

THE JOURNAL of the Acoustical Society of America

Vol. 103, No. 2

February 1998

16th International Congress on Acoustics/135th Meeting of the Acoustical Society of America
Meeting Program Summary **Seattle, Washington** **20–26 June 1998**
 (see pp. 653–656)

SOUNDINGS SECTION

ACOUSTICAL NEWS—USA	631
USA Meetings Calendar	631
ACOUSTICAL NEWS—INTERNATIONAL	637
International Meetings Calendar	637
REPORTS OF RELATED MEETINGS	639
REVIEWS OF ACOUSTICAL PATENTS	641
SELECTED RESEARCH ARTICLES [10]	
Ultrasonic spectroscopy of imperfect contact interfaces between a layer and two solids	Anton I. Lavrentyev, S. I. Rokhlin 657
Development of a new standard laboratory protocol for estimating the field attenuation of hearing protection devices. Part III. The validity of using subject-fit data	Elliott H. Berger, John R. Franks, Alberto Behar, John G. Casali, Christine Dixon-Ernst, Ronald W. Kieper, Carol J. Merry, Ben T. Mozo, Charles W. Nixon, Doug Ohlin, Julia Doswell Royster, Larry H. Royster 665

GENERAL LINEAR ACOUSTICS [20]

Acoustic scattering on an elastic plate described by the Timoshenko model: Contact conditions and uniqueness of the solution	I. V. Andronov, B. P. Belinskiy 673
The Rayleigh equations for a multi-sinusoidal periodic surface	Anthony Purcell 683
Propagation of Love waves in a transversely isotropic fluid-saturated porous layered half-space	Yue-Sheng Wang, Zi-Mao Zhang 695
A three-dimensional finite difference code for the modeling of sonic logging tools	Yong-Hua Chen, Weng Cho Chew, Qing-Huo Liu 702

(Continued)

CONTENTS—Continued from preceding page

A recursive Green's function technique for acoustic scattering from heterogeneous objects	Michael A. Jensen	713
Calculation of acoustical scattering from a cluster of scatterers	S. Koc, W. C. Chew	721
Target scattering calculations with the parabolic equation method	Mireille F. Levy, Andrew A. Zaporozhets	735
An iterative solver of the Helmholtz integral equation for high-frequency acoustic scattering	S. N. Makarov, M. Ochmann	742
A stochastic model for wave localization in one-dimensional disordered structures	Yang Yang, Douglas M. Photiadis	751
Torsional waves in lossy cylinders	J. M. Carcione, G. Seriani	760
On the velocities of localized vibration modes in immersed solid wedges	Victor V. Krylov	767
Temporal deconvolution of laser-generated longitudinal acoustic waves for optical characterization and precise longitudinal acoustic velocity evaluation	Franck Enguehard, Lionel Bertrand	771
UNDERWATER SOUND [30]		
High-frequency backscattering enhancements by thick finite cylindrical shells in water at oblique incidence: Experiments, interpretation, and calculations	Scot F. Morse, Philip L. Marston, Gregory Kaduchak	785
Double wave of Stoneley type on the interface of a stratified fluid layer and an elastic solid half-space	A. Alenitsyn	795
Estimating the compressional and shear wave speeds of a shallow water seabed from the vertical coherence of ambient noise in the water column	Nicholas M. Carbone, Grant B. Deane, Michael J. Buckingham	801
Mode functions for the wide-angle approximation to the parabolic equation	Amy R. Smith, Kevin B. Smith	814
Low-frequency acoustic scattering by gas-filled prolate spheroids in liquids. II. Comparison with the exact solution	Zhen Ye, Emile Hoskinson	822
A unified approach to volume and roughness scattering	Anatoliy N. Ivakin	827
ULTRASONICS, QUANTUM ACOUSTICS, AND PHYSICAL EFFECTS OF SOUND [35]		
Sound propagation in dilute suspensions of rigid particles	S. Temkin	838
Nonlinear inversion of the <i>SH</i> wave equation in a half-space for density and shear modulus determination	Wenhao Zhu, Xu Jun, Joseph L. Rose	850
Evolution of phonon noise and phonon state preparation in a model for generation of hypersonic phonons by laser	Jin-Hua Chai, Guang-Can Guo	858
STRUCTURAL ACOUSTICS AND VIBRATION [40]		
Experiments on acoustic streaming in a fluid layer between vibrating surfaces and amplitude-dependent damping of vibrations	Adnan Akay, Zhaoshun Xu	865
Utilization of coupling effects in compensator design for structural acoustic systems	H. T. Banks, M. A. Demetriou, R. C. Smith	872
Harmonic Green's functions of a semi-infinite plate with clamped or free edges	R. Gunda, S. M. Vijayakar, R. Singh, J. E. Farstad	888
Inherent background coefficients for acoustic resonance scattering from submerged, multilayered, cylindrical structures	Young-Sang Joo, Jeong-Guon Ih, Myoung-Seon Choi	900
An analytical model for bandlimited response of acoustic-structural coupled systems. I. Direct sound field excitation	K. S. Sum, J. Pan	911
Feedback vibration control of a flexible plate at audio frequencies by using a physical state-space approach	Kazuto Seto, Mingzhang Ren, Fumio Doi	924
NOISE: ITS EFFECTS AND CONTROL [50]		
Wave attenuation in catalytic converters: Reactive versus dissipative effects	A. Selamet, V. Easwaran, J. M. Novak, R. A. Kach	935
Effects of reflective ground on the actively created quiet zones	Jingnan Guo, Jie Pan	944

CONTENTS—Continued from preceding page

ACOUSTICAL MEASUREMENTS AND INSTRUMENTATION [58]

A numerical and experimental investigation of the performance of sound intensity probes at high frequencies	Finn Jacobsen, Vicente Cutanda, Peter M. Juhl	953
Energy fields of partially coherent sources	Jing-Fang Li, Jean-Claude Pascal, Claude Carles	962

PHYSIOLOGICAL ACOUSTICS [64]

A descriptive model of the receptor potential nonlinearities generated by the hair cell mechano-electrical transducer	Andrei N. Lukashkin, Ian J. Russell	973
Distortion product otoacoustic emissions in human newborns and adults. I. Frequency effects	Robert E. Lasky	981
Distortion product otoacoustic emissions in human newborns and adults. II. Level effects	Robert E. Lasky	992
Analysis of the micropipet experiment with the anisotropic outer hair cell wall	Alexander A. Spector, William E. Brownell, Aleksander S. Popel	1001
Estimation of elastic moduli and bending stiffness of the anisotropic outer hair cell wall	Alexander A. Spector, William E. Brownell, Aleksander S. Popel	1007

PSYCHOLOGICAL ACOUSTICS [66]

Masking by sinusoidally amplitude-modulated tonal maskers	Melanie J. Gregan, Sid P. Bacon, Jungmee Lee	1012
Cross-modality matching and the loudness growth function for click stimuli	Yula C. Serpanos, Honor O'Malley, Judith S. Gravel	1022
Temporal integration at 6 kHz as a function of masker bandwidth	Andrew J. Oxenham	1033
Factors governing speech reception benefits of adaptive linear filtering for listeners with sensorineural hearing loss	Christine M. Rankovic	1043
The effects of different envelope patterns and uncertainty for the detection of a tone added to SAM complex tonal maskers	Virginia M. Richards, Emily Buss, Lijun Tian	1058
Auditory suppression and frequency selectivity in older and younger adults	Mitchell S. Sommers, Sara E. Gehr	1067
Relative intensity comparisons between a tone and spectrally remote noise: Effects of onset asynchrony	Nicholas I. Hill, Peter J. Bailey	1075
Perceptual segregation of a harmonic from a vowel by interaural time difference in conjunction with mistuning and onset asynchrony	C. J. Darwin, R. W. Hukin	1080
Comparison of relative and absolute sound localization ability in humans	Gregg H. Recanzone, Samia D. D. R. Makhamra, Darren C. Guard	1085
Consonant–vowel intensity ratios for maximizing consonant recognition by hearing-impaired listeners	Elizabeth Kennedy, Harry Levitt, Arlene C. Neuman, Mark Weiss	1098

SPEECH PRODUCTION [70]

Using joint geometry to determine the motion of the cricoarytenoid joint	W. Scott Selbie, Lei Zhang, William S. Levine, Christy L. Ludlow	1115
---	--	------

SPEECH PERCEPTION [71]

Speech recognition of hearing-impaired listeners: Predictions from audibility and the limited role of high-frequency amplification	Teresa Y. C. Ching, Harvey Dillon, Denis Byrne	1128
The recognition of vowels produced by men, women, boys, and girls by cochlear implant patients using a six-channel CIS processor	Philipos C. Loizou, Michael F. Dorman, Verelle Powell	1141
Pitches of concurrent vowels	Peter F. Assmann, D. Dwayne Paschall	1150
Language, context, and speaker effects in the identification and discrimination of English /r/ and /l/ by Japanese and Korean listeners	John C. L. Ingram, See-Gyoon Park	1161

CONTENTS—Continued from preceding page

MUSIC AND MUSICAL INSTRUMENTS [75]

- Chaos in segments from Korean traditional singing and Western singing Myeong-Hwa Lee, Jeong-No Lee, Kwang-Sup Soh 1175

BIOACOUSTICS [80]

- The relationship of scattered subharmonic, 3.3-MHz fundamental and second harmonic signals to damage of monolayer cells by ultrasonically activated Alburnex® Douglas L. Miller, Shiping Bao 1183
- Control of vocal intensity in budgerigars (*Melopsittacus undulatus*): Differential reinforcement of vocal intensity and the Lombard effect Kazuchika Manabe, Ehsanee I. Sadr, Robert J. Dooling 1190
- Underwater audiogram of a tucuxi (*Sotalia fluviatilis guianensis*) Matthias Sauerland, Guido Dehnhardt 1199

LETTERS TO THE EDITOR

- A note on transient underwater bubble sound [20] Johan L. Leander 1205
- Acoustic scattering from two junctions in a rectangular waveguide [20] Jae Y. Kwon, Hyun H. Park, Hyo J. Eom 1209
- Comparison of speech intelligibility between English and Chinese [55] Jian Kang 1213
- Transient wave response of a cymbal using double-pulsed TV holography [75] Staffan Schedin, Per O. Gren, Thomas D. Rossing 1217

ERRATA

- Erratum: "The perceptual relevance of locus equations" [J. Acoust. Soc. Am. 102, 2997–3008 (1997)] David Fruchter, Harvey M. Sussman 1221

TECHNICAL NOTES AND RESEARCH BRIEFS

- Transverse vibrations of circular, annular plates with a free inner boundary Daniel Vega, Sergio A. Vera, Miguel D. Sánchez, Patricio A. A. Laura 1225

CUMULATIVE AUTHOR INDEX

1228

NOTES CONCERNING ARTICLE ABSTRACTS

1. The number following the abstract copyright notice is a Publisher Item Identifier (PII) code that provides a unique and concise identification of each individual published document. This PII number should be included in all document delivery requests for copies of the article.
2. PACS numbers are for subject classification and indexing. See June and December issues for detailed listing of acoustical classes and subclasses.
3. The initials in brackets following the PACS numbers are the initials of the JASA Associate Editor who accepted the paper for publication.

Document Delivery: Copies of articles can be ordered from the AIP/Member Society service "Articles in Physics;" E-mail: articles@aip.org; URL: <http://www.aip.org/articles.html>

SOUNDINGS

This front section of the *Journal* includes acoustical news, views, reviews, and general tutorial or selected research articles chosen for wide acoustical interest and written for broad acoustical readership.

ACOUSTICAL NEWS—USA

Elaine Moran

Acoustical Society of America, 500 Sunnyside Boulevard, Woodbury, New York 11797

Editor's Note: Deadline dates for news items and notices are 2 months prior to publication.

New Fellows of the Acoustical Society of America



Robert J. Bernhard—For contributions to computational acoustics and active noise control.



Klaus Scherer—For contributions to the understanding of emotions in speech.



Arnold Tubis—For contributions to cochlear mechanics and musical acoustics.

Adnan Akay named Lord Professor in mechanical engineering at Carnegie Mellon



Adnan Akay, professor and head, Mechanical Engineering Department, has been named recipient of the Thomas Lord Professorship at Carnegie Mellon University.

Akay has been with Carnegie Mellon since 1992. As head of the Department of Mechanical Engineering, he has been instrumental in substantially reshaping the course curriculum and refocusing the research efforts of the department to allow for new initiatives. His research, which has resulted in extensive publications in professional research journals, reviews, abstracts and monographs, covers funda-

mental issues related to generation and transmission of sound and vibration, as well as engineering aspects of noise and vibration control.

Akay is a Fellow of the Acoustical Society of America and has received the American Society of Mechanical Engineers' (ASME) Dedicated Service Award.

USA Meetings Calendar

Listed below is a summary of meetings related to acoustics to be held in the U.S. in the near future. The month/year notation refers to the issue in which a complete meeting announcement appeared.

	1998
9–13 Feb.	1998 Ocean Sciences Meeting, San Diego, CA [American Geophysical Union, 2000 Florida Ave., N.W., Washington, DC 20009, Tel.: 202-462-6900; Fax: 202-328-0566; WWW: http://www.agu.org].
19–21 Feb.	23rd Annual National Hearing Conservation Association Conference, Albuquerque, NM [NHCA, 611 E. Wells St., Milwaukee, WI 53202; Tel.: 414-276-6045; Fax: 414-276-3349; E-mail: nhca@globaldialog.com].
5–8 April	NOISE-CON 98, Ypsilanti, MI [Noise Control Foundation, P.O. Box 2469, Arlington Branch, Poughkeepsie, NY 12603; Tel.: 914-462-4006; Fax: 914-463-0201; E-mail: noisecon98@aol.com ; WWW: users.aol.com/noisecon98/nc98_cfp.html].
4–7 June	7th Symposium on Cochlear Implants in Children, Iowa City, IA [Center for Conferences and Institutes, The University of Iowa, 249 Iowa Memorial Union, Iowa City, IA 52242-1317; Tel.: 800-551-9029; Fax: 319-335-3533]. Deadline for receipt of abstracts: 1 March
20–26 June	16th International Congress on Acoustics/135th meeting of the Acoustical Society of America, Seattle, WA [ASA, 500 Sunnyside Blvd., Woodbury, NY 11797, Tel.: 516-576-2360; Fax: 516-576-2377; E-mail: asa@aip.org , WWW: http://asa.aip.org].
26 Jun.–1 Jul.	International Symposium on Musical Acoustics, ISMA 98, Leavenworth, WA [Maurits Hudig, Catgut Acoustical Society, 112 Essex Ave., Montclair, NJ 07042, Fax: 201-744-9197; E-mail: catgutas@msn.com , WWW: www.boystown.org/isma98].
7–12 July	Vienna and the Clarinet, Ohio State Univ., Columbus, OH [Keith Koons, Music Dept., Univ. of Central

Florida, P.O. Box 161354, Orlando, FL 32816-1354, Tel.: 407-823-5116; E-mail: kkons@pegasus.cc.ucf.edu].

9–14 Aug.

International Acoustic Emission Conference, Hawaii [Karyn S. Downs, Lockheed Martin Astronautics, PO Box 179, M. S. DC3005, Denver, CO 80201; Tel.: 303-977-1769; Fax: 303-971-7698; E-mail: karyn.s.downs@lmco.com].

13–17 Sept.

American Academy of Otolaryngology—Head and Neck Surgery, San Francisco, CA [American Academy of Otolaryngology—Head and Neck Surgery, One Prince St., Alexandria, VA 22314 Tel.: 703-836-4444; Fax: 703-683-5100].

12–16 Oct.

136th meeting of the Acoustical Society of America, Norfolk, VA [ASA, 500 Sunnyside Blvd., Woodbury,

NY 11797, Tel.: 516-576-2360; Fax: 516-576-2377; E-mail: asa@aip.org, WWW: <http://asa.aip.org>].

1999

15–19 March

Joint meeting: 137th meeting of the Acoustical Society of America/Forum Acusticum 1999 [Acoustical Society of America, 500 Sunnyside Blvd., Woodbury, NY 11797, Tel.: 516-576-2360; Fax: 516-576-2377; E-mail: asa@aip.org; WWW: asa.aip.org].

27–30 June

ASME Mechanics and Materials Conference, Blacksburg, VA [Mrs. Norma Guynn, Dept. of Engineering Science and Mechanics, Virginia Tech, Blacksburg, VA 24061-0219; Fax: 540-231-4574; E-mail: nguynn@vt.edu; WWW: <http://www.esm.vt.edu/mmconf/>]. Deadline for receipt of abstracts: 15 January 1999.

ACOUSTICAL NEWS—INTERNATIONAL

Walter G. Mayer

Physics Department, Georgetown University, Washington, DC 20057

Brazil to host the first Iberoamerican Congress of Acoustics—April 1998

It was October 1995 when the Iberoamerican Federation of Acoustics (FIA) was officially established, in Valdivia in Chile, as a nonprofit scientific federation. The bylaws of FIA were approved in 1996 in Buenos Aires by member societies which today include the Asociación del Acústica Argentina (AdAA), the Sociedade Brasileira de Acústica (SOBRAC), the Sociedad Chilena de Acústica (SCHA), the Sociedad Española de Acústica (SEA), the Sociedad Peruana de Acústica, and the Sociedade Portuguesa de Acústica.

This Congress will be organized by SOBRAC. It will be held 5–8 April 1998 in Florianópolis-SC-Brasil. The 18th meeting of SOBRAC will be part of the Iberoamerican Congress, as will be the 1st Symposium of Metrology and Normalization in Acoustics and Vibrations. The official languages will be Portuguese, Spanish, and English. All events are scheduled to take place in a seashore hotel where apartments and chalets have been reserved for participants and their families.

The program includes contributed papers and invited lectures by speakers from South and North America, various European countries, and Australia. In addition to the lecture program there will be four mini courses (4 hours each) and four roundtable discussions. An exhibition of technological instrumentation and materials will be open during the Congress.

Further information can be obtained from SOBRAC, Universidade Federal de Santa Catarina, Departamento de Engenharia Mecânica, Laboratório de Vibrações e Acústica, Cx.P. 476-Florianópolis-SC-Brasil. Fax: +55 48 331 9677; e-mail: sobrac@gva.ufsc.br; Web: www.sobrac.ufsc.br

Papers published in JASJ(E)

A listing of Invited Papers and Regular Papers appearing in the latest issue of the English language version of the *Journal of the Acoustical Society of Japan*, JASJ(E), was published for the first time in the January 1995 issue of the *Journal*. This listing is continued below.

The November issue of JASJ(E), Vol. 18, No. 6 (1997) contains the following papers:

- Saleem Asghar and Tasawar Hayat "Acoustic diffraction near a penetrable strip"
T. Arai, K. Okazaki, S. Imatomi, and Y. Yoshida "Acoustical and perceptual cues of the palatalized articulation of /s/'"
H. Suda, M. Ukigai, and Y. Miida "Sound reflection from a fine board array of finite length in oblique incidence"
T. Sakuma and M. Yasuoka "Numerical vibro-acoustic analysis of sound fields coupled with a baffled membrane"
S. Iwamiya and Mingzhi Zhan "A comparison between Japanese and Chinese adjectives which express auditory impressions"
T. Hasegawa, C. Matsuoka, N. Inoue, and T. Tizuka "A new theory of Rayleigh radiation pressure"

International Meetings Calendar

Below are announcements of meetings to be held abroad. Entries preceded by an * are new or updated listings with contact addresses given in parentheses. Month/year listings following other entries refer to issues of the *Journal* which contain full calendar listings or meeting announcements.

February 1998

2–6 **Ultrasonic Technological Processes—98**, Moscow. 6/97

March 1998

4–5 **4th Annual Conference of the Society of Acoustics of Singapore**, Singapore. 10/97
11–12 ***1st Annual Conference of the German Audiological**

Society, Oldenburg, Germany. (B. Kollmeier, Medizinische Physik, Universität Oldenburg, 26111 Oldenburg, Germany; Fax: +49 441 798 3698; e-mail: biko@medi.physik.uni-oldenburg.de)

13–15 ***Nordic Noise (Medical and biological effects)**, Stockholm, Sweden. (Ms. G. Scholander, Otorhinolaryngology Department, Karolinska Hospital, 171 76 Stockholm, Sweden; Fax: +46 8 5177 6267; e-mail: gschol@ent.ks.se)

17–19 ***Spring Meeting Acoustical Society of Japan**, Tokyo, Japan. (Acoustical Society of Japan, Ikeda-Building, 2-7-7, Yoyogi, Shibuya-ku, Tokyo 151 Japan; Fax: +81 3 3379 1456)

23–27 **DAGA 98 (German Acoustical Society Meeting)**, Zürich. 8/96

31–2 **Acoustics 98**, Cranfield University, UK. 10/97

April 1998

5–8 ***1st Iberoamerican Congress of Acoustics**, Florianópolis-SC-Brazil (for contact address see notice above)

27–30 **Waves in Two-phase Flows (EUROMECH Colloquium)**, Istanbul. 12/97

May 1998

10–14 **6th Meeting of the European Society of Sonochemistry**, Rostock-Warnemünde. 10/97

18–22 **7th Spring School on Acoustooptics and Applications**, Gdańsk. 8/97

25–27 **Noise and Planning 98**, Naples. 2/97

June 1998

8–10 **EAA/EEAA Symposium "Transport Noise and Vibration"**, Tallinn. 10/96

9–12 **8th International Conference on Hand-Arm Vibration**, Umea. 6/97

20–28 **Joint Meeting of the 16th International Congress on Acoustics and 135th Meeting of the Acoustical Society of America**, Seattle. 6/97

July 1998

1–12 **NATO ASI "Computational Hearing"**, Il Ciocco (Tuscany). 12/97

September 1998

7–9 **Nordic Acoustical Meeting 98**, Stockholm. 10/97

14–16 **Biot Conference on Poromechanics**, Louvain-la-Neuve. 10/97

14–16 **ACUSTICA 98**, Lisbon. 10/97

14–18 **35th International Conference on Ultrasonics and Acoustic Emission**, Chateau de Trešt'. 10/97

November 1998

16–18 **Inter-Noise 98**, Christchurch. 4/96

20 **Recreational Noise**, Queenstown. 10/97

23–27 **ICBEN 98: Biological Effects of Noise**, Sydney. 12/96

30–4 **5th International Conference on Spoken Language Processing**, Sydney. 6/97

March 1999

15–19 **Joint Meeting of DAGA, EAA Forum Acusticum, and 137th Meeting of the Acoustical Society of America**, Berlin. 6/97

June 1999
28–30

1st International Congress of the East European Acoustical Association, St. Petersburg. *10/97*

July 1999
4–9

10th British Academic Conference in Otolaryngology, London. *10/97*

5–8

***6th International Congress on Sound and Vibrations**, Copenhagen, Denmark. (F. Jacobsen, Department

of Acoustic Technology, Building 352, Technical University of Denmark, 2800 Lyngby, Denmark; Fax: +45 45 88 05 77; e-mail: fjac@dat.dtu.dk; Web: www.dat.dtu.dk)

September 1999
1–4

15th International Symposium on Nonlinear Acoustics (ISNA-15), Göttingen. *10/97*

REPORTS OF RELATED MEETINGS

PSQ '97 on Cape Cod

PSQ '97, a meeting on Product Sound Quality, was held on Cape Cod, Massachusetts in September. This two-day workshop, which had 18 presentations by 30 participants, was sponsored by the Acoustical Society of America and the Institute of Noise Control Engineering. The participants were from the appliance, aircraft, automotive, and telecommunications industries, and from consultation and academia.

The goal of the workshop was to allow sound quality (SQ) practitioners to exchange experiences and viewpoints about the rapidly developing activities concerned with how products sound, and not merely with their loudness or annoyance (although those attributes are clearly important). A great deal of discussion centered on the ability of physical measurements in general, and the value of certain algorithms or "metrics" in particular, to correlate with the subjective response to product sounds.

A few of the participants had considerable experience with the food, flavor, and aroma industries where the aesthetic values of odor, taste, and texture are typically of concern. The correlation between subjective responses for these senses and physical measurements is highly problematic, and the use of jury studies and experimental design has long been exploited. In some cases, sound quality studies have also benefited by adapting the techniques pioneered in these industries. However, the link between target designs resulting from such studies and "recipes" or modifications is much less straightforward for product sound. This indicates an area where more work is needed. In fact, the pursuit of the ability to "listen to a design" before it is built is currently being emphasized in the automotive industry.

The value of physical metrics for SQ is clear: it is much more convenient and less costly to process a signal and predict SQ directly than it is to conduct jury studies. However, the predictive capacity of current metrics is being questioned. In that event, is there a way to map directly from subjective reaction to product design? Two different approaches—one used in the automotive industry, and another used for appliance studies were described at PSQ '97. The former uses a genetic algorithm to lead in the search over the physical parameter space to optimize for SQ. The latter uses jury testing and analysis of variance and a "response surface method" to search for preferred designs. But the metrics have not been discarded. Several presenters gave examples of their successful use in specific cases.

Was the workshop successful (or even useful)? Participants expressed unsolicited enthusiasm for the experience. The combination of beautiful early fall weather on Cape Cod, a casual atmosphere, productive interactions, and camaraderie made for a fruitful and enjoyable workshop. The opportunity to disclose various methods and approaches, to hear how others have made the tests and calculations, and to reflect on the strengths and shortcomings of various programs was educational, with a lot of learning involved. Will there be another PSQ 'XX'? In '98, a special seminar on sound quality will be sponsored by INCE in conjunction with Noise Con 98. Perhaps there will be a PSQ '99.

This reporter thanks the ASA and INCE for their assistance with PSQ '97, and is grateful to his fellow organizing committee members, Bob Bernhard, Bennett Brooks, and Imdad Imam. A special thanks to George Maling of INCE for his assistance.

RICHARD H. LYON

REVIEWS OF ACOUSTICAL PATENTS

Daniel W. Martin

7349 Clough Pike, Cincinnati, Ohio 45244

The purpose of these acoustical patent reviews is to provide enough information for a Journal reader to decide whether to seek more information from the patent itself. Any opinions expressed here are those of reviewers as individuals and are not legal opinions. Printed copies of United States Patents may be ordered at \$3.00 each from the Commissioner of Patents and Trademarks, Washington, DC 20231.

Reviewers for this issue:

GEORGE L. AUGSPURGER, Perception Incorporated, Box 39536, Los Angeles, California 90039

RONALD B. COLEMAN, BBN Acoustic Technologies, 70 Fawcett Street, Cambridge, Massachusetts 02138

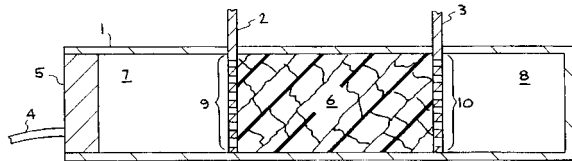
D. LLOYD RICE, 11222 Flatiron Drive, Lafayette, Colorado 80026

5,673,561

43.35.Ud THERMOACOUSTIC REFRIGERATOR

William C. Moss, assignor to the University of California
7 October 1997 (Class 62/6); filed 12 August 1996

In this thermoacoustic refrigerator transducer 5 is sealed at one end of housing 1 to generate a quarter-wavelength standing wave within the housing by reflection from closed end 8. The standing wave is created within helium or other noble gas, passing through porous thermal stack 6 disposed between perforated heat exchangers 2 and 3. The compression and decompression of the gas moving within thermal stack 6 creates a temperature gradient between the ends of the stack at the heat exchangers, with a higher



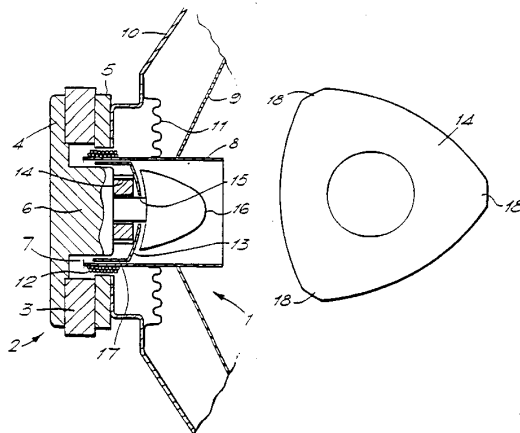
temperature at exchanger 3 and a lower temperature at exchanger 2 for refrigeration purposes. The porous stack material may be reticulated vitreous carbon open-cell foam which is said to provide "a desirable ratio of thermoacoustic area to viscous area, which has a low resistance to flow, which minimizes acoustic streaming and which has a high specific heat and low thermal conductivity..."—DWM

5,602,930

43.38.Ja LOUDSPEAKER

Roger N. Walton, assignor to Harman-Motive Limited
11 February 1997 (Class 381/192); filed in the United Kingdom 17 July 1992

The skirt of conductive dome 13 is inductively coupled to voice-coil 12. High-frequency energy emanates from the horn formed between phasing



plug 16 and former 8. The dome is supported at several discrete points by insulating gasket 14. This method of attachment is said to reduce suspended mass and improve the performance of the tweeter.—GLA

5,639,996

43.38.Ja ASYMMETRICALLY RESONANCE TUNED SPEAKER BOX

Yu-Wah Tan, Fremont, CA
17 June 1997 (Class 181/199); filed 16 November 1995

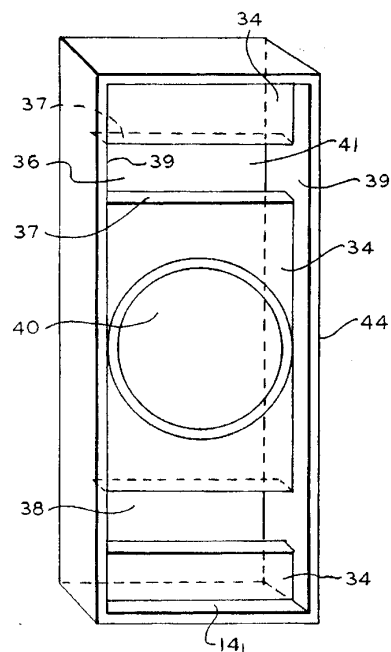
The panels that make up this loudspeaker box are built up to various thicknesses in a nonsymmetrical manner so as to sound "less boxy."—GLA

5,659,155

43.38.Ja ACOUSTICAL TRANSDUCER ENCLOSURE

Louis B. Porzilli, Sparta, NJ
19 August 1997 (Class 181/0.5); filed 19 July 1995

This is a simplified version of the inventor's earlier design in U.S. patent 5,327,985. A single loudspeaker can be located between two rectangular vents as shown, or a single vent can be located between two loudspeakers. In either case, the three-point projection geometry is supposed to



concentrate frequencies below 90 Hz into a tight directional pattern "...previously thought impossible." Assuming that the box is about 1.5 m high, most loudspeaker designers will *still* think it impossible.—GLA

5,613,010

43.38.Lc APPARATUS FOR REPRODUCING SOUND WITH A REDUCED DYNAMIC RANGE

Lawrence F. Heyl and Steven E. Austin, assignors to Apple Computer, Incorporated
18 March 1997 (Class 381/117); filed 30 March 1994

A Class D audio power amplifier is driven by two input signals. A modulation signal represents the audio program. The second input is a reference signal. A relatively simple mapping function unit modifies the dynamic range of the first signal more or less, or not at all, according to instructions from the user.—GLA

5,652,642

43.38.Ne COMBINATION DIGITAL AND ANALOG SOUNDTRACK SYSTEM AND METHOD

James A. Cashin, Tarzana, CA
29 July 1997 (Class 352/27); filed 13 March 1995

In this motion picture audio recording system, optical digital and analog audio-frequency signals both occupy the space traditionally reserved for the analog sound track. The trick is to record them in different colors and then add some digital processing to minimize interference between the two signals. Additional refinements suppress hiss and errors caused by dirt on the sound track.—GLA

5,646,990

43.38.Si EFFICIENT SPEAKERPHONE ANTI-HOWLING SYSTEM

Xu Li, assignor to Rockwell International Corporation
8 July 1997 (Class 379/390); filed 21 September 1995

Back-to-back, full duplex speakerphones have occasionally been used in audio teleconferencing for many years. For successful full duplex operation, each station had to be set up in advance and carefully tweaked to prevent howling and to minimize audible echo. Now that digitized computerized audio is commonplace, one might expect that all of the problems could be detected and corrected automatically in real time. The patent makes it clear that this is no trivial task. What is described as a "cost effective" system would probably have been impossible to implement only a dozen years ago. The patent document is short, easy to follow, and includes a lot of useful information.—GLA

5,594,800

43.38.Vk SOUND REPRODUCTION SYSTEM HAVING A MATRIX CONVERTER

Michael A. Gerzon, Oxford, United Kingdom
14 January 1997 (Class 381/120); filed in the United Kingdom 15 February 1991

This is a long patent with lots of mathematics and 35 pages of illustrations. A hierarchical system of multi-channel encoding and decoding is described which, among other benefits, allows for realistic stereophonic reproduction through a given number of loudspeakers, even if the original recording was intended for a different number of loudspeakers.—GLA

5,633,993

43.38.Vk METHOD AND APPARATUS FOR PROVIDING A VIRTUAL WORLD SOUND SYSTEM

William G. Redmann and Kerry M. Perkins, assignors to The Walt Disney Company
27 May 1997 (Class 395/119); filed 10 February 1993

The patent describes a well-designed method for delivering realistic 3-D sound in virtual reality systems, yet encoding the audio information in a reasonable number of channels. The apparatus employs a flexible resource scheduling method that accurately localizes only a few key sounds while less important sources are nonlocalized.—GLA

5,603,387

43.40.Tm ACTIVE VEHICLE SUSPENSION SYSTEM

Andrew M. Beard and Andreas H. von Flotow, assignors to Applied Power, Incorporated
18 February 1997 (Class 180/89.12); filed 6 September 1995

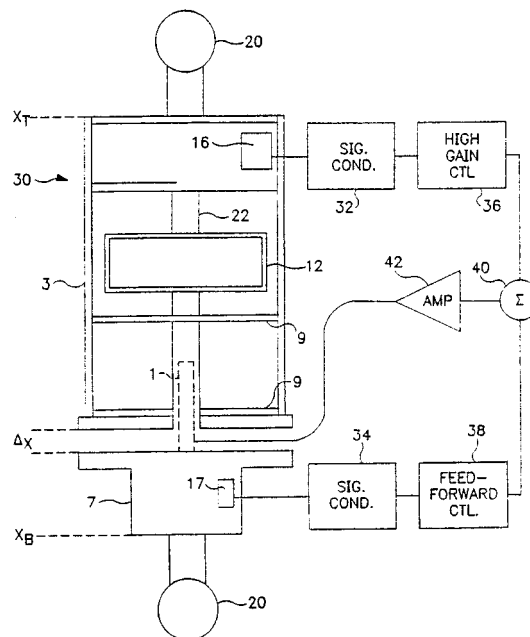
An active vehicle suspension system is described that is dynamically soft, yet is stiff to quasi-static excitations. The mount is discussed in relation to the isolation of chassis vibrations in tractors and trucks. Static stiffness is provided by an air bag controlled through a pneumatic valve. Dynamic control forces are applied using a hydraulic actuator to minimize chassis motion in the low-frequency range (from 1–10 Hz). Passive vibration isolation elements are included to provide additional attenuation at higher frequencies. The mount design and control system are stated to provide broadband vibration attenuation, starting at below 1 Hz and extending into the thousands of Hertz, not only for bounce, but for pitch and roll movement as well.—RBC

5,626,332

43.40.Tm VIBRATION ISOLATION SYSTEM USING PLURAL SIGNALS FOR CONTROL

Douglas J. Phillips *et al.*, assignors to Harris Corporation
6 May 1997 (Class 267/140.14); filed 29 July 1994

A device to provide active isolation of base motion X_B from exciting top motion X_T is described. The top body is connected to the base through a rod 22 containing a compliant damping element 12. Accelerometers on the upper and lower bodies (16 and 17) are used as feedback and feedforward sensors, respectively, to control a piezoceramic actuator 1 located in the load



path. Multiple devices are used to control six degrees of freedom at connections between the top and base structures. The design of the device is said to transmit forces primarily through the longitudinal axis. As such, the authors contend that cross coupling between mounts does not need to be addressed in the controller.—RBC

5,592,791

43.40.Vn ACTIVE CONTROLLER FOR THE ATTENUATION OF MECHANICAL VIBRATIONS

Camille M. D'Annunzio and Charles E. Chassaing, assignors to Radix Systems, Incorporated
14 January 1997 (Class 244/1N); filed 24 May 1995

A method is described for controlling building vibrations using an active control system. The approach uses an array of reference sensors to sense incoming earthquake vibration. Reaction-mass actuators are used to impart control forces to the upper floor and supports of the building structure. The residual vibration is sensed using arrays of sensors located on orthogonal sides of the building to monitor the first three vibrational modes. Controller complexity is reduced by sensing and controlling orthogonal responses independently. The control algorithm is the Block Underdetermined Covariance (BUC) algorithm developed by Slock, which is a modified block least squares method. The convergence properties of this algorithm are stated to be relatively insensitive to the condition number of the reference input correlation matrix, and therefore are well suited to this application.—RBC

5,595,372

43.40.Vn SEMI-ACTIVE VIBRATION MITIGATION ASSEMBLY

William N. Patten, assignor to University of Oklahoma
21 January 1997 (Class 267/64.13); filed 7 June 1995

An approach for suppressing structural vibrations of bridges and buildings using a semi-active vibration damping assembly is described. The assembly includes a double-rod hydraulic cylinder connected to a structure. The relative motion between the attachment points and the pressure differential in the fluid chambers of the hydraulic cylinder are measured to control the fluid flow between chambers. The assembly can be used to dissipate as well as store elastic energy. To take advantage of dissipative and energy storage capabilities (i.e., nondissipative) effects of the hydraulic fluid, the patent states that utilizing hydraulic fluid having entrained air is beneficial for enhancing stability of the semi-active control algorithms that are presented.—RBC

5,596,931

43.40.Vn DEVICE AND METHOD FOR DAMPING MECHANICAL VIBRATIONS OF A PRINTING PRESS

Georg Rössler and Bernhard Wagensommer, assignors to Heidelberger Druckmaschinen AG
28 January 1997 (Class 101/484); filed in Germany 16 October 1992

A device is described for damping asynchronous mechanical vibrations of a printing press to reduce ghosting and improve printing quality. Vibration sensors mounted to the press are processed to extract the asynchronous vibration responses. These responses are used to modulate the electrical signals input to the drive motors. These modulations produce control torques which oppose the asynchronous vibrations. The net effect is said to be the damping of the asynchronous vibrations. Several configurations are discussed including the use of multiple sensors and motors, as well as actuators operating directly on the drive train.—RBC

5,609,230

43.40.Vn VIBRATION CANCELLING DEVICE

Malcolm A. Swinbanks, assignor to MAS Research Limited
11 March 1997 (Class 188/267); filed in the United Kingdom 10 June 1993

This is an interesting patent about a magnetically levitated reaction-mass shaker. A hollow steel sphere is located in the spherical space interior of an outer shell secured to a structure to be controlled. Magnets on the inner sphere and outer shell are used to levitate and orient the steel sphere magnetically inside the shell. When the structure vibrates, proximity sensors detect changes in the proximity of the sphere. These sensor responses are used as feedback sensors to cause magnetic forces to be applied between the sphere and shell (i.e., structure), which oppose local vibration of the structure while restoring the sphere toward its rest position.—RBC

5,621,656

43.40.Vn ADAPTIVE RESONATOR VIBRATION CONTROL SYSTEM

Andrew J. Langley, assignor to Noise Cancellation Technologies, Incorporated
15 April 1997 (Class 364/508); PCT filed 15 April 1992

An active control system is described for modifying the apparent input impedance of tuned dynamic absorbers mounted on a structure so as to adjust the resonance frequency of the resonator. Sensors on the structure and dynamic mass of the absorber, together with a tonal reference signal, are inputs to a controller. The controller modifies the properties of the absorber (e.g., changes the apparent stiffness) so that its resonance frequency tracks the frequency of the tonal disturbance. The patent states that multiple adaptive resonators can be used to effectively damp vibrations from disturbances containing excitation at multiple tonal frequencies.—RBC

5,515,444

43.50.Ki ACTIVE CONTROL OF AIRCRAFT ENGINE INLET NOISE USING COMPACT SOUND SOURCES AND DISTRIBUTED ERROR SENSORS

Ricardo Burdisso et al., assignors to Virginia Tech Intellectual Properties
7 May 1996 (Class 381/71); filed 7 October 1994

An active control scheme to reduce noise radiated from the inlet of a turbofan engine is discussed. Experimental results using a multiple-input-multiple-output (MIMO) controller suggest that tonals associated with fan blade passage (BP) frequencies and high-pressure compressor BP fundamental can be significantly reduced using a filter-x least-mean-square (LMS) control algorithm. The test configuration uses tachometer reference sensors, acoustic horns, and loudspeakers to generate the control pressures, and a large area polyvinylidene fluoride (PVDF) microphone to measure the residual sound pressure. Sets of disturbance rods were installed in the engine to generate plane wave and spinning modes similar to those found in ultra-high bypass engines. A concept for a compact sound source capable of being flush mounted to the inside of the inlet duct is presented. In addition, an approach for locating distributed error sensors along the leading edge of the inlet is discussed.—RBC

5,577,127

43.50.Ki SYSTEM FOR RAPID CONVERGENCE OF AN ADAPTIVE FILTER IN THE GENERATION OF A TIME VARIANT SIGNAL FOR CANCELLATION OF A PRIMARY SIGNAL

Michiel W. R. M. Van Overbeek, assignor to Nederlandse Organisatie Voor Toegepast-Natuurwetenschappelijk Onderzoek Tno
19 November 1996 (Class 381/71); filed in Netherlands 19 November 1993

Rapidly changing signals tend to confuse active noise-reduction systems because adaptive digital filters converge at their own unhurried pace. "Means are provided for updating the filter coefficients with the aid of the so-called 'projection algorithm'...and for generating the reference signal in such a way that an input correlation matrix...has an eigenvalue distribution which has a value substantially equal to one after a few steps as possible."—GLA

5,584,447

43.50.Ki NOISE CONTROL USING A PLATE RADIATOR AND AN ACOUSTIC RESONATOR

Frederic G. Pla, assignor to General Electric Company
17 December 1996 (Class 244/1N); filed 19 December 1994

This patent describes a method for using active control to reduce discrete tonal noise produced by aircraft engines. The method uses the equivalent of Helmholtz resonators imbedded in the nacelle wall. In each cavity, piezoceramic actuators are mounted on bendable plates to create controlled volume velocities within each cavity. By tuning the plate and cavity resonances to coincide, the author states that loud canceling noise can be generated to control tonal noise sources in the engine. Methods are presented for tuning the resonance frequency of the Helmholtz cavities using quasi-static control of the cross-sectional area and length of the inlet duct (i.e., the acoustic mass).—RBC

5,588,800

43.50.Ki BLADE VORTEX INTERACTION NOISE REDUCTION TECHNIQUES FOR A ROTORCRAFT

Bruce D. Charles *et al.*, assignors to McDonnell Douglas Helicopter Company
31 December 1996 (Class 416/24); filed on 31 May 1994

An active control device is described for reducing blade-vortex interaction (BVI) noise generated by a rotorcraft, such as a helicopter. Trailing edge flaps located near the tip of each of the rotorcraft's rotor blades are controlled to follow a predetermined deflection schedule during each rotation of the blade. Through careful deflection and retraction of the flaps, the authors state that blade tip vortices, which are the primary source for BVI noise, are (a) made weaker and (b) pushed farther away from the rotor disk. Both of these effects will reduce BVI noise according to the authors. A tradeoff is noted for this approach between maximizing noise reduction and increasing drag (i.e., reducing efficiency of the rotor blade) when the flaps are deflected.—RBC

5,590,849

43.50.Ki ACTIVE NOISE CONTROL USING AN ARRAY OF PLATE RADIATORS AND AN ACOUSTIC RESONATOR

Frederic G. Pla, assignor to General Electric Company
7 January 1997 (Class 244/1N); filed on 19 December 1994

This patent represents a slight extension of the concept contained in patent 5,584,447 reviewed above. This patent differs from the prior patent in that a second layer of activated cavities, with different resonance frequen-

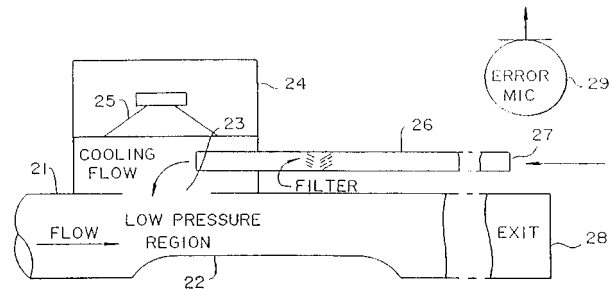
cies from the first, is included to extend the frequency range of control. As pointed out by the author, finding space for such extra sets of panels/resonators can be a problem in certain noise control applications such as in aircraft engines.—RBC

5,600,106

43.50.Ki ACTIVELY SOUND REDUCED MUFFLER HAVING A VENTURI EFFECT CONFIGURATION

Andrew J. Langley, assignor to Noise Cancellation Technologies, Incorporated
4 February 1997 (Class 181/206); filed 15 May 1996

This patent describes an active muffler system designed to minimize the acoustic mass between the loudspeaker and the error microphone, and to minimize the ingestion of hot exhaust gases into the loudspeaker enclosure. The acoustic mass is kept small by mounting the loudspeaker enclosure **24** directly to the muffler pipe **21**. A smooth Venturi **22** is used to generate



locally in the exhaust pipe a region that is below atmospheric pressure. A bleed pipe **26** in the front cavity of the loudspeaker enclosure permits air from outside to flow toward the low-pressure region, thereby reducing ingestion of exhaust gases into the loudspeaker enclosure, and also providing cooling. This patent is a division of U.S. Patent No. 5,550,334 (previously reviewed).—RBC

5,602,928

43.50.Ki MULTI-CHANNEL COMMUNICATION SYSTEM

Larry J. Eriksson and Cary D. Bremigan, assignors to Digisonix, Incorporated
11 February 1997 (Class 381/71); filed on 5 January 1995

A multi-channel communication system is discussed for reducing noise at passenger locations in a vehicle, while preserving the speech between passengers. Reference sensors that are well correlated with noise sources (e.g., engine noise, road noise, etc.) are used within the context of an adaptive recursive least-mean-square (RLMS) algorithm to minimize the contribution of these noise sources in the responses of microphones located in close proximity to each passenger. The residual microphone signals at the passenger locations are assumed to carry only the speech from the local passenger. These signals are used then as inputs to loudspeakers to enhance reception of speech from one passenger to another.—RBC

5,602,929

43.50.Ki FAST ADAPTING CONTROL SYSTEM AND METHOD

Steven R. Popovich, assignor to Digisonix, Incorporated
11 February 1997 (Class 381/71); filed on 30 January 1995

This patent describes an adaptive filter structure that provides for faster convergence than filtered-X or filtered-U least-mean-squares (LMS) algorithms for transfer functions between actuators and residual sensors having propagation delays. The system includes an additional digital filter to remove the effect of the control signal to the actuator in the electrical signal from the residual sensor. This modified residual signal, which represents an

estimate of the open-loop residual response, is used for adapting the coefficients of the control filter relating the reference signals to the output control signal. A similar approach is described for a feedback implementation. In both cases, the approach described is basically the well-known Youla transformation to recover the open-loop residual response, after which an assortment of LMS-based algorithms can be used to adapt control filter coefficients.—RBC

5,606,622

43.50.Ki ACTIVE NOISE CONTROL IN A DUCT WITH HIGHLY TURBULENT AIRFLOW

Terry N. Christenson, assignor to The Boeing Company
25 February 1997 (Class 381/71); filed 29 September 1994

This patent discusses an approach for using active control to attenuate sound wave propagation inside a duct with turbulent flow. The interaction of the turbulent flow with the reference and residual microphones typically results in low coherence between the microphone responses, and, consequently, limits achievable performance of an active system. The proposed method uses turbulent airflow control devices (i.e., perforated plates, wire screens, honeycomb material, or combination thereof) to smooth the turbulent air flow reaching the reference and residual microphones. In addition, aerodynamically designed microphones are also used to reduce the amount of noise created by the interaction of the airflow with the microphones. These aspects of the design improve the coherence between the microphones. The associated pressure drop is briefly discussed.—RBC

5,617,479

43.50.Ki GLOBAL QUIETING SYSTEM FOR STATIONARY INDUCTION APPARATUS

Stephen Hildebrand and Ziqiang Hu, assignors to Noise Cancellation Technologies, Incorporated
1 April 1997 (Class 381/71); filed 12 December 1995

An active control system to control sound radiation from power transformers and shunt reactors is described. The system uses piezoceramic actuators mounted directly to the transformer tank, as well as on separately supported plates, to control the local pressure field around the tank at 120 and 240 Hz. Actuator and sensor placements are determined based on spatial maps of the tank vibration and acoustic intensity. A multichannel filter-X least-mean-squares (LMS) algorithm is used to minimize microphone response by filtering a line-voltage reference signal through adaptive filters to drive the piezoceramic actuators. The authors state that significant reductions in sound pressure levels at a distance of 10 m were obtained with the active system in operation.—RBC

5,618,010

43.50.Ki ACTIVE NOISE CONTROL USING A TUNABLE PLATE RADIATOR

Frederic G. Pla and Harindra Rajiyah, assignors to General Electric Company
8 April 1997 (Class 244/1N); filed 19 December 1994

This patent represents a slight extension of the concepts contained in patents 5,584,447 and 5,590,849 reviewed above. The approach uses the equivalent of Helmholtz resonators imbedded in the nacelle wall of an aircraft engine. In each cavity, piezoceramic actuators are mounted on bendable plates to create controlled volume velocities within each cavity. By tuning the plate and cavity resonances to coincide, the authors state that loud cancelling noise can be generated to control tonal noise sources in the engine. This patent differs from the prior patents in that the resonance frequencies of the activated plates are tuned by controlling the static pressure on the back side of the plate, or by mechanically changing the volume of the backing cavity.—RBC

5,619,581

43.50.Ki ACTIVE NOISE AND VIBRATION CANCELLATION SYSTEM

Matthew K. Ferguson *et al.*, assignors to Lord Corporation
8 April 1997 (Class 381/71); filed 18 May 1994

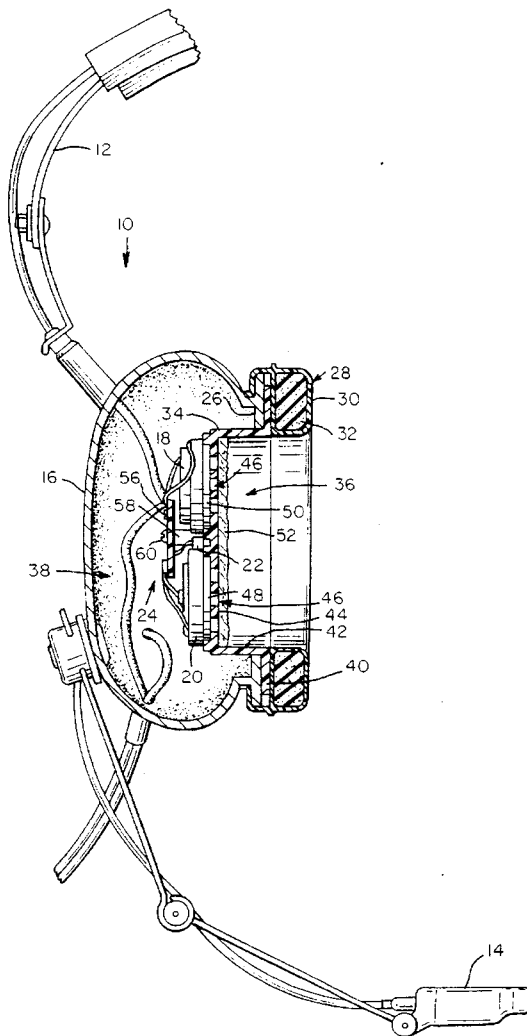
This patent relates to alternative hardware configurations for implementing adaptive feedforward controllers. In-line control filtering is performed using analog circuitry (i.e., waveform generators, phase-lock loops, switch-capacitor filters, etc.) or field-programmable gate arrays instead of digitally using digital signal processors (DSPs). The coefficient adaptation is performed using DSP's. By off-loading the in-line filtering from the DSPs, fewer DSPs are required, which according to this patent reduces cost, board area, power requirements, and component costs of the overall controller.—RBC

5,675,658

43.50.Ki ACTIVE NOISE REDUCTION HEADSET

Thomas Paige Brittain, Amarillo, TX
7 October 1997 (Class 381/72); filed 27 July 1995

An earphone 16 of this headset contains microphone 22 connected to a signal processing unit 24 that produces for reproduction by noise reduction transducer 20 a sound canceling the ambient noise in the earcup picked up



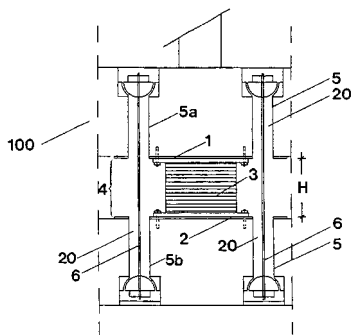
by the microphone. A second transducer 18 receives the communication signals desired for reproduction through cavity 36 to the wearer's ear.—DWM

5,669,189

43.55.Vj ANTISEISMIC CONNECTOR OF LIMITED VIBRATION FOR SEISMIC ISOLATION OF A STRUCTURE

Ioannis Logiadis *et al.*, Athens, Greece
23 September 1997 (Class 52/167.4); filed in Greece 24 December 1992

The antiseismic connector 10 between the superstructure of a building and its foundation is intended to allow a limited amount of relative motion laterally during an earthquake while restoring the relative position of structure and foundation at the completion of the vibration. The weight of the



structure is transmitted from iron plate 1 through sliding bearing 3, which is a stack of parallel plates, to steel plate 2 resting upon the foundation. Cables 6 within hollow casings 5 are under tension between cup-shaped terminations in the structure and in the foundation. The antiseismic connector "connects the superstructure to the foundation through prestressed tendons from special material which not only permit the relative movement of the foundation to the superstructure but also create horizontal recentering forces and receive tensile forces that may be encountered at the isolation system due to overturning moments of the superstructure, thus creating a safe seismic isolation of the structure."—DWM

5,631,678

43.58.Ls ACOUSTIC PRINTHEADS WITH OPTICAL ALIGNMENT

Babur B. Hadimioglu and Martin Lim, assignors to Xerox Corporation
20 May 1997 (Class 347/46); filed 5 December 1994

The acoustic printhead of this patent has an optically transparent substrate with at least two optical lenses that may be part of the substrate which also is part of an acoustic droplet ejector having an acoustic lens that is fabricated on the optically transparent substrate.—DWM

5,629,985

43.66.Qp APPARATUS AND METHODS FOR AUDITORY CONDITIONING

Billie M. Thompson, Phoenix, AZ
13 May 1997 (Class 381/68.4); filed 23 September 1994

The methods and apparatus of this patent are intended for the analysis of listening disorders, and for conditioning the listeners to changes that will enhance their listening capability. The apparatus contains a variety of signal sources including a microphone, recorded sounds, white and pink noise, computer generation; various high-pass and low-pass filters, with conventional bass and treble tone color circuits; and transducers for both air and bone conduction to each ear. The variety of speech, hearing, and neurological (e.g., dyslexia) disorders to which the system may be applicable is indicated by the listing of 34 different "objects of the invention." Examples of assessment and training procedures are included.—DWM

5,664,577

43.66.Yw METHOD AND APPARATUS FOR DISTORTION PRODUCT EMISSION TESTING OF HEARING

Brenda L. Lonsbury-Martin and Glen K. Martin, assignors to Baylor College of Medicine
9 September 1997 (Class 128/746); originally filed 25 January 1990

This is a method and apparatus for recording distortion product emissions (DPEs) of human ears, especially for recording DPE audiograms. Two pure tones f_1 and f_2 are simultaneously presented to the ear canal from separate transducers through tubes leading to a foam eartip placed in the ear canal. A miniature microphone in the eartip picks up otoacoustic emission tones (in addition to the input tones) which are supplied to a frequency spectrum analyzer. By controlling f_1 and f_2 in a constant ratio and selecting $2f_1 - f_2$ for isolation it is possible to create a DPE audiogram and a DPE input/output function as bases for an objective hearing test, both for normal and hearing impaired ears. Use of two microphones provides reduction of body noise. Much of the text of the patent is an Appendix describing the associated computer program.—DWM

5,662,477

43.70.Hs DEMONSTRATIVE PUPPET FOR PHONETIC TRAINING OF PERSONS HAVING SPEECH AND/OR HEARING DISORDERS

Janet A. Miles, Caza, CA
2 September 1997 (Class 434/185); filed 17 July 1995

This patent shows the design and use of a puppet for demonstrating the preferred positioning of the jaws, tongue, and incisor teeth for making a variety of audible phonetic sounds, especially in the training of people who have speech or hearing disorders. For training children the puppet head resembles that of a dog. The opening of the mouth and the position of the tongue relative to the lips and teeth are controlled by the hands of the puppet operator who is a qualified speech pathologist.—DWM

5,634,086

43.71.Hw METHOD AND APPARATUS FOR VOICE-INTERACTIVE LANGUAGE INSTRUCTION

Dimitry Rtischev *et al.*, assignors to SRI International
27 May 1997 (Class 395/2.79); filed 12 March 1993

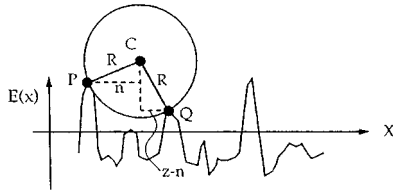
By constraining the syntax to the set of utterances included in a foreign language lesson, this hidden Markov model-based phonetic recognition system is able to tolerate a wide variety of word articulations and to provide feedback to the user on the accuracy of pronunciation. Three or more levels of error tolerance allow detection of mispronunciations while reading a script, wrong answers or pronunciations during a question/answer interaction and utterance endpoint detection in a conversational mode.—DLR

5,644,678

43.72.Ar METHOD OF ESTIMATING VOICE PITCH BY ROTATING TWO DIMENSIONAL TIME-ENERGY REGION ON SPEECH ACOUSTIC SIGNAL PLOT

Benedetto Giuseppe Di Ronza, assignor to Alcatel N. V.
1 July 1997 (Class 395/2.16); filed in Italy 3 February 1993

This pitch period detection system is based on a simple calculation of certain distances on a time plot of the speech waveform. The measures computed may be given a geometric interpretation corresponding to a circle



of fixed radius rolling along the tops of the waveform peaks. A pitch period is assigned based on which peaks are touched by the circle as it rolls along.—DLR

5,651,094

43.72.Ar ACOUSTIC CATEGORY MEAN VALUE CALCULATING APPARATUS AND ADAPTATION APPARATUS

Keizaburo Takagi and Hiroaki Hattori, assignors to NEC Corporation
22 July 1997 (Class 395/2.53); filed in Japan 7 June 1994

This patent covers a component of a speech recognition system concerned with classification of analysis vectors into phonetic clusters. A dynamic time warping calculation locates matches between input vectors and stored reference vectors. At that point, a weighted running average in each phonetic class is updated with the new input vector. The weight for each class is then also updated by the degree of fit found by the match.—DLR

5,647,006

43.72.Dv MOBILE RADIO TERMINAL COMPRISING A SPEECH

Rainer Martin, assignor to U.S. Philips Corporation
8 July 1997 (Class 381/66); filed in Germany 22 June 1994

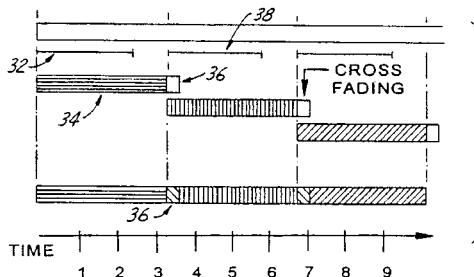
This speech processor, intended for vehicular applications, operates on the signals from two or more microphones and results in a speech output signal having a better signal-to-noise ratio than any of the input signals. It uses a type of beamforming in which the inputs are individually delayed based on their Hilbert transforms. A gradient smoothing arrangement provides a means of estimating the delays to fractions of a sample interval.—DLR

5,647,005

43.72.Ew PITCH AND RATE MODIFICATIONS OF AUDIO SIGNALS UTILIZING DIFFERENTIAL MEAN ABSOLUTE ERROR

Yen-Hui Wang and Der-Chwan Wu, assignors to Electronics Research & Service Organization
8 July 1997 (Class 381/62); filed 23 June 1995

This speech pitch or rate modification system divides the incoming speech signal into blocks, adjusts the sample rate to achieve the desired pitch, and then deletes or duplicates blocks as required for the desired



speech duration. A method of summing the sample differences across regions of block fade in/out is then used to determine how the blocks should be aligned in order to reconstruct the output speech signal.—DLR

5,644,679

43.72.Gy METHOD AND DEVICE FOR PREPROCESSING AN ACOUSTIC SIGNAL UPSTREAM OF A SPEECH CODER

Sophie Scott and William Navarro, assignors to Matra Communication
1 July 1997 (Class 395/2.33); filed in France 3 June 1994

Low bitrate speech coding techniques are typically optimized for best performance when the input signal is band limited to the "toll quality" telephone band. This system places a bandpass filter in front of such a coder when it is to be used with a microphone, or other input not limited to the telephone bandwidth, such as is often the case for speakerphones.—DLR

5,649,051

43.72.Gy CONSTANT DATA RATE SPEECH ENCODER FOR LIMITED BANDWIDTH PATH

Joseph Harvey Rothweiler *et al.*, Ellicott City, MD
15 July 1997 (Class 395/2.31); filed 1 June 1995

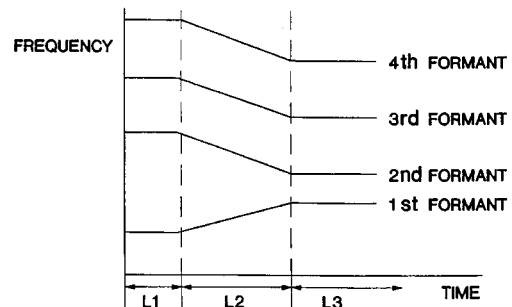
This speech coder could perhaps be called a Line Spectral Frequencies (LSF) vocoder. The transmitted spectral values are not the LSF coefficients themselves but, rather, one of four codes resulting from concurrent codebook searches spanning one, two, three, or four frames of the input signal. The pitch estimate includes a one-bit jitter flag, which governs a randomization of the fundamental frequency in the receiver. Before transmission, frames are compressed using a differential coding method.—DLR

5,649,058

43.72.Ja SPEECH SYNTHESIZING METHOD ACHIEVED BY THE SEGMENTATION OF THE LINEAR FORMANT TRANSITION REGION

Yoon-Keun Lee, assignor to Gold Star Company
15 July 1997 (Class 395/2.77); filed in Republic of Korea 31 March 1990

This speech synthesizer uses a formant coding technique to reduce the memory space required to store spectral vector sequences representing the speech phonetic units. The formant trajectory encoding method is geared



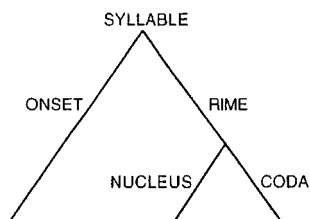
primarily toward the efficient representation of linear transitions of the formant frequencies.—DLR

5,651,095

43.72.Ja SPEECH SYNTHESIS USING WORD PARSER WITH KNOWLEDGE BASE HAVING DICTIONARY OF MORPHEMES WITH BINDING PROPERTIES AND COMBINING RULES TO IDENTIFY INPUT WORD CLASS

Richard Ogden, assignor to British Telecommunications
22 July 1997 (Class 395/2.69); filed in European Patent Office 4 October 1993

This speech synthesis component parses words from the text input and checks a word class dictionary for each input word. If found, the dictionary entry includes morpheme structure and phonological information pertaining



to morpheme bindings. A syllable parser provides additional phonological and stress structure information for synthesis parameter generation.—DLR

5,649,055

43.72.Kb VOICE ACTIVITY DETECTOR FOR SPEECH SIGNALS IN VARIABLE BACKGROUND NOISE

Prabhat K. Gupta *et al.*, assignors to Hughes Electronics
15 July 1997 (Class 395/2.42); filed 26 March 1993

This voice presence detector is presented in the context of a CELP vocoder, but is not specific to that application. It operates on time domain measures of the incoming signal, comparing these measures to adjustable thresholds for better amplitude independence. Measures include low-pass filtered versions of the PCM and mu-law waveforms and slope and zero-crossing counts of these low-pass signals.—DLR

5,640,485

43.72.Ne SPEECH RECOGNITION METHOD AND SYSTEM

Jukka Tapio Ranta, assignor to Nokia Mobile Phones Limited
17 June 1997 (Class 395/2.6); filed in Finland 5 June 1992

It is quite common for current speech recognition systems to select dynamically a syntax based on the current situation, or even to construct such a syntax based on current information pertaining to the interaction. The system described here goes a step farther, adjusting the probabilities of the occurrences of particular words when a recognition error has occurred.—DLR

5,640,488

43.72.Ne SYSTEM AND METHOD FOR CONSTRUCTING CLUSTERED DICTIONARY FOR SPEECH AND TEXT RECOGNITION

Jean-claude Junqua and Craig Demel, assignors to Panasonic Technologies, Incorporated
17 June 1997 (Class 395/2.54); filed 5 May 1995

The patent describes a way of organizing a speech processing dictionary into clusters of similar items for faster lookup accesses. The usual clustering methods involve exhaustive cross-comparisons of items. In this

approach, the word list is first grouped by a simple rule such as first letter or length. An iterative “reclustering” process then compares each item to the cluster centers of the previous iteration. The procedure description is fairly broad, such that the use of phonetic or linguistic clustering rules may be included.—DLR

5,640,490

43.72.Ne USER INDEPENDENT REAL-TIME SPEECH RECOGNITION SYSTEM AND METHOD

C. Hal Hansen *et al.*, assignors to Fonix Corporation
17 June 1997 (Class 395/263); filed 14 November 1994

This patent is a study in excesses; it includes over 300 literature references, 40 pages of electronic circuit diagrams, and over 300 pages of C source code. The speech recognizer described consists of a large number of fairly typical speech processing elements, filter bank, zero crossings, FFT, peak search pitch period analysis, and harmonic amplitude formant analysis, to name a few.—DLR

5,644,680

43.72.Ne UPDATING MARKOV MODELS BASED ON SPEECH INPUT AND ADDITIONAL INFORMATION FOR AUTOMATED TELEPHONE DIRECTORY ASSISTANCE

Gregory J. Bielby *et al.*, assignors to Northern Telecom Limited
1 July 1997 (Class 395/2.49); filed 25 May 1995

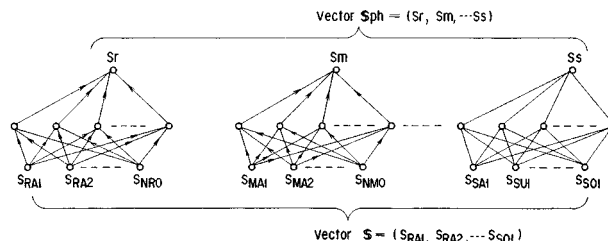
The patent discloses the use of a speech recognizer in a telephone directory search application. In use, the callers may speak a variety of items related to the desired number, such as city names, street names, and business names. Once correct recognition has been confirmed, the acoustic features for the spoken items are stored in association with the recovered phone number. This information may be used in future searches or in further training passes of the recognizer system.—DLR

5,649,056

43.72.Ne SPEECH RECOGNITION SYSTEM AND METHOD WHICH PERMITS A SPEAKER’S UTTERANCE TO BE RECOGNIZED USING A HIDDEN MARKOV MODEL WITH SUBSEQUENT CALCULATION REDUCTION

Tsuneo Nitta, assignor to Kabushiki Kaisha Toshiba
15 July 1997 (Class 395/2.65); filed in Japan 22 March 1991

The patent describes a hidden Markov model (HMM)-based speech recognizer with a novel matrix quantizer to determine the phonetic segment units. Matrices formed by adjacent frames of mel cepstral linear prediction vectors are used to search a codebook of such matrices. This is, of course,



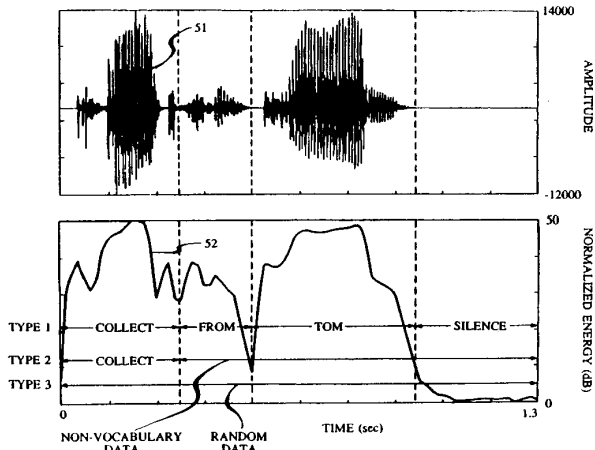
just a way of computing clusters of frames sequences, resulting in phonetic segment classes. Various applications use vector or matrix quantization or a neural network for the clustering process. All versions use HMM classifiers to convert phonetic sequences to words.—DLR

5,649,057

43.72.Ne SPEECH RECOGNITION EMPLOYING KEY WORD MODELING AND NON-KEY WORD MODELING

Chin-Hui Lee *et al.*, assignors to Lucent Technologies, Incorporated
 15 July 1997 (Class 395/2.65); originally filed 17 May 1989

This telephone-based continuous speech recognizer uses hidden Markov modeling of a relatively small key word vocabulary together with additional HMMs for silence, nonspeech events, and extraneous words not



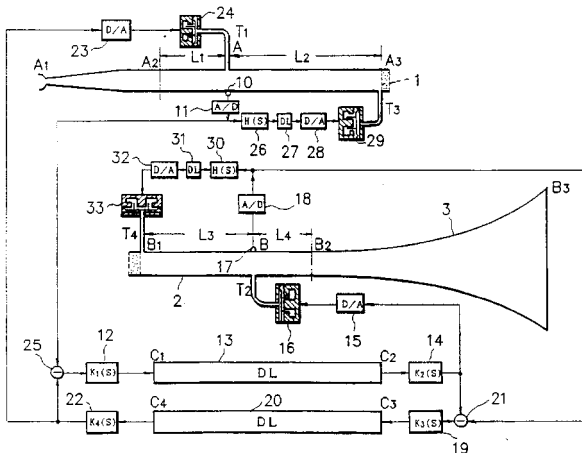
included in the key word set. Mel cepstral LP vectors and their time derivatives are used directly as the inputs for searching the HMM space. A grammar of the allowable sequences allows non-key word sequences to be interspersed freely among the key words in finding the best matching pathway through the HMMs.—DLR

5,668,340

43.75.Fg WIND INSTRUMENTS WITH ELECTRONIC TUBING LENGTH CONTROL

Hikaru Hashizume and Yutaka Washiyama, assignors to Kabushiki Kaisha Kawai Gakki
 16 September 1997 (Class 84/742); filed in Japan 22 November 1993

This electronic control system for wind instruments is intended to substitute for the standing wave system in instrument tubing on which conventional wind instruments operate. The example shown here is for brass wind instruments, but other examples are for reed instruments and flutes. In place of one continuous air column, this instrument uses a straight pipe segment of uniform diameter with a mouthpiece **A1** and a sound absorber **A3**, separated acoustically from a second flared segment with a sound absorber **B1** at one end and the instrument bell **B3** at the other. Microphone **10**



receives a pulse from the lips at **A1**, and the signal is converted to digital for delay line **13**, then converted back to analog to drive transducer **16**, which transmits the pulse into the flared tube. In turn the wave reflected from **B3** is picked up by microphone **17**, passed through delay line **20** to transducer **29** to create a return wave to the mouthpiece. Changes in delay time change the frequency of the musical tone. The sound absorbers at the ends of the tubes are intended to be totally nonreflective, as if connected to an infinite length of pipe. Since this is difficult to approximate practically, the patent proposes active means for achieving nonreflection using transducers **29** and **35**.—DWM

5,656,789

43.75.St ELECTRONIC MUSICAL INSTRUMENT HAVING A FUNCTION TO INDICATE KEYS TO BE OPERATED

Akira Nakada *et al.*, assignors to Yamaha Corporation
 12 August 1997 (Class 84/477 R); filed in Japan 15 April 1994

This electronic musical instrument provides indicators (e.g., illuminators) for its individual keyboard keys which assist in the training of keyboard players by showing which keys are to be played either simultaneously or in sequence, depending upon the stored musical information and the timing of its presentation. "Individual notes of a musical phrase may be sequentially indicated quickly in advance of the actual phrase performance."—DWM

5,559,298

43.75.Tv WAVEFORM READ-OUT SYSTEM FOR AN ELECTRONIC MUSICAL INSTRUMENT

Seiji Okamoto, assignor to Kabushiki Kaisha Kawai Gakki
 24 September 1996 (Class 84/607); filed in Japan 13 October 1993

"An electronic musical instrument produces musical tones based on waveform data, while providing smooth changes between different timbres and at the same time avoiding reduction in the efficiency of waveform compression. The timbre change is carried out in an interpolation interval, the magnitude of which varies in accordance with the magnitude of the timbre change. The data necessary to establish the interpolation interval may be stored and read out of a memory or may be determined by interpolation according to a linear function."—DWM

5,597,970

43.75.Tv WAVEFORM PROCESSING APPARATUS AND AN ELECTRONIC MUSICAL INSTRUMENT USING THE OUTPUT WAVEFORM THEREOF

Hiroshi Sato and Kaoru Matsunaga, assignors to Kabushiki Kaisha Kawai Gakki
 28 January 1997 (Class 84/604); filed in Japan 28 October 1993

In an electronic musical instrument of the waveform processing type the apparatus of this patent avoids sudden changes in tone spectrum by dividing the original sound signal into bands or ranges and effecting the necessary changes in each band gradually.—DWM

5,496,962

**43.75.Wx SYSTEM FOR REAL-TIME MUSIC
COMPOSITION AND SYNTHESIS**

**Sidney K. Meier, Hunt Valley, MD and Jeffrey L. Briggs,
Freeland, MD**

5 March 1996 (Class 84/601); filed 31 May 1994

This is a computerized system “for automatically generating musical compositions on demand one after another without duplication. The system can produce such compositions upon demand in a variety of genres and forms so that concerts based on generated compositions will have a varied mix of pieces incorporated therein. The system incorporates a ‘weighted exhaustive search’ process that is used to analyze the various aspects in developing the composition, from small-scale, note-to-note melodic construction to large-scale harmonic motions. The process maintains a balance between melodic, harmonic and contrapuntal elements in developing the composition. In general, the ‘weighted exhaustive search’ process involves generating a plurality of solutions for producing each element of the composition. Each one of the plurality of solutions is analyzed with a series of

‘questions.’ Each solution is then scored based upon how each question is ‘answered’ or how much that particular solution fits the parameters of the question.”—DWM

5,668,338

**43.75.Wx WAVETABLE AUDIO SYNTHESIZER
WITH LOW FREQUENCY OSCILLATORS
FOR TREMOLO AND VIBRATO EFFECTS**

**Larry D. Hewitt *et al.*, assignors to Advanced Micro Devices,
Incorporated**

16 September 1997 (Class 84/629); filed 2 November 1994

The tones generated by this wavetable audio synthesizer are intended for use in digital system boards and add-in cards for desktop and portable computers such as in a PC-based sound card. The application for this patent is related to 17 other patent applications filed simultaneously and identified by title in the introduction to the patent application. One of the features is the use of the wavetable data addressing rate for creating frequency vibrato (modulation) effects and/or amplitude vibrato. Delay-based effects are also possible, along with chorus and “flange” effects. Although the synthesizer can be very small, the patent document has 122 figures and 95 pages of text.—DWM

Ultrasonic spectroscopy of imperfect contact interfaces between a layer and two solids^{a)}

Anton I. Lavrentyev^{b)} and S. I. Rokhlin

The Ohio State University, Nondestructive Evaluation Program, 190 West 19th Avenue, Columbus, Ohio 43210

(Received 17 March 1997; accepted for publication 13 September 1997)

Ultrasonic waves reflected from the front and back surfaces of a thin layer are often not separated in the time domain, and interfere. The spectrum of the resulting interference signal depends on (a) the thickness of the layer and the elastic moduli and density of the layer and the surrounding material (substrates), and (b) properties of the layer/substrate interface which can be described in terms of the interfacial stiffness. In this paper the effect of interfacial stiffness is isolated by considering the ultrasonic wave interaction with a solid layer compressed between two substrates of the same material. Since the layer and the substrate have identical properties the effect of impedance difference on the layer reflection vanishes. An aluminum system is selected for the experiment; the contacting surfaces are roughened and varying pressure is applied to model imperfect interface changes. It is shown both theoretically and experimentally that the contact pressure increase results in increase of the interfacial stiffness and spectral minima shift to higher frequency. A simple analytical expression relating the reflection minimum position to the interfacial stiffness is derived and shows good agreement with experimental results. It is shown that in the high-interfacial-stiffness limit the resonance minima positions are given by the condition $h = \lambda/4 + n\lambda/2$, $n = 0, 1, 2, \dots$. In the limit of low interfacial stiffness the first minimum shifts to zero and higher order resonances are given by $h = n\lambda/2$. Since the resonance minima measurements can be done with high precision it is proposed to use the frequency minimum shift for determination of interfacial stiffness and, consequently, the quality of the interfacial contact. © 1998 Acoustical Society of America. [S0001-4966(98)06201-8]

PACS numbers: 43.10.Ln, 43.20.Fn, 43.35.Sx, 43.35.Zc [ANN]

INTRODUCTION

It is well known that the strength of many engineering structures depends critically on the bonding between structural components. Examples include, but are not limited to, solid state bonds formed by inertial or friction welding or brazing and adhesive/adherend bonds in adhesive joints. Imperfections along the bondline such as cracks, porosity, inclusions, etc. can significantly degrade the performance of the joint. Very often the imperfections are confined to a very thin layer in the form of an interphase separating the joining materials which is difficult to characterize. The ultrasonic method is one of the most promising for nondestructive evaluation of interphases. When the interphasial layer is thin and the imperfections are flat the interphasial layer can be modeled as an infinitely thin interface connected by distributed springs to account for interfacial stiffness reduction due to imperfections.¹ The mechanical behavior of such an interface can be modeled using spring boundary conditions. Significant effort has been put into experimental and theoretical studies of ultrasonic wave interaction with imperfect interfaces.¹⁻¹⁷ The goal of these studies was to characterize interface imperfections using the ultrasonic signature. The coefficient of reflection from an interface with spring bound-

ary conditions depends on frequency. By measuring this frequency response one can determine the interfacial spring stiffness.

Characterization of imperfect interfaces between a layer and two substrates is important, for example, for adhesive joint evaluation. It has been shown that in humid environments the adhesive bond deteriorates predominantly along the adhesive/adherend interface.^{18,19} Also interfacial layers are often used in solid state bonding to improve material bonding compatibility. The distinctive feature in characterizing two interfaces simultaneously is that in most practical systems the ultrasonic signals reflected (normally or obliquely) from the front and back sides of the adhesive layer are not separated in the time domain and interfere. In this paper we apply ultrasonic spectroscopy to characterize two imperfect interfaces separated by a layer of thickness h . To exclude the effect of the impedance mismatch between the layer and substrates a homogeneous model system consisting of an aluminum layer between two aluminum substrates is considered. The layer and substrate surfaces are roughened and varying pressure is applied across the system to simulate different degrees of interface imperfection. In this system the impedances of the plate and substrates are identical and thus the reflection from the layer is a function only of the plate/substrate interfacial contact which is defined by the applied pressure and the surface roughnesses. While the theory considered is identical for normal incidence of both longitudinal and shear waves, the experimental results are given for the

^{a)}“Selected research articles” are ones chosen occasionally by the Editor-in-Chief that are judged (a) to have a subject of wide acoustical interest, and (b) to be written for understanding by broad acoustical readership.

^{b)}Now with United Technologies Research Center, 411 Silver Lane, M/S 129-86, East Hartford, CT 06108.

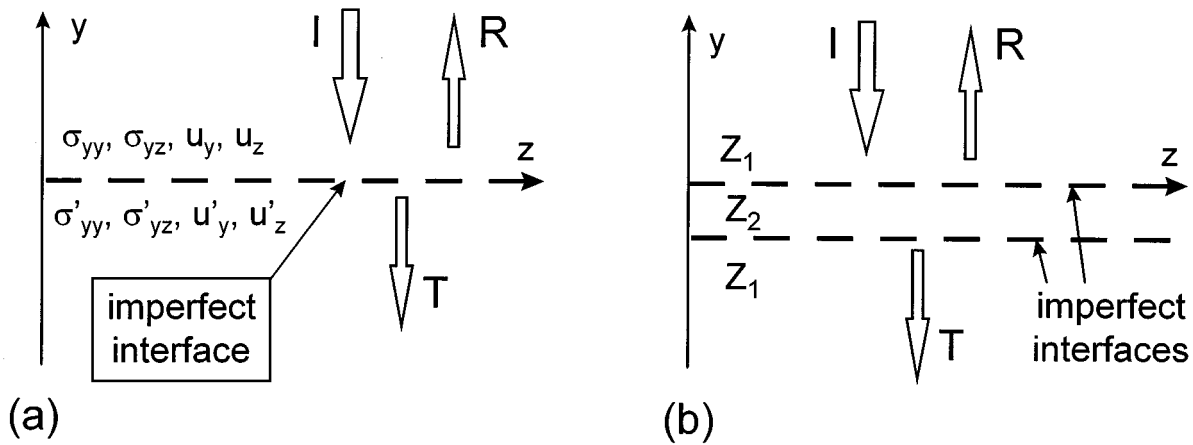


FIG. 1. Illustration of the problem: (a) imperfect interface between two solids; (b) layer imperfectly bonded to two solids.

incident longitudinal wave. Examples of shear wave incidence are given elsewhere.

I. THEORY

A. Single imperfect interface

Consider two bonded solids as shown in Fig. 1(a). If the bonding is imperfect and the size and spacing between the imperfections is much smaller than the wavelength then the ultrasonic wave interaction with this interface can be described using spring boundary conditions:^{7,8}

$$\begin{aligned} \sigma'_{yy} &= K_n(u_y - u'_y), & \sigma'_{yz} &= K_t(u_z - u'_z), \\ \sigma'_{yy} &= \sigma_{yy}, & \sigma'_{yz} &= \sigma_{yz}, \end{aligned} \quad (1)$$

where σ_{yy} , σ_{yz} , u_y , u_z are normal and shear stresses and displacements in the y and z directions at the interface; primed values correspond to the lower semispace ($z < 0$); K_n, K_t are distributed spring constants per unit area [(N/m)/m²]. At $K_n, K_t = 0$ the boundary conditions (2) become those for a free semispace; as $K_n, K_t \rightarrow \infty$ the conditions for welded contact are satisfied. (An alternative way to define the interfacial stiffness is given in Ref. 1.)

The ultrasonic wave normal incidence reflection and transmission coefficients from the imperfect interface modeled by springs are given by:⁵

$$\begin{aligned} R_{12} &= \frac{Z_2 - Z_1 + i(\omega/K_n)Z_1Z_2}{Z_2 + Z_1 - i(\omega/K_n)Z_1Z_2}, \\ T_{12} &= \frac{2Z_2}{Z_2 + Z_1 - i(\omega/K_n)Z_1Z_2}, \end{aligned} \quad (2)$$

where Z_1, Z_2 are the impedances of the contacting solids and ω is the angular frequency. An important feature of the reflection and transmission coefficients given by (2) is the existence of the frequency-dependent term. It appears physically due to the inertia of the response of the bottom substrate to the force applied from the top substrate. With frequency increase the substrates tend to decouple.

From equations (2) one can see that two factors determine the reflection coefficient at each given frequency: (a)

impedance difference between contacting materials and (b) interfacial stiffness. When the materials in contact are identical equation (2) reduces to

$$R_I = \frac{i(\omega/\Omega)}{1 - i(\omega/\Omega)}, \quad T_I = \frac{1}{1 - i(\omega/\Omega)}, \quad (3)$$

where Ω is the characteristic frequency¹¹

$$\Omega = \frac{2K_n}{Z_1}. \quad (4)$$

Subscript I in (3) corresponds to reflection (transmission) from an interface between identical materials.

B. Wave interaction with two imperfect interfaces separated by a layer

Let us consider an ultrasonic wave incident from the top semispace on a layer imperfectly bonded to two identical semispaces as shown in Figure 1b. The theory is identical for normal incidence of longitudinal and shear waves with selection of appropriate wave velocity V_l or V_t and interface stiffness K_n and K_t . The reflection from the layer R can be separated into two interfering signals:²⁰ (a) reflection from the top surface of the layer (first-reflection signal) with amplitude R_{12} and (b) reflection from the bottom which is the sum of all possible multiple reflections inside the layer R_Σ (multiple-reflection signal):

$$R_L = R_{12} + R_\Sigma, \quad (5)$$

where

$$R_\Sigma = \frac{T_{12}T_{21}e^{2ikh}}{1 - R_{12}^2e^{2ikh}}R_{21}, \quad (6)$$

where R_{ij} and T_{ij} are stress reflection and transmission coefficients at the interface between media i and media j defined by Eq. (2), h is the layer thickness. The reflection from the layer is controlled by two factors: impedance difference between the substrates and the layer, and the interfacial stiffness.

Let us consider the resonance effects of wave scattering from the layer. First, assume that $K_n \rightarrow \infty$ (perfect bonding) and $Z_1 \neq Z_2$. At $kh = \pi$ ($h = \lambda/2$) the multiple-reflection signal R_Σ reduces to

$$R_\Sigma = \frac{T_{12}T_{21}e^{2i\pi}}{1 - R_{12}^2 e^{2i\pi}} R_{21} = R_{21}. \quad (7)$$

(It is taken into account that at $K_n \rightarrow \infty$ the product $T_{12}T_{21} = 1 - R_{12}^2$.) Since for $Z_1 \neq Z_2$ the reflection coefficient $R_{21} = -R_{12}$ the multiple-reflection signal is equal in amplitude and opposite in phase to the first-reflection signal [first term (R_{12}) in (5)]. Thus they cancel each other and the reflectivity of the layer equals zero: $R=0$. At $kh = \pi/2$ ($h = \lambda/4$) we analogously obtain that

$$R_\Sigma = \frac{T_{12}T_{21}e^{i\pi}}{1 - R_{12}^2 e^{i\pi}} R_{21} = \frac{(1 - R_{12}^2)}{1 + R_{12}^2} R_{12}. \quad (8)$$

At $h = \lambda/4$ the first- and multiple-reflection signals are in phase and give maximum reflection

$$R^{\max} = R_{12} + R_\Sigma = \frac{2R_{12}}{1 + R_{12}^2}. \quad (9)$$

The conditions of maxima and minima in the case of a perfect interface and $Z_1 \neq Z_2$ can be summarized as follows:

$$(kh)_{\min}^{(R)} = n\pi, \quad n = 0, 1, 2, \dots, \quad (10)$$

$$(kh)_{\max}^{(R)} = \frac{\pi}{2} + n\pi, \quad n = 0, 1, 2, \dots \quad (11)$$

Let us consider the effect of the second factor—interfacial stiffness ($0 < K_n < \infty$)—on the reflection from the layer assuming that the impedances of the layer and substrates are equal: $Z_1 = Z_2$. Then the coefficients for the reflection (transmission) from the single interface are given by (3). The reflection and transmission coefficients from two spaced interfaces are

$$R = R_I + R_\Sigma = R_I + \frac{T_I^2 e^{2ikh}}{1 - R_I^2 e^{2ikh}} R_I, \quad (12)$$

$$T = \frac{T_I^2 e^{2ikh}}{1 - R_I^2 e^{2ikh}}. \quad (13)$$

Two principal differences from the previous case (perfect bond, different materials) must be noted:

- The signs of the reflection coefficient from the front and back interfaces are the same: $R_{12} = R_{21} = R_I$.
- The frequency dependence of the reflection coefficient is defined not only by the distance between interfaces but also by the frequency dependence of T_I and R_I . This results in more complicated conditions for spectral minima and maxima.

At $kh = \pi$ the multiple-reflection signal amplitude

$$R_\Sigma = \frac{1}{1 - 2i(\omega/\Omega)} R_I. \quad (14)$$

In the limit $K_n \rightarrow \infty$ ($\Omega \rightarrow \infty$) the multiple-reflection amplitude $R_\Sigma \rightarrow R_I$; thus, the first- and multiple-reflection signals are in phase and condition (10) corresponds to the maximum.

Analogously, at $kh = \pi/2$:

$$R_\Sigma = \frac{-1}{1 - 2i(\omega/\Omega) - 2(\omega^2/\Omega^2)} R_I. \quad (15)$$

In the limit $K_n \rightarrow \infty$ coefficient $R_\Sigma \rightarrow -R_I$; thus, the first- and multiple-reflection signals are in opposite phase and condition (11) corresponds to the minimum. One must note that in the limit $K_n \rightarrow \infty$ the reflection spectrum degenerates as $R \rightarrow 0$.

To find the condition for minimum reflection when $0 < K_n < \infty$ let us represent the complex reflection and transmission coefficient given by Eq. (3) in exponential form:

$$T_I = \frac{1}{\sqrt{1 + (\omega/\Omega)^2}} e^{i\varphi_T}, \quad \varphi_T = \arctan \frac{\omega}{\Omega}, \quad (16)$$

$$R_I = \frac{\omega/\Omega}{\sqrt{1 + (\omega/\Omega)^2}} e^{i\varphi_R}, \quad \varphi_R = \arctan \left(-\frac{\Omega}{\omega} \right) = \varphi_T + \frac{\pi}{2}. \quad (17)$$

Note that the reflection and transmission coefficients have a phase difference of $\pi/2$. Substituting (16) and (17) in (12) and (13) we obtain for the layer reflection and transmission coefficients:

$$R = \frac{[1 + (\omega/\Omega)^2](1 + e^{2i(\varphi_T + kh)})}{1 + (\omega/\Omega)^2 + (\omega/\Omega)^2 e^{2i(\varphi_T + kh)}} R_I, \quad (18)$$

$$T = \frac{e^{i(2\varphi_T + kh)}}{1 + (\omega/\Omega)^2 + (\omega/\Omega)^2 e^{2i(\varphi_T + kh)}}. \quad (19)$$

The reflection coefficient is zero when:

$$(kh)_{\min}^{(R)} = \frac{\pi}{2} - \varphi_T + n\pi, \quad n = 0, 1, 2, \dots, \quad (20)$$

or, in terms of frequency:

$$f_{\min}^{(R)} = \frac{V}{h} \left(\frac{1 + 2n}{4} - \frac{\varphi_T}{2\pi} \right), \quad n = 0, 1, 2, \dots, \quad (21)$$

where V is the velocity for longitudinal V_l or shear V_t wave. Note that Eq. (21) is transcendental since φ_T on the right hand side depends on frequency. The frequency of minimum reflection can be found by numerical solution of Eq. (21). The maximum reflection (minimum transmission) is observed near

$$(kh)_{\max}^{(R)} = n\pi - \varphi_T, \quad n = 0, 1, 2, \dots, \quad (22)$$

$$f_{\max}^{(R)} = \frac{V}{h} \left(\frac{n}{2} - \frac{\varphi_T}{2\pi} \right), \quad n = 0, 1, 2, \dots \quad (23)$$

The conditions (22), (23) are not exact due to the presence of the frequency-dependent phase term in the coefficients R_I [(17), (18)].

Figure 2 shows the dependence of the frequency for reflection minima on interfacial stiffness calculated from Eq. (21) using Newton's method (the calculation converged in only 2 or 3 iterations). One can see that as $K_n \rightarrow \infty$ (perfect bonding) the minima are at $kh = \pi/2, 3\pi/2, \dots$ (or $h = \lambda/4, 3\lambda/4, \dots$). The physical meaning of the $h = \lambda/4$ resonance is obvious: The waves reflected from the second inter-

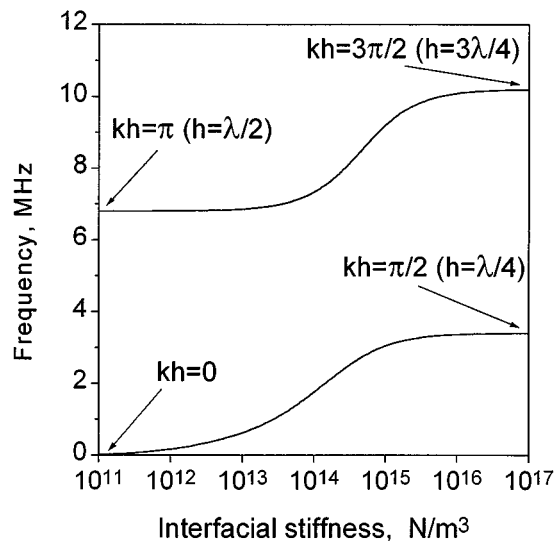


FIG. 2. Reflection spectrum minima positions for aluminum plate between aluminum substrates as a function of interfacial stiffness. Calculations are done for aluminum plate thickness $h_{Al}=0.47$ mm.

face travel an additional distance $2h=\lambda/2$ and arrive at the top interface in antiphase with the first-reflection signal, thus nullifying the reflection from the layer. The interfacial stiffness decrease results in minima shift to lower frequency. In the limit $K_n \rightarrow 0$ the minima shift to $kh=0, \pi, \dots$ ($h=0, \lambda/2, \dots$). The $K_n \rightarrow 0$ case corresponds to the resonance of a free layer. The $K_n \rightarrow \infty$ is a special case of a layer with impedance Z_2 bonded to two semispaces with impedances Z_1 and Z_3 . When $Z_2=(Z_1 Z_3)^{1/2}$ the condition for full transmission is $kh=\pi/2+n\pi$, $n=0,1,2,\dots$ (Ref. 20) ($h=\lambda/4, 3\lambda/4, \dots$) which in the limit $Z_1 \rightarrow Z_2 \rightarrow Z_3$ transforms to our case.

Note that the first and higher order minima positions are sensitive to the interfacial stiffness in different frequency ranges. For example for the case considered in Fig. 2 the maximum sensitivity point (deflection point) for the first minimum is about 10^{14} N/m³ and for the second $5 \cdot 10^{14}$ N/m³. Thus, simultaneous measurement of minima positions of several resonances widens the range of sensitivity to the interfacial stiffness.

Figure 3 shows calculated spectra of the signal reflected from the 0.47-mm-thick aluminum plate enclosed between aluminum substrates. The change of interfacial stiffnesses between ∞ and 0 results in a $\pi/2$ increase of φ_T and corresponding spectral minimum shift. This shift corresponds to that calculated from Eq. (21) and shown in Fig. 2. One can see from Fig. 3 that as $K_n \rightarrow \infty$ (perfect bonding) all the ultrasonic energy is transmitted through the plate and the reflection coefficient $R_L=0$. For an imperfect interface ($K_n < \infty$) part of the energy is reflected from the layer and the minima are at frequencies slightly lower than $kh=\pi/2+n\pi$. Further decrease of interfacial stiffness results in spectral minima shift to lower frequency. In the limit $K_n \rightarrow 0$ the minima are close to the condition $kh=n\pi$. At zero interfacial stiffness all the ultrasonic energy is reflected, the reflection coefficient equals 1 and no minima are observed. The above results are identical for the normally incident

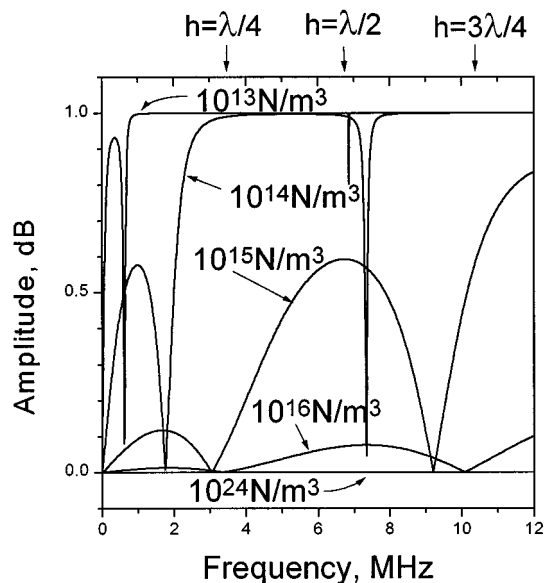


FIG. 3. Spectra of the signals reflected from the aluminum plate imperfectly bonded to aluminum substrates. Calculations are done for different interfacial stiffnesses.

shear wave with substitution of V_l by V_t and K_n by K_t .

Analogous phenomena were observed for environmental interfacial degradation of an Al/Al adhesive joint.¹⁸ Due to exposure to a severe environment (saturated NaCl solution at 68 °C under load) the adhesive/aluminum bond deteriorated with formation of the interfacial fluid-filled microdisbonds. The evolution of bonds was modeled by decrease of the shear interfacial stiffness $0 < K_t < \infty$ assuming normal stiffness $K_n = \infty$. Both the experiment and model showed that the interface degradation was accompanied by a strong shift of the spectral minimum (measured at oblique incidence) to lower frequency. This phenomenon—spectral minimum shift—is a characteristic effect of changing the boundary conditions (interfacial stiffness). It can be used to measure the interface stiffness as demonstrated experimentally in the following section.

II. EXPERIMENTAL APPROACH

A. Experimental concept

As discussed above, two major factors determine the spectra of the reflection from the layer: (a) layer thickness and layer and substrate properties and (b) properties (stiffness) of the layer/substrate interface. We consider here the effect of interface stiffness separately. Two model systems are considered: a single imperfect interface between two aluminum substrates and a system with two interfaces formed by an aluminum plate (about 0.5 mm thick) compressed between two aluminum substrates. The surfaces of the aluminum plate and substrates are roughened and varying pressure is applied across the system to simulate different degrees of interface imperfection.

B. Experimental apparatus

The experiments were done using a computer controlled ultrasonic experimental system shown in Fig. 4. The contact

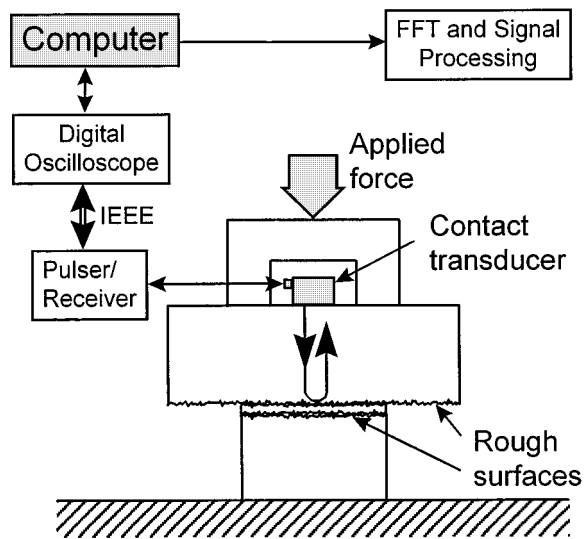


FIG. 4. Schematic of the experiment system for ultrasonic measurement of interfacial stiffness.

specimens consisted of a 50-mm-thick flat aluminum block (top) and a 40 mm long aluminum cylinder of 25-mm diameter (bottom). The block surfaces were machined to parallel. The contact surfaces were polished and then roughened as described below. The blocks were placed between plates of the press (Buehler Ltd.). The pressure was applied through a Π -shaped block. Contact broadband longitudinal ultrasonic transducers with central frequencies at 5 and 10 MHz were placed on top of the upper block. For the measurements with two interfaces a thin (less than 0.5 mm thick) aluminum plate 25 mm in diameter was placed between the aluminum blocks. The plate surfaces were roughened in the same way as the surfaces of the blocks. The reflected ultrasonic signals were amplified, digitized, averaged by a HP 54504A 400-MHz digital oscilloscope, and collected by a computer through an IEEE-488 interface. The data were then processed in the frequency domain using an FFT program and

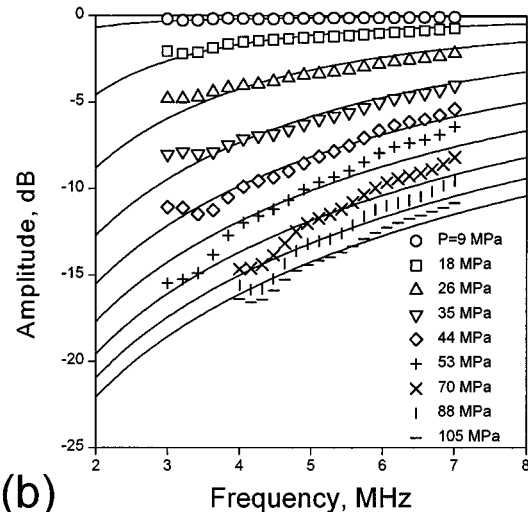
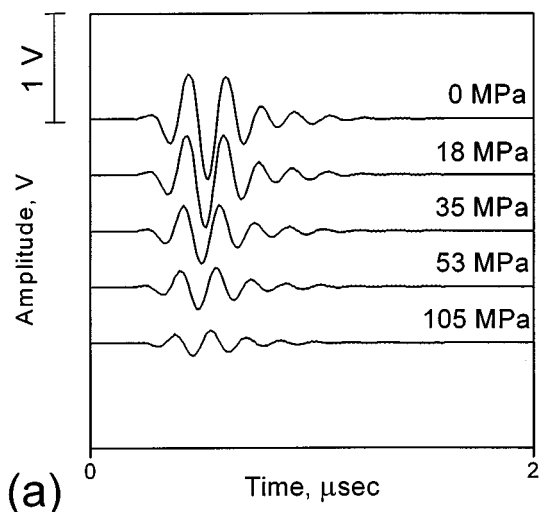


FIG. 5. (a) Typical time-domain signals reflected from the interface between two contacting rough aluminum surfaces at different pressures applied across the interface; (b) corresponding reflection spectra.

TABLE I. Estimated roughness of the aluminum samples.

	Surface preparation	Roughness h_{rms} , μm
A	Sandpaper, grit 500	0.34
B	Sandpaper, grit 120	1.40
C	Sandblasted	5.65
D	4.5 mm steel balls	5.54

deconvolved with a reference signal taken from the aluminum-aluminum interface at zero applied pressure.

C. Sample preparation and characterization

The contact surfaces before roughening were polished on the disk by 5 μm alumina particles. Three types of surface roughening were used: sandpapering (grit 120 and grit 500), sandblasting using 0.22 mm diameter glass beads, and dropping 4.5 mm steel balls from about 200 mm height. The average surface roughness h_a (the average variance of the surface height distribution) and h_{rms} (the square root of the variance of the height distribution) were measured for each sample by a Wyko Topo-3D stylus profilometer. The results are shown in Table I. In the table, the samples are labeled A, B, C, and D. Note that the roughness obtained from the line surface profile is always smaller than the real value because the stylus usually does not go over the summits and valleys but rather traverses the shoulders of individual asperities. Possible corrections are discussed in Refs. 21, 22, and 23.

III. EXPERIMENTAL RESULTS AND DISCUSSION

A. Single imperfect interface: measurements of interfacial stiffness

The interfacial stiffness between two contracted rough surfaces has been measured ultrasonically by several authors.^{12,15,16} Also, several studies have been performed to estimate it theoretically.²¹⁻²³

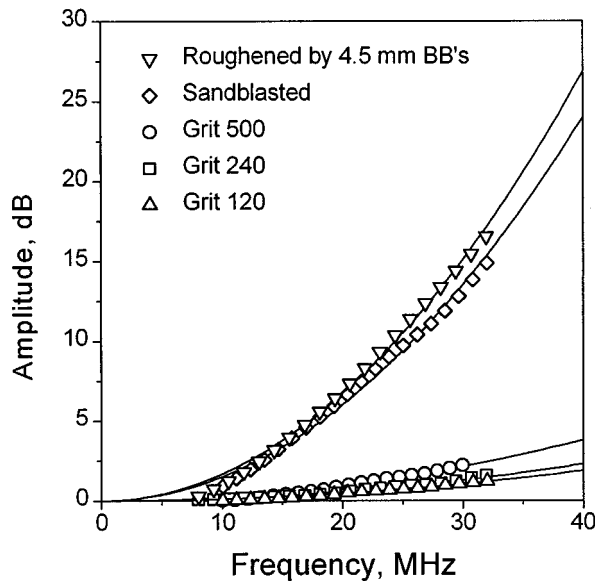


FIG. 6. Frequency spectra of the signals reflected from water/rough Al surface interface.

In this study we measure reflection from a single imperfect interface prior to the measurement from two imperfect interfaces. As an example, Fig. 5(a) shows typical time-domain reflected signals recorded at different pressures applied across the single interface between contacting surfaces of two aluminum blocks roughened by 500 grit sandpaper. (A broadband 5-MHz longitudinal wave ultrasonic transducer was used to collect these data.) Corresponding frequency spectra (deconvolved with the spectrum at zero applied pressure) are shown in Fig. 5(b). The theoretical curves shown in the same figure (solid lines) are calculated using Eq. (2) where the interfacial stiffness is optimized to get the best fit to the experimental data.

One must note that the ultrasonic wave scattering from rough surface asperities may be significant and, in certain conditions, may affect the results of the interfacial stiffness measurement. Figure 6 shows spectra of the signals reflected from a water/rough aluminum interface along with the best fitting f^2 curves. The measurements were performed using an immersion ultrasonic transducer with a frequency band from 10 to 35 MHz placed at about 50 mm from the reflecting surface. One can see that at frequencies below 10 MHz the scattering effect is insignificant and can be neglected.

The dependence of the interfacial stiffness on the applied pressure for different surface roughnesses is shown in Figure 7. One can see that the greatest interfacial stiffness values are achieved with the smoothest surface ($h_{\text{rms}}=0.34 \mu\text{m}$)— K_n is up to $1.4 \cdot 10^{15} \text{ N/m}^3$ at 105 MPa. This result is in line with the intuitive notion that the smooth surfaces provide better contact (i.e., the greatest interfacial stiffness).

However, the lowest interfacial stiffness is measured for sample D which has smaller $h_{\text{rms}}=5.54 \mu\text{m}$ than sample C ($h_{\text{rms}}=5.65 \mu\text{m}$). This result can be explained qualitatively using the theoretical predictions of Yoshioka and Scholtz.^{22,23} These authors modeled the individual asperities on the rough surface as sections of spheres of radius R ,

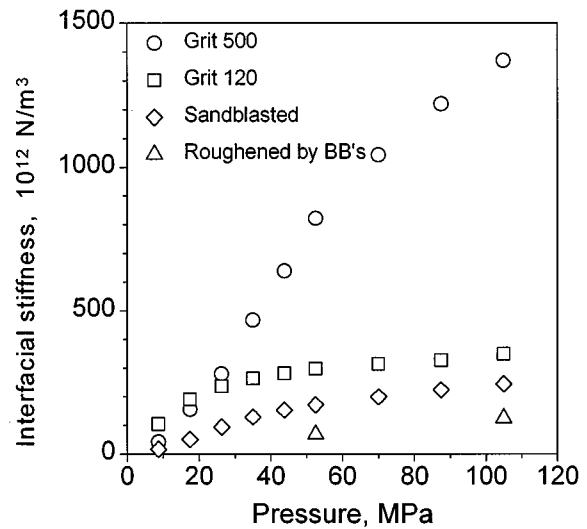


FIG. 7. Dependence of the interfacial stiffness on the pressure applied across the interface.

spherical segment base radius a , and asperity effective height h_e (close to h_{rms}). They showed that the interfacial stiffness $K_n \sim n^2 R^{3/2}$, where n is the surface density of asperities. Since $n \sim a^{-2}$ and $R \approx a^2 / (2R)$ (in approximation $R \gg a$) the interfacial stiffness $K_n \sim 1 / (ah_e^{3/2})$. Thus, the base radius a which characterizes the horizontal size of the asperities also affects the measured interfacial stiffness. Since the steel balls used for preparation of sample D (4.5 mm) are much larger than the glass beads (0.22 mm) used for preparation of sample C the corresponding base radius a is much larger for sample D resulting in smaller interfacial stiffness.

B. Spectroscopy of two spaced imperfect interfaces

Reflection spectra of the 0.47-mm aluminum plate between aluminum substrates were measured with different stresses across the interface. A 10-MHz broadband ultrasonic transducer was used for this experiment. Figure 8(a) shows typical time-domain signals recorded at different pressures applied across the Al/Al/Al sandwich with contacting surfaces roughened by 500 grit sandpaper. At zero applied pressure all the energy is reflected from the front Al/Al interface. The pressure increase results in decrease of the front interface reflection amplitude accompanied by appearance of signals reflected from the back interface. At 105 MPa the signals reflected from the top and bottom interfaces are separated in the time domain with the second signal amplitude about half that of the first. Figure 8(b) shows the corresponding spectra of the reflected signals (deconvolved with the reflection at zero pressure). One can see that as predicted theoretically the spectral minima shift to higher frequency occurs with pressure increase as indicated by dashed lines in the figure. For example, the second minimum shifts from 8.3 MHz at 26 MPa to 9.2 MHz at 88 MPa. Another example obtained for contact surfaces roughened by grit 120 sandpaper is shown in Fig. 9. The observed shifts of the spectral minima are smaller than in the previous case which is due to smaller interfacial stiffness change produced by the same applied pressure (Fig. 7).

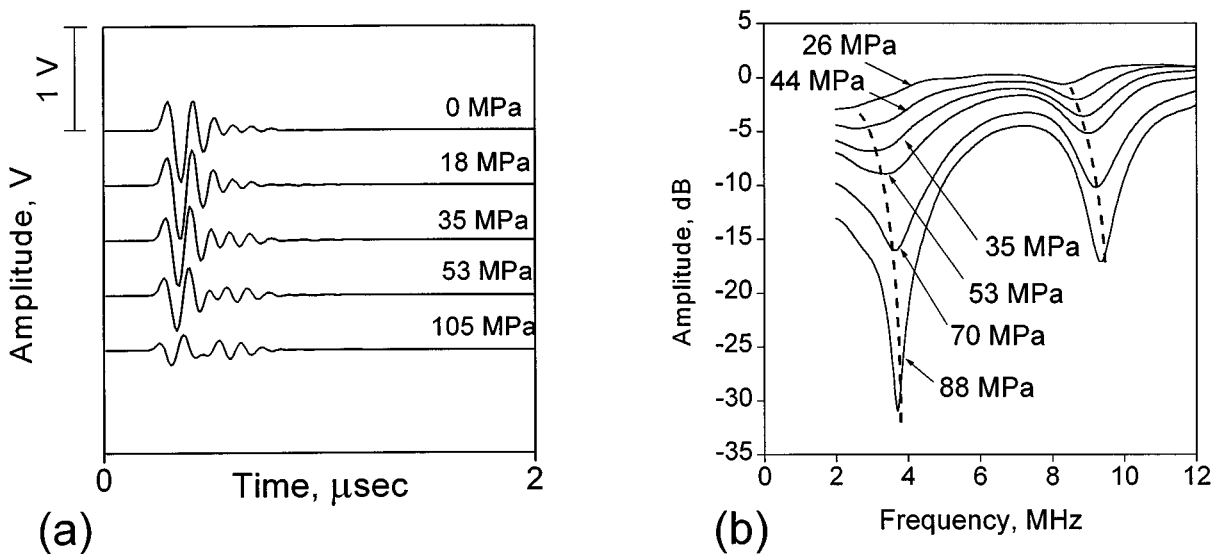


FIG. 8. (a) Typical time-domain signals reflected from the aluminum plate between aluminum substrates at different pressures applied across the imperfect interfaces confining the plate; (b) corresponding reflection spectra. Plate thickness is 0.47 mm, all the surfaces are roughened by 500 grit sandpaper.

The dependence of the second spectral minimum position on the interfacial stiffness is given in Fig. 10. The figure summarizes the data shown in Figs. 8(b), 9, and Fig. 7. The minimum frequency positions plotted on the vertical axis are determined from the spectra measured at different applied pressures (circles—from spectra in Fig. 8(b) squares—from spectra in Fig. 9). For each frequency point at given pressure the corresponding interfacial stiffness was determined from the dependence of the interfacial stiffness on pressure (Fig. 7) established in experiments on a single interface. This stiffness value was used on the horizontal axis as the coordinate for experimental frequency minimum. The figure also shows the theoretical curve (solid line) calculated for frequency minimum position versus interfacial stiffness using Eq. (21)

for an aluminum interface layer with thickness of 0.47 mm used in the experiment. One can see that the experimental and theoretical data are in good agreement. Eq. (21) (Fig. 10) allows one to determine interfacial stiffness from the measured frequency minimum position.

IV. CONCLUSIONS

This paper describes the effect of imperfect interfaces between a layer and substrates on the reflected ultrasonic signal. The ultrasonic wave interaction with an aluminum layer between aluminum substrates is studied when the layer and the substrate properties are identical and thus the effect of impedance differences on the layer reflection is removed.

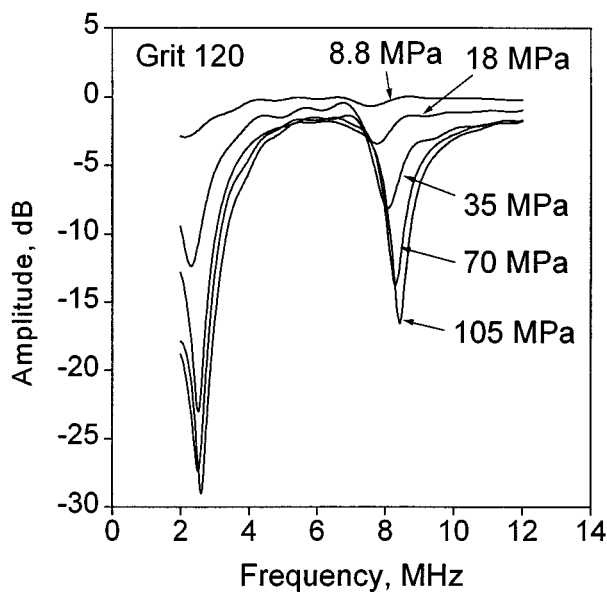


FIG. 9. Spectra of the signals from the aluminum plate between aluminum substrates at different pressures applied across the imperfect interfaces confining the plate. Plate thickness is 0.47 mm; all the surfaces are roughened by 120 grit sandpaper.

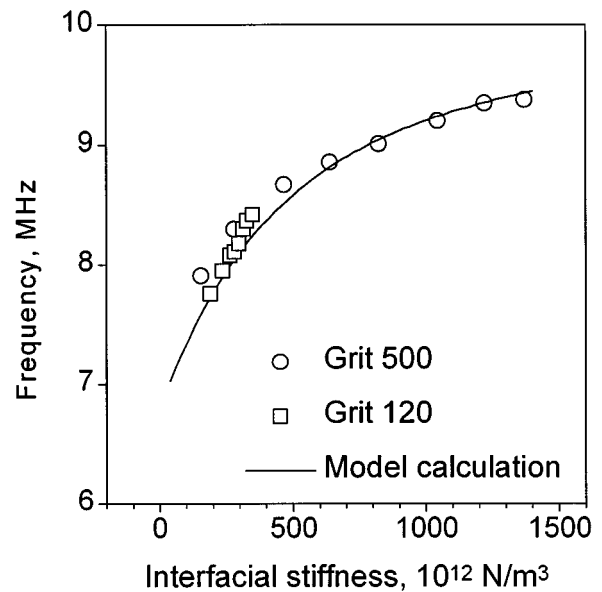


FIG. 10. Dependence of the second spectral minimum position on the interfacial stiffness for a 0.47 mm thick aluminum plate between aluminum blocks with contact surfaces roughened by (a) grit 120 sandpaper and (b) grit 500 sandpaper.

The contacting surfaces of the aluminum substrates and the layer are roughened and pressed together to model an imperfect interface. The interaction of the ultrasonic wave with these interfaces is described using spring boundary conditions. The interfacial spring stiffness is varied by applying different pressures across the interfaces.

It is shown both theoretically and experimentally that change in the interfacial stiffness results in shift of the spectral minima to lower frequency. A simple analytical expression relating the reflection minimum position to the interfacial stiffness is derived. Experiments were performed on interfaces of different roughnesses (h_{rms} from 0.34 to 5.65 μm). The greatest minimum shift was observed for interfaces with lowest roughness. The minima shifts measured experimentally and calculated theoretically are in good agreement. Since the resonance minima measurements can be done with high precision it is proposed to utilize the effect described for determination of the interfacial stiffness and, consequently, the quality of the interfacial bond.

¹J.-M. Baik and R. B. Thompson, "Ultrasonic scattering from imperfect interfaces: A quasi-static model," *J. Nondestruct. Eval.* **4**, 177–196 (1984).
²F. J. Margetan, R. B. Thompson, and T. A. Gray, "Interfacial spring model for ultrasonic interactions with imperfect interfaces: Theory of oblique incidence and application to diffusion-bonded butt joints," *J. Nondestruct. Eval.* **7**, 131–152 (1988).
³Y. C. Angel and J. D. Achenbach, "Reflection and transmission of elastic waves by a periodic array of cracks," *J. Appl. Mech.* **52**, 33–41 (1985).
⁴D. A. Sotiropoulos and J. D. Achenbach, "Reflection of elastic waves by a distribution of coplanar cracks," *J. Acoust. Soc. Am.* **84**, 752–759 (1988).
⁵M. Schoenberg, "Elastic wave behavior across linear slip interfaces," *J. Acoust. Soc. Am.* **68**, 1516–1521 (1980).
⁶M. de Billy and G. Quentin, "Backscattering of acoustic waves by randomly rough surfaces of elastic solids immersed in water," *J. Acoust. Soc. Am.* **72**, 591–601 (1982).
⁷S. I. Rokhlin and Y. J. Wang, "Analysis of boundary conditions for elastic wave interaction with an interface between two solids," *J. Acoust. Soc. Am.* **89**, 503–515 (1991).
⁸S. I. Rokhlin and Y. J. Wang, "Equivalent boundary conditions for thin

orthotropic layer between two solids: Reflection, refraction, and interface waves," *J. Acoust. Soc. Am.* **91**, 1875–1887 (1992).
⁹S. I. Rokhlin and W. Huang, "Ultrasonic wave interaction with a thin anisotropic layer between two anisotropic solids: exact and asymptotic-boundary-condition methods," *J. Acoust. Soc. Am.* **92**, 1729–1742 (1992).
¹⁰S. I. Rokhlin, M. Hefetz, and M. Rosen, "An elastic interface wave guided by a thin film between two solids," *J. Appl. Phys.* **52**, 2847–2851 (1981).
¹¹P. B. Nagy, "Ultrasonic classification of imperfect interfaces," *J. Nondestruct. Eval.* **11**, 127–139 (1992).
¹²P. B. Nagy and L. Adler, "Ultrasonic NDE of solid-state bonds: inertial and friction welds," *J. Nondestruct. Eval.* **7**, 199–215 (1988).
¹³J. H. Rose, M. Bilgen, and P. B. Nagy, "Acoustic double-reflection and transmission at rough water–solid interface," *J. Acoust. Soc. Am.* **95**, 3242–3251 (1994).
¹⁴B. Drinkwater, R. Dwyer-Joyce, and P. Cawley, "A study of the transmission of ultrasound across solid-rubber interfaces," *J. Acoust. Soc. Am.* **101**, 970–981 (1997).
¹⁵A. B. Wooldridge, "The effects of compressive stress on the ultrasonic response of steel–steel interfaces and of fatigue cracks," CEGB Report NW-SSD-RR-42-79, Berkley Nuclear Laboratories, 1979.
¹⁶L. J. Pyrak-Nolte, L. Myer, and N. G. W. Cook, "Transmission of seismic waves across single natural fractures," *J. Geophys. Res.* **95**, 8617–8630 (1990).
¹⁷L. J. Pyrak-Nolte, L. Myer, and N. G. W. Cook, "Anisotropy in seismic velocities and amplitudes from multiple parallel fractures," *J. Geophys. Res.* **95**, 11345–11357 (1990).
¹⁸A. I. Lavrentyev and S. I. Rokhlin, "Models for ultrasonic characterization of environmental degradation of interfaces in adhesive joints," *J. Appl. Phys.* **76**, 4643–4650 (1994).
¹⁹A. I. Lavrentyev, A. Balatazar, and S. I. Rokhlin, "Ultrasonic spectroscopy of two imperfect interfaces using longitudinal and shear waves," in *Review of Progress in Quantitative NDE*, Vol. 17, edited by D. O. Thompson and D. E. Chimenti (Plenum, New York, 1998).
²⁰L. M. Brekhovskikh, *Waves in Layered Media* (Academic, New York, 1960).
²¹S. R. Brown and C. H. Scholtz, "Closure of random elastic surfaces in contact," *J. Geophys. Res.* **90**, 5531–5545 (1985).
²²N. Yoshioka and C. H. Scholtz, "Elastic properties of contacting surfaces under normal and shear loads. 1. Theory," *J. Geophys. Res.* **94**, 17681–17690 (1989).
²³N. Yoshioka and C. H. Scholtz, "Elastic properties of contacting surfaces under normal and shear loads. 2. Comparison of theory with experiment," *J. Geophys. Res.* **94**, 17691–17700 (1989).

Development of a new standard laboratory protocol for estimating the field attenuation of hearing protection devices. Part III.^{a)} The validity of using subject-fit data^{b)}

Elliott H. Berger

E-A-R/Aearo Company, Indianapolis, Indiana 46268

John R. Franks

National Institute for Occupational Safety and Health, Cincinnati, Ohio 45226

Alberto Behar

Behar Noise Control, Scarborough, Ontario M1M 2X8, Canada

John G. Casali

Virginia Tech, Blacksburg, Virginia 24061

Christine Dixon-Ernst

ALCOA, Pittsburgh, Pennsylvania 15219

Ronald W. Kieper

E-A-R/Aearo Company, Indianapolis, Indiana 46268

Carol J. Merry

National Institute for Occupational Safety and Health, Cincinnati, Ohio 45226

Ben T. Mozo

U. S. Army Aeromedical Research Laboratory, Fort Rucker, Alabama 36330

Charles W. Nixon

Systems Research Laboratories, Wright-Patterson Air Force Base, Ohio 45433

Doug Ohlin

U. S. Army Center for Health Promotion and Preventive Medicine, Aberdeen Proving Ground, Maryland 21010

Julia Doswell Royster

Environmental Noise Consultants, Inc., Raleigh, North Carolina 27622

Larry H. Royster

North Carolina State University, Raleigh, North Carolina 27695

(Received 13 May 1997; accepted for publication 19 September 1997)

The mandate of ASA Working Group S12/WG11 has been to develop "laboratory and/or field procedure(s) that yield useful estimates of field performance" of hearing protection devices (HPDs). A real-ear attenuation at threshold procedure was selected, devised, tested via an interlaboratory study, and incorporated into a draft standard that was approved in 1997 [J. D. Royster *et al.*, "Development of a new standard laboratory protocol for estimating the field attenuation of hearing protection devices. Part I. Research of Working Group 11, Accredited Standards Committee S12, Noise," *J. Acoust. Soc. Am.* **99**, 1506–1526 (1996); ANSI S12.6-1997, "American National Standard Methods for Measuring Real-Ear Attenuation of Hearing Protectors" (American National Standards Institute, New York, 1997)]. The real-world estimation procedure utilizes a subject-fit methodology with listeners who are audiometrically proficient, but inexperienced in the use of HPDs. A key factor in the decision to utilize the subject-fit method was an evaluation of the representativeness of the laboratory data *vis-à-vis* attenuation values achieved by workers in practice. Twenty-two field studies were reviewed to develop a data base for comparison purposes. Results indicated that laboratory subject-fit attenuation values were typically equivalent to or greater than the field attenuation values, and yielded a better estimate of those values than did

^{a)}This paper is the last of three parts of a body of work that represents the research and analyses of S12/WG11 in conjunction with the development of ANSI S12.6-1997. Part I appeared in 1996 in *J. Acoust. Soc. Am.* **99**, 1506–1526 (1996). It referenced two succeeding parts, one of which Part II is still in press and hence will appear out of chronological order. Additionally the advance citation of this paper in Part I, listed the first two authors in the reverse order from that which appears above.

^{b)}"Selected research articles" are ones chosen occasionally by the Editor-in-Chief that are judged (a) to have a subject of wide acoustical interest, and (b) to be written for understanding by broad acoustical readership.

experimenter-fit or experimenter-supervised fit types of results. Recent data which are discussed in the paper, but which were not available at the time of the original analyses, confirm the findings.
© 1998 Acoustical Society of America. [S0001-4966(98)03001-X]

PACS numbers: 43.10.Ln, 43.50.Hg, 43.66.Vt, 43.15.+s [GAD]

INTRODUCTION

A quantity of fundamental concern to the understanding and description of the performance of hearing protection devices (HPDs) is the attenuation provided by such devices under conditions of actual use. Since the mid-1970's, studies have been published with increasing regularity (Berger *et al.*, 1996) indicating that the standardized laboratory test procedures utilized in North America do a very poor job of predicting such performance (ANSI S3.19-1974, ANSI S12.6-1984). This discrepancy between laboratory and real-world data is especially troubling considering the importance that many hearing protector purchasers and users ascribe to published attenuation values. As a result, Accredited Standards Committee S12, Noise, assigned its Working Group 11, "Hearing Protector Attenuation and Performance," the task of developing a procedure that would yield useful estimates of "achievable field performance" i.e., the noise reduction that properly trained and motivated workers receive from wearing their hearing protectors in occupational settings. Such results were defined as among the higher values of attenuation attained by groups of informed users in well-managed and well-supervised industrial and military hearing conservation programs.

This paper describes analyses conducted by the members of Working Group 11 to evaluate the suitability of a proposed standardized laboratory test procedure for measuring real-ear attenuation at threshold (REAT) in a manner that estimates achievable field performance. A prior paper described an interlaboratory comparison study undertaken by Working Group 11 that was used as the basis for the development and evaluation of the proposed protocol (Royster *et al.*, 1996). The reader is referred to that report and to the final approved standard that was developed as the outcome of the Working Group's efforts (ANSI S12.6-1997) for the rationale behind the experiments, a description of the overall work effort, the details of the test procedures, and a presentation of the actual results of the interlaboratory study. This paper will focus on a comparison of the interlaboratory test results to available field studies, in order to draw inferences about the degree to which the laboratory data can appropriately be used to predict field results.

The Working Group's interlaboratory protocol involved two distinctly different methods, an informed user-fit and a subject-fit approach. The latter procedure involved test subjects who were audiometrically proficient, but naive in the use of hearing protection. Prior research had suggested that the subject-fit method would provide better field estimates (Berger, 1988; Casali and Epps, 1986), but the informed user-fit (later somewhat modified and implemented as an experimenter-supervised fit in the final approved standard) was also included in the interlaboratory protocol because of the concern that the subject-fit might lead to large inter- and

intralaboratory variability and thus be unsuitable for standardization. However, the outcome of the experiments and subsequent analyses failed to justify such concerns, instead demonstrating that the subject-fit method was even preferable in terms of reproducibility (Royster *et al.*, 1996). With this in mind, as well as the fact that the subject-fit data had already been shown to predict the approximate upper bound estimate of field performance, and that experimenter-supervised fitting only diminished the usefulness of the prediction, the decision was made to focus attention on the subject-fit data for the analyses in this report.

I. METHODS

A. The laboratory data sample

The HPDs which were selected for the interlaboratory study, and hence for the real-world comparison, are described in Sec. II C and Fig. 1 of Royster *et al.* (1996). They include the Aearo Company E-A-R[®] Classic foam earplug, the PlasMed, Inc. V-51R premolded earplugs (5 sizes), the Willson Safety Products EP100 premolded earplugs (2 sizes), and the Bilsom UF-1 earmuffs. The devices were selected because they were products for which the greatest amount of real-world data were available in the literature, because of their popularity in the marketplace at the time of the study, and because they represented a diverse range of product types with a focus on earplugs, which were the type of hearing protector that the Working Group had deemed provided a greater real-world estimation problem than did earmuffs.

The laboratory-based attenuation values used in the following analyses are the average of each test subjects' two trials in the Subject-Fit 1 test session, and their two trials in the Subject-Fit 2 test session, from the interlaboratory study as reported in Table II of Royster *et al.* (1996). This provided a single attenuation value for each of 24 subjects at each of four laboratories, based on four attenuation measurements per subject. In this paper, trials were averaged together as in the original analyses by Royster *et al.* Furthermore, sessions were also averaged together since the ANOVAs indicated no effect of practice, i.e., no difference between the Subject-Fit 1 and Subject-Fit 2 test sessions. And finally, the data were also averaged together across the four laboratories since an ANOVA involving only the subject-fit data indicated no overall laboratory effect, albeit with a significant effect for a few cases—1000 and 2000 Hz for the Bilsom earmuff and 1000 Hz for the E-A-R Plug, due to lower attenuation values from one laboratory. However, the interlaboratory differences between subject-fit data for the EP100 and V-51R earplug were not significant at any frequency. Therefore all of the subject-fit data were pooled across 96 subjects with four trials per subject to create a benchmark

TABLE I. E-A-R classic foam earplug. Mean subject-fit (SF) data from the interlaboratory study, manufacturer's labeled values, and 16 real-world studies. N is number of subjects, SD is standard deviation, shaded values are significantly less than Interlab values at $p < 0.05$, and underlined values are significantly greater at $p < 0.05$.

		Interlab		N		Mfg.'s		N	
		SubjectFit		96		Labeled		10	
Freq.	Mean	SD	Mean	SD	Mean	SD	Mean	SD	t
125	21.4	7.8	37.4	5.7	6.30				
250	22.0	7.3	40.9	5.0	7.98				
500	24.2	7.8	44.8	3.3	8.25				
1000	25.2	6.9	43.8	3.6	8.38				
2000	31.0	4.7	36.3	4.9	3.38				
4000	38.4	5.8	42.6	3.1	2.25				
8000	38.3	7.0	47.3	2.7	4.02				
$t_{0.05,104}=1.984$									

Crawford/Nozza (1981)				Hachey/Roberts (1983)				Edwards et al. (1983)				Edwards/Green (1987)			
Study #		N		Study #		N		Study #		N		Study #		N	
021150		58		021160		31		021170		56		021175		28	
Frequency	Mean	SD	t	Mean	SD	t	Mean	SD	t	Mean	SD	t	Mean	SD	t
125	24	11	1.71	10.2	6.8	7.16	15.0	9.1	4.59	22.6	7.5	0.72			
250	24	11	1.36	11.2	5.5	7.56	15.0	7.7	5.59	23.6	8.3	0.99			
500	26	10	1.25	11.8	5.5	8.21	16.1	7.2	6.35	23.9	8.0	0.18			
1000	28	9	2.17	14.7	6.5	7.47	18.2	7.6	5.81	24.7	7.6	0.33			
2000	36	9	4.52	23.4	7.2	6.80	28.3	10.2	2.22	33.7	7.7	2.28			
4000	39	6	0.61	28.3	8.4	7.50	33.2	8.8	4.39	41.5	7.6	2.31			
8000	35	10	2.40	22.4	7.6	10.77	26.5	9.4	8.81	37.1	7.8	0.78			
$t_{0.05,152}=1.97$				$t_{0.05,125}=1.98$				$t_{0.05,150}=1.97$				$t_{0.05,122}=1.98$			

Edwards/Green (1987)				Edwards et al. (1983)				Abel et al. (1982)				Abel et al. (1982)			
Study #		N		Study #		N		Study #		N		Study #		N	
021176		28		021180		56		021190		55		021200		24	
Frequency	Mean	SD	t	Mean	SD	t	Mean	SD	t	Mean	SD	t	Mean	SD	t
125	17.7	8.8	2.14	9.5	9.8	8.24	12.8	8.3	6.37	13.1	7.8	4.66			
250	17.5	8.0	2.81	9.6	8.8	9.35	14.2	10.0	5.50	14.0	9.3	4.53			
500	19.7	8.0	2.67	11.5	9.2	9.06	14.5	8.7	7.05	14.6	8.7	5.27			
1000	20.2	8.7	3.17	13.3	9.1	9.10	18.0	7.7	5.91	17.5	8.5	4.66			
2000	28.9	8.8	1.67	24.9	12.0	4.44	24.5	7.5	6.55	24.4	9.8	4.79			
4000	38.7	8.5	0.22	26.2	9.5	9.84	25.2	8.5	11.31	26.4	10.0	7.70			
8000	30.8	9.1	4.65	23.5	9.7	10.87									
$t_{0.05,122}=1.98$				$t_{0.05,150}=1.97$				$t_{0.05,149}=1.97$				$t_{0.05,118}=1.98$			

Pfeiffer et al. (1989)				Casali/Park (1991)				Casali/Park (1991)				Hempstock/Hill (1990)			
Study #		N		Study #		N		Study #		N		Study #		N	
021240		69		021250		10		021251		10		021260		72	
Frequency	Mean	SD	t	Mean	SD	t	Mean	SD	t	Mean	SD	t	Mean	SD	t
125	15	11	4.37	13.7	10.1	2.89	25.0	8.7	1.37	15.4	9.0	4.62			
250	11	9	8.65	14.4	12.0	2.93	27.3	8.5	2.15	16.2	8.7	4.69			
500	17	10	5.19	16.5	13.3	2.75	31.1	9.6	2.60	18.1	8.8	4.75			
1000	23	10	1.67	16.7	13.1	3.35	30.8	7.9	2.41	21.1	7.8	3.60			
2000	27	8	4.03	26.6	13.1	2.24	33.5	5.2	1.59	28.1	7.5	3.07			
4000	33	9	4.68	30.0	11.5	3.89	36.8	4.4	0.85	33.1	8.6	4.77			
8000	30	8	7.07	27.6	10.6	4.36	36.3	6.6	0.86	32.1	10.2	4.67			
$t_{0.05,163}=1.97$				$t_{0.05,104}=1.98$				$t_{0.05,104}=1.98$				$t_{0.05,166}=1.97$			

Behar (1985)				Behar (1985)				P-Vermeer et al. (1993)				Berger/Kieper (1991)			
Study #		N		Study #		N		Study #		N		Study #		N	
021220		42		021222		24		021270		58		121516		22	
Frequency	Mean	SD	t	Mean	SD	t	Mean	SD	t	Mean	SD	t	Mean	SD	t
125							19.5	8.1	1.44	23.9	9.5	1.30			
250	16.2	6.5	4.44	16.9	6.0	3.16	22.5	9.2	0.37	25.0	10.7	1.58			
500	19.5	8.6	3.16	20.0	9.1	2.28	24.5	11.1	0.20	28.8	11.5	2.27			
1000	19.8	6.8	4.25	22.5	6.4	1.74	25.6	9.4	0.30	30.1	10.5	2.70			
2000	32.8	7.5	1.71	30.2	5.2	0.73	35.5	7.4	4.62	32.4	6.4	1.17			
4000	37.3	6.5	0.99	38.8	6.8	0.29	42.3	9.3	3.21	40.1	4.4	1.29			
8000	32.8	10.7	3.59	33.3	9.1	2.94	43.8	9.1	4.21	37.5	8.1	0.47			
$t_{0.05,136}=1.97$				$t_{0.05,118}=1.98$				$t_{0.05,152}=1.97$				$t_{0.05,163}=1.97$			

against which the real-world mean attenuations and standard deviations of attenuations could be compared. These averaged values, across practice and across laboratory, are reported in Tables I–IV of this report, in the cells labeled “Interlab Subject Fit.”

Also reported in Tables I through IV are the manufacturers’ published values based upon testing according to the

experimenter-fit protocol of ANSI S3.19 as interpreted by the U. S. Environmental Protection Agency (EPA, 1979). The EPA’s specific implementation does not use the first step of the S3.19-specified experimenter fit (namely, a subject fit of the device), thereby causing the fitting to become a purely experimenter-controlled procedure. In effect, the current EPA interpretation and test lab practices utilize the subject as

TABLE II. V-51R earplug. Mean subject-fit (SF) data from the interlaboratory study, manufacturer's labeled values, and 5 real-world studies. *N* is number of subjects, SD is standard deviation, shaded values are significantly less than Interlab values at $p < 0.05$, and underlined values are significantly greater at $p < 0.05$.

Frequency	Interlab Subject Fit 96		Mfg.'s Labeled 10		<i>t</i>	
	Mean	SD	Mean	SD		
125	11.5	10.4	<u>20</u>	2	2.57	
250	10.9	10.0	<u>22</u>	2	3.49	
500	11.6	10.0	<u>24</u>	2	3.90	
1000	14.1	10.2	<u>28</u>	2	4.28	
2000	21.3	9.9	<u>34</u>	2	4.03	
4000	22.8	7.9	<u>37</u>	3	5.62	
8000	18.6	11.2	<u>37</u>	3	5.16	
$t_{0.05,104}=1.98$						
Royster et al. (1991)				Abel et al. (1982)		
Study #		N		Study #		N
017222		12		017802		20
Frequency	Mean	SD	<i>t</i>	Mean	SD	<i>t</i>
125				10.8	10.2	0.27
250				13.3	10.1	0.97
500	14.6	14.5	0.93	12.3	9.5	0.29
1000	14.8	11.5	0.22	10.5	9.3	1.46
2000	18.8	8.7	0.83	<u>13.9</u>	8.6	3.11
4000	22.0	10.3	0.32	<u>15.6</u>	9.4	3.59
8000						
$t_{0.05,106}=1.98$				$t_{0.05,114}=1.97$		
Edwards et al. (1978)				Fleming (1980)		
Study #		N		Study #		N
019901		84		019902		9
Frequency	Mean	SD	<i>t</i>	Mean	SD	<i>t</i>
125	9.0	11.0	1.57	8.6	5.4	0.82
250	9.0	10.0	1.27	9.4	7.1	0.44
500	9.0	11.0	1.66	11.4	8.7	0.06
1000	13.0	11.0	0.70	15.9	6.3	0.52
2000	20.5	14.0	0.45	21.9	9.9	0.17
4000	<u>20.0</u>	11.0	1.98	21.3	8.4	0.54
8000	<u>14.0</u>	12.0	2.66	18.4	12.6	0.05
$t_{0.05,178}=1.97$				$t_{0.05,104}=1.98$		
Padilla (1976)				P-Vermeer et al. (1993)		
Study #		N		Study #		N
019903		183		018919		12
Frequency	Mean	SD	<i>t</i>	Mean	SD	<i>t</i>
125				7.9	8.4	1.95
250				8.3	10.7	1.76
500	<u>5.5</u>	9.1	5.14	9.2	11.8	1.63
1000				<u>9.6</u>	6.7	2.41
2000				<u>15.4</u>	6.7	2.97
4000				<u>19.6</u>	13.4	3.02
8000				<u>17.1</u>	13.4	2.32
$t_{0.05,114}=1.97$				$t_{0.05,106}=1.98$		

TABLE III. Wilson EP-100 earplug. Mean subject-fit (SF) data from the interlaboratory study, manufacturer's labeled values, and 5 real-world studies. *N* is number of subjects, SD is standard deviation, shaded values are significantly less than Interlab values at $p < 0.05$, and underlined values are significantly greater at $p < 0.05$.

Frequency	Interlab Subject Fit 96		Mfg.'s Labeled 10		<i>t</i>	
	Mean	SD	Mean	SD		
125	14.7	11.7	<u>27</u>	3.9	3.29	
250	14.5	11.6	<u>29</u>	2.9	3.92	
500	15.4	12.5	<u>31</u>	3.0	3.92	
1000	17.5	11.1	<u>33</u>	3.0	4.38	
2000	24.4	10.2	<u>37</u>	4.0	3.86	
4000	30.1	11.1	<u>45</u>	3.6	4.21	
8000	27.0	14.0	<u>36</u>	4.3	2.02	
$t_{0.05,104}=1.98$						
Crawford/Nozza (1981)				Edwards et al. (1978)		
Study #		N		Study #		N
018901		22		018903		28
Frequency	Mean	SD	<i>t</i>	Mean	SD	<i>t</i>
125	8	12	2.41	<u>5</u>	8	4.11
250	8	12	2.36	<u>4</u>	8	4.48
500	10	11	1.87	<u>5</u>	8	4.15
1000	<u>12</u>	13	2.03	<u>6</u>	8	5.10
2000	22	15	0.90	<u>13</u>	13	4.88
4000	<u>20</u>	11	3.86	<u>18</u>	10	5.18
8000	<u>14</u>	12	4.03	<u>9</u>	12	6.17
$t_{0.05,116}=1.97$				$t_{0.05,122}=1.97$		
Abel et al. (1982)				Smoorenburg et al. (1986)		
Study #		N		Study #		N
018904		45		018906		46
Frequency	Mean	SD	<i>t</i>	Mean	SD	<i>t</i>
125	16.5	10.8	0.87			
250	17.4	9.9	1.45	<u>6.8</u>	9.7	3.89
500	18.7	9.3	1.58	<u>7.7</u>	12.5	3.44
1000	20.9	9.8	1.76	<u>9.0</u>	12.9	4.05
2000	23.2	9.3	0.67	<u>19.4</u>	14.9	2.34
4000	28.8	9.6	0.68	<u>24.2</u>	14.1	2.71
8000				<u>15.2</u>	15.0	4.59
$t_{0.05,139}=1.97$				$t_{0.05,140}=1.97$		

though she or he were a test fixture to which the experimenter applies the HPD being tested. This type of manufacturers' data represents the information most commonly available to customers in North America today for purposes of specifying and selecting HPDs.

B. The real-world data sample

The first reported data on field performance of HPDs were published by Reagan in 1975. Since then, at least 21 additional studies of which the authors are aware have become available worldwide (Abel *et al.*, 1982; Behar, 1985; Berger and Kieper, 1991; Casali and Park, 1991; Chung *et al.*, 1983; Crawford and Nozza, 1981; Durkt, 1993; Edwards *et al.*, 1983; Edwards and Green, 1987; Edwards *et al.*, 1978; Fleming, 1980; Goff and Blank, 1984; Hachey

and Roberts, 1983; Hempstock and Hill, 1990; Mendez *et al.*, 1986; Padilla, 1976; Pekkarinen, 1987; Pfeiffer *et al.*, 1989; Royster *et al.*, 1991; Passchier-Vermeer *et al.*, 1993; and Smoorenburg *et al.*, 1986). The total data base of 22 studies comprises results from over 90 different industries, in seven countries (Argentina, Canada, Finland, Germany, Netherlands, UK, and U.S.) with a total of approximately 2900 subjects. Of those studies, 16 included data on the four HPDs which were tested in the interlaboratory comparison. For additional details on the studies, readers are referred to the individual reports and to the complete summary by Berger *et al.* (1996).

Measurements in the field studies were conducted by independent researchers, government-sponsored investigators, and by staff employed at the industries which supplied the data. In all cases, the test subjects were private-sector

TABLE IV. Bilsom UF-1 earmuff. Mean subject-fit (SF) data from the interlaboratory study, manufacturer's labeled values, and 3 real-world studies. *N* is number of subjects, SD is standard deviation, shaded values are significantly less than Interlab values at $p < 0.05$, and underlined values are significantly greater at $p < 0.05$.

	Interlab	N	Mfg.'s		N
	Subject Fit	96	Labeled	10	
Frequency	Mean	SD	Mean	SD	<i>t</i>
125	7.4	3.6	<u>17.1</u>	1.9	8.37
250	14.0	3.4	<u>19.9</u>	1.3	5.43
500	20.7	3.3	<u>25.6</u>	2.4	4.56
1000	29.2	3.8	<u>32.8</u>	1.7	2.96
2000	31.7	4.2	<u>40.3</u>	1.5	6.41
4000	35.6	4.0	<u>46.7</u>	1.4	8.69
8000	34.8	4.9	<u>43.9</u>	2.8	5.76
$t_{0.05, 104} = 1.98$					

	Hachey/Roberts (1983)			Casali/Park (1991)		
	Study #	N		Study #	N	
	056403	31		056416	10	
Frequency	Mean	SD	<i>t</i>	Mean	SD	<i>t</i>
125	7.8	4.1	0.52	8.3	4.2	0.74
250	8.8	5.0	6.55	12.2	4.4	1.55
500	16.8	6.2	4.51	19.3	5.2	1.20
1000	27.6	4.4	1.96	26.5	6.6	1.97
2000	30.5	6.3	1.21	26.2	5.5	3.82
4000	29.5	9.2	5.18	36.0	6.6	0.28
8000	24.0	8.6	8.71	35.3	7.0	0.29
$t_{0.05, 125} = 1.98$			$t_{0.05, 104} = 1.98$			

	Casali/Park (1991)		
	Study #	N	
	056417	10	
Frequency	Mean	SD	<i>t</i>
125	9.4	2.5	1.71
250	13.9	2.8	0.09
500	21.0	2.8	0.28
1000	27.3	3.7	1.51
2000	28.6	3.8	2.24
4000	38.4	5.2	2.05
8000	36.0	5.6	0.73
$t_{0.05, 104} = 1.98$			

workers or military personnel exposed to noise who were tested in most cases while wearing their own HPDs.

The facilities that have been examined most likely represent the better hearing conservation programs in existence. This presumption is based upon the increased likelihood of finding higher-quality programs among companies and organizations interested in and choosing to participate in the complicated, time consuming, and costly research of the type required for real-world evaluations. In fact, in at least two of the more recent studies, the locations were selected specifically because the authors believed them to be exemplary (Edwards and Green, 1987; Pfeiffer *et al.*, 1989).

Due to the variety of authors who have been involved and the diversity of countries in which the research has been conducted, the real-world data base spans a number of different procedures. Some of the most interesting parameters that could potentially influence the data and are germane to the analyses of this paper include: how the participation of the subjects was arranged (candid versus scheduled testing), and how the attenuation was measured (REAT using large circumaural earcups versus REAT in a small test booth). Berger *et al.* (1996) in their comprehensive review paper examined these aspects and others, and concluded that within

the limits of the variability of the available data, it was appropriate to collapse the results across scheduling method, and across methods of measuring attenuation as well.

A very recent evaluation of real-world hearing protector performance was also reviewed for this paper (Scott, 1995), but not included in the data tables. This extensive study of 350 subjects at 9 sites included E-A-R Classic foam earplugs, one of the four HPDs evaluated in this study, and the one for which substantial data already existed. Although the Scott results were not available in time for full inclusion in this study and statistical analyses, qualitative comparison to the 16 existing measurements on the foam plug indicated that the newer values only served to confirm that which had already been observed.

The real-world data for the four HPDs of this study are presented in Tables I–IV, along side the previously mentioned interlaboratory results. A blank cell indicates the authors did not test attenuation at that frequency, most notable being Padilla (1976) who only tested at 500 Hz. For each study, the reference is provided (see the references), as is the number of employees who were tested, and the study identification number (for the author's internal purposes).

C. Analysis

It was not possible to use a statistical tool such as an ANOVA to provide a basis for comparison of the real-world (RW), interlaboratory subject-fit (SF), and manufacturers' published (MFG) data, since raw RW and MFG values were not available. However, when the means and variances of two populations are compared with the assumption being that the two populations will have equal means and variances, $\mu_1 = \mu_2$ and $(\sigma_1)^2 = (\sigma_2)^2 = \sigma^2$, the distribution is that of the *t*-test (Mendenhall, 1975). The *t*-tests were run for independent samples of differing size, with a presumption of normal distributions and equal variances in both samples. The equal-variance assumption was appropriate for the SF-to-RW comparisons, but not for the SF-to-MFG comparisons, since in the latter case the MFG variances were substantially smaller. The effect of the inhomogeneity of variance in this instance, wherein the distribution with the lesser variance also has less than or equal to the sample size of the other distribution, is to make the *t*-test more conservative, i.e., it is less likely to reach significance. In spite of this, all SF-to-MFG differences were found to be significantly different.

The computed *t*-values are also listed in Tables I–IV, along with the associated degrees of freedom indicated in the subscript. The mean RW values which are significantly less than the SF values (at $p < 0.05$) are shaded, and those which are significantly greater are underlined.

II. RESULTS

The product for which the greatest amount of data are available is the E-A-R® Classic foam earplug (see Table I and Fig. 1). There are 16 separate measurements from 11 different reports with a total subject count of 633. For 61% of the 108 possible *t*-test comparisons the SF values are statistically greater than the RW data, 28% of the time there

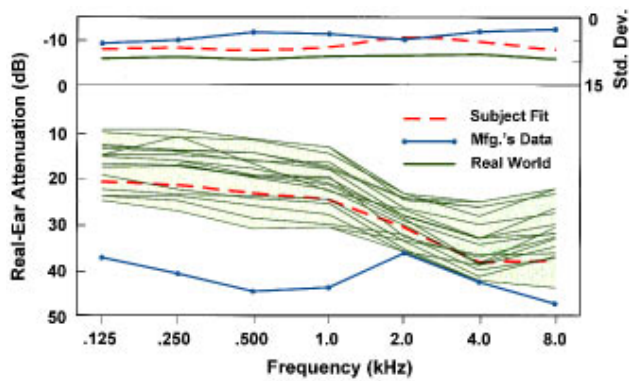


FIG. 1. E-A-R® Classic foam earplug: Mean subject-fit (SF) data from interlaboratory study and mfg.'s labeled values compared to 16 real-world studies. Individual real-world studies shown by thin green lines w/out symbols; bold green line w/out symbols is avg. real-world standard deviation and shading shows range of real-world data.

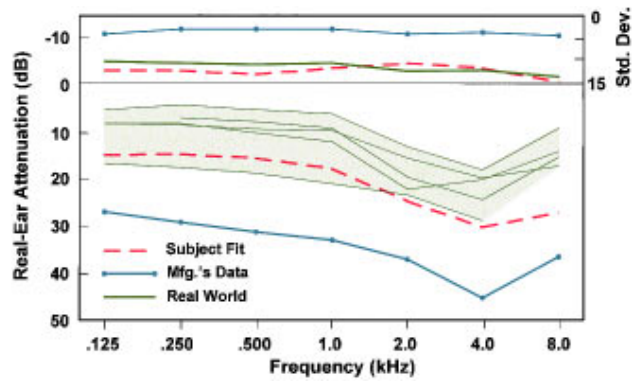


FIG. 3. EP100 earplug: Mean subject-fit (SF) data from interlaboratory study and mfg.'s labeled values compared to five real-world studies. Individual real-world studies shown by thin green lines w/out symbols; bold green line w/out symbols is avg. real world standard deviation and shading shows range of real-world data.

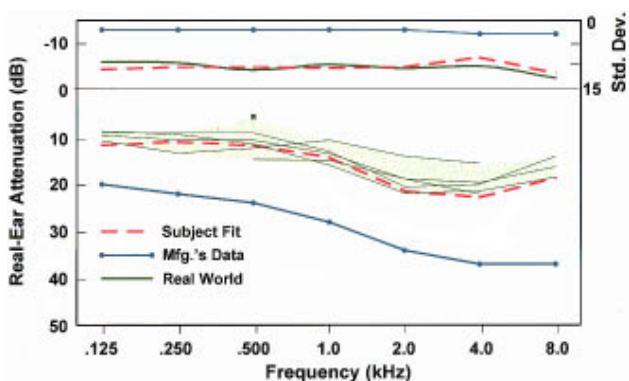


FIG. 2. V-51R earplug: Mean subject-fit (SF) data from interlaboratory study and mfg.'s labeled values compared to five real-world studies. Individual real-world studies shown by thin green lines w/out symbols and by filled box; bold green line w/out symbols is avg. real-world standard deviation and shading shows range of real-world data.

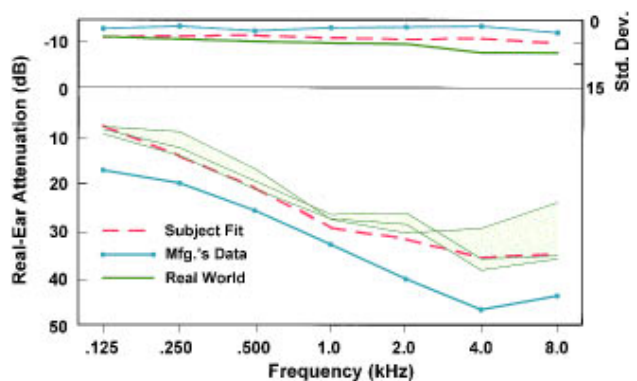


FIG. 4. UF-1 earmuff: Mean subject-fit data (SF) from interlaboratory study and mfg.'s labeled values compared to three real-world studies. Individual real-world studies shown by thin green lines w/out symbols; bold green line w/out symbols is avg. real world standard deviation and shading shows range of real-world data.

were no significant differences, and only 11% of the time did the RW values exceed the SF values. Stated alternatively, in 89% of the comparisons the SF values equaled or exceeded the RW data. This can be appreciated visually in Fig. 1, wherein it is clear the SF data represent approximately the upper quartile of the field values. In all cases the MFG data were statistically greater than the SF values, and in the figure the MFG values can be seen to be well outside the range of field data, except at 2 and 4 kHz.

The data for the remaining two earplugs tell a similar story (Tables II and III, and Figs. 2 and 3), although the fact that fewer field studies are available for examination makes it difficult to ascertain whether the SF data represent an upper bound, an upper quartile, or some other value. There are five studies of the V-51R earplug with a total subject count of 308, although 183 of those subjects were from one study (Padilla, 1976) who only measured attenuation at 500 Hz, albeit a frequency that has been shown to be an excellent indicator of overall protection (Berger, 1989). For 20% of the 25 possible *t*-test comparisons the SF values were statistically greater than the RW data, and in the remaining 80% there were no significant differences. In no instances did the field values significantly exceed the SF measurements.

There are also five studies of the EP100 earplug, with a total subject count of 153. For 67% of the 33 possible *t*-test comparisons the SF values are greater than the RW data, and in the remaining 33 of the comparisons there were no differences. In no instances did the field values significantly exceed the SF measurements. For both the V-51R and the EP100, the MFG data significantly exceeded the SF data at all frequencies.

With earmuffs, the expectation was that there would be less difference between the lab and field data since there is less to go wrong with the fitting of earmuffs under field conditions and since there is also less potential for the experimenter to "over fit" the earmuff for high attenuation in the laboratory setting. However, the reduced variance of the earmuff data caused smaller measured differences to reach significance. There were three separate measurements of the UF-1 earmuffs from two different reports with a total subject count of 51, and the values may be found in Table IV and are plotted in Fig. 4. For 33% of the 21 possible *t*-test comparisons the SF values are greater than the RW data, and in the remaining 67% there were no significant differences. In no instances did the field values significantly exceed the SF measurements. As noted with all of the other products, the

MFG data significantly exceeded the SF data at all frequencies.

III. DISCUSSION

In order to create a procedure that generates "valid" data, the question of course has to be asked, "Valid with respect to what?" In practice, a wide range of HPD attenuation values may be observed in the workplace, from essentially no attenuation at all for devices poorly fitted by untrained users who incorrectly and inconsistently wear their HPDs, to much higher levels of protection that may be obtained under ideal conditions in workplaces with the most successful hearing conservation programs. It makes no sense to excessively derate hearing protector performance to estimate worst-case attenuation values, since worst-case values are much more heavily influenced by factors other than the hearing protectors themselves, such as substantial misuse of products. Neither is it appropriate to utilize optimum laboratory-fit values to estimate field performance, since such laboratory-based values are in essence estimates of idealized protection obtained under pristine conditions and/or performance attained by unusually well-trained and motivated users.

In developing a procedure to estimate field performance, the decision was made by the Working Group to attempt to approximate "achievable" results. Such results were defined as among the higher values of attenuation attained by *groups* of informed users in well-managed industrial and military hearing conservation programs. The validity of the estimates was assessed and substantiated by the analyses in this report, and by prior analyses (Franks and Casali, 1993).

Ideally, the approach to reduction of laboratory versus real-world discrepancies would be to improve field performance to match laboratory data, keeping in mind that under no circumstances can one hope to duplicate optimum laboratory data for groups of users under field conditions. Regardless, most agree that industrial hearing conservation practice must be enhanced so that better real-world HPD performance can be realized (Berger, 1992). However, it is also clear that a laboratory method of measuring hearing protector attenuation that yields data which more closely correlate with existing, or even potential field performance, would be a valuable predictive tool. The development of such a tool has been one of the principal goals of Working Group 11.

The assessment of the degree to which the Working Group achieved its goal was based on comparison of the laboratory data measured via use of the new proposed protocol, to field performance data. The field data were taken from a wide range of available studies. Although some would argue that certain of the real-world studies might represent less than ideal field practice, the general agreement across studies, as well as the reasoning expressed earlier in this paper regarding the types of companies and hearing conservation programs that would be likely to participate, strongly argue that the current real-world data base provides a favorable representation of hearing conservation practice in the latter part of the twentieth century. As such, the fact that the laboratory-based data from the protocol proposed herein predicts the upper bounds of field-measured hearing protec-

tor attenuation is, in these authors' opinion, a reasonable measure of the suitability of that protocol. This suggests that the laboratory data are *achievable by groups of users* in the field, but are not guaranteed. Certainly, sincerely interested and/or highly motivated individual users may exceed these values (and of course others will fall short), but the purpose of such laboratory-based data is to provide a statistical indicator, not an absolute guarantee, of what hearing conservationists can expect to attain in an overall hearing conservation program. How the mean laboratory data are adjusted by the subtraction of one or more standard deviations in order to reflect what 84%, or 98%, or some other proportion of the users will achieve, is up to those who regulate safety or who implement programs based on these data (Berger and Royster, 1996).

With this discussion in mind, the results of the analyses provide strong support for the use of SF data, and a strong contraindication for use of existing U.S. laboratory-based test data for the estimation of field performance. The SF data were shown to provide essentially an upper-bound estimate for the premolded earplugs and the earmuff, and something closer to an upper-quartile estimate for the foam earplug. One could argue that the SF data provide too high a prediction of RW attenuation, but certainly not one that is too low. However, with the precision that is available in subjective testing of this nature, the Working Group agreed that the appropriate balance between over- and underestimation of field performance had been achieved. The MFG data, based on EPA-required testing using the 1974 standard were shown to always significantly exceed SF data, and to also always exceed field performance data by a substantial amount.

It is concluded that the data that results from the subject-fit method of Working Group 11, as implemented in the recently approved standard S12.6-1997, provide an improved estimate of the field performance of HPDs. Furthermore, this estimate represents the upper range of attenuation values which are achievable by groups of users in well-managed and well-supervised industrial and military hearing conservation programs.

ACKNOWLEDGMENTS

This study would not have been possible without the careful, patient, and dedicated efforts of those individuals who collected and recorded the interlaboratory subject-fit data, and maintained cheerful rapport with the subjects throughout the process. Each of these individuals is gratefully acknowledged for this considerable effort: at Armstrong Laboratory, U. S. Air Force personnel Captain Nancy Green and Captain Denise West; at NIOSH Taft Laboratories, Curtis W. Sizemore; and at U. S. Army Aeromedical Research Laboratory, Barbara A. Murphy. Edward F. Krieg of NIOSH is acknowledged for his assistance with statistical analysis of the data.

Abel, S. M., Alberti, P. W., and Riko, K. (1982). "User fitting of hearing protectors: Attenuation results," in *Personal Hearing Protection in Industry*, edited by P. W. Alberti (Raven, New York), pp. 315-322.

- ANSI (1974). S3.19-1974, "American National Standard Method for the measurement of real-ear protection of hearing protectors and physical attenuation of earmuffs" (American National Standards Institute, New York).
- ANSI (1984). S12.6-1984, "American National Standard Method for the measurement of the real-ear attenuation of hearing protectors" (American National Standards Institute, New York).
- ANSI (1997). S12.6-1997, "American National Standard Methods for measuring real-ear attenuation of hearing protectors" (American National Standards Institute, New York).
- Behar, A. (1985). "Field evaluation of hearing protectors," *Noise Control Eng. J.* **24**, 13–18.
- Berger, E. H. (1988). "Can real-world hearing protector attenuation be estimated using laboratory data?," *J. Sound Vib.* **22**, 26–31.
- Berger, E. H. (1989). "Exploring procedures for field testing the fit of earplugs," in *Proceedings, 1989 Industrial Hearing Conservation Conference*, Off. Eng. Serv. (University of Kentucky, Lexington, KY), pp. 7–10.
- Berger, E. H. (1992). "Development of a laboratory procedure for estimation of the field performance of hearing protectors," in *Proceedings, Hearing Conservation Conference*, Off. Eng. Serv. (University of Kentucky, Lexington, KY), pp. 41–45.
- Berger, E. H., Franks, J. R., and Lindgren, F. (1996). "International review of field studies of hearing protector attenuation," in *Scientific Basis of Noise-Induced Hearing Loss*, edited by A. Axelsson, H. Borchgrevink, R. P. Hamernik, P. Hellstrom, D. Henderson, and R. J. Salvi (Thieme Medical, New York), pp. 361–377.
- Berger, E. H., and Kieper, R. W. (1991). "Measurement of the real-world attenuation of E-A-R[®] foam and Ultrafit[®] brand earplugs on production employees," E-A-R Tech. Rept. 91-30/HP, Indianapolis, IN.
- Berger, E. H., and Royster, L. H. (1996). "In search of meaningful measures of hearing protector effectiveness," *Spectrum Suppl.* **1**, **13**, 29.
- Casali, J. G., and Epps, B. W. (1986). "Effects of user insertion/donning instructions on noise attenuation of aural insert hearing protectors," *Hum. Factors* **28**, 195–210.
- Casali, J. G., and Park M. Y. (1991). "Laboratory vs field attenuation of selected hearing protectors," *Sound and Vibration* **25**(10), 28–38.
- Chung, D. Y., Hardie, R., and Gannon, R. P. (1983). "The performance of circumaural hearing protectors by dosimetry," *J. Occup. Med.* **15**, 679–682.
- Crawford, D. R., and Nozza, R. J. (1981). "Field performance evaluation of wearer-molded ear inserts," presented at Am. Ind. Hyg. Conf., Abstract #398, Portland, OR.
- Durkt, Jr., G. (1993). "Field evaluations of hearing protection devices at surface mining environments," *Mine Safety and Health Admin.*, IR 1213, Pittsburgh, PA.
- Edwards, R. G., Broderson, A. B., Green, W. W., and Lempert, B. L. (1983). "A second study of the effectiveness of earplugs as worn in the workplace," *Noise Control Eng. J.* **20**, 6–15.
- Edwards, R. G., and Green, W. W. (1987). "Effect of an improved hearing conservation program on earplug performance in the workplace," *Noise Control Eng. J.* **28**, 55–65.
- Edwards, R. G., Hauser, W. P., Moiseev, N. A., Broderson, A. B., and Green, W. W. (1978). "Effectiveness of earplugs as worn in the workplace," *Sound and Vibration* **12**(1), 12–22.
- EPA. (1979). "Noise labeling requirements for hearing protectors," U. S. Environmental Protection Agency, Fed. Regist. 44(190), 40CFR Part 211, 56130-56147.
- Fleming, R. M. (1980). "A new procedure for field testing of earplugs for occupational noise reduction," Doctoral Thesis at Harvard School of Public Health, Boston, MA.
- Franks, J. R., and Casali, J. G. (1993). "Hearing protector attenuation from subject-fit methods at the work site and in the laboratory," *J. Acoust. Soc. Am.* **94**, 1791–1792.
- Goff, R. J., and Blank, W. J. (1984). "A field evaluation of muff-type hearing protection devices," *Sound and Vibration* **18**(10), 16–22.
- Hachey, G. A., and Roberts, J. T. (1983). "Real world effectiveness of hearing protection," presented at Am. Ind. Hyg. Conf., Abstract #462, Philadelphia, PA.
- Hempstock, T. I., and Hill, E. (1990). "The attenuations of some hearing protectors as used in the workplace," *Ann. Occup. Hyg.* **34**, 453–470.
- Mendenhall, W. (1975). *Introduction to Probability and Statistics*, 4th ed. (Duxbury Press, North Scituate, MA), pp. 222–224.
- Mendez, A., Salazar, E., and Bontti, H. (1986). "Attenuation measurement of hearing protectors in workplace," 12th Int. Congr. on Acoustics, Toronto, Vol. 1, paper B10-2.
- Padilla, M. (1976). "Ear plug performance in industrial field conditions," *Sound and Vibration* **10**(5), 33–36.
- Passchier-Vermeer, W., van den Berg, R., and Crijns, H. (1993). "Development of a simplified attenuation test method for personal hearing protection devices and for determining the attenuation values in real working situations," TNO, NIPG Pub. No. 93.004, The Netherlands.
- Pekkarinen, J. (1987). "Industrial impulse noise, crest factor and the effects of earmuffs," *Am. Ind. Hyg. Assoc. J.* **48**, 861–866.
- Pfeiffer, B. H., Kuhn, H-D., Specht, U., and Knipfer, C. (1989). "Sound attenuation by hearing protectors in the real world (in German)," *Berufsgenossenschaftliches Institut für Arbeitssicherheit Report 5/89*, West Germany.
- Regan, D. E. (1975). "Real ear attenuation of personal ear protective devices worn in industry," Doctoral Thesis at Kent State University, University Microfilms Int., Ann Arbor, MI.
- Royster, J. D., Ostendorf, J. S., Royster, L. H., and Berger, E. H. (1991). Personal communication.
- Royster, J. D., Berger, E. H., Merry, C. J., Nixon, C. W., Franks, J. R., Behar, A., Casali, J. G., Dixon-Ernst, C., Kieper, R. W., Mozo, B. T., Ohlin, D., and Royster, L. H. (1996). "Development of a new standard laboratory protocol for estimating the field attenuation of hearing protection devices. Part I. Research of Working Group 11, Accredited Standards Committee S12, Noise," *J. Acoust. Soc. Am.* **99**, 1506–152.
- Scott, R. F. (1995). "Study of factors affecting at-work protection afforded by hearing protection devices on steelworks," British Steel plc, Doc. FR S373-5 942, London, UK.
- Smoorenburg, G. F., ten Raa, B. H., and Mimpen, A. M. (1986). "Real-world attenuation of hearing protectors," 12th Int. Congr. on Acoustics, Toronto, Vol. 1, paper B9-6.

Acoustic scattering on an elastic plate described by the Timoshenko model: Contact conditions and uniqueness of the solution

I. V. Andronov^{a)}

*Scientific Research Institute in Physics, The University of St. Petersburg, 1-1 Ulianovskaya Str.,
198904 St. Petersburg, Russia*

B. P. Belinskiy^{b)}

*Department of Mathematics, The University of Tennessee at Chattanooga, 615 McCallie Avenue,
Chattanooga, Tennessee 37403-2598*

(Received 28 March 1997; accepted for publication 31 August 1997)

It is shown that the known solution of the acoustic scattering problem on a supported elastic plate, described by the Timoshenko model, should be corrected. The general formulation of the contact conditions that imply the reciprocity principle is given. Sommerfeld's formula and the "optical" theorem for the model are formulated. They lead to the uniqueness of the solution. The numerical comparison of the effective cross section of scattering from supported elastic plate described by the Kirchhoff and by the Timoshenko models is presented. © 1998 Acoustical Society of America. [S0001-4966(98)04201-5]

PACS numbers: 43.20.Bi, 43.20.Tb, 43.40.Dx, 43.40.Rj [ANN]

INTRODUCTION

The 2-D problem of acoustic scattering by a supported infinite elastic plate is a subject of regular interest.¹⁻⁷ The reason for this lies in the simplicity of the formulas for the scattered field, which give a quantitative analysis for the energy distribution between different scattering channels. Supporting ribs and other pointwise non-homogeneities appear to be very important in increasing the energy scattered from an elastic plate. Many distinguished specialists were involved in the analysis of scattering effects from supported elastic plates. Reference 1 contains the detailed review of the results published up to 1982. In particular, the heavy fluid loading limit is discussed. Recent efforts in the area required rather advanced mathematical methods to be used. The effects of varying junction conditions were considered by Guo.² The scattering on a periodically supported plate lies beyond the topic of this paper, and we mention only a few results. The scattering from an orthogonally supported plate was examined in Refs. 3 and 4. The influence of the surface of the supporting ribs was analyzed in Ref. 5. The influence of irregularity in location of ribs and their parameters was studied by Photiadis.⁶ The scattering from two semi-infinite plates with a support was analyzed by Rebinsky and Norris.⁷

In those papers the Kirchhoff model of the plate is accepted. This model is valid if the wave thickness of the plate kh is small. The consideration of moderate, but not small values of kh requires the Timoshenko model to be used (see Refs. 8 and 9). In this paper we show that the formulas and even the statement of the boundary value problems in Refs. 8 and 9 contradict the reciprocity principle and should be corrected. The correction deals with the description of the junction of the rib and plate. We give the general formulation of

the contact conditions on an arbitrary body attached to the plate that imply the reciprocity principle. In particular we present correct contact conditions for pointwise non-homogeneity. We prove the uniqueness of the solution based on Sommerfeld's formula¹⁰ and the "optical" theorem for the model. The last two results are known for the Kirchhoff model (see Refs. 11 and 12-14, respectively), and are reformulated in this paper for the Timoshenko model. Sommerfeld's formula is of independent interest for the inverse problems of finding the parameters of the scattering obstacle. The "optical" theorem serves as the identity for independent control of computations.

This paper is closely connected with Ref. 15 where the eigen-oscillations of a liquid in a bounded cavity with an elastic plate on the boundary are discussed. In Ref. 15 both Kirchhoff and Timoshenko models of the plate are used. The problem is reduced to a Fredholm type equation with a self-adjoint operator. The reason for self-adjointness lies in the correct contact conditions. Other than correct contact conditions would lead to a non-self-adjoint operator and complex fundamental frequencies which are unacceptable for a physical model without damping.

The problem of scattering from a plate reinforced by a set of ribs is considered in Ref. 16. The statement of the boundary value problem there is mathematically correct and the amplitude of the scattered field appears to be symmetric with respect to the angles of incidence and observation. However, only force impedances of ribs are taken into account. Our numerical calculations show that at high frequencies moment impedance plays an important role in the process of scattering.

The paper is organized as follows. In Sec. I the model is described and auxiliary representations for Green's function are given. In Sec. II the scattering on an elastic plate with an arbitrary compact inhomogeneity (boundary value problem)

^{a)}E-mail address: ivan.andronov@pobox.spbu.ru

^{b)}E-mail address: bbelinsk@cecasun.utc.edu

is considered. The representation for the solution of the boundary value problem is derived by means of Green's second formula. The asymptotic expansion of this formula allows Sommerfeld's formula to be found, i.e., the representation of the scattered field in terms of the scattering amplitude and its analytic continuation. In Sec. III the general form of contact conditions is given. The "optical" theorem for the model is formulated. Sommerfeld's formula and "optical" theorem imply the uniqueness of the solution for the correctly formulated boundary value problem. In Sec. IV the solution of the scattering problem on a supported plate is presented. In contrast with Ref. 8, the scattering amplitude appears to be a symmetric function of the angles of incidence and observation. The amplitudes of the surface waves traveling along the plate are found by means of the analytic continuation of the scattering amplitude for complex angles.¹⁷ Numerical results are presented in Sec. V. The analysis of the scattered energy distribution between different channels is given.

I. TIMOSHENKO MODEL

Consider harmonic oscillations of a semi-infinite fluid space $\{-\infty < x < \infty, 0 < y < \infty\}$ with an elastic plate on its boundary $\{-\infty < x < \infty, y = 0\}$. The factor $e^{-i\omega t}$ describes the time dependence and is omitted. The acoustic pressure satisfies the Helmholtz equation

$$(\nabla^2 + k^2)p = 0, \quad (1)$$

with the wave number $k = \omega/c$, where c is the fluid sound speed. The behavior of the plate is modeled by the Timoshenko theory (e.g., see Ref. 18). It means that shear deformation and rotatory inertia are taken into consideration. Thus, the thickness of the plate is assumed to be not small compared to the modal wavelength of the highest frequency of interest. This model requires the consideration of two functions: the plate displacement $\xi(x)$ in the y direction and the angle $\psi(x)$ between the tangent line to the plate and the x axis. These functions satisfy the following equations (prime denotes derivation with respect to x):

$$D\psi'' - \kappa^2 Gh(\xi' + \psi) + \frac{\rho h^3 \omega^2}{12} \psi = 0, \quad (2)$$

$$\kappa^2 Gh(\xi'' + \psi') + \rho h \omega^2 \xi = p(x, 0). \quad (3)$$

Here D is the bending stiffness of the plate, G is the shear modulus, ρ is the density of the material and h is the thickness of the plate. The parameter κ introduced in (2) and (3) is the shear correction factor usually taken equal to $\pi^2/12$. The acoustic pressure $p(x, 0)$ plays in (3) the role of external force applied to the plate. The displacement is related to the pressure by the continuity condition

$$\rho_0 \omega^2 \xi(x) = \frac{\partial p(x, 0)}{\partial y}, \quad (4)$$

where ρ_0 is the density of the fluid.

Equations (2), (3), and (4) allow us to exclude the functions ξ and ψ and to formulate the boundary condition in terms of pressure only:¹⁸

$$\left(\frac{d^4}{dx^4} + F_1 \frac{d^2}{dx^2} + F_2 \right) \frac{\partial p(x, 0)}{\partial y} + \left(F_5 - F_3 \frac{d^2}{dx^2} \right) p(x, 0) = 0. \quad (5)$$

Here convenient notations similar to those introduced in Ref. 8 are used:

$$F_1 = \frac{\rho \omega^2}{\kappa^2 G} + \frac{\rho h^3 \omega^2}{12D}, \quad F_2 = -k_0^4(1 - \varepsilon), \quad F_3 = \frac{\rho_0 \omega^2}{\kappa^2 Gh},$$

$$F_5 = \nu(1 - \varepsilon), \quad \varepsilon = \frac{\rho h^2 \omega^2}{12\kappa^2 G}.$$

The wave number k_0 and parameter ν above are the same as in the Kirchhoff theory:

$$k_0^4 = \frac{\rho h \omega^2}{D}, \quad \nu = \frac{\rho_0 \omega^2}{D}.$$

Letting $F_1 = F_3 = 0$ and $\varepsilon = 0$, i.e., $F_2 = -k_0^4$ and $F_5 = \nu$, the boundary condition of the Kirchhoff model appears instead of (5). For the system (2) and (3), this corresponds to taking the limit as

$$\kappa^2 Gh \rightarrow +\infty \quad \text{and} \quad \frac{\rho h^3 \omega^2}{12} \rightarrow 0. \quad (6)$$

Let $G(\mathbf{r}, \mathbf{r}_0)$ be Green's function of the model ($\mathbf{r} = (x, y), \mathbf{r}_0 = (x_0, y_0)$). It satisfies the Helmholtz equation (1) with the Dirac delta function on the right-hand side and the (homogeneous) boundary condition (5). Let $\xi_G(x, \mathbf{r}_0)$ and $\psi_G(x, \mathbf{r}_0)$ be the corresponding fields of displacements and angles. The formulas for these fields can be easily found by means of the Fourier transform

$$G(\mathbf{r}, \mathbf{r}_0) = -\frac{1}{4\pi} \int \frac{1}{\gamma(\mu)} e^{i\mu(x-x_0)} \left(e^{-\gamma(\mu)|y-y_0|} + \frac{l^*(\mu)}{l(\mu)} e^{-\gamma(\mu)(y+y_0)} \right) d\mu, \quad (7)$$

$$\xi_G(x, \mathbf{r}_0) = \frac{1}{2\pi\rho_0\omega^2} \int \frac{F_5 + F_3\mu^2}{l(\mu)} e^{i\mu(x-x_0) - \gamma(\mu)y_0} d\mu, \quad (8)$$

$$\psi_G(x, \mathbf{r}_0) = \frac{-i}{2\pi D} \int \frac{\mu}{l(\mu)} e^{i\mu(x-x_0) - \gamma(\mu)y_0} d\mu. \quad (9)$$

Here the Fourier symbol $l(\mu)$ of the boundary operator (5) and an auxiliary function $l^*(\mu)$ are introduced as follows:

$$l(\mu) = (\mu^4 - F_1\mu^2 + F_2)\gamma(\mu) - (F_5 + F_3\mu^2),$$

$$l^*(\mu) = (\mu^4 - F_1\mu^2 + F_2)\gamma(\mu) + (F_5 + F_3\mu^2),$$

$$\gamma(\mu) = \sqrt{\mu^2 - k^2}.$$

The function $\gamma(\mu)$ is defined on the complex plane cut along the vertical lines $\{\mu = k + i\tau\}$ and $\{\mu = k - i\tau\}$, $\tau \in [0, \infty)$, and $\gamma(\mu) > 0$ for $\mu > k$. The path of integration in (7)–(9) is shown in Fig. 1(a). It coincides with the real μ -axis except for small neighborhoods of the real zeros of the symbol $l(\mu)$ and the points $\mu = \pm k$. These points are avoided in accordance with the limiting absorption principle. One introduces a small imaginary part of k , so that $\text{Im } k > 0$. Then the zeros

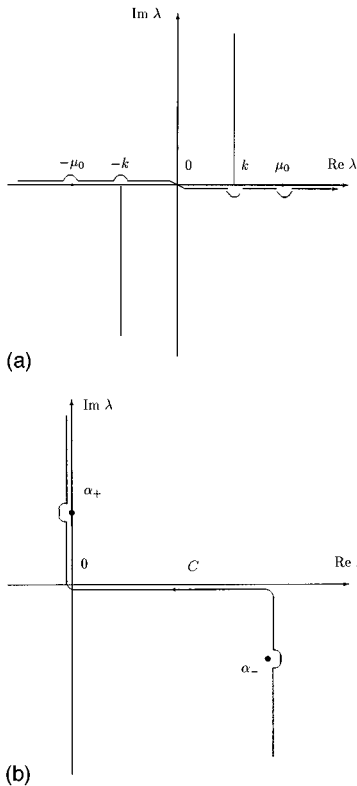


FIG. 1. Paths of integration.

of the symbol $l(\mu)$ shift from the real axis of μ into the complex plane and the integration contour can be taken along the real axis. The limit procedure as $\text{Im } k \rightarrow 0$ requires deforming the contour to avoid the singularities.

The dispersion equation

$$l(\mu) = 0 \quad (10)$$

can be rewritten as a fifth order algebraic equation for $s = \mu^2$. Its analysis shows that if $\varepsilon \leq 1$, there exists only one positive root $s = s_0$. That is, only one pair of real roots of (10) exists. For $\varepsilon > 1$ there could appear extra real roots, but we restrict our derivations in this paper to the case

$$\varepsilon < 1. \quad (11)$$

(Note, the second mode in the isolated Timoshenko plate appears as $\varepsilon > 1$.) Let the positive root of the dispersion equation be denoted as μ_0 . This root is the wave number of the surface wave that propagates along the plate and exponentially decreases in the orthogonal direction.

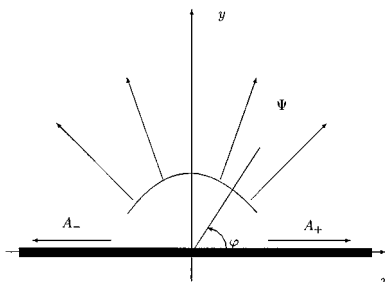


FIG. 2. Scattering far field geometry.

The method of steepest descent for the integral (7) yields the asymptotic representation for Green's function at large distances from the source

$$G(\mathbf{r}, \mathbf{r}_0) = \sqrt{\frac{2\pi}{kr}} e^{ikr - i\pi/4} \Psi_G(\varphi) + o(r^{-1/2})$$

$$\text{as } r \rightarrow \infty, \quad 0 < \varphi < \pi, \quad (12)$$

$$G(\mathbf{r}, \mathbf{r}_0) = A_G^\pm e^{\pm i\mu_0 x - \gamma(\mu_0)y} + o(1) \text{ as } x \rightarrow \pm\infty. \quad (13)$$

The asymptotic formula (12) represents the field as the radial distance $r \rightarrow \infty$ and the angle of observation φ is fixed. The asymptotic formula (13) represents the field as the distance along the plate $x \rightarrow \pm\infty$ and the y coordinate is fixed. The far field scattering geometry is presented on Fig. 2.

The scattering amplitude Ψ_G of the outgoing cylindrical wave is given by the formula

$$\Psi_G(\varphi, \mathbf{r}_0) = \frac{1}{4\pi i} e^{-ikx_0 \cos \varphi} (e^{-iky_0 \sin \varphi} + \mathcal{R}(\varphi) e^{iky_0 \sin \varphi}). \quad (14)$$

Here \mathcal{R} is the coefficient of reflection from a homogeneous infinite plate

$$\mathcal{R}(\varphi) = \frac{l^*(k \cos \varphi)}{l(k \cos \varphi)} = \frac{L^*(\varphi)}{L(\varphi)}, \quad (15)$$

$$L(\varphi) = ik \sin \varphi (k^4 \cos^4 \varphi - F_1 k^2 \cos^2 \varphi + F_2) + (F_5 + F_3 k^2 \cos^2 \varphi), \quad (16)$$

$$L^*(\varphi) = ik \sin \varphi (k^4 \cos^4 \varphi - F_1 k^2 \cos^2 \varphi + F_2) - (F_5 + F_3 k^2 \cos^2 \varphi).$$

The amplitudes of two surface waves traveling to the right and to the left from the source are

$$A_G^\pm = -\frac{i(F_5 + F_3 \mu_0^2)}{l'(\mu_0) \gamma(\mu_0)} e^{\mp i\mu_0 x_0 - \gamma(\mu_0)y_0}. \quad (17)$$

The following asymptotic representations can be easily found by using (13), (17), and boundary conditions (2)–(4):

$$\xi_G(x, \mathbf{r}_0) = B_G^\pm e^{\pm i\mu_0 x} + o(1), \quad (18)$$

$$\psi_G(x, \mathbf{r}_0) = C_G^\pm e^{\pm i\mu_0 x} + o(1) \text{ as } x \rightarrow \pm\infty.$$

Here

$$B_G^\pm = K_1 A_G^\pm, \quad C_G^\pm = K_2 A_G^\pm, \quad (19)$$

constants K_1 and K_2 depend on the parameters of the model only, and their precise values are not needed below.

The substitution $\mu = k \cos \alpha$ in the formula (7) leads to the following representation for Green's function:

$$G(\mathbf{r}, \mathbf{r}_0) = - \int_C e^{ikr \cos(\varphi - \alpha)} \Psi_G(\alpha, \mathbf{r}_0) d\alpha, \quad \text{for } y > y_0 \quad (20)$$

(see Ref. 11 for the details of derivation in case of the Kirchhoff model). This is the so-called Sommerfeld's formula.¹⁰ The path of integration C coincides with the standard Sommerfeld contour¹⁰ $(\pi - i\infty, \pi) \cup (\pi, 0) \cup (0, i\infty)$ except for

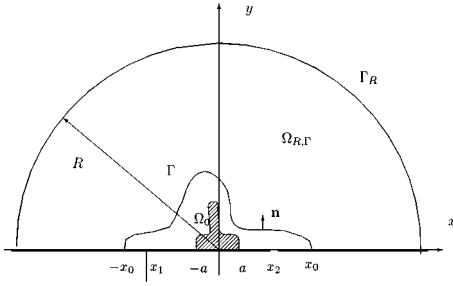


FIG. 3. Geometry of the problem of scattering and domain $\Omega_{R,\Gamma}$.

small neighborhoods of the points α_{\pm} such that $k \cos \alpha_{\pm} = \pm \mu_0$ [see Fig. 1(b)]. Those points are the poles of $\Psi_G(\alpha, \cdot)$ and are avoided from the right and from the left correspondingly. Therefore Sommerfeld's formula (20) assumes analytic continuation of the scattering amplitude (14) for complex angles. It appears in particular that

$$A_G^{\pm} = \mp 2\pi i \operatorname{Res}_{\alpha=\alpha_{\pm}} \Psi_G(\alpha, \cdot) \quad (21)$$

(see Ref. 17 for the details of derivation in case of the Kirchhoff model). Therefore the amplitudes of the surface waves can be found if the scattering amplitude is known (for complex angles).

It is important to note that the formulas (20) and (14) can be differentiated by x and y . In particular that allows one to find Sommerfeld's formulas for ξ_G and ψ_G . The corresponding scattering amplitudes are

$$\Psi_{\xi}(\varphi, x_0) = \frac{-1}{2\pi\rho_0\omega^2} \frac{k \sin \varphi}{L(\varphi)} \times (F_5 + F_3 k^2 \cos^2 \varphi) e^{-ikx_0 \cos \varphi}, \quad (22)$$

$$\Psi_{\psi}(\varphi, x_0) = \frac{i}{2\pi D} \frac{k^2 \sin \varphi \cos \varphi}{L(\varphi)} e^{-ikx_0 \cos \varphi}. \quad (23)$$

II. SOMMERFELD'S FORMULA

Consider now the scattering on a plate with a scatterer Ω_0 (see Fig. 3) that occupies a finite domain. In this section we derive fundamental relations for the scattered field such that the particular type of the scatterer is not important. Some examples of particular scatterers are presented in Sec. III. The total acoustic pressure $p(\mathbf{r})$ is the sum of the incident wave p_i , reflected wave p_r , which appears in the problem without scatterer, and scattered field p_s . The asymptotic representations (12), (13) and (18), (19) allow the radiation conditions for the scattered field p_s to be formulated:

$$p_s(\mathbf{r}) = \sqrt{\frac{2\pi}{kr}} e^{ikr - i\pi/4} \Psi_s(\varphi) + o(r^{-1/2})$$

as $r \rightarrow \infty$, $0 < \varphi < \pi$, (24)

$$p_s(\mathbf{r}) = A_s^{\pm} e^{\pm i\mu_0 x - \sqrt{\mu_0^2 - k^2} y} + o(1) \quad \text{as } x \rightarrow \pm \infty, \quad (25)$$

$$\xi_s(x) = B_s^{\pm} e^{\pm i\mu_0 x} + o(1), \quad \psi_s(x) = C_s^{\pm} e^{\pm i\mu_0 x} + o(1)$$

as $x \rightarrow \pm \infty$. (26)

Here

$$B_s^{\pm} = K_1 A_s^{\pm}, \quad C_s^{\pm} = K_2 A_s^{\pm}, \quad (27)$$

where constants K_1 and K_2 are the same as in (19). The scattering amplitude Ψ_s and the amplitudes A_s^{\pm} of surface waves are not known beforehand. Their determination and analysis represent the main problem of the scattering theory.

The physical meaning of the radiation conditions is the separation of those solutions which carry no energy from infinity. It is sufficient to assume that the scattering amplitude Ψ_s in (24) belongs to $L_2(0, \pi)$. However, after the scattering amplitude is found, it can be proved to be an analytic function.

In this section the structure of the scattered field is discussed. Sommerfeld's formula for it is derived and the scattering amplitude is analyzed.

Let Γ be an auxiliary smooth path that starts at the point $(-x_0, 0)$ and ends at the point $(x_0, 0)$ on the plate and belongs to the upper half plane $\{y > 0\}$ (see Fig. 3). Let the scatterer be below Γ . Further, let $\Omega_{R,\Gamma}$ denote the domain bounded by Γ , the plate, and semicircle $\Gamma_R = \{r = R, 0 \leq \varphi \leq \pi\}$ of sufficiently large radius R . Suppose $\mathbf{r}_0 \in \Omega_{R,\Gamma}$. Applying Green's second formula to the functions $p_s(\mathbf{r})$ and $G(\mathbf{r}, \mathbf{r}_0)$ in the domain $\Omega_{R,\Gamma}$ yields

$$p_s(\mathbf{r}_0) = \int_{\Gamma} \left(-p_s(\mathbf{r}) \frac{\partial}{\partial \mathbf{n}} + \frac{\partial p_s(\mathbf{r})}{\partial \mathbf{n}} \right) G(\mathbf{r}, \mathbf{r}_0) ds$$

$$+ R \int_0^{\pi} \left(p_s(\mathbf{r}) \frac{\partial}{\partial r} - \frac{\partial p_s(\mathbf{r})}{\partial r} \right) G(\mathbf{r}, \mathbf{r}_0) \Big|_{r=R} d\varphi$$

$$+ \int_{R > |x| > x_0} \left(-p_s(\mathbf{r}) \frac{\partial}{\partial y} + \frac{\partial p_s(\mathbf{r})}{\partial y} \right) \times G(x, 0, \mathbf{r}_0) dx. \quad (28)$$

Here \mathbf{n} is the outer unit normal to Γ . The third integral is simplified by using the continuity condition (4) and integrating by parts with the help of the boundary conditions (2) and (3):

$$p_s(\mathbf{r}_0) = \int_{\Gamma} \left(-p_s(\mathbf{r}) \frac{\partial}{\partial \mathbf{n}} + \frac{\partial p_s(\mathbf{r})}{\partial \mathbf{n}} \right) G(\mathbf{r}, \mathbf{r}_0) ds$$

$$+ R \int_0^{\pi} \left(p_s(\mathbf{r}) \frac{\partial}{\partial r} - \frac{\partial p_s(\mathbf{r})}{\partial r} \right) G(\mathbf{r}, \mathbf{r}_0) \Big|_{r=R} d\varphi$$

$$- \rho_0 \omega^2 (\xi_s(x) \mathbf{F}(G(x, \mathbf{r}_0)) + \psi_s(x) \mathbf{M}(G(x, \mathbf{r}_0)))$$

$$- \mathbf{M}(p_s(x)) \psi_G(x, \mathbf{r}_0) - \mathbf{F}(p_s(x)) \xi_G(x, \mathbf{r}_0) \Big|_{-R}^{-x_0} \Big|_{x_0}^R. \quad (29)$$

Here the displacements ξ_s and angles ψ_s are generated by the scattered field p_s . The quantities ξ_G and ψ_G are generated by Green's function (see (8) and (9)). The operators \mathbf{F} and \mathbf{M} in (29) are defined by the formulas

$$\mathbf{F}(p) = -\kappa^2 G h(\xi' + \psi), \quad \mathbf{M}(p) = -D \psi'. \quad (30)$$

Note, the expression $\mathbf{F}(p)$ in (30) represents the force and the expression $\mathbf{M}(p)$ represents the moment applied to the plate.¹⁸ By taking the limit (6) the formulas (30) reduce to

the expressions for the force and moment for the Kirchhoff model.

The radiation conditions (12), (13) and (24), (25) allow us to check that the integral along the large arc in (29) vanishes as $R \rightarrow \infty$. The radiation conditions (18), (19) and (26), (27) allow us to check that the substitutions at $x = \pm R$ in (29) vanish as $R \rightarrow \infty$. Finally the following representation for the scattered field appears:

$$p_s(\mathbf{r}_0) = \int_{\Gamma} \left(-p_s(\mathbf{r}) \frac{\partial}{\partial \mathbf{n}} + \frac{\partial p_s(\mathbf{r})}{\partial \mathbf{n}} \right) G(\mathbf{r}, \mathbf{r}_0) ds + \rho_0 \omega^2 (\xi_s(x) \mathbf{F}(G(x, \mathbf{r}_0)) + \psi_s(x) \mathbf{M}(G(x, \mathbf{r}_0)) - \mathbf{M}(p_s(x)) \psi_G(x, \mathbf{r}_0) - \mathbf{F}(p_s(x)) \xi_G(x, \mathbf{r}_0)) \Big|_{-x_0}^{x_0}. \quad (31)$$

This representation is valid for any field that satisfies the Helmholtz equation (1), boundary conditions (2) and (3) on the plate outside Γ , and radiation conditions (24)–(27).

Substituting the representation for Green's function from (20) and similar formulas for the functions ξ_G and ψ_G and changing the order of integration yields Sommerfeld's formula for the field $p_s(\mathbf{r}_0)$:

$$p_s(\mathbf{r}) = - \int_C e^{ikr \cos(\varphi - \alpha)} \Psi_s(\alpha) d\alpha, \quad (32)$$

$$\Psi_s(\varphi) = \int_{\Gamma} \left(-p_s(\mathbf{r}) \frac{\partial}{\partial \mathbf{n}} + \frac{\partial p_s(\mathbf{r})}{\partial \mathbf{n}} \right) \Psi_G(\varphi, \mathbf{r}) ds + \rho_0 \omega^2 (\xi_s(x) \mathbf{F}(\Psi_G(\varphi, x)) + \psi_s(x) \mathbf{M}(\Psi_G(\varphi, x)) - \mathbf{M}(p_s(x)) \Psi_{\psi}(\varphi, x) - \mathbf{F}(p_s(x)) \Psi_{\xi}(\varphi, x)) \Big|_{-x_0}^{x_0}. \quad (33)$$

Here the action of the operators \mathbf{F} and \mathbf{M} on the scattering amplitude $\Psi_G(\varphi, x)$ is defined as in (30):

$$\mathbf{F}(\Psi_G(\varphi, x)) = -\kappa^2 Gh(\Psi_{\xi}'(\varphi, x) + \Psi_{\psi}(\varphi, x)),$$

$$\mathbf{M}(\Psi_G(\varphi, x)) = -D\Psi_{\psi}'(\varphi, x),$$

and the scattering amplitudes Ψ_G , Ψ_{ξ} and Ψ_{ψ} are defined in (14), (22), and (23).

The formulas (32) and (33) are valid for $y > \max(y: y \in \Gamma)$.¹¹ Below this level, the field $p(\mathbf{r})$ can be prolonged as a solution of the Helmholtz equation (1). The possibility to use the formula (32) below this level is related to the well known Rayleigh hypothesis.¹⁹ If the scatterer is located completely above or on the plate, then the curve Γ in (31) can be taken as the boundary of the scatterer. For the scatterers that are located completely below or on the plate, the formulas (32) and (33) are valid for any $y > 0$. The curve Γ for that case can be taken as a segment (or union of segments) on the line $y = 0$. Note that Green's function (7) is not defined for $y < 0$. Generally speaking, that prohibits Γ to be below $y = 0$.

The geometrical part of the field $p_g(\mathbf{r}) = p_i(\mathbf{r}) + p_r(\mathbf{r})$ when substituted into the right-hand side of (33) gives zero. This can be easily shown by applying Green's second for-

mula to $p_g(\mathbf{r})$ and $G(\mathbf{r}, \mathbf{r}_0)$ in the domain Ω_{Γ} bounded by Γ and the plate. Indeed, \mathbf{r}_0 is located outside Ω_{Γ} and the similar derivations as above yield

$$0 = \int_{\Gamma} \left(-p_g(\mathbf{r}) \frac{\partial}{\partial \mathbf{n}} + \frac{\partial p_g(\mathbf{r})}{\partial \mathbf{n}} \right) G(\mathbf{r}, \mathbf{r}_0) ds + \rho_0 \omega^2 (\xi_g(x) \mathbf{F}(G(x, \mathbf{r}_0)) + \psi_g(x) \mathbf{M}(G(x, \mathbf{r}_0)) - \mathbf{M}(p_g(x)) \psi_G(x, \mathbf{r}_0) - \mathbf{F}(p_g(x)) \xi_G(x, \mathbf{r}_0)) \Big|_{-x_0}^{x_0}.$$

Adding this identity term by term to the formula (31) and combining the fields p_g and p_s yields the representation (33) with the total field $p(\mathbf{r})$ on the right-hand side.

Analysis of the formula (33) shows that the scattering amplitude $\Psi_s(\varphi)$ preserves the analytic properties of the scattering amplitude $\Psi_G(\varphi, \cdot)$ (see Sec. I). Therefore the scattering amplitude is a meromorphic function of the complex angle φ , it has simple poles that coincide with the zeros of the dispersion equation $l(k \cos \varphi) = 0$, and the identity similar to (21) is valid:

$$A_s^{\pm} = \mp 2\pi i \operatorname{Res}_{\alpha=\alpha_{\pm}} \Psi_s(\alpha, \cdot). \quad (34)$$

Let Φ be any subinterval of $(0, \pi)$. Analyticity of $\Psi_s(\varphi)$ implies that if the scattering amplitude Ψ_s is equal to zero on Φ , then it is identically equal to zero. Sommerfeld's formula (32) implies then that the field $p_s(\mathbf{r})$ is identically zero. This result will be used below in Sec. III.

III. "OPTICAL" THEOREM

In the previous section the scatterer and the boundary conditions on its surface were not specified. In this section the set of possible contact conditions for the Timoshenko model is described. It is shown that with those conditions, the scattering problem has a unique solution. In particular, the conditions on the rib correct the conditions used in Refs. 8 and 9.

We first give the brief derivation of the "optical" theorem (see Refs. 12–14 for the details of derivation in case of the Kirchhoff model). Let the incident field be a plane wave

$$p_i(\mathbf{r}) = \exp(ikx \cos \varphi_0 - iky \sin \varphi_0). \quad (35)$$

The reflected wave then is also the plane wave

$$p_r(\mathbf{r}) = \mathcal{R}(\varphi_0) \exp(ikx \cos \varphi_0 + iky \sin \varphi_0),$$

where $\mathcal{R}(\varphi_0)$ is the reflection coefficient (15). Let $(\pm x_0, 0)$ be the end points of the curve Γ (see Sec. II). Apply Green's second formula to the field $p(\mathbf{r})$ and its complex conjugate $\bar{p}(\mathbf{r})$ in the domain $\Omega_{R, \Gamma}$. Then let $R \rightarrow \infty$ and separate the imaginary part. The derivation is similar to that in Sec. II, except that the integral over large arc and the substitutions at the points $(\pm R, 0)$ do not vanish. The following identity appears:

$$-\frac{4\pi}{k} \operatorname{Re}(\bar{\mathcal{R}}(\varphi_0) \Psi(\varphi_0)) = \frac{2\pi}{k} \int_0^{\pi} |\Psi(\varphi)|^2 d\varphi + Q(|A^+|^2 + |A^-|^2) + E,$$

$$E = \frac{1}{k} \operatorname{Im} \int_{\Gamma} p \frac{\partial \bar{p}}{\partial \mathbf{n}} ds + \frac{\rho_0 \omega^2}{k} \operatorname{Im}(\mathbf{F}(p) \bar{\xi} + \mathbf{M}(p) \bar{\psi})|_{-x_0}^{x_0}. \quad (36)$$

Here

$$Q = \frac{\gamma(\mu_0) l'(\mu_0)}{2k(F_5 + F_3 \mu_0^2)}.$$

It is important to note that the quantity Q is positive.

All the terms in (36) have explicit physical meaning of energies normalized by the density of energy in the incident plane wave. If there is no scattered field, all the energy that is brought by the incident wave is carried away by the reflected wave. If there is a scattered field, then some energy is taken from the reflected wave. The left-hand side of (36) expresses this energy. The first term on the right-hand side expresses the energy that is carried away by the cylindrical wave (24). The second term gives the energy of the surface waves. It combines the energies carried over by the acoustic waves (25) and the elastic waves (26) in the plate. The last term is the energy absorbed or irradiated in the domain bounded by the curve Γ . If the scatterer represents a combination of bodies attached to the plate or located separately, inhomogeneities in the plate (cracks, ribs, segments with different parameters), open resonators below the plate, etc., the energy E is the sum of energies absorbed or irradiated by each of these bodies, inhomogeneities, and resonators.

The identity (36) describes the balance of energy in the system. If there are no active sources of energy in any finite domain, the natural restriction on the system is non-negativity of all the terms on the right-hand side of (36). Let the scatterer consist of a body Ω attached to the plate on a segment $(-a, a)$, a point crack at $x = x_1$, and a point rib at $x = x_2$ (see Fig. 3). Let $\partial\Omega$ be the boundary of the body and $\partial\Omega_0$ be the part of $\partial\Omega$ which contacts fluid. The contour Γ in (36) can be chosen as $\Gamma = \partial\Omega_0 \cup S_\varepsilon(x_1) \cup S_\varepsilon(x_2)$ with $\varepsilon \rightarrow 0$, where $S_\varepsilon(x_n)$ is the semicircle of the radius ε with the center at $(x_n, 0)$, $n = 1, 2$. In this case the energy E can be expressed as

$$E = E_0 + E_1 + E_2,$$

$$E_0 = \frac{1}{k} \operatorname{Im} \int_{\partial\Omega_0} p \frac{\partial \bar{p}}{\partial \mathbf{n}} ds + \frac{\rho_0 \omega^2}{k} \times \operatorname{Im}(\mathbf{F}(p) \bar{\xi} + \mathbf{M}(p) \bar{\psi})|_{-a}^a, \quad (37)$$

$$E_j = \frac{\rho_0 \omega^2}{k} \operatorname{Im}[\mathbf{F}(p) \bar{\xi} + \mathbf{M}(p) \bar{\psi}]_{x_j}, \quad j = 1, 2. \quad (38)$$

Here and below $[f]_x$ denotes the jump of function f at the point x .

The energy E_0 is associated with the body Ω . The integral over $\partial\Omega_0$ represents the energy absorbed by the surface of the body and the substitutions at $x = \pm a$ describe the energy of interaction of the body and the plate vibrations.

Consider the following (most general linear) conditions:

$$\begin{pmatrix} p(s) \\ \mathbf{F}(p(-a)) \\ \mathbf{M}(p(-a)) \\ \mathbf{F}(p(a)) \\ \mathbf{M}(p(a)) \end{pmatrix} = \mathbf{Z} \begin{pmatrix} \frac{\partial p(s)}{\partial \mathbf{n}} \\ \xi(-a) \\ \psi(-a) \\ \xi(a) \\ \psi(a) \end{pmatrix}. \quad (39)$$

Here \mathbf{Z} is the matrix operator that characterizes the interaction of the oscillations of the body Ω and the plate (see Refs. 5 and 20 for particular cases of conditions (39) for a body of finite mass). If the body is infinitely heavy, it can be considered as a body not contacting the plate and two separate fixed points on the plate. The matrix operator in such a case splits into two blocks, and the condition (39) can be rewritten in the form of two conditions:

$$p(s) = Z_\Omega(s) \frac{\partial p(s)}{\partial \mathbf{n}} \quad (40)$$

on $\partial\Omega_0$ and

$$\begin{pmatrix} \mathbf{F}(p) \\ \mathbf{M}(p) \end{pmatrix} = \mathbf{Z}_\pm \begin{pmatrix} \xi \\ \psi \end{pmatrix} \quad (41)$$

at $x = \pm a$. Here Z_Ω is proportional to the acoustic impedance of the surface $\partial\Omega_0$, the matrices \mathbf{Z}_+ and \mathbf{Z}_- are proportional to the impedance matrices of the junctions at the points $x = a$ and $x = -a$.

The two terms in (37) are non-negative if

$$\operatorname{Im} \mathbf{Z}(s) \geq 0$$

or

$$\operatorname{Im} Z_\Omega \geq 0, \quad \operatorname{Im} \mathbf{Z}_\pm \geq 0.$$

The last inequality for the matrices \mathbf{Z}_\pm is known as the condition of the passive four-pole network. The particular case of $Z_\Omega = 0$ or $Z_\Omega = \infty$ lead to the Dirichlet or Neumann boundary conditions on $\partial\Omega_0$. Then the integral over $\partial\Omega_0$ in (37) disappears, i.e., the body does not accept the energy.

In the formulas (38) for the energies of the crack and pointwise rib, the integrals over S_ε are not presented due to the Meixner conditions that are included in the formulation of the boundary value problem at the points $(\pm a, 0)$, $(x_1, 0)$, $(x_2, 0)$, and all the points of $\partial\Omega_0$ where the smoothness of the boundary is violated or the impedance $Z_\Omega(s)$ is discontinuous.

The energy E_1 that is absorbed by the crack is zero due to the contact conditions of free edges

$$\mathbf{F}(p) = 0, \quad \mathbf{M}(p) = 0, \quad x = x_1 \pm 0.$$

The conditions on the rib can be taken in the most general form similar to (41):

$$\begin{pmatrix} [\mathbf{F}(p)] \\ [\mathbf{M}(p)] \end{pmatrix} = \mathbf{Z}_r \begin{pmatrix} \xi \\ \psi \end{pmatrix}, \quad x = x_2.$$

These conditions involve an impedance matrix \mathbf{Z}_r (see Sec. IV below). The displacement ξ and the angle ψ are supposed to be continuous at the point $x = x_2$ where the rib is attached to the plate.

The formula (36) for the correctly stated boundary value problem expresses the ‘‘optical’’ theorem (see Ref. 12). It is usually written in the form of two expressions for the effective cross section

$$\begin{aligned} \Sigma &= -\frac{4\pi}{k} \operatorname{Re}(\overline{\mathcal{R}}(\varphi_0)\Psi(\varphi_0)), \\ \Sigma &= \frac{2\pi}{k} \int_0^\pi |\Psi(\varphi)|^2 d\varphi + Q(|A^+|^2 + |A^-|^2) + E, \\ E &= \frac{1}{k} \int_{\partial\Omega} \operatorname{Im} Z_s \left| \frac{\partial p}{\partial n} \right|^2 ds \\ &\quad + \frac{\rho_0 \omega^2}{k} \operatorname{Im} \left\langle \mathbf{Z}_+ \begin{pmatrix} \xi \\ \psi \end{pmatrix}, \begin{pmatrix} \xi \\ \psi \end{pmatrix} \right\rangle \Big|_{x=a} \\ &\quad - \frac{\rho_0 \omega^2}{k} \operatorname{Im} \left\langle \mathbf{Z}_- \begin{pmatrix} \xi \\ \psi \end{pmatrix}, \begin{pmatrix} \xi \\ \psi \end{pmatrix} \right\rangle \Big|_{x=-a} \\ &\quad + \frac{\rho_0 \omega^2}{k} \operatorname{Im} \left\langle \mathbf{Z}_r \begin{pmatrix} \xi \\ \psi \end{pmatrix}, \begin{pmatrix} \xi \\ \psi \end{pmatrix} \right\rangle \Big|_{x=x_2}. \end{aligned} \quad (42)$$

The ‘‘optical’’ theorem (42) serves as the universal independent control of accuracy of computations which together with internal control of convergence is often incorporated in the numerical procedure (e.g., see Refs. 5 and 21). The numerical results in Sec. V are checked by means of this identity.

The ‘‘optical’’ theorem (42) and Sommerfeld’s formula (32) allow us to prove the uniqueness of the solution. Suppose there exist two different solutions p_1 and p_2 . Then their difference is the solution of the boundary value problem without an incident field. In this case the left-hand side in (36) is zero, and hence $\Sigma=0$. Due to (42) the scattering amplitude is identically zero. Sommerfeld’s formula (32) yields $p_1 - p_2 = 0$. Thus the solution is unique.

In Refs. 8 and 9 the contact conditions at supporting ribs are taken using the formal analogy with those for the Kirchhoff model. The mistake in the expression for the force and moment (see (30)) leads to a model, for which the ‘‘optical’’ and uniqueness theorems are not valid. Though the difference in computed scattering characteristics is not large, we believe there is no use to compare the numerical results presented in the next Section with those of Refs. 8 and 9 not satisfying the energy conservation law.

IV. SCATTERING FROM A SUPPORTED PLATE

Consider now the scattering from a plate supported by a pointwise rib and correct the results of Ref. 8. The rib is supposed to be on the opposite side from fluid. The contact conditions that describe the scatterer are taken in the form

$$[\mathbf{F}(p)] = Z_f \xi, \quad [\mathbf{M}(p)] = Z_m \psi. \quad (43)$$

Here the force and moment impedances depend on the mass M and rotatory inertia J per unit length of the rib

$$Z_f = M \omega^2, \quad Z_m = J \omega^2.$$

The exact solution of the boundary value problem (1)–(4) and (43) can be constructed by means of the Fourier

transform.²² Here the final formulas for the scattering amplitude Ψ are presented only. For the special case of the plane incident wave (35), the scattering amplitude is given by the formula

$$\begin{aligned} \Psi(\varphi, \varphi_0) &= \frac{i}{\pi} \frac{k^2 \sin \varphi \sin \varphi_0}{L(\varphi)L(\varphi_0)} \{ \eta_f m(\varphi) m(\varphi_0) \\ &\quad - \eta_m k^2 \cos \varphi \cos \varphi_0 \}. \end{aligned} \quad (44)$$

Here $L(\varphi)$ is defined in (16),

$$\begin{aligned} m(\varphi) &= F_5 + F_3 k^2 \cos^2 \varphi, \\ \eta_f &= \left(F_5 D_0 - F_3 D_2 - \frac{\rho_0 \omega^2}{Z_f} \right)^{-1}, \\ \eta_m &= \nu \left(D_2 + F_3 \frac{\rho h}{\rho_0} D_0 + F_3 B_0 + \frac{D}{Z_m} \right)^{-1}, \end{aligned}$$

and the following contact integrals are introduced:

$$\begin{aligned} D_j &= \frac{1}{2\pi} \int \frac{\gamma(\mu)(i\mu)^j}{l(\mu)} d\mu, \quad j=0,2, \\ B_0 &= \frac{1}{2\pi} \int \frac{d\mu}{l(\mu)}. \end{aligned} \quad (45)$$

The paths of integration are the same as in (7)–(9).

Note, letting $Z_m=0$ yields the formula presented in Ref. 16. As it was mentioned in Sec. I, for the Kirchhoff model $F_1 = F_3 = 0$, $F_2 = -k_0^4$, and $F_5 = \nu$. The formula (44) comes to the well known result (e.g., see Refs. 1 and 20)

$$\begin{aligned} \Psi(\varphi, \varphi_0) &= \frac{i\nu k^2 \sin \varphi \sin \varphi_0}{\pi L_K(\varphi)L_K(\varphi_0)} \left\{ \frac{1}{D_0 - D/Z_f} \right. \\ &\quad \left. - \frac{k^2 \cos \varphi \cos \varphi_0}{D_2 + D/Z_m} \right\}. \end{aligned} \quad (46)$$

Here

$$L_K(\varphi) = ik \sin \varphi (k^4 \cos^4 \varphi - k_0^4) + \nu.$$

The identity (34) yields the formulas for the amplitudes of the surface waves:

$$\begin{aligned} A^\pm(\varphi_0) &= 2 \frac{k \sin \varphi_0 \sqrt{\mu_0^2 - k^2}}{L(\varphi_0)l'(\mu_0)} \{ \eta_f (F_5 + F_3 \mu_0^2) m(\varphi_0) \\ &\quad \mp \eta_m k \cos \varphi_0 \mu_0 \}. \end{aligned} \quad (47)$$

For the case of the incident surface wave

$$p_i = \exp(i\mu_0 x - \sqrt{\mu_0^2 - k^2} y), \quad (48)$$

the scattering amplitude can be expressed as follows:

$$\begin{aligned} \Psi(\varphi) &= \frac{1}{2\pi} \frac{k \sin \varphi \sqrt{\mu_0^2 - k^2}}{L(\varphi)(F_5 + F_3 k^2 \cos^2 \varphi)} \{ \eta_f (F_5 \\ &\quad + F_3 \mu_0^2) m(\varphi) - \eta_m k \cos \varphi \mu_0 \}. \end{aligned} \quad (49)$$

It should be noted that the scattering amplitude (44) satisfies the reciprocity principle, i.e., is symmetric with respect to the angle of incidence φ_0 and the angle of observation φ . The result of Ref. 8 based on the wrong contact conditions violates the energy conservation law and the reciprocity prin-

principle. Note also the symmetry between the expression (47) for the amplitudes of the surface waves and the expression (49) for the scattering amplitude. This symmetry represents the reciprocity between different channels of scattering.

V. NUMERICAL RESULTS

This section presents numerical results on acoustic scattering from an elastic plate supported by a pointwise rib of rigidity. Both the Kirchhoff and the Timoshenko models are used and the characteristics of scattering are compared.

The explicit formulas (44) and (46) for the amplitude of the scattered field contain special integrals D_j ($j=0,2$) and B_0 [see (45)]. These integrals converge slowly and their regularization²² is necessary. However, they can be reduced to sums of residues of auxiliary functions at the zeros of the denominator $l(\mu)$ (see Ref. 22 for contact integrals in the Kirchhoff theory). Thus the computational problems are reduced to finding all zeros of the fifth degree polynomial

$$P_5(s) = (s^2 - F_1s + F_2)^2(s - k^2) - (F_5 + F_3s)^2 \quad (50)$$

in the complex plane of $s = \mu^2$.

The control of accuracy of computations is based on the identities for the integrals

$$D_1 = D_5 = 0, \quad D_3 = 1.$$

The integrals D_3 and D_5 are understood as the following limits. First, the exponential $e^{i\kappa\mu}$ with $\kappa > 0$ is introduced in (45) and the path of integration is moved into the upper half-plane of μ . Then the limit for $\kappa \rightarrow +0$ is taken as the value of the integral.

Besides that control, the final results for the scattering amplitude are checked with the help of the ‘‘optical’’ theorem (42). Ribs that do not absorb energy are considered only, i.e., $E = 0$ in (42). For all the numerical dependencies presented in this paper ‘‘optical’’ theorem is satisfied to within 0.001%.

The main characteristic used for the comparison of the models is the effective cross section Σ . This quantity is defined as the ratio of the energy carried to infinity by the scattered field to the energy concentrated on the unit length of the incident wave front. On the figures the logarithmic scale is used; that is, the effective cross section is expressed in dB. Figure 4 corresponds to a steel plate in water supported by the ribs of different width and height. The curves computed for the Timoshenko model are given by thin lines and the curves for the Kirchhoff model are marked with bold dots. The results in Fig. 4(a) are given for the rib oriented perpendicularly to the plate, that is, its height H is larger than its width W , whereas the results in Fig. 4(b) are given for the ribs oriented parallel to the plate ($H < W$). The difference between the effective cross-sections computed for the Kirchhoff and for the Timoshenko models of plate vibrations almost does not depend on the parameters of the rib. However, this difference is slightly greater for orthogonal ribs than for ribs oriented parallel to the plate.

The influence of the moment impedance Z_m is shown on Fig. 5. The dependencies of effective cross-section are presented for $M = 1$ kg/m and different values of J . At low fre-

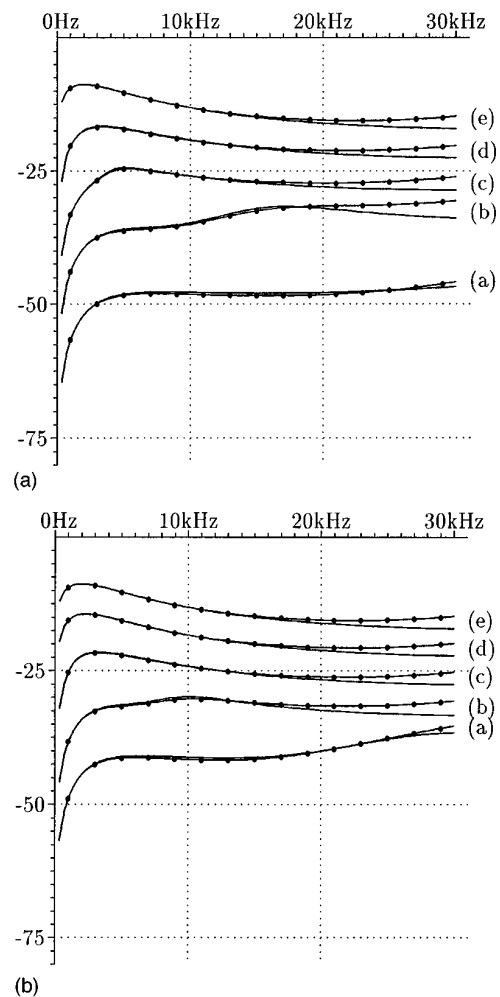


FIG. 4. (a) Dependencies $\Sigma(f)$ for steel plate in water: $\varphi_0 = 45^\circ$, $h = 1$ cm, and $W = 1$ cm. (a) $H = 1$ cm (curve is shifted -20 dB); (b) $H = 2.5$ cm (shift -15 dB); (c) $H = 5$ cm (shift -10 dB); (d) $H = 15$ cm (shift -5 dB); and (e) $H = 1$ m (no shift). (b) Dependencies $\Sigma(f)$ for steel plate in water: $\varphi_0 = 45^\circ$, $h = 1$ cm, and $H = 1$ cm, (a) $W = 2.5$ cm (curve is shifted -20 dB); (b) $W = 5$ cm (shift -15 dB); (c) $W = 15$ cm (shift -10 dB); (d) $W = 50$ cm (shift -5 dB); (e) $W = 1$ m (no shift).

quencies, the force impedance determines the process of scattering. At high frequencies, the moment impedance becomes more significant.

Figure 6 presents the angular dependence of the effective cross-section at the frequency of 20 kHz for the same ribs as in Fig. 4(a). These curves show that the maximum difference appears for the angle of incidence of about 20° .

Figure 7 describes the distribution of the scattered energy between the channels of scattering. The ratio of the energy carried away by the surface waves to the total scattered energy is plotted. The coincidence frequency f_0 at which the phase velocities of the flexural waves in an isolated plate and the acoustic waves in the fluid coincide plays an important role in the processes of scattering. The distribution of energy between the channels of scattering changes significantly at this frequency. At low frequencies, most energy is carried away by the surface waves propagating along the plate. For a plate in water, the increase of the frequency leads to the decrease of this portion to the level of about 75% up to the coincidence frequency. For the plates in air, up to

the coincidence frequency, the portion of energy carried away by surface waves remains at the level close to 100%. At the coincidence frequency, the balance of energy rearranges, and for $f > f_0$ the energy is mainly carried away by the cylindrical wave. This is seen more evidently in Fig. 7(b) for steel plate in air and in Fig. 7(c) for plexiglas plate in air.

For the Kirchhoff model, the flexural wave number in isolated plate is equal to k_0 , whereas for the Timoshenko model, this wave number is larger:

$$k_t = \sqrt{\frac{F_1}{2} + \sqrt{k_0^4(1 - \varepsilon) + F_1^2/4}}$$

This fact causes the difference of coincidence frequencies f_0 in the two models. The shift of curves corresponding to the Kirchhoff and to the Timoshenko models is seen in Fig. 7(c) for the Plexiglas plate in air when the difference of coincidence frequencies is the largest.

For the plates in water, the coincidence frequency lies in the domain of $kh \approx 0.9$ where the models of thin plates (at least the Kirchhoff model) are not valid. For the plates in air, this frequency corresponds to smaller values of kh . Figure 8 presents the dependence of the effective cross-section for the supported steel plate in air. Sharp maxima are noticed at frequencies of non-specular reflection when the velocity of the trace of the incident wave on the plate coincides with the velocity of flexural wave in isolated plate. Again, these frequencies are different for the Kirchhoff and for the Timoshenko models.

VI. CONCLUSION

We have derived Sommerfeld's formula (32) and "optical" theorem (42) for the acoustic scattering from an elastic plate described by the Timoshenko theory. These results, being also of independent interest, allow us to prove the uniqueness theorem for the problem of acoustic scattering from a plate with any compact scatterer. In the case of a pointwise rib, we have corrected the statement of the scattering problem examined in Ref. 8 and presented numerical

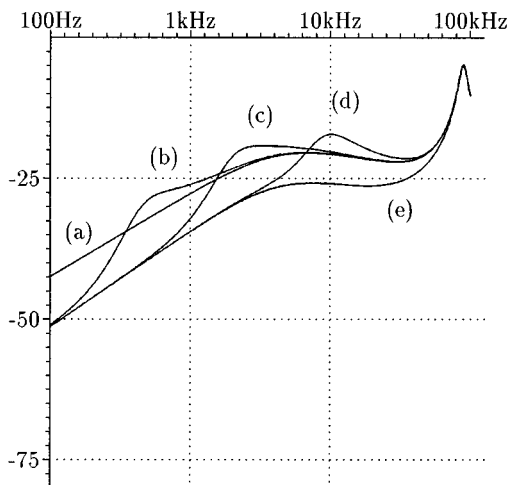


FIG. 5. Dependencies $\Sigma(f)$ for steel plate in water: $\varphi_0 = 45^\circ$, $h = 1$ cm, $M = 1$ kg/m; (a) $J = \infty$; (b) $J = 0.1$ kg m; (c) $J = 0.01$ kg m; (d) $J = 0.001$ kg m; and (e) $J = 0$.

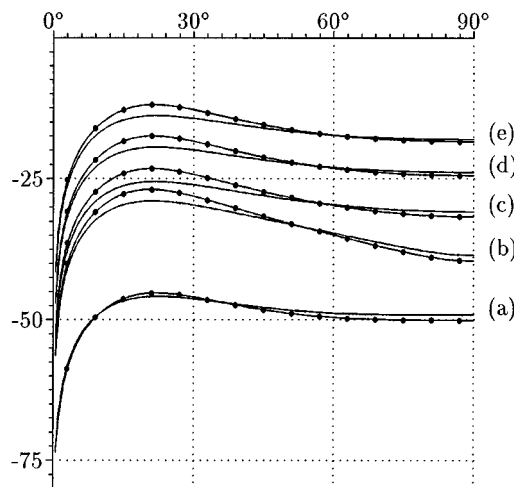


FIG. 6. Dependencies $\Sigma(\varphi_0)$ for steel plate in water at frequency $f = 20$ Hz. The parameters h , W , H and the shifts of curves are the same as in Fig. 1(a).

dependencies of the effective cross-section on frequency, angle of incidence, and parameters of the rib. These numerical results are checked with the help of an "optical" theorem. Comparison of the effective cross-section for the Kirchhoff and Timoshenko models shows that for not high frequencies the discrepancy is small. It can be explained by the slight difference in the frequencies of non-specular reflection that these models give.

The advantage of the Timoshenko model is in the much wider range of parameters (frequency, thickness) for which the model remains valid. The assumption $\varepsilon < 1$ accepted in this paper is an artificial one; Fig. 9 presents the effective

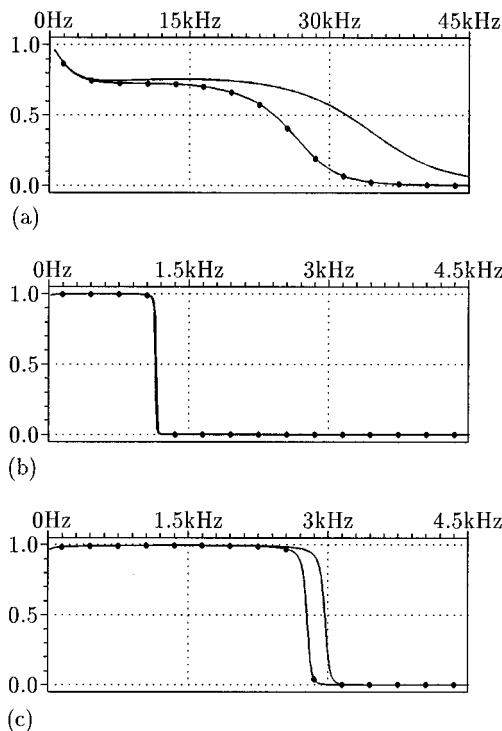


FIG. 7. Distribution of energy (a) for steel plate in water, (b) for steel plate in air and (c) for plexiglas plate in air: $\varphi_0 = 45^\circ$, $h = 1$ cm, $W = 1$ cm, and $H = 1$ cm.

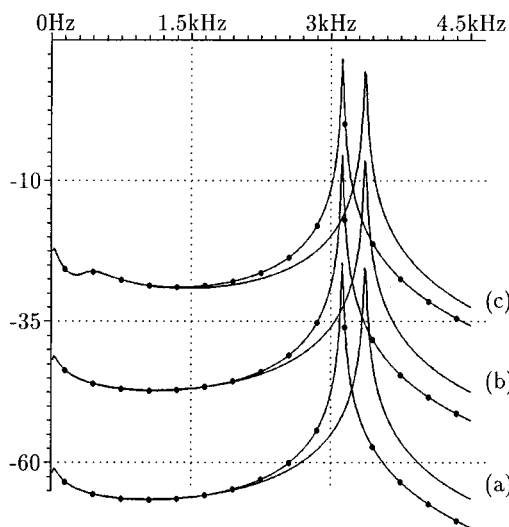


FIG. 8. Dependencies $\Sigma(f)$ for plexiglas plate in air: $\varphi_0=20^\circ$, $h=1$ cm, and $W=1$ cm; (a) $H=0.1$ cm; (b) $H=1$ cm; and (c) $H=10$ cm.

cross section as a function of the frequency for high frequencies, when this condition is violated. The Kirchhoff model gives wrong results in that domain. One can note a deep minimum on the curve corresponding to the Timoshenko model. At this frequency, the second anti-symmetric mode in the plate appears. The numerical results in Fig. 9 are presented for the following hypothetical model. The mass of the rib is chosen to be zero, though the moment of inertia is infinite. In this case the effect is the maximal. The curves corresponding to the plates supported by ribs with comparably large mass do not have this minimum of the effective cross section.

Analysis of the effect of the moment impedance that was not considered in Ref. 16 shows that at high frequencies the rotation of a rib is essential.

In this paper we assumed that the frequency is not very

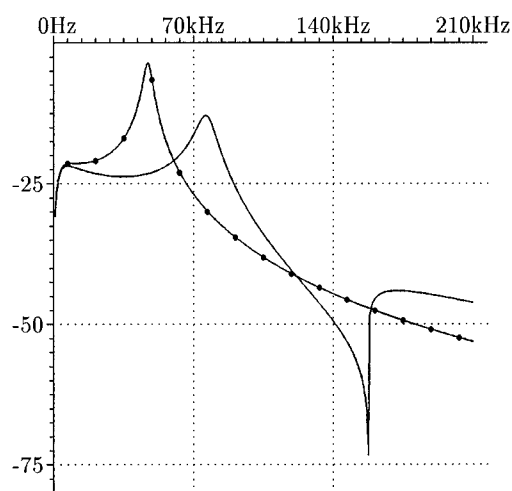


FIG. 9. Cross-section of scattering by a rib in steel water loaded plate, $h=1$ cm, mass of rib $M=0$, inertia $J=\infty$, and incidence at 45° .

high and the condition (11) is satisfied. As a result, only one surface wave propagates along the plate. However, this restriction is not crucial for our derivations. If more than one wave propagates along the plate in each direction, then additional terms appear in the "optical" theorem (42).

ACKNOWLEDGMENT

The second author was partially supported by the University of Tennessee at Chattanooga Center of Excellence in Computer Applications Scholarship.

- ¹D. G. Crighton and D. Innes, "Low frequency acoustic radiation and vibration response of locally excited fluid-loaded structures," *J. Sound Vib.* **91**, 293–314 (1983).
- ²Y. P. Guo, "Effect of structural joints on sound scattering," *J. Acoust. Soc. Am.* **93**, 857–863 (1993).
- ³B. R. Mace, "Sound radiation from fluid loaded orthogonally stiffened plates," *J. Sound Vib.* **79**, 439–452 (1981).
- ⁴B. P. Belinskiy, "Diffraction of plane wave by an infinite elastic plate stiffened by a doubly periodic set of rigid ribs," *PMM USSR* **47**, 962–971 (1983) [English translation: *J. Appl. Math. Mech.* **47**, 767–774 (1983)].
- ⁵B. P. Belinskiy, "Radiation of sound from a plate reinforced by a set of protruding beams under the action of a driving force," *Akust. Zh.* **29**, 420–427 (1983) [English translation: *Sov. Phys. Acoust.* **29**, 251–255 (1983)].
- ⁶D. M. Photiadis, "The effect of irregularity on the scattering of acoustic waves from a ribbed plate," *J. Acoust. Soc. Am.* **91**, 1897–1903 (1992).
- ⁷D. A. Rebinsky and A. N. Norris, "Acoustic and flexural wave scattering from a three-member junction," *J. Acoust. Soc. Am.* **98**, 3309–3319 (1995).
- ⁸B. L. Woolley, "Acoustic scattering from a submerged plate. I. One reinforcing rib," *J. Acoust. Soc. Am.* **67**, 1642–1653 (1980).
- ⁹B. L. Woolley, "Acoustic scattering from a submerged plate. II. Finite number of reinforcing ribs," *J. Acoust. Soc. Am.* **67**, 1654–1662 (1980).
- ¹⁰A. Sommerfeld, *Vorlesungen Über Theoretische Physik* (Wiesbaden, 1950), Vol. VI.
- ¹¹I. V. Andronov and B. P. Belinskiy, "Sommerfeld's formula and uniqueness for the boundary value contact problems," *J. Sound Vib.* [submitted].
- ¹²B. P. Belinskiy and D. P. Kousov, "The optical theorem for the plate-liquid system," *Akust. Zh.* **26**, 13–19 (1980) [English translation: *Sov. Phys. Acoust.* **26**, 8–11 (1980)].
- ¹³G. A. Kriegsmann, A. N. Norris, and E. L. Reiss, "An 'optical' theorem for acoustic scattering by baffled flexible surfaces," *J. Sound Vib.* **99**, 301–307 (1985).
- ¹⁴B. P. Belinskiy, "Comments on 'An 'optical' theorem for acoustic scattering by baffled flexible surfaces'," *J. Sound Vib.* **139**, 522–523 (1990).
- ¹⁵A. V. Badanin and B. P. Belinskiy, "Oscillations of a liquid in a bounded cavity with a plate on the boundary," *Zh. Vychisl. Mat. Mat. Phys.* **33**, 936–944 (1993) [English translation: *USSR Comput. Math. Math. Phys.* **33**, 829–835 (1993)].
- ¹⁶P. R. Stepanishen, "The acoustic transmission and scattering characteristics of a plate with line impedance discontinuities," *J. Sound Vib.* **58**, 257–272 (1978).
- ¹⁷I. V. Andronov, B. P. Belinskiy, and J. P. Dauer, "The connection between the scattering diagram and the amplitudes of the surface waves for acoustic scattering by a baffled flexible plate," *J. Sound Vib.* **195**, 667–673 (1996).
- ¹⁸W. Soedel, *Vibrations of Shells and Plates* (Dekker, New York, 1993), 2nd ed., Chap. 12.
- ¹⁹Lord Rayleigh, *Proc. R. Soc. London, Ser. A* **79**, 399–416 (1907).
- ²⁰B. P. Belinskiy, "Sound radiation from a plate with protruding stiffener," *Akust. Zh.* **24**, 326–333 (1978) [English translation: *Sov. Phys. Acoust.* **24**, 183–187 (1978)].
- ²¹G. A. Kriegsmann, "The Galerkin approximation of the iris problem: conservation of power," *Appl. Math. Lett.* **10**(1), 41–44 (1997).
- ²²D. P. Kousov, "Diffraction of a plane wave on a crack in an elastic plate," *PMM USSR* **27**, 1037–1043 (1963).

The Rayleigh equations for a multi-sinusoidal periodic surface

Anthony Purcell

Box 1388, Lunenburg, Nova Scotia B0J 2C0, Canada

(Received 12 May 1997; accepted for publication 4 November 1997)

It was shown by Purcell [J. Acoust. Soc. Am. **100**, 2919–2936 (1996)] that the Rayleigh equations in the Fourier domain for the reflection coefficients for scattering of a plane wave from a pressure-release sinusoid are valid if the maximum slope of the sinusoid $Kd < 0.6627$. This current work finds the corresponding constraint sufficient for the validity of Rayleigh's equations for a more general periodic surface consisting of a finite sum of sinusoids. The mathematical basis of the derivation of the Rayleigh equations from the Helmholtz integral formula is a Fourier series given by Oberhettinger. Unlike the single sinusoid case developed by Purcell (referenced above), the analysis of the general periodic surface given here requires an analytic continuation argument. In addition, a set of (infinite linear) equations of the "second kind" is derived for the reflection coefficients for the general periodic surface. This guarantees that the truncation solutions for the reflection coefficients converge and are unique. The matrix elements involved in these equations of the second kind require the numerical evaluation of a finite integral (a generalization of Bessel's integral for the integer index Bessel functions) and all calculations required can be performed by desktop computing. © 1998 Acoustical Society of America. [S0001-4966(98)04502-0]

PACS numbers: 43.20.Bi, 43.20.Fn, 43.30.Hw [ANN]

INTRODUCTION

The study of scattering of plane waves from a sinusoid was initiated some ninety years ago by Lord Rayleigh.¹ In the region above the maximum elevation of the surface, the periodicity of the surface implies that the scattered field is a sum over out-going plane waves scattered into discrete angles as given by the diffraction grating equation. Rayleigh postulated the same form for the scattered field within the grooves of the surface corrugations, including the surface itself. By applying the boundary conditions to this form of the scattered field, Rayleigh was able to find an infinite set of linear equations for the amplitudes of the out-going scattered waves—the reflection coefficients R_m . No existence or uniqueness theorems were available for such equations and the general validity of Rayleigh's approach was unknown.

In 1965, J. L. Uretsky² used the Helmholtz integral formula to derive an infinite set of linear equations, with matrix elements $V_{m,n}^0$, for the ψ_n coefficients—the Fourier components (apart from a phase factor) of the normal derivative of the pressure on the surface. Uretsky expressed the reflection coefficients R_m as an infinite sum over the ψ_n and derived an integral formula for the matrix elements $V_{m,n}^0$. From this integral formula Uretsky was able to find a series representation of the matrix $V_{m,n}^0$ consisting of two distinct terms, the first term a sum over Bessel functions and the second term expressible as (an integral over) a sum of Weber functions. Combined with his formula expressing the R_m as sums over the ψ_n , this result for $V_{m,n}^0$ led Uretsky to conclude (see Sec. E of Ref. 2) that his results were inconsistent with the Rayleigh equations. This in turn suggested that Rayleigh's assumption of out-going waves only in the grooves of the surface roughness was incorrect.

However, a series of papers by Millar³ and Petit and Cadilhac⁴ established that the Rayleigh assumption of out-going waves only everywhere in the grooves of the surface

corrugations is correct if and only if $Kd \leq 0.448$. Recently, Purcell⁵ used exact results for two generalized Kapteyn sums to rewrite Uretsky's series expression for $V_{m,n}^0$ in a form that immediately leads to the Rayleigh equations in the Fourier domain. Demanding that these Kapteyn sums converge absolutely gives the constraint $Kd < 0.6627$. This leads to the conclusion that the Rayleigh equations in the Fourier domain are valid more generally than Rayleigh's expansion in out-going plane waves. An attempt to reconcile the apparent discrepancy between these two different constraints is given in Sec. VI of this paper.

On a purely numerical level, solving the Rayleigh equations directly (by truncation) for the R_m is much easier than Uretsky's procedure of solving for the ψ_n coefficients, then expressing the R_m as (suitably truncated) sums over the ψ_n . The disadvantage is that the Rayleigh equations are only valid for a sufficiently small surface slope. This would correspond to a slope angle of $\arctan(0.6627) \approx 34^\circ$; this is still large enough to include many surfaces of practical interest. Some well-known difficulties connected with the condition number and with proving existence and uniqueness of the truncation solutions of the Rayleigh equations are also discussed in Purcell.⁵

This current work is an extension of the results of Ref. 5 [the single sinusoid surface $z = d \cos(Kx)$] to the case of a more general periodic surface consisting of a finite sum of sinusoids in the form $z = \sum_{n=1}^M d_n \cos(nKx + \omega_n)$. It is found that for such a composite surface, the Rayleigh equations in Fourier form are valid provided the maximum slopes nKd_n of the individual sinusoids satisfy a certain non-linear constraint that can be solved numerically. In any event, the slopes of the individual sinusoids may not exceed the single sinusoid limit $Kd < 0.6627$. Results for the simplest possible extension of the sinusoid case, namely $z = d \cos(Kx) + d' \cos(3Kx)$ (a ripple of period $L/3$ superimposed on a si-

nusoid of period $L \equiv 2\pi/K$), are presented in graphical form.

In this paper, the mathematical basis of the derivation of the Rayleigh equations is a Fourier series given by Oberhettinger.⁶ Hence the proof of the Rayleigh equations for the general periodic surface case requires an analytic continuation argument. This is in contrast to the work in Purcell⁵ for the single sinusoid, which was based on the Kapteyn sums of the form $\sum_{n=1}^{\infty} J_{2n}(2nZ)/n^{2M}$ given on p. 558 of Watson,⁷ and which did not require analytic continuation arguments. Also a set of linear equations of the ‘‘second kind’’ is derived for the reflection coefficients R_m for the general periodic surface. This guarantees that the truncation solutions for the reflection coefficients converge and are unique. The matrix elements for these equations of the second kind require the numerical evaluation of a generalization of Bessel’s integral for the integer index Bessel functions.

This work concludes that the Rayleigh equations are valid for composite surfaces consisting of a finite sum of sinusoids, provided the slopes are sufficiently small. Such surfaces have been used by Berman⁸ and Kachoyan and Macaskill⁹ (using methods applicable to arbitrary slope surfaces) to model bistatic scattering from the randomly rough cylindrical surfaces. The study of such surfaces, using techniques accessible to desktop computing, is the primary motivation for this current work. The reader should note that there is an extensive literature on scattering from periodic surfaces; this paper cites only a narrow selection of references relevant to the specific technical approach employed in this paper. There are other approaches to analyzing scattering from a sinusoid that bypass Uretsky’s integral formula completely. For references to the older literature there is the review by Fortuin,¹⁰ for more recent material see the review by Bishop and Smith.¹¹ Periodic surfaces have previously been investigated by Hill and Celli¹² and Van den Berg and Fokkema.¹³ In the limit of the single sinusoid case their results reduce to Millar’s constraint $Kd \leq 0.448$ (see Sec. V of Ref. 13) on the general validity of the Rayleigh expansion everywhere above the rough surface; in this paper the single sinusoid case reduces to the constraint $Kd < 0.6627$ on Rayleigh equations in the Fourier domain.

I. PRELIMINARY THEORY

Generally the notation in this paper will be chosen to be consistent with Holford¹⁴ and Purcell.⁵ Let the periodic surface be described by the coordinate system shown in Fig. 1, where the fluid occupies the half-space $z > \epsilon(x)$. In this paper it will be assumed that the periodic surface is given by a finite sum of M sinusoids of the form $z = \epsilon(x) = \sum_{n=1}^M d_n \cos(K_n x + \omega_n)$, where the phase factors $0 \leq \omega_n \leq 2\pi$. The wave numbers K_n of the sinusoids are assumed to be integral multiples of the lowest wavenumber $K_1 \equiv K$ i.e. $K_n = nK$. Hence the period of this surface is $L = 2\pi/K$. This is not the most general periodic surface that can be constructed from a finite sum of sinusoids, but it is sufficiently general to have some interesting applications. For example such a surface is used by Berman [see Eq. (A1) of Ref. 8] to model scattering from a random two-dimensional surface.

For simplicity consider an incident plane wave of the

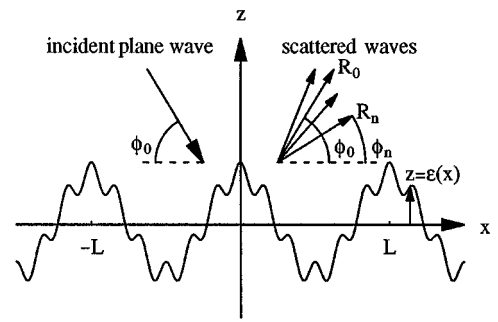


FIG. 1. Definition of the coordinates for the scattering of a plane wave from a periodic surface with period L . The fluid occupies the half-space $z > \epsilon(x)$ above the pressure-release periodic surface. In the example pictured above $z = \epsilon(x) = d_1 \cos(Kx) + d_2 \cos(7Kx)$, where the surface wave number $K = 2\pi/L$.

form $p_{\text{inc}}(x, z) = \exp[ik(x \cos \phi_0 - z \sin \phi_0)]$, where ϕ_0 is the grazing angle. The total pressure must satisfy the wave equation

$$\frac{\partial^2 p(x, z)}{\partial x^2} + \frac{\partial^2 p(x, z)}{\partial z^2} + k^2 p(x, z) = 0. \quad (1)$$

The boundary condition requires that the total pressure vanishes on the surface

$$p(x, \epsilon(x)) = 0. \quad (2)$$

The radiation condition requires that the scattered field consist only of out-going waves as $z \rightarrow \infty$.

As the x axis is shifted by an amount L , p_{inc} is shifted by the factor $\exp(ikL \cos \phi_0)$. Since the boundary conditions are periodic in x , $\exp(-ikL \cos \phi_0)p(x, z)$ must also be periodic in x . This leads to the expansion for the pressure in the form

$$p(x, z) = p_{\text{inc}}(x, z) + \sum_{n=-\infty}^{\infty} R_n e^{ik(x \cos \phi_n + z \sin \phi_n)}, \quad (3)$$

$$z > \text{Maximum}\{\epsilon(x)\},$$

where the diffraction grating equation gives

$$\cos \phi_n = \cos \phi_0 + \frac{K}{k} n. \quad (4)$$

To satisfy the radiation condition, choose the square root such that

$$\sin \phi_n = |\sqrt{1 - \cos^2 \phi_n}|, \quad +i|\sqrt{1 - \cos^2 \phi_n}|, \quad (5)$$

for $\cos \phi_n < 1$ and $\cos \phi_n > 1$ respectively.

From an application of Green’s theorem to the pressure $p(\mathbf{r}')$ and the Hankel function $H_0^1(k|\mathbf{r} - \mathbf{r}'|)$ and by inserting the pressure-release boundary conditions $p(x, \epsilon(x)) = 0$, follows the Helmholtz integral formula

$$p(\mathbf{r}) = p_{\text{inc}}(\mathbf{r}) - \frac{1}{4i} \int ds' \frac{\partial p(\mathbf{r}')}{\partial n'} H_0^1(k|\mathbf{r} - \mathbf{r}'|), \quad (6)$$

where the integral over the arc length s' extends over the infinite surface and n' is the downward normal. The field point $\mathbf{r} = (x, z)$ lies anywhere above the periodic surface and the point $\mathbf{r}' = (x', \epsilon(x'))$ lies on the periodic surface. This is

just Eq. (21) of Holford. Now define the shorthand notation for the normal derivative of the pressure on the surface in terms of the $\psi(x)$ function

$$\begin{aligned} \psi(x') &= \left(\frac{i}{k} \frac{\partial p(x', z')}{\partial n'} \frac{ds'}{dx'} \right) \Bigg|_{z'=\epsilon(x')} \\ &= \frac{i}{k} \left(-\frac{\partial p(x', z')}{\partial z'} + \frac{d\epsilon(x')}{dx'} \frac{\partial p(x', z')}{\partial x'} \right) \Bigg|_{z'=\epsilon(x')} \end{aligned} \quad (7)$$

Since the normal derivative of the pressure is also periodic up to a phase factor, it can be decomposed into the Fourier sum

$$\psi(x) = \sum_{n=-\infty}^{\infty} \psi_n e^{ikx \cos \phi_n} \quad (8)$$

Since the surface is assumed to be periodic with period $L = 2\pi/K$, this gives the Fourier sum

$$e^{-iP\epsilon(x)} = \sum_{r=-\infty}^{\infty} e^{iKxr} C_r(P) \quad (9)$$

This can be viewed as the generating function for the C_r functions.

Multiplication by the factor $\int_0^L dx \exp(-iKxr)/L$ gives the integral definition of the $C_r(P)$ functions

$$\begin{aligned} C_r(P) &= \frac{1}{L} \int_0^L dx e^{-iKxr - iP\epsilon(x)} \\ &= \frac{1}{2\pi} \int_{-\pi}^{\pi} d\theta e^{-ir\theta - iP\xi(\theta)} \end{aligned} \quad (10)$$

For convenience define the shorthand notation $\xi(\theta) \equiv \epsilon(\theta/K)$ i.e. set $Kx = \theta$ and hence $\xi(\theta + 2\pi) = \xi(\theta)$. Eq. (10) can be regarded as a generalization of the Bessel integral definition of the Bessel functions; such functions have been previously investigated by Wassiljeff.¹⁵ The special case $\epsilon(x) = d \cos Kx$ yields $C_r(P) = i^{-r} J_r(P)$.

Now let the field point approach the surface i.e. $\mathbf{r} = (x, z) \rightarrow (x, \epsilon(x))$ and use Meecham's result¹⁶ that this limit commutes with the integral to obtain

$$\frac{1}{4i} \int ds' \frac{\partial P(\mathbf{r}')}{\partial n'} H_0^1(k|\mathbf{r} - \mathbf{r}'|) = -p_{\text{inc}}(\mathbf{r}) \quad (11)$$

Substitution of Eqs. (7), (8) into Eq. (11) yields

$$\frac{k}{4} \sum_{n=-\infty}^{\infty} \psi_n \int_{-\infty}^{\infty} dx' e^{ikx' \cos \phi_n} H_0^1(k|\mathbf{r} - \mathbf{r}'|) = -p_{\text{inc}}(\mathbf{r}) \quad (12)$$

Multiplication of Eq. (12) by the operator $L^{-1} \int_0^L dx \times \exp(-ikx \cos \phi_m)$ gives the form

$$\sum_{n=-\infty}^{\infty} \psi_n V_{m,n}^0 = -2C_m(k \sin \phi_0), \quad (13)$$

where

$$\begin{aligned} V_{m,n}^0 &= \frac{k}{2} \frac{1}{L} \int_0^L dx e^{-ikx \cos \phi_m} \int_{-\infty}^{\infty} dx' e^{ikx' \cos \phi_n} \\ &\quad \times H_0^1(k\sqrt{(x-x')^2 + (\epsilon(x) - \epsilon(x'))^2}). \end{aligned} \quad (14)$$

By introducing the plane wave representation of the Hankel function one obtains Uretsky's well-known integral representation

$$V_{m,n}^0 = -\frac{i}{\pi} \sum_{l=-\infty}^{\infty} \int_{-\infty}^{\infty} dX \frac{C_{l-n}(kX) C_{m-l}(-kX)}{X^2 - \sin^2 \phi_l} \quad (15)$$

Following Uretsky, the contour is chosen by demanding that $\sin \phi_l$ have a positive imaginary part. This expression is the starting point of this paper; additional details of the intermediate steps can be found in Uretsky, Holford, Bishop and Smith, or Purcell. In addition, by returning to Eq. (6), and assuming that the field point z lies above the high point of the surface excursions, Uretsky was able to derive the important formula expressing the reflection coefficients R_l as a sum over the ψ_n coefficients

$$R_l = \sum_{n=-\infty}^{\infty} \frac{C_{l-n}(k \sin \phi_l)}{2 \sin \phi_l} \psi_n \quad (16)$$

This is Eq. (27) of Holford.

II. THE GENERAL PERIODIC SURFACE

To illustrate the next step required, for the moment return to the special case of the sinusoid $\epsilon(x) = d \cos(Kx)$. In that case the functions $C_r(kX) = i^{-r} J_r(k dX)$. By using Uretsky's method [see Appendix C of Uretsky, Appendix C of Bishop and Smith or Eq. (A2) of Purcell⁵ for details] combined with two generalized Kapteyn sums [see Eqs. (B3) and (B43) of Purcell⁵] one may derive a series representation for $V_{m,n}^0$ [set $C_r(x) = i^{-r} J_r(dx)$ in Eq. (25)] which when substituted into Eq. (13) immediately gives the Rayleigh equations.

The same conclusion [that Uretsky's formula Eq. (15) leads to the Rayleigh equations] holds for the general periodic surface, although the details of the proof must be modified. The proof depends on using a Fourier series and an analytic continuation argument. In the sinusoid case, the formulae given in Eqs. (B3) and (B43) of Purcell⁵ did not require analytic continuation but so far this seems necessary for the general periodic surface.

From the integral definition of Eq. (10)

$$\begin{aligned} C_{l-n}(P) C_{m-l}(-P) &= \frac{1}{4\pi^2} \int_{-\pi}^{\pi} d\theta \int_{\pi}^{-\pi} d\vartheta \\ &\quad \times e^{-i(l(\theta-\vartheta) + in\theta - im\vartheta - iP\{\xi(\theta) - \xi(\vartheta)\})} \end{aligned} \quad (17)$$

Now let $\theta - \vartheta = 2\chi$ and $\theta + \vartheta = 2\psi$. From the discussion in Sec. 2.6 of Watson, the integrand in Eq. (17) is unchanged if $\{\chi, \psi\} \rightarrow \{\chi \pm \pi, \psi \pm \pi\}$ or $\{\chi, \psi\} \rightarrow \{\chi \mp \pi, \psi \pm \pi\}$. Therefore the limits of integration can be taken as $0 \leq \chi \leq \pi$ and $-\pi \leq \psi \leq \pi$ and this gives

$$\begin{aligned}
& C_{l-n}(P)C_{m-l}(-P) \\
&= \frac{1}{2\pi^2} \int_0^\pi d\chi \int_{-\pi}^\pi d\psi e^{-i2l\chi+i(m+n)\chi-i(m-n)\psi} \\
&\quad \times e^{-iP\{\xi(\chi+\psi)-\xi(\psi-\chi)\}}. \tag{18}
\end{aligned}$$

Now substitute this result into Uretsky's formula Eq. (15) to obtain

$$\begin{aligned}
V_{m,n}^0 &= -\frac{i}{2\pi^3} \int_0^\pi d\chi \int_{-\pi}^\pi d\psi e^{i(m+n)\chi-i(m-n)\psi} \\
&\quad \times \sum_{l=-\infty}^\infty e^{-i2l\chi} \int_{-\infty}^\infty dX \frac{e^{-ikX\{\xi(\psi+\chi)-\xi(\psi-\chi)\}}}{X^2-\sin^2\phi_l}. \tag{19}
\end{aligned}$$

Again following Uretsky, the contour over the X integral is defined in the usual way by requiring that $\sin\phi_l$ have a positive imaginary part. Hence by closing the contour (in either the upper or lower half-plane) one obtains

$$\begin{aligned}
& \int_{-\infty}^\infty dX \frac{e^{-ikX\{\xi(\psi+\chi)-\xi(\psi-\chi)\}}}{X^2-\sin^2\phi_l} \\
&= \frac{i\pi e^{ik\sin\phi_l|\xi(\psi+\chi)-\xi(\psi-\chi)|}}{\sin\phi_l}, \tag{20}
\end{aligned}$$

provided $\sin\phi_l$ has a positive imaginary part.

Substituting this result into Eq. (19) gives

$$\begin{aligned}
V_{m,n}^0 &= \frac{1}{2\pi^2} \int_0^\pi d\chi \int_{-\pi}^\pi d\psi e^{i(m+n)\chi-i(m-n)\psi} \\
&\quad \times \sum_{l=-\infty}^\infty e^{-i2l\chi} \frac{e^{ik\sin\phi_l|\xi(\psi+\chi)-\xi(\psi-\chi)|}}{\sin\phi_l}. \tag{21}
\end{aligned}$$

So far this is similar to the analysis presented by Uretsky. For the sinusoid case, Uretsky continued this argument by (in effect) splitting the integrations over χ and ψ into the ranges $0 \leq \chi \leq \pi/2$, $0 \leq \psi \leq \pi/2$. He then observed that for the sinusoid $z = d \cos(Kx)$, $|\xi(\psi+\chi) - \xi(\psi-\chi)| = 2d \sin\chi \times \sin\psi \neq 0$. Then he split the factor

$$\begin{aligned}
e^{ik\sin\phi_l|\xi(\psi+\chi)-\xi(\psi-\chi)|} &\equiv e^{2ikd\sin\phi_l\sin\chi\sin\psi} \\
&= \cos(2kd\sin\phi_l\sin\chi\sin\psi) \\
&\quad + i\sin(2kd\sin\phi_l\sin\chi\sin\psi).
\end{aligned}$$

The $\cos(2kd\sin\phi_l\sin\chi\sin\psi)$ factor then leads to the first term in Eq. (A2) of Ref. 5; the $\sin(2kd\sin\phi_l\sin\chi\sin\psi)$ factor leads to the second term in Eq. (A2) of Ref. 5.

Instead of trying to generalize this lengthy argument, consider the case in which the surface wave number K (and $\cos\phi_0$) is assumed to be pure imaginary. From Eq. (5.1) of Oberhettinger⁶ or Eq. (16.1.5) of Hansen¹⁷ one has the Fourier series

$$\begin{aligned}
& \sum_{l=-\infty}^\infty e^{ilx} \frac{\sin\{a\sqrt{b^2+(y+lc)^2}\}}{\sqrt{b^2+(y+lc)^2}} \\
&= \frac{\pi}{c} \sum_{m=m_1}^{m_2} \exp\left[-(2\pi m+x)\frac{iy}{c}\right] \\
&\quad \times J_0(b[a^2-c^{-2}(2\pi m+x)^2]^{1/2}), \tag{22}
\end{aligned}$$

where the integers $m_1 \geq -[(ac+x)/(2\pi)]$ and $m_2 \leq [(ac-x)/(2\pi)]$. (If $[(ac \pm x)/(2\pi)]$ is an integer, one half the the corresponding term in the sum is to be taken. The parameters a , b , c , x , and y are real.) This means that the finite sum on the rhs of Eq. (22) is over all integers that lie between the values $-[(ac+x)/(2\pi)]$ and $[(ac-x)/(2\pi)]$. Assume the parameter values $0 > [(ac-x)/(2\pi)] > -[(ac+x)/(2\pi)] > -1$, and hence the finite sum is an empty sum and the rhs vanishes; i.e.,

$$\begin{aligned}
& \sum_{l=-\infty}^\infty e^{ilx} \frac{\sin\{a\sqrt{b^2+(y+lc)^2}\}}{\sqrt{b^2+(y+lc)^2}} = 0, \\
& 0 > [(ac-x)/(2\pi)] > -[(ac+x)/(2\pi)] > -1. \tag{23}
\end{aligned}$$

This series may be easily verified numerically in the case $0 > [(ac-x)/(2\pi)] > -[(ac+x)/(2\pi)] > -1$. The use of this series is the crucial part of the derivation of the Rayleigh equations given in this paper.

Now by making the identifications $x \equiv -2\chi$, $a \equiv k|\xi(\psi+\chi) - \xi(\psi-\chi)|$, $b \equiv 1$, $ic \equiv K/k$, $iy \equiv \cos\phi_0$ (hence K is pure imaginary) one can apply this result to the sum over l in Eq. (21). This means that the factor $\exp(ik\sin\phi_l|\xi(\psi+\chi) - \xi(\psi-\chi)|)$ in Eq. (21) can be rewritten as $\exp(ik\sin\phi_l\{\xi(\psi+\chi) - \xi(\psi-\chi)\})$ with no loss of generality, since the sum over the $\sin\{k\sin\phi_l|\xi(\psi+\chi) - \xi(\psi-\chi)\}$ factor vanishes by Eq. (23). Hence

$$\begin{aligned}
V_{m,n}^0 &= \frac{1}{2\pi^2} \int_0^\pi d\chi \int_{-\pi}^\pi d\psi e^{i(m+n)\chi-i(m-n)\psi} \\
&\quad \times \sum_{l=-\infty}^\infty e^{-i2l\chi} \frac{e^{ik\sin\phi_l\{\xi(\psi+\chi)-\xi(\psi-\chi)\}}}{\sin\phi_l}. \tag{24}
\end{aligned}$$

Now one can now reuse the integral formula for the product of the C functions given by Eq. (18), to rewrite Eq. (24) as

$$V_{m,n}^0 = \sum_{l=-\infty}^\infty \frac{C_{l-n}(k\sin\phi_l)C_{m-l}(-k\sin\phi_l)}{\sin\phi_l}. \tag{25}$$

The proof of this relation is valid along the finite line segment joining the parameter points $[(ac-x)/(2\pi)] \equiv -\delta_1$ and $-[(ac+x)/(2\pi)] \equiv -\delta_2$ provided the real numbers δ_1 , δ_2 satisfy $0 < \delta_1 < \delta_2 < 1$. In terms of the parameter K , it is valid along the finite segment of the complex K axis passing through the origin and joining the parameter points

$$\begin{aligned}
K_1 &= -i[2\pi\delta_1 + 2\chi]/|\xi(\psi+\chi) - \xi(\psi-\chi)|, \\
K_2 &= i[2\pi\delta_2 + 2\chi]/|\xi(\psi+\chi) - \xi(\psi-\chi)|.
\end{aligned}$$

Note that since Eq. (23) is certainly true if $a=0$, one can assume $a \neq 0$ without loss of generality. In particular since

$a \equiv k|\xi(\psi + \chi) - \xi(\psi - \chi)| = 0$ if $\chi = 0$ or $\chi = \pi$, then only the values $0 < \chi < \pi$ need be considered.

If two functions are equal along a finite line segment lying in a region in which both functions are analytic, then the functions must be equal throughout the entire region in which both functions are analytic (finite and differentiable). Hence by analytic continuation Eq. (25) must be valid for all parameter values for which the series in Eq. (25) is an analytic function (provided the finite line segment of the complex K axis passing through the origin and connecting the points K_1, K_2 is included in this region).

Substitution of Eq. (25) into Eq. (13), the interchange of the sums over n and l and the use of Uretsky's relation

$$\sum_{l=-\infty}^{\infty} \frac{C_{l-n}(k \sin \phi_l) C_{m-l}(-k \sin \phi_l) - C_{l-n}(-k \sin \phi_l) C_{m-l}(k \sin \phi_l)}{\sin \phi_l} = 0. \quad (27)$$

In the special case $z = d \cos(Kx)$, then Eq. (27) reduces to Eq. (B3) of Ref. 5, which was proven using a lengthy argument based on power series expansions and did not require any analytic continuation arguments. For the general series in Eq. (27), so far it seems necessary to use Fourier series and analytic continuation. The method to determine the parameter values for which these series represent analytic functions is given in the following section.

III. REGION OF VALIDITY FOR THE RAYLEIGH EQUATIONS

Provided the surface $\epsilon(x)$ consists of a finite sum of sinusoids and if the $\sin \phi_l \neq 0$ then each term in the series in Eq. (25) is differentiable. Furthermore the series can be differentiated term by term if the series is uniformly convergent. From the Weierstrass M-test, uniform convergence will be implied by absolute convergence within a finite region of the complex K plane. Hence the function represented by the series in Eq. (25) will be analytic if it converges absolutely within some finite region of the complex K plane. In addition one must ensure that the region of convergence includes a finite section of the complex K axis surrounding the origin. It will follow (see Fig. 3) that the region of convergence in the complex K plane includes the origin. One may therefore conclude that Eq. (25) is valid for all parameter values for which the series converges absolutely.

From the Cauchy root test for absolute convergence this means that

$$\begin{aligned} \lim_{|l| \rightarrow \infty} |C_{l-n}(k \sin \phi_l) C_{m-l}(-k \sin \phi_l)|^{1/|l|} \\ = \lim_{|l| \rightarrow \infty} |C_l(iK|l)| C_{-l}(-iK|l)|^{1/|l|} < 1. \end{aligned} \quad (28)$$

Hence the problem amounts to determining the asymptotic behavior, for large argument and large index, of the $C_r(x)$ functions defined through the generalized Bessel integral of Eq. (10). Since complex arguments of the C functions are

connecting the R_m and the ψ_n then leads to the Rayleigh equations for the general periodic surface in the form

$$\sum_{l=-\infty}^{\infty} C_{m-l}(-k \sin \phi_l) R_l = -C_m(k \sin \phi_0), \quad (26)$$

valid for all parameter values for which the generalized sum in Eq. (25) represents an analytic function. This is the form of the Rayleigh equations which are investigated in this paper.

Note that by using Eqs. (18) and (23) and making the same analytic continuation argument as above one can find the following generalized Kapteyn sums:

required for the analytic continuation argument, the method employed in Sec. 8.7 of Watson is required rather than the saddle point methods used by Hill and Celli, and van den Berg and Fokkema.

To illustrate this method in a detailed manner, consider the simplest possible extension (in terms of the symmetry properties of the C functions) of the single sinusoid case: $\epsilon(x) = d \cos(Kx) + d' \cos(3Kx)$. In this special case one has the additional properties $C_{-r}(x) = C_r(x)$ and $C_{-r}(-x) = (-1)^r C_r(x)$; this reduces Eq. (28) to the single constraint

$$\lim_{|l| \rightarrow \infty} |C_{|l|}(iK|l)|^{1/|l|} < 1. \quad (29)$$

(Note that the subsequent analysis is valid for any surface of the form $z = d \cos(Kx) + d' \cos[(2N+1)Kx]$, by making the replacement $3 \rightarrow (2N+1)$.) The following analysis can be made to correspond to Kapteyn's derivation of the Carlini formula as written in Sec. 8.7 of Watson. Rewrite the integral representation of Eq. (10) by making the substitution $t = \exp(i\theta)$ to yield

$$\begin{aligned} C_{|l|}(iK|l) = \frac{1}{2\pi i} \oint \frac{dt}{t^{|l|+1}} \exp\left\{\frac{1}{2}|l|\left(Kd\left[t + \frac{1}{t}\right] \right. \right. \\ \left. \left. + Kd'\left[t^3 + \frac{1}{t^3}\right]\right)\right\}, \end{aligned} \quad (30)$$

where the contour circles the origin once in the positive direction. Now set $t = \exp(i\theta + u)$ where the radius $\exp[u]$ of the contour circling the origin is to be chosen, i.e.,

$$\begin{aligned} C_{|l|}(iK|l) = \frac{1}{2\pi} \int_{-\pi}^{\pi} d\theta \exp\left[|l|\left\{\frac{1}{2}Kd(e^u e^{i\theta} + e^{-u} e^{-i\theta}) \right. \right. \\ \left. \left. + \frac{1}{2}Kd'(e^{3u} e^{i3\theta} + e^{-3u} e^{-i3\theta}) - u - i\theta\right\}\right]. \end{aligned} \quad (31)$$

Now if M is the maximum value of

$$\begin{aligned} |\exp\{\frac{1}{2}Kd(e^u e^{i\theta} + e^{-u} e^{-i\theta}) \\ + \frac{1}{2}Kd'(e^{3u} e^{i3\theta} + e^{-3u} e^{-i3\theta}) - u - i\theta\}| \end{aligned} \quad (32)$$

then one has the upper bound

$$|C_{|l|}(iK|l)| \leq M^{|l|}. \quad (33)$$

Now for simplicity, for the moment assume that K is a real parameter. In that case the real part of

$$\frac{1}{2} Kd(e^u e^{i\theta} + e^{-u} e^{-i\theta}) + \frac{1}{2} Kd'(e^{3u} e^{i3\theta} + e^{-3u} e^{-i3\theta}) - u - i\theta \quad (34)$$

is

$$Kd \cosh(u) \cos(\theta) + Kd' \cosh(3u) \cos(3\theta) - u. \quad (35)$$

This reaches its maximum value w.r.t. θ when $\theta=0$ and its value is

$$Kd \cosh(u) + Kd' \cosh(3u) - u. \quad (36)$$

Hence for all positive u

$$|C_{|l|}(iK|l)| \leq \exp\{ |l| [Kd \cosh(u) + Kd' \cosh(3u) - u] \}. \quad (37)$$

To obtain the strongest inequality possible, choose u to minimize the rhs of the previous equation, i.e.,

$$Kd \sinh(u) + 3Kd' \sinh(3u) = 1. \quad (38)$$

In the case of the single sinusoid $d'=0$, then Eq. (38) can be solved analytically as $u = \sinh^{-1}(1/Kd)$ and Eq. (29) reduces to $|(Kd)e^{\sqrt{1+(Kd)^2}/(1+\sqrt{1+(Kd)^2})}| < 1$. As noted in Eq. (31) of Purcell,⁵ the numerical solution of this constraint for Kd real gives $Kd < 0.6627$ and this is the region of validity (for Kd real) of the Rayleigh equations for the single sinusoid. In the case of Eq. (38), the solution for u is determined numerically as $u = u_{\min}(Kd, Kd')$. From Eq. (29) the Rayleigh validity constraint then amounts to

$$Kd \cosh[u_{\min}(Kd, Kd')] + Kd' \cosh[3u_{\min}(Kd, Kd')] - u_{\min}(Kd, Kd') < 0. \quad (39)$$

In terms of the maximum slopes of the individual sinusoids Kd and $3Kd'$, the numerical solution of Eqs. (38), (39)

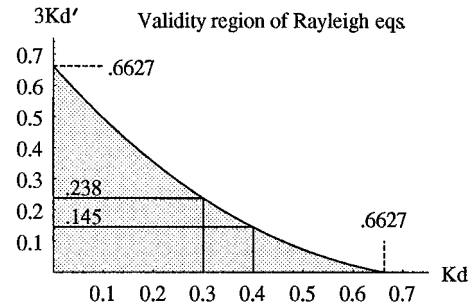


FIG. 2. The region of validity of the Rayleigh equations in the Fourier form. The shaded area gives the allowed values of the slopes Kd and $3Kd'$ for a composite surface $z = d \cos(Kx) + d' \cos(3Kx)$. In the interior of this region the generalized Kapteyn series $V_{m,n}^0 = \sum_{l=-\infty}^{\infty} C_{l-m}(k \sin \phi_l) C_{m-l} \times (-k \sin \phi_l) / \sin \phi_l$ converges absolutely and this implies that the Rayleigh equations [Eq. (26)] are valid. For use in Fig. 5, note the boundary values $(Kd, 3Kd') = (0.3, 0.238)$ and $(Kd, 3Kd') = (0.4, 0.145)$.

gives the shaded region shown in Fig. 2. In any event, the Rayleigh validity constraint requires both $Kd < 0.6627$ and $3Kd' < 0.6627$. Now observe that for the parameter values $Kd=0.3$ and $Kd=0.4$, Fig. 2 predicts that the region of convergence extends out to the values $3Kd'=0.238$ and $3Kd'=0.145$, respectively. These values can be easily obtained by the following recipe: (1) find the value of $u = u_{\min}(3Kd', Kd)$ which minimizes $Kd \cosh u + Kd' \cosh 3u - u$, (2) substitute this value of u into the equation $Kd \cosh u + Kd' \cosh 3u - u = 0$, (3) the numerical solution of the previous equation then gives the boundary of the region in the $3Kd' - Kd$ plane in which the constraint given in Eq. (39) holds. As an illustration of the simplicity of the numerical analysis required, in the Mathematica¹⁸ computer language, this procedure can be implemented by the following computer code:

```
In[1] := s2[s1_] := s2/.FindRoot[FindMinimum[s1*Cosh[u]+s2*Cosh[3*u]/3-u,
{u,0}][[1]]==0,{s2,0,.1}];{s2.[3],s2.[4]}
Out[1] = {0.238046,0.145195}.
```

The program variables $s2$, $s1$ have the physical meaning $s2 \equiv 3Kd'$, $s1 \equiv Kd$. (These values will be used in Fig. 5 to examine truncation solutions for the R_m .)

The case $\epsilon(x) = d \cos(Kx) + d' \cos(3Kx + \omega)$ with the phase factor $0 \leq \omega \leq 2\pi$ can also be treated by an extension of this approach. In that case the value of θ that maximizes the integrand [Eq. (31)] in the integral definition of the functions $C_{|l|}(iK|l)$ and $C_{-|l|}(-iK|l)$ must also be found numerically. For reasons of brevity this case will not be developed here. One finds that as the phase ω increases from 0, the region of validity of the Rayleigh equations shown as the

shaded area in Fig. 2 increases. The maximal extension of the validity region occurs for the phase difference $\omega = \pi$. Similar comments apply for the most general case $z = \sum_{n=1}^M d_n \cos(nKx + \omega_n)$.

In the foregoing it was assumed that the surface wave number K was a real parameter. These previous results may be generalized to allow complex values of the surface wave number K . If it is assumed that d' , d are real parameters and K is allowed to be complex $K \equiv |K|e^{i\alpha}$, then in place of Eq. (39) the convergence constraint for the series expression for $V_{m,n}^0$ becomes

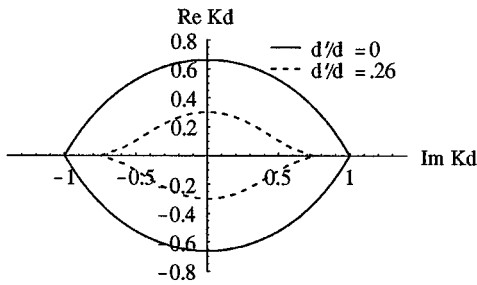


FIG. 3. The region of convergence of the series expression for $V_{m,n}^0$ for complex values of the surface wave number K , for a composite surface $z = d \cos(Kx) + d' \cos(3Kx)$. The interior of the oval region surrounding the origin of the complex Kd plane gives the complex values of Kd for which the generalized Kapteyn series $V_{m,n}^0 = \sum_{l=-\infty}^{\infty} C_{l-n}(k \sin \phi_l) C_{m-l} \times (-k \sin \phi_l) / \sin \phi_l$ converges absolutely. The solid curve is for the case $d'/d=0$ and this is just the "domain K " from Sec. 8.7 of Watson. The dashed line is the case $d'/d=0.264$; note that the dashed curve crosses the real axis at $Kd=0.3$ and this gives $3Kd'=0.238$, consistent with Fig. 2. The effect of adding extra sinusoids to the rough surface is therefore to shrink the region of convergence in the complex Kd plane.

$$\begin{aligned} & \frac{1}{2} |K| d \{ e^u \cos(\theta + \alpha) + e^{-u} \cos(\theta - \alpha) \} \\ & + \frac{1}{2} |K| d' \{ e^{3u} \cos(3\theta + \alpha) + e^{-3u} \cos(3\theta - \alpha) \} \\ & - u < 0. \end{aligned} \quad (40)$$

The value of $\theta = \theta(u, |K|, \alpha, d, d')$ is determined by maximizing the lhs of Eq. (40) w.r.t. θ (if $\alpha=0$, this value would be $\theta=0$). The value of $u = u(|K|, \alpha, d, d')$ is obtained by minimizing the lhs w.r.t. u . This gives a single constraint involving $|K|$, α , d , and d' . The numerical solution of Eq. (40) gives the allowed complex values as a finite area surrounding the origin of the complex K plane as shown in Fig. 3. Since the region of convergence includes a finite section of the complex K axis passing through the origin, Fig. 3 validates the analytic continuation argument in Sec. II. Further details follow the same arguments as in Sec. 8.7 of Watson and are left to the reader.

IV. THE EQUATIONS OF THE SECOND KIND

The Rayleigh equations for the periodic surface suffer from the same technical problems as in the single sinusoid case. In attempting to solve Eq. (26) by truncation, one may observe that the condition number of the truncated matrix of coefficients

$$\mathcal{M}_{j,l} \equiv \begin{cases} C_{j-l}(-k \sin \phi_l), & \{|j|, |l|\} \leq N \\ 0, & \text{otherwise.} \end{cases}$$

increases without bound (even for parameters within the region of validity of the Rayleigh equations) as the size of the truncation matrix increases (see Fig. 2 of Ref. 5). This will eventually require that the precision of the calculations be increased at the cost of extra computing time. In addition there are no existence or uniqueness theorems available for such infinite sets of linear equations of the "first kind." For the periodic surface, Holford observed that this deficiency could be removed by obtaining equations of the "second kind" for the ψ_m coefficients. To obtain these equations,

take the normal derivative of the Helmholtz formula first, then take the limit as the field point approaches the surface. In this manner Holford obtained the equations [see Eqs. (39), (40), and (42) of Holford¹⁴]

$$\psi_m + \sum_{n=-\infty}^{\infty} V_{m,n}^1 \psi_n = 2 \hat{\psi}_m, \quad (41)$$

where

$$\hat{\psi}_m = - \left[\sin \phi_0 - \frac{mK \cos \phi_0}{k \sin \phi_0} \right] C_m(k \sin \phi_0). \quad (42)$$

The matrix $V_{m,n}^1$ is given by

$$\begin{aligned} V_{m,n}^1 &= \frac{ik}{2L} \int_0^L dx e^{-iKx(m-n)} \int_{-\infty}^{\infty} dx' e^{ik(x'-x)\cos \phi_n} \\ & \times \frac{H_1^1(k \sqrt{(x-x')^2 + (\epsilon(x) - \epsilon(x'))^2})}{\sqrt{(x-x')^2 + (\epsilon(x) - \epsilon(x'))^2}} \\ & \times \left[\epsilon(x') - \epsilon(x) - (x'-x) \frac{d\epsilon(x)}{dx} \right]. \end{aligned} \quad (43)$$

By manipulating this integral expression for $V_{m,n}^1$, Holford was able to prove that these are equations of the "second kind," and hence proved existence and uniqueness of the truncation solutions for the ψ_m .

By following the same procedure as for the $V_{m,n}^0$ matrix one may derive an analogue of Uretsky's integral representation i.e. by substituting the plane wave integral representation for the Hankel function one obtains Eq. (44) of Purcell⁵

$$\begin{aligned} V_{m,n}^1 &= \frac{i}{2L\pi^2} \int_0^L dx e^{-iKx(m-n)} \int_{-\infty}^{\infty} d\tau e^{ik\tau \cos \phi_n} \\ & \times \int_{-\infty}^{\infty} dP_x \int_{-\infty}^{\infty} dP_z \frac{e^{iP_x \tau + iP_x(\epsilon(x) - \epsilon(x+\tau))}}{P_x^2 + P_z^2 - k^2} \\ & \times \left[P_z + P_x \frac{d\epsilon(x)}{dx} \right]. \end{aligned} \quad (44)$$

Now expand the exponential factors using Eq. (9), perform the τ integral in terms of a Dirac delta function, and the x integral in terms of Kronecker delta functions {use the generating function [Eq. (9)] to rewrite the $d\epsilon(x)/dx$ factor} to obtain

$$\begin{aligned} V_{m,n}^1 &= \frac{i}{\pi} \int_{-\infty}^{\infty} dX \frac{C_{m-l}(-kX) C_{l-n}(kX)}{X^2 - \sin^2 \phi_l} \\ & \times \left[X + \frac{K(l-m) \cos \phi_l}{kX} \right]. \end{aligned} \quad (45)$$

Now by introducing the integral formula Eq. (18), the Fourier series given in Eq. (23) and the analytic continuation argument used in Sec. II, one obtains the series representation

$$\begin{aligned} V_{m,n}^1 &= - \sum_{l=-\infty}^{\infty} C_{m-l}(-k \sin \phi_l) C_{l-n}(k \sin \phi_l) \\ & \times \frac{[1 - \cos \phi_l \cos \phi_m]}{\sin^2 \phi_l} + \delta^{m,n}. \end{aligned} \quad (46)$$

Furthermore, by applying the Cauchy root test for absolute convergence, it follows that the region of convergence for this series representation of $V_{m,n}^1$ is the same as the region of convergence of the series representation of $V_{m,n}^0$ given in Eq. (25).

Substitution into Eq. (41) and the use of Eq. (16) leads to

$$\begin{aligned} \psi_m - \sum_{l=-\infty}^{\infty} C_{m-l}(-k \sin \phi_l) \frac{[1 - \cos \phi_l \cos \phi_m]}{\sin \phi_l} R_l \\ = - \frac{[1 - \cos \phi_m \cos \phi_0]}{\sin \phi_0} C_m(k \sin \phi_0). \end{aligned} \quad (47)$$

For most applications it is the reflection coefficients which are required, not the ψ_m coefficients. These equations of the second kind for the ψ_m may be converted to equations of the second kind for the reflection coefficients. Multiply both sides by $\sum_{m=-\infty}^{\infty} C_{j-m}(k \sin \phi_j)/2 \sin \phi_j$ to obtain

$$\begin{aligned} R_j - \sum_{l,m=-\infty}^{\infty} C_{j-m}(k \sin \phi_j) C_{m-l}(-k \sin \phi_l) \\ \times \frac{[1 - \cos \phi_l \cos \phi_m]}{2 \sin \phi_j \sin \phi_l} R_l \\ = - \sum_{m=-\infty}^{\infty} \frac{[1 - \cos \phi_m \cos \phi_0]}{2 \sin \phi_j \sin \phi_0} \\ \times C_{j-m}(k \sin \phi_j) C_m(k \sin \phi_0). \end{aligned} \quad (48)$$

The sum over the index m above can be performed analytically using analogues of the Bessel function summation formulae $\sum_{r=-\infty}^{\infty} J_r(x) J_{p-r}(y) = J_p(x+y)$ and so on.

To derive the required summation formulae, return to the generating function for the $C_r(x)$ functions. From Eq. (9)

$$e^{-ix\xi(\theta)} = \sum_{r=-\infty}^{\infty} e^{ir\theta} C_r(x), \quad (49)$$

$$e^{-iy\xi(\theta)} = \sum_{r'=-\infty}^{\infty} e^{ir'\theta} C_{r'}(y).$$

As for the Bessel function case in Sec. 2.4 of Watson, multiply these two formulae together and equate powers of $\exp(i\theta)$ to obtain

$$\sum_{r=-\infty}^{\infty} C_r(x) C_{p-r}(y) = C_p(x+y). \quad (50)$$

By differentiation of the first of the formulae in Eqs. (49) w.r.t. θ and then following the same procedure as above gives the results

$$\begin{aligned} \sum_{r=-\infty}^{\infty} r C_r(x) C_{p-r}(y) = \frac{px}{(x+y)} C_p(x+y), \\ (x+y) \neq 0, \end{aligned} \quad (51)$$

$$\sum_{r=-\infty}^{\infty} r C_r(x) C_{-r}(-x) = 0. \quad (52)$$

These last three summation formulae yield the following collection of sums:

$$\begin{aligned} \sum_{m=-\infty}^{\infty} C_{m-l}(-k \sin \phi_l) C_{j-m}(k \sin \phi_j) \\ = C_{j-l}(k[\sin \phi_j - \sin \phi_l]), \end{aligned} \quad (53)$$

$$\begin{aligned} \sum_{r=-\infty}^{\infty} (m-l) C_{m-l}(-k \sin \phi_l) C_{j-m}(k \sin \phi_j) \\ = \frac{-(j-l) \sin \phi_l}{(\sin \phi_j - \sin \phi_l)} C_{j-l}(k[\sin \phi_j - \sin \phi_l]), \quad j \neq l, \end{aligned} \quad (54)$$

$$\sum_{m=-\infty}^{\infty} (m-j) C_{m-j}(-k \sin \phi_j) C_{j-m}(k \sin \phi_j) = 0, \quad (55)$$

$$\begin{aligned} \sum_{m=-\infty}^{\infty} C_m(k \sin \phi_0) C_{j-m}(k \sin \phi_j) \\ = C_j(k[\sin \phi_j + \sin \phi_0]), \end{aligned} \quad (56)$$

$$\begin{aligned} \sum_{m=-\infty}^{\infty} m C_m(k \sin \phi_0) C_{j-m}(k \sin \phi_j) \\ = \frac{j \sin \phi_0}{\sin \phi_j + \sin \phi_0} C_j(k[\sin \phi_j + \sin \phi_0]). \end{aligned} \quad (57)$$

Equations (51)–(57) allow one to rewrite Eq. (48) as

$$R_j - \sum_{l=-\infty}^{\infty} M_{j,l} R_l = \tilde{\psi}_j, \quad (58)$$

where

$$\begin{aligned} \tilde{\psi}_j = - \frac{[1 - \cos \phi_0 \cos \phi_j + \sin \phi_0 \sin \phi_j]}{\sin \phi_j (\sin \phi_0 + \sin \phi_j)} \\ \times C_j(k[\sin \phi_0 + \sin \phi_j]), \\ M_{j,j} = 0, \end{aligned} \quad (59)$$

$$\begin{aligned} M_{j,l} = \frac{C_{j-l}(kd[\sin \phi_j - \sin \phi_l])}{\sin \phi_j} \\ \times \frac{[1 - \cos \phi_l \cos \phi_j - \sin \phi_l \sin \phi_j]}{(\sin \phi_l - \sin \phi_j)}, \end{aligned}$$

$$j \neq l.$$

These equations are the generalization of Eqs. (63) of Purcell,⁵ valid for an arbitrary periodic surface consisting of a finite sum of sinusoids. Now following Holford, these are equations of the second kind provided

$$\sum_{j,l=-\infty}^{\infty} |M_{j,l}|^2 < \infty, \quad \sum_{m=-\infty}^{\infty} |\tilde{\psi}_m|^2 < \infty. \quad (60)$$

By generalizing the arguments in Appendix C of Purcell,⁵ these conditions are valid for the same parameter values for which the generalized Kapteyn series for $V_{m,n}^0$ converges absolutely.

A useful observation (but not of course a new one) is that the rhs of Eq. (58) is just the unshadowed Kirchhoff approximation $\partial p(x, z)/\partial n|_{z=\epsilon(x)} = 2\partial p_{\text{inc}}(x, z)/\partial n|_{z=\epsilon(x)}$ for the periodic surface, i.e.,

$$R_j^{\text{Kirchhoff}} = - \frac{[1 - \cos \phi_0 \cos \phi_j + \sin \phi_0 \sin \phi_j]}{\sin \phi_j (\sin \phi_0 + \sin \phi_j)} \times C_j(k[\sin \phi_0 + \sin \phi_j]). \quad (61)$$

V. SOME ADDITIONAL NUMERICAL RESULTS

Now consider a truncation solution of Eqs. (58) for the particular coefficient R_M , i.e.,

$$\sum_{l=-\infty}^{\infty} a_{j,l} R_l = b_j, \quad (62)$$

$$b_j = \begin{cases} \tilde{\psi}_j, & -P+M \leq j \leq P+M, \\ 0, & -P+M > j > P+M, \end{cases} \quad (63)$$

$$a_{j,l} = \begin{cases} \delta^{j,l} - M_{j,l}, & -P+M \leq \{j, l\} \leq P+M, \\ 0, & \text{otherwise.} \end{cases}$$

Denote the solution obtained by solving these $(2P+1)$ equations in $(2P+1)$ unknowns as $R_M(2P+1)$. Note that in the single sinusoid case $z = d \cos(Kx)$, the $C_r(x)$ functions reduce to $i^{-r} J_r(x)$, which are easy to numerically evaluate. For the general periodic surface case the $C_r(x)$ are evaluated by numerically integrating the Bessel type integral given by Eq. (10); simple trapezoidal integration seems to work the best. About 10–15 lines of computer code are required to construct a program to solve Eqs. (62).

To show the effect on the reflection coefficients of superimposing a ripple of period $L/3$ on a sinusoid of period L , again consider the simplest possible extension of the sinusoid case $z = d \cos(Kx) + Kd' \cos(3Kx)$. Numerical values for $R_m(N)$ for a specific choice of the parameters m, k, d, d', K, ϕ_0 take on order of one minute (for $N \approx 29$) by circa 1996 desktop computing (a 66 MHz processor). For the parameter values $\phi_0 = 45^\circ$, $Kd = 0.3$, and $3Kd' = \{0, 1\}$ ($d'/d = \{0, 1/9\}$), plots of $|R_0|$ and $|R_{-1}|$ vs kd are shown in Fig. 4. By inspection of these plots, it is clear that the ripple is important at higher frequencies. For the specular component, the effect of the ripple is considerable for $kd > 2$. Note that the positions of the Rayleigh anomalies $\sin \phi_n = 0$, indicated by the presence of certain cusps in the plots of $|R_0|$ and $|R_{-1}|$, are of course unchanged by the addition of the ripple. Figure 4 may be useful as a simple benchmark for the reader to test code for solving for reflection coefficients.

To demonstrate the convergence of the truncation solution of Eqs. (58) for the reflection coefficients again consider the simplest possible extension of the sinusoid case $z = d \cos(Kx) + Kd' \cos(3Kx)$. Return to Fig. 2 and recall that for the particular parameter choices $Kd = 0.3$ and $Kd = 0.4$, Fig. 2 predicted that the region of convergence of the series representations for $V_{m,n}^0$ (and $V_{m,n}^1$) extends out to the values $3Kd' \leq 0.238$ and $3Kd' \leq 0.145$ respectively. Now consider a truncation solution of Eqs. (58) for the particular coefficient R_M . The relative change in the truncation solutions as the size N of the truncation matrix $a_{j,l}$ is increased by 2 is

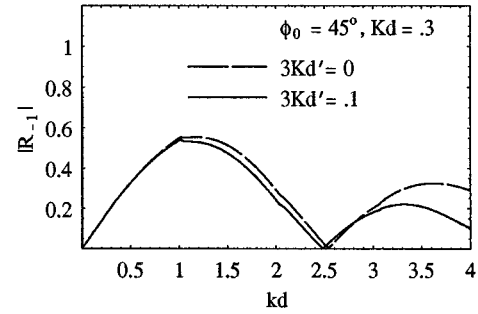
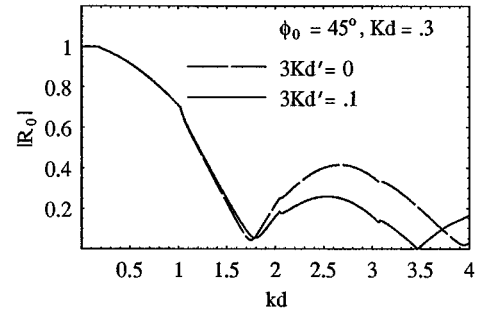


FIG. 4. Plots of the reflection coefficients $|R_0|$ and $|R_{-1}|$, for the periodic surface $z = d \cos(Kx) + d' \cos(3Kx)$. The parameter values $\phi_0 = 45^\circ$, $Kd = 0.3$, and $3Kd' = \{0, 0.1\}$ ($d'/d = \{0, 1/9\}$) are used in this illustration. By comparing the cases $d'/d = \{0, 1/9\}$, it is clear that the effect of the ripple increases as the frequency increases.

just $|1 - |R_M(N)/R_M(N+2)||$. Provided the truncation solutions are converging this means that this quantity should be small for N large. A plot of $|1 - |R_0(N)/R_0(N+2)||$ versus $3Kd'$ is shown in Fig. 5 for several large values of the truncation matrix size N . The predictions of Fig. 2 are confirmed in Fig. 5. For the parameter values $Kd = 0.3$ and $Kd = 0.4$, the relative changes in the value of the truncation solutions remain small for values $3Kd' \leq 0.238$ and $3Kd' \leq 0.145$ respectively and diverge thereafter. The parameter values $\phi_0 = 45^\circ$ and $kd = 1.0$ are used in this illustration. Fig. 5 can be regarded as the generalization of Fig. 4 of Purcell.⁵

VI. RELATIONSHIP BETWEEN DIFFERENT FORMS OF THE RAYLEIGH EQUATIONS

During the course of the review process for this paper some interesting arguments have been exchanged with one of the reviewers (hereafter referred to as reviewer ‘‘C’’) regarding the regions of validity of different forms of the Rayleigh equations. Some of these are points are sketched below. For the purposes of the subsequent discussion, only the sinusoid case will be considered, hence $\epsilon(x) \equiv d \cos Kx$. The two equations under discussion in this section are Rayleigh’s equations in the form analyzed in this current paper

$$\sum_{l=-\infty}^{\infty} i^{l-m} J_{l-m}(kd \sin \phi_l) R_l = -i^{-m} J_m(kd \sin \phi_0) \quad (64)$$

and Rayleigh’s expansion for the pressure on the surface of the pressure-release sinusoid

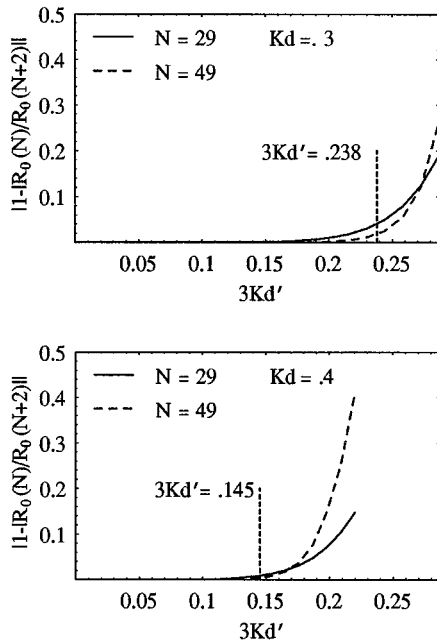


FIG. 5. The region of convergence of the truncation solution of the equations of the second kind, Eqs. (58), for the periodic surface $z = d \cos(Kx) + d' \cos(3Kx)$. The vertical axis gives the relative change in succeeding truncation solutions of Eq. (58) for $|R_0|$, i.e., $|1 - |R_0(N+2)||$ versus the slope $3Kd'$, where $R_0(N)$ denotes the solution obtained by taking N equations in N unknowns. Note that the solutions are well-behaved for the parameter values predicted by Fig. 2; namely if $Kd = .3$ the solutions are well-behaved up to the value $3Kd' \leq 0.238$, for $Kd = 0.4$ for values $3Kd' \leq 0.145$. The parameter values $\phi_0 = 45^\circ$ and $kd = 1.0$ are used in this illustration.

$$\sum_{l=-\infty}^{\infty} R_l e^{ik(x \cos \phi_l + \epsilon(x) \sin \phi_l)} = -e^{ik(x \cos \phi_0 - \epsilon(x) \sin \phi_0)}. \quad (65)$$

“C” refers to Eqs. (64) and (65) as the Rayleigh equations in “Fourier” and “coordinate” representation respectively.

As expressed by “C,” from Eqs. (8), (9), and (16), one has the integral representation

$$R_l = \frac{1}{4\pi \sin \phi_l} \int_{-\pi}^{\pi} d\theta \psi(\theta/K) e^{-ik\theta \cos \phi_l/K - ik \sin \phi_l \epsilon(\theta/K)}. \quad (66)$$

As $|l| \rightarrow \infty$ then $\sin \phi_l \rightarrow iK|l|/k$. “C” now points out that the resulting integral for R_l can be estimated by steepest descent (see Millar’s work for example) giving the asymptotic result

$$R_l \rightarrow \text{const} \frac{1}{\sqrt{3/2}} \exp[K(-ix_* + \epsilon(x_*))l], \quad (67)$$

where the saddle point x_* is defined by $\epsilon'(x_*) = i$ or equivalently $Kx_* = -i \sinh^{-1}(1/Kd)$. “C” then considers the special point $Kx = \pi$ and applies the Cauchy root test to the series on the l.h.s. of Eq. (65), to obtain the following necessary and sufficient condition for absolute convergence

$$e^{K[\text{Re}(-ix_* + \epsilon(x_*)) + d]} < 1. \quad (68)$$

This can be rewritten as

$$\text{Re}(-ix_* + \epsilon(x_*)) < -d. \quad (69)$$

This is Millar’s criterion and leads to the constraint $Kd \leq 0.448$. Since $\epsilon(x) = \min[\epsilon(x)]$ at $Kx = \pi$, this is a necessary and sufficient condition for demanding absolute convergence at all points on the surface. [From Art. 22 of Bromwich,¹⁹ it may also be noted that the series in Eq. (65) converges, in contrast to absolute convergence, for all values of the slope and for all points on the surface with the possible exception of the points $Kx = 0, \pi, 2\pi$.]

In response Purcell pointed that by a trivial rewriting of Eq. (67) by substituting $Kx_* = -i \sinh^{-1}(1/Kd)$, one has

$$\lim_{l \rightarrow \infty} |R_l|^{1/l} = \left| \frac{(Kd)e^{\sqrt{1+(Kd)^2}}}{1 + \sqrt{1+(Kd)^2}} \right|. \quad (70)$$

From the Carlini formula in (1) 8.7 of Watson it follows that

$$\lim_{l \rightarrow \infty} |J_{l-m}(kd \sin \phi_l)|^{1/l} = \lim_{l \rightarrow \infty} |J_l(ikdl)|^{1/l} \leq \left| \frac{(Kd)e^{\sqrt{1+(Kd)^2}}}{1 + \sqrt{1+(Kd)^2}} \right|. \quad (71)$$

Hence by applying the Cauchy root test one obtains the sufficient condition for the absolute convergence of the series in Eq. (64)

$$\left| \frac{(Kd)e^{\sqrt{1+(Kd)^2}}}{1 + \sqrt{1+(Kd)^2}} \right| < 1 \quad (72)$$

This is the domain “K” from the theory of Kapteyn series (see Chapters 8.7 and 17 of Watson) and as was stated in Ref. 5 of the manuscript, the numerical solution of this constraint gives the sufficient condition $Kd < 0.6627$ (Note that the boundary value $Kd = 0.6627$ was not investigated in Ref. 5, hence this condition is sufficient only.)

On the other hand one can multiply Eq. (65) by $L^{-1} \exp[-ikx \cos \phi_m]$, integrate over $\int_{-L/2}^{L/2} dx$ term by term (the assumed absolute convergence implies uniform convergence) and obtain Eq. (64). Furthermore one can multiply Eq. (64) by $\exp[ikx \cos \phi_m]$, take the sum $\sum_{m=-\infty}^{\infty}$, interchange the sums over m and l , perform the sum over m using the generating function for Bessel functions, and get Eq. (65). This leads to what “C” characterizes as a contradiction, namely that Eqs. (64) and (65), hitherto assumed to be completely equivalent, have different regimes of validity (defined by the requirement of absolute convergence). “C” proposes to resolve this contradiction by stating that Eqs. (64), (65) are not completely equivalent, that the interchange of the sums required in deriving Eq. (64) from Eq. (65), can only be carried out if Millar’s more restrictive assumption holds. “C” avers that statements such as “... the Rayleigh equations are valid if $Kd < 0.6627$...” must be sharpened to specify that this constraint refers to the Fourier form of the Rayleigh equations, Eq. (64). Likewise the meaning of Millar’s constraint $Kd \leq 0.448$ must be associated with Eq. (65), what “C” terms the coordinate form of the Rayleigh equations.

It appears that “C’s” ideas regarding the absolute convergence of the sum in Eq. (65) can be extended. Instead of

demanding absolute convergence at all points on the surface, consider an arbitrary point $(x, \epsilon(x))$ where $-\pi/2 \leq Kx \leq \pi/2$ (modulo multiples of 2π); this point lies somewhere on the “hills” of the sinusoid. If $\pi/2 < Kx < 3\pi/2$ (modulo multiples of 2π) then the point lies somewhere on the “valleys” of the sinusoid. From the Cauchy root test and Eq. (70), the series in Eq. (65) converges absolutely if

$$\left| \frac{(Kd)e^{-kd \cos Kx} e^{\sqrt{1+(Kd)^2}}}{1 + \sqrt{1+(Kd)^2}} \right| < 1. \quad (73)$$

If one demanded that this hold at $Kx = \pi$, then this gives $|(Kd)e^{Kd} e^{\sqrt{1+(Kd)^2}} / (1 + \sqrt{1+(Kd)^2})| < 1$ which is a trivial rewriting of Millar’s criterion with solution $Kd \leq 0.448$. But if the point lies somewhere on the “hills” of the sinusoid $-\pi/2 \leq Kx \leq \pi/2$, then $-Kd \cos Kx \leq 0$ and Eq. (73) becomes

$$\left| \frac{(Kd)e^{-\mu Kd} e^{\sqrt{1+(Kd)^2}}}{1 + \sqrt{1+(Kd)^2}} \right| < 1, \quad 0 \leq \mu \leq 1. \quad (74)$$

For $\mu=1$ this constraint is satisfied for all finite values of $Kd < \infty$, for $\mu=0$ the constraint is satisfied for $Kd < 0.6627$; in the general case $0 \leq \mu \leq 1$ numerical analysis shows that $Kd < 0.6627$ is sufficient. Hence in the range $Kd < 0.6627$, the series in Eq. (65) converges absolutely if $-\pi/2 \leq Kx \leq \pi/2$. The situation can be summarized by stating that the series in Eq. (65) converges absolutely at all points on the surface if and only if $Kd \leq 0.448$, in the range $0.448 < Kd < 0.6627$ it converges absolutely on the hills, but will fail to converge absolutely at least at some points on the valleys. This raises an intriguing possibility. Can Eq. (64) be derived by requiring that Eq. (65) holds (i.e., that the series converges absolutely) only on the hills of the surface rather than demanding that it be valid everywhere on the surface?

Assume that $Kd < 0.6627$ and hence that Eq. (65) is valid for $-\pi/2 \leq Kx \leq \pi/2$. Multiply Eq. (65) by $2L^{-1} \exp[-ikx \cos \phi_p]$, integrate over $\int_{-L/4}^{L/4} dx$ term by term and obtain

$$\sum_{l=-\infty}^{\infty} i^{l-p} \{J_{l-p}(kd \sin \phi_l) - iE_{l-p}(kd \sin \phi_l)\} R_l = -i^{-p} \{J_p(kd \sin \phi_0) + iE_p(kd \sin \phi_0)\}. \quad (75)$$

The $E_p(X)$ are the Weber functions defined in Chapter 10 of Watson, with elementary properties $E_{-n}(X) = (-1)^n E_n(X)$, $E_n(-X) = -(-1)^n E_n(X)$, $E_{2n}(0) = 0$, and $E_{2n+1}(0) = 2/[\pi(2n+1)]$. [The asymptotic behaviour of the $E_n(X)$ functions is the same as the Bessel functions, i.e., Eq. (71) also holds with $E_{l-m}(kd \sin \phi_l)$ replacing $J_{l-m}(kd \sin \phi_l)$. This means that the sum over the Weber functions in Eq. (75) is absolutely convergent if $Kd < 0.6627$.] The Weber functions can be expressed as sums over the Bessel functions of opposite parity. From Chapters 1 and 10 of Watson [see also Eqs. (59.3.12), (59.3.23) of Hansen] one has

$$E_j(X) = \frac{1}{2\pi} \sum_{\substack{r=-\infty \\ r \neq j}}^{\infty} [1 - (-1)^{j-r}] \frac{J_r(X)}{(j-r)}, \quad (76)$$

$$J_j(X) = \frac{1}{\pi} \sum_{\substack{r=-\infty \\ r \neq j}}^{\infty} [1 - (-1)^{j-r}] \frac{E_r(X)}{(r-j)}. \quad (77)$$

Hence by multiplying Eq. (64) by $(i/2\pi)i^{m-p}[1 - (-1)^{p-m}]/(p-m)$, summing over $\sum_{m \neq p}$, interchanging the sums over m and l , and using Eq. (76), one obtains

$$-i \sum_{l=-\infty}^{\infty} i^{l-p} E_{l-p}(kd \sin \phi_l) R_l = -i i^{-p} E_p(kd \sin \phi_0). \quad (78)$$

Adding Eqs. (64) and (78) then gives Eq. (75). The converse can be shown by multiplying Eq. (75) by $(1/i\pi)i^{p-m}[1 - (-1)^{p-m}]/(p-m)$, summing over $\sum_{p \neq m}$, interchanging the sums over p and l , and using Eqs. (76), (77) yielding

$$\sum_{l=-\infty}^{\infty} i^{l-m} \{J_{l-m}(kd \sin \phi_l) - 2iE_{l-m}(kd \sin \phi_l)\} R_l = -i^{-m} \{J_m(kd \sin \phi_0) + 2iE_m(kd \sin \phi_0)\}. \quad (79)$$

Multiplying Eq. (75) by 2 and subtracting Eq. (79) then gives Eq. (64). Hence Eq. (64) is completely equivalent to Eq. (75), provided the interchanges of summation can be rigorously justified.

These arguments make it clear that Purcell’s original attempt (see line 18, p. 2925 of Ref. 5) to reconcile the apparent discrepancy between the constraints $Kd < 0.6627$ and $Kd \leq 0.448$ (namely the postulate that Eq. (65) remains valid at all points on the surface in the range $Kd < 0.6627$) is incorrect. Instead the author proposes a modified resolution, namely the Rayleigh expansion [Eq. (65)] in terms of outgoing plane waves remains valid on the hills of the sinusoid if $Kd < 0.6627$, and this is sufficient to derive the Rayleigh equations in the form of Eq. (64). In the absence of a rigorous proof of the permissibility of commuting the repeated sums in the previous derivation, “C’s” caveat that the sufficient constraint $Kd < 0.6627$ applies only to the Rayleigh equations in the Fourier form of Eq. (64) would have to be added to subsequent discussions. The sufficient conditions derived in this paper, apply to the Rayleigh equations in the Fourier form of Eq. (26).

VII. CONCLUSION

The chief new insight in this paper is the use of the Fourier series in Eq. (23) to derive the series representation $V_{m,n}^0 = \sum_{l=-\infty}^{\infty} C_{l-n}(k \sin \phi_l) C_{m-l}(-k \sin \phi_l) / \sin \phi_l$, valid for any periodic surface consisting of a finite sum of sinusoids. This result implies that the Rayleigh equations in the form of Eq. (26), remain valid for such periodic surfaces provided the slopes of the individual sinusoids satisfy the constraint that this series for $V_{m,n}^0$ converges absolutely. For such periodic surfaces the region of convergence can be deduced from the Cauchy root test in a straightforward generalization of Kapteyn’s derivation of the Carlini formula given in 8.7 of

Watson. In particular for the special case of the double sinusoid $z = d \cos(Kx) + d' \cos[(2N+1)Kx]$, the Rayleigh equations are valid provided the constraint

$$Kd \cosh[u_{\min}(Kd, Kd')] + Kd' \cosh[(2N+1)u_{\min}(Kd, Kd')] - u_{\min}(Kd, Kd') < 0$$

is satisfied, where the function u_{\min} is chosen to minimize the quantity

$$Kd \cosh(u) + Kd' \cosh((2N+1)u) - u.$$

In the case of a surface consisting of a finite sum of sinusoids of the form $z = \sum_{n=1}^M d_n \cos(nKx + w_n)$, this problem of determining the region of convergence is somewhat more difficult but still numerically tractable by desktop computing. For the special case $z = d \cos(Kx) + d' \cos(3Kx)$, the Rayleigh validity constraint is particularly simple and can be numerically solved to allow any slopes Kd and $3Kd'$ that fall within the shaded area given in Fig. 2. The predictions of Fig. 2, are confirmed by examining the truncation solutions for the equations of the second kind Eqs. (58). Figure 5 shows that the truncation solutions converge for parameter values within the shaded region shown in Fig. 2.

One important application of this work is to allow the relatively quick (compared to more general methods²⁰⁻²²) calculation of reflection coefficients for scattering from surfaces consisting of finite sums of sinusoids whose surface wave numbers are integer multiples of the lowest wave number. Such surfaces have been used by Kachoyan and Macaskill, Berman, and others in the modeling of scattering from random cylindrical surfaces. Although the derivation of the parameter region for which the Rayleigh equations given by Eq. (26) [or the equations of the second kind, Eq. (58)] are valid is mathematically complex, the calculation of the reflection coefficients themselves is within reach of anyone with access to special function software. This means that the solution for the reflection coefficients for periodic surfaces consisting of sums of many sinusoids can be found by desktop computing rather than requiring supercomputer type calculations as in Berman.⁸

ACKNOWLEDGMENTS

The author would like to thank Dale Ellis and Dave Chapman of DREA for supporting this work. Funding was provided by the Defence Research Establishment Atlantic under Contact No. W7707-5-3266/01-HAL.

- ¹ Lord Rayleigh, *The Theory of Sound* (Dover, New York, 1945), Vol. 2.
- ² J. L. Uretsky, "The scattering of plane waves from periodic surfaces," *Ann. Phys. (N.Y.)* **33**, 400-427 (1965).
- ³ R. F. Millar, "On the Rayleigh assumption in scattering by a periodic surface," *Proc. Cambridge Philos. Soc.* **65**, 773-791 (1969).
- ⁴ R. Petit and M. Cadilhac, "Sur la diffraction d'une onde plane par un réseau infiniment conducteur," *C. R. Acad. Sci. Paris, Ser. B* **262**, 468-471 (1966).
- ⁵ A. Purcell, "Reflection coefficients for scattering from a pressure-release, sinusoidal surface," *J. Acoust. Soc. Am.* **100**, 2919-2936 (1996).
- ⁶ F. Oberhettinger, *Fourier Expansions* (Academic, New York, 1973).
- ⁷ G. N. Watson, *A Treatise on the Theory of Bessel Functions* (Cambridge U.P., New York, 1980), 2nd ed.
- ⁸ D. Berman, "Simulations of rough interface scattering," *J. Acoust. Soc. Am.* **89**, 623-636 (1991).
- ⁹ B. J. Kachoyan and C. Macaskill, "Acoustic scattering from an arbitrarily rough surface," *J. Acoust. Soc. Am.* **82**, 1721-1726 (1987).
- ¹⁰ L. Fortuin, "Survey of literature on reflection and scattering of sound waves at the sea surface," *J. Acoust. Soc. Am.* **47**, 1209-1228 (1970).
- ¹¹ G. C. Bishop and J. Smith, "A scattering model for nondifferentiable periodic surface roughness," *J. Acoust. Soc. Am.* **91**, 744-770 (1992).
- ¹² N. R. Hill and V. Celli, "Limit of convergence of the Rayleigh method for surface scattering," *Phys. Rev. B* **79**, 2478-2481 (1978).
- ¹³ P. M. van den Berg and R. J. Fokkema, "The Rayleigh hypothesis in the theory of reflection by a grating," *J. Opt. Soc. Am.* **69**, 27-31 (1979).
- ¹⁴ R. L. Holford, "Scattering of sound waves at a periodic, pressure-release surface: An exact solution," *J. Acoust. Soc. Am.* **70**, 1116-1128 (1981).
- ¹⁵ V. A. Wassiljeff, "Verallgemeinerung einer Summenformel von Neumann und Lommel," *Z. Angew. Math. Phys.* **20**, 389-403 (1969).
- ¹⁶ W. C. Meecham, "On the use of the Kirchhoff approximation for the solution of reflection problems," *J. Rational Mech. Anal.* **5**, 323-334 (1956).
- ¹⁷ E. R. Hansen, *A Table of Series and Products* (Prentice-Hall, Englewood Cliffs, NJ, 1973), Eq. 57.17.31.
- ¹⁸ Stephen Wolfram, *The Mathematica Book* (Wolfram Media/Cambridge U.P., New York, 1996), 3rd ed.
- ¹⁹ T. J. Bromwich, *An Introduction to the Theory of Infinite Series* (Chelsea, New York, 1991), 3rd ed.
- ²⁰ D. F. McCammon and S. T. McDaniel, "Application of a new theoretical treatment to an old problem-Sinusoidal pressure release boundary scattering," *J. Acoust. Soc. Am.* **78**, 149-156 (1985).
- ²¹ D. F. McCammon and S. T. McDaniel, "Surface reflection: On the convergence of a series solution to a modified Helmholtz integral equation and the validity of the Kirchhoff approximation," *J. Acoust. Soc. Am.* **79**, 64-70 (1986).
- ²² D. Berman and J. Perkins, "Rayleigh method for scattering from random and deterministic interfaces," *J. Acoust. Soc. Am.* **88**, 1032-1044 (1990).

Propagation of Love waves in a transversely isotropic fluid-saturated porous layered half-space

Yue-Sheng Wang

Institute of Engineering Mechanics, Northern Jiaotong University, Beijing 100044, People's Republic of China

Zi-Mao Zhang

Department of Civil Engineering, Northern Jiaotong University, Beijing 100044, People's Republic of China

(Received 20 November 1996; revised 3 September 1997; accepted 18 September 1997)

The dispersion equation for Love wave propagation in a layer lying over a half-space is derived. Both media are assumed to be transversely isotropic fluid-saturated poroelastic solids with principal axes perpendicular to the surface. The analysis is based on the Biot's theory. The dissipation due to fluid viscosity is considered and therefore the dispersion equation is complex and intractable analytically. An iterative procedure is developed to solve this equation. Two situations are discussed in detail: (i) an elastic layer overlying a poroelastic half-space and (ii) a poroelastic layer lying over an elastic half-space. Dispersion curves and attenuation curves of Love waves are plotted for these two cases. In addition, the upper and lower bounds of Love wave speeds are also explored. © 1998 Acoustical Society of America. [S0001-4966(98)04601-3]

PACS numbers: 43.20.Bi, 43.20.Jr, 43.35.Pt, 43.40.Ph [JEG]

INTRODUCTION

Wave propagation in fluid-saturated porous media has received considerable attention in recent years because of its practical importance in various fields such as earthquake engineering, soil dynamics, geophysics, and hydrology, etc. Biot^{1,2} developed a phenomenological theory and discussed the plane-wave propagation in isotropic porous media.

The geologic materials with pores saturated with fluid are usually anisotropic due to bedding, compaction, and the presence of aligned microcracks. The anisotropy may have significant effects on the wave characteristics. Biot³ formulated the constitutive equations and equations of motion for anisotropic porous solids. More recently, many investigators studied the propagation of waves in anisotropic poroelastic media.⁴⁻¹³ The present paper will consider Love waves in a transversely isotropic porous layered half-space.

It is well known that Love waves, first attacked by Love¹⁴ for isotropic elastic solids, play an important role in seismology, geophysics, and earthquake engineering. Deresiewicz, in his series papers, discussed Love waves in a porous layer on an elastic half-space,¹⁵ in a double surface layer on an elastic half-space,¹⁶ and in a porous layer between two elastic half-spaces.¹⁷ The last case was also considered by Paul¹⁸ for the case of small porosity. Deresiewicz's work presented an approximate scheme to determine the phase velocity and measure of dissipation valid for porous materials in which the mass of the interstitial liquid is smaller than that of the solid. Recently, Sharma and Gogna¹⁹ discussed Love waves in an initially stressed medium consisting of a slow elastic layer lying over a liquid-saturated porous half-space with small porosity. However, no attenuation curves of Love waves were given in the papers mentioned before.

The main contributions of the present paper are the fol-

lowing: (i) dispersion equation is derived for Love waves in a transversely isotropic porous layer overlying a transversely isotropic porous half-space, with consideration of dissipation due to fluid viscosity, (ii) the upper and lower bounds of Love wave speeds are presented analytically, (iii) an effective iterative procedure is developed to solve the complex dispersion equation for arbitrary values of porosity and frequency, (iv) dispersion curves and attenuation curves are plotted for two special cases: an elastic layer on a porous half-space and a porous layer on an elastic half-space.

I. BASIC EQUATIONS

A. Biot's theory

Take the principal axis of transversely isotropic media as z axis. Following Biot,³ the constitutive equations in the presence of dissipation are given by

$$\begin{aligned}\tau_{xx} &= (2B_1 + B_2)e_{xx} + B_2e_{yy} + B_3e_{zz} + B_6\zeta, \\ \tau_{yy} &= B_2e_{xx} + (2B_1 + B_2)e_{yy} + B_3e_{zz} + B_6\zeta, \\ \tau_{zz} &= B_3e_{xx} + B_3e_{yy} + B_4e_{zz} + B_7\zeta, \\ \tau_{yz} &= 2B_5e_{yz}, \quad \tau_{zx} = 2B_5e_{zx}, \quad \tau_{xy} = 2B_1e_{xy}, \\ p &= B_6e_{xx} + B_6e_{yy} + B_7e_{zz} + B_8\zeta,\end{aligned}\tag{1}$$

where τ_{xx} , τ_{xy} , etc., are the total stress components on the bulk material; e_{xx} , e_{yy} , etc., are the components of the strain tensor of the solid matrix; p is the pore fluid pressure, and ζ is the increment of fluid content per unit volume. In terms of the displacement components of bulk material and saturant fluid, u_i and U_i (with $i=1,2,3$ corresponding to x,y,z), e_{ij} and ζ may be expressed as

$$e_{ij} = \frac{1}{2}(u_{i,j} + u_{j,i}), \quad \zeta = -w_{i,i},\tag{2}$$

where $w_i = \phi(U_i - u_i)$ and ϕ is the porosity of the medium. The eight material coefficients $B_1 - B_8$ in Eq. (1) can be expressed in terms of the elastic coefficients of the skeleton, the bulk modulus of the constitutive grains, and the bulk modulus of the saturant fluid by using the homogenization technique.²⁰

The equations of motion presented by Biot³ for wave propagation in porous media are

$$\begin{aligned} \tau_{ij,j} &= \rho u_i + \rho_f w_i, \\ -p_{,i} &= \rho_f u_i + m_{ii} w_i + r_{ii} \dot{w}_i, \end{aligned} \quad (3)$$

where $\rho = (1 - \phi)\rho_s + \phi\rho_f$ is the mass density of the porous material, with ρ_s and ρ_f denoting the mass densities of the skeleton and the fluid, respectively. m_{ii} and r_{ii} are the coefficients introduced by Biot. Here, for transversely isotropic porous materials, we have $m_{11} = m_{22} = m_1$, $m_{33} = m_3$, $r_{11} = r_{22} = r_1$, and $r_{33} = r_3$. They are functions of angular frequency ω and may be expressed as

$$m_i = \text{Re}[\alpha_i(\omega)]\rho_f/\phi, \quad r_i = \eta/\text{Re}[K_i(\omega)], \quad i=1,3, \quad (4)$$

where η is the viscosity of the fluid; $\alpha_i(\omega)$ and $K_i(\omega)$ are, respectively, the dynamic tortuosity and permeability with the relation:²¹

$$\alpha_i(\omega) = i\eta\phi/[K_i(\omega)\omega\rho_f], \quad (5)$$

where $i=1$ refers to quantities in the x and y direction and $i=3$ to those in z direction.

B. Dynamic tortuosity and permeability

For porous solids with pores of simple form (for example, cylindrical tubes), the dynamic permeability/tortuosity can be obtained in closed form.^{22,23} Johnson *et al.*²¹ presented an asymptotic expression for general isotropic porous media, which can be extended to the transversely isotropic case:

$$\begin{aligned} K_i(\omega) &= K_i(0) \left\{ \left[1 - \frac{4i\alpha_i^2(\infty)K_i^2(0)\omega\rho_f}{\eta a_i^2 \phi^2} \right]^{1/2} \right. \\ &\quad \left. - \frac{i\alpha_i(\infty)K_i(0)\omega\rho_f}{\eta\phi} \right\}^{-1}, \end{aligned} \quad (6)$$

where a_i is the characteristic length of pores in the x , y , or z direction. The dynamic tortuosity $\alpha_i(\omega)$ may be obtained by Eq. (5). In general, $\alpha_i(\infty)$, $K_i(\infty)$, and a_i are unrelated and independently measurable, but if the pores are a set of non-intersecting tubes, these parameters are related to each other by²¹

$$\frac{8\alpha_i(\infty)K_i(0)}{\phi a_i^2} = 1. \quad (7)$$

Similar to the isotropic case, the viscous and inertial forces are of the same order of magnitude at a critical frequency,⁸ $f_{ci} = \omega_{ci}/2\pi = 3\eta\phi/[8\pi K_i(0)\alpha_i(\infty)\rho_f]^{-1}$. In terms of f_{ci} and the frequency $f = \omega/2\pi$, the dynamic permeability and tortuosity may be written as

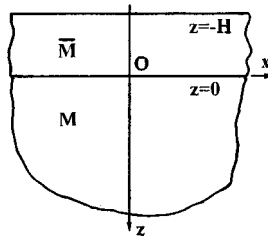


FIG. 1. A transversely isotropic porous layered half-space.

$$\begin{aligned} \eta[\omega K_i(\omega)]^{-1} &= i\phi^{-1}\rho_f\alpha_i(\omega) \\ &= i\phi^{-1}\rho_f\alpha_i(\infty) \left[1 + \frac{4if_{ci}}{3f} \right. \\ &\quad \left. \times \left(1 - \frac{3if}{8f_{ci}} \right)^{1/2} \right]. \end{aligned} \quad (8)$$

II. DISPERSION EQUATION OF LOVE WAVES

A. Wave fields in the layer and half-space

Consider a transversely isotropic poroelastic layer of thickness H bonded to a transversely isotropic poroelastic half-space. The coordinate system is taken to be a rectangular Cartesian with the z axis pointing vertically downwards and the x axis along the interface as shown in Fig. 1. Since we are considering the antiplane shear motion, the nonzero displacement components are those along the y axis (i.e., u_y and U_y or w_y). Combining Eqs. (1)–(3), we have

$$B_1 \frac{\partial^2 u_y}{\partial x^2} + B_5 \frac{\partial^2 u_y}{\partial z^2} = \rho \ddot{u}_y + \rho_f \ddot{w}_y, \quad (9)$$

$$0 = -\rho_f \ddot{u}_y - m_1 \ddot{w}_y - r_1 \dot{w}_y.$$

We assume the harmonic wave solution with the form

$$\{u_y, w_y\} = \{f(z), g(z)\} \exp[i(kx - \omega t)], \quad (10)$$

where k is the wave number. Substitution of Eq. (10) to Eq. (9) yields

$$f(z) = a_1 \exp(i\gamma z) + a_2 \exp(-i\gamma z), \quad (11)$$

$$g(z) = -\frac{\rho_f}{m_1 + ir_1/\omega} f(z), \quad (12)$$

where a_1 and a_2 are constants determined by the boundary conditions, and γ is given by

$$\gamma^2 = -\frac{B_1 k^2 - \omega^2 \rho}{B_5} - \frac{\omega^2 \rho_f^2}{B_5(m_1 + ir_1/\omega)}. \quad (13)$$

Hence the displacement components in the layer and half-space can be, respectively, expressed as

$$\bar{u}_y = [\bar{a}_1 \exp(i\bar{\gamma}z) + \bar{a}_2 \exp(-i\bar{\gamma}z)] \exp[i(kx - \omega t)], \quad (14)$$

$$u_y = a_1 \exp(i\gamma z) \exp[i(kx - \omega t)],$$

and

$$\{\bar{w}_y, w_y\} = \left\{ -\frac{\bar{\rho}_f \bar{u}_y}{\bar{m}_1 + i\bar{r}_1/\omega}, -\frac{\rho_f u_y}{m_1 + ir_1/\omega} \right\}, \quad (15)$$

where bars refer to the quantities of the layer. $\bar{\gamma}^2$ is of the same form as Eq. (13) with B_1 , B_5 , ρ , ρ_f , m_1 , r_1 replaced by those with bars.

For the Love surface waves expressed by Eq. (14), we must have $\text{Im } \gamma > 0$ and $\text{Re } \bar{\gamma} \neq 0$ (without loss of generality, we assume $\text{Re } \bar{\gamma} > 0$), which actually determine the region of the Love wave speeds.

B. Boundary conditions and dispersion equation

The boundary conditions to be satisfied in the present problem are

$$\begin{aligned} \bar{u}_y &= u_y, & \text{at } z=0, \\ \bar{\tau}_{zy} &= \tau_{zy}, & \text{at } z=0, \\ \tau_{zy} &= 0, & \text{at } z=-H, \end{aligned} \quad (16)$$

which when substituted upon by Eqs. (1), (2), (14), and (15) yield

$$\begin{aligned} \bar{a}_1 + \bar{a}_2 &= a_1, \\ \bar{B}_5 \bar{\gamma} (\bar{a}_1 - \bar{a}_2) &= B_5 \gamma a_1, \\ \bar{a}_1 e^{-i\bar{\gamma}H} - \bar{a}_2 e^{i\bar{\gamma}H} &= 0. \end{aligned} \quad (17)$$

Eliminating the unknown constants, we obtain the dispersion equation

$$\tan(\bar{\gamma}H) = \frac{B_5 \gamma}{iB_5 \bar{\gamma}}, \quad (18)$$

which is generally complex because of the dissipation of the system, even it is identical in appearance with the classical dispersion equation of Love waves in a transversely isotropic elastic half-space.²⁴ In fact, the wave number k is complex and thus may be written as

$$k = k_1 + ik_2 = k_1(1 + i\delta), \quad (19)$$

where k_1 and k_2 are real; $\delta = k_2/k_1$ is the attenuation coefficient. The phase velocity c can be evaluated by $c = \omega/k_1$. It is convenient to introduce the following contractions:

$$c_s = \left[\frac{B_1}{\rho - \rho_f^2 m_1 / (m_1^2 + r_1^2 / \omega^2)} \right]^{1/2}, \quad (20)$$

$$\bar{c}_s = \left[\frac{\bar{B}_1}{\bar{\rho} - \bar{\rho}_f^2 \bar{m}_1 / (\bar{m}_1^2 + \bar{r}_1^2 / \omega^2)} \right]^{1/2},$$

$$2\delta^* = \frac{\rho_f^2 r_1 / \omega}{\rho(m_1^2 + r_1^2 / \omega^2) - \rho_f^2 m_1}, \quad (21)$$

$$2\bar{\delta}^* = \frac{\bar{\rho}_f^2 \bar{r}_1 / \omega}{\bar{\rho}(\bar{m}_1^2 + \bar{r}_1^2 / \omega^2) - \bar{\rho}_f^2 \bar{m}_1}.$$

Then γ^2 and $\bar{\gamma}^2$ may be rewritten as

$$\gamma^2 = \frac{B_1}{B_5} k_1^2 \{ [(c/c_s)^2 - (1 - \delta^2)] + 2i[\delta^*(c/c_s)^2 - \delta] \}, \quad (22)$$

$$\bar{\gamma}^2 = \frac{\bar{B}_1}{B_5} \bar{k}_1^2 \{ [(c/\bar{c}_s)^2 - (1 - \delta^2)] + 2i[\bar{\delta}^*(c/\bar{c}_s)^2 - \delta] \}.$$

To satisfy the requirements of $\text{Im } \gamma > 0$ and $\text{Re } \bar{\gamma} > 0$, we must have

$$\bar{c}_s \sqrt{1 - \delta^2} < c < c_s \sqrt{1 - \delta^2}. \quad (23)$$

Consequently, γ and $\bar{\gamma}$ are given by

$$\gamma = i\sqrt{B_1/B_5} k_1 q, \quad \bar{\gamma} = \sqrt{\bar{B}_1/B_5} k_1 \bar{q} \quad (24)$$

with

$$\begin{aligned} q &= \{ [(1 - \delta^2) - (c/c_s)^2] + 2i[\delta - \delta^*(c/c_s)^2] \}^{1/2}, \\ \bar{q} &= \{ [(c/\bar{c}_s)^2 - (1 - \delta^2)] + 2i[\bar{\delta}^*(c/\bar{c}_s)^2 - \delta] \}^{1/2} \end{aligned} \quad (25)$$

being the branches of $\text{Re } q$ and $\text{Re } \bar{q} > 0$. Substitution of Eq. (24) to Eq. (18) yields

$$\tan(\sqrt{\bar{\mu}\bar{q}} k_1 H) = \lambda \sqrt{\mu/\bar{\mu}} \frac{q}{\bar{q}}, \quad (26)$$

where $\mu = B_1/B_5$, $\bar{\mu} = \bar{B}_1/\bar{B}_5$, and $\lambda = B_5/\bar{B}_5$.

We further set

$$\bar{q} = \bar{q}_1 + i\bar{q}_2, \quad \lambda \sqrt{\frac{\mu q}{\bar{\mu} \bar{q}}} = a + ib \quad (27)$$

with \bar{q}_1 , \bar{q}_2 , a , and b being real. Then Eq. (26), upon separation of real and imaginary parts, yields two real equations

$$\tan(\sqrt{\bar{\mu}\bar{q}_1} k_1 H) = a/[1 - b \tanh(\sqrt{\bar{\mu}\bar{q}_2} k_1 H)], \quad (28)$$

$$\tanh(\sqrt{\bar{\mu}\bar{q}_2} k_1 H) = b/[1 + a \tan(\sqrt{\bar{\mu}\bar{q}_1} k_1 H)] \quad (29)$$

from which the dispersion curves (c vs $k_1 H$) and the attenuation curves (δ vs $k_1 H$) can be determined. However, the analytical solution of Eqs. (28) and (29) is impossible, and the numerical solution is also difficult. Here we suggest an iterative procedure as follows based on the fact that the attenuation of SH waves in porous media is very small,^{7,13} (i.e., $\delta \ll 1$):

- (i) Set $\delta = 0$ in Eq. (28) and solve it for c with $k_1 H$ being fixed;
- (ii) Insert c obtained in the previous step to Eq. (29) and solve it for δ ;
- (iii) Insert δ obtained in the previous step to Eq. (28) and solve it for c .

Repeat steps (ii) and (iii) until the difference between the values of c (and/or δ) obtained by the two nearby iterations is within the expected errors. Numerical examples will be given afterwards.

Now let us reexamine Eq. (8). It implies that m_1 and r_1/ω [see Eq. (4)] are the functions of f/f_{c1} , a parameter which may be rewritten as

$$\frac{f}{f_{c1}} = \frac{c}{\hat{c}_s} \frac{k_1 H}{2\pi f_{c1} H / \hat{c}_s}, \quad (30)$$

where \hat{c}_s is a characteristic velocity introduced for nondimensionalization. With this result in hand, we can conclude that the dispersion curves (c vs $k_1 H$) and the attenuation curves (δ vs $k_1 H$) determined by Eqs. (28) and (29) depend upon the parameter $k_{c1} H$ with $k_{c1} = 2\pi f_{c1} / \hat{c}_s$. The choice of the characteristic velocity \hat{c}_s depends on the particular problem considered.

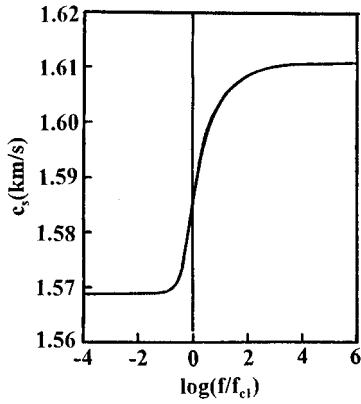


FIG. 2. Dependence of c_s on the frequency.

The dispersion equation (26) reduces to a real equation in two special cases. One is the case when the porous solid is saturated by nonviscous fluid, i.e., $\eta=0$. In this case, we have $m_1 = \alpha_1(\infty)\rho_f/\phi$, $r_1=0$ (\bar{m}_1 and \bar{r}_1 have similar properties). Thus $\delta = \bar{\delta} = \delta^* = \bar{\delta}^* = 0$ and

$$c_s = \left[\frac{B_1}{\rho - \phi\rho_f/\alpha_1(\infty)} \right]^{1/2} \quad (31)$$

with the similar behavior for \bar{c}_s . Equation (31) is exactly the antiplane shear wave velocity along x direction with no dissipation. Another case is for the dried porous solid, i.e., $\rho_f = 0$. In this situation, m_1 , \bar{m}_1 , r_1 , and \bar{r}_1 all vanish. Therefore $\delta = \bar{\delta} = \delta^* = \bar{\delta}^* = 0$ and

$$c_s = \sqrt{\frac{B_1}{(1-\phi)\rho_s}}, \quad \bar{c}_s = \sqrt{\frac{\bar{B}_1}{(1-\bar{\phi})\bar{\rho}_s}}. \quad (32)$$

The dispersion relation in these two situations is identical to its classical counterpart in an elastic system. When $\alpha_1(\infty) = 1$, the results of these two cases are exactly the same.

C. Range of love wave speed

Determination of the lower and upper bounds of the Love wave speed is of interest in both theoretical and practical aspects and is helpful in solving Eqs. (28) and (29). In fact, inequality (23) defines the range of the Love wave speed. Unfortunately, δ is unknown and should be determined by solving the dispersion equation. However, we have indicated before that $\delta \ll 1$ for SH waves (see Refs. 7 and 13). Therefore, c_s and \bar{c}_s may be approximately viewed as the upper and lower bounds of the Love wave speed. Both c_s and \bar{c}_s depend on the frequency. Here c_s is calculated numerically and plotted in Fig. 2 against the frequency. In the calculation, we take the material constants of the porous solid as

$$\begin{aligned} B_1 &= 6.4 \text{ GPa}, & B_5 &= 8.0 \text{ GPa}, \\ K_1(0) &= 1.0 \text{ Darcy}, & \alpha_1(\infty) &= 1.5, \\ \rho_s &= 3000 \text{ kg/m}^3, & \rho_f &= 1000 \text{ kg/m}^3, \\ \eta &= 10^{-3} \text{ Pa s}, & \phi &= 0.2. \end{aligned} \quad (33)$$

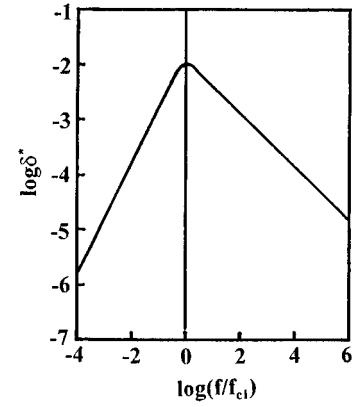


FIG. 3. Dependence of δ^* on the frequency.

It is seen from Fig. 2 that c_s possesses a rapid change near the critical frequency f_{c1} but almost remains unchanged at lower and higher frequencies. The limiting values of c_s at $f=0$ and $f=\infty$ are, respectively, given by

$$c_s(0) = \sqrt{\frac{B_1}{\rho}}, \quad c_s(\infty) = \sqrt{\frac{B_1}{\rho - \phi\rho_f/\alpha_1(\infty)}}, \quad (34)$$

where $c_s^{(\infty)}$ is of the same form as Eq. (31). The similar behavior may be expected for \bar{c}_s .

It is well known that a cut-off frequency exists for the n th mode of Love waves. That is to say, only waves whose frequency is higher than the cut-off frequency can propagate in the layer. The cut-off frequency of the n th mode (denoted by f_n^c) may be obtained by solving the following equations

$$\sqrt{\mu}q_1 k_1 H = (n-1)\pi, \quad n = 1, 2, 3, \dots, \quad (35)$$

$$q_1 = q_2 = 0,$$

where the second equation leads to

$$c^2 = c_s^2(1 - \delta^2), \quad c_s^2 \delta = c^2 \delta^* \quad \text{at } f = f_n^c \quad (36)$$

from which we obtain the exact upper bound of Love wave speed corresponding to the n th mode:

$$c = c_s \left[\frac{\sqrt{1 + 4\delta^{*2}} - 1}{2\delta^{*2}} \right]^{1/2}, \quad f = f_n^c, \quad (37)$$

which is nothing but the SH wave speed of the half-space in the x direction in the presence of dissipation (see the Appendix). The variation of δ^* with frequency is shown in Fig. 3 with the material constants taken as Eq. (33). It is seen that δ^* reaches a peak value at the critical frequency f_{c1} and tends to zero at the infinite frequency. Generally, $\delta^* \ll 1$, and thus we have, from Eq. (37),

$$c^2 \approx c_s^2 \left(1 + \delta^{*2} - \frac{1}{4} \delta^{*4} + \frac{1 \cdot 3}{4 \cdot 6} \delta^{*6} + \dots \right), \quad f = f_n^c, \quad (38)$$

which implies that $c_s(f_n^c)$ may provide a good approximation for the upper bound of the Love wave speed of the n th mode. If the half-space is nondissipative, we may have $\delta^*(f_n^c) = 0$ and $c_s(f_n^c) = 0$.

It may be verified easily that, as $k_1H \rightarrow \infty$ (equivalently, $f \rightarrow \infty$), $\{c, \delta\} = \{c_s(\infty), 0\}$ is the solution of the dispersion equation (26). But it is worth notice that $\bar{c}_s(\infty)$ is not the lower bound of the Love wave speed. Later we will show numerically that the Love wave speed may be lower than $\bar{c}_s(\infty)$ at finite frequencies.

For the first mode, no cut-off frequency exists, i.e., $f_1^c = 0$, which means that all of the waves with arbitrary frequency can propagate in the layer. When $k_1H \rightarrow 0$ (or $f \rightarrow 0$), $\{c, \delta\} = \{c_s(0), 0\}$ satisfies Eq. (26). $c_s(0)$ is the exact upper bound of the Love wave speed of the first mode.

III. NUMERICAL RESULTS AND DISCUSSION

Numerical calculation will be performed for two situations. First, we consider a slow elastic layer overlying a poroelastic half-space. As the second example, we consider a slow poroelastic layer lying on an elastic half-space. The first model may describe the oil- or water-saturated porous solid under a sandy layer. The second one may be used to examine the Love waves in a oil-saturated porous layer under the sea (note that a shear wave cannot propagate in the fluid). The material constants of the porous solids are selected as given by Eq. (33) in the following calculations.

A. An elastic layer on a porous half-space

Consider an elastic layer overlying a porous half-space. The shear moduli and mass density of the elastic layer are taken to be

$$\bar{B}_1 = \bar{B}_5 = 3 \text{ GPa}, \quad \bar{\rho}_s = 3000 \text{ kg/m}^3. \quad (39)$$

The dispersion curves are illustrated in Fig. 4(a) for Love waves of the first three modes ($n=1,2,3$), with different values of the parameter $k_{c1}H$ (where $k_{c1} = 2\pi f_{c1}/\bar{c}_s$). The dashed lines are for the nondissipative case, i.e., $\eta=0$ or equivalently, $k_{c1}H=0$. The lower bound of the Love wave speed is $\bar{c}_s = \sqrt{\bar{B}_1/\bar{\rho}_s} = 1 \text{ km/s}$, while the upper bound ranges between $c_s(0) = 1.5689 \text{ km/s}$ and $c_s(\infty) = 1.6108 \text{ km/s}$ for different modes. (See the dotted lines for $k_{c1}H=1$. The solid lines for $k_{c1}H=10^3$ do not show this fact clearly because c_s , in this case varies slightly in the frequency range we considered.) The upper bound for the nondissipative case is $c_s(\infty)$. A fact shown in the figure is that little difference exists between the curves except near the upper bounds.

Figure 4(b) demonstrates the attenuation of Love waves. The solid lines refer to the first three modes with $k_{c1}H = 10^3$. For the lowest mode, the attenuation reaches a peak value at a low frequency, and decreases to zero as $k_1H \rightarrow 0$ or $k_1H \rightarrow \infty$. While for the higher mode, the maximum value of the attenuation appears at the cut-off frequency and decreases with the increase of k_1H . The bigger the value of the n order of the mode is, the higher the attenuation is. The attenuation curves for $k_{c1}H = 1$ and 10^{-3} are also depicted in the figure with the dotted line and dot-dashed line, respectively. It is shown that the attenuation is higher for $k_{c1}H = 1$ than for $k_{c1}H = 10^3$ and 10^{-3} , which implies that there must be a value of $k_{c1}H$ at which the attenuation is the highest.

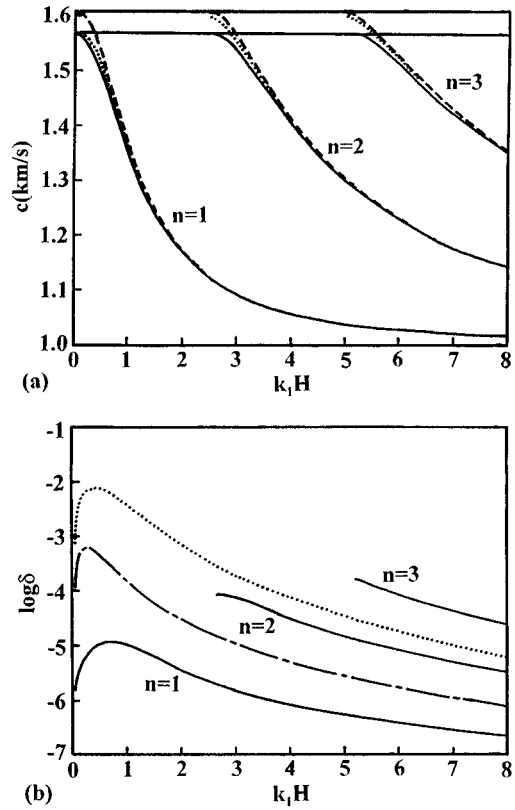


FIG. 4. Dispersion curves (a) and attenuation curves (b) of the first three modes of Love waves in an elastic layer overlying a porous half-space. The solid lines are for $k_{c1}H = 10^3$, the dotted lines for $k_{c1}H = 1$, the dashed lines for $k_{c1}H = 0$, and the dot-dashed line for $k_{c1}H = 10^{-3}$.

B. A porous layer on an elastic half-space

Contrary to the previous example, we assume a porous layer lying over an elastic half-space of which the shear moduli and mass density are given by

$$B_1 = B_5 = 12 \text{ GPa}, \quad \rho_s = 3000 \text{ kg/m}^3. \quad (40)$$

The dispersion curves of the first three modes are shown in Fig. 5(a) for $k_{c1}H = 10^3$ (the solid lines) and $k_{c1}H = 0$ (the dashed lines), where $k_{c1} = 2\pi f_{c1}H/\bar{c}_s(\infty)$. The upper bound of the Love wave speed is $c_s = \sqrt{B_1/\rho_s} = 2 \text{ km/s}$. The lower bound for $k_{c1}H = 0$ (i.e., $\eta=0$) is $\bar{c}_s(\infty)$, but it is not the case for $k_{c1}H = 10^3$ although $c \rightarrow \bar{c}_s(\infty)$ as $k_1H \rightarrow \infty$ (see the discussion in Sec. II C). It is seen that the phase velocity of the first mode is lower than $\bar{c}_s(\infty)$ but higher than $\bar{c}_s(0)$ when k_1H is higher than 6.4.

The attenuation of the first three modes is plotted in Fig. 5(b) against k_1H for $k_{c1}H = 10^3$. It follows from the figure that, for all three modes, the attenuation increases rapidly at first and then slowly as k_1H increases. We have argued before that the attenuation vanishes both at the critical frequency and at the infinite frequency. Thus we can infer that the attenuation must reach a maximum value at some finite frequency that is not shown in the figure.

IV. CONCLUSIONS

The dispersion equation for Love waves in a porous layered half-space has been derived. The equation is complex.

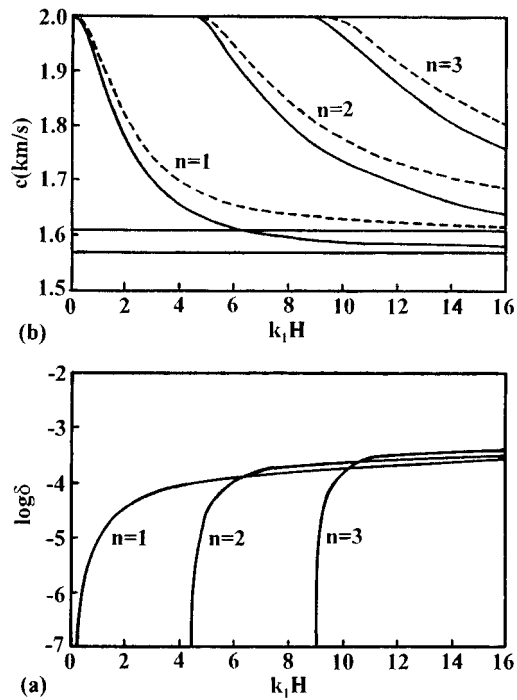


FIG. 5. Dispersion curves (a) and attenuation curves (b) of the first three modes of Love waves in a porous layer overlying an elastic half-space. The solid lines are for $k_{c1}H=10^3$ and the dashed lines for $k_{c1}H=0$.

An iterative method is suggested to solve it for the phase velocity and attenuation. It is demonstrated that the solution depends upon a parameter involving the critical frequency f_{c1} and the thickness of the layer. Two examples, which may be of practical interest, are discussed in detail. The phase velocity and attenuation are plotted against the dimensionless frequency k_1H . The attenuation is generally very small for the lower modes but may be higher for the higher modes. At zero frequency or infinite frequency, the attenuation vanishes.

The range of the Love wave speed is discussed in detail. The upper and lower bounds are functions of the frequency, and consequently are different for various modes. (It is self-evident that the upper or lower bound is a constant when the half-space or layer is elastic.) The upper bound is exactly the *SH* wave speed of the half-space in *x* direction. But for the lower bound, we cannot obtain its exact form. What is definite is that, at the infinite frequency, the phase velocities of all modes tend to the same constant, the limiting value of the *SH* wave speed of the layer in the *x* direction at the infinite frequency. The phase velocity may be beyond this limiting value at finite frequencies.

It is expected that the present work may be useful in the further theoretical or observational studies of wave propagation in the more realistic models of the porous solids present in the earth.

ACKNOWLEDGMENTS

Support by the China National Science Foundation under Grant No. 19372001 is acknowledged.

APPENDIX: *SH* WAVES IN A TRANSVERSELY ISOTROPIC POROUS MEDIUM

Consider an *SH* wave propagating in a transversely isotropic porous medium. Suppose that the propagating direction is in the *xz* plane and makes an angle of θ with the *z* axis, the material principal axis. Then the *SH* wave may be expressed as

$$\{u_y, w_y\} = \{a_y, b_y\} \exp[ik(x \sin \theta + z \cos \theta - c_T t)], \quad (\text{A1})$$

which when substituted into Eq. (9) yields

$$\begin{aligned} [\rho - (B_1 \sin^2 \theta + B_5 \cos^2 \theta)k^2/\omega^2]a_y + \rho_f b_y &= 0, \\ \rho_f a_y + (m_1 + ir_1/\omega)b_y &= 0. \end{aligned} \quad (\text{A2})$$

It follows from this equation that

$$k = \omega \left[\frac{\rho - \rho_f^2/(m_1 + ir_1/\omega)}{B_1 \sin^2 \theta + B_5 \cos^2 \theta} \right]^{1/2}. \quad (\text{A3})$$

The phase velocity and attenuation coefficient are given by

$$c_T = \omega/\text{Re}(k), \quad \delta_T = \text{Im}(k)/\text{Re}(k). \quad (\text{A4})$$

Combining (A3) and (A4), we have

$$c_T = \sqrt{\sin^2 \theta + B_5/B_1 \cos^2 \theta} c_s \left[\frac{\sqrt{1 + 4\delta^{*2}} - 1}{2\delta^{*2}} \right]^{1/2}, \quad (\text{A5})$$

$$\delta_T = \delta^* c_T^2 / c_s^2 \quad (\text{A6})$$

with c_s and δ^* given by Eqs. (20) and (21). The phase velocity for a wave propagating in the *x* direction ($\theta=90^\circ$) is

$$c_T = c_s \left[\frac{\sqrt{1 + 4\delta^{*2}} - 1}{2\delta^{*2}} \right]^{1/2}, \quad (\text{A7})$$

which is of the same form as Eq. (37).

- ¹M. A. Biot, "Theory of elastic waves in a fluid-saturated porous solid, I. Low frequency range," J. Acoust. Soc. Am. **28**, 168–178 (1956).
- ²M. A. Biot, "Theory of elastic waves in a fluid-saturated porous solid, II. High frequency range," J. Acoust. Soc. Am. **28**, 179–191 (1956).
- ³M. A. Biot, "Mechanics of deformations and acoustic propagation in porous media," J. Appl. Phys. **33**, 1482–1489 (1962).
- ⁴M. Badiely and T. Yamamoto, "Propagation of acoustic normal modes in a homogeneous ocean overlying layered anisotropic porous beds," J. Acoust. Soc. Am. **77**, 954–981 (1985).
- ⁵C. H. Yew and X. Weng, "A study of reflection and refraction of waves at the interface of water and porous sea ice," J. Acoust. Soc. Am. **82**, 342–353 (1987).
- ⁶M. N. Kazi-Aoual, G. Bonnet, and P. Jouanna, "Green's functions in an infinite transversely isotropic saturated poroelastic medium," J. Acoust. Soc. Am. **84**, 1883–1889 (1988).
- ⁷P. D. Schmitt, "Acoustic multipole logging in transversely isotropic poroelastic formations," J. Acoust. Soc. Am. **86**, 2397–2421 (1989).
- ⁸M. D. Sharma and M. L. Gogna, "Wave propagation in anisotropic liquid-saturated porous solids," J. Acoust. Soc. Am. **90**, 1068–1073 (1991).
- ⁹A. Ben Menahem and R. L. Gibson, "Directional attenuation of *SH* waves in anisotropic poroelastic media," J. Acoust. Soc. Am. **93**, 3057–3065 (1993).
- ¹⁰A. N. Norris, "Low-frequency dispersion and attenuation in partially saturated rocks," J. Acoust. Soc. Am. **94**, 359–370 (1993).
- ¹¹M. Badiely, I. Jaya, and A. H.-D. Cheng, "Propagator matrix for plane wave reflection from inhomogeneous anisotropic poroelastic seafloor," J. Comput. Acoust. **2**, 11–27 (1994).
- ¹²J. M. Carcione, "Wave propagation in anisotropic, saturated porous me-

- dia: Plane-wave theory and numerical simulation," J. Acoust. Soc. Am. **99**, 2655–2666 (1996).
- ¹³Y. S. Wang and Z. M. Zhang, "Propagation of plane waves in transversely isotropic fluid-saturated porous media" (in Chinese), Acta Mech. Sin. **29**, 257–268 (1997).
- ¹⁴A. E. H. Love, *Some Problems of Geodynamics* (Cambridge U.P., Cambridge, England, 1991).
- ¹⁵H. Deresiewicz, "The effect of boundaries on wave propagation in a liquid-filled porous solid: II. Love waves in a porous layer," Bull. Seismol. Soc. Am. **51**, 51–59 (1961).
- ¹⁶H. Deresiewicz, "The effect of boundaries on wave propagation in a liquid-filled porous solid: VI. Love waves in a double surface layer," Bull. Seismol. Soc. Am. **54**, 417–423 (1964).
- ¹⁷H. Deresiewicz, "The effect of boundaries on wave propagation in a liquid-filled porous solid: IX. Love waves in a porous internal stratum," Bull. Seismol. Soc. Am. **54**, 919–923 (1964).
- ¹⁸M. K. Paul, "Propagation of Love waves in a fluid-saturated porous layer lying between two elastic half-spaces," Bull. Seismol. Soc. Am. **54**, 1767–1778 (1964).
- ¹⁹M. D. Sharma and M. L. Gogna, "Propagation of Love waves in an initially stressed medium consisting of a slow elastic layer lying over a liquid-saturated porous solid half-space," J. Acoust. Soc. Am. **89**, 2584–2588 (1991).
- ²⁰J. L. Auriault, "Mécanique des milieux poreux saturés déformables," Tech. Report, Institute de Mécanique de Grenoble, Grenoble, France (1986).
- ²¹D. L. Johnson, J. Koplik, and R. Dashen, "Theory of dynamic permeability and tortuosity in fluid-saturated porous media," J. Fluid Mech. **176**, 379–402 (1987).
- ²²A. Bedford, R. D. Costley, and M. Stern, "On the drag and virtual mass coefficients in Biot's equations," J. Acoust. Soc. Am. **76**, 1804–1809 (1984).
- ²³J. L. Auriault, L. Borne, and R. Chambon, "Dynamics of porous saturated media, checking of the generalized law of Darcy," J. Acoust. Soc. Am. **77**, 1641–1950 (1985).
- ²⁴R. G. Payton, *Elastic Wave Propagation in Transversely Isotropic Media* (Martinus Nijhoff, The Hague, 1983).

A three-dimensional finite difference code for the modeling of sonic logging tools

Yong-Hua Chen and Weng Cho Chew

*Center for Computational Electromagnetics, Department of Electrical and Computer Engineering,
University of Illinois, Urbana, Illinois 61801*

Qing-Huo Liu

*Klipsch School of Electrical and Computer Engineering, New Mexico State University, Las Cruces,
New Mexico 88003*

(Received 12 March 1997; accepted for publication 13 October 1997)

This paper presents a numerical program for the simulation of elastic wave propagation and scattering in three-dimensional (3-D) cylindrical coordinates based on the first-order velocity-stress finite-difference scheme on staggered grids. Both Liao's and Lindman's absorbing boundary conditions are implemented for the exterior boundaries to efficiently truncate the computation domain for elongated 3-D well logging problems. Symmetric and anti-symmetric boundaries in azimuthal and axial directions are also implemented in the code to further reduce the size of the problem. Included for the first time with this code are very large and complex geometrical structures such as the whole slotted sleeve housing of a sonic well-logging tool which typically involves hundreds of millions of unknowns. The calculation for such a large problem only takes a couple of days on a four-processor SGI Power Challenge machine. Different types of slotted sleeve models are studied for sonic logging tools. Simulation results show that different slotted sleeves vary widely in delaying and attenuating the pipe waves which travel along the tool housing. A new slotted sleeve structure with three horizontal slot sections for every vertical slot period is proposed for better performance. A dipole source is found to produce much cleaner waveforms than a monopole source. © 1998 Acoustical Society of America. [S0001-4966(98)00702-4]

PACS numbers: 43.20.Fn, 43.20.Gp, 43.20.Jr [ANN]

INTRODUCTION

Sonic logging is one of the most widely used geophysical methods in borehole environments. A typical sonic logging tool includes one or more transmitters and several receivers in addition to its electronic circuits. A slotted sleeve housing is generally used to hold the sonde components and support other logging tools in combination. The slotted sleeve, as a major part of the sonic tool, is made of a steel pipe with many slots on it. Very finely-structured slots are designed to attenuate and delay the pipe waves traveling along the tool housing so that the existence of the steel pipe does not have a large effect on the elastic wave fields. In order to optimize the design of sonic tools, researchers have performed many numerical and experimental studies related to the transducers. For slotted sleeves, however, only experimental studies have been conducted. Due to the restrictions of cost and time, past experimental studies performed on the slotted sleeve are quite limited. In this paper, we present a finite difference code which can model the whole slotted sleeve for sonic logging tools. Some simulation results will be given for certain slotted sleeve designs.

Various studies have been done to model sonic waves in borehole environments. The real axis integration (RAI) and the branch-cut integration (BCI) have been used to compute sonic waveforms in concentric-layered formations (Biot, 1952; Tsang and Rader, 1979; Cheng and Toksoz, 1981; Kurkjian, 1985; Kurkjian and Chang, 1986; Liu and Chang, 1994, 1996; Lu and Liu, 1995). The numerical mode match-

ing (NMM) technique and the two-dimensional finite difference (FD) method are generally used for axisymmetrical problems where horizontally-layered formations are involved in addition to the concentric-layered borehole structures (Stephen *et al.*, 1985; Tsang, 1986; Randall *et al.*, 1991; Leslie and Randall, 1992). For nonaxisymmetrical media, a full three-dimensional (3-D) problem has to be solved. Due to the large number of unknowns involved in a 3-D elastic wave problem, the finite difference (FD) method is used predominantly (Daube and Randall, 1991; Yoon and McMechan, 1992; Cheng *et al.*, 1995; Liu *et al.*, 1996). Unlike other numerical methods such as the boundary element method (BEM) and the finite element method (FEM), FD is easy and straightforward to implement, and can be easily parallelized on a modern parallel supercomputer. Furthermore, the memory requirement of a FD code is only $O(N)$, where N is the total number of unknowns. Most of the previous 3-D FD studies, however, are for Cartesian coordinates. It is very difficult and too expensive to fit a finely-structured slotted sleeve into a numerical code in rectangular coordinates. For well logging simulations, a cylindrical coordinate formulation is more pertinent because the discretization is more conformal to a borehole environment. Due to the usual nonaxisymmetric property of acoustic well logging tools and borehole structures, a full 3-D cylindrical FD program is important not only in designing and analyzing the tools, but also in understanding the elastic wave propagation in the presence of the tool and in interpreting the measured data. In this paper, we present a 3-D FD code in cylindrical

coordinates for elastic wave propagation and scattering simulation. In what follows, we will first present the formulation and discretization scheme, then validate the code against the RAI method for layered media, and finally apply the code to simulate some typical slotted sleeve structures in fluid and in a borehole environment.

I. ELASTIC WAVE EQUATIONS AND THEIR DISCRETIZATION

For an inhomogeneous isotropic elastic medium characterized by the mass density $\rho(\mathbf{r})$ and Lamé constants $\lambda(\mathbf{r})$ and $\mu(\mathbf{r})$, the first-order partial differential equations for the particle velocity vector \mathbf{v} and the stress tensor $\bar{\boldsymbol{\tau}}$ in cylindrical coordinate system are given as (Liu *et al.*, 1996; Randall *et al.*, 1991; Aki and Richards, 1980; Auld, 1990)

$$\rho \frac{\partial v_r}{\partial t} = \frac{1}{r} \frac{\partial(r\tau_{rr})}{\partial r} + \frac{1}{r} \frac{\partial\tau_{r\theta}}{\partial\theta} + \frac{\partial\tau_{rz}}{\partial z} - \frac{\tau_{\theta\theta}}{r} + f_r, \quad (1)$$

$$\rho \frac{\partial v_\theta}{\partial t} = \frac{1}{r} \frac{\partial(r\tau_{r\theta})}{\partial r} + \frac{1}{r} \frac{\partial\tau_{\theta\theta}}{\partial\theta} + \frac{\partial\tau_{\theta z}}{\partial z} + f_\theta, \quad (2)$$

$$\rho \frac{\partial v_z}{\partial t} = \frac{1}{r} \frac{\partial(r\tau_{rz})}{\partial r} + \frac{1}{r} \frac{\partial\tau_{r\theta}}{\partial\theta} + \frac{\partial\tau_{zz}}{\partial z} + f_z, \quad (3)$$

$$\frac{\partial\tau_{rr}}{\partial t} = \lambda \left[\frac{1}{r} \frac{\partial(rv_r)}{\partial r} + \frac{1}{r} \frac{\partial v_\theta}{\partial\theta} + \frac{\partial v_z}{\partial z} \right] + 2\mu \frac{\partial v_r}{\partial r} + g_{rr}, \quad (4)$$

$$\frac{\partial\tau_{\theta\theta}}{\partial t} = \lambda \left[\frac{1}{r} \frac{\partial(rv_r)}{\partial r} + \frac{1}{r} \frac{\partial v_\theta}{\partial\theta} + \frac{\partial v_z}{\partial z} \right] + 2\mu \left(\frac{v_r}{r} + \frac{1}{r} \frac{\partial v_\theta}{\partial\theta} \right) + g_{\theta\theta}, \quad (5)$$

$$\frac{\partial\tau_{zz}}{\partial t} = \lambda \left[\frac{1}{r} \frac{\partial(rv_r)}{\partial r} + \frac{1}{r} \frac{\partial v_\theta}{\partial\theta} + \frac{\partial v_z}{\partial z} \right] + 2\mu \frac{\partial v_z}{\partial z} + g_{zz}, \quad (6)$$

$$\frac{\partial\tau_{r\theta}}{\partial t} = \mu \left[\frac{1}{r} \frac{\partial v_r}{\partial\theta} + r \frac{\partial}{\partial r} \left(\frac{v_\theta}{r} \right) \right] + g_{r\theta}, \quad (7)$$

$$\frac{\partial\tau_{rz}}{\partial t} = \mu \left(\frac{\partial v_r}{\partial z} + \frac{\partial v_z}{\partial r} \right) + g_{rz}, \quad (8)$$

and

$$\frac{\partial\tau_{\theta z}}{\partial t} = \mu \left(\frac{\partial v_\theta}{\partial z} + \frac{1}{r} \frac{\partial v_z}{\partial\theta} \right) + g_{\theta z}, \quad (9)$$

where f_α ($\alpha=\{r,\theta,z\}$) is a force source, and $g_{\alpha\beta}$ ($\alpha,\beta=\{r,\theta,z\}$) is a stress source (Liu *et al.*, 1996). In the numerical simulation, we use

$$g_{\alpha\alpha}(\mathbf{r},t) = \frac{1}{2\pi r} F(t) \cos(m\theta) \delta(r-r_0) \delta(z-z_0) \quad (10)$$

to simulate a multipole ring source of order m in a fluid, where $F(t)$ is some source time function and $\alpha=r,\theta,z$. All the other source terms are set to zero.

To solve the problem using FD, we discretize the partial differential equations (1)–(9) using central differencing scheme with staggered grids (Yee, 1966; Madariaga, 1976; Virieux, 1984, 1986; Levander, 1988). Figure 1 shows one cell of the staggered grids, where the three compressional stress components are located at the center of the cell and the

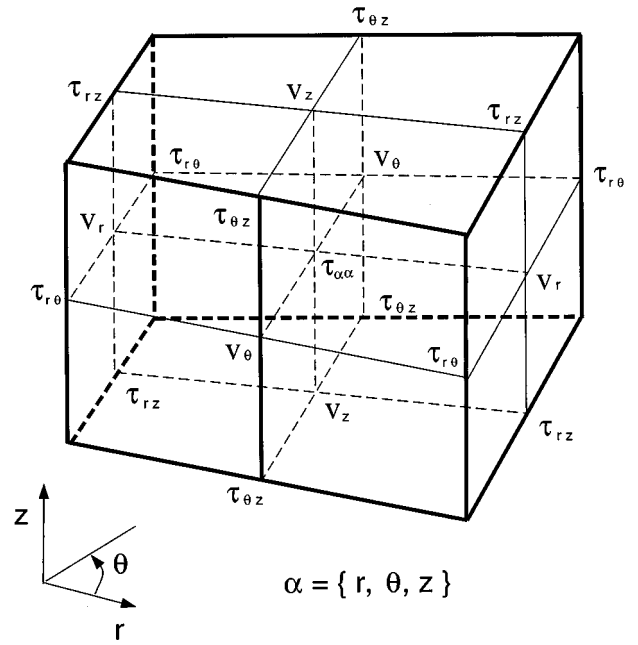


FIG. 1. Staggered grids with discretized points of velocity and stress components.

shear stresses are sampled at the cell edges. The velocity components are discretized at the center of each cell face. If the problem to be solved is in the domain of $r_{\min} \leq r \leq r_{\max}$, $0 \leq \theta \leq \theta_{\max}$, $0 \leq z \leq z_{\max}$, and we want to discretize the problem into $j_{\max} \times l_{\max} \times k_{\max}$ cells, then the grid points are located at

$$r_j = r_{\min} + j\Delta r, \quad j=0,1,2,\dots,j_{\max},$$

$$\theta_l = l\Delta\theta, \quad l=0,1,2,\dots,l_{\max},$$

and

$$z_k = k\Delta z, \quad k=0,1,2,\dots,k_{\max},$$

where $\Delta r = (r_{\max} - r_{\min})/j_{\max}$, $\Delta\theta = \theta_{\max}/l_{\max}$, and $\Delta z = z_{\max}/k_{\max}$. According to the staggered grid scheme, the field unknowns are sampled as follows in the spatial and temporal domains:

$$\tau_{\alpha\alpha}^n(j,l,k) = \tau_{\alpha\alpha}^n(r_{j+1/2}, \theta_{l+1/2}, z_{k+1/2}),$$

$$\tau_{rz}^n(j,l,k) = \tau_{rz}^n(r_j, \theta_{l+1/2}, z_k),$$

$$\tau_{r\theta}^n(j,l,k) = \tau_{r\theta}^n(r_j, \theta_l, z_{k+1/2}),$$

$$\tau_{\theta z}^n(j,l,k) = \tau_{\theta z}^n(r_{j+1/2}, \theta_l, z_k),$$

$$v_r^{n+1/2}(i,j,k) = v_r^{n+1/2}(r_j, \theta_{l+1/2}, z_{k+1/2}),$$

$$v_\theta^{n+1/2}(j,l,k) = v_\theta^{n+1/2}(r_{j+1/2}, \theta_l, z_{k+1/2}),$$

and

$$v_z^{n+1/2}(j,l,k) = v_z^{n+1/2}(r_{j+1/2}, \theta_{l+1/2}, z_k),$$

where n is the index for time at $n\Delta t$. Note that if an unknown is located at any integer grid point in a direction, then the corresponding index for the unknown is from 0 to the maximum number of points in that direction. If an unknown is located at a half grid point in a direction, then the corre-

sponding index for the unknown is from 0 to the maximum number of points minus one in that direction. It can be proved that with the central differencing on the staggered grids, the approximation made in discretizing the equations is of second order accuracy in terms of the grid size (Taflove, 1995). Due to its complexity, we have not seen yet any published stability criterion for the FD scheme in cylindrical coordinates. An empirical strict requirement would be

$$\Delta t \leq \frac{1}{c_{\max} \sqrt{(\Delta r)^{-2} + (r_{\min} \Delta \theta)^{-2} + (\Delta z)^{-2}}}, \quad (11)$$

according to the literatures for rectangular coordinates, if the maximum wave velocity in the medium is c_{\max} . However, our experience shows that this criterion can be relaxed. Further research is needed on the stability criterion of FD in cylindrical coordinates.

II. BOUNDARY CONDITIONS

The treatment on the exterior boundaries has always been an important issue for FD in simulating wave propagation problems. A good absorbing boundary condition (ABC) not only reduces the requirements of the simulation time and computer memory, but also guarantees that the solution is not contaminated by boundary reflections. In this section, we will summarize the boundary treatment, especially the implementation of Lindman's ABC for the 3-D cylindrical elastic wave propagation problem.

We implemented both Liao's ABC (Liao *et al.*, 1984), and Lindman's ABC (Lindman, 1975; Randall, 1989; Chew, 1990) in the 3-D FD code. Lindman's ABC is superior to Liao's ABC since it has smaller reflections. However, it is applicable only for media homogeneous near the boundary. Liao's ABC is used for boundaries at $z = z_{\min}$ and $z = z_{\max}$ because the medium is inhomogeneous and the wave incident angle is small over those end regions. It is well-known that Liao's ABC is good for small incident angle and is easy to implement. However, Liao's ABC is not adequate for the outer radial boundary at $r = r_{\max}$, although available as a choice for the boundary condition in the code. Lindman's ABC is implemented for the $r = r_{\max}$ boundary, since it absorbs waves very well up to an incident angle of 89° . The formulation of Lindman's ABC for elastic waves is based on Randall's work in 1989. Here we expand the idea to a 3-D elastic wave propagation problem in cylindrical coordinates.

Consider an isotropic, homogeneous, elastic medium with compressional and shear velocities c and s , respectively. The velocity field \mathbf{v} satisfies the vector wave equation

$$\frac{\partial^2 \mathbf{v}}{\partial t^2} = c^2 \nabla (\nabla \cdot \mathbf{v}) - s^2 \nabla \times \nabla \times \mathbf{v}, \quad (12)$$

and can always be represented as

$$\mathbf{v} = \nabla \Phi + \nabla \times \mathbf{A}, \quad (13)$$

where Φ is the scalar compressional potential and \mathbf{A} is the vector shear potential. If we set $\nabla \cdot \mathbf{A} = 0$ and substitute Eq. (13) into Eq. (12), then the potentials satisfy the following wave equations:

$$\frac{\partial^2 \Phi}{\partial t^2} = c^2 \nabla^2 \Phi \quad (14)$$

and

$$\frac{\partial^2 \mathbf{A}}{\partial t^2} = s^2 \nabla^2 \mathbf{A}. \quad (15)$$

Using Eq. (13), the above wave equations can be further expressed in terms of the velocity components in cylindrical coordinates as follows:

$$\frac{\partial^2 \Phi}{\partial t^2} = c^2 \left[\frac{1}{r} \frac{\partial (rv_r)}{\partial r} + \frac{1}{r} \frac{\partial v_\theta}{\partial \theta} + \frac{\partial v_z}{\partial z} \right], \quad (16)$$

$$\frac{\partial^2 A_r}{\partial t^2} = -s^2 \left(\frac{1}{r} \frac{\partial v_z}{\partial \theta} - \frac{\partial v_\theta}{\partial z} \right), \quad (17)$$

$$\frac{\partial^2 A_\theta}{\partial t^2} = -s^2 \left(\frac{\partial v_r}{\partial z} - \frac{\partial v_z}{\partial r} \right), \quad (18)$$

and

$$\frac{\partial^2 A_z}{\partial t^2} = -s^2 \frac{1}{r} \left(\frac{\partial (rv_\theta)}{\partial r} - \frac{\partial v_r}{\partial \theta} \right). \quad (19)$$

Since the compressional potential Φ and the three cylindrical components of the shear potential \mathbf{A} satisfy uncoupled scalar wave equations, we can treat them individually by the scheme of Lindman's ABC. We used the following modified Lindman's ABC scheme for the 3-D cylindrical coordinate problem:

$$\frac{\partial \Phi}{\partial t} + c \left(\frac{\partial \Phi}{\partial r} + \frac{\Phi}{2r} \right) = - \sum_{m=1}^M h_{\Phi_m} \quad (20)$$

and

$$\frac{\partial \Psi}{\partial t} + s \left(\frac{\partial \Psi}{\partial r} + \frac{\Psi}{2r} \right) = - \sum_{m=1}^M h_{\Psi_m}, \quad (21)$$

where Ψ represents shear potentials A_r , A_θ , and A_z , respectively and the correction functions h_{Φ_m} and $h_{\Psi_m} = \{h_{A_{r_m}}, h_{A_{\theta_m}}, h_{A_{z_m}}\}$ satisfy

$$\frac{\partial^2 h_{\Phi_m}}{\partial t^2} - \beta_m c^2 \frac{\partial^2 h_{\Phi_m}}{\partial z^2} = \alpha_m c^2 \frac{\partial^2}{\partial z^2} \left(c \frac{\partial \Phi}{\partial r} + c \frac{\Phi}{2r} \right) \quad (22)$$

and

$$\frac{\partial^2 h_{\Psi_m}}{\partial t^2} - \beta_m s^2 \frac{\partial^2 h_{\Psi_m}}{\partial z^2} = \alpha_m s^2 \frac{\partial^2}{\partial z^2} \left(s \frac{\partial \Psi}{\partial r} + s \frac{\Psi}{2r} \right), \quad (23)$$

respectively, where α_m, β_m with $m=1,2,3$ are constants (Chew, 1990). The implementation of Lindman's ABC in the FD code basically consists of three steps. First, Eqs. (16)–(19) are used to interpolate the compressional and shear potentials from velocity field. Next, Eqs. (20)–(23) are used to extrapolate the potentials at the boundary. Finally, Eq. (13) is employed to update the velocity at the boundary from the potentials. In implementing Lindman's ABC, a strict central-differencing staggered grid scheme is followed in both spatial and temporal domains. Thus a second order accuracy in

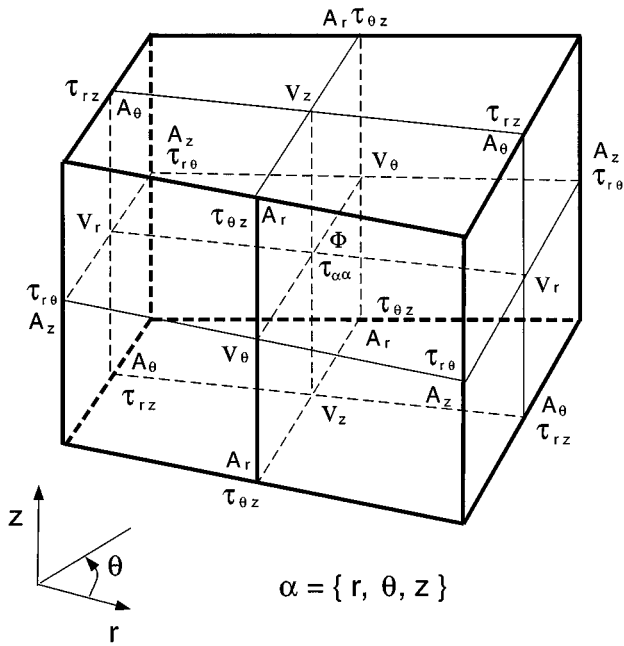


FIG. 2. Staggered grids at the outer radial boundary with discretized points of compressional and shear potentials in relation to velocity and stress components.

space and time is also achieved at the boundary. Figure 2 is the layout of the potential discretization points corresponding to the velocity and stress locations at the boundary. Our results show that the above ABC implementation works excellently for the exterior boundary at $r=r_{\max}$.

III. VALIDATION

In this section, numerical results will be shown to validate the finite difference program and to demonstrate applications to 3-D problems. In what follows, we use rings as the transmitter and receivers in all models. We apply sources to the diagonal stress terms all over the transmitter ring. For a monopole source, the receivers are of the same size as the transmitter and are vertically located at different positions. We record the diagonal stress at a same fixed azimuthal angle for all the receivers. For a dipole source, we record the radial velocity in the same way as we do for the monopole, but the radius of receivers is smaller than that of monopole receivers by one half of the radial grid size. The first 10 received waveforms for each figure in this section are normalized individually to give the same maximum amplitude. The rest of the waveforms as a group for each figure are normalized by the maximum value of that group. We will compare the numerical results for cylindrically layered media with the analytical solutions based on RAI (Lu and Liu, 1995). Three types of materials are used for different cases. They are fluid ($c=1500$ m/s, $s=0$ m/s, $\rho=1000$ kg/m³), steel ($c=5970$ m/s, $s=3120$ m/s, $\rho=7900$ kg/m³), and formation ($c=3000$ m/s, $s=1100$ m/s, $\rho=2200$ kg/m³). For reference, we name them as medium A, B, and C, respectively. The acoustic sources used in this study operate at center frequencies of either 5 or 10 kHz, with a waveform of

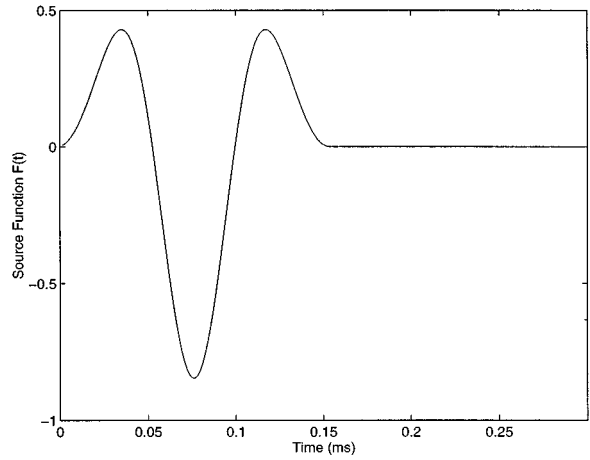


FIG. 3. The second derivatives of the Blackman–Harris window function was used in the simulation as the excitation source.

the second derivatives of the Blackman–Harris window function which is shown in Fig. 3 for 10 kHz (Liu *et al.*, 1996).

A. Homogeneous fluids

We first check FD results against RAI solutions for sources in a homogeneous fluid. Figure 4 shows the waveform comparison for a monopole ring source with a radius of 0.10 m in the fluid A. The center frequency used is 10 kHz. The solution domain is defined by $r_{\min}=0.0025$ m, $r_{\max}=0.5025$ m ($j_{\max}=100$), $z_{\max}=1$ m ($k_{\max}=200$), $\theta_{\max}=\pi$ ($l_{\max}=16$) with $\Delta t=1.5$ μ s. The two results agree very well. The direct arrivals travel at the fluid speed, and no dispersion is observed. The figure also justifies the use of the ring source, as we can see in the far-field region, the received waveforms are the same as those from a point source. In the near-field region, however, the receivers see two arrivals from the two sides of the ring, which is exaggerated in Fig. 5 where we doubled the ring source size. Notice that the number of sampling points in the azimuthal direction is not very

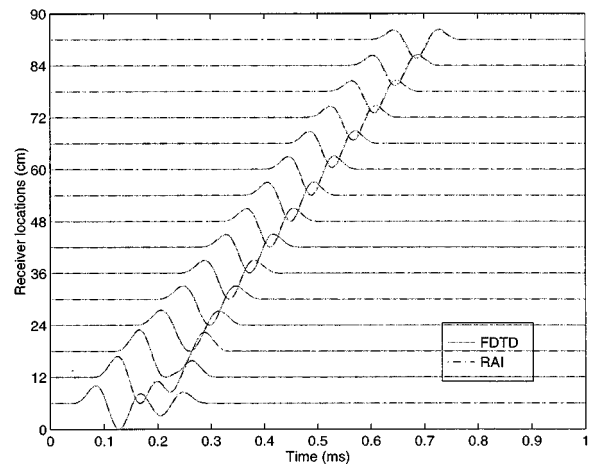


FIG. 4. The pressure waveforms calculated by FD (solid curves) are compared with those by RAI (dot-dashed lines) for a monopole source in fluid A (source radius = receiver radius = 10 cm, center frequency = 10 kHz).

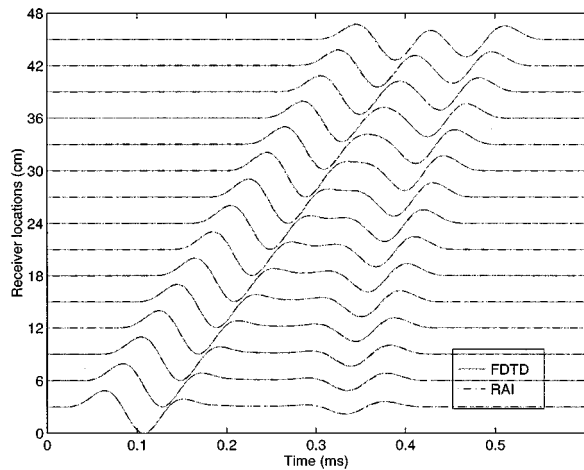


FIG. 5. The pressure waveforms simulated by FD (solid curves) are compared with those by RAI (dot-dashed lines) for a monopole source in fluid A (source radius = receiver radius = 20 cm, center frequency = 10 kHz).

critical when the wave fields are axisymmetrical for a monopole source. However, a coarse grid in such a case allows a larger time step in the simulation.

Figure 6 is a large homogeneous fluid case with a monopole source. For this case, we used $r_{\min}=0.0008$ m, $r_{\max}=0.5008$ m ($j_{\max}=100$), $z_{\max}=4.01$ m ($k_{\max}=802$), $\theta_{\max}=\pi/4$ ($l_{\max}=2$), and $\Delta t=1.8$ μ s. The minimum θ_{\max} is $\pi/2$ ($l_{\max}=4$) for a dipole source. Note that this model is much longer (4 m) than the previous one (1 m), and yet we use $r_{\max}=0.5008$ m. Very good ABC is required at the radial boundary for such a model, because the incident fields at the boundary are at near-grazing angles. Our experience shows that very large cases (both spatially and temporally) need to be calculated in order to decide if an implementation of an ABC scheme is acceptable.

B. Formation with a borehole

In Figs. 7 and 8, waveforms are simulated in homogeneous formations with a fluid-filled borehole for the mono-

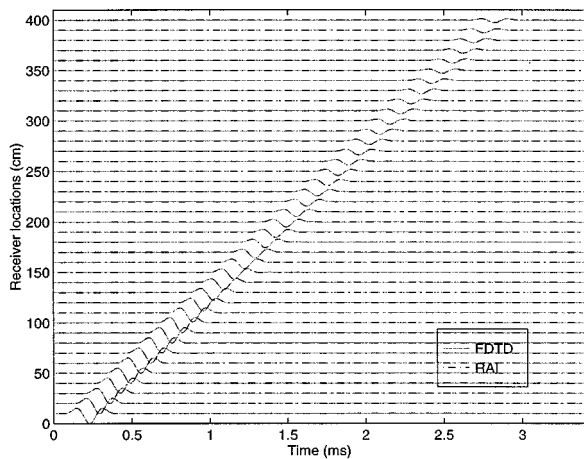


FIG. 6. The pressure waveforms calculated by FD (solid curves) are compared with those by RAI (dot-dashed lines) for a monopole source in fluid A (source radius = receiver radius = 3.83 cm, center frequency = 5 kHz).

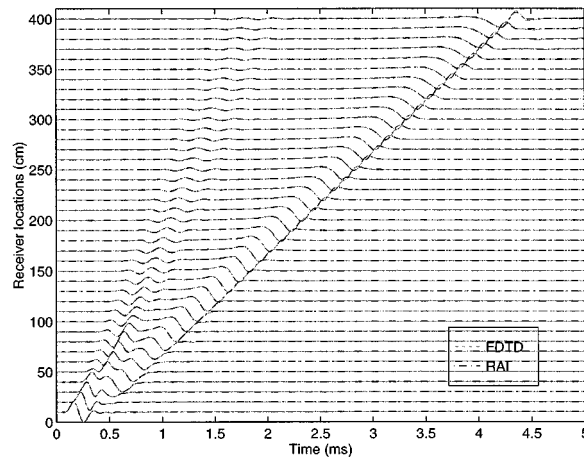


FIG. 7. The comparison of the pressure waveforms calculated by FD (solid curves) and RAI (dot-dashed lines) for a monopole source in formation (medium type: A-C, borehole radius = 10.08 cm, source radius = receiver radius = 4.33 cm, center frequency = 5 kHz).

pole and dipole ring sources. In these simulations, the center frequency of the source is 5 kHz. The medium is A-C, i.e., fluid A inside the borehole, and solid C as the formation. The radius of the ring source is 0.0433 m and that of the borehole is 0.1008 m. The parameters associated with the solution domain and its discretization are given as $r_{\min}=0.0008$ m, $r_{\max}=0.5008$ m ($j_{\max}=100$), $z_{\max}=4.01$ m ($k_{\max}=802$), $\theta_{\max}=\pi/4$ ($l_{\max}=8$), and $\Delta t=0.8$ μ s. Again, $\theta_{\max}=\pi/2$ ($l_{\max}=16$) for a dipole source. Excellent agreement is observed between the FD and the RAI results. The reflections are barely noticeable, because all boundaries have been properly taken care of. The compressional head waves are first recorded in the wave traces in Fig. 7. They decay as expected and travel at the formation compressional speed. No dispersion is observed for the head waves. After the head waves, the Stoneley waves follow in the waveforms. The Stoneley waves of the monopole case show some dispersion as they propagate, as do the flexural waves of the dipole source.

Notice that the azimuthal gridding becomes coarse as

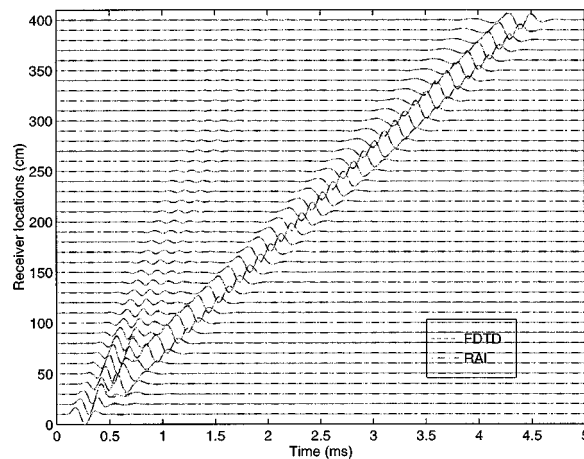


FIG. 8. Same as in Fig. 7 except that the source is a dipole and v_r is recorded (source radius = 4.33 cm, receiver radius = 4.08 cm, center frequency = 5 kHz).

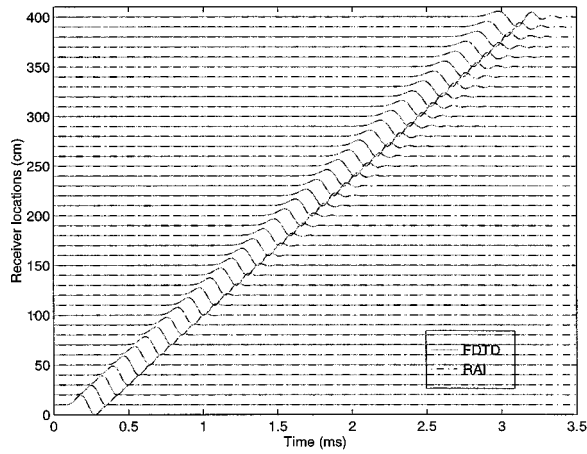


FIG. 9. The comparison of the pressure waveforms simulated by FD (solid lines) and RAI (dash-dotted curves) with a monopole source in fluid with steel pipe (medium type: *A-B-A*, pipe inner radius = 4.08 cm, pipe outer radius = 4.83 cm, source radius = receiver radius = 2.705 cm, center frequency = 5 kHz).

the radius increases and the fields simulated far beyond the borehole are not accurate due to the grid dispersion. In this paper, however, we are interested in the wave propagation and scattering phenomena near the borehole. All the transmitters and receivers are located inside the borehole. It is obvious that the method may not be used directly if scatterers far away from the borehole are involved such as in a sonic imaging situation.

C. Steel pipe in a borehole

Figure 9 simulates a monopole source in a medium *A-B-A*, that is, a steel pipe in fluid *A*. The inner radius of the steel pipe is 0.0408 m and the outer radius is 0.0483 m. The parameters associated with the solution domain and its discretization are given as $r_{\min}=0.0008$ m, $r_{\max}=0.5008$ m ($j_{\max}=200$), $z_{\max}=4.01$ m ($k_{\max}=802$), $\theta_{\max}=\pi$ ($l_{\max}=8$), and $\Delta t=0.24 \mu s$. Again, good agreement between the FD

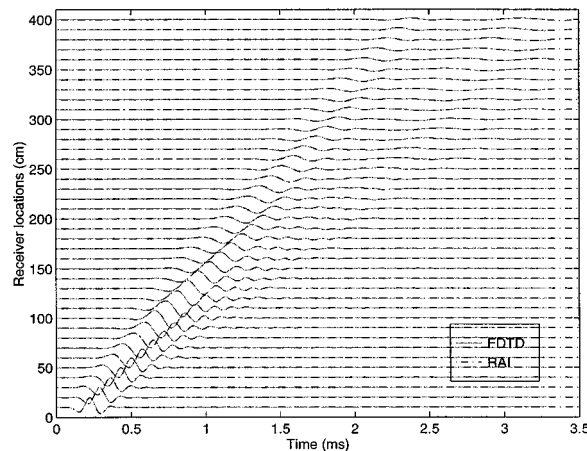


FIG. 10. The FD velocity (v_r) waveforms (solid lines) are compared with those by RAI (dash-dotted curves) for a dipole source in borehole with steel pipe (medium type: *A-B-A-C*, pipe inner radius = 4.08 cm, pipe outer radius = 4.83 cm, borehole radius = 10.08 cm, source radius = 2.705 cm, receiver radius = 2.58 cm, center frequency = 5 kHz).

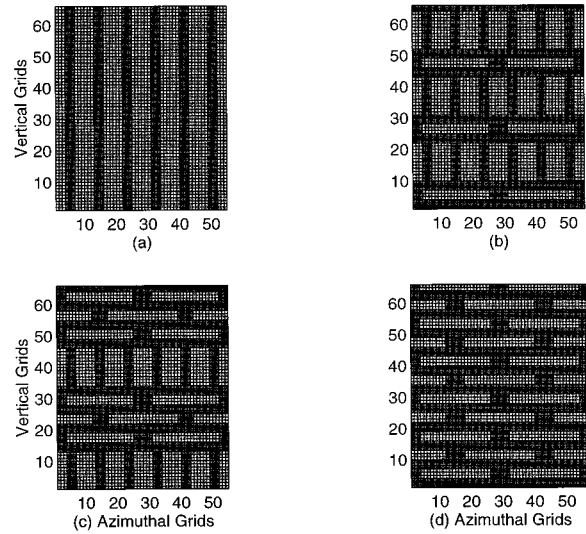


FIG. 11. Different slotted sleeve models are used for simulation.

and RAI results is achieved. As we can see from Fig. 9, the waveforms are dominantly controlled by the tube modes. There are extension waves traveling along the pipe in the early time for the monopole source, but they are too small to show up in the figure due to the larger amplitudes of the pipe modes.

The last model we used is *A-B-A-C*, simulating a uniform steel pipe in a slow formation with fluid-filled borehole. The radii of the medium interfaces are 0.0408 m, 0.0483 m and 0.1008 m. The dipole result is given in Fig. 10. The compressional head waves due to the borehole can be observed before the flexural waves if we amplify the dipole waveforms.

IV. SLOTTED SLEEVE MODELING

The 3-D FD code has been used to model the slotted sleeve housing of sonic logging tools. In this section, we will present some of the modeling results. Our focus of modeling is to show that we have developed a code which can be used

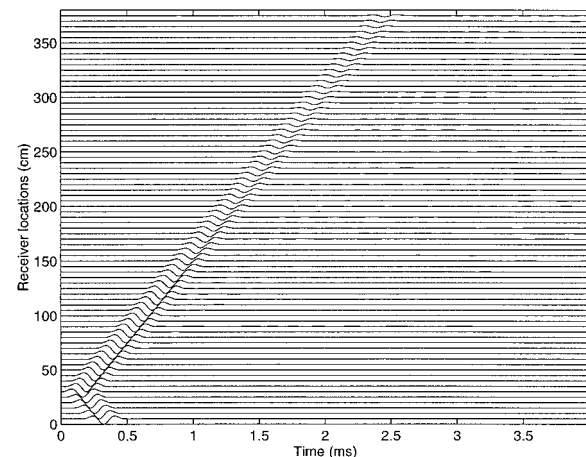


FIG. 12. Simulated waveforms of model 1 in fluid *A* with a monopole source.

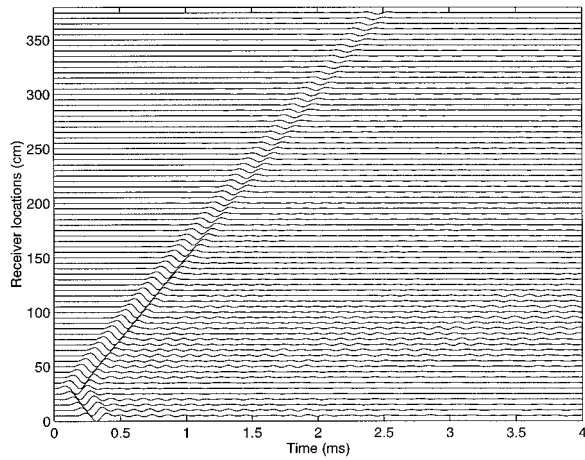


FIG. 13. Simulated waveforms of model 2 in fluid A with a monopole source.

to model and design the slotted sleeves for sonic logging. Through this initial modeling, we hope to provide some insight about the design of slotted sleeves.

Some of the slotted sleeve models used in the simulation are shown in Fig. 11, where the material mappings are shown for an azimuthal angle of 90° . The meshes are the actual discretization in our simulation models: Although different slots can be used for sonic logging, we use rectangular slots in the simulation because of their wide adoption in practice. The slotted sleeves are periodic and infinite in length in the z direction. For simplicity, we call these models described in Fig. 11(a)–(d) as model 1, model 2, model 3, and model 4, respectively. Model 1 has 12 uniformly distributed slots. Each of the slots is infinite in the z direction and spans an angle of 20° in the azimuthal direction. Model 4 has horizontal slots only, each of which spans 70° and has a width of 0.015 m. The adjacent slots in the vertical direction are separated by 0.015 m solid steel and are shifted by 45° to block the direct waves along the pipe. Models 2 and 3 are the combination of models 1 and 4. The vertical slots have a height of 0.06 m and all the solid steel sections have a height of 0.015 m. The inner and outer radii of the slotted sleeve

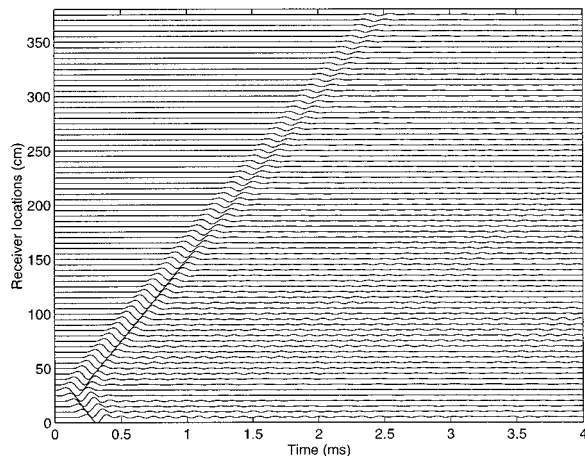


FIG. 14. Simulated waveforms of model 3 in fluid A with a monopole source.

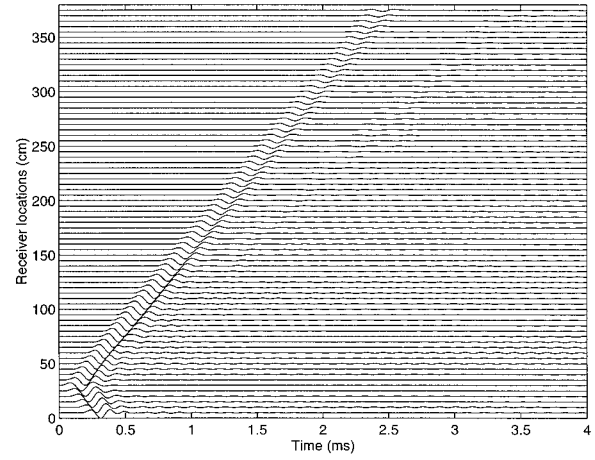


FIG. 15. Simulated waveforms of model 4 in fluid A with a monopole source.

housing are 0.045 m and 0.051 m, respectively.

Some basic requirements on the structure of the slotted sleeve models are imposed based on intuition. We require that the slotted sleeves be strong enough to avoid noticeable permanent deformation under various working conditions. Large slots are also avoided, because they might cause the tool to be stuck in a borehole while logging. Of course, model 1 does not meet these criteria, but we think that it will be interesting to compare its properties with those of the rest of the models. In the following simulations, the ring source radius is 0.025 m. The receiver radius is 0.025 m for a monopole source and 0.024 m for a dipole source. The center frequency is 5 kHz. The borehole radius, if applicable, is 0.105 m. Due to the fine structure of the slotted sleeves, the grid sizes have to be very small in all directions. Vertical and radial grid sizes are 0.005 and 0.002 m, respectively. There are approximately 810 sampling points in the vertical direction and 251 points in the radial direction. The simulation range in the θ direction depends on source type. For a monopole source, a sector region of 45° is solved (discretized with

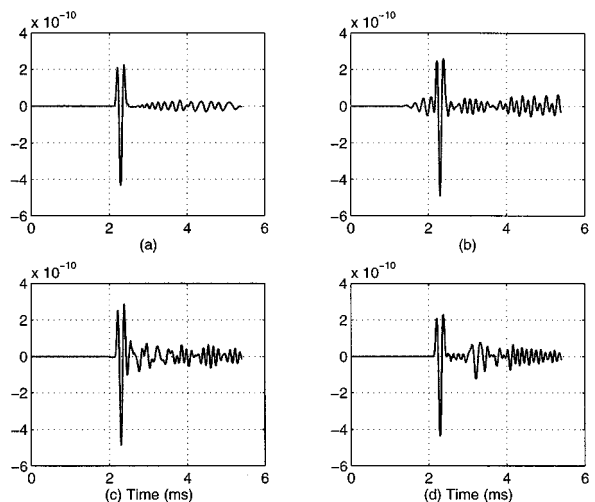


FIG. 16. The amplified waveform traces of receiver at $z=3.7$ m in Figs. 12–15.

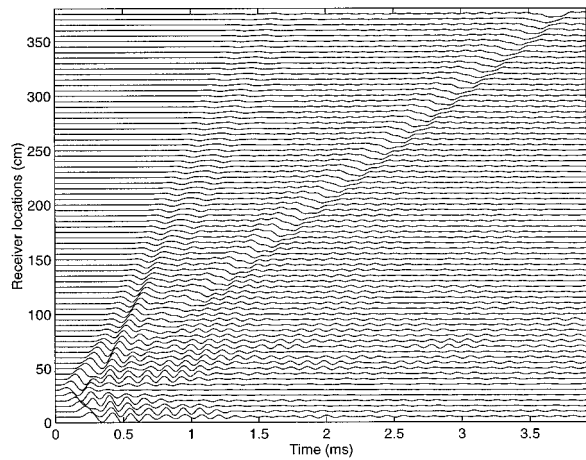


FIG. 17. Simulated waveforms of model 3 in a slow formation with a fluid-filled borehole.

15 points) with symmetrical boundary condition. For a dipole source, the solution range covers 90° (30 points) with anti-symmetrical boundary condition. The time step size is $0.18 \mu\text{s}$. The computers used for the simulations are SGI Power Challenge Array. Each of the simulations typically takes about 1–2 days on a four CPU machine. In what follows, we present the modeling results in terms of the sources we used.

A. Monopole source

Figures 12–15 show the simulated waveforms of the four slotted sleeves in fluid A. Note that for these figures, the first 24 waveforms are normalized trace by trace to give the same maximum amplitude of one, while the rest of the waveforms as a group in each figure are normalized by the maximum value of their group. If we compare the waveforms of these slotted sleeves with those of a steel pipe as shown in Fig. 9, we see that the major waveform variations here are caused by the direct arrivals in the fluid instead of the tube waves. The slotted sleeves have effectively destroyed the tube waves which would otherwise manifest themselves as in Figure 9. The small ripples on the waveforms are due to the

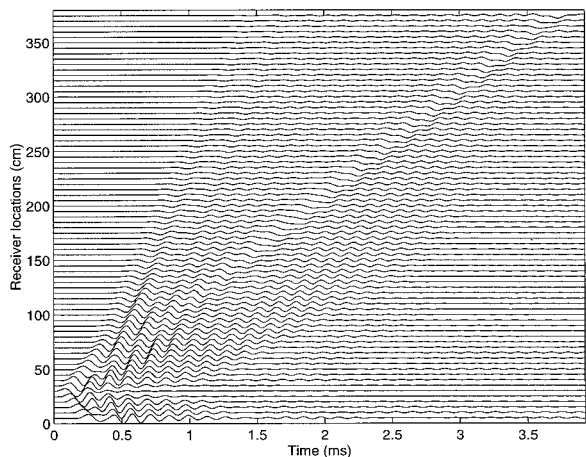


FIG. 18. Simulated waveforms of model 4 in a slow formation with a fluid-filled borehole.

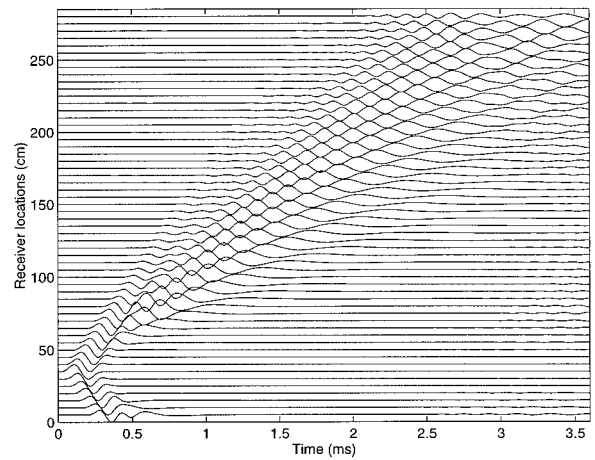


FIG. 19. Simulated waveforms of model 1 in fluid A with a dipole source.

scattering of the slotted sleeves. If there were no scattering by the slotted sleeves, the wave field traces would be as clean as those given by Fig. 6 for a homogeneous fluid.

In comparison with the other three models, model 1 gives the cleanest waveforms (see Fig. 12 and compare it with Figs. 13, 14, and 15) because the model does not have any vertical variation. For this case, extension waves exist and can be observed if we amplify the curves [see Fig. 16(a)]. The extension waves which travel along the steel strips are not perturbed in such a structure and can be easily removed by time gating or data processing. However, this kind of slotted sleeve is not very practical.

For a realistic slotted sleeve model, horizontal structure must also be used. In model 2, the vertical and horizontal slots are used alternatively. Its simulated waveforms are shown in Fig. 13. The horizontal slot sections are seen by the propagating wavefields as impedance mismatches, and stronger scatterings (ripples) can be observed in the waveforms. Enlarged waveform shows that the extension waves are smeared and delayed [see Fig. 16(b)]. Such signals cannot be easily removed by time gating or data processing. However, we can reduce them by using more horizontal slots as shown in model 4. The simulated results based on model 3 are given in Fig. 14, and an amplified curve is shown in Fig. 16(c).

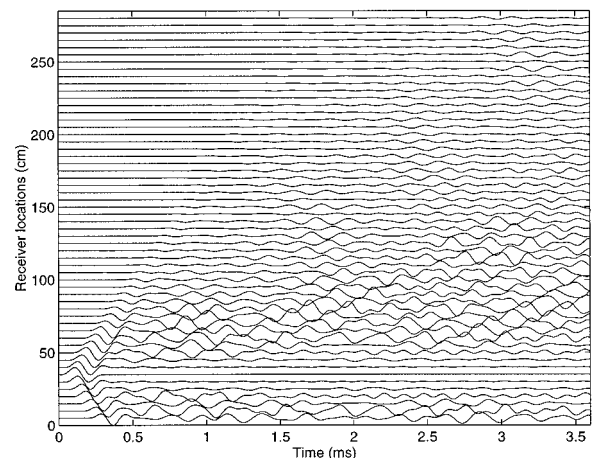


FIG. 20. Simulated waveforms of model 2 in fluid A with a dipole source.

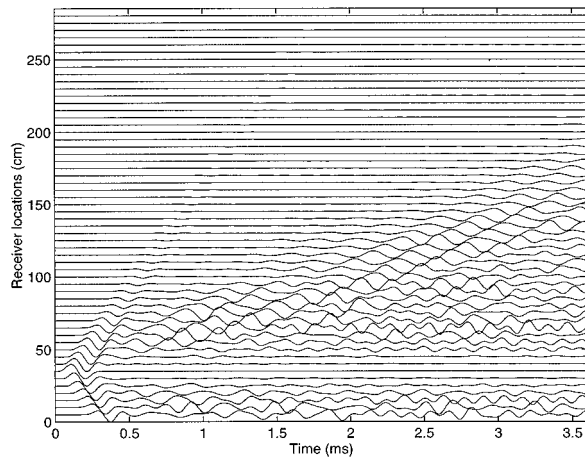


FIG. 21. Simulated waveforms of model 3 in fluid A with a dipole source.

As we can see from the previous results, the use of horizontal slots can efficiently delay the waves caused by the slotted sleeves. However, there are drawbacks associated with the horizontal slots. The percentage of the slotted area over the pipe surface in a horizontal slot section is much smaller than that in a vertical slot section because the latter can have much longer slots. The wave fields due to the pipe modes become stronger as more horizontal slots are used. This phenomena can be observed from the results of model 4 in Fig. 15 where no vertical slots are used.

Figures 17 and 18 are the simulation results for models 3 and 4 in a homogeneous slow formation with a fluid-filled borehole. The waveforms are comparable with Fig. 7 except that ripples show up in the wave traces due to the slotted sleeve scatterings. All the ripples seem to travel at the same speed as the compressional head waves. This is because the strongest scatterings occur near the source point, and all the scattered fields, once coupled into the formation, start to propagate at these speeds. Here, model 3 is shown to give less ringing after the compressional head waves than model 4. Thus, model 3 gives a better performance in a borehole structure for a monopole source. For model 3, slightly different structures have been simulated by changing the length

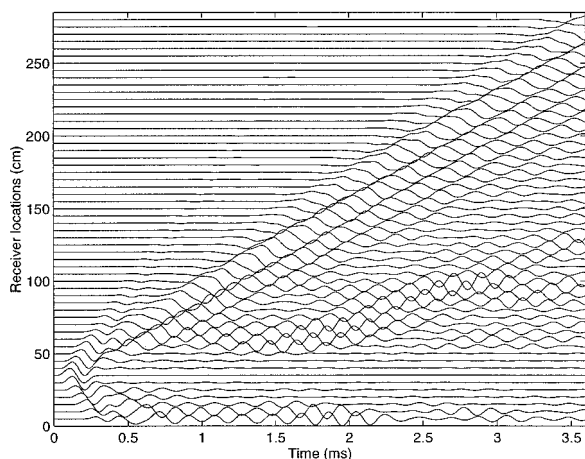


FIG. 22. Simulated waveforms of model 4 in fluid A with a dipole source.

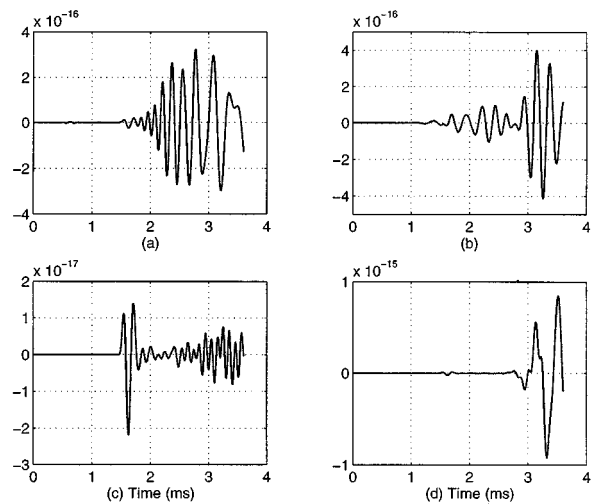


FIG. 23. The amplified waveform traces of receiver at $z=2.55$ m in Figs. 19–22.

of the vertical slots, the length of the solid steel junctions between the slots sections, and the number of slots in the vertical slot sections. Similar results have been consistently observed, with model 3 giving the smallest ringing.

B. Dipole source

For a dipole source, the simulated waveforms in the fluid A are given in Figs. 19, 20, 21, and 22, respectively, for slotted sleeve models 1–4. The first fifteen waveforms in these figures have been normalized trace by trace, while the rest of the waveforms as a group in each figure are normalized by the maximum value of their group. From these figures, we see that the pipe waves have been reduced and delayed by the slots. Thus, the weak direct arrivals in the fluid are clearly seen. However, unlike the monopole case discussed previously, the slotted sleeve effects on the waveforms vary widely depending on the slotted sleeve structure.

For model 1 (Fig. 19), the slender steel strips are seen to excite strong flexural modes right after the direct fluid arrivals, and extension waves are observed on the nonaxisym-

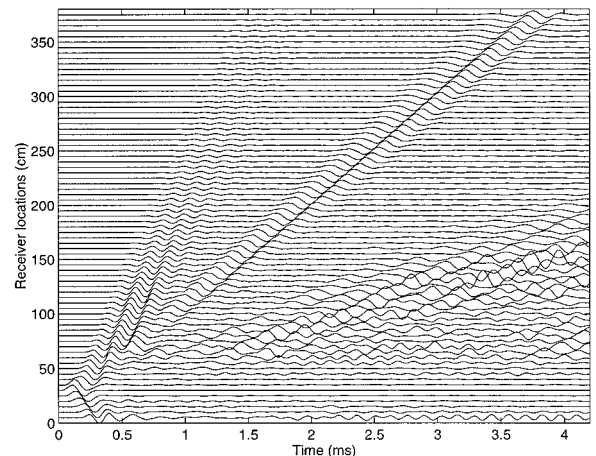


FIG. 24. Simulated waveforms of model 3 in a slow formation with a fluid-filled borehole.

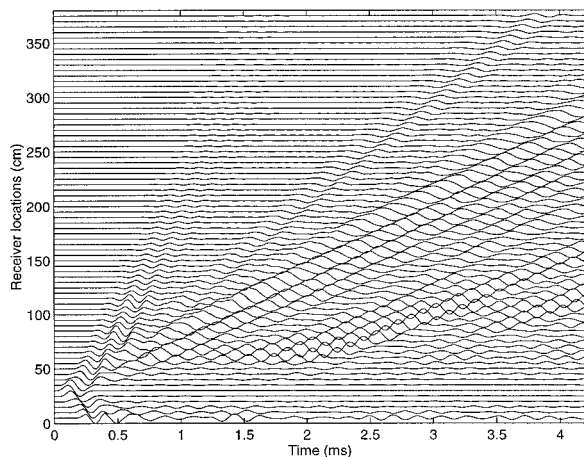


FIG. 25. Simulated waveforms of model 4 in a slow formation with a fluid-filled borehole.

metrical structure in Fig. 23(a) (the first ripple). Similar to the monopole case, the horizontal slots sections are seen as strong scatterers for the extension waves propagating along the steel strips for model 2 (Fig. 20). It is now difficult to identify the fluid direct arrivals due to the scattering fields and more horizontal slots are needed to further reduce and delay the pipe modes. Figure 21 presents the simulated waveforms for model 3 where three horizontal slot sections are used for every vertical slot section. The model generates the smallest scattering fields in the early time among the four test models for the dipole source. The model comprised of only horizontal slots is seen to give rise to strong tube modes as shown in Fig. 22 and Fig. 23(d).

Similar phenomena are observed for waveforms in slow formation with a fluid-filled borehole. The simulated results are given in Figs. 24 and 25 for the slotted sleeve models 3 and 4. In these figures, both the compressional head waves and the borehole flexural waves show up well before the scattered fields of the slotted sleeve. The borehole flexural waves travel approximately at the speed of the formation shear waves and can be used to estimate the formation shear velocity. Based on the simulation results, the third slotted sleeve model gives the best performance for both dipole and monopole sources. The slotted sleeve is very effective in delaying and attenuating the scattered wave fields by itself when a dipole source is used. However, it does not seem to work as well for a monopole source. The ringing noise starts right after the compressional headwaves when a monopole source is used. We do not know yet what causes the large difference between the two sources.

V. CONCLUSIONS

We have developed a three-dimensional finite difference time domain code to simulate elastic wave propagation in cylindrical coordinate system. Both Liao's and Lindman's absorbing boundary conditions are implemented in the code to reduce the simulation region. The combination of the two ABCs is shown to absorb waves at the boundary very effectively for the elongated well logging problems. The code has

been extensively validated by the solution of real axis integration for various layered media. Excellent agreement is achieved for all the test problems.

We have applied the code to model some typical slotted sleeves for sonic logging tools. Different slotted sleeves are found to vary widely in delaying and attenuating the pipe waves. Based on the simulation results, new slotted sleeve structure with three horizontal slot sections for every vertical slot period is proposed for better performance. With this new slotted sleeve structure, both the compressional head waves and the borehole flexural waves show up well before the scattered fields of the slotted sleeve for a dipole source. A dipole source is found to produce much cleaner than a monopole source.

ACKNOWLEDGMENTS

This work was supported by the Air Force Office of Scientific Research under Grant No. F49620-96-1-0025, the National Science Foundation under Grant No. NSF ECS93-02145, the Office of Naval Research under Grant No. N00014-95-1-0872, a gift from Schlumberger-Doll Research, and the National Center for Supercomputing Applications (NCSA) for providing the computer time. The first author would like to thank Chaur-Jian Hsu, Mike Prange, Ping Lee, and Chung Chang for some useful discussions.

- Aki, K., and Richards, P. G. (1980). *Quantitative Seismology: Theory and Methods* (Freeman, San Francisco).
- Auld, B. A. (1990). *Acoustic Fields and Waves in Solids* (Freeman, San Francisco), Vol. 1.
- Biot, M. A. (1952). "Propagation of elastic waves in a cylindrical bore containing a fluid," *J. Appl. Phys.* **23**, 997-1005.
- Chew, W. C. (1990). *Waves and Fields in Inhomogeneous Media* (Van Nostrand Reinhold, New York), pp. 211-269.
- Cheng, C. H., and Toksoz, M. N. (1981). "Elastic wave propagation in a fluid-filled borehole and synthetic acoustic logs," *Geophysics* **46**, 1042-1053.
- Cheng, N., Cheng, C. H., and Toksoz, M. N. (1995). "Borehole wave propagation in three dimensions," *J. Acoust. Soc. Am.* **97**, 3483-3493.
- Daube, F., and Randall, C. J. (1991). "3-D elastic wave propagation on the connection machine," SLCS Research Report, No. TR/C-91-07 (released for public reference).
- Kurkjian, A. L. (1985). "Numerical computation of individual far-field arrivals excited by an acoustic source in a borehole," *Geophysics* **50**, 852-866.
- Kurkjian, A. L., and Chang, S.-K. (1986). "Acoustic multipole sources in fluid-filled boreholes," *Geophysics* **51**, 148-163.
- Leslie, H. D., and Randall, C. J. (1992). "Multipole sources in boreholes penetrating anisotropic formations: Numerical and experimental results," *J. Acoust. Soc. Am.* **91**, 12-27.
- Levander, A. R. (1988). "Fourth-order finite difference P-SV seismograms," *Geophysics* **53**, 1425-1436.
- Liao, Z. P., Wong, H. L., Yang, B. P., and Yuan, Y. F. (1984). "A transmitting boundary for transient wave analysis," *Sci. Sin.* **27**, 1063-1076.
- Lindman, E. L. (1975). "Free space boundary conditions for the time dependent wave equation," *J. Comput. Phys.* **18**, 66-78.
- Liu, Q.-H., and Chang, C. (1994). "Compressional head waves in attenuative formations," *Proc. 64th Annual Meeting of Soc. Explor. Geophys.*, pp. 12-15.
- Liu, Q.-H., and Chang, C. (1996). "Compressional head waves in attenuative formations: Forward modeling and inversion," *Geophysics* **61**, 1908-1920.
- Liu, Q.-H., Schoen, E., Daube, F., Randall, C., Liu, H.-L., and Lee, P. (1996). "A three-dimensional finite difference simulation of sonic log-

- ging," J. Acoust. Soc. Am. **100**, 72–79.
- Lu, C.-C., and Liu, Q.-H. (1995). "A three-dimensional dyadic Green's function for elastic waves in multilayer cylindrical structures," J. Acoust. Soc. Am. **98**, 2825–2835.
- Madariaga, R. (1976). "Dynamics of an expanding circular fault," Bull. Seismol. Soc. Am. **65**, 163–182.
- Randall, C. J. (1989). "Absorbing boundary condition for the elastic wave equation: Velocity-stress formulation," Geophysics **54**, 1141–1152.
- Randall, C. J., Scheibner, D. J., and Wu, P. T. (1991). "Multipole borehole acoustic waveforms: Synthetic logs with beds and borehole washouts," Geophysics **56**, 1757–1769.
- Stephen, R. A., Cardo-Casas, F., and Cheng, C. H. (1985). "Finite-difference synthetic acoustic logs," Geophysics **50**, 1588–1609.
- Taflove, A. (1995). *Computational Electromagnetics: The Finite-Difference Time-Domain Method* (Artech House, Boston), pp. 36–38.
- Tsang, L. (1986). "Transient acoustic waves in a fluid-filled borehole with a horizontal bed boundary separating two solid formations," J. Acoust. Soc. Am. **81**, 844.
- Tsang, L., and Rader, D. (1979). "Numerical evaluation of transient acoustic waveforms due to a point source in a fluid-filled borehole," Geophysics **44**, 1706–1720.
- Virieux, J. (1986). "P-SV wave propagation in heterogeneous media: Velocity-stress finite-difference method," Geophysics **51**, 889–901.
- Virieux, J. (1984). "SH-wave propagation in heterogeneous media: Velocity-stress finite-difference method," Geophysics **49**, 1933–1957.
- Yee, K. S. (1966). "Numerical solution of initial boundary value problems involving Maxwell's equations in isotropic media," IEEE Trans. Antennas Propag. **AP-14**, 302–307.
- Yoon, K. H., and McMechan, G. A. (1992). "3-D finite-difference modeling of elastic waves in borehole environments," Geophysics **57**, 793–804.

A recursive Green's function technique for acoustic scattering from heterogeneous objects

Michael A. Jensen

Department of Electrical and Computer Engineering, 459 Clyde Building, Brigham Young University, Provo, Utah 84602-4099

(Received 5 May 1997; accepted for publication 14 October 1997)

A fast, efficient algorithm for computing acoustic fields scattered by inhomogeneous objects in an otherwise homogeneous space is presented. The algorithm, called the Recursive Green's Function Method (RGFM), constructs the domain Green's function by recursively combining known Green's functions from smaller subdomains. The fields on the scatterer surface are then computed using a boundary integral formulation. Proper implementation of the RGFM results in a storage requirement of $O(N)$ and computational costs of $O(N^{3/2})$ and $O(N^2)$ for two- and three-dimensional problems, respectively, where N is the total number of discrete points in the inhomogeneous region. Results are compared with those obtained from exact solutions to show the accuracy of the method.

© 1998 Acoustical Society of America. [S0001-4966(98)00602-X]

PACS numbers: 43.20.Fn, 43.30.Gv [ANN]

INTRODUCTION

Determining the behavior of acoustic fields in and near inhomogeneous domains finds practical application in such areas as medical imaging, geophysical exploration, seismic engineering, and underwater acoustics. For complex, heterogeneous geometries where closed-form solutions¹ are impractical, such analysis must be performed using numerical schemes such as the finite element,^{2,3} finite difference,^{3,4} boundary integral,^{5,6} T-matrix,⁷ and multipole expansion^{8,9} techniques. These latter three methods are particularly efficient for unbounded domains since their formulations are based upon integral equations which incorporate radiation conditions. However, they are typically limited to homogeneous or piecewise homogeneous media.

Given these observations, it is evident that a beneficial contribution involves extending integral equation techniques to efficiently accommodate heterogeneous domains. The difficulty with this concept is that the Green's function for the inhomogeneous region must be known to apply the boundary integral equations.¹⁰ This Green's function generally cannot be determined analytically, and therefore must be constructed using numerical schemes which are typically computationally costly, making this approach impractical for most realistic configurations.

The goal of this paper is to present an efficient scheme, known as the Recursive Green's Function Method (RGFM),¹¹ for computing the Green's function of an inhomogeneous domain and subsequently using it to compute the fields scattered by and internal to the object. The technique, which finds root in one-dimensional optical waveguide analysis,¹²⁻¹⁴ incrementally constructs the desired solution by cleverly combining Green's functions for smaller domains. The algorithm is similar to the T-matrix method, particularly the Nested Equivalence Principle Algorithm (NEPAL)^{15,16} for electromagnetic modeling. However, the present formulation differs from NEPAL in the selection of boundary conditions on the Green's function which simplifies the derivation and application. In this paper we provide a

firm theoretical basis for the method and demonstrate its application to two- and three-dimensional acoustic problems. Analysis shows that the computational costs of the algorithm are $O(N^{3/2})$ and $O(N^2)$ for two- and three-dimensional problems, respectively, where N is the number of cells in the discretized domain. The storage remains at $O(N)$ for both cases. Computational examples are provided which show the flexibility of the method in modeling general material profiles. Where possible, comparisons are made with exact solutions to illustrate the accuracy of the RGFM results.

I. THEORY

The problem of interest involves the scattering of a single-frequency incident wave field $P^{\text{inc}}(\mathbf{r})$ from a finite-sized inhomogeneous region Ω^i embedded in a homogeneous space Ω^o , as implied in Fig. 1. Throughout the derivation, we will use the notation $\partial\Omega$ to represent a domain boundary. A pressure wave $P^\gamma(\mathbf{r})$ propagating in either region is governed by the general Helmholtz equation

$$\{\nabla \cdot [\rho^{-1}(\mathbf{r})\nabla] + \rho^{-1}(\mathbf{r})k^2(\mathbf{r})\}P^\gamma(\mathbf{r}) = 0, \quad (1)$$

where $\gamma = i, o$ for $\mathbf{r} \in \Omega^{i,o}$. The parameters $k(\mathbf{r})$ and $\rho(\mathbf{r})$ represent the spatially varying wavenumber and mass density, respectively.

To facilitate the solution to Eq. (1), we define the Green's function $G^\gamma(\mathbf{r}, \mathbf{r}')$ which is a solution to the equation

$$\{\nabla \cdot [\rho^{-1}(\mathbf{r})\nabla] + \rho^{-1}(\mathbf{r})k^2(\mathbf{r})\}G^\gamma(\mathbf{r}, \mathbf{r}') = -\delta(\mathbf{r} - \mathbf{r}'), \quad (2)$$

where $\delta(\cdot)$ represents the Dirac delta function. Use of Eqs. (1) and (2) in conjunction with Green's integral theorem allows expression of the solution $P^\gamma(\mathbf{r})$ of Eq. (1) as¹

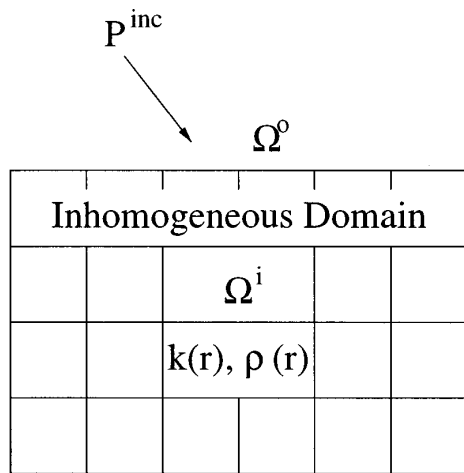


FIG. 1. Inhomogeneous domain Ω^i embedded in an otherwise homogeneous region Ω^o along with the divisions required for the RGFM.

$$P^i(\mathbf{r}) = \oint_{\partial\Omega^i} \frac{1}{\rho(\mathbf{r}')} \left[G^i(\mathbf{r}, \mathbf{r}') \frac{\partial P^i(\mathbf{r}')}{\partial n'} - P^i(\mathbf{r}') \frac{\partial G^i(\mathbf{r}, \mathbf{r}')}{\partial n'} \right] dS', \quad \mathbf{r} \in \Omega^i, \quad (3)$$

$$P^o(\mathbf{r}) = P^{\text{inc}}(\mathbf{r}) - \oint_{\partial\Omega^i} \frac{1}{\rho_o} \left[G^o(\mathbf{r}, \mathbf{r}') \frac{\partial P^o(\mathbf{r}')}{\partial n'} - P^o(\mathbf{r}') \frac{\partial G^o(\mathbf{r}, \mathbf{r}')}{\partial n'} \right] dS', \quad \mathbf{r} \in \Omega^o, \quad (4)$$

where n' represents the outward normal coordinate to Ω^i and ρ_o is the constant mass density in Ω^o .

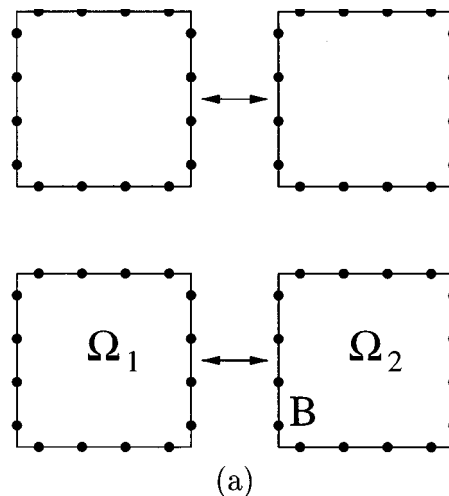
A. Green's function construction

If the Green's functions G^i and G^o are known, then Eqs. (3) and (4) may be solved for the fields on $\partial\Omega^i$ using a numerical approach such as the boundary element method.⁵ The difficulty here is that the Green's function G^i for the inhomogeneous domain is difficult and costly to construct. To facilitate this construction, consider subdividing the domain Ω^i into N small subdomains Ω_p , $1 \leq p \leq N$, as implied in Fig. 1. We will assume that within Ω_p , $k(\mathbf{r}) = k_p$ and $\rho(\mathbf{r}) = \rho_p$ remain constant. Also, to simplify the derivation, we will assume that G_p satisfies homogeneous Neumann boundary conditions on $\partial\Omega_p$. Appendix A provides expressions for G_p for two- and three-dimensional domains.

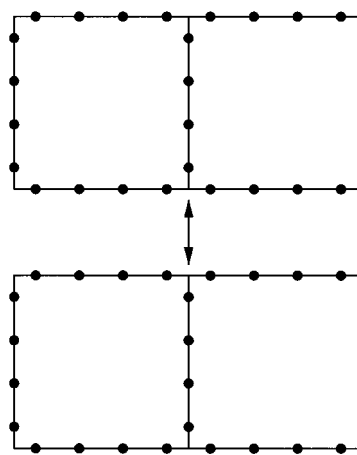
Consider now the scenario shown in Fig. 2(a) where the Green's functions G_1 and G_2 are known on two adjacent domains Ω_1 and Ω_2 with interface $B = \Omega_1 \cap \Omega_2$. Let the Green's function $G(\mathbf{r}, \mathbf{r}')$ for the composite domain $\Omega = \Omega_1 \cup \Omega_2$ be divided into four parts according to the definition

$$G_{pq}(\mathbf{r}, \mathbf{r}') = G(\mathbf{r}, \mathbf{r}'), \quad \mathbf{r} \in \Omega_p, \mathbf{r}' \in \Omega_q, \quad (5)$$

where $p, q \in [1, 2]$. Since G_{pp} and G_p satisfy the same differential equation, their first argument dependence must dif-



(a)



(b)

FIG. 2. (a) Horizontal and (b) vertical combining of two-dimensional domains to make a single composite domain using the RGFM equations.

fer only by a homogeneous solution of Eq. (2). Similarly, G_{pq} , $p \neq q$, must be a homogeneous solution of Eq. (2) in its first argument. As discussed in Appendix B, these homogeneous solutions can be constructed from the subdomain Green's functions, resulting in

$$G_{pp}(\mathbf{r}, \mathbf{r}') = G_p(\mathbf{r}, \mathbf{r}') + \int_B G_p(\mathbf{r}, \mathbf{r}'') A_{pp}(\mathbf{r}'', \mathbf{r}') d\mathbf{r}'', \quad (6)$$

$$G_{pq}(\mathbf{r}, \mathbf{r}') = \int_B G_p(\mathbf{r}, \mathbf{r}'') A_{pq}(\mathbf{r}'', \mathbf{r}') d\mathbf{r}'', \quad p \neq q, \quad (7)$$

where the A_{pq} represent unknown functions.

To solve for the unknown A_{pq} , we must apply the continuity of the expressions in Eqs. (6) and (7) and their normal derivatives on B . To begin, consider the condition¹⁷

$$\frac{1}{\rho_p} \frac{\partial}{\partial n} G_{pq}(\mathbf{r}_B, \mathbf{r}') = \frac{1}{\rho_q} \frac{\partial}{\partial n} G_{qq}(\mathbf{r}_B, \mathbf{r}'), \quad (8)$$

where $\mathbf{r}_B \in B$, $p \neq q$, and n represents the coordinate normal to B . Application of this expression to Eqs. (6) and (7) results in the relation

$$\begin{aligned} & \lim_{\mathbf{r}_p \rightarrow \mathbf{r}_B} \int_B \frac{1}{\rho_p} \frac{\partial}{\partial n} G_p(\mathbf{r}_p, \mathbf{r}'') A_{pq}(\mathbf{r}'', \mathbf{r}') d\mathbf{r}'' \\ &= \lim_{\mathbf{r}_q \rightarrow \mathbf{r}_B} \int_B \frac{1}{\rho_q} \frac{\partial}{\partial n} G_q(\mathbf{r}_q, \mathbf{r}'') A_{qq}(\mathbf{r}'', \mathbf{r}') d\mathbf{r}'', \end{aligned} \quad (9)$$

where \mathbf{r}_p approaches \mathbf{r}_B in the direction of n from the side of Ω_p . Note that the homogeneous Neumann boundary condition has been used to eliminate the term $\partial G_q(\mathbf{r}_B, \mathbf{r}')/\partial n$ from the right hand side of Eq. (9). The normal derivatives within the integrands in Eq. (9) are more difficult to evaluate since the source point \mathbf{r}'' is already on the interface B as the observation points approach B . To illustrate the procedure for evaluating these derivatives, consider the case where $n = x$ such that the boundary B lies parallel to the yz plane. In this case, we can use the jump condition on G_p which requires that¹⁷

$$\begin{aligned} & \lim_{\epsilon \rightarrow 0} \left[\frac{1}{\rho_p} \frac{\partial}{\partial x} G_p(\mathbf{r}^+, \mathbf{r}') - \frac{1}{\rho_p} \frac{\partial}{\partial x} G_p(\mathbf{r}^-, \mathbf{r}') \right] \\ &= -\delta(y-y')\delta(z-z'), \end{aligned} \quad (10)$$

where $\mathbf{r}^\pm = (x' \pm \epsilon, y, z)$. Now, consider the case where $p=1$ in Eq. (10) and let \mathbf{r}' approach the interface coordinate \mathbf{r}'' . Since the observation point \mathbf{r}^+ in the first term of Eq. (10) will reach the interface before the source point \mathbf{r}' in the limiting process, application of the homogeneous Neumann boundary condition will cause this term to vanish. In contrast, the observation point \mathbf{r}^- of the second term will arrive at the interface after the source point, in which case the Neumann boundary condition will not apply. A similar argument can be made for the case where $p=2$, resulting in the general expression

$$\lim_{\mathbf{r}_p \rightarrow \mathbf{r}_B} \frac{1}{\rho_p} \frac{\partial}{\partial x} G_p(\mathbf{r}_p, \mathbf{r}'') = \pm \delta(y_B - y'') \delta(z_B - z''), \quad (11)$$

where the upper and lower signs are used for $p=1$ and 2, respectively. Similar derivations can be completed for $n=y$ and $n=z$. Substitution of these results into Eq. (9) provides the result

$$A_{pq}(\mathbf{r}_B, \mathbf{r}') = -A_{qq}(\mathbf{r}_B, \mathbf{r}'), \quad p \neq q. \quad (12)$$

The next step in the derivation requires enforcing continuity of the Green's function on B , or

$$G_{pq}(\mathbf{r}_B, \mathbf{r}') = G_{qq}(\mathbf{r}_B, \mathbf{r}'). \quad (13)$$

Using this relation on the expressions in Eqs. (6) and (7) and utilizing the result of Eq. (12) generates the integral equation

$$\begin{aligned} G_q(\mathbf{r}_B, \mathbf{r}') &= - \int_B [G_p(\mathbf{r}_B, \mathbf{r}'') + G_q(\mathbf{r}_B, \mathbf{r}'')] \\ &\quad \times A_{qq}(\mathbf{r}'', \mathbf{r}') d\mathbf{r}'', \end{aligned} \quad (14)$$

which must be solved for the unknown function A_{qq} . To perform this solution, we project the \mathbf{r} and \mathbf{r}' dependence of G_p and G_q and the \mathbf{r}' dependence of A_{qq} onto basis sets complete on either $\partial\Omega_p$ or $\partial\Omega_q$, and the \mathbf{r}'' dependence of A_{qq} onto a basis complete on B . For simplicity, we assume the basis functions are of compact support, so that the basis

representation on B is a subset of that on $\partial\Omega_p$ or $\partial\Omega_q$. This expansion can be written as

$$G_p(\mathbf{r}, \mathbf{r}') = \sum_{mn} g_{p,mn} \psi_m(\mathbf{r}) \psi_n(\mathbf{r}'), \quad (15)$$

$$A_{qq}(\mathbf{r}_B, \mathbf{r}') = \sum_{ij} a_{qq,ij} \psi_i(\mathbf{r}_B) \psi_j(\mathbf{r}'), \quad (16)$$

where the coefficients $g_{p,mn}$ are elements of the matrix \mathbf{g}_p obtained from

$$\mathbf{g}_p = \mathbf{S}^{-1} \mathbf{H}_p \mathbf{S}^{-1}, \quad (17)$$

$$H_{p,mn} = \int_{\partial\Omega_p} \int_{\partial\Omega_p} \psi_m(\mathbf{r}) G_p(\mathbf{r}, \mathbf{r}') \psi_n(\mathbf{r}') d\mathbf{r} d\mathbf{r}', \quad (18)$$

$$S_{mn} = \int_{\partial\Omega_p} \psi_m(\mathbf{r}) \psi_n(\mathbf{r}) d\mathbf{r}. \quad (19)$$

Given this representation, it is clearly advantageous to use orthonormal basis sets in order to avoid computation of \mathbf{S}^{-1} .

With this notation, let $\bar{\mathbf{g}}_p$ represent the matrix of coefficients for which $\mathbf{r}, \mathbf{r}' \in B$ and $\hat{\mathbf{g}}_p$ represent the matrix of coefficients for which $\mathbf{r} \in B$ and $\mathbf{r}' \in \partial\Omega_p$. Then the solution of Eq. (14) results in

$$\mathbf{a}_{qq} = -(\bar{\mathbf{g}}_p + \bar{\mathbf{g}}_q)^{-1} \hat{\mathbf{g}}_q = -\mathbf{T} \hat{\mathbf{g}}_q. \quad (20)$$

Inserting this result into discrete forms of Eqs. (6) and (7) and using Eq. (12) results in the matrix expressions

$$\mathbf{g}_{pp} = \mathbf{g}_p - \hat{\mathbf{g}}_p^t \mathbf{T} \hat{\mathbf{g}}_p, \quad (21)$$

$$\mathbf{g}_{pq} = \hat{\mathbf{g}}_p^t \mathbf{T} \hat{\mathbf{g}}_q, \quad (22)$$

where t denotes a transpose. Note that these results imply construction of the Green's function G based only upon knowledge of G_1 and G_2 .

B. Recursive construction

The above development indicates how to combine two unit section Green's functions into a new Green's function for the composite domain. This approach forms the basis for a recursive procedure to systematically construct the Green's function for an arbitrary domain. The simplest procedure involves starting with unit cells which use only one basis function per side or face. To obtain reasonable accuracy, these unit cells should have a maximum dimension of $\lambda/10$ per side, where λ is the sound wavelength in the medium. If the material composition is complex, even smaller cells may have to be used to accurately model rapid variations in the medium parameters. For two-dimensional problems, the methodology consists of grouping the unit cells in the domain into adjacent pairs, and then combining these pairs using Eqs. (21) and (22) as depicted in Fig. 2(a). The resulting regions are then again grouped and combined with adjacent domains, as implied in Fig. 2(b). This combining scheme can be recursively repeated with the newly formed Green's functions until the composite Green's function for the entire domain has been constructed. A similar recursive combining procedure can be performed in three dimensions.

It is important to recognize that if only the fields external to the domain are required, then at each combining step the points internal to the domain can be discarded, so that only Green's functions with source and observation points on the domain boundary are computed. With reference to Fig. 2(a), this means that points on B need not be computed. If fields internal to the domain are desired as well, then Green's functions with observation points internal to the domain must be preserved and updated at each combination step.

This discussion reveals that the RGFM is similar to NEPAL^{15,16} in that both methods use a nested recursion concept to transform a volume scattering problem to a surface one. However, unlike NEPAL, the RGFM recursion works on the Green's function with carefully chosen boundary conditions rather than the isolated T matrix of subscatterers. This difference allows simplification of the formulation, avoids requiring expansion of the scattered fields in terms of cylindrical and spherical harmonics, and results in interaction matrices (\mathbf{T} in this development) whose sizes correspond to the number of interface points on B rather than the number of boundary points on $\partial\Omega_p$. This latter benefit allows reduction in the computational complexity of the method, as discussed below.

C. Field evaluation

Following construction of the Green's function G^i on Ω^i , we apply the continuity relations

$$P(\mathbf{r}) = P^i(\mathbf{r}) = P^o(\mathbf{r}), \quad (23)$$

$$P'(\mathbf{r}) = \frac{1}{\rho(\mathbf{r})} \frac{\partial P^i(\mathbf{r})}{\partial n} = \frac{1}{\rho_o} \frac{\partial P^o(\mathbf{r})}{\partial n}, \quad (24)$$

for $\mathbf{r} \in \partial\Omega^i$ to Eqs. (3) and (4). This step, in conjunction with the homogeneous Neumann boundary condition for G^i results in the integral equations

$$P(\mathbf{r}) = \oint_{\partial\Omega^i} G^i(\mathbf{r}, \mathbf{r}') P'(\mathbf{r}') dS', \quad (25)$$

$$\begin{aligned} \frac{1}{2} P(\mathbf{r}) = & P^{\text{inc}}(\mathbf{r}) - \text{pv} \oint_{\partial\Omega^i} \left[G^o(\mathbf{r}, \mathbf{r}') P'(\mathbf{r}') \right. \\ & \left. - \frac{1}{\rho_o} P(\mathbf{r}') \frac{\partial G^o(\mathbf{r}, \mathbf{r}')}{\partial n'} \right] dS', \end{aligned} \quad (26)$$

for $\mathbf{r} \in \partial\Omega^i$, where the 1/2 arises due to the singularity in the derivative of G^o , and "pv" signifies a principal value interpretation for the integral.

Solution of Eqs. (25) and (26) can be accomplished by projecting P and P' onto the basis functions ψ_n , to obtain the vectors \mathbf{P} and \mathbf{P}' , respectively. Subsequent projection of Eqs. (25) and (26) onto weighting functions $w_m(\mathbf{r})$ results in the matrix equations

$$\begin{bmatrix} \frac{1}{2} \mathbf{U} - \tilde{\mathbf{g}}^o & \mathbf{g}^o \\ \mathbf{I} & -\mathbf{g}^i \mathbf{S} \end{bmatrix} \begin{bmatrix} \mathbf{P} \\ \mathbf{P}' \end{bmatrix} = \begin{bmatrix} \mathbf{P}^{\text{inc}} \\ 0 \end{bmatrix}, \quad (27)$$

where \mathbf{S} is defined in Eq. (19), \mathbf{g}^i is the recursively obtained Green's matrix, and

$$\tilde{\mathbf{g}}_{mn}^o = \frac{1}{\rho_o} \int_{\partial\Omega^i} \int_{\partial\Omega^i} w_m(\mathbf{r}) \psi_n(\mathbf{r}') \frac{\partial G^o(\mathbf{r}, \mathbf{r}')}{\partial n'} dS dS', \quad (28)$$

$$\mathbf{g}_{mn}^o = \int_{\partial\Omega^i} \int_{\partial\Omega^i} w_m(\mathbf{r}) \psi_n(\mathbf{r}') G^o(\mathbf{r}, \mathbf{r}') dS dS', \quad (29)$$

$$U_{mn} = \int_{\partial\Omega^i} w_m(\mathbf{r}) \psi_n(\mathbf{r}) dS, \quad (30)$$

$$P_m^{\text{inc}} = \int_{\partial\Omega^i} w_m(\mathbf{r}) P^{\text{inc}}(\mathbf{r}) dS. \quad (31)$$

Inversion of Eq. (27) results in the solution of the fields on the boundary. These solutions can then be used with discrete forms of Eqs. (3) and (4) to obtain the fields at any desired location.

II. COMPUTATIONAL COMPLEXITY

Consider now the computation of the fields exterior to a square two-dimensional domain discretized into N cells with \sqrt{N} cells per side. The cost of computing the Green's functions for all of the unit cells is $O(N)$. The recursive procedure requires $\log_2 \sqrt{N}$ steps to complete the construction, where each cell contains $K=2^i$ points at the i th step. The combination of 4 such cells involves two matrix inversions for the \mathbf{T} matrices as well as two evaluations of Eqs. (21) and (22), with each computation requiring $O(K^3)$ operations. Since $N/4K^2$ such combinations are required per step, the overall RGFM cost C can be expressed as

$$C = \frac{N}{4} \sum_{i=0}^{\log_2 \sqrt{N} - 1} \alpha 2^i = \alpha \frac{N}{4} (\sqrt{N} - 1) \quad (32)$$

$$\approx O(N^{3/2}), \quad (33)$$

where α is a platform-dependent constant. Since the cost of solving Eq. (27) is also $O(N^{3/2})$, this represents the algorithm asymptotic complexity. The algorithm storage requirements are dominated by the $8\sqrt{N} \times 8\sqrt{N}$ matrix in Eq. (27), resulting in a storage complexity of $O(N)$. In three dimensions, the computational and storage complexities become $O(N^2)$ and $O(N)$, respectively. If the fields internal to the domain are also required, then the computational and storage costs increase respectively to $O(N^2)$ and $O(N^{3/2})$ for two-dimensional problems and $O(N^{7/3})$ and $O(N^{4/3})$ for three-dimensional domains.

III. RESULTS

In this section, we illustrate the performance of the RGFM in computing the fields scattered from various inclusions. Where possible, comparisons are made with results from exact solutions for canonical geometries. Numerical investigations have shown that use of a five-point Gaussian quadrature integration for all required integrals provides relatively good accuracy. A simple LU Decomposition scheme is used for all matrix solutions. The symbol $c = \omega/k$ will be used to denote the speed of sound in the relevant medium.

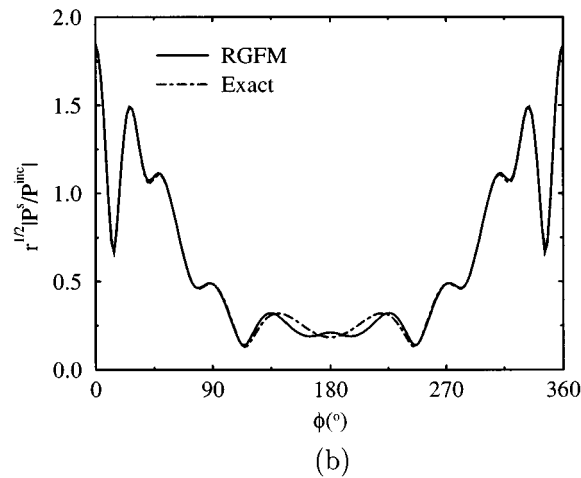
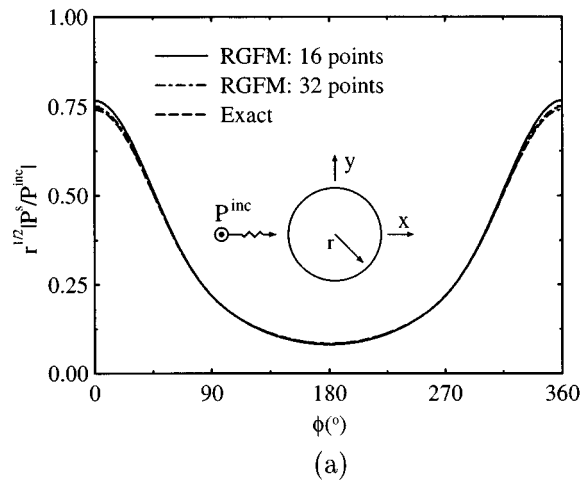


FIG. 3. Scattered normalized pressure field $\sqrt{r}|P^s/P^{inc}|$ as a function of angle for a circular cylindrical inclusion at a distance far from the scatterer. The background velocity is 2 km/s, the inclusion velocity is 3 km/s, and the density in both is 2000 kg/m³. The cylinder radius is (a) $a=0.4\lambda$ and (b) $a=1.5\lambda$, where λ is the wavelength of the excitation field.

A. Circular cylinder

As a first test case, consider the simple geometry of a plane wave scattered from a homogeneous circular cylinder. The velocity inside the cylinder is $c=3$ km/s, while the velocity in the surrounding medium is $c_s=2$ km/s. The density in both regions is $\rho=2000$ kg/m³. Because the RGFM formulation uses rectangular unit cells, the cylinder surface must be approximated using a stair-step contour. Figure 3(a) illustrates the geometry and the results from the RGFM and the exact series solution¹ for a cylinder of radius $a=0.4\lambda$, where λ is the wavelength in the background medium. The scattered field P^s is measured at a distance r far enough from the cylinder surface that the field variation with r becomes proportional to e^{-jkr}/\sqrt{r} . For this computation, when a 16×16 RGFM grid is used, some small error occurs in the plot, most likely due to the stair-stepped cylinder surface. This modeling error can be reduced by using more unit cells, as shown in the curve obtained using a 32×32 RGFM grid. Figure 3(b) illustrates the result when the cylinder radius is

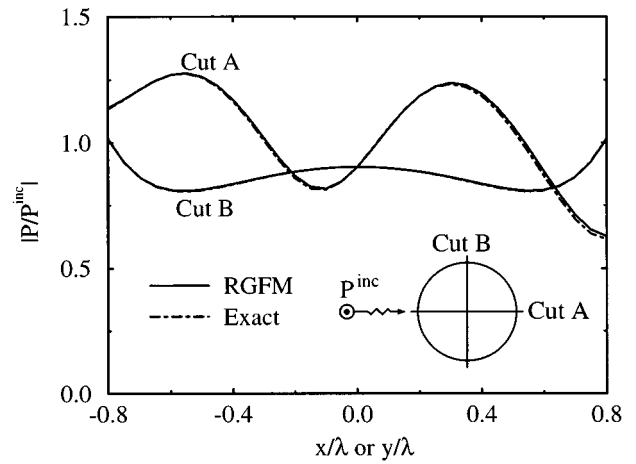


FIG. 4. Scattered normalized pressure field $|P/P^{inc}|$ in two cuts through the cylinder described in Figure 3 with radius $a=0.8\lambda$ computed using the RGFM and the exact series solution.

$a=1.5\lambda$ using a 32×32 RGFM grid. Here again, the RGFM result compares favorably with the exact solution. For these computations, the Green's function construction requires 1 s for the small grid and 7 s for the large grid, while the boundary integral equation solution requires 2 s for the small grid and 15 s for the large grid on a HP 9000 J210 workstation. These times indicate that the cost of performing the recursive operations is similar to and even less than the cost of the boundary integral solution.

Figure 4 illustrates the fields internal to the cylinder with the same material parameters as used in Fig. 3 but with a radius of $a=0.8\lambda$. The normalized pressure field is plotted along two different cuts through the center of the cylinder, as depicted in the figure inset. The results from the exact series solution are also plotted. As can be seen, the RGFM accurately predicts the field features. Such a capability can be important for applications in imaging and inverse scattering.

B. Two-layer circular cylinder

To further test the capabilities of the RGFM, we next apply it to compute the scattering from the two-layer cylinder shown in the inset of Figure 5. For this geometry, the surrounding medium has parameters $c_s=2$ km/s and $\rho_s=2000$ kg/m³. The inclusion has parameters $c_1=2.8$ km/s and $\rho_1=2800$ kg/m³ for $r \leq 0.75\lambda$, and $c_2=4$ km/s and $\rho_2=2400$ kg/m³ for $0.75\lambda \leq r \leq 1.5\lambda$. A 32×32 grid is used for the RGFM computations. An exact solution has also been developed for this geometry by extending the series solution¹ to accommodate two layers. The normalized scattered field P^s at a distance far from the scatterer obtained using the RGFM and exact solutions is depicted in Figure 5. Once again, we see some error in the RGFM result, particularly near $\phi=180^\circ$, which is likely due to the stair-stepped approximation to the cylindrical surface. Overall, however, the RGFM very accurately predicts the field behavior even for this inhomogeneous structure.

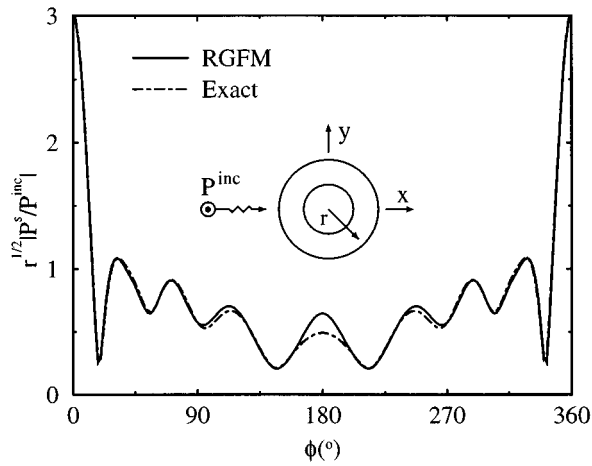


FIG. 5. Scattered normalized pressure field $\sqrt{r}|P^s/P^{inc}|$ as a function of angle for a two-layer circular cylindrical inclusion at a distance far from the scatterer. The background has velocity 2 km/s and density 2000 kg/m³, and the inclusion has parameters $c_1=2.8$ km/s and $\rho_1=2800$ kg/m³ for $r \leq 0.75\lambda$, and $c_2=4$ km/s and $\rho_2=2400$ kg/m³ for $0.75\lambda \leq r \leq 1.5\lambda$.

C. Synthetic seismograms

The RGFM can also be used to compute seismograms for acoustic pulse scattering. Consider the geometry shown in Figure 6, which depicts a square inclusion embedded in an otherwise homogeneous medium. Two different cases are considered: (1) all four regions in Figure 6 are identical, and (2) the four regions have different material properties, as indicated in the figure caption. Again, the surrounding medium has a velocity of 2 km/s and a density of 2000 kg/m³. A line source excitation emits a pulse whose shape is given by

$$s(t) = -\frac{(t-t_o)}{2\sigma^2} \exp\left[-\frac{(t-t_o)^2}{2\sigma^2}\right], \quad (34)$$

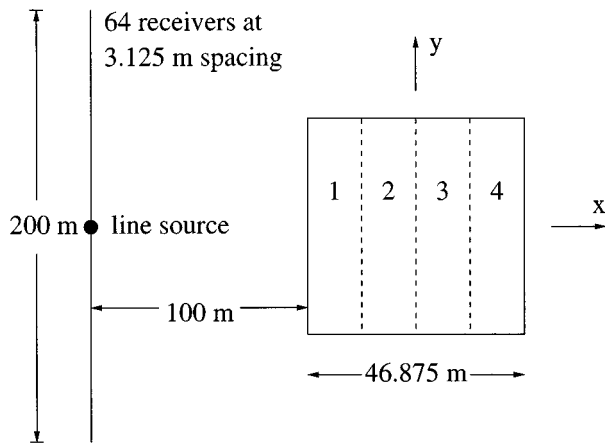
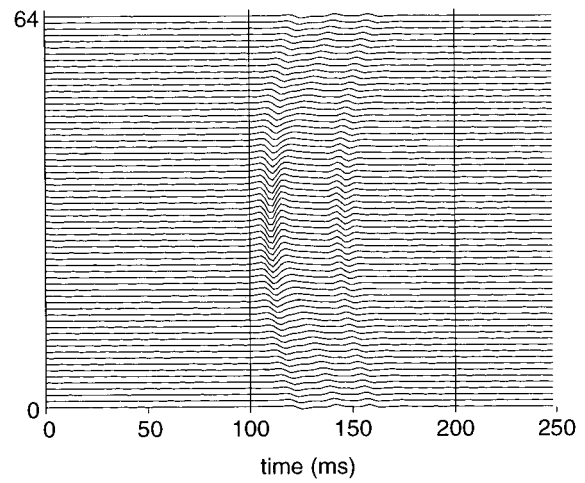
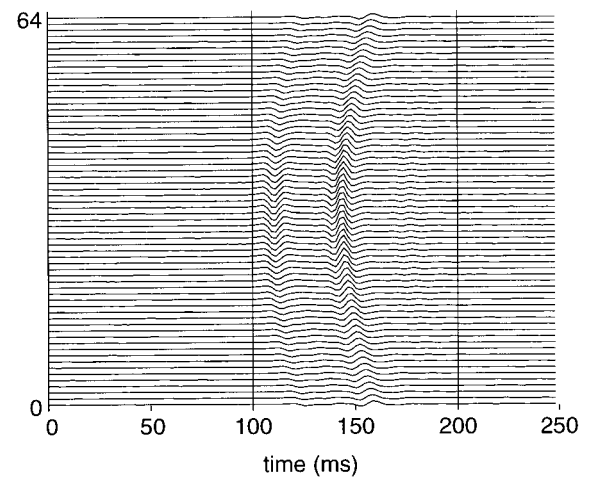


FIG. 6. Geometry for computing synthetic seismograms using the RGFM. In the first case, regions 1–4 are identical, with $c=2.8$ km/s and $\rho=2800$ kg/m³. In the second case, the regions have parameters $c_1=2$ km/s, $\rho_1=3200$ kg/m³, $c_2=2.3$ km/s, $\rho_2=2800$ kg/m³, $c_3=2.8$ km/s, $\rho_3=2400$ kg/m³, $c_4=6.3$ km/s, $\rho_4=2000$ kg/m³. The surrounding medium has parameters $c_s=2$ km/s and $\rho_s=2000$ kg/m³.



(a)



(b)

FIG. 7. Synthetic seismograms for the square inclusion shown in Figure 6 for the two cases described.

where $\sigma=2.5$ ms and $t_o=4\sigma$. This pulse contains no zero frequency components, has a bandwidth of approximately 256 Hz, and possesses a dominant frequency of 68 Hz (29 m dominant wavelength). Sixty-four receivers are used to record the scattered signal. Figure 7(a) and (b) illustrates the synthetic seismograms for each of the two cases described. As can be seen, the seismograms for the two inclusions are similar, although the inhomogeneous domain results in a noticeably stronger late-time return due to the strong reflection from the last interface. This example illustrates the need for incorporating small-scale variations in the modeling capabilities.

D. Three-dimensional scattering: Sphere

As a final example, we consider a three-dimensional problem involving a spherical inclusion with velocity $c=3$ km/s embedded in a medium with velocity $c_s=2$ km/s. Both media have a mass density of 2000 kg/m³. The sphere radius is $a=0.5\lambda$, and an $8 \times 8 \times 8$ RGFM grid is used. Figure 8

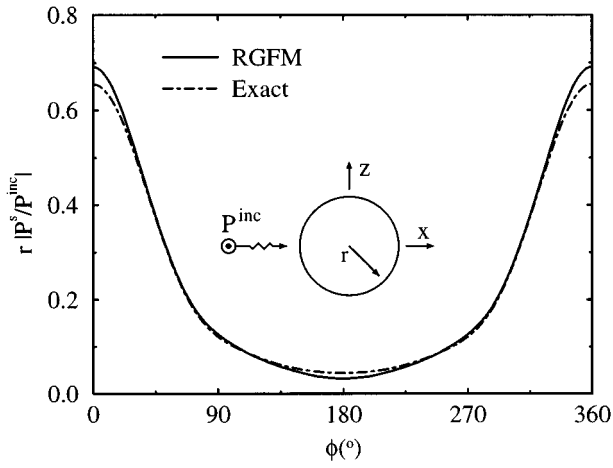


FIG. 8. Scattered normalized pressure field $r|P^s/P^{\text{inc}}|$ as a function of angle for a spherical inclusion at a distance far from the scatterer. The background has velocity 2 km/s and the inclusion has velocity $c=3$ km/s, and the density in both is 2000 kg/m^3 . The sphere radius is $a=0.5\lambda$.

illustrates the scattering configuration as well as the results from the RGFM and an exact solution obtained using a series expansion.¹⁸ Once again, we see that the RGFM provides high accuracy, with the error most likely due to the stair-stepped approximation of the curved spherical surface. This result shows that the RGFM is equally applicable to three-dimensional scattering problems.

IV. CONCLUSIONS

This paper has presented a novel numerical technique for analysis of the acoustic behavior of inhomogeneous domains embedded in a homogeneous space. The methodology uses a recursive scheme to efficiently construct the Green's function of the region using known Green's functions from smaller subdomains. Boundary integral equations are then formulated and solved to determine the pressure fields on the domain boundary for a given incident field. A comparison of the numerical results with solutions obtained from analytical expressions shows that the RGFM faithfully constructs the Green's function for heterogeneous domains and provides highly accurate results for scattering from various structures. Additionally, it allows simulation of domains for multiple source configurations with an asymptotic computational complexity of $O(N^{3/2})$ and $O(N^2)$ for two- and three-dimensional structures, respectively, and a storage requirement of $O(N)$. This allows solution of larger problems with less computational time as compared to traditional schemes for analyzing heterogeneous structures.

APPENDIX A: GREEN'S FUNCTIONS

Consider the rectangular domain Ω_1 with sides of length a and b in the x and y directions, respectively. The Green's function satisfying Eq. (2) with $k(\mathbf{r})=k$ and $\rho(\mathbf{r})=\rho$ being constants can be derived by performing an eigenfunction expansion in the y coordinate.¹⁸ When this series is substituted into Eq. (2), the resulting differential equation in x can be solved in closed-form,¹⁸ resulting in the representation

$$G(\mathbf{r}, \mathbf{r}') = -\frac{2\rho}{b} \sum_{m=0}^{\infty} \alpha_m \frac{\cos(k_m x) \cos[k_m(x' - a)]}{k_m \sin(k_m a)} \times \cos\left(\frac{m\pi y}{b}\right) \cos\left(\frac{m\pi y'}{b}\right), \quad x \leq x', \quad (\text{A1})$$

where

$$\alpha_m = \begin{cases} 1/2, & m=0, \\ 1, & m>0, \end{cases} \quad (\text{A2})$$

$$k_m = \sqrt{k^2 - (m\pi/b)^2}. \quad (\text{A3})$$

If $x > x'$, then the positions of x and x' must simply be reversed in Eq. (A1).

The difficulty with Eq. (A1) is that it is typically slowly convergent, and it does not converge when $\mathbf{r} = \mathbf{r}'$. However, because of the integrable nature of this singularity, if proper basis functions are chosen in Eq. (15), then the integration in Eq. (18) can be performed on the series term-by-term, resulting in a highly convergent series for all source/observation point pairs. Pulse basis functions provide this result, and additionally are orthogonal so that the matrix \mathbf{S}^{-1} can be easily determined. The exact number of series terms required in this case depends upon the dimensions a and b . For most computations where $a, b = \lambda/10$, typically fewer than four terms are needed for the series to converge within 0.001% of its value. Even using this scheme, however, the representation of Eq. (A1) has convergence difficulties when the boundary integrations occur in x and x' (i.e., $y, y' = 0$ or b) and $x = x'$. To avoid this difficulty, it is simplest to use the equivalent form of Eq. (A1) obtained by reversing the positions of x and y, x' and y' , and a and b in the expressions.

In three dimensions, the Green's function for a domain of side lengths a, b , and c in the x, y , and z directions, respectively, can be expressed as

$$G(\mathbf{r}, \mathbf{r}') = -\frac{4\rho}{bc} \sum_{m,n=0}^{\infty} \alpha_m \alpha_n \frac{\cos(k_{mn} x) \cos[k_{mn}(x' - a)]}{k_{mn} \sin(k_{mn} a)} \times \cos\left(\frac{m\pi y}{b}\right) \cos\left(\frac{m\pi y'}{b}\right) \cos\left(\frac{n\pi z}{c}\right) \times \cos\left(\frac{n\pi z'}{c}\right), \quad x \leq x', \quad (\text{A4})$$

where

$$k_{mn} = \sqrt{k^2 - (m\pi/b)^2 - (n\pi/c)^2}. \quad (\text{A5})$$

Replacements similar to those discussed above for the two-dimensional case can be made in Eq. (A4) as well.

APPENDIX B: HOMOGENEOUS WAVE EQUATION SOLUTIONS

Consider finding a homogeneous solution to Eq. (2) in the domain Ω_1 which satisfies homogeneous Neumann boundary conditions on all sides except the boundary B (at $x=a$). It is important to recognize that Eqs. (A1) and (A4) are homogeneous solutions to the wave equation and must be combined with the forms for $x \geq x'$ to provide the particular solutions. Additionally, as indicated by the jump condi-

tion in Eq. (10), the form for $x \leq x'$ does not satisfy the homogeneous Neumann boundary condition at $x = a$ if $\mathbf{r}' \in B$, as is the case in Eqs. (6) and (7). These observations indicate that the forms in Eqs. (A1) and (A4), when used in Eqs. (6) and (7), provide the solutions necessary for the RGFM construction.

¹Y. H. Pao and C. C. Mow, *Diffraction of Elastic Waves and Dynamic Stress Concentrations* (Crane, Russak & Co., New York, 1973).

²J. E. Murphy and S. A. Chin-Bing, "A finite-element model for ocean acoustic propagation and scattering," *J. Acoust. Soc. Am.* **86**, 1478–1483 (1989).

³K. J. Marfurt, "Accuracy of finite-difference and finite-element modeling of the scalar and elastic wave equations," *Geophysics* **49**, 533–549 (1984).

⁴K. R. Kelly, R. W. Ward, S. Treitel, and R. M. Alford, "Synthetic seismograms: a finite difference approach," *Geophysics* **41**, 2–27 (1976).

⁵G. T. Schuster and L. C. Smith, "A comparison among four direct boundary integral methods," *J. Acoust. Soc. Am.* **77**, 850–864 (1985).

⁶G. Chen and H. Zhou, "Boundary element modeling of nondissipative and dissipative waves," *Geophysics* **59**, 113–118 (1994).

⁷P. C. Waterman, "New formulation of acoustic scattering," *J. Acoust. Soc. Am.* **45**, 1417–1429 (1969).

⁸M. G. Imhof, "Multiple multipole expansions for acoustic scattering," *J. Acoust. Soc. Am.* **97**, 754–763 (1995).

⁹M. G. Imhof, "Scattering of acoustic and elastic waves using hybrid multiple multipole expansions—finite element technique," *J. Acoust. Soc. Am.* **100**, 1325–1338 (1996).

¹⁰W. C. Chew, *Waves and Fields in Inhomogeneous Media* (Van Nostrand Reinhold, New York, 1990).

¹¹J. D. Freeze and M. A. Jensen, "The recursive Green's function method for surface integral equation analysis of inhomogeneous media," *IEEE AP-S Intl. Symp. Dig.* **4**, 2342–2345 (1997).

¹²K. B. Kahen, "Analysis of distributed-feedback lasers using a recursive Green's functional approach," *IEEE J. Quantum Electron.* **29**, 368–373 (1993).

¹³K. B. Kahen, "Analysis of distributed-feedback lasers: A recursive Green's function approach," *Appl. Phys. Lett.* **61**, 2012–2014 (1992).

¹⁴J. D. Freeze, M. A. Jensen, and R. H. Selfridge, "A unified Green's function analysis of complicated DFB lasers," *IEEE J. Quantum Electron.* **33**, 1253–1259 (1997).

¹⁵W. C. Chew and C. C. Lu, "The use of Huygens' equivalence principle for solving the volume integral equation of scattering," *IEEE Trans. Antennas Propag.* **41**, 897–904 (1993).

¹⁶C. C. Lu and W. C. Chew, "The use of Huygens' equivalence principle for solving 3-D volume integral equation of scattering," *IEEE Trans. Antennas Propag.* **43**, 500–507 (1995).

¹⁷J. Mathews and R. L. Walker, *Mathematical Methods of Physics* (Benjamin, New York, 1970).

¹⁸C. A. Balanis, *Advanced Engineering Electromagnetics* (Wiley, New York, 1989).

Calculation of acoustical scattering from a cluster of scatterers

S. Koc^{a)} and W. C. Chew

Center for Computational Electromagnetics, Electromagnetics Laboratory, Department of Electrical and Computer Engineering, University of Illinois at Urbana-Champaign, Urbana, Illinois 61801-2991

(Received 12 May 1997; accepted for publication 15 August 1997)

The problem of determining the field scattered by a cluster of scatterers when they are insonified by a known acoustical field is addressed. The problem is formulated by using the T -matrix method and the resulting system of linear equations is solved by using the multilevel fast multipole algorithm (MLFMA) and the fast multipole method–fast Fourier transform (FMMFFT) method, and the efficiency of the two methods is compared. It was observed that, in general, the MLFMA performs better than the FMMFFT algorithm. However, when the scatterers are distributed uniformly on a rectangular grid, the FMMFFT algorithm performs as good as the MLFMA. The accuracy of the methods is evaluated by modeling a spherical scatterer as composed of many small spheres.

© 1998 Acoustical Society of America. [S0001-4966(97)00812-6]

PACS numbers: 43.20.Fn [ANN]

INTRODUCTION

Solution of multiple scattering from a system of scatterers is a classical problem that has preoccupied researchers for many years. There are basically two different approaches for the solution of this problem. In the first approach the distribution of the scatterers is assumed to be random and an average value of the scattered field (or power) is sought.¹⁻³ The second approach is to write down the pertinent equations and try to solve the resulting large linear system.⁴⁻⁷ The number of unknowns is then proportional to $\bar{\mu}N$, where N is the number of the scatterers and $\bar{\mu}$ is the average number of spherical harmonics used in the expansion of the fields scattered by the scatterers. The first approach has the advantage of producing analytical results that give insight to the scattering phenomena. However, these results are only valid in a statistical sense. The second approach, on the other hand, can produce the scattering solution for a specific distribution of the scatterers. This allows one to model a large scatterer as being composed of many small scatterers and a solution to the resulting system can be obtained. The basic disadvantage of this approach is that the numerical work is excessive, especially for three dimensional problems. If Gaussian elimination is used to solve for the unknowns, the solution time scales as $(\bar{\mu}N)^3$ which quickly exhausts the resource of even a supercomputer.

Several methods have been proposed to solve the matrix equation effectively. Many of these methods are summarized in Ref. 5. The purpose of this work is to compare the performances of the FMM,⁸⁻¹⁰ and FFT^{11,12} methods.

Throughout this paper $e^{-i\omega t}$ time convention is used.

I. PROBLEM FORMULATION

A. Geometry and definitions

Consider N scatterers located at points described by the position vectors \mathbf{p}_i , $i=1,\dots,N$ in some coordinate frame,

with known scattering solutions expressed in terms of their isolated T -matrices denoted by $\bar{\mathbf{T}}_i$. The problem is to determine the field scattered by this cluster of scatterers when they are insonified by a known acoustical field. The incident field is expressed in terms of its multipole coefficients expanded about a point \mathbf{p}_s ,

$$\Phi^{\text{inc}}(\mathbf{r}_s) = \sum_{n=0}^{n_s} \sum_{m=-n}^n a_{nm}^s j_n(kr_s) Y_{nm}(\theta_s, \phi_s), \quad (1)$$

where n_s is the order at which the multipole expansion of the incident field is truncated, a_{nm}^s are the multipole coefficients, j_n is the spherical Bessel function, and $\mathbf{r}_s = \mathbf{r} - \mathbf{p}_s$ is the vector from the point \mathbf{p}_s to the observation point \mathbf{r} , whose spherical coordinates are (r_s, θ_s, ϕ_s) . The spherical harmonics Y_{nm} are given by

$$Y_{nm}(\theta, \phi) = (-1)^m \left[\frac{(n-m)!}{(n+m)!} \frac{2n+1}{4\pi} \right]^{1/2} P_n^m(\cos\theta) e^{im\phi}, \quad (2)$$

where $P_n^m(x)$ denotes the associated Legendre functions as defined in Ref. 13. The short-hand notation $Y_{nm}(\hat{\mathbf{s}})$ will also be used to denote the spherical harmonics where $\hat{\mathbf{s}}$ is a unit vector whose direction is defined by the spherical angles θ and ϕ .

A simpler notation is achieved by combining the two indices n and m into a single index $L:(0,0),(1,-1), (1,0),(1,1),\dots,(n,m),\dots$ and Eq. (1) can be written as

$$\Phi^{\text{inc}}(\mathbf{r}_s) = \sum_{L=(0,0)}^{\mathcal{L}} \mathcal{R}g\Psi_L(k, \mathbf{r}_s) a_L^s, \quad (3)$$

where $\mathcal{R}g\Psi_L(k, \mathbf{r}_s) = j_n(kr_s) Y_{nm}(\theta_s, \phi_s)$ are the spherical wave functions. A further notational simplification is achieved by adopting a vector notation as

$$\Phi^{\text{inc}}(\mathbf{r}_s) = \mathcal{R}g\Psi^l(k, \mathbf{r}_s) \cdot \mathbf{a}^s, \quad (4)$$

where

^{a)}Permanent address: Department of Electrical and Electronics Engineering, Middle East Technical University, 06531, Ankara, Turkey.

$$\mathcal{R}g\mathbf{\Psi}^t(k, \mathbf{r}) = [\mathcal{R}g\mathbf{\Psi}_{(0,0)}(k, \mathbf{r}) \quad \mathcal{R}g\mathbf{\Psi}_{(1,-1)}(k, \mathbf{r}) \\ \mathcal{R}g\mathbf{\Psi}_{(1,0)}(k, \mathbf{r}) \quad \mathcal{R}g\mathbf{\Psi}_{(1,1)}(k, \mathbf{r}) \quad \cdots], \quad (5)$$

$$\mathbf{a}^s = [a_{(0,0)}^s \quad a_{(1,-1)}^s \quad a_{(1,0)}^s \quad a_{(1,1)}^s \quad \cdots]^t, \quad (6)$$

and $(\cdot)^t$ denotes the transpose of the vector. In this notation, the field scattered by the i th scatterer is

$$\Phi_i^{\text{sca}}(\mathbf{r}_i) = \mathbf{\Psi}^t(k, \mathbf{r}_i) \cdot \mathbf{b}^i = \sum_{n=0}^{n_i} \sum_{m=-n}^n b_{nm}^i h_n^{(1)}(kr_i) \\ \times Y_{nm}(\theta_i, \phi_i), \quad (7)$$

where $\mathbf{r}_i = \mathbf{r} - \mathbf{p}_i$ is the vector from the i th scatterer to the observation point and $h_n^{(1)}$ denotes the spherical Hankel functions of the first kind. It must be noted that the multipole expansions of both the incident and the scattered fields contain infinitely many terms. However, these expansions converge rapidly and they are truncated at n_s and n_i , respectively. The error bounds in these truncations are discussed in Ref. 14.

The total scattered field can now be written as

$$\Phi^{\text{sca}} = \sum_{i=1}^N \mathbf{\Psi}^t(k, \mathbf{r}_i) \cdot \mathbf{b}^i. \quad (8)$$

Each term of the above summation is an outgoing multipole expansion at a different point with

$$\Psi_L(k, \mathbf{r}) = h_n^{(1)}(kr) Y_{nm}(\theta, \phi) \quad (9)$$

being the outgoing wave functions.

To obtain a solution we must express all the fields in Eq. (8) as multipole fields expanded at the position of the j th scatterer. This can be achieved by using the addition theorems for the wave functions.

B. Scalar addition theorem

An outgoing wave function with the origin at the position of the i th scatterer can be expanded into a sum of regular wave functions with the origin at the position of the j th scatterer, since these fields do not have a singularity at \mathbf{p}_j . This expansion, known as the addition theorem for the scalar wave functions, is given below:^{15,16}

$$\Psi_{nm}(k, \mathbf{r}_i) = \sum_{\nu=0}^{\infty} \sum_{\mu=-\nu}^{\nu} \mathcal{R}g\Psi_{\nu\mu}(k, \mathbf{r}_j) \alpha_{\nu\mu, nm}(k, \mathbf{r}_{ji}), \quad (10)$$

where $\mathbf{r}_{ji} = \mathbf{r}_i - \mathbf{r}_j = \mathbf{p}_j - \mathbf{p}_i$ is a vector from the i th scatterer to the j th scatterer. This relation is valid provided that $|\mathbf{r}_j| < |\mathbf{r}_{ji}|$.

Similarly a regular wave function with origin at \mathbf{p}_s can be expanded into a sum of regular wave functions with origin at \mathbf{r}_j as

$$\mathcal{R}g\Psi_{nm}(k, \mathbf{r}_s) = \sum_{\nu=0}^{\infty} \sum_{\mu=-\nu}^{\nu} \mathcal{R}g\Psi_{\nu\mu}(k, \mathbf{r}_j) \beta_{\nu\mu, nm}(k, \mathbf{r}_{js}), \quad (11)$$

where $\mathbf{r}_{js} = \mathbf{r}_s - \mathbf{r}_j = \mathbf{p}_j - \mathbf{p}_s$ is a vector from the source point to the position of the j th scatterer. This relation is valid at any observation point. The α coefficients are

$$\alpha_{\nu\mu, nm}(k, \mathbf{r}) = \sum_{n'=|n-\nu|}^{n+\nu} i^{(\nu+n'-n)} Y_{n', m-\mu}(\theta, \phi) h_{n'}^{(1)}(kr) \\ \times (-1)^\mu \left[\frac{4\pi(2n+1)(2\nu+1)}{(2n'+1)} \right]^{1/2} \\ \times (n\nu 00 | n\nu n' 0) \\ \times (n\nu -m\mu | n\nu n' -m + \mu), \quad (12)$$

where $(j_1 j_2 m_1 m_2 | j_3 j_4 m_3)$ are the Clebsch–Gordan coefficients as defined in Ref. 13. The β coefficients are obtained by replacing the spherical Hankel functions of the first kind in Eq. (12) by the spherical Bessel functions.

C. T-matrix formulation

The T -matrix of a scatterer relates the field scattered from the scatterer to the incident field only when the scatterer is present. When there are more than one scatterer, multiple scattering between the scatterers occurs. The following matrix formulation of scattering from many scatterers is presented in Refs. 4, 5, and 17.

The total field due to N scatterers can be written as

$$\Phi = \Phi^{\text{inc}} + \Phi^{\text{sca}} = \mathcal{R}g\mathbf{\Psi}^t(k, \mathbf{r}_s) \cdot \mathbf{a}^s + \sum_{i=1}^N \mathbf{\Psi}^t(k, \mathbf{r}_i) \cdot \mathbf{b}^i, \quad (13)$$

where \mathbf{b}^i are yet to be determined. Consider a single term in the summation in Eq. (13). By using the addition theorem to express the field in the coordinate frame of the j th scatterer we get

$$\mathbf{\Psi}^t(k, \mathbf{r}_i) \cdot \mathbf{b}^i = \sum_{nm} \Psi_{nm}(k, \mathbf{r}_i) \mathbf{b}_{nm}^i \\ = \sum_{nm} \left\{ \sum_{\nu\mu} \mathcal{R}g\Psi_{\nu\mu}(k, \mathbf{r}_j) \alpha_{\nu\mu, nm}(k, \mathbf{r}_{ji}) \right\} \mathbf{b}_{nm}^i \\ = \sum_{\nu\mu} \mathcal{R}g\Psi_{\nu\mu}(k, \mathbf{r}_j) \left\{ \sum_{nm} \alpha_{\nu\mu, nm}(k, \mathbf{r}_{ji}) \mathbf{b}_{nm}^i \right\}. \quad (14)$$

We define the matrix

$$\bar{\alpha}(k, \mathbf{r}_{ji}) = \begin{bmatrix} \alpha_{0,0;0,0}(k, \mathbf{r}_{ji}) & \alpha_{0,0;1,-1}(k, \mathbf{r}_{ji}) & \alpha_{0,0;1,0}(k, \mathbf{r}_{ji}) & \cdots \\ \alpha_{1,-1;0,0}(k, \mathbf{r}_{ji}) & \alpha_{1,-1;1,-1}(k, \mathbf{r}_{ji}) & \alpha_{1,-1;1,0}(k, \mathbf{r}_{ji}) & \cdots \\ \alpha_{1,0;0,0}(k, \mathbf{r}_{ji}) & \alpha_{1,0;1,-1}(k, \mathbf{r}_{ji}) & \alpha_{1,0;1,0}(k, \mathbf{r}_{ji}) & \cdots \\ \vdots & \vdots & \vdots & \vdots \end{bmatrix}. \quad (15)$$

With this matrix notation we can now write

$$\Psi^l(k, \mathbf{r}_i) \cdot \mathbf{b}^i = \mathcal{R}g \Psi^l(k, \mathbf{r}_j) \cdot \bar{\alpha}(k, \mathbf{r}_{ji}) \cdot \mathbf{b}^i, \quad (16)$$

and

$$\mathcal{R}g \Psi^l(k, \mathbf{r}_s) \cdot \mathbf{a}^s = \mathcal{R}g \Psi^l(k, \mathbf{r}_j) \cdot \bar{\beta}(k, \mathbf{r}_{js}) \cdot \mathbf{a}^s, \quad (17)$$

where $\bar{\beta}$ is defined similar to $\bar{\alpha}$. The matrix $\bar{\alpha}$ transforms the scattering coefficients of the i th scatterer to the reference frame of the j th scatterer, and similarly the matrix $\bar{\beta}$ describes a transformation from the source to the j th scatterer. Using Eq. (16) and Eq. (17) in Eq. (13) gives

$$\Phi = \underbrace{\mathcal{R}g \Psi^l(k, \mathbf{r}_j) \cdot \bar{\beta}(k, \mathbf{r}_{js}) \cdot \mathbf{a}^s + \sum_{\substack{i=1 \\ i \neq j}}^N \mathcal{R}g \Psi^l(k, \mathbf{r}_j) \cdot \bar{\alpha}(k, \mathbf{r}_{ji}) \cdot \mathbf{b}^i}_{\text{Incident on the } j\text{th scatterer}} + \underbrace{\Psi^l(k, \mathbf{r}_j) \cdot \mathbf{b}^i}_{\text{Outgoing}} \quad (18)$$

The last term on the right hand side of Eq. (18) represents an outgoing wave which is singular at \mathbf{p}_j expressed in the coordinate frame of the j th scatterer, and the other terms represent incoming waves impinging upon it. Therefore, these fields must be related by the isolated T -matrix, $\bar{\mathbf{T}}_j$, of the scatterer, i.e.,

$$\mathbf{b}^j = \bar{\mathbf{T}}_j \cdot \left(\bar{\beta}(k, \mathbf{r}_{js}) \cdot \mathbf{a}^s + \sum_{\substack{i=1 \\ i \neq j}}^N \bar{\alpha}(k, \mathbf{r}_{ji}) \cdot \mathbf{b}^i \right), \quad (19)$$

$j = 1, \dots, N,$

which constitutes a set of N matrix equations for the N unknown vectors \mathbf{b}^i . Eq. (19) can be written as

$$\mathbf{b}^j - \bar{\mathbf{T}}_j \cdot \sum_{\substack{i=1 \\ i \neq j}}^N \bar{\alpha}(k, \mathbf{r}_{ji}) \cdot \mathbf{b}^i = \bar{\mathbf{T}}_j \cdot \bar{\beta}(k, \mathbf{r}_{js}) \cdot \mathbf{a}^s, \quad (20)$$

$j = 1, \dots, N,$

which is more suitable for iterative techniques.

Using the notation $\{\cdot\}_{ij}$ to represent the ij th block of a matrix and defining

$$\{\bar{\mathbf{T}}\}_{ij} = \begin{cases} \bar{\mathbf{T}}_i, & i = j, \\ 0, & i \neq j, \end{cases} \quad (21)$$

as a block diagonal matrix formed by the isolated T -matrices of the scatterers,

$$\{\bar{\mathbf{A}}\}_{ij} = \begin{cases} \bar{\alpha}(k, \mathbf{r}_{ij}), & i \neq j, \\ 0, & i = j, \end{cases} \quad (22)$$

$\{\mathbf{b}\}_i = \mathbf{b}^i$ and $\{\mathbf{a}\}_i = \bar{\beta}(k, \mathbf{r}_{is}) \cdot \mathbf{a}^s$, Eq. (19) can be written as

$$\mathbf{b} = \bar{\mathbf{T}} \cdot (\mathbf{a} + \bar{\mathbf{A}} \cdot \mathbf{b}) \quad (23)$$

or

$$[\bar{\mathbf{I}} - \bar{\mathbf{T}} \cdot \bar{\mathbf{A}}] \cdot \mathbf{b} = \bar{\mathbf{T}} \cdot \mathbf{a}. \quad (24)$$

In iterative solution of matrix equations, the product of the conjugate transpose of the coefficient matrix by the vector is also required which can be written as

$$\{[\bar{\mathbf{I}} - \bar{\mathbf{T}} \cdot \bar{\mathbf{A}}]^H \cdot \mathbf{b}\}_j = \mathbf{b}^j - \sum_{\substack{i=1 \\ i \neq j}}^N \bar{\alpha}^H(k, \mathbf{r}_{ij}) \cdot \bar{\mathbf{T}}_i^H \cdot \mathbf{b}^i, \quad (25)$$

where $(\cdot)^H$ denotes complex conjugate transpose of a matrix. It must be noted that certain relations exist between $\bar{\alpha}(k, \mathbf{r}_{ji})$ and $\bar{\alpha}^H(k, \mathbf{r}_{ij})$ some of which can be found in Refs. 15 and 18.

Equation (20) constitutes $\mathcal{M} = \sum_{i=1}^N \mu_i$ equations with \mathcal{M} unknowns and can be solved by using various linear algebraic techniques, where $\mu_i = (n_i + 1)^2$ is the number of harmonics required to represent the field scattered by the i th scatterer. If Gaussian elimination is used, the required number of operations is proportional to \mathcal{M}^3 . In a three dimensional problem, the number of scatterers, hence \mathcal{M} , increases very rapidly and the solution time and memory requirements quickly swamp the resource of even a super-computer. Hence, an effective solution method is highly desirable.

II. ITERATIVE METHODS

Iterative methods are techniques that use successive approximations to obtain more accurate solutions to a linear system at each step. The iterative methods are generally classified as *stationary* and *non-stationary* methods. These methods are discussed extensively in the literature.^{19,20} The rate of convergence of an iterative method depends greatly on the spectrum of the coefficient matrix. In general, the non-stationary methods converge much faster than the stationary methods. Most of the non-stationary methods rely on special properties of the coefficient matrix such as symmetry and positive definiteness. The conjugate gradient normalized residual (CGNR) method is quite general and can be used with

arbitrary coefficient matrices. However, the convergence rate of CGNR is relatively slow due to the squaring of the condition number.

Theoretically, the CGNR method will converge to the exact solution in \mathcal{M} steps. In this method, each iteration step requires two matrix-vector multiplications and three vector updates. Normally, each matrix-vector multiplication requires $\mathcal{O}(\mathcal{M}^2)$ operations. Thus the total number of operations is still proportional to \mathcal{M}^3 . However, if the iteration is stopped whenever the condition

$$\frac{\|\mathbf{r}_n\|}{\|\mathbf{y}\|} \leq \text{tol}$$

is satisfied, where tol is an arbitrary tolerance, $\mathbf{r}_n = \mathbf{y} - \bar{\mathbf{A}} \cdot \mathbf{x}_n$ is the residual, and \mathbf{x}_n is the solution at the n th iteration step, then the convergence can be achieved in $p < \mathcal{M}$ steps. The number of operations required to solve the system will then be proportional to $p \mathcal{M}^2 = p[\bar{\mu}N]^2$, where $\bar{\mu} = (1/N) \times \sum_i (n_i + 1)^2$ is the average value of the required number of harmonics over the scatterers.

Another iterative solution can be obtained by iterating Eq. (23) yielding

$$\mathbf{b} = \sum_{i=0}^{\infty} (\bar{\mathbf{T}} \cdot \bar{\mathbf{A}})^i \cdot \bar{\mathbf{T}} \cdot \mathbf{a}. \quad (26)$$

This is the Neumann series solution which was suggested in Refs. 6 and 7. The Neumann series will converge whenever $\bar{\mathbf{T}} \cdot \bar{\mathbf{A}}$ defines a contraction operator, in which case the convergence will be exponential.

III. GROUPING

To further decrease the order of the complexity of the algorithm, the special structure of the coefficient matrix must be used to perform the matrix-vector multiplication in less than $\mathcal{O}(\mathcal{M}^2)$ operations.

Assume that we divide the N scatterers into N/M groups each containing M scatterers. The scatterers are assumed to be evenly distributed so that each group occupies approximately the same volume. The idea in grouping the scatterers is to calculate the interactions between groups of scatterers simultaneously thus recycling information. The algorithm to perform a matrix-vector multiplication can be considered in four steps as outlined below:

- (1) **Aggregation.** Translate the outgoing multipole coefficients of all the scatterers in a group to the group center. The number of coefficients, R , required to represent the field at the center of the group is proportional to the square of the diameter of the group, hence $R \sim M^{2/3}$. Thus the number of operations required for this step is proportional to $\bar{\mu}RN \sim \bar{\mu}NM^{2/3}$.
- (2) **Group interactions.** Translate the outgoing multipole coefficients at each group center to local multipole coefficients at center of all the other groups. The number of operations required for this step is proportional to $R^2(N/M)^2 \sim N^2/M^{2/3}$.

- (3) **Disaggregation.** Translate the accumulated effect of all the other groups at a group center to the position of scatterers. This step is quite similar to the aggregation step and requires $\sim \bar{\mu}NM^{2/3}$ operations.
- (4) **Near Interactions.** Finally, calculate the interactions of the scatterers within the same group directly. This step requires $\sim \bar{\mu}^2NM$ operations.

In order to obtain an optimum algorithm, the computational load of these steps must be balanced. If we assume $M \sim N^x$, the value of x that minimizes the complexity is found to be $3/5$, or $\mathcal{O}(N^{8/5})$ operations per matrix-vector multiplication is required. Thus, if an iterative method is used and if the required number of iterations is p , then the problem complexity increases only by $pN^{8/5}$. The dependence of p on N for Helmholtz problem is hard to determine.

The algorithm complexity can be further reduced if plane wave expansions are used for translating an outgoing multipole expansion of a group to the center of another group, since in this case the translation of coefficients from one expansion center to another would require a number of operations that is proportional to the number of coefficients used. This is because each plane wave is translated into a single plane wave, or the translation operator for plane waves is a diagonal operator. Expanding the spherical waves into plane wave spectra is, therefore, sometimes referred to as the diagonalization of the spherical translation operators, or the fast multipole method, FMM.

IV. DIAGONALIZATION OF THE SPHERICAL TRANSLATION OPERATORS

In the formulation of the scattering problem, we need to transform spherical harmonic coefficients from the position of the i th scatterer to the position of the j th scatterer which is given by

$$\Psi_L(k, \mathbf{r}_i) = \sum_{L'} \mathcal{R}_g \Psi_{L'}(k, \mathbf{r}_j) \alpha_{L'L}(k, \mathbf{r}_{ji}), \quad r_j < r_{ji}. \quad (27)$$

Consider this transformation being done in three steps from the i th scatterer to \mathbf{r}_λ , the center of the group \mathcal{G}_λ which that scatterer belongs to, then to $\mathbf{r}_{\lambda'}$, the center of the group $\mathcal{G}_{\lambda'}$ which the j th scatterer belongs to, then to the j th scatterer. In matrix form we can write

$$\bar{\alpha}(k, \mathbf{r}_{ji}) = \bar{\beta}(k, \mathbf{r}_{j\lambda'}) \cdot \bar{\alpha}(k, \mathbf{r}_{\lambda'\lambda}) \cdot \bar{\beta}(k, \mathbf{r}_{\lambda i}). \quad (28)$$

By expanding the entries of these matrices in terms of plane waves, it can be shown that,²¹

$$\alpha_{L'L}(k, \mathbf{r}_{ji}) = \lim_{N_\alpha \rightarrow \infty} \oint i^{-n} Y_L(\hat{\mathbf{k}}) e^{i\mathbf{k} \cdot \mathbf{r}_{\lambda i}} \tilde{\alpha}_{N_\alpha; \lambda' \lambda}(\hat{\mathbf{k}}) i^{n'} Y_{L'}^*(\hat{\mathbf{k}}) \times e^{i\mathbf{k} \cdot \mathbf{r}_{j\lambda'}} d\hat{\mathbf{k}}, \quad (29)$$

where

$$\tilde{\alpha}_{N_\alpha; \lambda' \lambda}(\hat{\mathbf{k}}) = \sum_{n=0}^{N_\alpha} i^n (2n+1) h_n^{(1)}(kr_{\lambda' \lambda}) P_n(\hat{\mathbf{k}} \cdot \hat{\mathbf{r}}_{\lambda' \lambda}), \quad (30)$$

and $\hat{\mathbf{k}}$ and $\hat{\mathbf{r}}_{\lambda' \lambda}$ denote the unit vectors in the direction of respective vectors, and $(\cdot)^*$ denotes complex conjugation.

In order to obtain Eq. (29), the order of an integration and an infinite summation must be changed which is not permissible in the strict sense. As a result, the infinite sum in the expression of $\tilde{\alpha}_{N_\alpha; \lambda' \lambda}(\hat{\mathbf{k}})$ does not converge. However, we need to truncate the infinite sum at some N_α for numerical purposes. Thus, the series can be truncated first, and then exchanging the order of integration and a finite sum does not pose a problem. One must be careful in the evaluation of $\tilde{\alpha}_{N_\alpha; \lambda' \lambda}(\hat{\mathbf{k}})$. The number of terms that must be kept in the summation, N_α , depends on the value of kD , as well as the desired accuracy, where D is the diameter of the larger of the two spheres circumscribing the groups \mathcal{S}_λ and $\mathcal{S}_{\lambda'}$. As D is increased, more terms must be used to keep the accuracy at the desired level. On the other hand, if too many terms are used, the Hankel functions start to oscillate wildly, causing numerical inaccuracies. Since the Hankel functions start to oscillate rapidly when the order exceeds the argument, the condition

$$N_\alpha < kr_{\lambda' \lambda} \quad (31)$$

must be satisfied, otherwise the groups are too close to use FMM and they will be referred to as neighboring groups. A very good empirical formula for N_α is

$$N_\alpha = \lfloor kD + C_a \log(kD + \pi) \rfloor + 1, \quad (32)$$

where $\lfloor \cdot \rfloor$ denotes the integer part, C_a is a parameter to adjust the accuracy of the calculations, and D is the diameter of the sphere circumscribing the largest group.

The diagonal forms of the translation operators for the Helmholtz equation in three dimensions was first described by Rokhlin.¹⁴ The diagonal translation theory was later summarized by Epton and Dembart.²²

V. THE FAST MULTIPOLE METHOD, FMM

Again consider the grouping of the N scatterers described previously. The scatterers are divided into L_g groups and each group is indexed from 1 to L_g . The ℓ th group contains $M(\ell)$ scatterers, and the set of indices of scatterers belonging to that group is denoted by \mathcal{S}_ℓ . For each group we also construct a set \mathcal{N}_ℓ which contains the indices of the neighboring groups, including the group itself, where the condition for two groups to be neighbors of each other is given by Eq. (31). In view of these definitions, Eq. (20) can be written as

$$\begin{aligned} \mathbf{b}^j - \bar{\mathbf{T}}_j \cdot \left[\sum_{\ell \in \mathcal{N}'_\ell} \sum_{\substack{i \in \mathcal{S}_\ell \\ i \neq j}} \bar{\boldsymbol{\alpha}}(k, \mathbf{r}_{ji}) \cdot \mathbf{b}^i \right. \\ \left. + \sum_{\ell \in \mathcal{N}'_\ell} \sum_{i \in \mathcal{S}_\ell} \bar{\boldsymbol{\alpha}}(k, \mathbf{r}_{ji}) \cdot \mathbf{b}^i \right] = \bar{\mathbf{T}}_j \cdot \bar{\boldsymbol{\beta}}(k, \mathbf{r}_{js}) \cdot \mathbf{a}^s \end{aligned} \quad (33)$$

in which the index of the group which the j th scatterer belongs to is denoted by ℓ' . The first sum in Eq. (33) above represents the near interactions, which will be denoted by $\mathbf{S}_{\text{near}}(j)$. The last summation contains the bulk of the computations, and will be denoted by $\mathbf{S}_{\text{far}}(j)$. For this term, we can write an element of the matrix $\bar{\boldsymbol{\alpha}}(k, \mathbf{r}_{ji})$ as

$$\begin{aligned} \alpha_{\nu\mu, nm}(k, \mathbf{r}_{ji}) \\ = \oint i^{-n} Y_{nm}(\hat{\mathbf{k}}) e^{i\mathbf{k} \cdot \mathbf{r}_{\lambda i}} \tilde{\alpha}_{N_\alpha; \lambda' \lambda}(\hat{\mathbf{k}}) i^\nu Y_{\nu\mu}^*(\hat{\mathbf{k}}) e^{i\mathbf{k} \cdot \mathbf{r}_{j\lambda'}} d\hat{\mathbf{k}}. \end{aligned} \quad (34)$$

Thus the far interactions can be written as:

$$\begin{aligned} \mathbf{S}_{\text{far}}(j) = \bar{\mathbf{T}}_j \cdot \oint e^{i\mathbf{k} \cdot \mathbf{r}_{j\lambda'}} \mathbf{Y}^*(\hat{\mathbf{k}}) \sum_{\ell \in \mathcal{N}'_\ell} \tilde{\alpha}_{N_\alpha; \lambda' \lambda}(\hat{\mathbf{k}}) \\ \times \sum_{i \in \mathcal{S}_\ell} e^{i\mathbf{k} \cdot \mathbf{r}_{\lambda i}} \mathbf{Y}^t(\hat{\mathbf{k}}) \cdot \mathbf{b}^i d\hat{\mathbf{k}}, \end{aligned} \quad (35)$$

where the notation

$$\begin{aligned} \mathbf{Y}(\hat{\mathbf{k}}) = [Y_{00}(\hat{\mathbf{k}}) \quad (-i)Y_{1,-1}(\hat{\mathbf{k}}) \quad \cdots \\ (-i)^n Y_{nm}(\hat{\mathbf{k}}) \quad \cdots]^t \end{aligned} \quad (36)$$

has been adopted. In a similar way, the far interactions for the product $[\bar{\mathbf{I}} - \bar{\mathbf{T}} \cdot \bar{\mathbf{A}}]^H \cdot \mathbf{b}$ can be written as

$$\begin{aligned} \mathbf{Q}_{\text{far}}(j) = \oint e^{i\mathbf{k} \cdot \mathbf{r}_{j\lambda'}} \mathbf{Y}^*(\hat{\mathbf{k}}) \sum_{\ell \in \mathcal{N}'_\ell} \tilde{\alpha}_{N_\alpha; \lambda \lambda'}^*(\hat{\mathbf{k}}) \\ \times \sum_{i \in \mathcal{S}_\ell} e^{i\mathbf{k} \cdot \mathbf{r}_{\lambda i}} \mathbf{Y}^t(\hat{\mathbf{k}}) \cdot \bar{\mathbf{T}}_j^H \cdot \mathbf{b}^i d\hat{\mathbf{k}}. \end{aligned} \quad (37)$$

In order to calculate $\mathbf{S}_{\text{far}}(j)$ and $\mathbf{Q}_{\text{far}}(j)$ numerically by using Eqs. (35) and (37), the integrals must be evaluated by using a quadrature rule over the unit sphere. For this purpose we note that the product formula

$$\begin{aligned} \oint f(x, y, z) d\hat{\mathbf{s}} = \int_0^{2\pi} \int_0^\pi f(\theta, \phi) \sin \theta d\theta d\phi \\ = \sum_{i=1}^{N_\theta} \sum_{j=1}^{2N_\theta} w_i^s w_j^c f(\theta_i, \phi_j) \end{aligned} \quad (38)$$

is exact for polynomials $x^\alpha y^\beta z^\gamma$ if $\alpha + \beta + \gamma < 2N_\theta$, where θ_i are chosen as the Gauss–Legendre points, ϕ_j are $2N_\theta$ equally spaced points over the interval $[-\pi, \pi]$, w_i^s are the Gauss–Legendre weights, and $w_j^c = \pi/N_\theta$. Since the spherical harmonics, $Y_{nm}(\theta, \phi)$ are also polynomials of order n on the surface of the sphere, the above quadrature rule is exact for harmonics of order $n < 2N_\theta$. A more efficient method for numerical quadrature on the sphere is given in Ref. 23.

The number of sample points, N_θ , that must be used for an accurate integration depends on the harmonic content of the integrand. Since $\tilde{\alpha}_{N_\alpha; \lambda \lambda'}(\hat{\mathbf{k}})$ contains harmonics only up to $N_\alpha > n + \nu$, the choice of

$$N_\theta = N_\alpha + 1, \quad (39)$$

is sufficient for accurate integration.

If the accuracy control parameter, C_a , is chosen to be 1, then the relative error in the evaluation of Eq. (34) is about 10%, and each increase in C_a by 1 decreases the error roughly by an order of magnitude.

The algorithm for performing the matrix-vector multiplication can now be written as:

1. Aggregation. For each group form the scalar function u defined as

$$u(\hat{\mathbf{k}}) = \sum_{i \in \mathcal{G}_j} e^{i\mathbf{k} \cdot \mathbf{r}_{\lambda i}} \mathbf{Y}^t(\hat{\mathbf{k}}) \cdot \mathbf{b}^i$$

at the $2N_\theta^2$ quadrature points. Since $N_\theta \sim kD \sim M^{1/3}$, this step requires

$$C'_{\text{agg}} \sim (n_t + 1)^2 N (2N_\theta^2) \sim \bar{\mu} N M^{2/3}$$

operations, where $\bar{\mu} = (n_t + 1)^2$, n_t is the order of the harmonics used to represent a typical scatterer, and M denotes the average number of scatterers per group, which can be written as, $M = (1/L_g) \sum_{l=1}^{L_g} M(l) = (N/L_g)$.

2. Group interactions. For each group evaluate the scalar function v given by the sum

$$v(\hat{\mathbf{k}}) = \sum_{\ell \in \mathcal{N}'_j} \tilde{\alpha}_{N_\alpha; \lambda \lambda'}(\hat{\mathbf{k}}) u(\hat{\mathbf{k}})$$

at the $2N_\theta^2$ quadrature points. This step requires

$$C'_{\text{int}} \sim \left(\frac{N}{M}\right)^2 (2N_\theta^2) \sim \left(\frac{N^2}{M^{4/3}}\right)$$

operations.

3. Disaggregation. For each scatterer evaluate $\mathbf{S}_{\text{far}}(j)$ as

$$\mathbf{S}_{\text{far}}(j) = \bar{\mathbf{T}}_j \cdot \oint e^{i\mathbf{k} \cdot \mathbf{r}_{j\lambda'}} \mathbf{Y}^*(\hat{\mathbf{k}}) v(\hat{\mathbf{k}}) d\hat{\mathbf{k}}$$

using the $2N_\theta^2$ quadrature points. This step requires

$$C'_{\text{dis}} \sim (n_t + 1)^2 N (2N_\theta^2) \sim \bar{\mu} N M^{2/3}$$

operations.

4. Near interactions. Add the near interactions as described by the first sum in Eq. (33). This means that the effect of scatterers close to a scatterer is computed by translating $\bar{\mu}$ harmonics of each neighboring scatterer to the position of that scatterer, requiring $\bar{\mu}^2$ operations. This step requires

$$C'_{\text{near}} \sim \bar{\mu}^2 N B \sim \bar{\mu}^2 N M$$

operations, where B is the typical number of neighboring scatterers. For each scatterer, the number of nearby scatterers is proportional to the volume of the groups, which in turn is proportional to the number of scatterers in each group, i.e., $B \sim M$.

If the group size is chosen to be proportional to the x th power of the number of scatterers, $M \sim N^x$, then the number of operations required will be proportional to $N^{(1+2x/3)}$ in the aggregation and the disaggregation steps, to $N^{(2-4x/3)}$ in the far interaction step, and to $N^{(1+x)}$ in the near interaction step. Since $1+2x/3 < 1+x$, to obtain an optimum algorithm, the powers of N in the far interaction and near interaction steps must be equated, i.e.,

$$2 - \frac{4x}{3} = 1 + x \Rightarrow x = \frac{3}{7} \quad (40)$$

resulting in $\mathcal{O}(N^{10/7})$ operations per matrix-vector multiplication. If the number of iterations required for convergence is p , the problem complexity becomes $pN^{10/7}$.

A. Near interactions

An important point about the algorithm described above is that the proportionality constant should be proportional to $\bar{\mu}^2 = (n_t + 1)^4 \sim (ka_{\text{max}})^4$, where a_{max} is the maximum linear dimension of the scatterers. This shows that as the size of the scatterers or the frequency is increased, the number of unknowns and the overall algorithm order will increase by a power of 4. The transformation $\bar{\alpha}(k, \mathbf{r}_{ji})$ is in general represented by a full matrix. However, a rigid translation of a coordinate system can also be achieved by first rotating the coordinate system such that its z axis points to the final point of translation, followed by a translation of this system along its z axis, and finally rotating the system to reverse the initial rotation. The basic advantage of this approach is that the matrix representations of the intermediate steps are not full matrices.

Any arbitrary rotation of a coordinate axis can be achieved by three rotations performed successively by performing a rotation α about the z axis, followed by a rotation β about the y axis of the resulting coordinate frame, followed by a rotation γ about the z axis of the latter coordinate frame. The three angles α , β , and γ are known as the Euler angles. The notation used is that of Edmonds'.¹⁵ Thus, if the matrix representation of an arbitrary rotation is denoted by $\bar{D}(\alpha, \beta, \gamma)$, we can write

$$\bar{D}(\alpha, \beta, \gamma) = \bar{D}(0, 0, \gamma) \cdot \bar{D}(0, \beta, 0) \cdot \bar{D}(\alpha, 0, 0), \quad (41)$$

where $\bar{D}(0, 0, \gamma) \triangleq \bar{\mathcal{E}}(\gamma)$ and $\bar{D}(\alpha, 0, 0) \triangleq \bar{\mathcal{E}}(\alpha)$ are diagonal matrices with diagonal elements being $\exp(im\gamma)$ and $\exp(im\alpha)$, respectively. The desired rotation that brings the z axis along the translation direction can be achieved by

choosing $\alpha = \phi$, $\beta = \theta$, and $\gamma = 0$, where θ , and ϕ are the spherical angles corresponding to the translation direction.

A similarity transformation can be used to express a y -axis rotation in terms of a rotation about the z axis as¹⁵

$$\begin{aligned} \bar{D}(0, \beta, 0) = & \bar{D}\left(-\frac{\pi}{2}, 0, 0\right) \cdot \bar{D}\left(0, -\frac{\pi}{2}, 0\right) \cdot \bar{D}(\beta, 0, 0) \\ & \cdot \bar{D}\left(0, \frac{\pi}{2}, 0\right) \cdot \bar{D}\left(\frac{\pi}{2}, 0, 0\right). \end{aligned} \quad (42)$$

This reduces the problem of computing the matrix representation of any rotation to that of computing the one matrix $\bar{\mathcal{S}} \triangleq \bar{D}(0, \pi/2, 0) \cdot \bar{D}(\pi/2, 0, 0)$. This matrix is a block diagonal matrix with number of nonzero entries being proportional to²⁴ n_t^3 . The use of the $\bar{\mathcal{S}}$ matrix does not decrease the number of operations required for multiplication, however it does reduce the memory requirements since only a single $\bar{\mathcal{S}}$ matrix is required for all rotations, along with appropriate diagonal matrices for each particular rotation. It must be noted that the rotation operations, and hence their matrix representations are unitary.

The matrix representation of the z -axis translation, which will be denoted by $\bar{\mathcal{T}}(r)$, also has many of its entries as zero.²⁵ The number of non-zero entries of $\bar{\mathcal{T}}(r)$ is also proportional to²⁶ n_t^3 .

Using the definitions above, an arbitrary translation can be written as

$$\begin{aligned} \bar{\alpha}(k, \mathbf{r}) = & \bar{\mathcal{E}}^H(\phi) \cdot \bar{\mathcal{S}}^H \cdot \bar{\mathcal{E}}^H(\theta) \cdot \bar{\mathcal{S}} \cdot \bar{\mathcal{T}}(r) \cdot \bar{\mathcal{S}}^H \cdot \bar{\mathcal{E}}(\theta) \cdot \bar{\mathcal{S}} \\ & \cdot \bar{\mathcal{E}}(\phi), \end{aligned} \quad (43)$$

and the number of operations increase by n_t^3 instead of n_t^4 . This approach is also applicable for static problems and is presented in Ref. 27.

VI. MULTILEVEL FMA, MLFMA

The grouping idea described above can be applied repeatedly by dividing each group into subgroups. Group sizes at each level can be chosen to minimize the operation count. It can be shown that the complexity of the algorithm decreases to $\mathcal{O}(N)$ as the number of levels is increased. This idea of nested groups can be best implemented by defining a hierarchical tree of cells which refine the computational domain into progressively smaller regions. A cubical cell big enough to contain all the scatterers is defined as the computational domain which will be called the ‘‘root’’ cell. This root cell is divided into 8 cubical child cells, which are in turn divided into 8 cells until a desired level of divisions is achieved. The set of all cells constructed at a certain level is called a ‘‘level’’ and indexed from 0 upwards. Thus, the root cell constitutes the 0th level, its 8 children forms the 1st level, and so on. In the following, a level with a lower-(higher) index number will be referred to as a higher(lower) level. The number of distinct cells at level q is equal to 8^q . The algorithm consists of two passes over this tree structure.

1. Upward pass: Starting from the cells at the lowest level, a multipole expansion in terms of outgoing waves,

valid inside each cell, is obtained by using addition theorems. As the cell size increases, more terms in the multipole expansion is required. The number of multipole coefficients required to express the field inside a cell accurately is proportional to the square of the cell edge length.

2. Downward pass: There are two approaches for the downward pass.

(i) Barnes–Hut;²⁸ In this approach, the field expansion at the position of each scatterer is calculated directly from the expansions accumulated at the cell centers. Starting from the children of the root cell (root cell is the cell that encloses the whole cluster of scatterers), the outgoing wave expansion accumulated at each cell center (except for the cell containing the scatterer) is translated to a standing wave expansion at the position of the scatterer. This gives the total effect of the scatterers that are in other cells. The effect of the scatterers in the same cell are left for the next level. At the lowest level, the effect of scatterers in the same cell are calculated directly.

(ii) Greengard–Rokhlin;²⁹ At each level, the outgoing wave expansions of the cells that are not neighbors of the cell in consideration but whose parents are neighbors of the current cell’s parent are translated to a standing wave expansion at the center of that cell. The standing wave expansion of the parent cell is also translated to the center of the current cell. The effect of neighboring cells is left to the next level. At the lowest level, the effect of scatterers in the same and neighboring cells are taken into account directly.

If these methods are used directly (i.e., without diagonalization), the Barnes–Hut approach results in an $\mathcal{O}(N^{5/3})$ algorithm, and the Greengard–Rokhlin approach results in an $\mathcal{O}(N^{4/3})$ algorithm. By using the diagonalized forms of the translation operators, the orders of these algorithms can be reduced to $\mathcal{O}(N \log N)$ and $\mathcal{O}(N)$, respectively. However, to use the diagonalized forms of the translation operators, the condition given in Eq. (31) must be satisfied, meaning that the number of cells left for lower levels is increased. This results in an increase in the multiplicative factor of the algorithm order. Since the Greengard–Rokhlin approach has a lower complexity, only this algorithm making use of the diagonalized translation operators will be considered in detail. For Helmholtz wave problems, this algorithm has to be augmented by an interpolation and antinterpolation procedure which will be described next.

A. Interpolation and antinterpolation

Assume that Q levels are used and that the indices of the cells in q th level are denoted by m_q , where $q=0$ denotes the root cell and $q=Q$ denotes the lowest level. Let \mathcal{N}_{m_q} denote the set of indices of the neighbors of the m_q th cell including itself, \mathcal{I}_{m_q} denote the interaction list of the m_q th cell, and \mathcal{S}_{m_q} denote the index set of the m_q th cell’s elements. The interaction list of the m_q th cell consists of all the cells that are in the same level and are not neighbors of the m_q th cell, but whose parents are neighbors of the m_q th cell’s parent. With these definitions, we can write

$$\begin{aligned}
\mathbf{x}^j &= \sum_{\substack{i=1 \\ i \neq j}}^N \bar{\boldsymbol{\alpha}}(k, \mathbf{r}_{ji}) \cdot \mathbf{b}^i \\
&= \sum_{m_Q' \in \mathcal{N}_{m_Q}} \sum_{\substack{j \in \mathcal{J}_{m_Q'} \\ i \neq j}} \bar{\boldsymbol{\alpha}}(k, \mathbf{r}_{ji}) \cdot \mathbf{b}^i + \sum_{m_Q' \in \mathcal{J}_{m_Q}} \oint \mathbf{t}_{m_Q}(\hat{\mathbf{k}}) \\
&\quad \times \tilde{\alpha}_{N_{\alpha}(Q); \lambda_{m_Q} \lambda_{m_Q'}}(\hat{\mathbf{k}}) u_{m_Q'}(\hat{\mathbf{k}}) d\hat{\mathbf{k}} \\
&\quad + \sum_{m_{Q-1}' \in \mathcal{J}_{m_{Q-1}}} \oint \mathbf{t}_{m_{Q-1}}(\hat{\mathbf{k}}) \tilde{\alpha}_{N_{\alpha}(Q-1); \lambda_{m_{Q-1}} \lambda_{m_{Q-1}'}}(\hat{\mathbf{k}}) \\
&\quad \times u_{m_{Q-1}'}(\hat{\mathbf{k}}) d\hat{\mathbf{k}} + \dots, \tag{44}
\end{aligned}$$

where

$$u_{m_q}(\hat{\mathbf{k}}) = \sum_{i \in \mathcal{J}_{m_q}} e^{i(\mathbf{k} \cdot \mathbf{r}_{\lambda_{m_q} i})} \mathbf{Y}^t(\hat{\mathbf{k}}) \cdot \mathbf{b}^i, \tag{45}$$

$$\mathbf{t}_{m_q}(\hat{\mathbf{k}}) = \mathbf{Y}^*(\hat{\mathbf{k}}) e^{i(\mathbf{k} \cdot \mathbf{r}_{j\lambda_{m_q}})}, \tag{46}$$

and $\mathbf{r}_{\lambda_{m_q}}$ denotes the center of the m_q th cell, and cell m_{Q-1} is the parent of the cell m_Q which contains the j th scatterer. The first sum in Eq. (44) accounts for the near interactions between scatterers in neighboring cells which will be denoted by $\mathbf{S}_{\text{near}}(j)$. The function $u_{m_q'}(\hat{\mathbf{k}})$ is the outgoing multipole expansion for cell m_q' . The integrals are the diagonal forms of the translation operators. Thus the second sum in Eq. (44) takes into account the effects of all the scatterers in the interaction list of the cell m_Q in level Q , which contains the j th scatterer. The effects of the cells that are further away are given by similar expressions in lower levels which are represented by the remaining terms in Eq. (44)

We define

$$v_{m_q}(\hat{\mathbf{k}}) = \sum_{m_q' \in \mathcal{J}_{m_q}} \tilde{\alpha}_{N_{\alpha}(q); \lambda_{m_q} \lambda_{m_q'}}(\hat{\mathbf{k}}) u_{m_q'}(\hat{\mathbf{k}}), \tag{47}$$

and write Eq. (44) as

$$\begin{aligned}
\mathbf{x}^j &= \mathbf{S}_{\text{near}}(j) + \oint \mathbf{t}_{m_Q}(\hat{\mathbf{k}}) v_{m_Q}(\hat{\mathbf{k}}) d\hat{\mathbf{k}} \\
&\quad + \oint \mathbf{t}_{m_{Q-1}}(\hat{\mathbf{k}}) v_{m_{Q-1}}(\hat{\mathbf{k}}) d\hat{\mathbf{k}} + \dots \\
&= \mathbf{S}_{\text{near}}(j) + \sum_{n=1}^{K_Q} w_n^Q \mathbf{t}_{m_Q}(\hat{\mathbf{k}}_n^Q) v_{m_Q}(\hat{\mathbf{k}}_n^Q) \\
&\quad + \sum_{n'=1}^{K_{Q-1}} w_{n'}^{Q-1} \mathbf{t}_{m_{Q-1}}(\hat{\mathbf{k}}_{n'}^{Q-1}) v_{m_{Q-1}}(\hat{\mathbf{k}}_{n'}^{Q-1}) + \dots, \tag{48}
\end{aligned}$$

where the integrals are replaced by a quadrature rule and $\hat{\mathbf{k}}_n^q$ and w_n^q for $n=1, \dots, K_q$ denote the sampling points and weights at the $K_q = 2N_{\theta}^2(q)$ points used for integration at level q , respectively. The quadrature rule described previously in Eq. (38) is an appropriate choice. The u , v , and \mathbf{t} functions must be calculated at the sample points.

In the upward pass, the u functions, which represent the outgoing multipole expansion for the cells, are calculated at

the lowest level, and then the outgoing multipole expansions for cells in the higher levels are computed. The outgoing multipole expansion at a level q can be related to the outgoing multipole expansions at a lower level as

$$u_{m_q}(\hat{\mathbf{k}}) = \sum_{m_{q+1} \in \mathcal{C}_{m_q}} e^{i(\mathbf{k} \cdot \mathbf{r}_{\lambda_{m_q} \lambda_{m_{q+1}}})} u_{m_{q+1}}(\hat{\mathbf{k}}), \tag{49}$$

where \mathcal{C}_{m_q} denotes the set of the children of cell m_q . Since only $K_{q+1} < K_q$ samples of $u_{m_{q+1}}$ are available at level $q+1$, the value of u_{m_q} can be calculated only at these points. Its values at the quadrature points used for level q can be obtained by interpolation. Thus, we can write

$$\begin{aligned}
u_{m_q}(\hat{\mathbf{k}}_n^q) &= \sum_{m_{q+1} \in \mathcal{C}_{m_q}} e^{i(\hat{\mathbf{k}}_n^q \cdot \mathbf{r}_{\lambda_{m_q} \lambda_{m_{q+1}}})} \sum_{n'=1}^{K_{q+1}} W_{n'n} u_{m_{q+1}}(\hat{\mathbf{k}}_{n'}^{q+1}), \tag{50}
\end{aligned}$$

where $W_{n'n}$ are the entries of the interpolation matrix.

In a similar way, the function $\mathbf{t}_{m_{q-1}}$ can be related to a lower level as

$$\begin{aligned}
\mathbf{t}_{m_{q-1}}(\hat{\mathbf{k}}) &= \mathbf{Y}^*(\hat{\mathbf{k}}) e^{i(\mathbf{k} \cdot \mathbf{r}_{j\lambda_{m_{q-1}}})} \\
&= \mathbf{Y}^*(\hat{\mathbf{k}}) e^{i(\mathbf{k} \cdot \mathbf{r}_{j\lambda_{m_q}})} e^{i(\mathbf{k} \cdot \mathbf{r}_{\lambda_{m_q} \lambda_{m_{q-1}}})} \\
&= e^{i(\mathbf{k} \cdot \mathbf{r}_{\lambda_{m_q} \lambda_{m_{q-1}}})} \mathbf{t}_{m_q}(\hat{\mathbf{k}}) \tag{51}
\end{aligned}$$

which for the sample values becomes

$$\mathbf{t}_{m_{q-1}}(\hat{\mathbf{k}}_{n'}^{q-1}) = e^{i(\hat{\mathbf{k}}_{n'}^{q-1} \cdot \mathbf{r}_{\lambda_{m_q} \lambda_{m_{q-1}}})} \sum_{n=1}^{K_q} W_{n'n} \mathbf{t}_{m_q}(\hat{\mathbf{k}}_n^q), \tag{52}$$

where the values of $\mathbf{t}_{m_{q-1}}$ at the required sampling points are obtained by interpolation of the samples of \mathbf{t}_{m_q} . Now, a sum in Eq. (48) can be written as

$$\begin{aligned}
&\sum_{n'=1}^{K_{q-1}} w_{n'}^{q-1} \mathbf{t}_{m_{q-1}}(\hat{\mathbf{k}}_{n'}^{q-1}) v_{m_{q-1}}(\hat{\mathbf{k}}_{n'}^{q-1}) \\
&= \sum_{n'=1}^{K_{q-1}} w_{n'}^{q-1} \left\{ e^{i(\hat{\mathbf{k}}_{n'}^{q-1} \cdot \mathbf{r}_{\lambda_{m_q} \lambda_{m_{q-1}}})} \sum_{n=1}^{K_q} W_{n'n} \mathbf{t}_{m_q}(\hat{\mathbf{k}}_n^q) \right\} \\
&\quad \times v_{m_{q-1}}(\hat{\mathbf{k}}_{n'}^{q-1}) \\
&= \sum_{n=1}^{K_q} w_n^q \mathbf{t}_{m_q}(\hat{\mathbf{k}}_n^q) \\
&\quad \times \underbrace{\left\{ \sum_{n'=1}^{K_{q-1}} \frac{w_{n'}^{q-1}}{w_n^q} W_{n'n} v_{m_{q-1}}(\hat{\mathbf{k}}_{n'}^{q-1}) e^{i(\hat{\mathbf{k}}_{n'}^{q-1} \cdot \mathbf{r}_{\lambda_{m_q} \lambda_{m_{q-1}}})} \right\}}_{\bar{v}_{m_q}(\hat{\mathbf{k}}_n^q)}. \tag{53}
\end{aligned}$$

This result transforms an integral at level $q-1$ to an integral at level q , which is achieved by interpolating the kernel of

the integral operator, \mathbf{t} , at a lower level, then exchanging the order of interpolation and integration. As a result, the adjoint of the interpolation operator operates on the v function. This method was first proposed by Brandt³⁰ for solving integral equations with oscillatory kernels, who also coined the term *interpolation* standing for *adjoint interpolation*. Later, this technique was employed by Song and Chew,¹⁰ in the calculation of electromagnetic scattering from three dimensional scatterers. Through the use of this technique, it is possible to carry the multipole expansions without actually evaluating the integrals down to the lowest level where the integration is finally performed with the least cost.

Several points remain to be clarified in the foregoing description.

(i) The function $\tilde{\alpha}_{N_\alpha(q); \lambda_{m_q} \lambda_{m'_q}}(\hat{\mathbf{k}})$ is given by a summation truncated at $N_\alpha(q)$. Since each cell in a given level is a cube of edge d_q , and we desire the expressions to be valid inside this cube, the largest order of harmonics that should be retained is

$$N_\alpha(q) = [kD_q + C_d \log(kD_q + \pi)] + 1, \quad (54)$$

where $D_q \leq \sqrt{3}d_q + a_{\max}$ is the diameter of the sphere circumscribing all the scatterers in cells. The number of the quadrature points for accurate integration will then be

$$N_\theta(q) = N_\alpha(q) + 1. \quad (55)$$

(ii) The choice of $N_\alpha(q)$ determines the neighboring cells. If the distance between the centers of two cells satisfy the condition

$$N_\alpha(q) \geq k |\mathbf{r}_{\lambda_{m_q} \lambda_{m'_q}}|, \quad (56)$$

then these cells are neighbors of each other.

(iii) The samples of the functions at a higher level are expressed in terms of a lower level through interpolation. If all K_q points available at level q are used to interpolate the function at K_{q-1} points of level $q-1$, the interpolation would be exact since a spherical harmonic of order $N_\alpha(q)$ can be exactly recovered from K_q points. However, the algorithm order cannot be reduced. In order to reduce the algorithm order we must use a $P < K_q$ point interpolation formula where P is the same for each level. It can be shown that the best interpolation formula for band-limited functions (hence for spherical harmonics) from a finite and non-uniformly spaced points is the Lagrangian interpolation.³¹

(iv) If a Q level algorithm is used, there will be a total of $(8^Q - 1)/7$ cells which can be a very large number. However, by retaining only the non-empty cells, CPU requirements can be reduced.

The algorithm can now be described as follows:

1. Upward pass

(1) At the lowest level Q , for each cell calculate $u_{m_Q}(\hat{\mathbf{k}}_n^Q)$ using Eq. (45). This step requires

$$C'_{\text{up}}(Q) \sim \bar{\mu} N K_Q$$

operations, where $\bar{\mu}$ is the average value of harmonics required for the scatterers, as defined previously.

(2) Use Eq. (50) to find the outgoing wave expansions for each level up to the second level.³² This step requires

$$C'_{\text{up}}(q) \sim 8(K_q + PK_q)M_q$$

operations to generate the desired functions for level q , where M_q is the number of non-empty cells in this level, and P is the number of points used in interpolation.

2. Downward pass

(1) Starting from the second level, calculate $v_{m_q}(\hat{\mathbf{k}}_n^q)$ for each cell using Eq. (47). This accounts for the multipole expansions of interaction cells. Add $\tilde{v}_{m_q}(\hat{\mathbf{k}}_n^q)$ as defined in Eq. (53), where the cell m_{q-1} is the parent of the cell m_q . Thus, the multipole expansions of all cells except for the neighbors are translated to the cell center. The effect of the neighbors of the cell are left to a lower level. These calculations are repeated down to the lowest level and require

$$C'_{\text{down}}(q) \sim (I_q K_q + K_q + PK_q)M_q$$

operations for level q , where I_q is the average number of interacting cells of a cell.

(2) At the lowest level, evaluate

$$\mathbf{x}^j = \mathbf{S}_{\text{near}}(j) + \sum_{n=1}^{K_Q} w_n^Q \mathbf{t}_{m_Q}(\hat{\mathbf{k}}_n^Q) \{v_{m_Q}(\hat{\mathbf{k}}_n^Q) + \tilde{v}_{m_Q}(\hat{\mathbf{k}}_n^Q)\},$$

where $\mathbf{S}_{\text{near}}(j)$ is calculated directly. This step requires

$$C'_{\text{down}}(Q) \sim \bar{\mu} K_Q N + \bar{\mu}^2 B N,$$

where B is the average number of scatterers remaining in the neighboring region of a scatterer.

In order to calculate the overall algorithm order we will make certain assumptions:

- (1) The interpolation matrices for each level are calculated and stored;
- (2) The functions $\tilde{\alpha}_{N_\alpha(q); \lambda_{m_q} \lambda_{m'_q}}(\hat{\mathbf{k}})$ are calculated at the quadrature points for all possible pairs of interacting cells for all levels;
- (3) The number of quadrature points is roughly proportional to the cell sizes as depicted by Eq. (54) so that

$$K_q \sim 4K_{q+1} \sim 4^{Q-q} K_Q$$

since the cell size is halved at each level;

- (4) The scatterers are uniformly distributed so that all the cells are occupied at each level which gives

$$M_q = 8^q \quad \text{and} \quad N = 8^Q;$$

- (5) The average number of interacting cells for a given level is quite small for the first few levels, but then becomes large and independent of the level, determined solely by

the desired accuracy. Thus we will denote the limiting value of I_q as q increases by I .

We can now write the total number of operations for the upward pass as

$$\begin{aligned} C_{\text{up}} &\sim \bar{\mu} K_Q N + \sum_{q=2}^{Q-1} 8(K_q + PK_q) M_q \\ &= \bar{\mu} K_Q N + 8(P+1) K_Q N \end{aligned} \quad (57)$$

and the total number of operations for the downward pass as

$$\begin{aligned} C_{\text{down}} &\sim \bar{\mu} K_Q N + \bar{\mu}^2 B N + \sum_{q=3}^Q (IK_q + K_q + PK_q) M_q \\ &= \bar{\mu} K_Q N + \bar{\mu}^2 B N + 2(I+P+1) K_Q N \end{aligned} \quad (58)$$

from which it follows that the overall algorithm complexity is of $\mathcal{O}(N)$. The multiplicative factor of the algorithm depends basically on the value I of the average number of interacting cells. This value in turn depends on the desired accuracy.

VII. THE FFT METHOD

The translation matrix $\bar{\alpha}(k, \mathbf{r}_{ji})$ depends only on $\mathbf{r}_{ji} = \mathbf{r}_i - \mathbf{r}_j$ and hence the summation in Eq. (19) can be considered as a convolution, which can be effectively evaluated using the FFT algorithm. However, to use the FFT algorithm, the scatterers must be located on a regular grid.

The basic tool for the FFT method is the addition theorem depicted in Eq. (28) which is repeated here for convenience:

$$\bar{\alpha}(k, \mathbf{r}_{ji}) = \bar{\beta}(k, \mathbf{r}_{j\lambda'}) \cdot \bar{\alpha}(k, \mathbf{r}_{\lambda'\lambda}) \cdot \bar{\beta}(k, \mathbf{r}_{\lambda i}). \quad (59)$$

This expression is valid if $|\mathbf{r}_{\lambda'\lambda}| > |\mathbf{r}_{j\lambda'} + \mathbf{r}_{\lambda i}|$, i.e., if the two groups are disjoint. Using Eq. (28) in Eq. (33) and rearranging, we get

$$\begin{aligned} \mathbf{b}^j - \bar{\mathbf{T}}_j \cdot \left[\sum_{\ell \in \mathcal{N}'_{\ell'}} \sum_{\substack{i \in \mathcal{S}_{\ell} \\ i \neq j}} \bar{\alpha}(k, \mathbf{r}_{ji}) \cdot \mathbf{b}^i \right. \\ \left. + \bar{\beta}(k, \mathbf{r}_{j\lambda'}) \cdot \sum_{\ell \in \mathcal{N}'_{\ell'}} \bar{\alpha}(k, \mathbf{r}_{\lambda'\lambda}) \cdot \sum_{i \in \mathcal{S}_{\ell}} \bar{\beta}(k, \mathbf{r}_{\lambda i}) \cdot \mathbf{b}^i \right] \\ = \bar{\mathbf{T}}_j \cdot \bar{\beta}(k, \mathbf{r}_{js}) \cdot \mathbf{a}^s. \end{aligned} \quad (60)$$

The inner summation of the second term aggregates the outgoing multipole expansions of the scatterers contained in a group to the center of that group. The outer summation accounts for the group interactions. If the computational domain is divided into regular boxes, the translation between groups can be performed by using the FFT algorithm,¹¹ since in this case the outer sum can be cast into a matrix-vector multiplication involving a block Toeplitz matrix. Multiplication of the outer sum by $\bar{\beta}(k, \mathbf{r}_{j\lambda'})$ accounts for disaggregation and the first sum represents the near interactions which should be calculated directly. The set of neighbors of a group

consists of the adjacent groups due to the constraint on the addition theorem.

If we assume that each group contains $\mathcal{O}(1)$ scatterers, the aggregation, disaggregation, and near interactions steps can be performed in $\mathcal{O}(\bar{\mu}^2 N)$ operations while the group interactions require $\mathcal{O}(\bar{\mu}^2 N \log N)$ operations.

VIII. THE FMMFFT METHOD

The idea of diagonalization of the translation operator can be employed in conjunction with the FFT method to reduce the computational load.³³ In the FMM, the scalar functions $u(\hat{\mathbf{k}})$ are the outgoing wave expansions for each group. For far away groups, these outgoing wave expansions are translated to a standing wave expansion by

$$v(\hat{\mathbf{k}}) = \sum_{\ell \in \mathcal{N}'_{\ell'}} \tilde{\alpha}_{N_{\alpha}; \lambda' \lambda}(\hat{\mathbf{k}}) u(\hat{\mathbf{k}}).$$

This equation is a matrix-vector multiplication. If the group centers are located on a regular grid, the matrix whose entries are $\tilde{\alpha}_{N_{\alpha}; \lambda' \lambda}(\hat{\mathbf{k}})$ is a Toeplitz matrix and the multiplication can be done efficiently by using the FFT algorithm. In this approach, all the operations in a multilevel FMM, except for the lowest level, are replaced by the FFT algorithm.

The algorithm can be summarized as follows:

1. Aggregation. For each group form the scalar function u defined as

$$u(\hat{\mathbf{k}}) = \sum_{i \in \mathcal{S}_{\ell}} e^{i\mathbf{k} \cdot \mathbf{r}_{\lambda i}} \mathbf{Y}^t(\hat{\mathbf{k}}) \cdot \mathbf{b}^i$$

at the $2N_{\theta}^2$ quadrature points. For any given distribution of the scatterers, the number of FFT points, N_{FFT} , can be chosen to keep N_{θ} same. This means $N \sim N_{\text{FFT}}^3$. This step requires $\mathcal{O}(\bar{\mu} N)$ operations.

2. Group interactions. For each group evaluate the scalar function v given by the sum

$$v(\hat{\mathbf{k}}) = \sum_{\ell \in \mathcal{N}'_{\ell'}} \tilde{\alpha}_{N_{\alpha}; \lambda' \lambda}(\hat{\mathbf{k}}) u(\hat{\mathbf{k}})$$

at the $2N_{\theta}^2$ quadrature points by using the FFT algorithm. Assuming that each group contains $\mathcal{O}(1)$ scatterers, and hence $\bar{\mu} \sim 2N_{\theta}^2$, this step requires $\mathcal{O}(\bar{\mu} N \log N)$ operations.

3. Disaggregation. For each scatterer, evaluate $\mathbf{S}_{\text{far}}(j)$ as

$$\mathbf{S}_{\text{far}}(j) = \bar{\mathbf{T}}_j \cdot \oint e^{i\mathbf{k} \cdot \mathbf{r}_{j\lambda'}} \mathbf{Y}^*(\hat{\mathbf{k}}) v(\hat{\mathbf{k}}) d\hat{\mathbf{k}}$$

using the $2N_{\theta}^2$ quadrature points. This step is similar to the aggregation step and requires $\mathcal{O}(\bar{\mu} N)$ operations.

4. Near interactions. Compute the near interactions directly as described by the first sum in Eq. (33). This step requires $\mathcal{O}(\bar{\mu}^2 N)$ operations.

The order of the algorithm is determined by the second step and hence is $\mathcal{O}(\bar{\mu} N \log N)$. The basic advantage of using the diagonal forms of the translation operators is that the

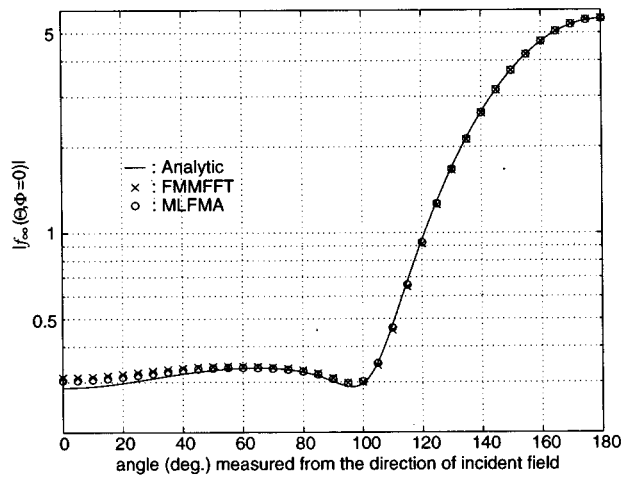


FIG. 1. The far field function $f_\infty(\theta, \phi=0)$ for a sphere of $ka=4.0$, $c_1=1.2$, $\rho_1=1$, in a background medium with parameters $c=1$, $\rho=1$. The analytic solution is obtained by spherical harmonic series expansion, while MLFMA and FMMFFT results are obtained by dividing the sphere into 3071 small spheres with the same parameters.

algorithm order is reduced by a factor of $\bar{\mu}$. However, the near neighbors are determined by the condition $N_\alpha < kr_{\lambda'}$, which results in a larger number of neighboring groups as compared to the FFT method. As a result, the total number of operations per matrix-vector multiplication for the FMMFFT method can exceed that of the FFT method, especially when the scatterers are densely packed.

IX. NUMERICAL RESULTS

In order to test the algorithms, a large sphere is divided into smaller spheres and the field scattered from this system of particles is calculated. Figure 1 shows the far field function for this sphere obtained by using both the analytic results (solid line, which are obtained by spherical harmonic series expansion), and the results obtained by using the MLFMA (“O”) and the FMMFFT (“x”) algorithms, where the far field function $f_\infty(\theta, \phi)$ is defined by

$$\Phi^s(\mathbf{r}) \sim f_\infty(\theta, \phi) \frac{e^{ikr}}{r}, \quad kr \rightarrow \infty, \quad (61)$$

and $\Phi^s(\mathbf{r})$ denotes the scattered field. The large sphere has a radius $ka = 4.0$ and it is divided into 3071 smaller spheres each having a radius $kr=0.1376$. The density of the spheres are the same as the background medium and the velocity of sound in the spheres is 1.2 times that of the background. The spherical harmonic expansion for the field scattered by the small spheres is truncated at $n_i=2$, hence there are 9 unknowns associated with each sphere, giving a total of 27 639 unknowns. The radii of the small spheres are calculated such that the total volume occupied by the 3071 spheres is equal to that of the large sphere, i.e.,

$$kr = \frac{ka}{3071^{1/3}} = 0.1376.$$

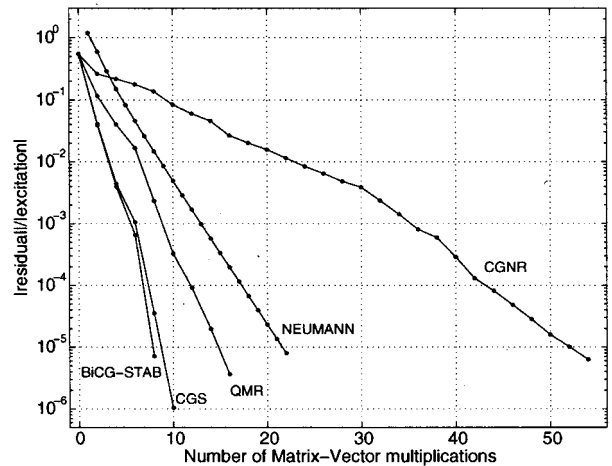


FIG. 2. Convergence rates for different iteration algorithms.

The errors in both the MLFMA and the FMMFFT results are less than 10% of the analytical result.

To solve the matrix equation, the conjugate gradient normalized residual (CGNR), conjugate gradient squared (CGS), biconjugate gradient stabilized (BiCG-STAB), quasi-minimal residual (QMR), and Neumann iteration techniques are used. Iteration is stopped when the norm of the residuals drop below 10^{-5} of the norm of the right hand side (excitation vector) of the matrix equation. The ratio of the norm of the residuals to the norm of the excitation vector for these methods is shown in Fig. 2. The results show that the CGS, BiCG-STAB, QMR algorithms have similar convergence behavior and they converge much more rapidly than the CGNR algorithm. This is basically due to the fact that CGNR method is applied to the positive definite Hermitian matrix $\bar{A}^H \cdot \bar{A}$ whose condition number is the square of the original coefficient matrix \bar{A} . However, the CGNR method is quite general and can be applied to any matrix whereas the convergence of the others depend on the properties of the matrix. The Neumann series converges exponentially and its convergence rate is intermediate for this example.

It must be mentioned that the rate of convergence of the algorithm depends on the distribution of the scatterers as well as their contrast. When the contrast is increased, the number of iterations required also increase. When the density of the scatterers is different from that of the background medium, it becomes necessary to use more terms in the expansion of the fields scattered by them, especially when the scatterers are small. This is because the dipole terms cannot be ignored for such scatterers as compared to the monopole term. Due to the increase in the number of iterations, the total time to solve high contrast problems takes much more time. Such cases have been successfully solved for a low number of unknowns.

In the implementation of the algorithms, the translation coefficients for neighboring scatterers are calculated each time it is required instead of keeping them in the memory. This decreases the memory requirements at the cost of in-

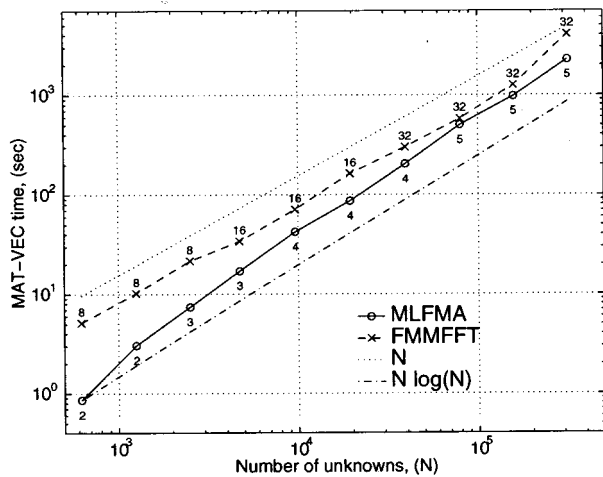


FIG. 3. The CPU times for the MLFMA and FMMFFT methods for a random distribution of scatterers. The numbers below (above) the curve for the MLFMA (FMMFFT) show the optimum number of levels (FFT size).

creasing the computation time for near interactions, but does not change the complexity of the algorithm.

The efficiency of the fast matrix-vector multiplication algorithms is tested by using different number of scatterers. As the number of the scatterers is increased, the computational domain is also enlarged to keep the density of scatterers approximately constant at $kD^3/N \approx 18$ where D is the edge of the cube that encloses all the scatterers. The acoustical parameters of all the scatterers are same with $\rho = 1$ and $c = 1.2$, whereas the location and the radii of the scatterers are randomly generated. The electrical radii of the scatterers, kr , are uniformly distributed between 0 and 1.75. Figure 3 shows the CPU time per matrix-vector multiplication for the MLFMA and FMMFFT methods. All the results presented are obtained on a 90 MHz, SGI Power Challenge with 2 GB of RAM. The numbers below (above) the curve for the MLFMA (FMMFFT) show the optimum number of levels (FFT size). It must be noted that the FFT algorithm used is a radix-2 algorithm, hence the FFT sizes are powers of 2. In the MLFMA, the accuracy parameter is chosen to be $C_a = 1.0$ and $P = 16$ point interpolation is used. The results confirm the complexity analysis for these algorithms.³⁴

Figure 3 reveals that the time per iteration is larger for the FMMFFT as compared to that of the MLFMA. As the number of levels used in MLFMA (or the FFT size in the FMMFFT) is increased, the cell size at the finest level decreases until it becomes about the size of the largest scatterer. However, due to random distribution of the scatterers, most of the cells at this level will be empty. The size of the cells at the finest level determines the neighboring cells through Eqs. (54) and (56). Therefore, increasing the number of levels (FFT size) can decrease the amount of work required for evaluating the near interactions drastically. In the MLFMA empty cells do not contribute to the computation, whereas in the FMMFFT algorithm empty cells require as much computation as the non-empty cells. As a result of the

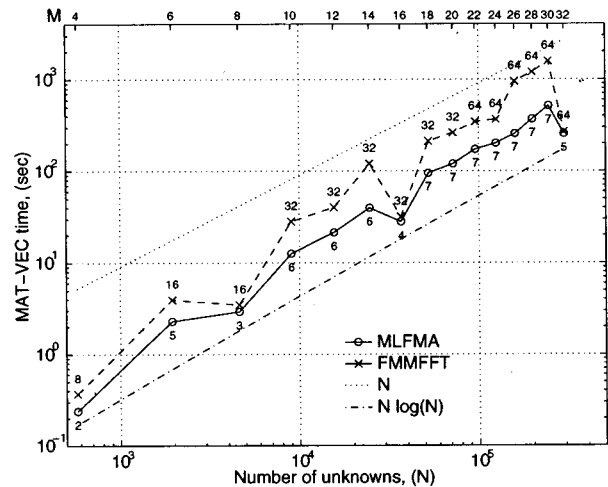


FIG. 4. The CPU times for the MLFMA and FMMFFT methods for closely packed scatterers located on a uniform rectangular grid. The numbers below (above) the curve for the MLFMA (item) show the optimum number of levels (FFT size).

adaptive nature of the MLFMA, the CPU requirements at the optimum number of levels are less stringent.

Figure 4 is similar to Fig. 3, except that the scatterers are located on a uniform rectangular grid and they are in contact with each other. The whole cluster forms a cube with M scatterers on each side. When $M = 2^m$, the scatterers are located at the center of a cell for m levels (FFT size = $2M$). For such cases, the matrix-vector multiplication times for both algorithms are very close to each other. These cases also present ideal situations in the sense that the assumptions made in the complexity analysis are very closely satisfied. It can be seen from the figure that the slope of the line passing through these points is very close to unity. When M is not a power of 2, there is an offset between the centers of the scatterers and the centers of the cells, for any choice of the

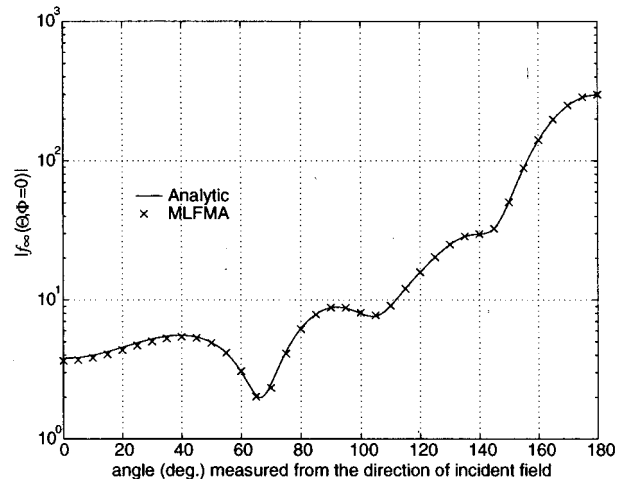


FIG. 5. The far field function $f_\infty(\theta, \phi = 0)$ for a sphere of $ka = 8.0$, $c_1 = 1.2$, $\rho_1 = 1$, in a background medium with parameters $c = 1$, $\rho = 1$. The MLFMA results are obtained by dividing the sphere into 137,376 small spheres with the same parameters and using $C_a = 0.0$.

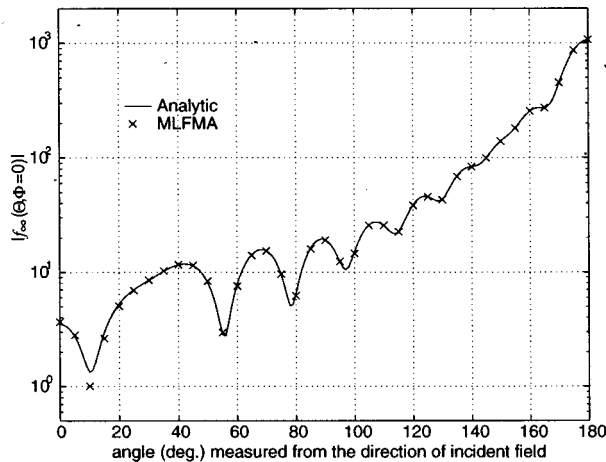


FIG. 6. The far field function $f_\infty(\theta, \phi=0)$ for a sphere of $ka=16.0$, $c_1=1.2$, $\rho_1=1$, in a background medium with parameters $c=1$, $\rho=1$. The MLFMA results are obtained by dividing the sphere into 1 099 136 small spheres with the same parameters and using $C_a=0.0$.

number of levels. However, this offset can be made smaller by using a large number of levels at the expense of creating many empty cells. Thus, for the same reason explained above, MLFMA performs better than the FMMFFT algorithm for such cases.

It must be noted that, in all the examples above, the accuracy parameter is $C_a=1.0$ and a $P=16$ point interpolation is used for the MLFMA. It can be shown that $C_a=1.0$ guarantees a 10% relative accuracy in the calculation of the elements of the translation matrix, $\bar{\alpha}(k, \mathbf{r}_{ij})$, even in the worst case, i.e., when the scatterers are located at the corners of the cells.³⁵ However, there is no reason to assume that all scatterers are located to yield a worst case error. The errors generally tend to cancel each other. Furthermore, comparing the error in an entry of $\bar{\alpha}(k, \mathbf{r}_{ij})$ to its actual value gives pessimistic results since the contribution of that term may be too small as compared to the total field. Figure 5 shows the far field function for a sphere of electrical radius $ka=8$ calculated by using 137 376 small spheres of radii $kr=0.1550$ using $n_i=0$ (corresponding to roughly 20 unknowns per wavelength) with $C_a=0.0$, and $P=16$ along with the spherical harmonic series expansion solution. The density of the spheres are the same as the background medium and the velocity of sound in the spheres is 1.2 times that of the background. Although a mathematical proof is not available, the agreement of the result with the spherical harmonic series expansion solution indicates that the constraint on the choice of C_a may be relaxed. Since C_a also determines the range of neighboring cells, a decrease in C_a results in a drastic decrease in the computation time. For this example, the solution time is ~ 2 hours for $C_a=0.0$ and ~ 12 hours for $C_a=0.5$. The far field function calculated by using $C_a=0.5$ is not shown in the figure since it would not be distinguishable from the result for $C_a=0.0$.

Figure 6 shows the far field function for a sphere of electrical radius $ka=16$ calculated by using 1 099 136 small spheres of radii $kr=0.1550$ using $n_i=0$, $C_a=0.0$, and

$P=16$ along with the spherical harmonic series expansion solution. The acoustical parameters are the same as in the previous case. The total solution time is ~ 20 hours.

X. CONCLUSIONS

The MLFMA and FMMFFT algorithms are implemented to solve the multiple scattering from a cluster of scatterers. The complexity analysis for both algorithms are given and verified by simulation. It was observed that the MLFMA performs better than the FMMFFT algorithm in general. However, when the scatterers are distributed uniformly on a rectangular grid, the FMMFFT algorithm is as good as the MLFMA. Since the implementation of the FMMFFT algorithm is much easier, it should be preferred in such cases. On the other hand, if the scatterer distribution is far from uniform, MLFMA can save both CPU time and memory owing to its adaptive nature.

The FMM is based on an approximation of the translation coefficients for far away points. The accuracy of this method is controlled by the parameter C_a . It is stated in Ref. 8 that for single precision (32-bit reals) $C_a=5$, and for double precision (64-bit reals) $C_a=10$ are appropriate. In Ref. 36, $C_a=1$ is used. The numerical results presented above show that, at least for sufficiently smooth problems, even a smaller value of C_a gives accurate results.

ACKNOWLEDGMENTS

The authors wish to thank J. M. Song for useful discussions. This work was supported by a grant from AFOSR via the MURI Program under Contract No. F49620-96-1-0025, the National Science Foundation under Grant No. NSF ECS 93-02145, and the Office of Naval Research under Contract No. N00014-95-1-0872.

- ¹L. L. Foldy, "The multiple scattering of waves," *Phys. Rev.* **67**, 107–109 (1945).
- ²U. Frisch, "Wave propagation in random media," in *Probabilistic Methods in Applied Mathematics*, edited by A.T. Bharucha-Reid (Academic, New York, 1968), Vol. 1, pp. 75–198.
- ³A. Ishimaru, *Wave Propagation and Scattering in Random Media* (Academic, New York, 1978).
- ⁴B. Peterson and S. Ström, "Matrix formulation of acoustic scattering from an arbitrary number of scatterers," *J. Acoust. Soc. Am.* **56**, 771–780 (1974).
- ⁵W. C. Chew, "Efficient computation of three-dimensional scattering of vector electromagnetic waves," *J. Opt. Soc. Am. A* **11**, 1528–1537 (1994).
- ⁶A. K. Hamid, I. R. Ciric, and M. Hamid, "Iterative solution of the scattering by an arbitrary configuration of conducting or dielectric spheres," *IEE Proc.-H* **138**, 565–572 (1991).
- ⁷F. de Daran, V. V. Lefebvre, and J. P. Parneix, "Modeling of electromagnetic waves scattered by a system of spherical particles," *IEEE Trans. Magn.* **31**, 1598–1601 (1995).
- ⁸R. Coifman, V. Rokhlin, and S. Wandzura, "The fast multipole method for the wave equation: A pedestrian prescription," *IEEE Antennas Propag. Mag.* **35**, 7–12 (1993).
- ⁹C. C. Lu and W. C. Chew, "A multilevel algorithm for solving a boundary integral equation of wave scattering," *Microw. Opt. Technol. Lett.* **7**, 466–470 (1994).
- ¹⁰J. M. Song and W. C. Chew, "Multilevel fast-multipole algorithm for solving combined field integral equations of electromagnetic scattering," *Microw. Opt. Technol. Lett.* **10**, 14–19 (1995).
- ¹¹W. C. Chew, J. H. Lin, and X. G. Yang, "An FFT T-matrix method for

- 3D microwave scattering solutions from random discrete scatterers," *Microw. Opt. Technol. Lett.* **9**, 194–196 (1995).
- ¹²H. Gan and W. C. Chew, "A discrete BCG-FFT algorithm for solving 3D inhomogeneous scatterer problems," *J. Electromagn. Waves Appl.* **9**, 1339–1357 (1995).
- ¹³*Handbook of Mathematical Functions*, edited by M. Abramowitz and I. A. Stegun (Dover, New York, 1972).
- ¹⁴V. Rokhlin, "Diagonal forms of translation operators for the Helmholtz equation in three dimensions," *Appl. Comput. Harmonic Anal.* **1**, 82–93 (1993).
- ¹⁵A. R. Edmonds, *Angular Momentum in Quantum Mechanics* (Princeton U. P., Princeton, NJ, 1957).
- ¹⁶S. Stein, "Addition theorems for spherical wave functions," *Q. Appl. Math.* **19**, 15–24 (1961).
- ¹⁷W. C. Chew, *Waves and Fields in Inhomogeneous Media* (Van Nostrand Reinhold, New York, 1990).
- ¹⁸W. C. Chew, "Recurrence relations for three-dimensional scalar addition theorem," *J. Electromagn. Waves Appl.* **6**, 133–142 (1992).
- ¹⁹R. Barrett, M. Berry, T. Chan, J. Demmel, J. Donato, J. Dongarra, V. Eijkhout, R. Pozo, C. Romine, and H. van der Vorst, *Templates for the Solution of Linear Systems: Building Blocks for Iterative Methods* (Society for Industrial and Applied Mathematics, Philadelphia, 1993).
- ²⁰G. H. Golub and C. F. van Loan, *Matrix Computations*, 2nd ed. (John Hopkins U. P., Baltimore, 1989).
- ²¹W. C. Chew, S. Koc, J. M. Song, C. C. Lu, and E. Michielssen, "A succinct way to diagonalize the translation matrix in three dimensions," *Microw. Opt. Technol. Lett.* **15**, 144–147 (1997).
- ²²M. A. Epton and B. Dembart, "Multipole translation theory for the three-dimensional Laplace and Helmholtz equations," *SIAM J. Sci. Comput.* **16**, 865–897 (1995).
- ²³A. D. McLaren, "Optimal numerical integration on a sphere," *Math. Comput.* **17**, 361–383 (1963).
- ²⁴The exact number of non-zero entries of the $\bar{\mathbf{S}}$ matrix is $\frac{4}{3}n_i^3 + 4n_i^2 + \frac{11}{3}n_i + 1$ where n_i is the order of harmonics.
- ²⁵With proper indexing, this matrix becomes a block diagonal, Toeplitz matrix. However, such an indexing changes the block diagonal form of the rotation matrices.
- ²⁶The exact number of non-zero entries of the $\bar{\mathbf{T}}$ matrix is $\frac{2}{3}n_i^3 + 2n_i^2 + \frac{7}{3}n_i + 1$, where n_i is the order of harmonics.
- ²⁷L. Greengard and V. Rokhlin, "A new version of the fast multipole method for the Laplace equation in three dimensions," Research Report YALEU/DCS/RR-1115, September 1996.
- ²⁸J. Barnes and P. Hut, "A hierarchical $O(N \log N)$ force-calculation algorithm," *Nature (London)* **324**, 446–449 (1986).
- ²⁹L. Greengard and V. Rokhlin, "A fast algorithm for particle simulations," *J. Comput. Phys.* **73**, 325–348 (1987).
- ³⁰A. Brandt, "Multilevel computations of integral transforms and particle interactions with oscillatory kernels," *Comput. Phys. Commun.* **65**, 24–38 (1991).
- ³¹*Advanced Topics in Shannon Sampling and Interpolation Theory*, edited by R. J. Marks (Springer-Verlag, New York, 1993).
- ³²Outgoing wave expansions for the root cell and its children are not necessary.
- ³³R. L. Wagner, J. M. Song, and W. C. Chew, "Monte Carlo simulation of electromagnetic scattering from two-dimensional rough surfaces," *IEEE Trans. Antennas Propag.* **45**, 235–245 (1997).
- ³⁴It must be noted that the last data point for the FMMFFT algorithm may not be for the optimum FFT size. The required memory becomes excessive for 64 point FFT hence the corresponding result is not available.
- ³⁵J. M. Song, C. C. Lu, and W. C. Chew, "MLFMA for electromagnetic scattering by large complex objects," Technical Report EM-WC-4-96, Center for Computational Electromagnetics, Department of Electrical and Computer Engineering, University of Illinois at Urbana-Champaign, 1996.
- ³⁶J. M. Song and W. C. Chew, "Fast multipole method solution using parametric geometry," *Microw. Opt. Technol. Lett.* **7**, 760–765 (1994).

Target scattering calculations with the parabolic equation method

Mireille F. Levy

Rutherford Appleton Laboratory, Chilton, Didcot OX11 0QX, United Kingdom

Andrew A. Zaporozhets

University of Southampton, Southampton SO17 1BJ, United Kingdom

and Rutherford Appleton Laboratory, Chilton, Didcot OX11 0QX, United Kingdom

(Received 20 June 1997; accepted for publication 29 October 1997)

The parabolic equation technique is used to solve the Helmholtz equation in the presence of scatterers of arbitrary shape, in two and three dimensions. The scattered field is computed directly, using non-homogeneous boundary conditions on the scattering object to represent the incident field. Effectively this decouples the PE paraxial direction from the direction of incidence. For convex objects the whole range of scattering angles can be covered with a small number of narrow-angle calculations. Finite-difference implementations involve tridiagonal matrices in two dimensions and more general sparse matrices in three dimensions. The resulting codes can be used to solve scattering problems for objects ranging in size from a few wavelengths to hundreds of wavelengths. The method has been tested against analytical solutions for soft and rigid circular cylinders in 2D and soft and rigid spheres in 3D, showing good agreement at all scattering angles. © 1998 Acoustical Society of America. [S0001-4966(98)03202-0]

PACS numbers: 43.20.Fn, 43.30.Gv [ANN]

INTRODUCTION

Parabolic equation (PE) techniques have been widely used to solve various types of wave propagation problems. They provide an efficient solution for long-range propagation of acoustical waves in the ocean or electromagnetic waves in the atmosphere.¹⁻⁴ More recently interest has arisen in the use of PE methods to solve scattering problems. Fast and accurate calculation of target strength is of course of great practical interest for defense applications. One approach is to couple the parabolic equation method with a scattering model to study target scattering in the ocean.⁵ However the PE can also be used to compute the scattered field directly.⁶⁻⁸ We show that complex three-dimensional acoustic scattering calculations can be carried out efficiently with appropriate PE techniques. We believe that the resulting algorithms bridge a gap between asymptotic methods, which can be difficult to apply in the low frequency regime, and finite-element codes, which can require huge computing resources for large targets.

In related previous work,^{7,8} the PE was used to solve for the total field. For forward scatter this method is identical to the conventional PE, while for computing the back-propagating field, it treats the scattering object as a sequence of reflecting facets. This approach gave quite encouraging results, but the method only coped approximately with the backscattered field and the field scattered at large angles. In the work presented here, rather than solving for the total field, we solve for the scattered field, incorporating information on the incident field through the use of non-homogeneous boundary conditions on the object surface. With this approach the PE paraxial direction is independent of the direction of the incident wave. As a consequence, the paraxial direction can be rotated to compute the field in a given an-

gular sector. With a small number of runs, scattering angles over the whole 360-deg domain can be covered.

In this paper we focus on the scattering calculations, limiting ourselves to the case of a homogeneous background medium. Scattering objects are assumed to be non-penetrable to sound. The PE algorithm is only used outside the scatterers, which are represented by appropriate boundary conditions. Far-field results are obtained from the near-field calculations through Fourier transform techniques.

I. MATHEMATICAL FRAMEWORK

In all that follows, we assume $\exp(-i\omega t)$ time dependence of the fields. We write the total field ψ_t as the sum of the incident field ψ_i that would be present without the scattering object of interest and of the scattered field ψ_s . Using Cartesian coordinates (x, y, z) , we introduce the reduced function u related to the scattered field ψ_s

$$u(x, y, z) = \exp(-ikx)\psi_s(x, y, z), \quad (1)$$

where k is a reference wave number. Choosing the positive x axis as the paraxial direction, we obtain the outgoing parabolic wave equation

$$\frac{\partial u}{\partial x} + ik(1 - Q)u = 0, \quad (2)$$

where the pseudo-differential operator Q is defined by

$$Q = \sqrt{\frac{1}{k^2} \frac{\partial^2}{\partial y^2} + \frac{1}{k^2} \frac{\partial^2}{\partial z^2} + n^2(x, y, z)} \quad (3)$$

and n is the refractive index of the medium. In this paper we investigate the idea of rotating the paraxial axis to cover the whole angular range of interest with a small number of PE runs. The narrow-angle PE, obtained by using the first-order

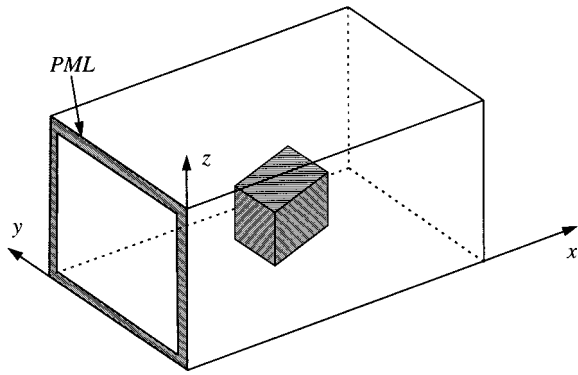


FIG. 1. Computational domain, showing PML layer.

Taylor approximation of the root, provides the simplest framework for this. It has the well-known expression

$$\left\{ \frac{\partial}{\partial x} - \frac{i}{2k} \left(\frac{\partial^2}{\partial y^2} + \frac{\partial^2}{\partial z^2} \right) + \frac{ik}{2}(n^2 - 1) \right\} u = 0. \quad (4)$$

We shall see that the resulting scattering algorithms treat convex objects very accurately. For more general shapes it will probably be necessary to resort to wider angle approximations, in particular investigating the use of the split-step Padé method.⁹

In what follows, we assume a homogeneous background medium, taking n constant equal to 1. This simplifies the treatment of boundary conditions and of far-field calculations. It is likely that the latter problem can be treated in more general environments by coupling the scattering model to a long-range PE code.⁵

Since we solve for the scattered field, the boundary conditions on the object are not homogeneous, as they involve the incident field. An acoustically soft object is modeled by the Dirichlet boundary condition: for a point P on the boundary of the object the total field is zero, giving the relation between the scattered field ψ_s and the incident field ψ_i in that point:

$$\psi_s(P) = -\psi_i(P). \quad (5)$$

Combining Eqs. (1) and (5), we get the boundary condition for the reduced function:

$$u(P) = -\exp(-ikx)\psi_i(P). \quad (6)$$

Acoustically rigid objects are modeled by the Neumann boundary condition, which can be written as

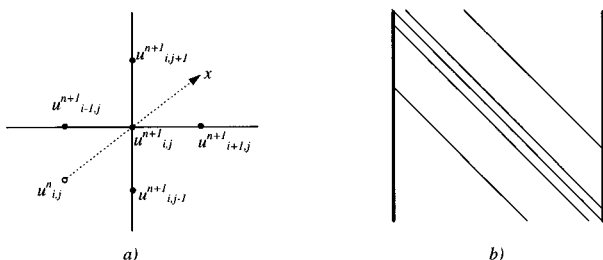


FIG. 2. Position of the grid points used by fully implicit solver (a) and the structure of the sparse matrix for the Dirichlet case (b).

$$n_x \frac{\partial \psi_s}{\partial x}(P) + n_y \frac{\partial \psi_s}{\partial y}(P) + n_z \frac{\partial \psi_s}{\partial z}(P) = -\frac{\partial \psi_i}{\partial \mathbf{n}}(P), \quad (7)$$

where P is a point on the surface and $\mathbf{n} = (n_x, n_y, n_z)$ is the outer normal to the surface at P . Using Eq. (1) and eliminating the range derivative using the parabolic equation (4), we get

$$\begin{aligned} \frac{in_x}{2k} \left(\frac{\partial^2 u}{\partial y^2} + \frac{\partial^2 u}{\partial z^2} \right) + ikn_x u + \frac{\partial u}{\partial y} n_y + \frac{\partial u}{\partial z} n_z \\ = -\exp(-ikx) \frac{\partial \psi_i}{\partial \mathbf{n}}. \end{aligned} \quad (8)$$

More general boundary conditions of surface impedance type can be expressed in a similar way.

The computational domain must be truncated in the transverse plane. Many types of absorbing boundary conditions have been considered in the literature.¹⁰ Here we use the Bérenger perfectly matched layer (PML) technique.^{11,12} A PML medium has the property that outgoing waves are fully transmitted at the interface without generating any reflections. The technique was originally designed to solve Maxwell's equations, but it can be adapted for the parabolic equation framework.¹³ The great advantage of the PML is its efficiency at all incidence angles, with a perfectly matched layer typically using a few gridpoints only.

We use a rectangular box-shaped domain containing the scatterer as shown in Fig. 1. The initial solution has to be defined at the plane $x=0$ in order to start the marching algorithm. Since we are solving for the scattered field in a paraxial cone centered on the positive x direction and all the scattering sources are located in the half-space $x>0$, the initial PE scattered field is zero.

This seemingly surprising initial condition is due to the fact that the PE extracts energy propagating in the paraxial cone: the PE initial scattered field is not the actual physical scattered field (which is of course not zero in front of the object), but only that part of it which is propagating in the paraxial direction (i.e., toward the object). Now since the object is the source of the scattered field, the scattered field propagates away from the object. This implies that at the $x=0$ plane, no component of the scattered field propagates in the paraxial cone towards the positive direction of the x axis, and hence the initial PE scattered field is zero.

II. NUMERICAL IMPLEMENTATION

We use a finite-difference implementation on a rectangular grid, together with a simple staircase representation of the object boundary. The grid spacing is fixed in the transverse (y - z) plane, but with variable range step for accurate representation of the scattering object. An important consideration is that for plane wave incidence, the boundary conditions [Eqs. (6) and (8)] contain an exponential term in x on the right hand side. This implies that the grid spacing must be reduced as the angle between the paraxial and incident directions increases, in order to represent phase variations accurately. Typical range steps are 1/10th of a wavelength or less. This is of course in total contrast with the more usual long-range applications of the PE, where range steps can be

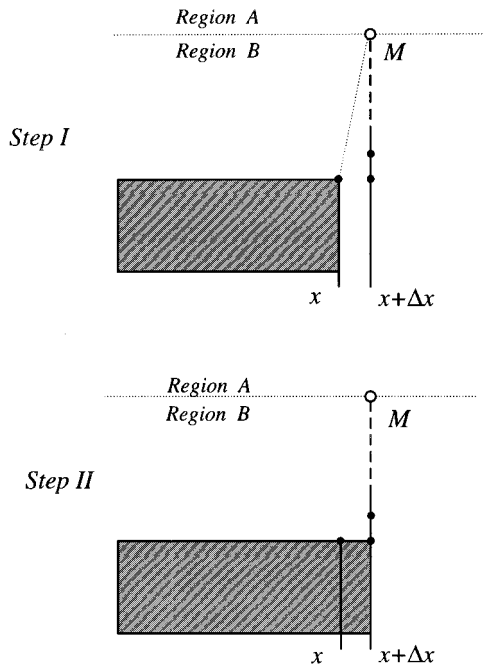


FIG. 3. Double pass method for Neumann boundary condition.

very large compared to the wavelength. For most applications the target dimensions are less than a few hundred wavelengths, and the small range steps are not a problem.

The Crank–Nicolson scheme is often used for finite-difference implementations of the PE. Here we use a slightly different implicit scheme, which has better stability properties than the Crank–Nicolson scheme¹⁴ and is easier to implement with irregular object boundaries. Basically, the second order derivatives in y and z are approximated at the

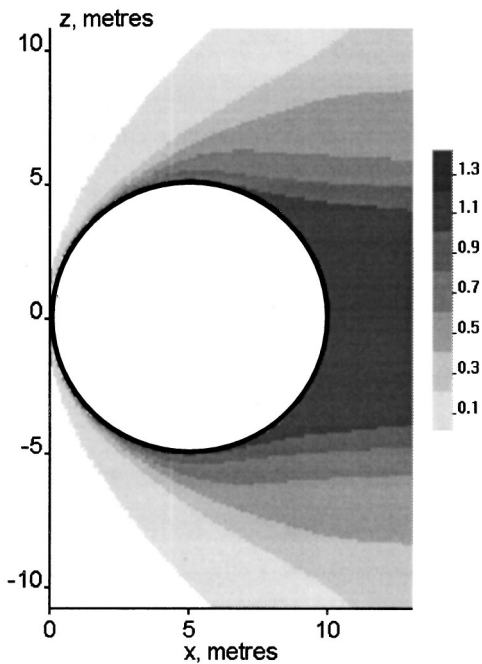


FIG. 4. Amplitude of the scattered field for a soft cylinder illuminated by a plane wave of unit amplitude coming from the left. Cylinder radius is 5 wavelengths. PE paraxial direction corresponds to the direction of the incident wave.

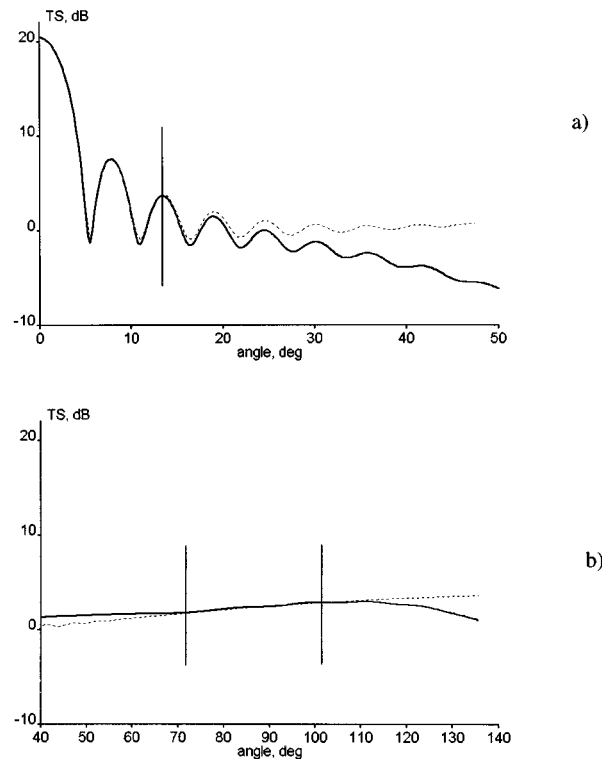


FIG. 5. Target strength for a soft cylinder of 5 wavelengths radius. The paraxial direction has angle 0° (a) and 90° (b) with the direction of the incident wave. Solid line—PE; dotted line—analytical solution. Vertical lines show $\pm 15^\circ$ sector around the paraxial direction.

forward range only, instead of averaging between previous and forward range as in the Crank–Nicolson scheme. One disadvantage is that this scheme is first-order accurate in range whereas the Crank–Nicolson scheme is second-order accurate, implying that smaller range steps are necessary. This is not a major drawback for the type of problem treated here, as range steps tend to be small anyway for accurate object boundary modeling and good phase representation.

For the standard PE, the scheme is described by

$$\frac{u_{i,j}^{n+1} - u_{i,j}^n}{\delta x} = \frac{i}{2k\Delta z^2} (u_{i-1,j}^{n+1} + u_{i,j-1}^{n+1} - 4u_{i,j}^{n+1} + u_{i+1,j}^{n+1} + u_{i,j+1}^{n+1}), \quad (9)$$

where δx is the range step size and Δz is the grid spacing in the transverse plane (for simplicity the same grid spacing is used here for the y and z coordinates). The superscript index relates to grid points along the range axis x , the subscript indexes i and j refer to the grid points along the y and z axes [Fig. 2(a)]. Boundary conditions on the object are approximated by single-sided finite-difference expressions.

In two dimensions, each range step requires the inversion of a tridiagonal matrix which can be carried out efficiently with the usual Gauss pivot method. In three dimensions, the tridiagonal matrix is replaced by a sparse matrix with a more complicated structure, as shown in Fig. 2(b) for the Dirichlet case: if the points in the transverse plane are numbered row by row, the matrix has three diagonals in the center and two diagonals further away. A very efficient in-

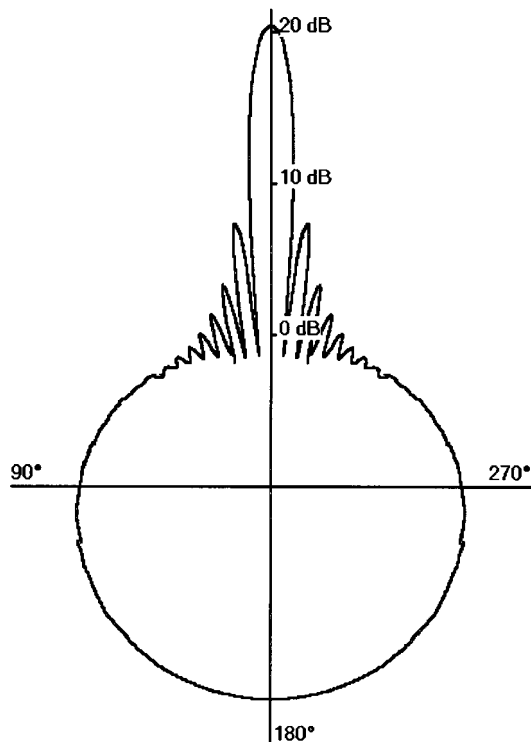


FIG. 6. Target strength for a soft cylinder of 5 wavelengths radius. Solid line—combined rotated PE runs; dotted line—analytical solution.

version technique is available for this case, based on factoring of the 3D operator into 2D operators for the y and z coordinates.¹⁵

This is not possible for the Neumann boundary condition [Eq. (8)], which is non-separable in general: the partial derivatives along the transverse coordinates are coupled, so that further non-zero entries are present and a sparse matrix solver is required. We have used a bi-conjugate gradient method with Jacobi preconditioner.¹⁶ Calculation times for the Neumann case can be reduced by decomposing the transverse domain into two regions, a small region B enclosing the object, and region A. In a first pass, the field at the next range is calculated in the whole transverse domain assuming the object is not present at that range. The PML is used to truncate the field at the outer boundaries of region A. The resulting field values are kept for region A. For region B, the field is then recalculated with the sparse matrix solver, this time in the presence of the object, using the first pass results at the boundary of region B. The method is described schematically in Fig. 3. Thinking in terms of the Huygens principle, we choose region A in such a way that the influence of the object between ranges x and $x + \Delta x$ on point M at the boundary between regions A and B is negligible, as it corresponds to deep shadow diffraction. The choice of region A is of course dependent on the range step. This double pass technique provides considerable speed-up for the Neumann case, but integration times are still several times longer than for the Dirichlet case which does not involve sparse matrix inversions. As calculations in region A are very fast, it is not necessary to use sophisticated procedures to optimize its size. Typically region A is taken to be two to three times the

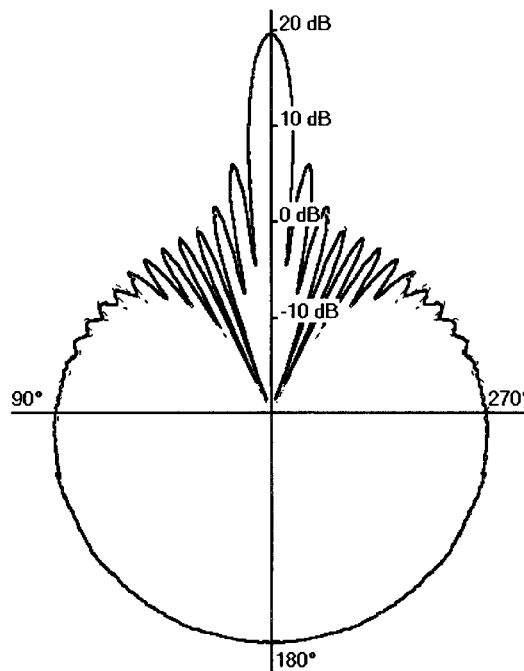


FIG. 7. Target strength for a rigid cylinder of 5 wavelengths radius. Solid line—combined rotated PE runs; dotted line—analytical solution.

maximum diameter of the scattering object in the transverse plane in order to obtain meaningful far-field patterns in the -15° to 15° sector around the paraxial direction.

The results of a single PE run are valid in a cone of roughly -15° to 15° around the paraxial direction, which can be chosen arbitrarily. For computing backscatter for example, one would take the paraxial direction as the opposite of the incident wave direction. To obtain the whole bistatic scattering pattern, a dozen runs would be required.

III. FAR-FIELD FORMULAE

Many problems require the calculation of target strength, which is a far-field notion. For a homogeneous background medium, target strength can be derived from near-field computations by solving the PE in closed form. In two dimensions, this involves a Hankel convolution kernel,⁷ with the formula:

$$\psi_s(x, z) = \frac{ik}{2} e^{-ik(x-x_0)} \int_{-\infty}^{\infty} \psi_s(x_0, z') \times \frac{x-x_0}{\rho(z')} H_1^{(1)}(k\rho(z')) dz', \quad (10)$$

where $x_0 < x$ are any ranges beyond the object, $H_1^{(1)}$ is the Hankel function of the first kind and $\rho(z')$

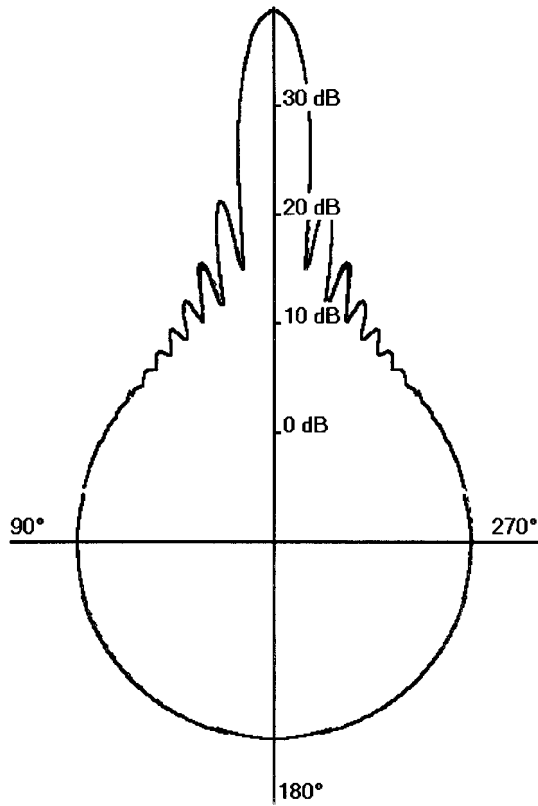


FIG. 8. Target strength of a soft sphere of 5 wavelengths radius. Solid line—PE; dotted line—analytical solution.

$= \sqrt{(x-x_0)^2 + (z-z')^2}$. The corresponding formula in three dimensions is

$$\psi_s(x, y, z) = -\frac{1}{2\pi} \int_{-\infty}^{\infty} \int_{-\infty}^{\infty} \psi_s(x_0, y', z') \cdot \left[ik \frac{(x-x_0)}{d(y', z')} - \frac{1}{d(y', z')} \right] \cdot \frac{\exp(ikd(y', z'))}{d(y', z')} dy' dz', \quad (11)$$

where $d(y', z') = \sqrt{(x_0-x')^2 + (y-y')^2 + (z-z')^2}$. By definition, the target strength¹⁷ in three dimensions in direction (θ, φ) is given by

$$TS(\theta, \varphi) = 10 \log \left[\lim_{r \rightarrow \infty} r^2 |\psi_s(x, y, z)|^2 / |\psi_i(x, y, z)|^2 \right], \quad (12)$$

where $x = r \cos \theta$, $y = r \sin \theta \cos \varphi$, $z = r \sin \theta \sin \varphi$. If the incident field ψ_i is a plane wave with unit amplitude, target strength in direction (θ, φ) is given by

$$TS(\theta, \varphi) = 10 \log \left[\frac{k^2 \cos^2 \theta}{4\pi^2} \times \left| \int_{-\infty}^{\infty} \int_{-\infty}^{\infty} \psi_s(x_0, y', z') \times \exp(-ik \sin \theta (y' \cos \varphi + z' \sin \varphi)) dy' dz' \right|^2 \right]. \quad (13)$$

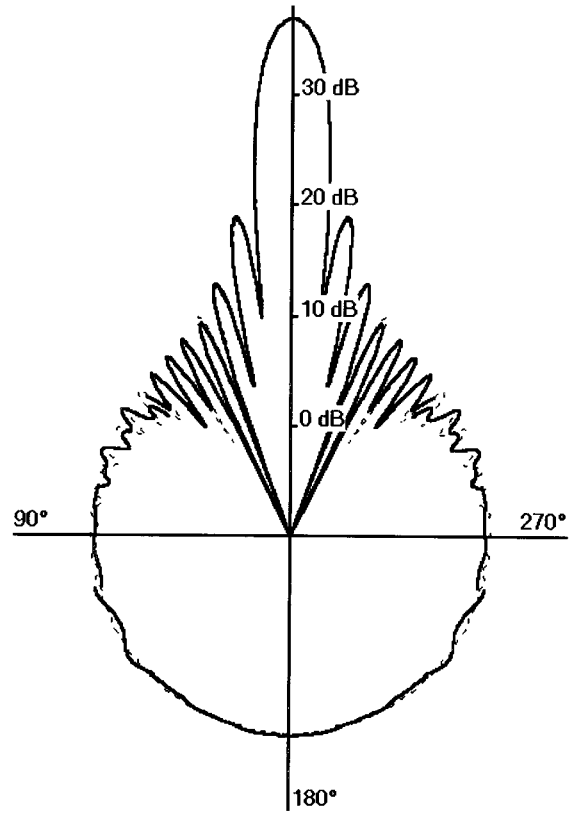


FIG. 9. Target strength for a rigid sphere of 5 wavelengths radius. Solid line—PE; dotted line—analytical solution.

The corresponding formula in two dimensions is

$$TS(\theta) = 10 \log \left[\frac{k \cos^2 \theta}{2\pi} \left| \int_{-\infty}^{\infty} \psi_s(x_0, z') \times \exp(-ikz' \sin \theta) dz' \right|^2 \right]. \quad (14)$$

These expressions show that target strength is obtained as the Fourier transform of the field in any transverse plane located beyond the object. Fast Fourier transforms can of course be used for the numerical calculations. However for the very small integration domains used here, it is more economical to compute the integrals directly with a standard Simpson scheme, thus avoiding sampling constraints in angle space.

IV. RESULTS AND DISCUSSION

We have compared PE results to analytical solutions for canonical shapes, using circular cylinders and spheres. In the examples below, the sound speed is 1500 m/c and the source frequency 1500 Hz, corresponding to a wavelength of 1 m.

We first look at two-dimensional examples. Figure 4 shows the amplitude of the scattered field computed with the PE for a soft circular cylinder of 5 wavelengths radius illuminated by a plane wave of unit amplitude coming from the left. The PE paraxial direction corresponds to the direction of the incident wave. As soon as the solution has been marched beyond the cylinder (i.e., for ranges more than 10 m in this case) we can use Eq. (14) to compute the far-field target strength. The result is shown in Fig. 5(a). The analytical

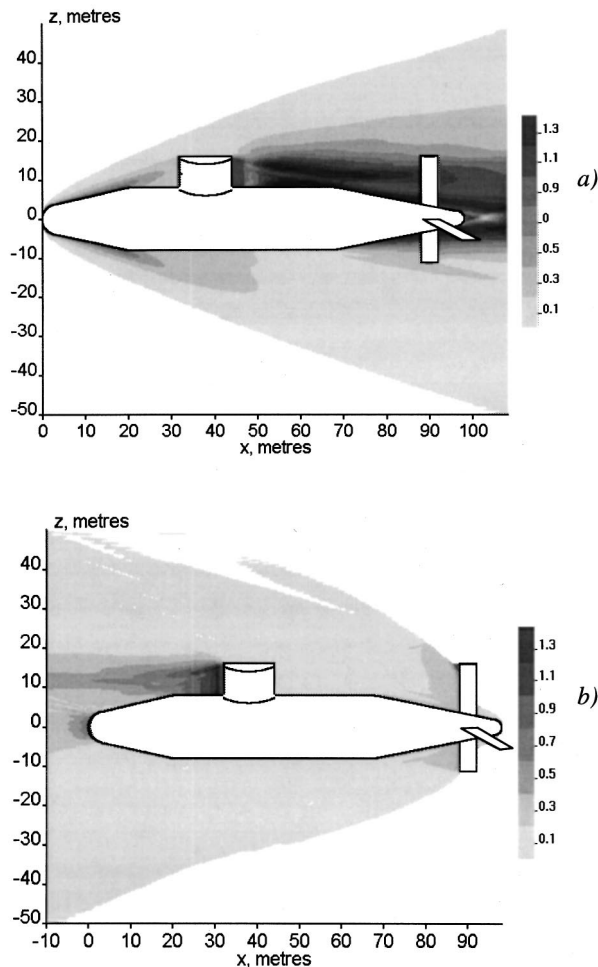


FIG. 10. Amplitude of the scattered field in a vertical plane for a rigid submarine-shaped 3D object illuminated by a plane wave of unit amplitude coming from the left. The field has been computed with forward (a) and backward (b) PE runs.

solution [dotted curve in Fig. 5(a)] is computed from a series of cosine functions.¹⁸ As expected, the standard parabolic equation provides accurate results in a sector of about 15° from the paraxial direction [marked with a vertical line in Fig. 5(a)], but the PE target strength field drops off much faster than the analytical solution away from the paraxial direction. Figure 5(b) shows target strength when the paraxial direction makes an angle of 90° with the direction of the incident wave. Again results are accurate within 15° from the paraxial direction. Figure 6 shows target strength calculated with the PE and with the analytical solution for the whole angular range. The PE curve was combined from 7 PE runs in angular patches rotated by 30° (i.e., the angle of the

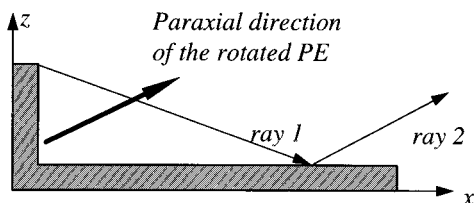


FIG. 11. Scattering by an L-shaped object. Height—3 wavelengths; length—10 wavelengths.

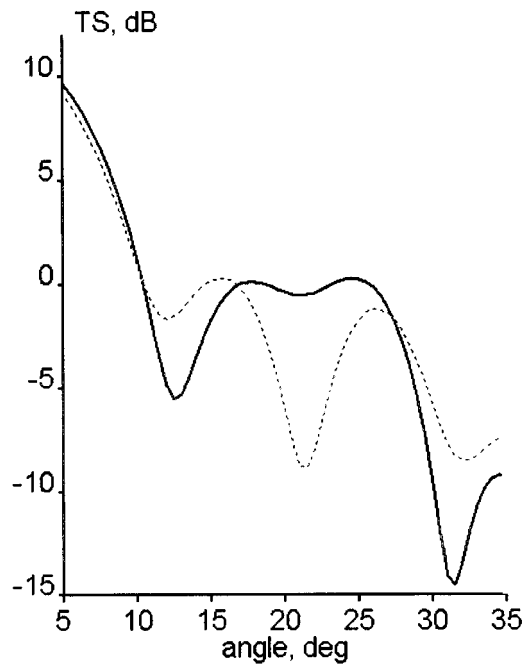


FIG. 12. Scattering by an L-shaped object. Narrow angle PE rotated by 20° —solid line; wide angle PE—dotted line.

paraxial direction was $0^\circ, 30^\circ, \dots, 180^\circ$) using the relevant PE results in each angular sector. Agreement with the analytical results is excellent.

The calculations were repeated for the acoustically rigid case. Figure 7 shows the full target strength results using the same angular patches as before. For both the soft and rigid cases, the grid spacing was 40 points per wavelength in all coordinates, the transverse domain size was 40 wavelengths and the execution time for each PE run was less than 15 s on a Pentium 133 MHz PC. As expected in view of the more complex integration scheme, accuracy is slightly less good in the rigid cylinder case.

Figures 8 and 9 show target strength results for soft and rigid spheres of radius 5 wavelengths, computed with the PE method and from the analytical solution, which is written as a series of Legendre functions.¹⁸ The grid spacing used for the PE simulations was 20 points per wavelength and the transverse domain size was 30 by 30 wavelengths. Execution times were 10 minutes for the soft case and 30 minutes for the rigid case on a Pentium PC. The longer execution time for the rigid sphere is due to the use of the sparse matrix solver for modeling the Neumann boundary condition. As in the 2D case, results are in excellent agreement for the soft sphere. The error is larger for the rigid sphere, but remains within 1 dB except in nulls of the scattering pattern.

To show that the method can be used for complex objects, we compute the acoustic field scattered by an acoustically rigid idealized 3D submarine shape. The object is quite large compared to the wavelength (maximum dimension of 100 m, while $\lambda = 1$ m). The incident field is a plane wave coming from the left. Figure 10 shows the scattered field in a longitudinal vertical plane passing through the axis of symmetry of the object. Figure 10(a) was obtained by marching the PE algorithm in the direction of the incident wave (for-

ward scatter), and Fig. 10(b) shows the field when the PE is marched in the opposite direction (backscatter). The grid spacing was 10 points per wavelength and the transverse domain size was 100 by 100 wavelengths. The execution time for each PE run was about an hour on a Pentium PC.

At the beginning of this paper, we stated that the rotating narrow-angle PE has limitations: This is due to the fact that energy scattered by one part of the object in a given direction may well contribute to scatter from another part of the object in a completely different direction. This is certainly the case for non-convex objects like the L-shaped object shown in Fig. 11. If the narrow-angle rotated PE is used with the paraxial direction indicated by the thick arrow, 20° from the horizontal, the contribution of ray 1 will be ignored. This is confirmed in the results shown in Fig. 12, where the narrow-angle rotated PE results are compared with a reference solution obtained with a split-step Padé code.^{8,9} The generalization of such a code to three-dimensional problems is not straightforward, particularly concerning domain truncation and the treatment of boundary conditions on the object.

A similar problem arises for the treatment of creeping waves: Their excitation by boundary conditions on the scatterer is automatically taken into account by the PE, but the difficulty is that they can undergo large changes of direction along the object. The accuracy with which creeping waves are handled by the rotating PE method depends on the size of the scattering object relative to the incident wavelength. Creeping waves can travel all the way around the scatterer and this "second time around" incident field is not taken into account by the rotating PE. The resulting error is small for objects of a size larger than or comparable to the wavelength.

It might be possible to extend the method to penetrable objects by using suitable boundary conditions for sloping interfaces,¹⁹ although accurate handling of resonance inside the object would probably require iterative procedures.

V. CONCLUSIONS

The potential of PE techniques for target scattering calculations has been demonstrated. By decoupling the paraxial direction from the incident direction, the field can be computed at all scattering angles by combining several PE runs. For a homogeneous background medium, far-field results are obtained with Fourier transform methods. The narrow-angle rotating PE code has been validated against analytical solutions for canonical shapes, using both Dirichlet and Neumann boundary conditions. For three-dimensional simulations, integration times are of the order of a few minutes for moderately large objects.

ACKNOWLEDGMENTS

This work has been carried out with the support of the Radiocommunications Agency of the Department of Trade and Industry and of the Engineering and Physical Sciences Research Council of the United Kingdom.

- ¹D. Lee and S. T. McDaniel, "Ocean acoustic propagation by finite difference methods," *Comput. Math. Appl.* **14**, 305–423 (1987).
- ²D. Lee and A. Pierce, "Parabolic equation development in recent decade," *J. Comput. Acoust.* **3**, 95–173 (1995).
- ³K. H. Craig and M. F. Levy, "Parabolic equation modeling of the effects of multipath and ducting on radar systems," *IEE Proc. F, Radar Signal Process.* **138**, 153–162 (1991).
- ⁴A. E. Barrios, "A terrain parabolic equation model for propagation in the troposphere," *IEEE Trans. Antennas Propag.* **42**, 90–98 (1994).
- ⁵M. D. Collins and M. F. Werby, "A parabolic equation model for scattering in the ocean," *J. Acoust. Soc. Am.* **85**, 1895–1902 (1989).
- ⁶N. Y. Zhu and F. M. Landstorfer, "Numerical determination of diffraction, slope and multiple diffraction coefficients of impedance wedges by the method of parabolic equation: Space waves," *IEEE Trans. Antennas Propag.* **43**, 1429–1435 (1995).
- ⁷M. F. Levy and P-P. Borsboom, "Radar cross-section computations using the parabolic equation method," *Electron. Lett.* **32**, 1234–1236 (1996).
- ⁸M. F. Levy, P-P. Borsboom, A. A. Zaporozhets, and A. Zebic-Le Hyaric, "RCS calculations with the parabolic wave equation" in *AGARD SPP Symposium on Radar Signature Analysis and Imaging of Military Targets*, October 1996, Ankara, Turkey.
- ⁹M. D. Collins, "A split-step Padé solution for the parabolic equation method," *J. Acoust. Soc. Am.* **94**, 1736–1742 (1993).
- ¹⁰D. Givoli, "Non-reflecting boundary conditions," *J. Comput. Phys.* **94**, 1–29 (1991).
- ¹¹J.-P. Bérenger, "A perfectly matched layer for the absorption of electromagnetic waves," *J. Comput. Phys.* **114**, 185–200 (1994).
- ¹²J.-P. Bérenger, "Perfectly matched layer for the FDTD solution of wave-structure interaction problems," *IEEE Trans. Antennas Propag.* **44**, 110–117 (1996).
- ¹³C. Vassalo and F. Collino, "Highly efficient absorbing boundary conditions for the beam-propagation method," *J. Lightwave Technol.* **14**, 1570–1577 (1996).
- ¹⁴G. D. Smith, *Numerical Solution of Partial Differential Equations* (Clarendon, London, 1985).
- ¹⁵D. Lee, Y. Saad, and M. H. Schultz, "An efficient method for solving the three-dimensional wide angle wave equation," in *Computational Acoustics, Wave Propagation*, edited by D. Lee, R. L. Sternberg, and M. H. Schultz (Elsevier Science, New York, 1988), pp. 75–88.
- ¹⁶R. Barrett, M. Berry, T. F. Chan, J. Demmel, J. M. Donato, J. Dongarra, V. Eijkhout, R. Pozo, C. Romine, and H. Van der Vorst, *Templates for the Solution of Linear Systems: Building Blocks for Iterative Methods* (SIAM, Philadelphia, 1994).
- ¹⁷R. J. Urick, *Principles of Underwater Sound* (McGraw-Hill, New York, 1983), 3rd ed.
- ¹⁸J. J. Bowman, T. B. A. Senior, and P. L. E. Uslenghi, *Electromagnetic and Acoustic Scattering by Simple Shapes* (North-Holland, Amsterdam, 1969).
- ¹⁹D. Lee and S. T. McDaniel, "A finite-difference treatment of interface conditions for the parabolic wave equation: The irregular interface," *J. Acoust. Soc. Am.* **73**, 1441–1447 (1983).

An iterative solver of the Helmholtz integral equation for high-frequency acoustic scattering

S. N. Makarov

Faculty of Mathematics and Mechanics, State St. Petersburg University, Bibliotchnaya 2,
St. Petersburg-Petrodvoretz 198904, Russia

M. Ochmann

Technische Fachhochschule Berlin, Fachbereich Mathematik und Physik, Luxemburger Strasse 10,
13353 Berlin, Germany

(Received 15 May 1997; accepted for publication 30 September 1997)

High-frequency scattering from convex and non-convex bodies is studied using an iterative algorithm. The key point of the method is a self-adjoint formulation of the Helmholtz integral equation, which ensures the convergence of the iteration process toward the true solution. For all investigated structures with different surface impedances fast convergence could be observed. The number of surface elements of the scatterer varies from about 6000 to 60 000 and the calculations are performed in the high-frequency range with Helmholtz numbers ka between 20 and 63. Even for a scattering structure with nearly 60 000 boundary elements, all computations could be carried out on a regular personal computer. © 1998 Acoustical Society of America. [S0001-4966(98)01202-8]

PACS numbers: 43.20.Fn, 43.30.Ft, 43.30.Gy [ANN]

INTRODUCTION

This paper presents an investigation of plane wave scattering from mainly non-convex bodies at high frequencies. The Helmholtz numbers ka of the problem range from about 20 to 63. The surface of the structure may be characterized by a local surface impedance.

Commonly used methods at high frequencies are approximate solutions like the plane wave approximation, the Kirchhoff approximation, the Rayleigh integral, or similar approaches.¹⁻³ Unfortunately, those approximations fail if multiple scattering appears, i.e., for non-convex bodies. But sometimes, they also give large errors for convex bodies.

An iterative method is presented here, which develops ideas of Kleinman and Roach^{4,5} and which allows one to approach the *exact* surface pressure by a (small) number of iterations N . The initial guess is the surface pressure found by using the plane wave approximation (PWA).¹ In principle, the accuracy of the method is limited only by the discretization error. Even a small number of iterations provides a much better approximation of the exact surface pressure, than the familiar high-frequency asymptotics, outlined above.

Unlike standard boundary element methods (BEM), which solve the system of equations directly, the iterative solver can handle structures consisting of several ten thousands of surface elements M on regular personal computers. Hereby, the required computing time is proportional to the square of M . In standard BEM the CPU-time is proportional to the cube of M if, for example, the Gaussian elimination is used.

Work is presently in progress to provide detailed information about the corresponding software package and some sample results on the Web under the URL <http://www.tfh-berlin.de/~ochmann/iter>.

I. THEORY

A. Rigid scatterer

The idea of an iterative solution of the Helmholtz integral equation based on a symmetric and positive definite formulation is realized numerically. Among other iterative methods, a formulation of Kleinman and Roach^{4,5} has been developed. The following notations are used in the calculations:

- x, y two arbitrary spatial points where y always lies on the structural surface S and x lies either in the exterior of S , or on S too,
- n_y the unit normal at y pointing into the exterior of the surface S ,
- p^i, p^s, p the incident, scattered, and the total pressure, respectively.

Assuming that the surface of the scatterer is rigid, we get the Helmholtz integral equation for the total surface pressure p in the form

$$p(x) = 2 \int_S p(y) \frac{\partial}{\partial n_y} g(x, y) ds_y + 2p^i(x), \quad x \in S \quad (1)$$

with the free-field Green's function $g(x, y) = \exp(-jk|x-y|)/(4\pi|x-y|)$. Here, $k = \omega/c$ denotes the wave number, ω the circular frequency, c the speed of sound in the fluid, and $j = \sqrt{-1}$. All time-varying quantities should obey the time dependence $\exp(+j\omega t)$. The operator L is introduced in the form

$$Lp = p - 2 \int_S p(y) \frac{\partial}{\partial n_y} g(x, y) ds_y \quad \text{on } S, \quad (2)$$

and Eq. (1) is rewritten as follows:

$$Lp = 2p^i \quad \text{on } S. \quad (3)$$

Further the adjoint operator L^* is defined by

$$L^*p = p - 2 \int_S p(y) \frac{\partial}{\partial n_x} \bar{g}(x,y) ds_y, \quad (4a)$$

where the overbar denotes the complex conjugate. Instead of Eq. (4a) we also use the operator

$$L^+p = p - 2 \int_S p(y) \frac{\partial}{\partial n_y} \bar{g}(x,y) ds_y, \quad (4b)$$

which is L^* without changing the differentiation from n_y to n_x . From Eq. (3), the expression

$$p = (p - \alpha L^*Lp) + 2\alpha L^*p^i \text{ on } S \quad (5)$$

is obtained. α denotes the relaxation parameter, which has to be chosen in an appropriate manner.⁶

Now, the surface of the structure is divided into M boundary elements. After this discretization, the function $p(y)$ is replaced by a vector \vec{p} which consists of the pressure values on different boundary elements. We have assumed that the pressure is constant over a single surface element. The operator $I - \alpha L^*L$ (I is the identity operator) in Eq. (5) is replaced by a square Hermitian matrix $\hat{A}(\alpha)$. The free term $2\alpha L^*p^i$ as a function of y is replaced by a vector \vec{b} consisting of the function values on different boundary elements. Then, Eq. (5) provides a linear system of equations

$$\vec{p} = \hat{A} \cdot \vec{p} + \vec{b}. \quad (5a)$$

Starting with the PWA, an iterative scheme is applied to Eq. (5a). If in Eq. (5) the operator L^+ is used instead of L^* , the corresponding matrix $\hat{A}(\alpha)$ fails to be Hermitian. However, it appears to be *very close* to a real, symmetric matrix in all of the considered examples of application. We have tried both formulations and found to our surprise that the use of L^+ enables a better convergence rate, especially for the cat's-eye structures (see below).

The relative error

$$E_N = \frac{\|Lp_N - 2p^i\|}{\|2p^i\|}, \quad (6)$$

where

$$\|p\| := \sqrt{\int_S |p(y)|^2 ds_y}$$

is the Euclidean norm, can be calculated at every iteration step N and is a measure of the accuracy of an iterative solution. The iteration process for the total surface pressure is completed when the relative error E_N becomes sufficiently small (cf. below). Then, in the far-field, the scattered pressure is simply obtained by using

$$p^s(x) = \int_S p(y) \frac{\partial}{\partial n_y} g(x,y) ds_y, \quad (7)$$

where x is a point lying in the exterior of the scatterer.

B. Impedance scatterer

Analogous integral equations as Eqs. (1), (5), and (7) can also be obtained for the general impedance boundary-value problem, where the impedance $Z = p/v_n$ is introduced

at each point on the surface S of the scatterer. Here, v_n is the normal surface velocity. The normalized impedance is defined by $Z_0 = Z/(\rho c)$, where ρ is the density of the surrounding fluid.

The generalization of Eq. (1) to an arbitrary surface velocity distribution takes the form

$$p(x) = 2 \int_S p(y) \frac{\partial}{\partial n_y} g(x,y) ds_y + 2 \int_S j\omega\rho v_n(y) g(x,y) ds_y + 2p^i(x), \quad x \in S. \quad (8)$$

Substitution of the impedance relation gives

$$p(x) = 2 \int_S p(y) \frac{\partial}{\partial n_y} g(x,y) ds_y + 2 \int_S \frac{jk}{Z_0(y)} p(y) g(x,y) ds_y + 2p^i(x), \quad x \in S. \quad (9)$$

Equation (1) is the particular case of Eq. (9), where $Z_0 \rightarrow \infty$ is uniformly on S . We emphasize that we consider a local impedance $Z_0(y)$ depending on the surface point y . This is a reasonable assumption for high Helmholtz numbers ka . In general Z_0 is also a function of the surface pressure itself, since the scattering from an elastic structure is a coupled system with fluid-structure interaction.⁷ The operators L, L^* , and L^+ as described above are introduced in accordance with Eq. (9). Instead of Eq. (7), we obtain

$$p^s(x) = \int_S p(y) \frac{\partial}{\partial n_y} g(x,y) ds_y + \int_S \frac{jk}{Z_0(y)} p(y) g(x,y) ds_y. \quad (10)$$

C. Discretization error as a limit for the iteration process

Although the values E_N from Eq. (6) formally tend to zero at $N \rightarrow \infty$, we realize that an infinitesimally small error with respect to the true solution cannot be achieved. The reason is simply a discretization error, which limits the accuracy of Eq. (1) or Eq. (9) from the very beginning. The iteration process no longer makes sense if the quantity E_N becomes smaller than some value E_L which characterizes the discretization error.

The discretization error E_L clearly depends on the boundary element structure, incidence direction, frequency, and the specific implementation scheme. An appropriate measure of the discretization error could be found if we knew some exact solution of Eq. (9). To get the simplest exact solution, consider the pressure distribution of the incident plane wave on the surface S , assuming for the moment, that the scatterer is sound transparent. The incident pressure on the closed surface S has to satisfy the well-known integral equation

$$p^i(x) = -2 \int_S p^i(y) \frac{\partial}{\partial n_y} g(x,y) ds_y + 2 \int_S \frac{\partial}{\partial n_y} p^i(y) g(x,y) ds_y, \quad x \in S, \quad (11a)$$

obtained from the Helmholtz formula for the interior domain. If we add $-2p^i(x)$ to both sides of this equation, multiply it with -1 , and substitute $(\partial/\partial n_y)p^i(y) = -jk \cos(n_y, \vec{k})p^i(y)$, the result can be written in the form of Eq. (9)

$$p^i(x) = 2 \int_S p^i(y) \frac{\partial}{\partial n_y} g(x,y) ds_y + 2 \int_S \frac{jk}{Z_0(y)} p^i(y) g(x,y) ds_y + 2p^i(x), \quad x \in S, \quad (11b)$$

where $Z_0(y)$ has to be chosen in the special form $Z_0(y) = 1/\cos(n_y, \vec{k})$. Here, we assume, that the incident wave has the form $p^i = \hat{p} \exp(-j\vec{k} \cdot x)$ with wave number vector \vec{k} . We see that the incident pressure is the exact solution of Eq. (9) at some specific value of the surface impedance. It is therefore straightforward to use this solution to characterize the discretization error. The discretization error E_L can be found if we substitute p^i instead of p_N into Eq. (6). It gives

$$E_L = \frac{\|Lp^i - 2p^i\|}{\|2p^i\|}. \quad (12)$$

The operator L for the impedance problem has the form

$$Lp = p - 2 \int_S p(y) \frac{\partial}{\partial n_y} g(x,y) ds_y - 2 \int_S \frac{jk}{Z_0(y)} p(y) g(x,y) ds_y \quad \text{on } S.$$

The calculation of the discretization error in Eq. (12) requires the choice $Z_0(y) = 1/\cos(n_y, \vec{k})$.

While performing the integration we assume that the surface pressure and the surface impedance are constant over each boundary element. Diagonal terms (at $x=y$) are ignored in the first integral on the right-hand side of Eq. (9), since they are zero if plane boundary elements are used.⁸ In the second integral, they are found by the integration of the Green function over a boundary element surface. The integration is made in polar coordinates. Then, a discretization error E_L of about 1%–2% is obtained for different structures with about 6 boundary elements per wavelength. We stop the iteration if

$$E_N < \varepsilon E_L, \quad (13)$$

where ε is some factor smaller than or equal to unity.

For the sake of simplicity, it is assumed that particular critical frequencies, caused by resonances of interior volumes and leading to nonunique solutions of the integral equations, do not occur with respect to all performed calculations. Established methods to overcome this uniqueness problem can be found in many papers (see the literature cited

in Ref. 9), and can be combined with the iteration method. For example, Kleinman and Roach^{4,5} used the modified Green's function technique for this purpose.

D. Starting pressure

The starting surface pressure is found from the impedance relation

$$p_{\text{start}} = p^i + p^s = Z(v_n^i + v_n^s) \quad (14)$$

coupled with some high-frequency approximation for p^s or for v^s . For example, with the assumption of the PWA

$$p^s = \rho c v_n^s \quad (15)$$

and taking into account that $Z = \rho c Z_0$ and $v_n^i = (1/\rho c) \times \cos(n_y, \vec{k})p^i$ on the surface S , we find

$$p_{\text{start}} = \frac{Z_0(1 - \cos(n_y, \vec{k}))}{Z_0 - 1} p^i. \quad (16)$$

Equation (16) is a local relation. It provides a reasonable approximation for $Z_0 \gg 1$ but leads to a considerably larger error at $Z_0 < 1$. Moreover, Eq. (16) fails in the vicinity of $Z_0 = 1$, where the approximation $p_{\text{start}} = p^i$ could be applied.

A simple way to slightly improve the PWA is to introduce a global proportionality factor γ into Eq. (15). After that, the starting pressure $p_{\text{start}} = p_{\text{start}}(\gamma)$ from Eq. (16) is substituted into Eq. (6) instead of p_N . It is easy to show that the relative error E_{start} found from Eq. (6), if $p_N = p_{\text{start}}(\gamma)$, will be a polynomial of second order with respect to γ . Its minimum gives us the desired value of γ . This value depends on the boundary element structure, incidence direction, frequency, and impedance. For the structures studied below in this paper, we have found that $0.8 < \gamma < 1.2$. However, the change in the relative error was usually not very high. It should be emphasized, that the formulation of a simple high-frequency approximation for the impedance problem is in general a difficult task, and is not the subject of this investigation.

II. RESULTS

A number of calculations were made to check the performance of the iterative method described above. Finite cylinders, a sphere, and cat's-eye structures were considered at various Helmholtz numbers $ka \gg 1$ and various incident angles. The cat's-eye structures are spheres without one octant (cf. subsection B and Fig. 3 below). Those structures have either rigid surfaces or locally/globally reacting surfaces with different values of the surface impedance Z . Here, we present some results for the sphere with 6096 boundary elements, for the cat's-eye structures with 7911, 24 832, and 57 470 boundary elements, and for the finite cylinder with 13 796 boundary elements, respectively. All calculations below were carried out on a PC (Intel Pentium 166 processor).

A. Rigid and impedance sphere

At first, we examined the well-known case of plane wave incidence on a sphere of radius a , with a constant surface impedance. In this case, a comparison with the analytical solution² is possible. The direction of incidence is

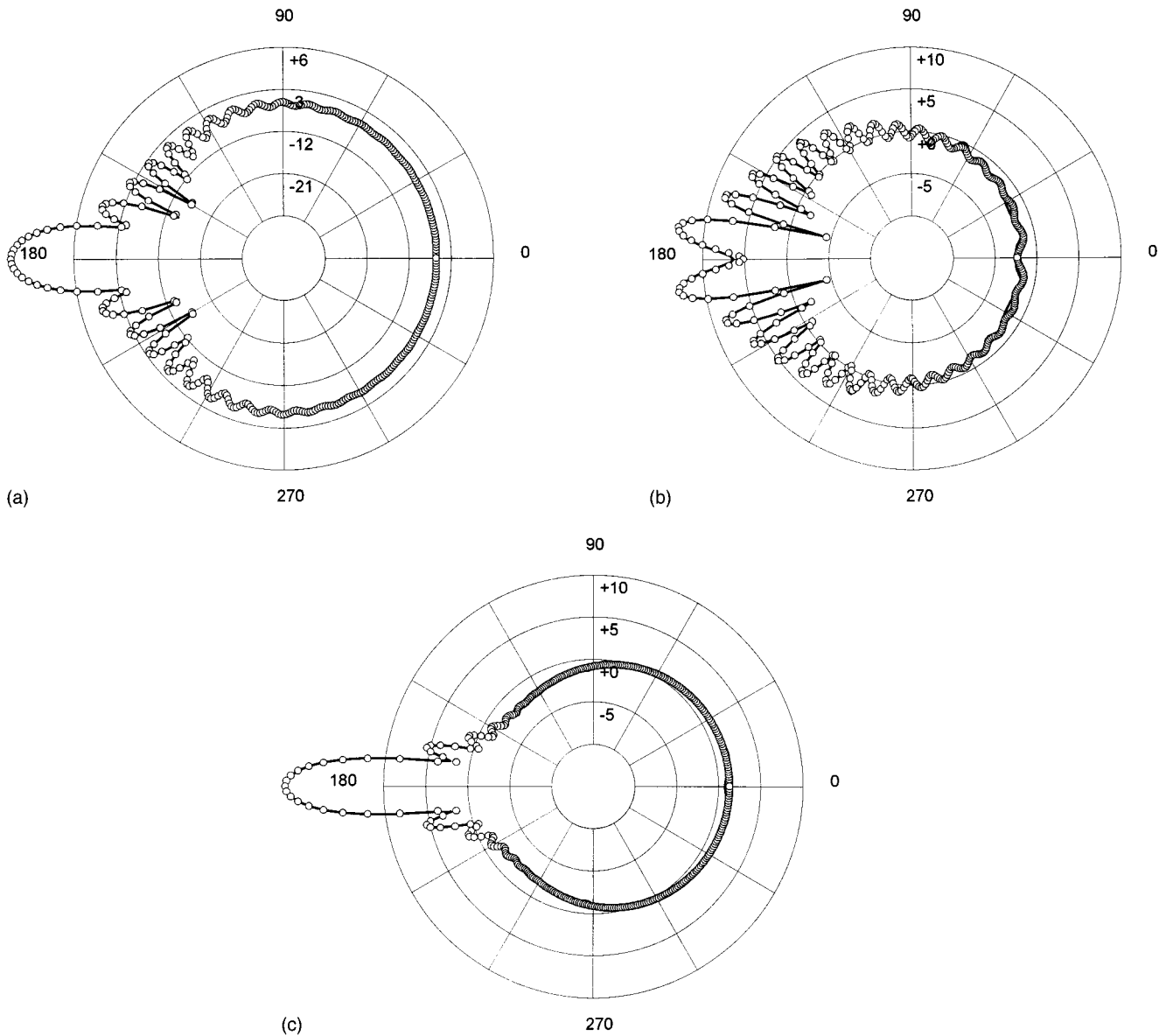


FIG. 1. Directivity patterns for the sphere at $ka = 20.9$ in terms of the polar angle θ . Vertical scaling gives the target strength TS in dB. (a) The exact solution (circles) in comparison with the iterative solution (thick line) at $Z_0 = \infty$; (b) the same at $Z_0 = 4$; (c) the same at $Z_0 = 0.4$.

along the negative z axis. We introduce spherical coordinates $x = R \sin \theta \cos \varphi$, $y = R \sin \theta \sin \varphi$, $z = R \cos \theta$. The field of the incident plane wave p^i is axisymmetric and does not depend on the azimuthal angle φ . Hence, the analytical solution takes the form

$$p^s(R, \theta) = p_0 \sum_{n=0}^{\infty} D_n h_n^{(2)}(kR) P_n(\cos \theta), \quad (17)$$

where θ is the polar angle, R is the radius of the observation sphere; $h_n^{(2)}$ are the spherical Hankel functions of the second kind and P_n are the Legendre polynomials. The coefficients D_n are given by

$$D_n = -(-j)^n (2n+1) \frac{j_n(ka) - jZ_0 j_n'(ka)}{h_n^{(2)}(ka) jZ_0 h_n^{(2)'}(ka)}, \quad (18)$$

where j_n are the spherical Bessel functions and the differentiation is made with respect to ka . The analytical solution for

the scattered pressure is calculated at $ka = 20.9$, which requires 30–35 terms in the series on the right-hand side of Eq. (17) to achieve an error smaller than 0.1%.

The directivity patterns of the far-field scattered pressure at $ka = 20.9$ are shown in Fig. 1 at $Z_0 = \infty, 4$, and 0.4 , respectively. The circles indicate the exact solution, whereas the thick curve represents the results of the iterative solver. There are nearly six elements per wavelength for the sphere with 6096 boundary elements. In Fig. 1, the target strength TS is given by¹⁰

$$\text{TS} = 10 \log \left. \frac{I_r}{I_i} \right|_{r=1m}, \quad (19)$$

where I_i is the incident intensity and I_r is the intensity of return at 1 m. (The target strength was calculated in the far field and then projected back to the distance of 1 m from the

TABLE I. Numerical data for the sphere.

Impedance	$Z_0 = \infty$	$Z_0 = 4$	$Z_0 = 0.4$
E_L , %	1.9	1.9	1.9
Starting error E_0 , %	22	38	53
Limiting error, %	0.6	0.4	1.1
Number of iterations	7	10	12
Maximum error of the scattered pressure level, dB	0.5	1.3	0.6

scatterer.) It is evident that the iterative solver agrees excellently with the exact solution.

The iteration data are presented in Table I (cf. also Fig. 4 below). The second row gives the error E_0 of the improved PWA (see previous section), according to Eq. (6). The improved PWA is used as the initial pressure. The limiting error is chosen 0.2–0.6 times smaller than the value E_L from Eq. (12). The last row of the table indicates the maximum difference in the directivity pattern of the scattered pressure,

in comparison with the exact solution. Note that the mean difference would be nearly five times smaller. Although very good convergence could be observed in any case, the number of required iterations increases with decreasing impedance. This increase is mainly related to the higher inaccuracy of the initial pressure.

For the purpose of comparison, we also present the corresponding data in Fig. 2 for the PWA. The maximum difference in the directivity pattern of the scattered pressure reaches 4, 9, and 12 dB, respectively. Thus, only for the rigid sphere, the PWA might be an acceptable quantitative approximation. The familiar Kirchhoff approximation as well as the Morse and Feshbach method (see Ref. 3, part II, p. 1551) provide nearly the same accuracy for the rigid sphere.

It should be pointed out that the solution at constant surface impedance of order unity predicts very large surface pressures. The surface pressure amplitude may reach $25|p_i|$ at $Z_0 = 1$ and $ka = 20.9$, which hardly seems possible from a physical point of view. The reason is that the choice $Z_0 = 1$ for a locally reacting surface impedance is a non-physical

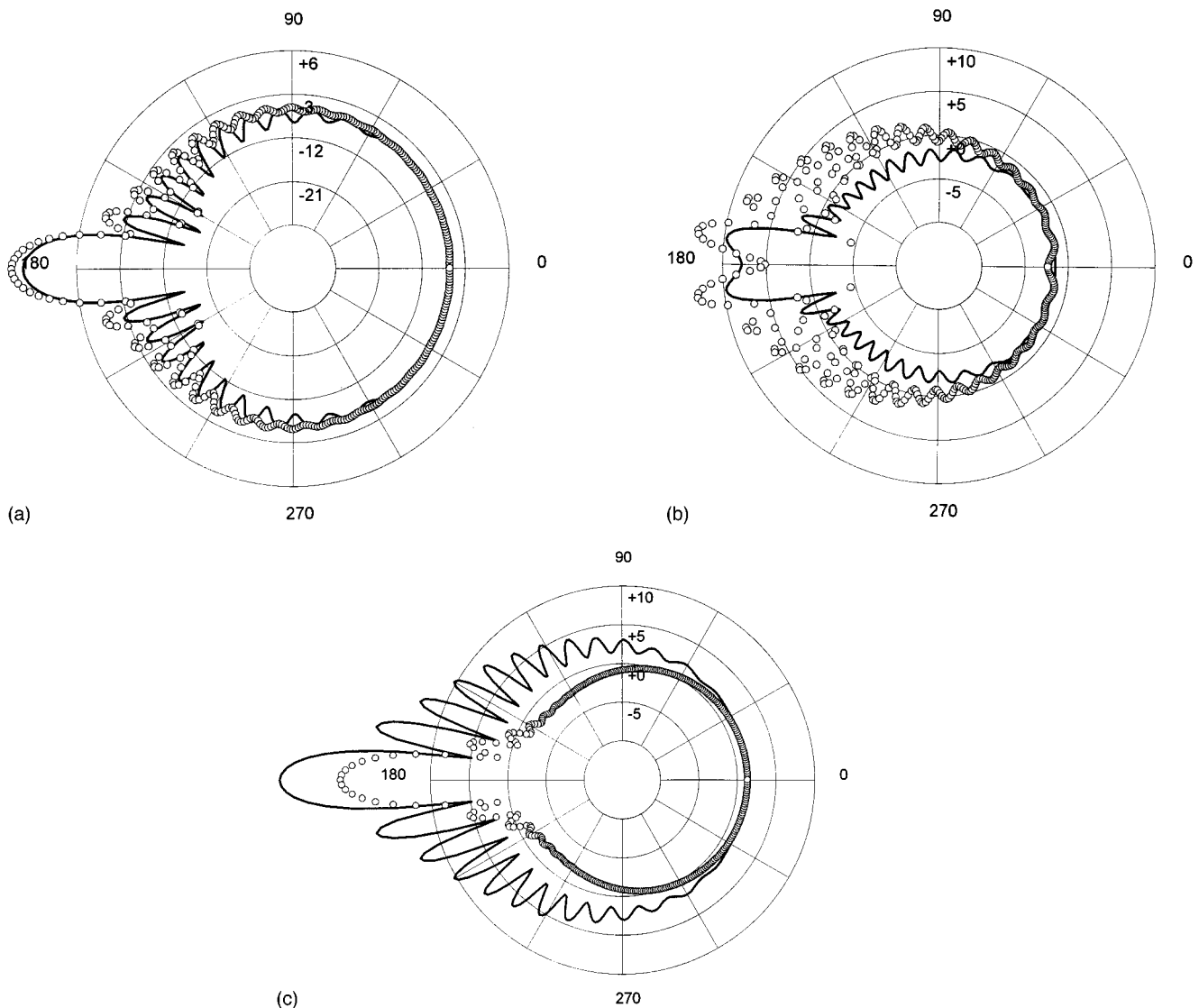


FIG. 2. Directivity patterns for the sphere at $ka = 20.9$ in terms of the polar angle θ . Vertical scaling gives the target strength TS in dB. (a) The exact solution (circles) in comparison with the PWA (thick line) at $Z_0 = \infty$; (b) the same at $Z_0 = 4$; (c) the same at $Z_0 = 0.4$.

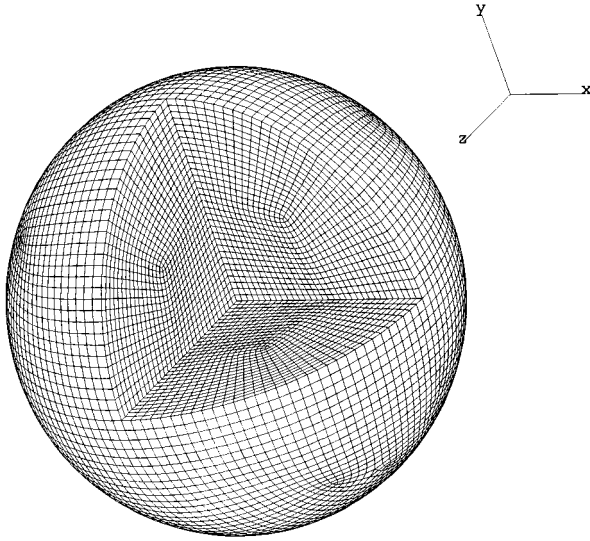


FIG. 3. Geometry of the non-convex cat's-eye structure. A part of the sphere corresponding to $x > 0$, $y > 0$, $z > 0$ was cut out. Incident angles are always given in spherical coordinates.

assumption. Due to extremely large amplitudes and pressure gradients the condition of six elements per wavelength becomes insufficient for numerical purposes. Nevertheless, the iterative solver still works, even at $Z_0 = 1$. However, the convergence rate and the corresponding accuracy are poor, indeed.

B. Non-convex structures with partially coated surfaces

The non-convex structure considered is shown in Fig. 3. It consists of a sphere, where the positive octant (i.e. the part corresponding to $x > 0$, $y > 0$, $z > 0$) is cut out. The region of the missing octant is called "cat's-eye," since it acts like a three-dimensional reflector. We have considered three such structures with the same geometry but with different numbers of boundary elements (7911, 24 832, and 57 470), to achieve large values of ka up to 62.8. They are called cat1, cat2, and cat3, respectively. The incident angles $\vartheta = 90 - \theta, \varphi$ are $(\vartheta, \varphi) = (45^\circ, 0^\circ)$ and $(\vartheta, \varphi) = (45^\circ, 45^\circ)$ in spherical coordinates. This system of coordinates is chosen in such a way that the direction of incidence is along the negative x , y , or z axis for $(\vartheta, \varphi) = (0^\circ, 0^\circ)$, $(\vartheta, \varphi) = (0^\circ, 90^\circ)$, and $(\vartheta, \varphi) = (90^\circ, 0^\circ)$, respectively. Hence, the incident wave illuminates the reflecting area of the cat's-eye, so that multiple reflection/scattering occurs.

For the uncoated cat's-eye, multiple reflection gives an important contribution to the backscattering pressure. The above mentioned approximation methods, like the PWA, etc., are unable to describe this effect. Therefore, we expect rather inaccurate results using those approximations.

Figure 4 shows the error of the total surface pressure as a function of the iteration number N at different $N < 10$. To find this error, Eq. (6) was applied again. The curves in this figure characterize the convergence rate of the iteration process. For the purpose of comparison, Fig. 4(a) indicates the convergence rate for the rigid sphere. The data at $N=0$ always give the relative error of the improved PWA (zeroth

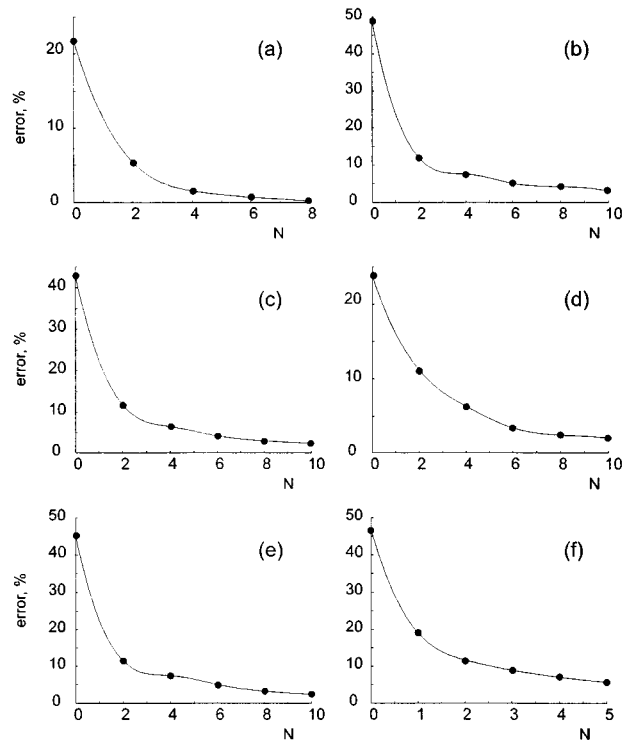


FIG. 4. Relative error E_N of the iterative solution depending on the number of iterations N . (a) Sphere with 6096 elements at $ka=20.9$, $Z_0=\infty$; (b) cat1 at $ka=20.9$, $(45^\circ, 0^\circ)$ incidence, and $Z_0=\infty$; (c) cat1 at $ka=20.9$, $(45^\circ, 45^\circ)$ incidence, and $Z_0=5.0$ over the whole surface; (d) the same as (c) but the cat's-eye surface is coated [Z_0 from Eq. (20) with $\hat{Z}_0=0.9$] and $Z_0=\infty$ otherwise; (e) cat2 at $ka=41.9$, $(45^\circ, 0^\circ)$ incidence, and $Z_0=\infty$; (f) cat3 at $ka=62.8$, $(45^\circ, 0^\circ)$ incidence, and $Z_0=\infty$.

iteration), which can reach 50%. The surface is either rigid [Fig. 4(a), (b), (e), (f)], or has a finite constant impedance Z_0 [Fig. 4(c)], or is only partially rigid and has a finite absorbing impedance $Z_0(y)$ on the reflecting surface of the cat's-eye [Fig. 4(d)]. The function $Z_0(y)$ was found in accordance with Snellius' law

$$Z_0(y) = - \frac{\hat{Z}_0}{\sqrt{1 - (c_a/c)^2 \sin^2(n_y, \vec{k})}}; \quad \hat{Z}_0 = \frac{\rho_a c_a}{\rho c}, \quad (20)$$

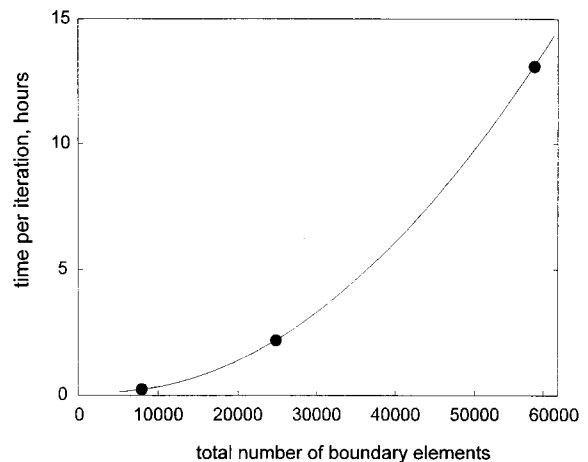


FIG. 5. Processor run-time per iteration as a function of the total number of boundary elements. A MS C++ 4.0 computer code was running by an Intel Pentium 166 processor. Circles show the data for the cat's-eye structure with a different number of boundary elements.

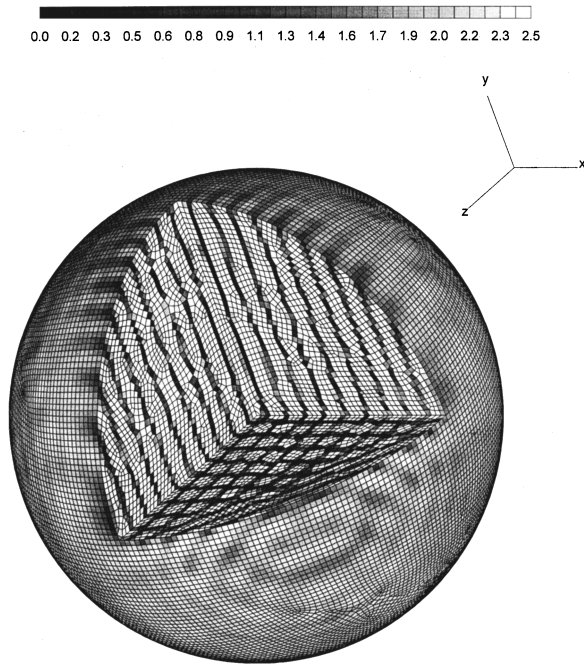


FIG. 6. Total surface pressure (amplitude distribution) normalized by the incident pressure for cat2 at $ka=41.9$, $(45^\circ, 0^\circ)$ incidence, and $Z_0=\infty$.

where the index a denotes the absorbing coating. The minus sign has to be chosen since the normal n_y is directed into the exterior of the scatterer S . If $c_a \approx c$ and $\cos(n_y, \vec{k}) < 0$, then $Z_0(y) = \hat{Z}_0 / \cos(n_y, \vec{k})$, which corresponds to the normal impedance of the incident plane wave on S [cf. Eq. (11b) above].

It is obvious that the primary inaccuracy of the PWA is improved very rapidly by only a few iterations. This has

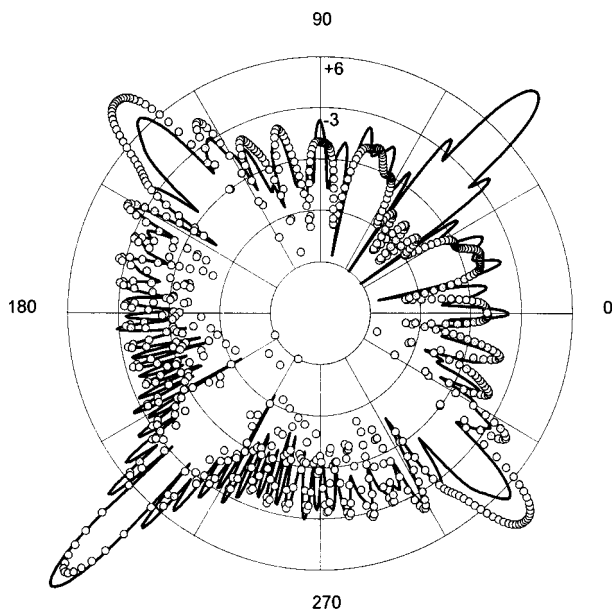


FIG. 7. Directivity pattern for cat3 in terms of the polar angle θ (xz plane) at $ka=62.8$, $(45^\circ, 0^\circ)$ incidence, and $Z_0=\infty$. Vertical scaling gives the target strength TS in dB. The thick curve shows TS obtained by the use of the iterative solver at $N=5$; the data corresponding to the PWA are indicated by circles.

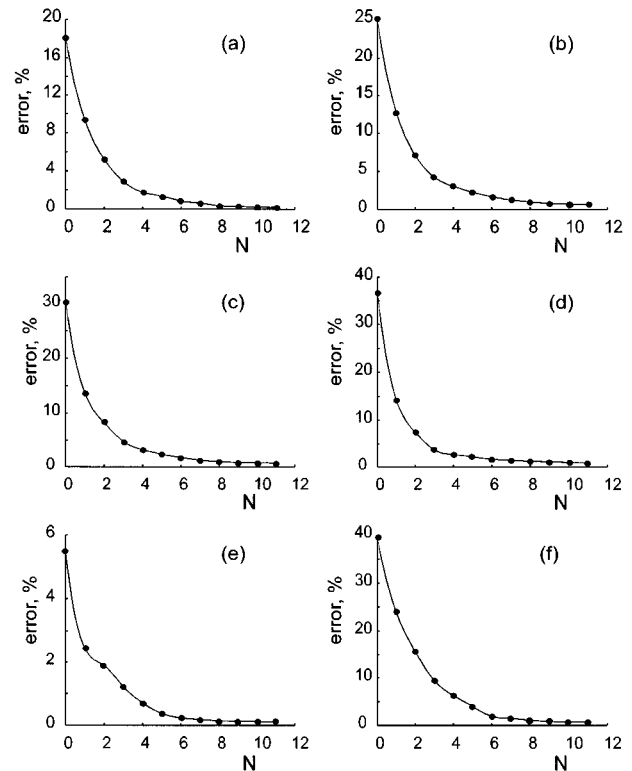


FIG. 8. Relative error E_N of the iterative solution depending on the number of iterations N for a finite cylinder with 13 796 elements at $ka=16.4$, $kl=61.2$. (a) $Z_0=\infty$, $(0^\circ, 0^\circ)$ incidence; (b) $Z_0=8$ over the whole surface and $(45^\circ, 0^\circ)$ incidence; (c) $Z_0=\infty$, $(60^\circ, 0^\circ)$ incidence; (d) $Z_0=\infty$, $(75^\circ, 0^\circ)$ incidence; (e) $Z_0=\infty$, $(90^\circ, 0^\circ)$ incidence; (f) $Z_0=8$, $(90^\circ, 0^\circ)$ incidence.

been observed for all investigated surface models with different numbers of boundary elements (6096–57 470) and at any ka from $20.9 \leq ka \leq 62.8$. Analogous results were obtained for scattering from different finite cylinders too (cf. below).

The results for $N > 10$ are not shown in Fig. 4. The convergence rate becomes smaller with increasing N , but the error always converges to zero. Nearly 20 iterations are required to obtain the accuracy of 1% in the total surface pressure for the cat's-eye structure. Note that the corresponding values of E_L from Eq. (12) are 1.78% (cat1, $ka=20.9$, $(45^\circ, 45^\circ)$ incidence), 1.87% (cat2, $ka=41.9$, $(45^\circ, 0)$ incidence), and 1.91% (cat3, $ka=62.8$, $(45^\circ, 0)$ incidence).

Figure 5 indicates the required processor run time to perform one iteration by the iterative solver. This is the most important information for applications. More precisely, one iteration step requires 8.4 min for the sphere, 0.23 hours for cat1, 2.2 hours for cat2, and 13.1 hours for cat3. The interpolation curve in Fig. 5 approximates the expected quadratic dependence with a relative accuracy of 9% in the considered domain. To give an idea of the data presented, recall, that a typical calculation for the cat's-eye structure with 7911 elements (accuracy of 1% in the total surface pressure is expected) takes 4–5 hours processor time (Intel Pentium 166 processor).

Figure 6 shows the total pressure on the surface of cat2 at $ka=41.9$ and $(45^\circ, 0^\circ)$ incidence. The surface is assumed

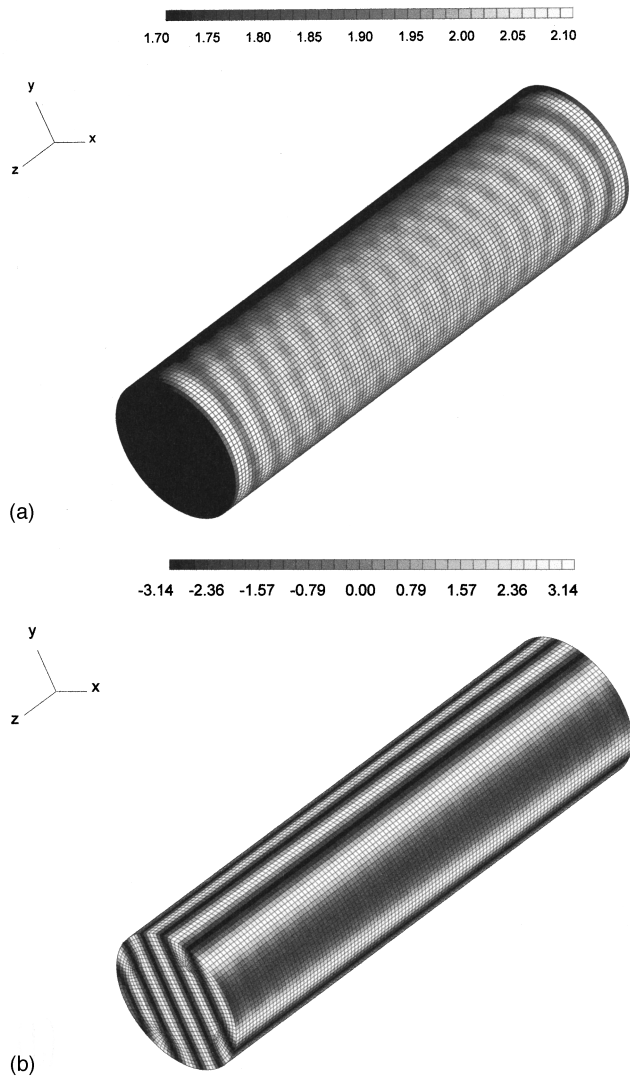


FIG. 9. Total surface pressure normalized by the incident pressure for a finite cylinder with 13 796 elements at $ka=16.4$, $kl=61.2$, $Z_0=\infty$, and $(0^\circ, 0^\circ)$ incidence. (a) Amplitude distribution; (b) phase distribution.

to be rigid. A well developed diffraction pattern is clearly seen on the surface of the cat's-eye.

Finally, Fig. 7 compares the far-field scattered pressure of cat3 corresponding to the PWA with the solution of the iterative solver at $N=5$ and $ka=62.8$. A difference of about 30 dB appears at backscattering. As mentioned before, the reason for this deviation is due to multiple reflection.

C. Finite cylinder

We studied three cylindrical structures: (i) with length to width ratio $l/2a=3.73$ and 3620 boundary elements; (ii) with length to width ratio $l/2a=3.73$ and 13 796 boundary elements; (iii) with length to width ratio $l/2a=5.60$ and 13 796 boundary elements. Figure 8 illustrates the convergence rate of the iteration process in case (ii). The error of the total surface pressure Eq. (6) as a function of the iteration number N is shown at different $N < 12$. The data at $N=0$ give the relative error of the improved PWA (zeroth iteration). The surface of the cylinder is either rigid [Fig. 8(a), (c), (d), (e)], or has a finite constant impedance $Z_0=8$ [Fig.

8(b), (f)]. The frequency was fixed to achieve $ka=16.4$, $kl=61.2$. This approximately corresponds to the condition of six boundary elements per wavelength. The angles of incidence are changed from $(0^\circ, 0^\circ)$ (plane wave incidence perpendicular to the cylinder axis) to $(90^\circ, 0^\circ)$ (plane wave incidence parallel to the cylinder axis). The corresponding values of E_L from Eq. (12) range from 1% to 2%.

The primary inaccuracy of the PWA is again improved rapidly by only a few iterations. Analogous results were observed in cases (i), (iii) for different frequencies and different angles of incidence also. Figure 9 shows the total pressure on the surface of cylinder (ii) at $ka=16.4$, $kl=61.2$ and $(0^\circ, 0^\circ)$ incidence, after 10 iterations. The surface is assumed to be rigid. Figure 9(a) gives the amplitude distribution, Fig. 9(b) shows the phase distribution. The diffraction pattern on the illuminated part of the surface can be seen in Fig. 9(a). However, it is only poorly developed in comparison with the case of the cat's-eye structures. This becomes evident if we compare amplitude scaling in Fig. 6 and Fig. 9(a), respectively. The phase distribution in Fig. 9(b) is very close to that of the incident wave.

III. CONCLUSIONS

The presented iterative solver of the Helmholtz integral equation makes it possible to calculate high-frequency scattering from complex impedance structures, consisting of several thousand boundary elements, in relatively short computing time on regular personal computers. Depending on the number of iterations, high-accuracy solutions can be obtained for both the surface pressure and the scattered far-field pressure. The error of the iterative solver is limited by the discretization error of the surface Helmholtz integral equation. These positive results give us confidence to extend the method to the application of sound radiation problems and to the computation of sound fields in closed rooms of arbitrary shape.

ACKNOWLEDGMENTS

The authors are grateful to Dr. H. G. Schneider and A. Homm from the Forschungsanstalt der Bundeswehr für Wasserschall und Geophysik (FWG), Kiel (Germany) for putting the structural models at their disposal and for many helpful discussions. We also thank the referees of the paper for helpful and valuable comments.

¹M. C. Junger and D. Feit, *Sound, Structures, and their Interaction* (The Massachusetts Institute of Technology, Edward Brothers Inc., Cambridge, 1972).

²E. Skudrzuk, *The Foundations of Acoustics: Basic Mathematics and Basic Acoustics* (Springer-Verlag, New York, 1971).

³P. M. Morse and H. Feshbach, *Methods of Theoretical Physics* (McGraw-Hill, New York, 1953).

⁴R. E. Kleinman, G. F. Roach, L. S. Schuetz, and J. Shirron, "An iterative solution to acoustic scattering by rigid objects," *J. Acoust. Soc. Am.* **84**, 385–391 (1988).

⁵R. E. Kleinman and G. F. Roach, "Iterative solutions of boundary integral equations in acoustics," *Proc. R. Soc. London, Ser. A* **417**, 45–57 (1988).

⁶R. Barrett, M. Berry, T. F. Chan, J. Demmel, J. M. Donato, J. Dongarra, V. Eijkhout, R. Pozo, Ch. Romine, and H. V. Vost, *Templates for the*

- Solution of Linear Systems: Building Blocks for Iterative Methods* (SIAM, Philadelphia, 1993).
- ⁷L. Kazandjian, "Comparison of the Rayleigh and T-matrix theories of scattering of sound from an elastic shell," *J. Acoust. Soc. Am.* **93**, 3139–3148 (1993).
- ⁸G. H. Koopmann and H. Benner, "Method for computing the sound power of machines based on the Helmholtz integral," *J. Acoust. Soc. Am.* **71**, 78–89 (1982).
- ⁹M. Ochmann, "The source simulation technique for acoustic radiation problems," *Acustica* **81**, 512–527 (1995).
- ¹⁰R. J. Urick, *Principles of Underwater Sound* (McGraw-Hill, New York, 1983), 3rd ed.

A stochastic model for wave localization in one-dimensional disordered structures

Yang Yang

SFA, Inc., 1401 McCormick Drive, Landover, Maryland 20785

Douglas M. Photiadis

Code 7131, Naval Research Laboratory, Washington, DC 20375-5000

(Received 21 March 1997; accepted for publication 14 October 1997)

This paper presents a probabilistic study of the effects of structural irregularity on wave propagation along an infinite 1-D chain. A general integral equation method based on Markov chain theory is used to determine the phase probability density function (pdf) at the scatterers distributed irregularly along the chain. The scatterers could be atoms in a one-dimensional crystal, or ribs on a flat plate or membrane. The integral equation derived for the phase pdf is simplified considerably when the scatterers are distributed completely randomly or quasi-periodically. In these cases, the integral equations may be asymptotically solved for the phase density functions in the limit of weak or strong scattering; the localization factors are then obtained. The present approach is quite general and is directly applicable to any disordered one-dimensional system consisting of identical scatterers that are arranged according to a probability distribution function. The validity of the present asymptotic solutions is examined and verified by comparing against the existing analytical solutions for simple atomic or mechanical disordered systems. © 1998 Acoustical Society of America. [S0001-4966(98)00402-0]

PACS numbers: 43.20.Fn, 43.30.Jx, 43.40.Rj [ANN]

INTRODUCTION

Wave propagation in periodic systems has been extensively explored for many decades. It is well known that there is a characteristic band structure in the dispersion relation of the propagating waves. Within certain frequency ranges, passbands, waves, or disturbances may propagate throughout the system without attenuation for a conservative system. Outside of these passbands, the stopbands, the waves exponentially decay as they travel through the system. In many engineering structures, however, certain imperfections or irregularities always occur. The occurrence of these irregularities generates a cutoff length for the passbands, thus preventing long-range propagation at all frequencies. As a result, the response of the system is exponentially localized near the source (Anderson localization¹). The large body of existing knowledge derived from periodic systems can not explain this phenomenon either qualitatively or quantitatively.

The phenomenon of energy localization due to structural irregularities was first discovered by Anderson in solid state physics.¹ A great many results have since been obtained from the study of quantum mechanical systems. Anderson's work was first extended to structural dynamics by Hodges,² who studied the localization of vibration along a one-dimensional chain of coupled pendula or a flexible beam with mass and spring constraints. The localization in other one-dimensional mechanical systems were discussed by many investigators with various statistical methods.³⁻⁶ An assumption commonly used in the existing literature is that the probability density function (pdf) of the phase of the standing wave is uniform and is independent of specific distributions of constraints or scatterers along the one-dimensional system.² This assumption often leads to the

single band approximation result, which is most valid within the central region of a passband and becomes singular near the edges of the band. Hodges and Woodhouse did realize the importance of the detailed form of a phase density function on the average energy density and the localization length, but they did not provide a systematic approach to determine the phase density function for any given configuration of a one-dimensional disordered system. The unique contributions that we try to make in the present paper are first to find a systematic approach for the determination of the phase density function, and second to derive a localization factor that is uniformly valid in both passbands and stopbands. One of the interesting results derived from our analysis is that the irregularity in a disordered system smooths out the singularity appearing at the edge of the passband. Furthermore, we will show that Hodges' results are the leading order terms of our asymptotic results in the limits of both weak and strong scattering.

In this paper, we consider wave propagation and localization along a general one-dimensional chain with an array of identical scatterers distributed according to a specific probability density function of the space separation. The system could be an array of atomic potentials, a ribbed membrane or a ribbed plate. The general problem is formulated within the framework of Markov chain theory. A systematic integral equation approach is used to determine the phase pdf at the scatterers along the chain. The main assumption used here is that the interaction among the scatterers is limited to nearest neighbor coupling. Thus Markov chain theory is directly applicable to the system. The paper is outlined as follows: A basic formalism is described in Sec. I. A traveling wave description is introduced so that the phase of the waves may be expressed in terms of single reflection and transmis-

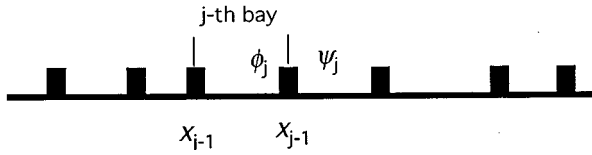


FIG. 1. A chain of randomly spaced scatterers.

sion coefficients of a scatterer. In addition, the ratio of the amplitudes in two adjacent bays (cells) depends only on the phase of the wave and the reflection and transmission coefficients. Then, a brief review of Borland's work^{7,8} is presented and a general integral equation for the phase density function is introduced. In Sec. II the integral equation is solved asymptotically at the limit of weak or strong scattering for two different chains of scatterers: one with completely randomly distributed scatterers and the other with quasi-periodically distributed scatterers. The asymptotic solutions are valid for a general one-dimensional system. The differences between two systems are characterized by their single reflection and transmission coefficients associated with each scatterer. In Sec. III, some examples are discussed in order to illustrate the application of the present approach and verify the asymptotic solutions against the existing results.

I. BASIC FORMALISM

A. Traveling wave description

In this section, we introduce a traveling wave description for the vibration in each bay along a disordered chain and characterize the behavior of each scatterer by its reflection and transmission coefficients. Consider a one-dimensional array of scatterers distributed according to a specific probability density function. The average spacing between two neighboring scatterers is assumed to be much larger than the attenuation length of any evanescent nearfield. Therefore, the nearfield in the vicinity of a scatterer may be ignored in the standing wave solutions, namely,

$$w(x) = A_j \cos[k_s(x - x_j) + \phi_j] \\ = \pm A_j \cos[k_s(x - x_{j-1}) + \psi_{j-1}], \quad (1)$$

where A_j is the amplitude in the j th bay, x_j is the coordinate of the j th scatterer, and ϕ_j and ψ_j are the reduced phases on the left and right sides of the j th scatterer (see Fig. 1), respectively (that is, $-\pi/2 \leq \phi_j \leq \pi/2$ and $-\pi/2 \leq \psi_j \leq \pi/2$). The uncertainty in sign is due to the fact that the phases are reduced to the interval $[-\pi/2, \pi/2]$. The above standing wave solution may be rewritten in terms of traveling waves scattered away from each scatterer:

$$w(x) = \frac{1}{2} A_j e^{ik_s(x-x_j) + i\phi_j} + \frac{1}{2} A_j e^{-ik_s(x-x_j) - i\phi_j} \\ = \pm \frac{1}{2} A_j e^{ik_s(x-x_{j-1}) + i\psi_{j-1}} \\ \pm \frac{1}{2} A_j e^{-ik_s(x-x_{j-1}) - i\psi_{j-1}}. \quad (2)$$

Let R and T be the single reflection and transmission coefficients of each scatterer. The continuity condition across each scatterer may be expressed as

$$\frac{1}{2} T A_j e^{i\phi_j} \pm \frac{1}{2} R A_{j+1} e^{-i\psi_j} = \pm \frac{1}{2} A_{j+1} e^{i\psi_j}, \quad (3)$$

$$\pm \frac{1}{2} T A_{j+1} e^{-i\psi_j} + \frac{1}{2} R A_j e^{i\phi_j} = \frac{1}{2} A_j e^{-i\phi_j}. \quad (4)$$

The above two equations give

$$\frac{A_{j+1}}{A_j} = \frac{\pm T e^{i\phi_j}}{e^{i\psi_j} - R e^{-i\psi_j}} = \frac{e^{-i\phi_j} - R e^{i\phi_j}}{\pm T e^{-i\psi_j}}. \quad (5)$$

Note from the above equation that the ratio of the amplitudes at two adjacent bays depends only on one random variable, i.e., ϕ_j or ψ_j . Define the ratio of the magnitudes of the response in adjacent bays:

$$f(\phi_j) = \frac{|A_{j+1}|^2}{|A_j|^2}. \quad (6)$$

From Eq. (5), we have

$$f(\phi_j) = \frac{1 + |R|^2 - 2|R|\cos(2\phi_j + \theta_R)}{|T|^2} \\ = \frac{|T|^2}{1 + |R|^2 - 2|R|\cos(2\psi_j - \theta_R)}, \quad (7)$$

where θ_R is the phase angle of the reflection coefficient. The relationship between the phases on the left and right sides of each scatterer may be obtained from the above as

$$\cos(2\phi_j + \theta_R) \\ = \frac{1 + |R|^2}{2|R|} - \frac{|T|^4}{2|R|} \frac{1}{1 + |R|^2 - 2|R|\cos(2\psi_j - \theta_R)}. \quad (8)$$

Note that Eqs. (7) and (8) are general and valid for all one-dimensional wave bearing systems. The only difference among the different systems lies in the single reflection and transmission coefficients associated with each scatterer. Furthermore, Eq. (7) implies that once the phase is determined then the amplitude may be obtained.

B. Markov chain model and localization length

In the previous section it was shown that the dynamic solution for a particular irregular chain is entirely contained in phase of the response, and further, that the phase may be determined iteratively in terms of an initial condition. Exploiting this fact, the expected behavior of an irregular system may be determined completely following a method due to Borland.⁷ The application of this method to structural acoustic problems was suggested in a recent review article.⁹

Suppose then that we have an ensemble of such chains (i.e., irregularly ribbed plates) and that the initial phase is specified in terms of a probability distribution $\rho_0(\phi_0)$. The distribution ρ_0 may be arbitrary. The probability distribution of the phase in the next bay is determined by both the phase discontinuity across the scatterer, Eq. (8), and the probability distribution of the scatterer's position $p(\phi)$. This relation must take the form of the Chapman-Kolmogorov equation

$$\rho_n(\phi_n) = \int_{-\pi/2}^{\pi/2} K(\phi_{n-1}, \phi_n) \rho_{n-1}(\phi_{n-1}) d\phi_{n-1}, \quad (9)$$

with

$$\int_{-\pi/2}^{\pi/2} \rho_n(\phi_n) d\phi_n = 1, \quad (10)$$

where we have written the recursion relation for the n th bay. Here, the kernel $K(\phi_{n-1}, \phi_n)$ is the one-step transition probability density function given by⁷

$$K(\eta, \phi) = \frac{1}{k_s} \sum_{n=1}^N p\left(\frac{\phi - D(\eta) + n\pi}{k_s}\right) + \frac{1}{k_s} p\left(\frac{\phi - D(\eta)}{k_s}\right) h(\phi - D(\eta)), \quad (11)$$

where k_s is the wave number and $h(\phi)$ is the Heaviside step function. The function $D(\eta)$ is the reduced phase at the right side of a scatterer given that the phase at the left side of this scatterer is η . Clearly, $D(\eta)$ can be determined by solving Eq. (8). The above equation may be simplified if unreduced phase is used:

$$K(\eta, \phi) = \frac{1}{k_s} p\left(\frac{\phi - D(\theta)}{k_s}\right). \quad (12)$$

After n steps of iteration, Eq. (9) becomes

$$\rho_n(\phi_n) = \int_{-\pi/2}^{\pi/2} K_n(\phi_0, \phi_n) \rho_0(\phi_0) d\phi_0, \quad (13)$$

where K_n is given recursively by

$$K_n(\phi_0, \phi_n) = \int_{-\pi/2}^{\pi/2} K_{n-1}(\phi_0, \phi_{n-1}) \times K(\phi_{n-1}, \phi_n) d\phi_{n-1}, \quad (14)$$

and $K_1 = K$.

It has been proved by Fréchet¹⁰ that $K_n(\phi_0, \phi)$ converges uniformly to a limiting function $\rho(\phi)$ independent of ϕ_0 , that is,

$$\lim_{n \rightarrow \infty} K_n(\phi_0, \phi) \rightarrow \rho(\phi), \quad (15)$$

if $K_n(\phi_0, \phi)$ satisfies certain conditions.^{8,10} In addition, the function $\rho(\phi)$ is the unique solution of the following integral equation,

$$\rho(\phi) = \int_{-\pi/2}^{\pi/2} K(\eta, \phi) \rho(\eta) d\eta, \quad (16)$$

with a normalization condition

$$\int_{-\pi/2}^{\pi/2} \rho(\phi) d\phi = 1. \quad (17)$$

As a result of Eqs. (15) and (10), ρ_n given by Eq. (13) converges uniformly to ρ , that is,

$$\lim_{n \rightarrow \infty} \rho_n(\phi) \rightarrow \rho(\phi), \quad (18)$$

and is independent of ρ_0 . Also, recall that ρ_n is the pdf for the phase in the n th bay.

Once the phase density function $\rho(\phi)$ is determined from Eq. (16), the localization factor may be calculated from the following definition:

$$\gamma = \langle \ln f(\phi) \rangle = \int_{-\pi/2}^{\pi/2} \rho(\phi) \ln f(\phi) d\phi, \quad (19)$$

where $f(\phi)$ is defined by Eq. (7). The localization length l is simply

$$l = 2b/\gamma, \quad (20)$$

where b is the average distance between two adjacent scatterers. The response due to any far away source hence decays exponentially according to $w(x) \propto \exp[-x/l]$ as the distance from the source increases.

In the rest of the paper we simplify the integral equations derived in this section and search for asymptotic solutions in the cases where the scatterers are distributed completely randomly or quasi-periodically.

II. ASYMPTOTIC SOLUTIONS

A. Chains of randomly distributed scatterers

In the case of completely randomly distributed scatterers, the probability density function of the separation between two adjacent scatterers is given by

$$p(s) = \frac{1}{b} \exp\left(-\frac{s}{b}\right), \quad (21)$$

where s is the spacing and b is the average spacing. It has been shown by Borland^{7,8} that inserting the above into the general integral equation (16) with some manipulations yields the following equation:

$$\rho(\phi) = A - \mu \int_{D^{-1}(\phi)}^{\phi} \rho(\theta) d\theta, \quad (22)$$

where A is a constant and $\mu = 1/(k_s b)$. Now let us seek the asymptotic expressions for the phase-density function $\rho(\phi)$ and the localization length in the limits of weak and strong scattering.

1. Weak scattering

In this case, the reflection coefficient is much smaller than unity and the transmission coefficient is close to unity, that is,

$$|R| \ll 1, \quad |T| \sim 1. \quad (23)$$

Furthermore, from energy conservation, we have

$$|T|^2 = 1 - |R|^2. \quad (24)$$

Solving Eq. (8) for ϕ_j in terms of ψ_j and R , and neglecting the terms of order higher than $|R|^2$, we obtained

$$\begin{aligned} \cos(2\phi_j + \theta_R) &= -\cos(2\psi_j - \theta_R) + 2|R| \sin^2(2\psi_j - \theta_R) \\ &\quad + 4|R|^2 \sin^2(2\psi_j - \theta_R) \cos(2\psi_j - \theta_R) \\ &\quad + O(|R|^3), \end{aligned} \quad (25)$$

and

$$\begin{aligned} \phi_j = D^{-1}(\psi_j) &= \frac{\pi}{2} + \psi_j - \theta_R + |R| \sin(2\psi_j - \theta_R) \\ &\quad + \frac{|R|^2}{2} \sin 2(2\psi_j - \theta_R) + O(|R|^3). \end{aligned} \quad (26)$$

Since the above equation is valid for all the identical scatterers, the subscript, j , may be dropped in the subsequent expressions.

At high frequencies, i.e., $k_s b \gg 1$ or $\mu \ll 1$, the integral equation (22) may be expanded asymptotically by iteration,

$$\begin{aligned} \rho(\phi) = & A - A\mu(\phi - D^{-1}(\phi)) \\ & + A\mu^2 \int_{D^{-1}(\phi)}^{\phi} \int_{D^{-1}(\psi)}^{\psi} \rho(\theta) d\theta d\psi. \end{aligned} \quad (27)$$

Inserting Eq. (26) into the above and neglecting the terms of order higher than $\mu|R|^2$ or $\mu^2|R|$ yield the asymptotic expression for the phase-density function at the left of the scatterer,

$$\begin{aligned} \rho(\phi) = & A - A\mu \left(\theta_R - \frac{\pi}{2} - |R| \sin(2\phi - \theta_R) \right. \\ & \left. - \frac{|R|^2}{2} \sin(2\phi - \theta_R) \right) + O(\mu^4), \end{aligned} \quad (28)$$

where we have used the fact that

$$|\phi - D^{-1}(\phi)| \sim O(|R|), \quad |R| \sim O(\mu). \quad (29)$$

Similarly, the function $f(\phi)$ defined by Eq. (6) may be expanded asymptotically at the limit of $|R| \ll 1$, and its logarithm may be written as

$$\begin{aligned} \ln f(\phi) = & -2|R| \cos(2\phi + \theta_R) + 2|R|^2 \sin^2(2\phi + \theta_R) \\ & + O(|R|^3). \end{aligned} \quad (30)$$

The localization factor may be obtained from Eqs. (19), (28) and (30),

$$\gamma = A|R|^2 \pi \left(1 - \mu \left(\theta_R - \frac{\pi}{2} \right) \right) + A\pi\mu|R|^2 \sin 2\theta_R + O(|R|^4), \quad (31)$$

where the constant A is determined by the normalization condition (17), that is,

$$A = \frac{1}{\pi(1 - \mu(\theta_R - \pi/2))}. \quad (32)$$

Substitution of the above into Eq. (31) yields

$$\gamma = |R|^2(1 + \mu \sin 2\theta_R) + O(|R|^4). \quad (33)$$

2. Strong scattering

Consider the case where

$$|T| \ll 1, \quad |R| \sim 1, \quad |R|^2 \sim 1 - |T|^2. \quad (34)$$

At this limit, Eq. (8) may be simplified in the following asymptotic form:

$$\cos(2\phi + \theta_R) = \frac{16\sin^2(\psi - \theta_R/2) - |T|^4}{16\sin^2(\psi - \theta_R/2) + |T|^4} + \frac{|T|^4}{8} + O(|T|^6), \quad (35)$$

where ϕ_j and ψ_j have been replaced by ϕ and ψ , respectively. Solving the above equation for ϕ gives

$$\begin{aligned} \phi = D^{-1}(\psi) = & -\frac{\theta_R}{2} \pm \left(\arctan \left[\frac{4}{|T|^2} \sin(\psi - \theta_R/2) \right] \right. \\ & \left. + \arctan \left(\frac{4}{|T|^2} \theta_R \right) \right) + O(|T|^4). \end{aligned} \quad (36)$$

Note that ϕ is the reduced phase, i.e., $-\pi/2 \leq \phi \leq \pi/2$. Thus, the plus sign should be chosen in Eq. (36). In general, $|\sin \theta_R| \gg |T|^2$, Eq. (36) may be further simplified as

$$\begin{aligned} \phi = D^{-1}(\psi) = & -\frac{\theta_R}{2} + \left(\frac{\pi}{2} \operatorname{sgn}(\theta_R) + \arctan \left[\frac{4}{|T|^2} \sin(\psi \right. \right. \\ & \left. \left. - \theta_R/2) \right] \right) + O(|T|^4). \end{aligned} \quad (37)$$

Inserting the above into Eq. (27) and ignoring all the terms of order higher than μ yields

$$\begin{aligned} \rho(\phi) = & A - A\mu \left(\phi + \frac{\theta_R}{2} - \left[\frac{\pi}{2} \operatorname{sgn}(\theta_R) \right. \right. \\ & \left. \left. + \arctan \left(\frac{4}{|T|^2} \sin(\phi - \theta_R/2) \right) \right] \right) + O(\mu^2), \end{aligned} \quad (38)$$

where the constant A is determined by the normalization condition Eq. (17):

$$A = \frac{1}{\pi} \left(1 + \mu \left[\theta_R - \frac{\pi}{2} \operatorname{sgn}(\theta_R) \right] \right) + O(\mu^2). \quad (39)$$

Thus, the final asymptotic solution for the phase density function may be written as

$$\begin{aligned} \rho(\phi) = & \frac{1}{\pi} + \frac{\mu}{\pi} \left(\frac{\theta_R}{2} - \phi + \arctan \left(\frac{4}{|T|^2} \sin(\phi - \theta_R/2) \right) \right) \\ & + O(\mu^2). \end{aligned} \quad (40)$$

Using the condition given by (34), we may expand Eq. (7)₁ as follows:

$$f(\phi) = 2 \frac{2 - |T|^2}{|T|^2} \sin^2(\phi + \theta_R/2) + O(|T|^2). \quad (41)$$

Then the localization factor can be obtained from Eqs. (19), (40) and (41) as

$$\begin{aligned} \gamma = & \ln \frac{2(2 - |T|^2)}{|T|^2} - 2 \ln 2 + \frac{\mu}{\pi} \int_{-\pi/2}^{\pi/2} \left(\frac{\theta_R}{2} - \phi \right) \ln \sin^2(\phi \\ & + \theta_R/2) d\phi + \frac{\mu}{\pi} \int_{-\pi/2}^{\pi/2} \arctan \left(\frac{4}{|T|^2} \sin(\phi - \theta_R/2) \right) \\ & \times \ln \sin^2(\phi + \theta_R/2) d\phi + O(\mu^2 |T|^2), \end{aligned} \quad (42)$$

where the identity

$$\int_{-\pi/2}^{\pi/2} \ln \sin^2(\phi + \theta_R/2) d\phi = -2\pi \ln 2 \quad (43)$$

has been used.

In the limit of high frequencies, $|T| \sim \mu \ll 1$, the first order approximation of the above equation corresponds to a uniform phase density function. The localization factor may be obtained as

$$\gamma = -\ln|T|^2 + O(\mu). \quad (44)$$

Hodges² showed via a much more elementary method that the transmitted intensity, $I_N = |A_N|^2/|A_0|^2$, through N randomly arranged scatterers behaves as $I_N \sim |T|^{2N}$, and, therefore,

$$\gamma \sim -\ln \frac{I_N}{I_{N-1}} \sim -\ln|T|^2, \quad (45)$$

which is exactly the first term in Eq. (45).

From the above discussion, one can see that Hodges' result, Eq. (45), is derived under assumption of uniform phase density function and is valid only in the limits of strong scattering and high frequencies. The error resulting from this assumption is of the order of $\mu = 1/(k_s b)$.

B. Chains of quasi-periodically distributed scatterers in the limit of weak scattering

For an array of quasi periodically distributed scatterers, the probability density function (pdf) of the separation of the adjacent scatterers may be expressed as

$$p(s) = \frac{1}{a}, \quad |s-b| \leq \frac{1}{2}a, \\ = 0, \quad |s-b| \geq \frac{1}{2}a, \quad (46)$$

where s is the spacing, b is the average spacing, and $\frac{1}{2}a$ is the largest possible deviation from b . For a nearly periodic or quasi-periodic array of scatterers, the following condition is implied:

$$k_s a \ll 1. \quad (47)$$

Inserting Eq. (46) into the integral equation (12) for unreduced phase yields

$$\rho(\phi) = \frac{1}{k_s a} \int_{U_1(\phi)}^{U_2(\phi)} \rho(\theta) d\theta, \quad (48)$$

where

$$U_1(\phi) = D^{-1}(\phi - k_s b - \frac{1}{2}k_s a), \quad (49)$$

$$U_2(\phi) = D^{-1}(\phi - k_s b + \frac{1}{2}k_s a). \quad (50)$$

The integral equation (48) can be solved asymptotically in the limit of weak scattering $|R| \ll 1$. In this limit, the unreduced form for the phase $D^{-1}(\phi)$ may be obtained from Eq. (25) as

$$D^{-1}(\phi) = n\pi + \frac{\pi}{2} + \phi - \theta_R + |R| \sin(2\phi - \theta_R) \\ + \frac{1}{2}|R|^2 \sin 2(2\phi - \theta_R) + O(|R|^3). \quad (51)$$

Note from the above that $D^{-1}(\phi) > 0$ at the limit, $|R| \ll 1$. Thus, $U_2(\phi) > U_1(\phi)$, and $\rho(\phi) \geq 0$ or $\rho(\phi) \leq 0$ for $-\infty < \phi < \infty$. Since ρ here is a probability density function, we

only choose the positive solution to Eq. (48). Let

$$\phi_1 = \phi - k_s b + \frac{\pi}{2} - \theta_R, \quad (52)$$

$$\epsilon = k_s a. \quad (53)$$

Substituting Eqs. (52), (53), and (51) into Eq. (48) and expanding the integral up to the first order of $|R|$, we obtain

$$\rho(\phi) = \frac{1}{\epsilon} \int_{\phi_1 - \epsilon/2}^{\phi_1 + \epsilon/2} \rho(\theta) d\theta - \frac{|R|}{\epsilon} \rho(\phi_1 + \epsilon/2) \sin(2\phi_1 \\ + \theta_R + \epsilon) + \frac{|R|}{\epsilon} \rho(\phi_1 - \epsilon/2) \sin(2\phi_1 + \theta_R - \epsilon) \\ + O(|R|^3). \quad (54)$$

It will be clear by the end of this subsection that the second and the third terms in the above are of the order of $|R|^2$.

Note the fact that the phase density function ρ is a periodic function of period equal to π and it must be a constant when the scattering strength is zero, i.e., $|R|=0$. Thus, we may expand ρ in the form of

$$\rho(\phi) = \rho_0 + |R| \sum_{n=1}^{\infty} (A_n \cos 2n\phi + B_n \sin 2n\phi), \quad |R| \ll 1, \quad (55)$$

where ρ_0 is a constant and may be determined later by using the normalization condition (17).

Inserting Eq. (55) into Eq. (54) and neglecting the terms of order higher than $|R|^2$, we obtain

$$\sum_{n=1}^{\infty} A_n \left(\frac{\sin n\epsilon}{n\epsilon} \cos 2n\phi_1 - (-1)^n \cos 2n(\phi_1 + k_s b + \theta_R) \right) \\ + \sum_{n=1}^{\infty} B_n \left(\frac{\sin n\epsilon}{n\epsilon} \sin 2n\phi_1 - (-1)^n \sin 2n(\phi_1 + k_s b \\ + \theta_R) \right) = \frac{2 \sin \epsilon}{\epsilon} \rho_0 \cos(2\phi_1 + \theta_R). \quad (56)$$

Multiplying $\cos 2n\phi_1$ and $\sin 2n\phi_1$, respectively, on both sides of Eq. (56) and then integrating the equation over $[-\pi/2, \pi/2]$ yield

$$\left(\frac{\sin n\epsilon}{n\epsilon} - (-1)^n \cos 2n(k_s b + \theta_R) \right) A_n \\ - (-1)^n \sin 2n(k_s b + \theta_R) B_n \\ = \frac{2 \sin \epsilon \cos \theta_R}{\epsilon} \rho_0 \delta_{n1}, \quad (57)$$

$$(-1)^n \sin 2n(k_s b + \theta_R) A_n + \left(\frac{\sin n\epsilon}{n\epsilon} - (-1)^n \cos 2n(k_s b \\ + \theta_R) \right) B_n = - \frac{2 \sin \epsilon \sin \theta_R}{\epsilon} \rho_0 \delta_{n1}, \quad (58)$$

where $\delta_{11} = 1$, and $\delta_{n1} = 0$ for $n \neq 1$. Solving the above two equations for A_n and B_n gives

$$A_1 = \frac{2\rho_0 \sin \epsilon}{\epsilon} \frac{(\sin \epsilon / \epsilon) \cos \theta_R + \cos(2k_s b + \theta_R)}{\sin^2 2(k_s b + \theta_R) + (\sin \epsilon / \epsilon + \cos 2(k_s b + \theta_R))^2}, \quad (59)$$

$$B_1 = \frac{2\rho_0 \sin \epsilon}{\epsilon} \frac{\sin(2k_s b + \theta_R) - (\sin \epsilon / \epsilon) \sin \theta_R}{\sin^2 2(k_s b + \theta_R) + (\sin \epsilon / \epsilon + \cos 2(k_s b + \theta_R))^2}, \quad (60)$$

and

$$A_n = B_n = 0, \quad n \geq 2. \quad (61)$$

Substituting the solutions given by Eqs. (59), (60) and (61) into Eq. (55) gives

$$\rho = \frac{1}{\pi} \left| 1 + \frac{2|R| \sin \epsilon}{\epsilon} \times \frac{[(\sin \epsilon / \epsilon) \cos(2\phi + \theta_R) + \cos(2\phi - 2k_s b - \theta_R)]}{\sin^2 2(k_s b + \theta_R) + ((\sin \epsilon / \epsilon) + \cos 2(k_s b + \theta_R))^2} \right|, \quad (62)$$

where the normalization condition has been used to determine ρ_0 .

The localization factor may be obtained from Eqs. (19), (30), and (62) as

$$\gamma = |R|^2 \frac{1 - \sin^2 \epsilon / \epsilon^2}{\sin^2 2(k_s b + \theta_R) + (\sin \epsilon / \epsilon + \cos 2(k_s b + \theta_R))^2}, \quad (63)$$

with $|R| \ll 1$. Within a passband, more precisely, $|k_s b + \theta_R - [(2m-1)/2] \pi| \gg O(\epsilon^2)$, the above equation may be further simplified as

$$\gamma = \frac{1}{3} \left(\frac{|R| \epsilon}{2 \sin k_s b} \right)^2 + O(\epsilon^4), \quad (64)$$

where k_b is the Floquet or Bloch wave number of the associated periodic array and is determined by the following dispersion equation:^{9,11}

$$\cos k_b b = \frac{1}{|T|} \cos(k_s b + \theta_T). \quad (65)$$

Here θ_T is the phase angle of the single scatterer transmission coefficient. Note that the facts $\theta_T \approx \theta_R + \pi/2$ and $|T|^2 = 1 - |R|^2 \approx 1$ have been used in deriving Eq. (64). The asymptotic result given by Eq. (64) is consistent with those derived by Hodges and Woodhouse¹² and Pierre.⁵ However, the simple asymptotic solution by Eq. (64) and those in references 5 and 12 become singular and fail near the edges of the passband, i.e., $|k_s b + \theta_R - [(2m-1)/2] \pi| \gg O(\epsilon^2)$, while Eq. (63) remains finite and valid.

It is also interesting to note from Eq. (63) that the localization factor is a periodic function of the dimensionless wave number, $k_s b$. This simple expression clearly exhibits the characteristics of band structure observed in quasi-periodic disordered systems.^{4,5} The localization factor reaches its local maxima

$$\gamma_{max} = |R|^2 \frac{1 + \frac{\sin \epsilon}{\epsilon}}{1 - \frac{\sin \epsilon}{\epsilon}} \quad (66)$$

at the centers of the stopbands in the dispersion relation, that is $k_s b = [(2m-1)/2] \pi - \theta_R$ for $m=1,2,3, \dots$. As a result, a stopband appears at every half-wavelength. Furthermore, the result in Eq. (63) implies that, in the absence of irregularity, i.e., $\epsilon = k_s a = 0$, which corresponds to a periodic system, the localization factor is zero within a passband, i.e., $k_s b \neq [(2m-1)/2] \pi - \theta_R$, and becomes singular within a stopband, $k_s b = [(2m-1)/2] \pi - \theta_R$. Therefore, along a regular chain, the waves may propagate throughout the system without attenuation within a passband but are completely cut off within a stopband. The presence of irregularity has a twofold effect on wave propagation: one is to generate a cutoff length for a passband; the other is to extend the cutoff length in a stopband.

III. EXAMPLES AND DISCUSSIONS

The results derived in the last section are valid for any one-dimensional disordered system consisting of identical scatterers that are distributed completely randomly or quasi-periodically. For a particular system, one first solves the wave equation for a single scatterer, determines the single reflection and transmission coefficients, then simply inserts these coefficients into the general expressions given in the last section and calculates the phase density function and the localization length. Here, we use a few examples to illustrate the application of the present approach and verify the present solutions with some existing results.

A. One-dimensional chains of randomly spaced identical atoms

The first example is that of electronic waves propagating along a one-dimensional infinite chain of randomly spaced atoms with δ -function potentials. A similar problem has been discussed by Borland⁸ in the weak scattering case. Here we present the results for both weak and strong scattering.

1. Single reflection and transmission coefficients

In order to determine single reflection and transmission coefficients, one needs to solve the single scattering problem which is much easier to deal with than the multiple scattering problem. The wave equation for a single scatterer (atom) δ function of strength $-U_0$ is

$$\frac{d^2 w(x)}{dx^2} + k_s^2 w(x) + U_0 \delta(x) w(x) = 0. \quad (67)$$

Consider a plane wave, $A e^{ik_s x}$, incident on the scatterer at the origin. We may express the solution in terms of reflected and transmitted waves as follows:

$$w(x) = \begin{cases} A e^{ik_s x} + R A e^{-ik_s x}, & x \leq 0, \\ T A e^{ik_s x}, & x \geq 0, \end{cases} \quad (68)$$

where R and T are the single reflection and transmission coefficients, respectively.

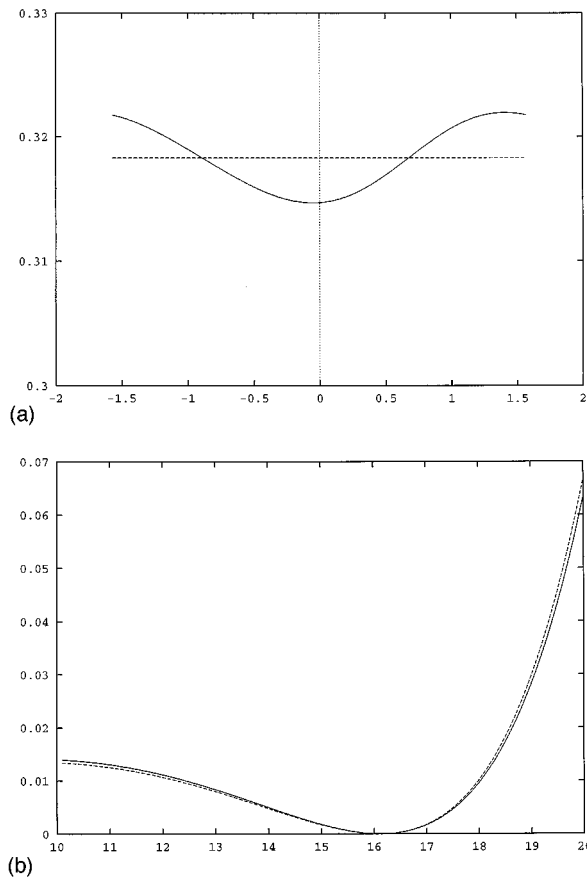


FIG. 2. Comparisons of the present asymptotic solutions (solid) with those of the first order approximation (dashed) at the limit of weak scattering for elastic flexural waves propagating along a flat plate with randomly distributed ribs. Each rib is a rectangular beam with dimension specified by the width $t=0.05$ (m) and the height $d=0.08$ (m). The average separation of two adjacent ribs is $b=1$ (m). (a) The phase density functions calculated at the dimensionless flexural wave number $k_s b=10$. (b) The localization factors or the averaged decay rates are calculated at the frequency range, $20 \leq k_s b \leq 30$.

Note that the wave function, $w(x)$, must be continuous across the scatterer at $x=0$, that is

$$A + RA = TA, \quad (69)$$

but its first derivative, $w'(x)$, is not continuous across $x=0$. Integrating Eq. (67) over the interval, $[-\epsilon, \epsilon]$, and letting $\epsilon \rightarrow 0$, we obtain

$$\frac{dw(0^+)}{dx} - \frac{dw(0^-)}{dx} + U_0 w(0) = 0. \quad (70)$$

Substituting Eq. (68) into the above yields

$$A i k_s (T - (1 - R)) + U_0 A T = 0. \quad (71)$$

Solving Eqs. (69) and (71) for R and T , we obtain

$$R = -\frac{q^2}{4 + q^2} + i \frac{2q}{4 + q^2}, \quad (72)$$

$$T = \frac{2}{2 - iq}, \quad (73)$$

where $q = U_0/k_s$. The phase angles of R and T can be found from the last two equations as

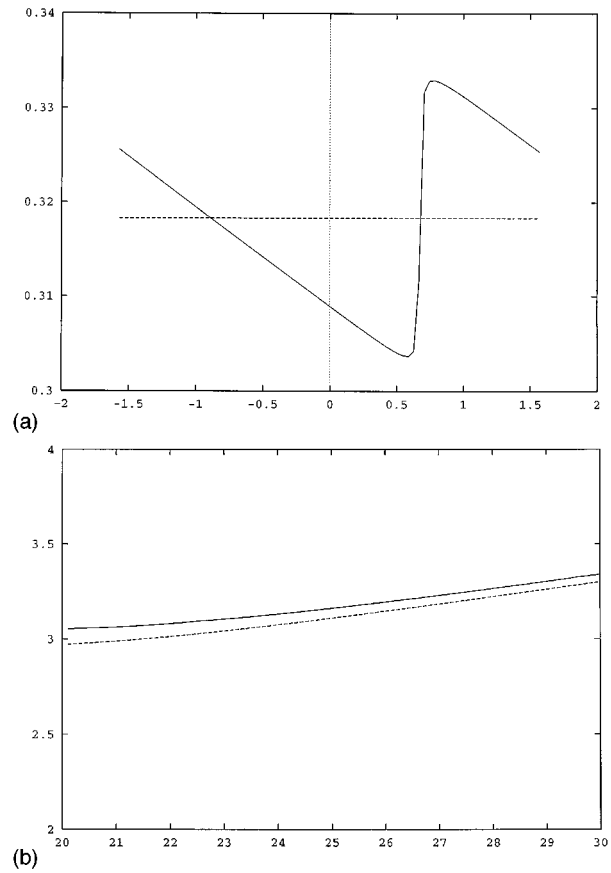


FIG. 3. Comparisons of the present asymptotic solutions [solid curves in (a) and (b)] with Hodge's result (the first order result) given by Eq. (45) [dashed curve in (b)] at the limit of strong scattering for elastic flexural waves propagating along a flat plate with randomly distributed ribs. Each rib is a rectangular beam with dimension specified by the width $t=0.05$ (m) and the height $d=0.25$ (m). The average separation of two adjacent ribs is $b=1$ (m). (a) The phase density functions calculated at the dimensionless flexural wave number $k_s b=30$. (b) The localization factors or the averaged decay rates are calculated at the frequency range, $20 \leq k_s b \leq 30$.

$$\theta_T = \theta_R - \frac{\pi}{2}, \quad \sin \theta_R = \frac{2}{\sqrt{4 + q^2}}. \quad (74)$$

2. Weak scattering

In the case of weak scattering, $q \ll 1$, Eqs. (72) and (74) are simplified as

$$|R| \rightarrow q/2, \quad \theta_R \rightarrow \pi/2 + q/2. \quad (75)$$

The phase density function follows from Eqs. (28) and (75) as

$$\begin{aligned} \rho(\phi) &= A - A\mu \left(\frac{q}{2} + \frac{q}{2} \cos(2\phi - q/2) \right. \\ &\quad \left. + \frac{q^2}{8} \sin 2(2\phi - q/2) \right) + O(\mu^4) \\ &= A - A\mu \left(q \cos^2 \phi + \frac{q^2}{2} \cos^2 \phi \sin 2\phi \right) + O(\mu^4), \end{aligned} \quad (76)$$

which yields the same result derived by Borland.⁸ The constant A is determined by the normalization condition (17), that is,

$$A = \frac{1 + \frac{1}{2}\mu q}{\pi} + O(\mu^4). \quad (77)$$

The localization factor then follows from Eqs (33) and (76) as

$$\gamma = \frac{q^2}{4}(1 - \mu \sin q) + O(\mu^4) = \frac{q^2}{4} - \frac{1}{4}\mu q^3 + O(\mu^4), \quad (78)$$

which reproduces the first two terms in Eq. (35) of Borland's paper.⁸

3. Strong scattering

In the limit of strong scattering and high frequencies, $q \gg 1$, or $U_0 b \gg k_s b \gg 1$, we have

$$|T| \rightarrow 2/q, \quad \theta_R \rightarrow \pi - 2/q. \quad (79)$$

The phase density function follows from Eqs. (40) and (79) as

$$\rho(\phi) = \frac{1}{\pi} + \frac{\mu}{\pi} \left(\frac{\pi}{2} - \frac{1}{q} - \phi - \arctan[q^2 \cos(\phi + 1/q)] \right) + O(\mu^2), \quad (80)$$

The localization factor then follows from Eqs (42) and (80) as

$$\begin{aligned} \gamma = & \ln(q^2 - 2) - 2\ln 2 + \frac{\mu}{\pi} \int_{-\pi/2}^{\pi/2} \left(\frac{\pi}{2} - \frac{1}{q} - \phi \right) \\ & \times \text{Incos}^2(\phi - 1/q) d\phi - \frac{\mu}{\pi} \int_{-\pi/2}^{\pi/2} \arctan(q^2 \cos(\phi \\ & + 1/q)) \text{Incos}^2(\phi - 1/q) d\phi + O(\mu^2 q^{-2}). \end{aligned} \quad (81)$$

B. Irregularly spaced ribs along a flat plate

Consider the examples of elastic flexural waves propagating along a flat plate with randomly or quasi-periodically distributed ribs. For simplicity, we consider the cases where the propagation direction is normal to the ribs. The scattering problem of a single rib has been given by many authors with various approaches.^{13,14} The well known results for the single reflection and transmission coefficients, given by Photiadis,¹⁴ may be written as

$$R = -\frac{Z_M g_\infty}{1 + Z_M g} + \frac{k_s^2 Z_I g_\infty}{1 - Z_I g''}, \quad (82)$$

$$T = 1 - \frac{Z_M g_\infty}{1 + Z_M g} - \frac{k_s^2 Z_I g_\infty}{1 - Z_I g''}, \quad (83)$$

where Z_M and Z_I are, respectively, the force and moment input impedances of the line scatterer and g is the line admittance of the plate. In the absence of fluid loading, these quantities are straightforward to obtain

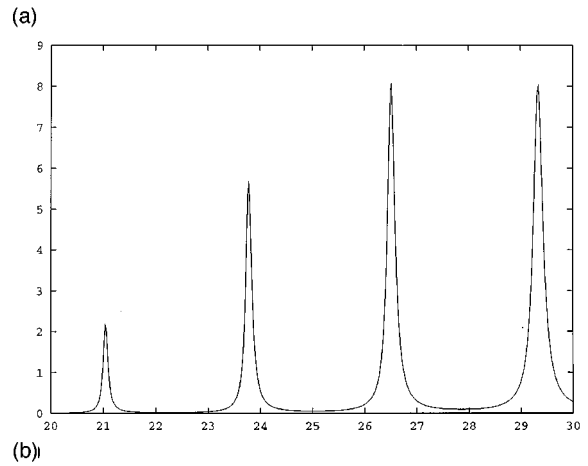
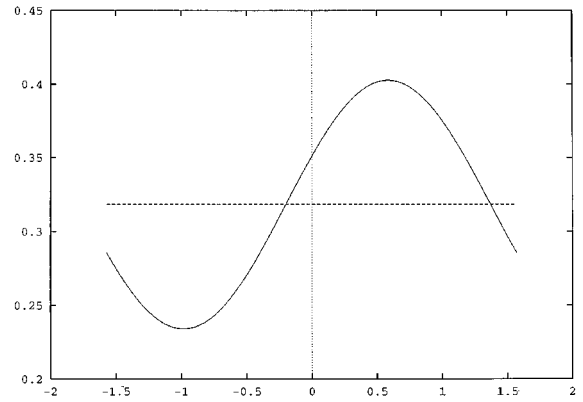


FIG. 4. The weak scattering results for elastic flexural waves propagating along a flat plate with quasi-periodically distributed ribs. Each rib is a rectangular beam with dimension specified by the width $t=0.05$ (m) and the height $d=0.25$ (m). The average separation of two adjacent ribs is $b=1$ (m). The maximum deviation from the average spacing is $a=0.04$ (m). (a) The phase density functions calculated at the dimensionless flexural wave number $k_s b=20$, where the solid curve is the present solution and the dashed curve is the first order result. (b) The localization factor or the average decay rate is calculated at the frequency range, $20 \leq k_s b \leq 30$.

$$g_\infty = \frac{k_s}{4\omega\rho_s h}, \quad g = \sqrt{2}e^{i\pi/4}g_\infty, \quad g'' = \sqrt{2}e^{i3\pi/4}k_s^2 g_\infty, \quad (84)$$

$$Z_m = -i\rho_s A\omega, \quad Z_I = -i\rho_s I_p^{eff}\omega, \quad (85)$$

where A is the area of the rib's cross section and I_p^{eff} is the moment of inertia about the line that the rib is attached to. For a $t \times d$ rectangular rib, we have

$$I_p^{eff} = \frac{1}{3}td^3 + \frac{1}{12}t^3d. \quad (86)$$

The weak scattering case corresponds to the frequency region, $k_s d \ll 1$ and $k_s b \gg 1$, while the strong scattering case corresponds to the frequency region, $k_s d \gg 1$, where b is the average spacing and d is the height of the rib. The phase density function and the localization factor may be calculated by substituting Eqs. (82) and (83) into Eqs. (28), (33), (40), (42), (62) and (63). The results for the chains of randomly distributed ribs are displayed in Fig. 2(a) and (b) for weak scattering, and in Fig. 3(a) and (b) for strong scattering, where the solid curves are the present asymptotic solutions given by Eqs. (28), (33) (40), and (42), and the dashed

curves are the first order results, i.e., the results based on the assumption of the uniform phase density function. It is clear to see from the comparisons that the uniform phase density function provides a good approximation for a chain of randomly distributed ribs in the limits of both weak and strong scattering.

The weak scattering results for a chain of quasi-periodically distributed ribs are shown in Fig. 4(a) and (b), where the solid curves are the present asymptotic solutions given by Eqs. (62) and (63), and the dashed curve in Fig. 4(a) is the result of the uniform phase density function (the first order result). At $k_s b = 20$, and $\epsilon = k_s a = 0.04$, the present result for the phase density function significantly deviates from the first order result. The most interesting result is the localization factor shown in Fig. 4(b), where the strong resonant peaks appear at every half wavelength, corresponding to the stopbands for the quasi-periodic system. The present asymptotic solution is uniformly valid within both the stopbands and the passbands.

IV. CONCLUSION

In the present paper, we have investigated wave propagation and localization in one-dimensional disordered systems, within the frame work of Markov chain theory. We have exploited the fact that the phase probability density function of the solution may be systematically determined by solving an integral equation. Using a traveling wave description, we have made this approach quite general. The scatterers could be atoms in a one-dimensional crystal, ribs on a flat plate or constraints on a membrane. The present method has been illustrated by its application to chains of randomly or quasi-periodically distributed scatterers. In these cases, the integral equations for the phase pdf's are simplified considerably and are solved asymptotically at the limit of weak or strong scattering; simple formulae are derived for the localization factors which are uniformly valid in both the passbands and the stopbands. The present asymptotic solutions agree well with the existing analytical solutions. As one may

see from the present analysis, the assumption of a uniform phase density function provides a good approximation to a chain of completely randomly distributed scatterers, but it becomes singular and fails near the edges of the passbands for a chain of quasi-periodically distributed scatterers.

ACKNOWLEDGMENTS

We would like to thank Dr. Luise S. Couchman for the valuable discussion. This work was supported by the Office of Naval Research and Naval Research Laboratory, Washington DC.

- ¹P. W. Anderson, "Absence of diffusion in certain random lattices," *Phys. Rev.* **109**, 1492–1505 (1958).
- ²C. H. Hodges, "Confinement of vibration by structural irregularity," *J. Sound Vib.* **82**, 411–424 (1982).
- ³C. H. Hodges and J. Woodhouse, "Confinement of vibration by one-dimensional disorder, I: theory of ensemble averaging," *J. Sound Vib.* **130**, 237–251 (1989).
- ⁴D. M. Photiadis, "Anderson localization of one-dimensional wave propagation on a fluid-loaded plate," *J. Acoust. Soc. Am.* **91**, 771–780 (1992).
- ⁵C. Pierre, "Weak and strong vibration localization in disordered structures: A statistical investigation," *J. Sound Vib.* **139**, 111–132 (1990).
- ⁶M. B. Sobnack and D. G. Crighton, "Anderson localization effects in the transmission of energy down an irregularly ribbed fluid-loaded structure," *Proc. R. Soc. London, Ser. A* **444**, 185–200 (1994).
- ⁷R. E. Boland, "One-dimensional chains with random spacing between atoms," *Proc. Phys. Soc. London* **77**, 705–711 (1961).
- ⁸R. E. Boland, "The nature of electronic states in disordered one-dimensional systems," *Proc. R. Soc. London, Ser. A* **274**, 529–545 (1963).
- ⁹D. M. Photiadis, "Fluid-loaded structures with one dimensional disorder," *Appl. Mech. Rev.* **49**, 100–125 (1996).
- ¹⁰M. Frechet, *Q. J. Math.* **5**, 106 (1934).
- ¹¹N. Ashcroft and D. Mermin, *Solid State Physics* (Saunders College, 1976), pp. 131–191.
- ¹²C. H. Hodges and J. Woodhouse, "Vibration isolation from irregularity in a nearly periodic structure: theory and measurements," *J. Acoust. Soc. Am.* **74**, 894–905 (1983).
- ¹³D. G. Crighton and G. Maidanik, "Acoustic and vibration fields generated by ribs on a fluid-loaded panel, I: Plane wave problems for a single rib," *J. Sound Vib.* **75**, 437–452 (1981).
- ¹⁴D. M. Photiadis, "Transport of energy across a discontinuity by fluid loading," *J. Acoust. Soc. Am.* **97**, 1409–1414 (1995).

Torsional waves in lossy cylinders

J. M. Carcione^{a)} and G. Seriani^{b)}

Osservatorio Geofisico Sperimentale, P.O. Box 2011 Opicina, 34016 Trieste, Italy

(Received 17 April 1997; revised 3 September 1997; accepted 10 October 1997)

The pure shear problem is one of relative mathematical simplicity and includes the essential physics common to more complicated cases, where multiple and coupled deformations occur. In this sense, the analysis of torsional waves serves as a pilot problem for investigating the influence of anisotropy and/or anelasticity on solution behavior. We obtain the kinematic and dynamic properties of torsional axially symmetric harmonic waves propagating in an infinitely long circular cylinder. The medium is transversely isotropic and dissipative, with its symmetry axis coincident with the axial axis of the cylinder. For an elastic cylinder each mode has a cutoff frequency and below that frequency there is no propagation. For tubes made of quartz and aluminum Lucite, we found that the existence of the cutoff frequencies depend on the degree of anisotropic attenuation, i.e., if the axial quality factor is greater than the transverse quality factor, the modes propagate at all frequencies. In contrast to the elastic case, the Poynting vector and the energy velocity have a component along the radial direction, whose values depend on the transverse attenuation. The presence of intrinsic attenuation confines the energy near the (elastic) cutoff frequencies while the radial distribution of the energy is governed by the geometrical features of the cylinder. © 1998 Acoustical Society of America. [S0001-4966(98)02002-5]

PACS numbers: 43.20.Jr, 43.20.Ks [JEG]

INTRODUCTION

Laboratory measurements of wave propagation in cylindrical samples provide a method for estimating the elastic and anelastic properties of rocks and metals. For instance, intrinsic attenuation can be obtained from measurements in cylindrical bars (Kolsky, 1953; White, 1965; Blair, 1990; Tang, 1992). Moreover, analysis of wave propagation through hollow cylinders and tubes has many engineering applications (Soldatos, 1994), ranging from nondestructive evaluation of oil and gas pipelines, acoustic telemetry (Drumheller, 1993) to attenuation of waves inside rigid pipes containing acoustic liners (Greenspon and Singer, 1995). In the exploration industry, the interest resides in the propagation of pulses through drill strings, since these pulses are used as pilot signals for the data processing of seismograms generated by the roller cone bit (Rector and Hardage, 1992).

In this work, we compute the phase and energy velocities of torsional oscillations propagating in a lossy anisotropic hollow cylinder. The theory is a generalization of previous works (Mirsky, 1965a, b; Armenakas and Reitz, 1973; Carcione and Seriani, 1994) where a purely elastic cylinder was assumed.

I. THE GOVERNING EQUATIONS

The problem is solved in cylindrical coordinates (r, φ, z) and an axially symmetric hollow cylinder of interior and exterior radii a and b is assumed. This implies that the symmetry axis of the medium coincides with the axial axis of the cylinder (z axis). In this case, the wave field does not depend on the azimuthal variable φ .

^{a)}Electronic mail: jcarcione@ogs.trieste.it

^{b)}Electronic mail: gseriani@ogs.trieste.it

In absence of body forces, the equations describing the motion of torsional viscoelastic waves are

$$\rho \ddot{u}_\varphi = \partial_r \sigma_{\varphi r} + \partial_z \sigma_{\varphi z} + \frac{2}{r} \sigma_{\varphi r}, \quad (1)$$

$$\sigma_{\varphi r} = \dot{\psi}_{66} * \left(\partial_r u_\varphi - \frac{u_\varphi}{r} \right), \quad (2)$$

$$\sigma_{\varphi z} = \dot{\psi}_{44} * \partial_z u_\varphi, \quad (3)$$

where u_φ is the displacement component, $\sigma_{\varphi r}$ and $\sigma_{\varphi z}$ are the stress components, ρ is the density, and ψ_{44} and ψ_{66} are (time-dependent) relaxation functions. The symbol * denotes time convolution, ∂ spatial differentiation, and a dot above a variable time differentiation.

Since the torsional waves are decoupled from the quasi-compressional and quasi-shear motions, they can be described, as in the isotropic case, by a potential function ϕ ,

$$u_\varphi = -\partial_r \phi. \quad (4)$$

Substituting the stresses into the conservation equation (1), and using Eq. (4), we obtain the equation of motion,

$$\rho \ddot{\phi} = \dot{\psi}_{44} * \partial_{zz} \phi + \dot{\psi}_{66} * \left(\partial_{rr} \phi + \frac{1}{r} \partial_r \phi \right). \quad (5)$$

II. THE SOLUTION

The time-harmonic solution has the form

$$\phi = F(r, z) \exp(i\omega t), \quad (6)$$

where ω is the angular frequency and $\iota = \sqrt{-1}$. Substitution of Eq. (6) into Eq. (5) gives the generalized Helmholtz equation

$$\frac{1}{\beta^2 r} \partial_r(r \partial_r F) + \partial_{zz} F + \frac{\omega^2}{V^2} F = 0, \quad (7)$$

where

$$\beta = \sqrt{\frac{p_{44}}{p_{66}}} \quad (8)$$

and

$$p_{44} = \mathcal{F}(\dot{\psi}_{44}), \quad p_{66} = \mathcal{F}(\dot{\psi}_{66}) \quad (9)$$

are the complex stiffnesses, with the operator \mathcal{F} denoting the time Fourier transform. Moreover,

$$V = \sqrt{\frac{p_{44}}{\rho}} \quad (10)$$

is the complex body wave velocity along the symmetry axis of the medium.

The general solution for time-harmonic waves along the positive z direction is

$$\begin{aligned} \phi(r, z, t; \gamma, \omega) = & [A_0 J_0(kr) + B_0 Y_0(kr)] \\ & \times \exp[\iota(\omega t - \gamma z)], \end{aligned} \quad (11)$$

where J_0 and Y_0 are Bessel functions of the first and second kinds, respectively, and A_0 and B_0 are arbitrary constants. The radial and vertical wave numbers k and γ are related by

$$k^2 = \beta^2 \left(\frac{\omega^2}{V^2} - \gamma^2 \right). \quad (12)$$

Application of the boundary conditions at the inner and outer surfaces of the cylinder,

$$\sigma_{\varphi r}(r=a) = 0 \quad \text{and} \quad \sigma_{\varphi r}(r=b) = 0, \quad (13)$$

imply

$$A_0 J_2(ka) + B_0 Y_2(ka) = 0, \quad (14)$$

$$A_0 J_2(kb) + B_0 Y_2(kb) = 0, \quad (15)$$

where the following properties were used: $\partial_r J_0(kr) = -kJ_1(kr)$ and $(\partial_{rr} - r^{-1}\partial_r)J_0(kr) = k^2 J_2(kr)$. Making zero the determinant of the linear system gives the period or dispersion equation

$$J_2(ka)Y_2(kb) - J_2(kb)Y_2(ka) = 0. \quad (16)$$

Equation (16) is identical to the purely elastic period dispersion, where the roots $k_1, k_2, \dots, k_j, \dots$ are real. Abramowitz and Stegun (1964, p. 374) give an approximate formula for the root $q_j \equiv k_j a$ that can be used for $b/a < 3$. Here, we compute the exact roots by using the Mathematica software.

The velocity of the lowest torsional mode is not appropriately obtained from Eq. (16). This mode corresponds to $k=0$ and the displacement to a rotation of each transverse section of the cylinder as a whole about its center [see, for instance, Christensen (1982), p. 47]. The dispersion of this mode is caused by the intrinsic attenuation along the radial direction. The phase velocity is

$$c_p = [\text{Re}(V^{-1})]^{-1}, \quad (17)$$

where Re denotes the real part.

III. PHYSICAL VELOCITIES AND DISSIPATION FACTORS

The location of a pulse traveling in the axial direction requires the explicit calculation of the energy velocity, since the concept of group velocity loses its physical meaning. The presence of attenuation considerably distorts the modulation envelope of the pulse (e.g., Carcione, 1994). Besides the presence of intrinsic attenuation, the energy velocity displays local information not contained in the group velocity (see the discussion in Simmons *et al.*, 1992).

A. Phase velocity and attenuation factor

The phase velocity and attenuation factor versus frequency corresponding to the j mode are

$$c_p(\omega) = \frac{\omega}{\text{Re}(\gamma)} \quad \text{and} \quad \alpha(\omega) = -\text{Im}(\gamma), \quad (18)$$

where

$$\gamma(\omega) = \frac{\omega}{c_p} - \iota\alpha = \text{p.v.} \left(\frac{\omega^2}{V^2(\omega)} - \frac{k_j^2}{\beta^2(\omega)} \right)^{1/2}, \quad (19)$$

with p.v. denoting the principal value and Im the imaginary part.

The calculation of the phase velocity and attenuation versus wavelength is not straightforward. Since

$$\lambda(\omega) \equiv G(\omega) = \frac{2\pi}{\text{Re}[\gamma(\omega)]}, \quad (20)$$

$\omega = G^{-1}(\lambda)$ and a formal solution is

$$c_p(\lambda) = \frac{\lambda}{2\pi} G^{-1}(\lambda) \quad \text{and} \quad \alpha = \text{Im}\{\gamma[G^{-1}(\lambda)]\}. \quad (21)$$

However, relation (20) is, in general, not invertible. The most simple procedure is to plot the pairs $[c_p(\omega), \lambda(\omega)]$ and $[\alpha(\omega), \lambda(\omega)]$.

B. Energy velocity and quality factor

Calculation of the energy velocity and quality factor requires energy considerations. The Umov–Poynting theorem, or energy balance equation, for time-harmonic fields in anisotropic-viscoelastic media (Carcione and Cavallini, 1993) is

$$\text{div } \mathbf{P} - 2\iota\omega(\langle \epsilon_s \rangle - \langle \epsilon_v \rangle) + \omega \langle \epsilon_d \rangle = 0, \quad (22)$$

where \mathbf{P} is the complex Umov–Poynting vector defined as

$$\mathbf{P} = -\frac{1}{2} \boldsymbol{\Sigma} \cdot \dot{\mathbf{u}}^*, \quad (23)$$

with $\boldsymbol{\Sigma}$ the stress tensor,

$$\langle \epsilon_v \rangle = \frac{1}{4} \rho \dot{\mathbf{u}}^T \cdot \dot{\mathbf{u}}^* \quad (24)$$

is the time-average kinetic energy density,

$$\langle \epsilon_s \rangle = \text{Re}(\mathcal{E}) \quad \text{and} \quad \langle \epsilon_d \rangle = 2 \text{Im}(\mathcal{E}) \quad (25)$$

are the time-average stored and dissipated energy densities, respectively, with

$$\mathcal{E} = \frac{1}{4} \mathbf{S}^T \cdot \mathbf{p} \cdot \mathbf{S}^* \quad (26)$$

the complex energy density, \mathbf{S} the strain vector, and \mathbf{p} the complex stiffness matrix. The asterisk used as superscript denotes complex conjugation, the symbol \cdot , ordinary matrix multiplication, and the superscript T , transpose.

The Poynting vector is

$$\mathbf{P} = -\frac{1}{2}(\sigma_{\varphi z}\hat{\mathbf{e}}_z + \sigma_{\varphi r}\hat{\mathbf{e}}_r)u_\varphi^* \quad (27)$$

Substituting the potential (11) into Eq. (4) and using Eq. (14) gives

$$u_\varphi = kA_0R_1 \exp(-\alpha z)\exp[i\omega(t-z/c_p)], \quad (28)$$

where

$$R_i(kr) = J_i(kr) - \frac{J_2(ka)}{Y_2(ka)} Y_i(kr), \quad i=1,2. \quad (29)$$

Note that $R_2(ka)=0$ and by virtue of the dispersion equation (16), $R_2(kb)=0$. The stress components are given by Eqs. (2) and (3),

$$\sigma_{\varphi z} = -i\gamma k p_{44} A_0 R_1 \exp(-\alpha z)\exp[i\omega(t-z/c_p)], \quad (30)$$

$$\sigma_{\varphi r} = -k^2 p_{66} A_0 R_2 \exp(-\alpha z)\exp[i\omega(t-z/c_p)]. \quad (31)$$

Then,

$$\mathbf{P} = \frac{1}{2}\omega k^2 |A_0|^2 R_1 (p_{44}\gamma R_1 \hat{\mathbf{e}}_z - i p_{66} k R_2 \hat{\mathbf{e}}_r) \exp(-2\alpha z). \quad (32)$$

From Eq. (26), the complex energy density is

$$\mathcal{E} = \frac{1}{4}(p_{44}|S_{\varphi z}|^2 + p_{66}|S_{\varphi r}|^2), \quad (33)$$

where

$$S_{\varphi z} = \partial_z u_\varphi \quad \text{and} \quad S_{\varphi r} = \partial_r u_\varphi - \frac{u_\varphi}{r} \quad (34)$$

are the strain components. Using Eq. (28) we obtain

$$\mathcal{E} = \frac{1}{4}k^2 |A_0|^2 (p_{44}|\gamma|^2 R_1^2 + p_{66}k^2 R_2^2) \exp(-2\alpha z). \quad (35)$$

The kinetic energy density is simply

$$\langle \epsilon_v \rangle = \frac{1}{4}\rho\omega^2 k^2 |A_0|^2 R_1^2 \exp(-2\alpha z). \quad (36)$$

In contrast to unbounded homogeneous and elastic media, the average kinetic and potential energy densities are different in elastic cylinders. This is shown in the Appendix.

The energy velocity \mathbf{v}_e is the ratio of the average power flow density $\text{Re}(\mathbf{P})$ to the mean energy density $\langle \epsilon_v + \epsilon_s \rangle$. Then,

$$\begin{aligned} \mathbf{v}_e &= \frac{\text{Re}(\mathbf{P})}{\langle \epsilon_v + \epsilon_s \rangle} \\ &= \frac{2\omega[\text{Re}(\gamma p_{44})R_1^2 \hat{\mathbf{e}}_z + k \text{Im}(p_{66})R_1 R_2 \hat{\mathbf{e}}_r]}{\rho\omega^2 R_1^2 + |\gamma|^2 R_1^2 \text{Re}(p_{44}) + k^2 R_2^2 \text{Re}(p_{66})}. \end{aligned} \quad (37)$$

Equation (37) becomes

$$\mathbf{v}_e = \frac{2\omega[\text{Re}(\gamma p_{44})\hat{\mathbf{e}}_z + k \text{Im}(p_{66})(R_2/R_1)\hat{\mathbf{e}}_r]}{\rho\omega^2 + |\gamma|^2 \text{Re}(p_{44}) + k^2 \text{Re}(p_{66})(R_2/R_1)^2}. \quad (38)$$

Note that the dependence on the radial variable r is contained in R_2/R_1 . While the energy velocity is constant for a plane wave in unbounded media, it is a function of r for

cylindrical systems and has a component in the radial direction. This component vanishes in the purely elastic case, since $\text{Im}(p_{66})=0$. At $r=a$ and $r=b$, R_2 vanishes and using Eq. (10),

$$\mathbf{v}_e = \frac{2\omega \text{Re}(\gamma V^2)}{\omega^2 + |\gamma|^2 \text{Re}(V^2)} \hat{\mathbf{e}}_z. \quad (39)$$

The quality factor can be obtained as the ratio of twice the stored energy to the dissipated energy, giving

$$Q = \frac{2\langle \epsilon_s \rangle}{\langle \epsilon_d \rangle} = \frac{\text{Re}(p_{44})|\gamma|^2 + k^2 \text{Re}(p_{66})(R_2/R_1)^2}{\text{Im}(p_{44})|\gamma|^2 + k^2 \text{Im}(p_{66})(R_2/R_1)^2}. \quad (40)$$

At $r=a$ and $r=b$ Eq. (40) reduces to

$$Q = \frac{\text{Re}(p_{44})}{\text{Im}(p_{44})}, \quad (41)$$

that is, the quality factor of the shear body wave traveling along the symmetry axis of the medium.

IV. EXAMPLES

We use a phenomenological model based on a viscoelastic rheology. The theory assumes a single standard linear solid element describing the anelastic deformations associated with the axial direction ($\nu=1$) and the radial direction ($\nu=2$). We take

$$p_{44} = c_{44}M_1, \quad p_{66} = c_{66}M_2, \quad (42)$$

where the complex moduli can be expressed as

$$M_\nu(\omega) = \frac{\sqrt{Q_{0\nu}^2 + 1} - 1 + i\omega Q_{0\nu}\tau_0}{\sqrt{Q_{0\nu}^2 + 1} + 1 + i\omega Q_{0\nu}\tau_0}. \quad (43)$$

The quality factor Q_ν , associated with of each moduli, is equal to the real part of M_ν divided by its imaginary part. The curve $Q_\nu^{-1}(\omega)$ has its peak at $\omega_0 = 1/\tau_0$, and the value of Q_ν at the peak is $Q_{0\nu}$. The high-frequency limit corresponds to the elastic case with $M_\nu \rightarrow 1$. The relaxation functions associated with the complex stiffnesses are $\psi_{44} = c_{44}\chi_1$ and $\psi_{66} = c_{66}\chi_2$, where

$$\chi_\nu(t) = \left[\frac{\tau_+^{(\nu)}}{\tau_-^{(\nu)}} - \left(\frac{\tau_-^{(\nu)}}{\tau_+^{(\nu)}} - 1 \right) \exp(-t/\tau_+^{(\nu)}) \right] H(t), \quad (44)$$

with $H(t)$ the Heaviside function, and

$$\tau_\pm^{(\nu)} = \frac{\tau_0}{Q_{0\nu}} [\sqrt{Q_{0\nu}^2 + 1} \pm 1]. \quad (45)$$

We introduce the anisotropic loss parameter

$$\eta = \frac{Q_{01}}{Q_{02}} \quad (46)$$

and assume that $\eta = 1.2\beta_\infty$, where $\beta_\infty = \beta(\omega \rightarrow \infty) = \sqrt{c_{44}/c_{66}}$.

We consider two materials (see Thomsen, 1986); quartz, with $c_{44} = 53.21$ GPa, $\rho = 2.65$ gr/cm³, $\beta_\infty = 1.21$ and $Q_{01} = 100$; and aluminum-Lucite composite with $c_{44} = 3.4$ GPa, $\rho = 1.86$ gr/cm³, $\beta_\infty = 0.53$ and $Q_{01} = 10$. The calculations are carried out for samples having $a = 1$ cm and $b = 2$ cm. If q_j

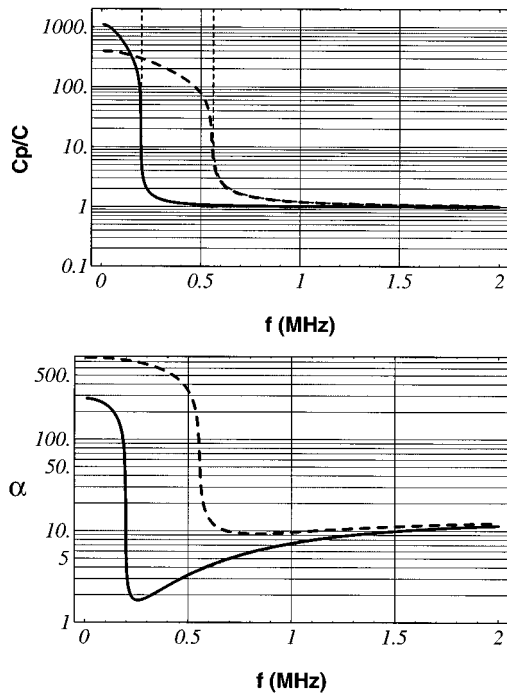


FIG. 1. Quartz: normalized phase velocity and attenuation versus frequency corresponding to the first and third propagation modes (continuous and broken lines, respectively). The normalization constant is the axial elastic velocity $c = (c_{44}/\rho)^{1/2}$. The thin broken lines are the respective elastic phase velocities.

$=k_j a$, the first three roots of the dispersion equation (16) are $q_1 = 3.4069$, $q_2 = 6.4278$, and $q_3 = 9.5228$. These roots are independent of the material properties.

A. Quartz

Normalized phase velocity and attenuation versus frequency corresponding to the first and third propagation modes are represented in Fig. 1 (continuous and broken lines, respectively). The thin broken lines are the respective elastic phase velocities, that tend to infinity at the cutoff frequencies $f_c = 201$ kHz and $f_c = 561$ kHz [$\gamma = 0$ in Eq. (12)]. There are no cutoff frequencies in the viscoelastic case, although the attenuations below f_c are so high that wave propagation is precluded in practice.

Figure 2 represents the normalized displacement field (32) for mode 3 as a function of frequency and radial distance (from $r = a$ to $r = b$). The upper picture corresponds to $z = 0$ and the lower picture to $z = 0.1$ m. In this case, the strong attenuation below the (elastic) cutoff frequency prevents any particle motion. Moreover, the viscoelasticity causes the dissipation at high frequencies.

The modulus of the normalized energy velocity, versus frequency and radial distance, is represented in Fig. 3. The surface practically shows the axial component of the energy velocity vector, since the radial component is very small. The energy velocity vanishes where there is no particle motion (see Fig. 2). These minima in the energy velocity are not due to the elasticity but to the geometrical features of the cylinder. As can be seen, the energy velocity displays local information not contained in the group velocity. It can be shown that the elastic energy velocity, when defined as the

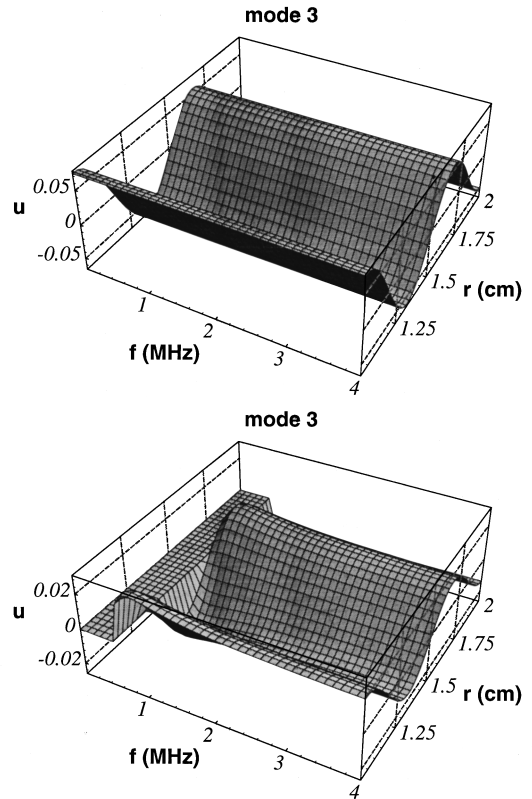


FIG. 2. Quartz: normalized displacement field for mode 3 as a function of frequency and radial distance. The upper picture corresponds to $z = 0$ and the lower picture to $z = 0.1$ m. The normalization constant is the displacement at $f = 1$ MHz, $r = a$ and $z = 0$.

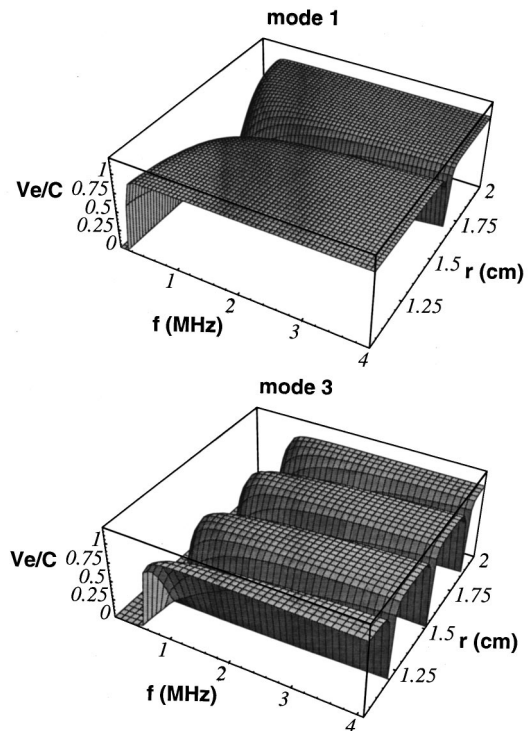


FIG. 3. Quartz: modulus of the normalized energy velocity, versus frequency and radial distance. The normalization constant is the axial elastic velocity $c = (c_{44}/\rho)^{1/2}$.

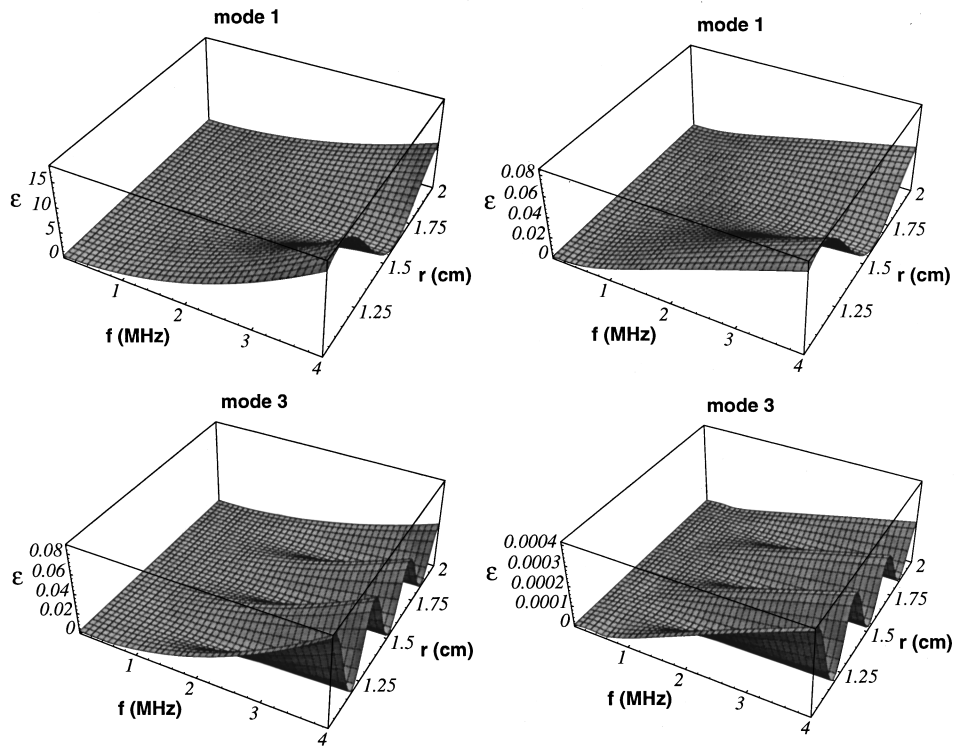


FIG. 4. Quartz: distribution of the energy along the radial distance, as a function of frequency. The left pictures correspond to the mean energy density $\langle \epsilon_v + \epsilon_s \rangle$ and the right pictures are the dissipated energy densities $\langle \epsilon_d \rangle$. The normalization constant ϵ_0 is the total energy at $f=1$ MHz, $r=a$ and $z=0$.

ratio of the time average of the power per cross section and the time average of the total energy per unit length of cylinder, equals the group velocity (e.g., Achenbach, 1973, pp. 214).

Figure 4 shows the distribution of the energy along the radial distance, as a function of frequency. The left pictures correspond to the mean energy density $\langle \epsilon_v + \epsilon_s \rangle$ and the right pictures are the dissipated energy densities $\langle \epsilon_d \rangle$. The first

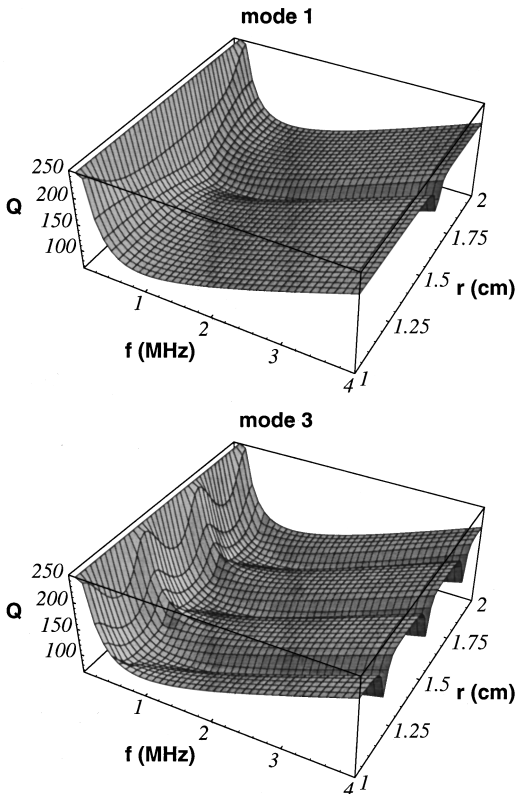


FIG. 5. Quartz: quality factors versus frequency and radial distance.

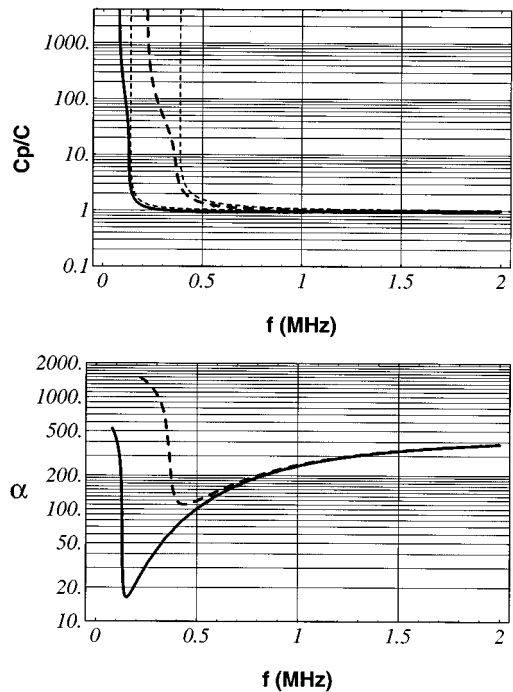


FIG. 6. Aluminum Lucite: phase velocity and attenuation curves versus frequency, corresponding to the first and third propagation modes (continuous and broken lines, respectively). The normalization constant is the axial elastic velocity $c = (c_{44}/\rho)^{1/2}$. The thin broken lines are the respective elastic phase velocities.

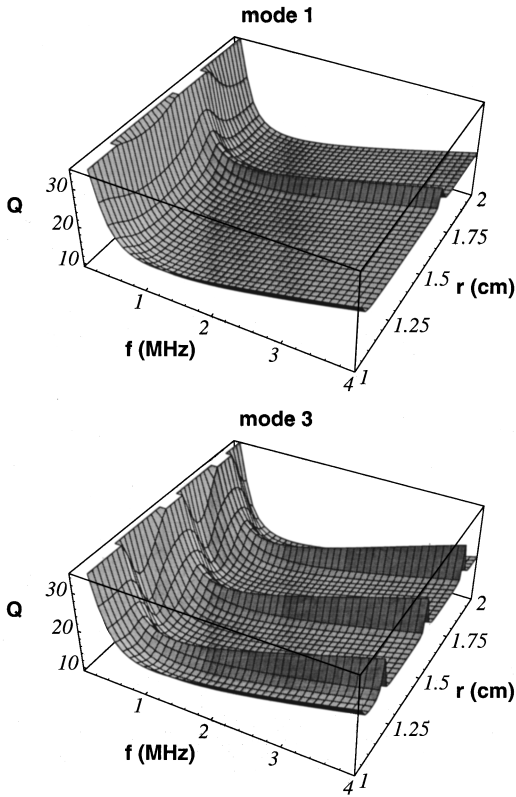


FIG. 7. Aluminum Lucite: quality factors versus frequency and radial distance.

mode is approximately 200 times stronger than the third mode, and both modes carry more energy at the high frequencies. This happens at the onset of the perturbation ($z = 0$), since for $z \neq 0$ the high frequencies are attenuated by the viscoelastic effects and the motion is confined near the (elastic) cutoff frequencies (Fig. 2).

Finally, the quality factors are represented in Fig. 5. They have a minimum value at ω_0 , the location of the relaxation peak. The location of the minima along the radial direction coincide with the positions of zero particle motion (see Fig. 2).

It is important to distinguish between two attenuation effects. One is of viscoelastic nature, that is reflected in the shape of the quality factors surface as a function of frequency. The other is geometrical effect that produce the minima along the radial direction and causes the strong attenuation below the elastic cutoff frequencies (see Fig. 1).

B. Aluminum Lucite

In contrast to quartz, this material has $\eta < 1$, and therefore, the attenuation is higher along the axial direction. Due to this fact, the physics of wave propagation is different. Figure 6 shows the phase velocity and attenuation curves versus frequency. In this case, there is a cutoff frequency even in the presence of anelasticity. The displacements energy densities and energy velocity surfaces are similar to those of quartz. The quality factors are represented in Fig. 7. They have a minimum value at ω_0 , the location of the relaxation peak, and, unlike quartz, the surfaces presents maxima along the radial direction.

APPENDIX: ENERGY BALANCE

In unbounded media $\text{div } \mathbf{P} = -2\boldsymbol{\alpha} \cdot \mathbf{P}$ (Carcione and Cavallini, 1993). If there are no losses, Eq. (22) implies that the average kinetic energy equals the average potential energy. An analysis based on Eq. (22) shows that this is not the case for cylinders. In order to verify the energy balance Eq. (22) we explicitly calculate the divergence of the Poynting vector (32). This can be written as

$$\mathbf{P} = P_r \hat{\mathbf{e}}_r + P_z \hat{\mathbf{e}}_z, \quad (\text{A1})$$

where

$$P_r = p_r R_1 R_2 \exp(-2\alpha z), \quad p_r = -\frac{i}{2} \omega k^3 |A_0|^2 p_{66} \quad (\text{A2})$$

and

$$P_z = p_z R_1^2 \exp(-2\alpha z), \quad p_z = \frac{1}{2} \omega k^2 |A_0|^2 \gamma p_{44}. \quad (\text{A3})$$

We have that

$$\text{div } \mathbf{P} = \partial_r P_r + \frac{P_r}{r} + \partial_z P_z. \quad (\text{A4})$$

For computing the radial derivatives we use the following recurrence relation for the cylinder functions $\mathcal{C}_\nu(z)$, where z is complex and ν any number (not necessarily an integer):

$$z \mathcal{C}'_\nu = \nu \mathcal{C}_\nu - z \mathcal{C}_{\nu+1} = -\nu \mathcal{C}_\nu + z \mathcal{C}_{\nu-1}. \quad (\text{A5})$$

We obtain

$$\partial_r P_r = p_r k \left(R_1^2 - R_2^2 - \frac{1}{r} R_1 R_2 \right) \exp(-2\alpha z). \quad (\text{A6})$$

Then,

$$\text{div } \mathbf{P} = [(k p_r - 2\alpha p_z) R_1^2 - k p_r R_2^2] \exp(-2\alpha z). \quad (\text{A7})$$

Note that in the elastic case the kinetic energy is not equal to the potential energy (in average), since

$$\langle \epsilon_s \rangle - \langle \epsilon_v \rangle = -\frac{1}{4} k^4 |A_0|^2 c_{66} (R_1^2 - R_2^2). \quad (\text{A8})$$

However, using properties of the cylinder functions, it can be shown that

$$\int [R_1^2(kr) - R_2^2(kr)] r dr = kr R_1(kr) R_2(kr), \quad (\text{A9})$$

Then, integration of Eq. (A8) over the cross section of the cylinder is zero since $R_2(ka) = 0$ and $R_2(kb) = 0$. This is in agreement with the result obtained by Achenbach (1973, pp. 214).

- Abramowitz, M., and Stegun, I. A., Eds. (1964). *Handbook of Mathematical Functions*, Applied Mathematical Series 55, p. 374, National Bureau of Standards, Washington, D. C.
- Achenbach, J. D. (1973). *Wave Propagation in Elastic Solids* (North-Holland, Amsterdam).
- Armenakas, A., and Reitz, E. S. (1973). "Propagation of harmonic waves in orthotropic circular cylindrical shells," *J. Appl. Mech.* **30**, 168–174.
- Blair, D. P. (1990). "The longitudinal pulse velocity in finite cylindrical cores," *J. Acoust. Soc. Am.* **88**, 1123–1131.
- Carcione, J. M. (1994). "Wavefronts in dissipative anisotropic media," *Geophysics* **59**, 644–657.
- Carcione, J. M., and Cavallini, F. (1993). "Energy balance and fundamental relations in anisotropic viscoelastic media," *Wave Motion* **18**, 11–20.
- Carcione, J. M., and Seriani, G. (1994). "Torsional oscillations of anisotropic hollow circular cylinders," *Acoust. Lett.* **18**, 99–102.
- Christensen, R. M. (1982). *Theory of Viscoelasticity. An Introduction* (Academic, New York).
- Drumheller, D. S. (1993). "Attenuation of sound waves in drill strings," *J. Acoust. Soc. Am.* **94**, 2387–2396.
- Greenspan, J. E., and Singer, E. G. (1995). "Propagation in fluids inside thick viscoelastic cylinders," *J. Acoust. Soc. Am.* **97**, 3502–3509.
- Kolsky, H. (1953). *Stress Waves in Solids* (Clarendon, Oxford), pp. 136–141.
- Mirsky, I. (1965a). "Wave propagation in transversely isotropic hollow circular cylinders, Part I: Theory," *J. Acoust. Soc. Am.* **37**, 1016–1021.
- Mirsky, I. (1965b). "Wave propagation in transversely isotropic hollow circular cylinders, Part II: Numerical results," *J. Acoust. Soc. Am.* **37**, 1022–1026.
- Rector III, J. W., and Hardage, B. A. (1992). "Radiation pattern and seismic waves generated by a working roller-cone drill bit," *Geophysics* **57**, 1319–1333.
- Simmons, J. A., Drescher-Krasicka, E., and Wadley, H. N. G. (1992). "Leaky axisymmetric modes in infinite clad rods," *J. Acoust. Soc. Am.* **92**, 1061–1090.
- Soldatos, K. P. (1994). "Review of three dimensional dynamic analyses of circular cylinders and cylindrical shells," *Appl. Mech. Rev.* **47**, 501–516.
- Tang, X. M. (1992). "A waveform inversion technique for measuring elastic wave attenuation in cylindrical bars," *Geophysics* **57**, 854–859.
- Thomsen, L. (1986). "Weak elastic anisotropy," *Geophysics* **51**, 1954–1966.
- White, J. E. (1965). *Seismic Waves, Radiation, Transmission and Attenuation* (McGraw-Hill, New York).

On the velocities of localized vibration modes in immersed solid wedges

Victor V. Krylov

Centre for Research into the Built Environment, The Nottingham Trent University, Burton Street, Nottingham NG1 4BU, United Kingdom

(Received 10 July 1997; accepted for publication 27 October 1997)

The approximate theory of localized elastic waves in immersed solid wedges earlier developed for wedges with small values of the apex angle [V. V. Krylov, Proc. IEEE Ultrason. Symp., Cat. #94, CHO 793–796 (1994)] has predicted that the effect of water loading results in velocity decrease for wedge modes travelling in the subsonic regime of wave propagation. The results of this theory, in particular the absolute values of wedge wave velocity calculated for slender Plexiglas wedges, agree well with the corresponding experiments. The present study demonstrates that for relative values of wedge wave velocity, as compared with those for wedges in vacuum, this theory provides good quantitative agreement with the experiments on Plexiglas samples also for large values of the apex angle. In addition to this, a generalization of the theory is undertaken to describe the effect of heavier wedge material and a supersonic regime of wave propagation. The corresponding results show good agreement with the existing velocity measurements in immersed brass wedges. © 1998 Acoustical Society of America. [S0001-4966(98)03102-6]

PACS numbers: 43.20.Jr [ANN]

INTRODUCTION

In a recently published work, De Billy¹ carried out measurements of the velocities of localized antisymmetric modes propagating along tips of elastic solid wedges immersed in water. The velocities of such modes (also called wedge acoustic waves) were measured on Plexiglas and brass samples with the apex angle varying from 20 to 90 degrees. For Plexiglas samples, for which a subsonic regime of wedge wave propagation takes place, the experiments showed a noticeable decrease in velocities due to water loading. As was mentioned in Ref. 1, this was in qualitative agreement with the predictions of the approximate analytical theory earlier developed by the present author for slender immersed wedges in subsonic regime of wave propagation.² However, no direct comparison with the theory was given in Ref. 1, probably because it was not expected from the theory to provide accurate results for large values of the wedge apex angle. Note in this connection that measurements of the absolute values of wedge wave velocities carried out by Chamuel³ on Plexiglas wedges with apex angles varying from about 8 to 13 degrees have shown excellent agreement with the theory.² Latest finite element calculations by Hladky-Hennion *et al.*⁴ carried out for Plexiglas wedges with angles in the range from 20 to 90 degrees demonstrated good quantitative agreement with the experiments.¹ However, in the case of brass wedges, which provide both subsonic and supersonic propagation regimes, only subsonic regime has been calculated.⁴

In what follows we demonstrate that (a) for relative values of wedge wave velocity, as compared with those for wedges in vacuum, the approximate analytical theory developed for slender immersed wedges² provides good quantitative agreement with the experiments on Plexiglas samples also for large values of the apex angle; and (b) a generalization of this theory to describe the effect of heavier wedge

material and a supersonic regime of wave propagation explains the results of the velocity measurements for immersed brass wedges.¹

I. THEORY

We remind the reader that the approximate theory of localized elastic waves in immersed solid wedges developed in Ref. 2 is based on the geometrical acoustics approach considering a slender wedge as a plate with a local variable thickness $d = x\Theta$, where Θ is the wedge apex angle and x is the distance from the wedge tip measured in the middle plane (Fig. 1). The velocities c of the localized wedge modes propagating in y direction are determined in the geometrical acoustics approximation as solutions of the Bohr–Sommerfeld type equation^{5–7}

$$\int_0^{x_t} [k^2(x) - \beta^2]^{1/2} dx = \pi n, \quad (1)$$

where $\beta = \omega/c$ is the yet unknown wave number of a wedge mode, $k(x)$ is a current local wave number of a flexural wave in a plate of variable thickness, $n = 1, 2, 3, \dots$ is the mode number, and x_t is the so called ray turning point being determined from the equation $k^2(x) - \beta^2 = 0$.

For example, in the case of wedge in vacuum $k(x) = 12^{1/4} k_p^{1/2} (\Theta x)^{-1/2}$, $x_t = 2\sqrt{3} k_p / \Theta \beta^2$, and $k_p = \omega/c_p$, where ω is circular frequency, $c_p = 2c_l(1 - c_l^2/c_t^2)^{1/2}$ is the so called plate wave velocity, c_l and c_t are propagation velocities of longitudinal and shear acoustic waves in plate material. Then, taking the integral in Eq. (1) and solving the resulting algebraic equation yields the extremely simple analytical expression for wedge wave velocities:^{5–7}

$$c = c_p n \Theta / \sqrt{3}. \quad (2)$$

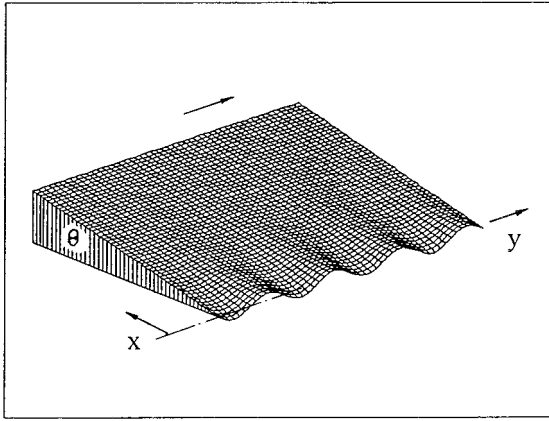


FIG. 1. Antisymmetric wedge waves.

Expression (2) agrees well with the other theories⁸⁻¹⁰ and with the experimental results.⁸ Note that, although, strictly speaking, the geometrical acoustics approach is not valid for the lowest order wedge mode ($n=1$),⁶ in practice it provides quite accurate results for wedge wave velocities in this case as well. The analytical expressions for amplitude distributions of wedge modes are rather cumbersome⁵⁻⁷ and are not displayed here.

To calculate the velocities of wedge waves in a wedge imbedded in liquid one has to make use of the expression for a plate wave local wave number $k(x)$ which takes into account the effect of liquid loading.² The starting point to derive $k(x)$ for this case is the well known dispersion equation for the lowest order flexural mode of a plate imbedded in liquid:

$$\frac{1}{2} \frac{\omega^4}{c_l^4 k^4} - \frac{1}{6} (c_l^2 - c_t^2) \frac{d^2}{c_l^2 c_t^2} \omega^2 + \frac{\rho_f}{\rho_s} \frac{\omega^4}{c_l^4 k^4} \frac{1}{d \sqrt{k^2 - \omega^2/c_f^2}} = 0, \quad (3)$$

where d is the plate thickness, $k = \omega/c$ is the wave number of propagating flexural mode, c is its phase velocity, $k_l = \omega/c_l$ and $k_t = \omega/c_t$ are respectively the wave numbers of longitudinal and shear acoustic waves in plate material, ρ_s and ρ_f are respectively the mass densities of solid and liquid. Note that, using the notation for flexural rigidity $D = (\rho_s c_p^2/12)d^3$, one can easily transform Eq. (3) to the more familiar form which is often used in the literature for flexural waves in thin plates faced to liquid at both sides.^{11,12} In the absence of liquid ($\rho_f = 0$) Eq. (3) reduces to the well known dispersion relation for flexural waves in a thin plate in vacuum.

In further consideration it is convenient to distinguish two characteristic cases of the relation between the mass densities of liquid and wedge material: $\rho_f/\rho_s \approx 1$ and $\rho_f/\rho_s \ll 1$.

For the case $\rho_f/\rho_s \approx 1$ typical for light solid materials in water we limit our analysis by subsonic regime of wave propagation ($k > \omega/c_f$). Moreover, for simplicity, we impose even more severe restriction considering very slow propagating plate flexural modes ($k \gg \omega/c_f$). In such a case one can use the approximation of incompressible liquid, i.e., neglect the ω/c_f term in (3), and the solution of Eq. (3) versus ω yields

$$\omega = \frac{1}{\sqrt{3}} \frac{c_t}{c_l} k^{5/2} \sqrt{\rho_s} \frac{d^{3/2}}{\sqrt{\rho_s k d + 2\rho_f}} \sqrt{c_l^2 - c_t^2}. \quad (4)$$

For $kd \ll 1$ typical for thin plates one can also neglect the term $\rho_s k d$ in Eq. (4), keeping in mind that $\rho_f/\rho_s \approx 1$. Then, taking into account that for a plate of variable thickness representing a wedge $d = d(x) = x\Theta$ and solving (4) versus k , one obtains the following expression for the local flexural wave number $k(x)$ describing the effect of liquid loading:

$$k(x) = \left[\sqrt{6} \frac{c_l}{c_t} \frac{1}{\sqrt{c_l^2 - c_t^2}} \frac{\sqrt{\rho_f}}{\sqrt{\rho_s}} \frac{\omega}{(x\Theta)^{3/2}} \right]^{2/5}. \quad (5)$$

Substituting (5) into (1) and introducing the nondimensional notations $\eta = c/c_t$ and $z = k_t d = x\Theta \omega/c_t$ one can derive the following equation versus η :²

$$\int_0^{(A\eta)^{5/3}} \left[\frac{A^2}{z^{6/5}} - \frac{1}{\eta^2} \right]^{1/2} dz = \pi n \theta, \quad (6)$$

where

$$A = 6^{1/5} (\rho_f/\rho_s)^{1/5} (1 - c_t^2/c_l^2)^{-1/5} \\ = 6^{1/5} (\rho_f/\rho_s)^{1/5} [2(1 - \sigma)]^{1/5} \quad (7)$$

is a nondimensional parameter dependent on the relation between the mass densities of liquid and solid ρ_f/ρ_s [the power of the mass density ratio 1/5 in Eq. (7) corrects the earlier misprinted value of 2/5 in Ref. 2] and on the Poisson ratio σ . Eq. (6) can be easily solved numerically using any appropriate algorithm, e.g., standard Mathcad package.² Note, however, that by change of variable $z = A^{5/3} \eta^{5/3} x$, it may be further simplified as

$$A^{5/3} \eta^{2/3} \int_0^1 (x^{-6/5} - 1)^{1/2} dx = \pi n \theta. \quad (8)$$

[The author's attention to this way of simplification of Eq. (6) has been drawn by A. N. Norris.] After numerical calculation of the integral in Eq. (8), one can easily derive the explicit analytical expression for wedge wave velocities:

$$c = c_l A^{-5/2} D^{-3/2} (\pi n)^{3/2} \Theta^{3/2}, \quad (9)$$

where $D = \int_0^1 (x^{-6/5} - 1)^{1/2} dx = 2.102$. According to Eq. (9), the dependence of c on Θ for immersed slender wedges is proportional to $\Theta^{3/2}$. This agrees well with the empirical power law $\Theta^{1.522}$ established by Chamuel³ by matching the numerical solution of Eq. (6).

In the case $\rho_f/\rho_s \ll 1$ typical for heavy solid materials in water and for any solids in gases, one can solve Eq. (3) approximately, to the first perturbation order versus ρ_f/ρ_s , seeking a solution for k in the form

$$k = k_{(0)} + k_{(1)}, \quad (10)$$

where $k_{(0)}$ is the solution of Eq. (3) for a plate in vacuum ($\rho_f/\rho_s = 0$) and $k_{(1)}$ is yet unknown small correction term which takes into account the effect of liquid loading. Substituting (10) into (3) and retaining terms of only the first order versus ρ_f/ρ_s , one can derive the following approximate expression for k :

$$k = k_{(0)} \left[1 + \frac{\rho_f}{2\rho_s d} \left(k_{(0)}^2 - \frac{\omega^2}{c_f^2} \right)^{-1/2} \right]. \quad (11)$$

Obviously, for $\rho_f/\rho_s=0$ Eq. (11) goes over to the well known expression for a wave number $k_{(0)}$ of a flexural plate wave in vacuum $k_{(0)} = [\sqrt{3}\omega c_l / (c_t \sqrt{c_l^2 - c_t^2} d)]^{1/2}$. The second term, proportional to ρ_f/ρ_s , gives a small correction $k_{(1)}$, describing liquid loading. It is seen that this term becomes imaginary in supersonic regime of wave propagation, when a local wave number of a plate wave in vacuum exceeds the wave number of sound in liquid. Note that Eq. (11) is not valid for very small values of d . It also becomes invalid for those values of d for which the velocity of flexural wave is equal to the velocity of sound in liquid. In both these cases the contribution of the second term in square brackets of (11) is not small and the perturbation solution can no longer be applied. Regarding wedge waves, this means that the above considered perturbation approach is not applicable for wedges with very small apex angles θ and for velocities of wedge waves approaching the velocity of sound in liquid.

To apply the Bohr–Sommerfeld type equation for calculating wedge wave velocities in the case considered, one should follow the well known way of generalization of geometrical acoustics for complex wave numbers¹³ and substitute real part of Eq. (11) into Eq. (1). Doing so and using the nondimensional notations $\eta = c/c_t$ and $z = k_t d = x\Theta \omega/c_t$, one can derive the following equation versus η :

$$\int_0^{B\eta^2} \left[\frac{B}{z} \operatorname{Re} \left(1 + \frac{\rho_f}{\rho_s} \frac{1}{z \sqrt{(B/z) - (c_t^2/c_f^2)}} \right) - \frac{1}{\eta^2} \right]^{1/2} dz = \pi n \theta, \quad (12)$$

where $B = \sqrt{3}c_l/\sqrt{c_l^2 - c_t^2}$. Note that the above described geometrical acoustics approach also allows calculation of the wedge wave energy loss factor 2γ due to the radiation of sound into liquid, so that the wave number of attenuated wedge waves can be written in the form $\beta' = \beta(1 + i\gamma) = (\omega/c)[1 + i\gamma]$. However, calculation of γ is out of the scope of this paper devoted to wedge wave velocities only.

II. RESULTS

The results of numerical calculations of wedge wave velocities for Plexiglas wedges in water obtained according to Eqs. (6) or (9) ($\rho_s = 1180 \text{ kg/m}^3$, $\rho_f = 1000 \text{ kg/m}^3$, $c_f = 1478 \text{ m/s}$, $c_l = 2732 \text{ m/s}$, $c_t = 1363 \text{ m/s}$, $\sigma = 0.334$; these yields $A = 1.466$) are shown in Fig. 2 for different apex angles. Following Ref. 1, they are presented as the ratio $c_{\text{wat}}/c_{\text{vac}}$ between the velocities of the first order localized modes in immersed wedges and in the same wedges in vacuum (solid curve). Note that the slope of the theoretical curve $c_{\text{wat}}/c_{\text{vac}}$ displayed in Fig. 2 decreases as the wedge angle increases. This reflects the fact that, according to Eqs. (2) and (9), the function $c_{\text{wat}}/c_{\text{vac}}$ is proportional to $\Theta^{1/2}$. The corresponding experimental results¹ are displayed in the same picture. It is clearly seen that the agreement between the theory and the experiment is remarkably good, although for values of the wedge apex angle larger than 30 degrees the geometrical acoustics theory is not expected to be

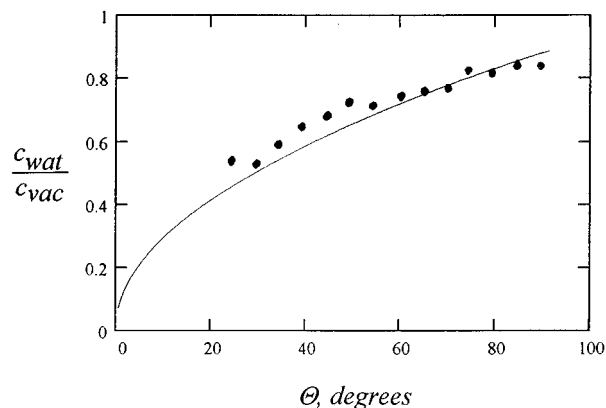


FIG. 2. Theoretically calculated ratio $c_{\text{wat}}/c_{\text{vac}}$ for Plexiglas wedges as a function of the apex angle (solid curve); points indicate the corresponding experimental results Ref. 1.

accurate.^{5,6} The most likely reason for such a good agreement is that, because of the presentation of the results in terms of relative values of wedge wave velocity, as compared with wedges in vacuum, the corresponding systematic errors caused by the limits of applicability of thin plate theory to plates of relatively high local thickness occurring for large apex angles Θ are expected to be the same for immersed wedges and for wedges in vacuum. Therefore, they might cancel each other.

The velocities for brass wedges in water ($\rho_s = 8600 \text{ kg/m}^3$, $\rho_f = 1000 \text{ kg/m}^3$, $c_f = 1478 \text{ m/s}$, $c_l = 4350 \text{ m/s}$, $c_t = 2127 \text{ m/s}$, $\sigma = 0.343$; these yields $B = 1.986$) were calculated in the process of numerical solution of Eq. (12). In doing so, we introduced a small artificial damping under square root in the second term of (12)—to avoid singularity when the value of local flexural wave velocity becomes equal to the velocity of sound in liquid. The results are shown in Fig. 3 as the ratio $c_{\text{wat}}/c_{\text{vac}}$ between the velocities of the first order wedge mode in immersed wedges and in the same wedges in vacuum (solid curve). Note that a small local minimum around $\Theta = 47$ degrees corresponding to the damped singularity indicates the values of the apex angle where the above theory is not accurate. It is not clear whether

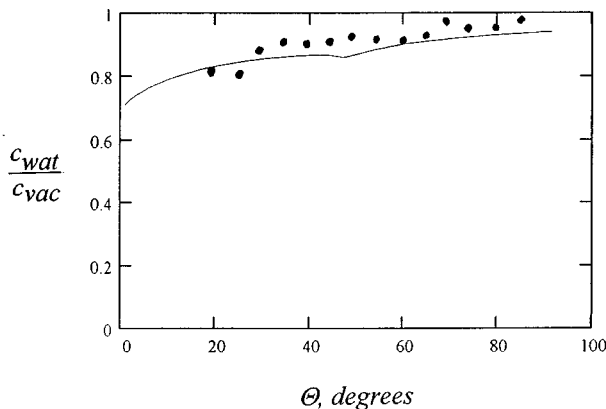


FIG. 3. Theoretically calculated ratio $c_{\text{wat}}/c_{\text{vac}}$ for brass wedges as a function of the apex angle (solid curve); points indicate the corresponding experimental results Ref. 1.

this small minimum is present in reality or it is just a sequence of limitation of the perturbational approach considered. The corresponding experimental results¹ displayed in the same picture fluctuate significantly due to experimental errors and do not clarify this question. Therefore, there is no point on this stage to investigate it in more detail. Regarding the average behavior of experimental points, it is fair to say that the agreement between the theory and the experiment in Fig. 3 is good enough for wedge angles from 20 to 90 degrees used in the experiment. One can expect that the reason for such a good agreement for brass wedges is the same as in the case of Plexiglas wedges. Making more definite conclusions on the limits of applicability of the simple thin plate theory approximation for both these cases would require using more advanced theories of plate flexural vibrations that goes beyond the scope of this paper.

III. CONCLUSIONS

Resuming the above, one can say that the geometrical acoustics approach to the theory of localized vibration modes in immersed solid wedges provides clear understanding of the phenomena involved and gives results which are in good agreement with the existing experiments for both subsonic and supersonic regimes of wave propagation. In particular, it has been demonstrated that for relative values of wedge wave velocity, as compared with those for wedges in vacuum, the theory provides good quantitative agreement with the experiments on Plexiglas samples also for large values of the apex angle. A generalization of the theory to describe the effect of heavier wedge material and a supersonic regime of wave propagation has been carried out. The results show good agreement with the existing velocity measurements for immersed brass wedges.

ACKNOWLEDGMENTS

The author would like to thank the referees of the paper for useful comments and the Associate Editor, Professor A.

N. Norris, for his idea of deriving the analytical expression (9) for velocities of localized vibration modes propagating in wedges made of light materials.

- ¹M. de Billy, "On the influence of loading on the velocity of guided acoustic waves in linear elastic wedges," *J. Acoust. Soc. Am.* **100**, 659–662 (1996).
- ²V. V. Krylov, "Propagation of wedge acoustic waves along wedges imbedded in water," *Proc IEEE Ultrasonics Symposium*, Cannes, France, Cat. #94, CHO 793–796 (1994).
- ³J. R. Chamuel, "Flexural edge waves along free and immersed elastic waveguides," in *Review of Progress in Quantitative Nondestructive Evaluation*, Vol. 16, edited by D. O. Thompson and D. E. Chimenti (Proc. 16th Symp. Quant. Nondestruct. Eval., 28 July–2 August 1996, Brunswick, Maine) (Plenum, New York, 1996), pp. 129–136.
- ⁴A.-C. Hladky-Hennion, P. Langlet, and M. de Billy, "Finite element analysis of the propagation of acoustic waves along waveguides immersed in water," *J. Sound Vib.* **200**, 519–530 (1997).
- ⁵V. V. Krylov, "Conditions for validity of the geometrical-acoustic approximation in application to waves in an acute-angle solid wedge," *Sov. Phys. Acoust.* **35**, 176–180 (1989).
- ⁶V. V. Krylov, "Geometrical-acoustics approach to the description of localized vibrational modes of an elastic solid wedge," *Sov. Phys. Tech. Phys.* **35**, 137–140 (1990).
- ⁷V. V. Krylov and D. F. Parker, "Harmonic generation and parametric mixing in wedge acoustic waves," *Wave Motion* **15**, 185–200 (1992).
- ⁸P. E. Lagasse, I. M. Mason, and E. A. Ash, "Acoustic surface waveguides—analysis and assessment," *IEEE Trans. Sonics Ultrason.* **20**, 143–154 (1973).
- ⁹S. L. Moss, A. A. Maradudin, and S. L. Cunningham, "Vibrational edge modes for wedges of arbitrary interior angles," *Phys. Rev. B* **8**, 2999–3008 (1973).
- ¹⁰J. McKenna, G. D. Boyd, and R. N. Thurston, "Plate theory solution for guided flexural acoustic waves along the tip of a wedge," *IEEE Trans. Sonics Ultrason.* **21**, 178–186 (1974).
- ¹¹M. C. Junger and D. Feit, *Sound, Structures and their Interaction* (Acoustical Society of America, Woodbury, NY, 1993).
- ¹²D. G. Crighton, A. P. Dowling, J. E. Ffowcs Williams, M. Heckl, and F. G. Leppington, *Modern Methods in Analytical Acoustics* (Springer-Verlag, London, 1992).
- ¹³Yu. A. Kravtsov and Yu. I. Orlov, *Geometrical Optics of Inhomogeneous Media*, Springer Ser. Wave Phen., Vol. 6 (Springer-Verlag, Berlin, 1990).

Temporal deconvolution of laser-generated longitudinal acoustic waves for optical characterization and precise longitudinal acoustic velocity evaluation

Franck Enguehard and Lionel Bertrand

Département de Génie Physique, École Polytechnique de Montréal, C. P. 6079, Succ. Centre-Ville, Montréal, Québec H3C 3A7, Canada

(Received 25 January 1996; revised 25 June 1997; accepted 23 September 1997)

The laser thermoelastic generation of ultrasound is a promising technique with many potential applications, but it is also a complicated process with many physical phenomena involved. Contrary to a conventional piezoelectric transducer generation, which is a surface phenomenon, a laser generation can activate acoustic sources within the material by optical penetration of the excitation wavelength, resulting in asynchronous wave arrivals at a given point. More generally, in the ideal case of a nondispersive isotropic material, the laser-ultrasonics displacement signals result from temporal convolutions between optical penetration, laser pulse duration, and laser spot extension effects. In this paper, a deconvolution technique is presented that extracts the laser pulse duration contribution from the experimental displacement signals. This deconvolution scheme applied to one-dimensional experiments, in which the laser excitation is spread over a sufficiently large area on the front side of the sample, allows the measurement of the optical absorption coefficient of the material at the excitation wavelength and also a precise evaluation of its longitudinal acoustic velocity. © 1998 Acoustical Society of America. [S0001-4966(98)04701-8]

PACS numbers: 43.20.Ye, 43.20.Gp, 43.35.Yb [JEG]

INTRODUCTION

Because of its noncontact nature, the laser-ultrasonics technique circumvents several important limitations of classical ultrasonics. But on the other hand, this technique, when used in the nondestructive thermoelastic regime, is not very efficient: Contrary to a highly directional acoustic source like a piezoelectric transducer, for example, a laser-activated thermoelastic source launches all types of acoustic waves in all the directions of the half-space, which dramatically reduces the efficiency of the generation in one given direction.

The ability of the material under study to bury thermal expansion sources has already been demonstrated to be a key factor for an improved efficiency of the laser ultrasound generation.¹⁻³ Depending on the physical properties of the material, this burying phenomenon can result from optical penetration^{1,2} or thermal diffusion.^{1,3} It gives rise to pulse-shaped longitudinal acoustic arrivals on the rear side of the sample (the first of these pulses being called the precursor), and it transforms a rather unfavorable longitudinal wave emissivity pattern into a highly directional one in the direction normal to the impinged surface.⁴

Thermal burying is usually a slow process compared to characteristic acoustic durations: the thermal diffusion length during an observation time of a few μs is only a few μm . Consequently, this process as the cause for larger precursors can be observed only on materials that are highly thermally conducting and highly optically opaque to the excitation wavelength. Metals belong to this category, and they have been at the center of the first theoretical works.^{3,5-7} On the other hand, optical burying is an instantaneous process and, depending on the matching of the excitation wavelength to the optical properties of the material, optical penetrations of

tens or even hundreds of μm can be reached, giving rise to huge longitudinal acoustic pulses. Thermal burying then becomes negligible compared to optical burying, which governs completely the thermoelastic generation.

The temporal information present in the precursor generated by optical burying has already been studied,^{2,4,8} and has been shown to result from temporal convolutions between the spatially distributed thermal expansion force (directly resulting from optical penetration) and the temporally and spatially distributed laser excitation (i.e., the pulse duration and the spot size, respectively). Optical characterization through the temporal analysis of the precursor is thus a complicated task, unless one can get rid of at least one of the two convolutions related to the laser excitation. A solution in this direction consists of focusing the laser beam so that the excitation becomes spatially pointlike, but the risk of damaging the sample obliges to use very low excitation energies and the displacements are too weak to be measured. On the other hand, extending the laser beam so that the irradiation can be considered as uniformly distributed is a satisfactory alternative: If the spot size-related convolution is still present (it is even extreme), this experimental configuration can easily be represented by a simple analytical one-dimensional (1-D) model in which the spot size-related convolution still exists but is no more apparent. In the following, we will develop this model, show how we can get rid of the last laser excitation-related convolution that is still apparent (i.e., the pulse duration), and present a technique of exploitation of the temporal shape of the convolution-free precursor for the quantitative evaluation of the optical penetration depth (or of the optical absorption coefficient) of the material at the excitation wavelength. Moreover, we will show that it is possible, with the help of the convolution-free normal displace-

ment signal, to evaluate the longitudinal acoustic velocity of the material with a precision of a few %, i.e., a precision attainable with classical ultrasonics but which to our knowledge has not yet been reached with laser-ultrasonics because of convolution-related problems and also because of the complexity of analyzing laser-ultrasonics signals in “non-1-D” configurations. Finally, we will validate our characterization schemes by performing two experiments with two different excitation durations (a “short” one and a “long” one) on a material with well-known optical properties.

I. THEORY

A. The analytical 1-D model

Let us consider an infinite orthotropic plate, cut in such a way that the normal to its surfaces is one of its principal axes, and impinged on its front side by a uniformly distributed laser pulse. In this configuration, the displacement vector is normal to the surfaces, and the temperature elevation and the mechanical displacement fields are functions of only one space variable, the depth in the plate. With the assumption of negligible thermal diffusion, the temperature elevation field $\Delta\theta$ reproduces the optical absorption space–time profile within the plate; its analytical expression is

$$\Delta\theta(z,t) = \frac{\beta I_0}{\rho C_p} e^{-\beta z} \int_0^t f(\tau) d\tau. \quad (1)$$

In this expression, z is the depth in the plate, and t the time. β , ρ , and C_p are physical properties of the plate, respectively, its optical absorption coefficient at the excitation wavelength, its density, and its specific heat. I_0 is the energy per surface unit “entering” the plate, which is equal to $(1-R)I_i$, where I_i is the incident energy per surface unit emitted by the excitation laser and R the reflection coefficient of the impinged front side at the excitation wavelength. Finally, the function $f(t)$ is the temporal profile of the laser pulse; this function is normalized through the relation:

$$\int_0^\infty f(t) dt = 1. \quad (2)$$

The component u_z normal to the surfaces of the mechanical displacement field is obtained by the resolution of its acoustic wave propagation equation containing a thermal expansion source term; this equation is

$$\frac{1}{v^2} \frac{\partial^2 u_z}{\partial t^2} = \frac{\partial^2 u_z}{\partial z^2} - \chi \frac{\partial(\Delta\theta)}{\partial z}. \quad (3)$$

In this equation, v is the longitudinal acoustic velocity of the plate in the z direction, and χ indicates an “apparent” thermal expansion coefficient of the plate, related to its rigidity and thermal expansion tensors [$\chi = (3\lambda + 2\mu)\alpha/(\lambda + 2\mu)$ for the particular case of an isotropic material, where λ and μ are the Lamé coefficients and α the linear thermal expansion coefficient]. Equation (3), plus the classical two initial conditions:

$$u_z = 0 \quad \text{and} \quad \frac{\partial u_z}{\partial t} = 0 \quad \text{at} \quad t = 0 \quad (4)$$

and the classical two boundary conditions:

$$\sigma_{zz} = 0 \quad \text{at} \quad z = 0 \quad \text{and} \quad z = L \quad (5)$$

[σ_{zz} being the (z,z) component of the stress tensor and L the thickness of the plate], allows the determination of the analytical expression of the normal displacement field $u_z(z,t)$.⁸ In the Laplace domain, this analytical expression is

$$U_z(z,s) = F(s) \times U_z^0(z,s) \quad (6)$$

with

$$U_z^0(z,s) = u_0 \frac{1/\beta v}{(s/\beta v)^2 - 1} \times \left[\frac{e^{-\beta L} \cosh(sz/v) - \cosh(s(L-z)/v)}{\sinh(sL/v)} + \frac{\beta v}{s} e^{-\beta z} \right] \quad (7)$$

and

$$u_0 = \frac{\chi I_0}{\rho C_p}. \quad (8)$$

In relations (6)–(8), s is the Laplace variable, $U_z(z,s)$ and $F(s)$ are the Laplace transforms of $u_z(z,t)$ and $f(t)$, respectively, and u_0 is a parameter group that has units of distance. Relation (6) shows that when the laser pulse becomes infinitely short, $f(t)$ becomes the Dirac function centered at $t = 0$, $F(s)$ is equal to 1, and $U_z(z,s)$ is equal to the function $U_z^0(z,s)$ defined in (7). Consequently, $U_z^0(z,s)$ is the Laplace transform of the normal displacement field $u_z^0(z,t)$ that would be generated in the plate if the laser excitation, instead of presenting a temporal profile $f(t)$ spread over a certain duration, was strictly instantaneous.

B. Procedure to extract the pulse duration-related convolution from the normal displacement curve

According to relation (6), $u_z(z,t)$, which is the quantity measured experimentally ($z = L$ for a rear-side detection), appears to be equal to the convolution product between the temporal profile $f(t)$ of the laser pulse and the normal displacement $u_z^0(z,t)$ that would be observed at the same point if the laser excitation was instantaneous:

$$u_z(z,t) = f(t) * u_z^0(z,t). \quad (9)$$

Then, a very simple way to cancel out the laser pulse duration effects in the experimental signal consists in deconvolving it as follows. The experimental temporal profile $f(t)$ of the laser pulse is recorded at the same time as the experimental normal displacement curve $u_z(z,t)$. As these two experimental signals are recorded over the same duration with the same sampling rate, a numerical Laplace transformation algorithm [based on the fast Fourier transform (FFT) algorithm] allows the evaluation of the Laplace transforms $F(s)$ and $U_z(z,s)$ over the same set $\{s_n\}$ of the Laplace variable. It

is then possible to evaluate the Laplace transform $U_z^0(z,s)$ over this set $\{s_n\}$ with the help of relation (6), and to deduce the convolution-free normal displacement curve $u_z^0(z,t)$ with the help of a numerical inverse Laplace transformation algorithm. That way, the curve $u_z^0(z,t)$ is evaluated over exactly the same time sequence as the initial curve $u_z(z,t)$. This deconvolution scheme has the advantage of involving the experimental temporal profile $f(t)$, so that no assumption needs to be made about an approximate analytical expression for it.

C. Evaluation of the longitudinal acoustic velocity and of the optical absorption coefficient from the convolution-free normal displacement curve

The analytical expression of $u_z^0(z,t)$ can be determined by analytical inverse Laplace transformation of $U_z^0(z,s)$,⁸ this expression is

$$u_z^0(z,t) = u_0 \times (u_z^0)^*(z,t) \quad (10)$$

with

$$\begin{aligned} (u_z^0)^*(z,t) = & e^{-\beta z} (\cosh(\beta vt) - 1) + e^{-\beta L} \sum_{n=0}^{\infty} H\left(t - \frac{(2n+1)L+z}{v}\right) \sinh\left[\beta v\left(t - \frac{(2n+1)L+z}{v}\right)\right] \\ & + e^{-\beta L} \sum_{n=0}^{\infty} H\left(t - \frac{(2n+1)L-z}{v}\right) \sinh\left[\beta v\left(t - \frac{(2n+1)L-z}{v}\right)\right] \\ & - \sum_{n=0}^{\infty} H\left(t - \frac{2nL+z}{v}\right) \sinh\left[\beta v\left(t - \frac{2nL+z}{v}\right)\right] - \sum_{n=0}^{\infty} H\left(t - \frac{2(n+1)L-z}{v}\right) \sinh\left[\beta v\left(t - \frac{2(n+1)L-z}{v}\right)\right], \end{aligned} \quad (11)$$

where the function $H(t)$ is the Heaviside function.

A dimensional analysis of expression (11) reveals that the dimensionless normal displacement $(u_z^0)^*(z,t)$ is a function of the two dimensionless space-time variables z/L and vt/L and of one dimensionless parameter $\beta L = L/\delta$ (δ being the optical penetration depth of the excitation wavelength in the material) that compares the thickness of the plate to the optical penetration. Figure 1 displays two dimensionless normal displacement curves $(u_z^0)^*(z/L, vt/L, \beta L)$ on the rear side ($z/L=1$) of the plate: one for a weakly absorbing material ($\beta L=1$) and one for a strongly absorbing one ($\beta L=10$).

As can be seen in this figure, the normal displacement on the rear side of the plate is a periodic function of time with a period equal to $2L/v$, and it exhibits peaks that are related to the multiple longitudinal wave arrivals. These longitudinal peaks reach their maxima at times $(2n+1)L/v$ (with n integer), so that the time delay between two successive peaks is exactly $2L/v$: this property thus allows a precise evaluation of the longitudinal acoustic velocity v .

Besides, the temporal broadening of the peaks appears to be closely related to the optical penetration phenomenon: the more the excitation wavelength penetrates in the material, the larger the full width at half maximum (FWHM) of the peaks. This temporal broadening related to the optical penetration is easy to interpret.⁸ When the excitation wavelength penetrates in the material down to a depth δ , it instantaneously activates thermal expansion sources over this depth. The normal displacement step functions emitted by these distributed sources arrive in an asynchronous way on the rear side of the plate, and the time delay between the first step function arrival (coming from the source located at $z=\delta$) and the last step function arrival (coming from the source

located at $z=0$) is δ/v . Hence this simple interpretation indicates that the FWHM of the longitudinal peaks should be proportional to $\delta/v = 1/\beta v$. This conclusion is confirmed by a rigorous analytical study of expression (11), which shows that the FWHM $\Delta t_{1/2}$ is expressed as

$$\Delta t_{1/2} = \frac{2}{\beta v} \ln\left(\frac{2}{1+e^{-\beta L}}\right). \quad (12)$$

The majority of our samples being opaque to the excitation radiation, $\exp(-\beta L) \ll 1$, and expression (12) reduces to:

$$\Delta t_{1/2} = \frac{\ln 4}{\beta v} \quad (13)$$

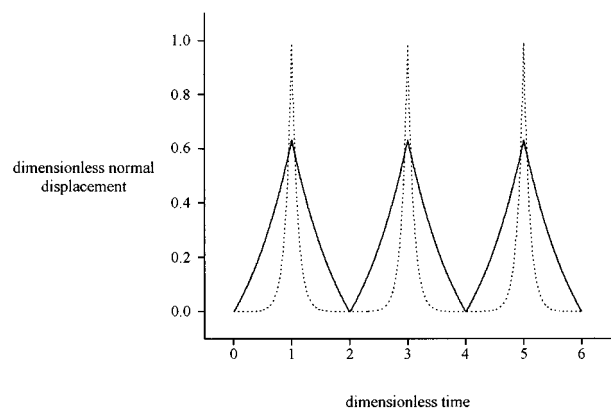


FIG. 1. Dimensionless normal displacement curves on the rear side of the plate for a weakly absorbing material ($\beta L=1$) (solid line), and for a strongly absorbing one ($\beta L=10$) (dashed line).

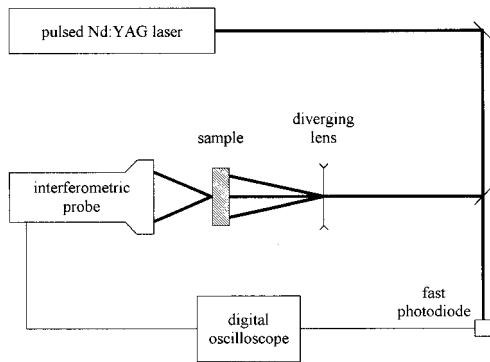


FIG. 2. Sketch of the experimental apparatus.

which allows the quantitative determination of the optical absorption coefficient β from the experimental measurement of the FWHM $\Delta t_{1/2}$.

Finally, it appears in Fig. 1 that the amplitude of the longitudinal peaks is also related to the value of the optical absorption coefficient. This amplitude a^0 can be derived from expressions (10) and (11), and is

$$a^0 = (1 - e^{-\beta L})u_0. \quad (14)$$

The amplitude a^0 is thus in the general case a fraction of the quantity u_0 , this fraction $(1 - e^{-\beta L})$ corresponding to the portion of the “entered” radiative flux which is absorbed by the bulk of the plate. For samples that are opaque to the excitation radiation, $\exp(-\beta L) \ll 1$, and the amplitude a^0 of the longitudinal peaks is exactly equal to u_0 , the expression of which is given by (8). This expression might then be the starting point of a technique for the quantitative measurement of the thermal expansion coefficient α through the experimental evaluation of the amplitude a^0 and the derivation of the value of the “apparent” thermal expansion coefficient χ .

II. EXPERIMENT

A. The experimental apparatus

The experimental apparatus is sketched in Fig. 2. Its main components are a pulsed Nd:YAG laser for the optical generation of ultrasound on the front side of the sample, a fast photodiode of 10-GHz bandpass for both triggering the data acquisition and recording the temporal profile of the laser pulse, a diverging lens of 10-cm focal distance for spreading the laser irradiation over a sufficiently large area on the front side of the sample so that the 1-D excitation regime can be reached, an interferometric probe for the optical detection of ultrasound on the rear side of the sample, and a digital oscilloscope for the data acquisition.

The pulsed Nd:YAG laser is composed of an oscillator part and an amplifier part. Depending on the voltage applied to the flash lamp of the oscillator part, the duration of the laser pulse can be varied from approximately 12 ns in the nominal operation mode, which corresponds to the maximum voltage applicable to the lamp, to about 100 ns for very low lamp voltages. This possibility of varying the pulse duration will allow us in the following to observe the intensities

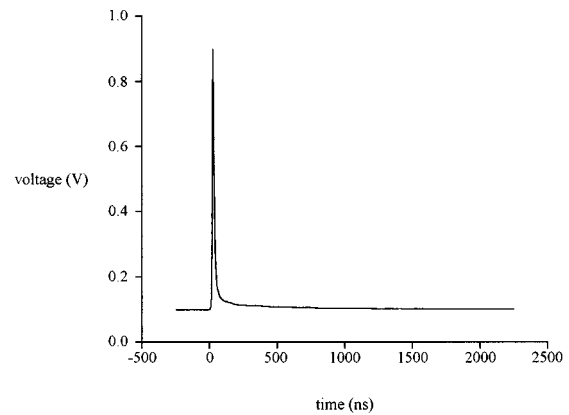


FIG. 3. “Short” pulse duration experiment, experimental temporal profile of the laser pulse.

of the pulse duration-related convolutions in the experimental normal displacement signals, and to test our deconvolution scheme. Besides, the laser is used in a multimode configuration instead of a monomode one for two reasons. First, the emitted energy must be quite high, as this energy is spread over a large area on the front side of the sample. Second, the multimode configuration, after the propagation of the laser beam through the amplifier Nd:YAG rod and then over a distance of approximately 2 m in the ambient air, produces a laser beam with a quite uniform energy surface distribution over a disk approximately 6 mm in diameter, which is quite appropriate for a 1-D excitation.

The interferometric probe is an Ultra-Optec OP35-I/O heterodyne interferometer that can perform quantitative measurements of both normal and parallel (in one given direction) displacements as functions of time over an area as small as a focused He-Ne laser beam. The detection limit of this interferometer is of the order of the Å, and its bandpass spreads from 1 kHz to 35 MHz.

Finally, the LeCroy 9450A digital oscilloscope records the signals with a sampling period of 2.5 ns, digitizes them over 16 bits, and averages them.

In the two experiments that follow, the sample used is a 3.0-mm-thick plate made of a Schott NG-9 colored glass. The optical absorption coefficient of this material at the Nd:YAG wavelength is given by the manufacturer to be $\beta = 3000 \text{ m}^{-1}$.

B. First experiment—“short” pulse duration

For this experiment, the nominal operation mode voltage was applied to the oscillator flash lamp, producing a laser pulse with an energy of 162 mJ. With such a laser intensity, the diverging lens could be placed at quite a large distance (approximately 30 cm) from the sample, ensuring an important spatial spreading of the laser beam while still keeping a good signal-to-noise ratio for the normal displacement detection.

As explained earlier, the experimental temporal profile of the laser pulse and the experimental normal displacement curve were recorded over the same duration with the same sampling rate. Figure 3 displays the former curve, as given

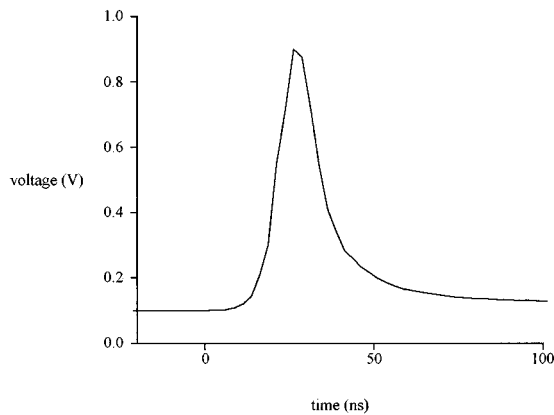


FIG. 4. Enlargement of Fig. 3 over the time interval $-20 \text{ ns} \leq t \leq 100 \text{ ns}$.

by the fast photodiode. The duration of the recording of this curve (equal to $2.5 \mu\text{s}$), imposed by the duration of the recording of the normal displacement curve, may look inadequate to the optimal determination of the temporal profile of the laser pulse, but it is to be reminded that no information was lost during this recording, since the sampling period of the digital oscilloscope for such recording durations remains equal to 2.5 ns . An enlargement of Fig. 3 over the time interval $-20 \text{ ns} \leq t \leq 100 \text{ ns}$ is shown in Fig. 4. From this figure, the FWHM of the pulse can be correctly evaluated: it is 14 ns .

In order for the experimental profile of Fig. 3 to become the normalized profile $f(t)$ of relations (1), (2), and (9), it was first shifted in the voltage direction (in order for its ground level to be brought to 0), then divided by its integral over the whole recording duration. Finally, a numerical Laplace transformation was applied to it. The experimental normal displacement curve recorded on the rear side of the sample is displayed in Fig. 5. This curve exhibits two intense longitudinal peaks that, for the moment, result from temporal convolutions between optical penetration and laser pulse duration effects.

In order to study to which extent the finite size of the surface irradiation affects the temporal features of the two longitudinal peaks, we simulated the experiment with the help of a

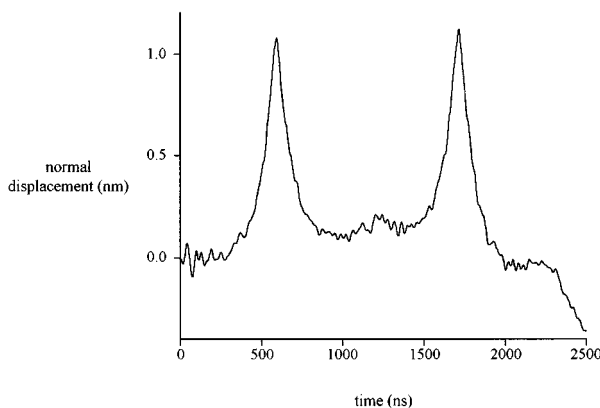


FIG. 5. Experimental normal displacement curve recorded on the rear side of the sample.

quasianalytical 3-D simulation model.⁹ This model solves the acoustic wave propagation equations containing thermal expansion source terms over an infinite plate of finite thickness with the restrictive assumptions of an axisymmetrical configuration and negligible thermal diffusion. The radial and normal displacement fields are derived analytically in the Hankel and Laplace spaces, and the only numerical step consists in performing numerical inverse Hankel and Laplace transformations to bring back the two displacement fields in the real spaces. A dimensional study of the acoustic wave propagation equations shows that, in the case of a uniformly distributed laser pulse impinging on the front side of an isotropic sample over a disk of radius Σ , the mechanical displacement field \mathbf{u} can be expressed as

$$\mathbf{u}(r, z, t) = u_0 \times \mathbf{u}^*(r, z, t). \quad (15)$$

In this relation, r is the radial space coordinate, and the quantity u_0 has units of distance, so that the mechanical displacement field \mathbf{u}^* is dimensionless. The expression of u_0 is given in (8), but this time the energy per surface unit “entering” the plate I_0 is limited to the irradiation disk and hence is equal to $E_0/\pi\Sigma^2$ where E_0 is the energy “entering” the plate. Finally, the dimensionless field \mathbf{u}^* can be shown to be a function of seven dimensionless parameters: (i) the three dimensionless space and time variables r/Σ , z/L , and vt/L , (ii) one dimensionless parameter related to the acoustic properties of the material, namely its Poisson coefficient ν , and (iii) three dimensionless parameters Σ/L , βL , and $\nu\tau/L$ (τ being a characteristic time of the temporal profile of the laser pulse⁹) that fully describe the features of the laser excitation. Further details about the model are reported in the Appendix.

The Poisson coefficient ν of our glass sample was evaluated to be 0.22 through classical piezoelectric transducer measurements of the longitudinal and shear acoustic velocities. Concerning the irradiation radius Σ , this quantity was estimated with the help of very simple geometrical optics. The sample being located a distance d away from the diverging lens of focal distance f , the radius Σ of the beam impinging on the sample is related to the one σ at the entrance of the diverging lens through the relation:

$$\frac{\Sigma}{\sigma} = 1 + \frac{d}{f}. \quad (16)$$

The values of the experiment ($\sigma = 3 \text{ mm}$, $d = 30 \text{ cm}$, and $f = 10 \text{ cm}$) yielded $\Sigma = 12 \text{ mm}$. Finally, the characteristic time τ of the temporal profile of the laser pulse was derived from its FWHM⁹ and was found to be 5.7 ns . All the data of the experiment being known, we calculated with the help of the 3-D simulation model the theoretical dimensionless normal displacement curve at the epicenter on the rear side of the sample $u_z^*(r/\Sigma = 0, z/L = 1, vt/L)$ generated by the uniform irradiation of its front side over a disk of radius Σ , and compared this curve to the one that would be obtained in the case of a truly uniformly distributed laser pulse presenting the same energy surface density [expressions (6)–(8) of the 1-D model]. This comparison is displayed in Fig. 6.

One notices first that the top curve of Fig. 6 is very similar to the experimental one of Fig. 5, which is a good sign of the validity of the parameters entered as data of the

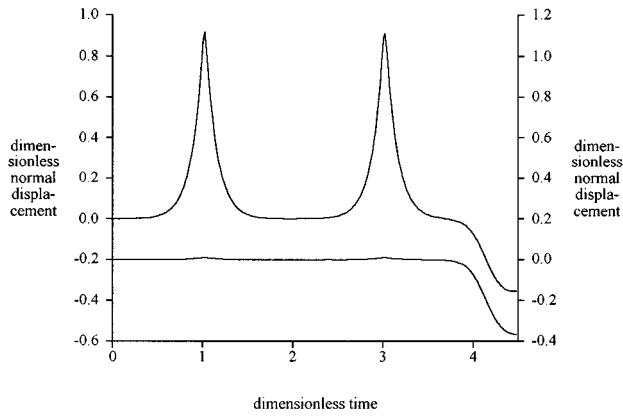


FIG. 6. Finite extension of the laser excitation and deviation from the 1-D model, theoretical dimensionless normal displacement curve at the epicenter on the rear side of the sample generated by the uniform irradiation of its front side over a disk of radius Σ (top curve, left scale), and this curve minus the one that would be obtained in the case of a truly uniformly distributed laser pulse presenting the same energy surface density (bottom curve, right scale).

3-D simulation model. Second, the bottom curve of Fig. 6 reveals that the normal displacement generated by the finite extension irradiation deviates from the 1-D model only after a dimensionless time vT/L that is approximately equal to 4 in Fig. 6 and that can be guessed to be a growth function of the laser spot extension dimensionless parameter Σ/L . These preceding two results could be expected. In an isotropic material, the acoustic information propagates with a velocity that cannot exceed the longitudinal acoustic velocity v . Consequently, from the point of view of the mechanical displacement at a given point of the sample, there is no difference between a uniform irradiation over a finite extension S and a truly uniformly distributed irradiation as long as there has not been enough time for the mechanical effects of the thermal expansion sources located outside S in the 1-D configuration to reach the point. In the case of a uniform irradiation over a disk of radius Σ , the mechanical displacement at the epicenter on the rear side of the sample is not different from the one that would result from a truly uniformly distributed excitation until a time T defined by

$$T = \frac{\sqrt{L^2 + \Sigma^2}}{v}, \quad \text{i.e.,} \quad \frac{vT}{L} = \sqrt{1 + \left(\frac{\Sigma}{L}\right)^2}. \quad (17)$$

The laser spot extension dimensionless parameter Σ/L of the experiment is 4, and relation (17) gives $vT/L \approx 4.1$, which means that the extension of the laser excitation in the experiment is sufficient to ensure that the normal displacement recorded at the epicenter on the rear side of the sample will not deviate from the 1-D model before a time T equal to 4.1 times the delay for a longitudinal trip through the sample. Consequently, the first two longitudinal arrivals will not be affected by “non-1-D” effects. Indeed, the two peaks set apart, the experimental normal displacement of Fig. 5 remains approximately equal to 0 over the time interval $0 \leq t \leq 2300$ ns that includes the two peaks. The “non-1-D” effects, which are related to the finite size and also the imperfect uniformity of the surface irradiation, start to affect the experimental normal displacement signal at $t = 2300$ ns, in-

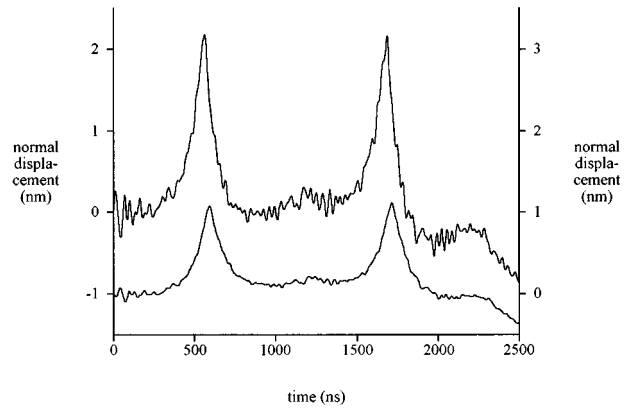


FIG. 7. Comparison of the convolution-free normal displacement curve (top curve, left scale) to the initial experimental curve of Fig. 5 (bottom curve, right scale).

cluding important negative displacements that constitute the “wash.”

A numerical Laplace transformation was applied to the experimental normal displacement curve of Fig. 5, this Laplace transform was then divided by the one of the experimental temporal profile of Fig. 3, and finally the convolution-free normal displacement curve was constructed with the help of a numerical inverse Laplace transformation.

Figure 7 compares the convolution-free normal displacement curve to the initial experimental curve of Fig. 5. First, one notices that the convolution-free curve is slightly noisier than the experimental one. This noise emergence is a direct consequence of the division of the Laplace transform of the experimental normal displacement curve by the one of the experimental temporal profile of the laser pulse, which results in an amplification of the high frequencies whereas the low frequencies are unchanged. Hence the high-frequency noise of the experiment happens to be amplified by the deconvolution operation. Second, one notices that the peaks of the convolution-free curve are larger and narrower than the ones of the experimental curve. Here again, these two points are direct consequences of the deconvolution operation: When the energy of the laser pulse is released instantaneously instead of over a certain duration, the longitudinal peaks are no longer flattened and broadened by temporal convolution ef-

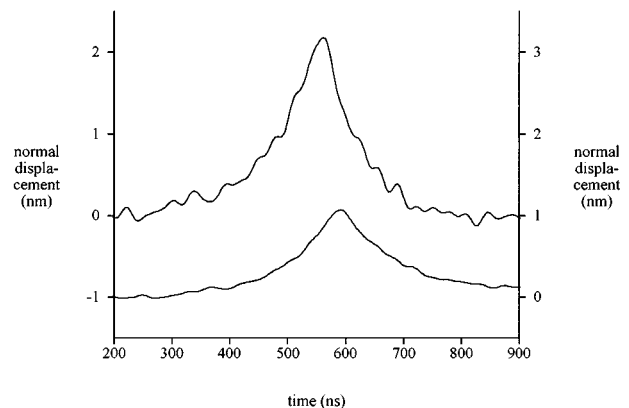


FIG. 8. Enlargement of Fig. 7 over the time interval $200 \text{ ns} \leq t \leq 900 \text{ ns}$.

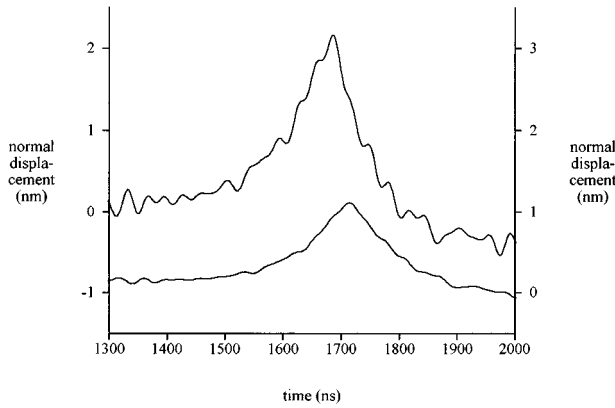


FIG. 9. Enlargement of Fig. 7 over the time interval $1300 \text{ ns} \leq t \leq 2000 \text{ ns}$.

fects. The FWHMs of the two longitudinal peaks before and after the deconvolution can readily be evaluated from Figs. 8 and 9, which are enlargements of the peaks of Fig. 7. The results are summarized in Table I: one can see that the deconvolution scheme reduces the FWHMs in a proportion of approximately 19%.

One also notices in Figs. 8 and 9 that the peaks of the convolution-free curve are slightly shifted to the left with respect to the ones of the experimental curve. This point could also be expected from the deconvolution operation, although the exact quantity of the shift is not a reliable value because of the imprecision in the definition of the time origin in the experimental temporal profile of the laser pulse. More generally, the absolute times of the experiments are not precisely defined because of an uncontrollable delay (of approximately 180 ns) induced by the demodulation unit of the interferometric probe in the recordings. On the other hand, the relative times are accurately measured and, reminding that two successive peaks of the convolution-free curve are separated by a delay of exactly $2L/v$, this quantity $2L/v$ can be determined with very good precision. For this evaluation, we used a cross-correlation technique based on the function:

$$\Phi(\tau) = \int_{t_1}^{t_2} u_z^0(L, t) u_z^0(L, t + \tau) dt. \quad (18)$$

In this expression, $u_z^0(L, t)$ is the experimental convolution-free normal displacement curve, and the time interval $[t_1, t_2]$ is the interval of occurrence of the first longitudinal peak. A plot of the function $\Phi(\tau)$ is displayed in Fig. 10. This plot exhibits an intense and quite symmetrical peak centered at $\tau = 1.117 \mu\text{s}$, which corresponds to the experimental evaluation of $2L/v$. Moreover, this value can be determined with an absolute precision of $\pm 5 \text{ ns}$, i.e., a relative precision of $\pm 5\%$. The quality of the evaluation of the longitudinal acoustic velocity v is then dependent upon the precision of

TABLE I. "Short" pulse duration experiment, FWHMs of the two longitudinal peaks before and after the deconvolution.

	First peak	Second peak
Before deconvolution	137 ns	139 ns
After deconvolution	110 ns	114 ns

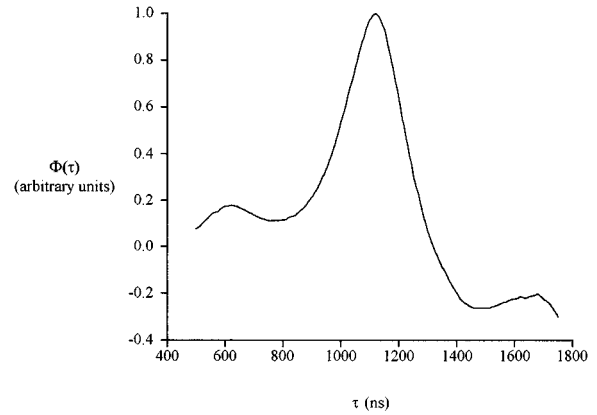


FIG. 10. Plot of the cross-correlation function $\Phi(\tau)$.

the measurement of the thickness L of the sample. This measurement was performed again with a finer apparatus, giving $L = 3.040 \text{ mm} \pm 3 \mu\text{m}$, i.e., $L = 3.040 \text{ mm} \pm 1\%$, and the value of the longitudinal velocity was derived: $v = 5443 \text{ m/s} \pm 6\%$.

Finally, the knowledge of the value of v and the measurement of the FWHMs of the longitudinal peaks of the experimental convolution-free normal displacement curve allow the experimental evaluation of the optical absorption coefficient β through relation (13). Taking $\Delta t_{1/2} = 112 \text{ ns}$, one obtains $\beta = 2300 \text{ m}^{-1}$. Figure 11 confronts the experimental convolution-free normal displacement curve to the one obtained from the analytical expression (11) of the normal displacement with the values derived previously for β , v , and L . A very satisfactory agreement between experiment and theory is observed, which gives credit to our evaluations of both the optical absorption coefficient and the longitudinal acoustic velocity.

C. Second experiment—"long" pulse duration

In order to test our deconvolution scheme in the case of more serious laser pulse duration effects, another experiment was performed on the colored glass sample with a lower

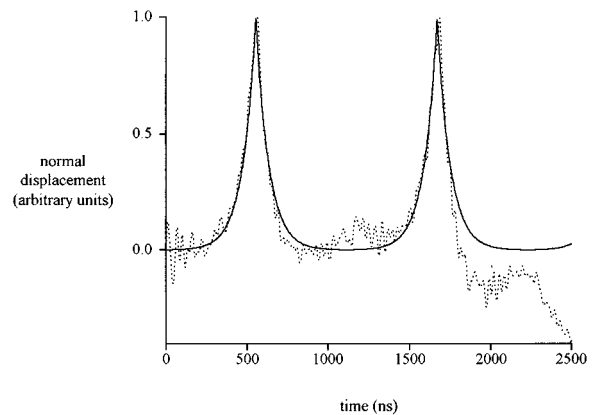


FIG. 11. Confrontation of the experimental convolution-free normal displacement curve (dashed line) to the one obtained from the analytical expression of the normal displacement with the values derived for β , v , and L (solid line).

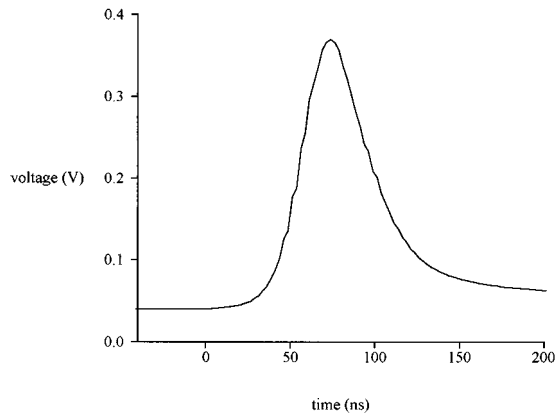


FIG. 12. “Long” pulse duration experiment, enlargement over the time interval $-40 \text{ ns} \leq t \leq 200 \text{ ns}$ of the experimental temporal profile of the laser pulse.

voltage applied to the oscillator flash lamp. This time, the laser pulse was only 63 mJ in energy, and, to compensate for this energy decrease and to keep a good signal-to-noise ratio for the normal displacement detection, the diverging lens had to be brought closer to the sample, at a distance of approximately 10 cm.

The same procedure as the one presented for the exploitation of the “short” pulse duration experiment was used here. Figure 12 displays an enlargement over the time interval $-40 \text{ ns} \leq t \leq 200 \text{ ns}$ of the experimental temporal profile of the laser pulse: the FWHM of the pulse is 45 ns, which this time is not small compared to the FWHMs of the convolution-free longitudinal peaks.

The experimental normal displacement curve observed on the rear side of the sample is shown in Fig. 13. As the diverging lens was brought closer to the sample, the laser irradiation was not as well distributed over its front side as in the preceding experiment, resulting in an earlier emergence of “non-1-D” negative normal displacements after $t = 1200 \text{ ns}$. This point is confirmed by the theory developed in the preceding section. The radius Σ of the laser excitation can be evaluated with the help of relation (16). The values of the experiment ($\sigma = 3 \text{ mm}$ and $d = f = 10 \text{ cm}$) yield $\Sigma = 6 \text{ mm}$. The laser spot extension dimensionless parameter

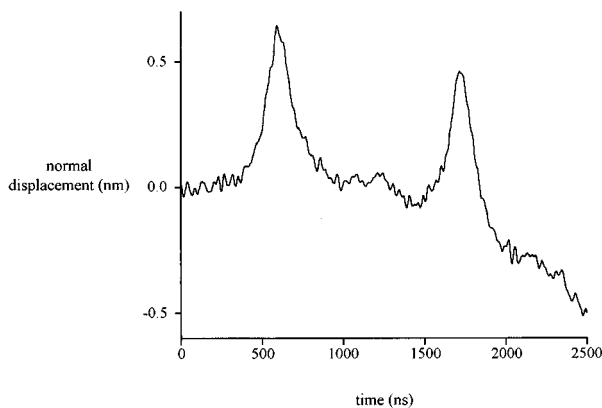


FIG. 13. Experimental normal displacement curve observed on the rear side of the sample.

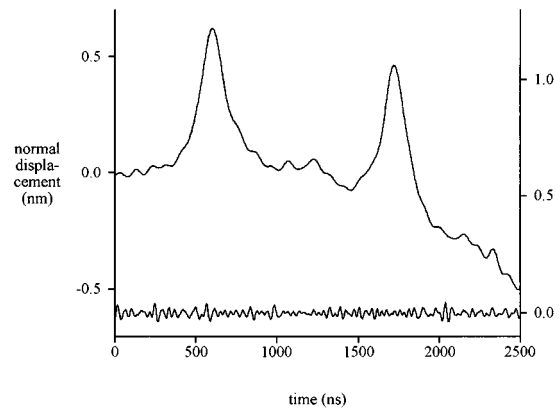


FIG. 14. Filtered normal displacement curve (top curve, left scale) and the difference between this curve and the initial experimental one of Fig. 13 (bottom curve, right scale).

Σ/L is then 2, and formula (17) allows the evaluation of the dimensionless time vT/L at which “non-1-D” effects start to alter the shape of the normal displacement curve: this dimensionless time vT/L is approximately 2.2. Consequently, the second longitudinal peak of Fig. 13 lies in the “wash” part of the signal, which is the part affected by “non-1-D” effects. But on the other hand, the time interval of occurrence of the first longitudinal peak is anterior to the emergence of the “wash,” and it is reasonable to assume that this peak has not been affected by “non-1-D” effects. We will thus in the following concentrate on the first longitudinal peak of Fig. 13.

The pulse duration being longer than in the preceding experiment, its frequency spectrum spreads over a smaller frequency range. Consequently, the phenomenon of experimental noise amplification induced by the division of the Laplace transform of the experimental normal displacement curve by the one of the experimental temporal profile of the laser pulse starts at lower frequencies. In the preceding experiment, the normal displacement signal was “naturally” filtered by the cut-off frequency (35 MHz) of the interferometric probe. Here, we had to perform an additional numerical filtering of the normal displacement signal with a cut-off frequency of 12 MHz in order to circumvent the noise amplification problem over the frequency range spreading from 12 to 35 MHz. Figure 14 displays the filtered normal displacement curve and the difference between this curve and the initial experimental one of Fig. 13. Figure 15 compares the convolution-free normal displacement curve to the filtered one of Fig. 14. The same remarks as the ones for the preceding experiment can be made about the noise of the convolution-free curve and the heights and widths and time positions of its longitudinal peaks. Concerning the FWHM of the first peak, this quantity goes from 175 ns on the filtered curve to 143 ns on the convolution-free one. The FWHM of the convolution-free curve is thus quite different from the one measured in the preceding experiment (112 ns), which is inconsistent with the theory developed previously. But in the “long” pulse experiment, we had to filter the experimental normal displacement curve of Fig. 13 with a cut-off frequency of 12 MHz, and doing so, we also filtered the convolution-free

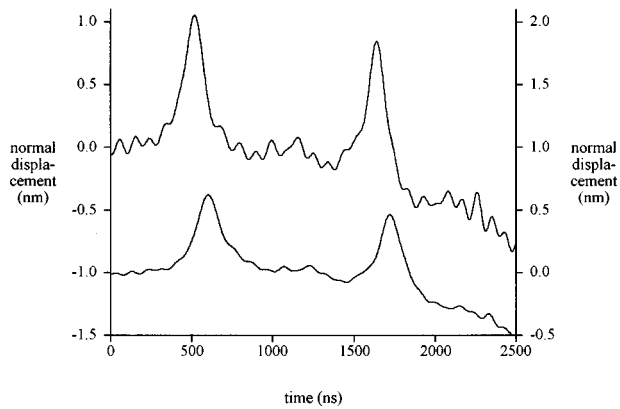


FIG. 15. Comparison of the convolution-free normal displacement curve (top curve, left scale) to the filtered one of Fig. 14 (bottom curve, right scale).

curve of Fig. 15. The discrepancy between the FWHM values of the two experiments is then maybe due to the fact that the contributions of the frequencies lying in the range between 12 and 35 MHz to the signal are lost in the “long” pulse experiment. In order to check the validity of this interpretation, we kept the values of β and v found in the preceding experiment, we calculated the theoretical convolution-free normal displacement curve from its analytical expression (11), and we filtered this curve with a cut-off frequency of 12 MHz. The confrontation of the theoretical filtered convolution-free normal displacement curve to the experimental one is shown in Fig. 16. The very good agreement that is obtained between the temporal shapes of the first longitudinal peaks of these two curves confirms our previous evaluations of β and v .

III. DISCUSSION AND CONCLUSION

If there cannot be any doubt about the evaluation of the longitudinal acoustic velocity v , on the other hand the optical absorption coefficient β measured experimentally (2300 m^{-1}) differs quite significantly from the value given by the manufacturer (3000 m^{-1}). In order to solve this ambiguity, we evaluated the optical absorption coefficient with

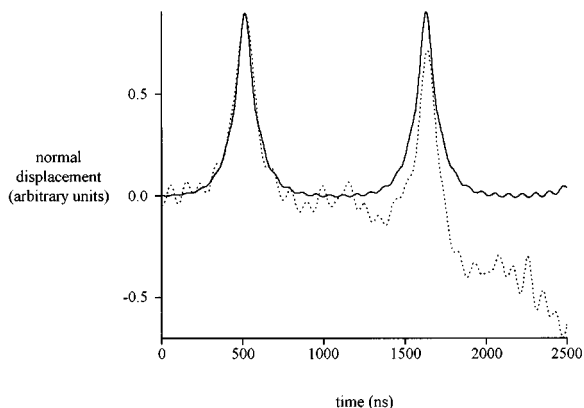


FIG. 16. Confrontation of the theoretical filtered convolution-free normal displacement curve (solid line) to the experimental one (dashed line).

a purely optical method consisting in the measurement of the radiative flux transmitted through the sample. The transmission being weak (of the order of a few ‰), this measurement was performed with the help of an intensity-modulated Nd:YAG laser and a lock-in detection. The transmission of the sample and the reflection coefficients of its two surfaces were evaluated to be 1.5‰ and 3‰, respectively (the reflection coefficients of the two surfaces were checked to be equal within the experimental precision), and from these values the internal transmission of the sample was calculated to be 1.6‰. This internal transmission being equal to $\exp(-\beta L)$, a new evaluation of the optical absorption coefficient β was derived: 2100 m^{-1} , which is much nearer to our laser-ultrasonics evaluation than to the value given by the manufacturer.

In conclusion, our deconvolution scheme has proved to be an efficient technique that allows us to extract one of the temporal convolutions that take place in a laser-ultrasonics experiment. As underlined earlier, some precautions need to be taken when dealing with “long” pulse durations (“long” meaning that the FWHM of the pulse is not small compared to the FWHM, given by expression (13), of the convolution-free longitudinal peaks), some additional numerical low-pass filtering may be necessary in order to circumvent the noise amplification phenomenon that affects lower and lower frequencies as the pulse duration is longer, and an obvious conclusion of that point is that the shorter the pulse duration, the easier and more efficient the deconvolution. Nevertheless, even with the shortest pulse duration attainable with our generation laser, the deconvolution has been shown to reduce substantially the FWHMs of the experimental longitudinal peaks, which allowed a better evaluation of the optical absorption coefficient as well as a very precise determination of the longitudinal acoustic velocity. We plan in the future to make use of this temporal deconvolution ability to derive experimental signals that are more directly affected and thus more “sensitive” to material-related physical phenomena such as the viscosity-induced acoustic dispersion in polymers, for example.

APPENDIX: DESCRIPTION OF OUR QUASIANALYTICAL 3-D MODEL FOR THE SIMULATION OF THE THERMOELASTIC GENERATION OF ULTRASOUND

For the purpose of simplicity, we will present the principle of resolution of the acoustic wave propagation equations in the case of an isotropic material. The following mathematical developments can easily be extended to the case of an anisotropic material presenting a cylindrical symmetry of axis (Oz).

Let us consider an infinite plate of thickness L impinged on its front side by a laser excitation presenting a radial symmetry. The configuration of the problem being axisymmetrical, we will in the following make use of the cylindrical coordinates (r, z) . With the assumption of negligible thermal diffusion, the temperature elevation field $\Delta\theta$ is simply the integration over time of the optically induced thermal source divided by ρC_p ; the analytical expression of $\Delta\theta$ is

$$\Delta\theta(r,z,t) = \frac{\beta E_0}{\rho C_p} e^{-\beta z} g(r) \int_0^t f(\tau) d\tau. \quad (\text{A1})$$

In this expression, E_0 is the energy ‘entering’ the plate, which is equal to $(1-R) E_i$, where E_i is the incident energy emitted by the excitation laser and R the reflection coefficient of the impinged front side at the excitation wavelength. The functions $g(r)$ and $f(t)$ are the radial and temporal profiles of the laser pulse; these two functions are normalized through the relations:

$$\int_0^\infty g(r) 2\pi r dr = 1 \quad \text{and} \quad \int_0^\infty f(t) dt = 1. \quad (\text{A2})$$

The radial component u_r and the normal component u_z of the mechanical displacement field are obtained by the resolution of the following two acoustic wave propagation equations containing thermal expansion source terms:

$$\rho \frac{\partial^2 u_r}{\partial t^2} = c_{11} \left(\frac{\partial^2 u_r}{\partial r^2} + \frac{1}{r} \frac{\partial u_r}{\partial r} - \frac{u_r}{r^2} \right) + c_{44} \frac{\partial^2 u_r}{\partial z^2} + (c_{11} - c_{44}) \times \frac{\partial^2 u_z}{\partial r \partial z} - (3c_{11} - 4c_{44}) \alpha \frac{\partial(\Delta\theta)}{\partial r}, \quad (\text{A3})$$

$$\rho \frac{\partial^2 u_z}{\partial t^2} = c_{44} \left(\frac{\partial^2 u_z}{\partial r^2} + \frac{1}{r} \frac{\partial u_z}{\partial r} \right) + c_{11} \frac{\partial^2 u_z}{\partial z^2} + (c_{11} - c_{44}) \times \left(\frac{\partial^2 u_r}{\partial r \partial z} + \frac{1}{r} \frac{\partial u_r}{\partial z} \right) - (3c_{11} - 4c_{44}) \alpha \frac{\partial(\Delta\theta)}{\partial z}. \quad (\text{A4})$$

In these two equations, c_{11} and c_{44} are the two principal components of the rigidity tensor $[c]$ (written with the two-index notation) of the isotropic material, and α is the linear thermal expansion coefficient of the material.

As a first step, we rewrite expression (A1) and Eqs. (A3) and (A4) with the help of dimensionless parameters. Introducing the dimensionless space and time variables $r^* = r/\Sigma$ (Σ being a characteristic length in the r direction), $z^* = z/L$ and $t^* = vt/L$ [v being the longitudinal acoustic velocity of the material, equal to $(c_{11}/\rho)^{1/2}$], and defining a dimensionless parameter $\beta^* = \beta L$ measuring the degree of opaqueness of the sample, the temperature elevation field $\Delta\theta$ can be rewritten in a dimensionless way by introducing the following three quantities:

$$\Delta\theta_0 = \frac{\beta E_0}{\rho C_p \pi \Sigma^2}, \quad (\text{A5})$$

$$\gamma^*(r^*) = \pi \Sigma^2 g(r) = \pi \Sigma^2 g(\Sigma r^*), \quad (\text{A6})$$

$$\varphi^*(t^*) = \frac{L}{v} f(t) = \frac{L}{v} f\left(\frac{L}{v} t^*\right). \quad (\text{A7})$$

One can note that the quantity $\Delta\theta_0$ has units of temperature and that, unlike the functions $g(r)$ and $f(t)$, the functions $\gamma^*(r^*)$ and $\varphi^*(t^*)$ are dimensionless. The dimensionless temperature elevation field $\Delta\theta^* = \Delta\theta/\Delta\theta_0$, when expressed with the help of the functions $\gamma^*(r^*)$ and $\varphi^*(t^*)$, takes the following form:

$$\Delta\theta^*(r^*, z^*, t^*) = e^{-\beta^* z^*} \gamma^*(r^*) \int_0^{t^*} \varphi^*(\tau^*) d\tau^*. \quad (\text{A8})$$

The same procedure can be applied to the two acoustic wave propagation equations (A3) and (A4). Introducing the quantity:

$$u_0 = \frac{\chi E_0}{\rho C_p \pi \Sigma^2} = \frac{3c_{11} - 4c_{44}}{c_{11}} \frac{\alpha E_0}{\rho C_p \pi \Sigma^2} \quad (\text{A9})$$

which has units of distance, the two equations governing the dimensionless radial displacement field $u_r^* = u_r/u_0$ and the dimensionless normal displacement field $u_z^* = u_z/u_0$ can be derived from Eqs. (A3) and (A4); they take the following forms:

$$\frac{\partial^2 u_r^*}{\partial t^{*2}} = \frac{1}{\Sigma^{*2}} \left(\frac{\partial^2 u_r^*}{\partial r^{*2}} + \frac{1}{r^*} \frac{\partial u_r^*}{\partial r^*} - \frac{u_r^*}{r^{*2}} \right) + c^* \frac{\partial^2 u_r^*}{\partial z^{*2}} + \frac{1-c^*}{\Sigma^*} \frac{\partial^2 u_z^*}{\partial r^* \partial z^*} - \frac{\beta^*}{\Sigma^*} \frac{\partial(\Delta\theta^*)}{\partial r^*}, \quad (\text{A10})$$

$$\frac{\partial^2 u_z^*}{\partial t^{*2}} = \frac{c^*}{\Sigma^{*2}} \left(\frac{\partial^2 u_z^*}{\partial r^{*2}} + \frac{1}{r^*} \frac{\partial u_z^*}{\partial r^*} \right) + \frac{\partial^2 u_z^*}{\partial z^{*2}} + \frac{1-c^*}{\Sigma^*} \left(\frac{\partial^2 u_r^*}{\partial r^* \partial z^*} + \frac{1}{r^*} \frac{\partial u_r^*}{\partial z^*} \right) - \beta^* \frac{\partial(\Delta\theta^*)}{\partial z^*} \quad (\text{A11})$$

in which two additional dimensionless parameters have been introduced: a geometrical parameter $\Sigma^* = \Sigma/L$ and a material parameter $c^* = c_{44}/c_{11}$ related to the Poisson coefficient ν through the relation $c^* = (2\nu - 1)/(2\nu - 2)$.

Equations (A10) and (A11) are solved in the Laplace and Hankel spaces. Applying a Laplace transformation (denoted L) and a Hankel transformation of order 1 (denoted H_1) to Eq. (A10), and a Laplace transformation and a Hankel transformation of order 0 (denoted H_0) to Eq. (A11), and introducing the following notations:

$$U_r^*(\xi^*, z^*, s^*) = LH_1[u_r^*(r^*, z^*, t^*)], \quad (\text{A12})$$

$$U_z^*(\xi^*, z^*, s^*) = LH_0[u_z^*(r^*, z^*, t^*)], \quad (\text{A13})$$

$$\Delta\Theta^*(\xi^*, z^*, s^*) = LH_0[\Delta\theta^*(r^*, z^*, t^*)] = \frac{\Gamma^* \Phi^*}{s^*} e^{-\beta^* z^*}, \quad (\text{A14})$$

with

$$\Gamma^*(\xi^*) = H_0[\gamma^*(r^*)] \quad (\text{A15})$$

and

$$\Phi^*(s^*) = L[\varphi^*(t^*)] \quad (\text{A16})$$

in which ξ^* is the dimensionless Hankel variable and s^* is the dimensionless Laplace variable, one comes to the following two equations:

$$c^* \frac{\partial^2 U_r^*}{\partial z^{*2}} - (1-c^*) \frac{\xi^*}{\Sigma^*} \frac{\partial U_z^*}{\partial z^*} - \left(s^{*2} + \left(\frac{\xi^*}{\Sigma^*} \right)^2 \right) U_r^* = -\beta^* \frac{\xi^*}{\Sigma^*} \Delta\Theta^* = -\beta^* \frac{\xi^*}{\Sigma^*} \frac{\Gamma^* \Phi^*}{s^*} e^{-\beta^* z^*}, \quad (\text{A17})$$

$$\begin{aligned} & \frac{\partial^2 U_z^*}{\partial z^{*2}} + (1-c^*) \frac{\xi^*}{\Sigma^*} \frac{\partial U_r^*}{\partial z^*} - \left(s^{*2} + c^* \left(\frac{\xi^*}{\Sigma^*} \right)^2 \right) U_z^* \\ & = \beta^* \frac{\partial(\Delta\Theta^*)}{\partial z^*} = -\beta^{*2} \frac{\Gamma^* \Phi^*}{s^*} e^{-\beta^* z^*}. \end{aligned} \quad (\text{A18})$$

This differential system [(A17),(A18)] is easy to integrate. Its general solution (U_r^*, U_z^*) can be expressed in the following way:

$$\begin{aligned} U_r^* = & \frac{\xi^*}{\Sigma^*} (-Zp_1^* e^{m_1^* z^*} + Zm_1^* e^{-m_1^* z^*}) \\ & + m_2^* (Rp_2^* e^{m_2^* z^*} + Rm_2^* e^{-m_2^* z^*}) + R_0^* e^{-\beta^* z^*}, \end{aligned} \quad (\text{A19})$$

$$\begin{aligned} U_z^* = & m_1^* (Zp_1^* e^{m_1^* z^*} + Zm_1^* e^{-m_1^* z^*}) + \frac{\xi^*}{\Sigma^*} \\ & \times (-Rp_2^* e^{m_2^* z^*} + Rm_2^* e^{-m_2^* z^*}) + Z_0^* e^{-\beta^* z^*}, \end{aligned} \quad (\text{A20})$$

in which we have introduced the following notations:

$$m_1^*(\xi^*, s^*) = \sqrt{\left(\frac{\xi^*}{\Sigma^*} \right)^2 + s^{*2}}, \quad (\text{A21})$$

$$m_2^*(\xi^*, s^*) = \sqrt{\left(\frac{\xi^*}{\Sigma^*} \right)^2 + \frac{s^{*2}}{c^*}}, \quad (\text{A22})$$

$$R_0^*(\xi^*, s^*) = \frac{\beta^*}{m_1^{*2} - \beta^{*2}} \frac{\xi^*}{\Sigma^*} \frac{\Gamma^* \Phi^*}{s^*}, \quad (\text{A23})$$

$$Z_0^*(\xi^*, s^*) = \frac{\beta^{*2}}{m_1^{*2} - \beta^{*2}} \frac{\Gamma^* \Phi^*}{s^*} \quad (\text{A24})$$

and in which the quantities Zp_1^* , Zm_1^* , Rp_2^* , and Rm_2^* are four constants of integration (functions of ξ^* and s^*) to be determined.

These four constants of integration are evaluated with the help of the four boundary conditions of the problem.

These conditions of zero mechanical stress on each boundary surface of the plate yield the following equations:

$$\sigma_{rz} = c_{44} \left(\frac{\partial u_r}{\partial z} + \frac{\partial u_z}{\partial r} \right) = 0 \quad \text{at } z=0 \quad \text{and } z=L, \quad (\text{A25})$$

$$\begin{aligned} \sigma_{zz} = & (c_{11} - 2c_{44}) \left(\frac{\partial u_r}{\partial r} + \frac{u_r}{r} \right) + c_{11} \frac{\partial u_z}{\partial z} - (3c_{11} - 4c_{44}) \\ & \times \alpha \Delta\theta = 0 \quad \text{at } z=0 \quad \text{and } z=L, \end{aligned} \quad (\text{A26})$$

in which σ_{rz} and σ_{zz} are, respectively, the (r,z) and the (z,z) components of the stress tensor. Rewriting condition (A25) in a dimensionless way and then applying a LH_1 transformation to the resulting dimensionless equation yields:

$$\frac{\partial U_r^*}{\partial z^*} - \frac{\xi^*}{\Sigma^*} U_z^* = 0 \quad \text{at } z^*=0 \quad \text{and } z^*=1. \quad (\text{A27})$$

In a similar fashion, rewriting condition (A26) in a dimensionless way and then applying a LH_0 transformation to the resulting dimensionless equation yields:

$$\begin{aligned} (1-2c^*) \frac{\xi^*}{\Sigma^*} U_r^* + \frac{\partial U_z^*}{\partial z^*} - \beta^* \Delta\Theta^* = 0 \\ \text{at } z^*=0 \quad \text{and } z^*=1. \end{aligned} \quad (\text{A28})$$

The four boundary conditions [(A27),(A28)] written with the analytical expressions (A19) and (A20) of U_r^* and U_z^* lead to a linear system of four equations allowing the evaluation of the four constants of integration Zp_1^* , Zm_1^* , Rp_2^* , and Rm_2^* . This system can be expressed in the following matrix form:

$$[A] \cdot \mathbf{x} = \mathbf{b}. \quad (\text{A29})$$

In this matrix equation, the vector

$$\mathbf{x} = \begin{pmatrix} Zp_1^* \\ Zm_1^* \\ Rp_2^* \\ Rm_2^* \end{pmatrix} \quad (\text{A30})$$

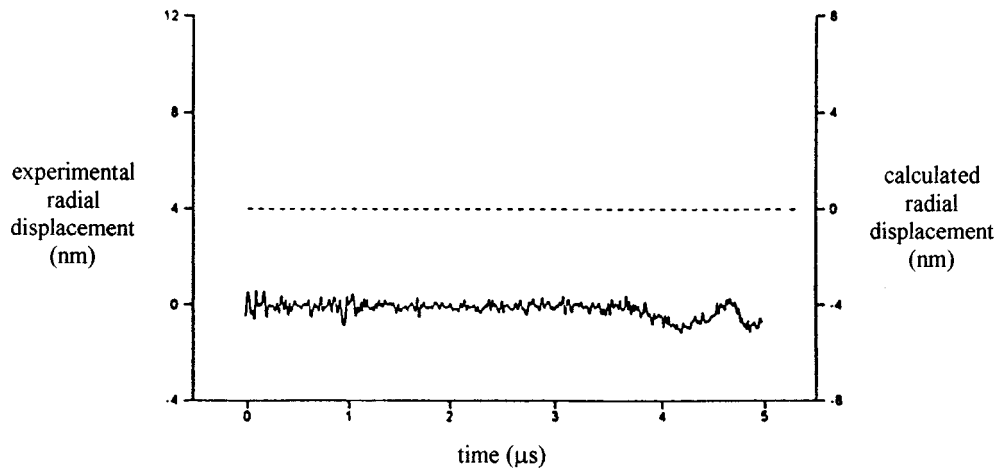


FIG. A1. Radial displacement curves on the rear side of the Schott BG-18 colored glass sample at the epicenter, comparison of the calculated curve (dashed line, right scale) to the experimental one (solid line, left scale).

is the unknown and the matrix $[A]$ and the vector \mathbf{b} are

$$[A] = \begin{pmatrix} A_{11} & A_{11} & A_{13} & -A_{13} \\ A_{11}e^{m_1^*} & A_{11}e^{-m_1^*} & A_{13}e^{m_2^*} & -A_{13}e^{-m_2^*} \\ A_{31} & -A_{31} & A_{33} & A_{33} \\ A_{31}e^{m_1^*} & -A_{31}e^{-m_1^*} & A_{33}e^{m_2^*} & A_{33}e^{-m_2^*} \end{pmatrix}$$

and

$$\mathbf{b} = \begin{pmatrix} b_1 \\ b_1 e^{-\beta^*} \\ b_3 \\ b_3 e^{-\beta^*} \end{pmatrix}, \quad (\text{A31})$$

in which we have introduced the following notations:

$$A_{11} = -2m_1^* \frac{\xi^*}{\Sigma^*}, \quad (\text{A32})$$

$$A_{13} = m_2^{*2} + \left(\frac{\xi^*}{\Sigma^*}\right)^2, \quad (\text{A33})$$

$$A_{31} = m_1^{*2} - (1 - 2c^*) \left(\frac{\xi^*}{\Sigma^*}\right)^2, \quad (\text{A34})$$

$$A_{33} = -2c^* m_2^* \frac{\xi^*}{\Sigma^*}, \quad (\text{A35})$$

$$b_1 = \beta^* R_0^* + \frac{\xi^*}{\Sigma^*} Z_0^*, \quad (\text{A36})$$

$$b_3 = \frac{m_1^{*2}}{\beta^*} Z_0^* - (1 - 2c^*) \frac{\xi^*}{\Sigma^*} R_0^*. \quad (\text{A37})$$

The problem is thus completely solved. Once the sample and the excitation laser are chosen, one can evaluate the three dimensionless parameters c^* , Σ^* (the characteristic length Σ in the r direction being taken to be, say, a measure of the size of the laser spot), and β^* . One can also determine the radial profile $g(r)$ and the temporal profile $f(t)$ of the laser excitation, and derive the values of the dimensionless trans-

formed profiles $\Gamma^*(\xi^*)$ and $\Phi^*(s^*)$. Then, for any value of the dimensionless depth z^* within the sample and of the two dimensionless spectral variables ξ^* and s^* , it is possible to calculate the values of $U_r^*(\xi^*, z^*, s^*)$ and $U_z^*(\xi^*, z^*, s^*)$ using the mathematical developments presented above. The last step in the resolution of the problem is also the only purely numerical step of the model: it consists in applying numerical inverse LH_1 transformations to $U_r^*(\xi^*, z^*, s^*)$ and numerical inverse LH_0 transformations to $U_z^*(\xi^*, z^*, s^*)$ in order to reach the real dimensionless displacements u_r^* and u_z^* in the real dimensionless spaces (r^*, z^*, t^*) .

Concerning the radial profile $g(r)$ of the laser excitation, two particular cases are worth considering because of their important practical applications: first, the Gaussian irradiation (produced by a monomode excitation), and second, the uniform irradiation over a disk (produced, with a certain degree of approximation, by a multimode excitation). In the case of a Gaussian irradiation, the function $g(r)$ has the following expression:

$$g(r) = \frac{1}{\pi \Sigma^2} e^{-(r/\Sigma)^2}, \quad (\text{A38})$$

in which Σ has been chosen as the radius at $1/e$ of the Gaussian profile. With the help of relations (A6) and (A15), one can derive the expressions of the dimensionless radial profile $\gamma^*(r^*)$ and of its H_0 -transform $\Gamma^*(\xi^*)$; these expressions are

$$\gamma^*(r^*) = e^{-r^{*2}}, \quad (\text{A39})$$

$$\Gamma^*(\xi^*) = \int_0^\infty \gamma^*(r^*) J_0(\xi^* r^*) r^* dr^* = \frac{1}{2} e^{-\xi^{*2}/4}. \quad (\text{A40})$$

In the case of a uniform irradiation over a disk, the function $g(r)$ has the following expression:

$$g(r) = \begin{cases} \frac{1}{\pi \Sigma^2}, & \text{for } 0 \leq r \leq \Sigma \\ 0, & \text{for } r > \Sigma, \end{cases} \quad (\text{A41})$$

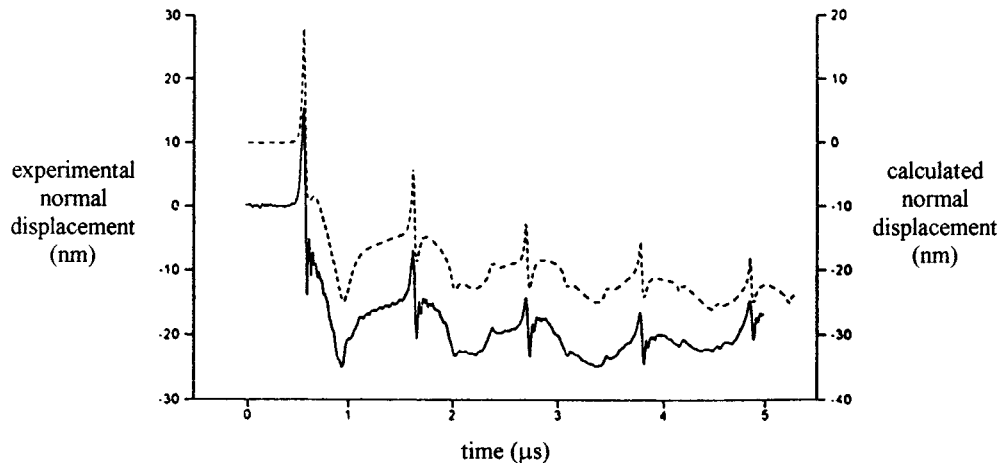


FIG. A2. Normal displacement curves on the rear side of the Schott BG-18 colored glass sample at the epicenter, comparison of the calculated curve (dashed line, right scale) to the experimental one (solid line, left scale).

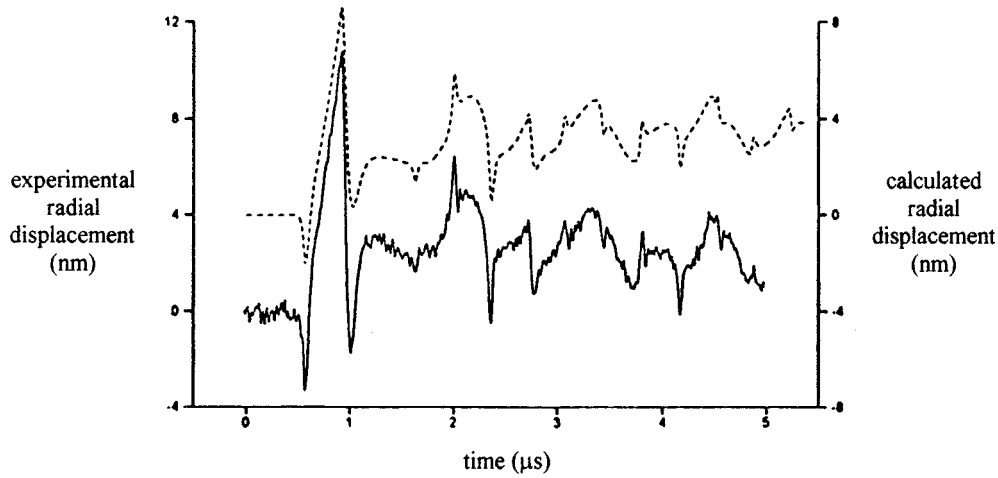


FIG. A3. Radial displacement curves on the rear side of the Schott BG-18 colored glass sample at a point situated 1 mm away from the epicenter, comparison of the calculated curve (dashed line, right scale) to the experimental one (solid line, left scale).

in which Σ , this time, has been chosen as the radius of the irradiation disk. Here again, with the help of relations (A6) and (A15), one can derive the expressions of the dimensionless radial profile $\gamma^*(r^*)$ and of its H_0 -transform $\Gamma^*(\xi^*)$; these expressions are

$$\gamma^*(r^*) = \begin{cases} 1, & \text{for } 0 \leq r^* \leq 1, \\ 0, & \text{for } r^* > 1, \end{cases} \quad (\text{A42})$$

$$\Gamma^*(\xi^*) = \int_0^\infty \gamma^*(r^*) J_0(\xi^* r^*) r^* dr^* = \frac{J_1(\xi^*)}{\xi^*}. \quad (\text{A43})$$

Concerning the temporal profile $f(t)$ of the laser excitation, for most applications involving irradiations from Q -switched lasers, this profile may reasonably be represented by the following analytical expression:

$$f(t) = \frac{t}{\tau^2} e^{-t/\tau}. \quad (\text{A44})$$

In this expression, τ is the rise time of the laser pulse, and the full width at half-maximum (FWHM) of the pulse is given by $\text{FWHM} \approx 2.45\tau$. With the help of relations (A7) and (A16), one can derive the expressions of the dimensionless temporal profile $\varphi^*(t^*)$ and of its L -transform $\Phi^*(s^*)$; these expressions are

$$\varphi^*(t^*) = \frac{t^*}{\tau^{*2}} e^{-t^*/\tau^*}, \quad (\text{A45})$$

$$\Phi^*(s^*) = \int_0^\infty \varphi^*(t^*) e^{-s^* t^*} dt^* = \frac{1}{(1 + \tau^* s^*)^2}, \quad (\text{A46})$$

in which we have introduced a new dimensionless parameter $\tau^* = v\tau/L$ that compares the rise time of the laser pulse to the duration of a longitudinal trip through the sample. Consequently, in the case of an isotropic material, the dimensionless radial and normal displacement fields u_r^* and u_z^* are functions of (i) the three dimensionless space and time variables r^* , z^* , and t^* , (ii) one dimensionless parameter c^* related to the acoustic properties of the material, and (iii) three dimensionless parameters Σ^* , β^* , and τ^* that fully describe the features of the laser excitation.

If the material is not isotropic but presents a cylindrical symmetry of axis (Oz), the mathematical resolution described above becomes more tedious but nevertheless can still be made. Under these circumstances, not one but five dimensionless parameters describe the anisotropy of the material. These five dimensionless parameters are $c_1^* = c_{11}/c_{33}$, $c_2^* = c_{12}/c_{33}$, $c_3^* = c_{13}/c_{33}$, $c_4^* = c_{44}/c_{33}$, and $\alpha^* = \alpha_r/\alpha_z$ in which the c_{ij} are the five principal components of the rigidity tensor $[c]$ (written with the two-index notation) of the hexagonal crystal describing the anisotropy of the material and α_r and α_z are the linear thermal expansion coefficients of the material in the r and z directions.

In order to validate our simulation model, we performed a laser-ultrasonics experiment on a 3.0-mm-thick plate made of a Schott BG-18 colored glass. This experiment consisted of the thermoelastic generation of ultrasonic waves on the front side of the plate with the help of our pulsed Nd:YAG laser and in the measurement of radial and normal displacement curves on the rear side of the plate with the help of our heterodyne interferometer. Measurements were made at two different locations, namely the epicenter and a point situated 1 mm away from the epicenter. The Nd:YAG laser was set in a monomode configuration, and the average radius at $1/e$ Σ of the Gaussian radial profile of the excitation, the average rise time τ of the laser pulse, and the average energy per pulse E_i were measured to be, respectively, 1.0 mm, 8.0 ns, and 31 mJ. Concerning the material properties of our sample, they were the following: isotropic material, longitudinal acoustic velocity $v = 5630$ m/s and shear acoustic velocity $w = 3330$ m/s (both determined experimentally with the help of longitudinal and shear piezoelectric transducers), and optical absorption coefficient at the excitation wavelength $\beta = 9700 \text{ m}^{-1}$ (given by the manufacturer).

The data listed above allowed the evaluation of the four dimensionless parameters characterizing the experiment, namely $c^* = c_{44}/c_{11} = (w/v)^2 = 0.35$, $\Sigma^* = \Sigma/L = 0.33$, $\beta^* = \beta L = 29$, and $\tau^* = v\tau/L = 0.015$. We ran the simulation model with these values, and calculated the dimensionless radial and normal displacement curves $u_r^*(t^*)$ and $u_z^*(t^*)$ on the rear side of the plate ($z^* = z/L = 1$) at the epicenter

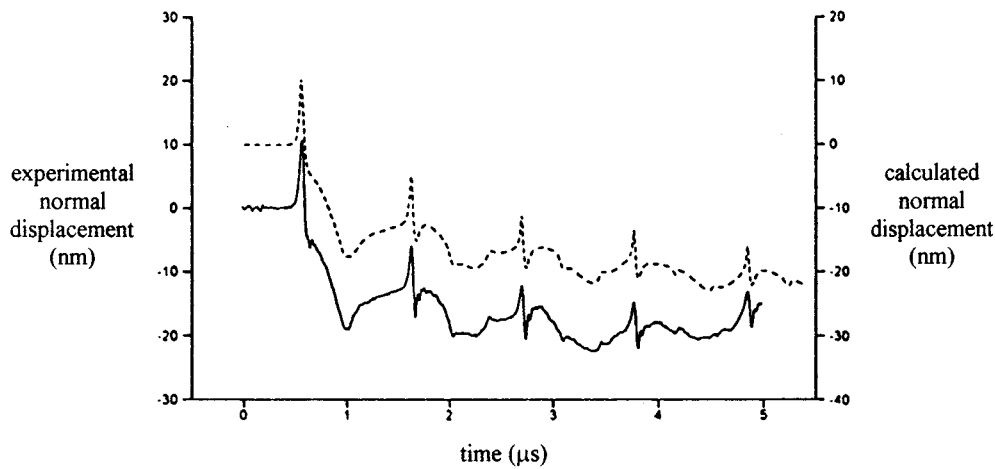


FIG. A4. Normal displacement curves on the rear side of the Schott BG-18 colored glass sample at a point situated 1 mm away from the epicenter, comparison of the calculated curve (dashed line, right scale) to the experimental one (solid line, left scale).

($r^* = r/\Sigma = 0$) and at a point situated 1 mm away from the epicenter ($r^* = r/\Sigma = 1$). Finally, we multiplied the horizontal scales (i.e., the t^* scales) of the dimensionless curves by a time constant $t_0^{\text{exp}} = 538$ ns in order to fit the acoustic arrival times of the calculated curves to the experimental ones, and we multiplied the vertical scales (i.e., the u^* scales) of the dimensionless curves by a distance constant $u_0^{\text{exp}} = 48$ nm in order to fit the displacement amplitudes of the calculated curves to the experimental ones.

Figure A1 compares the experimental and calculated radial displacement curves at the epicenter, and Fig. A2 compares the experimental and calculated normal displacement curves at that same point. A very good agreement between the experiment and the calculation can be observed on these two figures, which constitutes a good sign of the validity of our simulation model. From the axisymmetrical configuration of our problem, one can expect the radial displacement to be constantly zero at the epicenter, and this property is indeed verified on both the experiment and the calculation (see Fig. A1). Concerning the experimental and calculated normal displacement curves of Fig. A2, they both highlight the longitudinal and shear wave arrivals at the observed point as well as the multiple reflections and mode conversions at the two surfaces of the plate.

Figure A3 compares the experimental and calculated radial displacement curves at the point off epicenter, and Fig. A4 compares the experimental and calculated normal displacement curves at that same point. Here again, a very good agreement between the experiment and the calculation can be observed on these two figures. This time, the observed point being off epicenter, one can expect the radial displacement at that point not to be constantly zero any more, and indeed, both the radial displacement curves of Fig. A3 and the normal displacement curves of Fig. A4 exhibit the longitudinal and shear wave arrivals at the observed point as well as the multiple reflections and mode conversions at the two surfaces of the plate.

Finally, the multiplicative constants t_0^{exp} and u_0^{exp} determined experimentally must be confronted to their theoretical

values, namely $t_0^{\text{th}} = L/v$ and $u_0^{\text{th}} = \chi E_0 / \rho C_p \pi \Sigma^2$. With the numerical data listed above, t_0^{th} is 533 ns, which is in very good accordance with the value $t_0^{\text{exp}} = 538$ ns derived from the experiment. Concerning the quantity u_0^{th} , its numerical value can be determined with the help of (i) the relevant data of the experiment, namely $c^* = 0.35$, $E_i = 31$ mJ, and $\Sigma = 1.0$ mm, (ii) the reflection coefficient of the impinged surface at the excitation wavelength $R = 4\%$ (determined experimentally), allowing the evaluation of the energy “entering” the sample $E_0 = (1 - R)E_i \approx 30$ mJ, and (iii) the following material properties of the Schott BG-18 colored glass (given by the manufacturer): $\alpha = 6.8 \times 10^{-6} \text{ K}^{-1}$, $\rho = 2680 \text{ kg/m}^3$, $C_p = 700 \text{ J/kg K}$. The calculation yields $u_0^{\text{th}} = 55$ nm, which, given the complexity to calibrate our interferometer accurately, is in reasonably good accordance with the value $u_0^{\text{exp}} = 48$ nm derived from the experiment.

As a conclusion, the confrontation of our simulation model to a test experiment was successful and hence proves the quality of the calculations performed.

¹L. M. Lyamshev and B. I. Chelnokov, “Sound generation in a solid by penetrating radiation,” *Sov. Phys. Acoust.* **29**, 220–225 (1983).

²K. L. Telschow and R. J. Conant, “Optical and thermal parameter effects on laser-generated ultrasound,” *J. Acoust. Soc. Am.* **88**, 1494–1502 (1990).

³P. A. Doyle, “On epicentral waveforms for laser-generated ultrasound,” *J. Phys. D* **19**, 1613–1623 (1986).

⁴M. Dubois, F. Enguehard, L. Bertrand, M. Choquet, and J.-P. Monchalain, “Numerical and experimental studies of the generation of ultrasound by laser,” *J. Phys. IV, Colloq. C7, Suppl. J. Phys. III* **4**, 689–692 (1994).

⁵C. B. Scruby, R. J. Dewhurst, D. A. Hutchins, and S. B. Palmer, “Quantitative studies of thermally generated elastic waves in laser-irradiated metals,” *J. Appl. Phys.* **51**, 6210–6216 (1980).

⁶L. R. F. Rose, “Point-source representation for laser-generated ultrasound,” *J. Acoust. Soc. Am.* **75**, 723–732 (1984).

⁷F. A. McDonald, “On the precursor in laser-generated ultrasound waveforms in metals,” *Appl. Phys. Lett.* **56**, 230–232 (1990).

⁸F. Enguehard and L. Bertrand, “Effects of optical penetration and laser pulse duration on the features of the laser-generated longitudinal acoustic waves,” *J. Appl. Phys.* **82**, 1532–1538 (1997).

⁹E. Lafond, F. Enguehard, A. Cournoyer, A. Tanrats, and J.-P. Longuemard, “A two-dimensional model for sensitivity studies on laser-generated ultrasound,” in the Proceedings of the 1995 World Congress on Ultrasonics, Berlin, Germany, 1995, pp. 245–248.

High-frequency backscattering enhancements by thick finite cylindrical shells in water at oblique incidence: Experiments, interpretation, and calculations

Scot F. Morse and Philip L. Marston

Department of Physics, Washington State University, Pullman, Washington 99164-2814

Gregory Kaduchak

Advanced Sonar Division, Applied Research Laboratories, University of Texas, Austin, Texas 78713-8029

(Received 28 February 1997; accepted for publication 10 October 1997)

Impulse response backscattering measurements are presented and interpreted for the scattering of obliquely incident plane waves by air-filled finite cylindrical shells immersed in water. The measurements were carried out to determine the conditions for significant enhancements of the backscattering by thick shells at large tilt angles. The shells investigated are made of stainless steel and are slender and have thickness to radius ratios of 7.6% and 16.3%. A broadband PVDF (polyvinylidene fluoride) sheet source is used to obtain the backscattering spectral magnitude as a function of the tilt angle (measured from broadside incidence) of the cylinder. Results are plotted as a function of frequency and angle. These plots reveal large backscattering enhancements associated with elastic excitations at high tilt angles, which extend to end-on incidence in the coincidence frequency region. Similar features are present in approximate calculations for finite cylindrical shells based on full elasticity theory and the Kirchhoff diffraction integral. One feature is identified as resulting from the axial (meridional ray) propagation of the supersonic a_0 leaky Lamb wave. A simple approximation is used to describe circumferential coupling loci in frequency-angle space for several surface waves. The resulting loci are used to identify enhancements due to the helical propagation of the subsonic a_{0-} Lamb wave. © 1998 Acoustical Society of America. [S0001-4966(98)04302-1]

PACS numbers: 43.30.Gv, 43.20.Fn [DLB]

INTRODUCTION

Recent high-frequency sonar images of truncated cylindrical shells indicate that the visibility of the ends of the shell can be improved by an elastic response of the shell.¹ The enhancements are associated with a category of l th class of leaky ray shown in Fig. 1. The enhancement occurs when the tilt angle γ of the cylinder is close to the leaky wave coupling angle $\theta_l = \sin^{-1}(c/c_l)$, where c_l is the phase velocity of the leaky wave and c is the speed of sound in the surrounding water. This ray is referred to as a meridional ray² since it is propagated along the meridian defined by the direction of the incident wave vector and the cylinder's axis. An analysis shows that the backscattering enhancement is associated with the vanishing of Gaussian curvature of the wavefront backscattered in the direction of the receiver. The enhancements reported¹ were for tilts in the vicinity of 18° and 35° corresponding to the excitation of symmetric and antisymmetric (s_0 and a_0) generalizations of leaky Lamb waves on the stainless steel cylinder used in those experiments. The purpose of the present paper is to document the existence of high-frequency backscattering enhancements for tilted cylindrical shells relevant to larger values of the tilt γ and in some cases, extending to $\gamma=90^\circ$ (i.e., end-on incidence).

The method of our investigation concerns the global response in the *frequency-angle domain* rather than the spatial responses emphasized in Ref. 1. There are several reasons for identifying such high-frequency enhancement mechanisms. For example, such enhancements may be relevant to the use of backscattering by cylinders lying at random angles

on the sea bottom to facilitate detection at the greatest practical range. Other potential applications include remote ultrasonic detection of cracks or junctions in pipes. Scattering mechanisms of interest are not limited to meridional rays since in certain situations strong backscattering contributions from end-reflected helical leaky and subsonic rays are also evident. The frequency range investigated extends far above the coincidence frequencies of the thick and moderately thick shells studied. The combination of frequency range and shell thickness investigated are such that the elastic responses of the shell may not be adequately modeled by the assumptions of thin-shell mechanics.³⁻⁵ It is noteworthy, however, that frequency-angle domain displays of backscattering data used previously for thin fluid-loaded shells^{4,6} and various methods of approximation previously used for such systems (see Appendix A) are relevant to the present investigation.

The investigations mentioned above, as well as several by other authors,⁷⁻¹⁰ have demonstrated that significant backscattering enhancements from tilted cylindrical shells result from the reradiation of surface guided waves for a range of tilt angles somewhat near broadside incidence. Large backscattering levels arise from the launching of helical leaky waves which reflect off the shell truncation and reradiate into the backscattering direction. Leaky waves are launched at an angle θ_l with respect to the local shell normal according to the trace velocity matching condition $\theta_l = \sin^{-1}(c/c_l)$. (These waves are launched along the shell at helix angles Ψ_l defined with respect to the cylinder axis by

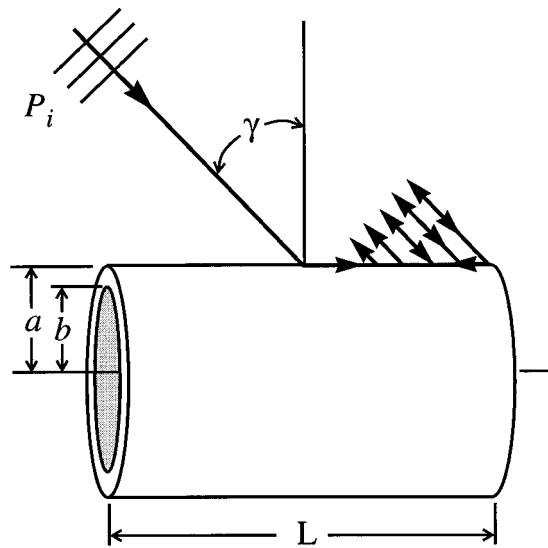


FIG. 1. Scattering geometry and ray diagram for a meridional leaky ray on a finite cylindrical shell.

cos $\Psi_l = \sin \gamma / \sin \theta_l$.) Two types of waves contribute strongly to the scattering: longitudinal and shear. For the general problem of propagation on tilted cylinders these waves are also known as quasicompressional and quasishear, since it is generally not possible to completely uncouple shear and compressional displacements. The compressional wave, whose behavior at low frequency is similar to a compressional wave in a plate, can be launched within the region from broadside incidence to a cutoff angle $\gamma_s = \sin^{-1}(c/c_p)$, defined by the plate speed c_p .¹¹ Shear waves can also be launched within a range of angles around broadside, limited by cutoff at an angle given by $\gamma_T = \sin^{-1}(c/c_s)$, where c_s is the shear speed in the shell material. Using the values given in Table I for SS304 these cutoff angles are $\gamma_s = 16.5^\circ$ and $\gamma_T = 28.2^\circ$. At each of these cutoff angles the helix angle Ψ_l is zero and propagation is strictly along the axial direction. For purely circumferential propagation on an infinite cylindrical shell these waves are identified in the lowest order case as the s_0 leaky Lamb wave and horizontally polarized shear wave T_0 , respectively. Acoustic coupling to these waves is cutoff for γ in excess of γ_s and γ_T , respectively. Coupling to the flexural wave, denoted by a_0 for broadside incidence, should be possible, however, for tilt angles greater than γ_T .¹² Section II of this paper describes the results of backscattering experiments carried out on two different

TABLE I. Shell and material parameters.

Shell	Outer radius a (cm)	Thickness h (cm)	Length L (cm)	h/a	L/a
A	1.91	0.145	22.86	0.076	12.0
B	2.10	0.342	24.51	0.163	11.7
Material	Density (g/cm ³)	Longitudinal velocity (km/s)	Shear velocity (km/s)		
Stainless steel 304	7.57	5.675	3.141		
Water	1.00	1.483			

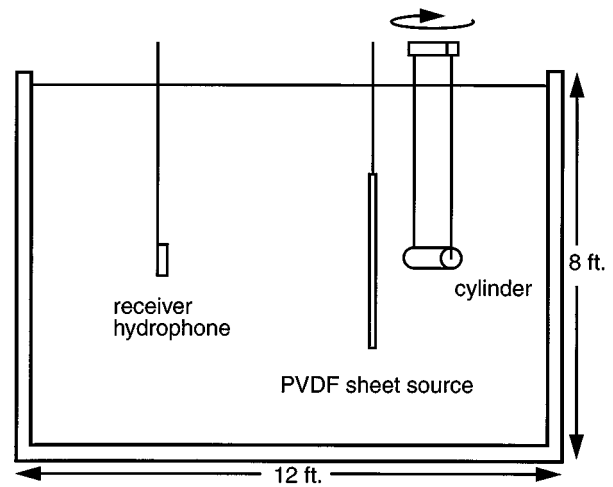


FIG. 2. Experimental setup. A cylindrical shell is suspended from a rotation stage in a cylindrical redwood tank. The sheet source generates an approximately unipolar pressure impulse from both its front and back sides. Backscattered signals from the shell propagate through the acoustically transparent sheet source to the hydrophone.

shells where the tilt of the cylinder was allowed to vary from broadside to end-on incidence. These results are compared with theoretical predictions of the backscattering spectral magnitude, which is presented in Appendix A. Section III describes an approximate calculation for the frequency-angle loci which correspond to launching and circumferential coupling conditions for helical surface waves of interest. These curves are used to identify the elastic responses observed at mid to high tilt angles.

I. SCATTERING EXPERIMENT

Broadband backscattering experiments were carried out for slender cylindrical shells in a large redwood water tank. A schematic of the experimental setup is given in Fig. 2. An air-filled finite cylindrical shell is placed in the *near field* of a PVDF sheet source, which radiates an approximately plane pressure impulse over the dimensions of the target. A hydrophone records the pressure response backscattered through the sheet. This nonconventional placement of the acoustically transparent PVDF source between the scatterer and receiver has been discussed previously.¹³ The cylindrical shell was suspended at each end cap by thin monofilament fishing line. Flat Plexiglas end caps were used, and a watertight seal was maintained by rubber O-rings and a light elastic strand stretched between the end caps inside the shell. The center of the target was placed approximately 25 cm from the source. The receiver, a pistonlike piezoelectric transducer (Panametrics, model V302), was placed oppositely a distance of approximately 100 cm from the source. The sheet source is constructed of 110- μm -thick PVDF film¹⁴ with silver surface metalization and a 1-mil layer of Mylar on each side. It measures 71 \times 71 cm. An approximately unipolar pressure pulse is generated when a voltage step is applied to the sheet. A discussion of the source spectral properties and normalization can be found in Appendix B. A high current pulse generator (Avtech Electrosystems LTD., model AVO-8C-C) was used to supply a long duration square wave input during

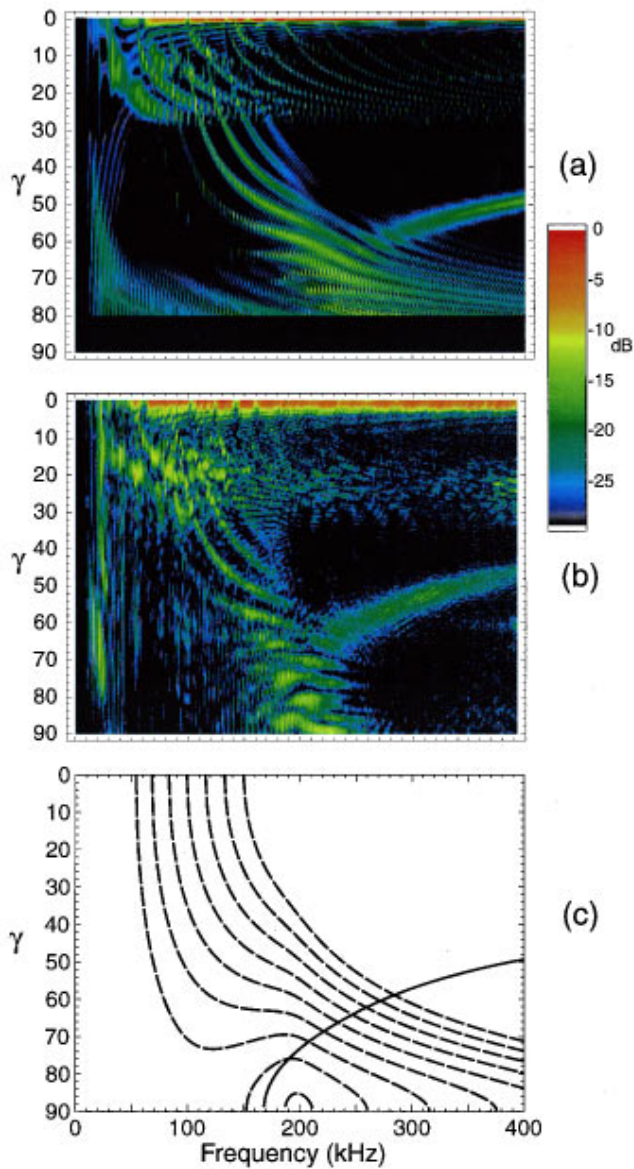


FIG. 3. Scattering from shell A: (a) Calculated and (b) measured backscattered spectral magnitude of the impulse response as a function of frequency and aspect angle for an empty SS304 cylindrical shell with thickness to radius ratio $h/a=0.076$ and slenderness $L/a=12.0$. The maximum frequency displayed ($f=400$ kHz) corresponds to $ka=32.3$. Calculated values beyond $\gamma=80^\circ$ in (a) have been floored (shown as black) due to increased error in the numerical calculation at high aspect angles. (c) The solid curve shows the frequency-angle locus for launching the meridional ray depicted in Fig. 1. It is calculated using the phase velocity for the a_0 wave on a fluid-loaded plate having the same thickness as the shell. The dashed curves show the approximate coupling loci ($m=6-14$) for a_0 -helical waves, calculated using Eq. (1) with phase velocity values calculated for an infinite, empty, thick cylindrical shell at broadside incidence as discussed in Appendix C.

the experiment. The trailing voltage step-down was delayed until after the backscattered signal was received. Due to the finite dimensions of the sheet source, edge contributions delayed relative to the initial pressure impulse will contribute to the measured backscatter. These edge contributions are delayed in proportion to the difference in path length between the scatterer and the center and edges of the sheet. Because the scatterer is placed near the sheet source the ef-

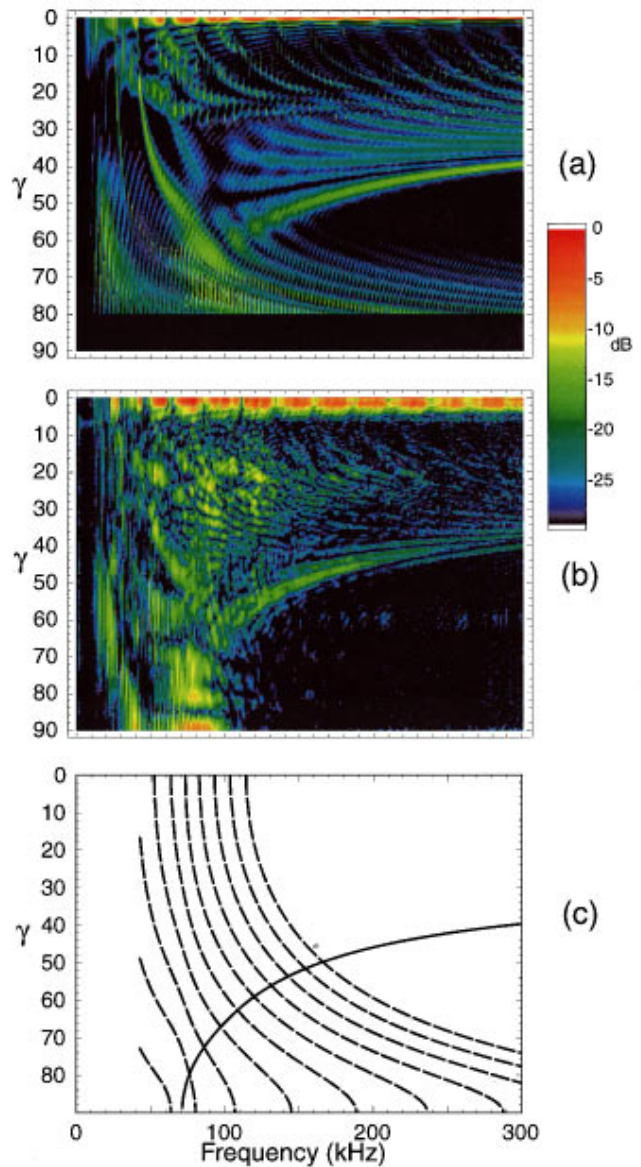


FIG. 4. Scattering from shell B: Same as Fig. 3 except $h/a=0.163$ and $L/a=11.7$. The maximum frequency displayed ($f=300$ kHz) corresponds to $ka=26.7$. The family of dashed curves in (c) correspond to resonance conditions $m=2-11$.

fects due to these contributions are expected primarily at low frequencies; no attempt has been made to incorporate these effects in the present analysis. Two stainless steel (SS304) scatterers with thickness to radius ratios of 7.6% and 16.3% were examined separately and are labeled A and B, respectively. Table I lists the dimensions of each shell and relevant material properties.

Time records were recorded for the full range of incidence angles, spanning end-on and broadside incidence. Multiple time signals were recorded and averaged at each angle; a background record, taken with the target removed, was then subtracted to remove signals arriving directly from the source. The time window chosen for the experiment excluded reflections from the tank walls. The background subtracted time series data was fast Fourier transformed (FFT) and the modulus normalized according to the source-receiver system impulse response to obtain the backscatter-

ing spectrum. In the region near end-on incidence, reflections from the flat end caps are clearly observable and quite localized in time. Because the scatterers in this experiment were slender, the specular reflection from the end cap closest to the source was well separated in time from the elastic responses of interest excited on the shell. To isolate the elastic backscattering response of the shell, a rectangular window which excluded the leading end-cap reflection was applied to all time records before computing an FFT.

II. MEASURED AND CALCULATED BACKSCATTERING SPECTRUM

Figures 3 and 4 compare measured and calculated spectral magnitudes for the two shells studied. Figure 3(b) shows the measured backscattering spectral magnitude from the thinner of the two shells, A, over a range of aspect angles from end-on ($\gamma=90^\circ$) to broadside ($\gamma=0^\circ$) incidence, in 0.3° increments. Figure 3(a) is the theoretical form function magnitude resulting from an *approximate* calculation for a simply supported finite cylindrical shell, which is presented in Appendix A. The relative scattering levels are set such that 0 dB corresponds to the maximum scattering response found at broadside incidence in each figure for the frequency range shown. The reader may wish to refer to the discussion of dispersion relations for thick shells given in Appendix C. The highest amplitude feature in each figure is found at $\gamma=0^\circ$. This feature corresponds to broadside incidence and includes the specular reflection from the cylinder. It is composed of broad peaks and oscillations which are not easily resolved in the figures due to the amplitude scale chosen. A comparison between the broadside records in Fig. 3(a) and (b) and the exact partial wave series (PWS) solution for backscattering at normal incidence from an infinite, air-filled thick cylindrical shell reveals good agreement in the location and spacing of the broad peaks and dips. This is the expected behavior for scattering from a slender finite shell at normal incidence when the length of the shell significantly exceeds the width of the first Fresnel zone,¹⁵ as is the case for most frequencies of interest here. These broad features are associated with the a_0 antisymmetric leaky Lamb wave in the region where that wave is supersonic.¹⁶ (For broadside incidence the narrow resonances are expected to be more strongly affected by the finite length of the cylinder.) Also clearly observable are regions of high backscatter between broadside incidence and the cutoff angle for shear wave propagation, corresponding to enhancements from helical leaky waves (s_0 and T_0) as discussed in the Introduction. This is evident by comparison with the loci shown in Fig. 5 discussed subsequently.

The most striking features evident in Fig. 3(a) and (b), and the principal focus of this paper, are the regions of high backscatter which extend beyond the cutoff angle for shear wave propagation ($\gamma = \gamma_T = 28.2^\circ$) to end-on incidence. Two features are distinguishable. The first is the broad peak curving from $\gamma=46^\circ$ at the right edge of each figure to $\gamma=90^\circ$ at $f \approx 200$ kHz. The peak value along this curve in the experimental result reaches approximately -17 dB. The second feature is composed of multiple frequency-angle curves which extend from broadside incidence to $\gamma=65^\circ$. The two

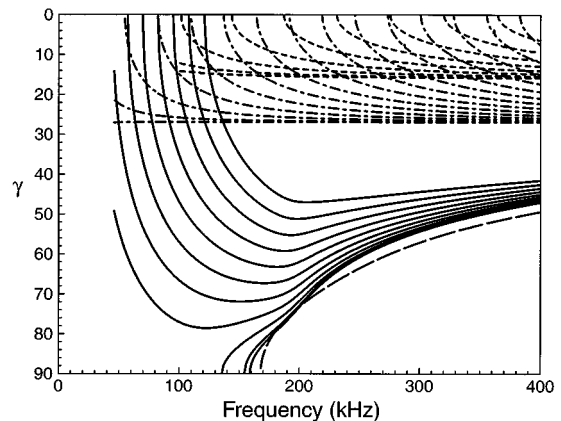


FIG. 5. Approximate coupling loci for shell A, calculated using Eq. (1). Phase velocity values are for an infinite, empty, thick cylindrical shell for purely circumferential propagation as discussed in Appendix C. Each family of curves is identified as follows: solid ($l=a_0$, $m=0-10$), alternating long and short dashes ($l=T_0$, $m=0-14$), and short dashes ($l=s_0$, $m=0-8$). The curve with long dashes is the solid curve in Fig. 3(c) for the meridional ray.

features merge near the coincidence frequency [$f=193$ kHz; $ka=15.6$, see Fig. C1(a)] and exhibit strong backscattering (up to -11 dB) out to end-on incidence. The first of these two features can be associated with the meridional (axial) propagation of the a_0 antisymmetric leaky Lamb wave along the front side of the cylinder, as shown in the ray diagram in Fig. 1. Recall that coupling to the meridional ray, and subsequent backscattering enhancement, occurs at tilt angles $\gamma = \theta_l = \sin^{-1}(c/c_l)$. To a good approximation in this frequency range the phase velocity of the a_0 wave can be modeled by the phase velocity calculated for a plate of the same material and thickness. The solid curve in Fig. 3(c) shows where the above launching condition is satisfied for the a_0 wave, using phase velocity values calculated with the exact solution for a plate fluid loaded on one side with water. Good agreement is found between this curve and the broad feature evident in both the experimental and theoretical figures. The dashed curves show the results of a similar approximation applied to the helical propagation of the subsonic Lamb wave a_0- which will be discussed in the following section.

Figure 4 shows theoretical and experimental results for a considerably thicker shell, labeled B in Table I. The coincidence frequency is now found at a lower frequency $f=82$ kHz ($ka=7.3$). Figure 4(c) displays phase matching conditions for the meridional propagation of the a_0 wave in the same way as for the thinner shell in Fig. 3(c). The broad curve extending from $\gamma=40^\circ$ at the right edge of the figure to $\gamma=90^\circ$ at $f \approx 80$ kHz is similarly identified as resulting, at least in part, from the launching of the a_0 wave in a meridional fashion. Also observable are what appear to be the higher-order circumferential resonances of the helical a_0 supersonic waves, whose coupling loci are discussed below (in conjunction with the discussion of Fig. 6). Near the coincidence frequency, within 25° of end-on incidence, backscattering levels are considerable, reaching -10 dB at $\gamma=80^\circ$ and -7 dB at $\gamma=90^\circ$. Below the coincidence frequency the backscattering response is generally high over a

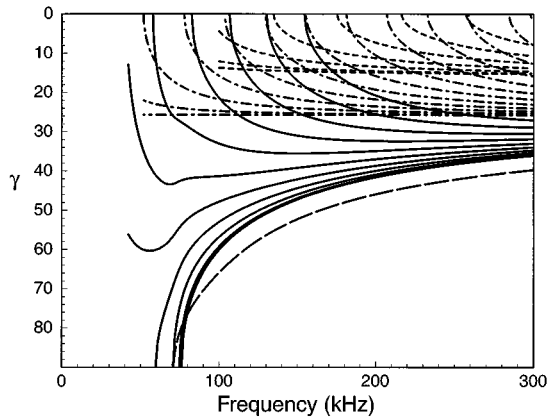


FIG. 6. Approximate coupling loci for shell B, calculated using Eq. (1), analogous to Fig. 5 for the thinner shell. Each family of curves is identified as follows: solid ($l = a_0$, $m = 0-10$), alternating long and short dashes ($l = T_0$, $m = 0-11$), and short dashes ($l = s_0$, $m = 0-7$). The curve with long dashes is the solid curve from Fig. 4(c) for the meridional ray.

large range of aspect angles although some frequency-angle ridges and valleys are distinguishable.

III. CIRCUMFERENTIAL RESONANCES

An approximation will now be discussed which describes the frequency-angle loci corresponding to circumferential resonances of helical waves. It is known that backscattering is enhanced when resonances of the shell are excited. For the tilted finite cylinder these are usually associated with circumferential and axial propagation. Only resonances associated with *circumferential* propagation will be examined here. Resonances associated with *axial* propagation are not considered in our analysis because for the high-frequency guided waves of interest, the radiation damping is usually sufficiently large to inhibit scattering contributions from repeated axial reflections. Consequently the frequency response is expected to depend only weakly on the length L when L is large. Circumferential resonance occurs for helical waves when the azimuthal wave path equals an integer number of wavelengths. If it is assumed that reflection of the surface wave off the truncation only introduces a change in sign of the axial wave vector, the previous condition combined with the launching condition serves to define specific frequency-angle combinations wherein high levels of backscattering are possible. In terms of the dimensionless frequency ka and the aspect angle γ , where k is the wave number in the fluid medium and a is the outer radius of the cylinder, the following relationship describes circumferential resonance conditions:¹⁷

$$(ka)^2 \left[\left(\frac{c}{c_l} \right)^2 - \sin^2 \gamma \right] = m^2, \quad m = 0, 1, 2, \dots, \quad (1)$$

where the integer m is the circumferential mode number. The solution for $m = 0$ does not correspond to a resonance, but rather describes purely axial propagation of a supersonic guided wave. For this case Eq. (1) reduces to the trace velocity matching condition of a meridional ray, $\gamma = \sin^{-1}(c/c_l)$. For sufficiently high frequencies the phase velocity for propagation of a guided wave on a tilted cylinder is

approximately independent of helix angle. In this frequency region the phase velocity for all angles of incidence in Eq. (1) can be approximated by the values calculated for broadside incidence. Figure 5 shows the frequency-angle loci which satisfy Eq. (1) for the s_0 , T_0 , and a_0 waves for shell A. For each set of loci, except the a_0 wave, the $m = 0$ curve enters at the lowest frequency while higher-order curves emerge with increasing frequency. For the a_0 wave the $m = 0$ curve corresponds to the limiting solid curve on the lower right side of the figure. For comparison the solid curve from Fig. 3(c), corresponding to propagation on a plate, has been included and is now described by the long dashed curve. Figure 6 displays analogous results for shell B. Phase velocity and radiation damping curves for the relevant waves, as well as a description of the method used to calculate them and a discussion of their applicability, are given in Appendix C. Due to the aforementioned approximation, the frequency-angle loci displayed in Figs. 3-6 are to be used in identifying the responses excited on the shell and are not meant to be a precise description of resonance locations. The agreement with calculated and measured results is quite good, which can be shown by overlaying the calculated resonance loci on the backscattering response figures, and the qualitative agreement serves to identify the wave types.

The regions of scattering below the coincidence frequency deserve attention. The resonance loci for the a_0 wave in Figs. 5 and 6 have been carried through to the region where the a_0 wave becomes subsonic. Any coupling to this wave in this latter region must occur through evanescent tunneling at the azimuthal angles $\psi = \pm \pi/2$. For shell A the scattering contribution is not expected to be significant due to the high radiation damping β_l for $l = a_0$ suggested by Fig. C1(b). The features evident in Fig. 3, primarily at and below the coincidence frequency at mid to high angles might be better associated with the slightly subsonic a_{0-} wave, which has been shown to lead to large backscattering enhancements from spherical and right-circular cylindrical shells.^{18,19} The dashed curves in Fig. 3(c) show the resonance loci for helical propagation of the a_{0-} wave, calculated using Eq. (1) with $m > 0$ and the cylindrical shell phase velocity. Coupling to the a_{0-} wave would occur at $\psi = \pm \pi/2$ through evanescent tunneling. Referring to Fig. C1(b) the radiation damping of the a_{0-} wave is small for $f < 100$ kHz and increases quickly through the coincidence frequency region.¹⁸ It is through this region where the a_{0-} wave moves from exhibiting “trapped wave” to “creeping wave” behavior as the thickness of the evanescent coupling layer decreases.²⁰ Significant coupling to this wave is expected in this region. The interpretation for shell B near and below the coincidence region does not follow directly from the thinner shell results and is not as clear from the present analysis. The radiation damping of the a_{0-} wave, seen in Fig. C2(b) is large near the coincidence frequency region while the damping of the a_0 wave is relatively low. For completeness the frequency-angle loci for helical propagation of the a_{0-} and a_0 waves are extended below the coincidence frequency in Figs. 4(c) and 6, respectively.

Comparison of the solid curves in Fig. 6 in the region above 100 kHz with the observations in Fig. 4(b) shows that several of the a_0 helical wave coupling loci are visible even

when m is not small. Inspection of Fig. C2(b) suggests that this may be a consequence of the relatively weak damping of the a_0 wave in comparison to the thinner shell case shown in Fig. C1(b). It is also noteworthy that for near end-on incidence in Fig. 4(b) there is a significant backscattering enhancement near 40 kHz. The cause of this enhancement was not identified.

IV. DISCUSSION AND CONCLUSIONS

The experimental data presented for backscattering from thick cylindrical shells clearly shows regions of high backscatter at aspect angles considerably beyond the cutoff for shear wave excitation on the shells. An approximate theoretical treatment of the scattering problem of a plane wave incident on a finite cylindrical shell using full elasticity theory has been presented. The agreement in the frequency-angle domain between the experimental data and the theoretical locations of the ridges of enhanced backscattering is very good, except in the region of aspect angles nearing end-on incidence where the numerical evaluation of Eq. (A8) becomes difficult. One feature evident for both shells in the region above the coincidence frequency is identified as the backscattering contribution of an end-reflected meridional ray. The location in frequency-angle space of this backscattering mechanism is easily approximated with knowledge of the phase velocity for the a_0 leaky Lamb wave on an infinite cylindrical shell or plate (the results for a plate in vacuum are very similar) in this frequency range. It should be emphasized that this mechanism does not depend on the back side of the shell and is a local synchronization, rather than a resonance phenomena in a global sense. The associated backscattering amplitude is expected to depend only weakly on the length L of the shell when, as in the present case, $\beta_1 L/a \gg 1$ where β_1/a approximates the spatial attenuation rate of the a_0 wave (see Appendix C). The one-way attenuation factor for propagation down the length of the shell becomes $\exp(-\beta_1 L/a) \ll 1$. A second feature, identified primarily for the thinner shell, is associated with helical wave coupling loci for the subsonic a_{0-} wave at and below the coincidence frequency. Distinct helical wave coupling loci can be resolved on the thick shell for the supersonic a_0 wave at high frequencies.

The frequency-angle domain response plots shown in Figs. 3 and 4 are only one of several multidimensional plots which may be used for identifying the large number of high-frequency elastic scattering contributions. Another example includes time-frequency domain response plots for a fixed scattering angle or target orientation.²¹⁻²³ The plots shown in Figs. 3 and 4 are especially relevant to the operation of high-frequency sonar systems because the dependence on aspect angle is displayed.

ACKNOWLEDGMENTS

This work was supported by the Office of Naval Research and the Applied Research Laboratory (ARL:UT). The experiments were carried out at research facilities at Washington State University.

APPENDIX A: APPROXIMATE CALCULATION OF THE FAR-FIELD SCATTERED PRESSURE FROM A THICK FINITE CYLINDRICAL SHELL

This Appendix describes the calculations performed to arrive at Figs. 3(a) and 4(a). The pressure at a distant point from a finite cylindrical shell is calculated by propagating the field quantities obtained at the cylindrical surface to the observation point. The propagation is accomplished by applying the Kirchhoff diffraction integral to the values of the velocity potential and its normal derivative on the cylindrical boundary. These values are approximated by the velocity potential at the surface of an *infinite* cylindrical shell constructed from the same material. [In contrast to other similar articles which address acoustic scattering from finite cylindrical shells, here the velocity potentials are obtained through the application of full 3-D elasticity theory as opposed to a thin shell theory (e.g., see Refs. 4, 8, and 10).] At the surface, the potentials are expanded in terms of the *in vacuo* eigenfunctions of a simply supported cylindrical shell leading to a periodic distribution of finite scatterers of length L . By limiting the domain of integration of the Kirchhoff integral to include only the section of the surface which corresponds to the finite shell ($-L/2 < z' < L/2$), the finite nature of the scatterer may be realized in the far field. Here the acoustic effects associated with excitation of the infinite shell outside the limits of integration as well as *elastic and acoustic end effects* associated with the approximate boundary conditions are ignored.

Figure A1 displays the coordinate system used in the calculation. The surface S defines the exterior surface of a circular cylindrical shell of radius a . An arbitrary point T located on S is described by cylindrical coordinates $(\rho' = a, \psi', z')$. The observation point P is likewise described by spherical coordinates (r, θ, ϕ) . In terms of the local coordinate systems, the distance between the observation point P and a point on the surface T is written

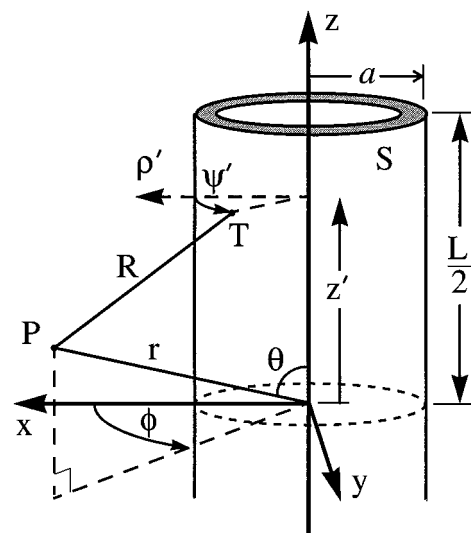


FIG. A1. Scattering geometry used in the approximate analysis. Defined with respect to the origin at the center of the cylinder, a point T on the surface is defined by the cylindrical coordinates $(\rho' = a, \psi', z')$; the observation point P is defined by the spherical coordinates (r, θ, ϕ) .

$$\begin{aligned}
R &= [(r \sin \theta \cos \phi - a \cos \psi')^2 \\
&\quad + (r \sin \theta \sin \phi - a \sin \psi')^2 + (r \cos \theta - z')^2]^{1/2} \\
&= r \left[1 + \frac{a^2}{r^2} + \frac{z'^2}{r^2} - \frac{2}{r} (a \sin \theta \cos (\psi' - \phi) \right. \\
&\quad \left. + z' \cos \theta) \right]^{1/2}. \tag{A1}
\end{aligned}$$

Assuming $r \gg a$, z' , the distance R may be written to leading order in a and z' as

$$R \approx r - a \sin \theta \cos (\psi' - \phi) - z' \cos \theta + \dots \tag{A2}$$

Inserting the above expression into the Kirchhoff diffraction integral^{10,24} yields the following equation for the velocity potential at a distant field point P

$$\begin{aligned}
\Phi(r, \theta, \phi) &= -\frac{1}{4\pi} \frac{e^{ikr}}{r} \oint_S e^{-ik(a \sin \theta \cos (\psi' - \phi) + z' \cos \theta)} \\
&\quad \times \left[\frac{\partial \Phi}{\partial \rho'} + ik \sin \theta \cos (\psi' - \phi) \Phi \right] dS'. \tag{A3}
\end{aligned}$$

Here R has been written to first order in a and z' in the exponential with only the leading term r kept in the denominator (Fraunhofer approximation). The solution to Eq. (A3) requires knowledge of both the velocity potential Φ and its normal derivative $\partial \Phi / \partial \hat{n}$ on the surface of the shell. An approximation for these values is discussed below.

Consider an infinite cylindrical shell insonified by plane waves propagating in the direction $\theta = \pi - \alpha$ and $\phi = 0$, where $\alpha = (\pi/2) - \gamma$ and γ is the tilt angle. The velocity potential of the total field may be written in terms of an incident and scattered potential

$$\Phi = \Phi_{\text{inc}} + \Phi_{\text{sc}}. \tag{A4}$$

By requiring the shell to satisfy simply supported boundary conditions at $z' = \pm qL/2$ (where q is an integer), the total potential Φ is expanded into the eigenfunctions of the *in vacuo* simply supported cylinder. The velocity potential resulting from the incident plane wave is written

$$\begin{aligned}
\Phi_{\text{inc}} &= \frac{i}{\rho \omega} \sum_{n=0}^{\infty} \sum_{p=1}^{\infty} \epsilon_n i^n J_n(k_{\perp} \rho') \cos(n \psi') \\
&\quad \times \sin \left[k_p \left(z' + \frac{L}{2} \right) \right] \beta(p), \tag{A5}
\end{aligned}$$

where the time dependence $e^{-i\omega t}$ has been suppressed, ρ is the density of the outer fluid, $k_p = p\pi/L$, and the radial projection of the incident wave vector is given by $k_{\perp} = k \sin \alpha$. The expansion coefficient $\beta(p)$ is written

$$\begin{aligned}
\beta(p) &= \frac{2}{L} i^{p-1} \left[-(-1)^p \frac{\sin((k \cos \alpha + k_p)(L/2))}{(k \cos \alpha + k_p)} \right. \\
&\quad \left. + \frac{\sin((k \cos \alpha - k_p)(L/2))}{(k \cos \alpha - k_p)} \right]. \tag{A6}
\end{aligned}$$

The velocity potential of the scattered field Φ_{sc} may be expressed by (compare with Ref. 7)

$$\begin{aligned}
\Phi_{\text{sc}} &= \frac{i}{\rho \omega} \sum_{n=0}^{\infty} \sum_{p=1}^{\infty} \epsilon_n i^n H_n^{(1)}(\xi_p \rho') \cos(n \psi') \\
&\quad \times \sin \left[k_p \left(z' + \frac{L}{2} \right) \right] X(n, p), \tag{A7}
\end{aligned}$$

where $\xi_p^2 = k^2 - k_p^2$ and X is the ratio of two 8×8 determinants $X(n, p) = D_{n,p}^{[1]}/D_{n,p}$, where $D_{n,p} = \det[M]$ and $D_{n,p}^{[1]} = \det[N_1]$. Notice that while k_{\perp} is determined by the tilt of the cylinder, ξ_p depends on the Fourier index p . The elements of the matrix M result from the boundary value problem for an infinite, elastic cylindrical shell interiorly and exteriorly fluid loaded. The shell is subject to periodic simply supported boundary conditions, and the shell mechanics are described by full three-dimensional elasticity theory. The elements of M may be obtained from Appendix B of Ref. 7 with a few minor adjustments. Using the notation of Ref. 7, the elements of M are obtained by replacing every occurrence of k_z by k_p , x_z by $-k_p a$, and y_z by $-k_p b$, where b is the inner radius of the shell. [This change is the result of replacing the axial eigenfunctions $e^{ik_z z}$ of Ref. 7 by eigenfunctions which satisfy simply supported boundary conditions $\sin(k_p(z' + L/2))$ along the axial coordinate.] In addition, the argument x_{\perp} in elements $M(1,1)$ and $M(3,1)$ must be replaced by $\xi_p a$, the term x_1^2 in $C(3)$ replaced by $(k_{\perp} a)^2 + (k_p a)^2$, and the argument $y_3 \cos \alpha'$ in $M(2,2)$ and $M(4,2)$ replaced by $\sqrt{(\omega b/c_3)^2 - (\xi_p b)^2}$. The matrix N_1 is the matrix M with its first column replaced by the column vector C .

The solution for the far-field scattered pressure of the finite, simply supported cylinder is obtained by inserting the velocity potentials from Eqs. (A5) and (A7) above into the Kirchhoff integral in Eq. (A3). Here, as is common with the Kirchhoff approximation,²⁴ Φ and $\partial \Phi / \partial \hat{n}$ are set to zero on the cylindrical surface S outside the aperture $-L/2 < z' < L/2$. (Even though the Kirchhoff problem suffers from mathematical inconsistencies outside the aperture, the inclusion of Dirichlet or Neumann boundary conditions in the region $|z'| > L/2$ would result in added specular contributions due to rigid or pressure release extensions of the finite cylinder. Such contributions are not of interest in the present study.) Integration over the domain of the aperture yields the solution for the velocity potential of the scattered field. For far-field backscattering

$$\begin{aligned}
\Phi_{\text{sc}}(r, \alpha, \pi) &= \frac{i}{\rho \omega} \frac{e^{ikr}}{2r} \sum_{n=0}^{\infty} \sum_{p=1}^{\infty} \epsilon_n (-1)^n \\
&\quad \times F(p) X(n, p) A(n, p), \\
A(n, p) &= [(k_{\perp} a) H_n^{(1)}(\xi_p a) J_n'(k_{\perp} a) \\
&\quad - (\xi_p a) H_n^{(1)'}(\xi_p a) J_n(k_{\perp} a)], \tag{A8} \\
F(p) &= \frac{L}{2} \beta(p).
\end{aligned}$$

The contribution from the incident field Φ_{inc} in Eq. (A5) is purposely ignored since only ‘‘outward’’ traveling waves at the far-field observation point are of interest. The pressure is easily obtained from Eq. (A8) by the relation

$$p(r, \theta, \phi) = -i\rho\omega\Phi(r, \theta, \phi), \quad (\text{A9})$$

and the far-field scattering form function f is defined by

$$p(r, \theta, \phi) = p_{\text{inc}} \frac{a}{2r} f(\theta, \phi) e^{ikr}, \quad (\text{A10})$$

where in the present case $P_{\text{inc}} = 1$.

The backscattered form function [$f(\alpha = \pi/2 - \gamma, \phi = \pi)$] in Figs. 3(a) and 4(a) is calculated via Eqs. (A8)–(A10). The material parameters used in the calculations are listed in Table I and the interior of the shell was taken to be a vacuum. The number of terms kept in the double infinite series of Eq. (A8) are p_{max} and n_{max} . Here n_{max} is chosen in accordance with the convention of Ref. 25 based on the localization principle. After several trials, it was necessary to choose the value of p_{max} to be slightly less than kL/π . Truncating the sum in this way appears necessary to avoid the singularity of the Hankel functions in the coefficients $A(n, p)$ in Eq. (A8) when the radial wave number $\xi_p \rightarrow 0$.

APPENDIX B: SOURCE SPECTRUM AND NORMALIZATION

This Appendix discusses the normalization used in the experimental spectral data [Figs. 3(b) and 4(b)] and a simple model used to describe the spectrum of the PVDF source. The system impulse response was measured with the hydrophone placed approximately at the target location. The solid line in Fig. B1 shows the fast Fourier transform (FFT) of the measured pulse. The smooth dashed curve is the expected spectrum from an idealized source–receiver model to be described subsequently. The spectrum of the source–receiver impulse response is taken to be the best fit of this model to the measured spectrum. The FFT of each time record in the scattering experiment was divided by this smooth estimate of the system impulse response to obtain the measured scattering spectrum.

To approximate the spectrum of the source a simple lumped electrical parameter circuit model was introduced. Figure B2 shows this circuit model where the source is taken to be an idealized capacitor in series with a small resistor.

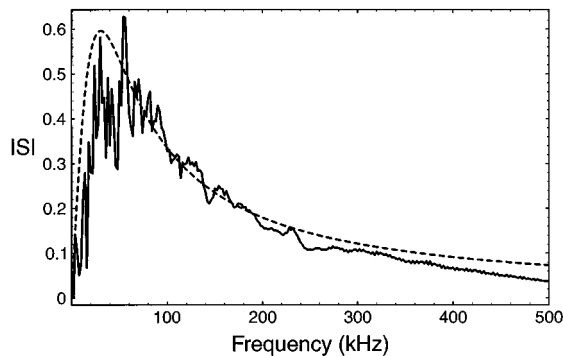


FIG. B1. Measured (solid line) spectrum of the pressure impulse generated by the sheet source. A simple lumped parameter model of the source and receiver system yields a good approximation (dashed line) of the measured spectrum.

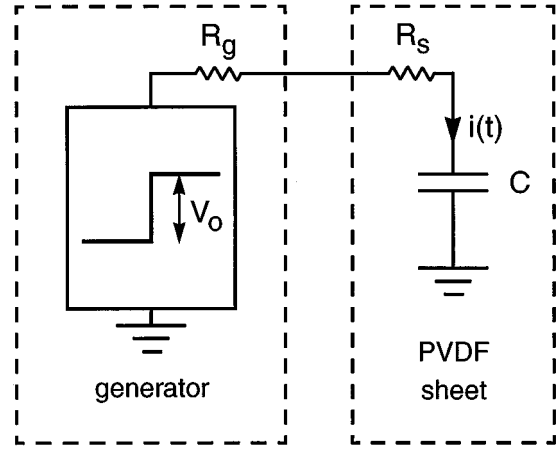


FIG. B2. Lumped electrical parameter circuit model which is used to model the frequency response of the PVDF sheet source.

The acoustic pressure generated by the PVDF is approximately proportional to the current (e.g., see Ref. 13), which for a step voltage input gives

$$p(t) = Ki(t) = K\Theta(t)i_o e^{-t/RC}, \quad (\text{B1})$$

$$i_o = V_o/R, \quad R = R_g + R_s,$$

where K is a constant determined by the piezoelectric properties, $\Theta(t)$ is the unit step function, C denotes the capacitance of the sheet, and R is the sum of the generator and effective sheet resistances. The magnitude of the spectrum associated with this pressure is

$$|S(\omega)| = [1 + (RC\omega)^2]^{-1/2}, \quad (\text{B2})$$

where $\omega = 2\pi f$. The spectral amplitude given in Eq. (B2) has a value of unity at zero frequency. In the experiment the low-frequency response is limited by the roll-off of the hydrophone, which is governed largely by the load resistance R_h and hydrophone capacitance C_h . The normalized low-frequency behavior of the receiver can be approximated as a high-pass filter with frequency response

$$|S_h(\omega)| = [1 + (R_h C_h \omega)^2]^{-1/2}. \quad (\text{B3})$$

At frequencies well below the fundamental hydrophone resonance the approximate spectrum of the source–receiver system is the product of $|S(\omega)|$ and $|S_h(\omega)|$. Figure B1 shows that this simple model overestimates the high-frequency response of the source above about 230 kHz; as a result, it is necessary to multiply Eq. (B2) by a slowly decaying function of ω for use in the actual normalization of Figs. 3(b) and 4(b). This function is $[1 + (RC\omega)^2]^{-0.25}$ and is thought to be a consequence of the specific receiver used, which was originally designed as an NDT (nondestructive testing) immersion transducer. The resulting fit to the experimental source spectrum is a four parameter fit: RC , $R_h C_h$, the exponent (0.25), and the overall amplitude factor. The values obtained for RC and $R_h C_h$ are compatible with the expected magnitudes for the apparatus used.

APPENDIX C: WAVE PROPERTIES FOR THICK CYLINDRICAL SHELLS

This Appendix discusses the guided wave properties for the thick cylindrical shell and their applicability to the circumferential resonance condition given in Sec. III. Figure C1 displays the wave properties for an infinite empty cylindrical shell having the same radii and material parameters as shell A. It displays the normalized phase velocity and radiation damping (in Np/rad) parameters as a function of frequency where the angular damping rate is for purely circumferential propagation. Figure C2 displays analogous results for a cylinder corresponding to shell B. The wave parameters given in these figures are calculated using the Watson methodology applied to the exact partial wave series (PWS) solution for an infinite cylindrical shell insonified at normal incidence.^{1,16} These curves are exact only for circumferential propagation (nonoblique incidence) on an infinite cylinder. In Figs. C1(a) and C2(a) the curve defined by the points corresponds to the normalized phase velocity for the a_0 Lamb wave on a plate of the same material and thickness in vacuum. Notice that unlike Fig. C1(a), in Fig. C2(a) the a_0 and a_{0-} curves for c_l/c cross in the coincidence region. This crossing behavior is representative of the coincidence behavior for thick shells in contrast to the repulsion for thin shells evident in Fig. C1(a).

The phase velocities calculated above for the case of broadside incidence are a good estimate for the phase velocities encountered at oblique incidence provided the frequency is sufficiently high. For the case of thin shells this criteria is

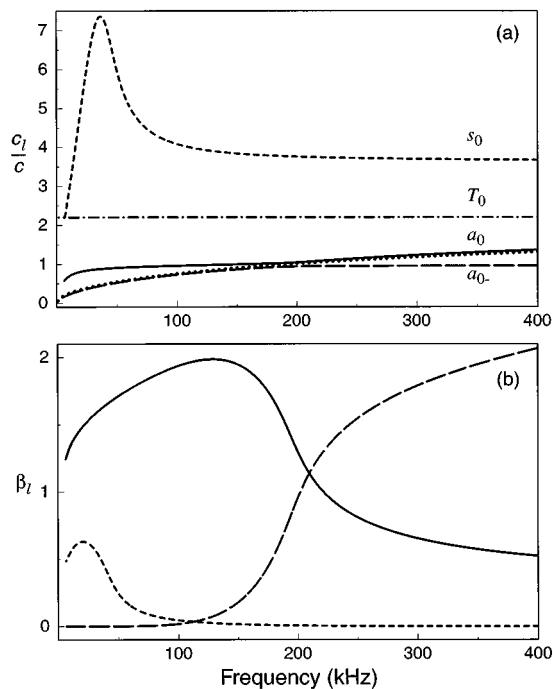


FIG. C1. (a) Normalized phase velocity and (b) radiation damping for guided waves on an infinite, empty, thick cylindrical shell corresponding to shell A for broadside incidence. The curve defined by the points shows the normalized phase velocity for the a_0 wave on a plate of the same thickness in vacuum. The coincidence frequency is defined as the frequency where this normalized phase velocity is equal to unity, which in this case is 193 kHz.

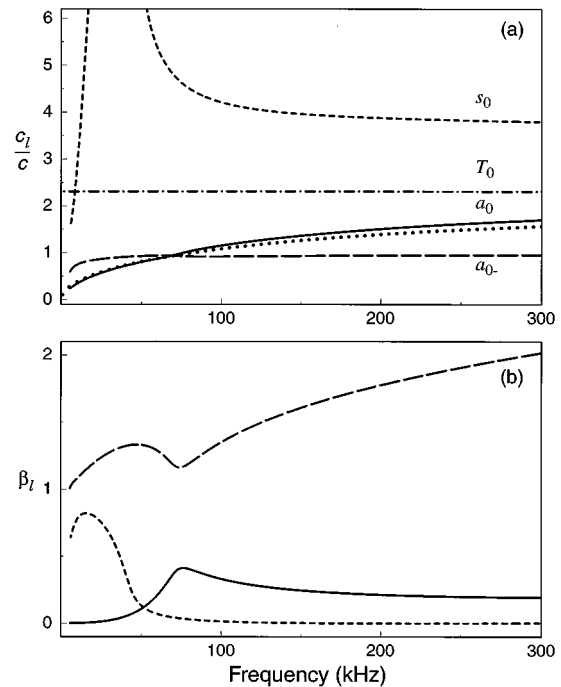


FIG. C2. (a) Normalized phase velocity and (b) radiation damping values for shell B. The coincidence frequency for this shell is 82 kHz.

usually that the frequency is sufficiently above the cylindrical “ring” frequency of the shell. In Figs. 3(c), 4(c), 5, and 6 the low end of the resonance loci are terminated at a somewhat arbitrary frequency, at or above an estimate of the “ring” frequency for each shell.

One consequence of using the phase velocities given above in Eq. (1) for the estimated resonance loci is apparent by noting the difference between the a_0 phase velocity curves for the cylinder compared with the plate. Evident in both Figs. C1(a) and C2(a) is a shift toward higher phase velocities for the cylinder above the coincidence frequency. This shift can be attributed to the effects of curvature present in the cylinder analysis.²⁶ For the meridional ray ($m=0$) the behavior of the a_0 wave would be expected to follow that for the plate, while for increasing m the behavior would tend toward that for the cylinder. In Figs. 5 and 6 the lower-order resonance loci for the supersonic a_0 wave (solid curves) tend to congregate very close together; furthermore, they are displaced relative to the plate curve. Removing the effect of curvature for low orders of m would have the effect of broadening the spacing of these curves toward the plate curve.

For situations where the phase velocity c_l is somewhat larger than c , it is anticipated that the spatial leaky wave damping rate depends only weakly on curvature for those waves where β_l is shown in Figs. C1(b) and C2(b). The spatial leaky wave damping rate may be estimated as β_l/a , where a is the radius of the cylinder. The relevant propagation distance is determined by the cumulative length of the meridional or helical leaky ray on the cylinder.

¹G. Kaduchak, C. M. Wassmuth, and C. M. Loeffler, “Elastic wave contributions in high resolution acoustic images of fluid-filled, finite cylindrical shells in water,” *J. Acoust. Soc. Am.* **100**, 64–71 (1996).

- ²P. L. Marston, "Approximate meridional leaky ray amplitudes for tilted cylinders: end-backscattering enhancements and comparisons with exact theory for infinite solid cylinders," *J. Acoust. Soc. Am.* **102**, 358–369 (1997).
- ³M. C. Junger and D. Feit, *Sound, Structures, and Their Interaction* (Acoustical Society of America, Woodbury, NY, 1993).
- ⁴M. L. Rumerman, "Contribution of membrane wave reradiation to scattering from finite cylindrical steel shells in water," *J. Acoust. Soc. Am.* **93**, 55–65 (1993).
- ⁵A. N. Norris and D. A. Rebinsky, "Acoustic coupling to membrane waves on elastic shells," *J. Acoust. Soc. Am.* **95**, 1809–1829 (1994).
- ⁶C. N. Corrado, "Mid-frequency acoustic backscattering from finite cylindrical shells and the influence of helical membrane waves," Ph.D. dissertation, Massachusetts Institute of Technology, Department of Ocean Engineering, 1993. See also M. Conti, "Mid-frequency acoustic scattering from finite internally-loaded cylindrical shells near axial incidence," Ph.D. dissertation, Massachusetts Institute of Technology, Department of Ocean Engineering, 1995.
- ⁷F. Léon, F. Lecroq, D. Décultot, and G. Maze, "Scattering of an obliquely incident acoustic wave by an infinite hollow cylindrical shell," *J. Acoust. Soc. Am.* **91**, 1388–1397 (1992).
- ⁸M. Tran-Van-Nhieu, "Scattering from a finite cylindrical shell," *J. Acoust. Soc. Am.* **91**, 670–679 (1991).
- ⁹X.-L. Bao, "Echoes and helical surface waves on a finite elastic cylinder excited by sound pulses in water," *J. Acoust. Soc. Am.* **94**, 1461–1466 (1993).
- ¹⁰V. V. Muzychenko and S. A. Rybak, "Low-frequency resonance scattering of sound by finite cylindrical shells (review)," *Sov. Phys. Acoust.* **34**, 325–333 (1988).
- ¹¹The plate speed is defined to be $c_p \equiv [E/\rho(1-\nu^2)]^{1/2}$, where E is Young's modulus, ρ is the density, and ν is Poisson's ratio. Alternately $c_p = 2c_s[2-(c_t^2-2c_s^2)/(c_t^2-c_s^2)]^{-1/2}$. Using the parameters listed in Table I, the plate speed for SS304 is $c_p = 5.232$ km/s.
- ¹²See, for example, V. V. Muzychenko, A. P. Paniklenko, and S. A. Rybak, "Dispersion curves for normal modes in cylindrical shell and conditions for spatial coincidence in the vicinity of the critical frequencies," *Sov. Phys. Acoust.* **30**, 47–51 (1984).
- ¹³G. Kaduchak, C. S. Kwiatkowski, and P. L. Marston, "Measurement and interpretation of the impulse response for backscattering by a thin spherical shell using a broad-bandwidth source that is nearly acoustically transparent," *J. Acoust. Soc. Am.* **97**, 2699–2708 (1995).
- ¹⁴The properties of this PVDF sheet differing from those found in Ref. 13 are its surface resistivity (0.1 Ω /square) and electrical capacitance (≈ 102 pF/cm²). The PVDF film was purchased from AMP Inc., Valley Forge, PA.
- ¹⁵I. B. Andreeva and V. G. Samovol'kin, "Sound scattering by elastic cylinders of finite length," *Sov. Phys. Acoust.* **22**, 361–364 (1977); P. L. Marston, "Leaky waves on curved scatterers. I. Fresnel width of coupling regions and elliptical Fresnel patches," *J. Acoust. Soc. Am.* **96**, 1893–1898 (1994).
- ¹⁶N. H. Sun and P. L. Marston, "Ray synthesis of leaky Lamb wave contributions to backscattering from thick cylindrical shells," *J. Acoust. Soc. Am.* **91**, 1398–1402 (1992); S. G. Kargl and P. L. Marston, "Ray synthesis of the form function for backscattering from an elastic spherical shell: Leaky Lamb waves and longitudinal resonances," *ibid.* **89**, 2545–2558 (1991).
- ¹⁷See, e.g., N. D. Veksler, V. M. Korsunskii, and S. A. Rybak, "Scattering of an obliquely incident plane wave by a circular cylindrical shell," *Sov. Phys. Acoust.* **36**, 5–7 (1990); J. M. Conoir, P. Rembert, O. Lenoir, and J. L. Izbicki, "Relation between surface helical waves and elastic cylinder resonances," *J. Acoust. Soc. Am.* **93**, 1300–1307 (1993).
- ¹⁸L. G. Zhang, N. H. Sun, and P. L. Marston, "Midfrequency enhancement of the backscattering of tone bursts by thin spherical shells," *J. Acoust. Soc. Am.* **91**, 1862–1874 (1992); G. Kaduchak and P. L. Marston, "Observation of the midfrequency enhancement of tone bursts backscattered by a thin spherical shell in water near the coincidence frequency," *ibid.* **93**, 224–230 (1993); P. L. Marston and N. H. Sun, "Backscattering near the coincidence frequency of a thin cylindrical shell: Surface wave properties from elasticity theory and an approximate ray synthesis," *ibid.* **97**, 777–783 (1995).
- ¹⁹M. Talmant, G. Quentin, J. L. Rousselot, J. V. Subrahmanyam, and H. Überall, "Acoustic resonances of thin cylindrical shells and the resonance scattering theory," *J. Acoust. Soc. Am.* **84**, 681–688 (1988); G. S. Sammelmann, D. H. Trivett, and R. H. Hackman, "The acoustic scattering by a submerged, spherical shell. I: The bifurcation of the dispersion curve for the spherical antisymmetric Lamb wave," *ibid.* **85**, 114–124 (1989).
- ²⁰L. B. Felsen, J. M. Ho, and I. T. Lu, "Three-dimensional Green's function for fluid-loaded thin elastic cylindrical shell: Alternative representations and ray acoustic forms," *J. Acoust. Soc. Am.* **87**, 554–569 (1990); *ibid.* **89**, 1463–1464 (1991).
- ²¹N. Yen, L. R. Dragonette, and S. K. Numerich, "Time-frequency analysis of acoustic scattering from elastic objects," *J. Acoust. Soc. Am.* **87**, 2359–2370 (1990).
- ²²D. H. Hughes, "Backscattering of sound by spherical shells in water," Ph. D. dissertation, Washington State University, 1992.
- ²³L. R. Dragonette, D. M. Drumheller, C. F. Gaumond, D. H. Hughes, B. T. O'Connor, N.-C. Yen, and T. J. Yoder, "The application of two-dimensional signal transformations to the analysis and synthesis of structural excitations observed in acoustical scattering," *Proc. IEEE* **84**, 1249–1262 (1996).
- ²⁴J. D. Jackson, *Classical Electrodynamics* (Wiley, New York, 1975), 2nd ed., Sec. 9.8; M. Born and E. Wolf, *Principles of Optics* (Permagon, Oxford, 1980), 6th ed., Sec. 8.3.2.
- ²⁵G. Kaduchak and P. L. Marston, "Traveling-wave decomposition of surface displacements associated with scattering by a cylindrical shell: Numerical evaluation displaying guided forward and backward wave properties," *J. Acoust. Soc. Am.* **98**, 3501–3507 (1995).
- ²⁶P. L. Marston, "Phase velocity of Lamb waves on a spherical shell: Approximate dependence on curvature from kinematics," *J. Acoust. Soc. Am.* **85**, 2663–2665 (1989).

Double wave of Stoneley type on the interface of a stratified fluid layer and an elastic solid half-space

A. Alenitsyn^{a)}

Department of Mathematical Physics, St. Petersburg University, 198904, St. Petersburg, Russia

(Received 15 July 1996; revised 16 April 1997; accepted 26 September 1997)

Sound propagation from a point time-harmonic source in a stratified water layer lying over an elastic solid half-space is investigated. It is assumed that the sound speed in the layer is less than the shear speed in the solid bottom, and that it increases with the depth. Numerical examples are given which show that the dependence of the wave field on the range between the source and the receiver can sharply change the character under rather small variations of the frequency. Namely, for some particular frequencies, the sound amplitude shows a periodical dependence on the range, while for other frequencies there is no periodicity. A theoretical explanation of this phenomenon is given in a mathematical development using the normal modes theory and high-frequency asymptotic approximations. The dispersion phase curves are found to have “quasi-intersections,” i.e., small domains where two adjacent curves almost intersect. The corresponding frequencies are called the “specific” frequencies. For any nonspecific frequency, there is *one* interface Stoneley (= Scholte) mode, whilst for each specific frequency there are *two* modes of the Stoneley type with close phase velocities. The periodicity of the field is a result of interference in the two Stoneley modes. © 1998 Acoustical Society of America. [S0001-4966(98)06101-3]

PACS numbers: 43.30.Bp, 43.30.Ma [SAC-B]

INTRODUCTION

In the process of calculating the acoustic time-harmonic wave fields in a shallow sea lying on a solid bottom, we met an unexpected phenomenon. For sound-speed profiles of a certain type, the dependence of the wave field amplitude on the range between the sound source and the receiver may considerably change character, along with an insignificant variation of the sound frequency. It is found that, at least in the sound frequency range 15–130 Hz, there exist some narrow intervals of specific frequencies for which this dependence has a periodic character, while for all other frequencies the dependence is rather chaotic. In order to understand the nature of the phenomenon, one must take into account the existence of two wave speeds in the solid bottom, the shear and the compressional ones, since no effect of this kind appears in models with a fluid bottom.

In Sec. I we set up the problem and give two numerical examples. Then in Sec. II we explain the discovered phenomenon theoretically; the explanation is based on the normal-mode theory.¹ In particular, we show that under certain conditions and for some specific frequencies, *two* (while normally *one*) modes of the Stoneley type exist. The effect mentioned above is caused by the mutual interference in these two modes.

Now we will briefly review some familiar facts concerning the Stoneley waves. It is well known^{1,2} that a specific acoustic wave can propagate along the interface of homogeneous fluid and solid half-spaces. The speed of this wave is less than the sound speed in fluid and both speeds—compressional and shear—in the elastic solid. Such a wave is called the Stoneley (or Scholte) wave. This wave is analo-

gous to Rayleigh’s wave^{1,2} on the free surface of an elastic half-space. The amplitude of Stoneley’s wave is concentrated near the fluid–solid interface and decreases exponentially with the distance from the interface in both fluid and solid. On the interface of a homogeneous fluid layer and a homogeneous elastic half-space a surface wave of the Stoneley type can also exist.³ The phase velocity of this wave depends on the frequency, so the wave is dispersive, in contrast to the classical Stoneley wave on the interface of two homogeneous half-spaces. This wave is also concentrated near the interface of two media.

In this work we consider acoustic waves in the model “an inhomogeneous stratified fluid layer on a homogeneous elastic half-space.” We show (Sec. II) that under certain conditions there exists a sequence of the frequency intervals which are specific in the following meaning: for each specific frequency, *two* waves of the Stoneley type arise instead of one Stoneley wave. The phase velocities of those waves differ slightly from each other. The following effect is found: Let the source and the receiver of sound be located in the water layer near the bottom, and the sound frequency be such that there are two close Stoneley-type modes, then the joint contribution of this Stoneley pair into the total field causes a periodic dependence of the field on the source–receiver range (Fig. 1).

I. THE PROBLEM AND NUMERICAL EXAMPLES

A. The problem

Let x , y , z be the Cartesian coordinates. Consider the acoustic waves in a layer $-\infty < x, y < +\infty$ lying on the elastic solid half-space $0 \leq z \leq h$. The acoustic waves are created by a point source of sound in the layer. Assume that the layer is filled by a fluid (the sea water) of a constant density ρ_0 ,

^{a)}Electronic mail: alenitsyn@mph.phys.spbu.ru

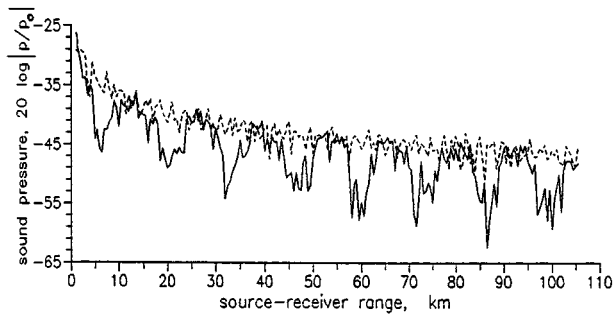


FIG. 1. Field amplitude as a function of range: the solid line for a specific frequency $f=42.1$ Hz, and the dashed line for a non-specific frequency $f=46$ Hz.

and that the sound speed depends on z , $c=c(z)$, i.e., the fluid is stratified. The half-space is a homogeneous elastic isotropic solid where the density is ρ and the wave speeds are c_p for the compressional wave and c_s for the shear wave. We suppose the wave process in both media to depend upon the time t according to the harmonic factor $\exp(-i\omega t)$, where $\omega=2\pi f$; f is a given frequency. The sound pressure $p(r, z)$ in water satisfies the Helmholtz equation

$$\nabla^2 p + \omega^2 n^2(z)p = \frac{1}{2\pi r} \delta(r) \delta(z - z_0),$$

where ∇^2 is the Laplace operator, δ is the Dirac function, and $r = \sqrt{x^2 + y^2}$, $n(z) = 1/c(z)$. The displacement vector $\mathbf{u}(x, y, z) = (u_x, u_y, u_z)$ in the solid base satisfies the system of elasticity equations:

$$c_p^2 \nabla (\nabla \cdot \mathbf{u}) - c_s^2 \nabla \times \nabla \times \mathbf{u} + \omega^2 \mathbf{u} = 0.$$

On the free water surface $z=0$ the sound pressure is taken to be zero. On the bottom $z=h$ the normal component v_z of the displacement velocity and the normal component τ_{zz} of the stress tensor are continuous, and the tangential components τ_{zx}, τ_{zy} vanish. As $z \rightarrow +\infty$, the displacement \mathbf{u} tends to zero. Our object is to investigate the acoustic pressure $p(r, z)$ as a function of the range r from the source to the receiver.

Using the familiar normal-mode method^{1,2} we can represent the sound field in the form

$$p(r, z) \approx \frac{e^{i\pi/4}}{\sqrt{8\pi}} \sum_{m=1}^M \Psi_m(z) \Psi_m(z_0) \frac{e^{ik_m r}}{\sqrt{k_m r}}. \quad (1)$$

Here $\Psi_m(z)$ is the m th eigenfunction of the spectral Sturm-Liouville boundary-value problem

$$\psi'' + k^2(n^2(z)\sigma^2 - 1)\psi = 0, \quad 0 \leq z \leq h, \quad (2)$$

$$\psi(0) = 0, \quad \psi'(h)g(\sigma) - k\psi(h) = 0, \quad (3)$$

where the phase velocity $\sigma = \sigma_m$ is the eigenvalue (to be calculated), $k_m = \omega/\sigma_m$, $n(z) = 1/c(z)$, and the function $g(\sigma)$ is defined as

$$g(\sigma) = \frac{\rho c_s^4}{\rho_0 \sigma^4} \left(4m_s - \frac{(1+m_s^2)^2}{m_p} \right), \quad (4)$$

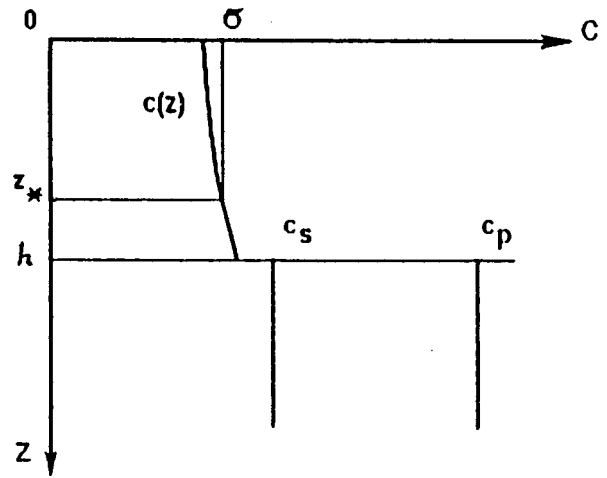


FIG. 2. Sound speeds and turning point z_* .

with $m_s = \sqrt{1 - \sigma^2/c_s^2}$, $m_p = \sqrt{1 - \sigma^2/c_p^2}$. The number M of all eigenfunctions depends on the given frequency ω , and $M \rightarrow \infty$ as $\omega \rightarrow \infty$. The eigenvalues are dispersive: σ_m are dependent on ω .

The spectral problem (2), (3) may be solved numerically with the help of finite-difference methods. In a special linear case, where $n^2(z) = \alpha - \beta z$, one can use the Airy functions Ai and Bi^4 as the exact solutions of Eq. (2).

B. Numerical examples

Consider two examples. In the first example the sound speed at the free surface is $c(0) = 1450$ m/s and at the bottom $c(h) = 1550$ m/s, the density is $\rho_0 = 1$ g/cm³, and the depth of the water layer $h = 250$ m. The sound-speed profile $c(z)$ is taken such that the squared refractive index $n^2(z)$ is a linearly decreasing function: $n^2(z) = \alpha - \beta z$, $\beta > 0$, i.e., $c(z)$ is monotonically increasing (see Fig. 2). In the solid half-space the compressional speed $c_p = 4000$ m/s, the shear speed $c_s = 1700$ m/s, and the density $\rho = 4$ g/cm³. The second example differs from the first one by only one parameter: $c_s = 2000$ m/s. The frequency values f were taken in the range 15–130 Hz. Calculations were performed with the help of a computer code using the Airy functions.

In both examples, we place the source and the receiver near the bottom: $z = z_0 = 248$ m. Then the surface waves will be well excited and hence give a significant contribution to the total field.

Remark: Such values of wave speeds are met in limestone, chalk, granite, schist, and solid sandstone. The value 4 g/cm³ for the density is not very realistic; this choice is done here only to illustrate the phenomenon as clear as possible. For instance, if $\rho = 2.7$ g/cm³, the sequence of the specific frequencies begins from $f = 37.5$ Hz, 79 Hz, ... For such ρ , the same phenomenon appears, but the graphs in Figs. 3–5, look not so indicative.

Figure 3 corresponds to the first example. We see here a family of the phase dispersion curves $\sigma = \sigma_m(\omega)$, with σ lying in the range $\sigma \in \Sigma = (c(0), c(h))$, and with f from 15 to 90 Hz. Note that a separate curve (the Stoneley-type

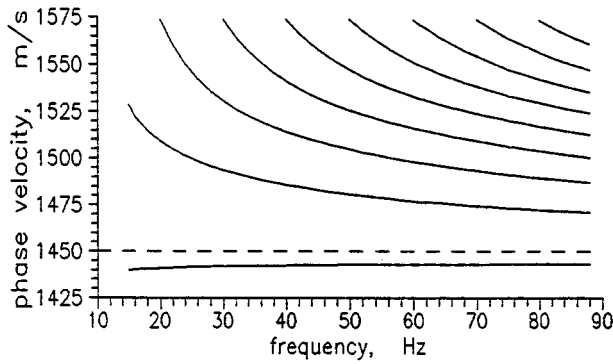


FIG. 3. The phase dispersion curves, first example: no quasi-intersections.

curve) lies below all other (water waveguide) curves. There are no quasi-intersections.

Figure 4 corresponds to the second example. We see here the *quasi-intersections* (QI) of the curves, i.e., the zones where two adjacent curves almost intersect. Such QI zones are centered near the “specific” frequencies 22, 42, 62, and 83 Hz. There are higher specific frequencies, e.g., 104 and 125 Hz (not shown in the plot).

Figure 5 shows the family of the group dispersion curves for the second example. The upper group curves fall abruptly and intersect. The intersection frequencies coincide with the quasi-intersection frequencies of the phase curves. Such intersections do not occur in example 1.

Table I shows the phase velocities σ_m and the group ones τ_m for the specific frequency $f=42.1$ Hz.

Figure 1 shows how the field amplitude depends upon the source–receiver range r . The solid line corresponds to a specific frequency 42.1 Hz, it is periodic with a period about 13.7 km. The dashed line corresponds to a nonspecific frequency 46 Hz, where the field is not periodic.

II. EXPLANATION

The phenomenon sketched above can be explained using the normal modes formula (1) and well-known WKB high-frequency asymptotic approximations^{4,5,6} for solutions of differential equation (2). Such approximations are effective for the frequency values of the order of $f \geq 20$ Hz, the higher the frequency the better the accuracy.

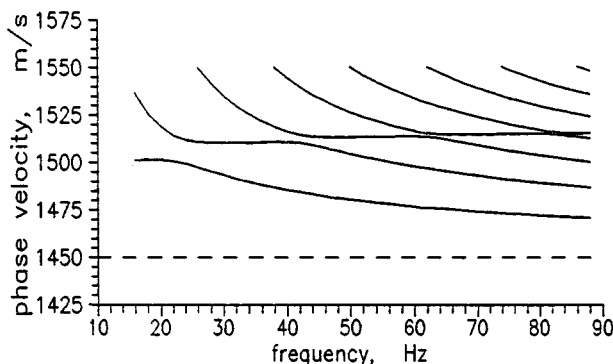


FIG. 4. The phase dispersion curves, second example: quasi-intersections.

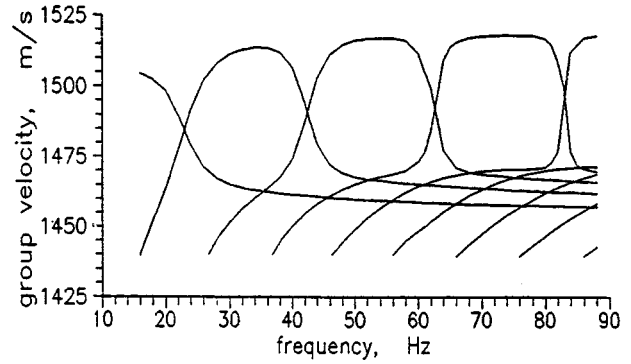


FIG. 5. The group dispersion curves, second example: intersections.

We shall now consider the phase velocity parameter σ only in the range $\Sigma = (c(0), c(h))$ because the above effect is directly related to this part of the whole spectral interval $(0, c_s)$. For $\sigma \in \Sigma$, inside the water layer there is a *turning point* z_* , i.e., the value, z such that $c(z_*) = \sigma$; see Fig. 2.

Asymptotic WKB formulas for two solutions $y_1(z)$ and $y_2(z)$ of (2) in the near-bottom domain $z_* < z \leq h$ can be written as follows:

$$y_{1,2}(z) = \frac{1}{(1 - \sigma^2 n^2(z))^{1/4}} \exp[\mp kF(z, \sigma)] \times [1 + O(\omega^{-1})], \quad (5)$$

where $F(z, \sigma) = \int_{z_*}^z \sqrt{1 - \sigma^2 n^2(t)} dt$, $k = \omega/\sigma$, $\omega \gg 1$, $n(z) = 1/c(z)$, and $\sigma \in \Sigma$.

In the near-surface waveguide domain $0 \leq z < z_*$ the asymptotic formulas are

$$y_1(z) = \frac{2}{(\sigma^2 n^2(z) - 1)^{1/4}} [\sin(k\Phi(z, \sigma) + \pi/4) + O(\omega^{-1})], \quad (5a)$$

$$y_2(z) = \frac{1}{(\sigma^2 n^2(z) - 1)^{1/4}} [\cos(k\Phi(z, \sigma) + \pi/4) + O(\omega^{-1})], \quad (5b)$$

where $\Phi(z, \sigma) = \int_z^{z_*} \sqrt{\sigma^2 n^2(t) - 1} dt$, $\sigma \in \Sigma$.

TABLE I. Phase and group velocities of normal modes. Second example, $f=42.1$ Hz.

Number	Phase velocity m/s	Group velocity m/s
1	1484.3591	1461.0133
2	1510.3491	1493.5510
3	1514.4412	1488.2941
4	1539.6915	1454.7201
5	1573.0870	1426.6350
6	1617.2800	1389.1291
7	1674.8621	1346.9117
8	1747.8225	1310.7239
9	1833.2078	1323.2978
10	1921.6700	1334.7152

Formulas like (5)–(5b) are obtained from a uniform asymptotics that uses the Airy functions of a spectral special integral argument; see Refs. 4–6.

Any solution $\psi(z)$ of Eq. (2) is a linear combination of $y_1(z)$ and $y_2(z)$: $\psi(z) = \alpha y_1(z) + \beta y_2(z)$ with coefficients α and β independent of z .

Inserting $\psi(z)$ into the boundary conditions (3) we come to an algebraic system for two unknowns α and β :

$$\begin{aligned} \alpha y_1(0) + \beta y_2(0) &= 0, \\ \alpha [g y_1'(h) - k y_1(h)] + \beta [g y_2'(h) - k y_2(h)] &= 0. \end{aligned} \quad (6)$$

System (6) admits nonzero α and β , and hence a non-zero solution $\psi(z)$, if the determinant of Eqs. (6) equals zero. The resulting *dispersion equation* may be written in the form:

$$y_1(0, \sigma, \omega) S_2(\sigma, \omega) - y_2(0, \sigma, \omega) S_1(\sigma, \omega) \varepsilon(\sigma, \omega) = 0, \quad (7)$$

where

$$\begin{aligned} S_2(\sigma, \omega) &= g(\sigma) - k y_2(h, \sigma, \omega) / y_2'(h, \sigma, \omega), \\ S_1(\sigma, \omega) &= g(\sigma) - k y_1(h, \sigma, \omega) / y_1'(h, \sigma, \omega), \\ \varepsilon(\sigma, \omega) &= y_1'(h, \sigma, \omega) / y_2'(h, \sigma, \omega). \end{aligned} \quad (8)$$

Here we have written down all three arguments of functions y_1 and y_2 .

Using Eq. (5) we obtain

$$S_j(\sigma, \omega) = g(\sigma) - (-1)^j (1 - \sigma^2 n^2(h))^{-1/2} + O(\omega^{-1}), \quad j=1,2,$$

$$\begin{aligned} \varepsilon(\sigma, \omega) &= -\exp\left(-2k \int_{z_*}^h \sqrt{1 - \sigma^2 n^2(z)} dz\right) \\ &\times [1 + O(\omega^{-1})]. \end{aligned}$$

Now let us discuss the physical sense of Eq. (7). First we see that the factor ε in (7) is a small number for $\omega \gg 1$. Therefore, Eq. (7) can be regarded as a result of a weak perturbation of the “unperturbed” equation

$$y_1(0, \sigma, \omega) \cdot S_2(\sigma, \omega) = 0. \quad (9)$$

The unperturbed equation (9) is decomposed into two simplest auxiliary equations: $y_1(0, \sigma, \omega) = 0$ and $S_2(\sigma, \omega) = 0$. Obviously, Eq. (9) may be satisfied by roots of either $y_1(0, \sigma, \omega)$ or $S_2(\sigma, \omega)$. Since the function $y_1(z, \sigma, \omega)$ is decreasing for $z > z_*$, the roots $\sigma_m^0(\omega)$ of the first auxiliary equation $y_1(0, \sigma, \omega) = 0$ may be regarded as the eigenvalues of a “water waveguide,” i.e., of a simplified environment model “the water stratified half-space with $h = \infty$ and without a bottom.” On the other hand, the second auxiliary equation $S_2(\sigma, \omega) = 0$ differs only by a small term $O(\omega^{-1})$ from the classical Stoneley equation

$$g(\sigma) - (1 - \sigma^2/c^2(h))^{-1/2} = 0. \quad (10)$$

This equation corresponds to the environment model “a homogeneous water half-space $z \leq h$ with $c(z) \equiv c(h)$ over an elastic solid half-space $z \geq h$.”

Equation (10) has a unique root σ_{St}^0 , we call it the classical Stoneley speed. It is known that $0 < \sigma_{St}^0 < c(h)$ (see Refs. 1–3). Since ε is a small number for $\omega \gg 1$, the roots of the perturbed equation (7) are close to either $\sigma_m^0(\omega)$ or σ_{St}^0 .

It is convenient to classify the models of environment in the original problem (see Sec. I) as belonging to one of the following two classes:

(A) the physical parameters are such that the classical Stoneley speed is less than the minimal value of the sound speed in the water layer: $\sigma_{St}^0 < c(0)$;

(B) the classical Stoneley speed is between the minimal and maximal values of the sound speed in the water layer: $c(0) < \sigma_{St}^0 < c(h)$.

Our first numerical example in Sec. I is of A class and the second one is of B class.

For A models, the Stoneley-type dispersion curve $\sigma = \sigma_{St}^0 + O(\omega^{-1})$ (corresponding to the solution of $S_2(\sigma, \omega) = 0$), does not intersect the water waveguide family $\sigma = \sigma_m^0 + O(\omega^{-1})$, as shown in Fig. 3.

For B models, the Stoneley-type curve forms quasi-intersections with the waveguide family; see Fig. 4. The mathematical reason is the following. Denote by $P_l = (\omega_l, \sigma_l)$, $l=1,2,3,\dots$ those points where both $y_1(0, \sigma, \omega)$ and $S_2(\sigma, \omega)$ are zero—the intersection points of the corresponding auxiliary unperturbed dispersion curves. For large ω , the last term in Eq. (7) is small but it is not exactly zero. As a result, we see the quasi-intersections—instead of intersections—with minimal distance between two adjacent curves of order $\exp(-k \int_{z_*}^h \sqrt{1 - \sigma^2 n^2(z)} dz)$. Namely, in a neighborhood of any point P_l two adjacent phase velocities are described by

$$\begin{aligned} \sigma_{\pm}(\omega) &= \sigma_{St}(\omega) \pm b_l \exp\left(-k \int_{z_*(\sigma)}^h \sqrt{1 - \sigma^2 n^2(z)} dz\right) \\ &\cdot [1 + O(\omega^{-1})], \end{aligned} \quad (11)$$

where $\sigma = \sigma_l$, and b_l are some constants. Evidently $\Delta\sigma = \sigma_+ - \sigma_- \rightarrow 0$ as $f \rightarrow \infty$.

Now let us look at the eigenfunctions. In case A the waveguide eigenfunctions are of the same order throughout all the water layer, and the Stoneley eigenfunction is rapidly increasing near the bottom. In case B, for f outside the QI zones, the eigenfunctions behave like those in case A. In case B, for f inside a QI zone, two eigenfunctions of the Stoneley type rapidly increase near the bottom, and other eigenfunctions behave like the waveguide ones in case A. The character of four first eigenfunctions in case B for a nonspecific frequency 46 Hz is shown in Fig. 6(a), and for a specific frequency 42.1 Hz it is shown in Fig. 6(b).

It should be pointed out that as soon as we have placed the sound source near the bottom, the main part of the wave energy must be transported to a large range by those modes whose amplitudes are dominant near the interface $z = h$. Such an effect is known in problems with a homogeneous layer⁷ and inhomogeneous layer.⁸ Numerical examples show that in some cases the contribution of the Stoneley wave near the bottom can increase the field amplitude up to 10–20 dB, so that this wave can transport the main part of wave energy. In case A for any frequency, and in case B for any nonspe-

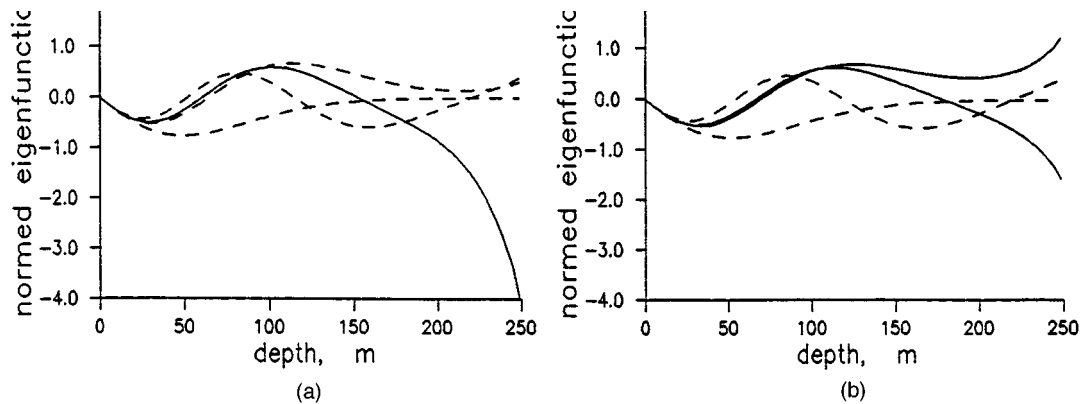


FIG. 6. Four first eigenfunctions, case B: the Stoneley-type eigenfunctions (continuous curves) grow rapidly near the bottom. (a) For nonspecific frequency 46 Hz; (b) for specific frequency, 42.1 Hz.

specific frequency, there is exactly one Stoneley normal mode and it transports the main part of the energy. In case B for any specific frequency, the two Stoneley modes described above will transport together the main part of wave energy. These normal modes contain the eigenfunctions $\Psi_+(z)$ and $\Psi_-(z)$ corresponding to Eq. (11).

Since the phase velocities σ_{\pm} of these modes are close to each other, it is natural to find their joint contribution V into the total sum (1) of all modes:

$$V(r, z) = \Psi_+(z)\Psi_+(z_0) \frac{e^{irk_+}}{\sqrt{rk_+}} + \Psi_-(z)\Psi_-(z_0) \frac{e^{irk_-}}{\sqrt{rk_-}}, \quad (12)$$

where $k_{\pm} = \omega/\sigma_{\pm}$; here the constant common factor $\exp(i\pi/4)/\sqrt{8\pi}$ is omitted.

Rewrite (12) as

$$V(r, k) = \frac{e^{irk_-}}{\sqrt{rk_+}} \Psi_+(z)\Psi_+(z_0) \cdot W, \quad (13)$$

where $W = e^{ir\Delta k} + A(z, z_0)$, $\Delta k = k_+ - k_-$,

$$A(z, z_0) = \sqrt{\frac{k_+}{k_-}} \Psi_-(z)/\Psi_+(z) \cdot \Psi_-(z_0)/\Psi_+(z_0).$$

The value $a = |A(z, z_0)|$ is approximately equal to 1, but, generally, $a \neq 1$. Let $A(z, z_0) = ae^{i\alpha}$, $\alpha = \arg A$, then

$$|W|^2 = |e^{i(\tau\Delta k - \alpha)} + a|^2 = 1 + a^2 + 2a \cos(\tau\Delta k - \alpha).$$

We see that $|V(r, z)|$ is a periodic function of the horizontal range r , with a period $R = 2\pi/|\Delta k| \approx \sigma^2/(f \cdot \Delta\sigma)$. Hence, the amplitude of the acoustic field is oscillating, the period being R . The amplitude decreases slowly as $1/\sqrt{r} \rightarrow 0$. Thus we conclude that the effect of r -periodicity of the sound field is the result of combination of two harmonic movements which have close frequencies. Note that the less $\Delta\sigma$, the greater the period R . For instance, at $f = 22$ Hz, $R = 7.5$ km, and at $f = 62$ Hz, $R = 22.5$ km.

Remark: In real media such as fluids and solids, there are losses of wave energy that cause an attenuation of the acoustic field. The energy loss may be simulated with addition of imaginary parts to the speeds. For example, let the compressional speed in the solid be complex, $c_p = \Re c_p + i\Im c_p$, $\Im c_p < 0$, and the relation $\Im c_p/\Re c_p$ be of the order

of 0.005 or less. Numerical calculations made for both examples of Sec. I with the complex c_p show that the amplitude of the acoustic field decreases with the source–receiver range more rapidly than in Fig. 1. However, the general character of the field is conserved up to the distances of the order of 100 km. At greater distances the structure of the field becomes more chaotic. Thus in case of small attenuations, the periodicity effect can be well seen. For greater imaginary parts of the speeds, this effect disappears nearer to the source. Addition of an imaginary part to the shear speed diminishes the field more than such an addition to the compressional speed does.

III. SUMMARY

A phenomenon is described that the sound field created by a point source in a shallow sea can depend periodically on the source–receiver range. The phenomenon is explained in terms of the normal modes theory and WKB asymptotic approximations: For each specific frequency, two normal modes of the Stoneley type with close phase velocities exist and interfere. The above effect appears for certain models of a stratified sea over a solid bottom. In short, it has place if the sound speed $c(z)$ in the sea is increasing with the depth, and the classical Stoneley speed is between the minimal and maximal values of $c(z)$. Such relations are not typical in fact, but they are possible.

The phenomenon described in this paper shows once more that the solidness of a bottom can present new effects in comparison with the simplest case of a liquid bottom; see also Refs. 7, 9, 10, and 11.

ACKNOWLEDGMENTS

The results of the work were announced at SIAM's Second International Conference of Mathematical and Numerical Aspects of Wave Propagation (June 1993, University of Delaware), and at the International Conference "Asymptotics in Mechanics" (August 1994, Marine Tech., St-Petersburg, Russia). This paper was partly supported by the Russian Foundation of Fundamental Researches.

¹L. M. Brekhovskikh and Yu. P. Lysanov, *Fundamentals of Ocean Acoustics* (Springer-Verlag, Berlin, 1982).

²J. A. Hudson, *The Excitation and Propagation of Elastic Waves* (Cambridge U.P., New York, 1980).

³D. I. Sherman, "On wave propagation in a fluid layer lying on an elastic

- half-space," Trudy Seismolog. Inst. AN SSSR (in Russian), No. **115**, 1–43 (1945).
- ⁴F. W. J. Olver, *Asymptotics and Special Functions* (Academic, New York, 1974).
- ⁵R. E. Langer, "The asymptotic solutions of certain linear ordinary differential equations of the second order," Trans. Am. Math. Soc. **36**, 90–106 (1934).
- ⁶F. W. J. Olver, "Error bounds for the Liouville–Green (or WKB) approximation," Proc. Cambridge Philos. Soc. **57**, 790–810 (1961).
- ⁷O. N. Grudski, S. M. Grudski, Yu. A. Kravtsov, E. A. Rivelis, and O. I. Sabirov, "Sound propagation in simplest hydroacoustic waveguides with liquid or elastic bottom," Moscow, Institut Obshtshej Fiziki AN SSSR (in Russian), preprint No. 57 (1989).
- ⁸A. G. Alenitsyn, "Influence of a Stoneley wave on the sound field of a point source in a fluid layer on an elastic half-space," Sov. Phys. Acoust. **33**, 545–548 (1987).
- ⁹K. E. Hawker, "Influence of Stoneley waves on plane-wave reflection coefficients," J. Acoust. Soc. Am. **64**, 548–555 (1978).
- ¹⁰N. E. Maltsev Mathematical simulation of sound fields in ocean, in *Ocean Acoustics. Modern Condition* (Nauka, Moscow, 1982), pp. 5–24 (in Russian).
- ¹¹F. Ingenito and S. N. Wolf, "Acoustic propagation in shallow water overlying a consolidated bottom," J. Acoust. Soc. Am. **60**, 611–617 (1976).

Estimating the compressional and shear wave speeds of a shallow water seabed from the vertical coherence of ambient noise in the water column

Nicholas M. Carbone, Grant B. Deane, and Michael J. Buckingham

Marine Physical Laboratory, Scripps Institution of Oceanography, University of California at San Diego, 9500 Gilman Drive, La Jolla, California 92093-0704

(Received 25 March 1997; accepted for publication 15 September 1997)

Due to the multiple bottom reflections encountered in shallow water environments, the spatial structure of the ambient noise field depends strongly on the geoacoustic properties of the seabed, which are invariant over time scales associated with most measurements. The vertical directionality and coherence are relatively stable features of the noise that are determined primarily by the seabed, rather than temporal variations in the surface source distribution. In this paper, estimates of the compressional and shear wave speeds are determined from ambient noise measurements over shear supporting seabeds. Using a model of wind-generated noise over an elastic seabed, it is shown that the noise is sensitive to the compressional and shear wave speeds in the upper few meters of seabed. An inversion procedure is developed based on a matched field of the complex, broadband coherence from a single hydrophone pair. Using ambient noise data from two shear supporting sites, compressional and shear wave estimates are obtained that are in good agreement with independent surveys. For one site where the bedrock is exposed, a half-space model of the seabed yields reasonable estimates of the seabed parameters. For the other site, the presence of a thin sedimentary layer results in a low estimate from the half-space model. However, when the layer is included in the model, the estimates of the underlying bedrock are in good agreement with a seismic survey. © 1998 Acoustical Society of America. [S0001-4966(98)05101-7]

PACS numbers: 43.30.Ma, 43.30.Pc [DLB]

INTRODUCTION

In shallow water, sound interacts strongly with the seabed. Sound emanating from a source undergoes multiple reflections between the sea surface and sea floor. The ambient noise field is a stochastic process of many such noise sources and the respective interactions of their wave fields with the environmental boundaries. As a consequence of the multipath interaction, the time-averaged ambient noise exhibits spatial structure that is largely determined by the characteristics of the seabed. In particular, the geoacoustic parameters of the seabed determine the relative reflection versus refraction of sound from the water column into the seabed as a function of grazing angle. In turn, this relationship affects the vertical directionality and vertical coherence of the ambient noise. These functions of the noise can therefore be measured in the ocean environment, and used to estimate the seabed parameters.

The dependence of the vertical directionality and coherence was examined by Chapman¹ who modeled typical variations in the noise structure for seabeds ranging from silt to chalk, and demonstrated good agreement of the real component of the coherence with data from two shallow water sites. Based on the seabed's effect on the vertical coherence, Buckingham and Jones² used a low-loss, fluid model to estimate the compressional wave speed from experimental measurements of the noise. In the present study, this idea is developed further to address shear-supporting seabed types. The dependencies of the ambient noise on the reflective properties of the seabed are presented and subsequently used

to invert for the compressional and shear wave speeds using the vertical coherence of the noise.

The inversion is based on the broadband vertical coherence from a single hydrophone pair. It utilizes the frequency band of 100 Hz to a few kilo-Hertz, where ambient noise often contains contributions from both natural source mechanisms and anthropogenic sources. The present study focuses solely on wind/wave-generated noise, which can be modeled as a uniform distribution of surface sources. Undoubtedly, other noise sources, particularly ships, can be important in many shallow water areas. These sources often have variable spatial distributions, and thus very different vertical noise structure compared to wind noise. The present study constitutes an initial investigation into the somewhat ideal situation where wind noise, which has a predictable spatial distribution, is the dominant source mechanism.

In this paper, the dominant environmental effects on the noise field are examined and used to estimate the compressional and shear wave speeds from ambient noise data. A normal mode model of wind-generated ambient noise over a shear-supporting basement is developed in Sec. I. In Sec. II, the noise is examined in terms of the narrowband vertical directionality and, alternatively, the broadband vertical coherence. The directionality is used because it is physically intuitive, whereas the coherence, which is easier to measure, forms the basis of the inversion. The fundamental effects of the seabed on the noise field are examined using a homogeneous half-space seabed. Then, a layered seabed is used to investigate the seabed penetration depth characterized by the broadband coherence. Finally, the effect of a sound speed

profile on the coherence is addressed. In Sec. III, ambient noise data are presented in order to demonstrate the stationarity of the noise field coherence with regard to temporally varying aspects of the ocean environment. In Sec. IV, the inversion procedure is introduced and subsequently applied to ambient noise data from two shear-supporting sites in Sec. V.

I. AMBIENT NOISE MODEL FOR A SHALLOW WATER DUCT OVER A SHEAR-SUPPORTING BASEMENT

Several models of ambient noise are currently in existence. A review of these models can be found in a paper by Hamson.³ One such model for the spatial correlation in the vertical was developed by Buckingham.⁴ This model accounts for uncorrelated omnidirectional noise sources over a low-loss, fluid basement in an isovelocity shallow water channel. The low-loss approximation made by Buckingham allowed for the continuous spectrum, which is often attributed to a branch line integral and can be difficult to compute, to be omitted from the calculation. However, as this energy represents the contribution from nearby sources, it can be an important component of the wind-generated ambient noise.⁵ A more general formulation, which allows for the continuous spectrum component, was expressed in the form of a wave number integral by Kuperman and Ingenito.⁶ This general expression is evaluated using the fast field program (FFP) OASES.^{7,8} Recently, Harrison⁹ has shown that equivalent results may also be obtained using a simple ray approach.

In this section, recent developments in the area of eigenvalue finding routines¹⁰ are incorporated with these previous approaches in order to express the entire wind-generated ambient noise field as a sum of normal modes. The expression accounts for lossy, elastic seabeds, and it incorporates the discrete and continuous spectra by including the trapped and leaky modes. It can be computed quickly and accurately for the isovelocity case and used to examine the seabed effects on the noise field.

The physical model is shown in Fig. 1. The wind noise generators are modeled as a plane of omnidirectional point sources which are Poisson distributed in space and time and are located just below a pressure release surface. The water column contains a sound speed c_{p1} and density ρ_1 . The seabed consists of an optional fluid layer of variable thickness overlying an elastic half-space. The parameters for the layer are the compressional wave speed and attenuation, c_{p2} and α_{p2} , and the density ρ_2 . The parameters for the half-space are the compressional wave speed and attenuation, c_{p3} and α_{p3} ; shear wave speed and attenuation, c_{s3} and α_{s3} ; and the density ρ_3 . A sensor array, shown as a single receiver pair, is located in the water column away from the interfaces.

The goal is to describe the second-order statistics as a function of the seabed parameters. To do this, the cross-spectral density between receivers will be expressed in terms of the Green's function, which in turn depends on the seabed parameters. The cross-spectral density will then be used to compute the vertical directionality and the vertical coherence, which will help to interpret the seabed's effect on the noise field.

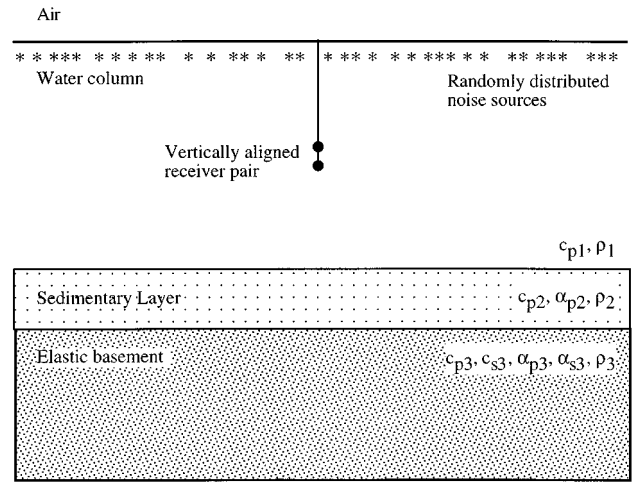


FIG. 1. Canonical shallow water ambient noise model showing an optional fluid layer of variable thickness and the viscoelastic parameters of the seabed half-space. The cross-spectral density between the two hydrophones is calculated from a random distribution of point sources just below the pressure release surface.

Considering an incremental surface area dA as shown in Fig. 2, the expected value of the cross-spectral density for a Poisson process is given by Carson's theorem,¹¹ which can be expressed as

$$\overline{dS_{ij}(\omega)} = 2\nu Q^2 G(r, \omega, z_{ri}) G^*(r, \omega, z_{rj}) dA, \quad (1)$$

where the overbar stands for ensemble average, ν is the source density per unit time, Q is the source strength, G are the Green's function at receiver depths z_{ri} and z_{rj} , ω is the angular frequency, and the asterisk denotes complex conjugate.

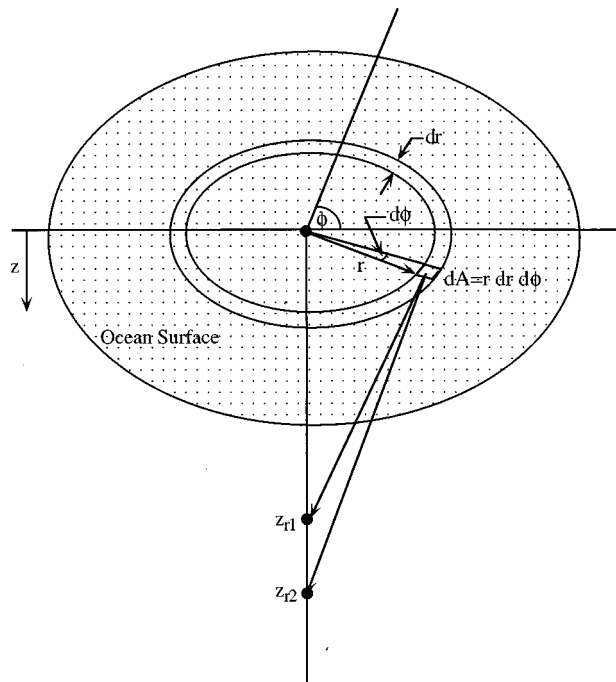


FIG. 2. Source model for the ambient noise field. The cross-spectral density of the ambient noise is derived using the Green's function within the incremental area dA and then integrating over azimuth and range.

gate. To obtain cross-spectral densities for the total surface, the incremental area $dA = r dr d\phi$ is integrated over range and angle. Assuming azimuthal symmetry, the integral over ϕ provides a factor of 2π and the resulting integral for the expected value of the total cross-spectral density is given by

$$\overline{S_{ij}}(\omega) = 4\pi\nu Q^2 \int_0^\infty r G(r, \omega, z_{ri}) G^*(r, \omega, z_{rj}) dr. \quad (2)$$

Thus, the expected value for the average cross-spectral density of the random process is expressed in terms of the deterministic Green's functions for a given environment. Considering the shallow water duct environment of Fig. 1, the Green's function solution to the wave equation is well known and can be expressed as a sum of normal modes

$$G(r, \omega, z_r) = i\pi \sum_n \varphi_n(z_r) \varphi_n(z_s) H_0^1(k_n r), \quad (3)$$

where n is the mode number, φ_n are the mode eigenvectors evaluated at the source and receiver, and H_0^1 is a Hankel function which depends on range r and the mode eigenvalues k_n .

Substituting the Green's function from Eq. (3) into the cross-spectral density in Eq. (2) and performing the range integration results in the following double sum of normal modes:

$$\begin{aligned} \overline{S_{ij}}(\omega) = 16\pi\nu Q \sum_{n=1}^\infty \varphi_n(z_s) \varphi_n(z_{ri}) \sum_{m=1}^\infty \varphi_m^*(z_s) \varphi_m^*(z_{rj}) \\ \times \frac{\ln(k_n/k_m^*) - i\pi}{k_m^{*2} - k_n^2}. \end{aligned} \quad (4)$$

The upper limit of infinity in the mode sum is due to choosing the Pekeris branch cut, which results in a finite sum of trapped modes plus an infinite sum of leaky modes plus a branch line integral, which can be neglected. Because the noise sources are distributed across the entire surface, the noise field includes overhead source contributions, and the continuous spectrum is an important contributor to the total noise field. The infinite sum provides an accurate description of the noise without the necessity for computing the branch line integral. In practice the sum may be truncated at mode cutoff for a rigid bottom. This corresponds to a maximum mode number of $N_{\text{modes}} = 2fh/c_{p1}$, where f is the frequency and h is the duct depth.

Some concern was raised by Stickler¹² as to whether the mode sum derived from the Pekeris cut provides a sufficiently complete solution for the field in the water column. However, Stickler's concern over the importance of the branch line integral is based on a specific example where a single trapped mode exists and is very near cutoff. For the geometries and frequencies used in this study, many modes exist in the water column. Consequently, the branch line integral can be neglected and the Pekeris mode sum provides an accurate representation of the field in the water column.

The seabed parameters couple into the noise field solution through the reflection coefficient which determines the mode eigenvalues k_n . For the case of an isovelocity profile in the water, the eigenfunctions are sines and the eigenvalue

solutions are obtained for the lossy, elastic seabed using the complex effective depth method of Zhang and Tindle.¹⁰ By allowing for an angle-dependent complex effective depth and iterating the eigenvalue solutions,¹³ the procedure provides the exact eigenvalues of both the trapped and leaky mode poles.

Once the eigenvalues have been obtained and the cross-spectral density computed, the vertical directionality may be obtained by beamsteering a multi-element array across the vertical span of the water column. To steer the array at an angle θ_s from the horizontal, the proper phase delay for a receiver at position z_i is given by

$$w_i(\theta_s) = a_i \exp\left(-i \frac{\omega z_i \sin(\theta_s)}{c_{p1}}\right), \quad (5)$$

where a_i is real-valued window weighting that may be used to provide array shading. The directional power for the angle θ_s is then the sum over all hydrophones according to the equation

$$F(\theta_s, \omega) = \sum_{i,j=1}^{N_{hyd}} w_i^*(\theta_s) \overline{S_{ij}}(\omega) w_j(\theta_s), \quad (6)$$

where again the asterisk denotes complex conjugate.

The vertical coherence is simply a normalized version of the cross-spectral density. It may be expressed for a variable receiver separation at a single frequency, or it may be expressed as a broadband calculation from a single receiver pair. For the purpose of this study, we desire the simplicity obtained in using a measurement from a single hydrophone pair. Consequently, the coherence is expressed as the following broadband function:

$$\Gamma_{ij}(\omega) = \frac{\overline{S_{ij}}(\omega)}{\sqrt{\overline{S_{ii}}(\omega) \overline{S_{jj}}(\omega)}}, \quad (7)$$

where $i=1$ and $j=2$. We note here that the coherence is a complex function, as is the cross-spectral density between the two receivers.

Having established a theoretical framework for the wind-generated ambient noise field, we can now interpret the seabed's effect on the ambient noise directionality and coherence.

II. INTERPRETING THE AMBIENT NOISE FIELD

A. Fundamental effects of a viscoelastic seabed on the ambient noise field

The ambient noise inversion will be based on the broadband coherence from a single hydrophone pair. However, as this function is not physically intuitive, the effect of the seabed on the ambient noise field will be described by first discussing the reflection coefficient, progressing to the vertical directionality, and finally arriving at the vertical coherence. The reflection coefficient describes the angular dependence of the reflection strength of a single plane wave as determined by the seabed parameters. The vertical directionality is a measurable quantity of the noise in which the properties of the reflection coefficient are manifest in the noise power per unit angle. Although the directionality has the

benefit of being easy to interpret, it has the drawback of requiring a multiple element array where the useful frequency band is limited by the minimum receiver separation. The coherence, on the other hand, requires only two elements, and its frequency band is limited only by the sampling frequency and receiver response. Consequently, the coherence has the benefits of being a simpler measurement and allowing a wider frequency band to be examined. Additionally, the use of a broadband measurement offers greater immunity to dominant shipping lines which tend to occur at lower frequencies. To relate the coherence to the vertical directionality, we will make use of the spatial Fourier transform relationship derived by Cox.¹⁴ This relationship relates the complex coherence to the vertical directionality, whereby the real component of the coherence represents the directional symmetry in the noise, and the imaginary component represents asymmetry in the noise. Although the relationship breaks down for nonhomogeneous noise fields, it will be useful in relating the coherence to the directionality and, thus, to the seabed reflection coefficient. Homogeneous noise is not, however, a necessary condition for performing ambient noise inversions based on the coherence or the directionality. Provided that an adequate representation of the field exists, inversions can be performed by matching the theory to the measurements in the water column.

To examine the fundamental seabed effects on the noise field, we consider the case of a viscoelastic half-space without the presence of the sedimentary layer. We will consider the compressional wave speed, c_{p3} ; the shear wave speed, c_{s3} ; and the compressional wave attenuation, α_{p3} . Computer simulations have shown that typical variations in the remaining parameters, ρ_3 and α_{s3} , are of lesser importance in determining the spatial structure of ambient noise. Consequently, they will not be considered in this analysis.

Figure 3 shows the reflection coefficient, vertical directionality, and vertical coherence for half-space parameter combinations of $[c_{p3}, c_{s3}, \alpha_{p3}]$ as follows: I, [1700, 0.01, 0.01]; II, [2400, 0.01, 0.01]; III, [2400, 750, 0.1]; and IV, [2400, 1000, 0.1], where the wave speeds are given in units of m/s and attenuation is in dB/λ. The line types are given by: case I (- -), case II (—), case III (- · -), and case IV (· ·).

Reflection coefficients for four seabed combinations are shown in Fig. 3(a). The effect of the compressional wave speed can be seen by comparing the solid line to the dash-dot line. The critical angle of total internal reflection derives from Snell's law which relates the refraction angle to the ratio of sound speeds at the interface. Increasing the value of c_{p2} results in an increased critical angle, and thus a larger range of angles where total internal reflection occurs. This is the most basic and dominant effect of the seabed on the acoustic wave energy. Because of the simplicity of the relationship, the critical angle is an easy identifier of the compressional wave speed.

Comparing the dashed and dotted lines to the solid line shows the result of increasing the shear wave speed in the seabed. Higher levels of shear result in decreased reflection of energy propagating at angles between grazing and the critical angle. Thus, with regard to energy in the water column, the conversion of compressional to shear waves is a

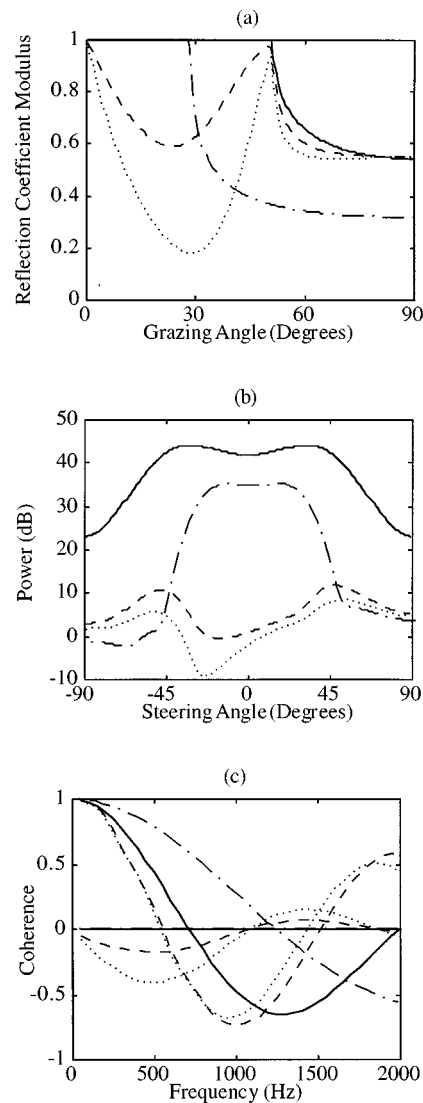


FIG. 3. The (a) reflection coefficient, (b) vertical directionality, and (c) vertical coherence are shown for varying seabed conditions. The parameters $[c_{p3}, c_{s3}, \alpha_{p3}]$ vary as follows: [1700, 0.01, 0.01], (- · -); [2400, 0.01, 0.01], (—); [2400, 750, 0.1], (- -); and [2400, 1000, 0.1], (· ·). The wave speeds are given in units of m/s and attenuation is in dB/λ.

loss mechanism that preferentially attenuates intermediate, subcritical angle energy.

In the absence of compressional wave attenuation, the reflection coefficient curves obtain a value of unity at the critical angle, even when shear is present. However, the presence of compressional wave attenuation decreases the reflection of critical and subcritical angle energy. Because of the compressional wave attenuation, the dashed and dotted curves in Fig. 3(a) obtain a value slightly less than unity at the critical angle.

Figure 3(b) shows the effect of the seabed parameters on the vertical directionality. The curves have been computed from an 11-hydrophone array using a Hanning window, an interelement spacing of 1.47 m, a frequency of 480 Hz, a 100-m channel, and a source strength of unity. Standard practice is to normalize these curves to absolute hydrophone level and to plot them on a polar plot. Rather than follow this

procedure, the unnormalized levels of the curves are plotted on a log-linear plot to show better the absolute effects of the loss mechanism.

It should be clear from the similarity in Fig. 3(a) and (b) that the character of the reflection coefficient manifests itself in the vertical power of the noise field. Comparing in Fig. 3(b) the solid line to the dash-dot line isolates the effect of varying the compressional wave speed. The angle span where total internal reflection occurs can be seen in the relative vertical power, where the faster compressional wave speed case has a broader peak around the horizontal. Furthermore, because a greater amount of energy has totally reflected along the multipath, the higher compressional wave speed case also has a higher absolute power level for an equal source strength.

In the dashed and dotted curves we see that the inclusion of shear results in intermediate mode stripping, creating a ‘‘rabbit ear’’ appearance to the directionality. The amount of mode stripping is dependent on the shear speed and the corresponding amount of compressional to shear wave conversion at the seabed. Because shear represents an energy loss mechanism, the directionality exhibits an asymmetry where more energy is present at upward-looking angles than at downward-looking angles. The compressional wave attenuation has a relatively minor effect on these curves, which is to clip the level of the peaks at the critical angle.

Figure 3(c) shows the complex coherence functions obtained from a 1-m receiver separation over the frequency band of 100–2000 Hz. The real part approaches unity at zero frequency; the imaginary part approaches zero. The solid and dash-dot curves demonstrate the effect of the compressional wave speed in the lossless environment. For these curves, the imaginary part is very close to zero because, for the lossless seabed, the noise field directionality is nearly symmetric about the horizontal. (A small amount of asymmetry always occurs due to penetration of high angle energy.) The effect of the compressional wave speed on the coherence is that increases in c_{p3} shift the zero crossings in the real component of the coherence to a lower frequency. In the limit, as c_{p3} becomes large, the noise field becomes isotropic (or entirely symmetric) and the zero crossing approaches a frequency of $f = c_{p1}/2s$, where s is the receiver separation.

The effect of shear can be seen in the dashed and dotted curves. Compared to the solid curves, the real coherence zero crossing frequency has decreased due to the loss of symmetry in the noise directionality. In addition, the magnitude of the imaginary component has increased due to the asymmetry associated with the intermediate mode stripping. Comparing the dashed and dotted curves indicates that these variations in the real and imaginary coherence increase with increasing shear wave speed.

In addition to shear, the compressional wave attenuation is a loss mechanism that can affect the asymmetry in the noise directionality. Although its properties differ from those of shear, attenuation can have similar effects on the vertical coherence. This raises uncertainty as to which parameter is causing the noise field asymmetry. One option would be to invert for the ‘‘effective attenuation’’¹⁵ which is a combination of all attenuation mechanisms including shear, attenua-

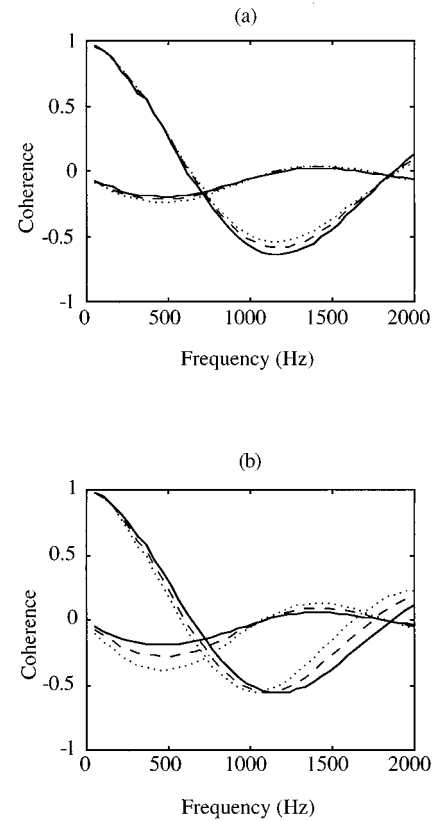


FIG. 4. The comparative effects of shear and compressional wave absorption for a moraine seabed showing (a) attenuation effects: $c_p = 2000$, $c_s = 600$, varying $\alpha_p = 0.1$ (—), 0.3 (---), 0.5 (· · ·); and (b) shear effects: $c_p = 2000$, $\alpha_p = 0.3$, varying $c_s = 500$ (—), 600 (---), 700 (· · ·). Sound speeds given in m/s, absorption given in dB/ λ .

tion, and scattering. However, it is known from numerous *in situ* studies by Hamilton^{16–18} and others that fast seabeds have high shear wave speeds and low attenuation values. Consequently, the effects of attenuation from a fast, shear-supporting seabed are expected to be small. The relative effects of shear and attenuation can be seen in Fig. 4 where the coherence is plotted for parameter variations typical of a moraine seabed.¹⁹ In Fig. 4(a) the attenuation has been varied from 0.1 to 0.5 dB/ λ ; in Fig. 4(b) the shear speed has been varied from 500 to 700 m/s. Comparing Fig. 4(a) and (b) shows that, for a moraine seabed, shear has a greater effect on the coherence than does the compressional wave attenuation. This will be increasingly true for progressively faster seabed types where attenuation values decrease and shear speeds increase. Consequently, typical variations in seabed attenuation should not provide significant error in the estimates of c_{p3} and c_{s3} , provided that the inversion is applied to sufficiently hard materials where shear speeds are high and attenuation is low. The presence of attenuation in unconsolidated sediments will, however, prohibit inverting for the low shear speeds associated with these materials. Therefore, we concentrate our inversions on fast, consolidated materials where shear is the dominant loss mechanism. To further minimize the error incurred in the inversion, empirically determined relationships will be used to correlate the attenua-

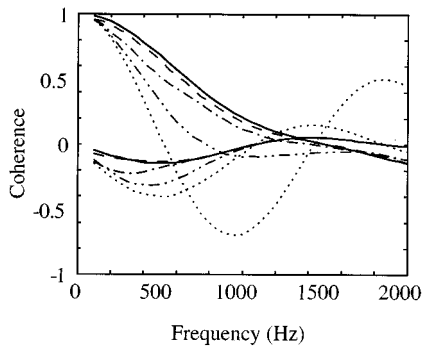


FIG. 5. The effect of a layer on the broadband coherence from a receiver pair separated by 1 m. The seabed model varies as follows: chalk half-space without a layer (\cdots), 1-m layer of sand over chalk ($-\cdot-\cdot-$), 2-m layer of sand over chalk ($- \cdot -$), 5-m layer of sand over chalk ($- -$), and sand half-space without a layer ($-$). The curves indicate that the coherence is only sensitive to the upper 5 m of seabed material.

tion with the compressional wave speed. This correlation is discussed in the Appendix.

B. The penetration depth

Using ambient noise to determine seabed parameters will provide an average estimate for some finite penetration depth into the seabed. This penetration depth will depend on the acoustic wavelength of the ambient noise used in the calculation. Narrowband simulations of the vertical directionality indicate that the noise is sensitive to approximately the upper one wavelength of seabed. Consequently, for frequencies varying from 100 to 2000 Hz, a vertical footprint of 15 to 0.75 m, respectively, may be obtainable provided an array of sufficient aperture is used. However, utilizing the broadband coherence does not allow for estimates at the individual frequency components. Rather, the coherence provides a single estimate which represents an intermediate value over the penetration depths delimited by the frequency band employed in the inversion.

To illustrate the vertical footprint obtained using the noise coherence, a fluid layer of variable thickness is now included in the model. The coherence curves for a sand layer over a chalk substrate seabed are shown in Fig. 5. The hydrophone pair is separated by 1 m and located at midwater depth in a 100-m channel. The thickness of the layer varies as 1 m ($-\cdot-\cdot-$), 2 m ($- \cdot -$), and 5 m ($- -$). The limiting cases are the chalk half-space with no layer (\cdots) and the sand half-space with no layer ($-$). The figure shows that the coherence is very sensitive to as little as 1 m of sediment over the chalk substrate. The curves for the three layered basements lie between the two half-space limits, representing a sort of average between the two materials. Furthermore, as the sand layer thickens, the coherence progressively approaches the sand half-space result. The coherence for the 5-m layer is barely distinguishable from the sand half-space. For the frequencies and receiver separations specified, these curves indicate that the coherence is only sensitive to the upper 5 m of seabed, and that this sensitivity is dominated by the surficial material. Consequently, the inversion technique will not be useful in determining deep sediment structure, but may pro-

vide an inexpensive means of monitoring seasonal variations in sediment overburden in shallow water areas.

C. The effect of a sound speed profile

The effect of a water column sound speed profile on the noise directionality and coherence has been considered previously by Hamson,⁵ Kuperman and Ingenito,⁶ and others. The presence of a sound speed profile will affect the ambient noise inversions in two ways: the noise field homogeneity and the perceived critical angle. In the isovelocity environment the noise field is approximately homogeneous away from the surface and bottom interfaces.⁴ As a consequence, the precise location of the receiver pair is not an important consideration, provided that the two receivers are not too far apart and that neither is near an interface. In the presence of a sound speed profile this simplifying factor breaks down. The sound speed profile results in bent rays, or vertically constrained mode shapes, depending on one's preferred point of view. Consequently, receiver placement within the profile dictates what collection of rays or what modal amplitudes contribute to the measured field. For this reason, placement of the receivers, even within the center of the water column, becomes a consideration that can affect the inversion calculations.

The second important factor related to the sound speed profile is that the energy is preferentially bent away from the horizontal. Upon first consideration it might appear that all energy is bent more vertically and is thus more likely to exceed the critical angle of the bottom. However, the effect is actually more prevalent on the horizontally propagating energy than on the energy near the critical angle. This can be understood very simply in terms of Snell's law. Consider a ray launched from the surface in a duct containing a sound speed profile. For a launch angle θ_{surf} from the horizontal, the angle of arrival at a given hydrophone will be

$$\theta_{\text{rec}} = \cos^{-1}((c_{\text{rec}}/c_{\text{surf}})\cos \theta_{\text{surf}}),$$

where c_{rec} and c_{surf} are the sound speeds at the receiver and surface, respectively. For a downward-refracting profile that varies 10 m/s from the surface to the receiver, a horizontally launched ray will have an arrival angle of $\theta_{\text{rec}} = 6.6^\circ$ whereas a ray launched at 30° will have an arrival angle of $\theta_{\text{rec}} = 30.7^\circ$, which is a much smaller deviation. Thus, the effect of the profile is not so much to bend energy beyond the critical angle of the bottom as it is to strip energy from the horizontal.

The profile effect can also be viewed as preferential alteration in the excitation strength of the lower-order modes. A downward-refracting profile will constrain a particular mode shape to the lower portion of the water column, making the mode less excitable by near surface sources. Conversely, an upward refracting profile will constrain the mode to the upper portion of the water column, increasing its excitation strength.

This effect creates a "noise notch" around the horizontal in the downward refracting case, and a filling in of the notch in the upward refracting case. This is illustrated in Fig. 6 for a moraine seabed. The velocity profiles are shown in Fig. 6(a), where there are two downward-refracting, one is-

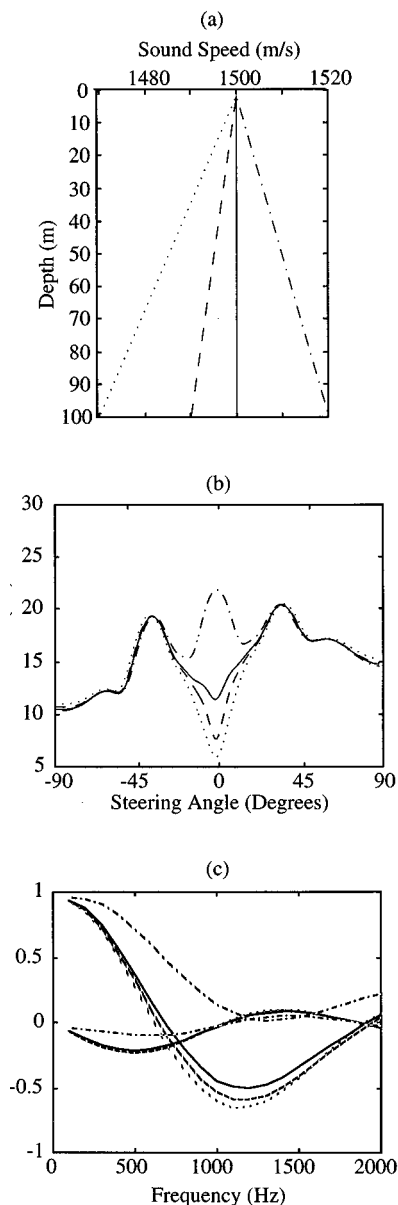


FIG. 6. The effect of a sound speed profile on the vertical directionality and the vertical coherence. (a) Sound speed profiles, (b) directionality for a moraine seabed, and (c) coherence for a moraine seabed. The line types are consistent with those given in (a).

ovelocity, and one upward-refracting profile. The line types are consistent throughout the figure, with solid representing isovelocity, dashed and dotted representing downward refracting, and the dash-dot representing upward refracting. The noise curves were calculated using OASES.^{7,8} Figure 6(b) shows the directionality at 480 Hz for the an 11-element array with 1.47-m interelement spacing and a source depth of 0.1 m. The broad dip below the critical angle is due to intermediate mode stripping associated with the shear-supporting moraine seabed. In addition, a narrow notch around the horizontal is present for isovelocity and downward-refracting profiles. In the isovelocity case, the notch is due to the source dipole radiation pattern used in the OASES program. However, the depth of the notch increases depending on the severity of the profile and the corresponding decrease in the

excitation of the lower-order modes. In the case of the upward refracting profile, the excitation of horizontal modes is enhanced, creating a hump around the horizontal.

The effect on the coherence of variations in the horizontal component of the noise field can be predicted by considering a purely horizontal noise component. In the case of horizontal plane wave noise there is no phase difference between two vertically separated sensors. In other words, the signals on the two sensors are perfectly coherent. Consequently, we expect enhancements in the horizontal component to increase the real coherence and drive the imaginary coherence toward zero. Conversely, notches in the horizontal component should place greater emphasis on higher-order modes, which are subject to attenuation and provide asymmetry to the directionality. This should decrease the real coherence and increase the imaginary part. This is shown in Fig. 6(c), where the vertical coherence is shown for a 1-m separated receiver pair centered at midwater depth above the moraine seabed. The noise notch associated with the downward-refracting case results in a reduced zero crossing frequency of the real coherence and a small increase in the magnitude of the imaginary coherence. In the upward-refracting case, the opposite effect is true.

Figure 6 indicates that the sound speed profile provides a measurable change in the coherence, and that including a measurement of the profile in the inversion could improve the accuracy of the inversion. In the upward-refracting case, it is clear that neglecting the profile from the inversion would result in substantial estimation error. For the downward-refracting case, however, the profile has a much smaller effect on the coherence, which remains dominated by the seabed. Consequently, only a small error will be incurred in an inversion if an isovelocity model is used when the actual *in situ* profile is downward refracting.

III. THE STATIONARITY OF THE NOISE COHERENCE

Because the ambient noise is a random process, it will naturally undergo random fluctuations over time. The use of noise in performing seabed inversions is based on the underlying tenet that the time-averaged noise coherence is a robust and repeatable measurement of the random process. Thus, the inversion assumes some level of stationarity whereby fluctuations in the coherence are of minor importance with respect to parameter estimation. Not all statistical measures of ambient noise are stationary. For instance, stationarity does not hold for the power spectral density which varies substantially with sea state. However, as the coherence is normalized with respect to the power spectral density, it is, in fact, a sufficiently stationary measurement of the random process to permit its use in the ambient noise inversion. This statement is justified below.

The broadband coherence is computed from a finite time measurement of the ambient noise field at two vertically separated receivers. Denote the time series on each receiver by $x_i(t)$ where $i=1,2$, and $X_i(f, \Delta T)$ is the corresponding finite Fourier transform over the time segment ΔT . The cross-spectral density estimate is obtained by averaging N segments, each of length ΔT , according to the following equation:

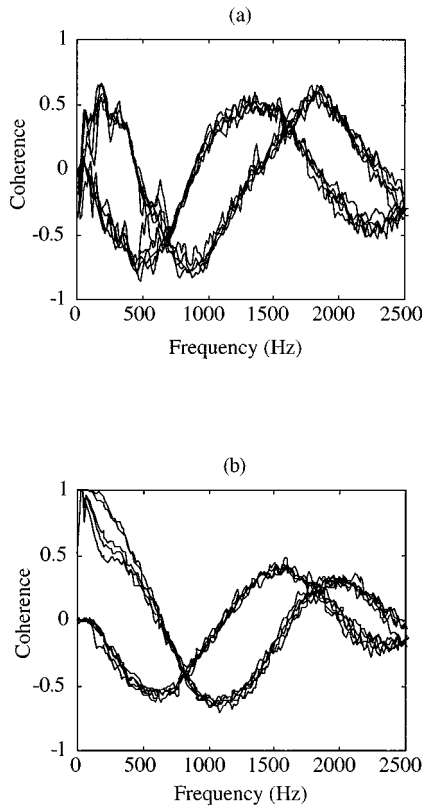


FIG. 7. The stationarity of the broadband vertical coherence is demonstrated using five individual estimates of the coherence spaced over a period of time. The coherence curves shown in (a) were obtained from the Cortes Bank using 20-s averages spaced over a 1-h period. The coherence curves shown in (b) were estimated from 40-s averages taken on five consecutive days at a site along the Florida Shelf.

$$\overline{\hat{S}_{ij}(f)} = \frac{1}{N} \sum_{n=1}^N X_i(f, \Delta T_n) X_j^*(f, \Delta T_n), \quad (8)$$

where the overbar stands for ensemble average and the hat indicates estimation. The coherence is then a normalized version of the cross-spectral density according to the equation

$$\hat{\Gamma}_m(f) = \frac{\overline{\hat{S}_{12}(f)}}{\sqrt{\overline{\hat{S}_{11}(f)} \overline{\hat{S}_{22}(f)}}}, \quad (9)$$

where $\hat{\Gamma}_m$ denotes measured coherence estimate.

In order to demonstrate the stationarity of the measured coherence, estimates obtained from two shallow water sites are shown in Fig. 7. For each site, coherence estimates are plotted from five distinct time intervals. The calculations were made using 512-point FFTs with 50% overlap and a Kaiser-Bessel²⁰ window with $\beta = \pi\alpha = 7.85$.

Figure 7(a) shows the coherence taken from the Cortes Bank in sea state 3. The data were digitized at a sampling frequency of 7 kHz. The five curves were obtained using relatively short 20-s averages spaced approximately equally over a 1-h measurement period. (The real coherence curves approach +1 at low frequency, but fall off toward zero at DC. The low-frequency falloff is attributed to flow noise which resulted from an imperfect decoupling of the array

from the surface movement.) The consistency in the five curves demonstrates the relative stationarity of the noise field coherence over the 1-h period. We have found similar consistency over these timescales in data from several other shallow water sites. The Cortes Bank is particularly noteworthy because the corresponding spectral levels vary by as much as 15 dB over this measurement period, but the coherence remains stable.

In Fig. 7(b) the coherence is plotted using data from five consecutive days at a muddy sand site along the Florida Shelf. During the five-day measurement period, the sea state varied between 1 and 3 and the spectral levels varied by up to 15 dB. The data were digitized at 6.34 kHz and the coherence curves were obtained from 40-s averages. On three of the five days intermittent dropout occurred in the data. The data were interpolated through the faulty points, which caused the coherence variations below about 300 Hz. Aside from the artifact at low frequency, the coherence shows a tremendous amount of consistency over the five-day period, despite the variation in sea state and spectral levels.

These and other observations strongly suggest that the wind-generated ambient noise coherence is a stable measurement which is dominated by time-invariant properties, rather than random fluctuations in the source distribution or ocean environment. As the average coherence structure is primarily controlled by seabed reflectivity, it should provide a suitable means of inverting for seabed parameters.

IV. INVERSION PROCEDURE

The inversion is based on a simple curve fit between the theoretical and measured coherence functions. The underlying philosophy is that, since the coherence is a function of the seabed parameters, the best fit will occur when the seabed parameter values used in the model are equal to the seabed parameters occurring at the experimental site. As the coherence is a broadband, complex function, the goal is to minimize the residual between real and imaginary parts across the frequency band of interest. The norm is therefore defined as the broadband, root-mean-square (rms) difference between the theoretical and experimental coherence curves. Because the real and imaginary parts provide separate information, the difference function is a linear combination of the two rms differences (real and imaginary). This allows for the option of unequal weighting of the real and imaginary parts, as discussed below. The norm may be written as

$$\Delta(c_{p3}, c_{s3}, z_s) = \frac{100}{\sqrt{N}} \left\{ \frac{1}{2} \sqrt{\sum_{i=1}^N \left[\frac{\Re(\hat{\Gamma}_m(f_i) - \Gamma_t(f_i))}{2} \right]^2} + \frac{1}{2} \sqrt{\sum_{i=1}^N \left[\frac{\Im(\hat{\Gamma}_m(f_i) - \Gamma_t(f_i))}{2} \right]^2} \right\}, \quad (10)$$

where N is the number of frequency points, $\hat{\Gamma}_m$ and Γ_t are the measured and theoretical coherence values, respectively, and \Re and \Im indicate real and imaginary parts. The normalization condition has been chosen such that the difference function varies between a minimum of 0 and a maximum of

100. Implicit in this normalization is the fact that the range of possible values for the real and imaginary coherence is from +1 to -1, meaning that the argument under each square root in Eq. (10) has a minimum value of 0 and a maximum value of N .

The sum over frequency implies equal weighting to all frequency components. This is a reasonable approach provided that the measured coherence contains sufficient structure at all frequencies. There is, however, some physical justification for other weighting functions. For instance, the lower-frequency components could be weighted preferentially over the higher-frequency components because surface scattering, which is unaccounted for in the model, would be more likely to alter the higher-frequency measurements. Or, the imaginary component, which is typically a factor of 2 to 3 smaller than the real component, could be preferentially weighted to account for the difference. Or, coherence values near zero magnitude could be deemphasized because they are more likely to be contaminated by electronic noise. These and other weighting functions may prove useful in future applications of the inversion, but will not be necessary in the current study.

The frequency band chosen for the inversion represents a compromise of the following factors. A low-frequency component is desirable in order to maximize the penetration depth into the sediment. However, focusing on only low frequencies increases the risk of error from shipping-contaminated noise, which is not being modeled here. Higher-frequency components are desirable in order to ensure the use of wind-generated noise and in order to obtain sufficient structure (i.e., zero crossings) in the coherence function. However, very-high-frequency noise is undesirable because it only samples the surficial sediment, and the coherence structure is more likely to be affected by surface scattering. Consequently, the frequency band of 100 Hz to a few kilo-Hertz is chosen to most reliably estimate the upper few meters of seabed using predominantly wind-generated noise. In the inversions results that follow, slight variations on these limits are applied because of hardware limitations imposed during the collection of data.

The inversion procedure is to minimize the norm between the theoretical and measured broadband, complex coherence functions for the three-dimensional parameter space c_{p3} , c_{s3} , and z_s . The source depth is considered as a free parameter here as it is unknown and can affect the higher-frequency components of the coherence.²¹ The theoretical coherence functions are computed for a matrix of the three parameters and saved in a look-up table for comparison with the data. The compressional wave speed is varied from 1550 to 2800 m/s, the shear wave speed is varied from 0 to 1400 m/s, and the source depth is varied from 0 to 1 m. The remaining seabed parameters are correlated using the relationships outlined in the Appendix. In the results that follow, the values of the norm are plotted on a two-dimensional (c_{p3} and c_{s3}) ambiguity surface for the source depth where the best fit occurs. The final estimate is the three-parameter combination that provides the minimum value of Eq. (10).

V. INVERSION RESULTS

At this point, we present inversions from two shallow water sites: the Cortes Bank and the North Celtic Sea.

A. The Cortes Bank

The Cortes Bank is a raised bank of volcanic origin located in the California Continental Borderland, 90 nautical miles from Pt. Loma, CA. The shallow area of the bank has a spatial extent of approximately 20 by 30 km. The top of the bank is characterized by large wave cut terraces of exposed bedrock, isolated areas of sediment pooling, and extensive areas of sediment deposits along the slopes. The areas of thin or absent sediment coverage were chosen for the experiment in order to maximize the chances of detecting the sandstone substrate, and measuring the shear speed. The exposed bedrock is composed of consolidated sedimentary and volcanic rock of probable Tertiary age.²² A generalized geoacoustic model from the neighboring Tanner Bank indicates a variable sediment overburden of 0 to 6 m with bedrock compressional and shear wave speeds of 2500 and 900 m/s, respectively.²³ Because of the proximity and similar geologic origin of the two banks, these parameters should be approximately representative of the Cortes Bank as well.

The experiment was conducted on 28 March 1995 using a 50-ft chartered vessel called the *Osprey*. The *Osprey* was equipped with a downward-looking sonar which was used to help select an experimental area where exposed bedrock was present. The experiment was performed at 32°27.997'N×119°10.454'W, in sea state 3, over an approximately 6 by 10-km area of exposed bedrock and in a water depth of 70 m. The receiver separation was 1 m and the hardware contained a low-pass filter at 2500 Hz. The coherence for five time segments is shown in Fig. 7(a). The corresponding spectra (not shown) display a spectral slope of about negative 3–4 dB/oct at the low frequencies, increasing to negative 5–6 dB/oct above 1 kHz.²⁴ These slopes are typical of wind-generated ambient noise, and suggest that there is little or no contamination from shipping. The five curves shown in Fig. 7(a) were averaged together to provide the final coherence estimate used in the inversion. Because the data were unreliable below 250 Hz, the inversion was performed on the coherence over the frequency band of 250–2500 Hz. The look-up tables were calculated using an isoveLOCITY profile and a homogeneous half-space basement. The theoretical coherence values were computed every 50 Hz, providing $N=46$ frequency points in the coherence curves. The measured coherence was computed using 512-point FFT's and interpolated to the 46 frequency points. The inversion results are shown in Fig. 8 for a source depth of 0.1 m where the best fit occurred. The ambiguity surface indicates a best fit at a value of $c_p=2350$ m/s and $c_s=1150$ m/s. The result is well resolved in the c_p and c_s dimensions and is in reasonable agreement with the model of Bucca and Fulford.²³ The estimates demonstrate that both compressional and shear wave speeds of the exposed bedrock can be measured from the ambient noise coherence.

The compressional wave speed estimate is lower than the 2500 m/s value given by Bucca and Fulford. One explanation for this comes from the depth-averaging property of

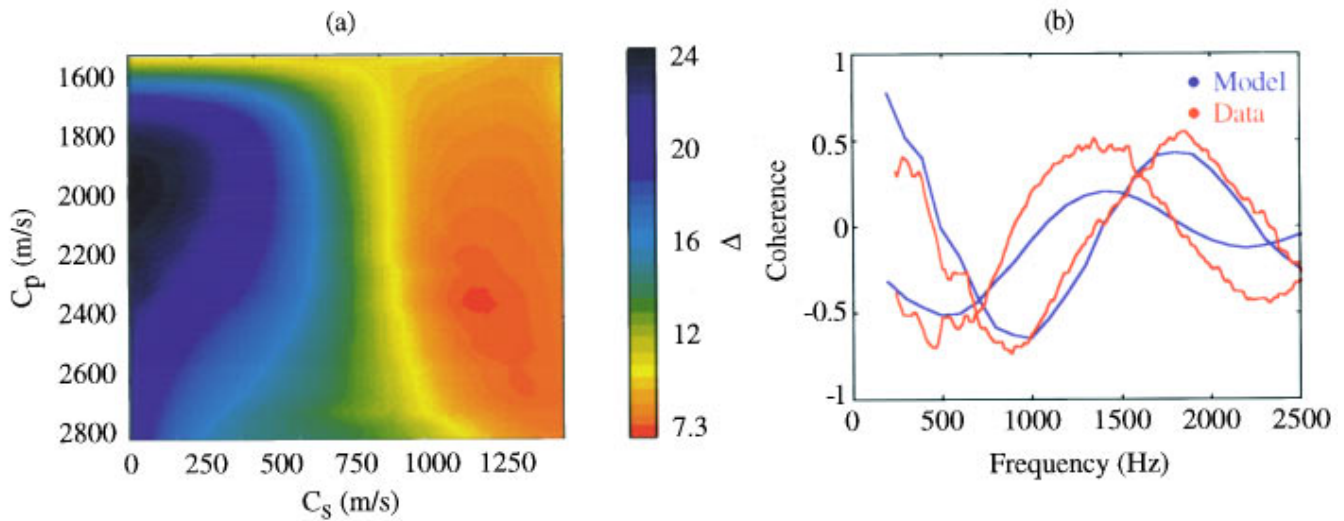


FIG. 8. Inversion result for the Cortes Bank data site. The best fit occurs at $c_p=2350$ m/s and $c_s=1150$ m/s for a value of $\Delta=7.3$.

the ambient noise technique. Since the site consists of exposed bedrock as well as areas of thin surficial sediment over the bedrock, the inversion estimate represents a reasonable average of these material properties. Another factor which might explain the low c_p estimate is the presence of a sound speed profile. A CTD (conductivity, temperature, and depth) cast was taken during the experiment to measure this profile, but the data were not recoverable. It is unlikely that a significant sound speed profile was present because of the turbulent mixing above the bank. However, since the experiment was conducted in the springtime when solar warming of the surface is prevalent, the existence of a weak downward-refracting sound speed profile is a reasonable possibility. To address this possibility, the look-up tables were recomputed assuming a modest downward-refracting profile. A linear profile was used that varied from 1518 to 1500 m/s over the 70-m channel depth. The inversion result showed little change from the isovelocity case. The best fit occurred at $c_p=2350$ m/s and $c_s=1200$ m/s. The reason that little change occurred is because the trapped modes were stripped out by the high shear speed basement, such that the noise incurred little additional mode stripping from the sound speed profile. The value of the norm increased from $\Delta=7.3$ in the isovelocity case to $\Delta=7.4$ in the downward-refracting case, indicating that the isovelocity profile provides a marginally better fit.

The best fit of the model to the data is also shown in Fig. 8. The real component shows a good fit over the entire frequency band. However, the imaginary component fit is somewhat less precise. The imaginary component of the data shows greater oscillations than the model, particularly at frequencies above 1 kHz. This may account for the high shear estimate, which is strongly dependent on the imaginary component. A possible explanation for the large imaginary component comes from surface scattering which preferentially influences the shorter wavelengths compared to the longer wavelengths. Scattering from the surface or bottom tends to displace low angle energy into high angle energy, which is more rapidly attenuated, and can thus be thought of as an

additional loss to the specularly reflected component. The increase in the imaginary component can easily be demonstrated using an exponential scattering model. During the experiment, the sea surface above the Cortes Bank exhibited considerable roughness and irregularity. Consequently, it is very likely that surface scattering contributed to the coherence of the measured field. A better theoretical fit to the measured coherence and a more accurate estimate might be obtained if a proper measurement of the rms surface roughness is included in the model. The omission of surface scattering from the model thus limits the accuracy of the seabed estimates for this site. However, as scattering represents a relatively minor modification which is mostly present at higher frequencies, the Cortes Bank inversions presented here demonstrate the feasibility of using the ambient noise coherence to estimate the shear wave speed over exposed consolidated materials.

B. The North Celtic Sea

The second inversion is presented for a site located in the North Celtic Sea at $51^{\circ}05'N \times 08^{\circ}12'W$. This site is characterized by a thin layer of sand over a chalk substrate. In Buckingham² the compressional wave speed at this site was inverted for using a low-loss fluid model. The inversion resulted in an erroneously low compressional wave speed estimate, which was attributed to the omission of shear from his model. This was one motivation for investigating the effects of shear in the present study.

An independent survey of the site was performed by measuring the propagation loss from explosive charges to a bottom-mounted array. These measurements were then fitted to the theoretical predictions of a shallow water Pekeris model with an elastic basement. The results are discussed by Ellis and Chapman^{25,26} and Staal.²⁷ In these studies, it was found that the inclusion of shear in the model was necessary to explain the very high losses below 300 Hz. The authors demonstrate good fits to these low-frequency data using typical chalk parameters of $c_p=2400$ m/s and $c_s=1000$ m/s, but

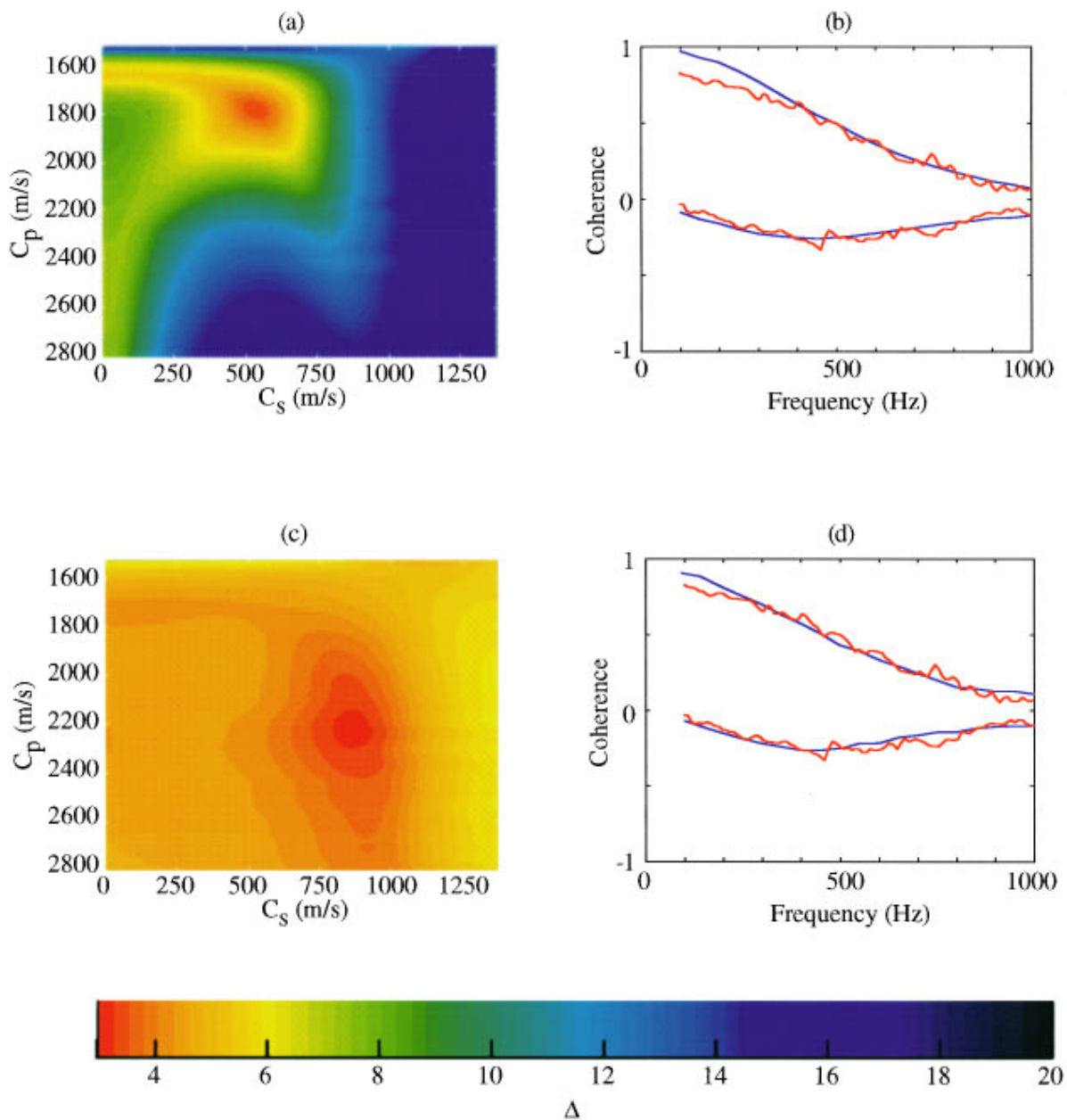


FIG. 9. Inversion results for the North Celtic site using an uncovered half-space bottom and a 1-m layer over a half-space substrate. (a) and (b) are respectively the ambiguity surface and best fit result obtained using the half-space model with no layer. The best fit occurs at 1775 m/s and 525 m/s with $\Delta=3.1$. (c) and (d) are the ambiguity surface and best fit result obtained using a 1-m layer of sand over a half-space substrate. The best fit for the layered model occurs at 2225 m/s and 875 m/s with $\Delta=2.9$.

state that better fits were achieved using slightly lower shear speeds. Furthermore, it was determined that the effects of a thin sediment layer, which they modeled as 1 m of sand, were important in the propagation loss measurements above 500 Hz. These estimates will serve as ground truth for the ambient noise analysis.

The North Celtic experiment was performed on 17 July 1983 in a water depth of 104 m. Data were collected for approximately 1 h using sonobuoy arrays described in Ref. 2, which have minimum receiver separation of 1 m and a low-pass filter cutoff of 1 kHz. The conditions during the experiment were sea state 1 with winds below 5 m/s. The spectra and coherence were computed from 2-min segments of data using 512-point FFTs with 50% overlap and a

Kaiser–Bessel²⁰ window $\beta = \pi\alpha = 7.85$. The spectra (not shown) exhibit a slope of -5 dB/oct over the 100–1000-Hz band, but do not display the characteristic wind noise rolloff below 500 Hz.²⁴ This lack of rolloff and a spectral line at 240 Hz suggest that shipping, or at least fishing vessels, may be a factor in the data.

The theoretical coherence curves were computed for 50-Hz increments, providing $N=19$ frequency points. The inversion results are shown in Fig. 9 for a source depth of 0.65 m where the best fits occurred. The ambiguity surface and best fit for a receiver pair separated by 1 m are shown in Fig. 9(a) and (b), respectively. The ambient noise estimates using the half-space model are $c_p=1775$ m/s and $c_s=525$ m/s. The results are low compared to the measured

values for the chalk substrate. This low estimate can be explained by the thin surficial sand layer that separates the chalk from the water column. The sand inhibits the compressional to shear wave conversion, and the inversion represents an average over the two materials.

For the frequencies used in the inversion we expect the average to represent the upper few meters of seabed. Ellis and Chapman found that a 1-m layer of sand was necessary to fit their propagation loss data above 500 Hz. Based on their findings, the look-up tables were recomputed for a variable homogeneous half-space covered by a fixed 1-m layer of sand. The layered inversion results are shown in Fig. 9(c) and (d). The estimate has moved out in parameter space to $c_p = 2225$ m/s and $c_s = 875$ m/s, which is in good agreement with the independent survey. Furthermore, the value of the norm has decreased from 3.1 to 2.9, indicating that the layered model has provided a marginally better fit.

Figure 9(a) and (c) is plotted on the same color scale. This is done to illustrate that the resolution in parameter space decreases when inverting for subsurface layers. This is not surprising because the noise is dominated by the uppermost sediment, whereas progressively deeper layers have less overall effect. Nonetheless, this result demonstrates the possibility of using ambient noise not only to estimate average seabed parameters, but also to measure a layered structure in the upper few meters. In this case we had the benefit of knowing the surficial sediment composition in advance. In general, when prior information is not available, a more systematic approach would need to be employed.

The results in this section demonstrate the ability of the ambient noise method to extract the seabed parameters, given the appropriate model. It is clear that the measured noise field can be altered substantially by the presence of a thin sedimentary layer. Given no prior knowledge of the seabed structure, this can lead to estimates that represent average seabed characteristics, and possibly estimates that mischaracterize the seabed. At the present time, the technique has not been refined to the point where the process of selecting the appropriate model can be automated. However, the improvement in the fit with the appropriate model selection suggests that such a procedure could be developed based on the minimum norm criterion.

VI. CONCLUDING REMARKS

Using a theoretical model of wind-generated ambient noise, it has been shown that the vertical directionality and vertical coherence of the noise are sensitive to both the compressional and shear wave speeds of the seabed. The compressional wave speed affects the symmetrical part of the noise directionality, which is manifest in the real component of the coherence. The conversion of compressional wave energy in the water column to shear waves in the seabed is a loss mechanism that strips intermediate trapped mode energy from the water column. As such, it decreases the symmetry in the noise and increases asymmetry. This is manifest as a decreased zero crossing in the real component and an increased magnitude in the imaginary component of the coherence.

The time-averaged directionality and coherence are relatively stable features of the noise and are relatively independent of temporal variations in the ocean environment. This has been demonstrated using distinct estimates of the coherence taken over time from two ocean sites. At one site, the structure of the coherence remained stable over a 1-h period while the power spectral density varied by up to 15 dB. At the other site, similar consistency was seen in the measured coherence taken from five separate days while the sea state varied between 1 and 3.

Based on the noise field dependence on the seabed, an inversion procedure was developed to estimate the compressional and shear wave speeds using the broadband coherence from a single hydrophone pair. Estimates obtained from the ambient noise will, by the very nature of ambient noise, represent an average over range and depth. Modeling of the coherence over a layered basement indicates the broadband coherence over the frequency band of 100 to 2000 Hz is determined by the upper few meters of seabed. In addition, a preliminary investigation into a range-dependent noise model indicates that the coherence represents a range footprint of 10–25 km.²⁴ Although these types of estimates will not be useful in detailed exploration of the ocean seabed, they provide a simple, cost effective means of estimating the average upper seabed properties.

The ambient noise inversion has been applied to ocean data from two shallow water sites. At the Cortes Bank, where the bedrock was exposed, a half-space model of the seabed provided reasonably accurate estimates of the compressional and shear wave speeds. For the North Celtic site, the half-space model proved to be insufficient due to the *in situ* presence of a thin sedimentary layer overlying the chalk substrate. However, by including the sedimentary layer in the model, the parameter estimates of underlying chalk improved significantly. This suggests that, by developing a systematic approach to focus on successive basement layers, the technique may be improved to not only give more accurate estimates, but to also determine a rough sound speed profile for the seabed.

ACKNOWLEDGMENTS

The authors wish to acknowledge the Naval Undersea Warfare Center for providing the data from the Florida Shelf and the Defence Research Agency—Farnborough for providing the data from the North Celtic. In addition, we thank Richard Bachman for supplying seismic profiling information from the Cortes Bank. This work has been supported by the Office of Naval Research under Contract No. N00014-91-J-1118.

APPENDIX: CORRELATION EQUATIONS FOR SEABED PARAMETERS

In the calculation of the coherence look-up tables, only two seabed parameters were held as free variables, c_{p3} and c_{s3} . The compressional wave speed is the primary parameter affecting the coherence, and is always included in the inversion. The absorption and shear wave speed are parameters that trade off in importance depending on whether the seabed

is fluidlike or shear supporting, respectively. For the consolidated seabed materials considered in this study, the loss due to shear outweighs absorption loss. As such, the value of α_{p3} was not included in the inversion, but was correlated with the compressional wave speed according to the following equation:

$$\alpha_{p3} = \{2.64 - 1.06 \times 10^{-3} c_{p3}\} \text{ dB}/\lambda. \quad (\text{A1})$$

The density and shear wave absorption are parameters of limited significance in the coherence calculation. Consequently, they were correlated with other parameters according to the following equations:

$$\rho_3 = \begin{cases} \frac{b + \sqrt{b^2 + 4a(c_{p3} - 2270.9)}}{2a} \text{ kg/m}^3, & 1.25 \leq \rho_3 \leq 2.1, \\ 1.62 + 2.61 \times 10^{-4} c_{p3} \text{ kg/m}^3, & 2.1 < \rho_3 \leq 2.4, \end{cases} \quad (\text{A2})$$

where

$$a = 474.6, \quad b = 1194.4,$$

and

$$\alpha_{s3} = [1.97 - 1.18 \times 10^{-3} c_{s3}] \text{ m/s}. \quad (\text{A3})$$

In addition to these correlations, lower limits of $\alpha_{p3} = 0.05 \text{ dB}/\lambda$ and $\alpha_{s3} = 0.1 \text{ dB}/\lambda$ were imposed as practical limits.

The correlations above are estimates based on a substantial body of *in situ* research conducted by Hamilton and others. The equations for α_{p3} and α_{s3} are linear fits to correlations found in Jensen *et al.*¹⁹ The quadratic equation correlating ρ_3 with c_{p3} comes from Hamilton,¹⁶ and is valid for the values of ρ_3 indicated. Above $\rho_3 = 2.1$, a linear fit to *in situ* data is again used.

As the coherence function does not have sufficient structure to resolve all five parameters, these correlations are an attempt to minimize the error that results from not actually knowing their values. Mismatch between the actual *in situ* values and those derived from Eqs. (A2) and (A3) are expected to have negligible effects on the coherence. Errors associated with Eq. (A1), on the other hand, are expected to be most significant when the absorption is largest. This means that shear speed measurements will be uncertain for low compressional wave speed seabeds where the effects of absorption become significant and where absorption levels are more variable in nature.

¹D. M. F. Chapman, in *Underwater Communication and Position Fixing* (Institute of Acoustics: University of East Anglia, Norwich, England, 1987), pp. 1–11.

²M. J. Buckingham and S. A. S. Jones, "A new shallow-ocean technique for determining the critical angle of the seabed from the vertical directionality of the ambient noise in the water column," *J. Acoust. Soc. Am.* **81**, 938–946 (1987).

- ³R. M. Hamson, "The modelling of ambient noise due to shipping and wind sources in complex environments," *Appl. Acoust.* **51**(3), 251–287 (1997).
- ⁴M. J. Buckingham, "A theoretical model of ambient noise in a low-loss, shallow water channel," *J. Acoust. Soc. Am.* **67**, 1186–1192 (1980).
- ⁵R. M. Hamson, "The theoretical responses of vertical and horizontal line arrays to wind-induced noise in shallow water," *J. Acoust. Soc. Am.* **78**, 1702–1712 (1985).
- ⁶W. A. Kuperman and F. Ingenito, "Spatial correlation of surface generated noise in a stratified ocean," *J. Acoust. Soc. Am.* **67**, 1988–1996 (1980).
- ⁷H. Schmidt, *OASES: Application and Upgrade Notes* (MIT, Cambridge, MA, 1994).
- ⁸H. Schmidt, *SAFARI: Seismo-acoustic Fast Field Algorithm for Range Independent Environments. User's Guide* (SACLANT Undersea Research Centre, La Spezia, Italy, 1988).
- ⁹C. H. Harrison, "Formulas for ambient noise level and coherence," *J. Acoust. Soc. Am.* **99**, 2055–2066 (1996).
- ¹⁰Z. Y. Zhang and C. T. Tindle, "Complex effective depth of the ocean bottom," *J. Acoust. Soc. Am.* **93**, 205–213 (1993).
- ¹¹S. O. Rice, "Mathematical analysis of random noise," *Bell Syst. Tech. J.* **23**, 46–156 (1945).
- ¹²D. C. Stickler, "Normal-mode program with both the discrete and branch line contributions," *J. Acoust. Soc. Am.* **57**, 856–861 (1975).
- ¹³P. Balasubramanian and M. M. Muni, "A note on 'The effective depth of a Pekeris ocean waveguide, including shear wave effects' [Chapman *et al.*, *J. Acoust. Soc. Am.* **85**, 648–653 (1989)]," *J. Acoust. Soc. Am.* **88**, 564–565 (1990).
- ¹⁴H. Cox, "Spatial correlation in arbitrary noise fields with application to ambient sea noise," *J. Acoust. Soc. Am.* **54**, 1289–1301 (1973).
- ¹⁵A. C. Kibblewhite, "Attenuation of sound in marine sediments: A review with emphasis on new low frequency data," *J. Acoust. Soc. Am.* **86**, 716–738 (1989).
- ¹⁶E. L. Hamilton, "Geoacoustic modeling of the sea floor," *J. Acoust. Soc. Am.* **68**, 1313–1340 (1980).
- ¹⁷E. L. Hamilton, "Compressional-wave attenuation in marine sediments," *Geophysics* **37**, 620–646 (1972).
- ¹⁸E. L. Hamilton, "Sound velocity, elasticity, and related properties of marine sediments, North Pacific," Naval Undersea Research and Development Center (1969).
- ¹⁹F. B. Jensen, W. A. Kuperman, M. B. Porter, and H. Schmidt, *Computational Ocean Acoustics* (American Institute of Physics, New York, 1994), 1st ed., Vol. 1.
- ²⁰F. J. Harris, "On the use of windows for harmonic analysis with the Discrete Fourier Transform," *Proc. IEEE* **66**, 51–83 (1978).
- ²¹M. J. Buckingham and N. M. Carbone, "Source depth and the spatial coherence of ambient noise in the ocean," *J. Acoust. Soc. Am.* **102**, 2637–2644 (1997).
- ²²H. G. Greene, S. H. Clarke, Jr., M. E. Field, F. I. Linker, and H. C. Wagner, "Preliminary report of the environmental geology of selected areas of the Southern California Continental Borderland," United States Department of the Interior Geological Survey (1975).
- ²³P. J. Bucca and J. K. Fulford, "Environmental variability during the Tanner Bank Phase of the Pacific Coast Operation," Naval Research Laboratory (1995).
- ²⁴N. M. Carbone, "Inverting for geoacoustic seabed parameters using ambient noise," Ph.D. Thesis, University of California at San Diego, Scripps Institution of Oceanography, 1996.
- ²⁵D. D. Ellis and D. M. F. Chapman, "Modelling of shear-wave related acoustic propagation on the U.K. continental shelf," DREA (1984).
- ²⁶D. D. Ellis and D. M. F. Chapman, "A simple shallow water propagation model including shear wave effects," *J. Acoust. Soc. Am.* **78**, 2087–2095 (1985).
- ²⁷P. R. Staal, in *Acoustics and the Sea Bed*, edited by N. G. Pace (Bath U.P., Bath, England, 1983), pp. 289–296.

Mode functions for the wide-angle approximation to the parabolic equation

Amy R. Smith and Kevin B. Smith

Department of Physics, Naval Postgraduate School, Monterey, California 93943

(Received 11 April 1997; accepted for publication 19 September 1997)

The parabolic approximation to the wave equation is examined within the context of normal mode theory. In a layered waveguide, the horizontal propagation constants and modal amplitudes of the field Ψ satisfying the standard parabolic equation (SPE) approximation can be mapped exactly into the amplitudes and wave numbers of the normal modes for the field p satisfying the Helmholtz wave equation. However, this is not the case for certain other parabolic approximations, such as the wide-angle parabolic equation (WAPE) approximation. Approximate mode functions for the WAPE approximation are developed. These mode functions are then used to decompose range-independent sound-pressure fields computed using the WAPE approximation. The resulting modal coefficients and eigenfunctions obtained using the WAPE mode functions are compared with those obtained using standard normal mode theory. © 1998 Acoustical Society of America.

[S0001-4966(98)03901-0]

PACS numbers: 43.30.Bp, 43.30.Zk [SAC-B]

INTRODUCTION

In 1974, Tappert introduced the parabolic approximation to the wave equation to the underwater acoustics community (Tappert, 1977). This approximation is valid to much lower frequencies than the geometrical acoustic (small wavelength) approximation, as it retains all the diffraction effects associated with the ocean sound channel. In contrast to separation of variables methods which are based on the approximation that the ocean is exactly horizontally stratified, the parabolic approximation retains full coupling between waveguide modes, thereby making it valid for more realistic, nonstratified oceans. These are just a few of the reasons why use of the parabolic approximation for acoustic propagation predictions has become commonplace

In Tappert's original paper, several approximations to the so-called "square root operator" of the parabolic approximation were introduced. One of these defines what is known as the standard parabolic equation (SPE). Over the last 20 years, there have been additional higher-order approximations made to the square root operator of the parabolic equation. One such approximation leads to the wide-angle parabolic equation (WAPE) introduced by Thomson and Chapman (1983). This WAPE approximation is based on an operator splitting by Feit and Fleck (1978), and extends the SPE approximation to accommodate wider angles of propagation. It is also generally less sensitive to the choice of a reference wave number, k_0 , although exceptions do exist. Furthermore, error analysis indicated that the effects of phase errors are greatly reduced with this operator. Subsequently, the WAPE approximation is favored over the SPE for predicting acoustic propagation, and is one of the approximations used in the Navy standard model (Holmes and Gainey, 1991).

In that PE-based methods are full wave methods providing the total acoustic field on a computational grid, they do not readily supply information regarding the propagation of individual modes. This modal information might assist in interpreting acoustic propagation behavior in a complex en-

vironment, or be useful for determining the relative adiabatic nature of a particular environment. Thomson (1993) addressed this issue for the standard parabolic approximation. In this work, he described a PE-based spectral method suitable for analyzing fields propagating in waveguides. Specifically, he demonstrated that the field p satisfying the Helmholtz wave equation is exactly related to the field ψ satisfying the SPE approximation. For this case, the modal amplitudes and wave numbers of ψ can be determined exactly, and the corresponding amplitudes and wave numbers of the normal modes of the acoustic field p are then obtained by simple mapping rules.

For certain other higher-order parabolic approximations, such as the WAPE and LOGPE (Berman *et al.*, 1989), the modal eigenfunctions, amplitudes, and wave numbers of Ψ can only be approximated. As we shall show, the eigenfunctions and eigenvalues of the WAPE are distinct from those of the Helmholtz equation and SPE. Furthermore, the dependence of WAPE eigenfunctions and eigenvalues on the choice of reference sound speed (or reference wave number) suggests an explanation for the apparent failure of the WAPE to converge to an accurate solution in some test cases, such as the leaky surface duct problem described by Porter and Jensen (1993). They also show this to be a problem for the LOGPE approximation.

In that the WAPE is generally the most common implementation for PE models using the split-step Fourier technique and is expected to yield more accurate results than the SPE, a better understanding of its "normal modes" is desired. This paper develops mode functions for the WAPE approximation. It is important to note in what follows that our use of the split-step Fourier (SSF) algorithm does not introduce any additional approximations in terms of the corresponding modal description.

I. THEORETICAL BACKGROUND

A time-harmonic acoustic field in a cylindrical coordinate system can be represented by

$$P(r, z, \varphi, \omega t) = p(r, z, \varphi) e^{-i\omega t}. \quad (1)$$

Substituting this into the homogeneous wave equation in cylindrical coordinates leads to the free field Helmholtz equation

$$\frac{1}{r} \frac{\partial}{\partial r} \left(r \frac{\partial p}{\partial r} \right) + \frac{1}{r^2} \frac{\partial^2 p}{\partial \varphi^2} + \frac{\partial^2 p}{\partial z^2} + k_0^2 n^2(r, z, \varphi) p = 0, \quad (2)$$

where $k_0 = \omega/c_0$ is the reference wave number, $n(r, z, \varphi) = c_0/c(r, z, \varphi)$ is the acoustic index of refraction, c_0 is the reference sound speed, and $c(r, z, \varphi)$ is the acoustic sound speed. Here, all of the features of the environment are represented within $c(r, z, \varphi)$. We shall neglect density variations in this work, but this could be incorporated without any loss of generality.

Treating the ocean as a cylindrical waveguide, acoustic energy primarily propagates outward from an acoustic source in the horizontal direction. Therefore, the pressure field can be represented by an outgoing Hankel function slowly modulated by an envelope function

$$p(r, z, \varphi) = \psi(r, z, \varphi) H_0^{(1)}(k_0 r), \quad (3)$$

or in the far field ($k_0 r \gg 1$),

$$p(r, z, \varphi) = P_0 \sqrt{\frac{R_0}{r}} \psi(r, z, \varphi) e^{ik_0 r}. \quad (4)$$

This is the standard definition of the so-called ‘‘PE field function’’ ψ scaled such that at $r = R_0$, $|\psi| = 1$ and $|p| = P_0$. Substituting this into the Helmholtz equation and assuming azimuthal symmetry, it can be shown that the far-field outgoing wave in layered media satisfies (e.g., Tappert, 1977; DeSanto, 1977)

$$\frac{\partial \psi}{\partial r} = ik_0 (Q_{\text{op}} - 1) \psi, \quad (5)$$

where the operators

$$Q_{\text{op}} = (1 + q)^{1/2}, \quad (6)$$

$$q = \mu + \varepsilon, \quad (7)$$

$$\mu = \frac{1}{k_0^2} \frac{\partial^2}{\partial z^2}, \quad \varepsilon = n^2 - 1. \quad (8)$$

The purpose of introducing the intermediate operator q will become apparent later.

The second-order differential wave equation is now reduced to a first-order one, thereby allowing solutions via a one-way (no backscatter) noniterative marching algorithm

$$\psi(r + \Delta r, z) = \exp\{ik_0 \Delta r (Q_{\text{op}} - 1)\} \psi(r, z). \quad (9)$$

However, use of the full-band, exact square root operator is not numerically efficient. Subsequently, approximations to Q_{op} have been introduced to reduce the computational burden. Note also that as approximations to Q_{op} are used, the pressure field computed from the exact relation in Eq. (4) also becomes approximate. The resulting approximate pressure field is therefore not exactly equivalent to the acoustic pressure field which solves the Helmholtz wave equation. The significance of this will become apparent as the SPE and WAPE mode functions are compared.

The SPE operator due to Tappert (1977) is obtained using the first-order binomial expansion

$$Q_{\text{op}} \approx 1 + \frac{1}{2}q = 1 + \frac{1}{2}\mu + \frac{1}{2}\varepsilon \quad \text{for } |\mu| \ll 1, \quad |\varepsilon| \ll 1. \quad (10)$$

This approximation requires that variation in the refractive index be small to some degree, and is limited to small propagation angles. Note that this expansion is linear in the operator q . Substituting Eq. (10) into Eq. (5) yields the well-known standard parabolic equation for underwater acoustics:

$$\frac{\partial \psi}{\partial r} = \frac{i}{2k_0} \frac{\partial^2 \psi}{\partial z^2} + \frac{ik_0}{2} (n^2 - 1) \psi. \quad (11)$$

Adopting the notation

$$Q_{\text{SPE}} = 1 + \frac{1}{2}q, \quad (12)$$

Eq. (11) becomes

$$\frac{\partial \psi}{\partial r} = ik_0 (Q_{\text{SPE}} - 1) \psi. \quad (13)$$

A higher-order approximation to Q_{op} introduced by Thomson and Chapman (1983) is based on an operator splitting by Feit and Fleck (1978). Commonly referred to as the ‘‘wide-angle’’ approximation, it has the form

$$Q_{\text{WAPE}} = (1 + \mu)^{1/2} + [(1 + \varepsilon)^{1/2} - 1]. \quad (14)$$

This operator extended the SPE operator to accommodate wider angles of propagation and was also found to be less sensitive to the choice of k_0 in many deep ocean environments. Error analysis indicated that for typical deep ocean conditions, the effects of phase errors were greatly reduced relative to the SPE operator. For these reasons, use of the WAPE is commonplace for predicting sound propagation. However, note that Q_{WAPE} is no longer a simple function of the operator q . This becomes significant when performing modal decompositions of the computed field.

These are but two widely used approximations to the exact square root operator Q_{op} defined by Eqs. (6)–(8). Other approximations exist, and use of any of these approximations to the exact square root operator will give rise to some phase error beyond some range in most environments. In the next section, we shall examine how various approximations to the propagator function affect the normal mode decomposition. In particular, we will develop equations defining the appropriate eigenfunctions for the WAPE approximation.

II. THEORETICAL DEVELOPMENT OF WIDE-ANGLE MODE FUNCTIONS

Normal mode decomposition theory uses the technique of *separation of variables* and is based on the approximation that the ocean is exactly stratified horizontally. Assuming constant water density, azimuthal symmetry, and range independence (sound speed varies only with depth), the time-harmonic acoustic field $p(r, z)$ satisfies the two-dimensional Helmholtz equation

$$\frac{1}{r} \frac{\partial}{\partial r} \left(r \frac{\partial p}{\partial r} \right) + \frac{\partial^2 p}{\partial z^2} + k_0^2 n^2(z) p = 0. \quad (15)$$

Seeking solutions in the form $p(r, z) = \Phi(r)\Psi(z)$ yields the well-known depth-dependent modal equation

$$\frac{d^2}{dz^2} \Psi_m(z) + [k_0^2 n^2(z) - k_m^2] \Psi_m(z) = 0, \quad (16)$$

which is subject to appropriate boundary conditions. In this equation, k_m^2 represents the separation constant and $\Psi_m(z)$ denotes the specific mode function associated with this separation constant. The complete sum of normalized modes is necessary to represent an arbitrary pressure field. Accordingly, the pressure is expressed as

$$p(r, z) = \sum_{m=1}^{\infty} \Phi_m(r) \Psi_m(z), \quad (17)$$

where

$$\Phi_m(r) = H_0^{(1)}(k_m r). \quad (18)$$

Note that we could rewrite Eq. (16) as

$$q \Psi_m(z) = \lambda_m \Psi_m(z). \quad (19)$$

The mode functions are then seen as eigenfunctions of the operator q with eigenvalues

$$\lambda_m = \frac{k_m^2 - k_0^2}{k_0^2}. \quad (20)$$

Returning to the relationship between the acoustic field and the envelope function defined by Eq. (4), an alternate approach employing the separation of variables technique to solve the standard parabolic equation, Eq. (13), yields an expansion into SPE modes. In this case, the range-independent expansion is shown by DeSanto (1977) to be

$$\psi(r, z) = \sum_{m=1}^{\infty} a_m u_m(z) \exp(is_m r), \quad (21)$$

where a_m are the SPE mode amplitudes, $u_m(z)$ are the SPE mode functions, and s_m are the SPE modal wave numbers.

Hardin and Tappert (1973) and later Thomson (1993) have shown that the depth-dependent SPE mode functions $u_m(z)$ satisfy an eigenvalue equation comparable to that for the normal mode functions of the Helmholtz wave equation,

$$\frac{d^2}{dz^2} u_m(z) + [k_0^2 n^2(z) - k_m^2] u_m(z) = 0, \quad (22)$$

where the SPE modal wave numbers s_m are given by

$$s_m = \frac{k_m^2 - k_0^2}{2k_0}, \quad (23)$$

and the horizontal wave numbers k_m are the corresponding normal mode eigenvalues of Eq. (16). Furthermore, the mode functions for the SPE approximation exactly match those which solve the Helmholtz wave equation, as may be noted by comparing Eqs. (16) and (22). Hereafter, these particular modes will be referred to as standard normal modes. As we shall see shortly, this is not the case when using the wide angle approximation.

An alternative approach to Eqs. (22) and (23) is to substitute Eq. (21) into Eq. (13) to obtain

$$\frac{\partial \psi}{\partial r} = ik_0 \left[\left(1 + \frac{1}{2} q \right) - 1 \right] \psi = \frac{ik_0}{2} q \psi \quad (24)$$

such that

$$q u_m(z) = \frac{2s_m}{k_0} u_m(z). \quad (25)$$

This indicates that the functions $u_m(z)$ are also eigenfunctions of q with eigenvalues

$$\frac{2s_m}{k_0} = \frac{k_m^2 - k_0^2}{k_0^2} \quad (26)$$

which are identical to the eigenvalues defined by Eq. (20). Thus, the eigenfunction basis set for the SPE approximation is identical to the Helmholtz equation. In general, this will be true for any approximation to Q_{op} which may be expressed in terms of integer powers of q since

$$q^n u_m(z) = \lambda_m^n u_m(z). \quad (27)$$

This includes rational linear functions such as the approximation due to Claerbout (1985) and Padé series expansions (e.g., Bamberger *et al.*, 1988; Collins, 1989).

An interesting PE formulation recently implemented is Tappert's c_0 -insensitive approximation (Tappert *et al.*, 1995). Analysis by Tappert and Brown (1996) shows that this approximation is accurate to second order in q , i.e.,

$$Q_{op} \approx Q_{INS} = 1 + \frac{1}{2} q - \frac{1}{8} q^2 + (\text{higher-order terms}). \quad (28)$$

It has been shown (Nghiem-Phu *et al.*, 1993) that this formulation does provide a stable, accurate solution to the leaky surface duct problem. While the depth-separated equation (hence, the eigenfunctions and eigenvalues) of the c_0 -insensitive model will not exactly match the Helmholtz equation (since the "higher-order terms" are not simply higher powers of q), the second-order accuracy of this approximation may practically eliminate the mismatch observed here with the WAPE.

We now seek approximate solutions to Eq. (5) replacing Q_{op} by the approximate propagator function Q_{WAPE} and assuming

$$\psi(r, z) = \sum_{m=1}^{\infty} \Gamma_m(r) \nu_m(z). \quad (29)$$

Here, $\Gamma_m(r)$ represents the WAPE range-dependent modal amplitude and $\nu_m(z)$ is the WAPE mode function. This expansion for $\psi(r, z)$ leads to the modal equation

$$\frac{ik_0}{\nu_m(z)} \left[\left(1 + \frac{1}{k_0^2} \frac{d^2}{dz^2} \right)^{1/2} + (n(z) - 1) - 1 \right] \nu_m(z) - \frac{1}{\Gamma_m(r)} \frac{d}{dr} \Gamma_m(r) = 0. \quad (30)$$

Setting the separation constant equal to $i\beta_m$, it can be shown that $\Gamma_m(r)$ has the simple range dependence

$$\Gamma_m(r) = b_m \exp(i\beta_m r), \quad (31)$$

where b_m is the range-independent modal amplitude and β_m is the associated WAPE modal wave number. Using this

separation constant, the WAPE depth-dependent modal equation becomes

$$\left[\left(1 + \frac{1}{k_0^2} \frac{d^2}{dz^2} \right)^{1/2} + (n(z) - 1) - \left(1 + \frac{\beta_m}{k_0} \right) \right] \nu_m(z) = 0. \quad (32)$$

To determine the approximate WAPE modal amplitudes, Eqs. (3) (4), (29), and (31) are used to establish the far-field WAPE modal solution for the computed WAPE field p in a layered waveguide:

$$p(r, z) \approx \left(\frac{2}{i\pi k_0 r} \right)^{1/2} \sum_m b_m \nu_m(z) \exp(i\beta'_m r), \quad (33)$$

where

$$\beta'_m = \beta_m + k_0. \quad (34)$$

To develop approximations for the WAPE modes, the square root operator in Eq. (32) is approximated using first- and second-order Taylor series expansions. This leads to the first-order approximate depth-dependent WAPE modal equation

$$\frac{d^2}{dz^2} \nu_m(z) + 2k_0^2 \left[n(z) - \frac{\beta'_m}{k_0} \right] \nu_m(z) \approx 0, \quad (35)$$

and to second order

$$\left[\frac{1}{8k_0^4} \frac{d^4}{dz^4} - \frac{1}{2k_0^2} \frac{d^2}{dz^2} - n(z) - \frac{\beta'_m}{k_0} \right] \nu_m(z) \approx 0. \quad (36)$$

Note that the terms ‘‘first order’’ and ‘‘second order’’ refer to the relative order of the Taylor series employed in the expansion of Eq. (32). It does not relate to the order of accuracy used during numerical implementation nor the overall accuracy of the WAPE approximation. The first-order approximation is essentially a return to a small angle approximation, and is not expected to provide highly satisfactory results in numerical implementation. However, it is included in the analysis to gain insight into the nature of the WAPE mode function and its relationship to the standard normal mode function.

The eigenfunctions satisfying Eqs. (32), (35), and (36) no longer match those normal mode eigenfunctions associated with the Helmholtz wave equation. The orthogonality (uniqueness) of the WAPE modes can be examined as follows. Here we shall only consider the first-order approximation, although the orthogonality of the WAPE modes can be shown to be more general. Multiply the first-order approximate depth-dependent WAPE modal equation (35) for $\nu_n(z)$ by $\nu_m(z)$ and for $\nu_m(z)$ by $\nu_n(z)$. Subtracting these two equations yields

$$\begin{aligned} \nu_m(z) \frac{d^2}{dz^2} \nu_n(z) - \nu_n(z) \frac{d^2}{dz^2} \nu_m(z) \\ = 2k_0(\beta_n - \beta_m) \nu_n(z) \nu_m(z) \end{aligned} \quad (37)$$

or

$$\begin{aligned} \frac{d}{dz} \left(\nu_m(z) \frac{d}{dz} \nu_n(z) - \nu_n(z) \frac{d}{dz} \nu_m(z) \right) \\ = 2k_0(\beta_n - \beta_m) \nu_n(z) \nu_m(z). \end{aligned} \quad (38)$$

Integrating over z and applying the boundary conditions for an ideal waveguide (pressure release surface, rigid bottom), Eq. (38) reduces to

$$(\beta_n - \beta_m) \int_0^\infty \nu_n(z) \nu_m(z) dz = 0. \quad (39)$$

Since each modal wave number is unique, i.e., $\beta_m \neq \beta_n$ if $m \neq n$,

$$\int_0^\infty \nu_n(z) \nu_m(z) dz = 0 \quad \text{for } m \neq n. \quad (40)$$

Therefore, the first-order approximate WAPE modes form an orthogonal basis set. A similar analysis could be performed on the second-order approximate WAPE modes.

III. NUMERICAL IMPLEMENTATION OF THE WIDE-ANGLE MODE FUNCTIONS

Finite-difference techniques are used to numerically approximate the wide-angle PE mode functions developed in Sec. II. Numerical schemes are developed for the first- and second-order Taylor series approximations given by Eqs. (35) and (36). For the first-order approximation, a numerical scheme closely following that developed by Jensen *et al.* (1994) for normal modes to the Helmholtz wave equation is developed. Defining a grid of N equally spaced points over the depth interval $0 \leq z \leq D$ gives the depth points $z_j = jh$, $j = 0, 1, \dots, N$, where h is the mesh width given by D/N . This then allows us to define the following $O(h^2)$ difference approximations for the first and second derivatives based on forward, centered, and backward difference approximations, respectively:

$$\nu'_j \approx \frac{\nu_{j+1} - \nu_j}{h} + \left[-2k_0 \left(\frac{\omega}{c(z)} - \beta'_m \right) \nu_j \right] \frac{h}{2}, \quad (41)$$

$$\nu''_j \approx \frac{\nu_{j-1} - 2\nu_j + \nu_{j+1}}{h^2} + O(h^2), \quad (42)$$

$$\nu'_j \approx \frac{\nu_j - \nu_{j-1}}{h} - \left[-2k_0 \left(\frac{\omega}{c(z)} - \beta'_m \right) \nu_j \right] \frac{h}{2}. \quad (43)$$

In the water column, the approximate mode functions must satisfy Eq. (35), which in terms of the difference approximations becomes

$$\begin{aligned} \nu_{j-1} + \left(-2 + h^2 2k_0 \left[\frac{\omega}{c(z_j)} - \beta'_m \right] \right) \nu_j + \nu_{j+1} = 0, \\ j = 1, 2, \dots, N-1. \end{aligned} \quad (44)$$

The top and bottom boundary conditions, continuity of pressure and normal velocity, in the continuous problem are represented by

$$f^T(\beta'_m) \nu(0) + \frac{g^T(\beta'_m)}{\rho} \frac{d}{dz} \nu(0) = 0, \quad (45)$$

$$f^B(\beta'_m) \nu(D) + \frac{g^B(\beta'_m)}{\rho} \frac{d}{dz} \nu(D) = 0, \quad (46)$$

and in the discrete problem by

$$\frac{f^T(\beta'_m)}{g^T(\beta'_m)} \nu_0 + \frac{1}{\rho} \left(\frac{\nu_1 - \nu_0}{h} + \left[-2k_0 \left\{ \frac{\omega}{c(z)} - \beta'_m \right\} \nu_0 \right] \frac{h}{2} \right) = 0, \quad (47)$$

$$\frac{f^B(\beta'_m)}{g^B(\beta'_m)} \nu_N + \frac{1}{\rho} \left(\frac{\nu_N - \nu_{N-1}}{h} - \left[-2k_0 \left\{ \frac{\omega}{c(z)} - \beta'_m \right\} \nu_N \right] \frac{h}{2} \right) = 0. \quad (48)$$

Collecting these equations together, we obtain the eigenvalue problem,

$$\mathbf{A}(\beta'_m) \mathbf{v} = 0, \quad (49)$$

where \mathbf{A} is a symmetric tridiagonal matrix with the diagonal elements defined by

$$d_0 = \frac{\left(-2 + h^2 2k_0 \left[\frac{\omega}{c(z_0)} - \beta'_m \right] \right)}{2h\rho} + \frac{f^T(\beta'_m)}{g^T(\beta'_m)}, \quad (50)$$

$$d_j = \frac{\left(-2 + h^2 2k_0 \left[\frac{\omega}{c(z_j)} - \beta'_m \right] \right)}{h\rho}, \quad j = 1, 2, \dots, N-1, \quad (51)$$

$$d_N = \frac{\left(-2 + h^2 2k_0 \left[\frac{\omega}{c(z_N)} - \beta'_m \right] \right)}{2h\rho} - \frac{f^B(\beta'_m)}{g^B(\beta'_m)}, \quad (52)$$

and the off-diagonal elements defined by

$$e_j = \frac{1}{h\rho}, \quad j = 1, 2, \dots, N. \quad (53)$$

The scaling factor $[1/(h\rho)]$ is introduced to allow for multiple layers. When the functions $f^{T,B}$ and $g^{T,B}$ are independent of β'_m , then the eigenvalues and eigenvectors for Eq. (49) can be solved using standard Matlab routines. For a pressure release surface, the ratio f^T/g^T goes to infinity and ν_0 vanishes. For a rigid bottom, the ratio f^B/g^B goes to zero.

To develop a numerical scheme to solve the second-order approximation, the following $O(h^4)$ centered difference approximations (Godunov and Ryabenkii, 1987) are employed

$$\nu_j''' = \frac{1}{h^4} \left[-\frac{1}{6} \nu_{j-3} + 2\nu_{j-2} - \frac{13}{2} \nu_{j-1} + \frac{28}{3} \nu_j - \frac{13}{2} \nu_{j+1} + 2\nu_{j+2} - \frac{1}{6} \nu_{j+3} \right], \quad (54)$$

$$\nu_j'' = \frac{1}{h^2} \left[-\frac{1}{12} \nu_{j-2} + \frac{4}{3} \nu_{j-1} - \frac{5}{2} \nu_j + \frac{4}{3} \nu_{j+1} - \frac{1}{12} \nu_{j+2} \right]. \quad (55)$$

Substituting into the governing equation

$$\nu'''' - 4k_0^2 \nu'' - 8k_0^3 \left(\frac{\omega}{c(z)} - \beta'_m \right) \nu = 0 \quad (56)$$

and using a mesh similar to that defined for Eqs. (41)–(53) gives the resulting equation which must be satisfied in the water column:

$$\begin{aligned} & \nu_{j-3} + (-12 - 2h^2 k_0^2) \nu_{j-2} + (39 + 32h^2 k_0^2) \nu_{j-1} \\ & + \left(-56 - 60h^2 k_0^2 + 48h^4 k_0^3 \left(\frac{\omega}{c(z)} - \beta'_m \right) \right) \nu_j \\ & + (39 + 32h^2 k_0^2) \nu_{j+1} + (-12 - 2h^2 k_0^2) \nu_{j+2} \\ & + \nu_{j+3} = 0, \quad j = 3, 4, \dots, N-3. \end{aligned} \quad (57)$$

This leads to a seven-diagonal banded matrix. To simplify computations, pressure release boundaries are assumed, giving $\nu_0 = 0$ and $\nu_N = 0$. For $j = 1, 2, N-2, N-1$, the pressure release assumption leads to the following equations:

$$\begin{aligned} & \left(-44 - 58h^2 k_0^2 + 48h^4 k_0^3 \left(\frac{\omega}{c(z)} - \beta'_m \right) \right) \nu_1 + (38 + 32h^2 k_0^2) \nu_2 \\ & + (-12 - 2h^2 k_0^2) \nu_3 + \nu_4 = 0, \quad j = 1, \\ & (38 + 32h^2 k_0^2) \nu_1 + \left(-56 - 60h^2 k_0^2 + 48h^4 k_0^3 \left(\frac{\omega}{c(z)} - \beta'_m \right) \right) \nu_2 \\ & + (39 + 32h^2 k_0^2) \nu_3 + (-12 - 2h^2 k_0^2) \nu_4 + \nu_5 = 0, \quad j = 2, \end{aligned} \quad (58)$$

$$\begin{aligned} & \nu_{N-5} + (-12 - 2h^2 k_0^2) \nu_{N-4} + (39 + 32h^2 k_0^2) \nu_{N-3} \\ & + \left(-56 - 60h^2 k_0^2 + 48h^4 k_0^3 \left(\frac{\omega}{c(z)} - \beta'_m \right) \right) \nu_{N-2} \\ & + (38 + 32h^2 k_0^2) \nu_{N-1} = 0, \quad j = N-2, \end{aligned} \quad (60)$$

$$\begin{aligned} & \nu_{N-4} + (-12 - 2h^2 k_0^2) \nu_{N-3} + (38 + 32h^2 k_0^2) \nu_{N-2} \\ & + \left(-44 - 58h^2 k_0^2 + 48h^4 k_0^3 \left(\frac{\omega}{c(z)} - \beta'_m \right) \right) \nu_{N-1} \\ & = 0, \quad j = N-1. \end{aligned} \quad (61)$$

In the following section, results from these numerical approximations will be shown.

The eigenvectors of the matrices defined by Eqs. (50)–(53) and (57)–(61) represent the first- and second-order Taylor series approximations, respectively, to the WAPE mode functions $\nu_m(z)$ in Eq. (32). The matrix eigenvectors represent the associated WAPE modal wave numbers β_m .

To determine the modal amplitudes, it is useful to write Eq. (32) as

TABLE I. Summary of UMPE input parameters for computing WAPE solution for the modeled range-independent deep ocean environment.

Parameter	Value
Reference sound speed, c_0	1490 m/s
Frequency, f	100 Hz
Source depth	1000 m
Bottom depth	4500 m
Computational depth	8000 m
Transform size	8192
Depth grid step	0.9765 m
Range grid step	2.5 m

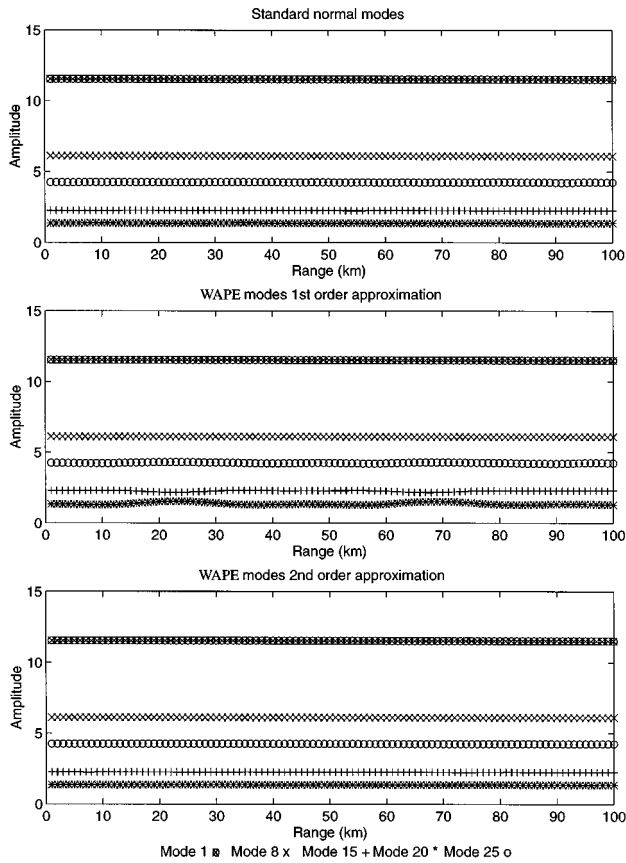


FIG. 1. Modal coefficient amplitudes as a function of range for modes 1, 8, 15, 20, and 25 of a range-independent Munk canonical sound-speed profile. Modes shapes were determined using standard normal mode theory and first- and second-order approximations to the WAPE mode function.

$$p(r, z) \approx \left(\frac{2}{i\pi k_0 r} \right)^{1/2} \sum_m b_m v_m(z) \exp(i\beta'_m r) \quad (62)$$

or

$$\begin{aligned} \sqrt{r} p(r, z) &\approx \left(\frac{2}{i\pi k_0} \right)^{1/2} \sum_m b_m v_m(z) \exp(i\beta'_m r) \\ &= \sum_m A_m(r) v_m(z), \end{aligned} \quad (63)$$

where A_m is the desired modal amplitude. This expression is general and does not depend on which approximation to the WAPE is used. Note that we have accounted for cylindrical spreading losses by scaling $p(r, z)$ by \sqrt{r} . Then assuming normalized modes and invoking orthogonality, it can be shown that at a given range the modal amplitude is given by

$$A_m(r) = \sqrt{r} \int_0^D \frac{p(z, r) v_m(z)}{\rho(z)} dz. \quad (64)$$

In the following section, modal amplitudes for a range-independent, deep ocean environment are computed.

IV. NUMERICAL RESULTS

The numerical schemes developed for the first- and second-order approximations to the WAPE mode function

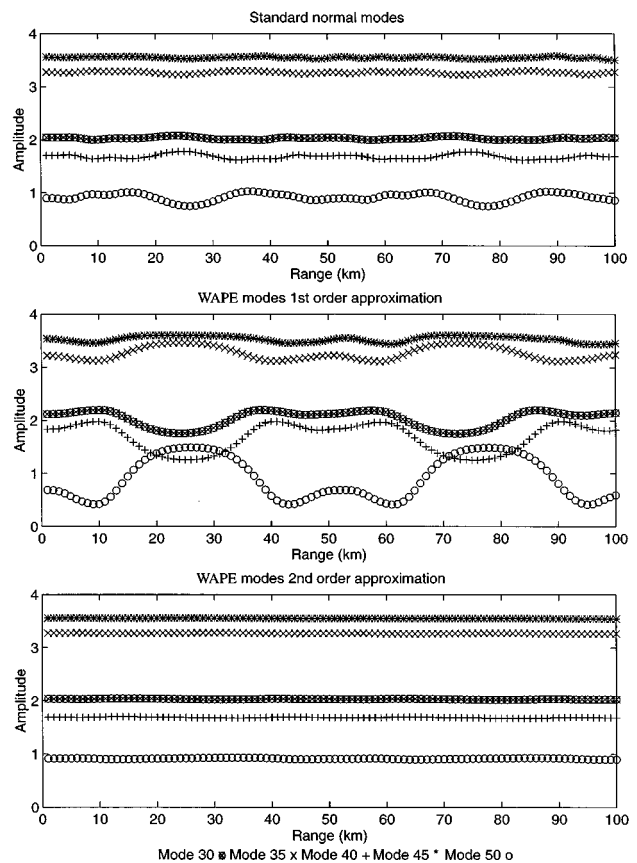


FIG. 2. Same as Fig. 1 except for modes 30, 35, 40, 45, and 50.

were tested assuming a range-independent, deep ocean environment characterized by Munk's canonical sound-speed profile (Munk, 1974)

$$[c(z) - c_0]/c_0 = \varepsilon(e^\eta - \eta - 1), \quad (65)$$

where $\varepsilon = 0.0057$, the scaled depth variable $\eta = 2(z - z_{\text{axis}})/B$, and the reference sound speed c_0 was chosen as 1490 m/s. Axis depth, z_{axis} , was assumed to be -1.0 km. The bottom depth was assumed to be -4.5 km.

The acoustic pressure field was computed out to a range of 100 km using the University of Miami PE (UMPE) model (Smith and Tappert, 1994) employing the wide angle PE approximation. Input run parameters are summarized in Table I. The resulting pressure field was then decomposed into standard normal modes using KRAKEN (Porter, 1991), and first- and second-order approximation WAPE modes by finding the eigenvectors of the matrices defined by Eqs. (50)–(53) and (57)–(61), respectively.

These mode functions were then used to compute the respective modal amplitude coefficients at 1-km intervals out to 100 km using Eq. (64). For a range-independent environment, these coefficients should remain constant with range. Plots of selected modal coefficient amplitudes for the three different mode functions are provided in Figs. 1–3. Modes were selected so as to minimize overlapping line segments on the plots. Only non-bottom interacting modes were considered, as the numerical scheme for the second-order WAPE mode functions currently only treats the bottom as a pressure release surface.

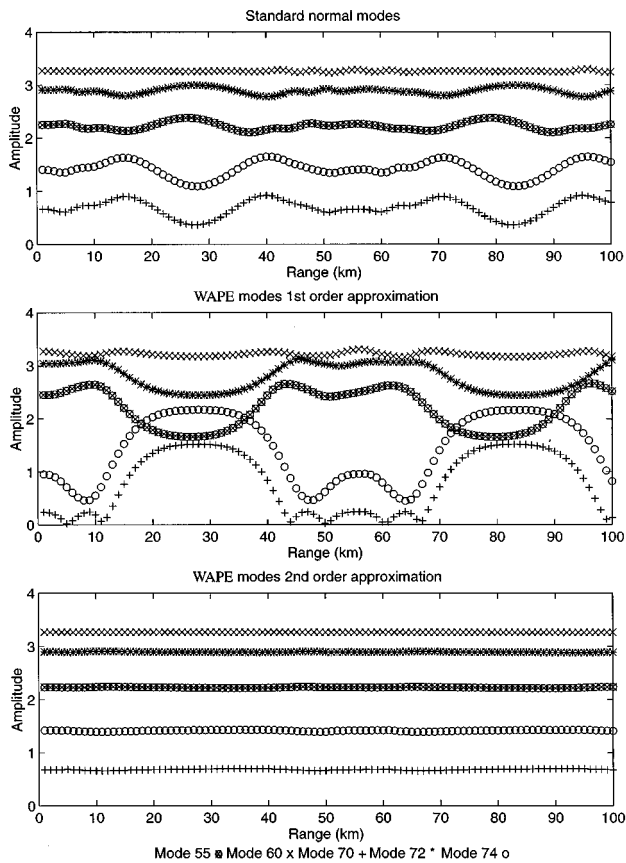


FIG. 3. Same as Fig. 1 except for modes 55, 60, 70, 72, and 74.

For the lower modes depicted in Fig. 1, all three methods provide satisfactory demonstration of range independence. However, the first-order WAPE mode function approximation starts to show some small fluctuations for mode numbers greater than 15. In Fig. 2, the first-order approximation clearly breaks down as the mode number increases. Additionally, the standard normal mode decomposition of the WAPE computed field begins to show noticeable fluctuations for modes above mode 35. Only the second-order WAPE mode function approximation demonstrates satisfactory range independence. As the mode number is increased further, the fluctuations in both the standard normal mode amplitudes and first-order WAPE approximation continue to increase. This is illustrated in Fig. 3. Again, the second-order approximation continues to correctly demonstrate the range-independent nature of the input sound-speed environment. This pattern was observed up through mode 100, the highest mode computed in this work.

The differences are relatively small between the mode shapes computed using standard normal mode theory and the second-order approximation to the WAPE mode function derived in this paper. Figure 4 illustrates the difference between these two mode functions for mode 70. For this particular sound-speed profile, the mode shapes derived using the two methods tended to converge at low mode numbers, and slowly diverge as the mode number increased.

For each mode function, the corresponding eigenvalue was also computed. The percentage differences between the first- and second-order approximate WAPE mode eigenval-

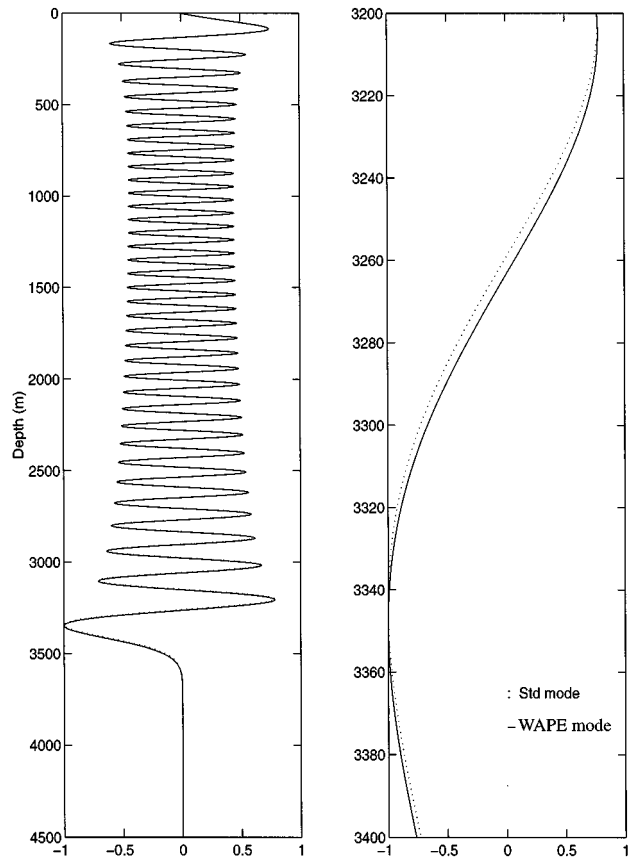


FIG. 4. Comparison of mode 70 mode shape as computed using standard normal mode theory and the second-order approximation to the WAPE mode function. The left-hand side depicts the mode shape over the entire water column. The right-hand side provides an enlargement of the 3200–3400-m depth to more clearly depict the difference in mode shape.

ues and the standard normal mode eigenvalues are plotted as a function of mode number in Fig. 5. As expected, the differences are small for the lower modes and increase with increasing mode number. Of significance is that none of the second-order WAPE mode eigenvalues differ by more than about 0.012% from the standard normal mode eigenvalues. The actual WAPE mode eigenvalue differences are expected to be even smaller. Thus, one may anticipate modal travel time differences to be very small. This was also suggested in a separate analysis by Smith (1997). The dramatic variability of the WAPE solution in the leaky surface duct problem is, therefore, possibly due more to modal amplitude fluctuations rather than relative modal phase interference.

V. SUMMARY

This paper has examined how approximations to the PE square root operator may alter the associated mode functions in a normal mode decomposition. Due to the popularity of the WAPE approximation in split-step Fourier algorithms, the corresponding mode functions and eigenvalues of this approximation were examined. Specifically, first- and second-order Taylor series approximations to the WAPE mode functions were developed and compared to the mode functions of the Helmholtz equation. Furthermore, it was shown that any PE approximation which can be defined as a

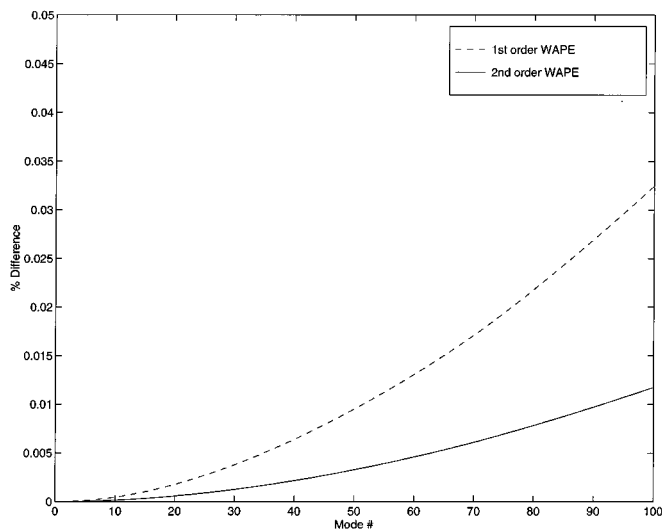


FIG. 5. Percent differences from the standard normal mode eigenvalues of the first- and second-order WAPE mode eigenvalues.

combination of integer powers of the operator q [defined in Eq. (7)] has the same basis set defined by the mode functions of the Helmholtz equation. This is not the case for the WAPE approximation. It was also conjectured that Tappert's c_0 -insensitive PE approximation may overcome this shortfall.

Numerical schemes were developed to compute the approximate WAPE mode functions and eigenvalues. The computed mode functions were then used to decompose a typical deep ocean range-independent sound-pressure field obtained using the WAPE approximation. The resulting modal amplitudes obtained using the WAPE mode functions were compared with those obtained using a standard normal mode decomposition of the WAPE field. The second-order approximation to the WAPE mode function showed noticeably less fluctuation in the computed modal amplitudes for the modeled range-independent environment in comparison to the standard mode shapes for modes above mode 35. The first-order approximation to the WAPE mode function, although simpler to implement numerically, did not provide an adequate representation of the range-independent nature of the modeled environment. While significant differences were observed between modal amplitudes, the errors in eigenvalues were quite small, typically less than 0.03% for all modes considered.

The purpose of this paper was to highlight the need for a different set of mode functions in normal mode expansions of certain parabolic approximations to the Helmholtz wave equation which do not have the same basis set. While the second-order Taylor series approximation to the WAPE mode function derived in this paper showed promising results for the simplified deep ocean environment, much remains to be done to develop proper numerical treatment of interfaces, bottom boundaries, and density gradients.

ACKNOWLEDGMENTS

This work was supported by the Student Research Fellowship Program sponsored by the Research, Development,

Test and Evaluation Division of the Naval Command, Control and Ocean Surveillance Center (NRaD), San Diego, CA, and the Research Initiation Program at the Naval Postgraduate School, Monterey, CA. The authors wish to thank Professors Ching-Sang Chiu, Fred Tappert, and Mike Brown for many useful discussions. Many thanks also to the reviewer whose comments were exceptionally helpful.

- Bamberger, A., Engquist, B., Halpern, L., and Joly, P. (1988). "Higher order parabolic wave equation approximation in heterogeneous media," SIAM (Soc. Ind. Appl. Math.) J. Appl. Math. **48**, 129–154.
- Berman, D. H., Wright, E. B., and Baer, R. N. (1989). "An optimal PE-type wave equation," J. Acoust. Soc. Am. **86**, 228–233.
- Claerbout, J. F. (1985). *Fundamentals of Geophysical Data Processing* (Blackwell, Oxford, UK, 1985), pp. 194–207.
- Collins, M. D. (1989). "Applications and time-domain solution of higher-order parabolic equations in underwater acoustics," J. Acoust. Soc. Am. **86**, 1097–1102.
- DeSanto, J. A. (1977). "Relation between the solutions of the Helmholtz and parabolic equations for sound propagation," J. Acoust. Soc. Am. **62**, 295–297.
- Feit, M. D., and Fleck, J. A. (1978). "Light propagation in graded-index fibers," Appl. Opt. **17**, 3990–3998.
- Godunov, S. K., and Ryabenkii, V. S. (1987). *Difference Schemes* (Elsevier, Amsterdam, 1987), pp. 94–109.
- Hardin, R. H., and Tappert, F. D. (1973). "Applications of the split-step Fourier method to the numerical solution of nonlinear and variable coefficient wave equations," SIAM Rev. **15**, 423.
- Holmes, E. S., and Gainey, L. A. (1991). "Software product specification for the PE model v.3.2," OAML-SPS-22 Naval Oceanography Office, Bay St. Louis, MS.
- Jensen, F. B., Kuperman, W. A., Porter, M. B., and Schmidt, H. (1994). *Computational Ocean Acoustics* (AIP, New York, 1994), Chap. 5, pp. 271–341.
- Munk, W. H. (1974). "Sound channel in an exponentially stratified ocean with application to SOFAR," J. Acoust. Soc. Am. **55**, 220–226.
- Nghiem-Phu, L., Smith, K. B., and Tappert, F. D. (1993). "FastPE, SlowPE, YourPE, MIPE: What are the Real Issues?" in *PE Workshop II: Proceedings of the Second Parabolic Equation Workshop*, edited by S. A. Chin-Bing, D. B. King, J. A. Davis, and R. B. Evans, Naval Research Laboratory NRL/BE/7181-93-0001 (U.S. Government Printing Office, Washington, DC, 1993), pp. 249–264.
- Porter, M. B. (1991). "The KRAKEN normal mode program," Rep. SM-245 (SACLANT Undersea Research Centre, La Spezia, Italy, 1991).
- Porter, M. B., and Jensen, F. B. (1993). "Anomalous parabolic equation results for propagation in leaky surface ducts," J. Acoust. Soc. Am. **94**, 1510–1516.
- Smith, A. R. (1997). "Analysis of Modal Travel Time Variability Due to Mesoscale Ocean Structure," Ph.D. Dissertation, Naval Postgraduate School, Monterey, CA, June 1997.
- Smith, K. B., and Tappert, F. D. (1994). "UMPE: The University of Miami Parabolic Equation Model, Version 1.1," Marine Physical Laboratory Tech. Memo 432 (Scripps Inst. of Oceanography, San Diego, 1994).
- Tappert, F. D. (1977). "The parabolic approximation method," in *Wave Propagation and Underwater Acoustics, Lecture Notes in Physics*, edited by J. B. Keller and J. S. Papadakis (Springer-Verlag, Berlin, 1977), Vol. 70, pp. 224–287.
- Tappert, F. D., and Brown, M. G. (1996). "Asymptotic phase errors in parabolic approximations to the one-way Helmholtz equation," J. Acoust. Soc. Am. **99**, 1405–1413.
- Tappert, F. D., Spiesberger, J. L., and Boden, L. (1995). "New full-wave approximation for ocean acoustic travel time predictions," J. Acoust. Soc. Am. **97**, 2771–2782.
- Thomson, D. J. (1993). "PE-Based Spectral Decomposition," in *PE Workshop II: Proceedings of the Second Parabolic Equation Workshop*, edited by S. A. Chin-Bing, D. B. King, J. A. Davis, and R. B. Evans, Naval Research Laboratory NRL/BE/7181-93-0001 (US Government Printing Office, 1993), pp. 296–320.
- Thomson, D. J., and Chapman, N. R. (1983). "A wide-angle split-step algorithm for the parabolic equation," J. Acoust. Soc. Am. **74**, 1848–1854.

Low-frequency acoustic scattering by gas-filled prolate spheroids in liquids. II. Comparison with the exact solution

Zhen Ye

*Institute of Ocean Sciences, Sidney, British Columbia, Canada
and Department of Physics, National Central University, Taiwan, Republic of China*

Emile Hoskinson

Department of Physics, University of British Columbia, Sidney, British Columbia, Canada

(Received 13 February 1997; accepted for publication 16 October 1997)

This sequential paper describes a comparison between the simple closed solution proposed in a previous paper [Z. Ye, *J. Acoust. Soc. Am.* **101**, 1945–1952 (1997)] with the exact solution for scattering of acoustic waves by gas-filled prolate spheroids at low frequencies. The analysis and comparison show that the low-frequency acoustic scattering by prolate spheroid gas bubbles has resonance features, and can be rather accurately described by the proposed simple formula. It is shown that the results from the simple analytic solution agree remarkably well with those obtained by the exact solution. © 1998 Acoustical Society of America. [S0001-4966(98)01402-7]

PACS numbers: 43.30.Gv, 43.20.Fn, 43.20.Bi. [DLB]

INTRODUCTION

When the acoustic wavelength is much larger than the dimension of a gas bubble, scattering by such a bubble has resonant features. Resonant scattering by a spherical gas-filled bubble in liquids has been studied in the past, and the scattering function expressed in a simple closed form [e.g., p. 1498 in Morse and Feshbach (1953)]. Until recently, however, few studies have considered nonspherical bubble shapes such as the prolate spheroid. Feuillade and Werby (1994) studied the resonant scattering by a prolate spheroid gas bubble using the T-Matrix numerical method. Their numerical result affirms the earlier theoretical prediction about the dependence of the resonance frequency on the elongation of the bubble (Strasberg, 1953). Unfortunately, the T-matrix method cannot express the sound scattering function in a closed form, and the numerical computation can be rather complicated.

Recently Ye (1997), referred to as Paper I, derived a simple closed formula describing the sound scattering by a prolate spheroid gas bubble in liquids with the use of the Kirchhoff integral theorem and an analogy between resonant scattering and electrostatic field phenomena. The result yields the same expression for the resonance frequency as a function of the aspect ratio of a prolate spheroid as first obtained by Strasberg (1953). For bubbles with small aspect ratios, the numerical results from the simple solution compare favorably with that from the T-matrix method with respect to the peak scattering value, the resonance frequency, and the quality factor Q . However, as the aspect ratio increases, differences between the two methods surface. Whereas the T-matrix method predicts that the resonant scattering pattern will become increasingly anisotropic as the aspect ratio increases, the simple solution predicts that it will remain close to isotropic. Concern may thus be raised with regard to the accuracy of the simple solution. Intuitively, an anisotropic scattering pattern for an elongated bubble seems reasonable. To resolve this ambiguity and test the accuracy

of the simple solution, it would be desirable to compare the simple solution with an exact solution. Although such an exact solution as a formalism has been known for many years, actual numerical implementation of the exact solution for spheroidal bubbles is not an easy task. The main difficulty arises in the construction of a series solution for the spheroidal wave functions which converges within the appropriate parameter space. To the best of our knowledge, no numerical result based on the exact solution for resonant scattering by a prolate spheroid gas bubble in liquids has been documented in the literature.

The purpose of this paper, a sequel to Paper I, is twofold. One, it is to report the first numerical result for resonant sound scattering by a prolate spheroid gas bubble based on the exact solution. Second, it is to compare the simple analytic solution with the exact result so as to inspect the accuracy of the simple solution. As will be illustrated by numerical examples, the results from the two approaches are in remarkable agreement, thereby providing a strong support for the simple solution.

I. THE SIMPLE ANALYTIC SOLUTION

A detailed derivation of the simple solution has been presented Paper I; here we just outline the solution. Consider a plane wave incident on a gas-filled prolate spheroid located at the origin (refer to Fig. 1 in Paper I). The surface of the spheroid is represented by the equation

$$\frac{x^2}{a^2} + \frac{y^2}{a^2} + \frac{z^2}{b^2} = 1, \quad (1)$$

where a and b are the minor and major radii, respectively, with $b \geq a$. The aspect ratio is given by b/a . (As a convention, we define ratio aspect as $e = a/b \leq 1$; thus the aspect ratio = $1/e$.)

The wave equation in the surrounding liquid can be written as

$$(\nabla^2 + k^2)p = 0. \quad (2)$$

The plane wave can be expressed as $p_i = \exp(i\mathbf{k}_i \cdot \mathbf{r})$ with suppressed time dependence $\exp(-i\omega t)$. Here ω is the angular acoustic frequency and \mathbf{k}_i is the incident wave vector with magnitude ω/c , c being the sound speed in the surrounding liquid.

From the Kirchhoff integral theorem, the scattering amplitude equation $f(\mathbf{k}_i, \mathbf{k}_s)$ can be derived as

$$f(\mathbf{k}_i, \mathbf{k}_s) = -\frac{1}{4\pi} \int_s ds \exp(-i\mathbf{k}_s \cdot \mathbf{r}) \times [i\mathbf{k}_s \cdot \mathbf{n} p_+ + i\omega \rho_l u_n], \quad (3)$$

where the integration is performed over the surface of the object, p_+ and u_n are the total field and the normal velocity at the surface, approached from the outside, \mathbf{n} is a unit outward vector normal to the surface, and ρ_l is the density of the surrounding liquid.

From Eq. (3), it is clear that the scattering wave and scattering amplitude can be calculated by the integral once their surface values are obtained. These surface values are determined by boundary conditions and thermodynamic relations. When the acoustic wavelength is much larger than the dimension of the bubble, the resulting formula for the scattering amplitude is (Ye, 1997)

$$f(\mathbf{k}_i, \mathbf{k}_s) = \frac{U_1 - U_2}{\frac{\omega_0^2}{\omega^2} - 1 - i \frac{kb}{B} \left[\frac{\ln[(1+\epsilon)/e]}{\epsilon} \right]^{-1}}, \quad (4)$$

where

$$\omega_0^2 = \frac{3\gamma P_0 B}{a^2 \rho_l \left[\frac{\ln[(1+\epsilon)/e]}{\epsilon} \right]}, \quad (5)$$

$$U_1 = \frac{1}{4\pi a^2 \left[\frac{\ln[(1+\epsilon)/e]}{\epsilon} \right]} \int_s ds \exp(-i\mathbf{k}_s \cdot \mathbf{r}) \times \frac{1}{\sqrt{x^2/a^4 + y^2/a^4 + z^2/b^4}}, \quad (6)$$

$$U_2 = \frac{\omega_0^2}{\omega^2} \frac{1}{4\pi} \int_s ds \exp(-i\mathbf{k}_s \cdot \mathbf{r}) (i\mathbf{k}_s \cdot \mathbf{n}). \quad (7)$$

In the long wavelength approximation, the quantities U_1 and U_2 can be simplified as

$$U_1 = \frac{b}{\left[\frac{\ln[(1+\epsilon)/e]}{\epsilon} \right]}, \quad (8)$$

$$U_2 = \frac{\omega_0^2}{\omega^2} \left[\frac{i}{4\pi} \int_s ds (\mathbf{k}_s \cdot \mathbf{n}) (1 - i\mathbf{k}_s \cdot \mathbf{r}) \right], \quad (9)$$

and

$$B = 1 + (ka)^2 \frac{1}{\epsilon} \sinh^{-1} \left(\frac{\epsilon}{e} \right) = 1 + (ka_e)^2 e^{2/3} \frac{1}{\epsilon} \sinh^{-1} \left(\frac{\epsilon}{e} \right), \quad (10)$$

where a_e is the radius of the equivalent sphere, and $\epsilon = \sqrt{1 - e^2}$. In the above, γ is the gas polytropic exponent. For diatomic air, γ can be approximated as 1.4. Here P_0 is the hydrostatic pressure, and ρ_l is the density of the surrounding liquid.

The scattering function in Eq. (4) clearly shows the resonance feature. The resonance frequency is ω_0 :

$$\omega_0^2 = \frac{3\gamma P_0 B}{a^2 \rho_l \left[\frac{\ln[(1+\epsilon)/e]}{\epsilon} \right]}. \quad (11)$$

In Eq. (4), the term $(kb/B) \{ [\ln[(1+\epsilon)/e]/\epsilon]^{-1} \}$ is identified as the damping factor due to acoustic radiation.

Under the low-frequency approximation, we can show that $B \approx 1$, and U_2 is of order of $(kb)^2$ and can thus be ignored. We finally get a simple analytic isotropic scattering function,

$$f = \frac{\epsilon b / \ln[(1+\epsilon)/e]}{\frac{\omega_0^2}{\omega^2} - 1 - i kb \left[\frac{\ln[(1+\epsilon)/e]}{\epsilon} \right]^{-1}}, \quad (12)$$

from which the quality factor Q at resonance is calculated as

$$Q^{-1} = k_0 b \left[\frac{\ln[(1+\epsilon)/e]}{\epsilon} \right]^{-1}, \quad (13)$$

where $k_0 = \omega_0/c$ with ω_0 given by Eq. (11).

Consider two special cases. (1) For a spherical bubble, i.e., when $a = b$, Eq. (12) reduces to the well-known result in the literature,

$$f = \frac{a}{\omega_0^2/\omega^2 - 1 - ika}, \quad (14)$$

with

$$\omega_s = \frac{1}{a} \sqrt{\frac{3\gamma P_0}{\rho_l}}.$$

(2) When $\omega \ll \omega_0$, the scattering function is simplified as

$$f = \frac{V}{4\pi} \frac{\rho_l}{\gamma P_0} \omega^2, \quad (15)$$

following Rayleigh volume scattering. Therefore at very low frequencies, the scattering will not depend on the aspect ratio.

II. THE EXACT SOLUTION

The exact solution for prolate spheroids is well known (e.g., Yeh, 1967). To facilitate reading, we outline the exact solution. Suppose that the foci of the spheroid are at $x = y = 0$, $z = \pm q/2$. The distances from the point (x, y, z) to these foci are

$$r_1 = \sqrt{(z + 1/2q)^2 + x^2 + y^2}, \quad r_2 = \sqrt{(z - 1/2q)^2 + x^2 + y^2}.$$

The prolate spheroidal coordinates ζ , η , and ϕ are defined as follows:

$$\zeta = (r_1 + r_2)/q, \quad \eta = (r_1 - r_2)/q, \quad \phi = \tan^{-1}(y/x),$$

and therefore

$$z = \frac{1}{2} q \xi \eta, \quad x = \frac{1}{2} q \sqrt{(\xi^2 - 1)(1 - \eta^2)} \cos \phi,$$

$$y = \frac{1}{2} q \sqrt{(\xi^2 - 1)(1 - \eta^2)} \sin \phi.$$

Here ξ goes from 1 to ∞ , η from -1 to 1, and ϕ from 0 to 2π . The major axis is thus $b = \frac{1}{2}\xi q$, and the minor axis $a = \frac{1}{2}q\sqrt{\xi^2 - 1}$.

The unit incident wave can be expressed in terms of spheroidal variables [p. 1502 in Morse and Feshbach (1953)],

$$\begin{aligned} p_i &= e^{i\mathbf{k}_i \cdot \mathbf{r}} = e^{ik(z \cos \theta_i + x \sin \theta_i)} \\ &= 2 \sum_{m=0}^{\infty} \sum_{n=m}^{\infty} \frac{\epsilon_m}{N_{mn}} i^n S_{mn}(h, \cos \theta_i) S_{mn}(h, \eta) \\ &\quad \times j e_{mn}(h, \xi) \cos m \phi, \end{aligned} \quad (16)$$

where the incident direction is denoted in spherical variables as $\hat{\mathbf{k}}_i = \mathbf{k}/k = (\sin \theta_i, 0, \cos \theta_i)$. Moreover, we define $h = kq/2$. Here, S_{mn} are the angular spheroidal functions, N_{mn} are their norms, and $j e_{mn}$ are the corresponding radial functions of the first kind. Similarly, the scattered wave can be represented in terms of the functions S_{mn} , and the linear combinations of radial functions of the first and second kinds $h_{mn} = j e_{mn} + i n e_{mn}$:

$$\begin{aligned} p_{\text{scat}}(\mathbf{r}) &= 2 \sum_{m=0}^{\infty} \sum_{n=m}^{\infty} \frac{\epsilon_m}{N_{mn}} i^n A_{mn} S_{mn}(h \cos \theta_i) \\ &\quad \times S_{mn}(h, \eta) h_{mn}(h, \xi) \cos m \phi. \end{aligned} \quad (17)$$

The unknown coefficients A_{mn} are determined by the boundary conditions that require that both the pressure field and the normal component of displacement be continuous across the scattering surface.

The scattering function is obtained in the far-field limit, i.e., $r \rightarrow \infty$, where $\xi \rightarrow \infty$, $\eta \rightarrow \cos \theta$, and

$$h_{mn} \rightarrow i^{-n-1} \frac{e^{ikr}}{kr}.$$

Thus we obtain

$$\begin{aligned} f(\mathbf{k}_i, \mathbf{k}_s) &= \frac{2}{ik} \sum_{m=0}^{\infty} \sum_{n=m}^{\infty} \frac{\epsilon_m}{N_{mn}} A_{mn} S_{mn}(h, \cos \theta_i) \\ &\quad \times S_{mn}(h, \cos \theta_s) \cos m \phi, \end{aligned} \quad (18)$$

where ϕ is the azimuthal angle between the incident and scattering wave vectors. We stress that the vectors \mathbf{k}_i and \mathbf{k}_s are represented in the spherical coordinates at the far field as

$$\mathbf{k}_i = k(\sin \theta_i, 0, \cos \theta_i),$$

$$\mathbf{k}_s = k(\sin \theta_s \cos \phi, \sin \theta_s \sin \phi, \cos \theta_s),$$

where θ_i and θ_s are the angles from \mathbf{k}_i and \mathbf{k}_s to the positive z -axis, respectively, and ranging from 0 to π .

TABLE I. Values for the resonance frequency (measured by ka_e) and the peak scattering amplitude from the simple analytic and exact solutions.

Aspect ratio	Resonance freq. ($ka_e \times 10^{-2}$)		$\sigma_R (\times 10^2)$	
	Analytic	Exact	Analytic	Exact
5	1.5274	1.5247	10.717	10.757
10	1.6971	1.6928	8.6802	8.7346
20	1.9299	1.9199	6.7125	6.8093

Owing to the complexity of the spheroidal wave functions, the computation of the scattering function, Eq. (18), is not an easy task. We have implemented a program, written in C, which calculates the spheroidal scattering function for values of h below about 40. It is based on the algorithms discussed by Flammer (1957). For the parameter range discussed in this paper, computation of the radial spheroidal wave functions of the second kind, $n e_{mn}$, is the most difficult task. For most values of h below 40, a standard series expansion in terms of spherical Bessel functions of the second kind is used to compute $n e_{mn}$; however, for the low frequencies used in this paper, this expansion becomes unstable, and a second expansion in terms of associated Legendre functions of the first and second kind is needed.

III. NUMERICAL RESULTS

For simplicity, we consider the case that the scattering direction lies in the plane spanned by the incident direction and the longitudinal axis of the prolate spheroid. The following usual parameters are used: $P_0 = 10^5$ kg/m² (hydrostatic pressure), $\gamma = 1.4$ (thermodynamic gas polytropic exponent), $\rho_l = 10^3$ kg/m³ (density of water), $\rho_g = 1.29$ kg/m³ (density of air), and $c = 1500$ m/s (sound speed in water). Accordingly, the sound speed in the air can be calculated as $c_a = \sqrt{\gamma P_0 / \rho_g} = 329$ m/s. The gas inside the bubble is assumed to be the air, and the bubble is immersed in water. We defined the normalized scattering cross section

$$\sigma_R = \left| \frac{f}{2a_e} \right|^2, \quad (19)$$

where f is the scattering function and a_e is the radius of the equivalent sphere which has the same volume as the prolate spheroid, i.e., $a_e = (ba^2)^{2/3} = be^{2/3}$. The normalized scattering cross section is a convenient quantity to calculate as it works out to be dependent only on e and the product ka_e , rather than e , k , and a_e . The reduced target strength is thus $\text{TS} = 10 \log_{10} \sigma_R$.

In Fig. 1, we plot the reduced backscattering target strength as a function of ka_e for three aspect ratios. The incidence is in the broadside direction ($\theta_i = 90^\circ$). As shown in this figure, the results from both the exact solution (18) and simple analytic solution (12) show resonance features, and the agreement between the two results is remarkable. In Table I, we compare the values for the resonance frequency (measured by ka_e) and the peak scattering amplitude from the two approaches. The two results are in excellent agreement, differing by less than 1.4%.

Figure 2 presents the azimuthal bistatic scattering pattern, i.e., σ_R versus the scattering angle θ_s , at three incident

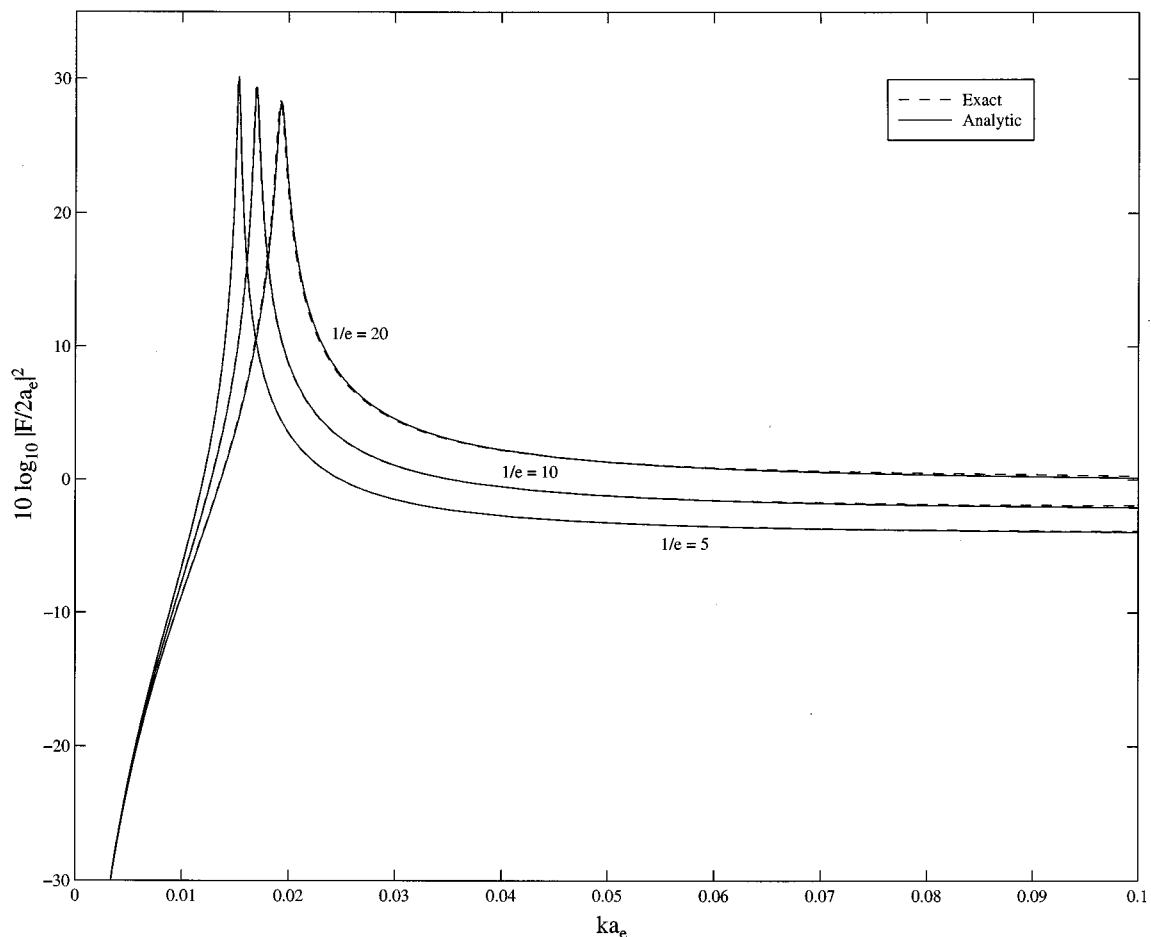


FIG. 1. The reduced target strength as a function of ka_e for three aspect ratios.

angles for the aspect ratio 20, i.e., $1/e = 20$. In the figure, the prolate spheroid bubble is positioned with its longitudinal axis along the horizontal axis of the plot. The analytic solution, Eq. (12), is given by the solid lines, the exact solution, Eq. (18), by the dashed lines. The plots (a1), (a2), and (a3) correspond to three values of ka_e , which are below, equal to, and above the resonance, respectively. There are actually three dashed lines in each plot, corresponding to the scattering patterns for the three incident directions indicated by the arrows. [For brevity, the arrows are only shown in plot (a1).]

Several observations can be noted from Fig. 2. (1) The

scattering pattern predicted by the exact solution matches the analytic solution quite well, the difference between the two not exceeding about 8% [the maximum difference is seen in (a2)]. (2) The scattering is nearly isotropic, particularly for frequencies near or below the resonance value. (3) A slight anisotropy begins to appear for frequencies above the resonance, as seen in (a3), where the inner, middle, and outer dashed lines correspond to end-on ($\theta_i = 0^\circ$), tilted ($\theta_i = 45^\circ$), and broadside ($\theta_i = 90^\circ$) incidences, respectively. However, the difference between the three directions is uniformly within 4%. Compared to the T-matrix method [see,

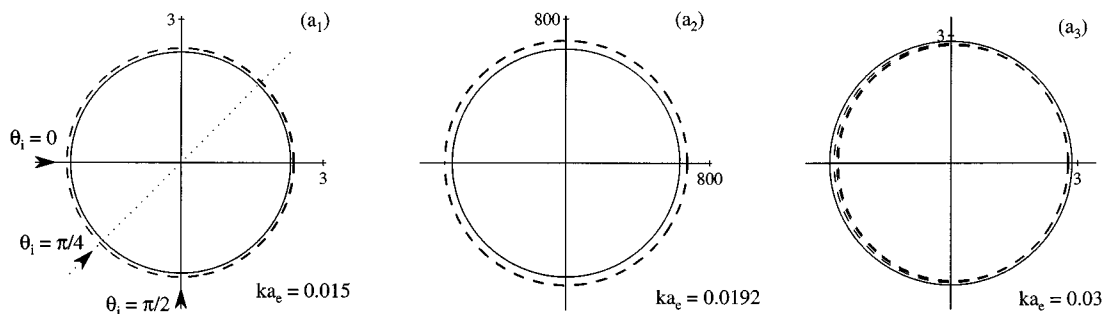


FIG. 2. The bistatic scattering pattern for the frequency below, at, and above the resonance at three incident angles. The aspect ratio is 20. The results from the analytic and exact solutions are represented by the solid and dashed lines, respectively. The three dashed lines in each plot refer to the scattering patterns of three incident directions. Plot (a1) is below resonance, (a2) is at resonance, and (a3) is above resonance.

e.g., Figs. 5(b) and 6(a) in Feuillade and Werby (1994)], both the exact and the simple analytic solutions predict much smaller anisotropy in the scattering pattern. The results from the T-matrix method indicate that the anisotropy, measured by the difference between the maximum and minimum scattering cross sections, can be as high as 29% for the bistatic scattering pattern and 48% for the monostatic scattering distribution, for the aspect ratio 20.

IV. CONCLUSION

In this paper, we have made an effort to compare the simple analytic solution developed in Paper I with the exact solution for resonant acoustic scattering by prolate spheroid gas bubbles in water. The analysis indicates that the resonant scattering is almost isotropic, and can be accurately described by the simple solution. It is shown, however, that as the aspect ratio increases, slight differences between the simple and exact solutions appear.

Since the simple solution is derived in the low-frequency limit, it cannot be extended to cases in which the acoustic wavelength is much shorter than the size of the bubble. Note, however, that while we considered only prolate spheroid gas bubbles, the method for obtaining the

simple solution (Ye, 1997) can be readily extended to consider other nonspherical bubbles, such as ellipsoidal or semi-capped cylindrical bubbles, for which an exact solution may either not exist or the implementation of such an exact solution is impossible.

ACKNOWLEDGMENTS

The work received support from the Department of Fisheries and Oceans, Canada, and Department of Physics, National Central University. Emile Hoskinson received support from the Institute of Ocean Sciences through a co-op studentship program.

- Feuillade, C., and Werby, M. F. (1994). "Resonances of deformed gas bubbles in liquids," *J. Acoust. Soc. Am.* **96**, 3684–3692.
- Flammer, C. (1957). *Spheroidal Wave Functions* (Stanford U.P., Stanford).
- Morse, P. M., and Feshbach, H. (1953). *Methods of Theoretical Physics* (McGraw-Hill, New York).
- Strasberg, M. (1953). "The pulsation frequency of nonspherical gas bubbles in liquids," *J. Acoust. Soc. Am.* **25**, 536–537.
- Ye, Z. (1997). "Low-frequency acoustic scattering by gas-filled prolate spheroids in liquids," *J. Acoust. Soc. Am.* **101**, 1945–1952.
- Yeh, C. (1967). "Scattering of acoustic waves by a penetrable prolate spheroid. I. Liquid prolate spheroid," *J. Acoust. Soc. Am.* **42**, 518–521.

A unified approach to volume and roughness scattering

Anatoliy N. Ivakin

Andreev Acoustics Institute, Shvernika 4, Moscow 117036, Russia

(Received 1 January 1997; accepted for publication 16 October 1997)

A unified approach is proposed to study scattering from a fluid medium with irregularities of different types: volume inhomogeneities (spatial fluctuations of the compressibility and density) and roughness of the interfaces. The approach considers the roughness as a volume perturbation of a specific kind near flat (unperturbed) interfaces. It permits a description of the scattering problem on the basis of a unique integral equation with a kernel including both types of irregularities. In the case of small perturbations, the first-order solution of this equation is used to obtain the scattering amplitude and scattering cross section for a stratified randomly inhomogeneous fluid medium with an arbitrary number of rough interfaces. Expressions for the roughness and volume scattering cross section are obtained involving cross-correlation matrixes between the roughness of different interfaces and between the volume fluctuations of different parameters. Also, an example is considered where roughness–volume correlations are important. The results are generalized to the case when the fluid is placed over an arbitrary basement characterized by its own reflection coefficient and scattering amplitude. © 1998 Acoustical Society of America.

[S0001-4966(98)01302-2]

PACS numbers: 43.30.Hw, 43.30.Ft, 43.30.Gv [DLB]

INTRODUCTION

Scattering from various irregular media, generally, can be attributed to two major mechanisms that are due to volume (spatial) inhomogeneities of the medium parameters and roughness of various interfaces. Usually the problem of scattering is considered separately for these two types of irregularities. Examples are known, however, where volume and roughness scattering are comparable for realistic values of medium parameters and it is difficult to separate them experimentally. This is common, e.g., in seabed scattering.¹⁻⁷ Also, in some cases, effects of volume and roughness scattering are essentially not additive.⁸ In such cases there is a practical need to examine different scattering mechanisms in the frame of a unified model based on realistic assumptions.

In many cases, inhomogeneous rough media can be assumed as stratified (plane layered on the average), i.e., having mean parameters dependent only upon the depth. For a number of particular medium models, it has been shown that such layering can have a strong effect on the scattered field.⁹⁻¹³ In this paper, the problem of scattering is considered for an arbitrarily stratified fluid medium. This model is then generalized to the case when the fluid is placed over an arbitrary basement having its own reflection and scattering properties which can be chosen, e.g., corresponding to an elastic irregular half-space and taken from Refs. 14–17.

In Sec. I, a general exact integral equation is considered for the field in a fluid medium with spatially varying density and compressibility, and it is shown how this equation can be applied to the case where the medium perturbation is in the form of roughness of an arbitrary number of interfaces. In Sec. II, a unified integral equation is obtained for the case of small volume–roughness perturbations. A plane wave expansion of the field is considered and a solution of the integral equation is written in the form of a multiple scattering series. In Sec. III, the first-order term is used to obtain the scattering

amplitude through which all the statistical characteristics of the scattered field can be expressed and related to the statistical properties of the scattering medium. Expressions for the scattering cross section are obtained involving cross-spectral and cross-correlation matrixes between roughness of the different interfaces and between the different kinds of volume inhomogeneities. Also, an example is considered where roughness–volume correlations are important. In Sec. IV, a summary is given.

I. INTEGRAL EQUATIONS

A. Volume perturbations

Consider an inhomogeneous fluid medium with spatially varying parameters, mass density, $\tilde{\rho}(\mathbf{r})$, and compressibility, $\tilde{\kappa}(\mathbf{r})$. Here and in following equations, $\mathbf{r}=(\mathbf{R},z)$ and $\mathbf{R}=(x,y)$ denote three-dimensional and two-dimensional position vectors. The spectral component of acoustic pressure, p , at frequency ω , in such a medium obeys the equation (see, e.g., Refs. 18 and 19)

$$\nabla \cdot \left(\frac{1}{\tilde{\rho}} \nabla p \right) + \omega^2 \tilde{\kappa} p = 0. \quad (1)$$

The boundary conditions are continuity at all the interfaces for the field, p , and the normal component of particle velocity, $\tilde{\rho}^{-1} \nabla p$.

The medium parameters, $\tilde{\rho}$ and $\tilde{\kappa}$, can be considered as spatially fluctuating with respect to their unperturbed values, ρ and κ , which can be, e.g., given functions of \mathbf{r} , so that the analytic or numerical solution for such a nonrandom medium, i.e., the field in unperturbed medium, p_0 , is known. This field obeys the Helmholtz equation

$$\hat{L} p_0 = 0, \quad (2)$$

with the unperturbed differential Helmholtz operator

$$\hat{L} = \rho \nabla \cdot \left(\frac{1}{\rho} \nabla \right) + k^2, \quad (3)$$

where $k = \omega/c$ is the unperturbed wave number with $c = (\kappa\rho)^{-1/2}$ as the unperturbed sound speed.

The spatial fluctuations of the bulk parameters, or *volume perturbations*, cause fluctuations of the pressure field relative to the unperturbed field, $p_s = p - p_0$, which obeys equation

$$\hat{L}p_s = -\rho\omega^2(\tilde{\kappa} - \kappa)p - \rho \nabla \cdot \left[\left(\frac{1}{\tilde{\rho}} - \frac{1}{\rho} \right) \nabla p \right]. \quad (4)$$

This results in an integral equation, which, after integration by parts, can be cast in the form

$$p(\mathbf{r}') = p_0(\mathbf{r}') - \int_{\Omega} \left[\omega^2(\tilde{\kappa} - \kappa)p(\mathbf{r})G(\mathbf{r}, \mathbf{r}') - \left(\frac{1}{\tilde{\rho}} - \frac{1}{\rho} \right) \nabla p(\mathbf{r}) \cdot \nabla G(\mathbf{r}, \mathbf{r}') \right] d^3r, \quad (5)$$

where Ω is the volume containing the medium fluctuations and G is the Green's function for the unperturbed medium, obeying equation

$$\hat{L}G(\mathbf{r}, \mathbf{r}') = \rho \delta(\mathbf{r} - \mathbf{r}'). \quad (6)$$

The Green's function and unperturbed field must satisfy the same boundary conditions, i.e., continuity at the unperturbed interfaces for the fields, p_0 and G , and the respective normal components of particle velocities, $\rho^{-1}\nabla p_0$ and $\rho^{-1}\nabla G$.

Integral equation (5) provides a relation between the spatial fluctuation in the field, $p - p_0$, and the fluctuations in the medium parameters, the compressibility and inverse density (specific volume). A number of general features of this equation can be mentioned. First, it is **exact** and, generally, can be used even when parameter fluctuations are not small. It can be represented in the general form

$$p(\mathbf{r}') = p_0(\mathbf{r}') + \int \hat{Q}(\mathbf{r}', \mathbf{r})p(\mathbf{r}) d^3r, \quad (7)$$

where the kernel operator, $\hat{Q}(\mathbf{r}', \mathbf{r})$, includes all the medium fluctuations. Then an approximate solution can be obtained using an iterative method in the form of a multiple scattering series (see Appendix A).

Note that the integral equation (7) and its solution have been examined only for certain simpler types of the kernel \hat{Q} than in (5), e.g., for the case where the density fluctuation are absent.^{20,21} The kernel in (5) is also more general than in the well-known equation¹⁸ where fluctuating density is included but the Green's function of free space is used as G and, correspondingly, the unperturbed field, p_0 , is replaced by the incident field. This case is contained in Eq. (5) as a particular case which corresponds to the unperturbed parameters, κ and ρ , considered as independent of spatial coordinates. This classical approach is simpler but is less efficient in the case when the mean values of medium parameters are different from those in free space, as this difference must be included into the medium parameters' variation in the kernel of Eq. (5), which can be bad for convergence of the multiple scattering series. Note, however, that the unperturbed param-

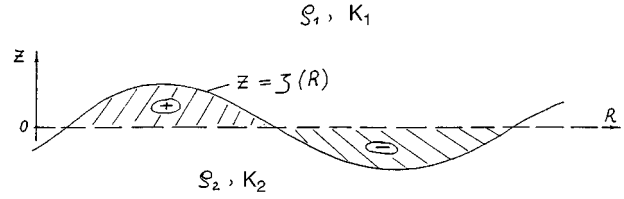


FIG. 1. Geometry of rough interface.

eters, ρ and κ , can be chosen, in particular, so as to provide vanishing mean fluctuations in the kernel of Eqs. (5) and (7). This assumption gives the following expressions:

$$\kappa = \langle \tilde{\kappa} \rangle, \quad \rho = \left\langle \frac{1}{\tilde{\rho}} \right\rangle^{-1}. \quad (8)$$

Note that, when defined this way, the unperturbed parameters can be rather arbitrary functions of \mathbf{r} . Both mentioned generalizations, considering the density fluctuations and spatial dependence of unperturbed parameters, can be important, e.g., in seabed volume scattering.^{5,9,11}

Note finally that Eq. (5) does not contain gradients of the density which permits its use not only in the case of continuous fluctuations, but also in the case of discontinuous volume fluctuations having correspondingly infinite gradients of the density at the interfaces. It also permits, in particular, the replacement of interface roughness by discontinuous volume inhomogeneity of a specific type and then the use of existing volume scattering theories to study roughness scattering. Analogous approaches, although using more complicated derivations, have appeared before, e.g., in Ref. 22 for the electromagnetic case, and for the case of small roughness in acoustical scattering.²³ In the present article it will be shown that the exact integral equation for roughness scattering can be easily obtained from the volume scattering equation (5) in the general case of an arbitrary roughness, or interface deviations.

B. Rough interface

Consider a rough interface, plane on the average, given by the equation

$$z = \zeta(\mathbf{R}), \quad (9)$$

where ζ is the deviation of the interface relative to its mean plane $z=0$ (see Fig. 1). The interface separates two media with parameters (ρ_1, κ_1) and (ρ_2, κ_2) , that is,

$$(\tilde{\rho}, \tilde{\kappa}) = \begin{cases} (\rho_1, \kappa_1), & z > \zeta(\mathbf{R}), \\ (\rho_2, \kappa_2), & z < \zeta(\mathbf{R}). \end{cases} \quad (10)$$

As the corresponding unperturbed medium, two half-spaces separated by the mean plane $z=0$ can be taken with parameters

$$(\rho, \kappa) = \begin{cases} (\rho_2, \kappa_2), & z > 0, \\ (\rho_1, \kappa_1), & z < 0. \end{cases} \quad (11)$$

As a result, fluctuations in the density and compressibility are of the form

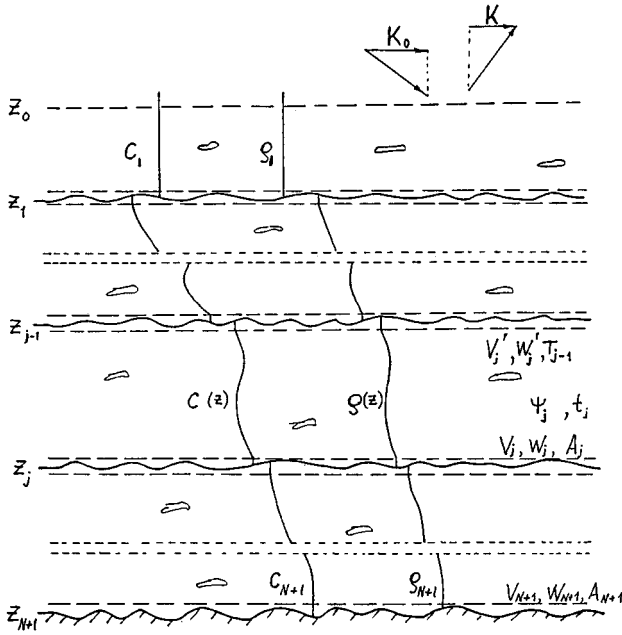


FIG. 2. Geometry of a multi-layered irregular medium.

$$(\tilde{\rho} - \rho) = \begin{cases} (\rho_2 - \rho_1), & 0 < z < \zeta(\mathbf{R}), \\ -(\rho_2 - \rho_1), & 0 > z > \zeta(\mathbf{R}), \end{cases} \quad (12)$$

$$(\tilde{\kappa} - \kappa) = \begin{cases} (\kappa_2 - \kappa_1), & 0 < z < \zeta(\mathbf{R}), \\ -(\kappa_2 - \kappa_1), & 0 > z > \zeta(\mathbf{R}). \end{cases} \quad (13)$$

Thus, roughness can be considered as a specific kind of volume (spatial) perturbation near the mean (unperturbed) flat interface, contained in the space between mean and rough interfaces and having different sign above and below the mean interface.

Note that fluctuations in the density and inverse density are related as follows:

$$\frac{1}{\tilde{\rho}} - \frac{1}{\rho} = -\frac{\tilde{\rho} - \rho}{\tilde{\rho}\rho}, \quad (14)$$

and $\tilde{\rho}\rho = \rho_1\rho_2$ is the same above and below the mean interface. Then taking into account Eqs. (12) and (13), one obtains from Eq. (5) the following integral equation for the field:

$$p(\mathbf{r}') = p_0(\mathbf{r}') - \int d^2R \int_0^{\zeta(\mathbf{R})} \left\{ (\kappa_2 - \kappa_1) \omega^2 p(\mathbf{r}) G(\mathbf{r}, \mathbf{r}') + \frac{(\rho_2 - \rho_1)}{\rho_1\rho_2} \nabla p(\mathbf{r}) \cdot \nabla G(\mathbf{r}, \mathbf{r}') \right\} dz. \quad (15)$$

A generalization of Eq. (15) onto the case of an arbitrary number of rough interfaces can be easily done. Let the j th interface be of the form

$$z = z_j + \zeta_j(\mathbf{R}), \quad j = 1, 2, \dots, N, \quad (16)$$

where ζ_j and z_j correspond to roughness and mean plane (see Fig. 2). Then the correspondent integral equation becomes of the form

$$p(\mathbf{r}') = p_0(\mathbf{r}') - \sum_j \int d^2R \times \int_{z_j}^{z_j + \zeta_j(\mathbf{R})} \left\{ (\kappa_{j+1} - \kappa_j) \omega^2 p(\mathbf{r}) G(\mathbf{r}, \mathbf{r}') + \frac{(\rho_{j+1} - \rho_j)}{\rho_{j+1}\rho_j} \nabla p(\mathbf{r}) \cdot \nabla G(\mathbf{r}, \mathbf{r}') \right\} dz. \quad (17)$$

Integral equations (15) and (17), as well as Eq. (5), are **exact**. They also can be represented in the general form (7). Then their approximate solution can be obtained with the help of iterative techniques in the form of a multiple scattering series (Appendix A). Note that when the difference in the parameters of the adjacent media is not too large, for example, for most sediment interfaces, the iterative solution of the integral equations (15) and (17) can be used at arbitrary roughness, without restriction to the case of small roughness. General considerations for the case of arbitrary roughness will be presented in a later paper. In the remainder of this article, the case of small perturbations of the medium is considered.

II. SMALL PERTURBATIONS IN LAYERED MEDIA

A. Unified integral equation

In the case of a single interface, for $|k_{1,2}\zeta| \ll 1$ and $|\nabla\zeta| \ll 1$, where $k_{1,2}$ are the corresponding wave numbers, the integral equation (15) can be written in the form (see Appendix B)

$$p(\mathbf{r}') = p_0(\mathbf{r}') - \int_{z=0} d^2R \zeta(\mathbf{R}) \hat{Q}_\zeta(\mathbf{r}', \mathbf{r}) p(\mathbf{r}). \quad (18)$$

where the kernel is

$$\hat{Q}_\zeta(\mathbf{r}', \mathbf{r}) = (\kappa_2 - \kappa_1) \omega^2 G(\mathbf{r}, \mathbf{r}') + (\rho_2 - \rho_1) \times [\rho_1^{-1} \rho_2^{-1} \nabla_R G(\mathbf{r}, \mathbf{r}') \cdot \nabla_R + \rho^{-2} \partial_z G(\mathbf{r}, \mathbf{r}') \partial_z] \quad (19)$$

Integral equation (18) and its generalization to the case of an arbitrary number N of rough interfaces can be easily presented in the general form (7), which then can include both volume and roughness perturbations of the medium. Define the dimensionless roughness and volume perturbations in the medium with N rough interfaces as follows:

$$\epsilon_\zeta(\mathbf{r}) = \sum_{j=1}^N \zeta_j(\mathbf{R}) \delta(z - z_j), \quad (20)$$

$$\epsilon_\rho = \frac{(\tilde{\rho} - \rho)}{\rho}, \quad \epsilon_\kappa = \frac{(\tilde{\kappa} - \kappa)}{\kappa}. \quad (21)$$

Assume that the medium is homogeneous in a small vicinity of all the unperturbed interfaces, $z = z_j$ (see Fig. 2). Then Eq. (18) can be replaced by an integral equation in the same form as for the volume perturbation case,

$$p(\mathbf{r}') = p_0(\mathbf{r}') - \int d^3r \epsilon_\zeta(\mathbf{r}) \hat{Q}_\zeta(\mathbf{r}', \mathbf{r}) p(\mathbf{r}). \quad (22)$$

A unified integral equation for the field in such a multi-layered medium with “unified” volume-roughness perturbations will be written in the form

$$p(\mathbf{r}') = p_0(\mathbf{r}') - \sum_{\beta} \int d^3r \epsilon_{\beta}(\mathbf{r}) \hat{Q}_{\beta}(\mathbf{r}', \mathbf{r}) p(\mathbf{r}),$$

$$\beta = \kappa, \rho, \zeta, \quad (23)$$

corresponding to the general form (7) with the kernel

$$\hat{Q}(\mathbf{r}', \mathbf{r}) = - \sum_{\beta} \epsilon_{\beta}(\mathbf{r}) \hat{Q}_{\beta}(\mathbf{r}', \mathbf{r}), \quad (24)$$

and with partial kernels defined as follows:

$$\hat{Q}_{\kappa}(\mathbf{r}', \mathbf{r}) = \omega^2 \kappa G(\mathbf{r}, \mathbf{r}'), \quad (25)$$

$$\hat{Q}_{\rho}(\mathbf{r}', \mathbf{r}) = \rho^{-1} \nabla G(\mathbf{r}, \mathbf{r}') \cdot \nabla, \quad (26)$$

$$\hat{Q}_{\zeta}(\mathbf{r}', \mathbf{r}) = D_{\kappa} \omega^2 G(\mathbf{r}, \mathbf{r}') - D_{1/\rho} \nabla_R G(\mathbf{r}, \mathbf{r}') \cdot \nabla_R + D_{\rho} \rho^{-2} \partial_z G(\mathbf{r}, \mathbf{r}') \partial_z, \quad (27)$$

where

$$D_{\beta}(z) = D(\beta) = \beta(z-0) - \beta(z+0), \quad \beta = \kappa, \rho, 1/\rho, \quad (28)$$

are the characteristic values for the parameters' discontinuity.

For the medium plane layered on the average, which is the case of interest in this paper, it is convenient to describe sound propagation and scattering in terms of plane waves. Below, such a description is introduced for the zeroth-order field and for the field perturbation.

B. Zeroth-order solution and Green's function

For calculation of the scattered field, the unperturbed field or zeroth-order solution, p_0 , and the Green's function, G , must be known. In terms of plane waves, they can be expressed in the following way. Let a plane wave of unit amplitude, having wave vector with transverse component \mathbf{K}_0 , be incident from a homogeneous half-space, $z > z_1$, i.e.,

$$p_{\text{inc}}(\mathbf{r}, \mathbf{K}_0) = \exp(i\mathbf{K}_0 \cdot \mathbf{R} - i\nu_1(K_0)(z - z_1)), \quad (29)$$

where $\nu_1(K) = \sqrt{k_1^2 - K^2}$ and k_1 is the wave number in the upper medium (first layer). The unperturbed field, or zeroth-order solution, is of the form

$$p_0(\mathbf{r}, \mathbf{K}_0) = \psi(z, K_0) \exp(i\mathbf{K}_0 \cdot \mathbf{R}), \quad (30)$$

where ψ is the complex amplitude of the field in a plane-layered medium with depth-dependent parameters, density and sound speed, $\rho(z)$ and $c(z)$ (see Appendix C).

The Green's function for such a plane-layered medium can be represented by the plane wave expansion

$$G(\mathbf{r}, \mathbf{r}') = \int d^2K g(z, z', K) \exp(i\mathbf{K} \cdot (\mathbf{R}' - \mathbf{R})), \quad (31)$$

where g is the corresponding 2-D spectrum, or the “depth-dependent Green's function” (see, e.g., Ref. 24), and $\mathbf{K} = (K_x, K_y)$ is its spectral parameter. The function g is a plane-wave solution of Eq. (6) and, like p_0 , can be expressed through the function ψ . For the case of a receiver in the

upper half-space, the function g is defined as follows:

$$g(z, z', K) = (8\pi^2 i \nu_1(K))^{-1} \rho_1 \psi(z, K) \exp(i\nu_0(K)z'),$$

$$z' \geq 0, z. \quad (32)$$

C. Field perturbation

The general integral equations (7) and (A1) and their iterative solution can be written for 2-D Fourier components. For that, consider the field perturbation, $p_s = p - p_0$, as a 2-D Fourier integral

$$p_s(\mathbf{r}, \mathbf{K}_0) = \int d^2K \Psi(z, \mathbf{K}, \mathbf{K}_0) \exp(i\mathbf{K} \cdot \mathbf{R}). \quad (33)$$

Then, from Eq. (A1), one obtains an integral equation

$$\Psi(z', \mathbf{K}', \mathbf{K}_0) = \Psi_1(z', \mathbf{K}', \mathbf{K}_0) + \int dz d^2K \hat{q}(z', \mathbf{K}'; z, \mathbf{K}) \Psi(z, \mathbf{K}, \mathbf{K}_0), \quad (34)$$

where

$$\hat{q}(z', \mathbf{K}'; z, \mathbf{K}) = (2\pi)^{-2} \int d^2R d^2R' \times \exp(-i\mathbf{K}' \cdot \mathbf{R}') \hat{Q}(\mathbf{r}', \mathbf{r}) \exp(i\mathbf{K} \cdot \mathbf{R}), \quad (35)$$

and the first-order term is of the form

$$\Psi_1(z', \mathbf{K}', \mathbf{K}_0) = \int dz \hat{q}(z', \mathbf{K}'; z, \mathbf{K}_0) \psi(z, K_0). \quad (36)$$

For the kernel, \hat{q} , in the case of small unified perturbations, taking into account Eqs. (35), (24), and (31), one obtains

$$\hat{q}(z', \mathbf{K}'; z, \mathbf{K}) = -(2\pi)^2 \sum_{\beta} \hat{\epsilon}_{\beta}(\mathbf{K}' - \mathbf{K}, z) \times \hat{q}_{\beta}(z', \mathbf{K}'; z, \mathbf{K}),$$

$$\beta = \kappa, \rho, \zeta, \quad (37)$$

where $\hat{\epsilon}_{\beta}$ is the 2-D Fourier transform of the corresponding perturbation with respect to transverse coordinates,

$$\hat{\epsilon}_{\beta}(\mathbf{K}, z) = (2\pi)^{-2} \int \epsilon_{\beta}(\mathbf{R}, z) \exp(-i\mathbf{K} \cdot \mathbf{R}) d^2R,$$

$$\beta = \kappa, \rho, \zeta, \quad (38)$$

and \hat{q}_{β} are the partial unperturbed kernel operators that, using Eq. (25), (26), and (27), are defined as follows:

$$\hat{q}_{\kappa}(z', \mathbf{K}'; z, \mathbf{K}) = \omega^2 \kappa g(z, z', K'), \quad (39)$$

$$\rho(z) \hat{q}_{\rho}(z', \mathbf{K}'; z, \mathbf{K}) = (\mathbf{K} \cdot \mathbf{K}') g(z, z', K') + \partial_z g(z, z', K') \partial_z \quad (40)$$

$$\hat{q}_{\zeta}(z', \mathbf{K}'; z, \mathbf{K}) = D_{\kappa}(z) \omega^2 g(z, z', K') - D_{1/\rho}(z) (\mathbf{K} \cdot \mathbf{K}') g(z, z', K') + D_{\rho}(z) \rho^{-2}(z) \partial_z g(z, z', K') \partial_z. \quad (41)$$

The formal solution of Eq. (34) can be presented in the form of multiple-scattering series

$$\Psi = \sum_{n=1}^{\infty} \Psi_n, \quad (42)$$

where Ψ_n is the n th-order term defined by the iterative expression

$$\begin{aligned} \Psi_n(z', \mathbf{K}', \mathbf{K}_0) \\ = \int dz d^2K \hat{q}(z', \mathbf{K}'; z, \mathbf{K}) \Psi_{n-1}(z, \mathbf{K}, \mathbf{K}_0), \\ n = 1, 2, 3, \dots, \end{aligned} \quad (43)$$

with

$$\Psi_0(z, \mathbf{K}, \mathbf{K}_0) = \psi(z, K) \delta(\mathbf{K} - \mathbf{K}_0). \quad (44)$$

III. FIRST-ORDER SOLUTION

Here we consider the first-order term in the perturbation expansion, often called the Born approximation, to determine the scattering amplitude and scattering cross section for the case of small volume and roughness perturbations in a multi-layered medium.

The function Ψ is related to the scattering amplitude, A (see Appendix D), as follows:

$$A(\mathbf{K}, \mathbf{K}_0) = \nu_1(K) \Psi(0, \mathbf{K}, \mathbf{K}_0), \quad (45)$$

through which all the statistical characteristics of the scattered field in the upper half-space can be expressed. A general expression for the first-order scattering amplitude, A_B , follows immediately from Eqs. (36) and (45):

$$A_B(\mathbf{K}, \mathbf{K}_0) = \nu_1(K) \int dz \hat{q}(0, \mathbf{K}; z, \mathbf{K}_0) \psi(z, K_0). \quad (46)$$

Taking into account Eq. (37), Eq. (46) can be presented in the form

$$A_B(\mathbf{K}, \mathbf{K}_0) = \sum_{\beta} A^{(\beta)}(\mathbf{K}, \mathbf{K}_0), \quad \beta = \kappa, \rho, \zeta, \quad (47)$$

where $A^{(\beta)}$ are the Born approximations for the corresponding scattering amplitudes (subscript B is omitted).

The scattering cross section (see Appendix D) is related to the first-order scattering amplitude through the equation

$$\langle A(\mathbf{K}, \mathbf{K}_0) A^*(\mathbf{K}', \mathbf{K}_0) \rangle = \delta(\mathbf{K} - \mathbf{K}') \sigma(\mathbf{K}, \mathbf{K}_0), \quad (48)$$

where superscript $*$ denotes the complex conjugation. The roughness scattering component, $A^{(\zeta)}$, and the volume component,

$$A^{(v)} = A^{(\kappa)} + A^{(\rho)}, \quad (49)$$

can be generally considered as partially correlated. The total scattering cross section can be presented as a sum of roughness, volume, and roughness-volume components,

$$\sigma = \sigma^{(\zeta)} + \sigma^{(v)} + \sigma^{(\zeta v)}, \quad (50)$$

with indices ζ , v , and ζv correspondingly. The last term vanishes when volume inhomogeneities and roughness are uncorrelated.

A. Roughness scattering

The roughness scattering amplitude, from (46) and (37), taking into account (41) and (32), is obtained in the form

$$A^{(\zeta)}(\mathbf{K}, \mathbf{K}_0) = \sum_j A_j^{(\zeta)}(\mathbf{K}, \mathbf{K}_0), \quad (51)$$

$$A_j^{(\zeta)}(\mathbf{K}, \mathbf{K}_0) = \hat{\zeta}_j(\mathbf{K} - \mathbf{K}_0) \phi_{\zeta}(z_j, \mathbf{K}, \mathbf{K}_0), \quad (52)$$

where ϕ_{ζ} is defined as follows:

$$\phi_{\zeta}(z_j, \mathbf{K}, \mathbf{K}_0) = \frac{ik_1^2}{2} \psi(z_j, K) \psi(z_j, K_0) f_j(\mathbf{K}, \mathbf{K}_0), \quad (53)$$

$$\begin{aligned} f_j(\mathbf{K}, \mathbf{K}_0) = D_j(\kappa/\kappa_1) - D_j(\rho_1/\rho)(\mathbf{K} \cdot \mathbf{K}_0) k_1^{-2} \\ - D_j(\rho/\rho_1) Y(z_j, K) Y(z_j, K_0), \end{aligned} \quad (54)$$

with $D_j(\beta) = D(\beta)_{z=z_j}$, $\beta = \kappa, \rho, 1/\rho$, and Y as the dimensionless continuous admittance of the plane-layered medium taken at the flat interface and defined through the function $\psi(z, K)$ as follows:

$$Y(z, K) = \frac{i\rho_1 \partial_z \psi(z, K)}{\kappa_1 \rho(z) \psi(z, K)}. \quad (55)$$

In terms of the reflection and transmission coefficients (see Appendix C) one obtains

$$\begin{aligned} \psi(z_j, K) = W_j(K) (1 + V_j(K)) \\ = W'_{j+1}(K) (1 + V'_{j+1}(K)), \end{aligned} \quad (56)$$

$$\begin{aligned} Y(z_j, K) = \left(\frac{1 - V_j(K)}{1 + V_j(K)} \right) Y_j(K) \\ = \left(\frac{1 - V'_{j+1}(K)}{1 + V'_{j+1}(K)} \right) Y'_{j+1}(K), \end{aligned} \quad (57)$$

$$Y_j(K) = Y^{(0)}(z_j + 0, K), \quad Y'_{j+1}(K) = Y^{(0)}(z_j - 0, K), \quad (58)$$

where

$$Y^{(0)}(z, K) = \frac{\rho_1 \nu(z, K)}{\kappa_1 \rho(z)} \quad (59)$$

is the local plane-wave dimensionless admittance of the unperturbed medium.

The roughness scattering cross section, from (48) and (51), is defined as follows:

$$\begin{aligned} \sigma^{(\zeta)}(\mathbf{K}, \mathbf{K}_0) = \sum_{j,l} \phi_{\zeta}(z_j, \mathbf{K}, \mathbf{K}_0) \phi_{\zeta}^*(z_l, \mathbf{K}, \mathbf{K}_0) \\ \times \Phi_{jl}^{(\zeta)}(\mathbf{K} - \mathbf{K}_0), \end{aligned} \quad (60)$$

$$\Phi_{jl}^{(\zeta)}(\mathbf{K}) = (2\pi)^{-2} \int B_{jl}^{(\zeta)}(\mathbf{R}) \exp(-i\mathbf{K} \cdot \mathbf{R}) d^2R, \quad (61)$$

$$B_{jl}^{(\zeta)}(\mathbf{R}) = \langle \zeta_j(\mathbf{R}') \zeta_l(\mathbf{R}' + \mathbf{R}) \rangle, \quad (62)$$

where $\Phi_{jl}^{(\zeta)}$ and $B_{jl}^{(\zeta)}$ are the cross-spectral and cross-correlation matrixes of the j th and l th interfaces roughness, assumed to be statistically uniform.

It is convenient to introduce the normalized form factor, $F_{\zeta j}$, as follows:

$$\phi_{\xi}(z_j, \mathbf{K}, \mathbf{K}_0) = W_j(K) W_j(K_0) F_{\xi_j}(\mathbf{K}, \mathbf{K}_0), \quad (63)$$

In the case when irregularities of the different interfaces are uncorrelated, i.e., $B_{ji}^{(\xi)} = \delta_{ji} B_j$, where δ_{ji} is the Kronecker symbol, using (63), we obtain

$$\sigma^{(\xi)}(\mathbf{K}, \mathbf{K}_0) = \sum_j |W_j(K) W_j(K_0)|^2 \sigma_j(\mathbf{K}, \mathbf{K}_0), \quad (64)$$

$$\sigma_j(\mathbf{K}, \mathbf{K}_0) = |F_{\xi_j}(\mathbf{K}, \mathbf{K}_0)|^2 \Phi_j(\mathbf{K} - \mathbf{K}_0), \quad (65)$$

where $\Phi_j = \Phi_{jj}^{(\xi)}$ is the spatial spectrum of the roughness of the j th interface.

Note, that Eqs. (60) and (64) generalize previous results obtained for a single rough interface onto the case of an arbitrary number of correlated or uncorrelated rough interfaces in an arbitrarily stratified fluid medium. In particular, in the case of scattering from the rough surface of a half-space ($N=1$, $W=1$), either from (60) and (63), or from (64) and (65), we find

$$\sigma^{(\xi)} = \sigma_1 = |F_1(\mathbf{K}, \mathbf{K}_0)|^2 \Phi_1(\mathbf{K} - \mathbf{K}_0). \quad (66)$$

This result corresponds to that obtained in Ref. 12 for the case of a rough surface of a half-space with the depth-dependent sound speed. In the particular case of a homogeneous rough half-space, the result is coincident with the well-known solution of Kuo,²⁵ taking into account that in this case the zeroth-order field below the interface, at $z < z_1$, is of the form (see Appendix C)

$$\psi(z, K) = W_2'(K) \exp[-i \nu_2'(K)(z - z_1)]. \quad (67)$$

B. Volume scattering

The volume scattering amplitudes for all the multiple-layered medium are obtained in the form

$$A^{(v)}(\mathbf{K}, \mathbf{K}_0) = \sum_{j, \beta} A_j^{(\beta)}(\mathbf{K}, \mathbf{K}_0), \quad (68)$$

where $A_j^{(\beta)}$ is the partial scattering amplitudes of the j th layer, $z_j < z < z_{j-1}$, defined as follows:

$$A_j^{(\beta)} = \int_{z_j}^{z_{j-1}} dz \hat{\epsilon}_{\beta}(\mathbf{K} - \mathbf{K}_0, z) \phi_{\beta}(z, \mathbf{K}, \mathbf{K}_0), \quad (69)$$

where ϕ_{β} is defined for different kinds of the volume fluctuations in the j th layer by the equations

$$-2i \frac{\rho(z)}{\rho_1} \phi_{\kappa}(z, \mathbf{K}, \mathbf{K}_0) = k^2(z) \psi(z, K) \psi(z, K_0), \quad (70)$$

$$-2i \frac{\rho(z)}{\rho_1} \phi_{\rho}(z, \mathbf{K}, \mathbf{K}_0) = (\mathbf{K} \cdot \mathbf{K}_0) \psi(z, K) \psi(z, K_0) + \partial_z \psi(z, K) \partial_z \psi(z, K_0). \quad (71)$$

As a simple example, let us consider a homogeneous (on the average) fluid half-space with spatial fluctuations of the density and compressibility. In this case, the zeroth-order solution is of the form (67). The volume scattering amplitude is defined by Eqs. (68)–(71). The result can be presented in the form

$$A^{(v)}(\mathbf{K}, \mathbf{K}_0) = W_2'(K) W_2'(K_0) A_2'(\mathbf{K}, \mathbf{K}_0), \quad (72)$$

$$A_2'(\mathbf{K}, \mathbf{K}_0) = i \pi \frac{\rho_1}{\rho_2} [k^2 \hat{\epsilon}_{\kappa}(\mathbf{k} - \mathbf{k}_0) + (\mathbf{k}_0 \cdot \mathbf{k}) \hat{\epsilon}_{\rho}(\mathbf{k} - \mathbf{k}_0)], \quad (73)$$

$$\hat{\epsilon}_{\beta}(\mathbf{q}) = (2\pi)^{-3} \int_{z < z_1} d^3 r \epsilon_{\beta}(\mathbf{r}) \exp(-i \mathbf{q} \cdot \mathbf{r}),$$

$$\beta = \kappa, \rho, \quad (74)$$

$$\mathbf{k}_0 = (\mathbf{K}_0, -\nu_2'(K_0)), \quad \mathbf{k} = (\mathbf{K}, \nu_2'(K)), \quad (75)$$

where \mathbf{k}_0 and \mathbf{k} are the wave vectors of the incident and scattered waves within the scattering half-space, and $\mathbf{q} = \mathbf{k} - \mathbf{k}_0$ is the scattering vector.

In the case of an arbitrary number of layers, it is convenient to introduce the normalized form factors, $\phi_{\beta j}$, as follows:

$$\phi_{\beta}(z, \mathbf{K}, \mathbf{K}_0) = W_j'(K) W_j'(K_0) \phi_{\beta j}(z, \mathbf{K}, \mathbf{K}_0). \quad (76)$$

Then the volume scattering cross section, using Eqs. (68) and (48), assuming that inhomogeneities of different layers are uncorrelated, is obtained in the form

$$\sigma^{(v)}(\mathbf{K}, \mathbf{K}_0) = \sum_j |W_j'(K) W_j'(K_0)|^2 \sigma_j'(\mathbf{K}, \mathbf{K}_0). \quad (77)$$

Here σ_j' is the normalized volume scattering cross section of the j th layer defined as follows:

$$\sigma_j'(\mathbf{K}, \mathbf{K}_0) = \sum_{\beta, \beta'} \int_{z_j}^{z_{j-1}} dz dz' \phi_{\beta j}(z, \mathbf{K}, \mathbf{K}_0) \times \phi_{\beta' j}^*(z', \mathbf{K}, \mathbf{K}_0) \Phi_{\beta \beta'}(\mathbf{K} - \mathbf{K}_0, z, z'), \quad (78)$$

$$\Phi_{\beta \beta'}(\mathbf{K}, z, z') = (2\pi)^{-2} \int B_{\beta \beta'}(\mathbf{R}, z, z') \times \exp(-i \mathbf{K} \cdot \mathbf{R}) d^2 R, \quad (79)$$

$$B_{\beta \beta'}(\mathbf{R}, z, z') = \langle \epsilon_{\beta}(\mathbf{R}', z) \epsilon_{\beta'}^*(\mathbf{R}' + \mathbf{R}, z') \rangle, \quad (80)$$

where $\Phi_{\beta \beta'}$ and $B_{\beta \beta'}$ are the 2-D cross-spectral and cross-correlation matrices of volume inhomogeneities, assumed to be statistically uniform in horizontal directions. If, moreover, the inhomogeneities are statistically uniform in the vertical direction, Eq. (78) can be presented in the form

$$\sigma_j'(\mathbf{K}, \mathbf{K}_0) = \sum_{\beta, \beta'} \int d\gamma F_{\beta j}(\mathbf{K}, \mathbf{K}_0, \gamma) \times F_{\beta' j}^*(\mathbf{K}, \mathbf{K}_0, \gamma) \Phi_{\beta \beta'}^{(j)}(\mathbf{K} - \mathbf{K}_0, \gamma), \quad (81)$$

where $F_{\beta j}$ is the form factor defined by the equation

$$F_{\beta j}(\mathbf{K}, \mathbf{K}_0, \gamma) = \int_{z_j}^{z_{j-1}} dz \phi_{\beta j}(z, \mathbf{K}, \mathbf{K}_0) \exp(i \gamma z) \quad (82)$$

and $\Phi_{\beta \beta'}^{(j)}(\mathbf{q})$ is the 3-D cross-spectral matrix of volume inhomogeneities,

$$\Phi_{\beta \beta'}^{(j)}(\mathbf{q}) = (2\pi)^{-3} \int B_{\beta \beta'}^{(j)}(\mathbf{r}) \exp(-i \mathbf{q} \cdot \mathbf{r}) d^3 r, \quad (83)$$

with $\mathbf{q} = (\mathbf{K} - \mathbf{K}_0, \gamma)$, $\mathbf{r} = (\mathbf{R}, z - z')$, and $B_{\beta \beta'}^{(j)}(\mathbf{r})$ as the 3-D cross-correlation matrices of volume inhomogeneities, assumed to be statistically uniform in all directions.

Note that in Eqs. (68) and (77) components with $j=1$, $A_1^{(v)}$ and σ_1 , correspond to scattering from the layer over the first interface, $z_1 < z < z_0$ (first layer, see Fig. 2) which is homogeneous on the average and for which the explicit form of the function ψ is known (see Appendix C). Note also that this layer in the frame of the first-order model is totally transparent with $|W_1'| = |W_1| = 1$.

Equations (77), (78), and (81) give first-order solution for the volume scattering cross section for an arbitrary number of stratified fluid layers with volume inhomogeneities of different kinds having arbitrary cross-spectral and cross-correlation functions. The only input for the above formulas is the function $\psi(z, K)$ defined once the depth dependence of the unperturbed medium parameters, $\rho(z)$ and $c(z)$, is given (see Appendix C).

C. Volume-roughness correlations

An expression for $\sigma^{(\zeta v)}$ can be obtained, using Eqs. (68), (69), and (52), in the form

$$\sigma^{(\zeta v)}(\mathbf{K}, \mathbf{K}_0) = 2 \operatorname{Re} \sum_{j, \beta} \phi_{\zeta}^*(z_j, \mathbf{K}, \mathbf{K}_0) \times \int dz \phi_{\beta}(z, \mathbf{K}, \mathbf{K}_0) \Phi_{\zeta\beta}(\mathbf{K} - \mathbf{K}_0, z, z_j), \quad (84)$$

$$\Phi_{\zeta\beta}(\mathbf{K}, z, z_j) = (2\pi)^{-2} \int B_{\zeta\beta}(\mathbf{R}, z, z_j) \times \exp(-i\mathbf{K} \cdot \mathbf{R}) d^2R, \quad (85)$$

$$B_{\zeta\beta}(\mathbf{R}, z, z_j) = \langle \epsilon_{\beta}(\mathbf{R}', z) \zeta_j(\mathbf{R}' + \mathbf{R}) \rangle, \quad (86)$$

where $\Phi_{\zeta\beta}$ and $B_{\zeta\beta}$ are the 2-D cross-spectral and cross-correlation functions of volume inhomogeneities and roughness and Re means real part of complex value.

As an example, let us consider an unperturbed plane-layered medium with one plane interface, $z = z_1$, and parameters being *continuous* functions of depth, $a_{\beta}(z)$, $z \neq z_1$. Surfaces of constant values of these parameters, the ‘‘iso-surfaces,’’ are the planes $z = \bar{z}$. Here, for brevity, denote notation of the unperturbed parameters by subscripts, i.e., $\rho = a_{\rho}$ and $\kappa = a_{\kappa}$. Small perturbations in such a medium can disturb the iso-surfaces so that they will be of the form

$$z = \bar{z} + \zeta(\mathbf{R}, \bar{z}), \quad (87)$$

where $\zeta(\mathbf{R}, \bar{z})$ is their deviation with respect to the unperturbed iso-surface $z = \bar{z}$, and $\zeta(\mathbf{R}, z_1) = \zeta_1(\mathbf{R})$. The parameters of such a slightly perturbed ‘‘quasi-layered’’ medium with rough iso-surfaces and one rough interface can be presented in the form

$$\tilde{a}_{\beta}(\mathbf{r}) = a_{\beta}(z - \zeta(\mathbf{R}, z)) \approx a_{\beta}(z) - \frac{da_{\beta}}{dz} \zeta(\mathbf{R}, z) \quad (88)$$

and have relatively small volume perturbations caused by and proportional to the iso-surface roughness

$$\epsilon_{\beta}(\mathbf{r}) = -\zeta(\mathbf{R}, z) \frac{da_{\beta}}{dz}, \quad \frac{|\epsilon_{\beta}(\mathbf{r})|}{a_{\beta}} \ll 1, \quad \beta = \kappa, \rho. \quad (89)$$

In this case, the cross-correlation function, $B_{\zeta\beta}$, is defined as follows:

$$B_{\zeta\beta}(\mathbf{R}, z, z_1) = -\frac{da_{\beta}}{dz} \langle \zeta(\mathbf{R}', z) \zeta(\mathbf{R}' + \mathbf{R}, z_1) \rangle. \quad (90)$$

D. How to include basement scattering

The above expressions for the scattering amplitude and scattering cross section, (51) and (52), (68) and (69), can be easily generalized to the case where the basement beneath a layered fluid medium not only reflects but also scatters. In this case, the expressions for the roughness and volume scattering amplitudes for the layered fluid (components with $j \leq N$) depend upon the reflection coefficient of the basement, $V_{N+1}(K)$, as an input parameter, through the function $\psi(z, K)$ (see Appendix C). All the scattering from the basement, in the framework of the first-order solution, is contained in the last term treated as the scattering amplitude of the basement,

$$A_{N+1}(\mathbf{K}, \mathbf{K}_0) = W_j(K) W_j(K_0) \bar{A}_{N+1}(\mathbf{K}, \mathbf{K}_0), \quad (91)$$

with $\bar{A}_{N+1} = \bar{A}_b^{(\zeta)} + \bar{A}_b^{(v)}$ as a sum of the normalized roughness and volume scattering amplitude of the basement. This amplitudes are defined for a plane incident pressure wave of a unit amplitude in an infinite homogeneous half-space with parameters ρ_{N+1} and c_{N+1} (see Fig. 2).

The explicit form of the basement scattering amplitude components, $\bar{A}_{N+1}^{(\beta)}(\mathbf{K}, \mathbf{K}_0)$, depends on the type of the basement medium. Generally, they can be presented as follows:

$$\bar{A}_b^{(\zeta)}(\mathbf{K}, \mathbf{K}_0) = \hat{\zeta}_{N+1}(\mathbf{K} - \mathbf{K}_0) F_{\zeta}(z_{N+1}, \mathbf{K}, \mathbf{K}_0), \quad (92)$$

$$\bar{A}_b^{(v)}(\mathbf{K}, \mathbf{K}_0) = \int_{z \leq z_{N+1}} dz \sum_{\beta} \tilde{\epsilon}_{\beta}(\mathbf{K} - \mathbf{K}_0, z) \times F_{\beta}(z, \mathbf{K}, \mathbf{K}_0), \quad (93)$$

where F_{ζ} and F_{β} are the roughness and volume scattering form factors.

As examples of perfectly scattering basements, hard or soft (impenetrable) rough surfaces can be used with $V_{N+1} = \pm 1$, respectively. Corresponding expressions for the scattering amplitude can be easily obtained from (63) and (53) as the limit cases,

$$F_{\zeta}(z_{N+1}, \mathbf{K}, \mathbf{K}_0) = F^{\pm}(\mathbf{K}, \mathbf{K}_0), \quad (94)$$

$$F^+(\mathbf{K}, \mathbf{K}_0) = -\frac{2i\rho_1}{\rho_{N+1}} (k_{N+1}^2 - \mathbf{K} \cdot \mathbf{K}_0), \quad (95)$$

$$F^-(\mathbf{K}, \mathbf{K}_0) = \frac{2i\rho_1}{\rho_{N+1}} \nu_{N+1}(K) \nu_{N+1}(K_0). \quad (96)$$

As a realistic example of a penetrable scattering basement, an elastic rough half-space with volume inhomogeneities can be used. In this case, the roughness and volume scattering amplitudes are of the form (92) and (93). Spatially fluctuating parameters are the density and compressional and shear speed, i.e., $\beta = \rho, c_p, c_t$. Expressions for the corresponding volume and roughness form factors, F_{β} and F_{ζ} , can be found in Refs. 14 and 15 respectively. Generalized

expressions for the scattering amplitude and scattering cross section of an elastic rough and inhomogeneous half-space and their analysis with a number of numerical examples are presented in Refs. 16 and 17.

IV. SUMMARY

In this paper, a unified approach is proposed for the study of scattering from a multi-layered fluid medium with irregularities of two different types: volume inhomogeneities (spatial fluctuations of the compressibility and density) and roughness of the interfaces between layers. The approach considers roughness as a volume perturbation of a specific kind near flat (unperturbed) interfaces. It permits a description of the scattering problem on the basis of a unique integral equation with a kernel including both types of perturbations in a multi-layered medium. In the case of small perturbations, its solution is presented in the form of a multiple scattering series. The first-order term is used to obtain the scattering amplitude for an arbitrarily stratified fluid medium with volume inhomogeneities and an arbitrary number of rough interfaces. All the statistical characteristics of the scattered field can be expressed through the scattering amplitude and then related to the statistical properties of the scattering medium. The expression for the scattering cross section is obtained in terms of cross-spectral and cross-correlation matrices between different types of medium perturbations. The results are generalized to the case for which the fluid is placed over an arbitrary basement characterized by its own reflection coefficient and scattering amplitude.

The model considered here is appropriate, e.g., for stratified marine sediments. Details of the application of the unified approach developed here to statistical modeling of seabed scattering with numerical examples will be presented in later papers.

ACKNOWLEDGMENTS

The author thanks Dr. Darrell R. Jackson of Applied Physics Laboratory, University of Washington, for a careful first reading of the manuscript and helpful discussions. This work was supported by the U.S. Office of Naval Research through the University of Washington.

APPENDIX A: MULTIPLE SCATTERING SERIES AND BORN APPROXIMATION

An integral equation for the field in an inhomogeneous medium can be presented in the general form (7) with the kernel operator, $\hat{Q}(\mathbf{r}', \mathbf{r})$, depending on the type of medium perturbations, see, e.g., Eqs. (5), (15), and (23). A similar integral equation can be written for the field perturbation, $p_s = p - p_0$, using the first-order solution, p_1 , as a starting term,

$$p_s(\mathbf{r}') = p_1(\mathbf{r}') + \int \hat{Q}(\mathbf{r}', \mathbf{r}) p_s(\mathbf{r}) d^3 r, \quad (\text{A1})$$

where p_1 is defined as follows,

$$p_1(\mathbf{r}') = \int \hat{Q}(\mathbf{r}', \mathbf{r}) p_0(\mathbf{r}) d^3 r, \quad (\text{A2})$$

and is called the single-scattered field or Born approximation.

A formal solution of Eq. (A1) can be presented in iterative form as a multiple-scattering series

$$p_s = \sum_{n=1}^{\infty} p_n, \quad (\text{A3})$$

where p_n is the n th order scattered field being defined analogously to the single-scattered term, Eq. (A2), by the iterative expression

$$p_n(\mathbf{r}') = \int \hat{Q}(\mathbf{r}', \mathbf{r}) p_{n-1}(\mathbf{r}) d^3 r, \quad n = 1, 2, 3, \dots \quad (\text{A4})$$

The expressions (A3) and (A4) are convenient for the development of multiple scattering models providing relations between statistical moments of the scattered field and medium fluctuations. For the case of the second-order moments in the Born approximation, taking into account Eq. (23), one obtains

$$\begin{aligned} \langle p_1(\mathbf{r}') p_1^*(\mathbf{r}'') \rangle &= \sum_{\beta_1 \beta_2} \int \int B_{\beta_1 \beta_2}(\mathbf{r}_1, \mathbf{r}_2) \\ &\quad \times \hat{Q}_{\beta_1}(\mathbf{r}', \mathbf{r}_1) \hat{Q}_{\beta_2}^*(\mathbf{r}'', \mathbf{r}_2) p_0(\mathbf{r}_1) \\ &\quad \times p_0^*(\mathbf{r}_2) d^3 r_1 d^3 r_2, \\ \beta_{1,2} &= \rho, \kappa, \zeta, \end{aligned} \quad (\text{A5})$$

where $B_{\beta_1 \beta_2}(\mathbf{r}_1, \mathbf{r}_2) = \langle \epsilon_{\beta_1}(\mathbf{r}_1) \epsilon_{\beta_2}^*(\mathbf{r}_2) \rangle$ is the cross-correlation matrix for different medium fluctuations.

APPENDIX B. SMALL ROUGHNESS

Let the interface roughness be small, i.e., $|k_{1,2}\zeta| \ll 1$. Then the functions appearing in the integrand of Eq. (15), pG and $\nabla p \cdot \nabla G$, can be continued onto the mean plane, $z = 0$, with the help of the boundary conditions

$$(p_1 - p_2)_{z=\zeta(\mathbf{R})} = 0, \quad (\text{B1})$$

$$\left(\frac{1}{\rho_1} \partial_N p_1 - \frac{1}{\rho_2} \partial_N p_2 \right)_{z=\zeta(\mathbf{R})} = 0, \quad (\text{B2})$$

$$(G_1 - G_2)_{z=0} = 0, \quad (\text{B3})$$

$$\left(\frac{1}{\rho_1} \partial_z G_1 - \frac{1}{\rho_2} \partial_z G_2 \right)_{z=0} = 0, \quad (\text{B4})$$

where G_1 and G_2 are the Green's functions, respectively, above and below the reference plane ($z = 0$), p_1 and p_2 are the pressures, respectively, above and below the rough interface, $z = \zeta(\mathbf{R})$, having the normal unit vector \mathbf{N} ,

$$\mathbf{N} = (-\nabla \zeta, 1) / \sqrt{1 + (\nabla \zeta)^2}, \quad (\text{B5})$$

with $\partial_N = \mathbf{N} \cdot \nabla$, $\nabla = (\nabla_R, \partial_z)$.

Note that $p_{1,2}$ and $G_{1,2}$ are continuous functions of \mathbf{r} . Using Eqs. (B1) and (B3), one obtains for $|k_{1,2}\zeta| \ll 1$

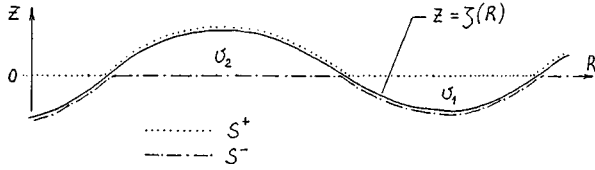


FIG. B1. Rough interface definitions.

$$(pG)_{v_{1,2}} \approx \begin{cases} (p_1 G_1)_{S^+} \approx (p_1 G_1)_{z=+0} \\ (p_2 G_2)_{S^-} \approx (p_2 G_2)_{z=-0} \end{cases}, \quad (\text{B6})$$

where S^\pm are the surfaces (see Fig. B1) defined as follows:

$$S^+ : z = \max\{\zeta(\mathbf{R}), +0\}, \quad S^- : z = \min\{\zeta(\mathbf{R}), -0\}, \quad (\text{B7})$$

and $v_{1,2}$ are subvolumes of integration in Eq. (15) defined as follows:

$$v_1 : \zeta(\mathbf{R}) < z < 0, \quad v_2 : 0 < z < \zeta(\mathbf{R}). \quad (\text{B8})$$

To find $(\nabla p \cdot \nabla G)_{v_{1,2}}$ note that the scalar (dot) product is independent of the angular orientation of the coordinate system, and

$$\begin{aligned} \nabla p \cdot \nabla G &= \nabla_{RP} \cdot \nabla_R G + \partial_z p \partial_z G \\ &= \nabla_t^\pm p \cdot \nabla_t^\pm G + \partial_N^\pm p \partial_N^\pm G, \end{aligned} \quad (\text{B9})$$

where $\partial_N^\pm = N^\pm \cdot \nabla$ is the normal derivative corresponding to the normal for the surface S^\pm , and ∇_t^\pm is the respective tangent gradient. Then using the boundary conditions (B2) and (B4), one obtains at $|k_{1,2}\zeta| \ll 1$

$$\begin{aligned} \frac{1}{\rho_1 \rho_2} (\nabla p \cdot \nabla G)_{v_{1,2}} &\approx \begin{cases} ((\rho_1 \rho_2)^{-1} \nabla_t^+ p_1 \cdot \nabla_t^+ G_1 + \rho_1^{-2} \partial_N^+ p_1 \partial_N^+ G_1)_{S^+}, \\ ((\rho_1 \rho_2)^{-1} \nabla_t^- p_2 \cdot \nabla_t^- G_2 + \rho_2^{-2} \partial_N^- p_2 \partial_N^- G_2)_{S^-}. \end{cases} \end{aligned} \quad (\text{B10})$$

If the roughness slope is small as well, i.e., $|\nabla \zeta| \ll 1$, then one obtains

$$\begin{aligned} \frac{1}{\rho_1 \rho_2} (\nabla p \cdot \nabla G)_{v_{1,2}} &\approx \begin{cases} ((\rho_1 \rho_2)^{-1} \nabla_{RP1} \cdot \nabla_R G_1 + \rho_1^{-2} \partial_z p_1 \partial_z G_1)_{z=+0}, \\ ((\rho_1 \rho_2)^{-1} \nabla_{RP2} \cdot \nabla_R G_2 + \rho_2^{-2} \partial_z p_2 \partial_z G_2)_{z=-0}. \end{cases} \end{aligned} \quad (\text{B11})$$

Taking into account Eqs. (B6) and (B11), one easily obtains from Eq. (15) the integral equation (18) for the small roughness perturbation case.

APPENDIX C: ZEROth ORDER FIELD

The complex amplitude of the field in a plane-layered medium with depth-dependent parameters, density and sound speed, $p(z)$ and $c(z)$, obeys the Helmholtz equation

$$[\rho \partial_z (\rho^{-1} \partial_z) + k^2 - K^2] \psi(z, K) = 0, \quad k = \omega/c(z), \quad (\text{C1})$$

and boundary (continuity) conditions at all the mean interfaces, $z = z_j$,

$$D_j(\psi) = \psi(z_j - 0) - \psi(z_j + 0) = 0, \quad D_j(\rho^{-1} \partial_z \psi) = 0, \quad (\text{C2})$$

where D_j denotes the contrast (difference) of the corresponding function at the j th interface.

For a description of the zeroth-order solution between interfaces, i.e., the function $\psi(z, K)$ within continuous layers, assume that the medium is homogeneous in a small vicinity of all the unperturbed interfaces, $z = z_j$. Then the unperturbed field above (and near) the j th interface, at the exit of the j th layer (see Fig. 2), is of the form

$$\psi(z, K) = W_j(K) \bar{\psi}_j(z, K), \quad (\text{C3})$$

$$\begin{aligned} \bar{\psi}_j(z, K) &= \exp[-i\nu_j(K)(z - z_j)] \\ &+ V_j(K) \exp[i\nu_j(K)(z - z_j)], \end{aligned} \quad (\text{C4})$$

where $\nu_j(K) = \nu(z_j + 0, K)$ and $\nu(z, K) = \sqrt{k^2(z) - K^2}$. Coefficients V_j and W_j are the reflection and transmission coefficients of the medium above the j th interface. Note that W_j corresponds to the amplitude of the incident field for the j th interface. In the first layer, $z_1 < z < z_0$, we have $W_1 = 1$ and $\psi = \bar{\psi}_1(z, K)$ defined by Eq. (C4) with V_1 as the total reflection coefficient of the inhomogeneous multi-layered half-space, $z \leq z_1$.

Below (and near) the $(j-1)$ th interface, at the entrance of the j th layer, the field is

$$\psi(z, K) = W'_j(K) \psi_j(z, K), \quad (\text{C5})$$

$$\begin{aligned} \psi_j(z, K) &= \exp[-i\nu'_j(K)(z - z_{j-1})] \\ &+ V'_j(K) \exp[i\nu'_j(K)(z - z_{j-1})], \end{aligned} \quad (\text{C6})$$

where $\nu'_j(K) = \nu(z_{j-1} - 0, K)$. Coefficients V'_j are the reflection coefficients of the medium at the entrance of the j th continuous layer, W'_j are the corresponding transmission coefficients and the amplitudes of the incident field. Within this layer, $z_{j+1} < z < z_j$, the function $\psi_j(z, K)$ obeys the Helmholtz equation (6) and boundary conditions, at the upper boundary of the layer,

$$\left[1 + \frac{i}{\nu'_j(K)} \partial_z \right]_{z=z_{j-1}-0} \psi_j(z, K) = 2, \quad (\text{C7})$$

and at the lower boundary,

$$\begin{aligned} \left[\frac{i \partial_z \psi_j(z, K)}{\psi_j(z, K)} \right]_{z=z_j+0} &= \left[\frac{i \partial_z \bar{\psi}_j(z, K)}{\bar{\psi}_j(z, K)} \right]_{z=z_j+0} \\ &= \nu_j(K) \frac{1 - V_j(K)}{1 + V_j(K)}. \end{aligned} \quad (\text{C8})$$

In the case of inhomogeneous (on the average) continuous layers, the functions $\psi_j(z, K)$ can be calculated by means of well-developed methods¹⁹ for any set of depth-dependent parameters, $\rho(z)$ and $c(z)$, as a plane-wave solution of Eq. (C1) with boundary conditions (C7) and (C8). Note that $V_j(K)$ is an input parameter for the function $\psi_j(z, K)$. If the function ψ_j has been found, the explicit form for $V'_j(K)$ and $V_{j-1}(K)$ can be determined as follows:

$$V'_j = \psi_j(z_j, K) - 1, \quad (\text{C9})$$

$$V_{j-1} = \frac{V_{j-1}^{(0)} + V_j'}{1 + V_{j-1}^{(0)} V_j'}, \quad (\text{C10})$$

where $V_{j-1}^{(0)}$ is the local reflection coefficient of the $(j-1)$ th interface,

$$V_j^{(0)} = \frac{Y_{j-1} - Y_j'}{Y_{j-1} + Y_j'}, \quad (\text{C11})$$

with Y_{j-1} and Y_j' defined by Eqs. (58) and (59).

The transmission coefficients of the j th layer, $t_j = W_j/W_j'$, and j th interface, $T_j = W_{j+1}'/W_j$, can be determined as follows:

$$t_j = \frac{\psi_{j+1}(z_{j+1}, K)}{1 + V_{j+1}(K)}, \quad (\text{C12})$$

$$T_j = \frac{1 + V_j}{1 + V_{j+1}'} = \frac{1 + V_j^{(0)}}{1 + V_j^{(0)} V_{j+1}'}. \quad (\text{C13})$$

When, by such a way, the transmission coefficients t_j and T_j are determined for all the fluid layers and interfaces, the amplitudes of incident field at different interfaces, W_j , are defined by the equation

$$W_{j+1} = W_j T_j t_{j+1}, \quad W_1 = 1. \quad (\text{C14})$$

APPENDIX D. SCATTERING AMPLITUDE

Regardless of the complexity of the random medium, whether scattering is due to roughness or volume inhomogeneity, the scattered field, $\tilde{p}_s = p - p_{\text{inc}}$, above the highest point on the interface can be expressed as a superposition of plane waves

$$\tilde{p}_s(\mathbf{r}, \mathbf{K}_0) = \int d^2K \tilde{A}(\mathbf{K}, \mathbf{K}_0) \exp(i\mathbf{K} \cdot \mathbf{R} + i\nu(K)z). \quad (\text{D1})$$

where $\tilde{A}(\mathbf{K}, \mathbf{K}_0)$ is the so-called scattering amplitude (see e.g., Refs. 26–29), $\nu(K) = \sqrt{k^2 - K^2}$, and k is the wave number in the upper medium. Note that this definition includes the zeroth-order component. It is convenient to introduce a scattering amplitude, A , for the perturbed part of the field, $p_s = p - p_0$, containing only higher-order components, as follows:¹⁴

$$p_s(\mathbf{r}, \mathbf{K}_0) = \int d^2K \nu^{-1}(K) A(\mathbf{K}, \mathbf{K}_0) \times \exp(i\mathbf{K} \cdot \mathbf{R} + i\nu(K)z), \quad (\text{D2})$$

where A is related to \tilde{A} by the equation

$$A(\mathbf{K}, \mathbf{K}_0) = [\tilde{A}(\mathbf{K}, \mathbf{K}_0) - \delta(\mathbf{K} - \mathbf{K}_0)V(\mathbf{K}_0)]\nu(\mathbf{K}_0), \quad (\text{D3})$$

with V being the zeroth-order reflection coefficient. The scattering amplitude, A , obeys the reciprocity relation

$$A(\mathbf{K}, \mathbf{K}_0) = A(-\mathbf{K}_0, -\mathbf{K}). \quad (\text{D4})$$

When the scattering amplitude or its perturbation have been found, all the basic characteristics of the scattered field in the upper medium can be determined. For example, the coherent reflection coefficient, $\bar{V}(\mathbf{K}_0)$, is defined by the fol-

lowing equation for the averaged scattering amplitude, or its coherent component

$$\langle \tilde{A}(\mathbf{K}, \mathbf{K}_0) \rangle = \delta(\mathbf{K} - \mathbf{K}_0) \bar{V}(\mathbf{K}_0). \quad (\text{D5})$$

The scattering amplitude or its perturbation can be used to obtain the scattering cross section, σ , through the equation

$$\langle A'(\mathbf{K}, \mathbf{K}_0) A'^*(\mathbf{K}', \mathbf{K}_0) \rangle = \delta(\mathbf{K} - \mathbf{K}') \sigma(\mathbf{K}, \mathbf{K}_0), \quad (\text{D6})$$

where

$$A'(\mathbf{K}, \mathbf{K}_0) = A(\mathbf{K}, \mathbf{K}_0) - \langle A(\mathbf{K}, \mathbf{K}_0) \rangle = \nu(\mathbf{K}_0) [\tilde{A}(\mathbf{K}, \mathbf{K}_0) - \langle \tilde{A}(\mathbf{K}, \mathbf{K}_0) \rangle] \quad (\text{D7})$$

is defined by the incoherent component of the scattering amplitude and it is assumed that the statistics of the scattering medium are stationary in the two transverse (horizontal) coordinates.

In this paper, $A(\mathbf{K}, \mathbf{K}_0)$ is called also the scattering amplitude for brevity. In the Born approximation we have $\langle A(\mathbf{K}, \mathbf{K}_0) \rangle = 0$ as all the medium fluctuations are defined so that they have vanishing average values. In this case, the scattering cross section is obtained through Eq. (48).

¹P. A. Crowther, "Some statistics of the sea-bed and acoustic scattering therefrom," in *Acoustics and Sea-Bed*, edited by N. G. Pace (Bath U.P., Bath, England, 1983), pp. 47–156.

²A. N. Ivakin, "Sound scattering by random volume inhomogeneities and small surface roughness of an underwater ground," *Voprosy sudostroeniya, Akustika*, No. 17, 20–25 (1983) (in Russian).

³D. R. Jackson and K. B. Briggs, "High-frequency bottom backscattering: roughness vs. sediment volume scattering," *J. Acoust. Soc. Am.* **92**, 962–977 (1992).

⁴N. G. Pace, "Low frequency acoustic backscatter from the sea bed," *Proc. Inst. Acoust.* **16**, 181–188 (1994).

⁵A. N. Ivakin, "Sound scattering by rough interface and volume inhomogeneities of the sea bottom," *Acoust. Phys.* **40**(3), 427–428 (1994).

⁶E. Y. T. Kuo, "Joint perturbation scattering characterization of a littoral ocean bottom reverberation: Theory, scattering strength predictions, and data comparisons," *IEEE J. Ocean Eng.* **20**, 198–210 (1995).

⁷D. Tang, "A note on scattering by a stack of rough interfaces," *J. Acoust. Soc. Am.* **99**, 1414–1418 (1996).

⁸A. N. Ivakin and Yu. P. Lysanov, "Underwater sound scattering by volume inhomogeneities of a bottom medium bounded by a rough surface," *Sov. Phys. Acoust.* **27**(3), 212–215 (1981).

⁹A. N. Ivakin, "Sound scattering by random inhomogeneities of stratified ocean sediments," *Sov. Phys. Acoust.* **32**(6), 492–496 (1986).

¹⁰S. T. McDaniel, "Effect of surficial sediment layering on high-frequency seafloor reverberation," *J. Acoust. Soc. Am.* **91**, 1353–1356 (1992).

¹¹P. D. Mourad and D. R. Jackson, "A model/data comparison for low-frequency bottom backscatter," *J. Acoust. Soc. Am.* **94**, 344–358 (1993).

¹²J. E. Moe and D. R. Jackson, "First-order perturbation solution for rough surface scattering cross section including the effects of gradients," *J. Acoust. Soc. Am.* **96**, 1748–1754 (1994).

¹³A. N. Ivakin, "Sound scattering by rough interfaces of layered media," in *Third International Congress on Air- & Structure-Borne Sound and Vibration* (International Public., Auburn, AL, 1994), Vol. 3, pp. 1563–1570.

¹⁴A. N. Ivakin, "Sound scattering by inhomogeneities of an elastic half space," *Sov. Phys. Acoust.* **36**(4), 377–380 (1990).

¹⁵H. H. Essen, "Scattering from a rough sedimental seafloor containing shear and layering," *J. Acoust. Soc. Am.* **95**, 1299–1310 (1994).

¹⁶D. R. Jackson and A. N. Ivakin, "Scattering from elastic sea beds: First-order theory," *J. Acoust. Soc. Am.* **103**, 336–345 (1998).

¹⁷A. N. Ivakin and D. R. Jackson, "Effects of shear elasticity on sea bed scattering: Numerical examples," *J. Acoust. Soc. Am.* **103**, 346–354 (1998).

¹⁸P. M. Morse and K. U. Ingard, *Theoretical Acoustics* (McGraw-Hill, New York, 1968).

¹⁹L. M. Brekhovskikh and O. A. Godin, *Acoustics of Layered Media I* (Springer-Verlag, Berlin, 1990).

- ²⁰S. M. Rytov, Yu. A. Kravtsov, and V. I. Tatarskii, *Principles of Statistical Radiophysics* (Springer-Verlag, Berlin, 1989).
- ²¹W. C. Chew, *Waves and Fields in Inhomogeneous Media* (VNR, New York, 1990).
- ²²M. L. Burrows, "A reformulated boundary perturbation theory in electromagnetism and in application to a sphere," *Can. J. Phys.* **45**, 1729–1743 (1967).
- ²³D. H. Berman, "Small-slope approximation for monostatic backscattering," *J. Acoust. Soc. Am.* **92**, 2093–2098 (1992).
- ²⁴*Ocean Acoustics*, edited by J. A. DeSanto (Springer-Verlag, Berlin, 1979).
- ²⁵E. Y. T. Kuo, "Wave scattering and transmission at irregular surfaces," *J. Acoust. Soc. Am.* **35**, 2135–2142 (1964).
- ²⁶G. G. Zipfel, Jr. and J. A. DeSanto, "Scattering of a scalar wave from a random rough surface: a diagrammatic approach," *J. Math. Phys.* **13**, 1903–1911 (1972).
- ²⁷E. I. Thorsos and D. R. Jackson, "The validity of the perturbation approximation for rough surface scattering using a Gaussian roughness spectrum," *J. Acoust. Soc. Am.* **86**, 261–277 (1989).
- ²⁸A. G. Voronovich, *Wave Scattering from Rough Surfaces* (Springer-Verlag, Berlin, 1994).
- ²⁹D. H. Berman, "Renormalization of propagation in a waveguide with rough boundaries," *J. Acoust. Soc. Am.* **92**, 309–314 (1992).

Sound propagation in dilute suspensions of rigid particles

S. Temkin

Department of Mechanical and Aerospace Engineering, Rutgers University, Piscataway, New Jersey 08855

(Received 20 February 1997; accepted for publication 8 September 1997)

This paper considers sound propagation in suspensions of rigid particles, when both heat and momentum are exchanged between the particles and the host fluid. A theory is developed for small-amplitude, single-frequency oscillatory motions, on the assumption that the temperature of each particle is uniform. This theory applies to dilute suspensions that have arbitrary particle and fluid material densities, and yields the attenuation and the speed of sound in the suspension in terms of the particles' velocity and temperature fluctuations. These quantities are not specified by the theory, but are available for some situations of interest which cover a very wide frequency range. In the particular case when the particle force and the heat transfer rate are not affected by the compressibility of the fluid, the particle's velocity and temperature are given by closed-form results that are used to obtain explicit formulas for the attenuation and sound speed. For this case, the present theory reproduces all fundamental predictions available in the literature, and yields new basic results where none seem to exist. Results are also shown for the important case when the particle force includes compressibility effects in the fluid. These provide a unified description for the attenuation and the dispersions which covers the viscous and the scattering regions, as well as the transition region between them. © 1998 Acoustical Society of America. [S0001-4966(98)01602-6]

PACS numbers: 43.35.Bf [HEB]

LIST OF SYMBOLS

e	suspension's internal energy per unit mass	$z = \sqrt{\omega a^2 / 2\kappa_f}$	ratio of particle radius to thermal penetration depth
e_f, e_p	internal energies, per unit mass, of fluid and of particles	$\bar{\alpha} = \alpha c_s(0) / \omega$	nondimensional attenuation based on the suspension's equilibrium sound speed
$k = \omega / c_s(0)$	wave number based on the suspension's equilibrium sound speed	$\hat{\alpha} = \alpha c_{sf} / \omega$	nondimensional attenuation based on the fluid's isentropic sound speed
P'_f	dilute-suspension fluid pressure fluctuation in a sound wave	$\hat{\alpha}_{tr}$	nondimensional translational attenuation coefficient
p	Pressure	$\hat{\alpha}_{th}$	nondimensional thermal attenuation coefficient
p'	imposed pressure fluctuation	β_f, β_p	coefficients of thermal expansion
p_f	fluid's thermodynamic pressure	$\hat{\beta} = \hat{\beta}_{tr} + \hat{\beta}_{th}$	dispersion coefficient, $c_{sf}^2 / c_s^2(0) - c_{sf}^2 / c_s^2(\omega)$
C_m	particle mass loading, ϕ_v / δ for dilute suspensions	$\hat{\beta}_{tr}$	translational dispersion coefficient
$c_s(0)$	suspension's equilibrium isentropic sound speed	$\hat{\beta}_{th}$	thermal dispersion coefficient
$c_s(\omega)$	suspension's frequency-dependent isentropic sound speed	γ_f, γ_p	specific heat ratios
c_{vf}, c_{vp}	specific heats at constant volume	$\delta = \rho_{f0} / \rho_{p0}$	material density ratio
c_{sf}, c_{sp}	isentropic sound speeds in fluid and particle materials	$\delta_{vf} = \sqrt{2\nu_f / \omega}$	viscous-wave penetration depth
c_{pf}, c_{pp}	specific heats at constant pressure	$\delta_{\kappa f} = \sqrt{2\kappa_f / \omega}$	thermal-wave penetration depth
F_D	fluid force on particle	$\delta\tau$	element of suspension volume
h	heat capacity ratio, $2\rho_p c_{pp} / 3\rho_f c_{pf}$	$\delta\tau_f, \delta\tau_p$	volumes of fluid and particles in a volume element of suspension
m_p	mass of one particle	Θ'_f	dilute-suspension fluid temperature fluctuation in sound wave
\dot{Q}_p	heat transfer rate to a particle	θ'_f	temperature fluctuation of disturbance produced by particle
T_0	ambient temperature	K_s	isentropic compressibility
T_f, T_p	fluid and particle temperatures	K_{sf}	isentropic compressibility of fluid phase
U_f	dilute-suspension fluid velocity in a sound wave	$K_s(0), K_{eq}$	equilibrium compressibility of the suspension
u_f, u_p	velocities of fluid and particulate phases	κ_f	thermal diffusivity
\dot{w}	compression work rate per unit mass of suspension	μ_f	dynamic viscosity
$y = \sqrt{\omega a^2 / 2\nu_f}$	ratio of particle radius to viscous penetration depth	ν_f	kinematic viscosity
		$\rho = \sigma_f + \sigma_p$	average suspension density
		ρ_f, ρ_p	material densities

σ_f, σ_p	densities of fluid and particulate <i>phases</i>
τ_d	dynamic relaxation time of particle, $2a^2/9\nu_f\delta$
τ_t	thermal relaxation time of particle, $(c_{pp}/c_{pf})a^2/3\kappa_p\delta$

ϕ_m	concentration of particles by mass
ϕ_v	concentration of particles by volume

INTRODUCTION

Among the motions that suspensions can sustain, the sound wave is one of the simplest and most general, owing to its linearity and to the wide variety of effects that play a role in its propagation. These include viscosity, compressibility, and heat conductivity, as well as particle and fluid inertia. Some of these can sometimes be disregarded because they are unimportant, for example, inertia effects in slowly changing Stokes flows, but for sound waves such effects must be generally considered. However, because of the linearity of acoustic equations these effects can be retained in the formulation, thereby providing another tool with which to study suspensions.

Of course, sound propagation in suspensions is an important subject on its own. As a result a large number of works dealing with the subject has been published dating back to Tyndall¹ and Rayleigh.² The initial work on the subject dealt with sound attenuation, and Sewell³ was the first to study it in viscous fluids. Since then many studies have appeared, but in spite of much work important questions remain. For rigid particle suspensions, these include the magnitude of the attenuation in liquid suspensions, and the dependence of the attenuation on the concentration.

In addition to attenuation, sound waves traveling in suspensions also experience dispersion. This has been given considerable attention in the cases of aerosols and bubbly liquids, but in the case of liquid suspensions of rigid particles, only a limited number of theoretical works have considered it from first principles. In these, various models are used to obtain a speed of propagation at finite frequencies. In some⁴⁻⁶ the suspension is treated as a two-phase fluid, whereas in others⁷⁻¹⁰ it is modeled as a porous solid whose rigidity can be varied by means of adjustable parameters. This model is more appropriate for sediments where a solid skeleton does exist, but for suspensions of *free* particles, such as those treated here, more fundamental theories can be developed, the two-phase model being an example. The main difficulties with this model are the mechanical and thermal interactions between the particulate and fluid phases. These play a central role in the problem, but there seems to be no consensus among investigators as to what values they should have. An exception is the case of dilute aerosols, where those interactions are well understood.^{4,11,12}

The dispersion problem has also been treated using the well-known effective-medium sound speed, known as Wood's equation¹³ (e.g., Refs. 14 and 15) but as this author has recently shown,¹⁶ that equation is only applicable to low-frequency waves in isothermal suspensions. Some authors (e.g., Fukumoto and Izuyama¹⁷ and Holmes *et al.*^{18,19}) obtain a frequency-dependent sound speed from a complex wave number obtained by the simple, but *ad hoc*, procedure of

adding to this sound speed an imaginary part that is equal to an attenuation coefficient.

Further methods used to obtain the speed of sound include those based on scattering theories (e.g., Refs. 20 and 21), and on the causality relations of Kramers and Kronig. The latter method has been used to study propagation in bubbly liquids,²² rigid-particle gaseous suspensions,¹² and phase-changing fluids.²³

In this work we present a new theory for the attenuation and the dispersion of sound in *dilute* suspensions of rigid particles having arbitrary densities relative the fluid. The results we obtain are mathematically simple, and give the attenuation and dispersion in terms of the particle velocity and temperature. Known values for these quantities are used to obtain explicit results for the attenuation and dispersion. These reproduce every known fundamental result and produce new ones in cases where no fundamental results exist.

I. ADIABATIC COMPRESSIBILITY

In what follows, we consider suspensions of rigid particles in fluids under the assumption that the particles have uniform temperatures. This assumption, like that of rigidity, is not met by actual particles if the frequency is very large, but in a fairly wide range, some solid particles can be treated as rigid bodies having a uniform but time-dependent temperature. An alternative approach leading to similar results would be in terms of a volume average of the particle temperature

The thermal and dynamic response of the suspension to applied forces may be studied in terms of the suspension's compressibility. To compute this, we consider a suspension enclosed by adiabatic walls, and focus our attention on a small volume element in it. At some time this volume element has a value $\delta\tau$ and contains a certain number of particles that occupy a volume $\delta\tau_p$. The corresponding volume occupied by the fluid is $\delta\tau_f$, so that $\delta\tau = \delta\tau_f + \delta\tau_p$. When the suspension moves under the influence of an imposed pressure, this volume element is deformed, and the deformation can, in principle, be quantified in terms of an adiabatic compressibility defined by

$$K_s = -\frac{1}{\delta\tau} \frac{d(\delta\tau)}{dp}. \quad (1)$$

This can be used in dynamic conditions, provided the physical quantities appearing in it can be properly defined for them.

A. Equilibrium conditions

Consider first sound waves whose frequency is so small that the suspension is in thermodynamic equilibrium. Here,

one can obtain the suspensions' compressibility in terms of its mean density ρ and of its relaxed-equilibrium *isentropic* sound speed $c_s(0)$ by means of

$$K_s(0) = \frac{1}{\rho c_s^2(0)}. \quad (2)$$

The suspension density is given by the sum of the particulate-phase density, $\sigma_p = \phi_v \rho_p$, and the fluid-phase density, $\sigma_f = (1 - \phi_v) \rho_f$. Thus

$$\rho = (1 - \phi_v) \rho_f + \phi_v \rho_p, \quad (3)$$

where ϕ_v is the volume concentration of particles and ρ_f and ρ_p are the densities of the fluid and particle materials, respectively.

The equilibrium isentropic speed, $c_s(0)$, cannot generally be written in such a simple manner as (3), but may be obtained from an equilibrium result for suspensions of elastic particles that applies when mass transfer, surface tension, and chemical and electrical effects are absent. That result is¹⁶

$$\frac{c_{sf}^2}{c_s^2(0)} = \gamma_f \frac{1 - \phi_v}{1 - \phi_m} \left(1 - \phi_v + \phi_v \frac{\rho_f c_{sf}^2 / \gamma_f}{\rho_p c_{sp}^2 / \gamma_p} \right) - (\gamma_f - 1) \frac{(1 - \phi_v + \phi_v \beta_p / \beta_f)^2}{1 + \phi_m (c_{pp} / c_{pf} - 1)}. \quad (4)$$

Here, ϕ_m is the mass concentration of particles, c_{sf} and c_{sp} are the isentropic sound speeds in the fluid and particle materials, γ_f and γ_p are the corresponding specific heat ratios, β_f and β_p are the coefficients of thermal expansion, and c_{pf} and c_{pp} are the fluid and particle specific heats at constant pressure. Because the propagation of small-amplitude sound waves in a suspension represents a motion around an equilibrium state in the suspension, it is useful to regard the speed $c_s(0)$ as the reference speed, although the corresponding fluid speed, c_{sf} , is often used instead. Now, for rigid particles, $1/c_{sp}^2 \rightarrow 0$ and $\beta_p \rightarrow 0$, so that

$$\frac{c_{sf}^2}{c_s^2(0)} = (1 - \phi_v)^2 (1 + C_m) \frac{1 + \gamma_f C_m c_{pp} / c_{pf}}{1 + C_m c_{pp} / c_{pf}}, \quad (5)$$

where we have expressed the mass concentration in terms of the mass loading, C_m , by means of $\phi_m = C_m / (1 + C_m)$, and have used $\rho = \rho_f (1 - \phi_v) (1 + C_m)$. The equilibrium adiabatic compressibility is, therefore,

$$K_s(0) = K_{sf} \frac{1 + \gamma_f C_m c_{pp} / c_{pf}}{1 + C_m c_{pp} / c_{pf}}, \quad (6)$$

where

$$K_{sf} = \frac{1 - \phi_v}{\rho_f c_{sf}^2}. \quad (7)$$

It should be added that although (5) was obtained by taking the limit $c_{sp} \rightarrow \infty$ in (4), it applies to real situations, provided the ratios of particle compressibility to fluid compressibility, and of particle to fluid thermal expansions, are very small. These conditions are met in some cases of practical interest. For example, in a suspension of kaolinite particles in water at STP, the ratio of compressibilities is equal to 0.05. On the other hand, the ratio of thermal expansion coefficients is of

order one and this will result in some differences if the volume concentration is not small. However, at least in the example given, the differences will be small because, in water, $\gamma_f - 1$ is small at normal temperatures.

B. Small-amplitude oscillations

For monochromatic acoustic motions, it is convenient to express the time dependence as $\exp(-i\omega t)$. When this is done, all variables become complex functions of the frequency. Thus, for example, $K_s \rightarrow \tilde{K}_s(\omega)$, where the tilde is used to represent a complex value. In analogy with (2) we write \tilde{K}_s as $\tilde{K}_s(\omega) = [\rho_0 \tilde{c}_s^2(\omega)]^{-1}$, where $\tilde{c}_s(\omega)$ is a complex sound speed and ρ_0 is the mean value of ρ . The main reason for a complex compressibility is that at finite frequencies there is attenuation. Because of this, it is preferable to work with a complex wave number, $\tilde{k} = \omega / \tilde{c}_s(\omega)$, where $\tilde{k} = \omega / c_s(\omega) + i\alpha(\omega)$, where α is the amplitude-attenuation coefficient, and $c_s(\omega)$ is real and represents the frequency-dependent speed of propagation. In terms of this wave number, the compressibility becomes $\tilde{K}_s(\omega) = K_s(0) \times [\tilde{k} c_s(0) / \omega]$, where $K_s(0)$ is explicitly given by (6). In general, there will be several irreversible mechanisms simultaneously at work, for example, viscosity and heat conductivity, each producing some changes in $\tilde{K}_s(\omega)$. To compute these changes, we make the assumption that they are additive. Thus, for each irreversible mechanism, we are interested in its contribution to $\tilde{K}_s(\omega) / K_s(0) - 1$. Taking the real and imaginary parts of this, and remembering that α must be positive in order for the amplitude of the waves to decay as they travel, we obtain

$$\frac{c_s^2(0)}{c_s^2(\omega)} - \bar{\alpha}^2 = 1 + \Re[\tilde{K}_s(\omega) / K_s(0) - 1]_1 + \Re[\tilde{K}_s(\omega) / K_s(0) - 1]_2 + \dots, \quad (8)$$

$$2\bar{\alpha} \frac{c_s(0)}{c_s(\omega)} = |\Im\{\tilde{K}_s(\omega)\} / K_s(0)|_1 + |\Im\{\tilde{K}_s(\omega)\} / K_s(0)|_2 + \dots, \quad (9)$$

where $\bar{\alpha} = \alpha c_s(0) / \omega$. It should be noted that in taking the absolute value of each separate term in (9) we have assumed that the corresponding irreversible mechanisms are independent of one another. If the mechanisms are coupled, then the absolute sign should be applied to the sum of the separate imaginary parts.

If the right-hand sides of these equations are denoted by $X(\omega)$ and $Y(\omega)$, respectively, we have

$$\frac{c_s^2(0)}{c_s^2(\omega)} - \bar{\alpha}^2 = X(\omega) \quad (10a)$$

and

$$2\bar{\alpha} \frac{c_s(0)}{c_s(\omega)} = Y(\omega). \quad (10b)$$

These may be easily solved for $\bar{\alpha}$ and $c_s(\omega)$ for any value of $X(\omega)$ and $Y(\omega)$. However, in some situations there may be reason to expect that attenuation per wavelength is very

small. In them we may neglect $\bar{\alpha}^2$ *a priori*, and obtain

$$\frac{c_s^2(0)}{c_s^2(\omega)} = X(\omega) \quad (11a)$$

and

$$\bar{\alpha} = \frac{1}{2} Y(\omega) / \sqrt{X(\omega)}. \quad (11b)$$

This pair gives a good approximation to the exact solution of (10a) and (10b) when $\bar{\alpha}$ is small. Of course, if the speed changes little throughout the frequency range, the last equation gives the simpler form

$$\bar{\alpha} = \frac{1}{2} \Im\{\tilde{K}_s(\omega)\}/K_s(0)|_1 + \frac{1}{2} \Im\{\tilde{K}_s(\omega)\}/K_s(0)|_2 + \dots \quad (12)$$

These relationships apply to general compressible media undergoing small changes about an equilibrium condition.

II. RIGID-PARTICLE SUSPENSIONS

We now consider the adiabatic compressibility for a suspension of rigid particles which is executing small-amplitude *translational* oscillations, produced, for example, by a small-amplitude, one-dimensional oscillatory motion of a plane wall. We will be interested only in changes to the compressibility that result from the particles' presence. Thus, the attenuation and dispersion of sound that viscosity and heat conductivity produce in the fluid alone will be ignored. Such effects are well understood and are small at frequencies that are of interest in suspension dynamics.

Now, in a suspension that is externally driven, both particles and fluid experience translational and temperature oscillations. Both of these fluctuations affect the suspension's compressibility, but because the oscillations are linear, the corresponding effects may be calculated separately. That is, we can consider contribution due to the translational oscillations without including temperature effects, and vice versa. The contribution due to the translational oscillations is simpler and is considered first.

A. Effects of relative translational oscillations

Consider a small volume element of suspension, $\delta\tau$, containing a large number of *identical* particles. The total mass of fluid and particles contained in $\delta\tau$ is $\rho\delta\tau$, where ρ is the average density of the suspension. Because of the oscillations, the fluid and particles generally move with different velocities, so that equilibrium does not generally exist. However, if we define $\delta\tau$ so that it contains the same fluid and particles during the motion, then the *total* mass contained in $\delta\tau$ will be conserved. Hence, the Lagrangian rate of change of the total mass in $\delta\tau$ is zero, or

$$\frac{d(\rho\delta\tau)}{dt} = 0. \quad (13)$$

Expanding this,

$$\frac{1}{\delta\tau} \frac{d(\delta\tau)}{dt} = -\frac{1}{\rho} \frac{d\rho}{dt}, \quad (14)$$

where $\rho\delta\tau = \delta M$ is the total mass in the element.

In *strict* equilibrium, the linearized rate of change of the density can be expressed as $-\rho_0(\partial u/\partial x)$, where $u = u_p = u_f$ is the velocity of *both* particles and fluid. This would give, in equilibrium,

$$\frac{1}{\delta\tau} \frac{d(\delta\tau)}{dt} = \frac{\partial u}{\partial x}. \quad (15)$$

Now, if the ambient pressure is ρ_0 , the total pressure is $p = p_0 + p'$, but since the changes have small magnitude, we have $|p'| \ll p_0$. Thus, $dp/dt = \partial p'/\partial t$. Dividing (15) by dp/dt we have an equilibrium compressibility

$$K_{\text{eq}} = -\frac{\partial u/\partial x}{\partial p'/\partial t}. \quad (16)$$

For a monochromatic time dependence, $\partial p'/\partial t = -i\omega\bar{p}'$. Further in a plane sound wave $\partial u/\partial x = ik\bar{u}$, where $k = \omega/c_s(0)$. Finally, the pressure and the velocity in a sound wave are related by means of $p' = \rho_0 c_s(0)u$. Hence,

$$K_{\text{eq}} = \frac{1}{\rho_0 c_s^2(0)}. \quad (17)$$

This is equal to $K_s(0)$, so that the strict thermodynamic equilibrium result is recovered.

Consider now a condition which is away from equilibrium. Here, the particles' and fluid velocities are generally different and it is advantageous to regard the suspension as a two-phase fluid, having densities σ_p and σ_f , defined as average values over the volume element, each phase obeying its own continuity equation. In linearized form these are

$$\frac{d\sigma_f}{dt} = -\sigma_{f0} \frac{\partial u_f}{\partial x} \quad (18a)$$

and

$$\frac{d\sigma_p}{dt} = -\sigma_{p0} \frac{\partial u_p}{\partial x}, \quad (18b)$$

where u_p is the velocity of each of the particles in the element, and where σ_{f0} and σ_{p0} are the linearized fluid-phase and particulate-phase densities. The velocity u_f appearing in (18a) is the fluid velocity in the element, also defined by an average value. Now, the suspension density is given by $\rho = \sigma_f + \sigma_p$, so that

$$\frac{d\rho}{dt} = -\left(\sigma_{f0} \frac{\partial u_f}{\partial x} + \sigma_{p0} \frac{\partial u_p}{\partial x}\right). \quad (19)$$

As before, we obtain the compressibility by dividing through $dp/dt = \partial p'/\partial t$. This gives

$$K_s = -\frac{\sigma_{f0}/\rho_0}{\partial p'/\partial t} \left[\frac{\partial u_f}{\partial x} + \frac{\sigma_{p0}}{\sigma_{f0}} \frac{\partial u_p}{\partial x} \right]. \quad (20)$$

For acoustic motions, $\partial/\partial x = ik$, where the exact value of k is complex, owing to the dissipation that must exist when a relative velocity exists. However, because the motions considered are near equilibrium, we may, on the right-hand side of (20), equate k to $\omega/c_s(0)$, where, as before, $c_s(0)$ is the relaxed-equilibrium sound speed in the suspension. Similarly, the rate of change of the pressure is equal to $-i\omega\bar{p}'$,

and since the wave is plane, we have $\tilde{p}' = \rho_0 c_s(0) \tilde{u}$. This gives

$$\tilde{K}_s = \frac{1}{\rho_0 c_s^2(0)} \frac{\sigma_{f0}}{\rho_0} \left[\frac{\tilde{u}_f}{\tilde{u}} + \frac{\sigma_{p0}}{\sigma_{f0}} \frac{\tilde{u}_p}{\tilde{u}} \right]. \quad (21)$$

The pressure \tilde{p}' used above, and the related velocity \tilde{u} , are imposed on the suspension. That is, they are the pressure and velocity produced by some plane boundary, whose amplitude can be adjusted so as to produce any desired small-amplitude velocity. There are two meaningful choices for \tilde{u} . One is the velocity that the whole suspension has at low frequencies. The other is the velocity that the fluid would have in a dilute suspension. Because it is of interest to compare particle and fluid velocities at the same, finite frequency, we choose the latter, and let \tilde{u} be the fluid velocity in a dilute suspension, \tilde{U}_f . Thus,

$$\tilde{K}_s = \frac{1}{\rho_0 c_s^2(0)} \frac{\sigma_{f0}}{\rho_0} \left[\frac{\tilde{u}_f}{\tilde{U}_f} + \frac{\sigma_{p0}}{\sigma_{f0}} \frac{\tilde{u}_p}{\tilde{U}_f} \right]. \quad (22)$$

Consider now the velocity \tilde{u}_f , defined earlier as an average fluid velocity in the suspension element. Although the definition might include particle interaction effects, these effects are not known for sound waves. We will therefore consider only small concentrations, so that $\tilde{u}_f = \tilde{U}_f$. Hence

$$\tilde{K}_s = \frac{1}{\rho_0 c_s^2(0)} \frac{\sigma_{f0}}{\rho_0} \left[1 + \frac{\sigma_{p0}}{\sigma_{f0}} \frac{\tilde{u}_p}{\tilde{U}_f} \right]. \quad (23)$$

The density ratios appearing here can be expressed as $\sigma_{f0}/\rho_0 = (1 + C_m)^{-1}$ and $\sigma_{p0}/\sigma_{f0} = C_m$, respectively. Hence

$$\tilde{K}_s = \frac{K_s(0)}{1 + C_m} \left(1 + C_m \frac{\tilde{u}_p}{\tilde{U}_f} \right), \quad (24)$$

where we have used (6). It should be noted that the mass loading can have finite values in some types of suspensions, e.g., dusty gases, even if the volume concentration is small. It is therefore necessary to retain, at this stage, quantities which are of the order of C_m . Further simplification is possible for suspensions so dilute that for all values of the density ratio, $\delta = \rho_f/\rho_p$, we have $\phi_v \ll \delta$.

Thus, the contribution to the complex compressibility of a dilute rigid-particle suspension due to the translational oscillations of the particles is

$$\left(\frac{\tilde{K}_s}{K_s(0)} - 1 \right)_{\text{tr}} = \frac{C_m}{1 + C_m} \left(\frac{\tilde{u}_p}{\tilde{U}_f} - 1 \right). \quad (25)$$

This simple result shows the importance of the relative motion between fluid and particles in determining the acoustical properties of a suspension. When there is no relative motion, we recover the equilibrium result $\tilde{K}_s = K_s(0)$. For other values of \tilde{u}_p differences occur, and these produce attenuation and dispersion, as prescribed by (10a) and (10b).

B. Effects of relative temperature oscillations

The changes of suspension's compressibility due to thermal effects are due to the oscillations of the particles' temperature, relative to the fluid. These result in irreversible heat

transfer between particles and fluid. The method used to calculate these effects is similar to that used for the translational case, with the temperature playing the role of the velocity. As with the translational case, thermal effects can be calculated separately from other effects that might be present. Now, in Sec. I we gave the equilibrium sound speed and compressibility for rigid-particle suspensions. Those results were obtained on the assumption that the temperature was uniform throughout. Outside equilibrium, the particles and the fluid are generally at different temperatures, and it is not possible to define a temperature for the suspension as a whole. However, for a wide frequency range, the temperature of all the particles in a suspension element can be taken to have a uniform (but time dependent) value T_p . The fluid in the element, on the other hand, does not have a uniform temperature owing to the presence of the particles, but we will assume that one can be defined in an average sense. This value will be denoted by T_f ; it will depend on the fluid density and pressure, ρ_f and p_f , respectively, also defined in some average sense. These quantities are sufficient to determine the internal energies of the particles and of the fluid.

As before, we consider volume element $\delta\tau$ of suspension being deformed by the passage of a sound wave. Because the deformation is adiabatic, the first law of thermodynamics gives

$$\frac{d(\delta E)}{dt} = \dot{W}, \quad (26)$$

where δE is the internal energy of the element and \dot{W} is the rate at which work is done on it. Since the energies are additive and the total mass is conserved, changes in the internal energy may be written as $d(\delta E) = de \delta M = (1 - \phi_m) de_f \delta M + \phi_m de_p \delta M$, where δM is the mass contained in $\delta\tau$, and e_f and e_p are the internal energy of the fluid per unit mass of fluid, and per unit mass of particles, respectively. Thus,

$$\frac{de}{dt} = (1 - \phi_m) \frac{de_f}{dt} + \phi_m \frac{de_p}{dt} = \dot{w}. \quad (27)$$

The internal energy of the particles depends only on their temperature, so that $de_p = c_{pp} dT_p$. On the other hand, the energy of the fluid depends on two variables, for example, the temperature, T_f , and the density, ρ_f . Thus,

$$de_f = c_{vf} dT_f + \frac{1}{\rho_f} (p_f - T_f \rho_f \beta_f c_{Tf}^2) d\rho_f, \quad (28)$$

where c_{Tf} is the isothermal sound speed in the fluid. The changes of fluid density may be expressed as

$$d\rho_f = -\rho_f \beta_f dT_f + \frac{1}{c_{Tf}^2} dp_f. \quad (29)$$

Substituting (28) and (29) into (27), we obtain

$$\begin{aligned} (1 - \phi_m) \left[c_{pf} \frac{dT_f}{dt} - \frac{T_f \beta_f}{\rho_f} \frac{dp_f}{dt} \right] + \phi_m c_{pp} \frac{dT_p}{dt} \\ = \dot{w} - (1 - \phi_m) \frac{p_f}{\rho_f} \frac{d\rho_f}{dt}, \end{aligned} \quad (30)$$

where we used the general-substance relationship between specific heats, $c_v = c_p - T\beta^2 c_T^2$.

Consider now \dot{w} . It represents the rate at which work is done on the suspension element, per unit mass, and is given by $\dot{w} = -p[d(\delta\tau)/dt]/\delta M$, where ρ is pressure imposed by a sound wave resulting from the motion of some plane wall, as described earlier. As we did with the imposed velocity, we will later select an appropriate value for this pressure. Now, since the particles are rigid, the only change of volume that can take place in the element occurs in the fluid. That is, $d(\delta\tau) = d(\delta\tau_f)$. The volume occupied by the fluid is $\delta\tau_f = (1 - \phi_m)\delta M/\rho_f$. Therefore $\dot{w} = p(1 - \phi_m)(d\rho_f/dt)/\rho_f^2$. Substituting this into (30) gives

$$\frac{dp_f}{dt} = \frac{\rho_f}{T_f\beta_f} \left[c_{pf} \frac{dT_f}{dt} + C_m c_{pp} \frac{dT_p}{dt} - \frac{p - p_f}{\rho_f^2} \frac{d\rho_f}{dt} \right]. \quad (31)$$

The changes of the fluid density can also be expressed in terms of the temperatures. Thus, using (29) and (31), we obtain

$$\frac{d\rho_f}{dt} = \frac{\rho_f^2 [c_{vf}(dT_f/dt) + C_m c_{pp}(dT_p/dt)]}{\rho_f T_f \beta_f c_{Tf}^2 + p - p_f}. \quad (32)$$

These changes can be used in the equation defining the compressibility. Thus, using $d(\delta\tau) = -\rho\delta\tau(1 - \phi_m)d\rho_f/\rho_f^2$, we can write

$$K_s = \frac{(1 - \phi_v)}{\rho_f} \frac{d\rho_f/dt}{dp/dt}. \quad (33)$$

All changes in a sound wave are small. That is, if $p = p_0 + p'$, $p_f = p_0 + p'_f$, $\rho_f = \rho_{f0} + \rho'_f$, $T_f = T_0 + T'_f$, and $T_p = T_0 + T'_p$, then all primed quantities are small compared to the corresponding equilibrium values. Now, as with the imposed translational velocity, we take p' to be equal to P'_f , the pressure changes in a dilute suspension. This is obtained from (31) by putting T'_f equal to the corresponding change in a dilute suspension, Θ'_f , and by linearizing the result. Thus,

$$\frac{dP'_f}{dt} = \frac{\rho_{f0}}{T_0\beta_f} \left[c_{pf} \frac{d\Theta'_f}{dt} + C_m c_{pp} \frac{dT'_p}{dt} \right].$$

Similarly, we linearize (32), noting that the pressure difference in the second term of the denominator may be neglected in comparison with the first term. Hence,

$$K_s = K_{sf} \frac{c_{vf}(dT'_f/dt) + C_m c_{pp}(dT'_p/dt)}{c_{pf}(d\Theta'_f/dt) + C_m c_{pp}(dT'_p/dt)}. \quad (34)$$

When the changes are monochromatic, this becomes

$$\tilde{K}_s = K_s(0) \frac{1 + C_m c_{pp}/c_{pf}}{1 + \gamma_f C_m c_{pp}/c_{pf}} \left[\frac{\tilde{T}'_f}{\tilde{\Theta}'_f} + \gamma_f C_m \frac{c_{pp}}{c_{pf}} \frac{\tilde{T}'_p}{\tilde{\Theta}'_f} \right] \left/ \left[1 + C_m \frac{c_{pp}}{c_{pf}} \frac{\tilde{T}'_p}{\tilde{\Theta}'_f} \right] \right., \quad (35)$$

where we have used (6). Finally, if we limit (35) to dilute suspensions, we have $\tilde{T}'_f = \tilde{\Theta}'_f$. Therefore, the thermal contribution to the changes in compressibility is given by

$$\left(\frac{\tilde{K}_s}{K_s(0)} - 1 \right)_{\text{th}} = \frac{(\gamma_f - 1)C_m c_{pp}/c_{pf}}{1 + \gamma_f C_m c_{pp}/c_{pf}} \frac{\tilde{T}'_p/\tilde{\Theta}'_f - 1}{1 + C_m(c_{pp}/c_{pf})\tilde{T}'_p/\tilde{\Theta}'_f}. \quad (36)$$

This is the thermal contribution to the compressibility changes; it vanishes when the particle's temperature equals that of the fluid, and when the fluid's specific heat ratio is equal to unity, as is nearly the case in many liquid suspensions.

III. TOTAL CHANGES

We now use the above results to obtain the adiabatic compressibility at *finite* frequencies, that is, outside equilibrium. Since the main interest here is in the sound speed and the attenuation, we use the basic equations derived in Sec. II to express those quantities in terms of the compressibility changes. Adopted to this case, those equations give

$$\frac{c_s^2(0)}{c_s^2(\omega)} - \bar{\alpha}^2 = 1 + \frac{C_m [\Re(\tilde{u}_p/\tilde{U}_f) - 1]}{1 + C_m} + \frac{(\gamma_f - 1)C_m c_{pp}/c_{pf}}{1 + \gamma_f C_m c_{pp}/c_{pf}} \times \Re \frac{\tilde{T}'_p/\tilde{\Theta}'_f - 1}{1 + C_m(c_{pp}/c_{pf})\tilde{T}'_p/\tilde{\Theta}'_f}, \quad (37a)$$

$$2\bar{\alpha} \frac{c_s(0)}{c_s(\omega)} = \frac{C_m |\Im(\tilde{u}_p/\tilde{U}_f)|}{1 + C_m} + \frac{(\gamma_f - 1)C_m c_{pp}/c_{pf}}{1 + \gamma_f C_m c_{pp}/c_{pf}} \times \left| \Im \frac{\tilde{T}'_p/\tilde{\Theta}'_f - 1}{1 + C_m(c_{pp}/c_{pf})\tilde{T}'_p/\tilde{\Theta}'_f} \right|. \quad (37b)$$

These equations are the most important contribution of this work. They succinctly define the attenuation and dispersion of sound in terms of the particle-to-fluid velocity and temperature ratios. If these are known in the entire frequency range, (37a) and (37b) provide the solution to the propagation problem in dilute suspensions of rigid particles.

IV. EXPLICIT RESULTS FOR $\phi_v \rightarrow 0$

To assess the validity of the results, we consider them in those situations where the velocity and temperature ratios are known. All of these refer to a single particle and thus are restricted to very small volume concentrations. For these, some results exist in the literature for the attenuation and the dispersion, so that comparison is possible.

Thus, we consider suspensions in which the volume concentration is so small that the mass loading, $C_m \approx \phi_v/\delta$, may be considered a small quantity for all values of the density ratio δ . Because the volume concentration is very small, it is convenient to use the isentropic sound speed in the fluid alone, c_{sf} , as the reference velocity instead of $c_s(0)$. Thus, when $\phi_v \ll 1$, (37a) and (37b) reduce to

$$\frac{c_{sf}^2}{c_s^2(\omega)} - \hat{\alpha}^2 = \frac{c_{sf}^2}{c_s^2(0)} + C_m \left[\Re \left(\frac{\tilde{u}_p}{\tilde{U}_f} \right) - 1 \right] + C_m(\gamma_f - 1) \frac{c_{pp}}{c_{pf}} \left[\Re \left(\frac{\tilde{T}'_p}{\tilde{\Theta}'_f} \right) - 1 \right], \quad (38)$$

$$2\hat{\alpha} \frac{c_{sf}}{c_s(\omega)} = C_m \left| \Im \frac{\tilde{u}_p}{\tilde{U}_f} \right| + C_m(\gamma_f - 1) \frac{c_{pp}}{c_{pf}} \left| \Im \frac{\tilde{T}'_p}{\tilde{\Theta}'_f} \right|, \quad (39)$$

where

$$c_{sf}^2/c_s^2(0) = 1 - 2\phi_v + \phi_v/\delta + (\gamma_f - 1)\phi_v\rho_{p0}c_{pp}/\rho_{f0}c_{pf} \quad (40)$$

is the low concentration limit of the speed ratio, (4), for rigid particles and $\hat{\alpha} = \alpha c_{sf}/\omega$.

If the right-hand sides of (38) and (39) are known, they may be solved exactly for the attenuation and for the speed. However, when $\hat{\alpha}$ is very small, its square may be neglected in (38), and the speed ratio in the left-hand side of (39) may be put equal to 1. The equations then become decoupled, and, furthermore, the attenuation and speed changes produced by the translational and thermal effects also become uncoupled. To emphasize this, we introduce a dispersion coefficient $\hat{\beta}$ which measures the departures of the sound speed from its equilibrium value by means of

$$\hat{\beta} = \frac{c_{sf}^2}{c_s^2(0)} - \frac{c_{sf}^2}{c_s^2(\omega)}. \quad (41)$$

In terms of $\hat{\beta}$, the first of our small dissipation results can be written as $\hat{\beta} = \hat{\beta}_u + \hat{\beta}_{th}$, where

$$\hat{\beta}_u = C_m [1 - \Re(\tilde{u}_p/\tilde{U}_f)] \quad (42a)$$

and

$$\hat{\beta}_{th} = C_m(\gamma_f - 1) \frac{c_{pp}}{c_{pf}} [1 - \Re(\tilde{T}'_p/\tilde{\Theta}'_f)]. \quad (42b)$$

The second equation can be similarly split. Thus, we put $\hat{\alpha} = \hat{\alpha}_u + \hat{\alpha}_{th}$, where

$$\hat{\alpha}_u = \frac{1}{2} C_m |\Im\{\tilde{u}_p/\tilde{U}_f\}| \quad (43a)$$

and

$$\hat{\alpha}_{th} = \frac{1}{2} (\gamma_f - 1) C_m \frac{c_{pp}}{c_{pf}} |\Im\{\tilde{T}'_p/\tilde{\Theta}'_f\}|. \quad (43b)$$

Since the mass loading is, by assumption, small, and since the magnitude of the complex ratios is, at most, equal to 1, we see that the attenuation is small, as assumed.

We now consider the particle velocity and temperature ratios. The first is available in the literature for a variety of limiting cases. The temperature ratio is available for low frequencies, and a more general theory is developed in the Appendix. For simplicity we consider, explicitly, only the case where the particles are much smaller than the wavelength of the sound wave. This covers a very wide frequency range which includes those frequencies where the most significant changes in speed occur. It is also the range where most existing results for the attenuation and dispersion can

be given in closed form. A more complete result, based on a velocity ratio that includes fluid compressibility effects²⁴ is given in graphical form.

Now, when the wavelength is much larger than the particle radius, the force acting on a particle oscillating with small amplitude, and the corresponding heat transfer rate can be calculated from incompressible-fluid theory. The incompressible force on a single, rigid sphere executing monochromatic translational oscillations in a fluid that is itself oscillating is given by (see, for example, Refs. 25 and 26)

$$F_D = m_p \delta \frac{dU_f}{dt} - 6\pi\mu_f a(1+y)(u_p - U_f) - \frac{1}{2} m_p \delta \left(1 + \frac{9}{2y} \right) \frac{d(u_p - U_f)}{dt}, \quad (44)$$

where m_p is the mass of one particle, and

$$y = \sqrt{\omega a^2/2\nu_f} \quad (45)$$

is the ratio of particle radius, a , to the fluid's viscous penetration depth, $\delta_{vf} = \sqrt{2\nu_f/\omega}$.

In comparable conditions, the heat transfer rate to a small, uniform temperature sphere immersed in a fluid whose temperature *far* from the sphere is Θ_f , is derived in the Appendix and is given by

$$\dot{Q}_p = -4\pi k_f a(1+z)(T_p - \Theta_f) - \frac{3\delta}{2} \frac{m_p c_{pf}}{z} \frac{d(T_p - \Theta_f)}{dt}. \quad (46)$$

Here $z = \sqrt{\omega a^2/2\kappa_f}$ is the thermal counterpart to y , and is related to it by means of $z = \text{Pr}_f^{1/2} y$, where Pr_f is the Prandtl number of the fluid.

The particle velocity and temperature can be obtained by using (44) and (46) in the corresponding conservation equations for the particle. These are, respectively

$$m_p \frac{du_p}{dt} = F_D \quad (47a)$$

and

$$m_p c_{pp} \frac{dT_p}{dt} = \dot{Q}_p. \quad (47b)$$

Because accurate results for *both* the dispersion and the attenuation are known only for the case of dusty gases, or aerosols, we consider this case first.

A. Aerosols

Here the particle force and heat transfer rate to an aerosol particle are well approximated by the simple expressions

$$F_D = -6\pi\mu_f a(u_p - U_f) \quad (48a)$$

and

$$\dot{Q}_p = -4\pi k_f a(T_p - \Theta_f). \quad (48b)$$

These follow from (44) and (46) when $\delta \ll 1$ and the frequency is not too large so that y may be considered small, and give

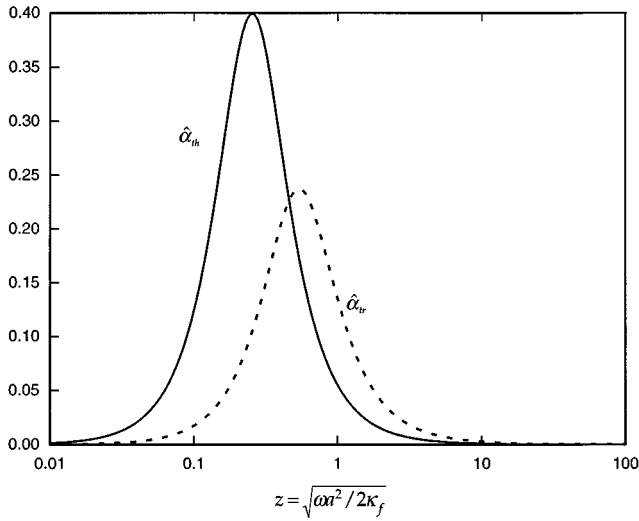


FIG. 1. Scaled thermal and translational attenuation coefficients of an aerosol composed of water droplets in air: —: thermal attenuation; ----: translational attenuation.

$$\frac{\tilde{u}_p}{\tilde{U}_f} = \frac{1}{1 - i\omega\tau_d} \quad (49a)$$

and

$$\frac{\tilde{T}'_p}{\tilde{\Theta}'_f} = \frac{1}{1 - i\omega\tau_t}, \quad (49b)$$

where $\tau_d = 2a^2/9\nu_f\delta$ and $\tau_t = (c_{pp}/c_{pf})a^2/3\kappa_p\delta$ are the dynamic and thermal relaxation times of a rigid spherical particle. Equations (49a) and (49b) are all that is needed to obtain the speed and attenuation. Thus, taking their real and imaginary parts and substituting them into (38) and (39), we obtain

$$\frac{c_{sf}^2}{c_s^2(\omega)} - 1 = C_m \left[\frac{1}{1 + \omega^2\tau_d^2} + \frac{(\gamma_f - 1)c_{pp}/c_{pf}}{1 + \omega^2\tau_t^2} \right], \quad (50)$$

$$\hat{\alpha} = \frac{1}{2} C_m \left[\frac{\omega\tau_d}{1 + \omega^2\tau_d^2} + (\gamma_f - 1) \frac{c_{pp}}{c_{pf}} \frac{\omega\tau_t}{1 + \omega^2\tau_t^2} \right]. \quad (51)$$

Equations (50) and (51) are identical to those obtained some time ago by Temkin and Dobbins¹⁰ on the basis of Marble's dusty gas system of equations.²⁷ They are also equal to those derived recently by the author on the basis of the Kramer-Kronig equations.²² Further, they have been confirmed experimentally.²⁸ Although graphs showing these results have been given before, we display them, again, in Figs. 1 and 2 to point out the dominant role that thermal effects play in aerosols.

B. Aerosols and hydrosols

The simple velocity and temperature results that were obtained above are valid when the frequency is not too high, and when the density ratio is small. When either condition is not satisfied, fluid inertia effects come into play that must be taken into account. This is particularly important in the case of hydrosols, because in them the density ratio is never

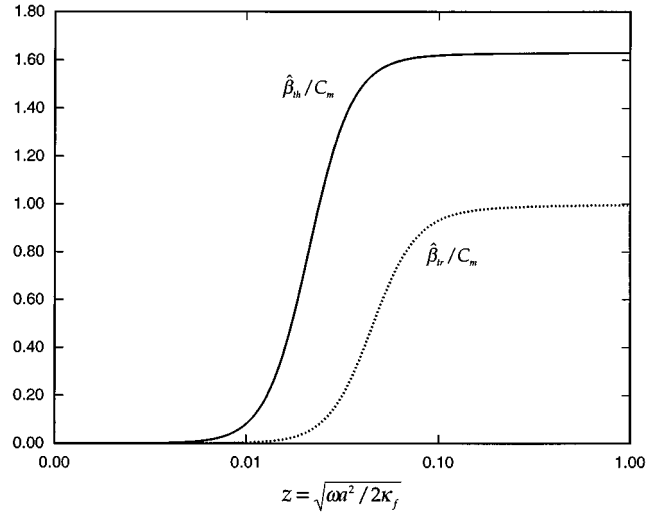


FIG. 2. Scaled thermal and translational dispersion coefficients of an aerosol composed of water droplets in air: —: thermal dispersion; ···: translational dispersion.

small. Thus, we need to retain all terms in the force and the heat transfer rate. Proceeding as before we now find, using (44)–(47),

$$\frac{\tilde{u}_p}{\tilde{U}_f} = 3\delta \frac{y(2y+3) + 3i(1+y)}{2y^2(2+\delta) + 9y\delta + 9i\delta(1+y)}, \quad (52)$$

$$\frac{\tilde{T}'_p}{\tilde{\Theta}'_f} = \frac{1+z-iz}{1+z-iz(1+hz)}, \quad (53)$$

where

$$h = \frac{2}{3} \frac{\rho_p c_{pp}}{\rho_f c_{pf}}.$$

The velocity ratio prescribed by (52) has been discussed elsewhere.²⁹ It reduces to the value given by Fuchs³⁰ for aerosols, i.e., when $\delta \ll 1$, in which case it closely agrees with the results predicted by (49a). The temperature ratio, on the other hand, seems to have received little attention, although

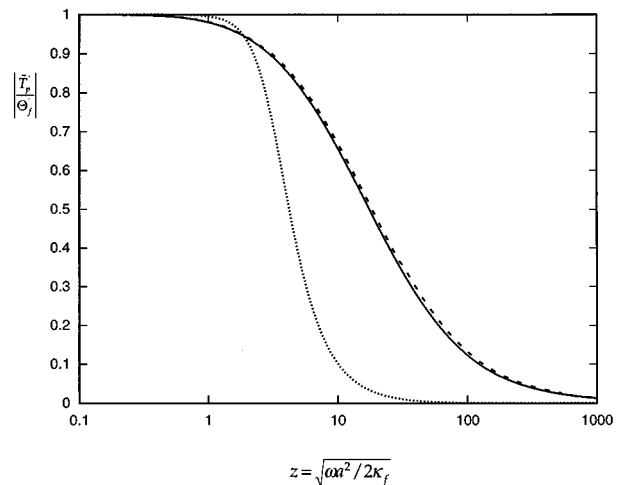


FIG. 3. Temperature magnitude ratio. Al_2O_3 particles in water. $\delta=0.37$: ···: Eq. (49b); —: Eq. (A8); ---: Eq. (53).

it plays an important role in any calculation of the thermal attenuation. As pointed out in the Appendix, (53) is derived from a more complete result, (A8). Both equations reduce to (49b) when $\delta \ll 1$, and z is small. However, when δ is finite, the more detailed results for the temperature ratio are significantly different from those predicted by (49b), as seen in Fig. 3 for the case of a 10- μm -diam alumina (Al_2O_3) particle in water. The figure also shows that, for this case, (53) and (A8) are in close agreement, so that use of (53) instead of (A8) is warranted.

Thus, the differences between the temperature ratios predicted by (49b) and (53) are similar to those between (49a) and (52) for the velocity ratio. Therefore, although (52) and (53) lack the simplicity of (49a) and (49b), they must be used when the frequency or the density ratio is not small. The main limitation of these equations is that they were obtained from a particle force and a heat transfer rate that does not include compressibility effects in the fluid. Later we will give a result that includes this effect and which shows that (52) is limited to frequencies that are below $\omega a/c_{sf} \approx 1$. For a 10- μm particle in water, this occurs at about 20 MHz. The corresponding limitations of (53) are not known, but are probably similar to those of (52).

Consider now the attenuation and the dispersion coefficients applicable to aerosols and hydrosols. To obtain these, we need only to take the real and imaginary parts of (52) and (53) and substitute them in (42a) and (43a). Because results exist in the literature only for the attenuation, we obtain that quantity first. Thus,

$$\hat{\alpha}_{tr} = 18C_m \delta |1 - \delta| \times \frac{(1+y)y^2}{y^4(2+\delta)^2 + 9\delta y^3(2+\delta) + (9\delta/2)^2(2y^2+2y+1)}. \quad (54)$$

and

$$\hat{\alpha}_{th} = \frac{3}{4} C_m \delta (\gamma_f - 1) \frac{(1+z)z^2}{z^4 + 2h^{-1}z^3 + h^{-2}(2z^2 + 2z + 1)}. \quad (55)$$

The first of these is identical to the viscous attenuation derived recently by this author.²⁹ Except for a difference in the power of $|1 - \delta|$, it is equal to the viscous attenuation derived some time ago by Sewell,³ Lamb,³¹ and Epstein³² from the scattering problem that arises when a plane sound wave encounters a spherical obstacle. With the same exception, it is also equal to a result obtained by Urick³³ on the basis of energy dissipation. The result has also been derived more recently by others, including Epstein and Carhart,³⁴ and Allegra and Hawley.³⁵ As described elsewhere,²⁹ the difference in the power of $|1 - \delta|$ can be traced to the omission of the first term in the force equation, Eq. (44), which is due to the acceleration of the fluid in the sound wave. Inclusion of that term in the approach used by Urick³³ leads to (54).

The thermal attenuation coefficient given by (55) may be shown to be equal to that derived by Epstein and Carhart,³⁴ when their equations (10.1) and (14.4) are reduced for the case of small, *rigid* particles. The result was apparently derived earlier by Isakovich.³⁶ A similar result was

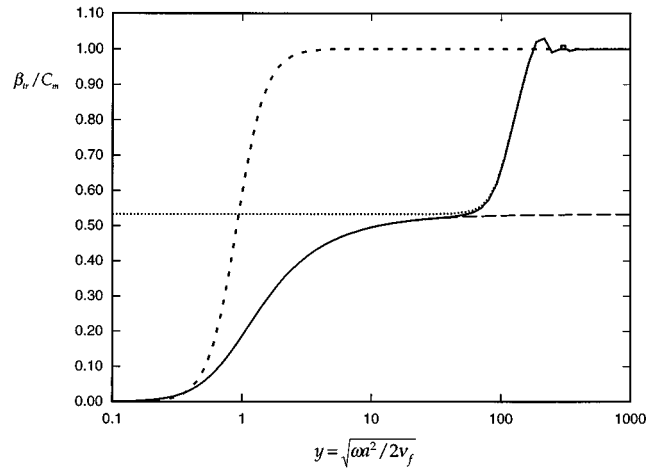


FIG. 4. Scaled translational dispersion coefficient for a suspension of Al_2O_3 particles in water: ---: Eq. (56); —: viscous, compressible theory; ···: inviscid, compressible theory; -·-: Stokes' law theory.

derived later by Chow,³⁷ but the coefficient of h^{-2} appearing in the denominator of his results lacks certain terms.

We now consider the phase velocity changes due to the translational and thermal effects, given by $\hat{\beta}_{tr}$ and $\hat{\beta}_{th}$. To obtain these, we take the real parts of (52) and (53) and substitute them into (42b) and (43b) to obtain

$$\hat{\beta}_{tr}/C_m = 1 - 3\delta \times \frac{4y^4(2+\delta) + 12y^3(1+2\delta) + 27\delta(2y^2+2y+1)}{4y^4(2+\delta)^2 + 36\delta y^3(2+\delta) + 81\delta^2(2y^2+2y+1)} \quad (56)$$

and

$$\hat{\beta}_{th}/C_m = 1 - \frac{3}{2}(\gamma_f - 1) \times \frac{z^3 + h^{-1}(2z^2 + 2z + 1)}{z^4 + 2h^{-1}z^3 + h^{-2}(2z^2 + 2z + 1)}. \quad (57)$$

Both results appear to be new and apply to arbitrary values of δ . When $\delta \ll 1$, the first may be shown to be equal to an unpublished result of Chu and Chow.³⁸ These investigators also presented some results for the thermal dispersion, which are similar to (57). The differences are of the same nature as those appearing in the translational attenuation coefficient derived by Chow.^{36,37}

These results are displayed graphically in Figs. 4–7 for a suspension of alumina particles in water. They can, of course, be used for other particle–fluid combinations. The main difference between different cases is the relative magnitude of the translational and thermal changes. For example, thermal changes are small for hydrosols, but, as shown earlier, can be dominant for aerosols.

Figure 4 shows the dependence of the translational dispersion on $y = \sqrt{\omega a^2 / 2\nu_f}$ for the case of alumina (Al_2O_3) particles in water. Because y is proportional to $a\sqrt{\omega}$, the curves give both the variations of the dispersion with frequency for a given particle radius, and with size for a given frequency. For comparative purposes, three other results are shown in the figure. One is the Stokes' law result, given by

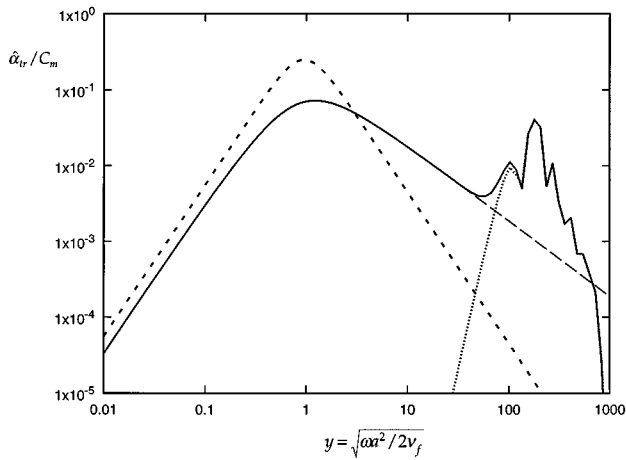


FIG. 5. Scaled translational attenuation coefficient, for a suspension of Al_2O_3 particles in water: ---: Eq. (54); —: viscous, compressible theory; ···: inviscid, compressible theory; ····: Stokes' law theory.

the first term in (50). The other two results include the effects of compressibility, and will be described below. We see that the viscous results tend to the same limit as $y \rightarrow 0$, where the particles move with the fluid. At the other end of frequency range, the viscous, unsteady theory predicts a finite value for $\hat{\beta}_{tr}/C_m$, which is given by $2(1-\delta)/(2+\delta)$. This value derives from the very small thickness, at high frequencies, of the viscous layer around a sphere, relative to the sphere radius, and corresponds the well-known result from irrotational, incompressible flow-field theory for velocity of a rigid particle in an oscillating fluid (see, for example, Refs. 31, 39, and 40), which predicts that at very high frequencies the ratio of particle to fluid velocities is given by $3\delta/(2+\delta)$. This result does not apply to real sound waves. For them, compressibility effects at high frequencies must be included when calculating the fluid force on the particle. As shown earlier,^{24,25} when the frequency is very high, those effects keep the particle at rest for all values of the density ratio.

The corresponding effects on the dispersion are shown by the two additional curves given in the figure. One is based

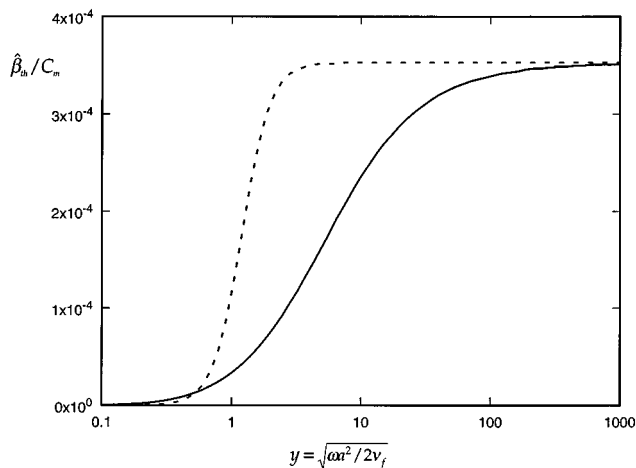


FIG. 6. Scaled thermal dispersion coefficient for a suspension of Al_2O_3 particles in water: —: Eq. (57); ---: second term in Eq. (50).

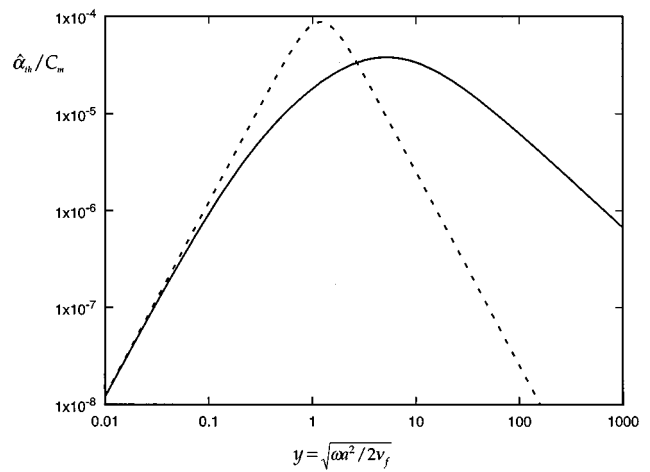


FIG. 7. Scaled thermal attenuation coefficient for a suspension of Al_2O_3 particles in water: —: Eq. (55); ---: second term in Eq. (51).

on the velocity ratio for a particle in an inviscid, compressible fluid.²⁵ The second is based on the results of Temkin and Leung,²⁴ which include both viscosity and compressibility. To save space, we do not give those equations here; they can be found in the works cited. When they are used in (38) and (39), they provide the most complete description sound propagation in dilute suspensions of rigid particles. They can also be used to assess the validity of the various limiting forms obtained with other theories. Now, the viscous, compressible results depend on the parameter y accounting for viscous effects, and on the ratio of particle radius to wavelength, which accounts for compressibility effects. In order to show the dependence of the attenuation and dispersion as a function of y alone, we have selected a particle radius equal to $10 \mu\text{m}$ to reduce the viscous, compressible results. Other sizes give similar trends.

Figure 5 gives the corresponding attenuation results. Here the effects of fluid inertia and compressibility are more apparent. Contrary to the case of the dispersion, where regions of overlap were found between the steady and unsteady Stokes results, here they differ at all frequencies. This is due to the large value of δ used in the figure. On the other hand, the unsteady Stokes theory [that is, the viscous, incompressible velocity ratio given by Eq. (52)] agrees with the full compressible theory in a wide range of frequencies that include the first peak in the attenuation curve. In this range, compressibility effects are negligible. Beyond that first peak, however, they become more significant, and produce subsequent peaks in the attenuation curve which are due to scattering. The first of these has a magnitude which is nearly equal to that produced by viscosity alone for the case shown in the figure. For this case, the first scattering peak occurs at about 10 MHz.

In Figs. 6 and 7, we show the thermal dispersion and attenuation coefficients, respectively, as a function of y for the case of alumina particles in water. The simple results given by the second terms in (50) and (51) are also shown there. Comparison with Figs. 4 and 5 shows that for this case the changes produced by the thermal effects are small compared to those produced by the translational effects. This is

due to the smallness, in water, of $\gamma_f - 1$. However, for liquid suspensions of nearly particles whose densities are close to that of the liquid, both effects produce comparable attenuations. However such cases refer to emulsions, or to suspensions of solid particles whose coefficient of thermal expansion are not negligible compared to that of the liquid, e.g., polystyrene particles, for which the assumption of rigidity is invalid.

V. CONCLUSIONS

We have presented a new theory for the attenuation and dispersion of sound in suspensions containing rigid particles that have arbitrary densities relative to the fluid. The theory has been reduced for the case of very dilute suspensions of spheres, where the particle velocity is known as a function of the frequency, radius, viscosity, and density ratio, and have found exact agreement with results available in the literature. The new theory also gives results for the sound speed in arbitrary-density ratio suspensions, where no theoretical results exist.

The present theory has also been used to obtain the attenuation and dispersion due to translational effects when compressibility in the fluid is included in the computations of the velocity ratio. These extend the range of applicability of the theory to very high frequencies, where scattering is the dominant effect. Finally, the results show that the velocity and temperature ratios play a key role in determining the propagation characteristics of sound waves in suspensions and therefore point to a possible means for the study of finite-concentration effects.

ACKNOWLEDGMENTS

Parts of this work were done while the author was on leave at the Royal Institute of Technology in Stockholm, and at the Consejo Superior de Investigaciones Cientificas in Madrid. Their kind hospitality and interest in this work is gratefully acknowledged.

APPENDIX: TEMPERATURE OF A RIGID SPHERE IN AN OSCILLATING TEMPERATURE FIELD

We consider the temperature and the heat transfer rate for a small, rigid sphere in a fluid whose temperature, far from the sphere, oscillates harmonically in time with a small amplitude. That is, far from the particle the temperature of the fluid is given by $\Theta_f = T_0 + T'_{f0} \cos(\omega t)$, where $T'_{f0} \ll T_0$. Because all quantities vary sinusoidally in time, it is convenient to use the complex factor $\exp(-i\omega t)$. Thus, the fluid's temperature fluctuation, far from the sphere, will be expressed as

$$\tilde{\Theta}'_f = T'_{f0} e^{-i\omega t}, \quad (\text{A1})$$

with the real part implied. To obtain the temperature distribution in the fluid when a sphere is suspended in it, we superimpose the uniform temperature fluctuation given above with a temperature-disturbance field, $\tilde{\theta}'_f$, produced in the fluid by a sphere whose surface temperature varies as

$$\tilde{T}'_s = T_0 + \tilde{T}'_{s0} e^{-i\omega t}, \quad (\text{A2})$$

where the amplitude \tilde{T}'_{s0} is to be determined.

The disturbance field may be obtained from Fourier's heat conduction equation reduced for a monochromatic time dependence:

$$\nabla^2 \tilde{\theta}'_f + K_f^2 \tilde{\theta}'_f = 0. \quad (\text{A3})$$

Here $K_f = \sqrt{i\omega/\kappa_f} = \pm(1+i)/\delta_{\kappa_f}$, where $\delta_{\kappa_f} = \sqrt{\omega/2\kappa_f}$ is the fluid's thermal-penetration depth. If the origin of the coordinate system is placed on the sphere's center, $\tilde{\theta}'_f$ will depend only on the radial distance from the origin, and the solution of (A3) which is bounded at infinity will be $A h_0^{(1)} \times (K_{f1} r)$, where $h_0^{(1)}(K_{f1} r)$ is the spherical Bessel function of the third kind and of zeroth order, and K_{f1} is the root of K_f that has a positive imaginary part.

Adding this field to the uniform field given by (A1), and applying the boundary condition on the sphere's surface to determine A , we obtain

$$\tilde{T}'_f = T'_{f0} e^{-i\omega t} + (\tilde{T}'_{s0} - T'_{f0}) \frac{h_0(K_{f1} r)}{h_0(K_{f1} a)} e^{-i\omega t}, \quad (\text{A4})$$

where we have dropped, for convenience, the superscript on $h_0^{(1)}$.

To obtain the surface temperature, we consider the temperature field within the spherical particle. For monochromatic time variations, this satisfies

$$\nabla^2 \tilde{T}'_p + K_p^2 \tilde{T}'_p = 0. \quad (\text{A5})$$

Here $K_p = \sqrt{i\omega/\kappa_p} = \pm(1+i)/\delta_{\kappa_p}$, where $\delta_{\kappa_p} = \sqrt{\omega/2\kappa_p}$ is the particle's thermal-penetration depth. The solution of (A5) which is finite at the origin is $B j_0(K_{p1} r)$, where $j_0(K_{p1} r)$ is the spherical Bessel function of the first kind and order zero. Thus,

$$\tilde{T}'_p = \tilde{T}'_{s0} \frac{j_0(K_{p1} r)}{j_0(K_{p1} a)} e^{-i\omega t}. \quad (\text{A6})$$

To obtain the surface temperature, we apply the condition that the heat flux be equal on both sides of the surface, that is, $k_p(\partial T_p/\partial r)_{r=a} = k_f(\partial \Theta_f/\partial r)_{r=a}$, where k_f and k_p are the thermal conductivities of fluid and particle material, respectively. Using (A4) and (A6), and solving for \tilde{T}'_{s0} , we obtain

$$\tilde{T}'_{s0} = T'_{f0} \frac{1 - iK_{f1} a}{1 - iK_{f1} a + (k_p/k_f) K_{p1} a j'_0(K_{p1} a)/j_0(K_{p1} a)}, \quad (\text{A7})$$

where we have used the definition of $h_0(\zeta)$ to write $\zeta h'_0(\zeta)/h_0(\zeta) = i\zeta - 1$.

Now, our derivation of (36) assumes that the temperature of the particle can be represented by some uniform value. A suitable one can be obtained by averaging (A6) over the volume of the particle. Thus, we take the particle temperature to be given by $v_p^{-1} \int_{v_p} T'_p dv$, where $v_p = 4\pi a^3/3$ is the volume of the particle. This gives

$$\tilde{T}'_p = \frac{i}{hz^2} \left[\frac{1}{1+z-iz} + \frac{k_f}{k_p} \frac{\tan(K_{p1} a)}{K_{p1} a - \tan(K_{p1} a)} \right]^{-1} \tilde{\Theta}'_f. \quad (\text{A8})$$

It should be pointed out that the function enclosed by square brackets in (A8) is identical to the function F in equation

(16.1) of Ref. 34 and to the function $1/H$ in Eq. (20) of Ref. 35.

As given by (A8), the average temperature of a rigid particle is, generally, a fairly involved function of the frequency, but for particles that can be considered rigid in comparison to the fluid outside, and that have a thermal conductivity larger than that of the host fluid, it can be closely approximated by

$$\tilde{T}'_p = \frac{1+z-iz}{1+z-iz(1+hz)} \tilde{\Theta}'_f, \quad (\text{A9})$$

where $h = 2\rho_p c_{pp}/3\rho_f c_{pf}$ and $z = \sqrt{\omega a^2/2\kappa_f}$. Instances where (A9) provides a good approximation to (A8) include water droplets in air, and alumina particles in water.

Finally, we consider the rate at which heat is transferred to the particle. This may be computed from either the particle or fluid temperature fields. The latter gives, directly, the form desired. Thus, since the temperature field is uniform around the sphere, we have $\dot{Q}_p = -4\pi a^2 k_f (\partial T_f / \partial r)_{r=a}$, or

$$\tilde{Q}_p = -4\pi a k_f (1+z-iz)(\tilde{T}'_{p0} - T'_{f0})e^{-i\omega t}. \quad (\text{A10})$$

This can be expressed in the real form

$$\dot{Q}_p = -4\pi k_f a (1+z)(T_p - \Theta_f) - \frac{3\delta m_p c_{pf}}{2z} \frac{d(T_p - T_f)}{dt}. \quad (\text{A11})$$

If the frequency is low, or the density ratio δ is very small, (A11) reduces to (48b). However, for liquid suspensions in general, (A11) is required.

¹J. Tyndall, *Sound* (Appleton, New York, 1875), 3rd ed.

²Lord Rayleigh, "Investigation of the disturbance produced by a spherical obstacle on the waves of sound," *Proc. London Math. Soc.* **IV**, 253–383 (1872); *Theory of Sound* (Dover Reprint, New York, 1945), pp. 282–284.

³C. J. T. Sewell, "On the extinction of sound in a viscous atmosphere by small obstacles of cylindrical and spherical form," *Philos. Trans. R. Soc. London, Ser. A* **210**, 239–256 (1910).

⁴S. Temkin and R. A. Dobbins, "Attenuation and dispersion of sound by particulate relaxation processes," *J. Acoust. Soc. Am.* **40**, 317–324 (1966).

⁵C. M. Atkinson and H. K. Kytömaa, "Acoustic wave speed and attenuation in suspensions," *Int. J. Multiphase Flows*, **18**, 577–592 (1992).

⁶A. H. Harker and J. A. G. Temple, "Velocity and Attenuation of Ultrasound in Suspensions of Particles in Fluids," *J. Phys. D* **21**, 1576–1588 (1988).

⁷D. L. Johnson, "Recent developments in the acoustic properties of porous media," in *Frontiers in Physical Acoustics*, edited by D. Sette (North-Holland, Amsterdam, 1986), pp. 255–290.

⁸R. L. Gibson, Jr. and M. Nafi Toksöz, "Viscous attenuation of acoustic waves in suspensions," *J. Acoust. Soc. Am.* **85**, 1925–1934 (1989).

⁹J. M. Hovem, "Viscous attenuation of sound in suspensions and high porosity sediments," *J. Acoust. Soc. Am.* **67**, 1559–1563 (1980). See also his erratum: *J. Acoust. Soc. Am.* **68**, 1531 (1980).

¹⁰P. R. Ogushwitz, "Applicability of the Biot Theory. II. Suspensions," *J. Acoust. Soc. Am.* **77**, 441–452 (1985).

¹¹F. E. Marble, "Dynamics of dusty gases," *Annu. Rev. Fluid Mech.* **2**, 397–446 (1970).

¹²S. Temkin, "Particle force and heat transfer in a dusty gas sustaining an acoustic wave," *Phys. Fluids* **5**, 1296–1304 (1993).

¹³A. B. Wood, *A Textbook of Sound* (Bell, London, 1941), pp. 361–362.

¹⁴R. J. Urick, "A sound velocity method for determining the compressibility of finely divided substances," *J. Appl. Phys.* **18**, 983–987 (1947).

¹⁵L. Ye, D. A. Weitz, S. Ping, S. Bhattacharya, J. S. Huang, and M. J. Higgins, "Dynamic rigidity percolation in inverted miscelles," *Phys. Rev. Lett.* **63**, 263 (1989).

¹⁶S. Temkin, "Sound speeds in suspensions in thermodynamic equilibrium," *Phys. Fluids A* **11**, 2399–2409 (1992).

¹⁷Y. Fukumoto and T. Izuyama, "Thermal attenuation and dispersion of sound in a periodic emulsion," *Phys. Rev. A* **46**, 4905–4921 (1992).

¹⁸A. K. Holmes and R. E. Challis, "A wide bandwidth study of ultrasound velocity and attenuation in suspensions: comparison of theory and experimental measurements," *J. Colloid Interface Sci.* **156**, 261–268 (1993).

¹⁹A. K. Holmes, R. E. Challis, and D. J. Wedlock, "A wide bandwidth ultrasonic study of suspensions: the variation of velocity and attenuation with particle size," *J. Colloid Interface Sci.* **168**, 339–348 (1994).

²⁰K. F. Herzfeld, "Propagation of sound in suspensions," *Philos. Mag.* **9**, 741–751, 752–768 (1930).

²¹D. J. McClements and M. J. W. Povey, "Scattering of ultrasound by emulsions," *J. Phys. D* **22**, 38–47 (1989).

²²S. Temkin, "Dispersion of sound in bubbly liquids via the Kramers-Kronig relationships," *J. Fluid Mech.* **211**, 61–72 (1990).

²³A. Onuki, "Sound propagation in phase-separating fluids," *Phys. Rev. A* **43**, 6740–6755 (1991).

²⁴S. Temkin and C. M. Leung, "On the velocity of a rigid sphere in a sound wave," *J. Sov. Laser Res.* **49**, 75–92 (1976).

²⁵S. Temkin, *Elements of Acoustics* (Wiley, New York, 1981).

²⁶M. R. Maxey and J. J. Riley, "Equations of motion for a small rigid sphere in nonuniform flow," *Phys. Fluids* **26**, 883–889 (1983).

²⁷F. E. Marble, "Dynamics of a gas containing small solid particles," *Proc. AGARD Combustion Propulsion Colloq.*, 57th (1963), pp. 175–215.

²⁸S. Temkin and R. A. Dobbins, "Measurements of the attenuation and dispersion of sound by an aerosol," *J. Acoust. Soc. Am.* **40**, 1016 (1966).

²⁹S. Temkin, "Viscous attenuation of sound in dilute suspensions of rigid particles," *J. Acoust. Soc. Am.* **100**, 825–831 (1996).

³⁰N. A. Fuchs, *The Mechanics of Aerosols* (Pergamon, London, 1964), p. 85.

³¹H. Lamb, *Hydrodynamics* (Dover, New York, 1945), 6th ed., Sec. 363.

³²P. S. Epstein, "On the absorption of sound by suspensions and emulsions," in *Contributions to Applied Mechanics, Theodore von Karman Anniversary Volume* (California Institute of Technology, Pasadena, 1941), pp. 162–188.

³³R. J. Urick, "The absorption of sound of irregular particles," *J. Acoust. Soc. Am.* **20**, 283–289 (1948).

³⁴P. S. Epstein and R. R. Carhart, "The absorption of sound in suspensions and emulsions. I. Water fog in air," *J. Acoust. Soc. Am.* **25**, 553–565 (1953).

³⁵J. R. Allegra and S. A. Hawley, "Attenuation of sound in suspensions and emulsions: Theory and experiments," *J. Acoust. Soc. Am.* **51**, 1545–1564 (1971).

³⁶M. A. Isakovich, "On the propagation of sound in emulsions," *Zh. Eksp. Teor. Fiz.* **18**, 907–912 (1948).

³⁷C. F. Chow, "Attenuation of acoustic waves in dilute emulsions and suspensions," *J. Acoust. Soc. Am.* **36**, 2395–2401 (1964).

³⁸B. T. Chu and J. C. F. Chow, "On a macroscopic theory of a two-phase fluid," Paper No. 65-8, AIAA 2nd Aerospace Sci. Meeting, New York, 25–27 January 1965 (unpublished).

³⁹L. D. Landau and E. M. Lifshitz, *Fluid Mechanics* (Pergamon, New York, 1959).

⁴⁰G. K. Batchelor, *An Introduction to Fluid Dynamics* (Cambridge U.P., Cambridge, 1967).

Nonlinear inversion of the *SH* wave equation in a half-space for density and shear modulus determination

Wenhao Zhu

Department of Engineering Science and Mechanics, The Pennsylvania State University, University Park, Pennsylvania 16802

Xu Jun

Department of Mechanics, Huazhong University of Science and Technology, Wuhan, 430074, People's Republic of China

Joseph L. Rose

Department of Engineering Science and Mechanics, The Pennsylvania State University, University Park, Pennsylvania 16802

(Received 27 February 1997; accepted for publication 8 October 1997)

This paper deals with the problem of multi-parameter nonlinear inversion of the *SH* wave equation in an elastic half-space. A numerical approach combining Born iteration and a regularizing technique is presented for simultaneously reconstructing 2-D distributions of density and shear modulus in a scatterer embedded in a half-space. The well-to-well source–receiver scheme commonly used in geophysical exploration is considered in the model in which two incident frequencies are used to uncouple the parameters in frequency domain. The weighted residual method, along with bilinear interpolating functions, are used in the discretization procedure. Computer simulations have been conducted on several examples with different density and shear modulus configurations. The numerical results show that the approach proposed has a uniformly convergence for the given objects and has a feature of treating the limited-source well-to-well scheme that causes a more ill-conditioned equation in the inversion procedure. © 1998 Acoustical Society of America. [S0001-4966(98)05102-9]

PACS numbers: 43.35.Cg, 43.35.Zc, 43.20.Bi [HEB]

INTRODUCTION

The problem of inverse scattering has received much attention for its potential application in many practical fields. Intensive study has been performed on linear inverse problems, such as ray CT, diffraction tomography, Born or Rytov inversion, etc.,^{1–5} for the situations of weak scattering or high-frequency approximation. Recently, many efforts have been made to avoid the linearizing assumption and to involve the diffracting and multiple scattering effects in inverse problems. Newton⁶ generalized the Gelfand–Levitan–Marchenko integral equation into three dimensions. Since analytical solutions are hardly sought in this case, many numerical methods have been developed. Johnson and Tracy⁷ used method of moment along with sinc basis functions. Tarantala⁸ applied an iterative method combined with an optimization procedure to investigate seismic inversion. Chew *et al.*⁹ presented a distorted Born iterative method to solve the inverse scattering problem of the EM wave equation for permittivity reconstruction. However, most previous works were restricted for single parameter inversion in an infinite medium. A more practical application is to consider the elastic wave inversion in a half-space as in seismic exploration and NDT, where the boundary surface effects cannot be neglected.

In this paper, the multi-parameter nonlinear inversion of *SH* waves in an elastic half-space is investigated numerically. In the problem, the source–receiver scheme is arranged in a form of well-to-well format as in seismic exploration (see Fig. 1). The point sources on the excitation array

are assumed monochromatic and horizontally polarized to produce *SH* waves. The forward scattered fields are measured by the receiver array and then used in the inversion procedure. A numerical algorithm is developed that reforms the Born iterative procedure for inversion into a regularized optimization procedure. Detailed numerical results with various types of density and shear modulus configurations are presented.

I. PROBLEM FORMULATION

The density ρ and shear modulus μ in an isotropic elastic half-space containing an inhomogeneous scatterer Ω are written as follows:

$$\rho(\mathbf{r}) = \rho_0[1 + \alpha(\mathbf{r})], \quad \mu(\mathbf{r}) = \mu_0[1 + \beta(\mathbf{r})], \quad (1)$$

where ρ_0 , μ_0 are the density and shear modulus of the background medium, respectively, and α , β are the corresponding deviations from ρ_0 , μ_0 , which vanish outside the scatterer Ω . The governing equation for the *SH* wave in frequency domain yielded by a point source can be written as follows, omitting the time dependency of $\exp(-i\omega t)$:

$$\begin{aligned} \mu(\mathbf{r})\nabla^2 w(\mathbf{r}, \mathbf{r}_s) + \nabla \mu(\mathbf{r}) \cdot \nabla w(\mathbf{r}, \mathbf{r}_s) + \omega^2 \rho(\mathbf{r})w(\mathbf{r}, \mathbf{r}_s) \\ = -s(\omega)\delta(\mathbf{r} - \mathbf{r}_s) \end{aligned} \quad (2)$$

with the boundary condition

$$\left. \frac{\partial w}{\partial y} \right|_{y=0} = 0, \quad (3)$$

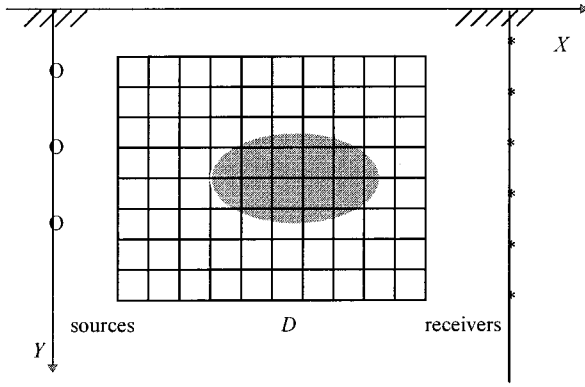


FIG. 1. The geometry of the well-to-well scheme.

where $w(\mathbf{r}, \mathbf{r}_s)$ is the out of plane displacement field at \mathbf{r} due to a point source loaded at \mathbf{r}_s , and $s(\omega)$ is the spectrum of the source. We can express the total fields $w(\mathbf{r}, \mathbf{r}_s)$ as a sum of incident fields and the scattered fields $w^{\text{tot}}(\mathbf{r}, \mathbf{r}_s) = w^{\text{in}}(\mathbf{r}, \mathbf{r}_s) + w^{\text{sc}}(\mathbf{r}, \mathbf{r}_s)$ with the incident field $w^{\text{in}}(\mathbf{r}, \mathbf{r}_s)$ satisfying the following boundary value problem:

$$\begin{aligned} \nabla^2 w^{\text{in}}(\mathbf{r}, \mathbf{r}_s) + k_0^2 w^{\text{in}}(\mathbf{r}, \mathbf{r}_s) \\ = -s(\omega) \delta(\mathbf{r} - \mathbf{r}_s) / \mu_0, \quad \left. \frac{\partial w^{\text{in}}}{\partial y} \right|_{y=0} = 0, \end{aligned} \quad (4)$$

where $k^2 = \omega^2 \rho_0 / \mu_0$, k is the wave number of the background medium. From Eqs. (1)–(4), we have

$$\begin{aligned} \nabla^2 w^{\text{sc}}(\mathbf{r}, \mathbf{r}_s) + k^2 w^{\text{sc}}(\mathbf{r}, \mathbf{r}_s) = -\{k^2 \alpha(\mathbf{r}) w^{\text{tot}}(\mathbf{r}, \mathbf{r}_s) + \nabla \\ \cdot [\beta(\mathbf{r}) \nabla w^{\text{tot}}(\mathbf{r}, \mathbf{r}_s)]\}. \end{aligned} \quad (5)$$

Applying Green's theorem to Eq. (5), integrating by parts the second term on the right side of Eq. (5), and using the condition that β vanishes outside the scatter Ω , we obtain the integral equation:

$$\begin{aligned} w^{\text{sc}}(\mathbf{r}, \mathbf{r}_s) = \int \int_{\Omega} [k^2 \alpha(\mathbf{r}_0) G(\mathbf{r}, \mathbf{r}_0) w^{\text{tot}}(\mathbf{r}_0, \mathbf{r}_s) \\ - \beta(\mathbf{r}_0) \nabla G(\mathbf{r}, \mathbf{r}_0) \cdot \nabla w^{\text{tot}}(\mathbf{r}_0, \mathbf{r}_s)] d\mathbf{r}_0, \end{aligned} \quad (6)$$

where \mathbf{r} is on the receiver array, $G(\mathbf{r}, \mathbf{r}_0)$ is the half-plane Green's function having the form

$$G(\mathbf{r}, \mathbf{r}_0) = \frac{i}{4} [H_0^{(1)}(k|\mathbf{r} - \mathbf{r}_0|) + H_0^{(1)}(k|\mathbf{r}' - \mathbf{r}_0|)], \quad (7)$$

and where $H_0^{(1)}$ is the zeroth-order Hankel function of first kind, \mathbf{r}' is the mirror point of \mathbf{r} about the surface plane.

Obviously, Eq. (6) is a nonlinear integral equation in α , β , w , and some supplement equations are needed to enclose Eq. (6). For the well-to-well scheme used here, each point source on the source array produces forward scattered fields that are measured by all of the receivers on the receiving array and then used as known data on the left side of Eq. (6). When the point source is excited over the entire source array, we obtain a 2-D data set for one frequency ω_1 . Repeating the above procedure for another frequency ω_2 , we then obtain two equations for α , β :

$$\begin{aligned} w^{\text{sc}}(\mathbf{r}, \mathbf{r}_s, \omega_i) = \int \int_{\Omega} [k_i^2 \alpha(\mathbf{r}_0) G(\mathbf{r}, \mathbf{r}_0, \omega_i) w^{\text{tot}}(\mathbf{r}_0, \mathbf{r}_s, \omega_i) \\ - \beta(\mathbf{r}_0) \nabla G(\mathbf{r}, \mathbf{r}_0, \omega_i) \cdot \nabla w^{\text{tot}}(\mathbf{r}_0, \mathbf{r}_s, \omega_i)] d\mathbf{r}_0, \\ i = 1, 2. \end{aligned} \quad (8)$$

Because $w^{\text{tot}}(\mathbf{r}, \mathbf{r}_s, \omega_i)$ ($i = 1, 2$) are unknown, we write the total fields for ω_i in the region of Ω as

$$\begin{aligned} w^{\text{tot}}(\mathbf{r}, \mathbf{r}_s, \omega_i) = w^{\text{in}}(\mathbf{r}, \mathbf{r}_s, \omega_i) \\ + \int \int_{\Omega} [k_i^2 \alpha(\mathbf{r}_0) G(\mathbf{r}, \mathbf{r}_0, \omega_i) w^{\text{tot}} \\ \times (\mathbf{r}_0, \mathbf{r}_s, \omega_i) - \beta(\mathbf{r}_0) \nabla G(\mathbf{r}, \mathbf{r}_0, \omega_i) \\ \cdot \nabla w^{\text{tot}}(\mathbf{r}_0, \mathbf{r}_s, \omega_i)] d\mathbf{r}_0, \\ \mathbf{r} \in \Omega, \quad i = 1, 2, \end{aligned} \quad (9)$$

which are the direct scattering equations to be employed in calculating the field w^{tot} in Ω . Combining Eqs. (8) and (9), we can solve numerically for the two 2-D functions: α , β , and the wave fields w^{tot} of two frequencies in the object. As a part of the computer simulations in the paper, the forward scattered wave fields on the receiving line are calculated by Eq. (6) for the given objects.

II. DISCRETIZATION AND REGULARIZED ITERATION ALGORITHMS

Two inverse scattering Eqs. (8) for parameters α , β , and two direct scattering Eqs. (9) for wave fields w^{tot} of two frequencies are therefore obtained. To implement the numerical solutions to Eqs. (8) and (9), a weighted residual method and a Born iteration algorithm using a regularization procedure are used.

A. Discretization and interpolation

Consider a rectangular imaging region D between the source and receiving lines, which is large enough to contain the scatterer region Ω . We discretize the region D into N small square elements $D = D_1 \cup D_2 \cdots \cup D_N$, and $D_i \cap D_j = \emptyset$, when $i \neq j$. In each element, the unknown parameters α , β , and wave field w are interpolated by a set of bilinear base functions along with their values at the four nodes of the element:

$$\phi(\mathbf{r}) = \sum_{i=1}^4 \phi_i f_i(\mathbf{r}), \quad (10)$$

where $\phi(\mathbf{r})$ is any of α , β , w^{tot} , ϕ_i is its value at the i th node of the element, and $f_i(\mathbf{r})$ ($i = 1, 2, 3, 4$) are bilinear interpolating functions about the spatial variables x , y , which satisfy $f_i(\mathbf{r}_j) = \delta_{ij}$ ($i, j = 1, 2, 3, 4$), where \mathbf{r}_j is the coordinate of the j th node of the element. The detailed forms of f_i and its derivatives $d_i = \partial f_i(\mathbf{r}) / \partial x$ and $t_i = \partial f_i(\mathbf{r}) / \partial y$ are given in the Appendix.

Now the domain integral (on D) of Eq. (8) can be discretized into a sum of element integrals. In each of them, the unknown functions α , β , w^{tot} are approximated by expan-

sions like Eq. (10). Then, the residual of such an approximation compared with the left side of Eq. (8) are forced to be a minimum by simply using a set of δ functions as the weighted functions (point match), where the matching points are chosen on the receiving line. If M number receivers are used in the problem, from Eq. (8) we have

$$w^{sc}(\mathbf{r}_m, \mathbf{r}_s, \omega_i) = \sum_{l=1}^L \alpha_l A_{ml}(w^{tot}, \omega_i) - \sum_{l=1}^L \beta_l B_{ml}(w^{tot}, \omega_i),$$

$$m = 1, \dots, M, \quad i = 1, 2, \quad (11)$$

where

$$A_{ml}(w^{tot}, \omega) = k^2 \sum_{j=1}^4 \int_{D_{lj}} \int e_{lj}(\mathbf{r}) G(\mathbf{r}_m, \mathbf{r}, \omega) f_j$$

$$\times \left(\sum_{i=1}^4 w_{lj,i}^{tot} f_i \right) d\mathbf{r}, \quad (12a)$$

$$B_{ml}(w^{tot}, \omega) = \sum_{j=1}^4 \int_{D_{lj}} \int e_{lj}(\mathbf{r}) f_j \left[\frac{\partial G(\mathbf{r}_m, \mathbf{r}, \omega)}{\partial x} \right.$$

$$\times \sum_{i=1}^4 w_{lj,i}^{tot} d_i + \frac{\partial G(\mathbf{r}_m, \mathbf{r}, \omega)}{\partial y}$$

$$\left. \times \sum_{i=1}^4 w_{lj,i}^{tot} t_i \right] d\mathbf{r}$$

$$m = 1, \dots, M, l = 1, \dots, L, \quad (12b)$$

and where L is the total number of nodes in the discretization, the subscript lj is related to the j th element ($j = 1, \dots, 4$) neighboring the l th node, and $e_{lj}(\mathbf{r})$ is a character function defined as

$$e_{lj}(\mathbf{r}) = \begin{cases} 1, & \text{if } j\text{th element is connected to } l\text{th node,} \\ 0, & \text{if } j\text{th element is not connected to } l\text{th node.} \end{cases}$$

$$(13)$$

Similarly, the direct scattering Eq. (9) for w^{tot} can be discretized into the same form as Eq. (11):

$$w^{tot}(\mathbf{r}_k, \mathbf{r}_s, \omega_i) = w^{in}(\mathbf{r}_k, \mathbf{r}_s, \omega_i) + \sum_{l=1}^L w_l^{tot} C_{kl}(\alpha, \beta, \omega_i),$$

$$k = 1, \dots, L, \quad i = 1, 2, \quad (14)$$

where

$$C_{kl}(\alpha, \beta, \omega) = k^2 \sum_{j=1}^4 \int_{D_{lj}} \int e_{lj}(\mathbf{r}) G(\mathbf{r}_k, \mathbf{r}, \omega)$$

$$\times f_j \left(\sum_{i=1}^4 \alpha_{lj,i} f_i \right) d\mathbf{r} - \sum_{j=1}^4 \int_{D_{lj}} \int e_{lj}(\mathbf{r})$$

$$\times \left[\frac{\partial G(\mathbf{r}_k, \mathbf{r}, \omega)}{\partial x} d_i + \frac{\partial G(\mathbf{r}_k, \mathbf{r}, \omega)}{\partial y} t_i \right]$$

$$\times \left(\sum_{i=1}^4 \beta_{lj,i} f_i \right) d\mathbf{r} \quad k, l = 1, \dots, L. \quad (15)$$

Finally, if S number of point sources are employed in this scheme, we can rewrite Eqs. (11) and (14) as a couple of matrix equations:

$$\mathbf{W}^{sc} = \Gamma(\mathbf{W}^{tot}) \cdot \mathbf{X}, \quad (16a)$$

$$\mathbf{W}^{in} = T(\mathbf{X}) \cdot \mathbf{W}^{tot}, \quad (16b)$$

where

$$\Gamma(\mathbf{W}^{tot}) = \begin{bmatrix} \mathbf{A}(\mathbf{W}^{tot}, \omega_1) & \mathbf{B}(\mathbf{W}^{tot}, \omega_1) \\ \mathbf{A}(\mathbf{W}^{tot}, \omega_2) & \mathbf{B}(\mathbf{W}^{tot}, \omega_2) \end{bmatrix}, \quad (17)$$

$$T(\mathbf{X}) = \begin{bmatrix} \mathbf{1} & \mathbf{0} \\ \mathbf{0} & \mathbf{1} \end{bmatrix} - \begin{bmatrix} \mathbf{C}(\mathbf{X}, \omega_1) & \mathbf{0} \\ \mathbf{0} & \mathbf{C}(\mathbf{X}, \omega_2) \end{bmatrix},$$

$$\mathbf{W}^{sc} = [w_{1,1}^{sc}(\omega_1), \dots, w_{M,1}^{sc}(\omega_1), \dots, w_{1,S}^{sc}(\omega_1), \dots,$$

$$w_{M,S}^{sc}(\omega_1), \dots, w_{1,S}^{sc}(\omega_2), \dots, w_{M,S}^{sc}(\omega_2)]^T,$$

$$\mathbf{W}^I = [w_{1,1}^I(\omega_1), \dots, w_{L,1}^I(\omega_1), \dots, w_{1,S}^I(\omega_1), \dots, w_{L,S}^I(\omega_1),$$

$$\dots, w_{1,S}^I(\omega_2), \dots, w_{L,S}^I(\omega_2)]^T, \quad I = \text{in, tot}, \quad (18)$$

$$\mathbf{X} = [\alpha_1, \dots, \alpha_L, \beta_1, \dots, \beta_L]^T,$$

and where \mathbf{A} , \mathbf{B} are matrices of $M \times S$ rows and L columns with their elements defined by Eqs. (12a) and (12b), \mathbf{C} is a diagonal matrix composed of S number of same $L \times L$ submatrices on the diagonal line with their elements defined by Eq. (15), “ T ” denotes transpose. It is noted that $T(\mathbf{X})$ is a square matrix whereas $\Gamma(\mathbf{W}^{tot})$ does not need to be squared as a regularization procedure will be applied to Eq. (16a).

B. Regularizing procedure and Born iteration

It is known that the integral Eq. (6) for the parameters is a first kind Fredholm integral equation which is generally ill-posed and thus the discretized equation is ill-conditioned. In general, we should define a well-behaved problem with its solution as an acceptable approximation for the previous ill-conditioned problem. To realize this, we adapt the Tikhonov¹⁰ regularizing procedure, that is, instead of solving the ill-posed matrix equation directly, we solve an optimization problem which minimizes the cost function given by

$$\|\Gamma(\mathbf{W}^{tot}) \cdot \mathbf{X} - \mathbf{W}^{sc}\|^2 + \gamma \|H \cdot \mathbf{X}\|^2 = \min, \quad (19)$$

which leads to a normal equation,

$$\text{Re}[(\Gamma^*(\mathbf{W}^{tot}) \cdot \Gamma(\mathbf{W}^{tot}) + \gamma H^* \cdot H) \cdot \mathbf{X}] = \text{Re}[\Gamma^* \cdot \mathbf{W}^{sc}], \quad (20)$$

where H is a smoothing matrix, γ is the regularizing parameter, and $*$ denotes conjugation transpose. Generally, increasing γ may decrease the ill-posed condition or increase the convergence rate, that may also decrease the accuracy of the solution. So there is a trade-off between accuracy and computing time. Estimates for γ should be carried out during the numerical analysis. Furthermore, in most cases, the smoothing matrix H is selected as the unit matrix or some diagonal matrix. In the next section, Eq. (20) will be used to

replace Eq. (16a) as the inverse scattering iterative equation.

To solve the nonlinear Eqs. (16b) and (20), we make use of the Born iterative method alternatively to the inverse and direct scattering procedures. This method is described as follows:

- (1) First, substitute the total field \mathbf{W}^{tot} in the coefficient matrix of Eq. (20) by the incident field \mathbf{W}^{in} , and solve Eq. (20) for $\mathbf{X}^{(1)}$ as the first-order Born approximation of \mathbf{X} .
- (2) Then, substitute the parameter \mathbf{X} in the coefficient matrix of Eq. (16b) by $\mathbf{X}^{(1)}$, solve Eq. (16b) for $\mathbf{W}^{(2)}$ as the second-order Born approximation of \mathbf{W}^{tot} (the first-order Born approximation of \mathbf{W}^{tot} is $\mathbf{W}^{(1)} = \mathbf{W}^{\text{in}}$).
- (3) Next, substitute \mathbf{W}^{tot} in $\Gamma(\mathbf{W}^{\text{tot}})$ of Eq. (20) by $\mathbf{W}^{(2)}$, and solve the equation for $\mathbf{X}^{(2)}$ as the second-order Born approximation of \mathbf{X} .
- (4) Repeat steps (2) and (3) to obtain the higher-order Born approximations, and so on.

A diagram illustrating the cross iterative procedure is given in Fig. 2.

There are two criteria to control the iterative procedure: one is for the wave field (direct scattering phase) which is defined as relative residual error (RRE):

$$\text{RRE} = \frac{\|\mathbf{W}^{\text{sc}(j)} - \mathbf{W}^{\text{sc}}\|^2}{\|\mathbf{W}^{\text{sc}}\|^2}, \quad (21)$$

where \mathbf{W}^{sc} is the measured or synthetic scattered field, $\mathbf{W}^{\text{sc}(j)}$ is calculated from Eq. (6) with the total field in the integrand replaced by the j th-order Born approximation $\mathbf{W}^{(j)}$. The other is for the parameters (inverse scattering phase) which is defined as the mean-square error (MSE):

$$\text{MSE1} = \sqrt{\frac{\int_D (\alpha^{(j)} - \alpha)^2 d\mathbf{r}}{\int_D \alpha^2 d\mathbf{r}}}, \quad (22)$$

$$\text{MSE2} = \sqrt{\frac{\int_D (\beta^{(j)} - \beta)^2 d\mathbf{r}}{\int_D \beta^2 d\mathbf{r}}},$$

where $\alpha^{(j)}$, $\beta^{(j)}$ are j th-order Born approximations of α , β .

Since the aim of this paper is for the inverse scattering for α , β , criterion (22) is used in the numerical iterations presented in the next section. However, it is noted that for a practical case, the real parameters α , β are unknown, so only criterion (21) is available for controlling the iterative procedure.

III. NUMERICAL RESULTS AND CONCLUSION

Several examples with different density and shear modulus configurations are considered and the computer simulations are conducted to evaluate the algorithms proposed above. The synthetic data of the scattered fields are produced by Eq. (6) with the assumed various parameter functions.

A. Computer simulations

The SH wave velocity in the background medium is set to be $C_T = \sqrt{\mu_0/\rho_0} = 4000$ m/s. In examples 1–3, the imaging region D is discretized into 11×11 square elements with a side length of $h = 0.8$ m. Six point sources (spaced equally with 3.2-m interval) and 20 receivers (1.6-m interval) are used in these examples. This is an asymmetrical source–

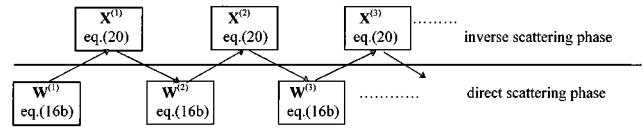


FIG. 2. The cross iterative procedure.

receiver arrangement but is more practical because the fewer the sources used, the less the experiments required. The two incident frequencies are $f_1 = 1000$ Hz and $f_2 = 1500$ Hz. For example 4, due to the complication of the parameter configurations, we use a net of 15×15 elements (16×16 nodes) along with eight point sources and thirty receivers.

1. Example 1

The parameters α, β are assumed to be ellipsoids with a distribution of the following form:

$$\alpha(\mathbf{r}) = -0.15 \sqrt{1 - \left(\frac{x-10}{2.4}\right)^2 - \left(\frac{y-12}{3.2}\right)^2}, \quad (23)$$

$$\beta(\mathbf{r}) = -0.1 \sqrt{1 - \left(\frac{x-10}{2.4}\right)^2 - \left(\frac{y-12}{2.4}\right)^2}.$$

This is shown in Fig. 3(a) and Fig. 4(a). The reconstructed results for the second, fourth, and ninth Born iterations are given in Fig. 3(b), (c), (d) and Fig. 4(b), (c), (d) for α and β , respectively. In the iterative procedure, the unit matrix is used as the smoothing matrix and γ is selected in the region of $10^{-7} - 10^{-6}$. After the ninth iteration, the criteria of convergence are $\text{MSE1} = 0.039$ and $\text{MSE2} = 0.127$. It is difficult to obtain the two criteria below a satisfactory value at the same time. Then, by changing the smoothing matrix by a diagonal matrix and recalculating the problem, it is realized that $\text{MSE1} = 0.028$ and $\text{MSE2} = 0.093$ at the ninth iteration, which are somewhat better than the previous results. The improved results are shown in Fig. 5(b), (c), (d), and Fig. 6(b), (c), (d).

2. Example 2

The parameter α is assumed to be a homogeneous square cylinder with a constant value -0.8 [shown in Fig. 7(a)] and β is assumed to be an ellipsoid [shown in Fig. 8(a)] with the distribution as follows:

$$\beta(\mathbf{r}) = -0.1 \sqrt{1 - \left(\frac{x-10}{3.2}\right)^2 - \left(\frac{y-12}{3.2}\right)^2}. \quad (24)$$

The results of the reconstruction for the second, fourth, and sixth Born iterations are shown in Fig. 7(b), (c), (d) and Fig. 8(b), (c), (d). After the 6th iteration, we have $\text{MSE1} = 0.030$ and $\text{MSE2} = 0.068$. It converges faster than the example 1.

3. Example 3

The parameter α is assumed to be a step function [a tower as shown in Fig. 9(a)] with two constant values -0.04 and -0.08 . β is assumed to be two homogeneous square cylinders with the same value of -0.05 , as shown in Fig.

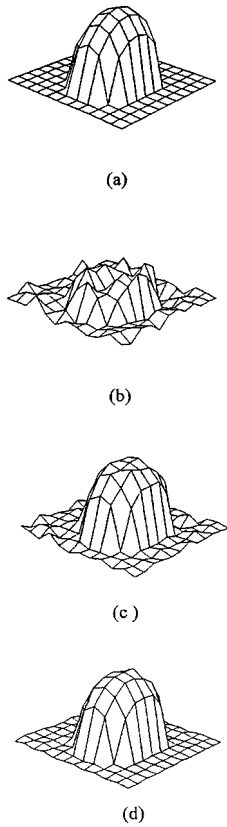


FIG. 3. Reconstruction for density with an original distribution as (a), at (b) second, (c) fourth, (d) ninth iterations, respectively.

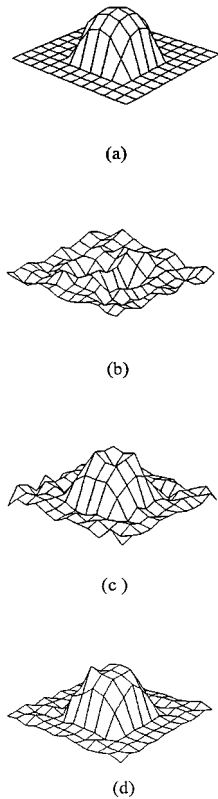


FIG. 4. Reconstruction for shear modulus with an original distribution as (a), at (b) second, (c) fourth, (d) ninth iterations, respectively.

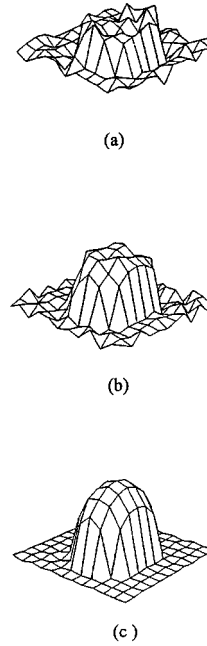


FIG. 5. Reconstruction for density with the same distribution as Fig. 3(a) by using, a diagonal smoothing matrix at (a) second, (b) fourth, (c) ninth iterations, respectively.

10(a). The two incident frequencies are selected as $f_1 = 1000$ Hz and $f_2 = 2000$ Hz. The reconstructed results for the first, third, and sixth Born iterations are given in Fig. 9(b), (c), (d) and Fig. 10(b), (c), (d). After the sixth iteration, $MSE1 = 0.021$ and $MSE2 = 0.078$. The convergence rate is faster also.

4. Example 4

The parameter α is assumed to be for two similar ellipsoids with the same maximum -0.05 , as shown in Fig.

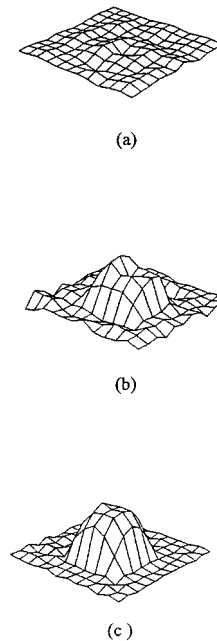
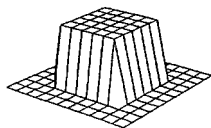
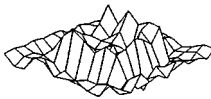


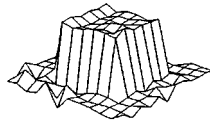
FIG. 6. Reconstruction for shear modulus with the same distribution as Fig. 4(a) by using a diagonal smoothing matrix at (a) second, (b) fourth, (c) ninth iterations, respectively.



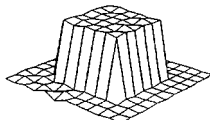
(a)



(b)

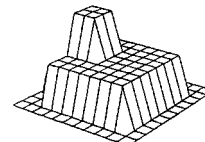


(c)



(d)

FIG. 7. Reconstruction for density with an original distribution as (a), at (b) second, (c) fourth, (d) sixth iterations, respectively.



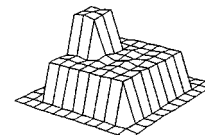
(a)



(b)

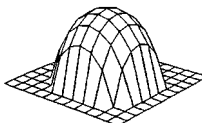


(c)



(d)

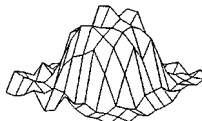
FIG. 9. Reconstruction for density with an original distribution as (a), at (b) first, (c) third, (d) sixth iterations, respectively.



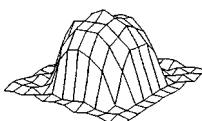
(a)



(b)

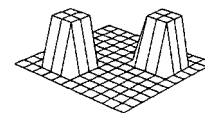


(c)



(d)

FIG. 8. Reconstruction for shear modulus with an original distribution as (a), at (b) second, (c) fourth, (d) sixth iterations, respectively.



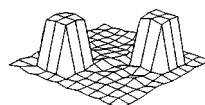
(a)



(b)



(c)



(d)

FIG. 10. Reconstruction for shear modulus with an original distribution as (a), at (b) first, (c) third, (d) sixth iterations, respectively.

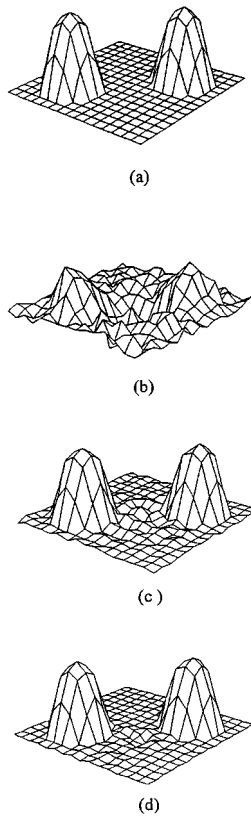


FIG. 11. Reconstruction for density with an original distribution as (a), at (b) first, (c) fourth, (d) sixth iterations, respectively.

11(a). β is assumed to be for a homogeneous square cylinder with a value of -0.05 , shown in Fig. 12(a). In this example, we use a net of 15×15 elements with 16×16 nodes and 8 sources plus 30 receivers. The incident frequencies are the same as in example 3. The results of the reconstructions for the first, fourth, and sixth Born iterations are shown in Fig. 11(b), (c), (d) and Fig. 12(b), (c), (d). After the sixth iteration, $MSE1 = 0.050$ and $MSE2 = 0.100$.

B. Discussions

The four examples presented here represents four types of parameter distributions: (1) both α and β are continuous; (2) α has jumps whereas β is continuous; (3) both α and β have jumps; and (4) β has jumps whereas α is continuous. All the examples in general show rapid convergence, i.e., both $MSE1$ and $MSE2$ fall below 0.1 within ten iterations. There is a trend in the results that the inversion accuracy for density α is better than that for shear modulus β . It is partly because in the discretization process the interpolation order for α 's coefficients is higher than that for β 's [see Eqs. (12) and (15)]. Example 1 also shows that if α and β cannot converge synchronically, we can try to use a nonuniform diagonal smoothing matrix. It is found after several tries that the optimizing factor γ for the regularization falls in the region of $10^{-7} - 10^{-6}$ which gives a rapid convergence and good accuracy. Finally, the algorithm presented above is stable enough to treat the more ill-conditioned equations as we have met in the examples where asymmetrical source-receiver schemes are used with fewer sources.

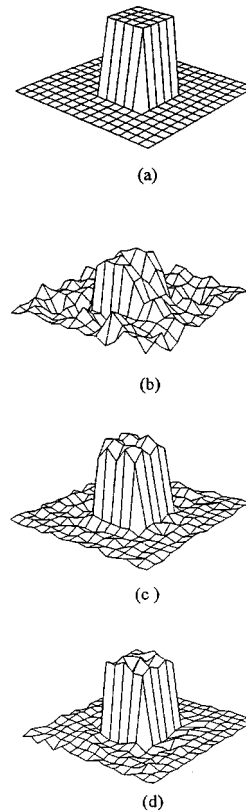


FIG. 12. Reconstruction for shear modulus with an original distribution as (a), at (b) first, (c) fourth, (d) sixth iterations, respectively.

IV. CONCLUSIONS

The problem considered in this paper represents a more practical case that concerns two parameters in a bounded medium. We have presented the inversion algorithms based on Born iteration and a regularizing procedure and a series of examples by numerical simulation to test the convergence and accuracy of the algorithms. The elementary results presented here show promise that the approach can be extended to the case of elastic vectoral waves.

APPENDIX: THE INTERPOLATING FUNCTIONS AND ITS DERIVATIVES

Defining coordinate transform:

$$x = \frac{1}{4} \sum_{i=1}^4 x_{i1} + \frac{1}{2} h \xi, \quad y = \frac{1}{4} \sum_{i=1}^4 y_{i1} + \frac{1}{2} h \eta, \quad (A1)$$

where (x_{i1}, y_{i1}) is the coordinate of i th node of l th element, and h is the side length of the element. Thus any element will be transformed into the standard element as shown in Fig. A1.

The interpolation functions used in the discretization are given as follows:

$$\begin{aligned} f_1 &= \frac{1}{4}(1 + \xi)(1 + \eta), & f_2 &= \frac{1}{4}(1 + \xi)(1 - \eta), \\ f_3 &= \frac{1}{4}(1 - \xi)(1 - \eta), & f_4 &= \frac{1}{4}(1 - \xi)(1 + \eta), \end{aligned} \quad (A2)$$

and its derivatives as:

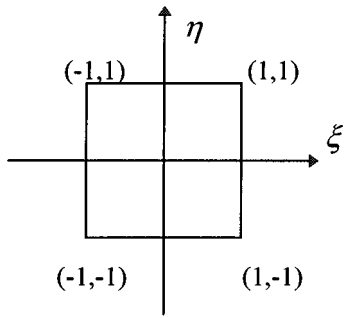


FIG. A1. The standard element in the ξ, η plane.

$$\frac{\partial f_i}{\partial x} = d_i, \quad d_1 = \frac{1}{2h} (1 + \eta), \quad d_2 = \frac{1}{2h} (1 - \eta),$$

$$d_3 = \frac{-1}{2h} (1 - \eta), \quad d_4 = \frac{-1}{2h} (1 + \eta),$$

(A3)

$$\frac{\partial f_i}{\partial y} = t_i, \quad t_1 = \frac{1}{2h} (1 + \xi), \quad t_2 = \frac{-1}{2h} (1 + \xi),$$

$$t_3 = \frac{-1}{2h} (1 - \xi), \quad t_4 = \frac{1}{2h} (1 - \xi).$$

(A4)

¹A. C. Kak, Proc. IEEE **67**, 1245–1272 (1979).

²A. J. Devaney, IEEE Trans. Geosci. Remote Sens. **GRS-22**, 3–13 (1984).

³S. J. Norton and M. Linzer, IEEE Trans. Biomed. Eng. **BME-28**, 202–220 (1984).

⁴J. D. Achenback, D. A. Sotiropoulos, and H. Zhu, ASME Trans. J. Appl. Mech. **54**, 754–760 (1987).

⁵W. H. Zhu, J. Acoust. Soc. Am. **87**, 2371–2375 (1990).

⁶R. G. Newton, J. Math. Phys. **21**, 1689–1715 (1980).

⁷S. A. Johnson and M. L. Tracy, Ultrason. Imaging **5**, 361–392 (1983).

⁸A. Tarantala, *Inverse Problem Theory* (Elsevier, Amsterdam, 1987).

⁹W. C. Chew and Y. M. Wang, IEEE Trans. Med. Imaging **MI-9**, 218–225 (1990).

¹⁰A. N. Tikhonov, *On the Problems with Approximately Specified Information in Ill-posed Problems in the Natural Science*, edited by A. N. Tikhonov and A. V. Goncharsky (MIR, Moscow, 1987).

Evolution of phonon noise and phonon state preparation in a model for generation of hypersonic phonons by laser

Jin-Hua Chai and Guang-Can Guo^{a)}

Department of Physics and Nonlinear Science Center, University of Science and Technology of China, Hefei, Anhui 230026, People's Republic of China

(Received 25 November 1996; accepted for publication 11 September 1997)

The evolution of phonon noise and the quantum correlation between phonon and photon in a model of the generation of hypersonic phonons by laser have been analyzed according to the quantum theory. The cases of perfect phase matching, phase mismatch, and losses have been discussed, respectively. It is shown that the phonon state preparation can be performed by measuring a quadrature component of the idle light field under certain conditions. © 1998 Acoustical Society of America. [S0001-4966(98)01702-0]

PACS numbers: 43.35.Ud [HEB]

INTRODUCTION

Generation and detection of hypersonic phonons with a frequency of up to 10^{12} Hz via the optical technique, and investigation of their behavior in solid state, is a significant research field in ultrasonic and solid physics.^{1,2}

Since 1971, Renk *et al.*³⁻⁶ have performed much work on the generation and detection of hypersonic phonons by optical method. In 1975, Weis and Grill⁷ first reported the generation of hypersonic phonons in a piezoelectric crystal using a far infrared pulse laser. Later, Bron's article⁸ showed how not one of the three other research groups has succeeded in replicating Weis and Grill's results, and has given the surface requirements for piezoelectric generation of high-frequency phonons. Monochromatic phonons can be generated through irradiation transition of impurity ions excited by laser, such as phonons with a frequency of 29 cm^{-1} in ruby with Cr^{3+} (Ref. 9) and tunable phonons in CaF_2 and SrF_2 with Eu^{2+} .⁶ Stimulated phonon emission can also be realized by laser pump.¹⁰⁻¹² On the other hand, the coherent detection of hypersonic phonons can be done by measuring a fluorescent emission induced by phonon absorption transition at excited impurity ions.^{3,6,13,14}

Although a great deal of work has been done on the generation of hypersonic phonons by lasers and their detection by the fluorescence, the study of phonon quantum noise properties in nonlinear interaction of hypersonic phonons and light field is a new subject. As we know, in quantum optics many quantum effects have been revealed, such as sub-Poissonian, antibunching, and the squeezed state,¹⁵⁻¹⁹ and quantum nondemolition (QND) measurements have been realized.²⁰ Because the hypersonic phonon field is a boson field as a light field, it can be studied by methods used in quantum optics and its quantum statistics properties can be revealed. In fact, many concepts in nonlinear optics have analogs in nonlinear acoustics. For example, the sum or difference-frequency generation and parametric amplification²¹⁻²³ are similar to the acoustics parametric arrays.²⁴⁻²⁸

In 1965, Yariv²⁹ first developed the quantum theory for parametric interactions of light and hypersound. In his work, the quantization of light field and acoustic field was performed, a set of differential equations which describe the coherent interaction of an arbitrary number of modes was obtained, and the problem of energy exchange between two light modes of different frequencies and an acoustic mode was formulated and solved.

In our paper, we will first describe a model of generation of hypersonic phonons by laser, then analyze the quantum noise evolution of the phonons and the correlation of phonons and idle photons using Yariv's equations of motion for a traveling wave interaction.

I. MODEL AND EQUATIONS

In Fig. 1, we show the model of generation of hypersonic phonons by laser. A beam of laser (with frequency ω_L , corresponding to the primary frequency of pump wave in the parametric arrays) is used to pump a crystal sample which is placed at very low temperature. Depending on parametric amplification or stimulated Brillouin scattering, a monochromatic phonon field (frequency ω_s , similar to the primary frequency of signal wave frequency in the parametric arrays) and an idle light field (frequency ω_i , identical to the difference frequency of parametric wave in the parametric arrays) can be generated.

We assume that the interaction between the three modes is exact resonant, namely $\omega_L = \omega_s + \omega_i$. We make a constant approximation for the pump field and describe it classically because it is usually intense enough. In addition, we need not consider the losses for the phonon and idle light because the crystal sample is placed at very low temperature and the size of the sample is small enough.

Under the above approximations, according to Ref. 29, we give the motion equations about traveling wave interaction:

^{a)}Electronic mail: gcguo@sun1x06.nsc.ustc.edu.cn

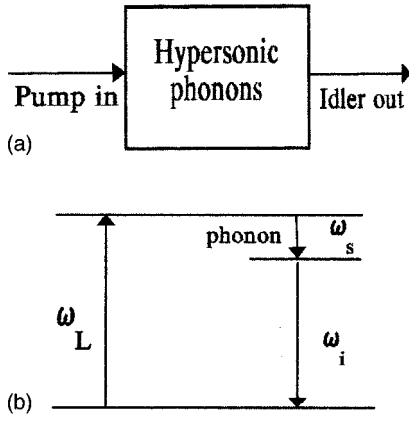


FIG. 1. (a) The model for generation of hypersonic phonons by laser. (b) The level diagram of the model.

$$\frac{da_s}{dz} = -ik_s a_s + i\eta^* \exp(-ik_p z) a_i^+, \quad (1)$$

$$\frac{da_i}{dz} = -ik_i a_i + i\eta^* \exp(-ik_p z) a_s^+,$$

where $a_s(a_s^+)$ and $a_i(a_i^+)$ are the annihilation (creation) operators of the phonon mode and the idle light mode, respectively. η is a coupling constant. k_p , k_s , and k_i are the wave vectors of the amplitude pump mode, phonon mode, and idle mode, respectively.

Making the following transformation:

$$a_s = A_s \exp(-ik_s z), \quad a_i = A_i \exp(-ik_i z), \quad (2)$$

we obtain

$$\frac{dA_s}{dz} = i\eta^* \exp(-i\Delta k z) A_i^+, \quad (3)$$

$$\frac{dA_i}{dz} = i\eta^* \exp(-i\Delta k z) A_s^+,$$

where Δk is the phase-mismatch coefficient,

$$\Delta k = k_p - k_s - k_i. \quad (4)$$

II. PERFECT PHASE-MATCHING CASE

Let $\Delta k = 0$ and η is real; from Eq. (3) we get

$$A_s(z) = A_s(0) \cosh(\eta z) + i A_i^+(0) \sinh(\eta z), \quad (5)$$

$$A_i(z) = A_i(0) \cosh(\eta z) + i A_s^+(0) \sinh(\eta z).$$

When $z=0$, both the phonon field and idle field are vacuum states. For the vacuum states, we have

$$a_j(0)|0\rangle = 0, \quad (6)$$

$$\langle 0|a_j(0)a_j^+(0)|0\rangle = 1,$$

$$[a_j(0), a_j^+(0)] = 1 \quad (j=s, i).$$

The phonon-number operator is defined as

$$n_s(z) = a_s^+(z)a_s(z) = A_s^+(z)A_s(z), \quad (7)$$

From Eqs. (5) and (7), we get

$$n_s(z) = \cosh^2(\eta z) A_s^+(0) A_s(0) + \sinh^2(\eta z) A_i(0) A_i^+(0) + i \sinh(\eta z) \cosh(\eta z) A_s^+(0) A_i(0) - i \sinh(\eta z) \cosh(\eta z) A_i(0) A_s(0). \quad (8)$$

Then we can obtain the mean phonon number from Eqs. (6) and (8)

$$\langle n_s(z) \rangle = \sinh^2(\eta z). \quad (9)$$

The fluctuation of phonon number is defined as

$$\langle \Delta n_s^2(z) \rangle = \langle n_s(z) n_s(z) \rangle - \langle n_s(z) \rangle \langle n_s(z) \rangle, \quad (10)$$

and from Eqs. (8) and (9), we obtain

$$\langle \Delta n_s^2(z) \rangle = \frac{1}{4} \sinh^2(2\eta z). \quad (11)$$

The fluctuation of idle photon number is also the same as Eq. (11). From Eqs. (9) and (11) we see that the mean value and the fluctuation of phonon number increase as the interaction distance z increases. These results are identical to those of parametric amplification in nonlinear optics.

In the following we consider the fluctuation of the quadrature components of phonon mode. The quadrature components are defined as

$$X_j(z) = A_j^+(z) + A_j(z), \quad (12)$$

$$Y_j(z) = i(A_j^+(z) - A_j(z)) \quad (j=s, i)$$

in which $X_j(z)$ is a quadrature amplitude and $Y_j(z)$ is a quadrature phase.

From Eqs. (5), we have

$$X_s(z) = X_s(0) \cosh(\eta z) + Y_i(0) \sinh(\eta z), \quad (13)$$

$$Y_s(z) = Y_s(0) \cosh(\eta z) + X_i(0) \sinh(\eta z),$$

$$X_i(z) = X_i(0) \cosh(\eta z) + Y_s(0) \sinh(\eta z),$$

$$Y_i(z) = Y_i(0) \cosh(\eta z) + X_s(0) \sinh(\eta z);$$

then we obtain the fluctuation of the quadrature components of phonon mode,

$$\langle \Delta X_s^2(z) \rangle = \langle \Delta Y_s^2(z) \rangle = \cosh(2\eta z). \quad (14)$$

For the idle mode we have the same expression for the quadrature component $\langle \Delta X_i(z) \rangle$ and $\langle \Delta Y_i(z) \rangle$ as in Eq. (14). From Eq. (14), it is clear that the fluctuations for both quadrature components are always equal and increase with distance.

Now we extend the concept of quantum nondemolition (QND) measurement to the model. We consider the measurement of the amplitude quadrature $X_s(z)$ of the phonon mode by detecting the phase quadrature $Y_i(z)$ of the idle mode. In this way we can prepare the phonon mode in a squeezed state.

The ability of phonon quantum state preparation (QSP) can be expressed by the conditional variance²⁰

$$W_{\text{QSP}} = \langle \Delta X_s^2(z) \rangle (1 - C^2(X_s(z), Y_i(z))), \quad (15)$$

where $C^2(X_s(z), Y_i(z))$ is the correlation coefficient between $X_s(z)$ and $Y_i(z)$, which can be expressed as

$$C^2(X_s(z), Y_i(z)) = \frac{|\langle X_s(z)Y_i(z) \rangle - \langle X_s(z) \rangle \langle Y_i(z) \rangle|^2}{\langle \Delta X_s^2(z) \rangle \langle \Delta Y_i^2(z) \rangle}. \quad (16)$$

If $W_{\text{QSP}}=0$, the system has a perfect state preparation. According to Ref. 20, if $W_{\text{QSP}}<1$, the system has the ability of a nonideal quantum state preparation; if $W_{\text{QSP}}=1$, the system lies in the classical limit of QSP; if $W_{\text{QSP}}>1$, the system operates in the classical domain.

From Eqs. (13)–(16), we obtain

$$C^2(X_s(z), Y_i(z)) = \tanh^2(2\eta z) \quad (17)$$

and

$$W_{\text{QSP}} = \cosh(2\eta z)(1 - \tanh^2(2\eta z)). \quad (18)$$

It is shown that, when $\eta z \gg 1$, $W_{\text{QSP}} \rightarrow 0$, which means the system has a good ability of phonon state preparation. In this case the phonon mode can be prepared in a eigenstate of $X_s(z)$ (which is known as a squeezed state) by detecting the light mode.

III. PHASE MISMATCH CASE

From Eq. (3) we obtain

$$A_s(z) = (f_1 + if_2)A_s(0) + (g_1 + ig_2)A_i^+(0), \quad (19)$$

$$A_i(z) = (f_1 + if_2)A_i(0) + (g_1 + ig_2)A_s^+(0),$$

where f_1, f_2, g_1, g_2 are all real functions of the distance z and are expressed as follows:

when $\Delta < 2\eta$,

$$\begin{aligned} f_1 &= \cos az \cosh(bz) + \frac{a}{b} \sin az \sinh(bz), \\ f_2 &= \frac{a}{b} \cos az \sinh(bz) - \sin az \cosh(bz), \\ g_1 &= \frac{\eta}{b} \sin az \sinh(bz), \\ g_2 &= \frac{\eta}{b} \cos az \sinh(bz), \end{aligned} \quad (20)$$

when $\Delta = 2\eta$,

$$\begin{aligned} f_1 &= \cos az + az \sin az, \\ f_2 &= az \cos az - \sin az, \\ g_1 &= \eta z \sin az, \\ g_2 &= \eta z \cos az, \end{aligned} \quad (21)$$

when $\Delta > 2\eta$,

$$\begin{aligned} f_1 &= \cos az \cos(bz) + \frac{a}{b} \sin az \sin(bz), \\ f_2 &= \frac{a}{b} \cos az \sin(bz) - \sin az \cos(bz), \\ g_1 &= \frac{\eta}{b} \sin az \sin(bz), \end{aligned} \quad (22)$$

$$g_2 = \frac{\eta}{b} \cos az \sin(bz),$$

where

$$a = \frac{\Delta k}{2}, \quad b = \frac{\sqrt{4\eta^2 - \Delta k^2}}{2}. \quad (23)$$

Similar to the analysis in Sec. III, we get the following expressions:

(1) The mean value and fluctuation of the phonon number:

$$\langle n_s(z) \rangle = g_1^2 + g_2^2, \quad (24)$$

$$\langle \Delta n_s^2(z) \rangle = (f_1^2 + f_2^2)(g_1^2 + g_2^2). \quad (25)$$

(2) The fluctuation of quadrature components:

$$\langle \Delta X_s^2(z) \rangle = \langle \Delta Y_s^2(z) \rangle = f_1^2 + f_2^2 + g_1^2 + g_2^2. \quad (26)$$

(3) The correlation coefficient of the quadrature components $X_s(z)$ and $Y_i(z)$:

$$C^2(X_s(z), Y_i(z)) = 4(f_1 g_2 + f_2 g_1)^2 / (f_1^2 + f_2^2 + g_1^2 + g_2^2). \quad (27)$$

According to Eqs. (20)–(27), we make plots and obtain the following results:

(1) As shown in Fig. 2(a)–(c), when $\Delta k < 2\eta$, the phonon fluctuations $\langle \Delta n_s^2(z) \rangle / \langle n_s(z) \rangle$ and $\langle \Delta X_s^2(z) \rangle \times \langle \Delta Y_s^2(z) \rangle$, and mean phonon number $\langle n_s(z) \rangle$ increase rapidly with interaction distance; when $\Delta k = 2\eta$, they first increase and then approach a fixed value.

(2) As shown in Fig. 3(a)–(c), when $\Delta k > 2\eta$, the phonon fluctuations and mean value change periodically as the distance increases, and the phonon field reverts back into the initial vacuum state periodically.

(3) Figures 4 and 5 are the plots of the conditional variance when $\Delta k \leq 2\eta$ and $\Delta k > 2\eta$, as functions of the interaction distance for different phase mismatch coefficient, respectively. It is shown that for some values of the distance and Δk values, we have $W_{\text{QSP}} < 1$, that is, QSP can be performed. The smaller Δk , the easier it is to perform QSP, and the optimum occurs for $\Delta k = 0$, as discussed in Sec. II, i.e., $\eta z \gg 1$, $W_{\text{QSP}} \rightarrow 0$, approaching the ideal QSP. However, when $\Delta k \gg \eta$, $W_{\text{QSP}} \rightarrow 1$, namely approaching the classical limit of QSP. This is because the ability of the phonon QSP depends on the correlation between $X_s(z)$ and $Y_i(z)$, and the smaller Δk , the larger $C^2(X_s(z), Y_i(z))$ and the more easier for QSP.

IV. LOSSES CASE

In any real material, there exists the scattering of hyper-sonic waves by defects and nonlinearity in the crystal. The scattering effects have been discussed in some papers.^{14,30} Now we consider the phonon loss term, corresponding to the effect of the scattering and anharmonic interactions. According to the Langevin quantum theory of damping,^{31,32} when discussing the quantum effects, we not only introduce the loss term as was done phenomenologically by Yariv in Sec. VIII in Ref. 29, but also add the fluctuation term in Eqs. (1) or (3); hence we give the following equation:

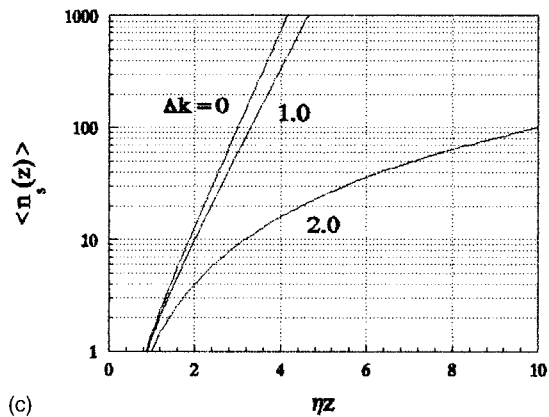
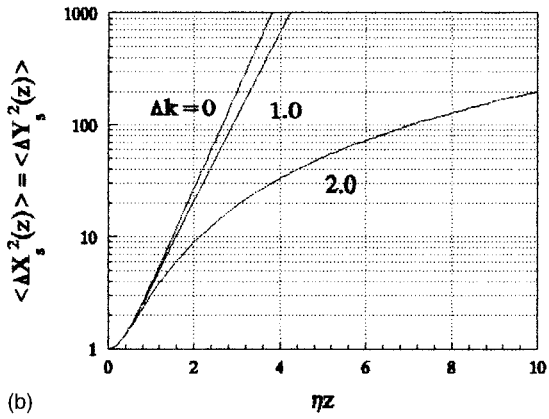
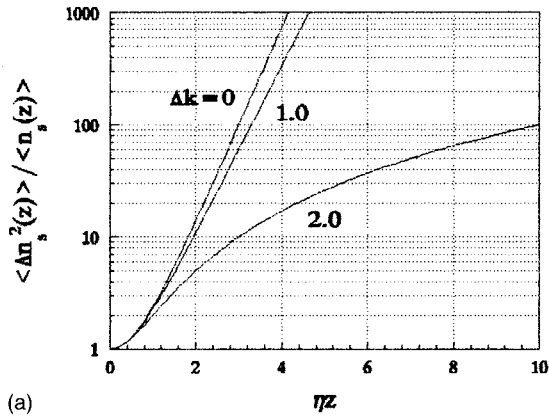


FIG. 2. (a) The fluctuation of phonon-number; (b) the fluctuation of quadrature component; and (c) the mean value of phonon number versus the scaled distance for $\Delta k=0, 1.0\eta$, and 2.0η .

$$\frac{dA_s}{dz} = -\gamma_s A_s + i\eta^* \exp(-i\Delta k z) A_i^+ + F_s, \quad (28)$$

$$\frac{dA_i}{dz} = -\gamma_i A_i + i\eta^* \exp(-i\Delta k z) A_s^+ + F_i,$$

where γ_s and γ_i are damping coefficients of the phonon mode and the idle mode, respectively, and F_s and F_i the noise operators of the two modes.

For simplicity, but not affecting the discussion of the effects caused by the losses, we assume $\gamma_s = \gamma_i = \gamma$ and $\Delta k = 0$; then from Eq. (28), we obtain

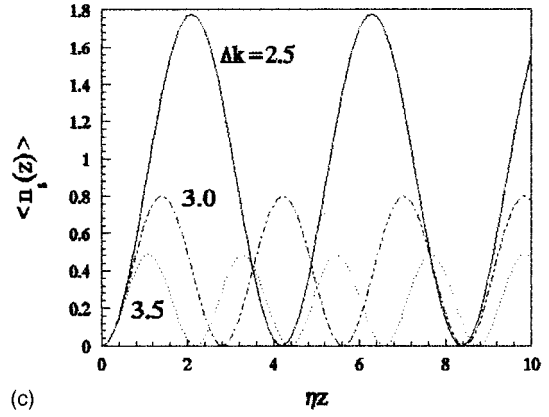
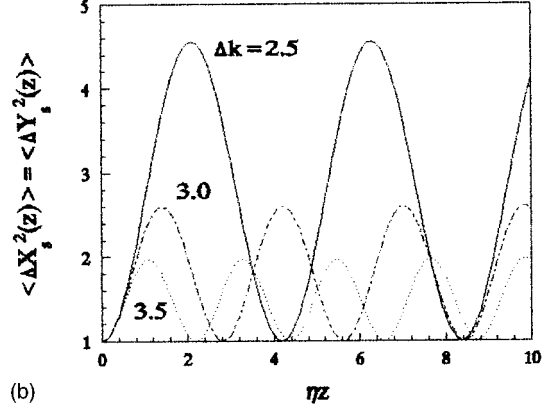
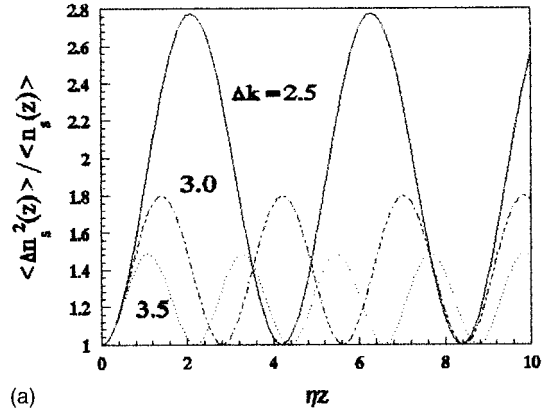


FIG. 3. (a) The fluctuation of phonon number; (b) the fluctuation of quadrature component; and (c) the mean value of phonon number versus the scaled distance for $\Delta k=2.5\eta, 3.0\eta, 3.5\eta$.

$$A_s(z) = a_1(z)A_s(0) + ia_2(z)A_i^+(0) + f_s, \quad (29)$$

$$A_i(z) = ia_2(z)A_s^+(0) + a_1(z)A_i(0) + f_s,$$

where

$$a_1(z) = \exp(-\gamma z) \cosh(\eta z), \quad (30)$$

$$a_2(z) = \exp(-\gamma z) \sinh(\eta z),$$

$$f_s = \int_0^z dz' [F_s(z') a_1(z-z') + ia_2(z-z') F_i(z')], \quad (31)$$

$$f_i = \int_0^z dz' [F_i(z') a_1(z-z') + ia_2(z-z') F_s(z')].$$

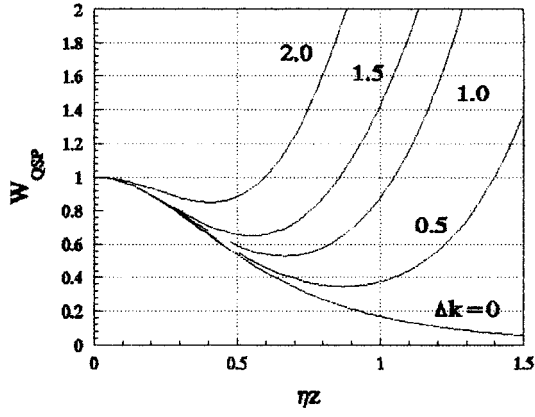


FIG. 4. The conditional variance versus the distance for $\Delta k=0, 0.5\eta, 1.0\eta, 1.5\eta, 2.0\eta$.

On the basis of the fluctuation-dissipation theorem^{31,32} from Eqs. (28), (30), and (31), we obtain the average values of f_s and f_i operators:

$$\begin{aligned}
 \langle f_s^+ f_s \rangle &= n_s(T)R_1(z) + n_i(T)R_2(z), \\
 \langle f_s f_s^+ \rangle &= (1 + n_s(T))R_1(z) + (1 + n_i(T))R_2(z), \\
 \langle f_i^+ f_i \rangle &= n_i(T)R_1(z) + n_s(T)R_2(z), \\
 \langle f_i f_i^+ \rangle &= (1 + n_i(T))R_1(z) + (1 + n_s(T))R_2(z), \\
 \langle f_s^+ f_i \rangle &= i(n_s(T) - n_i(T))R_3(z), \\
 \langle f_s f_i^+ \rangle &= -i(n_s(T) - n_i(T))R_3(z),
 \end{aligned} \tag{32}$$

where

$$\begin{aligned}
 R_1(z) &= \frac{1}{2} [1 - \exp(-2\gamma z)] \\
 &\quad + \frac{1}{4} \frac{\gamma}{\eta + \gamma} [1 - \exp(-2(\eta + \gamma)z)] \\
 &\quad - \frac{1}{4} \frac{\gamma}{\eta - \gamma} [1 - \exp(2(\eta - \gamma)z)], \\
 R_2(z) &= -\frac{1}{2} [1 - \exp(-2\gamma z)] \\
 &\quad + \frac{1}{4} \frac{\gamma}{\eta + \gamma} [1 - \exp(-2(\eta + \gamma)z)] \\
 &\quad - \frac{1}{4} \frac{\gamma}{\eta - \gamma} [1 - \exp(2(\eta - \gamma)z)], \\
 R_3(z) &= -\frac{\gamma}{\eta + \gamma} [1 - \exp(-2(\eta + \gamma)z)] \\
 &\quad - \frac{\gamma}{\eta - \gamma} [1 - \exp(2(\eta - \gamma)z)].
 \end{aligned} \tag{33}$$

Here $n_s(T)$ and $n_i(T)$ are the equilibrium numbers of the two modes at temperature T of the crystals, and when $T \rightarrow 0$, $n_s(T), n_i(T) \ll 1$.

As shown in Sec. II, the following results are obtained:

$$\langle n_s(z) \rangle = a_2^2 + \langle f_s^+ f_s \rangle, \tag{34}$$

$$\langle \Delta n_s^2(z) \rangle = a_1^2 a_2^2 + a_1^2 \langle f_s^+ f_s \rangle + a_2^2 \langle f_s f_s^+ \rangle, \tag{35}$$

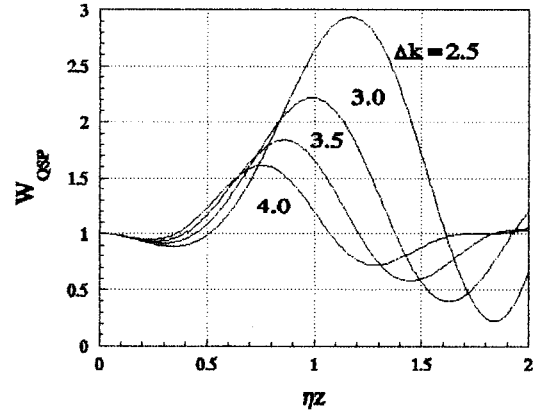


FIG. 5. The conditional variance versus the distance for $\Delta k=2.5\eta, 3.0\eta, 3.5\eta, 4.0\eta$.

$$\langle \Delta X_s^2(z) \rangle = \langle \Delta Y_s^2(z) \rangle = a_1^2 + a_2^2 + \langle f_s^+ f_s \rangle + \langle f_s f_s^+ \rangle, \tag{36}$$

$$\langle \Delta X_i^2(z) \rangle = \langle \Delta Y_i^2(z) \rangle = a_1^2 + a_2^2 + \langle f_i^+ f_i \rangle + \langle f_i f_i^+ \rangle, \tag{37}$$

$$C^2(X_s(z), Y_i(z)) = \frac{|2a_1 a_2 - i \langle f_s^+ f_i \rangle + i \langle f_s f_i^+ \rangle|^2}{\langle \Delta X_s^2(z) \rangle \langle \Delta Y_i^2(z) \rangle}. \tag{38}$$

In order to clearly see the effect of losses, we need a simple form of above expressions. In fact, the crystal sample is usually at very low temperature, hence we consider $T \rightarrow 0$ case; in this case, we have approximately, $n_s(T), n_i(T) \approx 0$. Thus from Eq. (32), $\langle f_s^+ f_s \rangle = \langle f_i^+ f_i \rangle = \langle f_s^+ f_i \rangle = \langle f_s f_i^+ \rangle = 0$, $\langle f_s f_s^+ \rangle = \langle f_i f_i^+ \rangle = R_1(z) + R_2(z)$, then we obtain

$$\langle n_s(z) \rangle = \exp(-2\gamma z) \sinh^2(\eta z), \tag{39}$$

$$\frac{\langle \Delta n_s^2(z) \rangle}{\langle n_s(z) \rangle} = \exp(-2\gamma z) \cosh^2(\eta z) + R_1(z) + R_2(z), \tag{40}$$

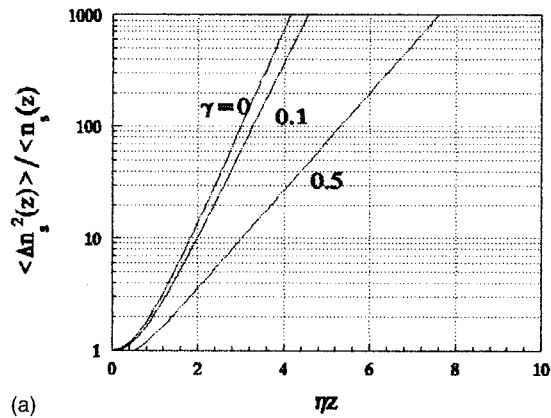
$$\langle \Delta X_s^2(z) \rangle = \langle \Delta Y_s^2(z) \rangle = \exp(-2\gamma z) \cosh(2\eta z) + R_1(z) + R_2(z), \tag{41}$$

$$\begin{aligned}
 C^2(X_s(z), Y_i(z)) &= \\
 &= \frac{\exp(-4\gamma z) \sinh^2(2\eta z)}{[\exp(-2\gamma z) \cosh(2\eta z) + R_1(z) + R_2(z)]^2}.
 \end{aligned} \tag{42}$$

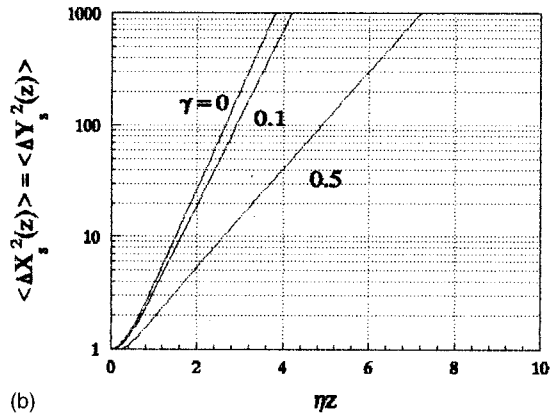
Figure 6(a)–(c) shows the phonon fluctuations $\langle \Delta n_s^2(z) \rangle / \langle n_s(z) \rangle$ and $\langle \Delta X_s^2(z) \rangle / \langle \Delta Y_s^2(z) \rangle$, and mean phonon number $\langle n_s(z) \rangle$, versus interaction distance ηz , for the damping coefficients $\gamma=0, 0.1\eta, 0.5\eta$, in the phase-matching case $\Delta k=0$. Here $\gamma=0$ corresponds to the case of no losses and phase matching discussed in Sec. II. We see that the losses will decrease the effect of evolution of phonon in $\gamma=0$.

Figure 7 shows the curves of the conditional variance W_{QSP} versus ηz for $\gamma=0, 0.1\eta, 0.5\eta$ in the case $\Delta k=0$. It is shown that the losses will pose serious limitation on the distance over which the system has the ability of quantum state preparation.

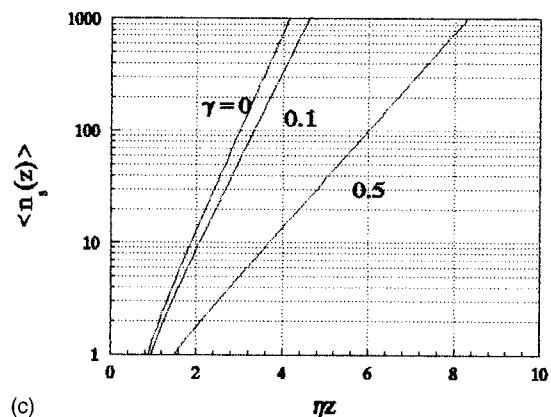
Similarly for the phase mismatch $\Delta k \neq 0$, we can also illustrate that the losses will destroy the oscillations and ability of quantum state preparation mentioned in Sec. III.



(a)



(b)



(c)

FIG. 6. (a) The fluctuation of phonon number; (b) the fluctuation of quadrature component; and (c) the mean value of phonon number versus the scaled distance for $\gamma=0, 0.1\eta, 0.5\eta$ in $\Delta k=0$.

V. SUMMARY AND DISCUSSIONS

According to the quantum theory for interaction of light and hypersound, we analyze the phonon evolution in the generation model of a hypersound by laser, including the noises of the phonon number and the quadrature components, and the phonon quantum state preparation ability. It is shown that, when the phase-mismatch coefficient Δk is small ($k < 2\eta$), the phonon noises increase as the distance increases; when Δk is large ($k > 2\eta$), the phonon mode goes back to the initial vacuum state periodically as the distance. The more interesting the phonon quantum state preparation can be performed under certain conditions, and the smaller the Δk , the easier for QSP, and an ideal QSP can be obtained for perfect phase matching.

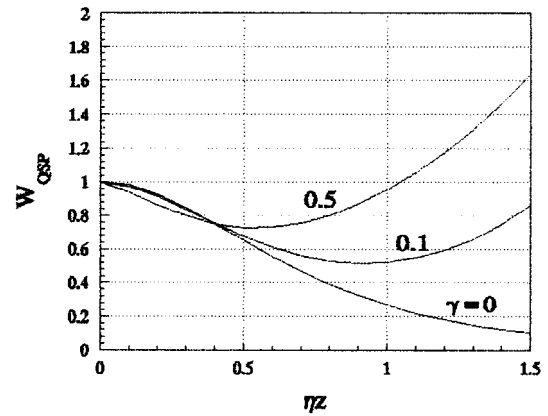


FIG. 7. The conditional variance versus the scaled distance for $\gamma=0, 0.1\eta, 0.5\eta$ in $\Delta k=0$.

It is worthwhile to indicate that the losses caused by the scattering and anharmonic interaction will limit the distance of the realization of such phenomena. Moreover, in the crystals for which the phenomena mentioned is relevant, the materials are significantly anisotropic and the group speed and phase speed of the traveling waves are usually in different directions; therefore the incident light beam and the generated acoustic wave will not overlap over an extended region. This will limit the efficiency in the phase match situation and probably ruin the oscillations in the phase-mismatch case. Moreover, it will limit the ability to create a squeezed phonon state. In our analysis, we omit these limitation, hence our concept will only apply to a very special set of circumstances.

In addition, we note that, since the maximum sound frequency which can be generated by parametric amplification or stimulated Brillouin scattering of acoustic phonons, is only 10^{-5} that of the laser pump frequency (as explained on page 35 of Ref. 29), experiments to test the prediction are not feasible for high-frequency (i.e., above 100 GHz) phonons. For example, for phonons in the 0.2–0.9 terahertz regime, one would therefore need a laser pump with a wavelength below 150 Å. On the other hand, since piezoelectric generation of acoustic phonons in the microwave regime has been demonstrated, experiments might be attempted there.

ACKNOWLEDGMENTS

This work was supported by the National Natural Science Foundation of China.

¹W. Y. Jia and L. W. Pei, "Generation of hypersonic phonons by lasers and their detection by fluorescence," *Prog. Phys. (China)* **4**, 287 (1984).

²W. N. Wybourne and J. K. Wigmore, "Phonon spectroscopy," *Rep. Prog. Phys.* **51**, 923 (1988).

³K. F. Renk and L. J. Deisehofer, "Imprisonment of resonant phonons observed with a new technique for the detection of 10 Hz phonons," *Phys. Rev. Lett.* **26**, 764 (1971).

⁴H. Lengfellner and K. F. Renk, "Detection of acoustic zone-boundary phonons by phonon difference absorption," *J. Phys. (France)* **C6**, 259 (1981).

⁵R. Baumgartner, M. Engelhardt, and K. F. Renk, "Spontaneous decay of high-frequency acoustic phonon in CaF₂," *Phys. Rev. Lett.* **47**, 1403 (1981).

⁶W. Einfeld and K. F. Renk, "Tunable optical detection and generation of terahertz phonon in CaF₂ and SrF₂," *Appl. Phys. Lett.* **34**, 481 (1979).

- ⁷W. Grill and O. Weis, "Excitation of coherent and incoherent Terahertz phonon pulse in quartz using infrared laser radiation," *Phys. Rev. Lett.* **35**, 588 (1975).
- ⁸W. E. Bron, M. Rossinelli, Y. H. Bai, and F. Keilmann, "Surface requirements for piezoelectric generation of high frequency phonons," *Phys. Rev. B* **27**, 1370 (1983).
- ⁹J. I. Dijkhuis, A. van der Pol, and H. W. de Wijn, "Spectral width of optically generated bottlenecked 29 cm^{-1} phonons in ruby," *Phys. Rev. Lett.* **37**, 1554 (1976).
- ¹⁰W. E. Bron and W. Grill, "Stimulated phonon emission," *Phys. Rev. Lett.* **40**, 1459 (1978).
- ¹¹P. Hu, "Stimulated emission of 29 cm^{-1} phonons in ruby," *Phys. Rev. Lett.* **44**, 417 (1980).
- ¹²D. J. Sox, J. E. Rives, and R. S. Meltzer, "Stimulated emission of 0.2 THz phonons in $\text{LaF}_3:\text{Er}^{3+}$," *Phys. Rev. B* **25**, 5064 (1982).
- ¹³R. S. Meltzer and J. E. Rives, "New high energy monoenergetic source for nanosecond phonon spectroscopy," *Phys. Rev. Lett.* **38**, 421 (1977).
- ¹⁴W. E. Bron and W. Grill, "Phonon spectroscopy, I. Spectral distribution of phonon pulse," *Phys. Rev. B* **16**, 5303 (1977).
- ¹⁵See papers contained in *J. Opt. Soc. Am. B* Special issue 4(1987); *J. Mod. Opt.* Special issue 34 (1987).
- ¹⁶H. P. Yuen, "Generation, detection, and application of high-intensity photon-number-eigenstate fields," *Phys. Rev. Lett.* **56**, 2176 (1986).
- ¹⁷R. E. Slusher, P. Grangier, A. LaPorta, B. Yurke, and M. J. Potasek, "Pulsed squeezed light," *Phys. Rev. Lett.* **59**, 2566 (1987).
- ¹⁸X. T. Zou and L. Mandel, "Photon-antibunching and sub-Poissonian photon statistics," *Phys. Rev. A* **41**, 475 (1990).
- ¹⁹P. Kumer, O. Aytur, and J. M. Huang, "Squeezed-light generation with an incoherent pump," *Phys. Rev. Lett.* **64**, 1015 (1990).
- ²⁰J. F. Roch, G. Roger, P. Grangier, J.-M. Courty, and S. Reynaud, "Quantum nondemolition measurement in optics: A review and some Recent experiment results," *Appl. Phys. B* **55**, 291 (1992).
- ²¹Y. R. Shen, *The Principles of Nonlinear Optics* (Wiley, New York, 1984), Chaps. 6–9.
- ²²M. Schubert and B. Wilhelmi, *Nonlinear Optics and Quantum Electronics* (Wiley, New York, 1986), Chap. 11.
- ²³R. W. Boyd, *Nonlinear Optics* (Academic, New York, 1992), Chap. 2.
- ²⁴O. V. Rudenko and S. I. Soluyan, *Theoretical Foundations of Nonlinear Acoustics* (Consultants, New York, 1977), Chap. 6.
- ²⁵P. J. Westervelt, "Parametric acoustic array," *J. Acoust. Soc. Am.* **35**, 535 (1963); **57**, 1352 (1975).
- ²⁶H. M. Merklinger, "Improved efficiency in the parametric transmitting array," *J. Acoust. Soc. Am.* **58**, 784 (1975).
- ²⁷M. B. Moffett and R. H. Mellen, "Model for parametric sources," *J. Acoust. Soc. Am.* **61**, 325 (1977).
- ²⁸N. G. Pace and R. V. Ceen, "Time domain study of the terminated transient parametric array," *J. Acoust. Soc. Am.* **73**, 1972 (1983).
- ²⁹A. Yariv, "Quantum theory for parametric interactions of light and hypersound," *IEEE J. Quantum Electron.* **QE-1**, 28 (1965).
- ³⁰T. E. Wilson, F. M. Lurie, and W. E. Bron, "Quasidiffusive transport of a broadband phonon distribution," *Phys. Rev. B* **30**, 6103 (1984).
- ³¹W. H. Louisell, *Quantum Statistical Properties of Radiation* (Wiley, New York, 1973), Chap. 7.
- ³²M. Sargent III, M. O. Scully, and W. E. Lamb, *Laser Physics* (Wesley, New York, 1974), Chap. 19.

Experiments on acoustic streaming in a fluid layer between vibrating surfaces and amplitude-dependent damping of vibrations

Adnan Akay and Zhaoshun Xu

Department of Mechanical Engineering, Carnegie Mellon University, Pittsburgh, Pennsylvania 15213

(Received 20 January 1997; revised 5 August 1997; accepted 11 November 1997)

The dynamic behavior of a thin fluid layer between two flat, vibrating surfaces is examined experimentally. The oscillatory motion of the surfaces is shown to generate a continuous flow of fluid within the layer in the form of eddies. Damping induced by the presence of the fluid layer is found to be amplitude-dependent and related to the generation of the steady streams within the layer.

© 1998 Acoustical Society of America. [S0001-4966(98)05302-8]

PACS numbers: 43.40.At, 43.40.Tm [CBB]

INTRODUCTION

A thin layer of fluid between two oscillating surfaces has the capability to both bear load and provide damping, as in the case of squeeze-film bearings. In cases of extended flexible structures, such as beams and plates, air between two closely spaced surfaces has been shown to be particularly effective in dissipating vibration energy at low frequencies; for example Ref. 1. Although the previous linear analyses suggest that the damping mechanism is the oscillatory viscous drag of the fluid in the layer [viz., Refs. 1–4], experiments described below show that the dissipation associated with the squeeze action on thin fluid films is amplitude dependent. The nonlinear increase of damping with the amplitude of oscillations was the motivation here to examine the motion of fluid in a thin layer. The sources of nonlinear damping are traced to the development of a continuous fluid flow within the fluid layer.

Fluid in a thin layer between two flat, parallel oscillating surfaces moves in and out through the perimeter of the layer in an oscillatory manner, following the compression and expansion the fluid layer undergoes. Experiments described in this paper show that, in addition to the oscillatory motion of the fluid, continuous flow streams are also developed in the layer. Fluid is continuously drawn in from and exhausted to the ambient medium at different locations along the perimeter of the layer. A similar, but more pronounced behavior is seen in the case of tilted rigid, flat bearings, as discussed later.

In the regimes where streams occur, at modest amplitudes of vibration, the continuous flow developed between two parallel surfaces exhibits eddy like patterns in the layer. The striations are seemingly laminar and follow stationary paths forming eddies that can be easily visualized. At increased vibration amplitudes, the speed of the continuous flow increases and the steady streams begin to diffuse, and with further increase of amplitude they become turbulent destroying the laminar structure of the eddies. Formation of streams in the layer is accompanied by the development of jets (turbulent exhaust) at its perimeter. The strength of the jets also increases with the vibration amplitude.

Development of eddies in the layer, and jets at the pe-

rimeter, coincides with the transition from a linear to a non-linear regime of the damping induced in the structure by the fluid layer. At high vibration amplitudes, where increased fluid transport is observed, amplitude dependence of damping is evident. The additional flow through the layer brought about by the steady flow of fluid is suggested here to be the cause of the increase in fluid-layer damping with the amplitude of oscillations.

In this paper, development of eddies in a fluid layer is demonstrated with experiments. The eddies are visualized and recorded for an air layer between two surfaces. Measurements of structural damping were made to correlate damping with the changes in the characteristics of the flow in the layer and the formation of jets at the edges. Experiments described here suggest that the eddies are formed as a result of the pressure field generated in a fluid layer between oscillating surfaces.

I. EXPERIMENTS

Experiments were designed both to visualize flow patterns and to simultaneously measure structural damping resulting from the motion of a thin layer of fluid between two closely spaced parallel surfaces. Measurements were conducted using pairs of flexible beams and plates as well as circular and rectangular rigid, flat bearings. In the experiments described here, one in each pair was excited by a shaker and the other was mounted rigidly to act as a “damper.”

Experiments were conducted in air where arrays of “point” smoke sources were placed along the free edges of the layers. The smoke sources were placed slightly below the plane of the fluid layer to avoid interference with the free flow of air in and out of the space between the surfaces. Flow visualization was realized with the use of a He–Ne laser, from which a sheet of light was obtained by using a cylindrical lens. The sheet of laser light passing through the fluid layer and its scattering due to the presence of smoke streams form the basis of visualization. The striations from the smoke sources were recorded photographically. In the case of flexible beams, experiments were also conducted in water using light reflecting particles. In addition, influence of the

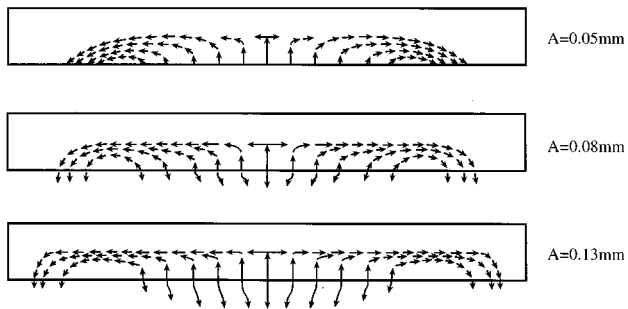


FIG. 1. Schematic depiction of the development of stream patterns in a thin air layer as observed under a beam vibrating in its first mode. The layer thickness is $h_0 = 1.8$ mm, $f = 29$ Hz, excitation point is located at $L/6$ from one end of the beam. A is rms value of vibration amplitude at the excitation point.

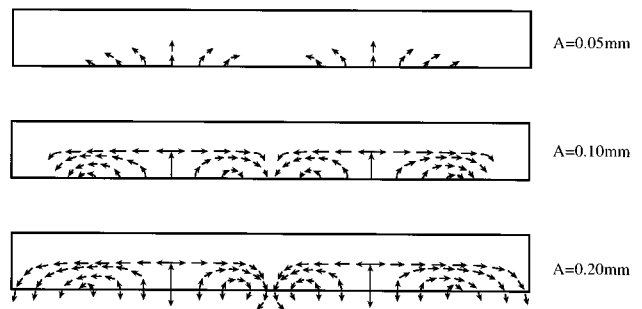


FIG. 2. Schematic depiction of the development of stream patterns in a thin air layer as observed under a beam vibrating in its second mode. $h_0 = 1.8$ mm, $f = 71$ Hz, the excitation point is at $L/6$ from one end of the beam. A is rms value of vibration amplitude at the excitation point.

length of the rigidly mounted damper beam on flow formation between it and a flexible beam was investigated. Damping values were obtained from the measurements of mechanical impedance.

In most studies involving thin fluid layers and squeeze films, the nondimensional *squeeze number* σ is used as a parameter to account for the effects of bearing size, oscillation frequency, and layer thickness. In the present case, the nonlinear characteristics of damping and formation of eddies also depend on the amplitude of oscillations. To better describe the conditions of the experiments in this paper, a modified version of σ is introduced; a nondimensional quantity, *streaming number* Σ , is defined as a product of the normalized value, ϵ , of the amplitude of oscillations of the layer thickness and the corresponding squeeze number, σ :

$$\Sigma = \epsilon \sigma,$$

where $\epsilon = A/h_0$, the nominal thickness of the layer is h_0 , and amplitude of layer thickness oscillation is A . Squeeze number σ is a quantity commonly used in lubrication studies and is defined as:

$$\sigma = 12\mu\omega B^2/p_0h_0^2,$$

where μ is the viscosity of the fluid, ω is the frequency of oscillations, and B is a characteristic size of the surfaces. The ambient pressure is p_0 .

A. Flexible beams

In the first set of experiments, a transparent Plexiglas beam, clamped at both ends, was excited at a point by a shaker to oscillate it at one of its natural frequencies with the corresponding mode shape. Below the flexible beam, a damper beam of the same size was positioned in parallel and in close proximity. The influence of the length of the damper beam is considered later in the paper.

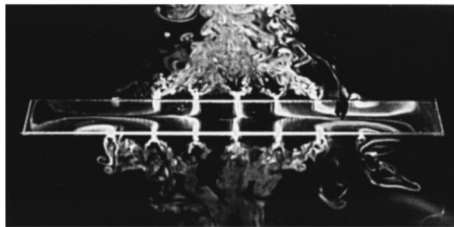
At low amplitudes of vibration, flow is entirely oscillatory and behaves as incompressible; air enters and exits in the normal direction to the edges all along the perimeter. The flow is largely confined to under the antinode(s) of the beam. The cycle of entry and exit follows the vibration frequency with which the layer volume undergoes expansion and compression. The distance of excursion of the fluctuating flow into the gap increases with the amplitude of vibrations.

As the vibration amplitude is increased, in addition to the fluctuating flow, a continuous flow pattern begins to develop in the layer. An example of the development of flow patterns is sketched in Fig. 1 for increasing values of vibration amplitude of the beam in its first mode. In this case, the flow pattern is in the form of an eddy in each quadrant of the layer. The arrows describe the direction of motion of the fluid and the travel distance of the streams in the layer. Steady streams of flow enter into the gap between the beams through both of the free edges at and near the antinode. The flow entering through each side meets at the longitudinal centerline of the layer. The combined flow bifurcates to travel in opposite directions along the centerline and each new flow again bifurcates to exit near the nodal lines on both sides, at each end of the beam. Around the core of each eddy, located in between the nodal and antinodal lines of the beam, flow enters and exits with a small radius near the free edge of the layer.

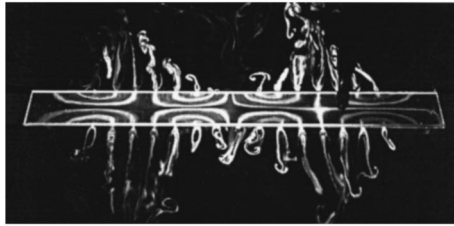
The flow activity is more intense under the antinodes of the beam than under the nodes. Flow under an antinode includes a strong fluctuating component that enters and exits the layer at the frequency of beam oscillation, superimposed on the continuous laminar streams that enter and travel. As the amplitude is increased further, the laminar structure of the steady stream patterns starts to break down; first the streams diffuse, later they vanish and are replaced by a turbulent flow.

The symmetry of the four quadrants of the streams about the center lines (in a plane parallel to the surfaces) of the fluid layer is a result of the symmetry of the boundary conditions at the edges of the fluid layer. When the symmetry of the edge conditions is altered, for example, by completely closing one of the free edges of the layer to prevent flow through it, the streams entering through the remaining free edge reach the closed edge and circulate to exit, forming only two eddy cells symmetric about the antinodal line of the beam.

At higher modes of vibration of the beam the number of eddies generated at the first mode are increased by the number of mode order, albeit with correspondingly smaller sizes. Under a beam of length L , vibrating at its n th mode, there are n nearly identical sets of eddies, each set with four symmetric quadrants, as depicted for the second mode of vibration in Fig. 2.



Mode # 1
 $h_0 = 2.1\text{mm}$
 $A = 0.84\text{mm}$
 $f = 31\text{Hz}$



Mode # 2
 $h_0 = 2.1\text{mm}$
 $A = 0.32\text{mm}$
 $f = 76\text{Hz}$



Mode # 3
 $h_0 = 1.1\text{mm}$
 $A = 0.17\text{mm}$
 $f = 136\text{Hz}$

FIG. 3. Visualization of stream patterns using smoke sources and a sheet of laser light in a fluid layer under a beam vibrating with different mode shapes. Formation of jets are also apparent at the free edges. Air layer thickness is h_0 , A is the amplitude of vibration at an antinode, and f is the frequency of vibration.

Photographic recordings of the flow patterns for the first three modes of vibration are shown in Fig. 3. The center of each set of eddies is under one of the antinodal lines of the beam and the boundaries of each set are under the adjacent nodal lines.

The oscillatory component of the flow which follows the frequency of the beam vibrations, accompanies the steady stream, but is not easily visible. The presence of such fluctuations is visualized as shown in Fig. 4 where a close-up view of the striae shows jagged patterns corresponding to the fluctuations in the flow.

Visualization of flow patterns were also made in water for a limited number of cases. The beams were placed in a tank containing water. As before, excitation was provided at a point on the beam by a vibration exciter. Light reflecting particles were used to visualize the motion of the fluid. Because of the heavy fluid loading, only the first mode of the beam was excited. The results showed existence of eddies in the water layer similar to those observed in the air layer. One notable difference is the speed with which the streams travel. In water the speed was much higher than in air.

B. Flexible plates

Flow of air into and out of a layer under a transparent plate was examined in the same manner as described above for beams. Stream patterns described in Fig. 5 are obtained by visually tracing the stream from each smoke source

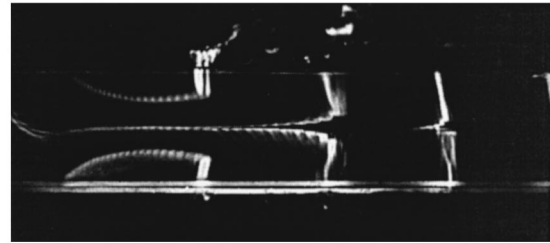


FIG. 4. Striations under the left half of a beam vibrating in its first mode. Jagged patterns correspond to the fluctuating component of the flow.

around the perimeter of the air layer. The plate was supported at four points near its corners and excited by a shaker off its center.

Stream patterns shown in Fig. 5 correspond to the vibration response of a rectangular plate simply supported near its four corners and vibrating at its (0,0) and (1,0) modes. Air enters at and near the antinode lines and exits beneath the nodal lines, as in the case for a beam. In the (0,0) mode, the antinode of the plate is at its center and the motion of the plate in this mode exhibits nodal lines near its corners as shown with dashed lines in Fig. 5. The corresponding antinodal lines coincide with the centerlines of the plate, thus each edge of the plate has an antinode at its center and nodes near its corners. As indicated by the arrows in Fig. 5, flow enters through the center of each edge and exits through the nearest corners. In the case of (1,0) mode, there is a nodal line along the length of the plate as well as two nodal lines (curves) near its shorter edges perpendicular to the nodal line along its length. In this case, again, flow enters through the two edges where the antinodes are located and exits through the remaining two edges that are in close proximity of the nodal lines. General characteristics of flow patterns under flexible beams and plates are essentially the same.

C. Size effects

Both the flow patterns in a thin layer of fluid and the resulting damping are influenced by the size and location of the damper beam (or plate). Experiments were conducted using rigid "damper" beams with shorter lengths than the flexible beam.

When a damper of length $l \geq L/2n$ is positioned between nodal lines of a vibrating beam, pressure distribution in the layer is influenced largely by the mode shape of the beam and the eddies developed have the same characteristics as those with a full-length damper as described earlier. When the damper length is small compared to the corresponding wavelength ($\lambda = 2L$) of the beam, i.e., $l \leq \lambda/4n$, eddies still can develop but with attributes more reminiscent of those between rigid flat bearings, which will be examined later. In such cases, pressure distribution in the layer is more or less similar to that between two rigid surfaces and the mode shapes of the flexible beam are not influential on the flow patterns.

D. Rigid bearings

Qualitatively, flow of fluid between a pair of parallel, rigid rectangular bearings exhibits the same characteristics as

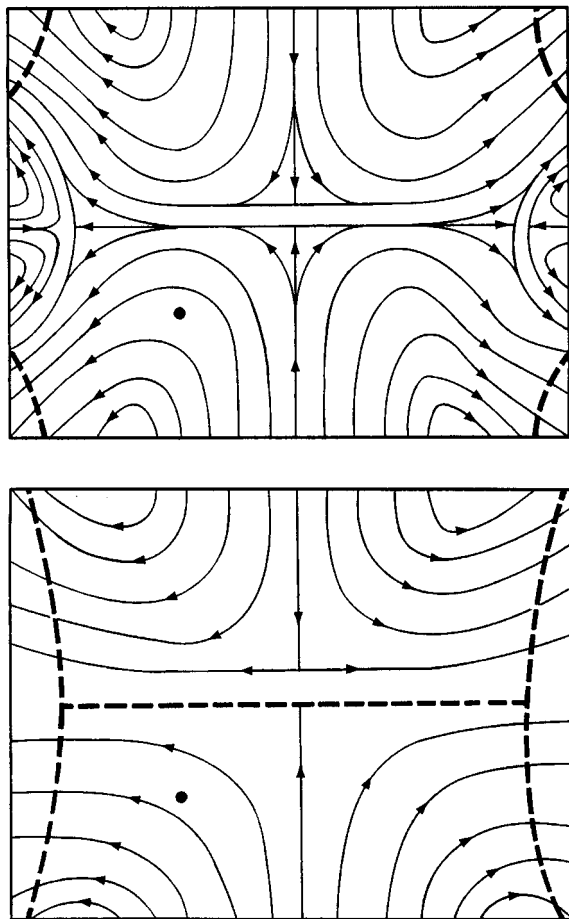


FIG. 5. Striations in a thin air layer under a rectangular plate vibrating at (0,0) mode (top) and (1,0) mode (bottom). Excitation is provided at the point marked by ● and dashed lines indicate the nodal lines.

that between flexible beams and plates. The major difference is in the spatial distributions of the pressure in the layer: In the case of rigid bearings, pressure distribution is determined by the edge conditions alone unlike the case of extended flexible structures, such as beams or plates, where the spatial distribution of pressure in the layer may be dominated by the spatial distribution of vibration of the flexible surface. The role of edge conditions is also observed in the different flow patterns between pairs of circular and rectangular rigid bearings.

Additional experiments were conducted to visualize flow patterns in an air layer between two rigid, parallel bearings with one oscillating in a direction normal to the other. The qualitative similarities of the streams to those under flexible beams notwithstanding, fluid in a layer between two rigid, parallel surfaces exhibits different behavior than between flexible beams, particularly, as the excitation levels are increased.

The boundary conditions at the perimeter of a layer alone determine the spatial distribution of pressure field in a fluid layer under a rigid bearing. Accordingly, the geometry of a bearing affects the patterns of striations. In the case of a pair of rectangular parallel bearings, pressure distribution is not azimuthally axisymmetric. As in the case of flexible plates and beams, with increasing vibration amplitude (or

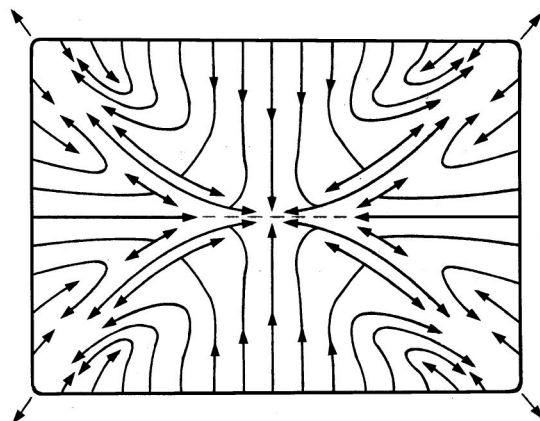
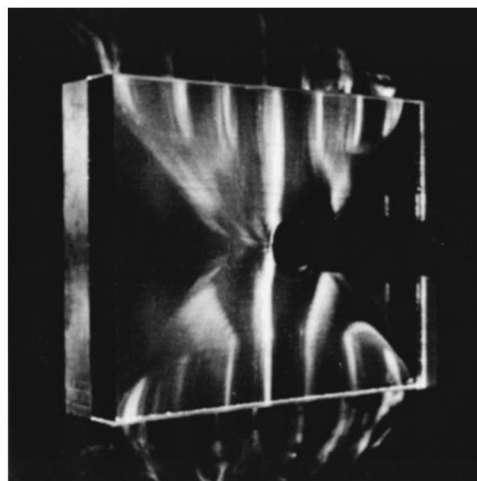


FIG. 6. Flow patterns between two rigid rectangular air bearings, tilt angle is zero, $h_0 = 1.8$ mm, $A = 0.5$ mm, and $f = 20$ Hz.

increasing streaming number), the behavior of the fluid shows a transition from that of a purely fluctuating motion to one that has a mix of fluctuating and continuous components. At very low streaming numbers, both the pressure in the layer and flow are purely fluctuating; fluid exits and reenters the layer through its edges as the volume between the surfaces decreases and increases, respectively, following the oscillation of the bearing. Fluid flow in the layer exhibits a parabolic profile. As before, the distance of excursion of the flow into the layer depends on the amplitude of vibration. Such behavior can be predicted by linear analysis.⁵

As the streaming number is increased (in the present experiments by either an increase in oscillation amplitude or a decrease in layer thickness), a subambient pressure is developed in the layer. The striae follow the gradient of the subambient pressure in the layer with a continuous flow of air which show characteristics of eddies similar to those generated by flexible beams described above. The motion of the oscillatory portion of the smoke is no longer discernible, but a steady flow develops. As visualized by striations of smoke, the steady flow also exhibits a parabolic profile and follows the patterns described earlier; entering the layer at the center of each edge and exiting near the corners, as shown in Fig. 6.

The motion of these streams is limited in the case of circular parallel bearings. The present experiments show

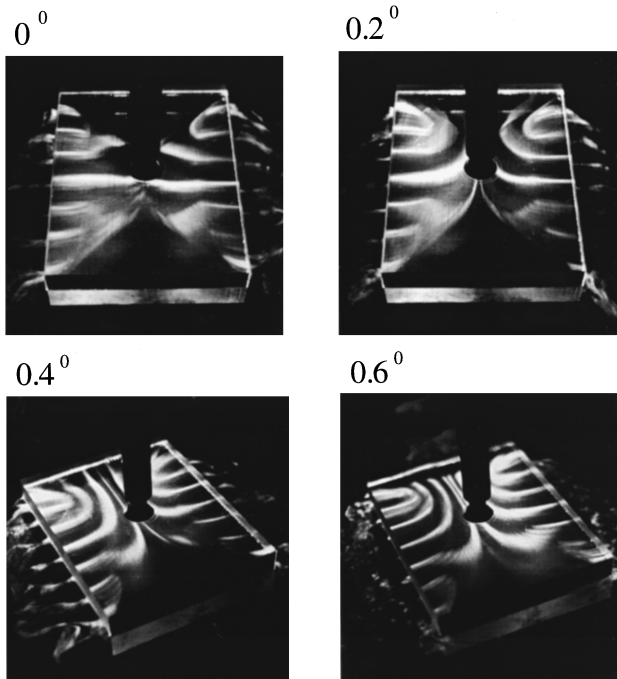


FIG. 7. Effects of tilt angle on flow patterns under a rigid air bearing. $h_0 = 1.8$ mm, $A = 0.5$ mm, and $f = 20$ Hz. As the tilt angle is increased, flow becomes more unidirectional.

that, in the case of circular bearings, where pressure distribution in the layer is azimuthally axisymmetric, initially, there is only a hint of residual smoke streams entering and staying at the center of the gap, without any chance to escape. In such a symmetric geometry streaming does not develop. If the symmetry is altered, for example, by positioning an obstacle near a part of the perimeter of the layer, the symmetry of the pressure distribution changes and streams develop.

The pressure field in the layer can also be altered by tilting one of the bearings upon which flow patterns become directional, flowing from the wider part of the gap to the narrower part. Generation of flow across bearing surfaces at high squeeze numbers has been identified previously (Tichy and Modest,⁶ Murray and Mote⁷), however, as shown in Fig. 7, present experiments show this flow to be not entirely unidirectional; air still enters and exits through the sides of the layer. As the tilt angle and streaming number are increased, flow through the sides decreases making it more unidirectional between the leading and trailing edges.

Further increase in streaming number shows another transition; this time, a superambient pressure field is developed in the layer. Associated with this development is a “lift” of the oscillating bearing from its nominal position with an effective increase in the mean thickness of the fluid layer, a phenomenon well known in bearings which was originally shown by Taylor and Saffman⁸ and Salbu.⁹

The development of flow patterns in the layer between two parallel surfaces is in a way similar to the case of tilted bearings. Unlike the case of circular bearings where the pressure field is azimuthally axisymmetric, pressure distribution between rectangular plates is not uniform. As a result of fluctuations in the layer, a time-invariant pressure field de-

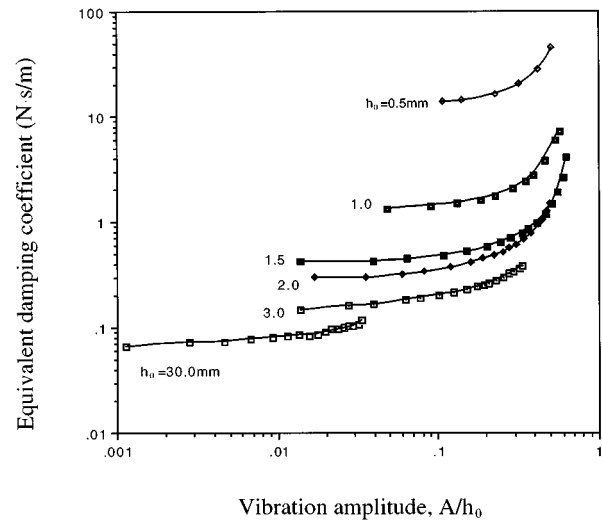


FIG. 8. Damping induced by the presence of a thin air layer adjacent to a beam vibrating in its first mode. Each plot corresponds to a different layer thickness, h_0 .

velops between the rigid bearings with a minimum, subambient pressure at its center. The resulting striations seen here follow the pressure gradients in the layer.

E. Damping measurements

Damping measurements were made at each stage of development of striations in the layer under a flexible beam. Damping values were obtained from the real part of the impedance measured at the excitation point of the flexible beam at its resonance frequencies.

For a given nominal layer thickness, damping is found to be amplitude dependent. The dependence of damping on vibration amplitude changes from linear to exponential as the amplitude of beam vibration increases. Transition from linear to exponential dependence on amplitude coincides with an increase in the intensity of the eddies in the layer, as indicated in Fig. 8 where damping values are plotted for several layer thicknesses. The same data shows a more universal relationship when plotted as a function of streaming number Σ , to take into account the amplitude of vibrations, as shown in Fig. 9. Damping values obtained in these experiments are equivalent damping and are due to a combination of mechanisms. At low streaming numbers viscous losses through the oscillatory flow dominate exhibiting a relatively constant value. At higher streaming numbers, losses due to steady streams in the layer and flow through the edges dominate.

II. DISCUSSION AND CONCLUDING REMARKS

A thin layer of fluid between two rigid or flexible parallel surfaces exhibits a new type of acoustic streaming. The development of the streams is gradual so that there is not a critical value above which streaming suddenly appears. Through flow visualization, it is demonstrated that the “ac” fluctuations of flow into and out of a thin layer lead to the development of “dc” steady streams. While the eddies generated are somewhat similar in appearance to those seen at

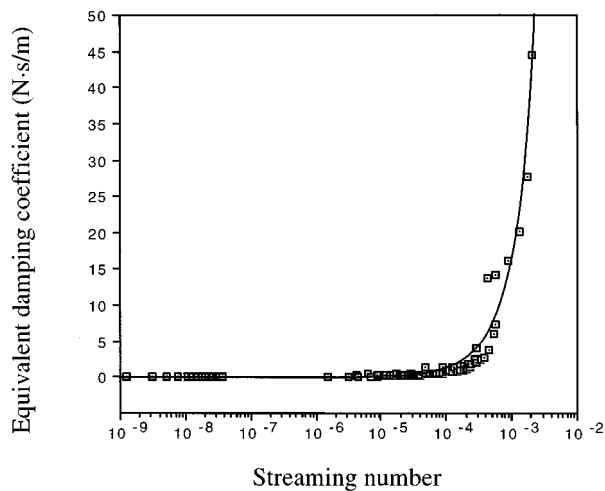


FIG. 9. Damping induced by a thin air layer under a beam vibrating in its first mode. This figure is a combination of the plots in Fig. 8 which are now plotted as a function of streaming number.

the onset of instability of a Couette flow in a narrow gap between rotating cylinders or even to Benard cells, the nature of the present vortices are different in that their circulations are not zero. Flow is drawn from and exhausted to the ambient surroundings. They are also reminiscent, in appearance only, of electric field lines of transverse magnetic waves between plane conductors.

It is known that vortices are generated at surfaces as a result of viscosity in the fluid and that they are characterized as a second-order phenomenon, often referred to as acoustic streaming.¹⁰ The early observations of their existence were made by Dvorak¹¹ in Kundt's tube which was later analyzed by Rayleigh and, more recently, by many other investigators (viz., Refs. 12, 13). Rayleigh extended the earlier analysis to explain the mechanism of generation of vortices between flat, parallel surfaces. These vortices are largely restricted to the acoustic viscous boundary layer. In the case of two closely spaced flat surfaces, there are two rows of periodically spaced vortices about a plane of symmetry between the surfaces with their axes parallel to the flat surfaces.

The streaming described here is different than those investigated earlier by Rayleigh and others. The axes of the two types of eddies are normal to each other, and in the present case, the eddies are not confined to the viscous boundary layer. It is possible that simultaneously with the development eddy cells across the width of a thin layer shown here, vortices due to second-order effects and viscosity, as described by Rayleigh, may also develop across the thickness of the layer. However, such vortices were not visible in the present examples under the conditions considered here.

The acoustic streaming described by Rayleigh and others depends on the presence of viscosity, and vanishes in its absence. The streaming developed in thin fluid layers between oscillating flat surfaces depends on the time-independent pressure distribution rather than the presence of viscosity.¹⁴ The vortices are not closed and, hence, each has a circulation that is different than zero. The axes of rotation of these striations are normal to the surfaces on either side of

the layer. The vortex patterns developed follow the gradient of the static pressure field in the layer. The striations generated in this manner are solely due to the oscillations of the parallel surfaces.

Pressure field between two closely spaced surfaces is influenced by both the boundary conditions of the layer and by the velocity distribution over the surfaces. In the case of rigid bearings, boundary conditions dominate whereas in the case of flexible surfaces, spatial distribution of the vibration velocity is the determining factor. As a result, flow patterns in the layer under a flexible beam are very pronounced when the vibration of, say, one of the surfaces closely represents one of its own mode shapes. Striations developed between a flexible beam and a damper beam with length shorter than $L/2n$ are similar to those between rigid bearings. However, damper beams of length $l \geq L/2n$ develop eddies characteristic of flexible beams as shown earlier.

An important consequence of the streaming described here is to increase structural damping due to a fluid layer. The presence of fluid in a thin layer is a source of structural damping (viz., Refs. 1–4), and such damping has been considered to be linear and due only to the oscillatory motion of the fluid in the layer. However, the influence of additional steady motion of the fluid described here has not been considered. It is also known that vortices generated in a fluid can dissipate the acoustical modes. In this paper experimental results show that vortices also extract energy from structural vibrations. In summary, based on the experimental observations, there is a strong suggestion that fluid layer damping is enhanced by the formation of eddies in the layer between two parallel surfaces. Structural damping may also be enhanced by the formation of jets to the extent that they are inevitable at the speeds of ejection of air from the thin layer. Such a transport mechanism between fluid in a layer and the surrounding medium may also be a desirable attribute in lubrication problems.

ACKNOWLEDGMENTS

The authors gratefully acknowledge the many discussions with Professor K. Uno Ingard during the course of this research. The authors also acknowledge the support provided by NSF (Grant No. MSS-9396104) and ONR (Code 334).

¹K. U. Ingard and A. Akay, "On the vibration damping of a plate by means of a viscous fluid layer," *ASME J. Vib. Acoust. Stress Reliab. Design* **109**, 178–184 (1987).

²E. E. Ungar and G. Maidanik, "High-frequency plate damping due to gas pumping in riveted joints," *J. Acoust. Soc. Am.* **44**, 292–295 (1968).

³G. Maidanik, "Energy dissipation associated with gas-pumping in structural joints," *J. Acoust. Soc. Am.* **40**, 1064–1072 (1966).

⁴M. J. H. Fox and P. N. Whitton, "The damping of structural vibrations by thin gas films," *J. Sound Vib.* **73**, 279–295 (1980).

⁵J. Kang, Z. Xu, and A. Akay, "Inertia effects on compressible squeeze films," *ASME J. Vib. Acoust.* **117**, 94–102 (1995).

⁶J. A. Tichy and M. F. Modest, "Squeeze film flow between arbitrary two-dimensional surfaces subject to normal oscillations," *J. Lubrication Technol.* **100**, 316–322 (1978).

⁷Y. D. Murray and C. D. Mote, Jr., "Analysis of a plane inclined guide bearing under transverse vibration and translation of a plate," *J. Lubrication Technol.* **105**, 335–341 (1983).

⁸G. I. Taylor and P. G. Saffman, "Effects of compressibility at low Reynolds numbers," *J. Aerosol Sci.* **24**, 553 (1957).

- ⁹E. O. J. Salbu, "Compressible squeeze films and squeeze bearings," *J. Basic Eng.* **86**, 355–366 (1964).
- ¹⁰John William Strutt, Lord Rayleigh, *The Theory of Sound* (Dover, New York, 1945), Vol. 2, pp. 333–342.
- ¹¹V. Dvorak, "Ueber einige neue Staubfiguren," and "Ueber die akustische Anziehung und Abstofsung," *Ann. Phys. (Leipzig)* **153**, 102–114 (1874); **157**, 42–72 (1876).
- ¹²W. L. Nyborg, "Acoustic streaming near a boundary," *J. Acoust. Soc. Am.* **30**, 329–339 (1958).
- ¹³C. P. Lee and T. G. Wang, "Outer acoustic streaming," *J. Acoust. Soc. Am.* **88**, 2367–2375 (1990).
- ¹⁴U. Ingard and D. C. Galehouse, "Second-order pressure distribution in an acoustic normal mode in a rectangular cavity," *Am. J. Phys.* **39**, 811–813 (1971).

Utilization of coupling effects in compensator design for structural acoustic systems

H. T. Banks

Center for Research in Scientific Computation, North Carolina State University, Raleigh, North Carolina 27695-8205

M. A. Demetriou

Department of Mechanical Engineering, Worcester Polytechnic Institute, Worcester, Massachusetts 01609

R. C. Smith

Department of Mathematics, Iowa State University, Ames, Iowa 50011

(Received 16 September 1996; accepted for publication 15 September 1997)

The quantification and utilization of coupling effects in a prototypical structural acoustic system are examined in this paper. In typical systems, the coupling mechanisms are manifested in two ways. The first leads to the transfer of energy from an ambient field to an adjacent structure and is often responsible for exogenous structural excitation. The second involves the transfer of energy from the vibrating structure to an adjacent field. This is the source of structure-borne noise and is ultimately the mechanism through which structural actuators are utilized to attenuate noise. The examples presented here demonstrate that in fully coupled systems, both mechanisms should be incorporated to accurately model system dynamics. The examples also illustrate advantages and limitations of compensators which utilize the accurate modeling of the structural coupling. © 1998 Acoustical Society of America. [S0001-4966(98)03401-8]

PACS numbers: 43.40.At, 43.50.Ki, 43.20.Tb, 43.40.Rj [PJR]

INTRODUCTION

The control of noise and vibration in structural acoustic systems has been intensely investigated in applications ranging from aircraft design to transformer construction. The trademark of all such applications and the mechanism ultimately utilized for control is the inherent coupling between the structure and adjacent acoustic fields. This mechanism is manifested in two ways. In the first, energy from a vibrant field is transmitted to a structure through pressure or force coupling. This is the mechanism responsible for fuselage vibrations due to propeller draft or vibrations in the casing surrounding a transformer. Unattenuated vibration due to the acoustic or fluid/structure coupling can lead to structural fatigue. It can also lead to the second mechanism of coupling in which energy is transmitted from the structure to an acoustic or compressible fluid field. This is the source of structure-borne noise and is ultimately the mechanism through which structural actuators are used to attenuate noise.

Accurate modeling of the acoustic, structural, and coupling components is a necessary first step for predicting the dynamics of structural acoustic systems and the design of model-based controllers. Substantial effort has been directed toward structural systems, and adequate linear models for various geometries have been developed. Moreover, as illustrated in Ref. 1, model-based controllers employing piezoceramic actuators have been experimentally implemented. The case for large displacements and hence nonlinear structural models is less complete.

Similarly, linear wave models have been successfully utilized for low sound-pressure level acoustic applications. Like the structural case, appropriate nonlinear models for

large sound-pressure levels are still under investigation. An important issue when modeling the acoustic field concerns the relatively low wave speeds at general atmospheric conditions. This leads to delays between the input of a signal to a structure-mounted actuator and measurement of the corresponding response at an acoustic sensor. If left unmodeled or uncompensated, this delay can destabilize a controller. This motivates the use of a dynamic wave model which incorporates the physical transmission time.

The analysis of coupling mechanisms is less complete than that of the other components. In the structural acoustic systems described in Refs. 2–4 and references therein, pressure coupling provided the mechanism for energy transfer from the field to the structure while velocity coupling yielded the converse effect. Modal coupling, radiation efficiency and radiation impedance were employed in Refs. 5–8 where the problem of attenuating structure-borne noise was considered. These coupling techniques are concerned with describing the transfer of energy from the structure to the field to address the objective of reducing the efficiency of structural radiation. The coupling between a nonlinear acoustic/fluid field and a structure through pressure balancing was employed in Refs. 9, 10 while pressure balancing was again used in Ref. 11 for modeling the converse effect of acoustic radiation from a vibrating panel. In these latter investigations, partial differential equations (PDE) derived from physical principles such as force and momentum balancing were used to model the fluid/acoustic/structural dynamics; however, these coupled models have not yet been utilized in acoustic control laws.

In this work, we quantify and utilize the two coupling effects for compensator design in a prototypical 3-D struc-

tural acoustic system. This significantly extends the results of Refs. 2 and 4 due to the higher dimensional complexity and analysis pertaining to compensator improvements through utilization of the coupling. It differs from Refs. 5–7 in that coupled PDE are used to model the system and provide a basis for the control laws. Modeling the system in this manner helps to provide insight for simulations and the development of model-based controllers.

The advantage of accurate quantification of the coupling mechanisms for the purpose of modeling system dynamics is obvious. The potential advantages from the perspective of control design can be indicated through a brief overview of various aspects concerning a feedback controller utilizing structural actuators.

In the idealized case of full state feedback control, information regarding the discretized structural acoustic model and control operator is used to compute a Riccati solution and corresponding gain. This gain is then applied to the state to compute a control signal which is fed back to the structural actuators. Control of the structure-borne noise is realized due to the natural coupling between structural and acoustic dynamics. In this case, the model provides the system information necessary for attaining an accurate Riccati solution and hence gain. Note that this case is idealized in the sense that it requires knowledge of the full structural (displacement, velocity) and acoustic (potential, pressure) states which is not possible with current instrumentation.

A more realistic scenario when implementing the controller is one in which a limited number of structural and/or acoustic measurements are available. In this case, the model is first used to provide system information for an observer Riccati equation necessary for estimating or reconstructing the state. The data for these calculations consists in part of the structural and/or acoustic measurements. The feedback gain is then applied to the state estimate to obtain the control signal. The model plays a dual role in this case since it provides system information used in calculating both the state estimate and the feedback gain.

The second source of system information is the data collected from structural and/or acoustic sensors. In applications involving an enclosed or interior field (e.g., an aircraft cabin), it may be possible to use both structural (e.g., accelerometers or piezoceramic patches) and acoustic (e.g., microphones) sensors. To reduce weight and hardware requirements, however, it is often advantageous to limit the number of sensors. This places the impetus for accurate system predictions on the model. In other applications such as reduction of exterior noise generated by an underwater vehicle, it is difficult, and in many cases impossible, to employ acoustic sensors. In such cases, the acoustic state and feedback gain must be calculated solely using the coupled model with structural data as input. For both interior and exterior noise control applications, the success of the controller is contingent upon the accuracy of the acoustic, coupling, and structural components of the model.

We consider here various aspects concerning the utilization of coupling in a 3-D structural acoustic system. In Sec. I, we present the model and outline the general feedback control methodology for the system. Numerical simulations

demonstrating the effects of the two coupling mechanisms are presented in Sec. II. It is demonstrated that for systems subjected to the two effects, both coupling mechanisms must be incorporated in the model to attain the correct system dynamics and frequencies. Control simulations for a system having the geometry and dimensions of an experimental device used in the Acoustics Division, NASA Langley Research Center, are presented in Sec. III. These results demonstrate that even with a limited number of structural and acoustic sensors, significant attenuation is attained with the model-based controllers. The dimensions of the acoustic cavity relative to the vibrating surface are significantly increased in Sec. IV. This illustrates certain controllability issues which must be addressed when employing structure-mounted actuators to control large acoustic fields. Section VI contains a summary of numerical results demonstrating the design of a purely structural controller. These results show that such a controller provides adequate attenuation for exogenous frequencies near *isolated* structural frequencies, but has minimal effect when acousticlike modes are excited. Taken in concert, these examples demonstrate advantages and limitations of controllers which utilize accurate modeling of the structural acoustic system.

From these results, the main contributions of this paper can be summarized as follows. With regard to modeling, the numerical simulations demonstrate the manner through which natural frequencies for the fully coupled system are modified from those of the isolated structural and acoustic components. The coupling between components also leads to corresponding modal changes. From a control perspective, the numerical examples demonstrate that for this geometry, little control authority is lost by employing a realizable output feedback compensator as compared with an impractical full state linear quadratic regulator (LQR) theory. It is further demonstrated that for this system, very adequate attenuation can be obtained via a compensator which incorporates the fully coupled model but utilizes only structural sensors. While the degree of attenuation achieved in this manner is application dependent, these results illustrate the potential for reduced hardware through accurate modeling. Finally, the results illustrate that the reduction of structural vibrations via isolated structural models is not adequate for controlling broadband structure-borne noise. The acoustic field and coupling mechanisms must also be incorporated in the model to attain effective noise reduction.

I. MODEL AND CONTROL FORMULATION

The first step in the development of a model-based control methodology is the derivation of a system model. This is illustrated here for a structural acoustic test apparatus used in the Acoustics Division, NASA Langley Research Center. This apparatus consists of a concrete cylinder with a thin aluminum plate mounted at one end as depicted in Fig. 1. The opposite end is closed so that interior acoustic waves are reflected back toward the plate. A loudspeaker adjacent to the plate provides an exterior acoustic source while surface-mounted piezoceramic patches are used as control elements.

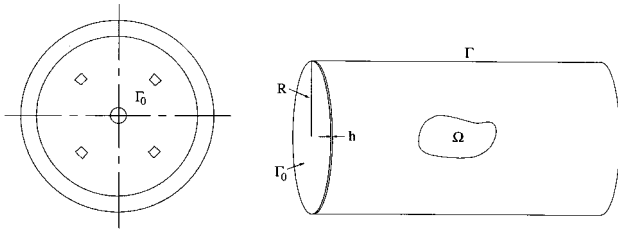


FIG. 1. Cylindrical structural acoustic system with a fixed plate at one end.

Note that in this system, both coupling between the plate and interior field and pressure interactions between the interior/exterior acoustic field and plate are present.

To specify the geometry, the cylinder is assumed to have length l and radius R with a thin plate of thickness h at one end. The interior acoustic domain is denoted by Ω while Γ_0 indicates the plate domain. The remaining boundary of the acoustic cavity is denoted by Γ and has an outward normal \hat{n} .

The test apparatus just described is a hybrid system in several senses. The generation of interior noise is due to structural acoustic coupling while control via the piezoceramic patches is due to electromechanical interactions. Finally, the system contains several electromagnetic components due to the hardware required for sensing and control. We describe here PDE modeling the structural, acoustic and structural acoustic coupling components as well as the electromechanical input from the patches. When spatially discretized, this provides a vector ordinary differential equation (ODE) which approximates the dynamics of the acoustic and mechanical components of the experimental system. Various uncertainties are then incorporated in the model to account for model and sensing uncertainties as well as the unmodeled electromagnetic components. The section concludes with an H^∞ /MinMax formulation appropriate for ODE system with uncertainties.

A. System model

1. Interior acoustic field

For the purpose of modeling the interior acoustic field dynamics, it is assumed that sound-pressure levels are below 120 dB and that acoustic field damping is negligible. These are reasonable and typical assumptions when considering the sound-pressure levels and dimensions of the experimental device or in applications such as control of fuselage noise. Furthermore, it is assumed that the acoustic cylinder and end cap are not influenced by the interior acoustic field; that is, no concrete pipe or end-cap frequencies are found in the system response. This latter assumption has been verified through accelerometer tests with the experimental apparatus.

With ϕ and c denoting an acoustic velocity potential and wave speed, respectively, an appropriate model for the interior acoustic dynamics is

$$\begin{aligned} \frac{\partial^2 \phi}{\partial t^2} &= c^2 \Delta \phi, \quad (r, \theta, z) \in \Omega, \quad t > 0, \\ \nabla \phi \cdot \hat{n} &= 0, \quad (r, \theta, z) \in \Gamma, \quad t > 0 \end{aligned} \quad (1)$$

with the Laplacian in cylindrical coordinates given by

$$\Delta \phi = \frac{\partial^2 \phi}{\partial r^2} + \frac{1}{r} \frac{\partial \phi}{\partial r} + \frac{1}{r^2} \frac{\partial^2 \phi}{\partial \theta^2} + \frac{\partial^2 \phi}{\partial z^2}.$$

The linear wave equation provides an adequate approximation of the acoustic dynamics for the sound-pressure levels under consideration. This includes the dynamic effects which account for the time required to propagate information from the plate to sensors in the cavity. The hardwall boundary conditions are justified by the inert nature of the concrete cylinder and end cap with the form of the boundary conditions resulting from the inherent relationship between the acoustic potential and velocity (i.e., $v = -\nabla \phi$). We note that the derivative boundary conditions employed in (1) to model the hardwall conditions are mathematically designated as Neumann boundary conditions and will be referred to as such throughout the remaining discussion. We also point out that the potential is related to the acoustic pressure through the relationship $p = \rho_f (\partial \phi / \partial t)$ where ρ_f denotes the equilibrium density of the interior acoustic field.

2. Plate dynamics

In developing dynamic equations for the plate, it is assumed that the displacements are within the range of linear theory and that rotational effects are negligible. Both of these assumptions have been validated through parameter estimation for the plate in the experimental setup (see Ref. 12). Furthermore, it is assumed that s piezoceramic patch pairs are bonded to the plate and driven out-of-phase so as to produce pure bending moments. Finally, it is assumed that boundary clamps are sufficiently tight to permit the use of clamped-edge boundary conditions. This latter assumption is again justified by the experimental results in Ref. 12.

As detailed in Refs. 13 and 14, an appropriate model for the circular plate derived under the assumption of negligible air damping is

$$\begin{aligned} \rho h \frac{\partial^2 w}{\partial t^2} - \frac{\partial^2 \mathcal{M}_r}{\partial r^2} - \frac{2}{r} \frac{\partial \mathcal{M}_r}{\partial r} + \frac{1}{r} \frac{\partial \mathcal{M}_\theta}{\partial r} - \frac{2}{r} \frac{\partial^2 \mathcal{M}_{r\theta}}{\partial r \partial \theta} \\ - \frac{2}{r^2} \frac{\partial \mathcal{M}_{r\theta}}{\partial \theta} - \frac{1}{r^2} \frac{\partial^2 \mathcal{M}_\theta}{\partial \theta^2} = g(t, r, \theta), \end{aligned}$$

$$w(t, R, \theta) = \frac{\partial w}{\partial r}(t, R, \theta) = 0,$$

where w is the transverse plate displacement, ρ is the structural density, and g is a general surface force input term. The general moments are given by

$$\mathcal{M}_r = M_r - (M_r)_{pe},$$

$$\mathcal{M}_\theta = M_\theta - (M_\theta)_{pe},$$

$$\mathcal{M}_{r\theta} = M_{r\theta},$$

where M_r , M_θ , and $M_{r\theta}$ are internal plate moments and $(M_r)_{pe}$ and $(M_\theta)_{pe}$ are the external moments generated by the patches.

The internal moments for the circular plate with s pairs of surface-mounted piezoceramic patches have the form

$$\begin{aligned}
M_r &= DK_r + \bar{D}K_\theta + c_D \dot{K}_r + \bar{c}_D \dot{K}_\theta, \\
M_\theta &= DK_\theta + \bar{D}K_r + c_D \dot{K}_\theta + \bar{c}_D \dot{K}_r, \\
M_{r\theta} = M_{\theta r} &= \frac{D}{2} \tau - \frac{\bar{D}}{2} \tau + \frac{c_D}{2} \dot{\tau} - \frac{\bar{c}_D}{2} \dot{\tau},
\end{aligned} \tag{2}$$

where

$$\begin{aligned}
K_r &= -\frac{\partial^2 w}{\partial r^2}, \quad K_\theta = -\frac{1}{r} \frac{\partial w}{\partial r} - \frac{1}{r^2} \frac{\partial^2 w}{\partial \theta^2}, \\
\tau &= -\frac{2}{r} \frac{\partial^2 w}{\partial r \partial \theta} + \frac{2}{r^2} \frac{\partial w}{\partial \theta}.
\end{aligned}$$

The global flexural rigidity parameters D , \bar{D} , and Kelvin–Voigt damping parameters c_D and \bar{c}_D are given by

$$\begin{aligned}
D(r, \theta) &= \frac{E_p h^3}{12(1-\nu_p^2)} + \frac{2}{3} \sum_{i=1}^s \left[\frac{E_{pe} a_{3pe}}{1-\nu_{pe}^2} + \frac{E_{b\ell} a_{3b\ell}}{1-\nu_{b\ell}^2} \right] \chi_i(r, \theta), \\
\bar{D}(r, \theta) &= \frac{E_p h^3 \nu_p}{12(1-\nu_p^2)} + \frac{2}{3} \sum_{i=1}^s \left[\frac{E_{pe} a_{3pe} \nu_{pe}}{1-\nu_{pe}^2} + \frac{E_{b\ell} a_{3b\ell} \nu_{b\ell}}{1-\nu_{b\ell}^2} \right] \\
&\quad \times \chi_i(r, \theta), \\
c_D(r, \theta) &= \frac{\hat{c}_{D_p} h^3}{12(1-\nu_p^2)} + \frac{2}{3} \sum_{i=1}^s \left[\frac{\hat{c}_{D_{pe}} a_{3pe}}{1-\nu_{pe}^2} + \frac{\hat{c}_{D_{b\ell}} a_{3b\ell}}{1-\nu_{b\ell}^2} \right] \\
&\quad \times \chi_i(r, \theta), \\
\bar{c}_D(r, \theta) &= \frac{\hat{c}_{D_p} h^3 \nu_p}{12(1-\nu_p^2)} \\
&\quad + \frac{2}{3} \sum_{i=1}^s \left[\frac{\hat{c}_{D_{pe}} a_{3pe} \nu_{pe}}{1-\nu_{pe}^2} + \frac{\hat{c}_{D_{b\ell}} a_{3b\ell} \nu_{b\ell}}{1-\nu_{b\ell}^2} \right] \chi_i(r, \theta),
\end{aligned} \tag{3}$$

where the Young's modulus, density coefficient, Poisson ratio, and Kelvin–Voigt damping coefficient for the plate are denoted by E_p , ρ_p , ν_p , and \hat{c}_{D_p} , respectively, while similar parameters for the patches and bonding layer are denoted by E_{pe} , ρ_{pe} , ν_{pe} , $\hat{c}_{D_{pe}}$ and $E_{b\ell}$, $\rho_{b\ell}$, $\nu_{b\ell}$, $\hat{c}_{D_{b\ell}}$, respectively. The constants $a_{3b\ell} \equiv (h/2 + T_{b\ell})^3 - (h/2)^3$, $a_{3pe} \equiv (h/2 + T_{b\ell} + T)^3 - (h/2 + T_{b\ell})^3$ arise from integration through the bonding layer $T_{b\ell}$ and patch thickness T while $\chi_i(r, \theta)$ denotes the characteristic function which has a value of 1 in the region covered by the i th patch and is 0 elsewhere. Finally, the mass density also exhibits a piecewise constant nature due to the presence of the patches and is given by

$$\rho(r, \theta) = \rho_p + \frac{2}{h} \sum_{i=1}^s [\rho_{b\ell} T_{b\ell} + \rho_{pe} T] \chi_i(r, \theta).$$

We point out that if the plate, patches, and bonding layers have the same Poisson ratios ($\nu_p = \nu_{pe} = \nu_{b\ell} = \nu$), then the internal moment expressions reduce to the familiar relations for a thin plate with variable thickness due to the bond-

ing layers and patches. For example, M_r in this case is given by

$$\begin{aligned}
M_r &= -D \left(\frac{\partial^2 w}{\partial r^2} + \frac{\nu}{r} \frac{\partial w}{\partial r} + \frac{\nu}{r^2} \frac{\partial^2 w}{\partial \theta^2} \right) \\
&\quad - c_D \left(\frac{\partial^3 w}{\partial r^2 \partial t} + \frac{\nu}{r} \frac{\partial^2 w}{\partial r \partial t} + \frac{\nu}{r^2} \frac{\partial^3 w}{\partial \theta^2 \partial t} \right)
\end{aligned}$$

with D and c_D defined in (3).

The external moments generated by the patches in response to an applied voltage (out-of-phase for the patch pair) are given by

$$(M_r)_{pe} = (M_\theta)_{pe} = - \sum_{i=1}^s \mathcal{V}_i^B u_i(t) \chi_i(r, \theta), \tag{4}$$

where $u_i(t)$ is the voltage into the i th patch pair and \mathcal{V}_i^B is a parameter which depends on the geometry, piezoceramic and plate material properties, and piezoelectric strain constant (see Ref. 15 for details). Note that (4) accounts for the electromechanical coupling through which an applied voltage is converted to mechanical input.

3. Structural acoustic coupling

Two structural acoustic coupling mechanisms are inherent in the system. The first accounts for the influence of the internal and external acoustic fields on the structure. It yields the input term

$$g(t, r, \theta) = f(t, r, \theta) - \rho_f \frac{\partial \phi}{\partial t}(t, r, \theta, w(t, r, \theta)),$$

where f is a surface force modeling the exogenous loudspeaker input and $\rho_f (\partial \phi / \partial t) = p$ is the backpressure force due to the interior field. The second mechanism is responsible for the transfer of energy from the plate to the interior field. It is modeled by the continuity of velocity condition

$$\frac{\partial \phi}{\partial z}(t, r, \theta, w(t, r, \theta)) = -\frac{\partial w}{\partial t}(t, r, \theta), \quad (r, \theta) \in \Gamma_0, \quad t > 0$$

(recall that due to the definition of the potential ϕ , $-\partial \phi / \partial z$ is the acoustic velocity in the z -direction). Because both conditions occur at the moving plate surface, they are inherently nonlinear. Under the assumptions of small displacements, however, it is reasonable to linearize about the rest state to obtain

$$g(t, r, \theta) = f(t, r, \theta) - \rho_f \frac{\partial \phi}{\partial t}(t, r, \theta, 0),$$

$$\frac{\partial \phi}{\partial z}(t, r, \theta, 0) = -\frac{\partial w}{\partial t}(t, r, \theta)$$

(see Ref. 3 for numerical investigations validating this assumption).

4. Strong form of system model

Consolidation of components yields the strong form of the coupled acoustic/structural/ electromechanical model

$$\begin{aligned} \frac{\partial^2 \phi}{\partial t^2} &= c^2 \Delta \phi, \quad (r, \theta, z) \in \Omega, \quad t > 0, \\ \nabla \phi \cdot \hat{n} &= 0, \quad (r, \theta, z) \in \Gamma, \quad t > 0, \\ \frac{\partial \phi}{\partial z}(t, r, \theta, 0) &= -\frac{\partial w}{\partial t}(t, r, \theta), \quad (r, \theta) \in \Gamma_0, \quad t > 0, \\ \rho h \frac{\partial^2 w}{\partial t^2} - \frac{\partial^2 M_r}{\partial r^2} - \frac{2}{r} \frac{\partial M_r}{\partial r} + \frac{1}{r} \frac{\partial M_\theta}{\partial r} - \frac{2}{r} \frac{\partial^2 M_{r\theta}}{\partial r \partial \theta} - \frac{2}{r^2} \frac{\partial M_{r\theta}}{\partial \theta} \\ &\quad - \frac{1}{r^2} \frac{\partial^2 M_\theta}{\partial \theta^2} \\ &= \frac{-\partial^2 (M_r)_{pe}}{\partial r^2} - \frac{2}{r} \frac{\partial (M_r)_{pe}}{\partial r} + \frac{1}{r} \frac{\partial (M_\theta)_{pe}}{\partial r} \\ &\quad - \frac{1}{r^2} \frac{\partial^2 (M_\theta)_{pe}}{\partial \theta^2} - \rho_f \frac{\partial \phi}{\partial t}(t, r, \theta, 0) + f(t, r, \theta), \\ w(t, R, \theta) &= \frac{\partial w}{\partial r}(t, R, \theta) = 0 \end{aligned} \quad (5)$$

with initial conditions

$$\begin{aligned} \phi(0, r, \theta, z) &= \phi_0(r, \theta, z), \quad w(0, r, \theta) = w_0(r, \theta), \\ \frac{\partial \phi}{\partial t}(0, r, \theta, z) &= \phi_1(r, \theta, z), \quad \frac{\partial w}{\partial t}(0, r, \theta) = w_1(r, \theta). \end{aligned}$$

It is noted that in this form, moments are differentiated in the plate component. Because the moments are discontinuous due to piecewise constant material parameters and control inputs, this leads to regularity problems associated with the differentiation of a Dirac delta “function.” To avoid ensuing difficulties with the differentiation and to reduce smoothness requirements on approximating bases, it is advantageous to reformulate the problem in a corresponding weak or variational form.

5. Weak formulation of system model

To provide classes of functions which are considered when defining a variational form of the problem, we consider the state space $X = \bar{L}^2(\Omega) \times L^2(\Gamma_0)$ and space of test functions $V = \bar{H}^1(\Omega) \times H_0^2(\Gamma_0)$ where $H_0^2(\Gamma_0) = \{\psi \in H^2(\Gamma_0) : \psi = \partial \psi / \partial r = 0 \text{ at } r = R\}$. Here $\bar{L}^2(\Omega)$ and $\bar{H}^1(\Omega)$ are the quotient spaces of $L^2(\Omega)$ and $H^1(\Omega)$ over the constant functions (the use of these spaces is due to the fact that the potentials are determined only up to a constant).

As detailed in Refs. 13 and 14, an appropriate variational form of the coupled system model is

$$\begin{aligned} \int_{\Omega} \frac{\rho_f}{c^2} \frac{\partial^2 \phi}{\partial t^2} \bar{\xi} \, d\omega + \int_{\Omega} \rho_f \nabla \phi \cdot \bar{\nabla} \xi \, d\omega + \int_{\Gamma_0} \rho h \frac{\partial^2 w}{\partial t^2} \bar{\eta} \, d\gamma \\ - \int_{\Gamma_0} M_r \frac{\partial^2 \eta}{\partial r^2} \, d\gamma - \int_{\Gamma_0} \frac{1}{r} M_\theta \frac{\partial \eta}{\partial r} \, d\gamma \end{aligned}$$

$$\begin{aligned} - \int_{\Gamma_0} \frac{1}{r^2} M_{r\theta} \frac{\partial^2 \eta}{\partial \theta^2} \, d\gamma - 2 \int_{\Gamma_0} \frac{1}{r} M_{r\theta} \frac{\partial^2 \eta}{\partial r \partial \theta} \, d\gamma \\ + 2 \int_{\Gamma_0} \frac{1}{r^2} M_{r\theta} \frac{\partial \eta}{\partial \theta} \, d\gamma + \int_{\Gamma_0} \rho_f \left(\frac{\partial \phi}{\partial t} \bar{\eta} - \frac{\partial w}{\partial t} \bar{\xi} \right) \, d\gamma \\ = \int_{\Gamma_0} \sum_{i=1}^s \mathcal{N}_i^B u_i(t) \bar{\nabla}^2 \eta \chi_i(r, \theta) \, d\gamma + \int_{\Gamma_0} f \bar{\eta} \, d\gamma \quad (6) \end{aligned}$$

for all test functions $(\xi, \eta) \in V$. In this formulation, $d\omega = r dr d\theta dz$ and $d\gamma = r dr d\theta$ while the overbars in (6) denote complex conjugates. An abstract formulation for this model, which leads to well-posedness results, is given in Refs. 13, 14, and 16.

B. Spatial approximation

To obtain a time-dependent ODE system suitable for simulations, parameter estimation, and control, a semidiscretization of the plate and acoustic states was performed. As detailed in Ref. 14, appropriate Galerkin approximations of the displacement and potential are given by

$$\begin{aligned} w^{\mathcal{N}}(t, r, \theta) &= \sum_{j=1}^{\mathcal{N}} w_j^{\mathcal{N}}(t) B_j^{\mathcal{N}}(r, \theta), \\ \phi^{\mathcal{M}}(t, r, \theta, z) &= \sum_{j=1}^{\mathcal{M}} \phi_j^{\mathcal{M}}(t) B_j^{\mathcal{M}}(r, \theta, z). \end{aligned}$$

The basis $\{B_j^{\mathcal{N}}(r, \theta)\}$ is constructed from modified cubic splines in r combined with periodic Fourier components in θ while modified Legendre polynomials in r and z were combined with Fourier components in θ to obtain $\{B_j^{\mathcal{M}}(r, \theta, z)\}$. In all examples which follow, a total of $\mathcal{M} = 99$ and $\mathcal{N} = 12$ basis functions were employed.

Projection of the system (6) onto the finite dimensional subspace spanned by the bases yields a $\mathcal{P} = 2(\mathcal{M} + \mathcal{N})$ dimensional ODE system

$$\begin{aligned} M^{\mathcal{P}} \dot{x}^{\mathcal{P}}(t) &= \bar{A}^{\mathcal{P}} x^{\mathcal{P}}(t) + \bar{B}^{\mathcal{P}} u(t) + \bar{F}^{\mathcal{P}}(t), \\ M^{\mathcal{P}} x^{\mathcal{P}}(0) &= \bar{x}_0^{\mathcal{P}}. \end{aligned} \quad (7)$$

The vector $x^{\mathcal{P}}(t)$ has the form $x^{\mathcal{P}}(t) = [\varphi(t), \vartheta(t), \dot{\varphi}(t), \dot{\vartheta}(t)]^T$, where $\varphi(t) = [\phi_1^{\mathcal{M}}(t), \dots, \phi_{\mathcal{M}}^{\mathcal{M}}(t)]$ and $\vartheta(t) = [w_1^{\mathcal{N}}(t), \dots, w_{\mathcal{N}}^{\mathcal{N}}(t)]$ contain the generalized Fourier coefficients for the approximate acoustic potential and plate displacement, respectively. The vector $u(t) = [u_1(t), \dots, u_s(t)]^T$ contains the s patch input variables. The system matrices and vectors have the form

$$M^{\mathcal{P}} = \begin{bmatrix} K_A & & & & \\ & \vdots & & & \\ & & K_P & & \\ & & & \vdots & \\ & & & & M_A \\ & & & & & \vdots \\ & & & & & & M_P \end{bmatrix}, \quad (8)$$

It is further assumed that errors proportional to the output are found in the observed data. To include these contributions, the observations are taken of the form

$$y^{\mathcal{P}}(t) = C^{\mathcal{P}}x^{\mathcal{P}}(t) + E^{\mathcal{P}}\eta(t),$$

where $[E^{\mathcal{P}}\eta(t)]_j = \hat{\alpha}_j(t)[C^{\mathcal{P}}x^{\mathcal{P}}(t)]_j$, $j = 1, \dots, m$. Here $\hat{\alpha}_j(t)$ is a random variable on $[-0.1, 0.1]$.

To summarize, the observed system with state and measurement uncertainties is given by

$$\begin{aligned} \dot{x}^{\mathcal{P}}(t) &= A^{\mathcal{P}}x^{\mathcal{P}}(t) + B^{\mathcal{P}}u(t) + D^{\mathcal{P}}\eta(t) + F^{\mathcal{P}}(t), \\ y^{\mathcal{P}}(t) &= C^{\mathcal{P}}x^{\mathcal{P}}(t) + E^{\mathcal{P}}\eta(t). \end{aligned} \quad (15)$$

C. Control formulation

We briefly summarize here the methodology for the H^∞ /MinMax periodic control of the finite dimensional structural acoustic system (see Ref. 17 for details). It is assumed that the only exogenous moments and forces being applied to the plate are periodic forces having a period τ ; hence $F(0) = F(\tau)$ in (15). Note that in accordance with usual finite dimensional control convention, we will drop all superscripts throughout the remainder of this work. It can be assumed throughout that the system dimension is $\mathcal{P} = 2(\mathcal{M} + \mathcal{N})$.

1. Full state feedback

For the case with *full state* information, the system to be controlled is

$$\begin{aligned} \dot{x}(t) &= Ax(t) + Bu(t) + D\eta(t) + F(t), \\ x(0) &= x(\tau). \end{aligned} \quad (16)$$

The performance output $z(t) \in Z$ is given by

$$z(t) = Hx(t) + Gu(t),$$

where Z is a performance output space (see Refs. 18 and 19). For the finite dimensional approximate system, the problem of determining a controlling voltage can then be posed as the problem of finding $u \in L^2(0, \tau; U)$ which minimizes the steady-state disturbance-augmented functional

$$\begin{aligned} J(u) &= \int_0^\tau \{ \langle Qx(t), x(t) \rangle_{\mathbb{R}^p} + \langle Ru(t), u(t) \rangle_{\mathbb{R}^s} \\ &\quad - \gamma^2 |\eta(t)|_W^2 \} dt, \end{aligned}$$

where $x(t)$ solves (16), $R = G^T G$ is an $s \times s$ diagonal matrix containing weights which penalize overly large voltages to the patches,²⁰ and W denotes the space in which disturbances evolve. An appropriate choice for the nonnegative matrix $Q = H^T H$, which stems from energy considerations, is a diagonal matrix multiple of the mass matrix in (7) (see Ref. 2). Here $\gamma \in \mathbb{R}$ is a fixed positive constant which is a design parameter to be chosen as small as possible. In this case, the H^∞ norm of the closed loop disturbance to performance output transfer function from $\eta(\cdot)$ to $z(\cdot)$ is bounded above by γ .

Under suitable conditions (see Ref. 21), optimal control theory can then be used to show that the optimal controlling voltage is given by

$$u(t) = -Kx(t) + R^{-1}B^T r(t), \quad (17)$$

where $K = R^{-1}B^T \Pi$ and Π is the unique nonnegative self-adjoint solution to the algebraic Riccati equation

$$A^T \Pi + \Pi A - \Pi \left(BR^{-1}B^T - \frac{1}{\gamma^2} DD^T \right) \Pi + Q = 0.$$

The tracking component $r(t)$ solves the adjoint equation

$$\begin{aligned} \dot{r}(t) &= - \left[A - \left(BR^{-1}B^T - \frac{1}{\gamma^2} DD^T \right) \Pi \right]^T r(t) + \Pi F(t), \\ r(0) &= r(\tau). \end{aligned} \quad (18)$$

2. Output feedback

The feedback law (17) is idealized in the sense that it requires knowledge of the full state (displacement, velocity, potential and pressure) which, using current instrumentation, is not possible. Instead, one typically has available measurements at a discrete number of points [see (10)]. From these observations y , the state is reconstructed or estimated by solving the MinMax state estimator equation

$$\begin{aligned} \dot{\hat{x}}(t) &= \left[A - F_c C - BK + \frac{1}{\gamma^2} DD^T \Pi \right] \hat{x}(t) + F_c y(t) \\ &\quad + F(t) + \left(BR^{-1}B^T - \frac{1}{\gamma^2} DD^T \right) r(t), \\ \hat{x}(0) &= \hat{x}(\tau) \end{aligned} \quad (19)$$

(see Refs. 4, 17, 20 and 21). The observer gain F_c has a form similar to that of the feedback gain K and is given by $F_c = [I - (1/\gamma^2)\Sigma\Pi]^{-1}\Sigma C^T \mathcal{N}_e^{-1}$. Here \mathcal{N}_e is a design matrix which is related to the effect of noise in the data and Σ solves a second algebraic Riccati equation

$$A\Sigma + \Sigma A^T - \Sigma \left(C^T \mathcal{N}_e^{-1} C - \frac{1}{\gamma^2} Q \right) \Sigma + DD^T = 0. \quad (20)$$

In addition to the self adjointness and non-negativity of the matrices Π and Σ , a supplementary condition is typically imposed, namely the boundedness of the spectral radius of $\Sigma\Pi$ by γ^2 (see Refs. 18–20). This latter condition can be expressed as

$$\rho_{sp}(\Sigma\Pi) < \gamma^2.$$

Once a state estimate $\hat{x}(t)$ is obtained, the controlling voltage is given by

$$u(t) = -K\hat{x}(t) + R^{-1}B^T r(t), \quad (21)$$

where $r(t)$ is again the unique τ -periodic solution of the adjoint or tracking equation (18).

II. OPEN LOOP SIMULATIONS

To illustrate the effects of coupling and the manner through which the plate and acoustic components contribute to the coupled system dynamics, we summarize here characteristic open loop dynamics for the system. The dimensions for the system were chosen to be compatible with those of

TABLE I. Physical parameters for the structure and acoustic cavity.

Parameter	Structure		Acoustic cavity	
	Plate	Plate + Pzt	Parameter	Cavity
$\rho \cdot \text{Thickness}$ (kg/m ²)	3.429	3.489	ρ_f (kg/m ³)	1.21
D (N·m)	13.601	13.901		
c_D (N·m·s)	1.150-4	2.250-4		
ν	0.33	0.32		
\mathcal{K}^B (N/V)		0.027		
			c (m/s)	343

the experimental cylinder at NASA Langley Research Center which has length $\ell = 1.067$ m (42 in.) and radius $R = 0.229$ m (9 in.). The end-mounted plate has thickness $h = 0.00127$ m (0.05 in.) with a pair of centered piezoceramic patches with respective thickness and radius $h_{pe} = 0.00018$ m (0.007 in.) and $R_{pe} = 0.019$ m (0.75 in.). These values were then used for the simulations reported here. The physical parameters for the simulations are summarized in Table I. As reported in Ref. 12, these values are also consistent with physical parameters for the experimental setup.

Throughout this section, control inputs are excluded [$u(t) = 0$] and impactlike spatial and acoustic inputs are used to generate transient system responses. A comparison of natural frequencies is then used to quantify the contributions of the structural and acoustic components and the two coupling mechanisms modeled by force (pressure) and velocity balancing.

To provide a baseline for comparison, natural frequencies for the *isolated* plate and acoustic field are summarized in Table II. As detailed in Refs. 13 and 14, where the full set of frequencies are provided, the plate frequencies were calculated under the assumption of no damping ($c_D = 0$) while the acoustic frequencies were calculated under the assumption of fully Neumann boundary conditions.

As discussed in Sec. I, force balancing is used to incorporate the acoustic effects on the structure; this leads to a pressure input term in the modeling acoustic equation. Velocity balancing incorporates the converse coupling mechanism through which energy is transmitted from the structure to the acoustic field. In terms of the component matrices in (7), these coupling components enter as input terms in the vector equations

$$M_A \ddot{\phi}(t) + K_A \phi(t) = -A_{c1} \dot{\vartheta}(t) + F_{\mathcal{A}} g(t), \quad (22)$$

$$M_P \ddot{\vartheta}(t) + C_P \dot{\vartheta}(t) + K_P \vartheta(t) = -A_{c2} \dot{\phi}(t) + F_{\mathcal{A}} f(t)$$

TABLE II. Axisymmetric natural frequencies for the *isolated* and *undamped* plate and cavity (in hertz). The cavity mode (m, n, p) , corresponding to frequency f_{mnp} , has m nodal lines in θ , n nodal circles in r and p nodal lines z (similarly for plate modes).

Plate (f_{mn})		Cavity (f_{mnp})			
(0,0)	62.0	(0,0,1)	160.8	(0,1,0)	915.0
(0,1)	241.2	(0,0,2)	321.5	(0,1,1)	929.0
(0,2)	540.5	(0,0,3)	482.3	(0,1,2)	969.9
(0,3)	959.5	(0,0,4)	643.0		
		(0,0,5)	803.8		
		(0,0,6)	964.6		

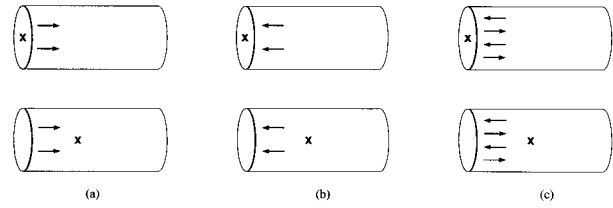


FIG. 2. Coupling combinations with plate and acoustic impulse forces at the point x ; (a) coupling from structure to field; (b) coupling from field to structure, and (c) full structural acoustic coupling.

[compare with (14)].

The vectors $F_{\mathcal{A}} g(t)$ and $F_{\mathcal{A}} f(t)$ incorporate the exogenous input to the cavity and plate, respectively. For an impact at time $t = t_0$ applied at the plate point (r_0, θ_0) , the components of $F_{\mathcal{A}} f(t)$ are given by

$$[F_{\mathcal{A}} f(t)]_k = \delta(t - t_0) \int_{\Gamma_0} \delta(r - r_0, \theta - \theta_0) B_k^{\mathcal{A}} d\gamma$$

$$= \delta(t - t_0) B_k^{\mathcal{A}}(r_0, \theta_0)$$

with a similar expression for the acoustic input. Note that one can consider $g(t) \equiv 0$ if no acoustic input is present as is the case in the coupled structural acoustic control problem. In all examples here, plate impacts are at $(r, \theta) = (0, 0)$ while cavity impacts are at $(r, \theta, z) = (0, 0, \ell/3)$.

By considering various coupling combinations (e.g., $A_{c1} \equiv 0$ eliminates the coupling mechanism through which energy is transmitted from the plate to the cavity) and force inputs $f(t), g(t)$, the effects of the two coupling mechanisms were isolated. The six coupling/input combinations are depicted in Fig. 2 and are summarized below.

Case (i): Coupling from structure to field

To illustrate the case in which coupling from the structure to the acoustic field is incorporated in the model but energy transfer from the field to the structure is neglected, we let $A_{c2} \equiv 0$ in (22) and (8). This case is depicted in Fig. 2(a). Note that the exogenous force $F_{\mathcal{A}} g(t)$ and velocity coupling provide input to the cavity while the only input to the plate is provided by the exogenous force $F_{\mathcal{A}} f(t)$.

Consider first the force choices $g(t) = 0, f(t) = \delta(t - t_0)$ which models an impact to the plate with no exogenous force to the cavity. Because the plate is unaffected by the acoustic field in this case, natural frequencies measured on the plate will be close to those summarized in Table II with differences due only to the Kelvin–Voigt damping. The structure acts as an input to the cavity with frequencies governed by the harmonics of the plate. Hence both plate and wave frequencies will be measured in the cavity. The frequencies obtained via (7) at the plate point $p_1 = (0, 0)$ and cavity point $c_2 = (0, 0, 0.35)$ depicted in Fig. 3 are summarized in Table III. Frequencies calculated at the plate point are indicated in the table by p while c denotes frequencies measured at c_2 . It should be noted that to within the sampling resolution, the frequencies calculated at both points agree with those for the isolated components which are summarized in Table II. Furthermore, Table III illustrates the transmission of plate frequencies into the cavity.

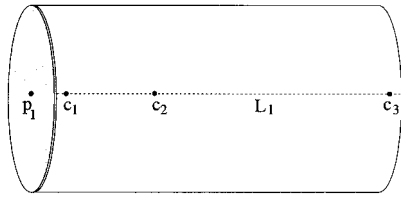


FIG. 3. The structural acoustic system with evaluation points $p_1=(0,0)$, $c_1=(0,0.05)$, $c_2=(0,0.35)$, $c_4=(0,0.1.0)$, and evaluation line L_1 .

The conclusion for general structural acoustic systems will be similar. The incorporation of *only* the velocity coupling in the model will lead to a system response similar to that of the components with structural frequencies propagated into the acoustic field. This type of model might be useful if considering far-field acoustics generated by a vibrating structure (e.g., transformer). As illustrated in Case (iii), however, it may provide inaccurate system frequencies in applications in which the acoustic oscillations couple back to the structure.

The second choice $g(t)=\delta(t-t_0), f(t)=0$ models an impact in the cavity with no exogenous force to the plate. The purely cavity frequencies summarized in Table II will be present at the cavity point c_2 . No response will be noted on the plate since the coupling between the field and plate is neglected in this case.

Case (ii): Coupling from field to structure

This case can be quantified by considering $A_{c1}\equiv 0$ in (8). As shown in (22) and depicted in Fig. 2(b), the model in this case incorporates the acoustic influence upon the structure but neglects structural influence upon the field. The dynamics can be predicted from those observed in Case (i) with the opposite mechanism. The acoustic frequencies are propagated to the structure when $g(t)=\delta(t-t_0), f(t)=0$ with both sets close to the those of the isolated components (the only deviation is a slight shift in the structural frequencies due to the Kelvin–Voigt damping). This model will be accurate *only* for systems in which the field strongly drives the structure with negligible feedback from the structure to the field.

Case (iii): Full coupling between field and structure

The case of primary interest for the system considered here is that in which both coupling mechanisms are incorporated in the system model. Hence both the matrix A_{c1} (velocity coupling) and matrix A_{c2} (pressure coupling) are included in the ODE system (8) or (22).

System frequencies for this case are summarized in Table IV. A comparison between these results and corre-

TABLE III. System frequencies obtained with $A_{c2}\equiv 0$; p : frequencies observed at the plate point $p_1=(0,0)$, c : frequencies observed at the cavity point $c_2=(0,0.35)$.

Natural system frequencies					
p, c	62.0	c	160.8	c	915.4
p, c	241.2	c	321.5	c	928.1
p, c	540.5	c	482.3	c	969.8
p	959.5	c	643.7		
		c	806.6		

TABLE IV. System frequencies obtained with full structural acoustic coupling conditions; p : frequencies observed at the plate point $p_1=(0,0)$, c : frequencies observed at the cavity point $c_2=(0,0.35)$.

Natural system frequencies					
p, c	59.5	p, c	163.4	c	915.6
p, c	239.5	p, c	324.1	p, c	929.3
p, c	538.2	p, c	483.1	p, c	971.0
		p, c	645.2		
		p, c	807.5		

sponding frequencies for the uncoupled plate and acoustic field (see Table II) indicates that while the system response reflects the structural and acoustic components, the system frequencies are shifted from those of the components due to the coupling. The three system frequencies corresponding to the plate component (59.5, 239.5, and 538.2 Hz) are lower than the corresponding frequencies of the isolated plate. Thus the coupled acoustic field effectively mass loads the structure. The remaining system frequencies correspond to the acoustic component. They are higher than those for the isolated wave fields which indicates that the coupling of the plate to the acoustic field provides a stiffening effect to the field. For the geometry investigated here, we observe frequency shifts of approximately 2.5 Hz ($\approx 5\%$) for lower frequencies and 3 to 4 Hz ($\approx 1\%$ to 2%) for higher frequencies. Hence in many applications, the uncoupled systems will provide sufficient modal information.

However, for many systems which are closed in the sense that both acoustic/structure and structure/acoustic interactions are present, both mechanisms may need to be incorporated in the model to accurately match dynamics. Omission of either mechanism will lead to model frequencies which match those of the isolated components but may *not* match those of the actual coupled system. Employment of a model which neglects coupling components in a PDE-based controller can lead to decreased control authority. If the neglected coupling is significant, the controller will be destabilized by the ensuing frequency inaccuracies.

III. CLOSED LOOP SIMULATIONS—SHORT CYLINDER

For compensator design, the spatially discretized model (15) with full structural acoustic coupling was considered. The performances of the full state H^∞ /MinMax feedback control, output feedback MinMax control, and linear quadratic Gaussian (LQG) feedback control (Kalman filter) were then compared with open loop system responses for a variety of sensor configurations and geometries. This provided a means of evaluating and utilizing the coupling in the model-based compensator.

To illustrate, two geometries for the structural acoustic system were considered. For the first, dimensions consistent with those of the experimental chamber in the Acoustics Division, NASA Langley Research Center were used (see the discussion in Sec. II and Table I). This provided simulation results which can be used to predict experimental dynamics and guide experiments involving that setup. The numerical results for this geometry are reported in this section. The second geometry involves an acoustic chamber whose length is significantly longer than the diameter of the vibrating

TABLE V. Full state and output feedback control laws with sensor numbers.

	Sensors			Sensor components for Riccati solution	Sensor components for control computation
	Mics.	Disp.	Vel.		
Compensator I	5	5	5	$N_p = N_w = N_v = 5$	$N_p = N_w = N_v = 5$
Compensator II	5 Virtual	5	5	$N_p = N_w = N_v = 5$	$N_p = 0, N_w = N_v = 5$
Compensator III	5 Virtual	5 Virtual	5	$N_p = N_w = N_v = 5$	$N_p = N_w = 0, N_v = 5$
Kalman filter	5	5	5	$N_p = N_w = N_v = 5$	$N_p = N_w = N_v = 5$
H^∞ Control				Full state	

plate. This illustrates the manner through which the acoustic wave equation describes the effective physical delays due to relatively slow wave speeds. It also indicates controllability issues which must be considered when designing controllers for such systems. Results for this geometry are summarized in Sec. IV.

The exogenous force to the plate was taken to be

$$f(t, r, \theta) = 28.8[\sin(2\pi 170t) + \sin(2\pi 330t) + \sin(2\pi 100t) + \sin(2\pi 250t)] \quad (23)$$

for $0 \leq r \leq R, 0 \leq \theta < 2\pi$. This models a plane acoustic wave with an rms sound-pressure level of 126 dB. This excites a combination of modes since the first two frequencies (170 Hz, 330 Hz) couple readily with cavitylike modes while the latter two frequencies strongly affect platelike frequencies (see Tables II and IV).

Consideration of the control laws outlined in Sec. I C indicates several design parameters which can be used to weight input and output values as well as various states and sensors. The specific design of the model uncertainty matrix D and output uncertainty matrix E also can be modified according to the application. Furthermore, the parameter γ which bounds the H^∞ norm of the transfer function from disturbance to performance output can be tuned to improve performance.

Various criteria are considered when choosing these design parameters. These include overall attenuation levels, control magnitude (overly large voltages will destroy the patches), conditioning of Riccati solutions and spectrum stability of the closed loop system. Many of these issues are addressed in Ref. 22 and the reader is referred to that reference for a general discussion of these design criteria. Reference 16 contains details regarding the specific choices for these simulations.

The design criteria involving the state, observation, and control weights, and MinMax parameter γ , arise from the formulation of the control law rather than the physics of the problem. The placement and number of sensors and actuators, however, is a design criterion which is directly related to the physics. As mentioned previously, a pair of circular, centered piezoceramic patches are employed as actuators in the experimental system. These actuators are glued to the plate and are considered as permanent throughout both experiments and simulations. The use of this single pair proved adequate for this geometry and axisymmetric force (23) but led to controllability problems in the long cylinder discussed in the next section.

The sensors are often more portable (unless piezoceramic patches or other permanently bonded materials are employed) and a variety of configurations were considered. Criteria which are considered when determining number and placement are hardware limitations (restricted number of input channels for data acquisition), physical constraints (sensors outside a transformer or submarine are unsuitable), Riccati solution conditioning, etc. The hardware constraints limit the available number of sensors while physical constraints often make it advantageous to limit the types and placement of sensors. The ideal case is to eliminate the acoustic sensors entirely and use the model with coupling along with structural data to reconstruct the acoustic state.

For the simulations presented here, three sensor configurations were considered as summarized in Table V. In all cases, the number of sensors measuring the potential was taken to be $N_\phi = 0$ in (11) when constructing the observation matrix (12). This is due to the fact that the potential is not a readily measured state.

For compensator I, 5 microphone, 5 velocity, and 5 displacement measurements at the observation points

$$\begin{aligned} \omega_{1p} &= (0, 0, 0.0334), & \gamma_{1w} &= \gamma_{1v} = (R/3, 0), \\ \omega_{2p} &= (R, 0, \ell/2), & \gamma_{2w} &= \gamma_{2v} = (R/3, \pi), \\ \omega_{3p} &= (R, \pi, \ell/2), & \gamma_{3w} &= \gamma_{3v} = (2R/3, \pi/2), \\ \omega_{4p} &= (R, \pi/2, \ell), & \gamma_{4w} &= \gamma_{4v} = (2R/3, 7\pi/6), \\ \omega_{5p} &= (R, 3\pi/2, \ell), & \gamma_{5w} &= \gamma_{5v} = (2R/3, 11\pi/6) \end{aligned}$$

were used for state reconstruction (see Fig. 4). This implies that $N_p = N_w = N_v = 5$ in (12).

Compensator II differs from compensator I in the manner through which the microphone observation submatrix C_p is employed. For the calculation of the observer gain through solution of the observer Riccati equation (20), this submatrix was retained so that the full observation matrix C had dimension $(N_p + N_w + N_v) \times (2\mathcal{N} + \mathcal{M})$. For the calculation of the

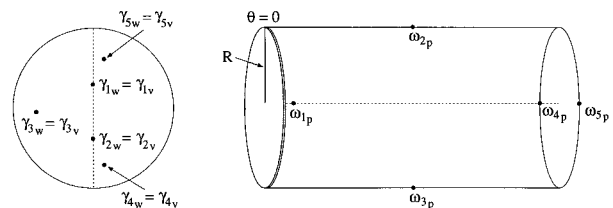


FIG. 4. Pressure and plate observation points for the structural acoustic system.

TABLE VI. Sound-pressure levels and displacements (rms) in the presence of 5% noise.

	Sound-pressure level (dB)			Displacement (m)
	c_1	c_2	c_3	p_1
Open loop	119.7	113.7	119.7	12.4×10^{-5}
MinMax full state	107.2	103.2	104.1	8.0×10^{-5}
Kalman filter (I)	111.3	105.9	110.9	8.0×10^{-5}
MinMax compensator (I)	111.3	105.9	110.9	8.0×10^{-5}
MinMax compensator (II)	112.8	106.9	112.3	8.0×10^{-5}
MinMax compensator (III)	112.8	106.9	112.3	8.0×10^{-5}

state output (15) and the state estimate $\hat{x}(t)$ solving (19), however, only plate measurements were considered so $N_p=0$ which results in a null submatrix C_p in (12). The acoustic sensors utilized in this manner are referred to as *virtual* microphones.

This second compensator is motivated by the goal of eliminating the acoustic sensors and utilizing the coupled model for state reconstruction using solely structural data. This is what is implemented in the state calculations (19). The motivation for including the pressure submatrix C_p when calculating the observer gain is the maintenance of conditioning for Riccati solutions, lower spectral radii, and closed loop spectrum bounds. As illustrated in Ref. 16, solution of the observer Riccati equation (20) with solely structural observation components leads to unacceptable conditioning and spectral radii when computing observer gains.

Compensator III utilizes both virtual microphones and virtual displacement sensors so that the only physical data used when estimating the state are velocity measurements. This is motivated by physical constraints on structural sensors. Displacement measurements using proximity sensors are typically difficult to obtain whereas velocity measurements can be obtained using laser vibrometers or integration of accelerometer data. Nonzero initial conditions for the state estimator were employed in all three compensators. As detailed in Ref. 16, this permitted additional comparison between the performance of the three compensators.

The construction of a controller using virtual sensors provides a great deal of flexibility. In addition to permitting the design of controllers utilizing certain state measurements, it provides the capability for developing controllers designed for a variety of environments. The observation gains are computed using the full observation matrix in each case. The observer submatrices C_p , C_w , C_v can then be incorporated or omitted in the state estimator computations depending on the available data. This allows for some latitude in sensor location as well as the disabling (in the data collection process) of damaged or superfluous sensors. While heuristic in nature, the dual incorporation of the observation submatrices to accommodate virtual sensors proves an effective technique for reducing the number of physical sensors while maintaining the conditioning of the gain and observer matrices.

The final control laws considered are the full state H^∞ /MinMax controller (17) and the Kalman filter which results with $\gamma=\infty$. These two laws provide benchmarks against which to compare the H^∞ /MinMax output feedback controllers.

Trajectories for the uncontrolled system and system controlled via the five control laws were computed over the time interval $[0,0.16]$ with 0%, 5%, and 10% relative noise added to the model and observations. The rms pressure values at the cavity points c_1 , c_2 , c_3 and the rms displacement at the plate center $p_1=(0,0)$ for the 5% noise case are summarized in Table VI. Time domain plots of the uncontrolled and controlled pressure at $c_1=(0,0,0.05)$ are given in Fig. 5 while the rms sound pressure values along the central axis L_1 (see Fig. 3) are plotted in Fig. 6.

As expected, the full state H^∞ /MinMax controller provides the best performance since it utilizes the most information. With 5% noise, it provides a 12.5-dB reduction at c_1 with equally significant reductions throughout the length of the cavity. The Kalman filter yields an 8.5-dB reduction at c_1 with performance less than the full state MinMax control due to the limited number of observations and the lack of robustness in the presence of noise. The three MinMax compensators yield 7 to 8 dB reductions at c_1 with similar performances throughout the cavity. In comparing the rms values and time plots of the three compensators, it is noted that the performance of compensator I with measurements of pressure, displacement, and velocity is only 1–2 dB better than that of compensators II and III. Recall from Table V that compensator III employs *only* 5 velocity sensors for the actual state reconstruction. The pre-computed gains and coupled model provide the remaining information required for accurate state estimation and control computation.

The global nature of the noise reduction should also be noted. Both time and rms plots illustrate that model-based controllers employing the structure-mounted actuator provide significant attenuation *throughout* the cavity.

These results demonstrate the possibility of obtaining very effective control attenuation using only structural observations with the coupled model used to estimate the structural and acoustic states. This is important in many interior field applications such as the structural acoustic system described here and crucial in exterior field applications (e.g., transformer or submarine) where acoustic measurements may be impossible to attain.

IV. CLOSED LOOP SIMULATIONS—LONG CYLINDER

Two physical mechanisms that contribute significantly to the difficulty in controlling structure-borne noise are the structural acoustic coupling and the relatively slow wave speed in the acoustic field. The effects and utilization of the coupling have been described in previous sections and will

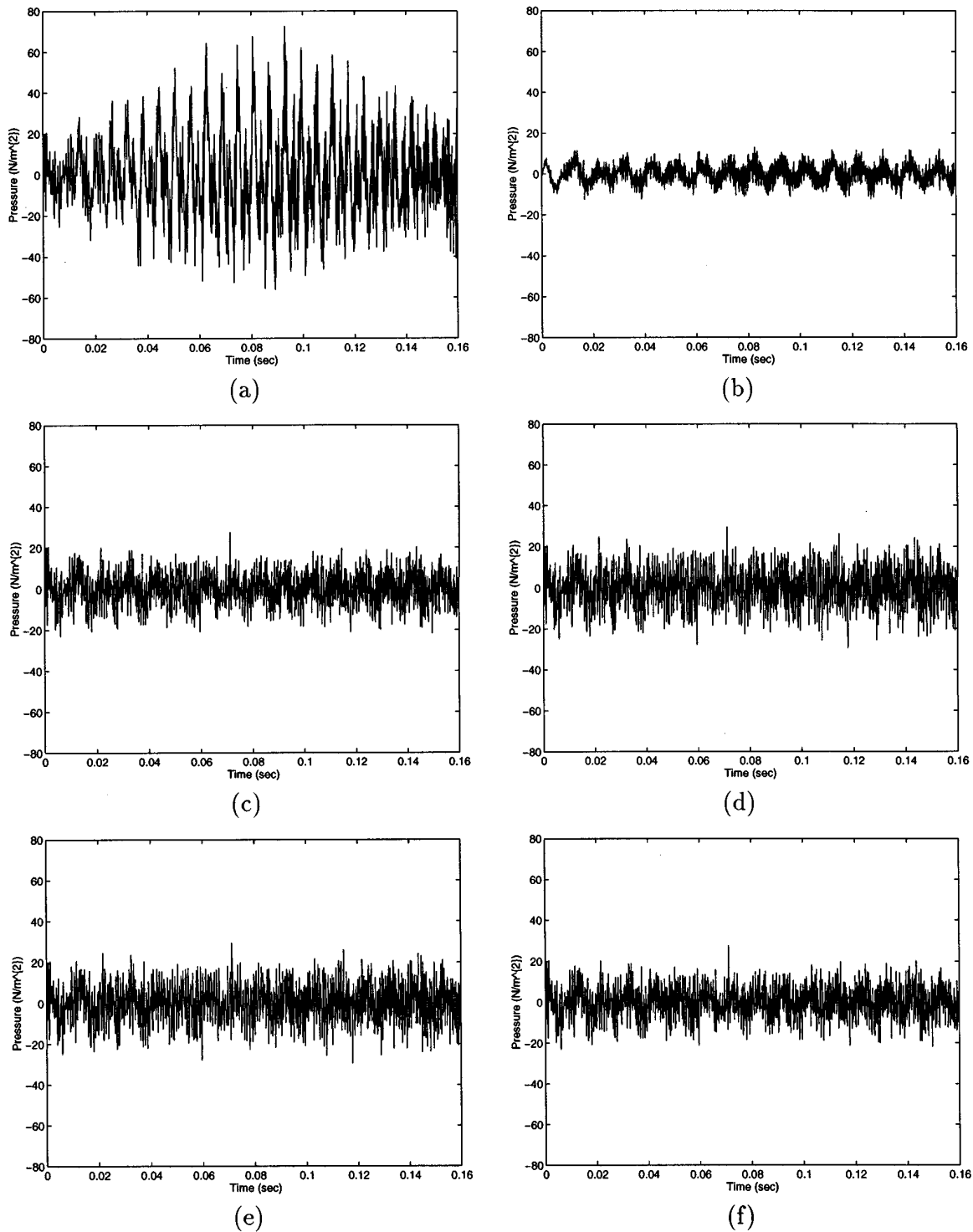


FIG. 5. Time history of sound-pressure level at $c_1 = (0,0,0.05)$ with 5% noise; (a) open loop, (b) full state MinMax controller, (c) MinMax compensator I, (d) MinMax compensator II, (e) MinMax compensator III, and (f) Kalman filter.

be readdressed in Sec. V. The efficacy of using the dynamic wave model to incorporate the wave speed is illustrated here through consideration of a cylinder whose length is significantly larger than the end-mounted vibrating plate [see Fig. 7(a)]. Specifically, the plate has the same dimensions as that in previous sections while the length of the cylinder is now 3.206 m. This yields a cylindrical length to plate diam-

eter ratio of 7 as compared to 2.33 in Sec. III. The forcing function in (23) was again used to model a uniform periodic acoustic field driving the plate.

For these simulations, three patch configurations were considered as depicted in Fig. 7. Specifically, two pairs were circular ($r_1 = 0, r_2 = R/12$ and $r_1 = 0, r_2 = R/4$) and one was ringlike ($r_1 = R/3, r_2 = R/2$). The smaller patch dimension

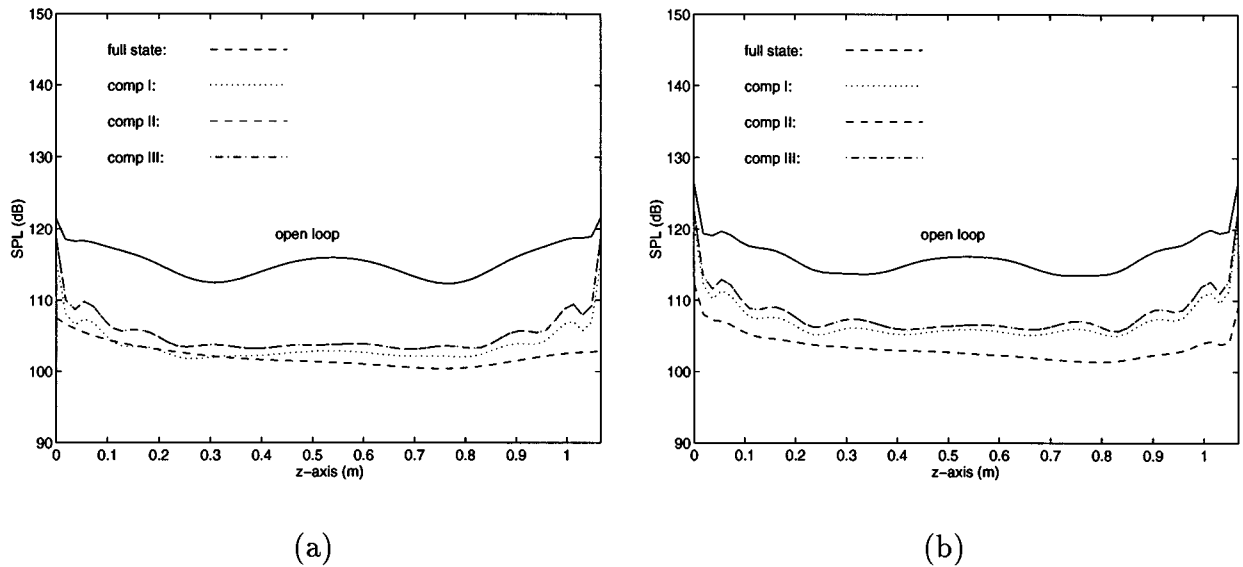


FIG. 6. Sound-pressure level along central z -axis L_1 over the time interval $[0,0.16]$; (a) 0% noise, (b) 5% noise. Compensators II and III provide graphically identical attenuation.

corresponds to that of the experimental setup used in the Acoustics Division, NASA Langley Research Center (see Sec. I). The MinMax parameter choice $\gamma=10$ provided an adequate balance between conditioning and stability.

For the full state feedback law (17), rms sound-pressure levels along the axes

$$A1: (\theta=0, r=0, 0 \leq z \leq \ell),$$

$$A2: (\theta=0, r=R/4, 0 \leq z \leq \ell),$$

$$A3: (\theta=0, r=R/2, 0 \leq z \leq \ell),$$

$$A4: (\theta=0, r=3R/4, 0 \leq z \leq \ell)$$

[see Fig. 7(a)] are plotted in Fig. 8. In each case, it is noted that the small circular patch pair ($r_1=0, r_2=R/12$) provides the least attenuation whereas the patch ring provides up to 30 dB attenuation. It is also noted that negligible attenuation is attained along the middle 1/3 of the central axis. This illustrates a controllability issue which arises when utilizing a single patch pair in a system whose length is significantly longer than the driving plate. Hence while significant attenu-

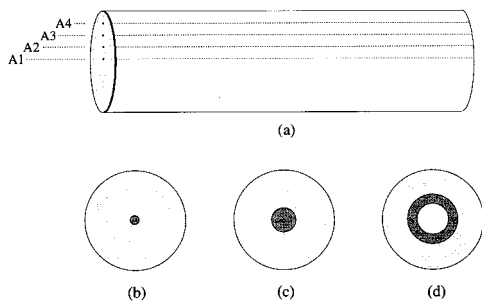


FIG. 7. (a) The acoustic cavity with observation axes 1,...,4; (b) patch with radius $r=R/12$; (c) patch with radius $r=R/4$; and (d) patch ring with $r_1=R/4, r_2=R/2$.

ation is achieved throughout most of the cavity, optimization issues concerning patch number and orientation should be investigated to attain global attenuation.

Similar results obtained with compensators I and III described in Table V are plotted in Fig. 9. The small patch having radius $R/12$ was employed as an actuator and rms sound-pressure levels along axis 2 are reported in the figure. For both cases (0% and 5% noise), 10–12-dB reductions were obtained along this axis, even with compensator III which employs only 5 velocity observations for state reconstruction. The tendencies along axes 3 and 4 are similar while the rms pressure along axis 1 still exhibits the central region with negligible control.

For both the full state feedback controller and the compensator, the information regarding propagation of the acoustic response is provided by the *dynamic* wave equation (1). Due to the low wave speed (343 m/sec), the time delay between the input of voltage to the patch and the acoustic response at a sensor is significant. If left unmodeled or uncompensated, this delay will destabilize a controller. This is one motivation for utilizing wave-based rather than modal-based controllers in many acoustic applications. For implementation purposes, the wave dynamics and hence delays must be discretized. Through the use of the Legendre-based Galerkin method, however, these approximations can be obtained to any desired accuracy. As illustrated by the results in Figs. 8 and 9, as well as the previous section, the use of a *dynamic* wave model with Legendre-based approximations very adequately accounts for the delay thus leading to strong attenuation for this system.

V. CLOSED LOOP SIMULATIONS—PLATE-BASED CONTROLLER

The fact that structure-borne noise is generated by a vibrating structure makes it tempting to reduce the noise solely by controlling the structure. The example we consider in this

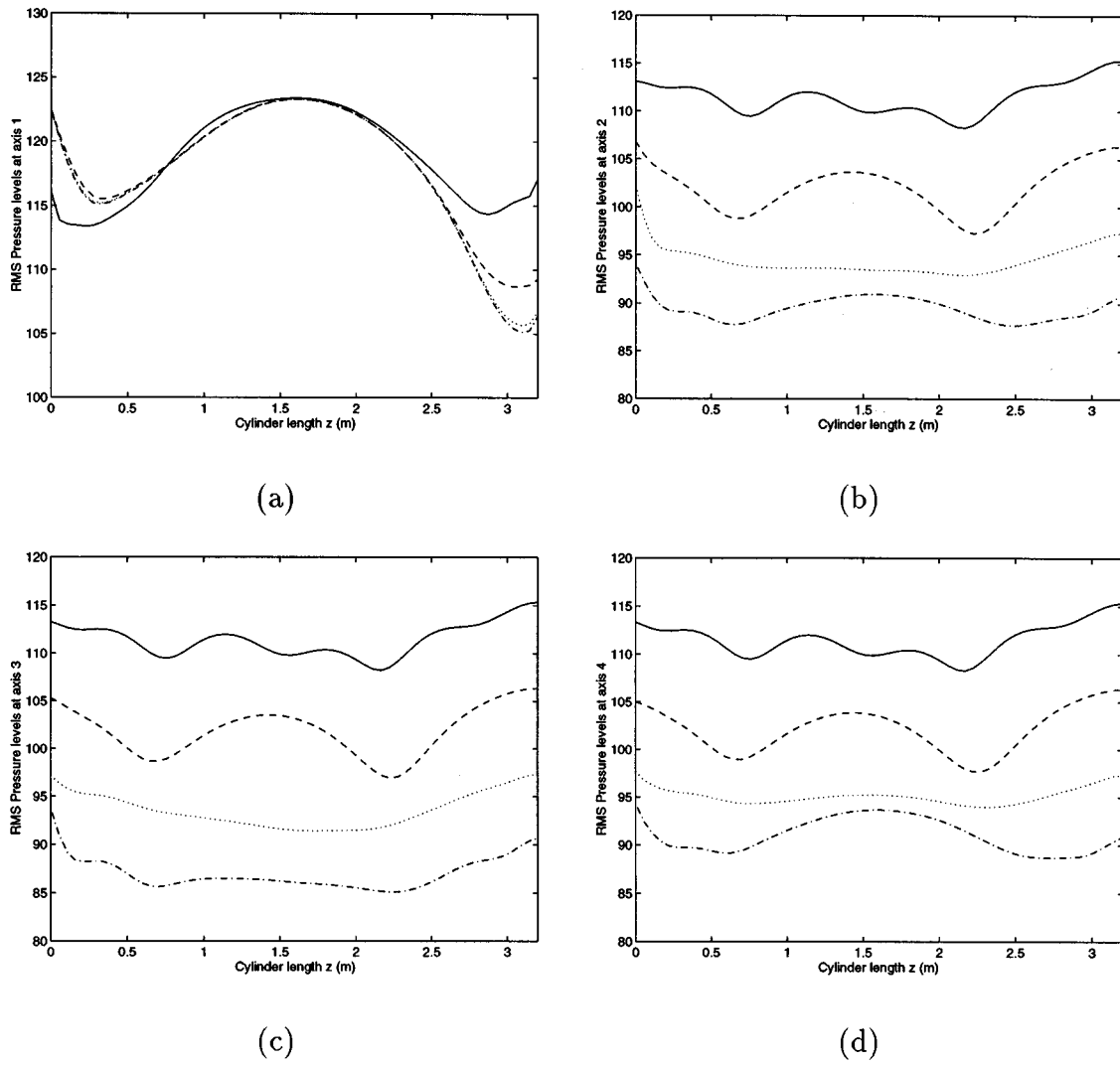


FIG. 8. Root-mean-square (rms) sound-pressure levels for 0% noise with full state feedback; — (open loop), --- (small circular patch), (large circular patch), - · - · - (patch ring); (a) axis 1, (b) axis 2, (c) axis 3, and (d) axis 4.

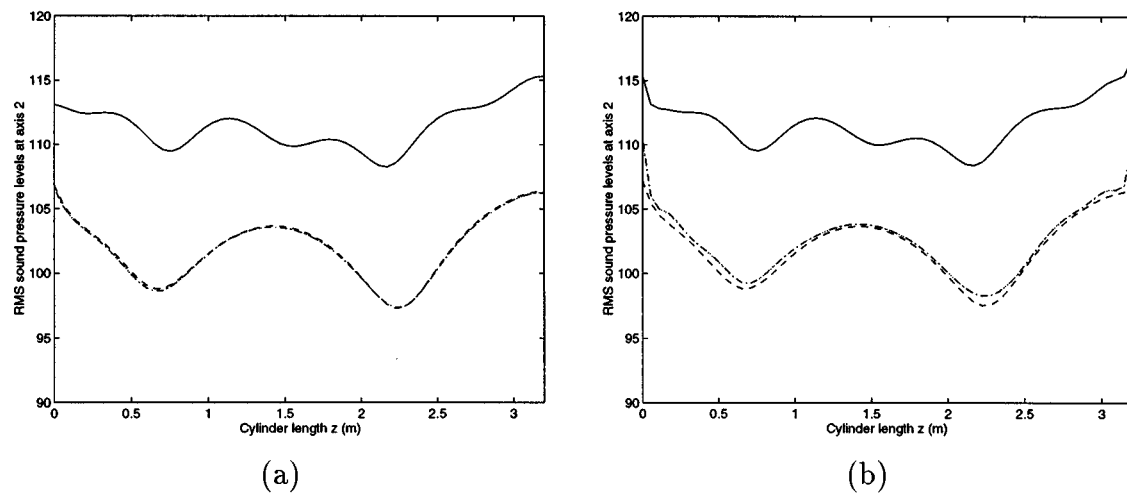


FIG. 9. rms sound-pressure levels along axis 2 with small patch as actuator; — (open loop), --- (full state MinMax control), (MinMax compensator I), - · - · - (MinMax compensator III); (a) 0% noise, and (b) 5% noise.

TABLE VII. Sound-pressure and displacement levels (rms) for the 65-Hz exogenous force $f_1(t)$.

	Pressure level (dB)			Displacement (m)
	c_1	c_2	c_3	p_1
Open loop	116.4	105.4	112.4	5.254×10^{-4}
H^∞ full state	107.7	101.4	105.2	0.464×10^{-4}
H^∞ compensator	109.5	103.4	109.2	0.950×10^{-4}

section reinforces the tenet held by many acousticians that this strategy is not effective in general and should be used only for certain exogenous frequencies (see, for example, Refs. 6 and 23). It also illustrates the benefits of utilizing a compensator for the coupled system which employs only structural sensors (see compensator III of Table V) rather than a purely structural controller.

For the structural acoustic system in this work, a purely structural controller would be designed for the discretized plate model

$$\begin{bmatrix} K_P & 0 \\ 0 & M_P \end{bmatrix} \begin{bmatrix} \dot{\vartheta}(t) \\ \ddot{\vartheta}(t) \end{bmatrix} = \begin{bmatrix} 0 & K_P \\ -K_P & -C_P \end{bmatrix} \begin{bmatrix} \vartheta(t) \\ \dot{\vartheta}(t) \end{bmatrix} + \begin{bmatrix} 0 \\ \hat{B} \end{bmatrix} u(t) + \begin{bmatrix} 0 \\ \hat{g}(t) \end{bmatrix} + \hat{D} \eta(t)$$

where again, $\vartheta(t)$ contains the generalized Fourier coefficients for displacement and M_P , K_P and C_P are the mass, stiffness, and damping matrices for the plate (see Sec. I). The control, exogenous force, and uncertainties are contained in $\hat{B}u(t)$, $\hat{g}(t)$, and $\hat{D}\eta(t)$, respectively. The observation matrix for this case is

$$y(t) = \begin{bmatrix} C_w & 0 \\ 0 & C_v \end{bmatrix} \begin{bmatrix} \vartheta(t) \\ \dot{\vartheta}(t) \end{bmatrix}$$

with 5 displacement and velocity observations ($N_w = N_v = 5$).

Control results for the forcing functions $f_1(t) = \sin(130\pi t)$, $f_2(t) = \sin(330\pi t)$ using the plate-based compensator with $N_w = N_v = 5$ are reported in Tables VII and VIII. The first frequency couples effectively with the 59.5-Hz platelike mode while $f_2(t)$ strongly drives the 163.4-Hz cavitylike mode. For comparison, the attenuation levels obtained with the plate-based H^∞ /MinMax full state control law are also summarized in the tables.

As noted by the rms sound-pressure levels in Table VII, the plate-based compensator is fairly effective in attenuating noise generated primarily by a platelike mode. The results in Table VIII illustrate that this strategy is ineffective (at some points, sound-pressure levels are actually increased) for exogenous frequencies driving cavitylike modes (this reinforces observations made in Refs. 6 and 23). While rms displacement levels are reduced by a factor of nearly 4 for the H^∞ full state controller, sound-pressure levels remain high due to the effective structural acoustic coupling. To attain an effective compensator for general frequencies, the coupling mechanisms and acoustic components *must* be incorporated in the model and control law.

TABLE VIII. Sound-pressure and displacement levels (rms) for the 165-Hz exogenous force $f_2(t)$.

	Pressure level (dB)			Displacement (m)
	c_1	c_2	c_3	p_1
Open loop	122.5	117.4	122.9	0.413×10^{-4}
H^∞ full state	124.9	119.8	125.3	0.133×10^{-4}
H^∞ compensator	125.5	120.4	125.9	0.342×10^{-4}

VI. CONCLUSION

The utilization of coupling effects in control design for structural acoustic systems was considered in this work. One objective in many such systems is the attenuation of structure-borne noise through the use of surface-mounted actuators such as piezoceramic patches. Models for such systems thus have a structural/actuator component, acoustic field components, and coupling mechanisms which model the acoustic/structure interactions. It is through these coupling mechanisms that feedback control of noise through the structural actuators can be accomplished.

The prototypical experimental setup considered here consisted of a cylindrical acoustic cavity with a driven circular plate mounted at one end. Piezoceramic patch pairs driven out-of-phase to produce pure bending moments were used as actuators. A PDE system was used to model the structural, acoustic, and coupling components for this setup. Galerkin approximations were used to obtain an ODE system suitable for simulation, parameter estimation and control applications.

For this modeled system with full coupling (backpressure and velocity) between the structure and adjacent acoustic field, numerical simulations demonstrated a 1–5-Hz shift in system frequencies from those observed for the isolated components. The backpressure from the field to the plate produced platelike system frequencies lower than those of the isolated plate; hence through the coupling, the field acts as added mass to the plate. The coupling of the plate to the acoustic field produces an opposite stiffening effect in that system frequencies of acousticlike modes are higher than isolated acoustic frequencies. For the geometry in these examples, the frequency shifts were fairly small and one might obtain reasonable modal information about the system through consideration of the uncoupled structure and acoustic field. In general, however, if coupling mechanisms are not included in the model, the frequency inaccuracies can nullify and possibly destabilize the controller.

The utilization of the coupling mechanisms can, on the other hand, lead to very effective controllers. To illustrate this, two sets of H^∞ /MinMax control laws were considered. Full state information was assumed for the first while the states were estimated from sensor measurements and then employed in an output feedback law in the second. In the latter (the MinMax compensator), a variety of sensor arrangements were compared to determine the extent to which the coupling could be utilized.

For various exogenous inputs, numerical simulations demonstrated high attenuation with both the full state feedback law and the output feedback law with states recon-

structed using pressure, velocity and displacement measurements. More importantly, the results demonstrated only a 1 to 2-dB loss of control when state measurements used for feedback were obtained *only* from structural velocity sensors. This latter case is important since it demonstrates that through the coupled structural acoustic model, accurate acoustic state information can be obtained *solely* from velocity measurements. This has important ramifications in a large number of structural acoustic systems since it demonstrates the possibility of eliminating pressure sensors (microphones) in the field (microphones in a fuselage can be unwieldy while microphones outside a submarine are unreasonable).

Finally, numerical results demonstrating the necessity of retaining the coupling and acoustic components when designing a general control law for noise attenuation were presented. These results demonstrate that while a control law based solely on the structural component can be effective for exogenous frequencies near platelike frequencies, it is totally ineffective for applications in which cavitylike modes are excited. This reinforces the necessity of careful modeling of the structural, acoustic, and coupling components and the design of a compensator which utilizes all three components.

ACKNOWLEDGMENTS

The authors thank R. J. Silcox, Acoustics Division, NASA Langley Research Center, for numerous discussions related to practical control implementation in structural acoustic systems. The research of H. T. Banks and M. A. Demetriou was supported in part by the Air Force Office of Scientific Research under Grant No. AFOSR F49620-95-1-0236 while support for M. A. Demetriou and R. C. Smith was provided by NASA under Grant No. NAG-1-1600. Research was also supported by NASA under Contract No. NAS1-19480 while H. T. Banks and R. C. Smith were visiting scientists at ICASE, NASA Langley Research Center.

¹H. T. Banks, R. C. Smith, D. E. Brown, R. J. Silcox, and V. L. Metcalf, "Experimental confirmation of a PDE-based approach to design of feedback controls," *SIAM J. Control Optimization* **35**, 1263–1296 (1997).

²H. T. Banks, W. Fang, R. J. Silcox, and R. C. Smith, "Approximation methods for control of structural acoustics models with piezoceramic actuators," *J. Intell. Mater. Syst. Struct.* **4**, 116 (1993).

³H. T. Banks and R. C. Smith, "Parameter estimation in a structural acoustic system with fully nonlinear coupling conditions," *Math. Comput. Modeling* **23**, 17–50 (1996).

⁴H. T. Banks, R. C. Smith, and Y. Wang, *Smart Material Structures: Modeling, Estimation and Control* (Masson/Wiley, Paris, 1996).

⁵W. T. Baumann, W. R. Saunders, and H. H. Robertshaw, "Active suppression of acoustic radiation from impulsively excited structures," *J. Acoust. Soc. Am.* **90**, 3202–3208 (1991).

⁶R. L. Clark and C. R. Fuller, "A model reference approach for implementing active structural acoustic control," *J. Acoust. Soc. Am.* **92**, 1534–1544 (1992).

⁷C. R. Fuller, C. A. Rogers, and H. H. Robertshaw, "Active structural acoustic control with smart structures," *Proceedings of the SPIE Conference 1170 on Fiber Optic Smart Structures and Skins II*, Boston, MA (1989).

⁸C. R. Fuller, S. D. Snyder, C. H. Hansen, and R. J. Silcox, "Active control of interior noise in model aircraft fuselages using piezoceramic actuators," *AIAA Paper 90-3922*, AIAA 13th Aeroacoustics Conference, Tallahassee, FL (1990).

⁹A. Frendi, L. Maestrello, and A. Bayliss, "Coupling between plate vibration and acoustic radiation," *J. Sound Vib.* **177**, 207–226 (1994).

¹⁰A. Frendi and J. Robinson, "Effect of acoustic coupling on random and harmonic plate vibrations," *AIAA J.* **31**, 1992–1997 (1993).

¹¹A. Frendi, L. Maestrello, J. Robinson, and A. Bayliss, "On acoustic radiation from a vibrating panel," *AIAA Paper 93-4367*, *Proceedings of the 15th AIAA Aeroacoustics Conference*, Long Beach, CA (1993).

¹²H. T. Banks, R. C. Smith, D. E. Brown, V. L. Metcalf, and R. J. Silcox, "The estimation of material and patch parameters in a PDE-based circular plate model," *J. Sound Vib.* **199**, 777–799 (1997).

¹³H. T. Banks and R. C. Smith, "The modeling and approximation of a structural acoustics problem in a hard-walled cylindrical domain," *CRSC Technical Report CRSC-TR94-26*, 1994; in *Dynamics and Control of Distributed Parameter Systems*, edited by H. S. Tzou and L. A. Bergman (Cambridge U.P., Cambridge, England, to appear).

¹⁴R. C. Smith, "A Galerkin method for linear PDE systems in circular geometries with structural acoustic applications," *SIAM J. Sci. Comput.* **18**, 371–402 (1997).

¹⁵H. T. Banks, R. C. Smith, and Y. Wang, "The modeling of piezoceramic patch interactions with shells, plates, and beams," *Q. Appl. Math.* **53**, 353–381 (1995).

¹⁶H. T. Banks, M. A. Demetriou, and R. C. Smith, "Utilization of coupling effects in compensator design for structural acoustic systems—numerical results," *CRSC Technical Report 96-24*, 1996.

¹⁷H. T. Banks, M. A. Demetriou, and R. S. Smith, "An H^∞ Min/Max periodic control in a 2-D structural acoustic model with piezoceramic actuators," *IEEE Trans Autom. Control* **41**, 943–959 (1996).

¹⁸B. V. Keulen, *H_∞ -Control for Distributed Parameter Systems: A State-Space Approach* (Birkhäuser, Boston, 1993).

¹⁹A. Stoorvogel, *The H^∞ Control Problem* (Prentice Hall, Englewood Cliffs, NJ, 1992).

²⁰T. Başar and P. Bernhard, *H^∞ -Optimal Control and Related Minimax Design Problems* (Birkhäuser, Boston, 1991).

²¹C. E. deSouza, U. Shaked, and M. Fu, "Robust H_∞ tracking: A game theory approach," *Int. J. Robust Nonlinear Control* **5**, 223–238 (1995).

²²H. T. Banks, M. A. Demetriou, and R. C. Smith, "Robustness studies for H^∞ feedback control in a structural acoustic model with periodic excitation," *Int. J. Robust Nonlinear Control* **6**, 453–478 (1996).

²³J. Pan and C. H. Hansen, "Active control of noise transmission through a panel into a cavity. II: Experimental study," *J. Acoust. Soc. Am.* **90**, 1488–1492 (1991).

Harmonic Green's functions of a semi-infinite plate with clamped or free edges

R. Gunda, S. M. Vijayakar, R. Singh,^{a)} and J. E. Farstad

Department of Mechanical Engineering, Acoustics and Dynamics Laboratory, The Ohio State University, 206 W. 18th Avenue, Columbus, Ohio 43210-1107

(Received 4 August 1997; accepted for publication 14 October 1997)

Harmonic Green's functions for a thin semi-infinite plate with clamped or free edges are developed starting from either simply supported or roller supported solutions and applying corrections to account for boundary excitation. This is achieved by connecting the solutions in terms of polar coordinates with the solutions in Cartesian coordinates. The formal solutions in the form of improper wave-number integrals are numerically evaluated using adaptive Clenshaw–Curtis integration. Alternate solutions obtained for each boundary condition compare well. Only harmonic point loads are considered in this article but the methodology may be extended to moment excitation and distributed loads. The methodology developed here will form the basis for advancing the ray tracing technique for vibration analysis of finite plates. © 1998 Acoustical Society of America. [S0001-4966(98)02302-9]

PACS numbers: 43.40.Dx, 43.40.At [CBB]

INTRODUCTION

The Green's functions for the harmonic response of semi-infinite plates serve as the basis for a ray tracing method used to construct solutions in finite domains and for boundary element models. The ray tracing technique has already been implemented successfully to predict harmonic responses in beams and rectangular plates with simply supported and roller supported boundary conditions.¹ New solutions needed for clamped and free edges are developed in this article.

A similar problem of interest to seismologists is the propagation of tremors over the surface of an elastic half-space due to harmonic line sources on the surface² or buried line sources radiating cylindrical³ or conical⁴ pulses. The main focus in elastic half-space problems is the wave propagation on the free surface. Other investigators have examined the acoustic radiation Green's functions for fluid-filled elastic plates governing the production of aerodynamic sound by sources near the edges of a semi-infinite plate⁵ or an infinite plate with discontinuities.⁶

To the best of our knowledge, two studies have specifically addressed the Green's functions for semi-infinite plates. Ortner⁷ uses the semi-infinite clamped beam solution to obtain the dynamic Green's function for a clamped semi-infinite plate with a special orthotropic property. He uses Laplace–Fourier transform techniques to derive the dynamic Green's function in the form of a double integral but it was not evaluated numerically. Static Green's function for a clamped semi-infinite plate on an elastic foundation was obtained by adding clamping terms to the simply supported solution. Similarly Kerr⁸ derives the static Green's functions for a clamped semi-infinite plate on a Winkler foundation by formulating an integral equation for an unknown distributed

load on the boundary line and by adding clamping terms to the roller supported solution.

I. PROBLEM FORMULATION

A. Governing equations

The equation governing the transverse motion $w(\mathbf{r}, t)$ of an isotropic homogeneous plate of constant thickness (h) is given by classical thin plate theory⁹ as

$$D\nabla^4 w(\mathbf{r}, t) + \rho h \frac{\partial^2 w(\mathbf{r}, t)}{\partial t^2} = p(\mathbf{r}, t) \quad \forall \mathbf{r} \in \Omega, \quad (1)$$

where $D = Eh^3/12(1 - \nu^2)$ is the flexural rigidity of the plate, E is the Young's modulus, ν is the Poisson's ratio, ∇^4 is the biharmonic operator, ρ is the mass density, $p(\mathbf{r}, t)$ is the normal force per unit area, \mathbf{r} the position vector, and t is the time. For harmonic excitation at a constant circular frequency ω , $p(\mathbf{r}, t) = \hat{p}(\mathbf{r}) \exp(-i\omega t)$, the response will be $w(\mathbf{r}, t) = \hat{w}(\mathbf{r}) \exp(-i\omega t)$, allowing us to suppress the time dependence from Eq. (1) and carry out the analysis in the frequency domain. Thus Eq. (1) can be rewritten as

$$(\nabla^4 - k^4) \hat{w}(\mathbf{r}) = \frac{\hat{p}(\mathbf{r})}{D}; \quad k^4 = \frac{\rho h \omega^2}{D}, \quad (2)$$

where k is the bending wave number. Structural damping behavior is incorporated in the formulation by substituting $D(1 - i\eta)$ for D in Eq. (2), η being the structural loss factor. The negative sign in $D(1 - i\eta)$ is chosen to yield behavior consistent with equivalent viscous damping for the $\exp(-i\omega t)$ time dependence.

B. Boundary conditions

At a regular point (not a corner) on a continuous boundary $\partial\Omega$, the bending moment $M_n(w)$, twisting moment $M_t(w)$, shear force $Q_n(w)$, and Kelvin–Kirchhoff edge reaction $V_n(w)$ are given by the following expressions:¹⁰

^{a)}Electronic mail: singh.3@osu.edu

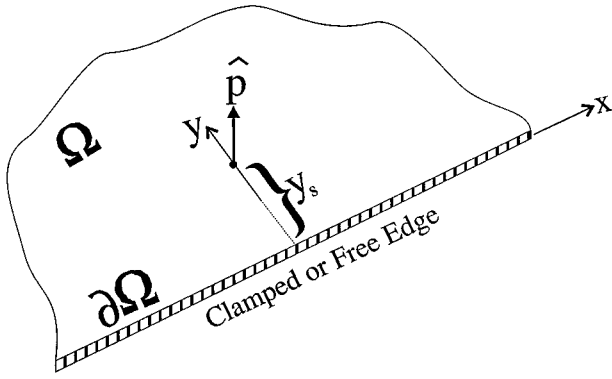


FIG. 1. The problem geometry, loading, and boundary conditions.

$$M_n(w) = \frac{D}{2} \left\{ -(1+\nu)\nabla^2 w + (1-\nu) \left[\left(\frac{\partial^2 w}{\partial y^2} - \frac{\partial^2 w}{\partial x^2} \right) \times \cos 2\alpha - 2 \frac{\partial^2 w}{\partial x \partial y} \sin 2\alpha \right] \right\} \mathbf{e}_n, \quad (3)$$

$$M_t(w) = \frac{D(1-\nu)}{2} \left[\left(\frac{\partial^2 w}{\partial y^2} - \frac{\partial^2 w}{\partial x^2} \right) \sin 2\alpha + 2 \frac{\partial^2 w}{\partial x \partial y} \cos 2\alpha \right] \mathbf{e}_t, \quad (4)$$

$$Q_n(w) = -D \frac{\partial}{\partial n} (\nabla^2 w) \mathbf{e}_n, \quad (5)$$

$$V_n(w) = \left\{ -D \frac{\partial}{\partial n} (\nabla^2 w) - \frac{\partial M_t}{\partial s} \right\} \mathbf{e}_z, \quad (6)$$

where $\cos \alpha = \mathbf{n} \cdot \mathbf{e}_x$ and $\sin \alpha = \mathbf{n} \cdot \mathbf{e}_y$ are the direction cosines of the outward normal \mathbf{n} , s is the tangential coordinate considered positive in the counterclockwise direction, $\mathbf{e}_x, \mathbf{e}_y, \mathbf{e}_z$ are the unit vectors in the coordinate directions, and $\mathbf{e}_n, \mathbf{e}_t$ are the unit vectors along $\mathbf{n}, \partial\Omega$, respectively. The four classical boundary conditions are simple supports, roller supports, clamped, and free edges, which satisfy the following relations on $\partial\Omega$:

$$\begin{aligned} \text{simple supports (S): } & w=0, \quad M_n(w)=0, \\ \text{roller supports (R): } & \partial w / \partial n=0, \quad V_n(w)=0, \\ \text{clamped edge (C): } & w=0, \quad \partial w / \partial n=0, \\ \text{free edge (F): } & M_n(w)=0, \quad V_n(w)=0. \end{aligned} \quad (7)$$

C. Statement of the problem

Figure 1 illustrates the plate geometry along with the excitation and boundary conditions. Without loss of generality, the semi-infinite plate is assumed to be oriented such that its edge coincides with the x axis of the coordinate system. The plate domain Ω is given by $\Omega = \{(x, y) / y \geq 0\}$. The plate is excited by a unit harmonic force concentrated at $\mathbf{r}_s = (0, y_s)$. Hence $\hat{p}(\mathbf{r}) = \delta(\mathbf{r} - \mathbf{r}_s)$, δ being the Dirac's delta function. On the plate edge ($y=0$), one of the four classical boundary conditions described by Eq. (7) is applied. In addition, the Sommerfeld radiation condition must be satisfied as the observation point approaches infinity in the y direction

(as $y \rightarrow \infty$). We seek to derive analytical harmonic Green's functions of Eq. (2) in Ω for the excitation and boundary conditions as described above.

D. Infinite plate solution

The Green's function for an infinite plate $G_\infty(\mathbf{r}|\mathbf{r}_s; k)$ represents the transverse deflection $\hat{w}(\mathbf{r})$ due to a unit concentrated harmonic load $\hat{p}(\mathbf{r}) = \delta(\mathbf{r} - \mathbf{r}_s)$ at \mathbf{r}_s :

$$G_\infty(\mathbf{r}|\mathbf{r}_s; k) = C[H_0^1(kr) - H_0^1(ikr)], \quad C = \frac{i}{8k^2 D}, \quad (8)$$

where $r = |\mathbf{r} - \mathbf{r}_s|$ is the distance of the observation point from the source location and H_0^1 is the zero order Hankel function of the first kind. The fundamental solution given by Eq. (8) satisfies the Sommerfeld radiation condition at infinity which requires the source to yield only outgoing waves. This is evident from the asymptotic expansion of the Hankel functions for large argument.¹¹

In this paper, the Green's functions for the semi-infinite plate are obtained by adding correction terms to the infinite plate fundamental solution $G_\infty(\mathbf{r}|\mathbf{r}_s; k)$ to account for the boundary conditions. The representation for $G_\infty(\mathbf{r}|\mathbf{r}_s; k)$ given by Eq. (8) contains both the arguments x, y under the radical as $\{(x-x_s)^2 + (y-y_s)^2\}^{1/2}$ making it inconvenient for applying boundary conditions along the edge $y=0$. Hence it is advantageous to transform $G_\infty(\mathbf{r}|\mathbf{r}_s; k)$ by decomposing the Hankel functions into their Cartesian components. This is accomplished by comparing two representations of the solution U to the two-dimensional Helmholtz equation (wave equation in frequency domain) excited by a unit harmonic point source at the origin:

$$\nabla^2 U + k^2 U = \delta(\mathbf{r}). \quad (9)$$

Equation (9) in cylindrical polar coordinates is

$$\frac{\partial^2 U}{\partial r^2} + \frac{1}{r} \frac{\partial U}{\partial r} + k^2 U = \frac{\delta(r)}{2\pi r}. \quad (10)$$

The solution U should in addition satisfy the Sommerfeld radiation condition. The homogeneous form of Eq. (10) is the Bessel's differential equation of order zero. The solution U is obtained by solving Eq. (10) in its homogeneous form and adjusting the coefficients to account for the source at the origin. Therefore $U(\mathbf{r}) = AH_0^1(kr)$. Integrating Eq. (10) over a small circle around the origin and taking the limit as the radius of the circle approaches zero yields $A = 1/4i$. Therefore

$$U(\mathbf{r}) = \frac{1}{4i} H_0^1(kr). \quad (11)$$

Equation (9) in Cartesian coordinates is

$$\frac{\partial^2 U}{\partial x^2} + \frac{\partial^2 U}{\partial y^2} + k^2 U = \delta(x)\delta(y). \quad (12)$$

Applying the spatial Fourier transform in the x direction to Eq. (12) yields

$$-k_x^2 \bar{U}(k_x, y) + \frac{\partial^2 \bar{U}(k_x, y)}{\partial y^2} + k^2 \bar{U}(k_x, y) = \frac{1}{\sqrt{2\pi}} \delta(y). \quad (13)$$

Let $k_y^2 = k^2 - k_x^2$. Equation (13) simplifies to

$$\frac{\partial^2 \bar{U}(k_x, y)}{\partial y^2} + k_y^2 \bar{U}(k_x, y) = \frac{1}{\sqrt{2\pi}} \delta(y). \quad (14)$$

Equation (14) is the one-dimensional wave equation in frequency domain whose solution¹² is

$$\bar{U}(k_x, y) = \frac{1}{\sqrt{2\pi}} \frac{1}{2ik_y} e^{ik_y|y|} \operatorname{Im}(k_y), \quad \operatorname{Re}(k_y) \geq 0. \quad (15)$$

Taking the inverse spatial Fourier transform of Eq. (15) in the x direction yields the required solution $U(\mathbf{r})$:

$$\begin{aligned} U(\mathbf{r}) &= \frac{1}{4\pi i} \int_{-\infty}^{\infty} \frac{e^{ik_x x} e^{ik_y|y|}}{k_y} dk_x \\ &= \frac{1}{2\pi i} \int_0^{\infty} \frac{\cos k_x x e^{ik_y|y|}}{k_y} dk_x. \end{aligned} \quad (16)$$

Comparing Eq. (11) with Eq. (16), we get the desired Cartesian decomposition of the zero order Hankel function of the first kind, and a representation of the fundamental solution suitable for applying boundary conditions along the straight edge ($y=0$) in terms of a wave-number integral as follows:

$$\begin{aligned} H_0^1(kr) &= \frac{1}{\pi} \int_{-\infty}^{\infty} \frac{\exp(ik_x x) e^{ik_y|y|}}{k_y} dk_x, \\ \operatorname{Im}(k_y), \quad \operatorname{Im}(k) &\geq 0, \end{aligned} \quad (17)$$

$$\begin{aligned} G_{\infty}(\mathbf{r}|\mathbf{r}_s; k) &= \frac{C}{\pi} \int_{-\infty}^{\infty} e^{ik_x(x-x_s)} \left[\frac{e^{i\sqrt{k^2-k_x^2}|y-y_s|}}{\sqrt{k^2-k_x^2}} \right. \\ &\quad \left. + i \frac{e^{-\sqrt{k^2+k_x^2}|y-y_s|}}{\sqrt{k^2+k_x^2}} \right] dk_x. \end{aligned} \quad (18)$$

II. FORMULATION FOR SEMI-INFINITE PLATE

A. Simply supported and roller supported edges

The solution for a semi-infinite plate with a simply supported edge excited by a point load at $\mathbf{r}_s = (0, y_s)$ is given by the method of images¹ as

$$G_s(\mathbf{r}|\mathbf{r}_s; k) = G_{\infty}(\mathbf{r}|\mathbf{r}_s; k) - G_{\infty}(\mathbf{r}|\mathbf{r}_i; k), \quad (19)$$

where $\mathbf{r}_i = (0, -y_s)$ is the location of image of \mathbf{r}_s in the plate edge. This solution satisfies the conditions of vanishing transverse displacement \hat{w} and the bending moment $M_n(\hat{w})$ on the plate edge. The normal slope $\partial\hat{w}/\partial n$ and the edge reaction $V_n(\hat{w})$ along the edge ($y=0$) are given by

$$\begin{aligned} \frac{\partial\hat{w}}{\partial n} &= -\frac{\partial\hat{w}}{\partial y} = \frac{2Ci}{\pi} \int_{-\infty}^{\infty} \exp(ik_x x) [e^{i\sqrt{k^2-k_x^2}y_s} \\ &\quad - e^{-\sqrt{k^2+k_x^2}y_s}] dk_x, \end{aligned} \quad (20)$$

$$\begin{aligned} V_n(\hat{w}) &= \frac{2CDi}{\pi} \int_{-\infty}^{\infty} \exp(ik_x x) \\ &\quad \times [\{k^2 + (1-\nu)k_x^2\} e^{i\sqrt{k^2-k_x^2}y_s} \\ &\quad + \{k^2 - (1-\nu)k_x^2\} e^{-\sqrt{k^2+k_x^2}y_s}] dk_x. \end{aligned} \quad (21)$$

Like the simply supported case, the solution for the roller supported edge is obtained from the method of images as

$$G_r(\mathbf{r}|\mathbf{r}_s; k) = G_{\infty}(\mathbf{r}|\mathbf{r}_s; k) + G_{\infty}(\mathbf{r}|\mathbf{r}_i; k). \quad (22)$$

This solution has zero normal slope $\partial\hat{w}/\partial n$ and zero edge reaction $V_n(\hat{w})$ on the plate edge. The transverse deflection \hat{w} and the bending moment $M_n(\hat{w})$ along the edge are given by

$$\begin{aligned} \hat{w} &= \frac{2C}{\pi} \int_{-\infty}^{\infty} \exp(ik_x x) \\ &\quad \times \left[\frac{e^{i\sqrt{k^2-k_x^2}y_s}}{\sqrt{k^2-k_x^2}} + i \frac{e^{-\sqrt{k^2+k_x^2}y_s}}{\sqrt{k^2+k_x^2}} \right] dk_x, \end{aligned} \quad (23)$$

$$\begin{aligned} M_n(\hat{w}) &= \frac{2CD}{\pi} \int_{-\infty}^{\infty} \exp(ik_x x) \\ &\quad \times \left[\{k^2 - (1-\nu)k_x^2\} \frac{e^{i\sqrt{k^2-k_x^2}y_s}}{\sqrt{k^2-k_x^2}} \right. \\ &\quad \left. - i\{k^2 + (1-\nu)k_x^2\} \frac{e^{-\sqrt{k^2+k_x^2}y_s}}{\sqrt{k^2+k_x^2}} \right] dk_x. \end{aligned} \quad (24)$$

B. Clamped edge via correction to roller supported edge

In this section, the Green's function for a clamped edge is obtained by adding to $G_r(\mathbf{r}|\mathbf{r}_s; k)$ given by Eq. (22), terms corresponding to certain waves which travel along the edge and decay or propagate in the plate interior. However, a simpler problem of a semi-infinite plate subjected to the following boundary excitation needs to be solved first: $\hat{w} = W(k_x) \exp(ik_x x)$ on $y=0$ and $\partial\hat{w}/\partial n = 0$ on $y=0$. A trial function which satisfies the homogeneous form of governing Eq. (2) is

$$\hat{w}(\mathbf{r}) = \exp(ik_x x) [A(k_x) e^{i\sqrt{k^2-k_x^2}y} + B(k_x) e^{-\sqrt{k^2+k_x^2}y}]. \quad (25)$$

The solution given by Eq. (25) is suitable for any type of boundary excitation since it yields bounded responses [waves propagating in the interior (first term if $k_x < k$), and waves traveling along the edge and decaying in the plate interior (second term and first term if $k_x > k$)]. Imposing the boundary conditions leads to the following system of equations for the coefficients $A(k_x)$ and $B(k_x)$:

$$\begin{bmatrix} 1 & 1 \\ -i\sqrt{k^2-k_x^2} & \sqrt{k^2+k_x^2} \end{bmatrix} \begin{Bmatrix} A(k_x) \\ B(k_x) \end{Bmatrix} = \begin{Bmatrix} W(k_x) \\ 0 \end{Bmatrix}. \quad (26)$$

The coefficient matrix in Eq. (26) is never singular. Solving Eq. (26) gives the solution as

$$\hat{w}(\mathbf{r}) = \frac{W(k_x)\exp(ik_x x)}{\sqrt{k^2+k_x^2+i\sqrt{k^2-k_x^2}}} \left[\sqrt{k^2+k_x^2} e^{i\sqrt{k^2-k_x^2}y} + i\sqrt{k^2-k_x^2} e^{-\sqrt{k^2+k_x^2}y} \right]. \quad (27)$$

In a roller supported plate, the transverse deflection along the edge is given by Eq. (23). The component of wave number k_x is

$$W(k_x) = \frac{2C}{\pi} \left[\frac{e^{i\sqrt{k^2-k_x^2}y_s}}{\sqrt{k^2-k_x^2}} + i \frac{e^{-\sqrt{k^2+k_x^2}y_s}}{\sqrt{k^2+k_x^2}} \right]. \quad (28)$$

The contribution of this edge displacement excitation has to be subtracted from $G_r(\mathbf{r}|\mathbf{r}_s;k)$ to realize the clamped boundary condition along $y=0$. Using the principle of superposition, the correction to the roller supported fundamental solution $G_r(\mathbf{r}|\mathbf{r}_s;k)$ to obtain the solution to the clamped boundary $G_c(\mathbf{r}|\mathbf{r}_s;k)$ is

$$\hat{w}_{cr}(\mathbf{r}|\mathbf{r}_s) = \frac{2C}{\pi} \int_{-\infty}^{\infty} \frac{\exp(ik_x x)}{\sqrt{k^2+k_x^2+i\sqrt{k^2-k_x^2}}} \left[\frac{e^{i\sqrt{k^2-k_x^2}y_s}}{\sqrt{k^2-k_x^2}} + i \frac{e^{-\sqrt{k^2+k_x^2}y_s}}{\sqrt{k^2+k_x^2}} \right] \left[\sqrt{k^2+k_x^2} e^{i\sqrt{k^2-k_x^2}y} + i\sqrt{k^2-k_x^2} e^{-\sqrt{k^2+k_x^2}y} \right] dk_x \quad (29)$$

$$= \frac{2C}{\pi} \int_{-\infty}^{\infty} \frac{\exp(ik_x x)}{\Delta_{cr}} f_{cr}(y) f_{cr}(y_s) dk_x, \quad (30)$$

where Δ_{cr} and $f_{cr}(y)$ are given by

$$\Delta_{cr} = \sqrt{k^2+k_x^2} \sqrt{k^2-k_x^2} \{ \sqrt{k^2+k_x^2} + i\sqrt{k^2-k_x^2} \}, \quad (31)$$

$$f_{cr}(y) = \sqrt{k^2+k_x^2} e^{i\sqrt{k^2-k_x^2}y} + i\sqrt{k^2-k_x^2} e^{-\sqrt{k^2+k_x^2}y}. \quad (32)$$

The fundamental solution for the clamped edge $G_c(\mathbf{r}|\mathbf{r}_s;k)$ is obtained by subtracting $\hat{w}_{cr}(\mathbf{r}|\mathbf{r}_s)$ from $G_r(\mathbf{r}|\mathbf{r}_s;k)$:

$$G_c(\mathbf{r}|\mathbf{r}_s;k) = G_r(\mathbf{r}|\mathbf{r}_s;k) - \hat{w}_{cr}(\mathbf{r}|\mathbf{r}_s). \quad (33)$$

The Green's function $G_c(\mathbf{r}|\mathbf{r}_s;k)$ given by Eq. (33) is convenient for calculating the effective shear force per unit length $V_n(\hat{w})$ along the edge $y=0$, since the roller solution $G_r(\mathbf{r}|\mathbf{r}_s;k)$ does not contribute and the contribution from correction term $-\hat{w}_{cr}(\mathbf{r}|\mathbf{r}_s)$ alone needs to be calculated. Along the edge, $V_n(\hat{w})$ is given by

$$V_n(\hat{w})|_{y=0} = \frac{-1}{2\pi} \int_{-\infty}^{\infty} \frac{\exp(ik_x x)}{\sqrt{k^2+k_x^2+i\sqrt{k^2-k_x^2}}} \times \left[\sqrt{k^2+k_x^2} e^{i\sqrt{k^2-k_x^2}y_s} + i\sqrt{k^2-k_x^2} e^{-\sqrt{k^2+k_x^2}y_s} \right] dk_x. \quad (34)$$

In the limiting case when y_s approaches zero, from Eq. (34), $V_n(\hat{w}) = -1/2\pi \int_{-\infty}^{\infty} \exp(ik_x x) dk_x$ which is nothing but $-\delta(x)$, as it should be.

C. Clamped edge via correction to simply supported edge

In this section, the Green's function for a clamped edge $G_c(\mathbf{r}|\mathbf{r}_s;k)$ is obtained by modifying $G_s(\mathbf{r}|\mathbf{r}_s;k)$ given by Eq. (19). The simpler problem whose solution is used to construct $G_c(\mathbf{r}|\mathbf{r}_s;k)$ is that of a semi-infinite plate with the following boundary excitation: $\hat{w}=0$ on $y=0$ and $\partial\hat{w}/\partial n = W_n(k_x)\exp(ik_x x)$ on $y=0$. Using the trial solution given by Eq. (25) and applying the boundary conditions leads to the following system of equations for the coefficients $A(k_x)$ and $B(k_x)$:

$$\begin{bmatrix} 1 & 1 \\ -i\sqrt{k^2-k_x^2} & \sqrt{k^2+k_x^2} \end{bmatrix} \begin{Bmatrix} A(k_x) \\ B(k_x) \end{Bmatrix} = \begin{Bmatrix} 0 \\ W_n(k_x) \end{Bmatrix}. \quad (35)$$

Solving Eq. (35) gives

$$\hat{w}(\mathbf{r}) = \frac{W_n(k_x)\exp(ik_x x)}{\sqrt{k^2+k_x^2+i\sqrt{k^2-k_x^2}}} \left[-e^{i\sqrt{k^2-k_x^2}y} + e^{-\sqrt{k^2+k_x^2}y} \right]. \quad (36)$$

In a simply supported plate, the component of wave number k_x of the normal slope along the edge is given by Eq. (20) as

$$W_n(k_x) = \frac{2Ci}{\pi} \left[e^{i\sqrt{k^2-k_x^2}y_s} - e^{-\sqrt{k^2+k_x^2}y_s} \right]. \quad (37)$$

The contribution of this slope excitation is subtracted from $G_s(\mathbf{r}|\mathbf{r}_s;k)$ to realize the clamped boundary condition along $y=0$. From superposition, the correction to the simply supported fundamental solution $G_s(\mathbf{r}|\mathbf{r}_s;k)$ to obtain the solution to the clamped boundary $G_c(\mathbf{r}|\mathbf{r}_s;k)$ is

$$\hat{w}_{cs}(\mathbf{r}|\mathbf{r}_s) = \frac{2Ci}{\pi} \int_{-\infty}^{\infty} \frac{\exp(ik_x x)}{\sqrt{k^2+k_x^2+i\sqrt{k^2-k_x^2}}} \times \left[e^{i\sqrt{k^2-k_x^2}y_s} - e^{-\sqrt{k^2+k_x^2}y_s} \right] \times \left[-e^{i\sqrt{k^2-k_x^2}y} + e^{-\sqrt{k^2+k_x^2}y} \right] dk_x \quad (38)$$

$$= \frac{2Ci}{\pi} \int_{-\infty}^{\infty} \frac{\exp(ik_x x)}{\Delta_{cs}} f_{cs}(y) f_{cs}(y_s) dk_x, \quad (39)$$

where Δ_{cs} and $f_{cs}(y)$ are given by

$$\Delta_{cs} = -\{ \sqrt{k^2+k_x^2} + i\sqrt{k^2-k_x^2} \}, \quad (40)$$

$$f_{cs}(y) = e^{i\sqrt{k^2-k_x^2}y} - e^{-\sqrt{k^2+k_x^2}y}. \quad (41)$$

The fundamental solution for the clamped edge $G_c(\mathbf{r}|\mathbf{r}_s;k)$ is obtained by subtracting $\hat{w}_{cs}(\mathbf{r}|\mathbf{r}_s)$ from $G_s(\mathbf{r}|\mathbf{r}_s;k)$:

$$G_c(\mathbf{r}|\mathbf{r}_s;k) = G_s(\mathbf{r}|\mathbf{r}_s;k) - \hat{w}_{cs}(\mathbf{r}|\mathbf{r}_s). \quad (42)$$

The Green's function $G_c(\mathbf{r}|\mathbf{r}_s;k)$ given by Eq. (42) is convenient for calculating the bending moment per unit length $M_n(\hat{w})$ along the edge $y=0$, since the simply supported solution $G_s(\mathbf{r}|\mathbf{r}_s;k)$ does not contribute and the contribution from correction term $-\hat{w}_{cs}(\mathbf{r}|\mathbf{r}_s)$ alone needs to be calculated. Along the edge, $M_n(\hat{w})$ is given by

$$M_n(\hat{w})|_{y=0} = \frac{-1}{2\pi} \int_{-\infty}^{\infty} \frac{\exp(ik_x x)}{\sqrt{k^2 + k_x^2 + i\sqrt{k^2 - k_x^2}}} \times [e^{i\sqrt{k^2 - k_x^2} y_s} - e^{-\sqrt{k^2 + k_x^2} y_s}] dk_x. \quad (43)$$

From Eqs. (33), (19), (22), and (42), we have

$$G_c(\mathbf{r}|\mathbf{r}_s; k) = G_\infty(\mathbf{r}|\mathbf{r}_s; k) - \frac{1}{2} [\hat{w}_{cr}(\mathbf{r}|\mathbf{r}_s) + \hat{w}_{cs}(\mathbf{r}|\mathbf{r}_s)]. \quad (44)$$

For a clamped edge, both displacement and normal slope must vanish on the boundary. In the derivation from the Green's function of a simply supported edge, the displacement on the boundary is already zero and we need to subtract only the contribution from the normal slope excitation on the boundary to get $G_c(\mathbf{r}|\mathbf{r}_s; k)$. Conversely, in the derivation from the roller supported edge, the normal slope along the edge being zero only the contribution from the displacement excitation is subtracted to get $G_c(\mathbf{r}|\mathbf{r}_s; k)$. In Eq. (44), we have the free space Green's function $G_\infty(\mathbf{r}|\mathbf{r}_s; k)$ which will yield nonzero displacement and normal slope along the line $y=0$. Hence subtract the contributions from both the boundary excitations to arrive at $G_c(\mathbf{r}|\mathbf{r}_s; k)$. The multiplicative factor 1/2 in Eq. (44) comes from the fact that the boundary excitations are half that of simply supported and roller boundary conditions. (The choice of image source annuls the two required conditions while doubling the other two.)

D. Free edge via correction to roller supported edge

The Green's function for a free edge $G_f(\mathbf{r}|\mathbf{r}_s; k)$ is obtained by modifying $G_r(\mathbf{r}|\mathbf{r}_s; k)$ as given by Eq. (22). The simpler problem whose solution is used to construct $G_f(\mathbf{r}|\mathbf{r}_s; k)$ is that of a semi-infinite plate with a boundary moment excitation: $M_n = M(k_x) \exp(ik_x x)$ and $V_n = 0$ on $y=0$. Using the trial solution given by Eq. (25) and applying the boundary conditions leads to the following system of equations for the coefficients $A(k_x)$ and $B(k_x)$:

$$D \begin{bmatrix} k^2 - (1-\nu)k_x^2 & -[k^2 + (1-\nu)k_x^2] \\ -i\sqrt{k^2 - k_x^2}[k^2 + (1-\nu)k_x^2] & -\sqrt{k^2 + k_x^2}[k^2 - (1-\nu)k_x^2] \end{bmatrix} \times \begin{Bmatrix} A(k_x) \\ B(k_x) \end{Bmatrix} = \begin{Bmatrix} M(k_x) \\ 0 \end{Bmatrix}. \quad (45)$$

Solving Eq. (45) gives

$$\hat{w}(\mathbf{r}) = \frac{M(k_x) \exp(ik_x x)}{D\Delta} [-\sqrt{k^2 + k_x^2} \times \{k^2 - (1-\nu)k_x^2\} e^{i\sqrt{k^2 - k_x^2} y + i\sqrt{k^2 - k_x^2} y} + \{k^2 + (1-\nu)k_x^2\} e^{-\sqrt{k^2 + k_x^2} y}], \quad (46)$$

where Δ is the determinant of the coefficient matrix given by

$$\Delta = -\sqrt{k^2 + k_x^2} \{k^2 - (1-\nu)k_x^2\}^2 - i\sqrt{k^2 - k_x^2} \times \{k^2 + (1-\nu)k_x^2\}^2. \quad (47)$$

The coefficient matrix in Eq. (45) is singular when

$$\frac{k_x}{k} = \sqrt[4]{\frac{-(3\nu - 1) + 2\sqrt{2\nu^2 - 2\nu + 1}}{(1-\nu)^2(3+\nu)}}. \quad (48)$$

For a steel plate with Poisson's ratio $\nu=0.28$, the coefficient matrix is singular when $k_x/k \approx 1.0007$. The null space of the coefficient matrix has dimension 1, which implies that $A(k_x)$ and $B(k_x)$ are nonzero even when there is no boundary excitation. Since we restrict k_x to be on the real (Re) line and k has a small imaginary (Im) part because of the mild dissipation included in the system, the coefficient matrix is never singular, but close to singular when $k_x \approx \text{Re}(k)$.

In a roller supported plate, the component of wave number k_x of the bending moment M_n along the edge is given by Eq. (24) as

$$M(k_x) = \frac{2CD}{\pi} \left[\{k^2 - (1-\nu)k_x^2\} \frac{e^{i\sqrt{k^2 - k_x^2} y_s}}{\sqrt{k^2 - k_x^2}} - i\{k^2 + (1-\nu)k_x^2\} \frac{e^{-\sqrt{k^2 + k_x^2} y_s}}{\sqrt{k^2 + k_x^2}} \right]. \quad (49)$$

The contribution of this bending moment excitation is subtracted from $G_r(\mathbf{r}|\mathbf{r}_s; k)$ to realize the free boundary condition along $y=0$. From superposition, the correction to the roller supported fundamental solution $G_r(\mathbf{r}|\mathbf{r}_s; k)$ to obtain the solution to the free boundary $G_f(\mathbf{r}|\mathbf{r}_s; k)$ is

$$\begin{aligned} \hat{w}_{fr}(\mathbf{r}|\mathbf{r}_s) &= \frac{2C}{\pi} \int_{-\infty}^{\infty} \frac{\exp(ik_x x)}{\Delta} \left[\{k^2 - (1-\nu)k_x^2\} \right. \\ &\quad \times \frac{e^{i\sqrt{k^2 - k_x^2} y_s}}{\sqrt{k^2 - k_x^2}} - i\{k^2 + (1-\nu)k_x^2\} \\ &\quad \times \frac{e^{-\sqrt{k^2 + k_x^2} y_s}}{\sqrt{k^2 + k_x^2}} \left. \right] [-\sqrt{k^2 + k_x^2} \\ &\quad \times \{k^2 - (1-\nu)k_x^2\} e^{i\sqrt{k^2 - k_x^2} y + i\sqrt{k^2 - k_x^2} y} \\ &\quad \times \{k^2 + (1-\nu)k_x^2\} e^{-\sqrt{k^2 + k_x^2} y}] dk_x \quad (50) \\ &= \frac{2C}{\pi} \int_{-\infty}^{\infty} \frac{\exp(ik_x x)}{\Delta_{fr}} f_{fr}(y) f_{fr}(y_s) dk_x, \quad (51) \end{aligned}$$

where $f_{fr}(y)$ and Δ_{fr} are given by

$$f_{fr}(y) = -\sqrt{k^2 + k_x^2} \{k^2 - (1-\nu)k_x^2\} e^{i\sqrt{k^2 - k_x^2} y} + i\sqrt{k^2 - k_x^2} \{k^2 + (1-\nu)k_x^2\} e^{-\sqrt{k^2 + k_x^2} y}, \quad (52)$$

$$\Delta_{fr} = -\Delta \sqrt{k^2 + k_x^2} \sqrt{k^2 - k_x^2}. \quad (53)$$

The Green's function for the free edge $G_f(\mathbf{r}|\mathbf{r}_s; k)$ is obtained by subtracting $\hat{w}_{fr}(\mathbf{r}|\mathbf{r}_s)$ from $G_r(\mathbf{r}|\mathbf{r}_s; k)$.

$$G_f(\mathbf{r}|\mathbf{r}_s; k) = G_r(\mathbf{r}|\mathbf{r}_s; k) - \hat{w}_{fr}(\mathbf{r}|\mathbf{r}_s). \quad (54)$$

E. Free edge via correction to simply supported edge

In this section, the Green's function for a free edge $G_f(\mathbf{r}|\mathbf{r}_s; k)$ is obtained by modifying $G_s(\mathbf{r}|\mathbf{r}_s; k)$ given by Eq.

(19). The simpler problem whose solution is used to construct $G_f(\mathbf{r}|\mathbf{r}_s; k)$ is that of a semi-infinite plate with a boundary force excitation: $M_n=0$ on $y=0$ and $V_n=V(k_x) \times \exp(ik_x x)$ on $y=0$. Using the trial solution given by Eq. (25) and applying the boundary conditions leads to the following system of equations for the coefficients $A(k_x)$ and $B(k_x)$:

$$D \begin{bmatrix} k^2 - (1-\nu)k_x^2 & -[k^2 + (1-\nu)k_x^2] \\ -i\sqrt{k^2 - k_x^2}[k^2 + (1-\nu)k_x^2] & -\sqrt{k^2 + k_x^2}[k^2 - (1-\nu)k_x^2] \end{bmatrix} \times \begin{Bmatrix} A(k_x) \\ B(k_x) \end{Bmatrix} = \begin{Bmatrix} 0 \\ V(k_x) \end{Bmatrix}. \quad (55)$$

Solving Eq. (55) gives

$$\hat{w}(\mathbf{r}) = \frac{V(k_x)\exp(ik_x x)}{D\Delta} [\{k^2 + (1-\nu)k_x^2\}e^{i\sqrt{k^2 - k_x^2}y} + \{k^2 - (1-\nu)k_x^2\}e^{-\sqrt{k^2 + k_x^2}y}], \quad (56)$$

where Δ is the determinant of the coefficient matrix given by Eq. (47). In a simply supported plate, the component of wave number k_x of the edge reaction V_n along the edge is given by Eq. (21) as

$$V(k_x) = \frac{2CDi}{\pi} [\{k^2 + (1-\nu)k_x^2\}e^{i\sqrt{k^2 - k_x^2}y_s} + \{k^2 - (1-\nu)k_x^2\}e^{-\sqrt{k^2 + k_x^2}y_s}]. \quad (57)$$

The contribution of this force excitation is subtracted from $G_s(\mathbf{r}|\mathbf{r}_s; k)$ to realize the free boundary condition along $y=0$. From superposition, the correction to the simply supported fundamental solution $G_s(\mathbf{r}|\mathbf{r}_s; k)$ to obtain the solution to the free boundary $G_f(\mathbf{r}|\mathbf{r}_s; k)$ is

$$\begin{aligned} \hat{w}_{f_s}(\mathbf{r}|\mathbf{r}_s) &= \frac{2Ci}{\pi} \int_{-\infty}^{\infty} \frac{\exp(ik_x x)}{\Delta} [\{k^2 + (1-\nu)k_x^2\} \\ &\times e^{i\sqrt{k^2 - k_x^2}y_s} + \{k^2 - (1-\nu)k_x^2\}e^{-\sqrt{k^2 + k_x^2}y_s}] \\ &\times [\{k^2 + (1-\nu)k_x^2\}e^{i\sqrt{k^2 - k_x^2}y} \\ &+ \{k^2 - (1-\nu)k_x^2\}e^{-\sqrt{k^2 + k_x^2}y}] dk_x \end{aligned} \quad (58)$$

$$= \frac{2Ci}{\pi} \int_{-\infty}^{\infty} \frac{\exp(ik_x x)}{\Delta_{f_s}} f_{f_s}(y) f_{f_s}(y_s) dk_x, \quad (59)$$

where $\Delta_{f_s} = \Delta$ and $f_{f_s}(y)$ is given by

$$f_{f_s}(y) = \{k^2 + (1-\nu)k_x^2\}e^{i\sqrt{k^2 - k_x^2}y} + \{k^2 - (1-\nu)k_x^2\}e^{-\sqrt{k^2 + k_x^2}y}. \quad (60)$$

The Green's function for the free edge $G_f(\mathbf{r}|\mathbf{r}_s; k)$ is obtained by subtracting $\hat{w}_{f_s}(\mathbf{r}|\mathbf{r}_s)$ from $G_s(\mathbf{r}|\mathbf{r}_s; k)$:

$$G_f(\mathbf{r}|\mathbf{r}_s; k) = G_s(\mathbf{r}|\mathbf{r}_s; k) - \hat{w}_{f_s}(\mathbf{r}|\mathbf{r}_s). \quad (61)$$

From Eqs. (54) and (61) we obtain the following relation which is similar to the clamped boundary condition solution:

$$G_c(\mathbf{r}|\mathbf{r}_s; k) = G_\infty(\mathbf{r}|\mathbf{r}_s; k) - \frac{1}{2}[\hat{w}_{f_r}(\mathbf{r}|\mathbf{r}_s) + \hat{w}_{f_s}(\mathbf{r}|\mathbf{r}_s)]. \quad (62)$$

III. CLENSHAW-CURTIS INTEGRATION OF WAVE-NUMBER INTEGRALS OVER FINITE INTERVALS

The wave-number integrals occurring in the expressions for the Green's functions of a semi-infinite plate are in the form of improper (infinite) integrals as given by Eqs. (29), (38), (50), and (58). For the purpose of numerical quadrature, these are broken down into many finite integrals. These integrals typically are of the form $\int_a^b g(x, k_x) \cos(k_x x) dk_x$ and $\int_a^b g(x, k_x) \sin(k_x x) dk_x$. Filon¹³ developed a method in which integrals of this type are approximately evaluated by fitting a quadratic polynomial to the function $g(x, k_x)$ over each sub-interval and integrating each term analytically. This method is accurate when $g(x, k_x)$ is slowly varying. In the case of integrals occurring in the Green's function expressions, $g(x, k_x)$ is often irregular, and sometimes almost singular. Clenshaw and Curtis¹⁴ developed a powerful method that can handle these irregularities. The function $g(x, k_x)$ is approximated by a finite series of Chebyshev polynomials of the first kind $T_m(z)$, followed by an analytical integration of each term in the series. Xu and Mal¹⁵ derived an error estimate for the eighth order formula using the Clenshaw and Curtis method. Dravinski and Mossessian¹⁶ demonstrated the use of Xu and Mal's approach in calculating the Green's functions for harmonic line loads in a viscoelastic half-space.

A brief outline of this method, commonly referred to as the Clenshaw-Curtis integration, is given next. Define, for later use, the functions $I_m(t)$ and $J_m(t)$ along with their recursive expressions as follows:

$$I_m(t) = \int_{-1}^1 T_m(z) e^{itz} dz, \quad (63)$$

$$I_0(t) = \frac{-i}{t} (e^{it} - e^{-it}),$$

$$I_1(t) = \frac{e^{it} + e^{-it}}{it} + \frac{1}{t^2} (e^{it} - e^{-it}), \quad (64)$$

$$I_2(t) = \left(\frac{4i}{t}\right) I_1(t) - \frac{i}{t} (e^{it} - e^{-it}),$$

$$\begin{aligned} I_{m+1}(t) &= \frac{2i(m+1)}{t} I_m(t) + \frac{m+1}{m-1} I_{m-1}(t) \\ &+ \frac{2i}{t(m-1)} (e^{it} + (-1)^m e^{-it}) \quad \text{for } m \geq 2, \end{aligned}$$

$$J_m(t) = \int_{-1}^1 T_m(z) e^{-itz} dz, \quad (65)$$

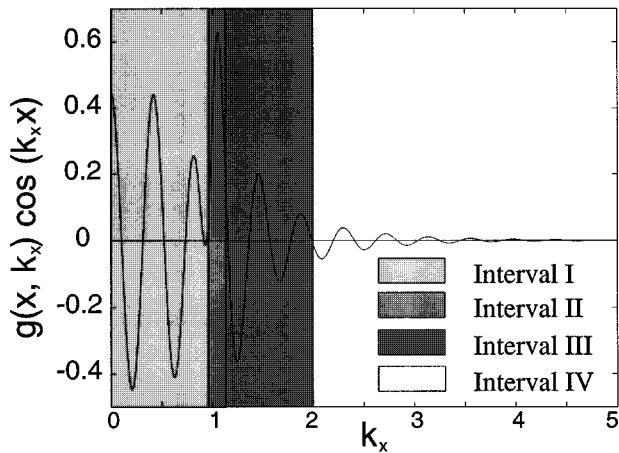


FIG. 2. A typical wave-number integrand with a near singularity at $k_x=1.0$.

$$\begin{aligned}
 J_0(t) &= \frac{i}{t}(e^{-it} - e^{it}), \\
 J_1(t) &= \frac{e^{-it} + e^{it}}{(-i)t} + \frac{1}{t^2}(e^{-it} - e^{it}), \\
 J_2(t) &= \frac{-4i}{t}J_1(t) + \frac{i}{t}(e^{-it} - e^{it}), \\
 J_{m+1}(t) &= \frac{-2i}{t}(m+1)J_m(t) + \frac{(m+1)}{(m-1)}J_{m-1}(t) \\
 &\quad + \frac{(-2i)}{t(m-1)}(e^{-it} + (-1)^m e^{it}) \quad \text{for } m \geq 2.
 \end{aligned} \tag{66}$$

Define $G_{m,j}$ and its recursive relations as

$$G_{m,j} = - \int_{-1}^1 T_m(z) z^j dz, \tag{67}$$

$$G_{0,j} = \frac{1 + (-1)^j}{j+1}, \tag{68}$$

$$G_{1,j} = G_{0,j+1},$$

$$G_{m,j} = 2G_{m-1,j+1} - G_{m-2,j} \quad \text{for } m \geq 2.$$

Given a function $g(x, k_x)$ that has to be integrated over the interval $k_x \in [a, b]$, first normalize the range of integration to $[-1, 1]$ by introducing the function $k_x = Az + B$, where $A = (b-a)/2$, $B = (b+a)/2$. This function is approximated by a finite Chebyshev series as follows:

$$g(x, k_x) = g(x, Az + B) = f(x, z) \approx \sum_{m=0}^N {}'' D_m(x) T_m(z). \tag{69}$$

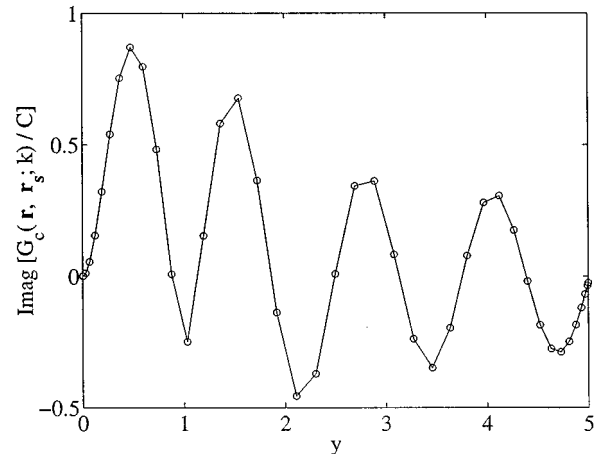
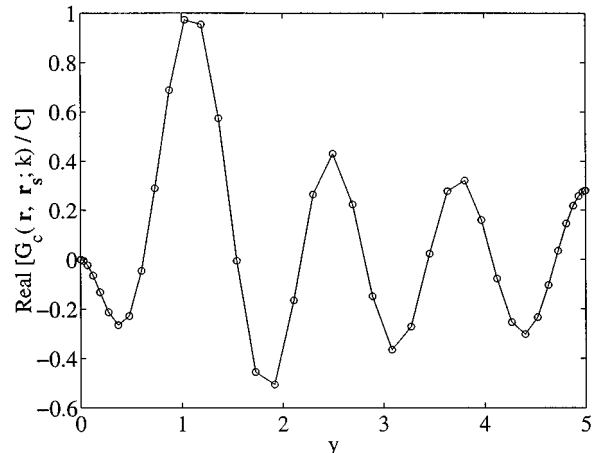


FIG. 3. Comparison of the $G_c(\mathbf{r}, \mathbf{r}_s; k)$ given by Eqs. (33) and (44) along $x=0$ for a semi-infinite plate with a clamped edge. Key: —, Eq. (33); \circ , Eq. (44).

The unknown constants $D_m(x)$ are calculated using

$$D_m(x) = \frac{2}{N} \sum_{j=0}^N {}'' f\left(x, \cos\left(\frac{j\pi}{N}\right)\right) \cos\left(\frac{mj\pi}{N}\right). \tag{70}$$

The double prime on the summation symbol denotes summation over a sequence whose first and last terms are halved:

$$\sum_{m=0}^N {}'' s_m = \frac{s_0}{2} + s_1 + s_2 + \cdots + s_{N-1} + \frac{s_N}{2}. \tag{71}$$

The Clenshaw–Curtis quadrature formula is expressed in terms of these functions as follows:

TABLE I. Numerical evaluation of the Hankel function H_0^1 using wave-number integral.

θ	$\text{Re}[H_0^1(\exp(i\theta))]$	$\text{Im}[H_0^1(\exp(i\theta))]$	NS	Error
1	0.751 678 646 346 771 8	8.059 102 803 424 181 3E-02	714	0.1234E-11
30	0.438 513 077 962 303 7	-0.112 818 452 396 018 9	265	0.2121E-10
60	0.204 526 564 082 411 5	-0.230 704 377 271 396 3	204	0.3614E-10
90	0.000 000 000 000 000 0	-0.268 032 482 033 987 1	170	0.4815E-10

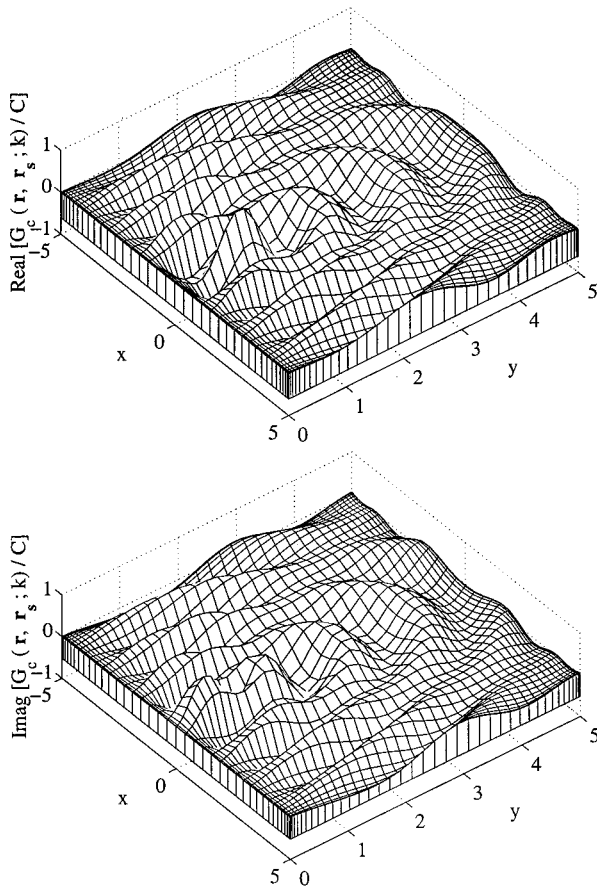


FIG. 4. Vibratory response $G_c(\mathbf{r}, \mathbf{r}_s; k)$ for $(x, y) \in [-5, +5] \times [0, 5]$ for a semi-infinite plate with a clamped edge.

$$\int_a^b g(x, k_x) e^{ik_x x} dk_x = \begin{cases} A e^{ixB} \sum_{m=0}^N D_m(x) I_m(Ax) & \text{for } |Ax| > 1 \\ A e^{ixB} \sum_{m=0}^N D_m(x) \sum_{j=0}^{\infty} G_{m,j} \frac{(iAx)^j}{j!} & \text{for } |Ax| \leq 1, \end{cases} \quad (72)$$

$$\int_a^b g(x, k_x) e^{-ik_x x} dk_x = \begin{cases} A e^{-ixB} \sum_{m=0}^N D_m(x) J_m(Ax) & \text{for } |Ax| > 1 \\ A e^{-ixB} \sum_{m=0}^N D_m(x) \sum_{j=0}^{\infty} G_{m,j} \frac{(-iAx)^j}{j!} & \text{for } |Ax| \leq 1. \end{cases} \quad (73)$$

When $N=8$, the error in these quadrature formulas is estimated by Xu and Mal¹⁵ as

$$\epsilon = \max(2.5|D_8(x)|, 2.0|D_7(x)|, 1.5|D_6(x)|, 1.2|D_5(x)|). \quad (74)$$

Using the definitions of the trigonometric functions in terms of the exponential functions,

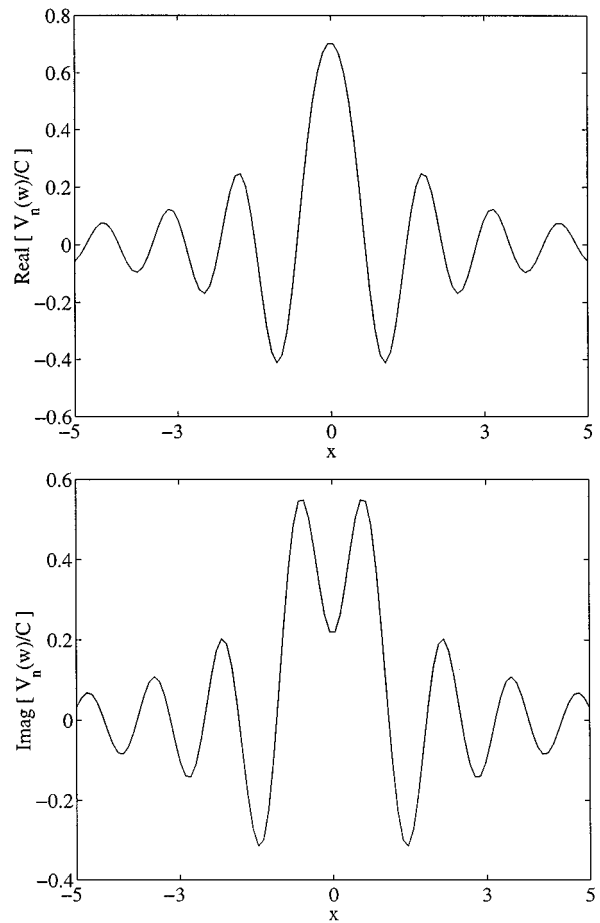


FIG. 5. Effective shear force distribution $V_n(\hat{w})$ along the x axis for a semi-infinite plate with a clamped edge.

$$\int_a^b g(x, k_x) \cos(k_x x) dk_x = \frac{1}{2} \left(\int_a^b g(x, k_x) e^{ik_x x} dk_x + \int_a^b g(x, k_x) e^{-ik_x x} dk_x \right), \quad (75)$$

$$\int_a^b g(x, k_x) \sin(k_x x) dk_x = \frac{1}{2i} \left(\int_a^b g(x, k_x) e^{ik_x x} dk_x - \int_a^b g(x, k_x) e^{-ik_x x} dk_x \right). \quad (76)$$

If the error estimate ϵ for numerically evaluated integrals is larger than a prescribed tolerance value, then the interval is subdivided into two halves, and the process is repeated for each of the subintervals. The interval subdivision is repeated until the error estimate becomes smaller than the tolerance value. Hence this method is designated as ‘‘adaptive integration.’’ More subdivisions are required when the function has a near singularity in the interval of integration.

IV. EVALUATION OF IMPROPER WAVE-NUMBER INTEGRALS OCCURRING IN GREEN’S FUNCTION FORMULAS

The previous section showed how to evaluate wave-number integrals over a finite interval. Green’s function ex-

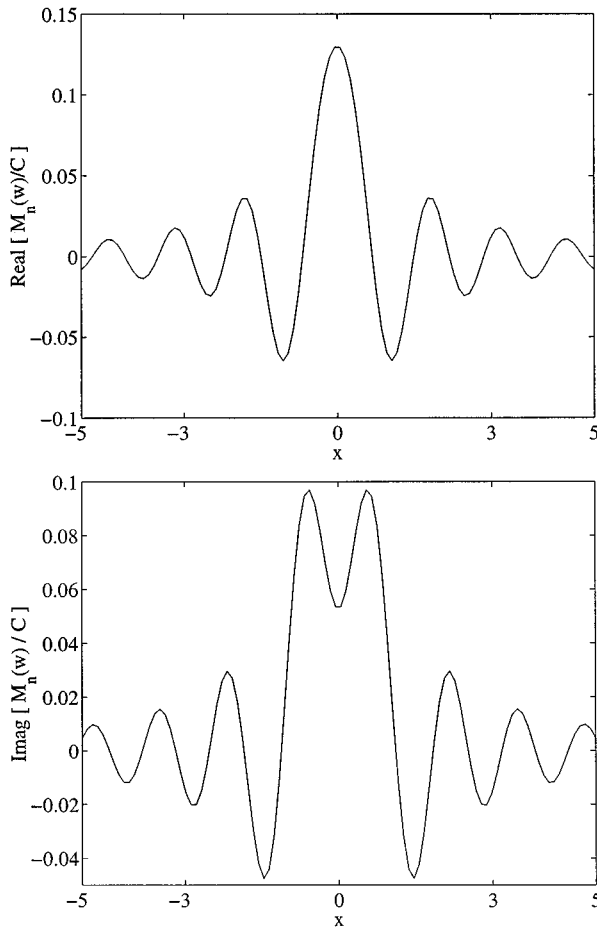


FIG. 6. Bending moment distribution $M_n(\hat{w})$ along the x axis for a semi-infinite plate with a clamped edge.

pressions contain improper wave-number integrals of the form $\int_0^\infty g(x, k_x) \cos(k_x x) dk_x$ and $\int_0^\infty g(x, k_x) \sin(k_x x) dk_x$. This section shows how these improper integrals are expressed as a series of finite integrals, and how the sum of the resulting series is calculated. The integrands in these improper integrals oscillate rapidly. The function $g(x, k_x)$ can have very sharp peaks at the particular values of k_x corresponding to the real part of a pole. Also, the functions $g(x, k_x)$ attenuate very slowly resulting in poor convergence. Because of these two reasons, conventional numerical integration methods are not satisfactory.

Figure 2 shows the behavior typical of such wave-number integrals. Let I be the wave-number integral of interest.

$$I = \int_0^\infty g(x, k_x) \cos(k_x x) dk_x, \quad (77)$$

where $k_x = s_0$ is the location of the peak in the integrand. Let s_1 be a multiple of π/x large enough that the irregularities at $k_x = s_0$ have died down before $k_x = s_1$. Here, s_1 is chosen such that the function $g(x, k_x)$ has no poles or zeroes when $k_x > s_1$. The integral I is divided into four parts as shown in Fig. 2:

$$I = I_I + I_{II} + I_{III} + I_{IV}, \quad (78)$$

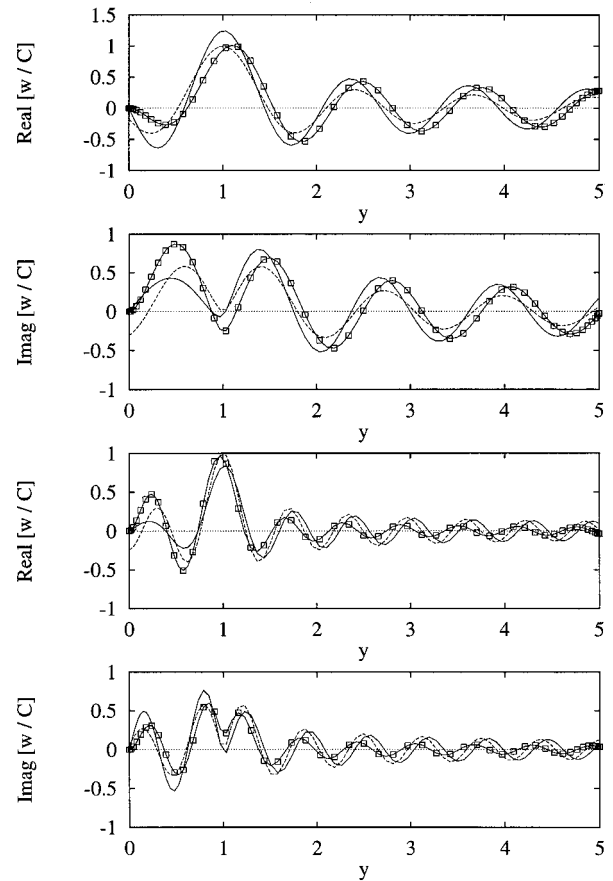


FIG. 7. Comparison of $G_c(\mathbf{r}, \mathbf{r}_s; k)$ with $G_s(\mathbf{r}, \mathbf{r}_s; k)$ for $y_s=1$, $k=5+0.005i$ (top two), and $k=10+0.01i$ (bottom two) along the y -axis for a semi-infinite plate with clamped and simply supported edges respectively. Key: \square —, $G_c(\mathbf{r}, \mathbf{r}_s; k)$; —, $G_s(\mathbf{r}, \mathbf{r}_s; k)$; dashed line, $G_\infty(\mathbf{r}, \mathbf{r}_s; k)$.

$$\begin{aligned} I_I &= \int_0^{s_0-\varepsilon} g(x, k_x) \cos(k_x x) dk_x, \\ I_{II} &= \int_{s_0-\varepsilon}^{s_0+\varepsilon} g(x, k_x) \cos(k_x x) dk_x, \\ I_{III} &= \int_{s_0+\varepsilon}^{s_1} g(x, k_x) \cos(k_x x) dk_x, \\ I_{IV} &= \int_{s_1}^\infty g(x, k_x) \cos(k_x x) dk_x. \end{aligned} \quad (79)$$

The first three integrals are evaluated using the adaptive Clenshaw–Curtis quadrature method that was described in Sec. III. The integral I_{II} is further subdivided into two equal subintervals before quadrature if the near singularity at $k_x = s_0$ is very strong. The last part, I_{IV} is an improper integral with the near singularity removed. The integral I_{IV} can be expressed as

$$\begin{aligned} I_{IV} = \int_{s_1}^\infty g(x, k_x) \cos(k_x x) dk_x &= \int_{s_1}^{s_2} (\dots) + \int_{s_2}^{s_3} (\dots) \\ &+ \int_{s_3}^{s_4} (\dots) + \dots, \end{aligned} \quad (80)$$

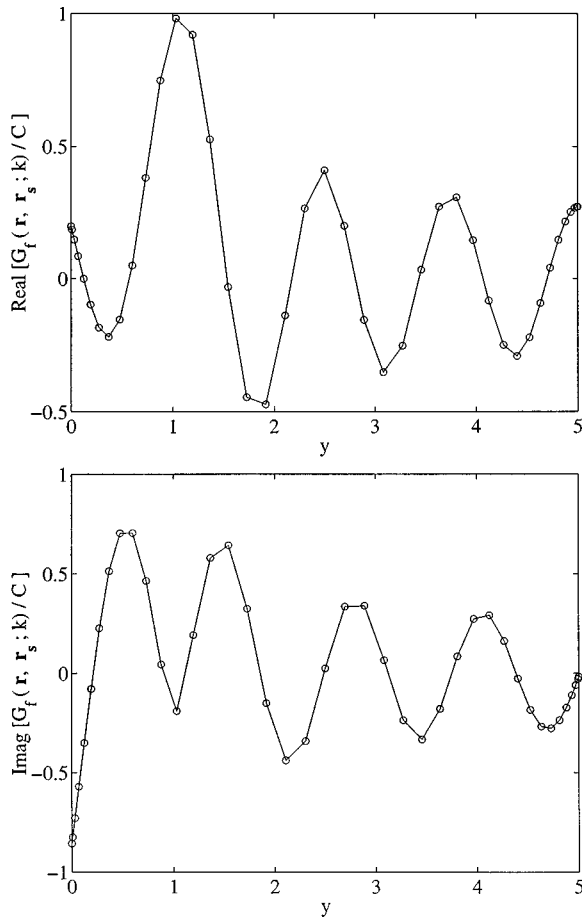


FIG. 8. Comparison of the $G_f(\mathbf{r}, \mathbf{r}_s; k)$ given by Eqs. (54) and (61) along $x=0$ for a semi-infinite plate with a free edge. Key: —, Eq. (54); ○, Eq. (61).

where s_2, s_3, s_4, \dots are the consecutive integer multiples of π/x . This infinite series of subintegrals is an alternating series, with each term being opposite in sign to its preceding term. Therefore I_{IV} can be expressed as

$$I_{IV} = A_1 - A_2 + A_3 - A_4 + A_5 - \dots \quad (81)$$

All of the terms $A_1, A_2, A_3, A_4, A_5, \dots$ have the same sign and each can be evaluated by the adaptive Clenshaw–Curtis method. The absolute series is monotonously decreasing. Longman¹⁷ described a method in which slowly converging alternating series of this kind can be transformed into swiftly converging series. According to Euler's transformation define the forward difference terms:

$$\Delta A_m = A_{m+1} - A_m, \quad (82)$$

$$\Delta^{r+1} A_m = \Delta^r A_{m+1} - \Delta^r A_m.$$

Then the series after transformation is

$$\sum_{m=0}^{\infty} (-1)^m A_m = \frac{1}{2} A_0 - \frac{1}{4} \Delta A_0 + \frac{1}{8} \Delta^2 A_0 - \frac{1}{16} \Delta^3 A_0 + \dots \quad (83)$$

The remainder R_p after p terms is bounded by $2^{-p} |\Delta^p A_0|$. Thus the slowly converging series has been converted to a rapidly converging series. This series summation is carried out with as many terms as are needed to make this error

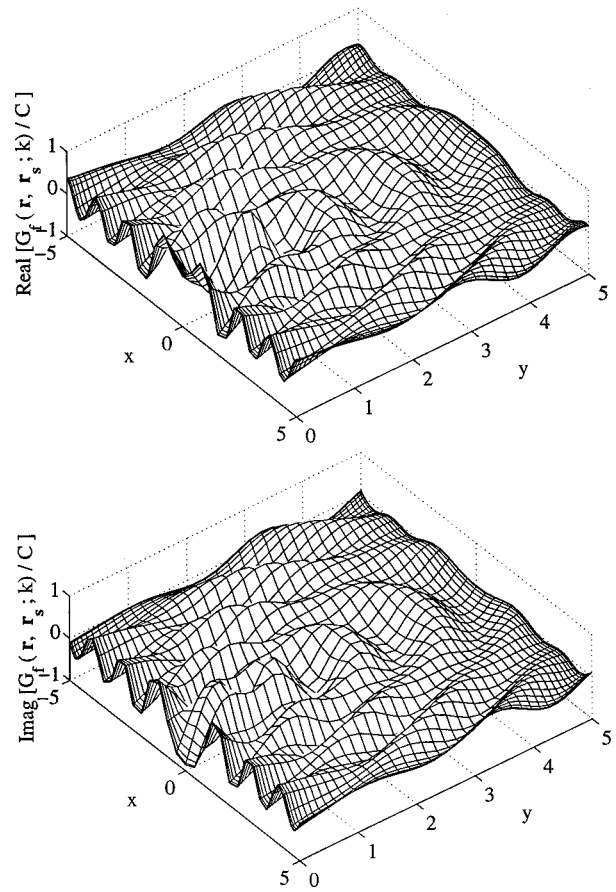


FIG. 9. Vibratory response $G_f(\mathbf{r}, \mathbf{r}_s; k)$ for $(x, y) \in [-5, +5] \times [0, 5]$ for a semi-infinite plate with a free edge.

smaller than the tolerance value. Shank's paper¹⁸ contains an extensive treatment of Euler's transformation and other non-linear sequence-to-sequence transformations. The effectiveness of these transforms in accelerating convergence in some slowly converging series and in inducing convergence in some diverging series is discussed. Difficulties which sometimes arise in the use of these transforms such as nonuniform convergence to the wrong answer, irregularity and the ambiguity of multivalued functions are also investigated. Dravinski and Mossessian¹⁶ have also successfully used Euler's transformation to evaluate wave-number integrals.

To demonstrate the accuracy of the adaptive integration technique described in the Sec. III, the zero order Hankel function of the first kind given in the wave-number integral form by Eq. (17) is compared with the conventional series summation form. The symbolic computational program MAPLE¹⁹ is used to calculate the Hankel function accurately to 20 decimal places and it is taken as the exact value with which the wave-number integral is compared. Figure 2 shows the real part of the integrand. The integral is evaluated in double precision with the tolerance set at $\epsilon = 1.0E-11$. In Table I, NS is the number of subintervals required, which is a measure of the number of function evaluations needed, and the error is the absolute distance between the exact and calculated values. From the results of Table I, it is clear that the adaptive integration technique is very accurate.

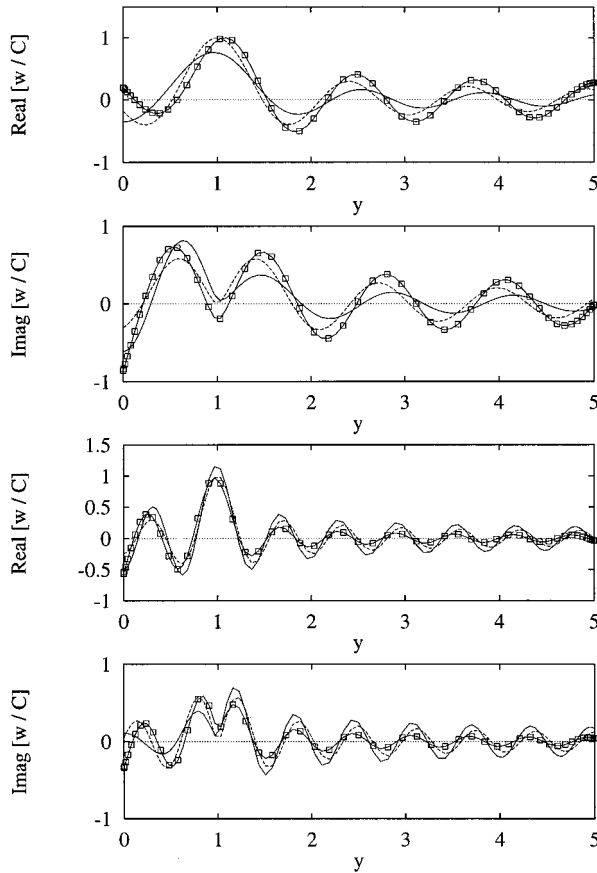


FIG. 10. Comparison of $G_f(\mathbf{r}, \mathbf{r}_s; k)$ with $G_r(\mathbf{r}, \mathbf{r}_s; k)$ for $y_s = 1$, $k = 5 + 0.005i$ (top two) and $k = 10 + 0.01i$ (bottom two) along the y -axis for a semi-infinite plate with free and roller supported edges, respectively. Key: \square —, $G_f(\mathbf{r}, \mathbf{r}_s; k)$; —, $G_r(\mathbf{r}, \mathbf{r}_s; k)$; dashed line, $G_\infty(\mathbf{r}, \mathbf{r}_s; k)$.

V. RESULTS AND DISCUSSION

For the sake of illustration, the excitation point is located at $(x_s, y_s) = (0, 1)$ and a bending wave number of $k = 5 + 0.005i$ is chosen for a semi-infinite plate with a clamped edge. The observation location in the semi-infinite plate is restricted to $(x, y) \in [-5, +5] \times [0, 5]$. The two representations for the Green's function $G_c(\mathbf{r}, \mathbf{r}_s; k)$ given by Eqs. (33) and (42) are compared in Fig. 3 from which it can be inferred that both solutions are practically identical. The calculation using Eq. (42) is faster because its integrand does not have a near singularity in the interval of integration. The vibratory response is depicted in Fig. 4. The shear force and bending moment distributions along the plate edge ($y = 0$) are plotted in Figs. 5 and 6, respectively. The solutions with clamped and simply supported boundary conditions $G_c(\mathbf{r}, \mathbf{r}_s; k)$ and $G_s(\mathbf{r}, \mathbf{r}_s; k)$ are compared in Fig. 7 to study the influence of the clamping term as the excitation frequency increases. As expected, from Fig. 7 it is seen that the solutions behave quite differently near the edge $y = 0$, but in the vicinity of the source ($y_s = 1$) the infinite plate Green's function $G_\infty(\mathbf{r}, \mathbf{r}_s; k)$ dominates the response. Away from the source and the edge, all the solutions fall off because of geometric spreading that is given by the $1/\sqrt{r}$ term.

Similarly, for the numerical study of a plate with a free edge, we choose the same excitation location $(x_s, y_s) = (0, 1)$, bending wave number of $k = 5 + 0.005i$, and the

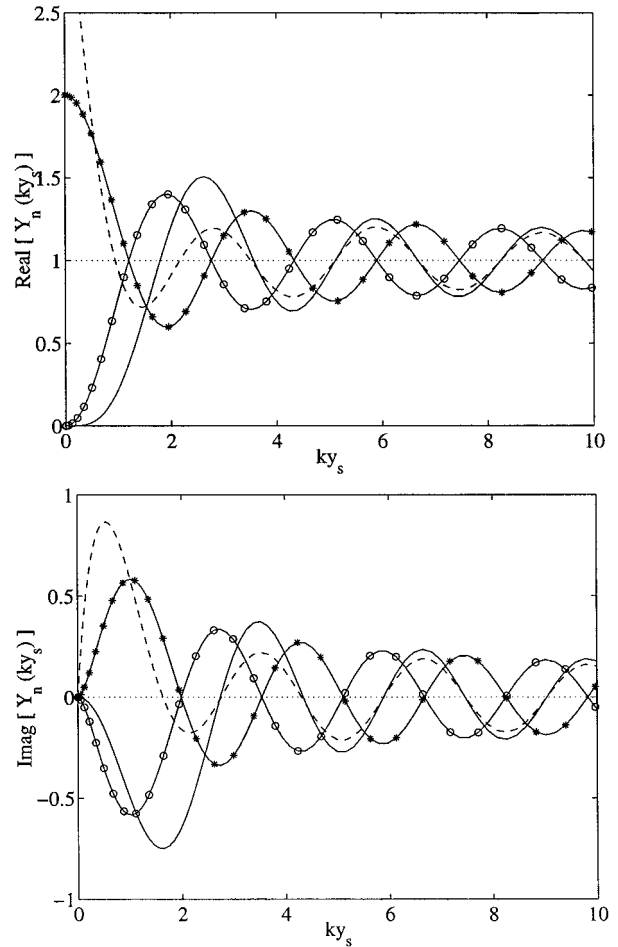


FIG. 11. Normalized driving point mobility $\hat{Y}_n(ky_s)$ for a semi-infinite plate with different edge conditions. Key: —, clamped edge; ---, free edge; —○—, simply supported edge; —*—, roller supported edge. Note that $\text{Re}(\hat{Y}_n) = 1$, $\text{Im}(\hat{Y}_n) = 0$ correspond to the driving point mobility of an infinite plate.

observation domain $(x, y) \in [-5, +5] \times [0, 5]$, as in the clamped case. The two representations for the Green's function $G_f(\mathbf{r}, \mathbf{r}_s; k)$ given by Eqs. (54) and (61) are compared in Fig. 8 and found to be identical. The vibratory response is shown in Fig. 9. The solutions with free and roller supported boundary conditions $G_f(\mathbf{r}, \mathbf{r}_s; k)$ and $G_r(\mathbf{r}, \mathbf{r}_s; k)$ are compared in Fig. 10 from which the edge and source effects are apparent.

It should be noted that Eqs. (30), (39), (51), and (59) are all symmetric with respect to \mathbf{r} and \mathbf{r}_s , since the solution should remain unchanged when the source and the observation locations are interchanged, because of reciprocity. It is well known that the driving point mobility of a infinite plate $\hat{Y}_\infty(k)$ is real valued and independent of excitation frequency. This result can be directly obtained from $G_\infty(\mathbf{r}, \mathbf{r}_s; k)$ as

$$\hat{Y}_\infty(k) = \lim_{\mathbf{r} \rightarrow \mathbf{r}_s} -i\omega G_\infty(\mathbf{r}, \mathbf{r}_s; k) = -i\omega C = \frac{1}{8\sqrt{\rho h D}}. \quad (84)$$

In Fig. 11, the normalized driving point mobilities $\hat{Y}_n(ky_s) = \hat{Y}(ky_s)/\hat{Y}_\infty$ are plotted. For all of the classical boundary conditions considered in this article, the mobility

curves approach that of a infinite plate asymptotically as $ky_s \gg 1$.

VI. CONCLUSION

New analytical harmonic Green's functions for a semi-infinite plate with clamped or free edges are developed. Two solutions are derived for each boundary condition starting from either roller or simply supported solutions. The formal solutions in terms of improper wave-number integrals are numerically evaluated using eighth order Clenshaw–Curtis adaptive quadrature. The procedure developed in this paper may be extended further to derive the Green's functions of semi-infinite plates with impedance type boundary conditions. These Green's functions will be of use to researchers interested in developing boundary element models for semi-infinite plates with arbitrary holes or cutouts, and to us in our continuing effort to build a ray tracing model for finite polygonal plates.

ACKNOWLEDGMENTS

This work has been supported by the U.S. Army Research Office (URI Grant No. DAAL-03-92-G-0120; Project Monitor: Dr. T. L. Doligalski).

¹R. Gunda, S. M. Vijayakar, and R. Singh, "Method of images for the harmonic response of beams and rectangular plates," *J. Sound Vib.* **185**, 791 (1995).

²H. Lamb, "On the propagation of tremors over the surface of an elastic solid," *Philos. Trans. R. Soc. London, Ser. A* **203**, 1–42 (1904).

³E. R. Lapwood, "The disturbance due to a line source in a semi-infinite

elastic medium," *Philos. Trans. R. Soc. London, Ser. A* **242**, 63–100 (1949).

⁴A. N. Jette and J. G. Parker, "Excitation of an elastic half-space by a buried line source of conical waves," *J. Sound Vib.* **67**, 523–531 (1979).

⁵D. M. Photiadis, "Approximations for the two-dimensional Green's function of a fluid-loaded plate," *J. Acoust. Soc. Am.* **93**, 42–47 (1993).

⁶J. M. Cuschieri and D. Feit, "A hybrid numerical and analytical solution for the Green's function of a fluid loaded elastic plate," *J. Acoust. Soc. Am.* **95**, 1998–2005 (1994).

⁷N. Ortner and P. Wagner, "The Green's functions of clamped semi-infinite vibrating beams and plates," *Int. J. Solids Struct.* **26**, 237–249 (1990).

⁸A. D. Kerr, "The clamped semi-infinite plate on a winkler base subjected to a vertical force," *Q. J. Mech. Appl. Math.* **46**, 457–470 (1993).

⁹A. W. Leissa, *Vibration of Plates* (Acoustical Society of America, Woodbury, NY, 1993), 2nd ed.

¹⁰Y. Niwa, S. Kobayashi, and M. Kitahara, "Eigen frequency analysis of a plate by the integral equation method," *Theor. Appl. Mech.* **29**, 287–367 (1981).

¹¹N. N. Lebedev, *Special Functions and their Applications* (Dover, New York, 1972).

¹²K. F. Graff, *Wave Motion in Elastic Solids* (Dover, New York, 1991).

¹³L. N. G. Filon, "On a quadrature formula for trigonometric integrals," *Proc. R. Soc. Edinburgh* **49**, 38–47 (1928).

¹⁴C. W. Clenshaw and A. R. Curtis, "A method for numerical integration on a automatic computer," *Numer. Math.* **2**, 197–205 (1960).

¹⁵P.-C. Xu and A. K. Mal, "An adaptive integration scheme for irregularly oscillatory functions," *Wave Motion* **7**, 235–243 (1985).

¹⁶M. Dravinski and T. K. Mossessian, "On the evaluation of Green's functions for harmonic line loads in a viscoelastic halfspace," *Int. J. Numer. Methods Eng.* **26**, 823–841 (1988).

¹⁷I. M. Longman, "Note on a method for computing infinite integrals of oscillatory functions," *Proc. Cambridge Philos. Soc.* **52**, 764–768 (1956).

¹⁸D. Shanks, "Non-linear transformations of divergent and slowly convergent sequences," *J. Math. Phys.* **34**, 1–42 (1955).

¹⁹Waterloo Maple Inc. *MAPLE V Release 4, Version 4.00f*, 1996.

Inherent background coefficients for acoustic resonance scattering from submerged, multilayered, cylindrical structures

Young-Sang Joo

Nondestructive Evaluation Division, Korea Atomic Energy Research Institute, P.O. Box 105, Yusong, Taejeon 305-600, Korea

Jeong-Guon Ih^{a)}

Center for Noise and Vibration Control, Department of Mechanical Engineering, Korea Advanced Institute of Science and Technology, Science Town, Taejeon 305-701, Korea

Myoung-Seon Choi

Nondestructive Evaluation Division, Korea Atomic Energy Research Institute, P.O. Box 105, Yusong, Taejeon 305-600, Korea

(Received 5 May 1997; revised 10 September 1997; accepted 28 October 1997)

For the scattering of acoustic waves by an elastic shell, the acoustical background coefficients are inherent in the scattering coefficients. The background coefficients for elastic empty shells, named the inherent background, can be obtained from the zero frequency limit of the modal acceleration in the scattering coefficients for analogous liquid shells. In this work, the concept of obtaining the inherent background is applied to multilayered elastic cylindrical structures. The inherent background manifests itself in the sound scattering by the liquid structures. The scattering *S*-function and the modal acceleration for the liquid system are determined by considering the incoming and outgoing waves. The acceleration of liquid layers is generalized so that the scattering function can be obtained by the recurrence relation for the accelerances of the adjacent liquid layers. From the zero frequency limit of the generalized acceleration of liquid structures, the constant modal acceleration is extracted and the general expression for the inherent background coefficients is obtained. The background coefficients depend on the densities of the layers and ambient fluid medium, the relative thickness of each layer, and the normal mode number. The acoustical background coefficients for solid cylinders, empty shells, fluid-filled shells, and double-layered shells can be obtained by the appropriate limit of the density ratio and the relative thickness of layers in the generalized inherent background coefficients. The usefulness of the proposed background is demonstrated for several examples of layered structures. © 1998 Acoustical Society of America. [S0001-4966(98)03302-5]

PACS numbers: 43.40.Ey, 43.30.Gv, 43.20.Fn, 43.20.Ks [CBB]

INTRODUCTION

The resonance scattering theory (RST), known as the resonance formalism of the nuclear reaction theory, has been applied to acoustic and elastic wave scattering problems.^{1,2} One of the important contributions of the RST is that each partial wave contained in the total scattering amplitude can be decomposed into two components: one is the background that is smooth and regular, and the other represents the set of modal resonances of the scatterer. The resonances in the partial waves can be isolated by the subtraction of the background, unknown *a priori*. Impenetrable, i.e., rigid or soft, background coefficients may be adopted as the backgrounds for certain cases of penetrable targets, but are not applicable to the extraction of the resonances of shells having intermediate thickness. A proper background should possess the transitional property from soft to rigid background in the appropriate limits of frequency and shell thickness.³ Although many models for describing the transitional background have been proposed, they were successful only for limited ranges of shell thickness and frequency.⁴⁻⁹ An acous-

tical background has been sought that has no limitation on the composition and thickness of penetrable targets over the whole frequency range of interest.

Recently, a general approach was proposed allowing an analytical expression of the exact background for empty spherical shells, named the *inherent* background.¹⁰ The inherent background coefficients for cylindrical shells were also obtained by a similar approach.¹¹ In these works, it was shown that there are two interacting components contributing to the modal accelerances. One is the nonresonant constant component independent of frequency and the other is the resonant one having narrow singularities near the resonance frequencies. The resonant components influence the nonresonant component so that the magnitude of the accelerances changes quickly at and near the resonance frequencies, and slowly out of the resonance frequencies. Since the interaction with the resonances occurs in all frequency ranges, the constant component hardly manifests its appearance in elastic shells. When the shear wave speed is set to be zero, like in the "liquid-shell background" by Veksler, the constant component can be observed. The coefficient of the constant component is extracted from the zero frequency limit of the modal acceleration of the analogous liquid shells. This is be-

^{a)}Electronic mail: ihih@sorak.kaist.ac.kr

cause the resonances interact negligibly with the background near zero frequency. The concept of this inherent background seems to have no limitation on its application to concentric layered shells and other canonical scatterers.

In most examples of acoustic resonance scattering, non-layered objects such as cylinders or spheres, either solid or hollow in structure, have been considered as the target geometry.^{12,13} However, practical scattering problems are concerned with more complicated targets having layered structures rather than nonlayered objects. The treatment of wave scattering for multilayered structures finds many potential applications and a generalized formulation is particularly important because the scattering problems of multilayered structures include those of the single layered structures. The acoustic resonance scattering from the layered shell has not been thoroughly understood yet, even though some study on the scattering cross section and absorption effects of shells coated with elastic¹⁴ or viscoelastic^{15,16} layers have been carried out. Models of the transitional background were proposed only for nonlayered shells with intermediate thickness. Resonance scattering from the spherical shell covered with viscoelastic layers¹⁷ has been studied using the intermediate background of Murphy *et al.*⁵ Recent works have proved that the acoustical background for submerged shells is mainly dependent on fluid loading and the modal mass of shells.^{10,11} The entire structure of the scatterers should be considered in the acoustical background because the waves can penetrate inside the target. The coating layer of layered shells, as well as the inner fluid in fluid-filled shells, obviously affect the acoustical background. In acoustic scattering problems, the transmitted waves in liquid cylinders was investigated using the Debye series expansion.¹⁸ In layered structures, the Debye series expansion using the notion of incoming and outgoing waves has been applied to the decomposition of the scattering process in a series of local interaction.¹⁸⁻²¹ The method clearly show the reflections and refractions at each interface of the scatterer and can also introduce the scattering *S*-function directly. This method brings a better physical understanding for the scattering process in layered structures.

The purpose of this paper is to give the general expression for the inherent background coefficients of multilayered cylindrical structures. In order to obtain the background coefficients for multilayered solid and/or fluid structures, the problem of acoustic wave scattering by the analogous liquid structure is presented. The scattering function and the modal acceleration of the multilayered fluid cylindrical structures are derived and generalized using the concept of incoming and outgoing waves.

I. SCATTERING FUNCTIONS AND MODAL ACCELERANCES

In order to extend the idea of the inherent background to multilayered cylindrical elastic structures, the interaction of a plane acoustic wave incident on analogous multilayered liquid structures is considered, assuming a harmonic excitation with a frequency ω . Figure 1 shows the geometry of a multilayered concentric cylindrical liquid system containing $m + 1$ layers with different compositions. The core fluid is numbered 0 and the fluid layers are consecutively numbered

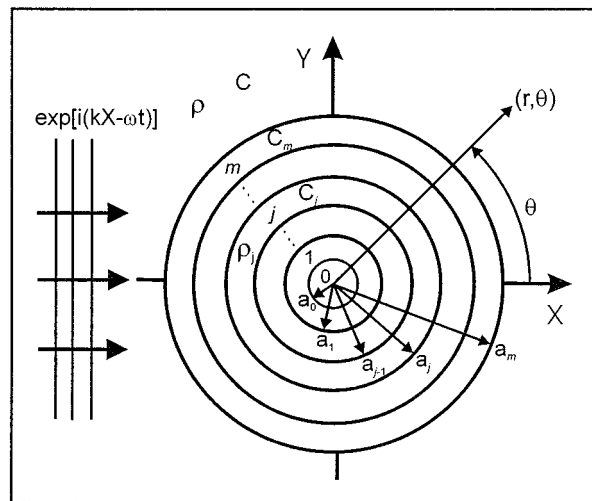


FIG. 1. Plane wave scattering from a multilayered cylindrical liquid structure.

1, 2, ..., m . The subscript of an ambient fluid is omitted. The radius of the outer boundary of the j th layer is $r = a_j$. The total radius of the system will be a_m and the radius of the core, a_0 . The thickness of the j th layer will be $d_j = a_j - a_{j-1}$ and the relative thickness of the j th layer will be $h_j = d_j / a_j$. The ρ_j and C_j denote the density and the longitudinal wave speed in the j th layer, respectively. The $k = \omega / C$ is the wave number of the incident wave in the ambient medium, while $k_j = \omega / C_j$ is the wave number for the longitudinal wave in the j th layer. The nondimensional frequencies of the incident and longitudinal waves in the layers are defined as:

$$x = ka_m, \quad y_j = k_j a_j, \quad x_j = k_j a_{j-1} \quad (j=0, 1, \dots, m), \quad (1)$$

where y_j and x_j correspond to the outside and inside boundary of the j th layer, respectively. The nondimensional frequencies are related to each other by $y_j = x_{j+1} (C_{j+1} / C_j)$ and $x_j = y_j (1 - h_j)$ ($j=0, 1, \dots, m$). At the core cylinder ($j=0$), $h_0 = 1$ and $x_0 = 0$, which means that there is no boundary inside the core.

A plane acoustic wave of unit amplitude $\exp[i(kX - \omega t)]$ interacts at normal incidence with a multilayered liquid structure in an ambient infinite fluid medium, as shown in Fig. 1. The scattered acoustic pressure can be expressed by the following normal mode series:²

$$p_{sc} = \sum_{n=0}^{\infty} \varepsilon_n i^n R_n^{(L)} H_n^{(1)}(kr) \cos n\theta. \quad (2)$$

Here, $\varepsilon_n = 1$ for $n=0$, $\varepsilon_n = 2$ for $n \geq 1$, the superscript (L) denotes the liquid media, $H_n^{(1)} (= J_n + iY_n)$ is the Hankel function of the first kind, and J_n and Y_n are the Bessel and Neumann functions of order n , respectively. The scattering coefficient $R_n^{(L)}$ can be given by:

$$R_n^{(L)} = - \frac{x J_n'(x) - (F_n^{(L)})_m J_n(x)}{x H_n^{(1)'}(x) - (F_n^{(L)})_m H_n^{(1)}(x)}, \quad (3)$$

which should be determined from the boundary conditions. Here, the subscript $()_m$ denotes the outermost layer of the

scatterer. The function $(F_n^{(L)})_m$ is called a modal acceleration of the layered structure because $(F_n^{(L)})_m$ has a dimension of acceleration per force that is equivalent to the modal admittance multiplied by frequency.²²

By introducing the scattering S -function, defined by $S_n^{(L)} = 1 + 2R_n^{(L)} \equiv e^{2i\delta_n}$, the scattered pressure of Eq. (2) can be rewritten as:

$$p_{sc} = \frac{1}{2} \sum_{n=0}^{\infty} \varepsilon_n i^n (S_n^{(L)} - 1) H_n^{(1)}(kr) \cos n\theta, \quad (4)$$

where δ_n is the scattering phase shift familiar from the nuclear scattering theory.² The scattering function $S_n^{(L)}$ brings a better physical understanding for the scattering process and can be directly obtained using the notion of incoming and outgoing waves in the layered structures.²¹

A. Fluid cylinder

As a limiting case of the multilayered cylindrical shell, a homogeneous fluid cylinder lying in the ambient medium (i.e., $m=0$) is considered here. In the ambient fluid medium, the total pressure field can be expressed by the sum of the incident incoming and the scattered outgoing waves as:

$$p = \sum_{n=0}^{\infty} \varepsilon_n i^n [H_n^{(2)}(kr) + S_n^{(L)} H_n^{(1)}(kr)] \cos n\theta, \quad (5)$$

where $H_n^{(2)}(=J_n - iY_n)$ is the Hankel function of the second kind. The pressure field in the liquid core ($j=0$) should be finite on the axis ($r=0$), that it can be expressed only with the Bessel function:

$$p_0 = \sum_{n=0}^{\infty} \varepsilon_n i^n [(W_n^{(L)})_0 J_n(k_0 r)] \cos n\theta. \quad (6)$$

The unknown coefficients $S_n^{(L)}$ and $(W_n^{(L)})_0$ can be determined from the boundary conditions for the fluid–fluid interface, that is the statement of continuities of pressures and particle velocities:

$$p = p_0, \quad \frac{1}{\rho} \frac{\partial p}{\partial r} = \frac{1}{\rho_0} \frac{\partial p_0}{\partial r} \quad \text{at } r = a_0. \quad (7)$$

Substitution of Eqs. (5) and (6) into Eq. (7) yields:

$$\begin{bmatrix} H_n^{(1)}(x) & -H_n^{(2)}(y_1) & H_n^{(1)}(y_1) & 0 \\ xH_n^{(1)'}(x) & -\frac{\rho}{\rho_1} y_1 H_n^{(2)'}(y_1) & -\frac{\rho}{\rho_1} y_1 H_n^{(1)'}(y_1) & 0 \\ 0 & H_n^{(2)}(x_1) & H_n^{(1)}(x_1) & -J_n(y_0) \\ 0 & x_1 H_n^{(2)'}(x_1) & x_1 H_n^{(1)'}(x_1) & -\frac{\rho_1}{\rho_0} y_0 J_n'(y_0) \end{bmatrix} \begin{Bmatrix} S_n^{(L)} \\ (T_n^{(L)})_1 \\ (U_n^{(L)})_1 \\ (W_n^{(L)})_0 \end{Bmatrix} = \begin{Bmatrix} -H_n^{(2)}(x) \\ -xH_n^{(2)'}(x) \\ 0 \\ 0 \end{Bmatrix}. \quad (13)$$

$$\begin{bmatrix} H_n^{(1)}(x) & -J_n(y_0) \\ xH_n^{(1)'}(x) & -\frac{\rho}{\rho_0} y_0 J_n'(y_0) \end{bmatrix} \begin{Bmatrix} S_n^{(L)} \\ (W_n^{(L)})_0 \end{Bmatrix} = \begin{Bmatrix} -H_n^{(2)}(x) \\ -xH_n^{(2)'}(x) \end{Bmatrix}. \quad (8)$$

Then, the scattering function $S_n^{(L)}$ can be obtained using Cramer's rule as:

$$S_n^{(L)} = -\frac{xH_n^{(2)'}(x) - (F_n^{(L)})_0 H_n^{(2)}(x)}{xH_n^{(1)'}(x) - (F_n^{(L)})_0 H_n^{(1)}(x)}, \quad (9)$$

where the modal acceleration of the liquid cylinder is given by

$$(F_n^{(L)})_0 = \frac{\rho}{\rho_0} y_0 \frac{J_n'(y_0)}{J_n(y_0)}. \quad (10)$$

Using the relation of $J_n(x) = [H_n^{(1)}(x) + H_n^{(2)}(x)]/2$, the acceleration $(F_n^{(L)})_0$ of a cylinder can be decomposed into the incoming and outgoing waves. For a physical description of the scattering process in the core, it is useful to use the local scattering function $(S_n^{(L)})_0$ in the core fluid. In such a case, $(S_n^{(L)})_0$ is unity because there is no boundary inside the core. This means that the scattering does not occur inside the core. The acceleration of Eq. (10) can be rewritten as:

$$(F_n^{(L)})_0 = \frac{\rho}{\rho_0} y_0 \frac{H_n^{(1)'}(y_0)(S_n^{(L)})_0 + H_n^{(2)'}(y_0)}{H_n^{(1)}(y_0)(S_n^{(L)})_0 + H_n^{(2)}(y_0)}. \quad (11)$$

Equation (11) implies that $(F_n^{(L)})_0$ can be determined from the scattering function $(S_n^{(L)})_0$ in the cylinder.

B. Double-layered fluid cylinder

As one of the most simple multilayered-structure geometries, a double layered fluid cylinder is considered here. The pressures in the ambient medium and liquid core ($j=0$) are the same as Eq. (5) and Eq. (6), respectively. The pressure of the liquid shell ($j=1$) can be expressed as:

$$p_1 = \sum_{n=0}^{\infty} \varepsilon_n i^n [(T_n^{(L)})_1 H_n^{(2)}(k_1 r) + (U_n^{(L)})_1 H_n^{(1)}(k_1 r)] \cos n\theta. \quad (12)$$

Substituting Eqs. (5), (6) and (12) into the boundary conditions, one can obtain the following 4×4 matrix equation:

The scattering function $S_n^{(L)}$ and modal accelerance $(F_n^{(L)})_1$ of the double-layered liquid cylinder are given as follows:

$$S_n^{(L)} = -\frac{xH_n^{(2)'}(x) - (F_n^{(L)})_1 H_n^{(2)}(x)}{xH_n^{(1)'}(x) - (F_n^{(L)})_1 H_n^{(1)}(x)}, \quad (14)$$

$$(F_n^{(L)})_1 = \frac{\rho}{\rho_1} y_1 \frac{H_n^{(1)'}(y_1)(S_n^{(L)})_1 + H_n^{(2)'}(y_1)}{H_n^{(1)}(y_1)(S_n^{(L)})_1 + H_n^{(2)}(y_1)}. \quad (15)$$

Since the local scattering function $(S_n^{(L)})_1$ comes from local interaction at the outer surface of the core, it is identical to Eq. (9), except for replacing x with x_1 . The accelerance $(F_n^{(L)})_0$ of the core cylinder ($j=0$) is the same as Eq. (10), but ρ should be replaced by ρ_1 .

C. Multilayered fluid structures

From the foregoing results of the cylinder and the double-layered cylinder, one can obtain the scattering function and the accelerance of multilayered liquid cylindrical structures. The scattering function $S_n^{(L)}$ of multilayered liquid structures is the same as Eq. (9), except for replacing $(F_n^{(L)})_0$

with $(F_n^{(L)})_m$. For an arbitrary liquid layer ($j=0,1,\dots,m$), the modal accelerance $(F_n^{(L)})_j$ of the j th liquid medium can be determined from the scattering function $(S_n^{(L)})_j$ of the layer:

$$(F_n^{(L)})_j = \frac{\rho_{j+1}}{\rho_j} y_j \frac{H_n^{(1)'}(y_j)(S_n^{(L)})_j + H_n^{(2)'}(y_j)}{H_n^{(1)}(y_j)(S_n^{(L)})_j + H_n^{(2)}(y_j)}. \quad (16)$$

Because the $(F_n^{(L)})_j$ are related to the outer surface of the j th layer, they depend on y_j explicitly. The local scattering function $(S_n^{(L)})_j$ are determined by the accelerance $(F_n^{(L)})_{j-1}$ of the inner surface in the j th layer as follows:

$$(S_n^{(L)})_j = -\frac{x_j H_n^{(2)'}(x_j) - (F_n^{(L)})_{j-1} H_n^{(2)}(x_j)}{x_j H_n^{(1)'}(x_j) - (F_n^{(L)})_{j-1} H_n^{(1)}(x_j)}. \quad (17)$$

The $(S_n^{(L)})_j$ are related to the inner boundary of the j th layer, and thus it explicitly depends on x_j .

By substituting Eq. (17) into Eq. (16), one can derive the following recurrence relation between the accelerances of the two adjacent layers:

$$(F_n^{(L)})_j = \frac{\rho_{j+1}}{\rho_j} y_j \frac{[x_j \{J_n'(y_j) Y_n'(x_j) - J_n'(x_j) Y_n'(y_j)\} - (F_n^{(L)})_{j-1} \{J_n'(y_j) Y_n(x_j) - J_n(x_j) Y_n'(y_j)\}]}{[x_j \{J_n(y_j) Y_n'(x_j) - J_n'(x_j) Y_n(y_j)\} - (F_n^{(L)})_{j-1} \{J_n(y_j) Y_n(x_j) - J_n(x_j) Y_n(y_j)\}]}. \quad (18)$$

The accelerance for any type of layered liquid structure can be obtained by this recurrence relation. The recurrence starts from the outer layer of the core (i.e., $j=1$) and ends at the system surface ($j=m$). In the final stage, ρ_{m+1} should be replaced by ρ .

In the case of a layered cylinder, the core cylinder ($j=0$) has no inner boundary. Therefore, there is no scattering interaction and the scattering function in the core has no phase change, i.e., $(S_n^{(L)})_0=1$. The $(F_n^{(L)})_0$ of the core cylinder ($j=0$) is identical to Eq. (10), if ρ is replaced by ρ_1 . The layered cylinder can be regarded as the empty shell when the density of the core is zero (i.e., $\rho_0=0$), and then $(F_n^{(L)})_0 \rightarrow \infty$. In this case, the scattering function of innermost shell layer ($j=1$) becomes equal to $(S_n^{(L)}(x_1))_1 = -H_n^{(2)}(x_1)/H_n^{(1)}(x_1) = S_n^{(s)}(x_1)$. Here, $S_n^{(s)}(x_1)$ denotes the soft background. From Eq. (16), the modal accelerance of the innermost layer can be expressed as:

$$(F_n^{(L)})_1 = \frac{\rho_2}{\rho_1} y_1 \frac{J_n(x_1) Y_n'(y_1) - J_n'(y_1) Y_n(x_1)}{J_n(x_1) Y_n(y_1) - J_n(y_1) Y_n(x_1)}. \quad (19a)$$

For a rigid core, $(F_n^{(L)})_0=0$ and $(S_n^{(L)})_1 = -H_n^{(2)'}(x_1)/H_n^{(1)'}(x_1) = S_n^{(r)}$, and the modal accelerance of the innermost shell can be written as:

$$(F_n^{(L)})_1 = \frac{\rho_2}{\rho_1} y_1 \frac{J_n'(x_1) Y_n'(y_1) - J_n'(y_1) Y_n'(x_1)}{J_n'(x_1) Y_n(y_1) - J_n(y_1) Y_n'(x_1)}. \quad (19b)$$

II. INHERENT BACKGROUND COEFFICIENTS

The constant part of the accelerance F_n of the elastic structures can be determined from the value $(F_n^{(L)}(0^+))_m$ near a zero frequency for an equivalent liquid structure. The inherent background for the multilayered cylindrical elastic structure can be described by the following scattering form functions and scattering coefficients corresponding to $(F_n^{(L)} \times (0^+))_m$:¹¹

$$f_n^{(b)}(\theta, x) = \frac{2\varepsilon_n}{\sqrt{\pi i x}} R_n^{(b)} \cos n\theta, \quad (20)$$

$$R_n^{(b)} = -\frac{x J_n'(x) - (F_n^{(L)}(0^+))_m J_n(x)}{x H_n^{(1)'}(x) - (F_n^{(L)}(0^+))_m H_n^{(1)}(x)}. \quad (21)$$

Here, the superscript (b) denotes the acoustical background. For very low frequencies of $x \ll (F_n^{(L)}(0^+))_m$, the scattering coefficients will be reduced to the soft background. For very high frequencies of $x \gg (F_n^{(L)}(0^+))_m$, the scattering coefficients will approach the rigid background. Therefore, the inherent background undergoes a transition from soft to rigid background with the increase of frequency. This transition is characterized by the frequency of $x^* = (F_n^{(L)}(0^+))_m$. The softer the target, the higher the transition frequency.

A. Multilayered cylindrical structures

The inherent background coefficients for multilayered elastic structures can be generally derived by substituting the following approximate expressions of cylinder functions for $x \ll 1$ into Eq. (18):

$$J_n(x) = \frac{x^n}{2^n n!}, \quad (22a)$$

$$Y_n(x) = \frac{2}{\pi} \ln x \quad \text{for } n=0, \quad (22b)$$

$$Y_n(x) = -\frac{(n-1)!}{\pi} \left(\frac{2}{x}\right)^n \quad \text{for } n \geq 1. \quad (22c)$$

Using the relation of the normalized frequencies $x_j = y_j(1 - h_j)$, the constant magnitude of $(F_n^{(L)})_j$ for each liquid layer ($j=1, 2, \dots, m$) can be obtained as:

$$(F_0^{(L)}(0^+))_j = \frac{\rho_{j+1}}{\rho_j} \frac{(F_0^{(L)}(0^+))_{j-1}}{[1 - \ln(1 - h_j)(F_0^{(L)}(0^+))_{j-1}]} \quad \text{for } n=0, \quad (23a)$$

$$(F_n^{(L)}(0^+))_j = \frac{\rho_{j+1}}{\rho_j} \frac{n^2 + q_j (F_n^{(L)}(0^+))_{j-1}}{q_j + (F_n^{(L)}(0^+))_{j-1}} \quad \text{for } n \geq 1, \quad (23b)$$

where

$$q_j = n \frac{1 + (1 - h_j)^{2n}}{1 - (1 - h_j)^{2n}}. \quad (24)$$

For multilayered cylindrical structures, each $(F_n^{(L)}(0^+))_j$ can be determined by utilizing Eqs. (23). The constant acceleration $(F_n^{(L)}(0^+))_m$ can be obtained by substituting $(F_n^{(L)}(0^+))_{j-1}$ into $(F_n^{(L)}(0^+))_j$ recurrently from $j=1$ to $j=m$. In the case of multilayered cylinders, $(F_n^{(L)}(0^+))_0$ for the core cylinder is given by

$$(F_n^{(L)}(0^+))_0 = \frac{\rho_1}{\rho_0} n. \quad (25)$$

In the case of multilayered empty shells, $(F_n^{(L)}(0^+))_1$ for the innermost layer of the shell can be expressed as:

$$(F_0^{(L)}(0^+))_1 = -\frac{\rho_2}{\rho_1} \frac{1}{\ln(1 - h_1)} \quad \text{for } n=0, \quad (26a)$$

$$(F_n^{(L)}(0^+))_1 = \frac{\rho_2}{\rho_1} n \frac{1 + (1 - h_1)^{2n}}{1 - (1 - h_1)^{2n}} \quad \text{for } n \geq 1. \quad (26b)$$

In the case of a rigid core cylinder, the following can be derived:

$$(F_n^{(L)}(0^+))_1 = \frac{\rho_2}{\rho_1} n \frac{1 - (1 - h_1)^{2n}}{1 + (1 - h_1)^{2n}}. \quad (27)$$

B. Cylinder

The constant acceleration for the cylinder (i.e., $m=0$ case) can be obtained from Eq. (25) by replacing ρ_1 to ρ :

$$(F_n^{(L)}(0^+))_0 = \frac{\rho}{\rho_0} n. \quad (28)$$

The constant acceleration is large for a very soft cylinder and becomes zero by approaching the rigid cylinder. It is obvious from Eq. (21) that for $(F_n^{(L)}(0^+))_0 \rightarrow \infty$, the inherent background approximates the soft background and for $(F_n^{(L)}(0^+))_0 \rightarrow 0$, the rigid background. The inherent back-

ground converges to the rigid or soft background for the appropriate limit of the density ratio and frequency. The magnitude $(F_n^{(L)}(0^+))_0$ is determined individually for each partial mode. The acoustic resonance scattering from a fluid cylinder submerged in another fluid medium was considered only for the case of a denser fluid loading or a denser cylinder because the proper background was not proposed.^{23,24} However, using the background coefficient of Eq. (28), any kind of fluid obstacle in another fluid medium can be dealt with.

For the zeroth ($n=0$) partial wave, the magnitude $(F_n^{(L)}(0^+))_0$ is always equal to zero. This leads to the obvious discrepancy that the modal inherent background becomes the rigid background regardless of the material properties of the target. This discrepancy always occurs in the case of nonempty cylindrical structures. This seems to be attributed to the fact that the giant monopole resonance is embedded in the background plot near the zero frequency.^{2,23} For the zeroth partial wave in nonempty structures, the constant acceleration seldom manifest itself near zero frequency due to the masking by the monopole resonance in the background. The constant acceleration cannot be determined from the zero frequency limit in the case of the zeroth partial wave of core-filled structures. Therefore, the methodology determining a constant acceleration should be modified for a zeroth partial wave. Fortunately, it is well known that the monopole resonance does not exist for very thick shells. This implies that $(F_0^{(L)}(0^+))_1$ of the shell can be used to obtain the background coefficient for the cylinder. The numerical calculation shows that the background amplitude of the zeroth order partial wave can be obtained from the inherent coefficients of the empty shell by approximating the cylinder with a very thick shell.

C. Empty shell

The modal acceleration of the empty liquid shell can be derived in Eqs. (26). The magnitude of the constant acceleration for an empty shell is obtained as follows:

$$(F_0^{(L)}(0^+))_1 = -\frac{\rho}{\rho_1} \frac{1}{\ln(1 - h_1)} \quad \text{for } n=0, \quad (29a)$$

$$(F_n^{(L)}(0^+))_1 = \frac{\rho}{\rho_1} n \frac{1 + (1 - h_1)^{2n}}{1 - (1 - h_1)^{2n}} \quad \text{for } n \geq 1. \quad (29b)$$

The background coefficients for the empty shell are presented in Ref. 11. The inherent background coefficients of the empty cylindrical shell are governed by the density ratio, the modal number, and the relative thickness. The background of the $n=0$ partial wave for the empty shell is not zero. When the relative thickness h_1 of the empty shell is getting close to 1, the empty shell becomes the cylinder. It is obvious from Eqs. (29) that for $h_1 \rightarrow 1$, the inherent background coefficients for an empty shell approach those for a cylinder, i.e., $(F_0^{(L)}(0^+))_1 \rightarrow 0$ and $(F_n^{(L)}(0^+))_1 \rightarrow (\rho/\rho_1)n$.

The function $(G_n^{(L)}(0^+))_1$, defined as the normalization of $(F_n^{(L)}(0^+))_1$ by the fluid-loading parameter ($\Omega = \rho/(\rho_1 h_1)$), is given as Eqs. (4) in Ref. 11. For thin shells with $h_1 \ll 1$, $(G_n^{(L)}(0^+))_1 \approx 1$ and $(F_n^{(L)}(0^+))_1$ reduces to the

fluid-loading parameter Ω . For shells with intermediate thickness, $(G_n^{(L)}(0^+))_1$ gives the modal and thickness correction for the shell by using the fluid-loading parameter of thin shells. For very thick shells with $h_1 \approx 1$, $(G_n^{(L)}(0^+))_1 \approx n$ and $(F_n^{(L)}(0^+))_1$ reduces to $(\rho/\rho_1)n$. For thick targets and large mode orders, the modal acceleration increases linearly with normal mode numbers as $(F_n^{(L)}(0^+))_1 \propto n$. As n increases, lesser part of the target mass is involved in the calculation of $(F_n^{(L)}(0^+))_1$ and the modal acceleration increases.

D. Fluid-filled shell

The constant modal acceleration of the fluid-filled liquid shell can be obtained by:

$$(F_n^{(L)}(0^+))_1 = \frac{\rho}{\rho_1} \frac{n^2 + q_1(F_n^{(L)}(0^+))_0}{q_1 + (F_n^{(L)}(0^+))_0}, \quad (30)$$

where

$$q_1 = n \frac{1 + (1 - h_1)^{2n}}{1 - (1 - h_1)^{2n}} \quad (31a)$$

and

$$(F_n^{(L)}(0^+))_0 = \frac{\rho_1}{\rho_0} n. \quad (31b)$$

The $(F_n^{(L)}(0^+))_1$ is influenced by the density ratio of the outside fluid and shell, the $(F_n^{(L)}(0^+))_0$ of the inner fluid, as well as the modal number. The $(F_n^{(L)}(0^+))_0$ is governed by the density ratio of the shell and the inner fluid. If the inner cylinder is vacuum, $(F_n^{(L)}(0^+))_0 \rightarrow \infty$ and Eq. (30) reduces to $(F_n^{(L)}(0^+))_1$ of the empty shells in Eqs. (29). Therefore, it can be concluded that, for the fluid-filled shell, the density of the inner fluid must be incorporated in the expression for the acoustical background.

E. Double-layered empty shell

The constant modal acceleration for the double-layered, empty shell can be obtained as:

$$(F_0^{(L)}(0^+))_2 = \frac{\rho}{\rho_2} \frac{(F_0^{(L)}(0^+))_1}{[1 - \ln(1 - h_2)(F_0^{(L)}(0^+))_1]} \quad \text{for } n=0, \quad (32a)$$

$$(F_n^{(L)}(0^+))_2 = \frac{\rho}{\rho_2} \frac{n^2 + q_2(F_n^{(L)}(0^+))_1}{q_2 + (F_n^{(L)}(0^+))_1} \quad \text{for } n \geq 1, \quad (32b)$$

where

$$(F_0^{(L)}(0^+))_1 = -\frac{\rho_2}{\rho_1} \frac{1}{\ln(1 - h_1)} \quad (33a)$$

and

$$(F_n^{(L)}(0^+))_1 = \frac{\rho_2}{\rho_1} q_1. \quad (33b)$$

It is noted that the inherent background coefficients of the double-layered shell are functions of the density ratios, the

TABLE I. Material properties of the substances for numerical calculations.

	Density $\times 10^3$ (kg/m ³)	Longitudinal wave velocity (m/s)	Transverse wave velocity (m/s)
Tungsten carbide	13.8	6860	4185
Aluminum	2.79	6380	3100
Stainless steel	7.9	5780	3090
Glycerin	1.26	1920	-
Hg	13.56	1450	-
Air	0.0012	340	-
Water	1	1480	-

relative thicknesses of the outer and inner shells, and the normal mode number. The appropriate limits of the inherent background coefficients approach those of the empty shells and the fluid-filled shells: If the thickness or density of the inner shell is getting close to zero (i.e., $h_1 \rightarrow 0$ or $\rho_1 \rightarrow 0$), $(F_n^{(L)}(0^+))_1 \rightarrow \infty$ and Eqs. (32) converge to Eqs. (29) for empty shells. If the inner shell becomes a cylinder (i.e., $h_1 \rightarrow 1$), Eqs. (32) reduce to Eq. (30) for fluid-filled shells. If the relative thickness h_2 of the outer shell equals 1, that is, if the outer shell becomes a solid or fluid cylinder, the inherent background coefficients for the solid and liquid cylinders can be obtained. The inherent background coefficients for the double-layered shell derived here include the coefficients for solid or liquid cylinders, empty single-layered shells, coated solid cylinders, fluid-filled shells, and double-layered empty shells.

III. NUMERICAL EXAMPLES

In order to examine the adequacy of the derived inherent backgrounds, examples for typical scatterers are dealt with that manifest pure resonance responses. The selected targets are solid and fluid cylinders, empty shells, fluid-filled shells, and coated shells. The pure resonances in the scattering amplitudes of the n th normal mode can be isolated by subtracting the inherent backgrounds from the form function as follows:

$$|f_n^{(res)}(\theta, x)| = |f_n(\theta, x) - f_n^{(b)}(\theta, x)| = \left| \frac{2\varepsilon_n}{\sqrt{\pi i x}} (R_n - R_n^{(b)}) \cos n\theta \right|. \quad (34)$$

The scattering coefficients R_n 's for the aforementioned scatterers can be determined from the ratio of secular determinants of the scattering matrix: $R_n = B_n/D_n$.²⁵ The elements of the determinants for these selected targets can be found in previous works.^{2,14,15,25,26} The modal form function $f_n(\theta, x)$ and inherent background $f_n^{(b)}(\theta, x)$ are calculated in the direction of the backscattering ($\theta = \pi$). The backscattering amplitudes of the partial waves ($n = 0 \sim 25$) are calculated within the intermediate frequency range of $x = 0 \sim 20$. Table I lists the material properties of the substances used for the numerical calculations.

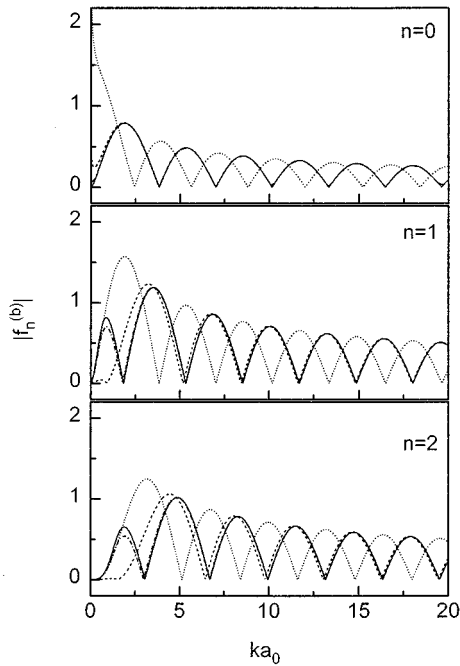


FIG. 2. Comparison of a rigid background (—) with the inherent backgrounds of the lowest three ($n=0,1,2$) partial waves for air (·····), glycerin (---), and WC (-·-·) cylinders submerged in the water.

A. Solid and fluid cylinders

Acoustic resonance scattering has many application examples to elastic cylinders or spheres as the scatterers for theoretical and experimental studies. The rigid background was used for isolating the resonances of elastic cylinders. The soft background has proved suitable in extracting the resonances of air cylinders in a fluid. Neither rigid nor soft backgrounds can be applied to the liquid targets submerged in a fluid medium, since their densities are of the same order of magnitude. In cases where the impedance ratio is close to unity, the proper background behaves intermediately between the rigid and soft backgrounds. The inherent background coefficients of the solid and fluid cylinders are determined uniquely by the density ratios and normal mode numbers. When the density of a scatterer is low (i.e., gas cylinder, $\rho/\rho_0 \gg 1$) and at lower frequencies, the inherent background converges to the soft background. When a scatterer becomes hard (i.e., solid cylinder, $\rho/\rho_0 \ll 1$), the inherent background converges to the rigid one. The adequacy of the inherent background for solid and fluid cylinders can be investigated by isolating the pure resonances. For this purpose, numerical calculations are performed for air, glycerin, mercury, aluminum and tungsten carbide cylinders. Figure 2 shows a comparison of a rigid background with the inherent backgrounds of three ($n=0,1,2$) partial waves for air, glycerin and tungsten carbide (WC) cylinders. Here, the inherent background amplitude of the zeroth order ($n=0$) partial wave is calculated from Eq. (29a) for an empty shell with $h_1=0.99999$. It is noted that the inherent background of the air cylinder approximates the soft background since the density ratio is very large. The inherent background of the WC cylinder is nearly the same as the rigid background for $ka_0 > 5$. The background amplitude of the glycerin cylinder is

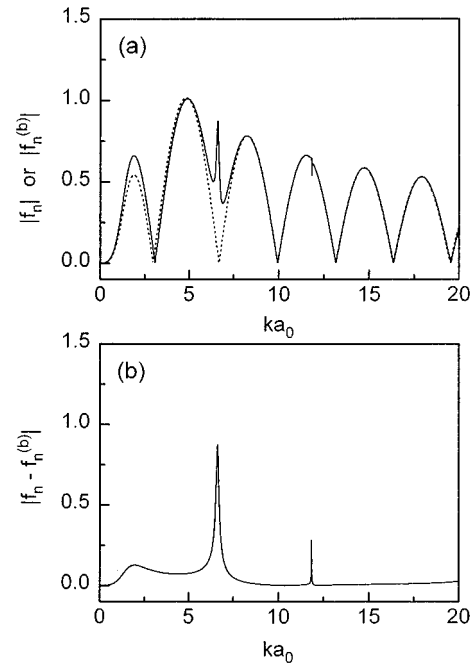


FIG. 3. (a) Comparison of the backscattering form function (—) and inherent background (·····) of a partial wave ($n=2$) for a WC cylinder in water, (b) isolated residual response, $|f_n - f_n^{(b)}|$, by removing the inherent background from the response curve.

between those of the air and solid cylinders because the density of glycerin has the same order of magnitude as that of water. In the lower frequency range, the background amplitudes of liquid cylinders make a large difference between the gas and the solid cylinders. Therefore, the acoustical backgrounds of the liquid cylinder show the characteristics of the intermediate background between the soft and rigid ones. Figures 3–6 show the backscattering responses, the inherent

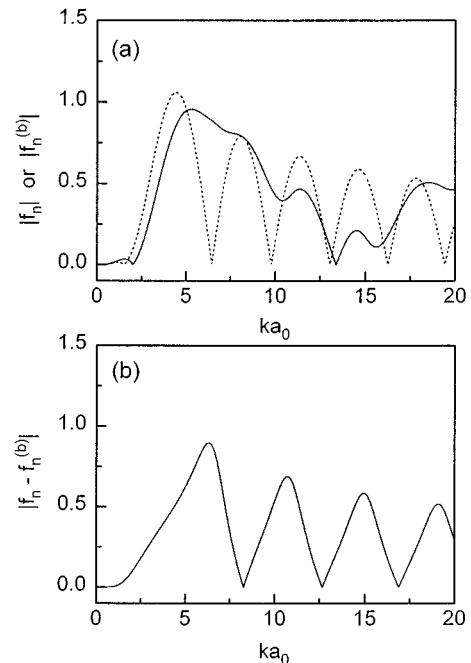


FIG. 4. Same as in Fig. 3, except for the glycerin cylinder.

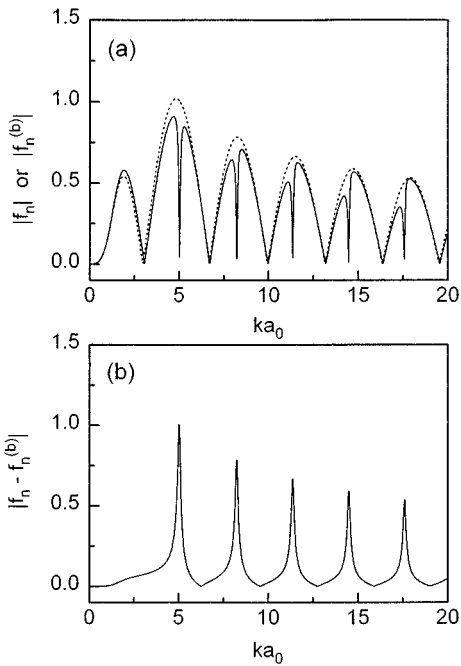


FIG. 5. Same as in Fig. 3, except for the Hg cylinder.

backgrounds and the isolated residual responses of the partial wave ($n=2$) for WC, glycerin, mercury (Hg) and air cylinders, respectively. The partial modes of each cylinder coincide completely with the corresponding partial mode of the background, excluding the resonance region. One can observe that the resonances can be isolated very clearly using the inherent background for cylinders of any substance.

B. Empty shells

The inherent background coefficients for an empty cylindrical shell have been proposed already in previous

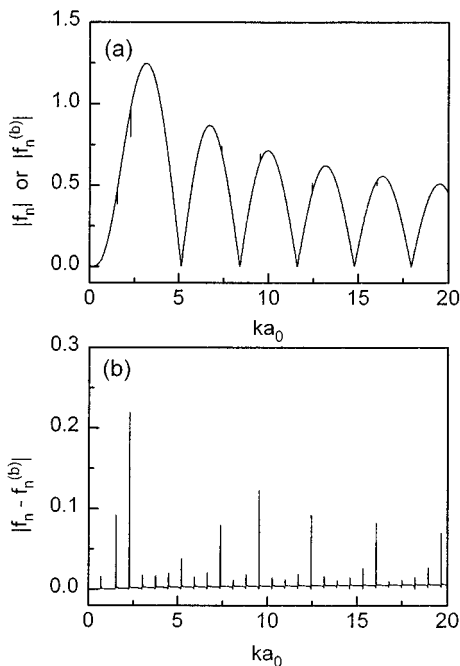


FIG. 6. Same as in Fig. 3, except for the air cylinder.

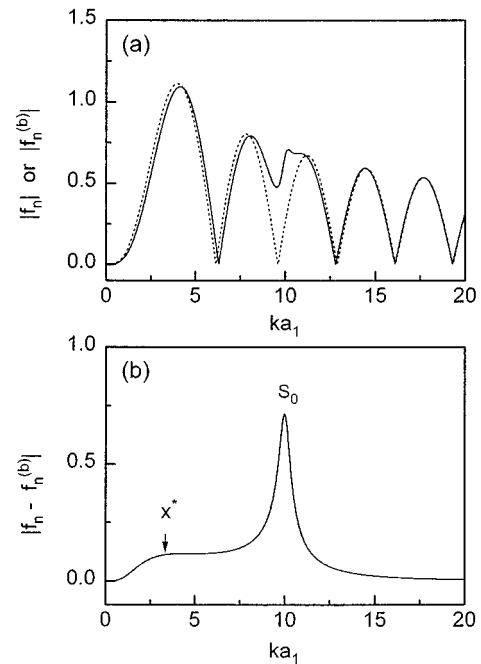


FIG. 7. (a) Comparison of the backsattering form function (—) with the inherent background (·····) of a partial wave ($n=2$) for a 2% thick, empty, WC shell in water, (b) residual response $|f_n - f_n^{(b)}|$.

work.¹¹ Through an example of stainless steel shells of 2% and 99% thickness, it was numerically shown that the inherent background describes the background for any cylindrical shell correctly over all frequencies.

In this study, an aluminum (Al) and a tungsten carbide (WC) shell of 2% thickness are adopted as test examples. Figures 7(a) and 8(a) show the backsattering form function

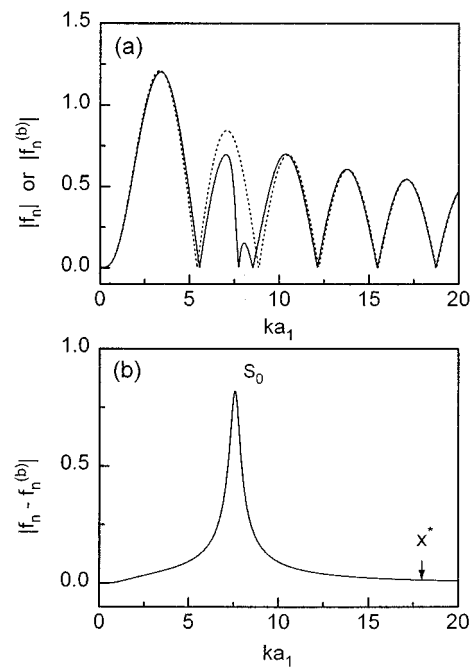


FIG. 8. (a) Comparison of the backsattering form function (—) with the inherent background (·····) of a partial wave ($n=2$) for a 2% thick, empty Al shell in water, (b) residual response $|f_n - f_n^{(b)}|$.

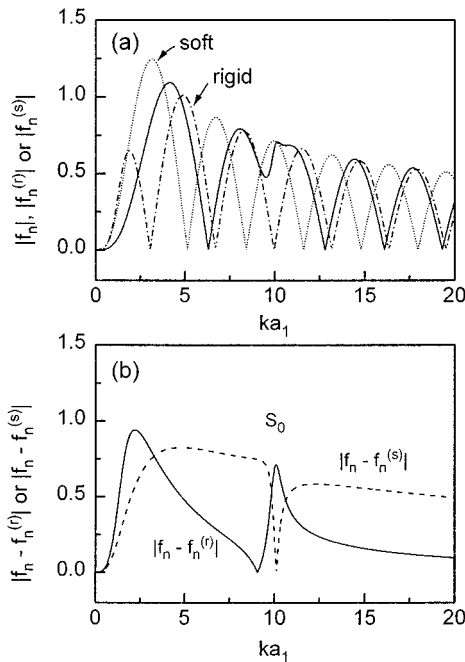


FIG. 9. (a) Comparison of the backscattering form function (—) with the soft background (·····) and rigid background (---) of a partial wave ($n = 2$) for a 2% thick, empty WC shell in water, (b) residual responses $|f_n - f_n^{(r)}|$ (---) and $|f_n - f_n^{(s)}|$ (—).

and the inherent background amplitude of the partial mode ($n=2$) for the 2% thick WC and Al shells, respectively. The modal backscattering amplitudes coincide with those of the inherent backgrounds, except in the resonance region. In Figs. 7(b) and 8(b), one can find that the resonances are cleanly isolated by subtracting the inherent background. The isolated resonance curves show the shape of the simple harmonic oscillator. On the other hand, Fig. 9 shows the residual response by the subtraction of a soft and rigid background for a 2% thick WC shell. Either a rigid or a soft background strongly distort the form of an isolated resonance curve. Figures 7 and 9 show an unambiguous example where the inherent background is more useful than the rigid or soft background for shells having intermediate thickness. The form function of the inherent backgrounds for the WC shell is shifted to a higher frequency than that of the Al shell because the former is more rigid. Also, the transition frequency, x^* , for the WC shell is marked lower than that of the Al shell because the WC shell is harder. The resonances are due to the circumferential wave corresponding to the lowest symmetric (S_0) Lamb wave. The resonance frequency of the WC shell is higher than the Al shell. This means that the S_0 circumferential wave in the WC shell has faster phase speed than that in the Al shell.

C. Fluid-filled shells

The proper background for fluid-filled shells has not been found, although it is known that the inner fluids substantially influence the acoustical background. The modal mass of a fluid-filled shell is related to its acoustical background. The modal mass of a gas-filled shell is the same as that of an empty shell. For a shell filled with a relatively

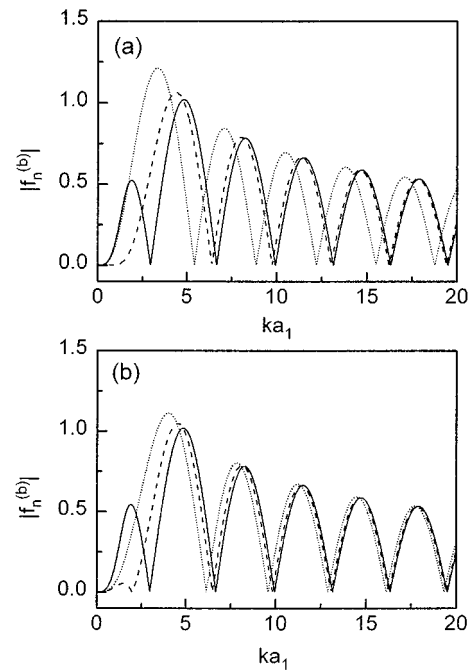


FIG. 10. Comparison of the inherent background of a partial wave ($n = 2$) for a 2% thick (a) Al shell and (b) WC shell filled with air (·····), water (---), and Hg (—).

dense liquid such as mercury, petroleum oil, etc., the inner liquid should be considered in the shell response and acoustical background. The inner liquid greatly affects the background for very thin shells. The inherent background coefficients of a fluid-filled shell have the analytic form considering the mass loading effect of the internal fluid. When a very thick shell containing a very sparse inner fluid filler (i.e., gas filler) is considered, the background coefficients of the fluid-filled shell reduce to those of the empty shell. For a very thin shell containing a dense fluid filler (i.e., liquid filler), the acoustical background should take into account the density of the inner fluid. To investigate the characteristics of the inherent background for fluid-filled shells, the backscattering background amplitudes of the 2% thick WC and Al shells filled with air, water and mercury are considered. Figure 10 shows the magnitude of the inherent background of a partial wave ($n=2$) for Al and WC shells. The results clearly illustrate the effect of the internal fluids on the acoustical background. In the low frequency region, the effect of internal fluid on the background is particularly large, so the consideration of the inner fluids is essential in the isolation of the resonances. In the high frequency region, the loading effect is relatively diminished and, in the case of a WC shell, the background amplitudes for three inner fluids are close to each other because the density of the WC shell is larger than those of the inner fluids.

D. Coated shells

Backscattering amplitudes are calculated for two kinds of 2% thick Al shells coated with a WC layer: one is the Al shell ($h_1 = 1.8\%$) coated with a thin WC layer ($h_2 = 0.2\%$) and the other is the Al shell ($h_1 = 1\%$) with a thick WC layer ($h_2 = 1\%$). For comparison purposes, the backscattering am-

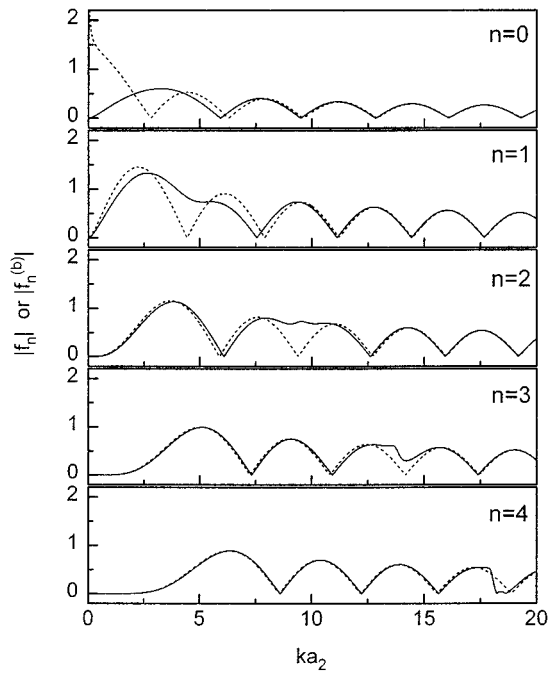


FIG. 11. Comparison of the shell response (—) for a 1% thick Al shell layered with a 1% thick WC outer layer and the corresponding inherent background (·····) varying the wave mode number n .

plitudes are calculated for the 2% thick Al and WC shells. Figure 11 shows the shell responses of the 1% thick Al shell layered with the 1% thick WC layer, and the corresponding inherent backgrounds for the lowest five partial waves. The modal amplitudes of the partial waves coincide with those of the inherent backgrounds, except in the resonance region. As

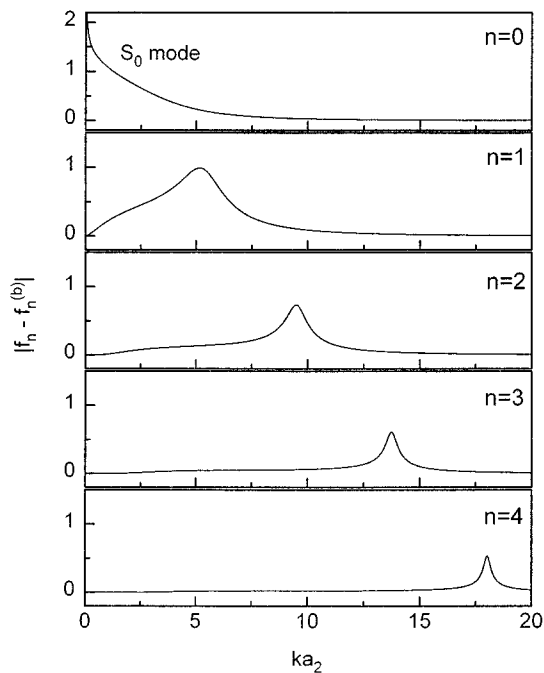


FIG. 12. Backscattering amplitudes of isolated resonances, $|f_n - f_n^{(b)}|$, for the lowest five ($n=0-4$) partial waves of a 1% thick Al shell layered with a 1% thick WC outer layer.

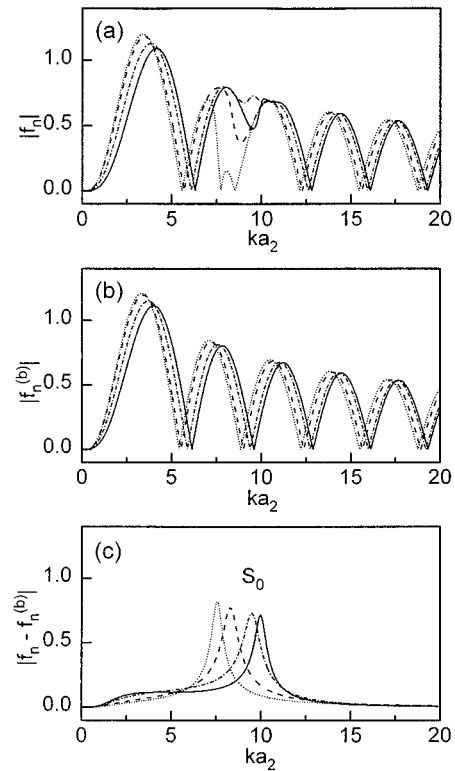


FIG. 13. (a) Backscattering amplitudes of the partial wave ($n=2$) of a shell response, (b) the inherent backgrounds, and (c) the isolated resonances for 2% thick shells (···, Al shell; —, WC shell) and the Al shells coated with WC outer layer (---, 1.8% thick Al shell coated with a 0.2% thick WC layer; -·-·-, 1% thick Al shell layered with a 1% thick WC outer layer).

depicted in Fig. 12, the extraction of the resonance is clearly done by subtracting the inherent background. The backscattering amplitudes of the partial wave ($n=2$) for the four cases (i.e., two single-layered shells and two double-layered shells with Al and WC) are shown in Fig. 13(a), and one can find that the elastic responses consist of a smooth background and a resonance. The difference in the shell responses implies that the rigidities of four shells are different. The total rigidity of the shells affect the acoustical background. The behavior of the elastic responses of the layered shells is between those of the Al and WC shells: the former is the low frequency bound and the latter the high frequency bound. The Al shell is the softest, while the Al shells with a WC layer have a medium rigidity, and the WC shell is the most rigid. Figure 13(b) illustrates the inherent backgrounds for those shells which reflect the different rigidities of the corresponding shells. Although the four shells have the same thickness, the resonances are different in location. The resonances of the four shells, which correspond to the S_0 circumferential wave, have different characteristics of propagation and radiation damping. In layered shells, the composition and thickness of layers affect the modal background, as well as the resonances. The coating layers have an influence on the propagation characteristics of the resonances. The inherent background provides a powerful tool for analyzing the effect of layers on the characteristics of the resonances for the layered shells.

IV. CONCLUSIONS

A theory of the acoustical background for layered cylindrical structures has been proposed. Inherent background coefficients for layered structures are obtained from the modal accelerance of equivalent liquid systems. The liquid systems have been analyzed by incorporating the notion of incoming and outgoing waves and then the scattering function and modal accelerances of the systems have been obtained. The scattering functions of the scatterer with fluid–fluid interfaces are simply correlated with the modal accelerances due to no mode conversion at the interfaces. The accelerance of each liquid layer is recurrently related to that of the adjacent layer. The scattering functions of the liquid structures can be obtained by the generalized modal accelerance. The generalized expression of the inherent background can be extracted from the zero frequency limit of the generalized accelerances. The acoustical background coefficients for all kinds of the layered structures can be derived from the generalized inherent coefficients, which converge analytically to the background of cylinders, empty shells, fluid-filled shells and layered shells in the appropriate limits. The exactness of the inherent backgrounds is numerically illustrated through examples of the typical cylindrical scatterers over very wide ranges of the physical parameters. The inherent background brings a powerful tool for interpreting the resonance scattering phenomena of layered shells and shells with internal structures.

- ¹L. Flax, L. R. Dragonette, and H. Überall, “Theory of elastic resonance excitation by sound scattering,” *J. Acoust. Soc. Am.* **63**, 723–731 (1978).
- ²L. Flax, G. C. Gaunaurd, and H. Überall, “Theory of resonance scattering,” in *Physical Acoustics XV* (Academic, New York, 1980), pp. 191–294.
- ³M. F. Werby and G. C. Gaunaurd, “Transition from soft to rigid behavior in scattering from submerged thin elastic shells,” *Acoust. Lett.* **9**, 89–93 (1986).
- ⁴J. D. Murphy, E. D. Breitenbach, and H. Überall, “Resonance scattering of acoustic waves from cylindrical shells,” *J. Acoust. Soc. Am.* **64**, 677–683 (1978).
- ⁵J. D. Murphy, J. George, A. Nagl, and H. Überall, “Isolation of the resonant component in acoustic scattering from fluid-loaded elastic spherical shells,” *J. Acoust. Soc. Am.* **65**, 368–373 (1978).
- ⁶N. D. Veksler, “Intermediate background in problems of sound waves scattering by elastic shells,” *Acustica* **76**, 1–9 (1992).

- ⁷M. F. Werby, “The acoustical background for a submerged elastic shell,” *J. Acoust. Soc. Am.* **90**, 3279–3287 (1991).
- ⁸G. C. Gaunaurd, “Hybrid background coefficients to isolate the resonance spectrogram of submerged shells,” *J. Acoust. Soc. Am.* **92**, 1981–1984 (1992).
- ⁹A. N. Norris and N. Vasudevan, “Acoustic wave scattering from thin shell structures,” *J. Acoust. Soc. Am.* **92**, 3320–3336 (1992).
- ¹⁰M.-S. Choi and Y.-S. Joo, “Theory of the background amplitudes in acoustic resonance scattering,” *J. Acoust. Soc. Am.* **101**, 2083–2087 (1997).
- ¹¹M.-S. Choi, Y.-S. Joo, and J.-P. Lee, “Inherent background coefficients for submerged cylindrical shells,” *J. Acoust. Soc. Am.* **101**, 1743–1745 (1997).
- ¹²G. C. Gaunaurd, “Elastic and acoustic resonance wave scattering,” *Appl. Mech. Rev.* **42**, 143–193 (1989).
- ¹³G. C. Gaunaurd and M. F. Werby, “Acoustic resonance scattering by submerged elastic shell,” *Appl. Mech. Rev.* **43**, 171–208 (1990).
- ¹⁴L. Flax and W. G. Neubauer, “Acoustic reflection from layered elastic absorptive cylinders,” *J. Acoust. Soc. Am.* **61**, 307–312 (1977).
- ¹⁵G. C. Gaunaurd, “The sonar cross section of a hollow coated cylinder in water,” *J. Acoust. Soc. Am.* **61**, 360–368 (1977).
- ¹⁶G. C. Gaunaurd, “High frequency acoustic scattering from submerged cylindrical shells coated with viscoelastic layers,” *J. Acoust. Soc. Am.* **62**, 503–512 (1977).
- ¹⁷G. C. Gaunaurd and A. Kalnins, “Resonances in the sonar cross sections of coated spherical shells,” *Int. J. Solids Struct.* **18**, 1083–1102 (1982).
- ¹⁸D. Brill and H. Überall, “Transmitted waves in the diffraction of sound from liquid cylinders,” *J. Acoust. Soc. Am.* **47**, 1467–1469 (1970).
- ¹⁹D. Brill and H. Überall, “Acoustic waves transmitted through solid elastic cylinders,” *J. Acoust. Soc. Am.* **50**, 921–939 (1971).
- ²⁰A. Gerard, “Scattering by spherical elastic layers: Exact solution and interpretation for a scalar field,” *J. Acoust. Soc. Am.* **73**, 13–18 (1983).
- ²¹E. B. Danila, J. M. Conoir, and J. L. Izbicki, “The generalized Debye series expansion: Treatment of the concentric and nonconcentric cylindrical fluid–fluid interfaces,” *J. Acoust. Soc. Am.* **98**, 3326–3342 (1995).
- ²²P. M. Morse and K. U. Ingard, *Theoretical Acoustics* (McGraw-Hill, New York, 1968), pp. 422–427.
- ²³J. D. Alemar, P. P. Delsanto, E. Rosario, A. Nagl, and H. Überall, “Spectral analysis of the scattering of acoustic waves from a fluid cylinder, I: Denser fluid loading,” *Acustica* **61**, 1–6 (1986).
- ²⁴J. D. Alemar, P. P. Delsanto, E. Rosario, A. Nagl, and H. Überall, “Spectral analysis of the scattering of acoustic waves from a fluid cylinder, II: Denser fluid inside,” *Acustica* **61**, 7–13 (1986).
- ²⁵G. C. Gaunaurd and D. Brill, “Acoustic spectrogram and complex-frequency poles of a resonantly excited elastic tube,” *J. Acoust. Soc. Am.* **75**, 1680–1693 (1984).
- ²⁶D. Brill and G. C. Gaunaurd, “Acoustic resonance scattering by a penetrable cylinder,” *J. Acoust. Soc. Am.* **73**, 1448–1455 (1983).

An analytical model for bandlimited response of acoustic-structural coupled systems. I. Direct sound field excitation

K. S. Sum and J. Pan

Department of Mechanical and Materials Engineering, The University of Western Australia, Nedlands, Western Australia 6907, Australia

(Received 2 June 1997; accepted for publication 10 September 1997)

An analytical model is proposed in this paper for predicting time-averaged energies of boundary structures and enclosed sound field. The sound field is directly driven by an acoustic source and the structures are excited through acoustic-structural coupling. The present model is based on the classical modal coupling method but is developed in such a way to improve the computational efficiency in estimating the bandlimited response of acoustic-structural coupled systems particularly in the medium frequency range where a large number of acoustic and/or structural modes is involved. In this frequency range, one often has to deal with manipulation of large complex matrices in order to obtain full mathematical solutions to the system response using the classical modal coupling method. However, this is avoided if the present bandlimited model is used. This paper describes the mathematical development of the model. Numerical examples for a panel-cavity system are presented and the proposed model is compared with the classical modal coupling method in terms of computational efficiency and accuracy in the prediction of the system energies. © 1998 Acoustical Society of America. [S0001-4966(98)03301-3]

PACS numbers: 43.40.Rj, 43.40.Dx [CBB]

INTRODUCTION

The interaction between flexible boundary structures of an enclosure and the enclosed sound field is an important practical problem as far as structural vibration and acoustic response are concerned. Dynamic analysis and design of acoustic-structural coupled systems require accurate modeling of boundary conditions of the systems and the corresponding acoustic-structural interaction/coupling. Numerous investigations have been done in this area not only to improve physical understanding of the nature of the acoustic-structural coupling and its effect on the response of such coupled systems but also to establish models for the response prediction.

Modal coupling method is one of the well-established theoretical methods for estimating response characteristics of acoustic-structural coupled systems. Using this method, the response of an acoustic-structural coupled system can be accurately evaluated by summing over the response of a finite number of system modes. Dowell *et al.*¹ and Pan² have experimentally validated this method. They have successfully performed acoustic-structural coupling analyses using this method on a sound field inside a rectangular parallelepiped cavity, which is coupled to one of its flexible vibrating boundary structures. However, it is known that the modal density of enclosed acoustic volumes increases rapidly as a quadratic function of frequency.³ Thus beyond the low-frequency regime, solutions to the coupled system response using the modal coupling method have to cope with manipulation of large complex matrices if the effect of acoustic-structural coupling is included in the analysis. Substantial computational effort is then required for the solution of a large number of coupled system equations. Computational effort is also very significant for medium- and high-frequency analyses of acoustic-structural coupled systems

using well-established deterministic techniques such as the finite element method (FEM) and the boundary element method (BEM). In these frequency ranges, details of boundary conditions are significant and accurate modeling of the system response requires information of a large number of system modes. The medium and high frequencies also correspond to shorter vibrational wavelengths. A large number of elements is then required for resolving the details of the system response. Therefore application of these deterministic techniques is not efficient in terms of computational time and computer storage requirement.⁴ These techniques are thus usually applied for low-frequency analysis.

Prediction of the response of acoustic-structural coupled systems has recently gained considerable interest. Numerous investigations have been aimed at establishing computationally efficient analytical, experimental, statistical, or numerical techniques capable of handling the large number of modes for analyses beyond the low-frequency range. A subdomain decomposition technique has been recently established for evaluating eigenproperties and frequency response of modally dense acoustic cavities.⁵ A large acoustic cavity is decomposed into smaller subcavities of lower modal densities and each subcavity is separated from the others by fictitious interfaces. Eigenproperties of each subcavity subject to continuity at all interfaces are then obtained numerically and eigenproperties of the original large cavity are synthesized by using a modal synthesis approach. Acoustical response of the cavity can then be predicted. A similar subdomain decomposition method has also been used by Terao and Sekine⁶ but in a later step they used a partial Gauss-Jordan elimination technique to numerically solve the sound pressure and particle velocity at the fictitious interfaces. Computer storage has been shown to be reduced if the subdomain decomposition method is used but the computational

time remains the same as for the prediction of response of the original large cavity without subdomain decomposition. This method has only been proposed for rigid⁵ and locally reactive boundaries⁶ of the cavity.

A new numerical method called the coupled wave method^{7,8} has also been developed recently for the prediction of response of acoustic-structural coupled systems. In contrast to the classical finite element technique where the structural and acoustical domains of the coupled system are divided into small elements and the dynamic equations within each element are solved, the entire subsystems are now described by complex structural and acoustical wave propagation functions. These functions are solutions of the structural and acoustical wave equations. By applying boundary conditions and using a weighted residual formulation where the acoustical plane-wave functions are chosen as weighting functions, a set of algebraic equations can be obtained and the system response can then be predicted. By comparison to the finite element method, improvement in calculation time has been achieved if this coupled wave method were used for the prediction of response of acoustic-structural coupled systems. The method has been used for a low-frequency analysis.

Simplified methods based on averaged quantities have also been developed to reduce computational effort. Analytical expressions for predicting response of acoustic-structural coupled systems were derived for statistical energy analysis (SEA)^{9,10} and asymptotic modal analysis (AMA).¹¹ However, these methods are more adapted to the prediction in the high-frequency range since the relevant quantities or parameters used to describe the system response are averaged over observation points, frequency, and excitation points. In the low and medium frequency ranges, applications of these methods become uncertain when the modal overlap indices of the system are low and/or the band of analysis contains few resonance modes.¹²

Different approaches for modeling the response of acoustic-structural coupled systems at frequencies where application of statistical methods is not reliable, have been developed. Techniques developed must be computationally efficient but yet have to be reliable in terms of accuracy of response prediction. Bonilha and Fahy¹³ developed a probabilistic-deterministic technique for an acoustic-structural coupled system in frequency bands where there is a large number of structural modes of a wall vibration interacting with a few resonance acoustic modes of the enclosed sound field. A probabilistic description is employed for the wall with modal density high enough to justify an SEA model while a deterministic description is employed for the sound field with sparsely distributed modes and amenable to FE modeling. This technique allows for the reduction in computational effort because the necessary information for the characterization of the system dynamics has been compressed. Analyses on the response of a master plate loaded with mass heterogeneities¹⁴ and on the response of coupled beams¹⁵ have been performed using a variational method called modal sampling method. The computational time is reduced since only a limited number of modes are used to interpolate the response of the system. Analysis of the band-

limited response of acoustic-structural coupled systems using this method is also possible although it is mathematically complicated.

Bandlimited power flow expressions have been derived by Pope and Wilby^{16,17} for sound transmission into enclosures about two decades ago. In this paper, an analytical method is established for predicting bandlimited energies of subsystems in acoustic-structural coupled systems. The present method is based on the classical modal coupling method and it reduces computational effort in summing the modal contribution of each subsystem mode given the information of the modes. It is relatively more computationally efficient especially for analysis in the medium frequency range because manipulation of large complex matrices as in the classical modal coupling method will be avoided. Improvement in calculation time can also be achieved with the present method since calculations of energies at each single frequency and subsequent frequency integrations for bandlimited energies have been avoided. For a 100-Hz frequency bandwidth for example, calculations of bandlimited energies using the classical modal coupling method must be performed 100 times if a 1-Hz step is used (or smaller steps if a more precise prediction is required) and then integrated over the frequency range. However, with the present method, the bandlimited energies can be predicted straight away in one calculation for each subsystem given the lower and upper limits of the frequency band.

Crandall and Mark¹⁸ have presented an exact solution for the mean-square response of a single degree-of-freedom system to bandlimited white noise and this response is proportional to the energy of the system. Based on this, Fang and Wang¹⁹ then derived the solution for multi-degree-of-freedom systems. Analytical expressions for bandlimited energies of acoustic-structural coupled systems developed in this paper have the same general form as the result in Ref. 19 but they are more complicated and dependent on various modal parameters and properties of the coupled systems. Numerical examples for a panel-cavity system are presented in this paper and accuracy in predicting bandlimited energies of subsystems using the present method is discussed by comparing the results with those obtained from the classical modal coupling method. Computational efficiency of the present method is also demonstrated.

I. ANALYSIS OF ACOUSTIC-STRUCTURAL COUPLED SYSTEMS

A. Review of the classical modal coupling method

The acoustic-structural coupled system considered in this analysis consists of an enclosed sound field described by the sound pressure $p(\mathbf{r}, \omega)$ and a vibration field in a flexible boundary structure described by the structural velocity $v(\boldsymbol{\sigma}, \omega)$. Using the modal coupling method, the modal coupling equations for the coupled system are expressed as follows:²

$$\begin{bmatrix} P_1 \\ \vdots \\ P_N \end{bmatrix} = \rho_0 c_0 \begin{bmatrix} B_{1,1}/\chi_{a1} & \cdots & B_{1,M}/\chi_{a1} \\ \vdots & \ddots & \vdots \\ B_{N,1}/\chi_{aN} & & B_{N,M}/\chi_{aN} \end{bmatrix} \begin{bmatrix} V_1 \\ \vdots \\ V_M \end{bmatrix} + \begin{bmatrix} Q_1 \\ \vdots \\ Q_N \end{bmatrix} \quad (1)$$

for the sound field and

$$-\rho_0 c_0 \begin{bmatrix} \chi_{s1} & & 0 \\ & \ddots & \\ 0 & & \chi_{sM} \end{bmatrix} \begin{bmatrix} V_1 \\ \vdots \\ V_M \end{bmatrix} = \begin{bmatrix} B_{1,1} & \cdots & B_{1,N} \\ \vdots & \ddots & \vdots \\ B_{M,1} & & B_{M,N} \end{bmatrix} \times \begin{bmatrix} P_1 \\ \vdots \\ P_N \end{bmatrix} \quad (2)$$

for the structural vibration. P_i and V_j are, respectively, the complex pressure and velocity amplitudes of the i th acoustic mode and j th structural mode. The sound field is directly excited using a distributed steady-state acoustic source in the enclosure while the structure is driven through coupling with the sound field. The quantities in Eqs. (1) and (2) are

$$\chi_{ai} = jM_{ai}(\omega_{ai}^2 - \omega^2 + j\eta_{ai}\omega_{ai}^2)/\omega\rho_0 c_0 A_s, \quad (3)$$

$$\chi_{sj} = jM_{sj}(\omega_{sj}^2 - \omega^2 + j\eta_{sj}\omega_{sj}^2)/\omega\rho_0 c_0 A_s, \quad (4)$$

$$Q_i = \frac{-\rho_0 c_0}{A_s \chi_{ai}} \int_{V_0} q \Phi_i dV, \quad (5)$$

$$B_{j,i} = \frac{1}{A_s} \int_{A_s} \Phi_i(\mathbf{r}) S_j(\boldsymbol{\sigma}) d\boldsymbol{\sigma}, \quad (6)$$

where M_{ai} , M_{sj} , ω_{ai} , ω_{sj} , η_{ai} , η_{sj} , $\Phi_i(\mathbf{r})$, $S_j(\boldsymbol{\sigma})$ are acoustic and structural modal masses, resonance frequencies, loss factors, and mode shape functions, respectively. $B_{j,i}$ is the modal coupling coefficient between the i th acoustic mode and j th structural mode, $q(\mathbf{r}, \omega)$ is the volume velocity of the sound source per unit volume of the enclosure, ρ_0 is air density, c_0 is speed of sound in air, and A_s is surface area of the structure. \mathbf{r} and $\boldsymbol{\sigma}$ are, respectively, the location vectors in the sound field and on the structural surface.

Substituting Eq. (2) into (1) and eliminating the structural velocity matrix, the complex amplitude of each acoustic mode can be obtained as

$$\begin{bmatrix} P \\ \vdots \\ P_N \end{bmatrix} = \begin{bmatrix} 1 + \sum_{j=1}^M \frac{B_{1,j}B_{j,1}}{\chi_{a1}\chi_{sj}} & \cdots & \sum_{j=1}^M \frac{B_{1,j}B_{j,N}}{\chi_{a1}\chi_{sj}} \\ \vdots & \ddots & \vdots \\ \sum_{j=1}^M \frac{B_{N,j}B_{j,1}}{\chi_{aN}\chi_{sj}} & & 1 + \sum_{j=1}^M \frac{B_{N,j}B_{j,N}}{\chi_{aN}\chi_{sj}} \end{bmatrix}^{-1} \times \begin{bmatrix} Q_1 \\ \vdots \\ Q_N \end{bmatrix}. \quad (7)$$

Since the modal density of the enclosed sound field increases relatively fast with respect to excitation frequency compared to that of the structure, one would deal with an inverse of a very large complex matrix shown in Eq. (7) at medium or high frequencies. Therefore substantial computational effort is required even though modal information of the coupled system is available. To avoid the inverse of such a large matrix, one can first solve for the velocity vector and then the sound-pressure vector. Substituting Eq. (1) into (2) and eliminating the sound-pressure vector, it can be shown that

$$\begin{bmatrix} V_1 \\ \vdots \\ V_M \end{bmatrix} = -\frac{1}{\rho_0 c_0} \begin{bmatrix} \chi_{s1} + \sum_{i=1}^N \frac{B_{1,i}B_{i,1}}{\chi_{ai}} & \cdots & \sum_{i=1}^N \frac{B_{1,i}B_{i,M}}{\chi_{ai}} \\ \vdots & \ddots & \vdots \\ \sum_{i=1}^N \frac{B_{M,i}B_{i,1}}{\chi_{ai}} & & \chi_{sM} + \sum_{i=1}^N \frac{B_{M,i}B_{i,M}}{\chi_{ai}} \end{bmatrix}^{-1} \begin{bmatrix} \sum_{i=1}^N B_{1,i}Q_i \\ \vdots \\ \sum_{i=1}^N B_{M,i}Q_i \end{bmatrix}. \quad (8)$$

In this case, one would deal with an inverse of a matrix which is smaller than before since the size of this matrix is dependent only on the number of structural modes. The sound-pressure vector can then be obtained from Eq. (1) once the velocity vector is solved. However, if sound-pressure calculation is only required, this alternative way has a disadvantage that it requires two sets of calculation using both Eqs. (1) and (8). The time- and space-averaged mean-square sound-field pressure and structural velocity can be obtained once the sound pressure and velocity vectors are solved and are given by

$$\langle \bar{p}^2 \rangle = \frac{1}{2\rho_0 V_0} \sum_{i=1}^N P_i P_i^* M_{ai}, \quad (9)$$

$$\langle \bar{v}^2 \rangle = \frac{1}{2m_s} \sum_{j=1}^M V_j V_j^* M_{sj}. \quad (10)$$

The asterisk denotes complex conjugate of the quantity, V_0 is the volume of the enclosure, and m_s is the mass of the structure. $\langle \bar{p}^2 \rangle$ and $\langle \bar{v}^2 \rangle$ are, respectively, related to the acoustic energy of the sound field and vibration energy of the structure. Equations (9) and (10) provide a way to evaluate the

coupled system responses at single frequencies. If frequency bandlimited responses are required then calculations are done at each single frequency and the results are averaged over the frequency band $\Delta\omega$ using numerical integrations.

B. Mathematical formulation for bandlimited response

In practice, a frequency bandlimited averaged energy level in each subsystem of an acoustic-structural coupled system often provides sufficient information for the analysis and design of such a system. It is therefore necessary to search for analytical expressions with computational efficiency and accuracy for prediction of energies in the subsystems. To formulate these expressions, a number of approximations will be used. Detailed derivations of the analytical expressions will be presented here whereas justifications of all the approximations will be provided in Sec. III.

1. Sound-field response

From Eqs. (1), (2), and (5), it can be shown that

$$P_i = H_{ai} \int_{V_0} q \Phi_i dV - H_{ai} A_s \sum_{j=1}^M V_j B_{j,i}, \quad (11)$$

$$V_j = H_{sj} \sum_{k=1}^N P_k B_{j,k}, \quad (12)$$

where

$$H_{ai} = -\rho_0 c_0 / A_s \chi_{ai}, \quad (13)$$

$$H_{sj} = -1 / \rho_0 c_0 \chi_{sj}. \quad (14)$$

Substituting Eq. (12) into (11) results in

$$P_i \left[1 + H_{ai} A_s \sum_{j=1}^M H_{sj} B_{j,i}^2 \right] = H_{ai} \int_{V_0} q \Phi_i dV - H_{ai} A_s \sum_{k \neq i}^N P_k \sum_{j=1}^M H_{sj} B_{j,i} B_{j,k}. \quad (15)$$

The first term on the right-hand side of Eq. (15) accounts for direct excitation of the i th acoustic mode through the sound source while the second term accounts for its indirect excitation by other acoustic modes through coupling with various structural modes. The second term was often interpreted as cross coupling of the acoustic mode. Neglecting the acoustic cross-coupling term, a simplified expression for the pressure amplitude of the i th acoustic mode is obtained as

$$P_i \approx H_{ai} \int_{V_0} q \Phi_i dV \left/ \left(1 + H_{ai} A_s \sum_{j=1}^M H_{sj} B_{j,i}^2 \right) \right. \quad (16)$$

Equation (16) is equivalent to setting all nondiagonal terms in the pressure transfer matrix in Eq. (7) (i.e., the matrix which is to be inverted) to zero. Using Eqs. (13) and (14) for H_{ai} and H_{sj} to expand Eq. (16), it can be shown that

$$P_i \approx j \omega \rho_0^2 c_0^2 \int_{V_0} q \Phi_i dV \left/ \left(M_{ai} \{ (\omega_{ai}^c)^2 - \omega^2 \} + j \eta_{ai}^c \omega_{ai}^2 \right) \right. \quad (17)$$

where

$$(\omega_{ai}^c)^2 = \omega_{ai}^2 - \frac{(A_s \rho_0 c_0)^2 \omega}{M_{ai}} \sum_{j=1}^M \frac{B_{j,i}^2}{\Delta \omega_{sj}^{3dB} M_{sj}} \left[\frac{\epsilon_{sj}}{\epsilon_{sj}^2 + 1} \right], \quad (18)$$

$$\eta_{ai}^c = \eta_{ai} + \frac{(A_s \rho_0 c_0)^2 \omega}{M_{ai} \omega_{ai}^2} \sum_{j=1}^M \frac{B_{j,i}^2}{\Delta \omega_{sj}^{3dB} M_{sj}} \left[\frac{1}{\epsilon_{sj}^2 + 1} \right]. \quad (19)$$

In the above, $\Delta \omega_{sj}^{3dB} = \eta_{sj} \omega_{sj}$ is the half-power bandwidth of the uncoupled j th structural mode. ω_{ai}^c and η_{ai}^c are, respectively, the coupled or effective resonance frequency and effective loss factor of the i th acoustic mode due to coupling. The ratio of difference between resonance and excitation frequencies to damping of the j th structural mode is

$$\epsilon_{sj} = (\omega_{sj}^2 - \omega^2) / \eta_{sj} \omega_{sj}^2. \quad (20)$$

Equation (18) describes the shift in ω_{ai} when the coupling effect is present. However, effect of resonance frequency shifts on the sound-field response is insignificant for analysis beyond the low-frequency range and it will be assumed that $\omega_{ai}^c \approx \omega_{ai}$. η_{ai}^c in Eq. (19) incorporates both the internal loss due to other enclosure boundaries and the loss due to coupling with the structure. The contribution of the j th structural mode to η_{ai}^c through ϵ_{sj} is only significant if the mode is excited to a sufficient degree such that

$$|\omega_{sj} - \omega| < \frac{1}{2} \Delta \omega_{sj}^{3dB}. \quad (21)$$

Equation (21) is actually a condition for proximate excitation of the j th structural mode. Considering this condition for the assumption that $\omega_{sj} \approx \omega$, it can be shown that Eq. (20) can be mathematically approximated as

$$\epsilon_{sj} \approx 2(\omega_{sj} - \omega) / \Delta \omega_{sj}^{3dB}. \quad (22)$$

Close to the first acoustic mode (0,0,0) with a natural frequency of 0 Hz, the sound-field response is controlled by air leakage and this mode is modeled as a Helmholtz resonator.²⁰ Therefore in Eqs. (18) and (19), ω_{ai} and η_{ai} for this mode should be, respectively, replaced by the Helmholtz resonance frequency and its loss factor.

The bandlimited time- and space-averaged mean-square sound-field pressure can be obtained by averaging the sound pressure over a frequency band. Thus Eq. (9) becomes

$$\langle \bar{p}^2 \rangle_{\Delta\omega} = \frac{\rho_0^3 c_0^4}{2V_0 \Delta\omega} \sum_{i=1}^N \frac{[\int_{V_0} q \Phi_i dV][\int_{V_0} q^* \Phi_i dV]}{M_{ai}} \times \int_{\Delta\omega} \frac{\omega^2}{(\omega_{ai}^2 - \omega^2)^2 + (\bar{\eta}_{ai}^c \omega_{ai}^2)^2} d\omega, \quad (23)$$

where

$$\bar{\eta}_{ai}^c = \bar{\eta}_{ai} + \frac{(A_s \rho_0 c_0)^2 \omega_0}{M_{ai} \omega_{ai}^2} \sum_{j=1}^M \frac{B_{j,i}^2}{\Delta \omega_{sj}^{3dB} M_{sj}} \left[\frac{1}{\bar{\epsilon}_{sj}^2 + 1} \right], \quad (24)$$

$$\bar{\epsilon}_{sj} = 2(\omega_{sj} - \omega_0) / \Delta \omega_{sj}^{3dB}. \quad (25)$$

$\bar{\eta}_{ai}$ and $\bar{\eta}_{ai}^c$ are, respectively, the band-averaged uncoupled and effective loss factors of the i th acoustic mode. The definition of $\bar{\eta}_{ai}^c$ where it is evaluated at the band center frequency ω_0 , is also one of the approximations made in the formulation of the present method. The analytical solution to the integral in Eq. (23) can be obtained as

$$\int_{\Delta\omega} = I(\omega_U, \omega_{ai}, \bar{\eta}_{ai}^c) - I(\omega_L, \omega_{ai}, \bar{\eta}_{ai}^c), \quad (26)$$

where

$$I(\omega, \omega_{ai}, \bar{\eta}_{ai}^c) = \frac{(c_{ai}A_{ai} + d_{ai}B_{ai})}{2(A_{ai}^2 + B_{ai}^2)} \ln \left[\frac{(\omega + A_{ai})^2 + B_{ai}^2}{(\omega - A_{ai})^2 + B_{ai}^2} \right] + \frac{(c_{ai}B_{ai} - d_{ai}A_{ai})}{2(A_{ai}^2 + B_{ai}^2)} \times \tan^{-1} \left[\frac{4B_{ai}\omega(\omega^2 - A_{ai}^2 - B_{ai}^2)}{(\omega^2 - A_{ai}^2 - B_{ai}^2)^2 - (2B_{ai}\omega)^2} \right], \quad (27)$$

$$A_{ai} = \omega_{ai} \sqrt{(1 + \sqrt{1 + \bar{\eta}_{ai}^c})/2} \quad (28a)$$

$$\approx \omega_{ai} \quad \text{if } \bar{\eta}_{ai}^c \ll 1, \quad (28b)$$

$$B_{ai} = \omega_{ai} \sqrt{(\sqrt{1 + \bar{\eta}_{ai}^c} - 1)/2} \quad (29a)$$

$$\approx \bar{\eta}_{ai}^c \omega_{ai}/2 \quad \text{if } \bar{\eta}_{ai}^c \ll 1, \quad (29b)$$

$$c_{ai} = -0.5, \quad (30)$$

$$d_{ai} = 0.5/\bar{\eta}_{ai}^c. \quad (31)$$

Here, ω_U and ω_L are, respectively, the upper and lower limits of the frequency band under consideration. The value of the inverse tangent term in Eq. (27) varies from 0 to 2π .

2. Structural vibration response

Mathematical formulation of an analytical expression for prediction of structural vibration response is similar to that for the sound-field response and all approximations used are analogous. Substituting Eq. (11) into (12), it can be shown that

$$V_j \left[1 + H_{sj} A_s \sum_{i=1}^N H_{ai} B_{j,i}^2 \right] = H_{sj} \sum_{i=1}^N B_{j,i} H_{ai} \int_{V_0} q \Phi_i dV - H_{sj} A_s \sum_{k \neq j}^M V_k \sum_{i=1}^N H_{ai} B_{j,i} B_{k,i}. \quad (32)$$

The first term on the right-hand side of Eq. (32) accounts for excitation of the j th structural mode through direct couplings with acoustic modes. The second term accounts for its excitation by other structural modes through coupling with various acoustic modes. The second term was also interpreted as cross coupling of the structural mode. Neglecting the struc-

tural cross-coupling term, a simplified expression for the velocity amplitude of the j th structural mode is obtained as

$$V_j \approx H_{sj} \sum_{i=1}^N B_{j,i} H_{ai} \int_{V_0} q \Phi_i dV \left/ \left(1 + H_{sj} A_s \sum_{i=1}^N H_{ai} B_{j,i}^2 \right) \right. \quad (33)$$

Equation (33) is equivalent to setting all nondiagonal terms in the velocity transfer matrix in Eq. (8) (i.e., the matrix which is to be inverted) to zero. Using Eqs. (13) and (14) for H_{ai} and H_{sj} to expand Eq. (33), it can be shown that

$$V_j \approx - \frac{(\omega \rho_0 c_0)^2 A_s}{M_{sj} \{ [(\omega_{sj}^c)^2 - \omega^2] + j \eta_{sj}^c \omega_{sj}^2 \}} \times \sum_{i=1}^N \frac{B_{j,i} \int_{V_0} q \Phi_i dV}{M_{ai} [(\omega_{ai}^c - \omega)^2 + j \eta_{ai} \omega_{ai}^2]}, \quad (34)$$

where

$$(\omega_{sj}^c)^2 = \omega_{sj}^2 - \frac{(A_s \rho_0 c_0)^2 \omega}{M_{sj}} \sum_{i=1}^N \frac{B_{j,i}^2}{\Delta \omega_{ai}^{3dB} M_{ai}} \left[\frac{\epsilon_{ai}}{\epsilon_{ai}^2 + 1} \right], \quad (35)$$

$$\eta_{sj}^c = \eta_{sj} + \frac{(A_s \rho_0 c_0)^2 \omega}{M_{sj} \omega_{sj}^2} \sum_{i=1}^N \frac{B_{j,i}^2}{\Delta \omega_{ai}^{3dB} M_{ai}} \left[\frac{1}{\epsilon_{ai}^2 + 1} \right]. \quad (36)$$

$\Delta \omega_{ai}^{3dB} = \eta_{ai} \omega_{ai}$ is the half-power bandwidth of the uncoupled i th acoustic mode. ω_{sj}^c is the coupled or effective resonance frequency and η_{sj}^c is the effective loss factor of the j th structural mode. If the i th acoustic mode is proximately excited such that

$$|\omega_{ai} - \omega| < \frac{1}{2} \Delta \omega_{ai}^{3dB}, \quad (37)$$

then it can be shown that the ratio of difference between resonance and excitation frequencies to damping of the i th acoustic mode in Eqs. (35) and (36) is

$$\epsilon_{ai} \approx 2(\omega_{ai} - \omega) / \Delta \omega_{ai}^{3dB}. \quad (38)$$

A similar explanation as for the proximate excitation of structural modes in the sound field response section holds for Eqs. (37) and (38). It will also be assumed that $\omega_{sj}^c \approx \omega_{sj}$ for medium- and high-frequency analyses where the effect of structural modal resonance frequency shifts on the structural vibration response is insignificant. Using this approximation in Eq. (34), Eq. (10) can be written as

$$\langle \bar{v}^2 \rangle = \frac{(\rho_0 c_0)^4 (\omega A_s)^2}{2 m_s} \times \sum_{j=1}^M \frac{F_j^D(\omega) + F_j^C(\omega)}{M_{sj} [(\omega_{sj}^2 - \omega^2)^2 + (\eta_{sj}^c \omega_{sj}^2)^2]}, \quad (39)$$

where the direct modal excitation function for the j th structural mode is

$$F_j^D(\omega) = \sum_{i=1}^N \frac{[B_{j,i} \omega]^2 [\int_{V_0} q \Phi_i dV] [\int_{V_0} q^* \Phi_i dV]}{M_{ai}^2 [(\omega_{ai}^2 - \omega^2)^2 + (\eta_{ai} \omega_{ai}^2)^2]} \quad (40)$$

and the cross-modal excitation function for the j th structural mode is

$$F_j^C(\omega) = 2 \sum_{i=1}^{N-1} \sum_{k=i+1}^N \frac{B_{j,i} B_{j,k} [\int_{V_0} q \Phi_i dV] [\int_{V_0} q^* \Phi_k dV]}{M_{ai} M_{ak}} \frac{\omega^2 [(\omega_{ai}^2 - \omega^2)(\omega_{ak}^2 - \omega^2) + (\eta_{ai} \eta_{ak} \omega_{ai}^2 \omega_{ak}^2)]}{[(\omega_{ai}^2 - \omega^2)^2 + (\eta_{ai} \omega_{ai}^2)^2][(\omega_{ak}^2 - \omega^2)^2 + (\eta_{ak} \omega_{ak}^2)^2]}. \quad (41)$$

Neglecting only F_j^C in Eq. (39) and averaging the structural velocity over a frequency band, the bandlimited time- and space-averaged mean-square structural velocity is

$$\langle \bar{v}^2 \rangle_{\Delta\omega} = \frac{(\rho_0 c_0)^4 A_s^2}{2 m_s \Delta\omega} \sum_{j=1}^M \frac{1}{M_{sj}} \sum_{i=1}^N \frac{B_{j,i}^2 [\int_{V_0} q \Phi_i dV] [\int_{V_0} q^* \Phi_i dV]}{M_{ai}^2} \times \int_{\Delta\omega} \frac{\omega^4}{[(\omega_{sj}^2 - \omega^2)^2 + (\bar{\eta}_{sj}^c \omega_{sj}^2)^2][(\omega_{ai}^2 - \omega^2)^2 + (\eta_{ai} \omega_{ai}^2)^2]} d\omega, \quad (42)$$

where

$$\bar{\eta}_{sj}^c = \bar{\eta}_{sj} + \frac{(A_s \rho_0 c_0)^2 \omega_0}{M_{sj} \omega_{sj}^2} \sum_{i=1}^N \frac{B_{j,i}^2}{\Delta \omega_{ai}^{3\text{dB}} M_{ai}} \left[\frac{1}{\bar{\epsilon}_{ai} + 1} \right], \quad (43)$$

$$\bar{\epsilon}_{ai} = 2(\omega_{ai} - \omega_0) / \Delta \omega_{ai}^{3\text{dB}}. \quad (44)$$

$\bar{\eta}_{sj}$ and $\bar{\eta}_{sj}^c$ are, respectively, the band-averaged uncoupled and effective loss factors of the j th structural mode. In the above, η_{sj}^c is defined to be evaluated at the band center frequency ω_0 . Analytical solution to the integral in Eq. (42) can be obtained as

$$\int_{\Delta\omega} = I_1(\omega_U, \omega_{ai}, \omega_{sj}, \eta_{ai}, \bar{\eta}_{sj}^c) - I_1(\omega_L, \omega_{ai}, \omega_{sj}, \eta_{ai}, \bar{\eta}_{sj}^c) + I_2(\omega_U, \omega_{ai}, \omega_{sj}, \eta_{ai}, \bar{\eta}_{sj}^c) - I_2(\omega_L, \omega_{ai}, \omega_{sj}, \eta_{ai}, \bar{\eta}_{sj}^c), \quad (45)$$

where

$$I_1(\omega, \omega_{ai}, \omega_{sj}, \eta_{ai}, \bar{\eta}_{sj}^c) = \frac{(c_{j,i} A_{sj} + d_{j,i} B_{sj})}{2(A_{sj}^2 + B_{sj}^2)} \ln \left[\frac{(\omega + A_{sj})^2 + B_{sj}^2}{(\omega - A_{sj})^2 + B_{sj}^2} \right] + \frac{(c_{j,i} B_{sj} - d_{j,i} A_{sj})}{2(A_{sj}^2 + B_{sj}^2)} \times \tan^{-1} \left[\frac{4B_{sj}\omega(\omega^2 - A_{sj}^2 - B_{sj}^2)}{(\omega^2 - A_{sj}^2 - B_{sj}^2)^2 - (2B_{sj}\omega)^2} \right], \quad (46)$$

$$I_2(\omega, \omega_{ai}, \omega_{sj}, \eta_{ai}, \bar{\eta}_{sj}^c) = \frac{(e_{j,i} C_{ai} + f_{j,i} D_{ai})}{2(C_{ai}^2 + D_{ai}^2)} \ln \left[\frac{(\omega + C_{ai})^2 + D_{ai}^2}{(\omega - C_{ai})^2 + D_{ai}^2} \right] + \frac{(e_{j,i} D_{ai} - f_{j,i} C_{ai})}{2(C_{ai}^2 + D_{ai}^2)} \times \tan^{-1} \left[\frac{4D_{ai}\omega(\omega^2 - C_{ai}^2 - D_{ai}^2)}{(\omega^2 - C_{ai}^2 - D_{ai}^2)^2 - (2D_{ai}\omega)^2} \right], \quad (47)$$

$$A_{sj} = \omega_{sj} \sqrt{(1 + \sqrt{1 + \bar{\eta}_{sj}^c})/2} \quad (48a)$$

$$\approx \omega_{sj} \quad \text{if } \bar{\eta}_{sj}^c \ll 1, \quad (48b)$$

$$B_{sj} = \omega_{sj} \sqrt{(\sqrt{1 + \bar{\eta}_{sj}^c} - 1)/2} \quad (49a)$$

$$\approx \bar{\eta}_{sj}^c \omega_{sj} / 2 \quad \text{if } \bar{\eta}_{sj}^c \ll 1, \quad (49b)$$

$$C_{ai} = \omega_{ai} \sqrt{(1 + \sqrt{1 + \eta_{ai}^2})/2} \quad (50a)$$

$$\approx \omega_{ai} \quad \text{if } \eta_{ai} \ll 1, \quad (50b)$$

$$D_{ai} = \omega_{ai} \sqrt{(\sqrt{1 + \eta_{ai}^2} - 1)/2} \quad (51a)$$

$$\approx \eta_{ai} \omega_{ai} / 2 \quad \text{if } \eta_{ai} \ll 1, \quad (51b)$$

$$c_{j,i} = -2 \eta_{ai} \bar{\eta}_{sj}^c \omega_{ai}^2 \omega_{sj}^2 [\omega_{ai}^2 (1 + \eta_{ai}^2) - \omega_{sj}^2 (1 + \bar{\eta}_{sj}^c)] / G_{j,i}, \quad (52)$$

$$d_{j,i} = \frac{\eta_{ai} \omega_{sj}^2 \{ \omega_{sj}^4 (1 + \bar{\eta}_{sj}^c)^2 + \omega_{ai}^2 [\omega_{ai}^2 (1 + \eta_{ai}^2) (1 - \bar{\eta}_{sj}^c) - 2 \omega_{sj}^2 (1 + \bar{\eta}_{sj}^c)] \}}{G_{j,i}}, \quad (53)$$

$$e_{j,i} = -c_{j,i}, \quad (54)$$

$$f_{j,i} = \frac{\bar{\eta}_{sj}^c \omega_{ai}^2 \{ \omega_{ai}^4 (1 + \eta_{ai}^2)^2 + \omega_{sj}^2 [\omega_{sj}^2 (1 - \eta_{ai}^2) (1 + \bar{\eta}_{sj}^c) - 2 \omega_{ai}^2 (1 + \eta_{ai}^2)] \}}{G_{j,i}}, \quad (55)$$

$$G_{j,i} = 2 \eta_{ai} \bar{\eta}_{sj}^c \{ \omega_{ai}^8 (1 + \eta_{ai}^2)^2 + \omega_{sj}^8 (1 + \bar{\eta}_{sj}^c)^2 - 2 \omega_{ai}^2 \omega_{sj}^2 [2(\omega_{ai}^2 - \omega_{sj}^2)^2 + 2(\eta_{ai}^2 \omega_{ai}^4 + \bar{\eta}_{sj}^c \omega_{sj}^4) + \omega_{ai}^2 \omega_{sj}^2 (1 - \eta_{ai}^2)(1 - \bar{\eta}_{sj}^c)] \} \quad (56a)$$

$$\approx 2 \eta_{ai} \bar{\eta}_{sj}^c \omega_{sj}^8 (\eta_{ai}^2 - \bar{\eta}_{sj}^c)^2 \quad \text{if } \omega_{ai} \approx \omega_{sj}. \quad (56b)$$

Values of inverse tangent terms in Eqs. (46) and (47) also vary from 0 to 2π .

II. NUMERICAL RESULTS AND DISCUSSION

Some numerical examples for a panel-cavity system used in Ref. 2 are presented in this section to validate the present model. The system consists of a rectangular simply supported aluminum panel backed by a rectangular parallelepiped acoustic cavity of dimensions (0.868, 1.150, 1.000) m with slightly absorptive walls. The panel is located at $z = 1.000$ m and a monopole sound source located at the origin of the coordinates, $(x, y, z) = (0, 0, 0)$ m is used to drive the sound field inside the cavity. This acoustic-structural coupled system is used because of the convenience in obtaining the *in-vacuo* panel modal details and the rigid wall (uncoupled) cavity modal details theoretically. However, the use of the derived analytical expressions for bandlimited response is not restricted to this kind of system with simple geometry. For structure and cavity with complicated shapes, numerical techniques can be used to first obtain the respective *in-vacuo* and rigid wall modal information²¹ and then the present approach can be used to include the coupling effect into the analysis of the system response.

Theoretical expressions for uncoupled modal resonance frequencies, loss factors, and mode shapes of the panel and cavity used here are provided in Ref. 22. For a steady-state harmonic monopole source,

$$q = Q_p \delta(\mathbf{r} - \mathbf{r}_0) e^{j(\omega t + \gamma)}, \quad (57)$$

where Q_p is the peak source strength. γ is the initial phase, $\delta(\mathbf{r} - \mathbf{r}_0)$ is a dirac delta function, and \mathbf{r}_0 is the location vector of the source inside the cavity. Substituting Eq. (57) into (23) and (42), we obtained

$$\langle \bar{p}^2 \rangle_{\Delta\omega} = \frac{\langle \bar{s} \rangle_{\Delta\omega} \rho_0^3 c_0^4}{2V_0} \sum_{i=1}^N \frac{\Phi_i^2(\mathbf{r}_0)}{M_{ai}} [I(\omega_U, \omega_{ai}, \bar{\eta}_{ai}^c) - I(\omega_L, \omega_{ai}, \bar{\eta}_{ai}^c)], \quad (58)$$

$$\begin{aligned} \langle \bar{v}^2 \rangle_{\Delta\omega} = & \frac{\langle \bar{s} \rangle_{\Delta\omega} (\rho_0 c_0)^4 A_s^2}{2m_s} \sum_{j=1}^M \frac{1}{M_{sj}} \sum_{i=1}^N \left[\frac{B_{j,i} \Phi_i(\mathbf{r}_0)}{M_{ai}} \right]^2 \\ & \times [I_1(\omega_U, \omega_{ai}, \omega_{sj}, \eta_{ai}, \bar{\eta}_{sj}^c) - I_1(\omega_L, \omega_{ai}, \omega_{sj}, \eta_{ai}, \bar{\eta}_{sj}^c) \\ & + I_2(\omega_U, \omega_{ai}, \omega_{sj}, \eta_{ai}, \bar{\eta}_{sj}^c) - I_2(\omega_L, \omega_{ai}, \omega_{sj}, \eta_{ai}, \bar{\eta}_{sj}^c)]. \end{aligned} \quad (59)$$

$\langle \bar{s} \rangle_{\Delta\omega} = Q_p^2 / \Delta\omega$ is the power spectral density of bandlimited noise emitted by the source.

Bandlimited sound-pressure level in the cavity and velocity level of the panel vibration predicted from Eqs. (58)

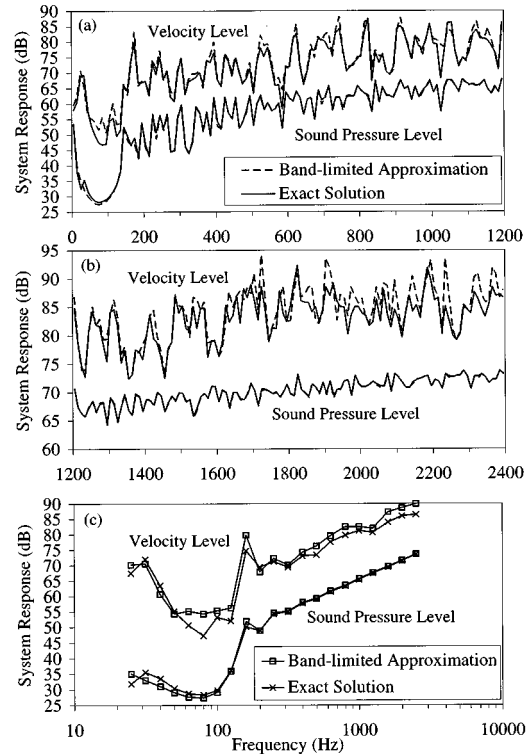


FIG. 1. System response for $Ta = 1.0$ s, $Tp = 0.4$ s, $h = 5.8$ mm, and $\Delta\omega = 9 \times 2\pi$ rad/s in (a) low-medium frequency regime, (b) medium-high frequency regime, and (c) 1/3-oct bands.

and (59) are shown in Fig. 1. The system response evaluated from the classical modal coupling method where full mathematical solutions are used, is also included for comparison. Sufficient acoustic and panel modes have been used in all calculations to avoid modal truncation errors. Analysis is done for narrow frequency bandwidths of 9 Hz. A panel with low modal density of 0.05788 Hz^{-1} (or panel thickness, $h = 5.8$ mm) is used and averaged modal decay times of the acoustic and panel modes are, respectively, $Ta = 1.0$ s and $Tp = 0.4$ s. For the narrow-band excitation, acoustic modal decay time, and cavity dimensions used here, the Schroeder frequency²³ which indicates the starting of the high-frequency range of the uncoupled sound field is approximately 2000 Hz. Also, the starting of the medium frequency range of the sound field is defined at the frequency where acoustic modes start to overlap.²⁴ For this cavity, overlapping of two or more acoustic modes on average is observable in the uncoupled sound-field frequency response at about 800 Hz. This will correspond to the starting of the medium frequency range of the uncoupled sound field. For the panel modal density and modal decay time used here, the medium frequency range of the uncoupled panel starts at about 200 Hz.²⁴ In Fig. 1, two subfigures are used to cover the system response in the low-medium frequency range and the medium-high frequency range. The figures show fairly good agreements between the results predicted from the present method and the classical modal coupling method at medium frequencies. Figure 1(c) shows results in 1/3-oct bands. For the panel response, a good agreement is achieved in the 200-Hz frequency band and above while for the sound-field

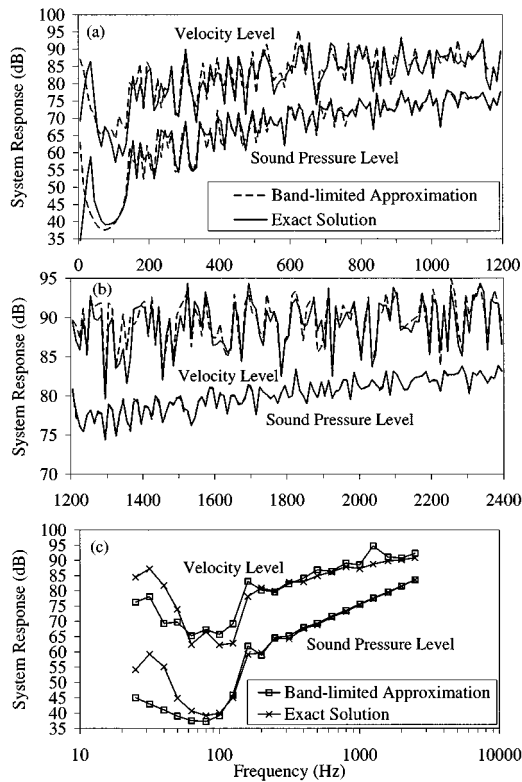


FIG. 2. System response for $Ta=1.0$ s, $Tp=1.0$ s, $h=1.0$ mm, and $\Delta\omega=9\times 2\pi$ rad/s in (a) low-medium frequency regime, (b) medium-high frequency regime, and (c) 1/3-oct bands.

response, a good agreement is achieved in almost all frequency bands.

In the second example, a panel with a high modal density of 0.336 Hz^{-1} ($h=1.0$ mm) and a modal decay time of 1.0 s is used. The system response evaluated using both the present method and the classical modal coupling method is shown in Fig. 2. There is now a larger number of panel mode distributed closer to the first few acoustic modes and the effect of coupling on the resonance frequency shift of both panel and acoustic modes becomes significant. In Fig. 2(a), there are distinguishable shifts in the resonance frequency of the first panel and acoustic modes in the system response obtained by the classical modal coupling method. However, these shifts have not been taken into account in the derivations of the present method and therefore are not shown in the predicted response. At frequencies away from the low-frequency range, the effect of resonance frequency shifts on the system response is insignificant as one deals with higher-order modes and thus the results agree well. Good agreements at medium and high frequencies between the results in Fig. 2 also indicate that the present method has a fairly good predictability with respect to variations in the modal densities of the panel as well as the cavity. The pronounced discrepancies between the panel responses obtained from both methods particularly at low frequencies (e.g., below 150 Hz) as observed in Figs. 1 and 2 are attributed to the negligence of cross-modal excitation of each structural mode [Eq. (41)] in the present method. On the other hand, the limited discrepancies observed in the 500-Hz frequency band and above in the 1/3-oct analysis are mainly attributed to the approxi-

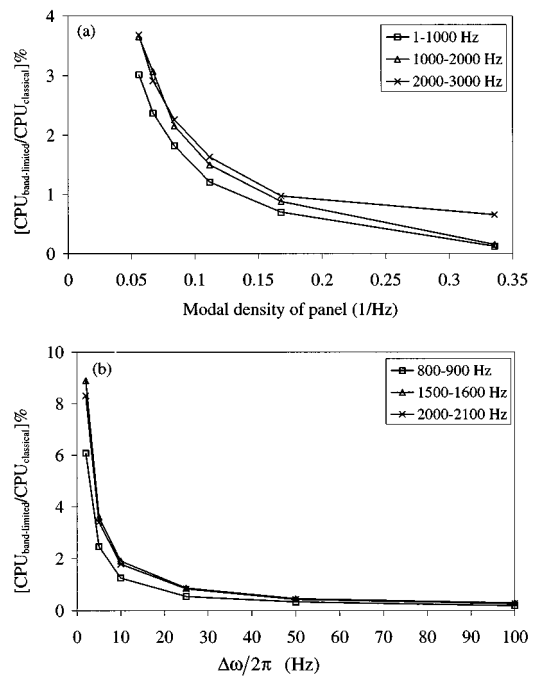


FIG. 3. Ratio of calculation time using the bandlimited model to calculation time using the classical modal coupling method for three frequency bands as (a) a function of panel modal density for 9-Hz frequency bandwidth and (b) a function of averaging frequency bandwidth for $h=3.0$ mm.

mation using band center frequencies to evaluate acoustic and panel effective loss factors [Eqs. (24) and (43)].

By using the present method, sound-pressure level prediction is distinguishably more accurate than velocity level prediction as can be seen in Figs. 1 and 2. The sound-field response is contributed by both the sound source and acoustic-panel coupling whereas the panel vibration directly obtains all its energy through coupling. However, in the previous section, all approximations were made towards the coupling effects for the convenience of mathematical formulation of the present method. Therefore any errors generated by the approximations will be shown directly in the velocity response while the errors may not be clearly shown in the pressure response because the contribution from the sound source is generally larger than that from the coupling. Furthermore, the number of approximations used in the derivation of the analytical solution to the bandlimited sound-pressure level is less than that for the velocity level.

The actual computational time for evaluating the coupled system response using the classical modal coupling method at 1-Hz steps has been recorded. Computational time using the present method has also been recorded. All calculations were performed on a DEC Alpha 3000 300X workstation. Figure 3(a) presents the percentage of actual calculation time used if the present method is used for prediction of bandlimited system response. The frequency bandwidth for averaging is 9 Hz and results are presented as a function of panel modal density for three different frequency bands. The computational time using the present method has been found to significantly improve when the panel modal density is increased because one has to deal with inversion of large complex matrices in Eqs. (7) and (8) if full mathematical

solutions of the classical modal coupling method are used. Figure 3(b) presents the results for three frequency bands as a function of the frequency bandwidth for averaging. In this example, $h=3.0$ mm. The computational efficiency using the present method is also improved significantly as the frequency bandwidth for averaging increases because calculations at each single frequency at 1-Hz step and subsequent frequency averaging for bandlimited response as used in the classical modal coupling method have been avoided. For example, 100 calculations are originally required in a 100-Hz band but only four calculations are required if analysis is performed in a bandwidth of 25 Hz or only one calculation if analysis is now performed in a bandwidth of 100 Hz. Therefore the computational time using the present method is shorter for broadband analysis than for narrow-band analysis.

III. JUSTIFICATIONS OF APPROXIMATIONS

In Sec. I B several approximations have been applied in the formulations of analytical expressions for bandlimited responses of acoustic-structural coupled systems without any justifications. For the enclosed sound field, the approximations are

- (1) negligence of acoustic modal cross-coupling terms,
- (2) negligence of shift in acoustic resonance frequency due to the coupling, i.e., $\omega_{ai}^c \approx \omega_{ai}$,
- (3) $\epsilon_{sj} = (\omega_{sj}^2 - \omega^2) / \eta_{sj} \omega_{sj}^2$ is approximated as $2(\omega_{sj} - \omega) / \Delta \omega_{sj}^{3\text{dB}}$ if the following condition is satisfied: $|\omega_{sj} - \omega| < \frac{1}{2} \Delta \omega_{sj}^{3\text{dB}}$,
- (4) $\bar{\eta}_{ai}^c$ is approximately evaluated at the band center frequency.

For the structure, the approximations are

- (1) negligence of structural modal cross-coupling terms,
- (2) negligible of shift in structural resonance frequency due to coupling, i.e., $\omega_{sj}^c \approx \omega_{sj}$,
- (3) $\epsilon_{ai} = (\omega_{ai}^2 - \omega^2) / \eta_{ai} \omega_{ai}^2$ is approximated as $2(\omega_{ai} - \omega) / \Delta \omega_{ai}^{3\text{dB}}$ if the following condition is satisfied: $|\omega_{ai} - \omega| < \frac{1}{2} \Delta \omega_{ai}^{3\text{dB}}$,
- (4) $\bar{\eta}_{sj}^c$ is approximately evaluated at the band center frequency,
- (5) negligence of cross-modal excitation of each structural mode.

Although some of the approximations used here are not new, it is still necessary to justify all approximations in order to obtain the significance of each approximation to the accuracy of response prediction using the present method. This is because any errors generated by the approximations may vary and in some cases, these errors are not attributed to all but only to a particular approximation depending on modal properties of the coupled system. The significance of each of the above approximation can be independently investigated by sequentially applying each approximation to exact solutions to the coupled system response from the classical modal coupling method.

A. Effect of acoustic and structural modal cross couplings

For enclosed sound-field response, it has been shown that cross coupling between various acoustic modes over locally reactive boundaries of an enclosure can be ignored if the equivalent specific acoustic impedance which represents the overall sound absorption property of all boundaries is in the order of 20.^{20,25} For the case of a modally reactive boundary as concerned here, acoustic and structural modal cross couplings are, respectively, insignificant to the sound field and structural response at medium frequencies or away from the first few low-order acoustic and structural modes.²⁶ This is because the cross couplings are strongly dependent on mode shape matching between acoustic and structural modes [see Eqs. (15) and (32)] and it can be shown that this matching which is measured by the modal coupling coefficient $B_{j,i}$ is only strong and significant for the first few system modes. Therefore the cross couplings can be reasonably neglected in the development of the present method for the medium frequency range. This approximation is well-adapted for the case of light fluid coupling.²⁷

B. Effect of shift in acoustic and structural resonance frequencies

The effect of acoustic-structural coupling on shift of resonance frequencies of acoustic modes has been studied by Pan and Bies.²² It has been shown that the effect of coupling on the shift is most significant for the first few acoustic modes. For the case of the structural response, change of structural resonance frequencies due to coupling has been found to be insignificant except for the first few volume-displacing structural modes which are well-coupled with the fundamental acoustic mode in terms of mode shape matching.²⁸ Therefore the effect of assuming $\omega_{ai}^c \approx \omega_{ai}$ and $\omega_{sj}^c \approx \omega_{sj}$ on the system response is insignificant at frequencies away from these modes.

C. Effect of approximation in ϵ_{ai} and ϵ_{sj}

The application of the approximation which concerns ϵ_{ai} and ϵ_{sj} was aimed to provide a useful physical description on the effect of excitation frequency on modal resonance frequency and loss factor of acoustic and structural modes. This approximation has been shown to have an insignificant effect on prediction accuracy at frequencies beyond the first few system modes.²⁶

D. Effect of adopting $\bar{\eta}_{ai}^c$ and $\bar{\eta}_{sj}^c$

The effect of adopting $\bar{\eta}_{ai}^c$ and $\bar{\eta}_{sj}^c$ on the prediction accuracy of the present method is directly related to the prediction accuracy in the effective loss factors. Figure 4 shows an example of variation of effective loss factors of cavity mode (2,4,9) and panel mode (5,11) with frequency in a medium frequency band for the coupled system which was used in Sec. II. In contrast to the low-frequency range, there is a lot of panel-cavity modal coupling pair at medium frequencies and therefore variation of the panel and cavity effective loss factors with frequency becomes very irregular. It

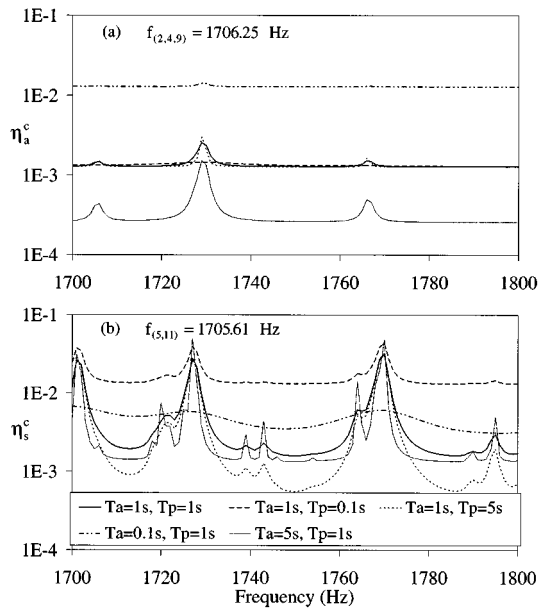


FIG. 4. Effective loss factor of mode (a) (2,4,9) and (b) (5,11) as a function of frequency for $h = 5.8$ mm and a number of different averaged panel and cavity modal decay times.

can be shown that other system modes at medium or high frequencies also exhibit such a feature. However, when the modal decay time of either the panel or cavity or both decrease, modal overlapping of the system increases and effective loss factors will vary more uniformly with frequency (e.g., see Fig. 4). In this case, approximated values of the effective loss factors can be reasonably evaluated at center frequencies and the use of these approximated values will produce smaller errors in the predicted system response than the case of highly fluctuating effective loss factors. Since the modal density of the cavity increases very fast with frequency, variation of effective loss factors of cavity modes with frequency is less irregular compared to variation of panel effective loss factors (e.g., see Fig. 4). This is because there is a large number of cavity mode dominating to the panel effective loss factors. Therefore the use of effective loss factors of cavity modes evaluated at center frequencies only produces small errors in the predicted sound field response whereas the use of panel effective loss factors evaluated at center frequencies can produce more distinguishable errors in the predicted panel response.

The system response is also analyzed as a function of $\Delta\omega$. Results have shown that discrepancies observed for broadbands such as that observed in the panel response in the 500-Hz 1/3-oct band and above in Figs. 1 and 2 are mainly associated with the approximation of evaluating panel effective loss factors at center frequencies. At medium frequencies, a broadband [for example, 100 Hz in Fig. 4(b)] covers a larger irregularity in variation of the effective loss factors than for the case of a narrow band (for example 10 Hz). Hence approximated values of the effective loss factors evaluated at the center frequency of the broadband can produce more distinguishable errors in the prediction of the system response than approximated values of the effective loss factors evaluated at the center frequency of the narrow band.

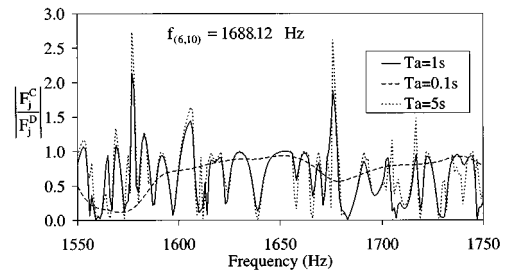


FIG. 5. Absolute ratio of a cross-modal to direct modal excitation function as a function of frequency for mode (6,10) for $h = 5.8$ mm and a number of different averaged cavity modal decay times.

E. Effect of cross-modal excitation of structural modes

The approximation of neglecting cross-modal excitation of structural modes is only applicable in the development of bandlimited structural velocity. Unlike the case for the sound field, the structure is only driven through modal coupling. Thus each structural mode is excited both directly through direct interaction with acoustic modes [described by Eq. (40)] and indirectly through the effect of mutual interaction between various acoustic modes [described by Eq. (41)]. The two forcing functions of the j th structural mode in Eqs. (40) and (41) (i.e., F_j^D and F_j^C) have the same general form as the frequency response function of a general structure excited either mechanically or by a random pressure field^{29,30} as well as of the enclosed sound field. Contribution of structural modal cross-products of the structural frequency response considered in Refs. 29 and 30 is negligibly small compared to the direct structural terms if the structure is lightly damped and/or natural frequencies of the structural modes are well-separated. This is actually analogous to ignoring acoustic cross products (i.e., the cross-modal excitation function, F_j^C) in our present case when acoustic modes of the enclosed sound field do not overlap. However, for analysis in the medium frequency range which is of interest here, acoustic modes start to overlap. Also discussions in Refs. 29 and 30 dealt with cross products in the structural frequency response function whereas in the present case, we deal with cross products in the forcing function of our structure. Thus some justifications are essential in order to explain the extent of significance of the cross-modal excitation to the predicted structural response.

The relative importance of the cross-modal excitation can be compared to the direct modal excitation. If the absolute ratio of F_j^C to F_j^D for any panel mode is approximately one or greater, then the cross-modal excitation of the panel mode is considered important. Figure 5 shows an example of the absolute ratio of F_j^C to F_j^D for panel mode (6,10). The corresponding variations of the excitation functions of the mode with frequency are presented in Fig. 6. Since F_j^C and F_j^D have the same general form as the frequency response function of the sound field [see Eqs. (40) and (41)], their variations with frequency are actually similar to the frequency response of the sound field. If the sound field is lightly damped then the ratio of F_j^C to F_j^D is highly fluctuating with frequency and the cross-modal excitation of the panel mode is only important within particular narrow band-

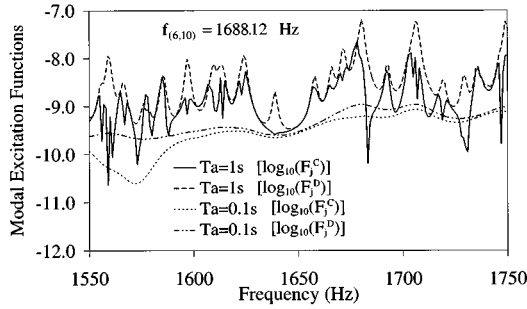


FIG. 6. Variation of cross-modal and direct modal excitation functions with frequency for mode (6,10) for $h = 5.8$ mm and two different averaged cavity modal decay times.

widths (e.g., $Ta = 1$ s or $Ta = 5$ s in Fig. 5). If the damping in the sound field is now increased (e.g., $Ta = 0.1$ s), overlapping of cavity modes increases and the ratio of F_j^C to F_j^D varies smoothly with frequency. The cross-modal excitation of the panel mode is also now becoming important over a broad frequency range. It can be shown that other panel modes also exhibit such a feature and thus the effect of neglecting the cross-modal excitation of each of those panel modes tends to easily superimpose. Therefore there is large error in the predicted panel velocity level over consecutive narrow medium frequency bands (e.g., see Fig. 8).

IV. CORRECTION TERMS

In the previous section, the fourth and fifth approximations have been identified to be the most significant to the prediction accuracy of system response using the present method. In this section, correction terms based on the above justifications are proposed in order to improve the prediction accuracy in the medium frequency range.

It has been shown that for cases where the structure and/or enclosed sound field is too lightly damped, η_{ai}^c and η_{sj}^c are highly fluctuating with frequency. Thus instead of evaluating $\bar{\eta}_{ai}^c$ and $\bar{\eta}_{sj}^c$ at the center frequency ω_0 , a band-averaged value of η_{ai}^c and η_{sj}^c is defined by integrating Eqs. (19) and (36) over the bandwidth $\Delta\omega$. It can be shown that

$$\bar{\eta}_{ai}^c = \bar{\eta}_{ai} + \frac{(A_s \rho_0 c_0)^2}{M_{ai} \omega_{ai}^2 \Delta\omega} \sum_{j=1}^M \frac{B_{j,i}^2}{M_{sj}} \times \int_{\Delta\omega} \frac{\omega^2}{(\omega_{sj}^2 - \omega^2)^2 + (\eta_{sj} \omega_{sj}^2)^2} d\omega, \quad (60)$$

$$\int_{\Delta\omega} = I(\omega_U, \omega_{sj}, \eta_{sj}) - I(\omega_L, \omega_{sj}, \eta_{sj}) \quad (61)$$

and

$$\bar{\eta}_{sj}^c = \bar{\eta}_{sj} + \frac{(A_s \rho_0 c_0)^2}{M_{sj} \omega_{sj}^2 \Delta\omega} \sum_{i=1}^N \frac{B_{j,i}^2}{M_{ai}} \times \int_{\Delta\omega} \frac{\omega^2}{(\omega_{ai}^2 - \omega^2)^2 + (\eta_{ai} \omega_{ai}^2)^2} d\omega, \quad (62)$$

$$\int_{\Delta\omega} = I(\omega_U, \omega_{ai}, \eta_{ai}) - I(\omega_L, \omega_{ai}, \eta_{ai}). \quad (63)$$

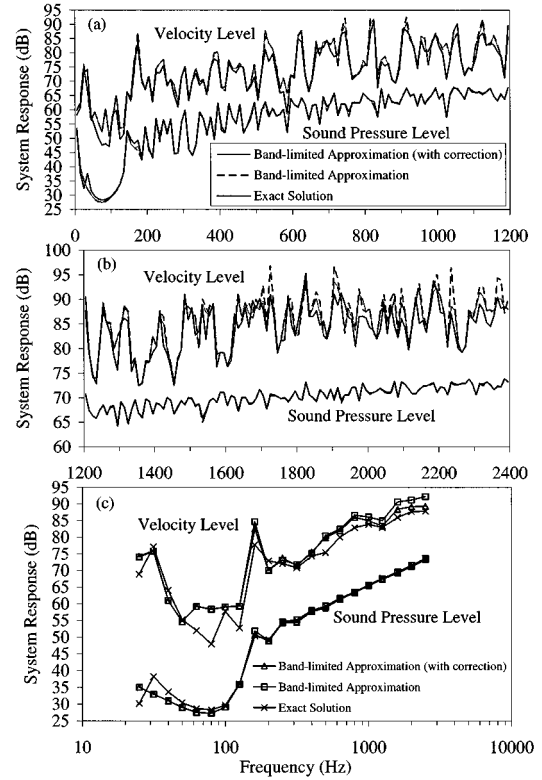


FIG. 7. System response with and without the fourth approximation and with correction term to the fourth approximation for $Ta = 1.0$ s, $Tp = 1.0$ s, $h = 5.8$ mm, and $\Delta\omega = 9 \times 2\pi$ rad/s in (a) low-medium frequency regime, (b) medium-high frequency regime, and (c) 1/3-oct bands.

The function I in Eqs. (61) and (63) can be, respectively, obtained from Eqs. (27) with all the corresponding coefficients evaluated from Eqs. (28) to (31) for ω_{sj} , η_{sj} and ω_{ai} , η_{ai} .

Figure 7 shows the system response for the panel-cavity system as used before for $Ta = 1.0$ s, $Tp = 1.0$ s, and $h = 5.8$ mm. Narrow-band results show that prediction errors in the system response are reduced when corrected $\bar{\eta}_{sj}^c$ and $\bar{\eta}_{ai}^c$ are used particularly at some peaks in the panel response at medium and high frequencies [Fig. 7(b)]. In the low-frequency range of the sound field, there are only a few cavity modes dominating to $\bar{\eta}_{sj}^c$ and thus the variation irregularity of effective loss factors of low-order panel modes is low. In this case, correction terms are not required because these can give no significant reduction in the prediction errors. For the case of 1/3-oct band analysis in Fig. 7(c), reduction in prediction errors in the panel response is shown to be achieved for the 500-Hz band and above where the broad frequency bandwidth covers a large variation irregularity of effective loss factor of higher-order panel modes [e.g., see Fig. 4(b)]. In all other bands where the irregularity for low-order panel modes is low, no significant improvements have been achieved and the correction terms are not required.

The fifth approximation has been shown to be significant if the modal overlap of the sound field is high. Because of the smooth variation of the cross-modal and direct modal excitation functions with frequency for high modal overlap of the sound field (e.g., see Fig. 6), these functions can be approximately evaluated at the band center frequency, i.e.,

$F_j^C(\omega_0)$ and $F_j^D(\omega_0)$. Combining these functions with some algebraic manipulation, Eq. (39) becomes

$$\langle \bar{v}^2 \rangle = \frac{(\rho_0 c_0)^4 (\omega A_s)^2}{2m_s} \times \sum_{j=1}^M \frac{K_j(\omega_0) K_j^*(\omega_0)}{M_{sj} [(\omega_{sj}^2 - \omega^2)^2 + (\eta_{sj}^c \omega_{sj}^2)^2]}, \quad (64)$$

where

$$K_j(\omega_0) = \sum_{i=1}^N \frac{B_{j,i} \omega_0 \int_{V_0} q \Phi_i dV}{M_{ai} [(\omega_{ai}^2 - \omega_0^2) + j \eta_{ai} \omega_{ai}^2]} \quad (65)$$

is a smooth function of frequency if the modal overlap of the sound field is high. The corrected bandlimited time- and space-averaged mean-square structural velocity can then be obtained by integrating Eq. (64) over the frequency bandwidth $\Delta\omega$:

$$\langle \bar{v}^2 \rangle_{\Delta\omega} = \frac{A_s^2 (\rho_0 c_0)^4}{2m_s} \sum_{j=1}^M \frac{K_j(\omega_0) K_j^*(\omega_0)}{M_{sj}} \times \int_{\Delta\omega} \frac{\omega^2}{(\omega_{sj}^2 - \omega^2)^2 + (\bar{\eta}_{sj}^c \omega_{sj}^2)^2} d\omega, \quad (66)$$

$$\int_{\Delta\omega} = I(\omega_U, \omega_{sj}, \bar{\eta}_{sj}^c) - I(\omega_L, \omega_{sj}, \bar{\eta}_{sj}^c). \quad (67)$$

It can be obtained from Eq. (27) with all the corresponding coefficients evaluated from Eqs. (28) to (31) for ω_{sj} and $\bar{\eta}_{sj}^c$. The panel response for $Ta=0.1$ s, $Tp=1.0$ s, and $h=5.8$ mm is shown in Fig. 8. In the 1/3-oct analysis, the corrected panel velocity reduces prediction errors for frequency bands above 630 Hz [Fig. 8(c)] since both the direct and cross-modal excitation functions vary smoothly with frequency when the modal overlap of the sound field is high (e.g., see Fig. 6). For the bands below 160 Hz, the corrected panel velocity also improves the prediction accuracy due to smooth variation of those functions as there are no resonance cavity modes to couple with the dominant panel modes. In other bands, either no significant improvements in the prediction accuracy have been achieved or prediction errors become even larger. This is because either the direct or cross-modal excitation function or both cannot be evaluated at the center frequency when their variation is highly fluctuating with frequency due to low modal overlap of the sound field. In this case, correction terms are not required. Improved prediction accuracy can also be achieved for the case of narrow-band analysis [Fig. 8(a) and (b)] where variation irregularity of the functions is small within each narrow band.

V. CONCLUSIONS

An analytical method has been proposed in this paper for modeling the bandlimited response of acoustic-structural coupled systems without substantial computational effort. Manipulation of large complex matrices particularly at medium frequencies has been avoided and only a small fraction of the actual calculation time using the classical modal coupling method has been used. The present method can also be useful for the case of narrow-band excitations where there

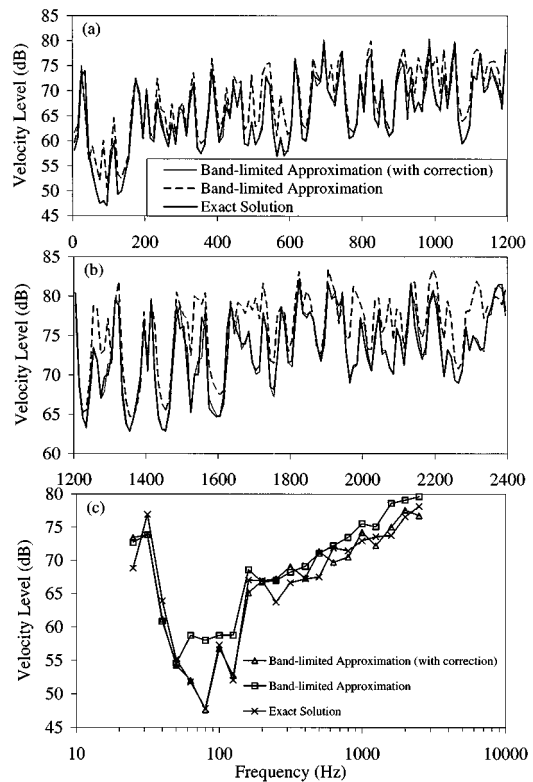


FIG. 8. System response with and without the fifth approximation and with correction term to the fifth approximation for $Ta=0.1$ s, $Tp=1.0$ s, $h=5.8$ mm, and $\Delta\omega=9 \times 2\pi$ rad/s in (a) low-medium frequency regime, (b) medium-high frequency regime, and (c) 1/3-oct bands.

are insufficient or even no resonance modes in the band for reliable estimates using statistical methods. Correction terms have been derived to improve prediction accuracy when prediction errors are either associated with the fourth approximation (evaluating acoustic and structural effective loss factors at band center frequencies) or the fifth approximation (negligence of structural cross-modal excitation in the modeling of structural response) or both. As a general criterion, correction terms are recommended for the medium frequency range as far as the fourth approximation is concerned if either the structure and/or enclosed sound field is too lightly damped and the averaged decay time of their modes is in the order of a second or higher. For the case of the fifth approximation, correction terms are recommended if the sound field modal overlap is high and is of that of the medium frequency range²⁴ or high-frequency range.

The case where the sound field is directly driven by an acoustic source and the structure is excited through acoustic-structural modal coupling has only been considered in this paper. Results for the case where the structure is directly excited by some external forces and the sound field is driven through coupling will be separately reported. Consideration will be given to problems of structure-borne sound where the sound field is subject to coupling with various vibrating structures. The analytical method proposed here can be further developed as a potential tool for medium frequency analysis and design of practical acoustic-structural coupled systems.

ACKNOWLEDGMENTS

Financial support from the Australia Research Council for this work is gratefully acknowledged. The second author would like to thank the Modern Acoustics Laboratory, Nanjing University for their financial support for his bandlimited energy flow project.

- ¹E. H. Dowell, G. F. Gorman, and D. A. Smith, "Acoustoelasticity: general theory, acoustic natural modes and forced response to sinusoidal excitation, including comparisons with experiment," *J. Sound Vib.* **52**, 519–542 (1977).
- ²J. Pan, "The forced response of an acoustic-structural coupled system," *J. Acoust. Soc. Am.* **91**, 949–956 (1992).
- ³P. M. Morse, "Standing waves of sound," in *Vibration and Sound* (American Institute of Physics, New York, 1976), Chap. 8.
- ⁴A. Pietrzyk, "Finite element modelling of low frequency air-borne sound transmission through building partitions," *Proceedings of the 15th International Congress on Acoustics* (TAPIR, Trondheim, Norway, 1995), pp. 149–152.
- ⁵F. Ramiandrasoa, M. A. Hamdi, and M. Haddar, "A subdomain decomposition method for large acoustic cavities," *Proceedings of Inter-Noise*, Liverpool, UK (Institute of Acoustics, London, 1996), pp. 2975–2978.
- ⁶M. Terao and H. Sekine, "A numerical analysis of sound field of a long space by a sub-region coupling approach," *Proceedings of Inter-Noise*, Liverpool, UK (Institute of Acoustics, London, 1996), pp. 3007–3010.
- ⁷W. Desmet, P. Sas, D. Vandepitte, and P. De Fonseca, "A new numerical technique for coupled vibro-acoustic predictions based on wave representation," *Proceedings of the 4th International Congress on Sound and Vibration*, St. Petersburg, Russia (1996), pp. 857–868.
- ⁸W. Desmet, P. Sas, and D. Vandepitte, "A new wave based prediction technique for coupled vibro-acoustic analysis: theoretical description and application to a double wall structure," *Proceedings of ISMA21, International Conference on Noise and Vibration Engineering*, Leuven, Belgium (1996), pp. 105–134.
- ⁹G. Maidanik, "Response of ribbed panels to reverberant acoustic fields," *J. Acoust. Soc. Am.* **34**, 809–826 (1962).
- ¹⁰F. J. Fahy, "Vibration of containing structures by sound in the contained fluid," *J. Sound Vib.* **10**, 490–512 (1969).
- ¹¹Y. Kubota, H. D. Dionne, and E. H. Dowell, "Asymptotic modal analysis and statistical energy analysis of an acoustic cavity," *J. Vib. Acoust. Stress Rel. Design*, **110**, 371–376 (1988).
- ¹²F. J. Fahy and A. D. Mohammed, "A study of uncertainty in applications of SEA to coupled beam and plate systems, Part I: computational experiments," *J. Sound Vib.* **158**, 45–67 (1992).
- ¹³M. W. Bonilha and F. J. Fahy, "A hybrid probabilistic-deterministic approach for vibroacoustic studies," *Proceedings of the 15th International Congress on Acoustics*, Trondheim, Norway (TAPIR, Trondheim, Norway, 1995), pp. 483–486.
- ¹⁴D. Trentin and J. L. Guyader, "Vibration of a master plate with attached masses using modal sampling method," *J. Acoust. Soc. Am.* **96**, 235–245 (1994).
- ¹⁵J. L. Guyader, "Modal sampling method for the vibration study of systems of high modal density," *J. Acoust. Soc. Am.* **88**, 2269–2276 (1990).
- ¹⁶L. D. Pope and J. F. Wilby, "Bandlimited power flow into enclosures," *J. Acoust. Soc. Am.* **62**, 906–911 (1977).
- ¹⁷L. D. Pope and J. F. Wilby, "Bandlimited power flow into enclosures. II," *J. Acoust. Soc. Am.* **67**, 823–826 (1980).
- ¹⁸S. H. Crandall and W. D. Mark, *Random Vibration in Mechanical Systems* (Academic, New York, 1963).
- ¹⁹T. Fang and Z. Wang, "Mean square response to band-limited white noise excitation," *AIAA J.* **24**, 860–862 (1986).
- ²⁰J. Pan and S. J. Elliott, "Analysis of sound field response in a damped rectangular enclosure for active control of noise," *Institute of Sound and Vibration Research Technical Memorandum No. 763*, University of Southampton (1995).
- ²¹S. H. Sung and D. J. Nefske, "A coupled structural-acoustic finite element model for vehicle interior noise analysis," *J. Vib. Acoust. Stress Rel. Design* **106**, 314–318 (1984).
- ²²J. Pan and D. A. Bies, "The effect of fluid-structural coupling on sound waves in an enclosure—Theoretical part," *J. Acoust. Soc. Am.* **87**, 691–707 (1990).
- ²³M. R. Schroeder and K. H. Kuttruff, "On frequency response curves in rooms. Comparison of experimental, theoretical, and Monte Carlo results for the average frequency spacing between maxima," *J. Acoust. Soc. Am.* **34**, 76–80 (1962).
- ²⁴K. S. Sum and J. Pan, "A study of the medium frequency response of sound field in a panel-cavity system," *J. Acoust. Soc. Am.* (submitted).
- ²⁵J. Pan, "A second note on the prediction of sound intensity," *J. Acoust. Soc. Am.* **96**, 2141–2144 (1994).
- ²⁶K. S. Sum, Study of medium frequency characteristics of sound field in enclosures, Ph.D. thesis, Department of Mechanical and Materials Engineering, The University of Western Australia, 1998.
- ²⁷J. L. Guyader and B. Laulagnet, "Structural acoustic radiation prediction: expanding the vibratory response on a functional basis," *Appl. Acoust.* **43**, 247–269 (1994).
- ²⁸A. J. Pretlove, "Free vibrations of a rectangular panel backed by a closed rectangular cavity," *J. Sound Vib.* **2**, 197–209 (1965).
- ²⁹A. Powell, "On the fatigue failure of structures due to vibrations excited by random pressure fields," *J. Acoust. Soc. Am.* **30**, 1130–1135 (1958).
- ³⁰Y. K. Lin, "Linear continuous structures," in *Probabilistic Theory of Structural Dynamics* (McGraw-Hill, New York, 1967), Chap. 7.

Feedback vibration control of a flexible plate at audio frequencies by using a physical state-space approach

Kazuto Seto

Department of Mechanical Engineering, Nihon University, 1-8 Kanda Surugadai, Chiyodo-ku, Tokyo 101, Japan

Mingzhang Ren and Fumio Doi

Vibration Control Laboratory, Kyowa Metal Works Co., Ltd., Fukuura 1-1-1, Kanazawa-ku, Yokohama 236, Japan

(Received 11 January 1997; accepted for publication 9 October 1997)

A study on feedback control of the vibration of a clamped elastic plate in the audio frequency range is presented in this paper. The study is specified by a discretization method based on an inverse modal analysis approach, through which a new lumped parameter system can be established to represent the dynamics of the low-order modes of the actual structure. With the discrete model the standard linear quadratic optimal control theory can be formulated in physical state space to design a controller, that will be later implemented in experiments to control the real structure. As an illustration, a lumped parameter model with 9DOFs has been created for the clamped plate. It is demonstrated by experiments under both impulse excitation and stationary random excitation that the corresponding nine vibration modes of the plate are quite well controlled with a collocation of two electromagnetic actuators and five sensors. © 1998 Acoustical Society of America. [S0001-4966(98)01102-3]

PACS numbers: 43.40.Vn, 43.40.Dx [PJR]

INTRODUCTION

In recent years, active structure control has come to real application in some fields such as civil engineering where the active means of protective design of tall structures such as buildings and bridge towers against adverse environmental loads has prevailed.¹ However, the research of active vibration control for the purpose of reducing mechanical noise has not yet seen so many successful applications. The main obstacle perhaps is that the mechanical noise and vibration are often in fairly high frequency, which may present some difficulties, in viewing the capacity of the current control hardware and software. Nevertheless, the research and development of this active vibration control technique, also known as active structural acoustic control (ASAC),² has been experiencing concrete progress owing to the fast development of microprocessors and control algorithms.

Perhaps due to the fact that the initial motive of ASAC lies in abating aircraft interior noise³ or noise radiation from submarine hull, in which the information of primary excitation of the system can be obtained somehow, the feedforward control based on adaptive signal processing technique⁴ has been widely accepted and successfully used in structural acoustic control, as in the case of active noise control (ANC).⁵ On the other hand, it is only recently that the feedback control strategy, such as the modern control theory, that is well developed for control of dynamic systems has comparatively received more attention in active noise and structural acoustic control.⁶⁻¹⁰ In many practical cases structures are under broadband or random excitation, the modal radiation of mechanical system plays the main role in total noise radiation, which is in general proportional to the vibration level. Therefore, control of the vibration modes with high

radiation efficiency will almost certainly result in reduction in noise level. The modes with high radiation can be determined numerically or experimentally. Under this condition, the structural acoustic control problem can be simplified to a problem of vibration mode control. It seems appropriate to construct the modal control schemes by making use of the modern control theories based on the state-space approach.⁷⁻¹⁰ Unlike the adaptive feedforward control, which involves little knowledge of the dynamics of structures, the feedback methods using modern control theories, such as the linear quadratic optimal controller (LQ control), require the modeling of structure dynamics.

The feedback structure control has been well studied in theory,¹¹ while its implementation on the distributed systems often presents some difficulties. Most of the work in the literature pertaining to controlling the continuous structures is designed in modal space for obtaining a simple system matrix, such as the well-known independent modal-space control (IMSC).¹¹ The state variables are in modal space and not directly measurable, "mode analyzer" and "mode synthesizer"² or "mode filter" and "inverse mode filter"¹⁰ are therefore required to transform between the modal space and the physical space. It is not easy to estimate the state quantities in modal space accurately if more controlled modes are concerned, unless large number of sensors or distributed sensors are used.^{2,10} In a theoretical study,⁹ Wu *et al.* introduced a feedback control for duct acoustic system in physical state space, where the states were physically measurable quantities. The method was based on a finite difference discretization of the system, which was possible in the case in which the system (one-dimensional acoustic wave in duct) was analytically describable. In other cases such as elastic structures, however, it would face various difficulties.

In this paper, another approach is therefore considered. It is aimed at developing a more practical method that can be applied conveniently to actual control experiments, hence, the directly measurable state variables are preferred. For this purpose, a modeling method via a so-called inverse modal analysis approach has been established, through which one can create a lumped parameter model, to represent the dynamics of the low-order vibration modes of real mechanical system at the designed modeling points. As will be demonstrated in the following section, this lumped parameter model is not simply a modal truncation of the original system with distributed parameters, as often used;^{8,10,11} it is a “new” system with physical, lumped parameters. With this discrete model, the standard linear quadratic control law can be easily formulated in physical state space with the state variables being directly measurable, thus making it dispensable to use “mode analyzer” and “mode synthesizer” or the like as required by the modal-space approach.^{2,10,11} The controller designed on the discrete model will be implemented in actual system to control the real structure. This method is demonstrated in the present paper on a study of active structure-borne noise control of a clamped flexible steel plate, a fundamental subject that can find application in wide noise and vibration problems encountered in practice. A lumped physical parameter system with 9DOFs is created to represent the dynamics of 9 of the first 12 vibration modes of the plate. The suboptimal control,¹² rather than the standard LQ theory, is employed to design the control system, in order to reduce the number of sensors. With a collocation of five displacement sensors and two electromagnetic actuators, successful control results, irrespective of impulsive excitation or stationary random excitation, have been achieved in experiments that 9 of the first 12 vibration modes of the plate are quite well controlled. In viewing that the experimental investigations in this area are rather thin on the ground, as pointed out by Fuller *et al.*,² it is intended that this paper could also supply some helpful materials in this aspect.

I. MODELING

A. The principle

For a thin-plate structure, the harmonic bending vibration is governed by the following motion equation:¹³

$$L[x(r)] - \rho_s \omega^2 x(r) = p(r), \quad (1)$$

where $x(r)$ is the normal surface displacement, L is the operator governing the elastic forces in the structure, ρ_s is the surface density (mass per unit area), and $p(r)$ is mechanically applied force per unit area. Solving the corresponding eigenvalue problem of Eq. (1), one can obtain the eigen frequency, ω_n , and the eigenfunction, $\psi_n(r)$, which satisfy the following eigen equation

$$L[\psi_n(r)] - \rho_s \omega_n^2 \psi_n(r) = 0, \quad (2)$$

and the orthogonality condition

$$\int_S \rho_s \psi_n(r) \psi_m(r) dS = 0, \quad m \neq n. \quad (3)$$

The vibration displacement at any position on the structure surface can be obtained through the modal superposition method, namely,

$$x(r) = \sum_{n=1}^{\infty} X_n \psi_n(r), \quad (4)$$

where, X_n is called the modal participation factor.

From the above equations and with some manipulations, the frequency response function of the plate, exciting at point q and monitoring the response at point r , is obtained as

$$H_c(\omega) = \frac{x(r)}{f(q)} = \sum_{n=1}^{\infty} \frac{\psi_n(r) \psi_n(q)}{(\omega_n^2 - \omega^2) \Lambda_n}, \quad (5)$$

where

$$\Lambda_n = \int_S \rho_s \psi_n^2(r) dS \quad (6)$$

is the modal-generalized mass. This equation describes the dynamics of the undamped continuous system. Rewrite Eq. (5) as

$$\begin{aligned} H_c(\omega) &= \sum_{n=1}^N \frac{\psi_n(r) \psi_n(q)}{(\omega_n^2 - \omega^2) \Lambda_n} + \sum_{n=N+1}^{\infty} \frac{\psi_n(r) \psi_n(q)}{(\omega_n^2 - \omega^2) \Lambda_n} \\ &= H_{\text{low}}(\omega) + H_{\text{res}}(\omega), \end{aligned} \quad (7)$$

it is then clear that as far as the low frequency is concerned, say, $\omega \ll \omega_{N+1}$, the second term $H_{\text{res}}(\omega)$ is very small compared with $H_{\text{low}}(\omega)$, therefore

$$H_c(\omega) \approx H_{\text{low}}(\omega) = \sum_{n=1}^N \frac{\psi_n(r) \psi_n(q)}{(\omega_n^2 - \omega^2) \Lambda_n}. \quad (8)$$

This fact makes it possible to represent the low-frequency dynamics of the structure by its N modes in the concerned frequency range. Actually, all the current work concerning modal control of continuous systems with the state-space approach^{8,10} is based on this approximation, that is, the modal truncation. It should be noted here that the coordinates r and q refer to any position on the structure surface.

On the other hand, for a discrete system with N degree of freedoms, the free vibration with no damping can be formulated in a general form as

$$m_i \ddot{x}_i + \left(k_{i0} + \sum_{\substack{j=1 \\ j \neq i}}^N k_{ij} \right) x_i - \sum_{\substack{j=1 \\ j \neq i}}^N k_{ij} x_j = 0, \quad i = 1 \sim N, \quad (9)$$

or, written more compactly,

$$\mathbf{M} \ddot{\mathbf{x}} + \mathbf{K} \mathbf{x} = \mathbf{0}. \quad (10)$$

Here, x_i refers to the displacement of mass i , m_i is the i th mass, k_{i0} is the stiffness of the spring connecting the i th mass and the ground, and k_{ij} refers to the spring constant between the i th mass and the j th mass. \mathbf{M} is the physical mass matrix and \mathbf{K} is the physical stiffness matrix. It is not difficult to show that the frequency response function (compliance) from mass j to mass i takes the form

$$H_d(\omega) = \sum_{n=1}^N \frac{\phi_n(i) \phi_n(j)}{(\omega_n^2 - \omega^2) m_n}, \quad (11)$$

where ϕ_n is the n th modal vector of the system, which satisfies the following orthogonality equation:

$$\phi_n^T \mathbf{M} \phi_m = \begin{cases} 0, & m \neq n, \\ m_n, & m = n \end{cases} \quad (12)$$

or, in matrix form,

$$\Phi^T \mathbf{M} \Phi = \mathbf{m}, \quad (13)$$

where m_n is the n th modal mass, \mathbf{m} is the diagonal modal mass matrix and Φ is the modal matrix of the discrete system.

Equation (8) and Eq. (11) are in similar form, except that the spatial coordinates are different: The modal shape of the former is a smooth and continuous function over the whole structure surface, while that of the latter is a vector containing information only at N mass points. If one can choose N typical discrete points on the surface of the structure as modeling points, and assume proper lumped masses and stiffnesses at these points in such a way that the motion of these points can approximate the dynamics of the continuous structure, then one can make a lumped parameter model for the distributed dynamic system. It is evident that in choosing the modeling points, which is something like a spatial sampling, the following principles should be observed:

- (1) The modeling points should be located, as long as possible, at maximum deformation positions of the concerned modes. In other words, they should not be placed at nodes of these modes.
- (2) The least number of modeling points along one dimension of the structure should be the maximum number of the node lines of the concerned modes along this dimension, plus one. Otherwise, the spatial information of the structural modes cannot be reflected in the model.
- (3) It is better to coincide the modeling points with the nodes of the unconsidered high modes, that is, the modes $N+1$ and the higher in Eq. (7). This will benefit modeling accuracy and control design based on the lumped model.

Suppose N points on the structure have been chosen, following the above guidelines, to form a N DOF system by assuming N lumped masses at the modeling points, one spring between each two masses, and an elastic connection between each mass and the ground, the motion of the system can then be described by Eq. (9). Now the question is how to determine the physical parameters involved, that is, the masses and the spring constants.

Manipulating Eq. (13) yields

$$\mathbf{M} = (\Phi \mathbf{m}^{-1} \Phi^T)^{-1} = (\bar{\Phi} \bar{\Phi}^T)^{-1}, \quad (14)$$

where $\bar{\Phi}$ is the normalized modal matrix. This relationship indicates that if $\bar{\Phi}$ is known, then \mathbf{M} is determined. Comparing Eq. (8) and Eq. (11), it is reasonable to assign the normalized mode shape values of the real structure at the locations of modeling points, which can be obtained through numerical or experimental modal analysis, to that of the lumped system, that is

$$\bar{\phi}_n(i) = \bar{\psi}_n(r_i) = \psi_n(r_i) / \sqrt{\Lambda_n}; \quad (15)$$

here, r_i refers to the position of the i th modeling point on the structure. However, thus formed the matrix $\bar{\Phi}$ is not guaranteed to satisfy Eq. (14) where both sides should be diagonal. Usually some nonzero values, although small, exist in the off-diagonal positions of the matrix $\bar{\Phi} \bar{\Phi}^T$. This problem can be solved by modifying the initial matrix $\bar{\Phi}$ through a sensitivity analysis procedure in order to satisfy Eq. (14).

Suppose an initial modal matrix for the lumped system has been obtained, from Eq. (15), as $\bar{\Phi}$, and assume that there are p different nonzero components in the off-diagonal positions of the matrix $\bar{\Phi} \bar{\Phi}^T$, an error vector can be defined here that consists of these p components, namely,

$$\boldsymbol{\varepsilon} = \{\varepsilon_1 \ \varepsilon_2 \ \varepsilon_3 \ \cdots \ \varepsilon_p\}^T, \quad (16)$$

in which each error ε_i is a function of some modal shape components of the matrix $\bar{\Phi}$. Suppose there are, in total, q independent modal shape components involved in Eq. (16), then it is reasonable to write

$$\varepsilon_i = f_i(\phi_1, \phi_2, \dots, \phi_q) = f_i(\boldsymbol{\phi}), \quad (17)$$

where $\boldsymbol{\phi}$ is a newly defined ($q \times 1$) vector consisting of ϕ_j ($j=1-q$; here the subscript j is only a sequence number and has nothing to do with the mode order or the position label). The purpose is to modify these modal shape components ϕ_j in order that the errors ε_i approach zero. It should be pointed out here that in constituting the initial modal matrix $\bar{\Phi}$, if use has been made of the symmetry feature of the mode shapes, the number of p and q can be greatly reduced.

Define the modification of $\boldsymbol{\phi}$ as $\delta\boldsymbol{\phi}$, which is assumed to change the error vector from its initial value $\boldsymbol{\varepsilon}$ to 0, then the following equation stands:

$$\left[\frac{\partial \boldsymbol{\varepsilon}}{\partial \boldsymbol{\phi}} \right] \delta\boldsymbol{\phi} = 0 - \boldsymbol{\varepsilon} = -\boldsymbol{\varepsilon}, \quad (18)$$

where $\partial \boldsymbol{\varepsilon} / \partial \boldsymbol{\phi}$ is a $p \times q$ matrix called the sensitivity matrix whose elements are partial differentiation of the errors, ε_i ($i=1-p$), with respect to the mode shape components, ϕ_j ($j=1-q$), namely

$$\left[\frac{\partial \boldsymbol{\varepsilon}}{\partial \boldsymbol{\phi}} \right] = \begin{bmatrix} \frac{\partial \varepsilon_1}{\partial \phi_1} & \frac{\partial \varepsilon_1}{\partial \phi_2} & \cdots & \frac{\partial \varepsilon_1}{\partial \phi_q} \\ \frac{\partial \varepsilon_2}{\partial \phi_1} & \frac{\partial \varepsilon_2}{\partial \phi_2} & \cdots & \frac{\partial \varepsilon_2}{\partial \phi_q} \\ \vdots & \vdots & \cdots & \vdots \\ \frac{\partial \varepsilon_p}{\partial \phi_1} & \frac{\partial \varepsilon_p}{\partial \phi_2} & \cdots & \frac{\partial \varepsilon_p}{\partial \phi_q} \end{bmatrix}_{p \times q}.$$

The modification vector can be obtained from Eq. (18) as

$$\delta\boldsymbol{\phi} = \left[\frac{\partial \boldsymbol{\varepsilon}}{\partial \boldsymbol{\phi}} \right]^T \left(\left[\frac{\partial \boldsymbol{\varepsilon}}{\partial \boldsymbol{\phi}} \right] \left[\frac{\partial \boldsymbol{\varepsilon}}{\partial \boldsymbol{\phi}} \right]^T \right)^{-1} (-\boldsymbol{\varepsilon}), \quad (19)$$

and the new vector is calculated by

$$\boldsymbol{\phi} \leftarrow \boldsymbol{\phi} + \delta\boldsymbol{\phi}. \quad (20)$$

Usually an iterative calculation is necessary in this procedure in order that $\boldsymbol{\varepsilon}$ converges to 0. Substituting the newly obtained $\boldsymbol{\phi}$ into Eq. (17) yields a new error vector, and this new $\boldsymbol{\varepsilon}$ can be substituted into Eq. (19) to generate a new

modification vector. After a certain iteration that a preset accuracy has been reached, a final modified modal matrix can be obtained that will satisfy the diagonal condition of Eq. (14). Consequently, \mathbf{M} can be obtained, and the stiffness matrix \mathbf{K} can also be determined

$$\mathbf{K} = (\bar{\Phi}^T)^{-1} \mathbf{\Omega} \bar{\Phi}^{-1}, \quad (21)$$

where $\mathbf{\Omega}$ is a diagonal matrix whose nonzero elements are square of the natural frequencies of the concerned modes of the real structure.

The above procedure, that is, determining the physical parameters of the lumped parameter system from the available modal data of the distributed parameter system [Eqs. (14) and (21)], is termed an inverse modal analysis approach in this paper. The established lumped parameter model should be regarded as a new system, that is supposed to represent the low-order dynamics of the structure at the designed modeling points.

It should be mentioned that in Ref. 14 Ewins has explored the feasibility of constructing a spatial model from the modal model based on the inverted orthogonality equations (14) and (21). Aiming at a model with full structure dynamics, he pointed out that it is usually impractical to deduce the mass and stiffness matrixes directly from these equations, since it is much more usual to have an incomplete modal model in which the eigenvector matrix is rectangular and, as such, noninvertible. But in the method presented in the above, there would be no such rank deficiency problem, because this method does not aim at a complete model of the structure dynamics, only the finite low modes of the structure are of interest. For example, if one is dealing with N modes, then one can accordingly choose N modeling points, so that the modal matrix of the lumped parameter model is always square and, thus, invertible. Usually, the order of the lumped parameter model is much lower than that of the modal model of the structure from experimental or numerical modal analysis.

It also should be pointed out that structural damping has been neglected in the above derivation. One reason is that the main purpose of the discrete spatial model is to represent the eigenvalues and the eigenfunctions of the corresponding modes, which are more crucial for control design. Another reason is due to the difficulties in identifying the damping matrix in this approach, except for the assumption of proportional damping, which is more an academic solution than a practical method. Nevertheless, the damping effect can be considered somehow in control system design as described in Sec. II.

B. Discrete model of the plate

The above modeling method suggests that the first step for making a lumped parameter model is to obtain the modal shapes of the real structure by modal analysis methods. The clamped plate under study in this paper is covered onto a rectangular box for the convenience of studying the noise transmission problem, as shown in Fig. 1. Therefore, the plate is backed by an air cavity. Experimental modal analysis is carried out to obtain the mode shapes. By examining the

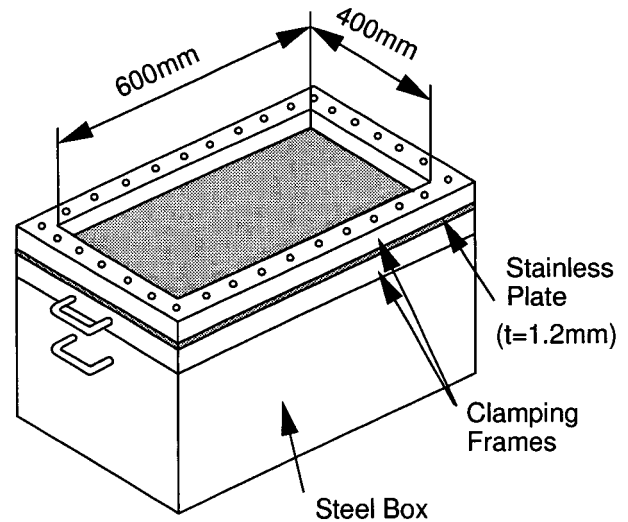


FIG. 1. The clamped plate and the supporting box.

modal shapes of the plate and following the guidelines for determining modeling points described in the previous section, it is decided that nine points on the plate surface are selected as modeling points, as shown in Fig. 2. (The mesh lines in this figure show the measurement points in experimental modal analysis. The peculiar numbering way results from an initial consideration that the first modeling point corresponds to the maximum deformation position of the first mode, the second point to the second mode, etc. It has no real meaning, and can be numbered in other ways.) The positions of these modeling points are clearly shown with small circles in Fig. 3, where node lines are used to roughly illustrate the first 12 mode shapes of the plate.

It should be mentioned that determination of the number and the position of the modeling points largely depends on how many and which modes are to be controlled. As stated in the introduction, ASAC can be simplified to an active vibration control (AVC) problem when only controlling those modes strongly coupled to the radiation field. The modeling points can be chosen in such a way that the modes with high radiation efficiencies are focused. (However, in the present paper we are concerned to control the vibration modes as many as possible.) In addition, it is presumed that the sensors and the actuators will be placed at these chosen modeling points; therefore, use of unobservability or uncon-

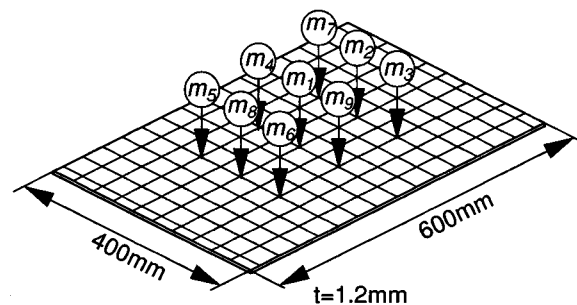


FIG. 2. The modeling points on the plate.

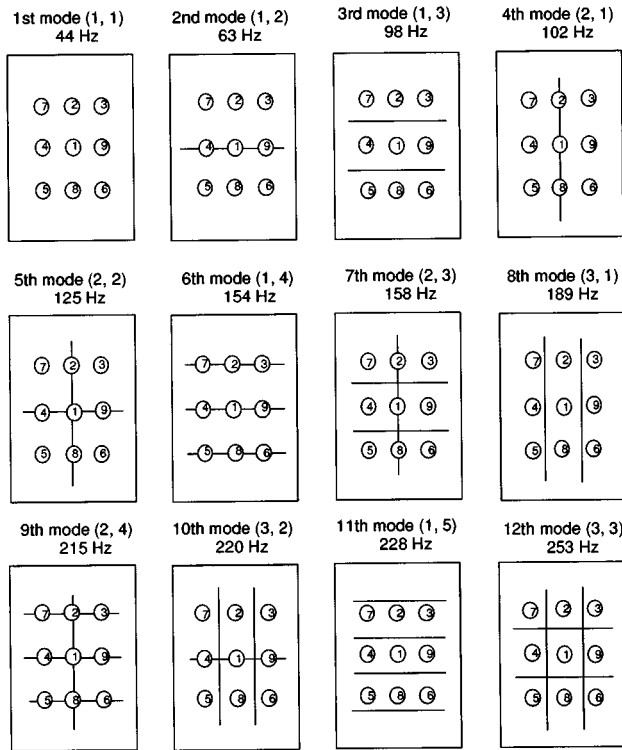


FIG. 3. The first 12 mode shapes illustrated by node lines. The circles and numbers refer to modeling points.

trollability for getting rid of influences of certain modes, preferably the omitted high modes, could also be considered at this stage.

Obviously, with this pattern of the modeling points, the sixth and the ninth modes are completely unobservable from the modeling points (this is not deliberately designed). Furthermore, the eleventh mode is not fully reflected as well. Nevertheless, nine other modes can be represented, that is, the first, second, third, fourth, fifth, seventh, eighth, tenth, and the twelfth mode, reaching to over 250 Hz. Given the number and location of the modeling points being determined, the physical parameters involved in setting up the lumped parameter model can be calculated following the inverse modal analysis approach described in the preceding section. This approach has been implemented into a piece of MATLAB (The MathWorks, Inc., MA) program. The lumped parameter system with 9DOFs is shown, intuitively, in Fig. 4. The lines in this figure refer to the springs, connecting each two masses, and each mass and the ground. The physical parameters (mass and spring constant) determined are not listed here for brevity.

II. CONTROL SYSTEM DESIGN

A. Optimal control in physical state space

Now that the lumped parameter model with nine DOFs has been established, which represents the dynamics of the nine modes of the plate of the concern; it is quite convenient to design a state feedback control system using the LQ theory on the basis of this discrete model, for the purpose of controlling the vibration of the real structure. In order to

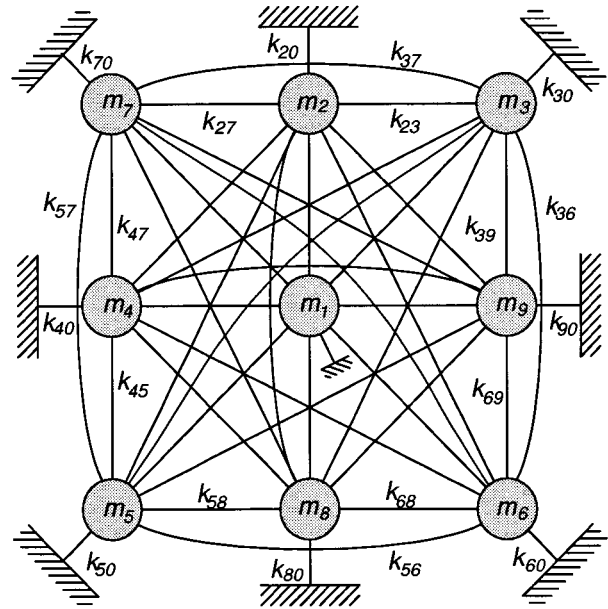


FIG. 4. The lumped parameter model with nine DOFs.

control all nine modes, two actuators are employed, that are supposed to be located at the mass points 1 and 3, respectively.

The motion equations of the 9DOF system with two electromagnetic actuators are as follows

$$m_1 \ddot{x}_1 + c \dot{x}_1 + \left(k_{10} + \sum_{j=1}^9 k_{1j} \right) x_1 - \sum_{j=2}^9 k_{1j} x_j = \lambda_f u_1, \quad (22a)$$

$$m_2 \ddot{x}_2 + \left(k_{20} + \sum_{j=1}^9 k_{2j} \right) x_2 - \sum_{j=1, j \neq 2}^9 k_{2j} x_j = 0, \quad (22b)$$

$$m_3 \ddot{x}_3 + \left(k_{30} + \sum_{j=1}^9 k_{3j} \right) x_3 - \sum_{j=1, j \neq 3}^9 k_{3j} x_j = \lambda_f u_3, \quad (22c)$$

$$m_i \ddot{x}_i + \left(k_{i0} + \sum_{j=1}^9 k_{ij} \right) x_i - \sum_{j=1, j \neq i}^9 k_{ij} x_j = 0, \quad i = 4-9, \quad (22d)$$

where u_1 and u_3 are the control signals of the two actuators, respectively, and λ_f is the voltage-force coefficient of the electromagnetic actuators. In deriving the lumped parameter model in the above section, the damping effect has been ignored. However, in the present study, the clamped plate is backed by an air cavity, which is found to have strong damping effect on the first mode of the plate. In addition, the electromagnetic actuators also exert passive damping to the plate. These damping effects, that mainly influence the first vibration mode of the plate, have been approximately accounted for by the measured damping coefficient c in Eq. (22a).

Define a state vector as

$$\mathbf{X} = [\dot{x}_1 \quad \dot{x}_2 \quad \cdots \quad \dot{x}_9 \quad x_1 \quad x_2 \quad \cdots \quad x_9]^T, \quad (23)$$

which consists of the physically measurable displacements and velocities at the modeling points of the real structure, the above motion equations can be denoted by the following state equation

$$\dot{\mathbf{X}} = \mathbf{A}\mathbf{X} + \mathbf{B}\mathbf{U}. \quad (24)$$

Here, the state matrix \mathbf{A} is given as

$$\mathbf{A} = \begin{bmatrix} -\mathbf{M}^{-1}\mathbf{C} & -\mathbf{M}^{-1}\mathbf{K} \\ \mathbf{I} & \mathbf{0} \end{bmatrix}, \quad (25)$$

where \mathbf{I} is a (9×9) unit matrix, $\mathbf{0}$ is a (9×9) null matrix, \mathbf{M} and \mathbf{K} are the physical mass matrix and stiffness matrix of the lumped parameter system, and \mathbf{C} is the damping matrix

$$\mathbf{C} = \text{diag}[c \ 0 \ 0 \ 0 \ 0 \ 0 \ 0 \ 0 \ 0].$$

The state matrix \mathbf{B} is

$$\mathbf{B} = \lambda_f \begin{bmatrix} \frac{1}{m_1} & 0 & 0 & 0 & 0 & 0 & 0 & 0 & 0 & 0 & 0 & 0 & 0 & 0 & 0 & 0 & 0 & 0 \\ 0 & 0 & \frac{1}{m_3} & 0 & 0 & 0 & 0 & 0 & 0 & 0 & 0 & 0 & 0 & 0 & 0 & 0 & 0 & 0 \end{bmatrix}^T. \quad (26)$$

The control signal matrix is

$$\mathbf{U} = [u_1 \ u_3]^T. \quad (27)$$

Based on the LQ control theory, this system can be optimally controlled as long as the quadratic performance index J reaches minimum

$$J = \int_0^\infty (\mathbf{X}^T \mathbf{Q} \mathbf{X} + \mathbf{U}^T \mathbf{R} \mathbf{U}) dt, \quad (28)$$

in which \mathbf{Q} is the state weighting matrix and \mathbf{R} is the control weighting matrix, both are diagonal matrixes. The corresponding control value is obtained as

$$\mathbf{U} = -\mathbf{R}^{-1} \mathbf{B}^T \mathbf{P} \mathbf{X} = -\mathbf{G} \mathbf{X}, \quad (29)$$

where \mathbf{G} is the feedback gain matrix and \mathbf{P} is the solution of the Riccati equation:

$$\mathbf{P} \mathbf{A} + \mathbf{A}^T \mathbf{P} - \mathbf{P} \mathbf{B} \mathbf{R}^{-1} \mathbf{B}^T \mathbf{P} + \mathbf{Q} = 0. \quad (30)$$

In order to reduce the sensor number required by the LQ control, the suboptimal control theory¹² is adopted here. Examining the modal shapes of the plate (see Fig. 3), it is possible to suppose only the state variables at five mass points (1, 3, 5, 6, and 7) being monitored for the feedback control. Set \mathbf{Z} being a substate vector representing those measured state variables in \mathbf{X} , then the following transformation stands:

$$\mathbf{Z} = \mathbf{S} \mathbf{X}, \quad (31)$$

$$\mathbf{S} = \begin{bmatrix} 1 & 0 & 0 & 0 & 0 & 0 & 0 & 0 & 0 & 0 & 0 & 0 & 0 & 0 & 0 & 0 & 0 & 0 \\ 0 & 0 & 1 & 0 & 0 & 0 & 0 & 0 & 0 & 0 & 0 & 0 & 0 & 0 & 0 & 0 & 0 & 0 \\ 0 & 0 & 0 & 0 & 1 & 0 & 0 & 0 & 0 & 0 & 0 & 0 & 0 & 0 & 0 & 0 & 0 & 0 \\ 0 & 0 & 0 & 0 & 0 & 1 & 0 & 0 & 0 & 0 & 0 & 0 & 0 & 0 & 0 & 0 & 0 & 0 \\ 0 & 0 & 0 & 0 & 0 & 0 & 1 & 0 & 0 & 0 & 0 & 0 & 0 & 0 & 0 & 0 & 0 & 0 \\ 0 & 0 & 0 & 0 & 0 & 0 & 0 & 0 & 1 & 0 & 0 & 0 & 0 & 0 & 0 & 0 & 0 & 0 \\ 0 & 0 & 0 & 0 & 0 & 0 & 0 & 0 & 0 & 0 & 1 & 0 & 0 & 0 & 0 & 0 & 0 & 0 \\ 0 & 0 & 0 & 0 & 0 & 0 & 0 & 0 & 0 & 0 & 0 & 0 & 1 & 0 & 0 & 0 & 0 & 0 \\ 0 & 0 & 0 & 0 & 0 & 0 & 0 & 0 & 0 & 0 & 0 & 0 & 0 & 0 & 1 & 0 & 0 & 0 \\ 0 & 0 & 0 & 0 & 0 & 0 & 0 & 0 & 0 & 0 & 0 & 0 & 0 & 0 & 0 & 1 & 0 & 0 \end{bmatrix}. \quad (32)$$

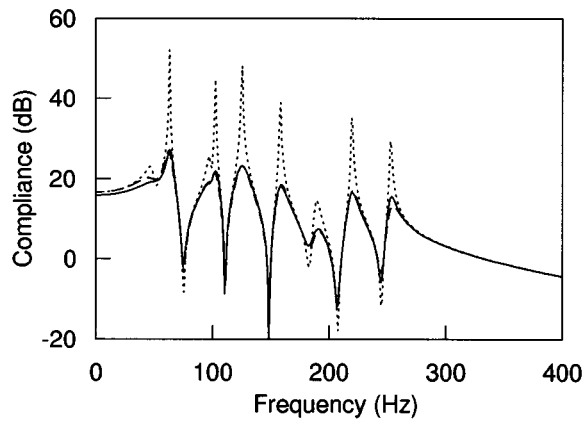
The control value thus can be expressed as

$$\mathbf{U} = -\mathbf{G}_s \mathbf{Z}, \quad (33)$$

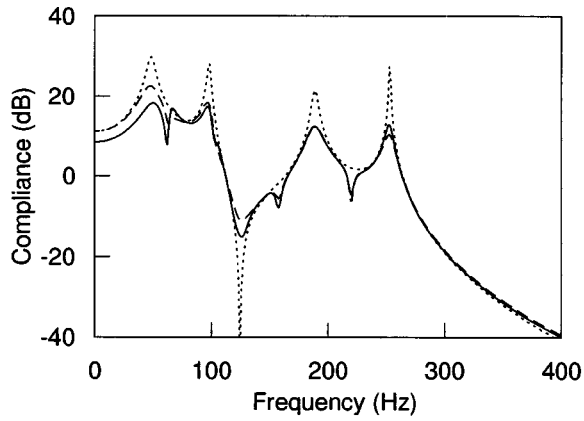
in which the suboptimal feedback gain \mathbf{G}_s can be determined by the minimum norm method¹² as follows:

$$\mathbf{G}_s = \mathbf{G} \mathbf{S}^T (\mathbf{S} \mathbf{S}^T)^{-1} \mathbf{S}. \quad (34)$$

It can be seen that with the use of the lumped parameter model, the controller design is very concise; no ‘‘mode analyzer’’ or ‘‘modal filter’’^{2,11} is required, making it quite con-



(a)



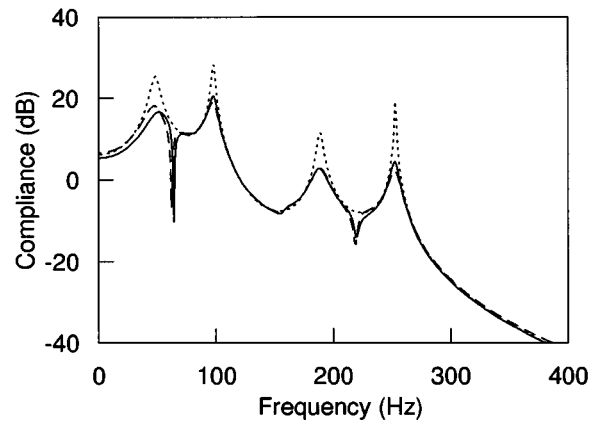
(b)

FIG. 5. The simulation results. Dotted line: without control; dashed line: with optimal control; solid line: with suboptimal control. (a) Excite and observe at mass point 3; (b) excite at mass point 1 and observe at mass point 3.

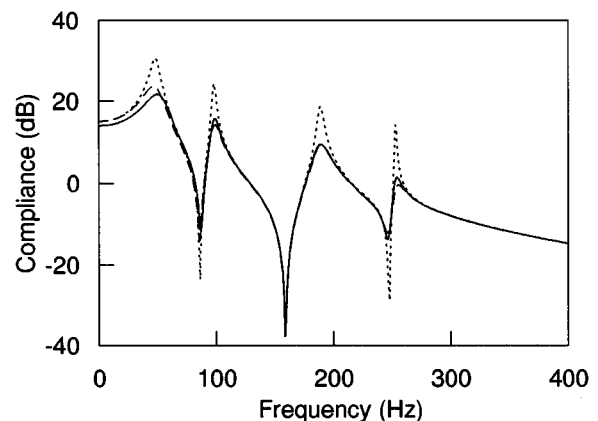
venient to manipulate in implementing a real control system. The damping effect of the mechanical system can also be considered somehow in this approach. The discrete system is designed to represent the dynamics of the low-order modes of the continuous system at the modeling points; the controller on the lumped parameter model is therefore capable of controlling the real system at these points. It goes without saying that in mode vibration, if a local point is controlled, global suppression can be achieved for the whole mode.

B. Numerical simulations

The numerical simulations of the discrete model are performed using MATLAB Control System Toolbox routines. In these simulations the values of the components that weight velocity terms in \mathbf{Q} are all taken as unity, while the components weighting displacements are taken as zero, since it has been examined by various simulations and experiments not mentioned in this paper that the weighting velocity terms seem more effective than weighting displacement terms or the both. The feedback gains are changed by adjusting the weighting matrix \mathbf{R} . The proper gains examined in simulation will be used in the experiments. Therefore, simulation is



(a)



(b)

FIG. 6. The simulation results. Dotted line: without control; dashed line: with optimal control; solid line: with suboptimal control. (a) Excite at mass point 2 and observe at mass point 1; (b) excite and observe at mass point 1.

not only a test of the model but also an indispensable procedure to prepare the feedback gains for the experiments. The values of \mathbf{R} used in this paper are 0.005.

In Fig. 5 are shown the calculated transfer functions (compliance) in the occasions when assuming an excitation at mass point 3 and picking up at the same point, and excit-

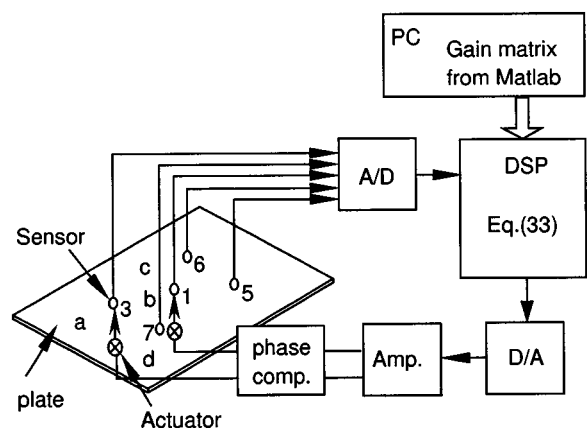


FIG. 7. The experimental setup.

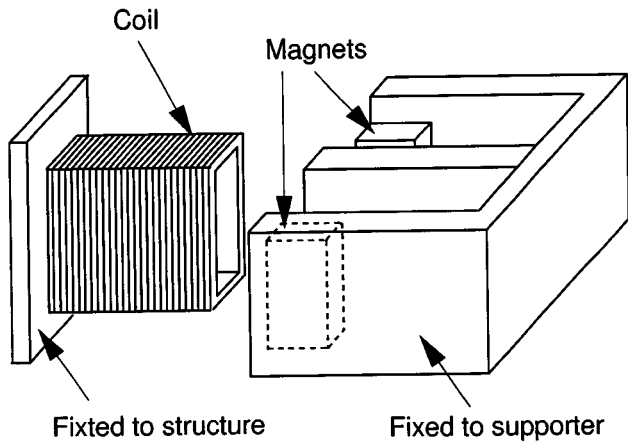


FIG. 8. The structure of the electromagnetic actuator.

ing at mass point 1 and picking up at mass point 3. In Fig. 6 are shown the occasions when exciting at mass point 2 and picking up at mass point 1, and exciting and picking up both at mass point 1. In these figures the dotted line refers to the system response without control (open loop); the dashed line

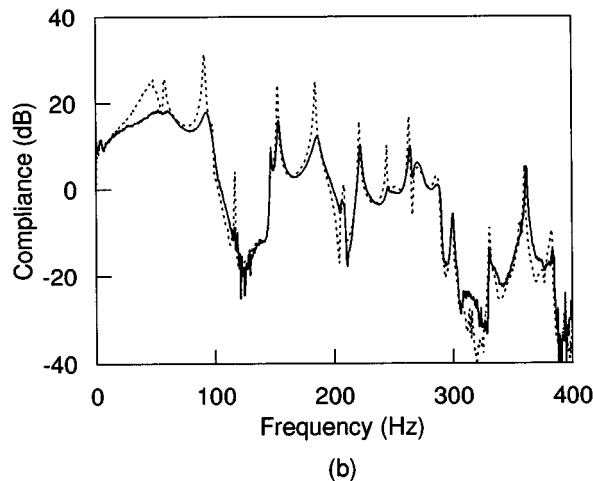
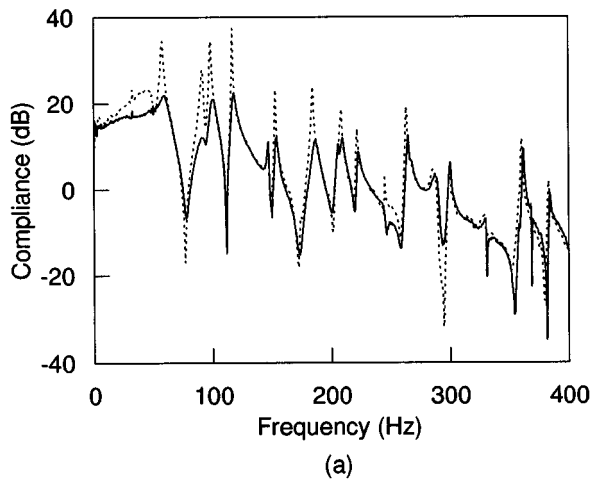


FIG. 9. The experimental results. Dotted line: without control; solid line: with control. (a) Excite near and pick up at modeling point 3; (b) excite near modeling point 1 and pick up at modeling point 3.

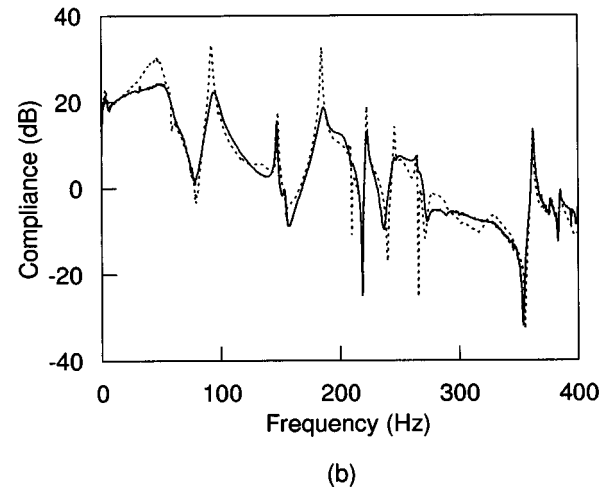
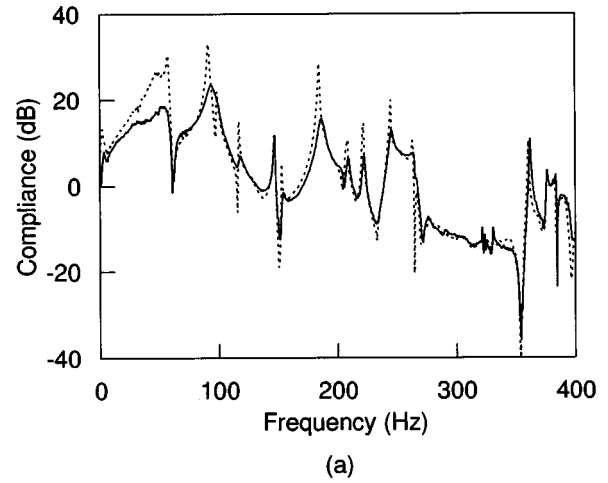
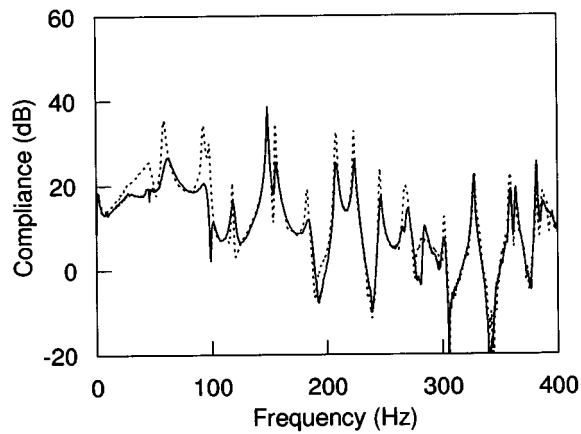


FIG. 10. The experimental results. Dotted line: without control; solid line: with control. (a) Excite near modeling point 2 and pick up at modeling point 1; (b) excite near and pick up at modeling point 1.

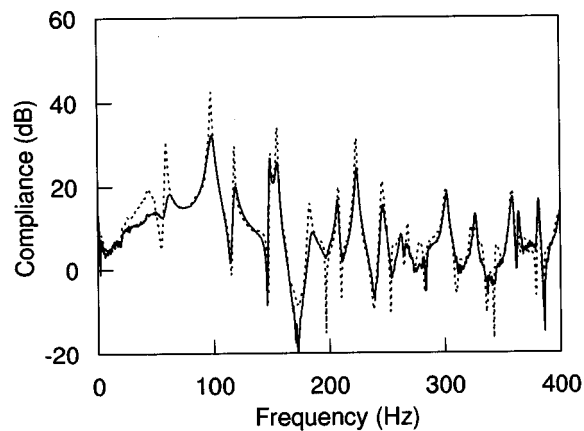
refers to that with LQ control and the solid line with suboptimal control (closed loop). Encouragingly, very good control results have been obtained, for all nine modes, by both the LQ control and the suboptimal control, as shown in these figures.

III. EXPERIMENTS

Experiments on the real structure are carried out to verify the discrete model and the control design. Five displacement sensors (at the modeling points 1, 3, 5, 6, and 7) and two electromagnetic actuators (fixed at the modeling points 1 and 3) are employed. By this collocation of sensors and actuators, 9 of the first 12 vibration modes of the plate, as depicted in Fig. 3, are expected to be controlled with the suboptimal control design. The velocities are not directly measured but estimated through the approximation differential of the displacements. A DSP device (TMS320C40) is used as the controller, and the sampling rate of A/D boards is set to be 0.01 ms (the reason for using such a high sampling rate, 100 KHz, can be found in Ref. 15). The feedback gains obtained on the discrete model in the numerical simulation are used to generate the control forces in the experiments [see Eq. (33)]. The experimental setup is illustrated in Fig. 7,



(a)

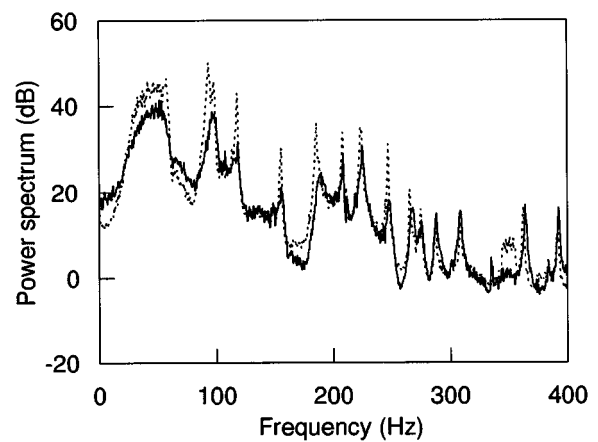


(b)

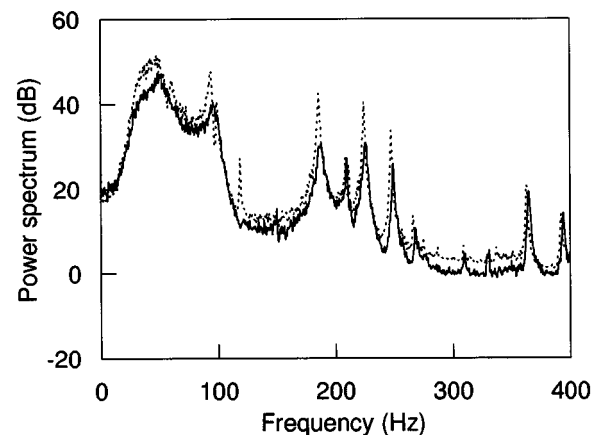
FIG. 11. The experimental results. Dotted line: without control; solid line: with control. (a) Excite at point *a* and pick up at point *b*; (b) excite at point *c* and pick up at point *d*.

and the structure of the electromagnetic actuator, through which both the passive damping and the active control force are applied to the plate, is depicted in Fig. 8. (The passive damping is always present no matter control on or off.) It should be mentioned here that in the control design of Sec. II, the physical system have been treated as an ideal one with no time delay. But, in practice, phase lag problems in the physical control system, particularly in the actuator, have detrimental influence on the control performance and robustness, as examined by Ren *et al.*¹⁵ Therefore, in the present study, a phase lead compensation network has been employed in experiments to improve the control performance. Readers are referred to Ref. 15 for details about this problem.

The vibration control effects are first evaluated by measuring the compliance of the plate under impulse excitation by hammer. In Fig. 9 are shown the occasions when exciting near modeling point 3 and picking up at modeling point 3, and exciting near modeling point 1 and picking up at modeling point 3. In Fig. 10 are shown the occasions when exciting at modeling point 2 and picking up at modeling point 1, and exciting near modeling point 1 and picking up at modeling point 1. As anticipated in the simulations, these experiments demonstrate very good control effects over all



(a)



(b)

FIG. 12. The experimental results of random excitation by loudspeaker. Dotted line: without control; solid line: with control. (a) Displacement measured at modeling point 3; (b) displacement measured at modeling point 1.

the nine concerned modes. It is interesting to notice that the eleventh mode (228 Hz) and some other high modes, which are not incorporated in the lumped parameter model, are also suppressed. This is probably due to the collocation effect. At nonmodeling points on the plate, such as the randomly chosen points *a*, *b*, *c*, and *d* (see Fig. 7), the same good control results have been observed, as shown by two occasions given in Fig. 11, demonstrating that global vibration control effects can be achieved with the methods presented in this paper. Since the actuators are very close to, if not exactly on, the nodes of the sixth mode (about 154 Hz), this mode is not controlled, as shown in these figures.

Another way for examining the control effect is exciting the plate, from inside the box, with a loudspeaker driven with 0–400 Hz white noise, and measuring the vibration response spectra. In Fig. 12 are shown the displacement power spectra measured at two points: the modeling point 1 and the modeling point 3. Evidently, the resonant peaks corresponding to the controlled modes below 300 Hz are well suppressed. This fact suggests that considerable control effects should also be achieved for noise transmission/radiation of the plate. However, this kind of experiments are not con-

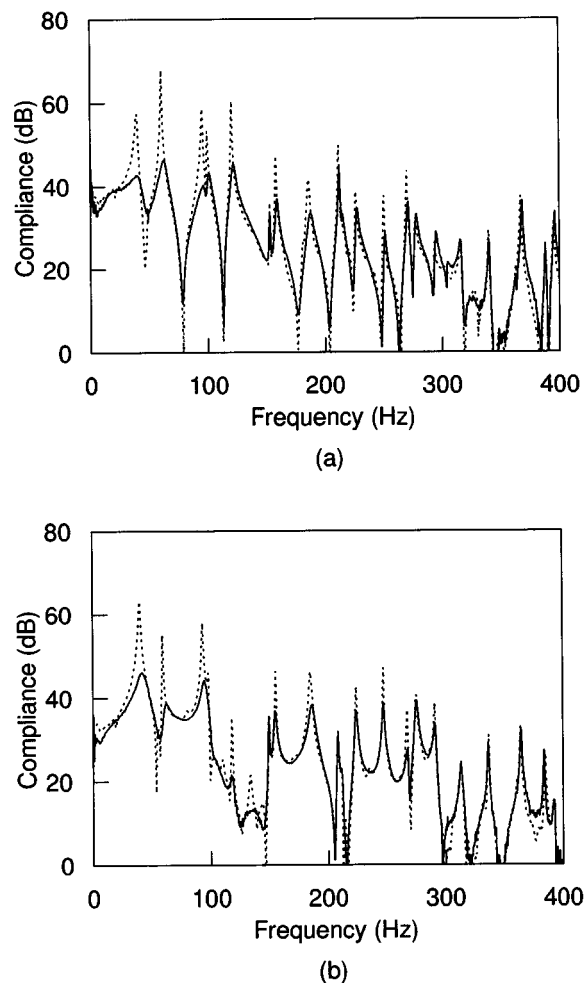


FIG. 13. The experimental results with the box opened. Dotted line: without control; solid line: with control. (a) Excite near and pick up at modeling point 3; (b) excite near modeling point 1 and pick up at modeling point 3.

ducted in this paper, and will be investigated later.

In these experiments, no spillover¹⁶ due to the unmodeled high modes of the structure is observed. This partially benefits from the collocation of two actuators with two sensors, partially benefits from the fact that at high frequencies, the output powers of the actuators are limited. It has been examined when very large control forces (large gains) are employed, some modes above 400 Hz do go unstable. Therefore, spillover problem remains to be a problem in this sense.

One may doubt that the feedback gains used in the experiments are determined beforehand on the basis of the discrete model; the control performance might be very sensitive to the change of the condition. It is sure that if the condition of the real structure alters greatly after the discrete model has been created, it is quite necessary to modify the parameters of the discrete model. But it is observed in this paper that slight change of the dynamics of the structure has little influence on the control performance and robustness. As an example of illustration, the experiment when the plate is not placed onto the box (so that it is not backed by the air cavity) is conducted, and the same controller as the case with the air cavity is used in this condition. As shown in Fig. 13, the transfer function of the plate with no control force on it dis-

plays sharp peak at the first mode, the natural frequency is also slightly shifted. Nevertheless, the control performance is not degraded. Usually, the dynamics of a structure does not change so much in ordinary condition that the mode shapes are completely different, it is considered that the controller designed on the discrete model of the structure would demonstrate fairly good robustness.

IV. CONCLUSIONS

By establishing a lumped parameter model to represent the dynamics of low-order modes of the continuous mechanical system, the well-developed linear quadratic optimal control theory can be easily formulated in physical state space, where state variables are directly measurable quantities. The feedback gains can be determined on the physical discrete system, and then be applied in experiment to generate active forces to control the real structure. This approach essentially gets rid of the problems involved in the widely used modal-space control method, when discrete sensors are used in the systems with distributed parameters. The discretization method based on an inverse modal analysis approach introduced in this paper, that is, to determine the physical parameters of the discrete model from the available modal data of the continuous system, is generally applicable to elastic structures. Since the modal data of a control object (structure) can be obtained either by experiment or by numerical methods in advance, the modeling method described in this paper is quite practical and easy to manipulate. The damping effects can also be considered somehow. This consideration has been examined in this paper by a study on active vibration control of a clamped elastic thin plate. By creating a lumped parameter model with 9DOFs for the clamped plate backed by an air cavity, and designing a state feedback controller using the suboptimal control theory, it has been confirmed by simulation and experiment that nine vibration modes of the plate, ranging from low frequency to fairly high frequency, are quite well controlled with a collocation of two electromagnetic actuators and five sensors. It has also been demonstrated that the suboptimal control design is an effective way to reduce the number of the sensors required by the LQ control theory.

¹K. Seto, "Trends on active vibration control in Japan," in *Proceedings of First International Conference on Motion and Vibration Control (1st MOVIC)*, edited by K. Yoshida and K. Nonami (Yokohama, Japan, 1992), Vol. 1, pp. 1-8.

²C. R. Fuller, S. J. Elliott, and P. A. Nelson, *Active Control of Vibration* (Academic, London, 1996). Chaps. 3, 6, and 8.

³C. R. Fuller, "Experiments on reduction of aircraft interior noise using active control of fuselage vibration," *J. Acoust. Soc. Am. Suppl. 1* **78**, S88 (1985).

⁴B. Widrow and S. D. Stearns, *Adaptive Signal Processing* (Prentice-Hall, Englewood Cliffs, NJ, 1985).

⁵P. A. Nelson and S. J. Elliott, *Active Control of Sound* (Academic, London, 1992).

⁶K. Seto and K. Sawatari, "Vibration control of a plate structure by an active control device for reducing noise," *JSME Int. J.* **33**, 453-459 (1990).

⁷W. T. Baumann, F. S. Ho, and H. H. Robertshaw, "Active structural acoustic control of broadband disturbances," *J. Acoust. Soc. Am.* **92**, 1998-2005 (1992).

⁸D. R. Thomas and P. A. Nelson, "Feedback control of sound radiation from a plate excited by a turbulent boundary layer," *J. Acoust. Soc. Am.* **98**, 2651-2662 (1995).

⁹Z. Wu, V. K. Varadan, V. V. Varadan, and K. Y. Lee, "Active absorption

- of acoustic waves using state-space model and optimal control theory," J. Acoust. Soc. Am. **97**, 1078–1087 (1995).
- ¹⁰M. R. Bai and C. Shieh, "Active noise cancellation by using the linear quadratic Gaussian independent modal space control," J. Acoust. Soc. Am. **97**, 2664–2674 (1995).
- ¹¹L. Meirovitch, *Dynamics and Control of Structures* (Wiley, New York, 1990), Chaps 6, 7, and 8.
- ¹²R. L. Kosut, "Suboptimal control of linear time-invariant systems subject to control structure constraints," IEEE Trans. Autom. Control. **AC-15**, 557–563 (1970).
- ¹³F. J. Fahy, *Sound and Structural Vibration* (Academic, London, 1985), p. 246.
- ¹⁴D. J. Ewins, *Modal Testing: Theory and Practice* (Wiley, New York, 1984), Sections 5.4 and 6.2.
- ¹⁵M. Z. Ren, K. Seto, and F. Doi, "Feedback structure-borne sound control of a flexible plate with electromagnetic actuator: The phase lag problem," J. Sound Vib. **205**, 57–80 (1997).
- ¹⁶M. J. Balas, "Feedback control of flexible structures," IEEE Trans. Autom. Control. **AC-23**, 673–679 (1978).

Wave attenuation in catalytic converters: Reactive versus dissipative effects

A. Selamet and V. Easwaran

The Ohio State University, Department of Mechanical Engineering and Center for Automotive Research,
206 West 18th Avenue, Columbus, Ohio 43210

J. M. Novak

Powertrain Operations, Ford Motor Company, Dearborn, Michigan 48121

R. A. Kach

Motorsport Technology Department, Ford Motor Company, Dearborn, Michigan 48121

(Received 28 April 1997; revised 8 September 1997; accepted 23 September 1997)

Acoustic wave propagation and attenuation in catalytic converters are investigated in the present study. The relationships for wave propagation in a catalytic monolith are derived first and then coupled to the wave propagation in tapered ducts which are commonly placed at either end of the monolith. Analytical and finite element approaches are used to solve the resulting coupled system of equations. Theoretical predictions are then compared with the experimental results for two different (one circular and the other oval) catalyst configurations. The attenuation characteristics of the catalyst with and without the monolith are also investigated. © 1998 Acoustical Society of America. [S0001-4966(98)03801-6]

PACS numbers: 43.50.Gf, 43.20.Mv [GAD]

LIST OF SYMBOLS

A	area
c	sound speed
c_p	specific heat at constant pressure
d	diameter
f	frequency
G_c	as defined by Eq. (11)
i	imaginary unit, $\sqrt{-1}$
J_n	Bessel function of the first kind of order n
k	wave number
K	as defined by Eq. (31)
l	length
M	mean flow Mach number
n	area normal
N	shape function
p	acoustic pressure
P	pressure
Pr	Prandtl number
r	radius
R	flow resistance
\mathcal{R}	as defined by Eq. (10)
Re	Reynolds number
s	as defined by Eq. (12)
t	time
T	temperature; transfer matrix
TL	transmission loss
\mathbf{u}	acoustic particle velocity vector
$\bar{\mathbf{u}}$	mean \mathbf{u}

U mean flow velocity

Greek symbols

α	shape factor
γ	ratio of specific heats
Γ	boundary
κ	thermal conductivity
μ	dynamic viscosity
ϕ	diameter; open-area ratio or porosity
Φ	equivalence ratio
ρ	density
θ	semi-cone angle
τ	transmission coefficient
ω	angular frequency, $2\pi f$
Ω	volume or area domain

Superscripts

+	forward moving wave
−	reflected wave
^	nodal values

Subscripts

$\mathbf{0}$	mean quantity
1	fluid domain
2	catalytic converter element
i	inlet
int	interface boundary
m	catalytic converter element
o	outlet

INTRODUCTION

Following the 1970 Clean Air Act, the need to comply with the emission standards has resulted in significant developments in the catalyst technology. The efforts that started

by retarding the ignition, the use of thermal reactors and the oxidation catalyst have led to the discovery of three-way catalysts in late 1970's (Gandhi *et al.*,¹ Heywood,² Stone³). Three-way catalysts are now an integral part of the exhaust

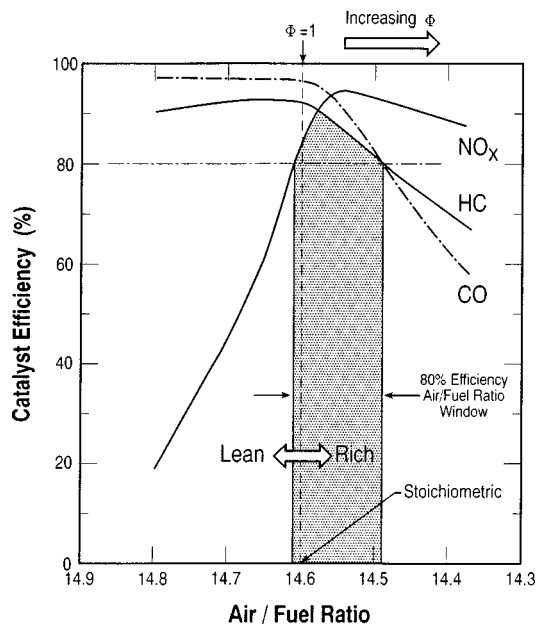


FIG. 1. Conversion efficiency for NO, CO, and HC for a three-way catalyst as a function of exhaust gas air/fuel ratio, modified from Kummer (Ref. 7).

system of spark-ignition engines due to their ability to convert all three pollutants (NO_x, CO, and HC) simultaneously by accelerating the associated kinetics reactions. The catalytically active coat, which may be composed of precious metals such as platinum, palladium, and rhodium, is applied to the washcoat (typically alumina, Al₂O₃) with a large surface area to enhance the oxygen storage capacity and key reactions. The washcoat is applied to either a ceramic or a metal substrate which is mounted in a metal housing by using a thin layer of swelling mat or wire mesh. A typical conversion efficiency near stoichiometric combustion and the associated narrow conversion window, for 80% conversion, for example, for a three-way catalyst is shown in Fig. 1. On the fuel rich side NO_x is reduced usually to N₂ by excess unburnt hydrocarbons, and by CO which is formed due to lack of sufficient oxygen, whereas on the fuel lean side, excess oxygen oxidizes hydrocarbons and CO. Thus the window width for conversion is determined by the NO conversion on the lean side, and by CO or HC conversion on the rich side. The details of some representative reactions are given in the literature (see, for example, Schäfer and van Basshuysen,⁴ and Oh and Cavendish⁵). The compression-ignition engines, on the other hand, use primarily oxidizing catalysts because of the lean operation.

The pollutant conversion behavior of catalysts has been studied in detail, for example, by Oh and his co-workers.^{5,6} Their earlier work is a one-dimensional model of simultaneous heat and mass transfer, and the chemical reactions. The effect of step increase in the feed stream temperature is examined on the lightoff behavior as a function of catalyst design and operating conditions. The later work involves a three-dimensional model facilitating the prediction of more realistic temperature gradients in both radial and axial directions, which have significant implications in terms of heat losses and structural durability, particularly for important

transients such as converter warm-up, sustained heavy load, and engine misfiring. They also included realistic kinetics to some extent (with the exception of NO_x) for the Pt-catalyzed oxidation reactions of hydrocarbons, CO, and H₂. A comprehensive review of catalysts for pollutant emission control is given by Kummer.⁷ Also, recent technologies for emission control have been discussed by numerous researchers.⁸

The emission control has clearly been the primary objective of the catalytic converters (CC) on the exhaust system of internal combustion engines, as just described. This challenging task naturally led to extensive research toward understanding the pollutant conversion behavior of CCs. The same element, however, is also effective in reflecting and dissipating the noise to a considerable extent, therefore acting as a reactive/dissipative silencer. Thus far, the wave attenuation behavior of CCs has received relatively little attention, and will be the focus of the present study. The monoliths have a large number of parallel tubes (or cells). The density of these cells vary, for example, from 300 to 600 per square inch (cpi) in a ceramic monolith. Thus the analysis of sound attenuation in a CC requires the knowledge of wave propagation in the tube bundles (or capillaries) and their interaction with the connecting ducts. Kirchhoff⁹ and Rayleigh¹⁰ investigated the sound propagation in narrow tubes containing a viscous, heat-conducting fluid. Exact solutions of their equations for circular tubes under simplifying conditions were given by Zwikker and Kosten.¹¹

Tijdeman¹² later obtained numerical solutions of Kirchhoff's equations and discussed the limitations of the work of Zwikker and Kosten. The idea of using a "shape factor" to account for noncircular tubes was introduced by Biot.¹³ Craggs and Hilderbrandt^{14,15} studied the wave propagation through noncircular capillaries via the finite element method, but neglected the thermal boundary layer in their modeling. Analytical solution in the form of a series solution was obtained by Roh *et al.*¹⁶ for viscous and thermal perturbation fields in rectangular tubes. Stinson and Champoux¹⁷ derived an exact solution for an equilateral triangular capillary. Recently, Cummings¹⁸ demonstrated the use of a variational method to study the wave propagation and attenuation in capillaries of arbitrary cross section.

The foregoing studies, i.e., Refs. 9–18, examined the wave propagation in capillaries when the medium is quiescent. Glav *et al.*¹⁹ described a simple model to study the wave propagation through the catalytic converter element. Their model was based on the heuristic work of Ingard and Singhal²⁰ and showed good agreement with the experimental results at low frequencies. At higher frequencies, however, their predictions deviated from the experimental results as their model was based on the low-frequency approximations for the visco-thermal boundary layer attenuation in circular capillaries. Recently, Peat²¹ studied the effect of flow on circular capillaries using the variational method. This work was followed up by Astley and Cummings²² who used the finite element method to study the attenuation and propagation in capillaries of arbitrary cross section in the presence of flow. Ih *et al.*²³ and Jeong and Ih²⁴ later developed analytical solutions for circular capillaries in the presence of small mean flow in terms of confluent hypergeometric functions.

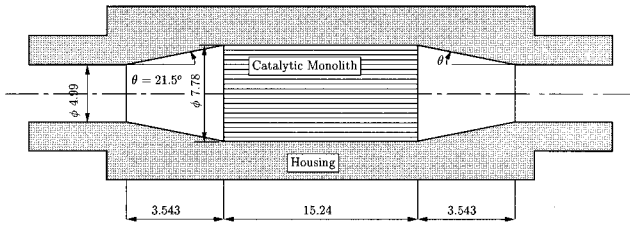


FIG. 2. Circular ceramic monolith and the housing (length is in [cm]).

References 9–24 dealt with the wave propagation in capillaries. The monolith consists of a large number of these capillaries and has a cross-sectional area considerably larger than the main exhaust duct. Utilization of the full cross-sectional area and therefore all the available actively coated surface is highly desirable.²⁵ Thus particularly on the upstream side, the duct is connected to the housing of the monolith via a diffuser with the hope that flow will expand to the full monolith surface relatively uniformly. This tapered section upstream is repeated to a degree at the downstream location primarily to reduce the flow losses, therefore reducing the back pressure to the engine and improving the engine performance through decreased pumping loop work. A typical configuration is shown in Fig. 2 which also represents one of the two configurations considered in this study.

In addition to investigating the wave propagation in the monolith, the objective of the present study is to combine the wave field in the monolith to the tapered ducts (diffuser and reducer) and the main duct. Unlike Oh and his co-workers,^{5,6} this work neglects the heat/mass transfer and chemical reactions aspects, and deals primarily with the acoustic wave propagation and attenuation. While a recently presented preliminary attempt²⁶ investigated a circular monolith only, the present study (i) considers two blank (without washcoat) ceramic monoliths: circular and oval, for both analytical and experimental work, the latter being more realistic because of the under-body space constraints; (ii) introduces a finite element treatment of the CC to provide an assessment of multi-dimensional versus one-dimensional wave propagation behavior; and (iii) uses a CFD approach to evaluate the validity of analytical relationships given for the flow resistance in capillaries, which is employed in the present attenuation model.

Following the Introduction, the theory underlying the wave propagation in the catalyst is described in Sec. I. Section II illustrates the analytical and finite element method to obtain the transmission loss characteristics, and Sec. III the different methods to determine the flow resistance. Section IV discusses the results of the present study, which is concluded in Sec. V with some final remarks.

I. THEORY

The treatment of the wave propagation in a system containing a catalytic converter (CC) element essentially requires the solution of a coupled system of equations: one for the wave propagation in the connecting tapered ducts, and

the other for the wave propagation in the CC element. The wave propagation in the connecting ducts is given by the well-known wave equation,

$$\nabla^2 p = \frac{1}{c_0^2} \frac{\partial^2 p}{\partial t^2}, \quad (1)$$

where p is the acoustic pressure and c_0 is the speed of sound in the connecting duct. The equation for wave propagation in the tube bundles of the CC element is, however, rather involved, and requires a few simplifying assumptions. The capillary tube walls are assumed to be impervious in the present investigation. For some combination of the ceramic monolith and the washcoat, the tube walls can exhibit microporosity. Such an effect can readily be included via a locally reacting wall impedance, and an effective open-area ratio as shown by Arnott *et al.*²⁷ On a macroscopic scale, the problem of wave propagation in the CC element is analogous to the problem of wave propagation in an equivalent fluid which has an effective density and an effective compressibility, both of which can be complex. These effective properties are derived as shown in the following.

The linearized version of the continuity, momentum and the energy equations for acoustic wave propagation are given, in the absence of flow, by²⁸

$$\frac{\partial \rho_m}{\partial t} + \rho_0 \nabla \cdot \mathbf{u}_m = 0, \quad (2)$$

$$\nabla p_m + \rho_0 \frac{\partial \mathbf{u}_m}{\partial t} - \mu \left[\nabla^2 \mathbf{u}_m + \frac{1}{3} \nabla (\nabla \cdot \mathbf{u}_m) \right] = 0, \quad (3)$$

and

$$\frac{\partial T_m}{\partial t} - \frac{1}{\rho_0 c_p} \frac{\partial p_m}{\partial t} = \frac{\kappa}{\rho_0 c_p} \nabla^2 T_m, \quad (4)$$

respectively, where ρ_m is the density, p_m is the acoustic pressure, \mathbf{u}_m is the acoustic particle velocity vector, T_m is the temperature, μ is the kinematic viscosity of the fluid, κ is the thermal conductivity of the fluid and c_p is the specific heat of the fluid at constant pressure. The subscript ‘‘m’’ is used here to denote the catalytic converter.

At low frequencies, or when the cross-sectional dimensions of the capillary are very small compared to the wavelength, acoustic laminar conditions exist in the capillaries.¹⁴ Even when the flow is present the Reynolds number (based on the capillary width) is small enough for the conditions within the tube to be laminar.²² Further, if the length of the capillary is large compared to the cross-sectional dimensions, the flow in the capillary can be assumed to be fully developed.²² Under such conditions, the momentum equation can be re-written in terms of the space-averaged mean velocity $\bar{\mathbf{u}}_m$ as follows:

$$\nabla p_m + \rho_0 \frac{\partial \bar{\mathbf{u}}_m}{\partial t} + \mathcal{R} \bar{\mathbf{u}}_m = 0, \quad (5)$$

where \mathcal{R} depends on the frequency and the cross-sectional shape of the capillary. In view of a harmonic time dependency, Eq. (5) may be reduced to

$$\nabla p_m + \rho_m \frac{\partial \bar{\mathbf{u}}_m}{\partial t} = 0, \quad (6)$$

where

$$\rho_m = \rho_0 + \frac{\mathcal{R}}{i\omega}, \quad (7)$$

which defines the equivalent density ρ_m . While viscous effects play a role in determining the effective density [through \mathcal{R} in Eq. (7)], thermal effects become important in obtaining the equivalent sound speed as described in the following. In terms of the linearized equation of state for an ideal gas,

$$\frac{p_m}{P_0} = \frac{\rho_m}{\rho_0} + \frac{T_m}{T_0}. \quad (8)$$

The speed of sound is then given by

$$c_m^2 \equiv \frac{p_m}{\rho_m} = \frac{1}{[\rho_0/P_0 - \rho_0 T_m/p_m T_0]}. \quad (9)$$

For isothermal conditions, $T_m = 0$. Then, in view of Eq. (9), $c_m = \sqrt{P_0/\rho_0}$, which is purely real. Craggs and Hilderbrandt¹⁴ assumed isothermal conditions and used the finite element method to predict the equivalent density for a capillary of arbitrary cross section. However, when the thermal boundary layer is accounted for, the solution of Eq. (4) yields T in terms of p . Because of the thermal diffusion term on the right side of Eq. (4), the variables p_m and T_m will be out-of-phase in their oscillations. Thus the equivalent sound speed defined by Eq. (9) would be complex. Stinson²⁹ obtained closed form solutions to Eqs. (2)–(4) for circular capillaries and for rectangular slits. Allard³⁰ has worked extensively on the modeling of porous materials and has developed simple relationships for the equivalent density and sound speed in porous materials of arbitrary cross section by expressing the parameter \mathcal{R} in Eqs. (5) and (7) as

$$\mathcal{R} = R\phi G_c(s), \quad (10)$$

where R is the flow resistance, ϕ is the open-area ratio, i.e., ratio of the cross-sectional area of the pores and the total cross-sectional area,

$$G_c(s) = \frac{-\frac{s}{4}\sqrt{-i}\frac{J_1(s\sqrt{-i})}{J_0(s\sqrt{-i})}}{1 - \frac{2}{s\sqrt{-i}}\frac{J_1(s\sqrt{-i})}{J_0(s\sqrt{-i})}} \quad (11)$$

with

$$s = \alpha \sqrt{\frac{8\omega\rho_0}{R\phi}}, \quad (12)$$

J_0 and J_1 are the Bessel functions of order zero and unity, respectively, and α is a factor which depends on the shape of the cross section of the capillary.³⁰ The factor α is used here

to account for noncircular cross section of the capillary, and should be distinguished from the tortuosity factor used elsewhere in the literature³⁰ to account for the randomness in the distribution of pores. For a given pore geometry, the viscosity μ and the flow resistance R are directly related if the boundary layer is assumed to be fully developed, as illustrated later in Sec. III.

The equivalent sound speed is given by³⁰

$$c_m = \frac{c_0}{\sqrt{\left[1 + \frac{\phi R}{i\omega\rho_0} G_c(s)\right] \left[\gamma - \frac{\gamma-1}{1 + (\phi R/i\rho_0\omega \text{Pr}) G_c(s\sqrt{\text{Pr}})}\right]}}, \quad (13)$$

where

$$\text{Pr} = \frac{\mu c_p}{\kappa} \quad (14)$$

is the Prandtl number (the ratio of momentum to thermal diffusivity). The wave propagation in the catalytic monolith is hence characterized by

$$\nabla^2 p_m = \frac{1}{c_m^2} \frac{\partial^2 p_m}{\partial t^2}. \quad (15)$$

Analysis of the wave propagation in a catalyst then involves the coupled solution of Eqs. (15) and (1).

II. TRANSMISSION LOSS (TL)

Transmission loss is proportional to the ratio of sound power incident on an acoustic filter and the sound power transmitted downstream into an anechoic termination. As it allows for the evaluation of the acoustic performance of a silencer independent of the acoustic source and termination, this desirable quantity is used in the present analysis to characterize the acoustic behavior of the catalyst. Two different theoretical approaches, (a) analytical, and (b) finite element method, are used to predict the transmission loss when the medium in the catalyst is quiescent.

A. Analytical method

A transfer matrix method is used to evaluate the TL characteristics analytically. Using pressure and volume velocity as the state variables, the transfer matrix for the uniform duct segment of the catalyst is given by²⁸

$$T_{\text{catalyst monolith}} = \begin{bmatrix} \cos k_m l & i \frac{\rho_m c_m}{A} \sin k_m l \\ \frac{iA}{\rho_m c_m} \sin k_m l & \cos k_m l \end{bmatrix}, \quad (16)$$

where $k_m = \omega/c_m$, A is the cross-sectional area of the CC element, c_m is given by Eq. (13), and ρ_m is given by Eqs. (7) and (10). The transfer matrix expression for a conical duct is given by³¹

$$T_{\text{conical duct}} = \begin{bmatrix} \frac{r_2}{r_1} \cos(k_0 l) - \frac{\tan \theta}{k_0 r_1} \sin(k_0 l) & i \rho_0 c_0 \frac{r_2}{r_1} \sin(k_0 l) \\ -i \frac{l \tan^2 \theta \cos(k_0 l)}{k_0 r_1^2} + i \left(\frac{r_2}{r_1} + \frac{\tan^2 \theta}{k_0^2 r_1^2} \right) \frac{\sin(k_0 l)}{\rho_0 c_0} & \frac{r_2}{r_1} \cos(k_0 l) + \frac{\tan \theta}{k_0 r_1} \sin(k_0 l) \end{bmatrix}, \quad (17)$$

where θ is the semi cone angle, l is the length, and r_1 and r_2 are the radii at the inlet and outlet of the conical duct section of the catalyst. The overall transfer matrix is then

$$T_{\text{catalyst}} = [T_{\text{diverging duct}}] \begin{bmatrix} 1 & 0 \\ 0 & \phi \end{bmatrix} [T_{\text{catalyst monolith}}] \begin{bmatrix} 1 & 0 \\ 0 & \frac{1}{\phi} \end{bmatrix} \times [T_{\text{converging duct}}]. \quad (18)$$

Transmission loss is evaluated using the following expression:

$$\text{TL} = 20 \log_{10} \left[\frac{1}{2} \sqrt{\frac{A_i}{A_o}} T_{11} + \frac{A_o}{\rho_0 c_0} T_{12} + \frac{\rho_0 c_0}{A_i} T_{21} + \frac{A_o}{A_i} T_{22} \right], \quad (19)$$

where A_i and A_o are the cross-sectional areas of the inlet and outlet ducts, respectively, where T_{ij} 's correspond to those of the matrix T_{catalyst} . Note that Eq. (19) is more general than the applications considered in the present study by allowing for different A_i and A_o . In the following section, a finite element approach to evaluate the TL characteristics is illustrated.

B. Finite element method

The wave propagation in the catalyst are characterized by Eqs. (1) and (15), or equivalently by

$$(\nabla^2 + k_0^2)p = 0 \quad \dots \quad \text{in } \Omega_1, \quad (20)$$

and

$$(\nabla^2 + k_m^2)p_m = 0 \quad \dots \quad \text{in } \Omega_2, \quad (21)$$

where domains Ω_1 and Ω_2 denote, respectively, the fluid domain and the CC element. In the Galerkin finite element method trial functions of the form,

$$p = \sum_i N_i \hat{p}_i, \quad \text{and} \quad p_m = \sum_i N_i (\hat{p}_m)_i, \quad (22)$$

are chosen to approximate the solution of Eqs. (20) and (21). Here, \hat{p}_i and $(\hat{p}_m)_i$ are the nodal pressure values, and N_i 's are the trial functions or the shape functions. The residues obtained by substituting Eq. (22) in Eqs. (20) and (21) are then weighted by the shape functions, and the residual error minimized over the entire domain. Thus

$$\int_{\Omega_1} N(\nabla^2 + k_0^2)p \, d\Omega = 0 \quad (23)$$

and

$$\int_{\Omega_2} N(\nabla^2 + k_m^2)p_m \, d\Omega = 0. \quad (24)$$

Using Gauss' divergence theorem, Eqs. (23) and (24) are expressed in the following form:

$$\int_{\Omega_1} (\nabla N \cdot \nabla p - k_0^2 N p) \, d\Omega = \int_{\Gamma_1} N \frac{\partial p}{\partial n} \, d\Gamma \quad (25)$$

and

$$\int_{\Omega_2} (\nabla N \cdot \nabla p_m - k_m^2 N p_m) \, d\Omega = \int_{\Gamma_2} N \frac{\partial p_m}{\partial n} \, d\Gamma, \quad (26)$$

where Γ_1 and Γ_2 are the boundaries of domains Ω_1 and Ω_2 , respectively, and n is the area normal. The following boundary conditions apply along the interface Γ_{int} of domains Ω_1 and Ω_2 :

$$p = p_m, \quad \text{and} \quad \mathbf{u} = \phi \mathbf{u}_m. \quad (27)$$

By virtue of the continuity, Eq. (2), and the corresponding equation for the fluid domain, the velocity boundary condition at the interface can be rewritten as

$$\frac{\nabla p \cdot \mathbf{n}}{\rho_0} = \phi \frac{\nabla p_m \cdot \mathbf{n}}{\rho_m}. \quad (28)$$

Multiplying Eq. (26) by $\phi \rho_0 / \rho_m$ and then adding it to Eq. (25), yields

$$\int_{\Omega_1} (\nabla N \cdot \nabla p - k_0^2 N p) \, d\Omega + \frac{\phi \rho_0}{\rho_m} \int_{\Omega_2} (\nabla N \cdot \nabla p_m - k_m^2 N p_m) \, d\Omega = \int_{\Gamma_i} N \frac{\partial p}{\partial n} \, d\Gamma + \int_{\Gamma_o} N \frac{\partial p}{\partial n} \, d\Gamma, \quad (29)$$

where Γ_i and Γ_o denote the inlet and outlet boundaries. The contribution due to the interface boundary integral drops out as a result of Eq. (28). Boundary integral at other boundaries vanish due to rigid wall conditions.

Assuming plane waves to be incident on the boundary Γ_i and the boundary Γ_o to be terminated anechoically, the solution of Eq. (29) can be obtained for a given incident pressure field. The ratio of the transmitted and incident pressures would then yield the transmission coefficient τ . In terms of τ , TL is then given by,

$$\text{TL} = 20 \log_{10} |1/\tau|. \quad (30)$$

Equation (30) is used to evaluate the transmission loss, numerically, by the finite element method. These results are then used to corroborate the analytical treatment of the preceding Sec. II A based on a simple one-dimensional approach.

III. FLOW RESISTANCE

In order to evaluate the TL characteristics of the catalyst, the geometry of the pore, the properties of the fluid filling the pores of the catalytic monolith and the flow resistance R , need to be known explicitly. The pore geometry and the properties of air which fills the pore are generally known *a priori*, leaving only the flow resistance to be determined. The flow resistance can either be measured directly or estimated theoretically. Various models^{32–34} exist in the literature for predicting the pressure drop along the length of the duct. While the theoretical model of Shapiro *et al.*³⁴ is limited to the region in the immediate vicinity of the flow entrance in the duct or tube, the model of Fargie *et al.*³² is valid over a small region along the length of the duct. The model of Sparrow and Lin,³³ however, is more elegant. The pressure drop in a tube of length l and of diameter d according to their model is given by

$$\frac{\Delta P_0}{\frac{1}{2}\rho_0 U^2} = \frac{64l/d}{\text{Re}} + K(l), \quad (31)$$

where P_0 is the mean pressure, U is the mean velocity, $\text{Re} = \rho_0 U d / \mu$ is the Reynolds number, and $K(l)$ is a function which depends on the length of the duct.

The first term on the right side of Eq. (31) corresponds to a fully developed flow, and the second term, the entrance region where the flow is developing. The value of K has been shown to increase from zero at the inlet to a constant value of 1.24 at a distance far from the entrance region where the flow is fully developed to the well-known Poiseuille profile.³³ Their analytical results were found to be in excellent agreement with the computational predictions obtained here from a commercial software, STAR-CD,³⁵ which solves the full Navier–Stokes equations for the fluid flow. The observed degree of agreement eliminated the need for a detailed comparison between the two approaches. Thus no further discussion on the computational approach is provided here. Equation (31) is then related to the flow resistance of the catalytic monolith as described next.

For a catalytic monolith at very low frequencies, $s \ll 1$ [refer to Eq. (12)]. In this limit,

$$G_c(s) \approx 1, \quad (32)$$

and at these low frequencies Eq. (6) reduces to

$$\mathcal{R}\bar{\mathbf{u}}_m \approx -\nabla p_m, \quad (33)$$

or, in terms of Eq. (10) to

$$R\phi G_c(s)\bar{\mathbf{u}}_m \approx -\nabla p_m. \quad (34)$$

Substituting the value of $G_c(s)$ for the low-frequency limit, i.e., Eq. (32) in Eq. (34), yields

$$R = \lim_{\omega \rightarrow 0} \frac{-\nabla p_m}{\phi \bar{\mathbf{u}}_m} \equiv \frac{\Delta P_0 / l}{U_i}, \quad (35)$$

which defines the static flow resistance. Here,

$$U_i = \phi U, \quad (36)$$

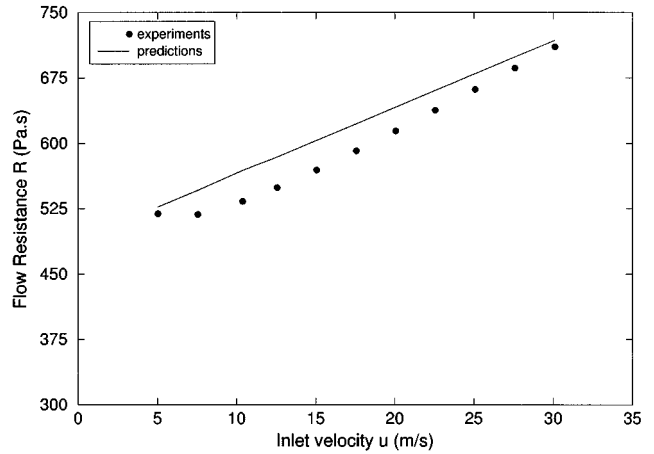


FIG. 3. Variation of flow resistance with inlet velocity.

where U_i is the free-stream velocity of the fluid outside the catalytic monolith. Substituting Eq. (31) for pressure loss in Eq. (35) would yield

$$R = \frac{\Delta P_0 / l}{\phi U} = \frac{32\mu}{\phi d^2} + \frac{\rho K(l)}{2l\phi^2} U_i, \quad (37)$$

where d is the diameter of the capillary tube. Equation (37) would provide a good estimate of R in actual steady flow measurements. However, the second term in this expression accounts for developing boundary layer, which is not incorporated in a conventional formulation such as that of Sec. I. Thus to retain consistency, only the first term on the right side of Eq. (37) is effectively used in the analytical expressions here by determining the limit when velocity tends to zero, as described in the following section. This first term also matches Eq. (4.77) in Allard.³⁰

IV. RESULTS

One circular and one oval blank (uncoated) ceramic monoliths are used in the present study. The circular configuration consists of a 350 cpi (cells per square inch) catalytic monolith connected to constant-diameter ducts on both sides with tapered sections (see Fig. 2). The circular monolith is made up of square capillaries and has an open area ratio of $\phi=0.8$ (equivalent to a square pore of 1.214 mm length). The flow resistance across the monolith was determined experimentally in a flow bench. The predicted [Eq. (37)] and the measured flow resistances are compared in Fig. 3. The flow resistance depends on the flow velocity, as expected. As the flow resistance is defined by Eq. (37), the value of R corresponding to the case where the velocity tends to zero, i.e., $R=500$ Pa s is used in the theoretical predictions. For the square capillaries, the value of parameter α [see Eq. (12)] is 1.07 (Ref. 30, Table 4.1).

The TL characteristics obtained experimentally (through impedance tube measurements, see for example, Selamet *et al.*³⁶ for the details of the experimental setup), analytically, and by finite element method are depicted in Fig. 4, which incorporates, $c_0=343$ m/s, $\rho_0=1.2$ kg/m³, and $\gamma=1.4$ for the ambient air. Theoretical predictions compare well

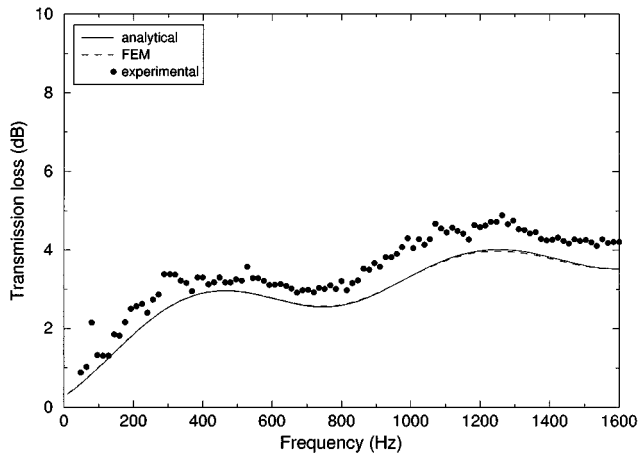


FIG. 4. Circular catalyst of Fig. 2 with the monolith (350 cpi, $\phi=0.8$)—Transmission loss.

with the experimental results. The difference between the one-dimensional analytical and the three-dimensional finite element results is nearly negligible, suggesting that one-dimensional treatment would be sufficiently accurate for these type of configurations. The discrepancy between the theoretical and the experimental results may be attributed to (i) the variation in the flow resistance, (ii) the variation in the open-area ratio from the manufacturer's specifications, and (iii) the finite porosity of the capillary walls. The effect of variation of the flow resistance and the open-area ratio on TL are illustrated in Figs. 5 and 6, respectively. As expected, increase in the flow resistance increases the transmission loss (since the dissipation of acoustic energy is higher). Increase in the open-area ratio exposes more of the pore fluid to viscous attenuation and this explains the observed increase in transmission loss with an increase in the open-area ratio. For the effect of finite wall porosity, Arnott *et al.*²⁷ may be referred to.

A comparison of the TL obtained with and without the catalytic monolith is shown in Fig. 7. The behavior of the tapered housing alone (without monolith) is depicted by dashed lines, which is based on purely reactive wave reflections. The difference between the dashed line and the solid

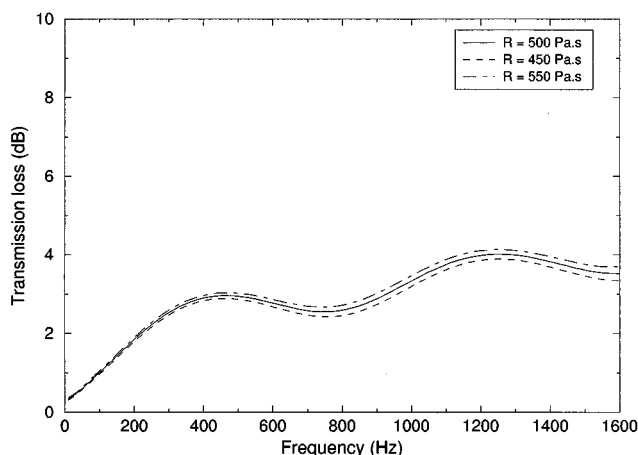


FIG. 5. Effect of the variation of flow resistance.

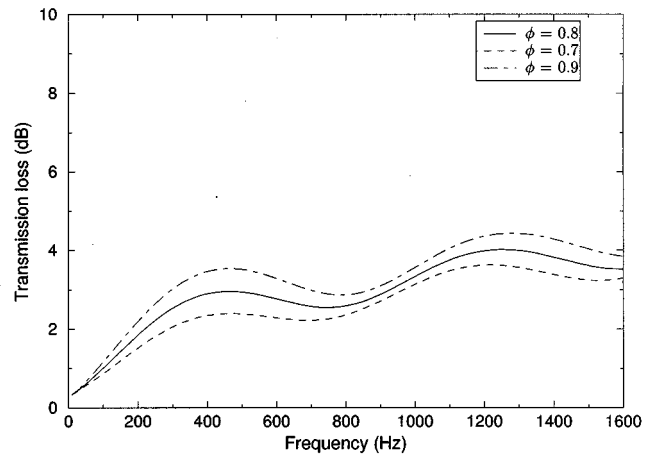


FIG. 6. Effect of the variation of open-area ratio.

line (with monolith) is due to the viscous dissipation in the catalytic monolith. Thus the introduction of the monolith increases the transmission loss at higher frequencies, away from the first peak. Also, for this particular configuration, the transmission loss remains fairly constant in the frequency range of interest in automotive applications. Therefore, in addition to increasing the reaction rates for the transformation of the pollutants to less hazardous substances, the catalyst also helps in reducing the sound transmission downstream of the catalyst. Note that in Figs. 4–7, as the frequency tends to zero, the transmission loss of catalyst housing coupled with the monolith does not reduce to zero. This is due to the dissipative nature of the catalyst [refer to Eqs. (7), (10), (11), and (32)].

Figure 8 shows the oval catalytic monolith connected to the same circular ducts of Fig. 2 at both ends through two tapered transitions. Figure 9 provides a comparison of the 3-D finite element analysis, the one-dimensional analytical solution, and the experimental data for the configuration of Fig. 8 with the housing alone (catalytic monolith removed). For the analytical solution the oval section is replaced by a circular duct of equal cross-sectional area. The TL behavior indicates that the higher order modes are not cut-on in the frequency range of interest, and the waves are predominantly one-dimensional along the oval section. Figure 10 shows the corresponding results for the oval catalyst of Fig. 8 in the presence of the catalytic monolith. While the theoretical predictions in general compare well with the experimental results, the sources of the deviations (as indicated earlier for the case of circular configuration) in Figs. 9 and 10 are currently being investigated. These two figures for the oval catalyst also reveal a minimal increase in the accuracy of predictions when employing a 3-D finite element method instead of a simple one-dimensional analytical solution. When multi-dimensional wave propagation becomes more significant at higher frequencies the need for finite element method would become obvious. However, the frequency range considered here at ambient conditions needs to be stretched proportional to the square root of the temperature in the hot exhaust system. A multiplying factor of 1.5 or slightly higher is not atypical. Therefore, for the symmetric configurations studied

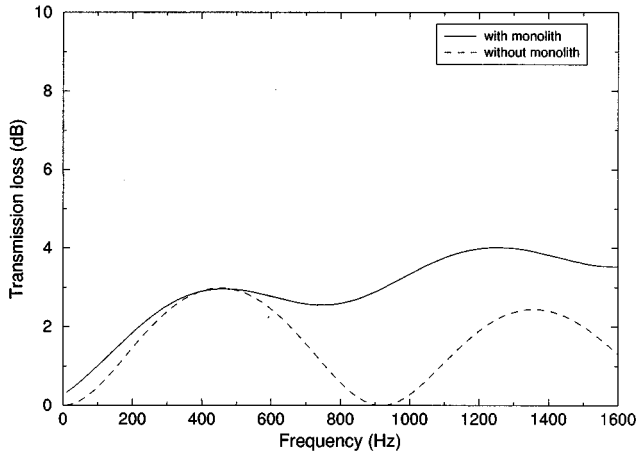


FIG. 7. Circular catalyst—transmission loss with and without the monolith.

here and for the dimensions considered, there is very little to be gained from a detailed finite element method relative to a simplistic one-dimensional analytical approach.

A 3-D finite element approach could prove to be useful for larger diameters and asymmetric CCs with offset or angled inlet and outlets. The effect of higher order modes might then be important at higher frequencies, particularly in the connecting ducts. Using finite elements to model the connecting ducts while retaining a simple one-dimensional model for the catalytic monolith might be a suitable approach for such a case.

The examination of Figs. 7, 9, and 10 also reveals that the first attenuation dome is dictated by the reactive effects based simply on the wave reflections due to cross-sectional area changes. The insertion of the monolith in the housing has a two-fold impact on the attenuation: (i) for the pure wave reflection, the expansion ratio of the housing alone is somewhat reduced because of the monolith walls. Depending

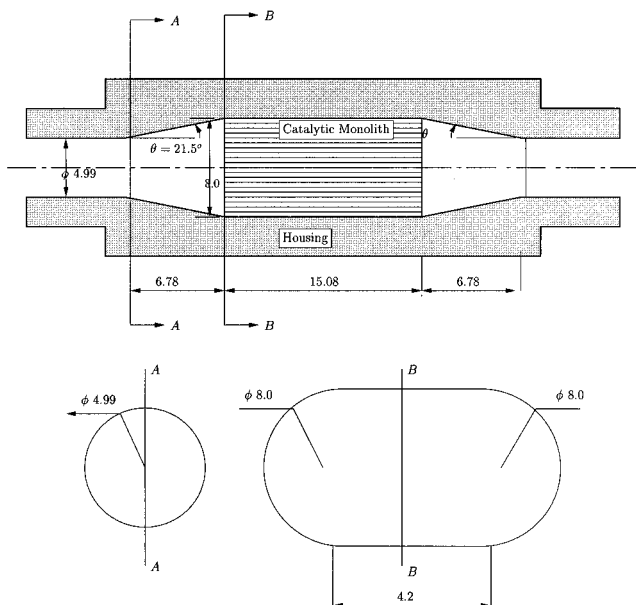


FIG. 8. Oval ceramic monolith and the housing (length is in [cm]).

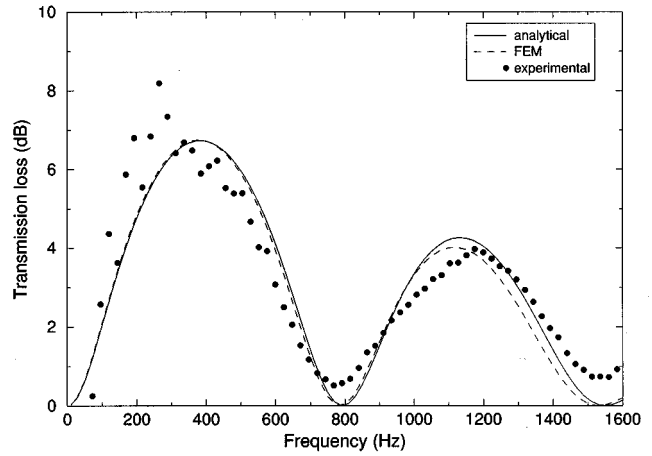


FIG. 9. Oval catalyst of Fig. 8 without the monolith (housing alone)—comparison of theoretical and experimental results.

on the configuration, this may result in some reduction in TL of the first dome; and (ii) beyond the first dome, the wave dissipation inside the capillaries of the monolith becomes significant. The fact that the behavior of the first dome is dictated primarily by wave reflections based on the available expansion ratio could prove to be useful for a number of different applications, particularly in view of frequency stretching due to high exhaust temperatures. Also note that the monoliths used in this study did not have a coating. With the application of the coating, the flow resistance is expected to increase somewhat, resulting in more dissipation.

V. CONCLUDING REMARKS

The present study determines the wave attenuation in catalytic converters by combining the wave field in the monolith to the tapered ducts and the main circular duct. Two different catalyst configurations, one circular and the other oval, are investigated both analytically and with the finite element method. The theoretical predictions presented in this study for these two configurations are shown, in general, to compare well with the experimental data. Compari-

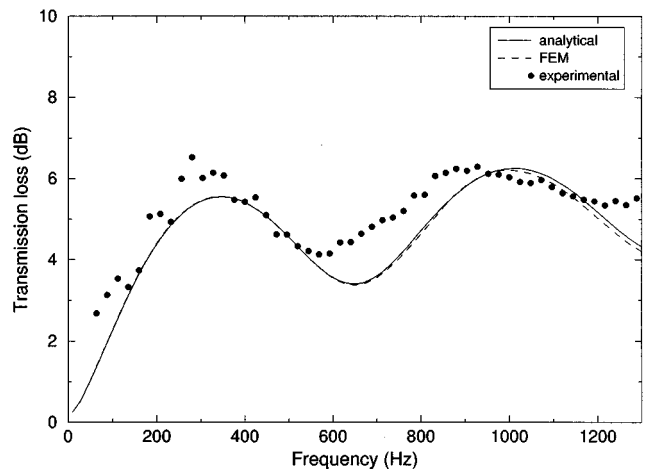


FIG. 10. Oval catalyst of Fig. 8 with the monolith (400 cpi, $\phi=0.75$)—comparison of theoretical and experimental results.

son of the results with and without the catalytic monolith indicates an improved acoustic performance in the presence of the monolith. Theoretical results for the oval catalyst indicate that for the frequency range of interest in automotive applications, the acoustic wave propagation is predominantly one dimensional. Thus a simple analytical treatment based on one-dimensional approach appears to be rather useful, if not sufficient, to determine the acoustic attenuation of a catalytic converter.

The results of Peat,²¹ and Astley and Cummings²² indicate that the effect of flow on the attenuation and phase speed is convective: i.e., the wave number k_m^+ for the forward moving wave is $k_m^+ = k_m / (1 + M)$ and the wave number k_m^- for the reflected wave is $k_m^- = k_m / (1 - M)$, where M is the mean flow Mach number. The present method can then be extended to include incompressible mean flow by constructing the transfer matrices of the conical and the straight ducts in the presence of flow according to Selamet and Easwaran³⁷ and evaluating the TL in the presence of flow according to Easwaran.³⁸ Axial temperature gradients inside catalytic converters³⁹ have been ignored in the present analysis. Also, the application of the present method, for example, to thermo-acoustic engines^{40,41} remains to be explored.

¹H. S. Gandhi, A. G. Piken, M. Shelef, and R. G. Delosh, "Laboratory evaluation of three-way catalysts," SAE 760201 (1976).

²J. B. Heywood, *Internal Combustion Engine Fundamentals* (McGraw-Hill, New York, 1988), Chap. 11.

³R. Stone, *Introduction to Internal Combustion Engines* (McGraw-Hill, SAE, Inc., Warrendale, PA, 1995), 2nd ed., Chap. 4.

⁴F. Schäfer and R. van Basshuysen, *Reduced Emissions and Fuel Consumption in Automobile Engines* (Springer-Verlag, New York, 1995), Chap. 5.

⁵S. H. Oh and J. C. Cavendish, "Transients of monolithic catalytic converters: response to step changes in feedstream temperature as related to controlling automobile emissions," *Ind. Eng. Chem. Prod. Res. Dev.* **21**, 29–37 (1982).

⁶D. K. S. Chen, S. H. Oh, E. J. Bissett, and D. L. van Ostrum, "A three-dimensional model for the analysis of transient thermal and conversion characteristics of monolithic catalytic converters," SAE 880282 (1988).

⁷J. T. Kummer, "Catalysts for automobile emission control," *Prog. Energy Combust. Sci.* **6**, 177–199 (1981).

⁸Society of Automotive Engineers, SP-1173, *Cold-Start Emission Control and Catalyst Technologies* (SAE, Inc., Warrendale, PA, 1996).

⁹G. Kirchhoff, "Ueber den Einfluss der Wärmeleitung in einem Gase auf die Schallbewegung," *Ann. Phys. Chem.* **134**, 177–193 (1868).

¹⁰J. W. Strutt (Lord Rayleigh), *Theory of Sound* (Dover, New York, 1945), Vol. II.

¹¹C. Zwikker and C. W. Kosten, *Sound Absorbing Materials* (Elsevier, Amsterdam, 1949).

¹²H. Tijdeman, "On the propagation of sound waves in cylindrical tubes," *J. Sound Vib.* **39**, 1–33 (1975).

¹³M. A. Biot, "Theory of propagation of elastic waves in fluid-saturated porous solid. II. Higher frequency range," *J. Acoust. Soc. Am.* **28**, 179–191 (1956).

¹⁴A. Craggs and J. G. Hilderbrandt, "Effective densities and resistivities for acoustic propagation in narrow tubes," *J. Sound Vib.* **92**, 321–331 (1984).

¹⁵A. Craggs and J. G. Hilderbrandt, "The normal incidence absorption coefficient of a matrix of narrow tubes with constant cross-section," *J. Sound Vib.* **105**, 101–107 (1986).

¹⁶H.-S. Roh, W. P. Arnott, J. M. Sabatier, and R. Raspet, "Measurement and calculation of acoustic propagation constants in arrays of small air-filled rectangular tubes," *J. Acoust. Soc. Am.* **89**, 2617–2624 (1991).

¹⁷M. R. Stinson and Y. Champoux, "Propagation of sound and the assignment of shape factors in model porous materials having simple pore geometries," *J. Acoust. Soc. Am.* **91**, 685–695 (1992).

¹⁸A. Cummings, "Sound propagation in narrow tubes of arbitrary cross-section," *J. Sound Vib.* **162**, 27–42 (1993).

¹⁹R. Glav, H. Boden, and M. Åbom, "An acoustic model for automotive catalytic converters," *Proc. InterNoise 88*, 1261–1266 (1988).

²⁰U. Ingard and V. K. Singhal, "Sound attenuation in turbulent pipe flow," *J. Sound Vib.* **55**, 535–538 (1974).

²¹K. S. Peat, "A first approximation to the effects of mean flow on sound propagation through cylindrical capillary tubes," *J. Sound Vib.* **175**, 475–489 (1994).

²²R. J. Astley and A. Cummings, "Wave propagation in catalytic converters: formulation of the problem and finite element solution scheme," *J. Sound Vib.* **188**, 635–657 (1995).

²³J. G. Ih, C. M. Park, and H. J. Kim, "A model for sound propagation in capillary ducts with mean flow," *J. Sound Vib.* **190**, 163–175 (1996).

²⁴K. W. Jeong and J. G. Ih, "A numerical study on the propagation of sound through capillary tubes with mean flow," *J. Sound Vib.* **198**, 67–79 (1996).

²⁵D. W. Wendland and W. R. Matthes, "Visualization of automotive catalytic converter internal flows," SAE 861554 (1986).

²⁶A. Selamet and V. Easwaran, "Wave propagation in catalytic converters: a preliminary investigation," SAE 971873 (1997).

²⁷W. P. Arnott, J. M. Sabatier, and R. Raspet, "Sound propagation in capillary-tube-type porous media with small pores in the capillary walls," *J. Acoust. Soc. Am.* **90**, 3299–3306 (1991).

²⁸A. D. Pierce, *Acoustics* (Acoustical Society of America, Woodbury, NY, 1991).

²⁹M. R. Stinson, "The propagation of plane sound waves in narrow and wide circular tubes, and generalization to uniform tubes of arbitrary cross-sectional shape," *J. Acoust. Soc. Am.* **89**, 550–558 (1991).

³⁰J. F. Allard, *Propagation of Sound in Porous Media* (Elsevier Applied Science, New York, 1993).

³¹A. Selamet, N. S. Dickey, and J. M. Novak, "Wave attenuation by universal venturi tubes: finite difference predictions with analytical and experimental comparisons," *Noise Control Eng. J.* **44**, 224–230 (1996).

³²D. Fargie and B. W. Martin, "Developing laminar flow in a pipe of circular cross-section," *Proc. R. Soc. London* **321**, 461–476 (1971).

³³E. M. Sparrow, S. H. Lin, and T. S. Lundgren, "Flow development in hydrodynamic entrance region of tubes and ducts," *Phys. Fluids* **7**, 338–347 (1964).

³⁴A. H. Shapiro, R. Siegel, and S. J. Kline, "Friction factor in laminar entry region of a smooth tube," in *Proceedings of the 2nd U.S. National Congress of Applied Mechanics*, Ann Arbor, Michigan, pp. 733–740 (1954).

³⁵Computational Dynamics Limited, London, *STAR-CD Manuals* (1995).

³⁶A. Selamet, N. S. Dickey, and J. M. Novak, "The Hersche–Quincke tube: A theoretical, computational and experimental investigation," *J. Acoust. Soc. Am.* **96**, 3177–3185 (1994).

³⁷A. Selamet and V. Easwaran, "Wave propagation in Herschel–Venturi tube," *J. Acoust. Soc. Am.* **101**, 936–942 (1997).

³⁸V. Easwaran, "Analysis of acoustic wave propagation in variable area flow ducts and anechoic linings," Ph.D. thesis, Indian Institute of Science, Bangalore, India 1993.

³⁹K. S. Peat, "Convected acoustic wave motion along a capillary duct with an axial temperature gradient," *J. Sound Vib.* **203**, 855–866 (1997).

⁴⁰G. W. Swift, "Thermoacoustic engines," *J. Acoust. Soc. Am.* **84**, 1145–1180 (1988).

⁴¹W. P. Arnott, H. E. Bass, and R. Raspet, "General formulation of thermoacoustics for stacks having arbitrarily shaped pore cross sections," *J. Acoust. Soc. Am.* **90**, 3228–3237 (1991).

Effects of reflective ground on the actively created quiet zones

Jingnan Guo and Jie Pan

Department of Mechanical and Materials Engineering, The University of Western Australia, Nedlands, WA 6907, Australia

(Received 7 May 1997; revised 26 September 1997; accepted 3 October 1997)

Previous studies on the local active control of noise in free space show that the size of the quiet zone and the total sound power output of the control system are mainly determined by the spatial arrangement of primary sources, secondary sources, and error sensors. When a nearby reflective surface is introduced, the size of the quiet zone and the total power output of the system will be affected. The research presented in this paper examines the influence of the presence of a nearby reflective plane on the control system with different alignments to the reflective surface. It is found that the reflective surface significantly affects the size of the quiet zone and the sound power output of the system, as compared with the same control system in free space. The effect is related to two important parameters of the control system: the heights of the sources and the error sensor above the surface and the distances between the primary and secondary sources and between the secondary source and the error sensor. While the quiet zones created by most arrangements of the control system in half-space are smaller than those for free space, the quiet zones created by the arrangements of the control system perpendicular to the reflective surface may be larger than those for free space. © 1998 Acoustical Society of America. [S0001-4966(98)05001-2]

PACS numbers: 43.50.Ki [GAD]

INTRODUCTION

Much of the literature addressing the active noise control (ANC) in an open space assumes free-field conditions.¹⁻⁵ Free-field conditions do not always exist in practical applications, and half-spaces are of more practical engineering concern.

There are several strategies of applying active noise control in free space; the two major strategies are global control (also known as optimal control) and local control. For the global control strategy, the cost function is the total sound power output and the source strengths of the control sources are adjusted to minimize the total power output of the control system. Nelson and Elliott pointed out that for the optimal control strategy, substantial reductions in total power output can be achieved only if the primary sources and control sources are closely located,¹⁻⁵ say less than one-half wavelength apart at the frequency of interest. In practical applications, the condition of a short separation distance between the primary and secondary sources may not be always satisfied. For these cases, to cancel the sound pressure in some areas and achieve quiet zones seems to be the only option for the active noise control in free space. This control strategy is called local control or zone of quiet control.

To extend the optimal control (minimum total sound power output) technique into half-spaces, Cunefare and Shepard modified the free-space equations derived by Nelson *et al.*, and examined the effect of the presence of a nearby reflective plane on the active control of sound radiated by a number of point sources and by extended acoustic sources. They found that the effect of the presence of the reflective plane on the optimal noise control can be ignored when the sources are more than one wavelength away from the reflective surface, regardless of the reflective properties of the surface.^{6,7}

The authors have investigated the quiet zone created by a control system with a single primary/secondary source in free space.⁸ The objective of this paper is to investigate the efficiency of the local control strategy in half-space and to examine the effect of the presence of a reflective surface on the performance of a local control system with single primary/secondary sources and an error sensor. The size of the quiet zone and the total power output of the system are used as measurements of the performance of the control system, and will be compared with those of the free-space control system. The computer simulation will focus on a rigid reflective plane, and on various alignments of the control system to the reflective surface.

For the analyses presented here, a feedforward control mechanism has been assumed with a reference signal obtained from the input to the primary source. The control sources are modeled as constant volume velocity sources, the outputs of which are linearly related to their inputs.

I. THEORETICAL ANALYSIS

A. A point source above a reflective plane

When a point source radiates above a large reflective plane in open space, the plane acts as an imaginary source,⁹⁻¹¹ as shown in Fig. 1. In Fig. 1, q is the strength of point source, $q_i = C_r q$ is the strength of the imaginary source, C_r is the reflection coefficient determined by the characteristics of the reflective plane, and h is the height of the point source above the reflective plane.

The sound pressure at the position of a receiver is

$$P = iZ_0q \left\{ \frac{e^{-ikr}}{kr} + \frac{C_r e^{-ikr_i}}{kr_i} \right\}, \quad (1)$$

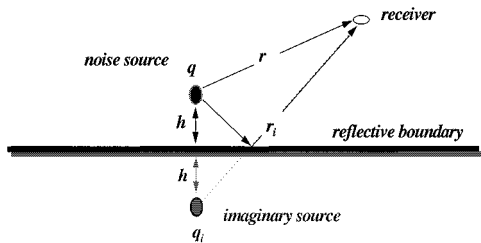


FIG. 1. A monopole point source over a reflective plane.

and the sound power output of the point source above a reflective plane is given as

$$W_h = W_0(1 + R_{p'p}), \quad (2)$$

where $W_0 = \frac{1}{2}Z_0|q|^2$ is the power output of the point source when the reflective plane is absent, $Z_0 = \omega^2\rho_0/4\pi c_0$, and $R_{p'p} = \text{Re}(iC_r e^{-i2kh}/2kh)$. For a rigid plane, $C_r = 1$, and the power output becomes

$$W_h = W_0(1 + (2kh)). \quad (3)$$

For a pressure release plane, $C_r = -1$, and so the power output in half-space is given by

$$W_h = W_0(1 - (2kh)). \quad (4)$$

The normalized power outputs of a monopole source over a rigid plane and a pressure release boundary are shown in Fig. 2. The figure shows that the reflective boundary affects the power output of the source when the source is close to the boundary. This effect can be ignored when the distance between the sound source and the boundary is longer than one wavelength.

B. Active noise control in free space

The simplest active noise control system in free space consists of one primary source, one control source, and/or one error microphone, as shown in Fig. 3. Here q_p and q_s are the strengths of the primary and secondary sources, and the error sensor is at E ; r_{ps} , r_{pe} , and r_{se} are the distances from

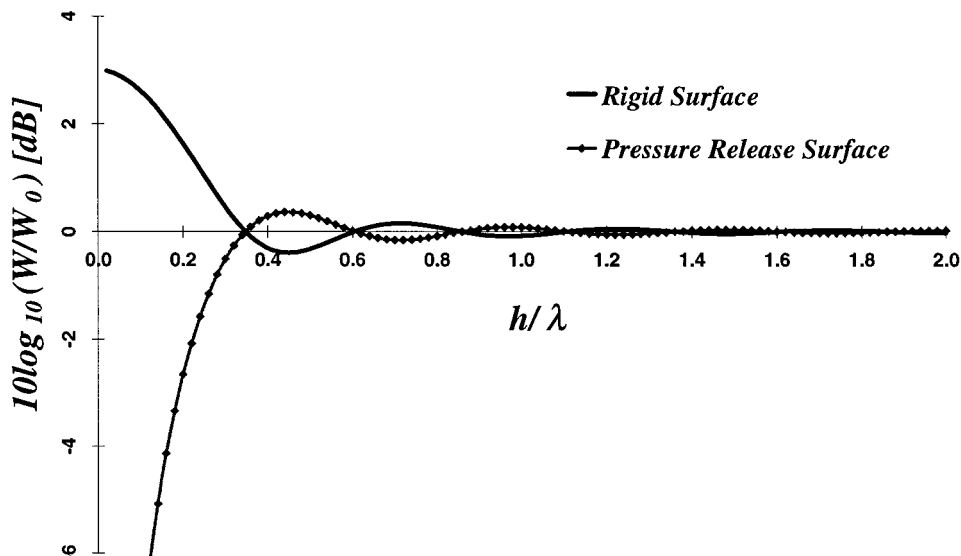


FIG. 2. The normalized power outputs of a monopole source over a rigid plane and a pressure release plane.

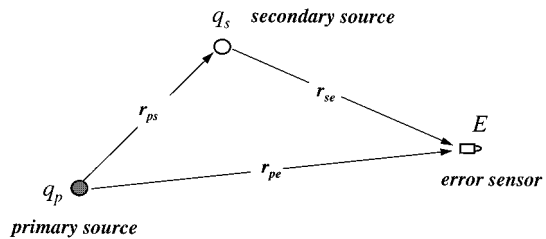


FIG. 3. Monopole primary and secondary source with an error sensor in free space.

the primary source to the secondary source, the primary source to the error sensor, and the secondary source to the error sensor, respectively.

For the local control strategy, the strength of the secondary source q_s is selected so as to drive the total sound pressure at position E to zero, i.e.,

$$q_s = -Z_{se}^{-1}Z_{pe}q_p. \quad (5)$$

In this case, $Z_{pe} = iZ_0 e^{-ikr_{pe}}/kr_{pe}$ and $Z_{se} = iZ_0 e^{-ikr_{se}}/kr_{se}$ are the acoustic transfer impedances between the primary source and the error sensor and between the secondary source and the error sensor, respectively. The control source strength can be rewritten as

$$q_s = -q_p \frac{r_{se} e^{-ik(r_{pe} - r_{se})}}{r_{pe}}. \quad (6)$$

Then the quiet zone can be created around the error sensor. A “quiet zone” is defined as the area where the sound pressure has been attenuated by more than 10 dB.¹²⁻¹⁴

The total power output of the system is given by³

$$W_{Tf} = \frac{1}{2} \text{Re}[q_p(Z_{pp}q_p + Z_{sp}q_s)^* + q_s(Z_{ss}q_s + Z_{ps}q_p)^*]. \quad (7)$$

Noted that when $\text{Re}(Z_{pp}) = \text{Re}(Z_{ss}) = Z_0$, $Z_{ps} = Z_{sp} = iZ_0 e^{-ikr_{ps}}/kr_{ps}$, and we substitute Eq. (6) into Eq. (7), the total power output becomes

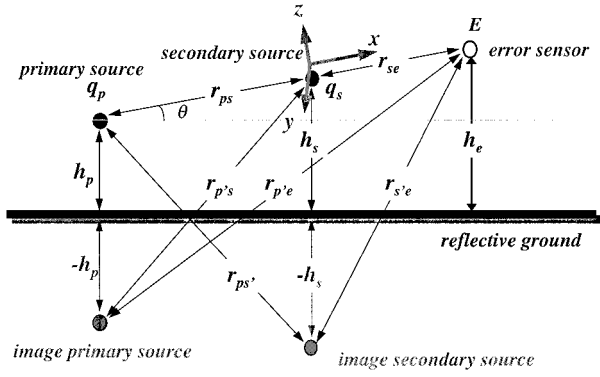


FIG. 4. Monopole primary and secondary sources with a canceling point in half-space.

$$W_{Tf} = W_0 \left[1 + \frac{r_{se}^2}{r_{pe}^2} - \frac{2r_{se}}{kr_{pe}r_{ps}} \cos k(r_{pe} - r_{se}) \sin kr_{ps} \right], \quad (8)$$

where W_0 is the power output of the primary source in free space when the control source is absent, which is defined in Eq. (2).

It has been found that when the wavefront matching area between the primary source and the secondary source is large, then the quiet zone area will also be large. For the control system shown in Fig. 3, the optimal configuration of the system is that the secondary source is in between the linking line of the primary source and error sensor,⁸ i.e., $r_{pe} = r_{ps} + r_{se}$, which results in a relatively large quiet zone with the shape of an ellipsoid. The following discussion of local control in half-space will also be based on this kind of configuration for both the sources and the error sensor.

C. Local control system in half-space

Figure 4 shows an active noise control system above a reflective plane. Here q_p and q_s are the strengths of primary and secondary sources; E is the position of error sensor; and r_{ps} , r_{pe} , and r_{se} are the distances from the primary source to the secondary source, the primary source to the error sensor, and the secondary source to the error sensor, respectively. As both the sources and the error sensor are all in a line with an angle θ to the reflective boundary, $r_{pe} = r_{ps} + r_{se}$. The $r_{p's}$, $r_{s'p}$, $r_{p'e}$, and $r_{s'e}$ are respectively the distances from the primary source to the secondary source, the secondary source to the primary source, the primary source to the error sensor, and the secondary source to the error sensor through the reflective plane. Here h_p , h_s , and h_e are the heights of the primary source, the secondary source, and the error sensor over the reflective plane.

For this case, the acoustic transfer impedances between the primary source and the error sensor and between the secondary source and the error sensor become

$$Z_{pe} = iZ_0 \left(\frac{e^{-ikr_{pe}}}{kr_{pe}} + C_r \frac{e^{-ikr_{p'e}}}{kr_{p'e}} \right), \quad (9)$$

$$Z_{se} = iZ_0 \left(\frac{e^{-ikr_{se}}}{kr_{se}} + C_r \frac{e^{-ikr_{s'e}}}{kr_{s'e}} \right). \quad (10)$$

If the sound pressure at the position of the error microphone is chosen as the cost function of the local control in half-space, the required source strength of the control source becomes

$$q_s = A q_p, \quad (11)$$

where $A = -Z_{pe}/Z_{se}$ is the ratio of the acoustic transfer impedances between the primary source and the error microphone to that between the secondary source and the error microphone. Using the transfer impedances expressed by Eqs. (9) and (10), A as the secondary/primary source strength ratio is expressed as

$$A = - \left(\frac{e^{-ikr_{pe}}}{r_{pe}} + C_r \frac{e^{-ikr_{p'e}}}{r_{p'e}} \right) / \left(\frac{e^{-ikr_{se}}}{r_{se}} + C_r \frac{e^{-ikr_{s'e}}}{r_{s'e}} \right). \quad (12)$$

Due to the acoustic reciprocity,

$$Z_{sp} = Z_{ps} = iZ_0 (e^{-ikr_{ps}}/kr_{ps} + C_r e^{-ikr_{p's}}/kr_{p's}), \quad (13)$$

the total sound power radiated by both primary and secondary sources in half-space becomes

$$\begin{aligned} W_{Th} = & W_0 [1 + R_{p'p} + 2(\text{sinc } kr_{ps} \\ & + \text{Re}(iC_r e^{-ikr_{p's}}/kr_{p's})) \text{Re}(A) \\ & + |A|^2 (1 + R_{s's})], \end{aligned} \quad (14)$$

where $R_{p'p}$ is defined in Eq. (2) and $R_{s's} = \text{Re}(iC_r e^{-i2kh_s}/2kh_s)$. Equation (14) shows that the total sound power output of the control system in half-space is largely dependent upon the secondary strength ratio A .

The total sound pressure at any position in upper space is

$$P = Z_{p'l} q_p + Z_{s'l} q_s, \quad (15)$$

where

$$Z_{p'l} = iZ_0 \left(\frac{e^{-ikr_{p'l}}}{kr_{p'l}} + C_r \frac{e^{-ikr_{p'l}}}{kr_{p'l}} \right), \quad (16)$$

$$Z_{s'l} = iZ_0 \left(\frac{e^{-ikr_{s'l}}}{kr_{s'l}} + C_r \frac{e^{-ikr_{s'l}}}{kr_{s'l}} \right). \quad (17)$$

Here $r_{p'l}$, $r_{p'l}$, $r_{s'l}$, and $r_{s'l}$ are respectively the distances from the observation point to the primary source, the image primary source, the secondary source, and the image secondary source. As ANC always deals with the low-frequency noise, in most practical cases the reflective plane can be regarded as a rigid plane, i.e., $C_r = 1$. The following discussion will focus on the rigid reflective surface.

Equation (14) also indicates that the total power output of the control system is determined by two reflective terms $R_{p'p}$ and $R_{s's}$. When the primary source and the secondary source are very close to the reflective plane, those two terms can also affect the total power output significantly. As will be shown later, a large control source strength causes a big increase in the total power output, which in return decreases the size of the quiet zone created by the control source.

Both Z_{pe} and Z_{se} are the functions of distances from the primary source to the error sensor and from the secondary source to the error sensor, both directly and through the re-

flective boundary. For some configurations with large Z_{pe} and/or small Z_{se} , the secondary source strength may become very large. When Z_{pe} is large and Z_{se} is small, the secondary source strength reaches its maximum value. This will result in a big increase in the total power output, and deteriorate the performance of the control system.

II. EFFECT OF REFLECTIVE GROUND ON TOTAL POWER OUTPUT

For the local active control system, the total sound power output is one of the major indicators of the control effectiveness.¹² The optimal configurations of the local control strategy correspond to the least increase in total sound power output and the largest quiet zone area.

According to Eqs. (12) and (14), the total power output of the local control system is determined by the arrangement of the sources and the error sensor, by the relative position between the control system and the reflective surface, and by the properties of the reflective plane. This section uses the results of the previous section to assess the effects of the presence of a reflective plane on the total power output of the control system. The effects of the reflective plane on the power output of local control will be evaluated by calculating the difference in power output of local control in the half-space and that in the free space. This difference is expressed as $10 \log_{10}(W_{Th}/W_{Tf})$ in dB, symbolled as ΔW , and referred as the free-space error,^{6,7} hereafter

$$\Delta W = 10 \log_{10} \left\{ \left[1 + R_{p'p} + 2(\text{sinc } kr_{ps} + \text{sinc } kr_{p's}) \right. \right. \\ \left. \left. \times \text{Re}(A) + |A|^2(1 + R_{s's}) \right] \middle/ \left[1 + \frac{r_{se}^2}{r_{pe}^2} - \frac{2r_{se}}{r_{pe}} \right. \right. \\ \left. \left. \times \cos k(r_{pe} - r_{se}) \text{sinc } kr_{ps} \right] \right\}, \quad (18)$$

where A is the secondary/primary strength ratio for a rigid reflective surface:

$$A = - \frac{r_{s'e}}{r_{p'e}} e^{-ik(r_{p'e} - r_{s'e})} \left[\frac{r_{p'e}}{r_{pe}} e^{-ik(r_{pe} - r_{p'e})} + 1 \right] \middle/ \\ \left(\frac{r_{s'e}}{r_{se}} e^{-ik(r_{se} - r_{s'e})} + 1 \right). \quad (19)$$

For this case, the secondary/primary strength ratio is a function of θ , h_p , h_s , h_e , r_{ps} , and r_{se} as shown in Fig. 4. It can be shown that the strength of the secondary source and the total power output of the control system have peak values when

$$k(r_{p'e} - r_{pe}) = 2n\pi \quad (20)$$

and

$$k(r_{s'e} - r_{se}) = (2n - 1)\pi, \quad n = 1, 2, \dots \quad (21)$$

With these spatial arrangements, the sound pressures at the error sensor both direct from the primary source and via the ground reflection are in phase, while the sound pressures direct from the secondary source and via the reflective surface are opposite in phase. This means that the output of the

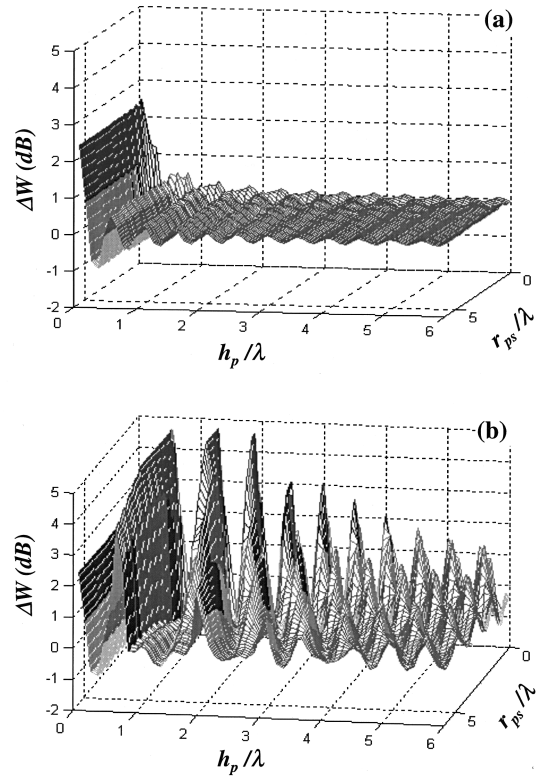


FIG. 5. Free-space error of the system with $\theta=0^\circ$, (a) $r_{se}=0.2\lambda$ and (b) $r_{se}=2\lambda$.

secondary source needs to be very large to cancel the sound pressure at the position of the error microphone. When both of the conditions specified in Eqs. (20) and (21) are satisfied, the power output of the control system in half-space reaches its maximum. As a result, the size of quiet zone created by the control system usually becomes smaller.¹²

Figure 5 shows the power output error in half-space versus h_p and r_{ps} in nondimensional units and when $r_{se} = 0.2\lambda$, 2.0λ and $\theta=0^\circ$. It is obvious that the effects of a reflective surface on the local control system are not only dependent on the height of the sources and the error sensor over the reflective plane, but also on the distances between the primary and secondary sources r_{ps} and that between the secondary source and the error sensor r_{se} . Furthermore, the distance between the secondary source and the error sensor r_{se} affects more significantly the free-space error of power output.

The free-space error ΔW decays with the increasing height of the sources and the error sensor h_p , and with the increasing distance between the primary and secondary source r_{ps} . It also increases as the distance between the secondary source and error sensor r_{se} increases. The influence of the reflective plane on the total power output of the control system ranges from -1 to 5 dB for the configuration noted in Fig. 5.

The contour plots in Fig. 6 suggest that the free-space error $|\Delta W| \geq 0.5$ dB is largely contained in an area, expressed by $h_p + r_{ps} \leq 6r_{se}$ (within the dashed line). When the angle between the control system and the reflective plane

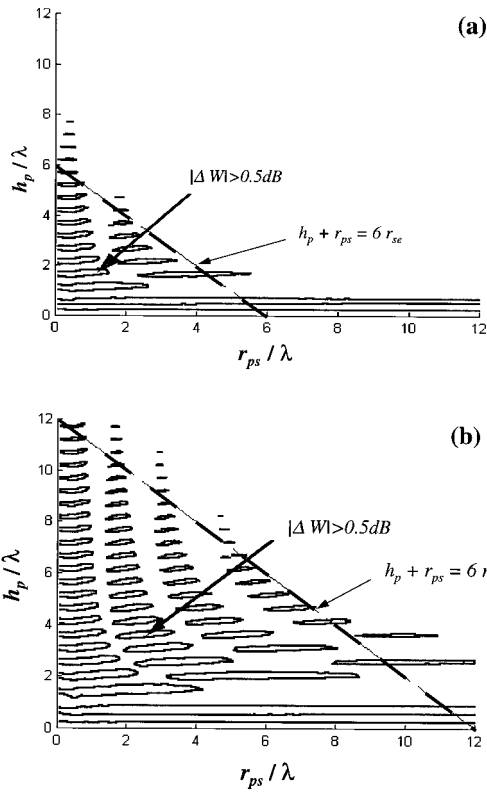


FIG. 6. Contour plots of free-space error for $|\Delta W| \geq 0.5$ dB with $\theta = 0^\circ$; (a) $r_{se} = \lambda$ and (b) $r_{se} = 2\lambda$.

increases from $\theta = 0^\circ$ to $\theta = 90^\circ$, the free-space error pattern changes, as shown in Fig. 7.

With different θ , it can be concluded that the free-space error ($|\Delta W| \geq 0.5$ dB) is largely constrained in the area described by

$$h_p + (1 + \sin \theta/2)r_{ps} \leq 6r_{se}. \quad (22)$$

The generality of this expression has been verified by calculating a large number of different configurations. It is clear that the effect of the reflective plane on the total sound power output decreases when either the height of the control system to the reflective plane and the distance between the primary and secondary sources increases, or the separation of the secondary source and the error sensor decreases. As the free-space error is more sensitive to the distance between the secondary source and the error sensor, decreasing the distance from the secondary source to the error sensor is a much more effective way to reduce the effect of the reflective plane on the power output of the system.

III. EFFECT OF REFLECTIVE GROUND ON SIZE OF QUIET ZONE

Another very important indicator of the efficiency of local control is the size of the quiet zone. The following discussion will be focused on the size of quiet zones created by local control in half-space, and their comparison to that created in free space.

The size of the quiet zone is observed on the plane containing both the sources and the error microphone at an angle

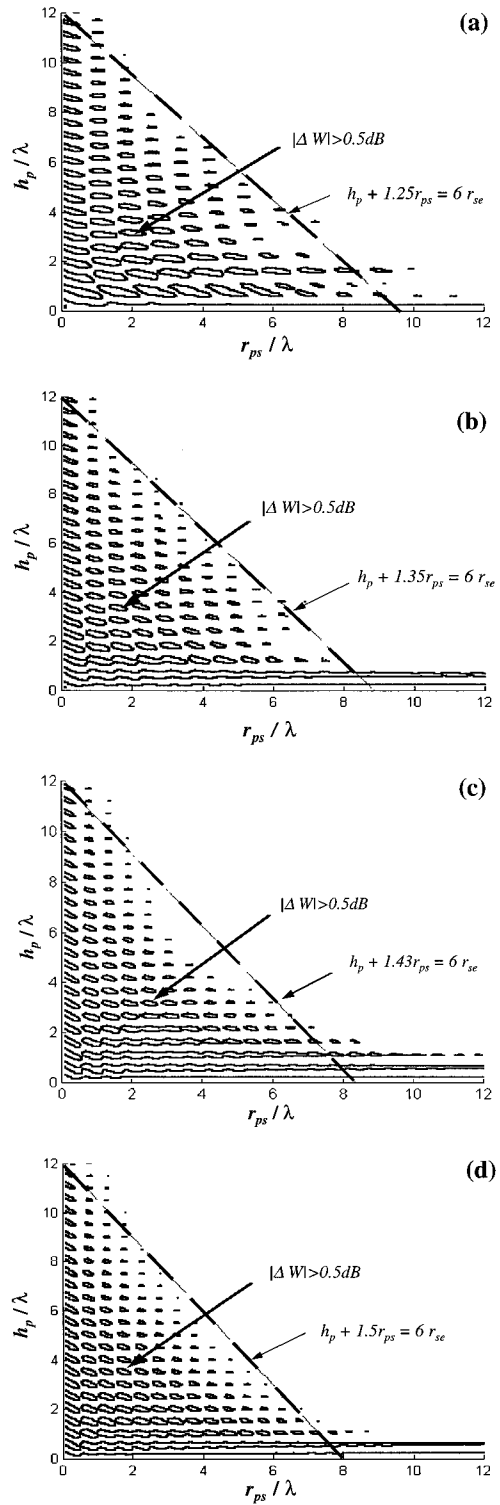


FIG. 7. Contour plots of free-space error for $|\Delta W| \geq 0.5$ dB with $r_{se} = 2\lambda$; (a) $\theta = 30^\circ$, (b) $\theta = 45^\circ$, (c) $\theta = 60^\circ$, and (d) $\theta = 90^\circ$.

of θ to the reflective ground. The primary source is at the position $(-r_{ps}, 0, 0)$, the secondary source at $(0, 0, 0)$, and the error sensor at $(r_{se}, 0, 0)$. The effect of the reflective ground on the size of quiet zone has been calculated for various configurations of the control system. Only a specific configuration of $r_{ps} = \lambda$ and $r_{se} = \lambda$ is demonstrated in the following discussion.

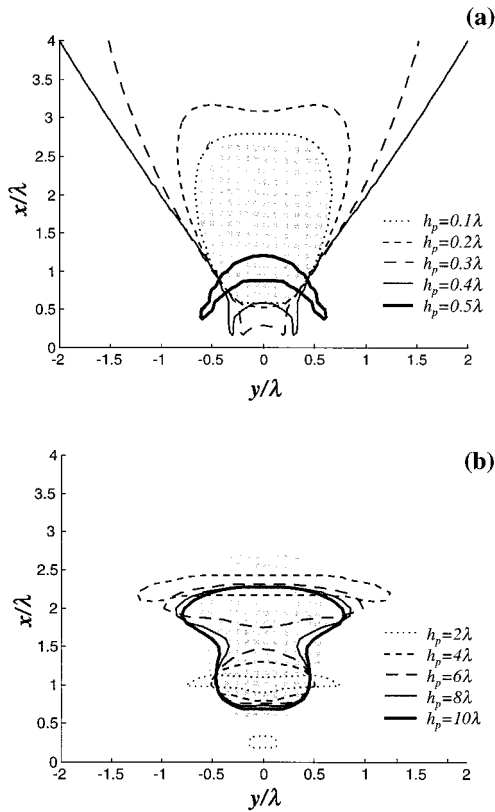


FIG. 8. The quiet zones created by a control system over a rigid plane when $\theta=0^\circ$, $r_{ps}=1\lambda$, $r_{se}=1\lambda$, (a) $h_p=0.1\lambda, 0.2\lambda, 0.3\lambda, 0.4\lambda, 0.5\lambda$, and (b) $h_p=2\lambda, 4\lambda, 6\lambda, 8\lambda, 10\lambda$.

A. The control system in a line parallel to the reflective plane

This is the case of $\theta=0^\circ$, and also the case corresponding to many practical configurations. Figure 8 shows the quiet zones created by a control system with this arrangement. In Fig. 8(a) the control system is very close to the reflective surface in terms of wavelength. The quiet zone is calculated for five heights of the control system: $h_p=0.1\lambda, 0.2\lambda, 0.3\lambda, 0.4\lambda$, and 0.5λ . In Fig. 8(b) the control system is several wavelengths away from the rigid plane; the five heights examined are $h_p=2\lambda, 4\lambda, 6\lambda, 8\lambda$, and 10λ . The shaded area is the quiet zone created by the system in free space, which is equivalent to the infinite height of the system over the reflective plane.

It can be seen clearly that the quiet zones created in half-space can be larger than those in free space when the height of the control system to the ground is less than a critical value. For this configuration, $h_p \leq h_c = 0.4\lambda$. Numerous numerical analyses for different heights and different configurations of the control system have shown that the critical height of the system increases with the distance from the secondary source and the error microphone only, which can be approximately expressed as

$$h_c = 0.4\lambda \sqrt{r_{se}/\lambda}.$$

When the height of the control system is larger than the critical height, the quiet zones created in half-space are always smaller than those in free space. The effect of the rigid boundary on the quiet zone decreases as the distance be-

tween the control system and the rigid surface increases, as demonstrated in Fig. 8(b).

B. The control system in a line with an angle to the reflective plane

The effects of the rigid boundary on the size of the quiet zone created by an active control system when the system is at the angles of $\theta=30^\circ, \theta=45^\circ, \theta=60^\circ$, and $\theta=90^\circ$ and with the heights of $h_p=1\lambda, 2\lambda, 3\lambda, 4\lambda$, and 5λ are shown in Fig. 9. The reflective rigid plane decreases the size of quiet zone for all angles except for $\theta=90^\circ$. In the case of $\theta=90^\circ$, the presence of a ground can even increase the size of the quiet zone. The effect of the ground on the size of the quiet zone becomes smaller as the height of the system to the ground increases.

For the case of $\theta=90^\circ$, the size of the quiet zone is not always increased as it is also a function of r_{ps} and h_p . For those configurations when both conditions expressed by Eqs. (20) and (21) are satisfied at the same time, large power output increase and reduced quiet zone size may result. It can be shown that Eqs. (20) and (21) now correspond to the configurations of $h_p = n\lambda/2$ and $r_{ps} = (2n-1)\lambda/4$. Figure 10 shows the quiet zones created by one of these configurations. It is clear that the reflective ground reduces the size of the quiet zone significantly for these specific system configurations.

So far, the effect of the reflective ground on the size of the quiet zone has been demonstrated in the x - y plane. In fact, the effect of ground reflection on the size of the quiet zone is three dimensional (i.e., over the whole volume of the quiet zone). The quiet zone is symmetrical about the x axis for the configuration of $\theta=90^\circ$, the change of quiet zone size can be seen in the x - y plane. For the configurations that the control system is at an angle to the reflective ground other than 90° , the quiet zone created by the control system in half-space is not symmetrical about the x axis any more. Figure 11 shows the quiet zone in the y - z plane for two typical configurations: $\theta=0^\circ$ and 45° , when $x=2\lambda$ and $h_p=1\lambda, 2\lambda, 3\lambda, 4\lambda$, and 5λ , respectively. It is shown that the size of quiet zone also decreases significantly in the y - z plane for these configurations. With the nearby reflective ground, the control system may create some quiet zones in other areas, making the quiet zone several separated pieces.

The size of the quiet zone is determined by the wavefront matching between the primary and control sound fields. The larger area of wavefront matching between the primary and control fields, the larger the area of the quiet zones. It has been found that when the primary source, the control source, and the error microphone are placed in a line, the area of wavefront matching reaches its maximum.⁸ When a nearby reflective boundary is present as for the configuration of the control system shown in Fig. 4, while the large area of wavefront matching of the direct sound fields from the sources can always be achieved, the amount of wavefront matching of the sounds reflected from the boundary depends on the angle and height of the system to the boundary. As a result, the size of the quiet zone may decrease.

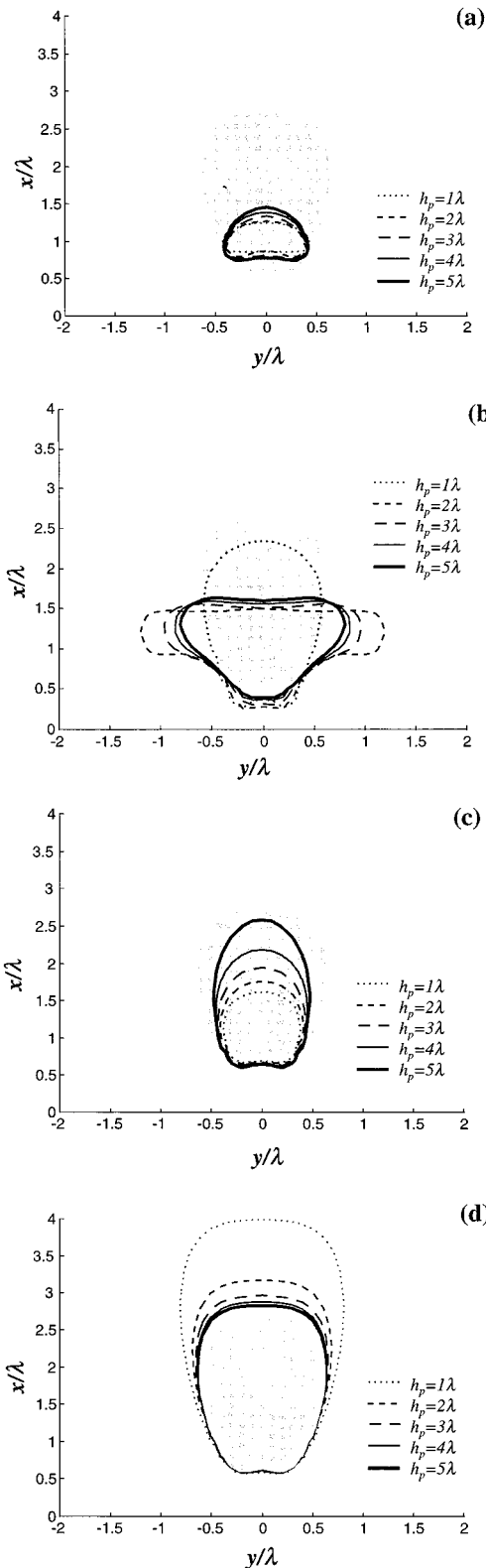


FIG. 9. The quiet zones created by a control system over a rigid plane when $r_{ps} = 1\lambda$, $r_{se} = 1\lambda$, $h_p = 1\lambda, 2\lambda, 3\lambda, 4\lambda, 5\lambda$, and (a) $\theta = 30^\circ$, (b) $\theta = 45^\circ$, (c) $\theta = 60^\circ$, and (d) $\theta = 90^\circ$.

IV. EXPERIMENTS

Experiments were carried out in an anechoic chamber, with the size of $4.2\text{ m} \times 4.2\text{ m} \times 4.2\text{ m}$, to verify the simulation results. The quiet zones created by the control system

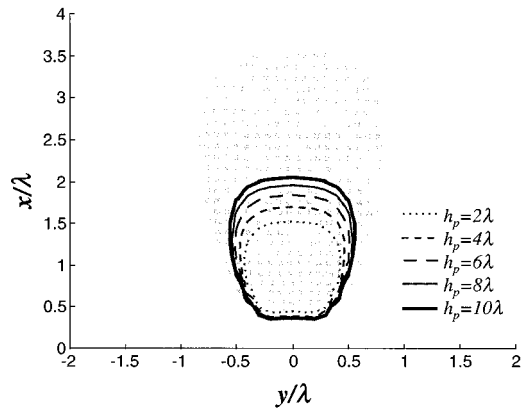


FIG. 10. The quiet zones created by a special control system configuration for the case of $\theta = 90^\circ$ when $r_{ps} = (2n - 1)\lambda/4$ and $h_p = n\lambda/2$.

both in free space and in half-space are compared; the effect of a reflective surface on the performance of an active noise control system is also demonstrated.

As shown in Fig. 12, the system has one primary source, one secondary source, and one error sensor. An adaptive controller called EZ-ANC is used for the minimization of the error signal. A pure tone signal from the signal generator is sent to the primary source, and is also used by the ANC controller as the reference signal. In this experiment, the frequency of the signal is 500 Hz. The sound pressure attenuation (ΔP) is measured in a plane containing the error sensor (observation plane). Altogether 168 measuring points are equally located in this plane with size of $1.4\text{ m} \times 2.1\text{ m}$. The

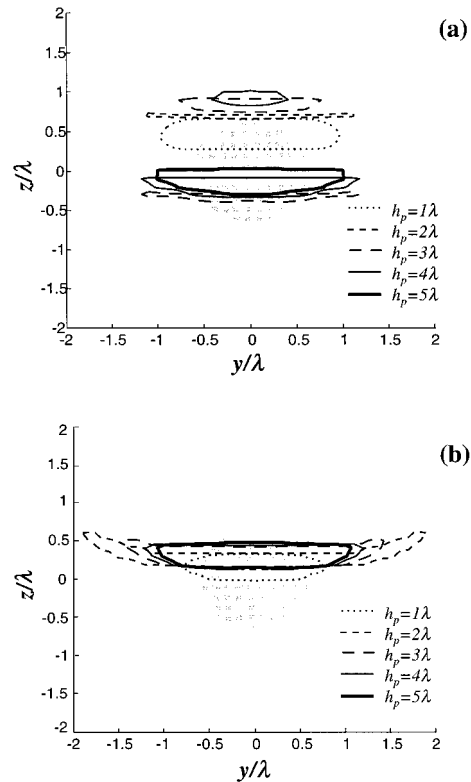


FIG. 11. The quiet zones created by a control system over a rigid plane in the y - z plane when $x = 2\lambda$, $r_{ps} = 1\lambda$, $r_{se} = 1\lambda$, $h_p = 1\lambda, 2\lambda, 3\lambda, 4\lambda, 5\lambda$, (a) $\theta = 0^\circ$, and (b) $\theta = 45^\circ$.

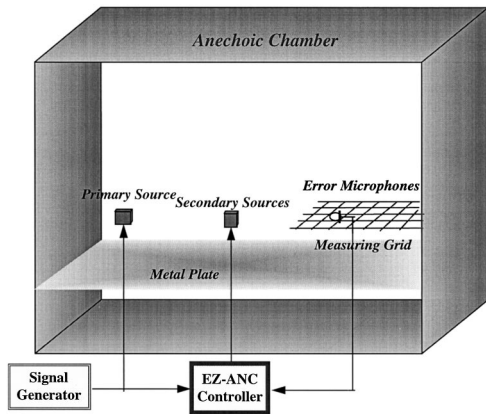


FIG. 12. Experimental setup with metal plates installed at $\theta=0^\circ$.

distance between the primary source and the secondary source is one wavelength ($r_{ps}=\lambda$), and that between the secondary source to the error sensor is also one wavelength ($r_{se}=\lambda$). Several aluminium plates are used as the reflective boundaries, and installed at angles of either $\theta=0^\circ$ or $\theta=90^\circ$ with respect to the control system. The thickness of the aluminium plates is 2 mm, which provides sufficient sound reflection to demonstrate the effect of reflection on the effectiveness of the control system.

Figure 13 shows the quiet zone created by the control system in the anechoic chamber when the reflective boundary is absent, which is the case of free field. The coordinates of the primary source, the secondary source, and the error microphone are $(-2.064,0,0)$, $(-1.376,0,0)$, and $(0,0,0)$, respectively. The sound attenuations were measured in both x - y and y - z planes, and Fig. 13 only gives the quiet zone obtained in the x - y plane containing the primary and secondary sources and the error microphone.

The experiments were then conducted for the case that the grid floor of the anechoic chamber was covered by the metal plates, which simulated the condition of $\theta=0^\circ$. Two heights of the control system to the metal plates, $h=0.55\lambda$ and $h=2\lambda$, are selected in this experiment to test the effects of reflective boundary on the size of quiet zone. Quiet zones created by the control system above the metal plates are also measured in both x - y and y - z planes. Figure 14 shows the

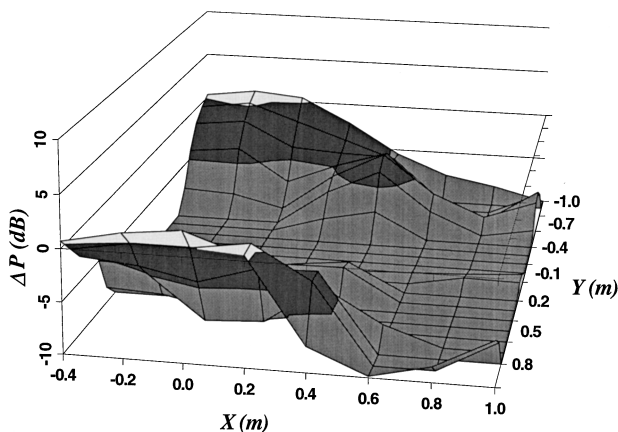


FIG. 13. Quiet zone created in free space.

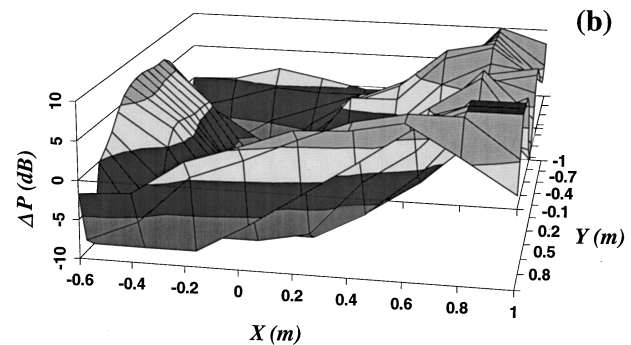
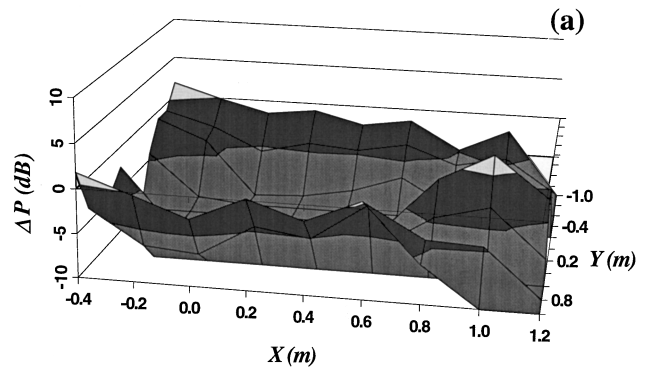


FIG. 14. Quiet zone created by a system above a ground ($\theta=0^\circ$) with $h=0.55\lambda$ and (b) $h=2\lambda$.

sound attenuations of the control system in x - y plane for $h=0.55\lambda$ and $h=2\lambda$.

The sound attenuation shown in Fig. 14(a) is the case when the system is very close to the reflective boundary. It can be calculated by Eq. (19) that the critical height for the

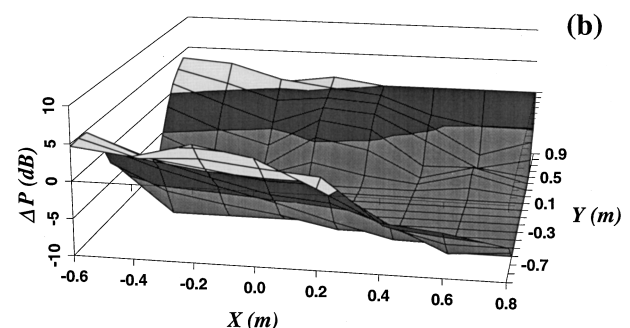
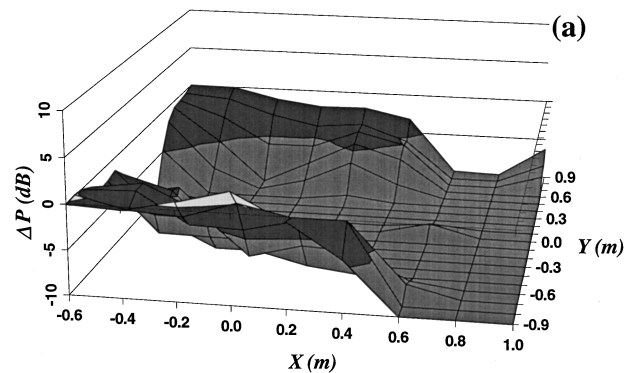


FIG. 15. Quiet zone created by a system in front of a reflective boundary ($\theta=90^\circ$) when (a) $r_{ps}=\lambda$ and (b) $r_{ps}=5\lambda/4$.

examined control system is $h_c=0.57\lambda$. Figure 14(a) indicates that the reflective boundary does not reduce the size of the quiet zone when the height of the system to the boundary is shorter than the critical height. For the case that the control system is $2\lambda (>h_c)$ above the boundary, the presence of the reflective ground not only largely decreases the size of the quiet zone in the space, but also increases the sound pressure in most places, as shown in Fig. 14(b). In some places, this increase can be more than 10 dB.

Figure 15 is the sound attenuations caused by a control system when the metal plates are placed behind the system. The control system is now perpendicular to the reflective boundary ($\theta=90^\circ$). The distance from primary source to the metal plates is $h=\lambda$, the distance from control source to the error microphone is $r_{se}=2\lambda$, and the separation between the primary and control sources is $r_{ps}=\lambda$ for Fig. 15(a) and $r_{ps}=5\lambda/4$ for Fig. 15(b).

Compared with Fig. 13, Fig. 15(a) shows some increase of quiet zone size. Figure 15(b) corresponds to a specific arrangement with large power output increase. It is shown that not only is the size of the quiet zone reduced, but also the sound pressure increase in some places becomes evident.

V. CONCLUSIONS

A nearby reflective boundary will affect both the total power output of the active noise control system and the size of the quiet zone created by the system. The effect of the reflective ground on the total power output of the control system decreases with the increase of the height of the system to the ground, which is in agreement with Cunefare and Shepard's results.^{6,7} This effect also decreases with the increase of the distance between the primary and control sources, and more significantly with the decrease of the separation between the control source and error microphone.

Compared with the results of local active noise control in free space, the presence of a nearby reflective boundary significantly reduces the size of the quiet zone created by the control system for most configurations. This size reduction

usually decreases as the height of the system to the boundary increases. For the case that the control system is arranged in parallel with the ground, there exists a critical height. The size of the quiet zone will not be reduced if the height of the control system to the ground is shorter than the critical height.

Although the quiet zone created by most arrangements of the control system in half-space is smaller than that in free space, the size of the quiet zone created by the arrangement where the control system is perpendicular to the reflective plane may be increased, except for the specific configurations described by Eqs. (20) and (21).

- ¹J. Tichy, "Current and future issues of active noise control," *J. Acoust. Soc. Jpn. (E)* **12**(6), 255–262 (1991).
- ²P. A. Nelson and S. J. Elliott, *Active Control of Sound* (Academic, San Diego, CA, 1992).
- ³P. A. Nelson and S. J. Elliott, "The minimum power output of a pair of free field monopole sources," *J. Sound Vib.* **105**, 173–178 (1986).
- ⁴P. A. Nelson, A. R. D. Curtis, S. J. Elliott, and A. J. Bullmore, "The minimum power output of free field point sources and the active control of sound," *J. Sound Vib.* **116**, 397–414 (1987).
- ⁵S. J. Elliott, P. Joseph, P. A. Nelson, and M. E. Johnson, "Power output minimization and power absorption in the active control of sound," *J. Acoust. Soc. Am.* **90**, 2501–2512 (1991).
- ⁶K. A. Cunefare and S. Shepard, "The active control of point acoustic sources in a half-space," *J. Acoust. Soc. Am.* **93**, 2732–2739 (1993).
- ⁷W. S. Shepard, Jr. and K. A. Cunefare, "Active control of extended acoustic sources in a half-space," *J. Acoust. Soc. Am.* **96**, 2262–2271 (1994).
- ⁸J. Guo and J. Pan, "Analysis of active noise control in a free field," in *Proceedings of Active 95*, Newport Beach, CA (1995), pp. 649–660.
- ⁹P. M. Morse and K. U. Ingrad, *Theoretical Acoustics* (McGraw-Hill, New York, 1968).
- ¹⁰E. Skudrzyk, *The Foundations of Acoustics: Basic Mathematics and Basic Acoustics* (Springer-Verlag, Vienna, 1971).
- ¹¹A. D. Pierce, *Acoustics: An Introduction to Its Physical Principles and Applications* (Acoustical Society of America, Woodbury, NY, 1989).
- ¹²J. Guo, J. Pan, and C. Bao, "Actively created quiet zones by multiple control sources in free space," *J. Acoust. Soc. Am.* **101**, 1492–1501 (1997).
- ¹³A. David and S. J. Elliott, "Numerical studies of actively generated quiet zones," *Appl. Acoust.* **41**, 63–79 (1994).
- ¹⁴P. Joseph, S. J. Elliott, and P. A. Nelson, "Near field zones of quiet," *J. Sound Vib.* **72**, 605–627 (1994).

A numerical and experimental investigation of the performance of sound intensity probes at high frequencies

Finn Jacobsen, Vicente Cutanda,^{a)} and Peter M. Juhl

Department of Acoustic Technology, Technical University of Denmark, Building 352, DK-2800 Lyngby, Denmark

(Received 18 February 1997; accepted for publication 5 November 1997)

The influence of scattering and diffraction on the performance of sound intensity probes has been examined using a boundary element model of an axisymmetric two-microphone probe with the microphones in the usual face-to-face arrangement. On the basis of calculations for a variety of sound field conditions and probe geometries it is concluded that the optimum length of the spacer between the microphones is about one microphone diameter; with this geometry the effect of diffraction and the finite difference error almost counterbalance each other up to about an octave above the frequency limit determined by the finite difference approximation. This seems to be valid under virtually any sound field condition that could be of practical importance in sound power determination. The upper frequency limit corresponds to about 10 kHz for an intensity probe with $\frac{1}{2}$ -in. microphones, which means that it should be possible to cover most of the audible frequency range, say, from 50 Hz to 10 kHz, with a single probe configuration. The numerical results have been confirmed by a series of experiments. © 1998 Acoustical Society of America.

[S0001-4966(98)04202-7]

PACS numbers: 43.58.Fm, 43.50.Yw, 43.38.Kb [SLE]

INTRODUCTION

All sound intensity probes in commercial production today are based on the "two-microphone" principle which employs two closely spaced pressure microphones.¹ One of the fundamental limitations of this measurement principle is due to the approximation of the particle velocity by a difference of pressures at two closely spaced points. This finite difference approximation obviously imposes an upper frequency limit. The interference of the microphones on the sound field also imposes an upper frequency limit. One of the results of the many investigations in the late 1970s and early 1980s was that the "face-to-face" arrangement is advantageous in this respect.^{2,3} In this configuration the microphones are mounted against each other with a solid plug, a "spacer," between the sensing parts, which means that the bulk of the probe in effect is a cylindrical body.

In the past decade research in this field has concentrated on problems at low and medium frequencies, and the most significant improvement of the instrumentation has been the development of microphones with reduced production tolerances of the phase characteristics and very low vent sensitivity.⁴ The purpose of this paper is to examine whether the performance of intensity probes could be improved at high frequencies.

I. HIGH-FREQUENCY LIMITATIONS

A. The finite difference approximation

Although the finite difference approximation error in principle depends on the sound field,⁵⁻⁷ practice has shown

that the influence of the error on measurement of sound power can be conservatively predicted from the expression for intensity estimation in a plane wave with a direction that coincides with the axis of the probe,¹

$$\hat{I}_r = I_r \frac{\sin k \Delta r}{k \Delta r}, \quad (1)$$

where \hat{I}_r is the estimate of the true intensity component I_r , k is the wave number, and Δr is the microphone separation distance. This expression, which is shown in Fig. 1, implies that the condition

$$k \Delta r < 1.15 \quad (2)$$

ensures that the error is less than 1 dB, corresponding to an upper frequency limit of about 5 kHz if the separation distance is 12 mm, which has usually been regarded as the minimum distance to give acceptably small diffraction errors with standard $\frac{1}{2}$ -in. condenser microphones. This combination is very common. One can, of course, use smaller microphones separated by a correspondingly shorter distance; with $\frac{1}{4}$ -in. microphones separated by a 6-mm spacer, for example, the upper frequency limit will be about 10 kHz, which is more acceptable. Unfortunately the influence of several other measurement errors, of which the most well known and most serious is phase mismatch, is inversely proportional to the length of the spacer.^{5,8-10} This means that an intensity probe with smaller microphones separated by a shorter distance will have a higher lower limiting frequency. To this can be added that, quite apart from the influence of the separation distance, $\frac{1}{4}$ -in. microphones are considerably more noisy than $\frac{1}{2}$ -in. microphones, they are difficult to use because of their low capacitance, and they are not commercially available in pairs as well matched as $\frac{1}{2}$ -in. microphones are.

^{a)}Present address: U.P.M., E.U.I.T. de Telecomunicación, Department of Audiovisual Engineering and Communications, Ctr de Valencia km 7, E-28031 Madrid, Spain.

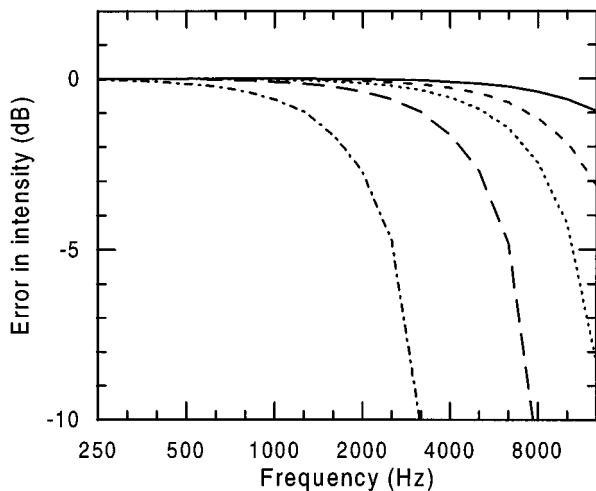


FIG. 1. Finite difference approximation error in plane wave of axial incidence for different spacer lengths; —, 5 mm; ---, 8.5 mm; ···, 12 mm; - · - ·, 20 mm; - - - -, 50 mm.

Another way of overcoming the relatively low upper frequency limit of the sound intensity technique might be to “correct” the finite difference error by multiplying with a factor of $k\Delta r/\sin k\Delta r$, as suggested by Balant *et al.*¹¹ However, this cannot be recommended in the general case; it tends to lead to overestimation because the intensity vector will usually not be perpendicular to the measurement surface used in sound power determination.

One can also extend the frequency range by combining measurements with a probe with $\frac{1}{2}$ -in. microphones separated by a relatively long spacer with measurements with $\frac{1}{4}$ -in. microphones and a 6-mm spacer—but that is not an attractive solution.

B. Scattering and diffraction effects

The foregoing considerations seem to be based on the assumption that the intensity probe actually measures the sound pressure at two discrete positions as it would be in the absence of the probe. However, because of the interference of the probe on the sound field, that is the case only at low frequencies.

Scattering and diffraction effects have been examined experimentally by many workers in the area.^{2,3,12-17} All these investigations have been restricted to examining the performance of intensity probes of various configurations in the simplest of all sound fields, a plane progressive wave, though; and in most cases only axial incidence has been considered. A general conclusion is that the face-to-face configuration with a solid spacer between the microphones is advantageous. With the microphones arranged in this configuration the phase difference between the two microphone signals increases nearly linearly with the frequency over a wider frequency range than with the same configuration without the spacer or with any other configuration, in particular for nonaxial incidence of the plane wave. It has also been observed that a long cylindrical probe (which cannot be used in practice) performs better than a similar short probe in this respect.¹⁶

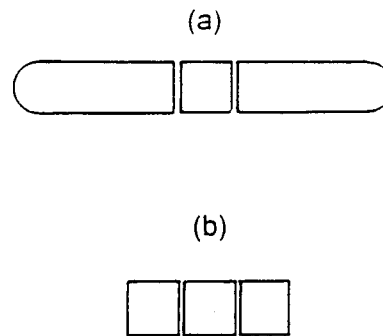


FIG. 2. Intensity probe geometries. (a) Long probe, (b) short probe.

One of the characteristics of the face-to-face arrangement with a spacer between the microphones is that there is a small cavity in front of the diaphragm of each microphone. This cavity is connected to the outside via the slots of the microphone grid. The experimental results published in Refs. 15 and 16 imply that diffraction effects due to the cylinder in combination with the resonance of the cavities give rise to a pressure increase on both diaphragms that amounts to about 5 dB at 10 kHz for a probe with $\frac{1}{2}$ -in. microphones subjected to a plane wave of axial incidence. Watkinson and Fahy suggest that this increase could be used to compensate for the finite difference error.¹⁵

Diffraction experiments are rather difficult to perform; they tend to be disturbed by the influence of supporting devices, imperfections of the anechoic room, etc. Therefore, numerical models would seem to have some advantages in studying the performance of various probe configurations. However, only one single numerical investigation of the behavior of sound intensity probes has been found in the literature.¹⁸ Also here the analysis was restricted to plane waves of axial incidence. Unfortunately, the face-to-face arrangement with a spacer between the microphones, which seems to be superior according to the experimental data presented in Refs. 2, 3, and 14–16, was not examined in this investigation.

It must be concluded that diffraction effects have been studied systematically only in very simple sound fields, and that existing sound intensity probes have not been optimized for high-frequency performance.

II. A BOUNDARY ELEMENT MODEL

The boundary element method based on the Helmholtz integral equation is particularly suited for solving scattering and diffraction problems.^{19,20} Such a model has been implemented for various axisymmetric probe configurations, two of which are shown in Fig. 2. Details of the model of intensity probes have been given elsewhere;²¹ here it suffices to say that each pressure signal is calculated as a weighted average of the pressure on the diaphragm, the weighting function being due to the shape of the dominating first membrane mode and the finite size of the backplate behind the diaphragm.²² The model is idealized in three respects: (i) nonaxisymmetric parts of the probe are ignored, (ii) a parabolic mode shape of the diaphragm is assumed, and (iii) the finite acoustic impedance of the diaphragm is not taken into

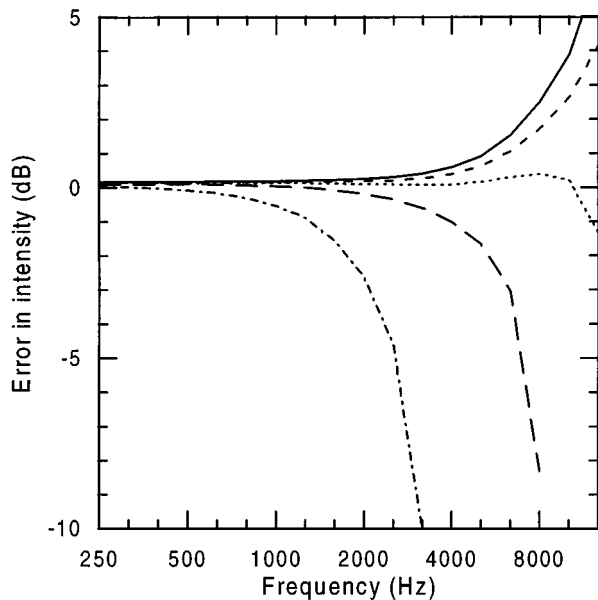


FIG. 3. Error of short probe with half-inch microphones in a plane wave of axial incidence. Length of spacer: —, 5 mm; ---, 8.5 mm; ···, 12 mm; -·-·-, 20 mm; - - - -, 50 mm.

account. The two last mentioned simplifications are certainly reasonable in the frequency range of concern here, well below the resonance frequency of the diaphragm.²² The first one, which leads to a significant reduction of the required computer memory and calculation time, is perhaps also reasonable since the diffraction behavior of existing probes with $\frac{1}{2}$ -in. microphones can be expected to be dominated by the bulk of the microphones and the spacer.

All results presented in the following have been calculated for $\frac{1}{2}$ -in. microphones, that is, for a cylinder with a diameter of 12.7 mm. There is a gap of 1.1 mm between the diaphragm and the solid spacer. The diameter of the diaphragm is 9 mm, and the diameter of the backplate is 7.2 mm. Two geometries are investigated here, a “long probe” of which each “microphone” is a 31.8-mm-long cylinder with a hemispherical end, and a “short probe,” the microphones of which are 12 mm long and have flat ends. (Various other geometries have also been examined.) The geometry of the short probe is actually modeled after a probe in commercial production, Brüel & Kjær’s type 3548 with 4181 microphones. Note that “length of spacer” includes one gap (i.e., half a gap at both ends), so the physical length of a “12-mm spacer” is 10.9 mm. The calculations have been carried out at the one-third octave center frequencies from 250 Hz to 12.5 kHz. Evidently, reducing all dimensions of the probe by a factor of 2 corresponds to doubling the frequency.

A. Numerical results; single position

Figure 3 shows the indicated sound intensity normalized with the true intensity, calculated for the short probe with five different spacers in a plane wave of axial incidence. The intensity has been determined from the two (complex) pressure signals as sensed by the probe, \hat{p}_1 and \hat{p}_2 , as follows:

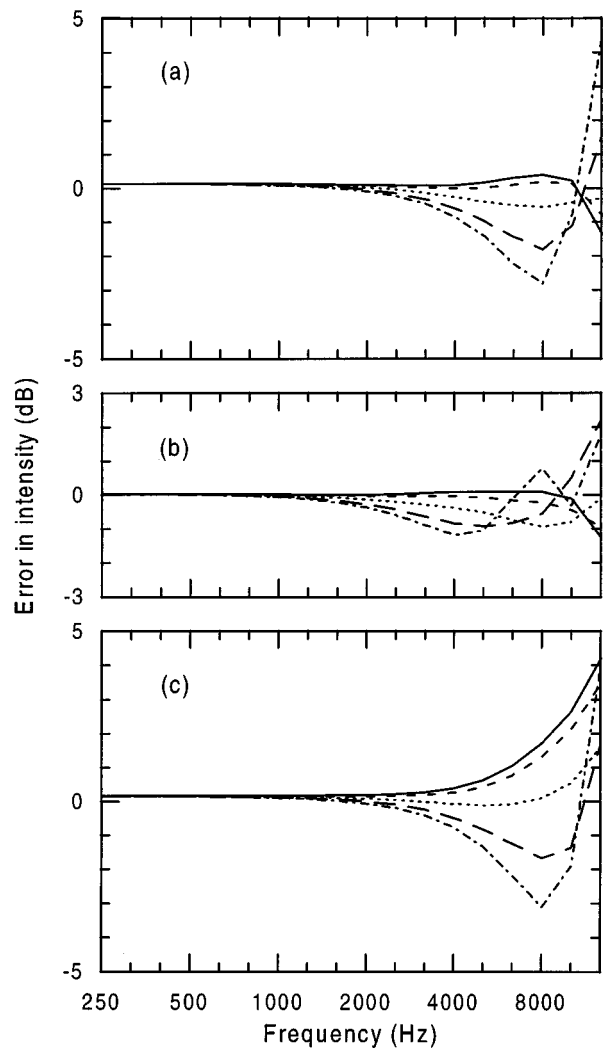


FIG. 4. Errors of intensity probes with $\frac{1}{2}$ -in. microphones. (a) Short probe, 12-mm spacer, (b) long probe, 12-mm spacer, (c) short probe, 8.5-mm spacer. Angle of incidence: —, 0°; ---, 20°; ···, 40°; -·-·-, 60°; - - - -, 80°.

$$\hat{I}_r = \frac{\text{Im}\{\hat{p}_1 \hat{p}_2^*\}}{2\rho c k \Delta r}, \quad (3)$$

where ρ is the density of air. At high frequencies the performance of the probe is essentially the result of the combined effect of the finite difference error shown in Fig. 1 and the pressure increase mentioned above, and it is apparent that the two effects very nearly counterbalance each other up to 10 kHz with the 12-mm spacer, as anticipated by Watkinson and Fahy.¹⁵ A shorter spacer leads to overestimation, and with a long spacer the upper frequency limit is determined by the sinc-function, Eq. (1). Results obtained with the long probe are quite similar. It is interesting that a probe with $\frac{1}{2}$ -in. microphones separated by a 12-mm spacer performs better at high frequencies than a probe with $\frac{1}{4}$ -in. microphones separated by a 12-mm spacer; this follows from the fact that the compensating pressure increase is shifted upwards by an octave in the latter case.

Figure 4 shows the errors for nonaxial incidence, calculated for the three different combinations of probe shapes

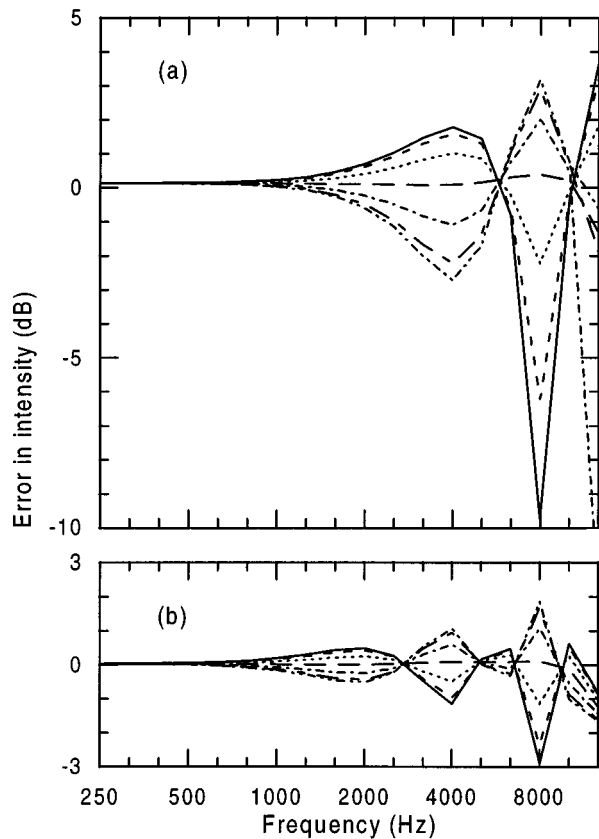


FIG. 5. Errors of intensity probes with half-inch microphones and a 12-mm spacer in an axial standing wave field with a standing wave ratio of 24 dB. (a) Short probe, (b) long probe. Phase angle between the two interfering plane waves: —, -90° ; ---, -60° ; ···, -30° ; — —, 0° ; - · - ·, 30° ; - - - -, 60° ; · · · · ·, 90° .

and spacer lengths. The figure demonstrates that the errors increase with the angle of incidence if the length of the spacer is optimized for axial incidence; they are much larger if the plane wave propagates in a direction almost perpendicular to the probe. With a shorter spacer the influence of the angle of incidence is increased. It can also be seen that the sharp edges of the short probe have an unfavorable influence for nonaxial incidence; the longer probe with rounded ends is clearly superior. Note that the short probe overestimates the intensity slightly at low frequencies irrespective of the angle of incidence, in agreement with the experimental observation that the “effective separation distance” is slightly larger than the actual distance.¹⁶

Finally Fig. 5 demonstrates that the errors vary with the position of the probe in a standing wave field. It is interesting and rather surprising that, irrespective of the standing wave ratio, the effect of diffraction is the same both at pressure maxima and minima as in a plane progressive wave, whereas diffraction has a more serious influence and increases with the standing wave ratio at positions midway between these positions. (See the Appendix.) It is also apparent that the longer the probe, the less the error.

The influence of the gap in front of each microphone diaphragm has also been examined; the gap has very little influence.

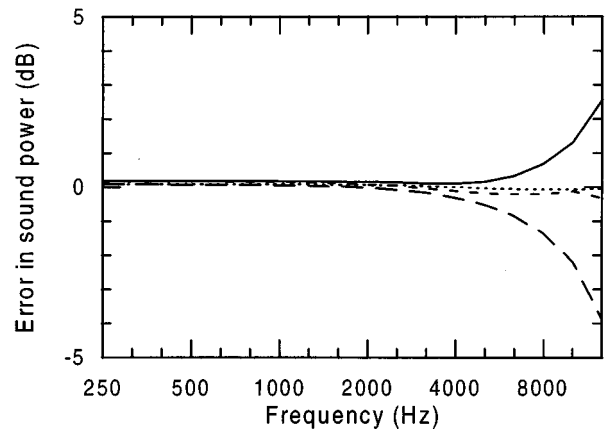


FIG. 6. Calculated error in sound power determination with the short probe in the absence of extraneous noise. —, $\frac{1}{2}$ -in. microphones, 8.5-mm spacer; ---, $\frac{1}{2}$ -in. microphones, 12-mm spacer; ···, $\frac{1}{4}$ -in. microphones, 6-mm spacer; - - -, $\frac{1}{4}$ -in. microphones, 12-mm spacer.

B. Numerical results; sound power determination

The most important application of sound intensity measurements is the determination of sound power, which involves integrating the normal component of the intensity over a surface that encloses the source under test. To examine the influence of scattering and diffraction on sound power determination, such measurements have been simulated by summing over the indicated intensity at a number of positions on a surface that encloses a monopole source in free field, with or without another monopole source outside the surface. The surface is a cube of $1 \times 1 \times 1$ m, and the normal component of the intensity is calculated at 36 points on each face of the surface. The calculations have been made for the short probe with $\frac{1}{2}$ -in. microphones and various spacers as described in the foregoing, but also for a similar probe with $\frac{1}{4}$ -in. microphones. (The latter is no longer a mere scaling, because the measurement surface is fixed.)

In Fig. 6 are shown the results of such a simulated sound power measurement without an extraneous source. As can be seen the errors are more or less as one would expect from Fig. 3, that is, in spite of the finite difference error the performance of a probe with $\frac{1}{2}$ -in. microphones and a 12-mm spacer is nearly perfect up to 12.5 kHz, whereas the sound power is overestimated with a shorter spacer. With a probe with $\frac{1}{4}$ -in. microphones and a 12-mm spacer the finite difference error dominates below 12.5 kHz; therefore the sound power is underestimated.

Figure 7 shows the results of similar “measurements” in the presence of background noise from an uncorrelated monopole source. “Uncorrelated” implies that the calculated sound intensity component due to the disturbing source at each position has been added to the calculated sound intensity component due to the primary source. (If both sources were included in one boundary element calculation the result would correspond to completely correlated sources, which generate an interference field.) In the results presented in Fig. 7(a) and (b) the extraneous source is 2 m from the center of one of the faces of the cube, and its sound

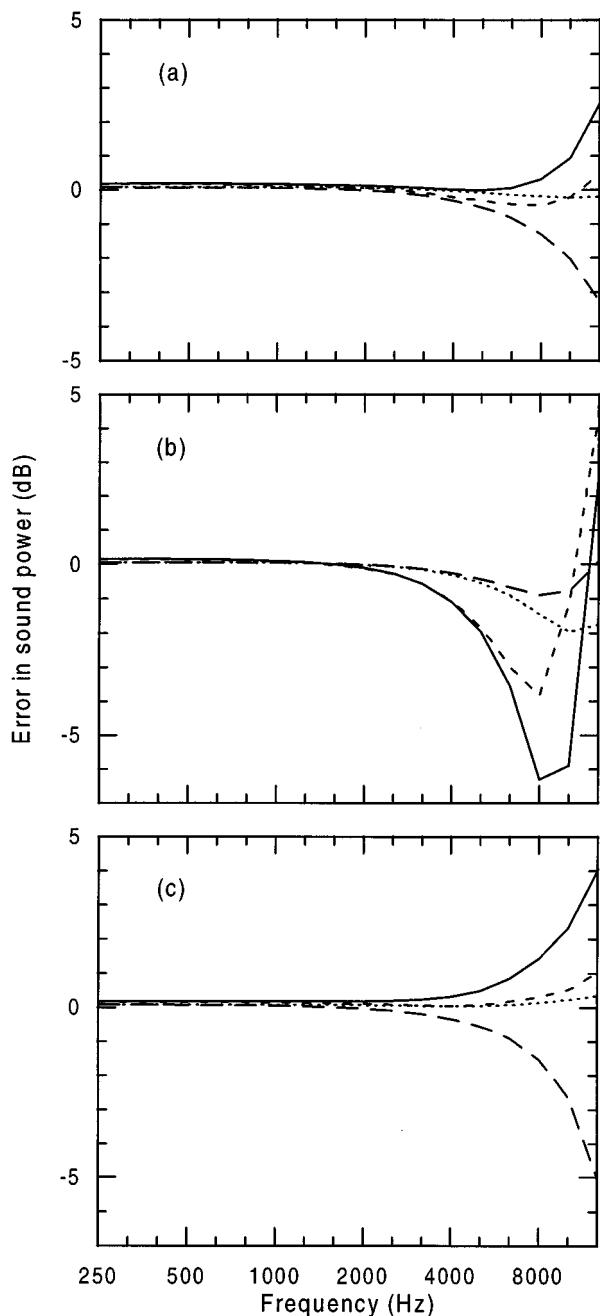


FIG. 7. Calculated error in sound power determination with the short probe in the presence of background noise from an uncorrelated source. (a) Extraneous source 10 dB stronger than the source under test, placed 2 m from one of the faces of the cubic measurement surface; (b) extraneous source 20 dB stronger than the source under test, placed 2 m from one of the faces of the cubic measurement surface; (c) extraneous source 20 dB stronger than the source under test, placed diagonally 2 m from an edge of the cubic measurement surface. —, $\frac{1}{2}$ -in. microphones, 8.5-mm spacer; ---, $\frac{1}{2}$ -in. microphones, 12-mm spacer; \cdots , $\frac{1}{4}$ -in. microphones, 6-mm spacer; - - , $\frac{1}{4}$ -in. microphones, 12-mm spacer.

power outputs are, respectively, 10 and 20 dB larger than the sound power of the source under test. It is apparent that the intensity probe with $\frac{1}{2}$ -in. microphones and a 12-mm spacer is able to suppress noise from an extraneous source only up to a certain level at high frequencies, the reason being that the surface integral of the intensity associated with the dis-

turbing source differs from zero because of diffraction effects. On the other hand, Fig. 7(c) demonstrates that the ability of suppressing disturbing noise depends on the position of the extraneous source. In this case the source is in a plane that bisects the cubic measurement surface diagonally, 2 m from the nearest edge, and although its sound power output is again 20 dB larger than the sound power of the source under test, the performance of the various combinations of probes and spacers is almost unaffected by the strong disturbing sound field. The influence of the position of the extraneous source on the performance of a probe with $\frac{1}{2}$ -in. microphones and an 8.5-mm spacer is particularly strong, in agreement with the observation that this configuration is more seriously affected by the angle of incidence of a plane wave.

III. DISCUSSION

The numerical results presented in the foregoing lead to the conclusion that the optimum length of the spacer is about 12 mm for a sound intensity probe with $\frac{1}{2}$ -in. microphones in the face-to-face configuration, and that such a probe performs tolerably well up to 10 kHz under a variety of sound field conditions. In other words, it covers just about the entire frequency range where sound power measurement is relevant. This is rather surprising in view of the fact that intensity probes that comply with this description have been on the market for about 15 years.²³ If one consults Fahy's monograph on sound intensity and its measurement one certainly gets the impression that the upper frequency range of such a probe is 5 kHz in accordance with the inequality (2).¹ According to a well-known manufacturer of sound intensity probes, their probes should be used up to 5 kHz with a 12-mm spacer,²⁴ and up to 6.3 kHz with an 8.5-mm spacer.²⁵ Moreover, an IEC standard on instruments for the measurement of sound intensity actually *requires* that the sound intensity response of the probe in a plane progressive wave of axial incidence shall follow the sinc-function [Eq. (1)] within a certain tolerance.²⁶

The most probable explanation of the remarkable fact that no one has discovered that the probe performs very well at much higher frequencies than 5 kHz is that Brüel & Kjær's sound intensity microphones of type 4181, which are rather dominating in this area, are overdamped, so-called free field microphones, that is, microphones designed to have a flat response in a plane wave of 0° incidence. Since, surprisingly, the free field responses of two microphones in the face-to-face arrangement with a solid spacer between them differ little from the free field response of one microphone, as pointed out by Fahy and Elliott,³ this means that the *pressure* response of a probe with $\frac{1}{2}$ -in. microphones of type B&K 4181 in a plane wave of axial incidence is essentially flat up to 10 kHz; the *intensity* response, however, is not. The resulting underestimation may well have been confounded with finite difference errors. Clearly, "pressure" microphones rather than "free field" microphones should be used, as also pointed out by Fahy and Elliott.³ However, whereas one cannot in the general case compensate for the finite difference approximation error, it is unproblematic to compensate for a frequency-dependent pressure response.

Both the IEC standard on sound intensity instruments²⁶ and the corresponding American ANSI standard²⁷ require a flat pressure response of the probe in a plane progressive wave of axial incidence (within a certain tolerance). However, a probe with $\frac{1}{2}$ -in. microphones of the “pressure field” type does not have a flat pressure response above 5 kHz.^{16,21} It seems reasonable to optimize the high-frequency performance of sound intensity probes with respect to the *intensity* response rather than the pressure response, the more so since the pressure response at high frequencies depends strongly on the angle of incidence whereas it seems to be possible to obtain an intensity response that is essentially flat.

Although the resonances of the cavities compensate very well for the finite difference error in some cases, the compensation is not perfect, cf. Figs. 4 and 5. It is apparent that fairly large errors can occur, also below the frequency that has hitherto been believed to be the upper frequency limit of this configuration, when the angle between the axis of the probe and the direction of the (true) intensity is nearly 90°. In fact, other numerical experiments, not presented here, have shown that arbitrarily large errors can occur under sufficiently extreme sound field conditions, also well below 5 kHz. However, this is unlikely to be a serious problem in sound power determination, because the component of the intensity in the direction of the probe is very small under such circumstances, which means that it does not contribute very much to the surface integral. This conclusion is supported by the simulated sound power measurements presented in Figs. 6 and 7: although errors occur in measurement of sound intensity at certain angles of incidence, they tend to be averaged out in sound power determination. In fact, it is easy to show that a plane wave generated by a distant extraneous source in free field would not in any way disturb sound power determination obtained by integrating the normal component of the intensity over a rectangular surface (in theory), irrespective of the relative strengths of the sources and irrespective of how much the sound field is disturbed by the presence of the intensity probe, provided that the probe is axisymmetric and symmetric about the spacer. (In practice the measurement accuracy would deteriorate because of spatial sampling errors if the extraneous sound field were sufficiently strong.)

For the same reason the shape of the intensity probe is probably not as important in sound power determination as Figs. 4 and 5 would seem to indicate. Although it is clear that the sharp edges of the short probe are unfavorable, it can be useful that the probe can be placed very near a vibrating surface, which means that it cannot be very long. A probe slightly longer than the “short” probe and with rounded ends would probably be the best compromise.

IV. EXPERIMENTAL RESULTS

The most important conclusion to be drawn from the numerical results presented in the foregoing is that the optimum length of the spacer between the two microphones of an intensity probe is about one microphone diameter; with this configuration the useful frequency range of the probe is extended by about an octave above the limit determined by the finite difference error. In particular, a probe with $\frac{1}{2}$ -in.

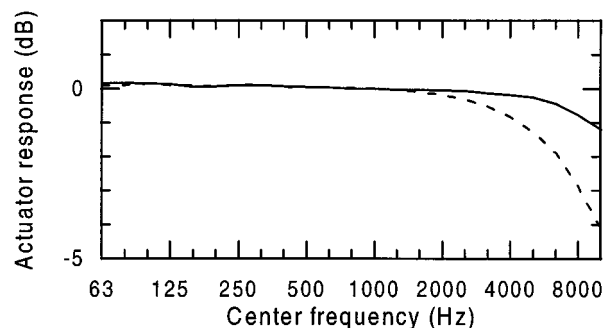


FIG. 8. Electrostatic actuator response of microphones of intensity probe. —, B&K type 4178; ---, B&K type 4181.

microphones separated by a 12-mm spacer should be able to cover the frequency range up to 10 kHz in sound power determination with insignificant errors under any realistic sound field condition.

To test this conclusion a series of experiments has been carried out: the sound power of a loudspeaker driven with pink noise, B&K 4205, was determined under a variety of acoustic conditions. The source was placed on the floor, and the radiated sound power was estimated by scanning manually with an intensity probe over the five faces of a cubic surface of $1 \times 1 \times 1$ m.

A frequency analyzer of type B&K 3550 was used in combination with an intensity probe of type B&K 3548, either with $\frac{1}{2}$ -in. microphones of type B&K 4181 or with $\frac{1}{4}$ -in. microphones of type B&K 4178. Since these microphones are so-called free-field microphones it is necessary to compensate for the drop of the pressure sensitivity at high frequencies. Figure 8 shows the pressure response of the two sets of microphones, determined with an electrostatic actuator. All the results presented in the following have been corrected with the corresponding actuator response. (In the frequency range well below the resonance frequency of the microphones the radiation impedance is much smaller than the acoustic impedance of the diaphragm, which means that the actuator response is proportional to the pressure response.)

The first series of measurements were carried out in a large (240 m^3) reverberant room with a reverberation time of about 4 s under three conditions: (i) without extraneous noise, (ii) with strong diffuse background noise from a distant source (Airap A14 from Électricité de France), and (iii) with strong nondiffuse and diffuse background noise from the same source placed about 2.5 m from the surface. In the last mentioned case the partial sound power of the nearest 1-m^2 segment was negative in the entire frequency range.

The measurements with $\frac{1}{4}$ -in. microphones were carried out with a 6-mm spacer and with a 12-mm spacer. The former measurement, which can be expected to be reliable at high frequencies, served as the reference in the frequency range from 4–10 kHz. The measurements with $\frac{1}{2}$ -in. microphones were carried out with an 8.5-mm spacer, a 12-mm spacer, and a 50-mm spacer. In order to reduce the effect of transducer phase mismatch as far as possible, all measure-

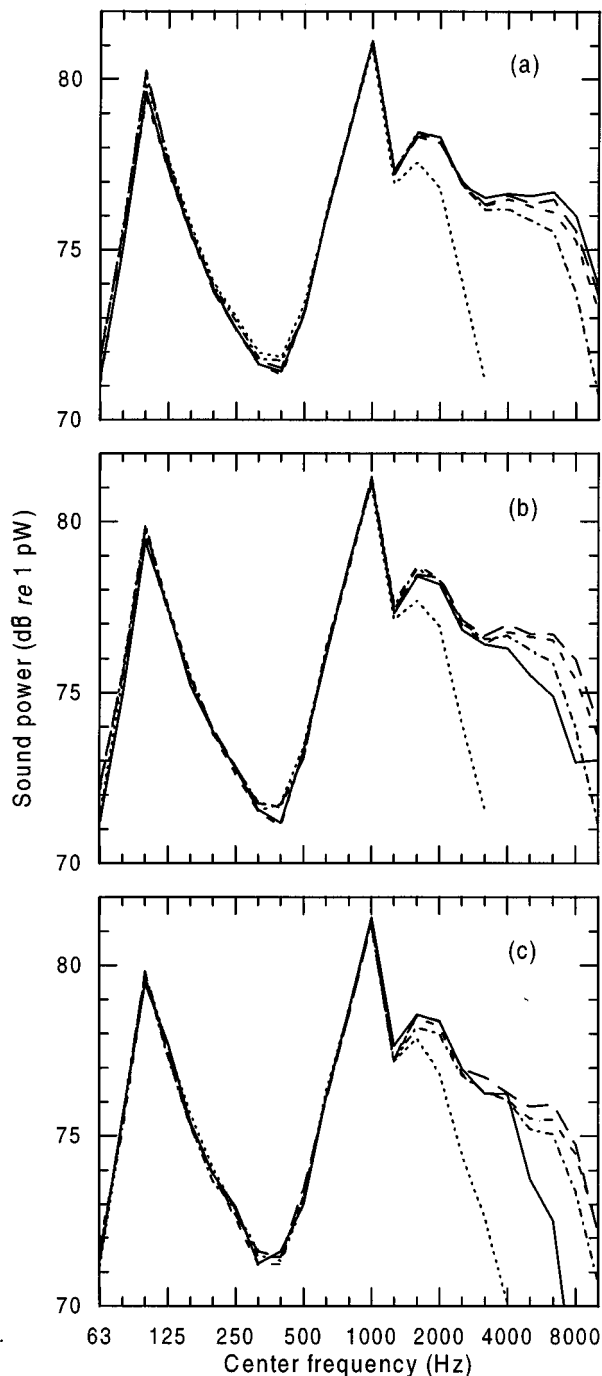


FIG. 9. Sound power of source in a reverberation room, measured with different combinations of microphones and spacers. (a) No extraneous noise, (b) strong diffuse background noise from an extraneous source, (c) strong diffuse and nondiffuse noise from an extraneous source. —, $\frac{1}{2}$ -in. microphones, 8.5-mm spacer; ---, $\frac{1}{2}$ -in. microphones, 12-mm spacer; \cdots , $\frac{1}{2}$ -in. microphones, 50-mm spacer; - - - , $\frac{1}{4}$ -in. microphones, 6-mm spacer; - · - · , $\frac{1}{4}$ -in. microphones, 12-mm spacer.

ments were repeated with the two microphones interchanged.²⁸

The results of the sound power measurements are presented in Fig. 9; Fig. 10, which shows the corresponding values of the pressure-intensity index, gives an impression of the acoustic conditions. It can be seen from Fig. 9 that prac-

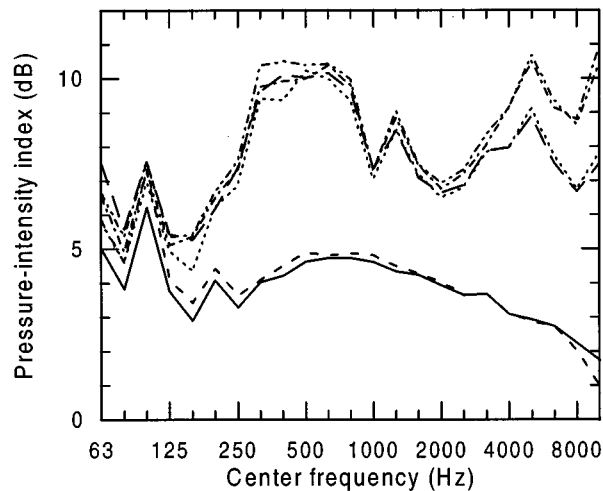


FIG. 10. Pressure-intensity index. —, $\frac{1}{4}$ -in. microphones, 6-mm spacer, no extraneous noise; ---, $\frac{1}{2}$ -in. microphones, 12-mm spacer, no extraneous noise; \cdots , $\frac{1}{4}$ -in. microphones, 6-mm spacer, diffuse noise; - - - , $\frac{1}{2}$ -in. microphones, 12-mm spacer, diffuse noise; - · - · , $\frac{1}{4}$ -in. microphones, 6-mm spacer, nondiffuse and diffuse noise; - - - - , $\frac{1}{2}$ -in. microphones, 12-mm spacer, nondiffuse and diffuse noise.

tically all measurements are in agreement from 63 Hz to 1.25 kHz. However, without compensation for phase mismatch significant errors occurred with the $\frac{1}{4}$ -in. microphones in most of the frequency range. From 1.6 kHz and upwards the combination of $\frac{1}{2}$ -in. microphones and the 50-mm spacer underestimates, but it is worth noting that the error is less than predicted by the idealized expression for an axial plane wave (Fig. 1), and that the size of the error depends on the sound field conditions, which leads to the conclusion that one cannot compensate for the finite difference error. The combination of $\frac{1}{4}$ -in. microphones and a 12-mm spacer leads to underestimation from 5 kHz and upwards, more or less as expected. The measurements with $\frac{1}{2}$ -in. microphones and the 12-mm spacer are in fair agreement with the reference measurements, confirming the predicted advantage of this combination. The behavior of the combination of $\frac{1}{2}$ -in. microphones and the 8.5-mm spacer is more complicated. As can be seen, it overestimates slightly under mild measurement conditions, but underestimates under more difficult conditions. It seems as if the ability to suppress extraneous noise at high frequencies deteriorates if the spacer is significantly shorter than the diameter of the microphones, in agreement with the numerical results (cf. Fig. 7).

Figure 11 summarizes the high-frequency performance of the sound intensity probe with the most favorable geometry, a probe with $\frac{1}{2}$ -in. microphones and a 12-mm spacer, in sound power determination under the three acoustic conditions described above. Clearly the probe performs quite well even at 8 and 10 kHz.

Many other sound power measurements have been carried out, with similar results. It should finally be mentioned that no difference has been found between the performance of the B&K 3548 probe and the newer, smoother, more robust version of the probe with an improved brace, UA 1250.²⁵ Likewise, plastic cones mounted on the B&K 3548

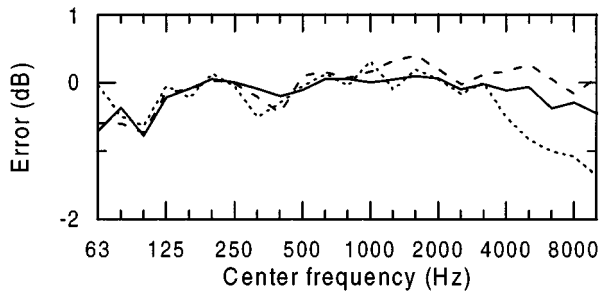


FIG. 11. Deviations between sound power measurements with an intensity probe with $\frac{1}{2}$ -in. microphones and a 12-mm spacer under three conditions and a sound power measurement with a probe with $\frac{1}{4}$ -in. microphones and a 6-mm spacer under the most favorable of these conditions. —, reverberation room, no extraneous noise, ---, reverberation room, diffuse noise from distant source; ···, reverberation room, noise from source close to measurement surface.

probe so as to taper the $\frac{1}{2}$ -in. microphones smoothly had no appreciable influence in sound power determination.

V. CONCLUSIONS

A numerical and experimental study of the performance of sound intensity probes with the microphones in the usual face-to-face arrangement has demonstrated that the optimum length of the spacer between the microphones is about one microphone diameter. With this geometry, diffraction effects tend to compensate for the finite difference approximation error inherent in the measurement principle, which means that the operational frequency range of the probe is significantly larger than hitherto believed.

A practical consequence is that a sound intensity probe with $\frac{1}{2}$ -in. microphones separated by a 12-mm spacer can cover the frequency range up to 10 kHz.

APPENDIX: DIFFRACTION EFFECTS IN A PLANE STANDING WAVE FIELD

Let \hat{p}_1 and \hat{p}_2 be the pressures as sensed by the microphones of a sound intensity probe in a plane progressive wave of axial incidence. If the intensity probe is symmetric about the spacer, it follows from the principle of superposition that the corresponding pressures are

$$\hat{p}_1^i = \hat{p}_1 + R\hat{p}_2, \quad (\text{A1a})$$

$$\hat{p}_2^i = \hat{p}_2 + R\hat{p}_1, \quad (\text{A1b})$$

in the interference field composed by the plane wave and another plane wave propagating in the opposite direction, where the latter wave is modified in amplitude and phase by the complex factor R . Therefore the indicated intensity in the standing wave field is

$$\begin{aligned} \hat{I}_r^i &= \frac{\text{Im}\{\hat{p}_1^i(\hat{p}_2^i)^*\}}{2\rho ck\Delta r} \\ &= \frac{\text{Im}\{(\hat{p}_1 + R\hat{p}_2)(\hat{p}_2^* + R^*\hat{p}_1^*)\}}{2\rho ck\Delta r} \\ &= \frac{\text{Im}\{\hat{p}_1\hat{p}_2^* + |R|^2\hat{p}_1^*\hat{p}_2\}}{2\rho ck\Delta r} + \frac{|\hat{p}_2|^2 - |\hat{p}_1|^2}{4\rho ck\Delta r} 2|R|\sin\theta \\ &= \hat{I}_r(1 - |R|^2) - 2\hat{J}_r|R|\sin\theta, \end{aligned} \quad (\text{A2})$$

where \hat{I}_r is the indicated intensity (subject to diffraction) in the plane progressive wave, \hat{J}_r is the corresponding indicated reactive intensity (which in this case is *the result of diffraction*—there is no reactive part in a plane wave),²⁹ and θ is the phase angle of R . (The phase angle θ corresponds to the distance between the position of the probe and a position where the pressure assumes a maximum or a minimum value.) Since the true intensity in the standing wave field is

$$I_r^i = I_r(1 - |R|^2), \quad (\text{A3})$$

where I_r is the true intensity in the plane progressive wave, it can be seen that, surprisingly, the relative diffraction error is the same as in the plane wave in the standing wave at positions where the pressure assumes maximum and minimum values.

Equation (A2) is also valid at the position halfway between two interfering monopole sources in free space; Eq. (A3), however, is not.

¹F. J. Fahy, *Sound Intensity* (Spon, London, 1995), 2nd ed. See sections 5.2, 5.6, and 6.2.

²G. Rasmussen and M. Brock, "Acoustic intensity measurement probe," in *Proceedings Recent Developments in Acoustic Intensity Measurement*, edited by M. Bockhoff (Senlis, France, 1981), pp. 81–88.

³F. J. Fahy and S. J. Elliott, "Practical considerations in the choice of transducers and signal processing techniques for sound intensity measurements," in *Proceedings Recent Developments in Acoustic Intensity Measurement*, edited by M. Bockhoff (Senlis, France, 1981), pp. 37–44.

⁴E. Frederiksen and O. Schultz, "Pressure microphones for intensity measurements with significantly improved phase properties," *Brüel & Kjær Tech. Rev.* **4**, 11–23 (1986).

⁵G. Pavić, "Measurement of sound intensity," *J. Sound Vib.* **51**, 533–545 (1977).

⁶J. K. Thompson and D. R. Tree, "Finite difference approximation error in acoustic intensity measurements," *J. Sound Vib.* **75**, 229–238 (1981).

⁷U. S. Shirahatti and M. J. Crocker, "Two-microphone finite difference approximation errors in the interference fields of point dipole sources," *J. Acoust. Soc. Am.* **92**, 258–267 (1992).

⁸S. Gade, "Sound intensity. Part I Theory," *Brüel & Kjær Tech. Rev.* **3**, 3–39 (1982).

⁹F. Jacobsen, "Sound intensity measurements at low levels," *J. Sound Vib.* **166**, 195–207 (1993).

¹⁰F. Jacobsen and E. S. Olsen, "The influence of microphone vents on the performance of sound intensity probes," *Appl. Acoust.* **41**, 25–45 (1994).

¹¹A. C. Balant, G. C. Maling, Jr., and D. M. Yeager, "Measurement of blower and fan noise using sound intensity techniques," *Noise Control Eng. J.* **33**, 77–88 (1989).

¹²J. Tichy, "Some effects of microphone environment on intensity measurements," in *Proceedings Recent Developments in Acoustic Intensity Measurement*, edited by M. Bockhoff (Senlis, France, 1981), pp. 25–30.

¹³G. Krishnappa, "Interference effects in the two microphone technique of acoustic intensity measurements," *Noise Control Eng. J.* **21**, 126–135 (1983).

¹⁴G. Krishnappa, "Scattering/diffraction effects in the two-microphone technique of measuring sound intensity at sound incidence angles other than 0°," *Noise Control Eng. J.* **22**, 96–102 (1984).

- ¹⁵P. S. Watkinson and F. J. Fahy, "Characteristics of microphone arrangements for sound intensity measurement," *J. Sound Vib.* **94**, 299–306 (1984).
- ¹⁶E. Frederiksen and M. Piil, "Characteristics of microphone pairs and probes for sound intensity measurements," Brüel & Kjær, Nærum, Report BA0077-11 (1987).
- ¹⁷J. C. Rébillat and S. Rifai, "Détermination expérimentale de la diffraction acoustique autour de sondes intensimétriques," *Acustica* **70**, 83–88 (1990).
- ¹⁸J. C. Rébillat, "Estimation numérique de la diffraction acoustique autour de sondes intensimétriques," *Acustica* **63**, 203–210 (1987).
- ¹⁹B. B. Baker and E. T. Copson, *The Mathematical Theory of Huygen's Principle* (Oxford U.P., Oxford, 1953), 2nd ed.
- ²⁰A. F. Seybert, B. Soenarko, F. J. Rizzo, and D. J. Shippy, "An advanced computational method for radiation and scattering of acoustic waves in three dimensions," *J. Acoust. Soc. Am.* **77**, 362–368 (1985).
- ²¹V. Cutanda, P. M. Juhl, and F. Jacobsen, "The influence of thin shapes and narrow gaps on the convergence of boundary element formulations," submitted to *J. Acoust. Soc. Am.*
- ²²P. Juhl, "A numerical investigation of standard condenser microphones," *J. Sound Vib.* **177**, 433–446 (1994).
- ²³O. Roth, "A sound intensity real-time analyzer," in *Proceedings Recent Developments in Acoustic Intensity Measurement*, edited by M. Bockhoff (Senlis, France, 1981), pp. 69–74.
- ²⁴Anon.: Product Data. Sound Intensity Probes Types 3520, 3545, 3547, 3548. Sound Intensity Microphone Pairs Types 4178, 4181 (Brüel & Kjær, Nærum, 1991).
- ²⁵S. Gade and K. B. Ginn, "Design of a new robust sound intensity probe," in *Proceedings of the Third International Congress on Air- and Structure-Borne Sound and Vibration*, edited by M. J. Crocker (Montréal, Canada, 1994), pp. 1037–1044.
- ²⁶IEC International Standard 1043, "Electroacoustics—Instruments for the measurement of sound intensity—Measurements with pairs of pressure sensing microphones" (1993).
- ²⁷ANSI S1.12-1994, "American National Standard Instruments for the measurement of sound intensity" (American National Standards Institute, New York, 1994).
- ²⁸F. Jacobsen, "A note on the accuracy of phase compensated intensity measurements," *J. Sound Vib.* **174**, 140–144 (1994).
- ²⁹F. Jacobsen, "Active and reactive, coherent and incoherent sound fields," *J. Sound Vib.* **130**, 493–507 (1989).

Energy fields of partially coherent sources

Jing-Fang Li^{a)} and Jean-Claude Pascal^{b)}

Centre Technique des Industries Mécaniques (CETIM), 60300 Senlis, France

Claude Carles

Conservatoire National des Arts et Métiers (CNAM), 75141 Paris Cedex 03, France

(Received 12 December 1995; accepted for publication 5 November 1997)

Random acoustic fields and their energetic quantities (acoustic active and reactive intensities, potential and kinetic energy densities) are described in terms of the mutual coherences between sources. Conditions to correctly construct the coherence matrix of sources in a multivariate random process are given. It is shown that the description of a sound field using the coherence matrix of source is equivalent to the superposition of a number of independent coherent fields, which do not correspond to the original localized sources. A method based on processing the principal components of the coherence matrix of sources is given to reduce the number of necessary fields. The coherence function between acoustic pressure and particle velocity and the curl of active intensity are proposed as two indicators for estimating the degree of coherence and the polarization of acoustic fields. These indicators are analyzed theoretically and experimentally. The description of the structure of partially coherent fields is generalized by the definition of the field matrix whose rank is an indicator of the local complexity of an acoustic field. © 1998 Acoustical Society of America. [S0001-4966(98)04102-2]

PACS numbers: 43.58.Fm, 43.20.Fn, 43.60.Cg [SLE]

INTRODUCTION

For a better comprehension of the characteristics of sound intensity fields observed around real sources, models consisting of point sources have often been used to simulate the complexity of interference fields.¹⁻⁴ It has been shown that the influence of the coherence between sources on the directivity of acoustic radiation is considerable.³ The relationship of the coherence between elementary sources is important when studying the structure of acoustic fields corresponding to harmonic (fully coherent) or random (partially coherent) fields. The latter case is the general situation encountered in industrial applications. However, many techniques, such as the holography reconstruction, the identification of models, and active control, are based on the relationships defined for coherent fields. Their adaptation to general fields requires a model for these random fields. Filippi and Mazzoni⁵ used the cross spectrum between two pressure points to describe these fields and gave a decomposition method in elementary fields.

The objective of this paper is to investigate an energy field produced by partially coherent sources using a source model composed of elementary sources (monopoles and dipoles). The definition of a coherence matrix of sources in Sec. I is a solution for the representation of a partially coherent field and allows all the energetic quantities to be expressed and calculated. Conditions are given to correctly construct the coherence matrix of sources. In Sec. II, the

relationships between partially coherent fields and their decomposed-independent fields are established by the analysis of the principal components of the coherence matrix of sources. It is shown that a partially coherent field can be represented as the superposition of independent fields. Section III presents how to characterize the structure of a partially coherent field using two measurable indicators which are expressed in terms of the coherence matrix of sources: the coherence function between acoustic pressure and particle velocity and the curl of active intensity. Finally we will show that the field matrix defined in this paper can be used to reveal the structure of an acoustic field from all the relationships between the energetic quantities.

I. REPRESENTATIONS OF ENERGY FIELD FROM A SOURCE MODEL

Energetic quantities, such as the active and reactive intensities and the potential and kinetic energy densities, are very useful for studying energy flow and source location. The purpose of this section is to show how to express energy fields of partially coherent sources. First, the fundamental relationships for energetic quantities in a coherent field are reviewed. Then, the expressions for a partially coherent sound field will be developed using a coherence matrix of sources.

A. Fundamental relationships of coherent fields

The time-averaged energetic quantities of an acoustic field can be expressed using the complex notation of the pressure p and the particle velocity \mathbf{u} . Thus, the active intensity \mathbf{I} and the reactive intensity \mathbf{J} can be written in the form of a complex intensity $\mathbf{\Pi}$ ^{6,7} as follows:

$$\mathbf{\Pi} = \mathbf{I} + j\mathbf{J} = \frac{1}{2}p\mathbf{u}^*, \quad (1)$$

^{a)}Present address: Department of Mechanical Engineering, University of British Columbia, 2324 Main Mall, Vancouver, British Columbia V6T 1Z4, Canada.

^{b)}Present address: Ecole Nationale Supérieure d'Ingénieurs du Mans (ENSIM), Université du Maine, Avenue Olivier Messiaen, 72000 Le Mans, France.

and the potential and kinetic energy densities V and T are expressed, respectively, as

$$V = \frac{|p|^2}{4\rho c^2} \quad (2a)$$

and

$$T = \frac{\rho}{4} \mathbf{u} \cdot \mathbf{u}, \quad (2b)$$

where ρ is the density of the medium and c is the speed of sound. The relationships between these quantities have been first given by Smith *et al.*,⁸

$$\nabla \cdot \mathbf{I} = 0, \quad (3a)$$

$$\nabla \cdot \mathbf{J} = 2kc(V - T), \quad (3b)$$

$$\nabla \times \mathbf{I} = \frac{-j\rho ck}{2} \mathbf{u} \times \mathbf{u}^*, \quad (3c)$$

$$\nabla \times \mathbf{J} = 0, \quad (3d)$$

where $k = \omega/c$ is the acoustic wave number and ω is the angular frequency. The spatial distribution of these different quantities has been studied in many configurations.⁹⁻¹³ The relationship (3d) is a consequence of the fact that the reactive intensity is proportional to the gradient of the potential energy density^{10,14}

$$\mathbf{J} = -\frac{c}{k} \nabla V. \quad (4)$$

The vortex formation in the strong interference region is a particularity of an active intensity field and has received much attention.^{9,11,13,15-18} This characteristic of the polarization of the acoustic field bears relation to the curl of the active intensity, which is expressed in terms of the angular momentum density of the fluid particles [see Eq. (3c)].¹⁷ Another expression using only energetic quantities has been derived^{9,12} for coherent fields:

$$\nabla \times \mathbf{I} = \mathbf{\Omega} = \frac{k}{c} \frac{\mathbf{I} \times \mathbf{J}}{V}. \quad (5)$$

In most cases only the coherent fields were taken into consideration. Jacobsen¹⁹ shows that the degree of coherence of an acoustic field can be described by the function of coherence between acoustic pressure and particle velocity $\gamma_{\mathbf{u}p}^2$. This indicator can be expressed by energetic quantities as follows:

$$\gamma_{\mathbf{u}p}^2 = \frac{|G_{\mathbf{u}p}|^2}{G_{pp}G_{\mathbf{u}\mathbf{u}}} = \frac{\mathbf{I}^2 + \mathbf{J}^2}{4c^2VT}, \quad (6)$$

where the energetic quantities can be written in the form of power-spectral densities (see Sec. II C). In the case of a coherent field, $\gamma_{\mathbf{u}p}^2 = 1$, and Eq. (6) provides an additional relationship between the energetic quantities, which allows us, for example, to omit kinetic energy T and to describe the field with only \mathbf{I} and V in Eqs. (3). However, in the noncoherent field, there are not obvious solutions to Eqs. (3), (5), and (6). It is necessary to validate these relationships. For this purpose, a model of partially coherent fields generated

by a set of elementary sources is used here. In practice, stationary processes are often assumed in the energy field studies. The instantaneous intensity has sometimes been used for understanding the phenomena in acoustic fields,^{17,20} especially for the interpretation of the exchange of energy during one time period in a vortex region³ or in interference fields.⁷ However, for stationary fields, the instantaneous complex intensity does not give supplementary information in comparison with its time-averaged value. Therefore, the time-averaged quantities are only considered in this article.

B. Representation of partially coherent fields

A field created by a set of harmonic sources is everywhere coherent and the phase between two points in the field is perfectly defined. On the contrary, uncorrelated broadband sources produce partially diffuse acoustic fields. Two field points are not, in general, fully coherent. Hence the phase between two field points can be expressed only for the coherent part of the fields. It is not possible to represent *a priori* the partially coherent fields by the superposition of pressures due to each elementary source. The amplitudes of two elementary sources (A_i and A_j) are stationary random functions whose interdependence relationships can be expressed by a cross-spectral density function:

$$G_{ij}(\omega) = \lim_{T \rightarrow \infty} \frac{2}{T} E[A_i^*(\omega, T)A_j(\omega, T)], \quad (7)$$

where $A_i(\omega, T)$ is the finite Fourier transform of $A_i(t)$ measured over the finite time interval T ,

$$A_i(\omega, T) = \int_{t_1}^{t_1+T} A_i(t) e^{-j\omega t} dt. \quad (8)$$

The coherence function between source amplitudes can then be given as

$$\gamma_{ij}^2(\omega) = \frac{|G_{ij}(\omega)|^2}{G_{ii}(\omega)G_{jj}(\omega)}, \quad (9)$$

where $0 \leq \gamma_{ij}^2(\omega) \leq 1$ and $G_{ii}(\omega)$ and $G_{ij}(\omega)$ are, respectively, auto- and cross-spectral density functions. This coherence function can be used to represent the energetic quantities of broadband acoustic fields using the complex notation. The energetic quantities (intensities and energy densities) in the field generated by a set of M sources are then expressed in the following forms:

$$\mathbf{I} = \mathbf{I} + j\mathbf{J} = \frac{1}{2} \sum_{i=1}^M \sum_{j=1}^M \sqrt{\gamma_{ij}^2} p_i \mathbf{u}_j^*, \quad (10a)$$

$$V = \frac{1}{4\rho c^2} \sum_{i=1}^M \sum_{j=1}^M \sqrt{\gamma_{ij}^2} p_i p_j^*, \quad (10b)$$

$$T = \frac{\rho}{4} \sum_{i=1}^M \sum_{j=1}^M \sqrt{\gamma_{ij}^2} \mathbf{u}_i \cdot \mathbf{u}_j^*. \quad (10c)$$

The relationships between elementary sources are written in terms of a coherence matrix $[\Gamma^2]$, whose elements γ_{ij}^2 were given by Eq. (9). The matrix γ_{ij}^2 represents the coherence between sources. As examples, consider two typical cases. In

the coherent case, all elements γ_{ij}^2 of the coherence matrix take the value 1. Only in this case, the complex pressure and particle velocity for the whole field can be defined by $p = \sum_{i=1}^M p_i$ and $\mathbf{u} = \sum_{i=1}^M \mathbf{u}_i$. In the case of independent sources, the coherence matrix becomes the identity matrix and the cross-terms are zero, $[\Gamma^2] = \text{diag}(1, 1, \dots, 1)$. The complex intensity is the vectorial sum of that generated by each source: $\mathbf{I} = \frac{1}{2} \sum_{i=1}^M p_i \mathbf{u}_i^* = \sum_{i=1}^M (\mathbf{I}_i + j\mathbf{J}_i)$.

II. COHERENCE MATRIX OF SOURCES

In the previous section it was shown that the coherence matrix of sources is a key to investigating a partially coherent field. However, not any matrix can be used to describe the coherence between sources. The symmetry of $[\Gamma^2]$ is not a sufficient condition for defining the matrix. For example, if two sources have coherent relationships with the third source, the coherence between these two sources depends on these relationships. We therefore seek the supplementary conditions to correctly construct the matrix $[\Gamma^2]$. The decomposition of this matrix using the principal component analysis allows the necessary numbers of the independent field to be obtained. This analysis finally leads to establishing the relationships between the partially coherent field and the reduced-number-independent fields.

A. Definition of the coherence matrix of sources

The amplitudes of sources $A_i(\omega, T)$ [Eq. (8)] can also be written as

$$A_i(\omega, T) = B_i(\omega) a_i(\omega, T), \quad (11)$$

where $B_i(\omega)$ is a complex coefficient and $a_i(\omega, T)$ is the finite Fourier transform of a stationary random signal with the auto-power-spectral density

$$\frac{2}{T} E[|a_i(\omega, T)|^2] = 1. \quad (12)$$

The random signals $a_i(\omega, T)$ are partially coherent among them. Substituting Eqs. (11) and (12) into Eq. (9) yields

$$\gamma_{ij}^2(\omega) = \left| \frac{2}{T} E[a_i^*(\omega, T) a_j(\omega, T)] \right|^2. \quad (13)$$

To obtain all elements of the matrix $[\Gamma^2]$, $a_i(\omega, T)$ can be expressed as the linear combinations of M independent stationary random signals $s_m(\omega, T)$:²¹

$$a_i(\omega, T) = \sum_{m=1}^M \xi_{im}(\omega) s_m(\omega, T). \quad (14)$$

According to Eq. (11), each real source is the superposition of a number of independent sources. Uncorrelated random signals $s_m(\omega, T)$ have the following property:

$$\frac{2}{T} E[s_m^*(\omega, T) s_n(\omega, T)] = \delta_{mn} = \begin{cases} 1, & \text{if } n = m, \\ 0, & \text{if } n \neq m, \end{cases} \quad (15)$$

and the coefficients $\xi_{im}(\omega)$ are real numbers such that $0 \leq \xi_{im}(\omega) \leq 1$. From Eqs. (12), (14), and (15), the coefficients $\xi_{im}(\omega)$ should satisfy the following condition:

$$\sum_{m=1}^M \xi_{im}^2(\omega) = 1. \quad (16)$$

A new expression of mutual coherence of sources is obtained by substituting Eq. (14) into Eq. (13)

$$\begin{aligned} \gamma_{ij}^2(\omega) &= \left(\sum_{m=1}^M \sum_{n=1}^M \xi_{im}(\omega) \xi_{jn}(\omega) \delta_{mn} \right)^2 \\ &= \left(\sum_{m=1}^M \xi_{im}(\omega) \xi_{jm}(\omega) \right)^2. \end{aligned} \quad (17)$$

The mutual coherence matrix $[\Gamma^2]$ is hence expressed by the matrix $[\xi]$ as follows:

$$[\Gamma^2] = ([\xi][\xi]^T)^2, \quad (18)$$

where $[\]^T$ designates the transpose of the matrix. The matrix $[\Gamma] = [\xi][\xi]^T$ whose coefficients are $\sqrt{\gamma_{ij}^2}$ is equally well used as the coherence matrix of sources. According to Dodds and Robson,²¹ the matrix $[\xi]$ that will correctly construct the matrix $[\Gamma^2]$ is a lower triangular matrix such as

$$\begin{aligned} \begin{bmatrix} a_1(\omega, T) \\ a_2(\omega, T) \\ a_3(\omega, T) \\ \vdots \\ a_M(\omega, T) \end{bmatrix} &= \begin{bmatrix} \xi_{11} & 0 & 0 & \cdots & 0 \\ \xi_{21} & \xi_{22} & 0 & \cdots & 0 \\ \xi_{31} & \xi_{32} & \xi_{33} & \cdots & 0 \\ \vdots & \vdots & \vdots & \ddots & \vdots \\ \xi_{M1} & \xi_{M2} & \xi_{M3} & \cdots & \xi_{MM} \end{bmatrix} \\ &\times \begin{bmatrix} s_1(\omega, T) \\ s_2(\omega, T) \\ s_3(\omega, T) \\ \vdots \\ s_M(\omega, T) \end{bmatrix}, \end{aligned} \quad (19)$$

and the only constraint of this definition is the normalization on each line according to Eq. (16) (which results in $\xi_{11} = 1$ in all cases).

As examples, consider two typical cases. In the case of M independent sources, it is evident that $a_i(\omega, T) = s_i(\omega, T)$ and that the matrix $[\xi]$ is an identity matrix $[\xi] = [\mathbf{E}] = \text{diag}(1, 1, \dots, 1)$. In the case of M coherent sources, each random signal $a_i(\omega, T)$ should be represented by the same linear combination $\sum_m \xi_{im}(\omega) s_m(\omega, T)$, which results in a matrix having only one nonzero column by using the definition of the triangular matrix (19). In Ref. 22 it was shown how to construct $[\xi]$ for a particular case where the coherence functions among sources are all identical: $\gamma_{ij}^2(\omega) = g^2$ for $j \neq i$, $i, j = 1, 2, 3, \dots, M$.

B. Analysis of the coherence matrix

The coherence matrix of sources can be determined by the coefficient matrix $[\xi]$. A method is shown here to obtain the independent fields from the coherence matrix of sources using the singular value decomposition (SVD).

1. Decomposition into independent fields

The rank of $[\xi]$ corresponds to the number of independent columns, therefore, to the number of independent primary sources $s_m(\omega, T)$ necessary to produce the signals

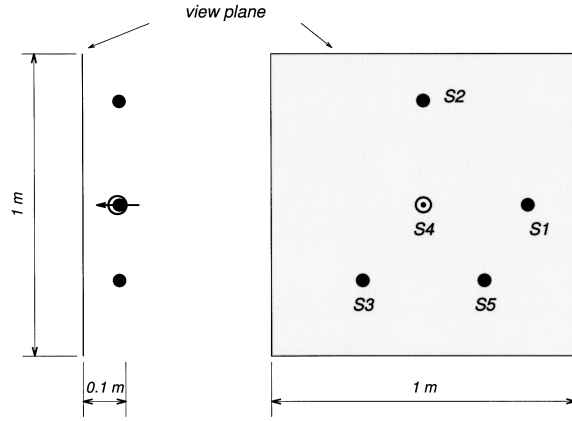


FIG. 1. Model of synthetic source: four monopoles (S_1, S_2, S_3, S_5) and one dipole (S_4) and position of the view plane.

$A_i(\omega, T)$. In the coherent case each random signal $a_i(\omega, T)$ should be represented by the same linear combination $\sum_m \xi_{im}(\omega) s_m(\omega, T)$. Thus the matrix $[\xi]$ has only one non-zero column: its rank is equal to 1, therefore only one primary source $s_1(\omega, T)$ is needed. On the contrary, in the case of noncoherence, $[\xi]$ is an identity matrix, $[\xi] = [\mathbf{E}] = \text{diag}(1, 1, \dots, 1)$, and its rank is equal to M . In the case of partially coherent sources, one encounters, in practice, many of these intermediate situations where one or several columns are linear combinations of the others. It is thus possible, in principle, to reduce the number of independent sources by using the principal component analysis (PCA).^{23,24} Calculating the singular value decomposition (SVD) of the matrix $[\Gamma] = [\xi][\xi]^T$ results in the following factorization:

$$[\Gamma]_{M \times M} = [\mathbf{H}]_{M \times M} [\Sigma^2]_{M \times M} [\mathbf{H}]_{M \times M}^T. \quad (20)$$

The diagonal matrix $[\Sigma^2]$ contains the eigenvalues of $[\Gamma]$ arranged in decreasing order,

$$[\Sigma^2]_{M \times M} = \text{diag}(\sigma_1^2, \sigma_2^2, \dots, \sigma_r^2, 0, \dots, 0). \quad (21)$$

If the matrix $[\Gamma]$ has r nonzero eigenvalues, its rank is r . It can be shown that for a Hermitian matrix, these eigenvalues are all real and positive. The columns of the orthonormal matrix $[\mathbf{H}]$ correspond to the complex eigenvectors, in which only the first r columns are significant. Therefore, if $r < M$, the sizes of the matrices $[\Sigma^2]$ and $[\mathbf{H}]$ can be reduced without loss of any information such that

$$[\Gamma]_{M \times M} = [\mathbf{H}']_{M \times r} [\Sigma'^2]_{r \times r} [\mathbf{H}']_{r \times M}^T, \quad (22)$$

where $[\Sigma'^2]_{r \times r} = \text{diag}(\sigma_1, \sigma_2, \dots, \sigma_r)$. From the reduced matrices $[\Sigma'^2]_{r \times r}$ and $[\mathbf{H}']_{M \times r}$, a reduced coefficient matrix $[\xi']$ can be constructed:

$$[\xi']_{M \times r} = [\mathbf{H}']_{M \times r} [\Sigma']_{r \times r}. \quad (23)$$

The replacement of $[\xi]$ with $[\xi']$ means, according to Eq. (19), that the random signals $a_i(\omega, T)$ representing the M partially coherent sources can be reconstituted from only r independent source signals $s_m(\omega, T)$, ($m = 1, 2, 3, \dots, r$).

2. Example

Figure 1 shows a source model synthesized by four monopoles (S_1, S_2, S_3, S_5) and one dipole (S_4) directing to

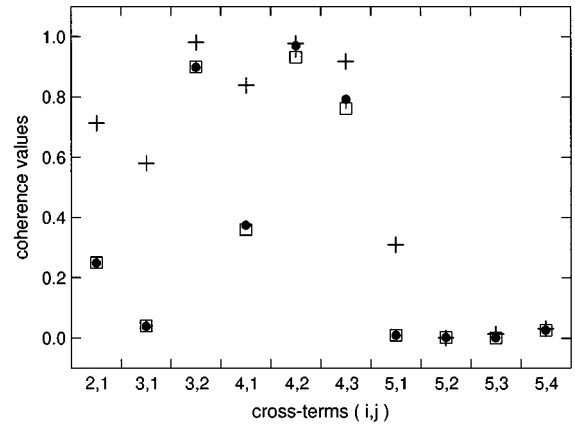


FIG. 2. Cross terms of the coherence matrix of sources: □, initial coherence matrix; ●, coherence matrix reduced to three independent components; +, coherence matrix reduced to two components.

the view plane. These five point sources have the same amplitude and are in phase. To generate a coherence matrix of a source in the general case, consider a matrix $[\xi]_{5 \times 5}$ that satisfies Eqs. (16) and (19), but one column of which is a linear combination of the others. The coherence matrix of sources $[\Gamma^2]$ can be calculated using Eq. (18). The cross-term values of $[\Gamma^2]$ are represented in Fig. 2. The diagonal matrix of eigenvalues is obtained by calculating the SVD of the matrix $[\xi][\xi]^T$,

$$[\Sigma^2] = \text{diag}(3.1399, 1.0251, 0.8075, 0.0275, \varepsilon), \quad (24)$$

with $\varepsilon \approx 3 \times 10^{-16}$ which can be neglected in comparison with the sum $\sum_{i=1}^M \sigma_i^2 = M = 5$. Since two columns in $[\xi]$ are not independent, the rank of $[\xi][\xi]^T$ is equal to 4 (inferior to $M = 5$). The reduced matrix $[\xi']_{5 \times 4}$ is obtained using Eq. (23). Then $[\xi']$ is used to calculate the coherence matrix of sources: $[\Gamma^2] = ([\xi'] [\xi']^T)^2$. It can be verified that it is identical to the initial matrix. The triangular matrix $[\xi]$ is replaced by a reduced matrix $[\xi']$ with elements varying between -1 and 1 .

To generalize the previous discussion, consider the first three eigenvalues of the matrix (24) which already take 99.45% of the total energy. The matrix of coherence deduced from the three components is calculated from a normalized matrix $[\xi'']_{5 \times 3}$ whose elements are obtained by $\xi''_{im} = \xi'_{im} (\sum_{m=1}^3 \xi'^2_{im})^{-1/2}$ to satisfy the condition (16). It results in an approximate expression of the initial coherence matrix

$$[\Gamma'^2] = ([\xi''] [\xi'']^T)^2. \quad (25)$$

If only the first two eigenvalues of the diagonal matrix (24) are taken into account, another approximation of the coherence matrix can be obtained from the normalized matrix $[\xi''']_{5 \times 3}$:

$$[\Gamma''^2] = ([\xi'''] [\xi''']^T)^2. \quad (26)$$

The cross terms of approximate coherence matrices given by Eqs. (25) and (26) are compared to those of the initial matrix in Fig. 2. The matrix $[\Gamma'^2]$ gives a good approximation to $[\Gamma^2]$, but $[\Gamma''^2]$ is very different from the initial matrix because a component of the independent field which represents

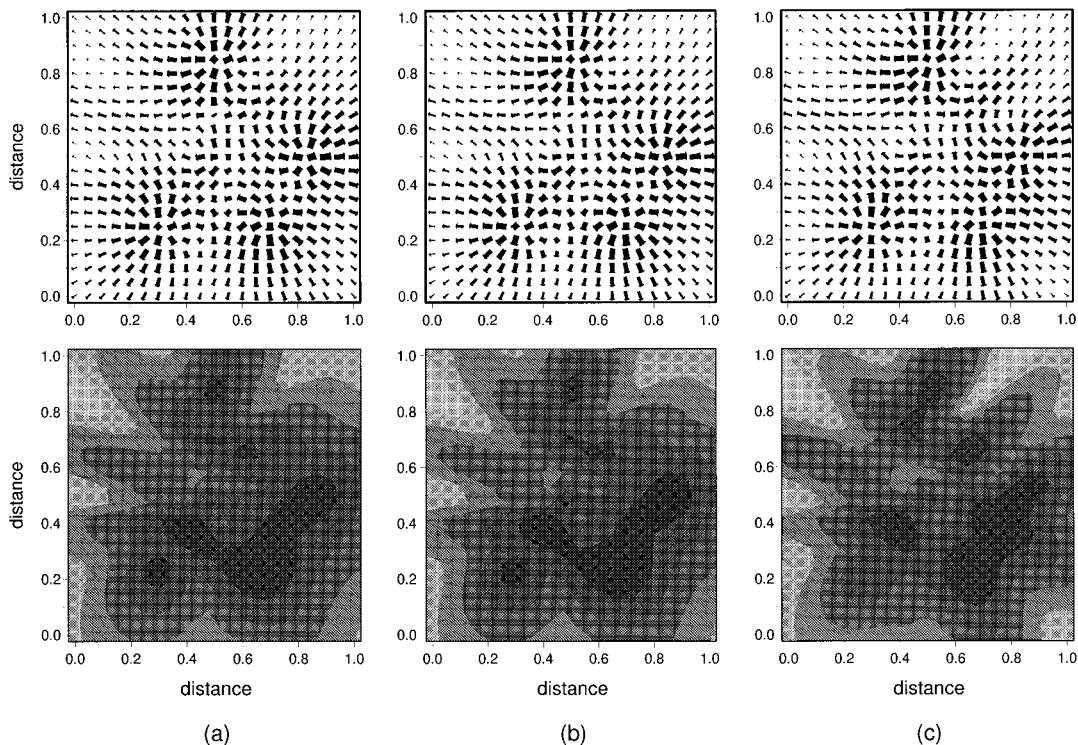


FIG. 3. Active acoustic intensity (top) and potential energy density (bottom) on the view plane shown in Fig. 1. Dynamic range of the arrow: 20 dB, grey-scale level: 2.5 dB. (a) Initial coherence matrix of sources; (b) coherence matrix of sources reduced to three independent components [Eq. (25)]; and (c) coherence matrix of sources reduced to two components [Eq. (26)].

approximately 16.7% of sound field energy has not been considered.

The active intensity and potential energy density fields created by the synthetic source in Fig. 1 at 1000 Hz were calculated using Eq. (10). The initial coherence matrix of sources shown in Fig. 2 and its approximate expressions Eqs. (25) and (26) were used, respectively, in the calculations. The results are shown in Fig. 3(a)–(c). Graphically, the potential energy density is represented by grey-scale plots. The three-dimensional active intensity vectors are presented with arrows which indicate the three components. The in-plane components are represented in amplitude by the lengths of arrows and in direction by the orientations of arrows. The out-of-plane component is represented in amplitude by the thicknesses of arrows and in direction by a filled arrow representing I_z pointing out of the view plane and an empty arrow pointing into the view plane. Comparing the results in Fig. 3(a) and (b), it is noted that Eq. (25) [Γ'^2] gives a very good approximation to the initial coherence matrix of sources [Γ^2] for the calculation of the energetic quantities \mathbf{I} and V . However, Fig. 3(c) shows the differences from the results in Fig. 3(a) and (b) because the third independent component cannot be negligible. Nevertheless, the structure of the field is not fundamentally changed and the deviations have approximately the same order as the measurement errors in industrial situations. The use of only three independent components instead of four has practical interests, for example, in the experimental realization of a synthetic source using a ξ -matrix where only three noise generators will be necessarily needed (see Fig. 4). A real field can often be

recreated from a synthetic field composed of a reduced number (often less than 5) of independent principal components.

C. Partially coherent fields and independent fields

Equation (10a) representing active and reactive intensities of partially coherent fields can also be expressed in the matrix form:

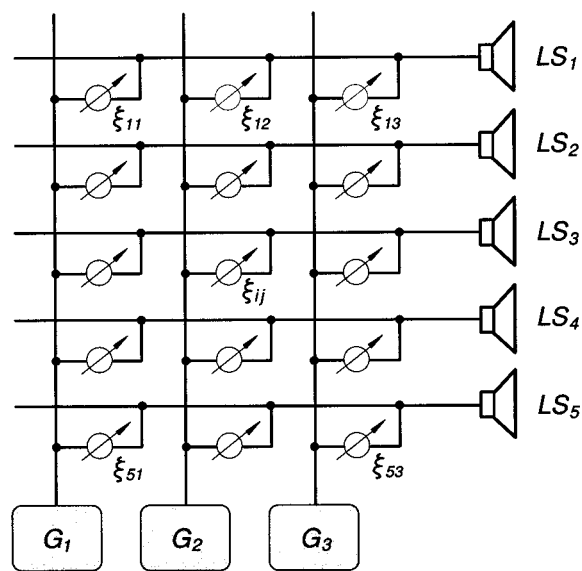


FIG. 4. Realization of a synthetic source from coefficients ξ_{ij} obtained by principal component analysis of the matrix of coherence of sources. LS_i : excitators or loudspeakers, G_j : independent noise generators.

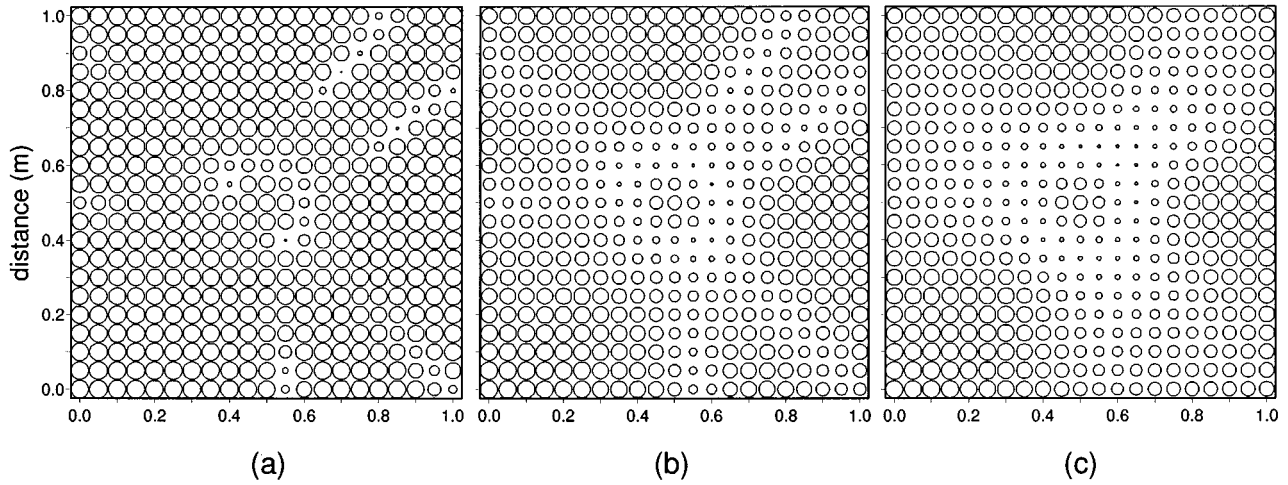


FIG. 5. The function of coherence γ_{up}^2 : (a) for $\gamma_{ij}^2=0.9$; (b) for $\gamma_{ij}^2=0.25$; and (c) for $\gamma_{ij}^2=0.01$. The frequency of the calculation is 1000 Hz and the dimension of the view plane is 1 m \times 1 m (2.9 λ \times 2.9 λ). γ_{up}^2 is represented by circles with radius varying linearly (identical scales).

$$\mathbf{\Pi} = \mathbf{I} + j\mathbf{J} = \frac{1}{2}[\mathbf{U}_S]_{1 \times M}^H [\mathbf{\Gamma}]_{M \times M} [\mathbf{P}_S]_{M \times 1}, \quad (27)$$

with H denoting the Hermitian transpose. The elements of the column matrices $[\mathbf{P}_S]$ and $[\mathbf{U}_S]$ are, respectively, the pressure p_i and the velocity \mathbf{u}_i of the field due to each primary point source. By the use of the reduced matrices Eqs. (22) and (23), we have

$$\mathbf{\Pi} = \mathbf{I} + j\mathbf{J} = \frac{1}{2}([\mathbf{\xi}]^T [\mathbf{U}_S])^H ([\mathbf{\xi}]^T [\mathbf{P}_S]) = \frac{1}{2}[\mathbf{U}_C]_{1 \times r}^H [\mathbf{P}_C]_{r \times 1}. \quad (28)$$

The elements in the column matrices $[\mathbf{P}_C]$ or $[\mathbf{U}_C]$ are given, respectively, as

$$p_m = \sum_{i=1}^M \xi_{im} p_i \quad \text{and} \quad \mathbf{u}_m = \sum_{i=1}^M \xi_{im} \mathbf{u}_i, \quad (29)$$

where p_m and \mathbf{u}_m are interpreted as the independent coherent fields ($m=1,2,3,\dots,r$), each of which is due to the combination contributions from the primary point sources. Hence the complex intensity is the vectorial superposition of r independent intensity fields

$$\mathbf{\Pi} = \mathbf{I} + j\mathbf{J} = \frac{1}{2} \sum_{m=1}^r p_m \mathbf{u}_m^* = \sum_{m=1}^r \mathbf{\Pi}_m. \quad (30)$$

Similarly, the kinetic and potential densities can be expressed as the superposition of r independent kinetic- and potential-density fields. It is advisable to note that Eq. (10) and Eq. (30) will give the identical results for the energetic quantities. Equation (30) shows that a partially coherent field due to M point sources can be expressed by r independent fields ($r < M$). However, one cannot get the information about location and coherence of the primary sources from the independent fields. Thus these r independent fields are termed ‘‘virtual fields.’’

III. CHARACTERIZATION OF PARTIALLY COHERENT ACOUSTIC FIELDS

Generally, for an acoustic field created by multiple sources, it is not possible to directly estimate the mutual coherence between sources from measurements. However,

the information about the degree of coherence of the acoustic field is important to evaluate measurement conditions, statistical errors, or the validity of the use of the algorithms derived from harmonic signals. The coherence function between pressure and particle velocity γ_{up}^2 and the curl of acoustic intensity $\nabla \times \mathbf{I}$ are used here to characterize the structure of acoustic fields. It is shown later that the complete information about the local structure of acoustic fields is provided by the definition of a field matrix.

A. Coherence function of sound fields

The superposition of independent fields leads to a loss of coherence between the acoustic pressure and the particle velocity.¹⁹ The characteristic of the acoustic field is represented by the coherence function γ_{up}^2 defined by Eq. (6), which is expressed in terms of measured (or calculated) energetic quantities in random acoustic fields. By using Eq. (10) associated with the coherence matrix of sources or Eq. (30) for r independent fields, the coherence function of an acoustic field takes the following form:

$$\begin{aligned} \gamma_{up}^2(\mathbf{r}, \omega) &= \frac{|\sum_{i=1}^M \sum_{j=1}^M \sqrt{\gamma_{ij}^2} p_i \mathbf{u}_j^*|^2}{(\sum_{i=1}^M \sum_{j=1}^M \sqrt{\gamma_{ij}^2} p_i p_j^*)(\sum_{i=1}^M \sum_{j=1}^M \sqrt{\gamma_{ij}^2} \mathbf{u}_i \cdot \mathbf{u}_j^*)} \\ &= \frac{|\sum_{m=1}^r p_m \mathbf{u}_m^*|^2}{\sum_{m=1}^r |p_m|^2 \sum_{m=1}^r \mathbf{u}_m \cdot \mathbf{u}_m^*}. \end{aligned} \quad (31)$$

This function can be used as an indicator of the coherence structure of the acoustic field: (i) when $\gamma_{ij}^2=1$, the field is produced by fully correlated random sources ($r=1$) and $\gamma_{up}^2(\mathbf{r}, \omega) = 1$; (ii) if $0 < \gamma_{ij}^2 < 1$, the sources are partially correlated ($1 < r < M$) and the coherence of the field $\gamma_{up}^2(\mathbf{r}, \omega)$ then has values between 0 and 1; (iii) when $\gamma_{ij}^2=0$ (hence $r=M$), the coherence function is zero only on some points of the sound field. Generally, $\gamma_{up}^2(\mathbf{r}, \omega) \neq 0$. Zero values of $\gamma_{up}^2(\mathbf{r}, \omega)$ correspond to a perfectly diffuse field, thus outside the acoustic near field.

If we consider the source model in Fig. 1 without the source S_5 , Fig. 5 demonstrates that the distribution of γ_{pu}^2 on

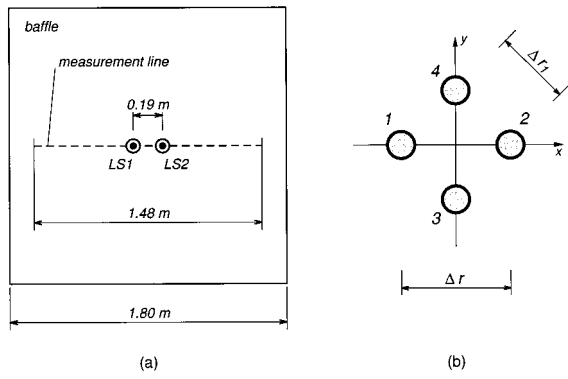


FIG. 6. (a) Plane of baffle and positions of loudspeakers. (b) Two-dimensional acoustic intensity probe with four microphones used in the measurements.

the view plane (at 1000 Hz) is very sensitive to the values of the coherence matrix of sources $[\gamma_{ij}^2]$. The experimental determination of this indicator from Eq. (6) will therefore provide the information about the nature of the radiating acoustic field, as well as about the source which is at the origin, as an example, a real source with a set of independent excitations. In practice, the coherence function between the pressure and a component of the particle velocity is often used to control the validity of the measurements of the corresponding component of the intensity vector.¹⁹ The coherence function between the pressure and x -component velocity, for example, is written as $\gamma_{u_x p}^2 = (I_x^2 + J_x^2)/4c^2VT_{xx}$, with $T_{xx} = \rho|u_x|^2/4$. The coherence function of the field [Eq. (16)] can be, therefore, written as

$$\gamma_{\mathbf{u}p}^2 = \frac{\gamma_{u_x p}^2 T_{xx} + \gamma_{u_y p}^2 T_{yy} + \gamma_{u_z p}^2 T_{zz}}{T_{xx} + T_{yy} + T_{zz}}. \quad (32)$$

In Fig. 7, the coherence function was determined experimentally in a horizontal line on the view plane, 4 cm from a baffle on which two loudspeakers were mounted [see Fig. 6(a)]. The experimental system was set up in an anechoic chamber. The components of the active intensity in the view plane parallel to the baffle were measured using a two-dimensional intensity probe consisted of four quarter-inch microphones [Fig. 6(b)] positioned by an automatic robot system. The coherence function calculated by

$$\gamma_{\mathbf{u}p|\text{plane}}^2 = \frac{\gamma_{u_x p}^2 T_{xx} + \gamma_{u_y p}^2 T_{yy}}{T_{xx} + T_{yy}} \quad (33)$$

is an incomplete form of Eq. (32), but it remains valid ($0 \leq \gamma_{\mathbf{u}p|\text{plane}}^2 \leq 1$) to characterize the measured data, for example, used in the acoustic holography processing. The energetic quantities are calculated using the well-known finite-difference approximation,^{6,7,14} for example, $I_x = \text{Im}\{G_{21}(\omega)\}/\rho\omega\Delta r$ and $J_x = [G_{11}(\omega) - G_{22}(\omega)]/2\rho\omega\Delta r$, where Δr is the distance between the two microphones shown in Fig. 6(b), G_{11} and G_{22} are the auto-power-spectral densities of signals measured by microphone 1 and microphone 2 respectively, and G_{21} is the cross-power-spectral density between the signals of microphones 1 and 2. A multichannel signal processing system (LMS Cada-X) was used

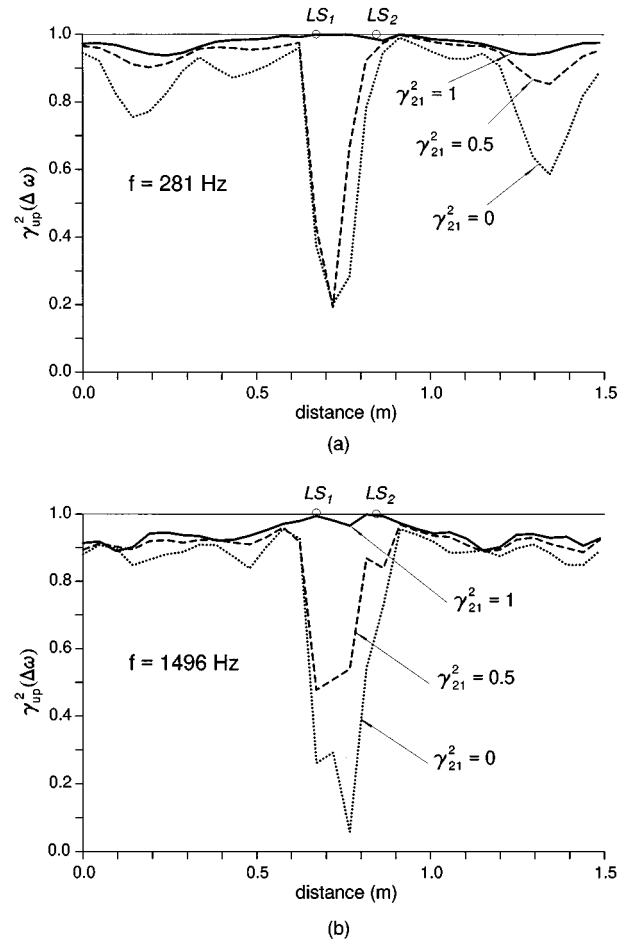


FIG. 7. Coherence function of fields measured in the view plane parallel to the baffle of Fig. 6 for values γ_{ij}^2 indicated; (a) $f=281$ Hz, (b) $f=1496$ Hz (frequency resolution=3.9 Hz).

for data acquisition. A mixer was used to obtain the coherence γ_{ij}^2 between two white noise signals built in (LMS Cada-X) by adjusting the amplitudes of the signals. Then the two mixed signals were used to drive the two loudspeakers. The energetic quantities used in Eq. (33) were determined with a frequency resolution Δf of 3.9 Hz. Figure 7 illustrates the coherence of field $\gamma_{\mathbf{u}p|\text{plane}}^2$ measured for different values of the coherence γ_{ij}^2 . The results presented at 281 Hz and at 1496 Hz show, when $\gamma_{ij}^2 < 1$, a sensitive coherence loss in the central area where the two loudspeakers were mounted.

B. Indicator of the polarization of fields

The polarization vector for a coherent field was defined by Uosukainen¹⁷ as

$$\mathbf{a} = -j \frac{\mathbf{u} \times \mathbf{u}^*}{\mathbf{u} \cdot \mathbf{u}^*}, \quad (34)$$

where $0 \leq |\mathbf{a}| \leq 1$. The vector \mathbf{a} is zero when the particle velocity is polarized linearly, i.e., the orientation of its instantaneous value is always the same during one time period (vectors of the active and reactive intensities are parallel with each other). In general, the velocity field has an elliptic polarization, that is, the orientation of its instantaneous particle velocity changes during one time period and traces an el-

lipse. The instantaneous velocity has often been decomposed into two parts: one is in phase and another is in quadrature with the pressure. The directions of the two components correspond to those of active and reactive intensities, respectively. Thus the magnitude of the polarization vector becomes maximum (equal to 1) when the two components of the particle velocity are the same magnitude but perpendicular (the ellipse becomes a circle). According to Eq. (3c), the polarization vector is the curl of acoustic intensity normalized by kinetic energy

$$\mathbf{a} = \frac{\nabla \times \mathbf{I}}{2kcT}. \quad (35)$$

It can be seen that a field is hence polarized when the curl of intensity is not zero. The curl, i.e., the polarization, depends strongly on interferences between sources. Thus, the field of a monopole possesses a zero curl. Several coherent monopoles will produce an interference field in which the curl vector characterizes the polarization of the field. On the contrary, if the monopole sources are independent, the zero curl indicates a nonpolarized field. In an intermediate situation, the curl measures the polarization of the coherent part. Thus, by calculating the curl of Eq. (10a) with the consideration of the relationships $\nabla p_i = -jk\rho c\mathbf{u}_i$ and $\nabla \times \mathbf{u}_i = 0$ (ideal nonviscous fluid), one obtains

$$\nabla \times \mathbf{I} = -\frac{jk\rho c}{2} \sum_{i=1}^M \sum_{j=1}^M \sqrt{\gamma_{ij}^2} \mathbf{u}_i \times \mathbf{u}_j^*. \quad (36)$$

Using the symmetric relationships between $\mathbf{u}_i \times \mathbf{u}_j^*$ and $\mathbf{u}_j \times \mathbf{u}_i^*$, Eq. (36) becomes

$$\nabla \times \mathbf{I} = \nabla \times \mathbf{I} = \frac{\rho kc}{2} \text{Im} \left\{ \sum_{i=1}^M \sum_{j=1}^M \sqrt{\gamma_{ij}^2} \mathbf{u}_i \times \mathbf{u}_j^* \right\}. \quad (37)$$

Multiplying the numerator and the denominator in Eq. (37) by $p_i^* p_j$ yields

$$\frac{\rho kc}{2} \text{Im} \{ \mathbf{u}_i \times \mathbf{u}_j^* \} = \frac{k}{2c} \text{Im} \left\{ \frac{\mathbf{I}_i^* \times \mathbf{I}_j}{V_{ij}} \right\}, \quad (38)$$

with $\mathbf{I}_i = p_i \mathbf{u}_i^*/2$ and $V_{ij} = p_i^* p_j / 4\rho c^2$. Using $(\mathbf{I}_i^* \times \mathbf{I}_j) + (\mathbf{I}_j^* \times \mathbf{I}_i) = 2j(\mathbf{I}_i \times \mathbf{J}_j) + 2j(\mathbf{I}_j \times \mathbf{I}_i)$, Eq. (38) can also be expressed in the form of the vector product of the active intensity and the reactive intensity of each individual source:

$$\nabla \times \mathbf{I} = \frac{k}{c} \sum_{i=1}^M \sum_{j=1}^M \sqrt{\gamma_{ij}^2} \frac{\mathbf{I}_i \times \mathbf{J}_j}{V_{ij}}. \quad (39)$$

Substituting values $\gamma_{ij}^2 = 1$ into Eq. (37), we get the expression of the curl of a coherent field ($\gamma_{up}^2 = 1$)

$$\begin{aligned} \nabla \times \mathbf{I} |_{\gamma_{up}^2 = 1} &= \frac{\rho kc}{2} \text{Im} \left\{ \sum_{i=1}^M \sum_{j=1}^M \mathbf{u}_i \times \mathbf{u}_j^* \right\} \\ &= \frac{\rho kc}{2} \text{Im} \left\{ \sum_{i=1}^M \mathbf{u}_i \times \sum_{j=1}^M \mathbf{u}_j^* \right\}, \end{aligned} \quad (40)$$

which is the same expression as $\mathbf{\Omega}$ given by Eq. (5) in which \mathbf{I} , \mathbf{J} , and V are defined by Eqs. (10a) and (10b) when $\gamma_{ij}^2 = 1$. In these conditions, according to Eq. (5) the polarization vector of the coherent field can be expressed as follows:

$$\mathbf{a} |_{\gamma_{up}^2 = 1} = \frac{\mathbf{I} \times \mathbf{J}}{2c^2 VT}. \quad (41)$$

In order that $|\mathbf{a}| = 1$, the active and reactive intensity vectors should be perpendicular to each other and $|\mathbf{I}| = |\mathbf{J}|$. Equation (39) demonstrates that the curl of a partially coherent field cannot be calculated from vector product of \mathbf{I} and \mathbf{J} and that Eq. (5) is valid only for a coherent field. This is illustrated obviously in Fig. 8 where the curl of the field produced by the source model in Fig. 1 without the source S_5 is calculated by Eqs. (39) and (5) respectively in the cases where $\gamma_{ij}^2 = 0, 0.25$ and 1 . It is noted that Eqs. (5) and (39) give the same results when $\gamma_{ij}^2 = 1$. There are, however, differences between the results calculated by Eq. (5) and by Eq. (39) when $\gamma_{ij}^2 \neq 1$. When $\gamma_{ij}^2 = 0$, it is obvious that Eq. (5) gives wrong results for the calculation of the curl of the intensity because in this case no interference between the sources exists and the polarization of the field is only due to the dipole source. The invalid use of Eq. (5) in noncoherent acoustic fields makes the nonexistent components appear, especially outside the representation plane. To explain this phenomenon, a field constituted by the superposition of two nonpolarized independent coherent fields ($\nabla \times \mathbf{I}_i = 0$, therefore $\mathbf{I}_i \times \mathbf{J}_i = 0$, $i = 1, 2$) is considered. The resultant active and reactive intensities in this field are written, respectively, as $\mathbf{I} = \mathbf{I}_1 + \mathbf{I}_2$ and $\mathbf{J} = \mathbf{J}_1 + \mathbf{J}_2 = a\mathbf{I}_1 + b\mathbf{I}_2$, where a and b are two scalar factors. In the general case when $a \neq b$, these resultant vectors are not parallel and $\mathbf{I} \times \mathbf{J}$ is not zero while the curl of the resultant field is always equal to 0.

By the use of the principal component decomposition to a partially coherent field according to Eq. (29), the curl of the resultant vector corresponds to the sum of the curl of the elementary vectors

$$\nabla \times \mathbf{I} = \sum_{m=1}^r \nabla \times \mathbf{I}_m = \frac{k}{c} \sum_{m=1}^r \frac{\mathbf{I}_m \times \mathbf{J}_m}{V_m}. \quad (42)$$

Similarly, the polarization vector of the field can be determined from the polarization vector and the kinetic energy density of each elementary field

$$\mathbf{a} = \left(\sum_{m=1}^r T_m \mathbf{a}_m \right) / T. \quad (43)$$

With regard to the experimental determination of the curl for partially coherent fields, Eq. (3c) is adapted to random signals by

$$\nabla \times \mathbf{I} = \rho ck \lim_{T \rightarrow \infty} \frac{2}{T} \text{Im} \{ E[\mathbf{u}(\omega, T) \times \mathbf{u}^*(\omega, T)] \}, \quad (44)$$

where $\mathbf{u}(\omega, T)$ is the finite Fourier transform defined by Eq. (8). Equation (44) can also be given as

$$\nabla \times \mathbf{I} = 4ck \text{Im} \{ T_{yz} \hat{\mathbf{i}} + T_{zx} \hat{\mathbf{j}} + T_{xy} \hat{\mathbf{k}} \}, \quad (45)$$

where $T_{ij} = (\rho/2) \lim_{T \rightarrow \infty} (2/T) \text{Im} \{ E[u_i u_j^*] \}$, with $i, j \in \{x, y, z\}$ ($i \neq j$). Using the same configuration mentioned above to determine the coherence function $\gamma_{up}^2|_{\text{plane}}$, the normal component of the curl is measured and calculated by the following expression derived from Eq. (45):

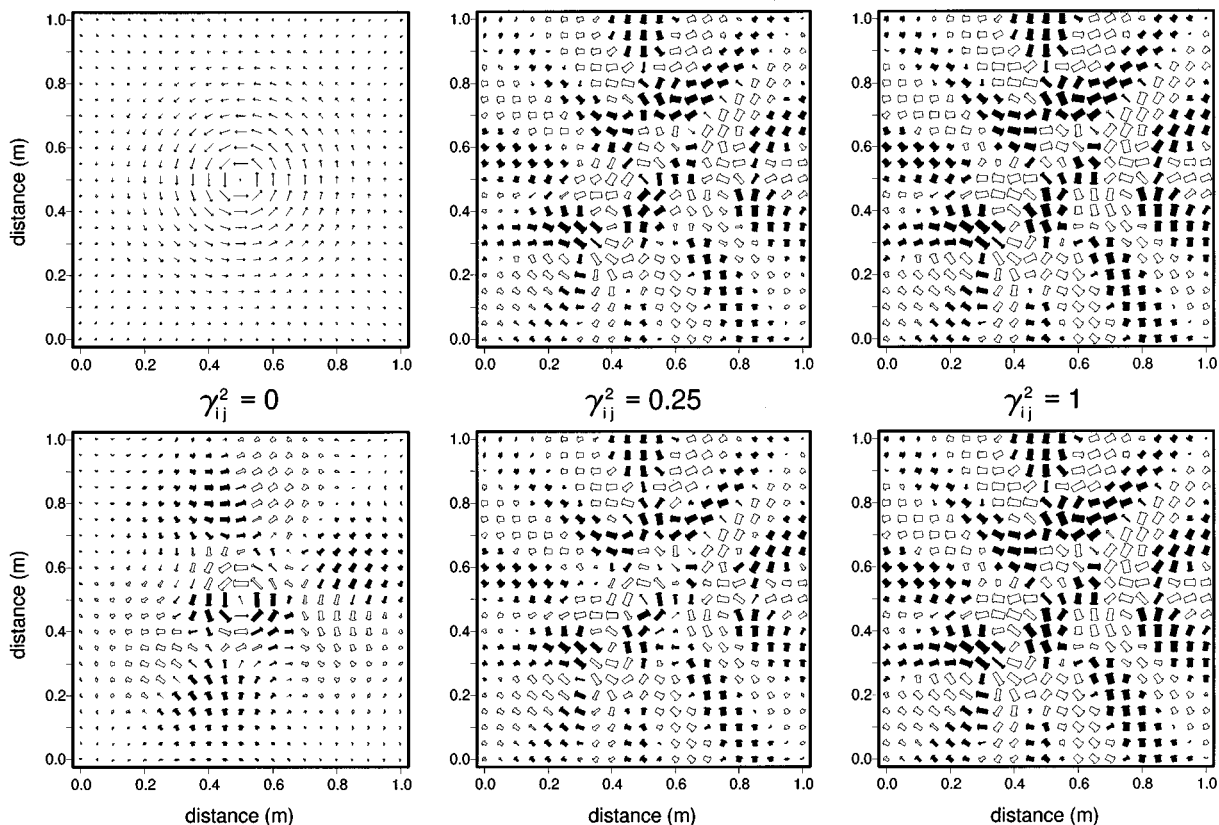


FIG. 8. Curl of the active acoustic intensity calculated with the model of Fig. 1 without S_5 with $\gamma_{ij}^2=0$ (left), $\gamma_{ij}^2=0.25$ (middle), $\gamma_{ij}^2=1$ (right): (a) use of Eq. (39) (top) and (b) use of Eq. (5) (bottom).

$$(\nabla \times \mathbf{I})_z = \frac{2}{\rho c k} \lim_{T \rightarrow \infty} \frac{2}{T} \text{Im} \left\{ \mathbf{E} \left[\frac{\partial p}{\partial x} \frac{\partial p^*}{\partial y} \right] \right\}. \quad (46)$$

Expressing the x component and y component of the pressure gradient in terms of the cross-power spectra $[G_{ij}(\omega); i, j = 1, 2, 3, 4; i \neq j]$ between the microphones of the two-dimensional sound intensity probe [see Fig. 6(b)] by the use of the finite-difference approximation, Eq. (46) becomes

$$(\nabla \times \mathbf{I})_z \approx \frac{2}{\rho c k (\Delta r_1)^2} \text{Im} \{ G_{31}(\omega) - G_{41}(\omega) - G_{32}(\omega) + G_{42}(\omega) \}, \quad (47)$$

where $\Delta r_1 = \Delta r / \sqrt{2}$ is the distance between the two microphones shown in Fig. 6(b). In the case of a coherent field, the normal component of the curl of the intensity can be derived using Eq. (5):

$$\Omega_z \approx \frac{k}{c} \frac{\tilde{I}_x \tilde{J}_y - \tilde{I}_y \tilde{J}_x}{\tilde{V}}, \quad (48)$$

where \tilde{I}_x , \tilde{I}_y , \tilde{J}_x , \tilde{J}_y , and \tilde{V} are determined by standard formulations using the finite-difference approximation.¹⁴ In order to validate Eqs. (47) and (48), the curl of the acoustic intensity was measured using the experimental set-up shown in Fig. 6. The experimental procedure was similar to that described in Sec. III A. The intensity probe was used to measure the four auto-power-spectral densities G_{ii} ($i = 1, 2, 3, 4$) and the six cross-power-spectral densities G_{ij} ($i > j$, i, j

$= 1, 2, 3, 4$) which were then used to calculate the curl of the intensity using, respectively, Eqs. (47) and (48). Figure 9 shows $(\nabla \times \mathbf{I})_z$ and Ω_z for the cases where $\gamma_{21}^2 = 0$ and $\gamma_{21}^2 = 0.5$. It is noted that there are differences between the results of Eqs. (47) and (48). The differences are larger when $\gamma_{21}^2 = 0$. The significant differences are found in the central area where the values of γ_{up}^2 are small and the two loudspeakers were mounted.

C. The field matrix

Locally, a coherent field can be completely described by quantities p , u_x , u_y , and u_z . Their relationships lead to an energetic representation of the field which can be generalized in the form of the field matrix:

$$[\mathbf{F}] = \frac{1}{2} [\mathbf{\Theta}] [\mathbf{\Theta}]^H, \quad (49)$$

where $[\mathbf{\Theta}] = [p / \sqrt{\rho c} \quad \sqrt{\rho c} u_x \quad \sqrt{\rho c} u_y \quad \sqrt{\rho c} u_z]^T$ is the column vector of acoustic quantities normalized in order to have the same dimension. The field matrix can be expressed by the energetic quantities as

$$[\mathbf{F}] = \begin{bmatrix} 2cV & \Pi_x & \Pi_y & \Pi_z \\ \Pi_x^* & 2cT_{xx} & 2cT_{xy} & 2cT_{xz} \\ \Pi_y^* & 2cT_{xy}^* & 2cT_{yy} & 2cT_{yz} \\ \Pi_z^* & 2cT_{xz}^* & 2cT_{yz}^* & 2cT_{zz} \end{bmatrix}. \quad (50)$$

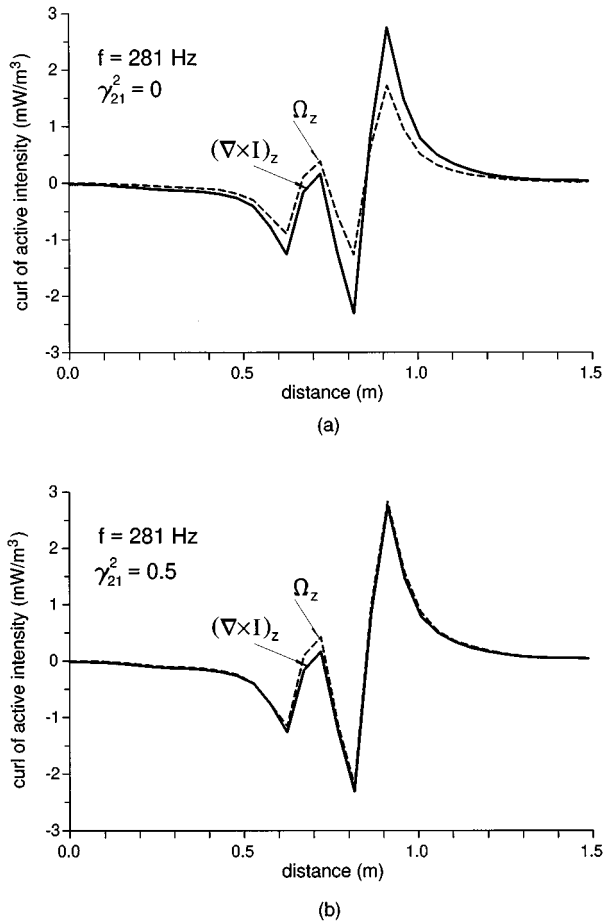


FIG. 9. Measured normal components of the curl of \mathbf{I} processed using the approximations $(\nabla \times \mathbf{I})_z$ [Eq. (47)] and Ω_z [Eq. (48)] for (a) $\gamma_{ij}^2 = 0$ and (b) $\gamma_{ij}^2 = 0.5$ at 281 Hz.

It has a Hermitian symmetry ($F_{ji} = F_{ij}^*$) and the sum of its diagonal elements corresponds to the total energy of the field: $2c(V+T)$. For a partially coherent sound field, the vector $[\Theta]$ cannot be defined and the matrix $[\mathbf{F}]$ must be characterized by the cross-power spectra $\lim_{T \rightarrow \infty} (2/T)E[\theta_i^*(\omega, T)\theta_j(\omega, T)]$, some of which have already been used in the expressions of the two previous indicators: the cross spectra between pressure and particle velocity for the coherence function of the field γ_{up}^2 and the imaginary parts of cross spectra between components of velocities for the curl. In what follows below, some properties of the field matrix are proven by choosing the coordinates (x', y', z') where the axis x' is in the direction of the vector of the active intensity \mathbf{I} and the plane (x', y') corresponds to the plane defined by vectors \mathbf{I} and \mathbf{J} . The field matrix obtained in these particular coordinates is denoted by $[\mathbf{F}_0]$, namely, the principal field matrix.

1. Case of a coherent field

Equation (5) is used to calculate the curl of the intensity of a coherent field. In the coordinates defined above, the curl of \mathbf{I} is oriented in the direction z' and is expressed by

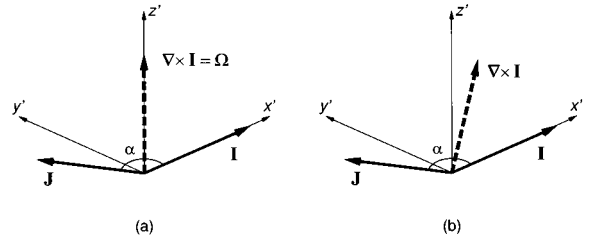


FIG. 10. Representation in the form of energetic quantities of information contained in the principal field matrix $[\mathbf{F}_0]$: (a) for a coherent field and (b) for a partially coherent field.

$|\nabla \times \mathbf{I}| = 4ck \operatorname{Im}\{T_{x'y'}\} = jk(F_{32} - F_{23})$ with $2cT_{x'y'} = \rho c u_{x'} u_{y'}^* / 2$. The field matrix of a coherent field is written, therefore, in the following form:

$$[\mathbf{F}_0] = \begin{bmatrix} 2cV & I_{x'} + jJ_{x'} & jJ_{y'} & 0 \\ I_{x'} - jJ_{x'} & 2cT_{x'x'} & 2cT_{x'y'} & 0 \\ -jJ_{y'} & 2cT_{x'y'}^* & 2cT_{y'y'} & 0 \\ 0 & 0 & 0 & 0 \end{bmatrix}. \quad (51)$$

In this configuration, the reactive intensity that forms an angle α with the active intensity has the components $J_{x'}$ and $J_{y'}$ (except for particular cases). An analytic expression of the particle velocity can be given by $u_{x'} = u_{x'R} - ju_{x'I}$, where $u_{x'R}$ and $u_{x'I}$ are, respectively, in phase and in quadrature with the pressure. The active and reactive intensities can be thus written as $I_{x'} = \frac{1}{2}p u_{x'R}$ and $J_{x'} = \frac{1}{2}p u_{x'I}$. In the coordinates (x', y', z') , $I_{y'} = 0$, $u_{y'}$ is in quadrature with $p(u_{y'} = -ju_{y'I})$ and hence $J_{y'} = (1/2)p u_{y'I}$. Similarly, $2cT_{x'y'} = \rho c u_{x'} u_{y'}^* / 2 = \rho c (u_{x'I} u_{y'I} + ju_{x'R} u_{y'I}) / 2$. The curl corresponding to the imaginary part of this last relationship will always be oriented in the direction of the z' axis. In the special case where the coherent field is nonpolarized, the velocity only has a component in the direction of x' and $J_{y'} = 0$, $T_{x'y'} = 0$ and $T_{y'y'} = 0$.

2. Case of a partially coherent field

Since any partially coherent field can be represented by the sum of r independent coherent fields, all elements of the matrix $[\mathbf{F}_0]$ will have a nonzero value, except for $F_{41} = F_{14} = 0$, which is the consequence of the choice of the coordinates system: there is no z' component of the resultant intensity vector, however, in general, $T_{z'z'} \neq 0$. If the independent fields are nonpolarized we have noted previously that a component $J_{y'}$ exists but the imaginary parts of $T_{x'y'}$, $T_{x'z'}$, and $T_{y'z'}$ are zero. This will not be true in the general case, where $\operatorname{Im}\{T_{x'z'}\}$ and $\operatorname{Im}\{T_{y'z'}\}$ are not zero: the curl of the resultant vector \mathbf{I} is no longer oriented in the direction z' , as shown in Fig. 10.

3. Use of the rank of the field matrix

A singular value decomposition of the field matrix $[\mathbf{F}]$ can also constitute a local indicator of the nature of the acoustic field. In the coherent case, the rank of the field matrix is equal to 1 and the eigenvector is proportional to the vector $[\Theta]$. For a partially coherent field, the rank of the field matrix may be 2, 3, or 4, which can be considered as a local

indicator of the complexity of the acoustic field. When the rank is superior to 2, the loss of coherence between pressure and particle velocity is accompanied by a loss of coherence between the orthogonal components of the particle velocity.

IV. CONCLUSION

Any random acoustic field can be represented by a model consisting of point sources or elementary fields whose relationships are defined by the coherence matrix of sources. The conditions that are required to correctly construct this matrix have been specified. Energetic quantities in a partially coherent field are expressed in terms of the coherence matrix of sources. It is shown that an acoustic field can be expressed as the superposition of independent fields which are coherent themselves but independent of each other. The investigation of the coherence matrix using the principal component analysis allows the number of the independent components to be minimized. The approximate model can be used for designing acoustic experiments, suppressing the weak components without appreciably modifying the structure of the field. To obtain measurable characteristics of the degree of coherence of an acoustic field, the function of coherence between the pressure and the particle velocity can be used. It is completed by the information about the polarization of the field in the form of an indicator determined from the measurement of the curl of acoustic intensity. It is shown that the curl of the intensity of a partially coherent field cannot be expressed in terms of the vector product of the resultant active and reactive intensities and Eq. (5) is valid only for a coherent field. Finally, we have shown that the definition of a field matrix made up of the relationships between the acoustic pressure and the three components of the particle velocity can completely take into account the local structure of an acoustic field and the rank of the field matrix can be used as an indicator of the local complexity of the acoustic field.

¹G. Krishnappa, "Acoustic intensity in the nearfield of two interfering monopoles," *J. Acoust. Soc. Am.* **74**, 1291–1294 (1983).

²S. Y. Ham, W. S. Kim, and M. G. Prasad, "Interference studies of acoustic pressure and intensity fields of two simple sources," *J. Acoust. Soc. Am.* **90**, 1149–1154 (1991).

³J.-C. Rebillat and S. Rifai, "Modèle plan du rayonnement acoustique de sources ponctuelles," *J. Acoust.* **3**, 263–271 (1990).

⁴F. Laville and J. Nicolas, "A computer simulation of sound power determination using two-microphone sound intensity measurements," *J. Acoust. Soc. Am.* **91**, 2042–2055 (1992).

⁵P. Filippi and D. Mazzoni, "Modélisation des sources de bruits à large bande et aléatoires," *Acustica* **74**, 77–80 (1991).

⁶J.-C. Pascal, "Intensimétrie et antennes acoustiques (Chap. XI)," in *Rayonnement acoustique des structures*, edited by C. Lesueur (Eyrolles, Paris, 1988).

⁷F. J. Fahy, *Sound Intensity* (Elsevier, London, 1989).

⁸P. W. Smith, T. J. Schultz, and C. I. Malme, "Intensity measurement in near fields and reverberant spaces," Bolt Beranek and Newman Inc., Report No. 1135 (1964).

⁹J.-C. Pascal, "Structure and patterns of acoustic intensity fields," Proc. 2nd Int. Cong. on Acoust. Intensity, Senlis, France, 23–26 September 1985, pp. 97–104.

¹⁰J.-C. Pascal, "Measurement of the active and reactive intensity in various acoustic fields," Proc. Conf. on Recent Dev. in Acoust. Intensity Meas., Senlis, France, 30 September–2 October 1981, pp. 11–19.

¹¹G. W. Elko, "Frequency domain estimation of the complex acoustic intensity and energy density," Ph.D. thesis, The Pennsylvania State University, 1984.

¹²J.-C. Pascal and J. Lu, "Advantage of the vectorial nature of acoustic intensity to describe sound field," Inter-Noise 84 Proc., Honolulu, 3–5 December 1984, pp. 1111–1114.

¹³J. A. Mann III, J. Tichy, and A. Romano, "Instantaneous and time-averaged energy transfer in acoustic fields," *J. Acoust. Soc. Am.* **82**, 17–30 (1987).

¹⁴J.-C. Pascal and C. Carles, "Systematic measurement errors with two microphone sound intensity meters," *J. Sound Vib.* **83**(1), 53–65 (1982).

¹⁵K. Pesonen and S. Uosukainen, "On rotationality of acoustic intensity field," Inter-Noise 84 Proc., Honolulu, 3–5 December 1984, 1125–1128.

¹⁶R. V. Waterhouse, D. G. Crighton, and J. E. Ffowcs-Williams, "A criterion for an energy vortex in a sound field," *J. Acoust. Soc. Am.* **81**, 1323–1326 (1987).

¹⁷S. Uosukainen, "Properties of acoustic energy quantities," Technical Research Centre of Finland, Report 656, Espoo (1990).

¹⁸A. N. Zhukov, A. N. Ivannikov, and V. I. Pavlov, "Identification of multipole sound sources," *Sov. Phys. Acoust.* **36**(3), 249–252 (1990).

¹⁹F. Jacobsen, "Active and reactive, coherent and incoherent sound fields," *J. Sound Vib.* **130**(3), 493–507 (1989).

²⁰F. Jacobsen, "A note on instantaneous and time-averaged active and reactive sound intensity," *J. Sound Vib.* **147**(3), 489–496 (1991).

²¹C. J. Dodds and J. D. Robson, "Partial coherence in multivariate random processes," *J. Sound Vib.* **42**(2), 243–249 (1975).

²²J.-F. Li, "Identification des sources industrielles par des techniques d'intensimétrie et d'holographie acoustique," Thèse de doctorat, Université de Technologie de Compiègne, 1993.

²³D. Otte, P. Sas, and P. Van de Pongeele, "Noise source identification by use of principal component analysis," Inter-Noise 88 Proc., Avignon, France, 30 August–1 September 1988, pp. 199–202.

²⁴D. Otte, "Development and evaluation of singular value analysis methodologies for studying multivariate noise and vibration problems," doctorate thesis, Catholic University of Leuven, 1994.

A descriptive model of the receptor potential nonlinearities generated by the hair cell mechano-electrical transducer

Andrei N. Lukashkin^{a)} and Ian J. Russell

School of Biological Sciences, University of Sussex, Falmer, Brighton BN1 9QG, United Kingdom

(Received 12 May 1997; accepted for publication 18 October 1997)

This paper describes a model for generating the hair cell receptor potential based on a second-order Boltzmann function. The model includes only the resistive elements of the hair cell membranes with batteries across them and the series resistance of the external return path of the transducer current through the tissue of the cochlea. The model provides a qualitative description of signal processing by the hair cell transducer and shows that the nonlinearity of the hair cell transducer can give rise to nonlinear phenomena, such as intermodulation distortion products and two-tone suppression with patterns similar to those which have been recorded from the peripheral auditory system. Particular outcomes of the model are the demonstration that two-tone suppression depends not on the saturation of the receptor current, but on the behaviour of the hair cell transducer function close to the operating point. The model also shows that there is non-monotonic growth and phase change for any spectral component, but not for the fundamental of the receptor potential. © 1998 Acoustical Society of America. [S0001-4966(98)02802-1]

PACS numbers: 43.64.Bt, 43.64.Kc, 43.64.Ld [RDF]

INTRODUCTION

All stages involved in the processing of auditory signals distort their input to some extent and contribute to the overall nonlinearity of the cochlea's response to sound (Rhode, 1971; Dallos, 1973; Russell and Sellick, 1978; Dallos *et al.*, 1982; Sellick *et al.*, 1982; Robles *et al.*, 1991; Zagaeski *et al.*, 1994). The mechano-electrical transducer of the hair cell is an early, crucial stage in auditory sensory processing with strong nonlinear characteristics. This nonlinear relationship between hair bundle displacement and transducer conductance has been fitted, in turtle hair cells (Crawford *et al.*, 1989) and outer hair cells (OHCs) from organotypic cultures of the mouse cochlea (Kros *et al.*, 1995) by a second-order Boltzmann function (SOB) which relates the probability of transducer channel opening to the displacement of the hair bundle. In 1985, Weiss and Leong provided a detailed description of the signal transformation by a sigmoidal transducer input-output function which was symmetrical to its point of inflection. According to these authors, the harmonic distortion pattern depends on the specific form of the transducer input-output function as well as on the operating point of the transducer. Therefore, in this paper we have examined the signal processing in a model based on a SOB transducer function with one open and two closed states and displacement-dependent transitions between them. The SOB is an approximation of an input-output function which is asymmetrical to its point of inflection. The parameters used in the model are based on the measurements by Kros *et al.* (1995). The model provides a qualitative description of signal processing by the hair cell transducer alone. It is not complicated by the feedback and mechanical filtering which is present in the cochlea *in situ*. However, the model shows that the nonlinearity of the hair cell transducer can give rise

to the nonlinear phenomena, including two-tone suppression, which have been recorded from the peripheral auditory system.

I. DESCRIPTION OF THE MODEL

The conductance of the transducer $G_{tr}(x(t))$ is given by

$$G_{tr}(x(t)) = R_{tr}(x(t))^{-1} = G_{tr \max} [1 + K_2 [1 + K_1]]^{-1}, \quad (1)$$

where R_{tr} is the transducer resistance and $G_{tr \max}$ is the maximal transducer conductance. K_1 and K_2 are the equilibrium constants for two transitions of the transducer channel. K_1 and K_2 can be described in terms of the position of the hair bundle (Crawford *et al.*, 1989)

$$K_1 = \exp[a_1[x_1 - x(t)]] \quad (2)$$

$$K_2 = \exp[a_2[x_2 - x(t)]],$$

where a_1 , a_2 , x_1 , x_2 are constants and $x(t)$ is the displacement of the hair bundle from its resting position. An example of $G_{tr}(x(t))$ as a function of hair bundle displacement for the mammalian OHC is given in Fig. 1(a). The function is a concave-convex asymmetrical function with a point of inflection which lies closer to the lower saturation level. Let us define the transducer operating point as a value of the transducer function with zero displacement of the hair bundle, i.e., the point $G_{tr}(0)$. Then biasing of the transducer operating point may be introduced as a steady state displacement x_{set} of the hair bundle and the biased transducer operating point is $G_{tr}(x_{set})$. When x_{set} is positive the operating point of the transducer moves in the direction indicated by the arrow in Fig. 1(a).

The nonlinearities of the receptor current through conductance $G_{tr}(x(t))$ are manifested in the changes in intracellular potential (the receptor potential). In order to compare the model of transduction, as described by a SOB function,

^{a)}Electronic mail: A.Lukashkin@sussex.ac.uk

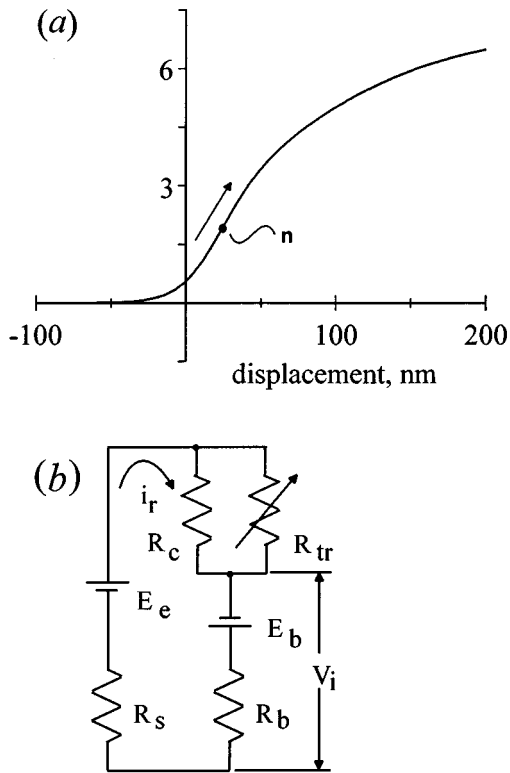


FIG. 1. Electrical circuit representing an OHC *in vivo*. (a) Transducer conductance of the mammalian OHC as a function of bundle displacement, according to Kros *et al.* (1995), was fitted to Eq. (1) with $G_{tr\max}=7$ nS, $a_1=0.065$ nm $^{-1}$, $a_2=0.016$ nm $^{-1}$, $x_1=24$ nm, $x_2=41$ nm. **n** indicates the point of inflection of the transducer function ($x=24.4$ nm). (b) Resistive circuit describing approximately the electrical properties of the hair cell *in vivo*. R_a is the resistance of the cell's apical pole which consists of the constant resistance R_c (500 M Ω) and the transducer resistance $R_{tr}(x)$ [Eq. (1) with parameters of Fig. 1] connected in parallel. R_b (50 M Ω) is the resistance of the basolateral membrane. These values correspond to a OHC about 50 μ m long from guinea pig cochleae (Housley and Ashmore, 1992). R_s is the resistance of the cochlear tissue. E_b (90 mV) is an electromotive force of the basolateral membrane determined by the potassium reversal potential (Housley and Ashmore, 1992). E_e is an endolymphatic potential of 80 mV.

with experimental results based on voltage responses recorded from the cochlear hair cells, it is necessary to introduce a simple electrical circuit that approximately describes the electrical properties of the hair cell *in vivo* [Fig. 1(b)]. A resistive model [Fig. 1(b)] may provide a useful basis for describing the distortion products created by the transducer itself because in this circuit the amplitudes of the distortion products are not modified by reactive elements of the cell's membranes. In fact, this circuit approximates the electrical properties of the hair cells *in vivo* in response to low frequency tones. For this circuit the resistance of the cell's apical pole $R_a(x(t))$ consists of a constant resistance R_c and a variable transducer resistance $R_{tr}(x(t))=1/G_{tr}(x(t))$ [Fig. 1(b)]. R_b is the resistance of the basolateral membrane and R_s is the series resistance of the external return path of the transducer current i_r through the tissue of the cochlea. According to the above mentioned definition one can write for the receptor potential V_r ,

$$V_r = V_i - V_{i0}, \quad (3)$$

where V_i is the basolateral membrane voltage and V_{i0} is the resting basolateral membrane voltage when displacement of the hair bundle $x=0$ [Eq. (1)] and, using the condition $R_s \ll R_a, R_b$, the basolateral membrane voltage V_i is

$$V_i = R_b i_r - E_b = (E_e + E_b) \frac{1}{1 + R_a(x(t))/R_b} - E_b, \quad (4)$$

where E_b is the electromotive force of the basolateral membrane determined by the potassium reversal potential (Housley and Ashmore, 1992) and E_e is the endolymphatic potential.

II. APPLICATION OF THE MODEL

The equations for all of the figures were solved numerically in the time domain with MATLAB software. The results were presented in a form which permitted comparison with the existing experimental results and which facilitated the planning of further experiments to investigate the role of the mechano-electrical transducer in generating the observed nonlinear phenomena.

A. Magnitude of the harmonic components of the receptor potential as functions of the bundle displacement and bias of the transducer operating point

Let us describe the transducer nonlinearity by the single valued input-output function $N_{tr}(x) = G_{tr}(x) - G_{tr}(x_{set})$. If an input signal has the form of $x = A \cos \theta$, where $\theta = 2\pi ft$, then the output signal may be expanded in a Fourier series

$$N_{tr}(\theta) = \sum_{n=0}^{\infty} a_n \cos(n\theta), \quad (5)$$

where a_n is the n th Fourier series coefficients of $N_{tr}(\theta)$. Weiss and Leong (1985) used a hyperbolic-tangent function, which is equivalent to a first-order Boltzmann function (FOB), in order to describe the input-output characteristic of the transducer. For a function of this kind, the zero frequency term and second harmonic may be positive (the phase angle is equal to 0 $^\circ$) or negative (the phase angle is equal to 180 $^\circ$) but they do not change their sign (i.e. the phase angle) when the level of the input signal changes as observed for the other spectral components (Weiss and Leong, 1985). The SOB function we are considering here [Eq. (1)] is asymmetrical to its point of inflection with the lower saturating level closer to its point of inflection [Fig. 1(a)] and shows non-monotonic growth and phase changes for any spectral component, but not for the fundamental. The latter characteristic can be shown easily for a few first harmonic components (see the Appendix). Figure 2 shows that with x_{set} above the point of inflection one can obtain non-monotonic level functions for the dc component. For small values of A the dc potential is negative but with large amplitude bundle displacements, it becomes positive again.

Figure 3 illustrates how variation in the resting position of the hair bundle (x_{set}) can produce non-monotonic growth of both even- and odd-order harmonics and the amplitude of the harmonics approaches zero and the phase angle changes

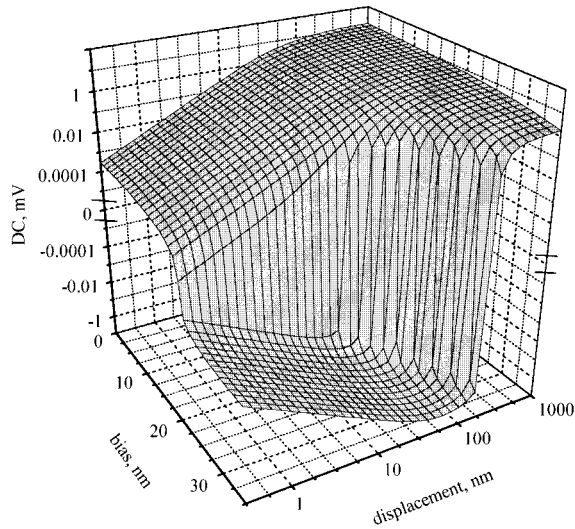


FIG. 2. Bipolar changes of the receptor potential dc component with bias of the transducer operating point. Direct numerical solution for circuit *b*. Bias is defined by the value of x_{set} (see text). Note the breaks of the vertical axis indicated by the short horizontal lines. The same model parameters as in Fig. 1 were used.

by 180° near the local minimum of the harmonics. The notches in the odd-order harmonics disappear with small positive values of x_{set} under the chosen model parameters [Fig. 3(b)]. This disappearance corresponds to a movement of the notches to levels of the harmonics below those shown in Fig. 3, i.e., in this case notches occur at very small hair bundle displacement, [note the change of the phase angle for the lowest amplitude of the 3rd and 5th harmonics shown in Fig. 3(a) and (b)]. This disappearance is followed by a range of x_{set} when all the harmonics grow monotonically for the observed output values. If x_{set} becomes larger again, then notches appear on even-order harmonics and, finally, when the value of x_{set} is increased still further (to 40 nm) all harmonics possess local minima over the plotted range of the harmonics' value. Thus it can be seen in Fig. 3 that the magnitudes of the odd and even-order harmonics alter reciprocally when the transducer operating point approaches and moves away from the point of inflection of the transducer function (Fig. 3).

B. Interference between two frequencies

If two harmonic signals f_1 and f_2 , with peak displacement amplitudes A_1 and A_2 , are present in the input then

$$\begin{aligned} x &= A_1 \cos(2\pi f_1 t) + A_2 \cos(2\pi f_2 t) \\ &= A_1 \cos \theta_1 + A_2 \cos \theta_2, \end{aligned} \quad (6)$$

and the output signal includes not only these primary frequencies but also intermodulation distortion components (IDCs). The output magnitude of the primaries is also a result of the interference between the input signals. Either the IDC magnitudes or the magnitudes of primaries depend upon whether the frequencies f_1 and f_2 are related (e.g., see Atherton, 1975). Therefore, the result of the interference will be different for commensurate frequencies (i.e., when the ratio f_2/f_1 is a ratio of integers) and incommensurate fre-

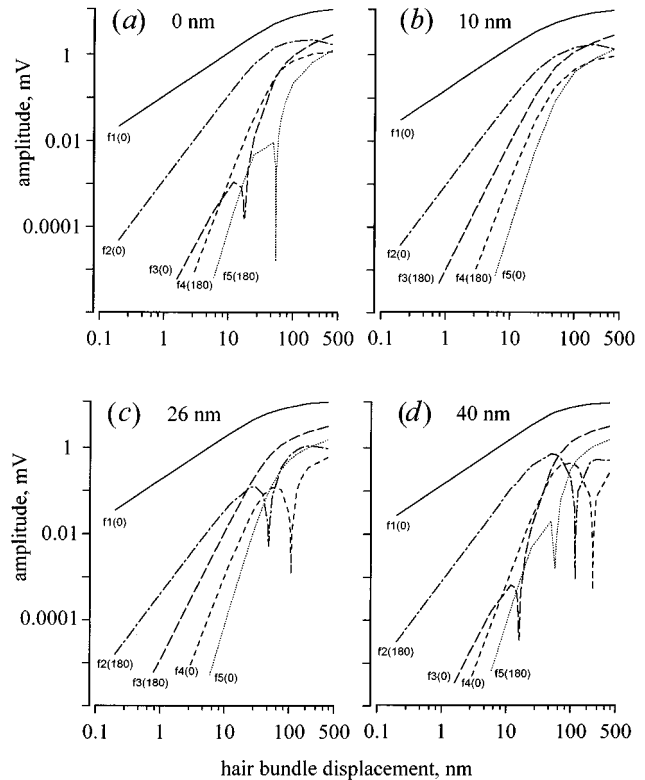


FIG. 3. Level functions of the fundamental and harmonics of the receptor potential with bias of the transducer operating point. Direct numerical solution for circuit *b*. f_1 is the fundamental. f_2 , f_3 , f_4 , and f_5 are the second, third, fourth and fifth harmonics, respectively. The phase of the lower part of each function re phase of the fundamental is indicated in degrees by the number in brackets and it changes by 180° near the minimum of the notches. (a), (b), (c) and (d) corresponds to x_{set} of 0, 10, 26, and 40 nm, respectively. The same model parameters as in Fig. 1 were used.

quencies. Furthermore, the output signal is unique for each particular ratio of commensurate frequencies and should be considered separately. Therefore, we have restricted our description to incommensurate frequencies only.¹

In order to account for the nonlinear interaction of two tones in the cochlea, Engebretson and Eldredge (1968) developed a model which showed that, when two signals were present at the input of a nonlinear system which had an input-output function that could be approximated by a power series, one could observe interference between the two signals. Notably, the output magnitude of one signal was linearised and suppressed when the input magnitude of the other signal was increased. A similar effect might also be expected for the transducer under consideration [Fig. 1(a)] because power series approximation is valid in this case.

In order to make estimates of the behaviour of the IDCs and fundamentals when two primary frequencies are used as an input signal to the model, let us expand the transducer input-output function $N_{tr}(x)$ in a Taylor's series about $x = x_{set}$

$$N_{tr}(x) = \sum_{n=0}^{\infty} a_n x^n, \quad (7)$$

where

$$a_n = \frac{1}{n!} \left[\frac{d^n N_{tr}(x)}{dx^n} \right]_{x=0}. \quad (8)$$

The remainder of series (7) approaches zero when $n \rightarrow \infty$ for any value of x . Therefore, it is identical to the function $N_{tr}(x)$ and all conclusions made on the basis of series expansion (7) are valid for any value of x . By substituting Eq. (6) into Eq. (7) one can find the output magnitude of $N_{tr}(x)$ of the frequency f_1 for incommensurate frequencies f_1 and f_2 when the peak displacement amplitude $A_1 \ll A_2$ [see Eq. (2) from Engebretson and Eldredge (1968)]:

$$N_{tr}(x)_{f_1} \approx A_1 \left[a_1 + \frac{3}{2} a_3 A_2^2 + \frac{15}{8} a_5 A_2^4 + \frac{35}{16} a_7 A_2^6 + \dots \right]_{A_1 \ll A_2}, \quad (9)$$

where $N_{tr}(x)_{f_1}$ is the magnitude $N_{tr}(x)$ at frequency f_1 . Therefore, $N_{tr}(x)_{f_1}$ depends linearly on the amplitude A_1 when $A_1 \ll A_2$. The slope of this dependence is defined by a linear combination of even-order powers of A_2 ; each power being weighted by a_n , which is defined by the appropriate order derivative of $N_{tr}(x)$ evaluated at the operating point. Some of the first odd-order derivatives of $N_{tr}(x)$ are shown in Fig. 4. It is seen from Fig. 4 that the sign and value of a_n is heavily dependent on the position of the operating point of the hair cell transducer function (in our notation on x_{set}). Therefore, if A_1 is held constant, magnitude of $N_{tr}(x)_{f_1}$ can decrease (suppression) or increase (facilitation) with varying A_2 [Eq. (9)] for different x_{set} . With some values of A_2 the magnitude of $N_{tr}(x)_{f_1}$ becomes negative. In other words, $|N_{tr}(x)_{f_1}|$ can change its phase angle by 180° . Examples of interference between two frequencies for different x_{set} are given in Fig. 5. One can see from Eq. (9) that $N_{tr}(x)_{f_1}$ does not depend on A_2 in one case only, when higher order terms of the series expansion (7) degenerate into zeros, i.e. when a system is linear.

From their measurement of the response of the CM to two tones, Geisler *et al.* (1990) proposed that saturation of the OHC receptor current causes two-tone suppression. In the model presented here, suppression is a particular case of the interference phenomena for two frequencies and depends only on the value of the derivatives of the transducer function $N_{tr}(x)$ at the operating point and, consequently, on the position of the operating point along x axis and does not depend on the behaviour of the function far away from the operating point and into saturation.

By using the same technique and expanding the transducer input–output function $N_{tr}(x)$ in a Taylor's series about $x = x_{set}$, one can show that it is possible to obtain non-monotonic level functions for the odd- and even-order IDCs of $N_{tr}(x)$. It is possible to derive the equation for the magnitude of any IDC from Eq. (7). For example, the $N_{tr}(x)$ magnitude of the distortion product $2f_1 - f_2$ for incommensurate frequencies f_1 and f_2 [Eq. (5) from Engebretson and Eldredge (1968)] is given by

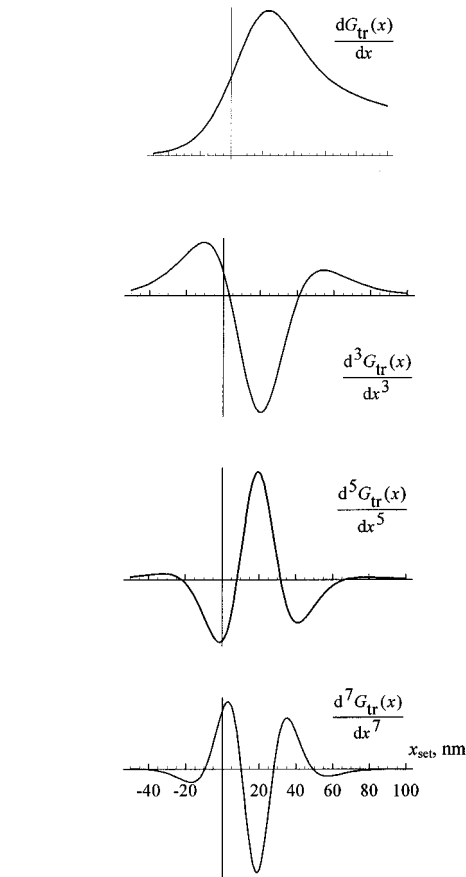


FIG. 4. First four even-order derivatives for the function $G_{tr}(x)$ that is shown in Fig. 1. The abscissa is x_{set} . The ordinate is $d^n G_{tr}(x)/dx^n$.

$$N_{tr}(x)_{2f_1 - f_2} = A_1^2 A_2 \left[\frac{3}{4} a_3 + \frac{5}{8} a_5 (2A_1^2 + 3A_2^2) + \frac{105}{64} a_7 (A_1^4 + 4A_1^2 A_2^2 + 2A_2^4) + \dots \right]. \quad (10)$$

The relative weight of different terms of the linear combination in Eq. (10) depends on the amplitude of the primaries and on the position of the transducer operating point because a_n depends on the n th order derivative of $N_{tr}(x)$ evaluated at the operating point. Therefore, it is possible to obtain monotonic as well as non-monotonic dependence of the amplitude of the distortion product $2f_1 - f_2$ as a function of displacement, depending on a particular form of nonlinearity and position of the operating point. The amplitude of IDCs of the receptor potential as a function of displacement are shown in Fig. 6 (upper panel) for two primary frequencies of equal amplitude when the set point of the transducer x_{set} is fixed at 26 nm. It is possible to see that the even IDCs show local minima together with monotonic growth of the fundamentals and the odd IDCs. These minima are also accompanied by a phase change of 180° . If, instead of keeping a constant operating point of the transducer, we fix the amplitude of the primaries and alter the operating point, we can observe the appearance and disappearance of the notches at the odd and even IDCs [Fig. 6 (lower panel)].

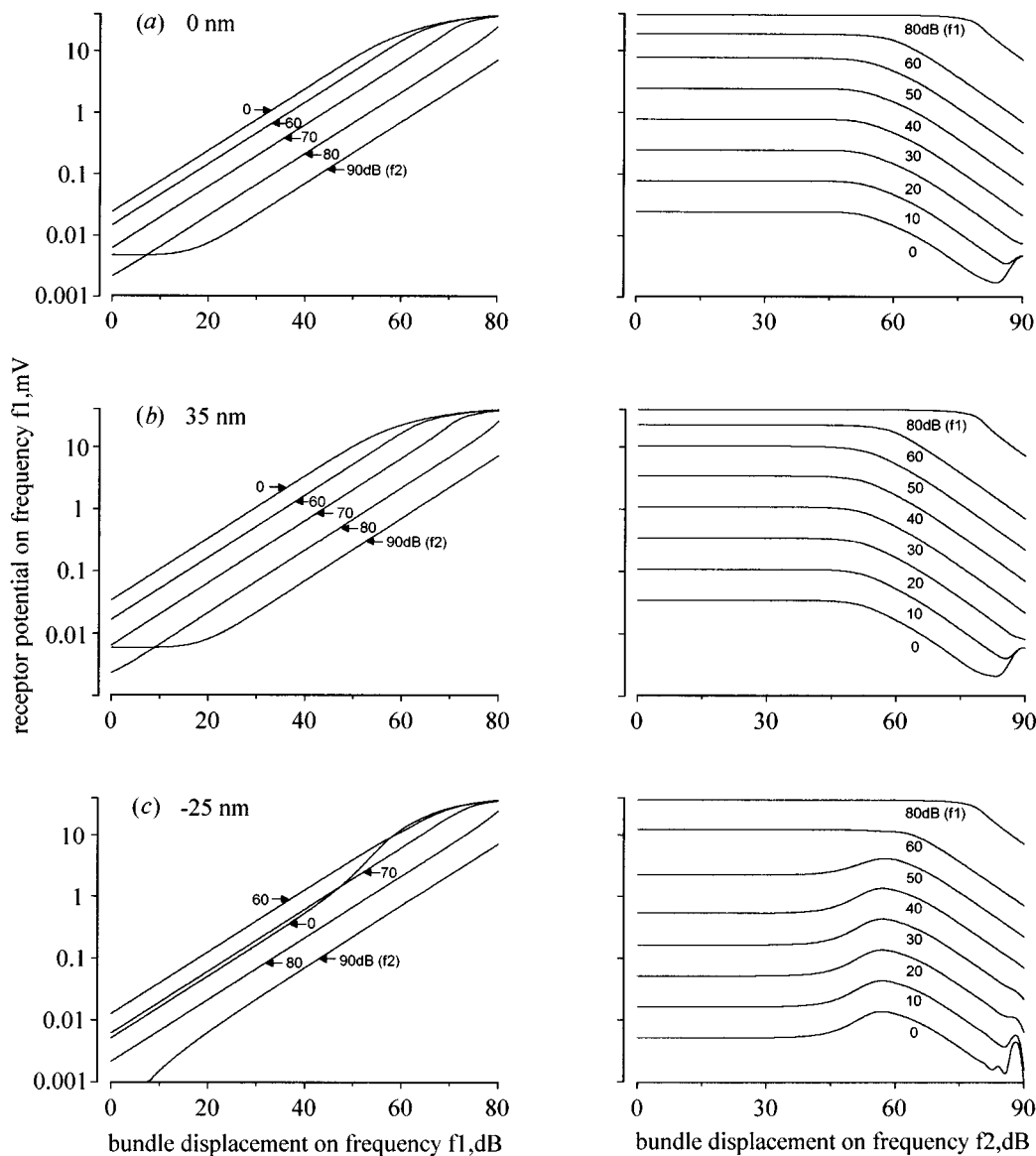


FIG. 5. Level functions for the spectral component of the receptor potential on frequency f_1 (left column) and changes of the spectral component of the receptor potential on frequency f_1 with increasing primaries amplitude (right column) evaluated at different transducer operating points when the input signal consists of two frequencies f_1 and f_2 . Direct numerical solution for circuit *b*. Frequency ratio f_1/f_2 is equal to $2^{-1/2}$. Panels (a), (b), and (c) present responses with $x_{\text{set}}=0$ nm, 35 nm, and -25 nm, respectively. Parameter indicated near each function is the amplitude of the bundle displacement at frequency f_2 (left column) and at frequency f_1 (right column) in decibels. 0 dB amplitude for the displacement is equal to 0.1 nm. The same model parameters as in Fig. 1 were used.

III. DISCUSSION

A. Notches and non-monotonic level functions

If it is assumed that the transducer function is labile and that the operating points can change, then, on the basis of the model, and depending on the level of bias of the operating point, it is possible to generate both monotonic and non-monotonic harmonics of the OHC receptor potential with notches accompanied by 180° changes in phase (Fig. 3). A change in the operating point of the transducer function could account for the non-monotonic behaviour and the notches observed in the even harmonics of receptor potentials recorded from both IHCs and OHCs in the third turn of the cochlea in response to tones close to their CF and their

monotonic growth for frequencies off CF (Dallos and Cheatham, 1989). A similar explanation might account for the appearance of notches in the harmonics, but not the fundamental, of OHC receptor potentials recorded in the basal turn of the guinea pig cochlea. The notches appear in response to low frequency tones when these are presented in combination with intense tones at frequencies a half octave below their CF (16 kHz) (Cody and Russell, 1992). The intense tones have been hypothesised to shift the operating point of the OHC transducer function (Cody and Russell, 1992, 1995). However, the model does not predict non-monotonic behaviour and sudden phase shifts and notches in the fundamental of the receptor potential. Both changes have

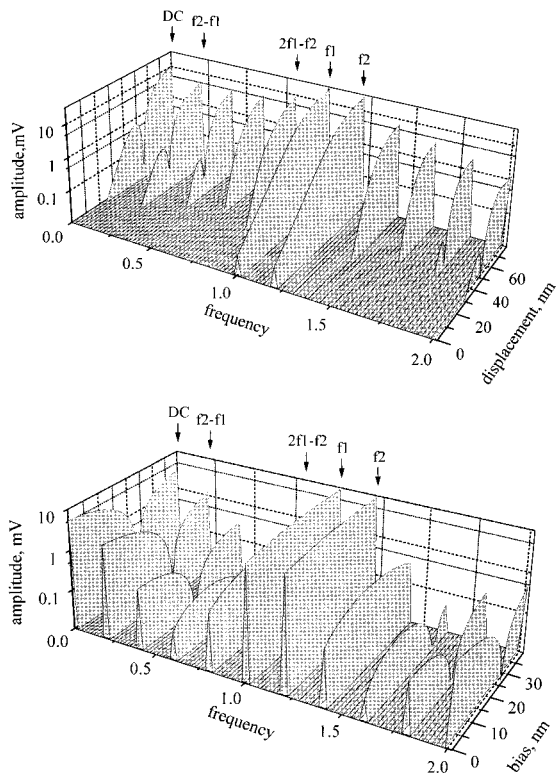


FIG. 6. Frequency spectrum of the receptor potential. Direct numerical solution for circuit *b*. Upper panel. Level function of the frequency spectrum. Amplitude of the frequencies are the same. Frequency ratio f_1/f_2 is equal to 1.2^{-1} . x_{set} is equal to 26 nm. Lower panel. Frequency spectrum with bias of the transducer operating point. Primary frequencies with ratio f_1/f_2 of 1.2^{-1} and of equal amplitude (100 nm peak-to-peak) were used as an input. The same model parameters as in Fig. 1 were used.

been seen in the fundamental of IHC receptor potentials recorded in the third turn of the cochlea to tones at their CF (Dallos and Cheatham, 1989), and in OHC receptor potentials recorded in the basal turn to intense tones a half octave below their CF (Kössl and Russell, 1992), but not in the BM displacements (Russell *et al.*, 1995). The phase changes and notches in the fundamental of the receptor potential are likely to be either direct, or indirect, consequences of changes in the relative vibration between the tectorial membrane and reticular lamina (Zwislocki, 1986).

The distinctive feature of the OHC dc receptor potential recorded from both the low frequency (Dallos *et al.*, 1982; Dallos, 1986) and the high frequency (Cody and Russell, 1987) regions of the cochlea is its frequency and level-dependent bipolarity. It has been suggested by Dallos and Cheatham (1992) that the bipolarity reflects interference of a recording electrode with the cochlear partitions. It can be seen from Fig. 2 that biasing of the operating point for several nanometers in the steepest region of the transducer function changes the sign and amplitude of the dc component dramatically. If the feedback process in the cochlea leads to the adjustment of the transducer operating point in this region (Russell *et al.*, 1986) then this could explain the polarity of the OHC dc potential without the need to propose that OHC feedback gain varies reciprocally with mechanical biasing of the basilar membrane (Dallos and Cheatham, 1992),

when either the lateral or scala tympani approaches are used for microelectrode registration of the OHC receptor potential. Namely, if the transducer operating points are situated above the point of inflection of the transducer function, one might expect a negative dc receptor potential for hair bundle displacements with small amplitude (Fig. 2), i.e. with low levels of stimulation or for stimulation with tones well below CF (Dallos, 1986; Cody and Russell, 1987). The dc receptor potential changes its polarity with increasing level of stimulation or when the frequency of a stimulating tone approaches CF (Dallos, 1986; Cody and Russell, 1987) and amplitude of hair bundle displacement increases (Fig. 2).

B. The generation of IDCs and two-tone suppression

The frequency selectivity of the basilar membrane was ignored when comparing the hair cell transducer model with experimental results involving the interaction of two tones. Instead, two stimuli of different frequencies but equal amplitude caused the same displacement of the hair bundle.

In accordance with direct measurements of distortion products in the forces exerted by hair bundles in response to two sinusoidal stimuli (Jaramillo *et al.*, 1993), it is clear from the data presented in Fig. 6 that the model of the hair cell transducer function is capable of generating both cubic and quadratic distortion products. Furthermore, the relative level of these products depends on the bias of the transducer function. A similar conclusion has been drawn by Frank and Kössl (1996) from a model of distortion generation in the cochlea in which the nonlinearity is also a SOB function. The transducer nonlinearity is not the only one which can participate in the generation of responses observed *in vivo* responses. Notable examples include the nonlinearities of the OHC electromotility and the voltage-dependent capacitance of the OHC membrane. However, according to a model proposed by Santos-Sacchi (1993) the transducer nonlinearity is the most dominant. Since, at the CF, the OHC transducer function controls the nonlinear growth of both the OHC receptor potential and BM displacement, it is likely that the OHC transducer function is the principal nonlinearity which determines the generation of low-level distortion products in the cochlea. Changes in the bias of the transducer operating point (Fig. 6) could be the primary cause of the complex, sometimes reciprocal, level-dependent changes in the magnitude of odd and even-order IDCs (Schmiedt and Adams, 1981; Brown, 1987, 1994; Whitehead *et al.*, 1992; Popelka *et al.*, 1993; Frank and Kössl, 1996).

An interesting outcome of the model is the demonstration that the phenomenon of two-tone suppression depends on the behaviour of the hair cell transducer function at the operating point and not only on the saturation of the OHC receptor current as suggested by Geisler *et al.* (1990) for two-tone suppression measured in the electrical responses of the cochlea. In the model under consideration, the existence of suppression or facilitation is an intrinsic attribute of the transducer with a nonlinear input-output function for any amplitudes of the input signals. In fact, if generation of the IDCs is a result of the interference between two input signals, then suppression characterises this interference when

the output signal is measured at the frequency of the primaries. This result has been known for a long time in control engineering (e.g., see Atherton, 1975). The two-tone suppression produced by the model has features similar to that observed for basilar membrane vibrations, hair cell receptor potentials, and neural responses recorded *in situ* and which are not completely accounted for by either the saturation model (Geisler *et al.*, 1990) or an attenuation model of suppression (Arthur *et al.*, 1971; Javel *et al.*, 1978; Sellick and Russell, 1979; Cheatham and Dallos, 1989, 1992; Robles *et al.*, 1989; Nuttall and Dolan, 1993). Although the model is very simple and is not complicated by the feedback and mechanical filtering which is present in the cochlear *in situ*, it does produce two-tone suppression between tones which would not be expected to saturate the OHC transducer conductance [Fig. 5(a)] and it can generate phenomena which are not accounted for by either the saturation or the attenuation models. Notable examples include, for low to moderate levels of the probe tone in the presence of a loud suppressor, that the level functions become straightened out (see Nuttall and Dolan, 1993 and Fig. 5) and the model can generate two-tone augmentation. According to the model, slight changes in the operating point of the transducer function [see Fig. 5(c)], can lead to two-tone augmentation or facilitation rather than to suppression as has been seen in the voltage responses of basal turn IHCs in insensitive preparations of the guinea pig cochlea (Russell and Kössl, 1992).

ACKNOWLEDGMENTS

We thank Dr. Ann Brown, Dr. Cornè Kros, Dr. Gunnar Sandberg, and Dr. Aleksandr Sobolev for valuable discussion and critical reading of early versions of this manuscript. This work was supported by grants from the Medical Research Council, Hearing Research Trust and Royal Society. A.N.L. is supported by a Wellcome Trust Prize Studentship.

APPENDIX

Let the transducer under consideration possess a memoryless nonlinearity which can be described by the input-output function $N(x)$. If an input signal for the transducer has the form of $x = A \cos \theta$, where $\theta = 2\pi ft$, then the output signal may be described by a Fourier series

$$N(\theta) = \sum_{n=0}^{\infty} a_n \cos(n\theta), \quad (\text{A1})$$

where

$$a_n = \frac{\epsilon_n}{2\pi} \int_{-\pi}^{\pi} N(\theta) \cos(n\theta) d\theta, \quad (\text{A2})$$

and $\epsilon_n = 1$ for $n = 0$ and $\epsilon_n = 2$ for $n > 0$.

The Fourier coefficients of the series expansion (A2) can be calculated directly from the function $N(x)$ (e.g., see Atherton, 1975). Using substitution $\theta = \arccos(x/A)$ and $N(\theta) = N(x)|_{x=A \cos \theta}$ for $-\pi \leq \theta \leq \pi$ we can write

$$\begin{aligned} a_n &= \frac{\epsilon_n}{2\pi} \int_{-A}^A N(x) \cos[n \arccos(x/A)] [(A^2 - x^2)^{-1/2}] dx \\ &\quad + \frac{\epsilon_n}{2\pi} \int_A^{-A} N(x) \cos[n \arccos(x/A)] \\ &\quad \times [-(A^2 - x^2)^{-1/2}] dx \\ &= \frac{\epsilon_n}{\pi} \int_{-A}^A N(x) \cos[n \arccos(x/A)] [(A^2 - x^2)^{-1/2}] dx \\ &= \epsilon_n \int_{-A}^A N(x) T_n(x/A) p(x) dx, \end{aligned} \quad (\text{A3})$$

where $T_n(x/A) = \cos[n \arccos(x/A)]$ is the Chebyshev polynomial of the first kind and $p(x) = (A^2 - x^2)^{-1/2}$.

Substituting $T_0(x/A) = 1$ into Eq. (A3) one can find the amplitude of the dc component

$$a_0 = \int_{-A}^A N_{tr}(x) p(x) dx. \quad (\text{A4})$$

$p(x) > 0$ for $-A \leq x \leq A$, $N_{tr}(x) > 0$ for $x > 0$ and $N_{tr}(x) < 0$ for $x < 0$. Therefore, the value of the integrand is negative for $-A \leq x \leq 0$ and positive for $0 \leq x \leq A$. If x_{set} is below the point of inflection of the transducer function ($d^2 G_{tr}/dx^2 < 0$), then $-N_{tr}(-x) < N_{tr}(x)$ for both FOB and SOB. Therefore, $a_0 > 0$ for any value of A . If x_{set} is above the point of inflection then, for FOB, $-N_{tr}(-x) > N_{tr}(x)$ and, therefore, $a_0 < 0$ for any A . The situation is different for SOB. For small values of A the dc potential is negative [$-N_{tr}(-x) > N_{tr}(x)$]. However, with large amplitude bundle displacements, it becomes positive again because, for large A , $-N_{tr}(-x) < N_{tr}(x)$.

Substituting $T_1(x/A) = x/A$ into Eq. (A3) one can find the amplitude of the fundamental

$$a_1 = \frac{2}{A} \int_{-A}^A N_{tr}(x) x p(x) dx. \quad (\text{A5})$$

The value of the integrand is positive for $-A \leq x \leq A$. Therefore, $a_1 > 0$ for any A and the level function of the fundamental is monotonic for both FOB and SOB for any x_{set} .

Substituting $T_2(x/A)$ into Eq. (A3) one can find the amplitude of the second harmonic

$$a_2 = 2 \int_{-A}^A N_{tr}(x) T_2(x/A) p(x) dx. \quad (\text{A6})$$

Resubstituting $x = A \cos \theta$ into Eq. (A6) gives

$$a_2 = \frac{1}{\pi} \int_{-\pi}^{\pi} N_{tr}(\theta) \cos(2\theta) d\theta. \quad (\text{A7})$$

Integrating Eq. (A7) by parts, we have

$$a_2 = -\frac{1}{2\pi} \int_{-\pi}^{\pi} N'_{tr}(\theta) \sin(2\theta) d\theta, \quad (\text{A8})$$

where $N'_{tr}(\theta) = dN_{tr}(\theta)/d\theta$. Using substitution $\theta = \arccos(x/A)$ for $0 \leq \theta \leq \pi$, $\theta = -\arccos(x/A)$ for $-\pi \leq \theta \leq 0$ and $N'_{tr}(\theta) = [dN_{tr}(x)/dx][dx/d\theta] = N'_{tr}(x)[dx/d\theta]$ we can write

$$a_2 = \frac{1}{\pi} \int_{-A}^A N'_{tr}(x) U_1(x/A) [1 - (x/A)^2]^{1/2} dx$$

$$= \frac{2}{A\pi} \int_{-A}^A N'_{tr}(x) x [1 - (x/A)^2]^{1/2} dx, \quad (\text{A9})$$

where $U_1(x/A) = 2x/A$ is the Chebyshev polynomial of the second kind $U_{n-1}(x/A) = \sin[n \arccos(x/A)] [1 - (x/A)^2]^{-1/2}$. In Eq. (A9) $N'_{tr}(x) > 0$ and $[1 - (x/A)^2]^{1/2} > 0$ for $-A < x < A$, the integrand is negative for $-A < x < 0$ and it is positive for $0 < x < A$. Therefore, this case is similar to the above mentioned case for the dc component. Again, for FOB a_2 can be either positive or negative, depending on x_{set} , but it does not change its sign for different A . For SOB, when x_{set} is above the point of inflection a_2 changes its sign with increasing A .

¹To illustrate frequency dependence of the interference between primaries let us consider a simple quadratic nonlinearity $y = x^2$. Substituting Eq. (6) into this equation, expanding the cosine powers and separating the cosine products, we have $y(t) = 1 + 0.5 \cos(2\theta_1) + 0.5 \cos(2\theta_2) + 0.5 \cos(\theta_1 + \theta_2) + 0.5 \cos(\theta_1 - \theta_2)$. If frequencies f_1 and f_2 are incommensurate then each term on the right hand side represents a unique frequency component. If frequencies f_1 and f_2 are commensurate then some of the terms could have the same frequency. For example, if $f_1/f_2 = 3$ then 3rd and 5th terms have the same frequency $2f_2$.

- Arthur, R. M., Pfeiffer, R. R., and Suga, N. (1971). "Properties of two-tone inhibition in primary auditory neurons," *J. Physiol. (London)* **212**, 593–609.
- Atherton, D. P. (1975). *Nonlinear Control Engineering* (Van Nostrand Reinhold, London).
- Brown, A. M. (1987). "Acoustic distortion from rodent ears: A comparison of responses from rats, guinea pigs and gerbils," *Hearing Res.* **31**, 25–38.
- Brown, A. M. (1994). "Modulation of the hair cell motor: A possible source of odd-order distortion," *J. Acoust. Soc. Am.* **96**, 2210–2215.
- Cheatham, M. A., and Dallos, P. (1989). "Two-tone suppression in inner hair cell responses," *Hearing Res.* **40**, 187–196.
- Cheatham, M. A., and Dallos, P. (1992). "Two-tone suppression in inner hair cell responses: Correlates of rate suppression in the auditory nerve," *Hearing Res.* **60**, 1–12.
- Cody, A. R., and Russell, I. J. (1987). "The responses of hair cells in the basal turn of the guinea-pig cochlea to tones," *J. Physiol. (London)* **383**, 551–569.
- Cody, A. R., and Russell, I. J. (1992). "The effects of intense acoustic stimulation on the nonlinear properties of mammalian hair cells," in *Noise-Induced Hearing Loss*, edited by A. L. Dancer, D. Henderson, R. J. Salvi, and R. P. Hamernik (Mosby-Year Book, St. Louis), pp. 11–27.
- Cody, A. R., and Russell, I. J. (1995). "Time-varying voltage responses of mammalian hair cells to isoamplitude acoustic stimulation," *Aud. Neurosci.* **1**, 351–361.
- Crawford, A. C., Evans, M. G., and Fettiplace, R. (1989). "Activation and adaptation of transducer currents in turtle hair cells," *J. Physiol. (London)* **419**, 405–434.
- Dallos, P. (1973). *The Auditory Periphery. Biophysics and Physiology* (Academic, New York).
- Dallos, P. (1986). "Neurobiology of cochlear inner and outer hair cells: Intracellular recordings," *Hearing Res.* **22**, 185–198.
- Dallos, P., and Cheatham, M. A. (1989). "Nonlinearities in cochlear receptor potentials and their origins," *J. Acoust. Soc. Am.* **86**, 1790–1796.
- Dallos, P., and Cheatham, M. A. (1992). "Cochlear hair cell function reflected in intracellular recordings in vivo," in *Sensory Transduction*, edited by D. P. Corey and S. D. Roper (The Rockefeller University Press, New York), pp. 372–393.
- Dallos, P., Santos-Sacchi, J., and Flock, A. (1982). "Intracellular recordings from cochlear outer hair cells," *Science* **218**, 582–584.
- Engelbreton, A. M., and Eldredge, D. H. (1968). "Model for the nonlinear characteristics of cochlear potentials," *J. Acoust. Soc. Am.* **44**, 548–554.

- Frank, G., and Kössl, M. (1996). "The acoustic two tone distortions $2f_1 - f_2$ and $f_2 - f_1$ and their possible relation to changes in the gain and the operating point of the cochlear amplifier," *Hearing Res.* **98**, 104–115.
- Geisler, C. D., Yates, G. K., Patuzzi, R. B., and Johnstone, B. M. (1990). "Saturation of outer hair cell receptor currents causes two-tone suppression," *Hearing Res.* **44**, 241–256.
- Housley, G. D., and Ashmore, J. F. (1992). "Ionic currents of outer hair cells isolated from the guinea-pig cochlea," *J. Physiol. (London)* **448**, 73–98.
- Jaramillo, F., Markin, V. S., and Hudspeth, A. J. (1993). "Auditory illusions and the single hair cell," *Nature (London)* **364**, 527–529.
- Javel, E., Geisler, C. D., and Ravindran, A. (1978). "Two-tone suppression in the auditory nerve of the cat: Rate-intensity and temporal analyses," *J. Acoust. Soc. Am.* **63**, 1093–1104.
- Kössl, M., and Russell, I. J. (1992). "The phase and magnitude of hair cell receptor potentials and frequency tuning in the guinea pig cochlea," *J. Neurosci.* **12**, 1575–1586.
- Kros, C. J., Lennan, G. W. T., and Richardson, G. P. (1995). "Transducer currents and bundle movements in outer hair cells of neonatal mice," in *Active Hearing*, edited by A. Flock, D. Otoson, and M. Ulfendahl (Elsevier Science, Amsterdam), pp. 113–125.
- Nuttall, A. L., and Dolan, D. F. (1993). "Two-tone suppression of inner hair cell and basilar membrane responses in the guinea pig," *J. Acoust. Soc. Am.* **93**, 390–400.
- Popelka, G. R., Osterhammel, P. A., Nielsen, L. H., and Rasmussen, A. N. (1993). "Growth of distortion product otoacoustic emissions with primary-tone level in humans," *Hearing Res.* **71**, 12–22.
- Rhode, W. S. (1971). "Observations of the vibrations of the basilar membrane in squirrel monkeys using the Mossbaver technique," *J. Acoust. Soc. Am.* **49**, 1218–1231.
- Robles, L., Ruggero, M. A., and Rich, N. C. (1989). "Nonlinear interactions in the mechanical response of the cochlea to two-tone stimuli," in *Cochlear Mechanisms*, edited by J. P. Wilson and D. T. Kemp (Plenum, New York), pp. 369–375.
- Robles, L., Ruggero, M. A., and Rich, N. C. (1991). "Two-tone distortion in the basilar membrane of the cochlea," *Nature (London)* **349**, 413–414.
- Russell, I. J., and Kössl, M. (1992). "Modulation of hair cell voltage responses to tones by low-frequency biasing of the basilar membrane in the guinea pig cochlea," *J. Neurosci.* **12**, 1587–1601.
- Russell, I. J., Kössl, M., and Murugasu, E. (1995). "A comparison between tone-evoked voltage responses of hair cells and basilar membrane displacements recorded in the basal turn of the guinea pig cochlea," in *Advances in Hearing Research*, edited by G. A. Manley, G. M. Klump, C. Köppl, H. Fastl, and H. Oeckinghaus (World Scientific, Singapore), pp. 136–144.
- Russell, I. J., Richardson, G. P., and Cody, A. R. (1986). "Mechanosensitivity of mammalian auditory hair cells *in vitro*," *Nature (London)* **321**, 517–519.
- Russell, I. J., and Sellick, P. M. (1978). "Intracellular studies of hair cells in the mammalian cochlear," *J. Physiol. (London)* **284**, 261–290.
- Santos-Sacchi, J. (1993). "Harmonics of outer hair cell motility," *Biophys. J.* **65**, 2217–2227.
- Schmiedt, R. A., and Adams, J. C. (1981). "Stimulated acoustic emissions in the ear canal of the gerbil," *Hearing Res.* **5**, 295–305.
- Sellick, P. M., and Russell, I. J. (1979). "Two-tone suppression in cochlear hair cells," *Hearing Res.* **1**, 227–236.
- Sellick, P. M., Patuzzi, R., and Johnstone, B. M. (1982). "Measurement of basilar membrane motion in the guinea pig using the Mossbauer technique," *J. Acoust. Soc. Am.* **72**, 131–141.
- Weiss, T. F., and Leong, R. (1985). "A model for signal transmission in an ear having hair cells with free-standing stereocilia. IV. Mechanoelectric transduction stage," *Hearing Res.* **20**, 175–195.
- Whitehead, M. L., Lonsbury-Martin, B. L., and Martin, G. K. (1992). "Evidence for two discrete sources of $2f_1 - f_2$ distortion-product otoacoustic emission in rabbit: I. Differential dependence on stimulus parameters," *J. Acoust. Soc. Am.* **91**, 1587–1607.
- Zagaeski, M., Cody, A. R., Russell, I. J., and Mountain, D. C. (1994). "Transfer characteristic of the inner hair cell synapse: Steady-state analysis," *J. Acoust. Soc. Am.* **95**, 3430–3434.
- Zwislocki, J. J. (1986). "Analysis of cochlear mechanics," *Hearing Res.* **22**, 155–169.

Distortion product otoacoustic emissions in human newborns and adults. I. Frequency effects

Robert E. Lasky^{a)}

Neurology Department, The University of Wisconsin, Madison Medical School, H6/528 Clinical Science Building, 600 Highland Avenue, Madison, Wisconsin 53792-5132

(Received 19 July 1996; revised 16 June 1997; accepted 23 October 1997)

This study varied stimulus frequency and recorded distortion product otoacoustic emissions (DPOAEs) in human newborns and adults. Because of outer and middle ear acoustics, the same auditory input resulted in higher newborn stimulus sound pressure levels across a broad frequency range in the occluded outer ear canal. Noise levels in the canal were 5–15 dB lower for adults at frequencies less than about 3 kHz. The $2f_1 - f_2$ DPOAE was the most reliably recorded DPOAE except at the lowest frequencies assessed. At the lowest frequencies the $2f_2 - f_1$ DPOAE was more frequently recorded than any other DPOAE. There were no striking developmental differences in the kinds of DPOAEs that were recorded. The amplitudes of consecutively recorded $2f_1 - f_2$ DPOAEs were generally within 1.5 dB of each other for all age groups (slightly better reproducibility for adults than newborns). The phases of consecutively recorded $2f_1 - f_2$ DPOAEs were generally within 15 degrees of each other (often less than 10 and 5 degrees for newborns and adults respectively). At the highest frequencies assessed ($f_2 = 4.2 - 9.9$ kHz) all subjects had similar amplitude $2f_1 - f_2$ DPOAEs. At lower frequencies adult $2f_1 - f_2$ amplitudes were significantly less than those of newborns. At the lowest frequencies reliably assessed ($f_2 = 1.5 - 2.1$ kHz) term newborns had significantly larger $2f_1 - f_2$ DPOAEs than preterm newborns. Newborn and adult $2f_1 - f_2$ DPOAE amplitude $\times f_2/f_1$ functions were quite similar although there were reliable differences. Age related differences in the outer and middle ears may explain some of the differences in DPOAEs that were observed. © 1998 Acoustical Society of America. [S0001-4966(98)02602-2]

PACS numbers: 43.64.Ha, 43.64.Jb, 43.64.Ri [BLM]

INTRODUCTION

Otoacoustic emissions are a by-product of cochlear mechanics (Brownell, 1990). A number of laboratories have described the development of emissions (primarily distortion product otoacoustic emissions, DPOAEs) in a variety of experimental animal species (Lenoir and Puel, 1987; Henley *et al.*, 1989; Norton *et al.*, 1991; Mills and Rubel, 1994, 1996; Tierney *et al.*, 1994). Although the species assessed differed, the results were consistent. The $2f_1 - f_2$ DPOAE was first recorded in response to middle- and high-frequency stimuli and last to low-frequency stimuli. Mills and Rubel (1996) have demonstrated that early in the gerbil's development DPOAEs are also absent at very high frequencies.

In the cat, Tierney *et al.* (1994) reported that: (1) DPOAE thresholds decreased with age (reaching adult values first in the $f_2 = 3$ kHz region); (2) for given primary levels DPOAE amplitudes increased with age and became more comparable across frequency (at the youngest ages tested DPOAE amplitudes at low and high frequencies were reduced relative to those in the mid-frequency range); (3) the DPOAE amplitude $\times f_2/f_1$ ratio functions became more sharply tuned with age; and (4) the ratio associated with the peak amplitude of those functions decreased with age.

Whether the developmental results observed in altricial experimental animals characterize humans depends on the

maturational status of the human auditory periphery at birth. Researchers have reported either similar or greater DPOAE amplitudes in human newborns at term compared to those of adults (Bonfils *et al.*, 1992; Lasky *et al.*, 1992; Brown *et al.*, 1995; Abdala, 1996; Abdala *et al.*, 1996). Smurzynski (1994) reported the results of a longitudinal study of seven preterm newborns tested from 31 through 41 weeks conceptional age (the majority of tests were conducted over a three week period). DPOAEs increased in amplitude with age but were present and relatively mature by 33 weeks. Popelka *et al.* (1995) reported no differences in DPOAE amplitudes between 34 and 42 weeks conceptional age on a larger cross-sectional sample. The frequencies (2 and 4 kHz) Popelka assessed were close to the frequencies expected to mature first. If they exist, developmental differences are more likely at lower and higher frequencies.

Pujol and Uziel (1988) have related the onset of cochlear function to the opening of the tunnel of Corti, the formation of Nuel's spaces, the final transformation of inner sulcus epithelium from tall to low cuboidal cells, and the release of the tectorial membrane from the inner sulcus epithelium (see Romand, 1983; Rubel, 1984; Pujol and Uziel, 1988; Walsh and Romand, 1992, for reviews of anatomical development). In the human these developments occur by approximately the twentieth week post conception. By that time inner hair cell (IHC) innervation seems almost mature.

Many of the anatomical changes that occur between 20 and 35 weeks post-conception in the human concern the

^{a)}Electronic mail: rlasky@facstaff.wisc.edu

outer hair cells (OHCs) and their support cells, the relationship between the tectorial membrane and the inner and outer hair cells, and the basilar membrane (Bredberg, 1968; Pujol *et al.*, 1980). There are other, more subtle, cochlear developments which extend beyond the thirty-fifth conceptional week in the human. For example, development of the lateral subsurface cisternae extends for a relatively long time (Pujol *et al.*, 1980). The lateral subsurface cisternae may play a role in OHC motility.

Pujol and colleagues (Pujol and Uziel, 1988) have concluded that functional development of the human cochlea begins by 20 weeks conceptional age and matures by 35 weeks conceptional age. They supported their hypothesis with functional data from human fetuses and preterm newborns. The human fetal heart rate changes in response to sound from the twentieth to the twenty-fourth conceptional week (Bench and Metz, 1974). By 25–29 weeks human fetuses show eye blink reflexes to acoustic stimuli delivered to the abdominal wall of the mother (Birnholtz and Benacerraf, 1983). These findings are consistent with the earliest recordings of the auditory brainstem evoked response (ABR) and the N1-P2 slow vertex potential in preterm newborns at 25 weeks post-conception (Weitzman and Graziani, 1968; Starr *et al.*, 1977). Thresholds are quite elevated at this age (Starr *et al.*, 1977). By term ABR thresholds are within 10–25 dB of adult thresholds (Schulman-Galambos and Galambos, 1975; Lary *et al.*, 1985; Adelman *et al.*, 1990; Lasky, 1991; Hall, 1992). ABR input/output (I/O) functions are also adult-like in the newborn (Hall, 1992).

Outer and middle ears also affect emissions and changes in those structures in humans from the birth to adulthood are significant (Saunders *et al.*, 1983; Eby and Nadol, 1986; Kruger and Rubin, 1987; Relkin, 1988; Keefe *et al.*, 1993, 1994; Ikui *et al.*, 1995; Margolis and Trine, 1997). Little is known about the development of the efferent pathways which may also affect emissions.

Within the range of stimulation of interest the outer and middle ears are linear systems. Consequently, they cannot explain nonlinearities in the newborns' response to stimulation but scale it accordingly. Differences accounted for by linear operations (e.g., changes in DPOAE amplitude across frequency) would be consistent with outer and middle ear effects. On the other hand, developmental differences in the distortion products recorded or the nonlinearity of the input/output (I/O) functions would support an interpretation of cochlear immaturity.

The purpose of the experiments to be presented in this and a companion article (Lasky, 1997) was to provide additional details concerning DPOAEs in human newborns. In this article DPOAEs evoked by stimuli varying in frequency were compared among human preterm newborns, full term newborns, and adults. In the companion article (Lasky, 1997) primary level effects are described and contrasted in human newborns and adults.

I. GENERAL METHODS

A. Subjects

Subjects were of three different ages: preterm newborns, full term newborns, and young adults. The preterm newborns

(1) were judged healthy by routine physical and neurologic examinations by the Pediatric House Staff, (2) did not require assisted ventilation at the time of testing, (3) were not receiving antibiotics, loop diuretics, or other medications at the time of testing, and (4) had no family history of congenital hearing loss. The full term newborns (1) were judged healthy by routine physical and neurologic examinations by the Pediatric House Staff, (2) had 1- and 5-min Apgar scores greater than seven, (3) were between 37 and 41 weeks post-conception according to the Pediatric House Staff's estimate of gestational age based on the Lubchenco (1970) exam, (4) did not receive antibiotics, loop diuretics, or other ototoxic medications prior to testing, and (5) had no family history of congenital hearing loss. All newborns were tested at more than 24 h after birth (Lasky *et al.*, 1987). The hearing of the adults was assessed as normal by pure-tone audiometry (i.e., no greater than a 10-dB loss at the octave frequencies from 250 through 8 kHz and the inter octave frequencies at 3 and 6 kHz).

The study was approved by the Internal Review Boards of The University of Wisconsin-Madison Medical School and The University of Texas Southwestern Medical Center at Dallas. Informed consent was obtained from all human subjects prior to study initiation. Permission for newborn study participation was obtained from the parents.

B. Apparatus and stimuli

The instrumentation used to collect the DPOAEs included an Intel microprocessor based computer, an Ariel DSP-16+ signal processing board that generated the stimuli and digitized the sound recorded from the ear canal, two Etymotic ER-2 earphones that converted the stimulus output from the signal processing board into sound pressure, a probe unit housing an Etymotic ER-10B ear canal microphone, and an amplifier providing signal conditioning and 40 dB of amplification to the microphone output which was then input to the signal processing board. Silicone tubing (0.95 mm o.d. × 0.5 mm i.d.) transmitted the sound generated by the two earphones through the probe housing and into the ear canal. The terminus of these tubes was more than 5 mm from the probe tip, varied from subject to subject, but was approximately the same for both stimulus channels.

Two different software programs were used to record the DPOAEs. A software program written at AT&T Bell Labs by Jont Allen and his colleagues (CUBEDIS™) was used to record the majority of the DPOAEs. It controlled stimulus generation and response recording. In addition to other functions, the software calculated and plotted the frequency responses of the two stimulus channels to chirps, the sound pressure levels (in dB SPL) of the primaries in the ear canal, the $2f_1 - f_2$ DPOAE, and the noise in the vicinity of the $2f_1 - f_2$ DPOAE (the mean of the three higher and the three lower Fourier transform frequency bins adjacent to the distortion product frequency). The software was modified to include artifact rejection capabilities, to calculate phase, to measure other DPOAEs and their respective noise levels (the mean of the three higher and the three lower Fourier transform frequency bins adjacent to each DPOAE), and to calculate the significance of the DPOAEs recorded on the basis

of general likelihood ratio tests (van Trees, 1968). A software program written by Stephen Neely and Zhiqiang Liu (Neely and Zhiqiang, 1993) at Boys Town National Research Hospital (EMAV) was also used. EMAV has the capability of the CUBEDIS™ program and additionally many of the modifications added to that program. It also permitted averaging to a criterion signal-to-noise ratio (SNR) rather than a defined number of trials.

The distortion generated by the instrumentation used in this study was measured in 1-, 2-, and 3-cc closed syringes to verify that our instrumentation at the levels presented did not distort the results. The volume of the syringes was varied to span the range characterizing human newborn and adult ear canal volumes. As a consequence, measurements were eliminated which could have reflected distortion generated by the instrumentation. Adult high level, high-frequency measurements were more likely to be affected.

C. Procedure

For each experiment the protocol was the same for newborns and adults. An otoscopic examination preceded probe placement. Canal debris was removed if necessary. The probe was inserted in the canal, and the frequency response of each earphone was determined. The probe was repositioned until the frequency responses from both earphones were similar and as flat as possible. A piece of surgical tubing around the probe maintained the seal of the probe unit in the newborn canal. In adults the probe unit was held in place by Grason–Stadler impedance probe tips. Once an acceptable frequency response from both earphones was achieved, emission recording commenced.

The DPOAEs were recorded by the CUBEDIS™ program to primaries presented for 4096 ms. The stimulus presentation interval was divided into 20.48-ms response periods which were averaged. An FFT was calculated on the averaged response. The sampling rates of both the analog-to-digital and digital-to-analog converters were 50 kHz. Noise levels greater than 3 s.d.'s above mean values for human adults tested in good conditions were rejected as artifact (Lasky *et al.*, 1992). In experiment IV responses were averaged until a SNR equal to 20 dB was recorded or 64 s of artifact free response averaging was completed.

In experiments I and III duplicate responses were recorded to each pair of primaries presented. DPOAE reproducibility was estimated from these duplicate measurements. It should be noted that these duplicate measurements were made without repositioning the probe. They represent the upper limit on reproducibility with this instrumentation and procedures (two measurements made one after the other to the same stimuli with the same probe placement).

The preterm newborns were tested in a quiet room in the continuing care newborn nursery at Parkland Memorial Hospital, Dallas. Full term newborns were tested in a different quiet room in the newborn nursery at Parkland Memorial Hospital. The newborns were assessed laying down, while asleep, and between feedings. The adults were tested in a single walled sound booth (IAC) in the Neurology Department at The University of Wisconsin-Madison Medical

School. Adult testing was conducted while the subjects were seated in a comfortable chair in an awake state.

D. Terminology

The primary frequencies in Hz are abbreviated by f . The level of the primaries in dB SPL is abbreviated by L . The subscript 1 refers to the lower-frequency primary, and the subscript 2 refers to the higher-frequency primary.

II. EXPERIMENTS

A. Experiment I

1. Introduction

Experiment I was conducted to contrast DPOAEs in human preterm newborns, full term newborns, and adults over a considerable frequency range. DPOAEs were recorded to primaries presented at 65 dB SPL ($L_1=L_2$). The f_2/f_1 ratio was held constant at 1.2, while f_2 was varied in 25 steps from 20.020 through 0.537 kHz. It was not possible to present distortion free stimuli at these levels to all subjects at all frequencies. Only results that were significantly ($p < 0.05$) greater than the noise floor and did not reflect the distortion produced by the system are presented.

The primary analyses were 3 (age) \times n (frequency) repeated measures analyses of variance (ANOVAs). N refers to the number of frequencies included in the analysis. The limitation of these analyses was missing data, generally at the lowest and highest frequencies. Data were missing for two reasons: (1) stimuli could not be presented due to ear canal acoustics and instrumentation limitations (generally high frequencies); and (2) DPOAEs were not significantly different from the noise (generally low frequencies). One-way ANOVAs (contrasting the three ages) were also conducted at each frequency. These analyses included data not included in the two-way ANOVAs. Data were analyzed only if at least six subjects in each group had data. Significant effects ($p < 0.05$) were explored by Student–Newman–Keuls *post hoc* contrasts. The repeated measures ANOVAs were used to identify significant age \times frequency interactions and main effects. The one-way ANOVAs further explored those interactions and commented on frequencies and data not included in the repeated measures ANOVAs.

Twelve preterm newborns (mean conceptional age at the time of testing=34.1 weeks, s.d.=1.1 weeks), 12 full term newborns (mean conceptional age at the time of testing=39.5 weeks, s.d.=1.2 weeks), and 12 young adults (mean age at the time of testing=21.5 years, s.d.=1.5 years) participated as subjects in this study.

2. Results

The frequency responses to chirps recorded from the probe in the occluded ear canal differed significantly in preterm newborns, full term newborns, and adults (see Fig. 1). The same voltage chirp resulted in higher sound pressure levels across a broad frequency range in newborns compared to adults. The difference was greatest between 3 and 9 kHz. Differences between preterm and full term newborns were small. At low frequencies the frequency response of term

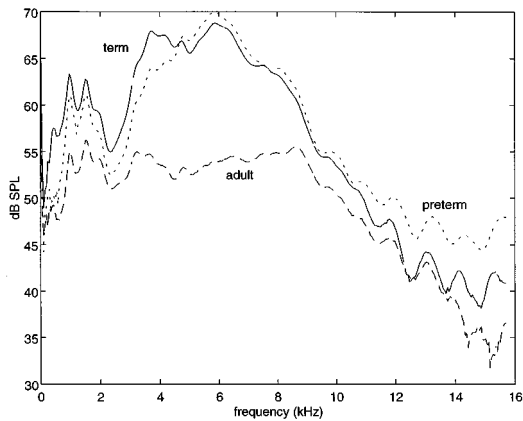


FIG. 1. Mean frequency responses in the occluded ear canal of preterm newborns (small dashed lines), full term newborns (solid line), and adults (large dashed lines).

newborns was of slightly greater amplitude than the frequency response of preterm newborns. At high frequencies (>5 kHz) the reverse was true.

Noise levels were calculated at each frequency by the mean of the three Fourier transform frequency bins above and below the distortion product frequency. That was the estimate of noise used in artifact rejection and all SNR calculations. Figure 2 presents those noise levels for the $2f_1 - f_2$ DPOAE for the three groups of subjects. For each frequency at least six same aged subjects had to have data in order to be included in Fig. 2. The age \times frequency interaction of a 3 (age) \times 14 (frequency) repeated measures ANOVA was significant [$F(26,390) = 7.05$; $p < 0.001$]. The 14 f_2 frequencies (1.1–7.5 kHz) included in that analysis were those having virtually complete data. One-way ANOVAs explored frequency specific age effects in greater detail. There was little difference in the noise levels of the preterm and full term newborns. In contrast, the noise levels of the adults were significantly lower (Student–Newman–Keuls contrasts) by 5–15 dB than those of newborns for DPOAE frequencies less than 3 kHz. Adults were tested in the nursery as well as the sound booth. Low-frequency noise levels were up to 5 dB higher in the low frequencies in the nursery accounting for some but not all of the differences between newborns and adults.

The emission data were explored for families of DPOAEs. The probe system generated relatively high levels of harmonics in the calibration cavities precluding meaning-

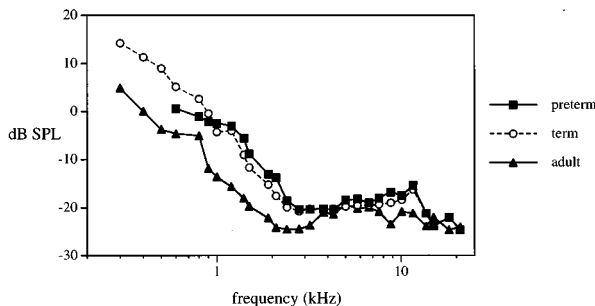


FIG. 2. Average noise levels of preterm and full term newborns and adults.

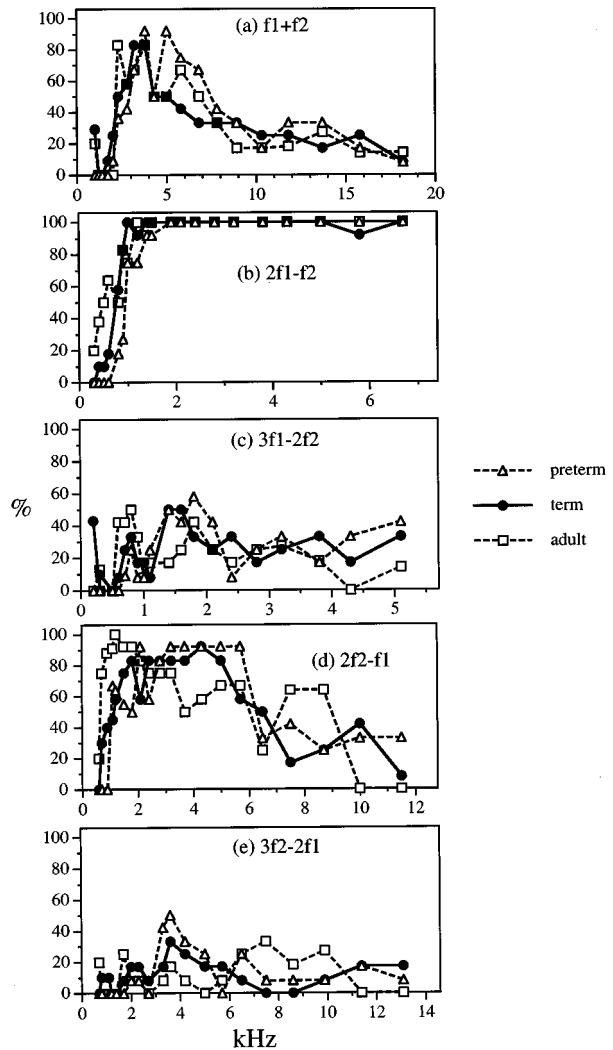


FIG. 3. Percentage of subjects with significant DPOAEs as a function of age, frequency, and DPOAE.

ful statements concerning cochlear generated harmonics. With one exception ($f_1 + f_2$), $nf_1 + nf_2$ summation DPOAEs were not reliably recorded. The $nf_2 - nf_1$ difference DPOAEs were not reliably recorded. The simple difference DPOAE ($f_2 - f_1$) can be reliably recorded at higher primary levels and lower frequencies than presented in this study. Difference DPOAEs from two families, $(n+1)f_1 - nf_2$ and $(n+1)f_2 - nf_1$ were reliably recorded. Higher than fifth-order difference DPOAEs were recorded infrequently. Other DPOAEs were not prominent after a preliminary scan of the data and are not presented. Thus five DPOAEs, $f_1 + f_2$, $2f_1 - f_2$, $3f_1 - 2f_2$, $2f_2 - f_1$, and $3f_2 - 2f_1$, were considered in subsequent analyses.

Figure 3 presents the percentage of subjects with significant DPOAEs as a function of age, frequency, and DPOAE. At each frequency all subjects presented stimuli were included in the analyses. The abscissa for each individual graph indicates the frequency of the DPOAE for that individual graph. Corresponding values on each graph were generated by the same frequency primaries (e.g., the last values on each graph were generated by the $f_2 = 9.9$ kHz, $f_1 = 8.3$ kHz primaries).

As expected, the $2f_1 - f_2$ DPOAE was reliably recorded to all but the lowest frequencies assessed in virtually all subjects. At the lowest frequencies significant $2f_1 - f_2$ DPOAEs were most likely to be recorded from adults and least likely to be recorded from preterm newborns. The $2f_2 - f_1$ DPOAE was recorded in 80% or more of the subjects at low frequencies for adults and at mid frequencies for newborns. At the lowest frequencies the $2f_2 - f_1$ DPOAE was more frequently recorded than any other DPOAE (including $2f_1 - f_2$). This was most obvious for adults but apparent for newborns as well. The $f_1 + f_2$ DPOAE was also reliably recorded in 80% or more of the subjects in each age group at some frequencies. The low-pass characteristics of the probe unit and canal may have contributed to the high-frequency fall-off in the $2f_2 - f_1$ and $f_1 + f_2$ DPOAEs. Relatively few quintic DPOAEs were recorded at any age.

Absolute amplitude and phase differences between duplicate DPOAE recordings were calculated at each frequency. These differences specified the within session reproducibility of the recorded DPOAEs (note that all of these DPOAEs were unlikely, $p < 0.05$, to be noise). Reproducibility of the $2f_1 - f_2$ DPOAE was relatively constant across frequency except at the extremes of the frequency range assessed. Absolute differences in amplitude were generally less than 1.5 dB for all age groups. Reproducibility was slightly better for adults than newborns although none of the age main effects were significant ($p < 0.01$; one-way ANOVAs). Absolute differences in phase were generally less than 15 degrees (for newborns often less than 10 degrees and for adults often less than 5 degrees). Again, none of the age main effects were significant. Because reliable DPOAEs other than $2f_1 - f_2$ were infrequently observed, statements concerning their within session reproducibility must be qualified. However, reproducibility of the other DPOAEs was generally poorer than for $2f_1 - f_2$.

Mean $2f_1 - f_2$ DPOAE amplitudes are plotted in Fig. 4 (top graph) for preterm newborns, full term newborns, and adults. The age \times frequency interaction of a 3 (age) \times 10 (frequency) repeated measures ANOVA was significant [$F(18,252) = 5.94$; $p < 0.001$]. The 10 f_2 frequencies (2.1–7.5 kHz) included in that analysis were those having virtually complete data (excluding frequencies that could not be presented and those with nonsignificant DPOAEs). One-way ANOVAs explored frequency specific age effects in greater detail. At the highest frequencies ($f_2 = 4.2$ – 9.9 kHz) all subjects had similar amplitude $2f_1 - f_2$ DPOAEs. At lower frequencies the $2f_1 - f_2$ amplitudes of adults were significantly smaller (Student–Newman–Keuls contrasts) than those of the preterm and full term newborns which were of similar amplitude. At the lowest frequencies ($f_2 = 1.5$, 1.8, and 2.1 kHz) the term newborns had significantly larger $2f_1 - f_2$ DPOAEs (Student–Newman–Keuls contrasts) than the preterm newborns. The bottom graph of Fig. 4 presents corresponding data for the $2f_2 - f_1$ DPOAEs. The pattern of results for the $2f_2 - f_1$ DPOAEs were similar to those for the $2f_1 - f_2$ DPOAE.

When present, the amplitudes of the other DPOAEs ($f_1 + f_2$, $3f_1 - 2f_2$, and $3f_2 - 2f_1$) were smaller than the amplitudes of the $2f_1 - f_2$ and $2f_2 - f_1$ DPOAEs. Because

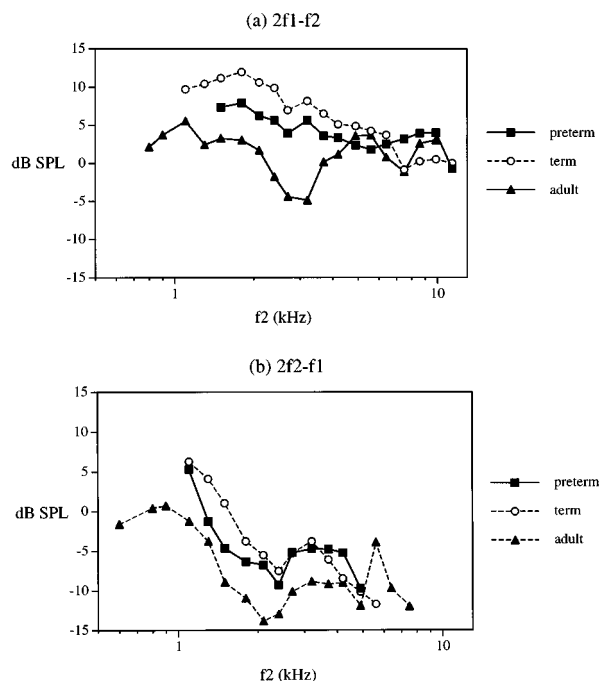


FIG. 4. Mean amplitudes of the significant $2f_1 - f_2$ (a) and $2f_2 - f_1$ (b) DPOAEs.

few of these DPOAEs were reliably recorded, little can be said about them. Between subject phases were highly variable. This was not unexpected because phase depended on probe position which varied from subject to subject.

B. Experiment II

1. Introduction

In cats Tierney *et al.* (1994) reported that DPOAE $\times f_2/f_1$ functions became more sharply tuned with age. Furthermore, the f_2/f_1 ratio associated with peak DPOAE amplitude decreased with age. Brown *et al.* (1995) has reported that at $f_2 = 4$ kHz human newborn DPOAE $\times f_2/f_1$ functions were broader than those of adults. Abdala (1996) reported that newborn and adult DPOAE $\times f_2/f_1$ functions at $f_2 = 1.5$ and 6 kHz were similar. Abdala (1996) offered two explanations for the differences between her results and those of Brown *et al.*—a frequency related developmental effect or a methodological confound. Experiment II investigated developmental differences in human DPOAE $\times f_2/f_1$ functions across a range of frequencies including those investigated by Brown *et al.* (1995) and Abdala (1996).

In experiment II the f_2/f_1 ratio was varied (1.05, 1.1, 1.15, 1.2, 1.25, 1.3, 1.35, and 1.4—the exact ratios were determined by the frequency resolution of the instrumentation) by varying f_1 for six different f_2 s (1, 2, 3, 4, 6, and 8 kHz). The primaries were equal level ($L_1 = L_2 = 60$ dB SPL). The same five DPOAEs that were initially considered in experiment I were also considered in experiment II. Results concerning three DPOAEs will be presented. Other DPOAEs were significant so infrequently to preclude further consideration. The three DPOAEs considered were $2f_1 - f_2$, $3f_1 - 2f_2$, and $2f_2 - f_1$.

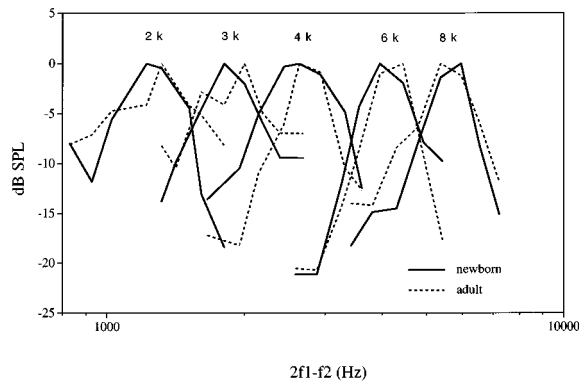


FIG. 5. Mean normalized $2f_1-f_2$ amplitude by f_2/f_1 functions for five f_2 's (2, 3, 4, 6, and 8 kHz) for newborns and adults.

If filtering by cochlear structures is responsible for lower amplitude DPOAEs at small f_2/f_1 s (Allen, 1990; Brown and Gaskill, 1990; Stover *et al.*, 1994; Abdala, 1996), the peaks in the $(n+1)f_1-nf_2$ DPOAE $\times f_2/f_1$ function for different DPOAEs should occur at the same frequency. Comparing $2f_1-f_2$ and $3f_1-2f_2$ DPOAE $\times f_2/f_1$ functions permitted a test of this hypothesis. There may be developmental differences in the structures responsible for this filtering.

Ten full term newborns (mean conceptional age at the time of testing = 39.4 weeks, s.d. = 0.9 weeks) and 8 adults (mean age at the time of testing = 21.4 years, s.d. = 1.8 years) served as subjects. In addition, two preterm newborns (both were 33 weeks conceptional age at testing) were also tested. Given the length of the protocol for newborns a single response was recorded to each stimulus.

2. Results

Figure 5 presents mean $2f_1-f_2$ amplitude $\times 2f_1-f_2$ frequency functions for five f_2 's (2, 3, 4, 6, and 8 kHz). It was difficult to interpret these functions at $f_2=1$ kHz because so few significant DPOAEs were recorded. For that reason they were not included in this figure. Newborn and adult DPOAE amplitudes differed at low frequencies replicating experiment I results. In order to facilitate direct comparisons of newborn and adult functions, those differences were eliminated in Fig. 5 by normalizing DPOAE amplitudes (i.e., assigning the peak value of each function as the referent sound pressure, 0 dB).

Distortion product amplitudes in Fig. 5 increased from noise to their peak values and then declined into noise again as f_2/f_1 increased. Because few values were sampled and these functions can be quite sharp, eliminating all measurements indistinguishable from the noise floor can distort these functions (e.g., in the extreme a very sharp function could have only one value significantly different from the noise floor which would clearly not characterize that function well). Consequently, nonsignificant values at the extremes of the f_2/f_1 range were included to more accurately portray these functions.

At $f_2=2-8$ kHz adult and newborn functions were comparably shaped. Two (age) \times n (frequency) repeated measures analyses of variance were computed at each f_2 . None of the age \times frequency interactions were significant.

These results are consistent with those reported by Abdala (1996). However, it is difficult to conclude these results are inconsistent with those of Brown *et al.* (1995) given the small sample sizes. In particular, newborn 4-kHz functions were broader than those of adults even though the difference was not statistically significant ($p=0.203$).

For both age groups the $3f_1-2f_2$ DPOAE peaked at $f_2/f_1=1.1$ for f_2 's = 4, 6, and 8 kHz and either 1.1 or 1.2 for f_2 's = 2 and 3 kHz. These peaks were approximately 1/2 an octave down from f_2 in line with the cochlear filtering hypothesis (Allen, 1990; Brown and Gaskill, 1990b; Stover *et al.*, 1994). With increasing f_2/f_1 , the $2f_2-f_1$ DPOAE declined from a peak amplitude (generally at $f_2/f_1=1.05$ for all f_2 frequencies). There were no striking developmental differences.

The superior robustness of the $2f_2-f_1$ DPOAE reported in experiment I at low frequencies was replicated. For the newborns few significant ($p<0.05$) DPOAEs were recorded to the $f_2=1$ kHz stimuli. However, more significant $2f_2-f_1$ than $2f_1-f_2$ DPOAEs were recorded.

The results from the two preterm newborns tested were similar to the results from the full term newborns and the adults. However, it was not possible to interpret the $f_2=1$ and 2-kHz data for these preterm newborns because few significant DPOAEs were recorded at those frequencies.

C. Experiments III and IV

1. Introduction

Experiments III and IV were conducted to extend and confirm the results of experiment II at select frequencies. In experiment III the f_2/f_1 's were more densely sampled in order to more accurately evaluate the DPOAE amplitude $\times f_2/f_1$ functions. The same paradigm and procedure as in experiment II were used. Only three f_2 's (2, 4, and 8 kHz) were presented. Ten f_2/f_1 's were presented at all three f_2 's (1.02, 1.05, 1.08, 1.11, 1.14, 1.17, 1.21, 1.24, 1.28, 1.32). An additional six f_2/f_1 's were presented at $f_2=4$ kHz (1.06, 1.12, 1.19, 1.22, 1.30, 1.34). In addition, duplicate measurements were recorded in order to comment on reproducibility as a function of f_2/f_1 .

The difficulty in recording the $2f_1-f_2$ DPOAE function at $f_2=1$ kHz may be explained by a poor SNR. A poor SNR may also explain the failure to consistently record other members of the $(n+1)f_1-nf_2$ family of DPOAEs at all frequencies. Pisorski *et al.* (1995) recorded very high order $(n+1)f_1-nf_2$ DPOAEs in normal hearing adults. Consequently, in experiment IV data were collected for 64 s (rather than 4 s in experiments I-III) or until the SNR = 20 dB. DPOAE $\times f_2/f_1$ functions were recorded at f_2 's = 1, 2, 4, and 8 kHz. The f_2/f_1 's sampled (5 for $f_2=1$ kHz, 10 for $f_2=2$ kHz, and 16 for $f_2=4$ and 8 kHz) ranged from 1.025 through 1.344.

Eight full term newborns (mean conceptional age at the time of testing = 39.5 weeks, s.d. = 1.5 weeks) and seven adults (mean age at the time of testing = 21.4 years, s.d. = 1.7 years) served as subjects in experiment III. In experiment IV six full term newborns (mean conceptional age

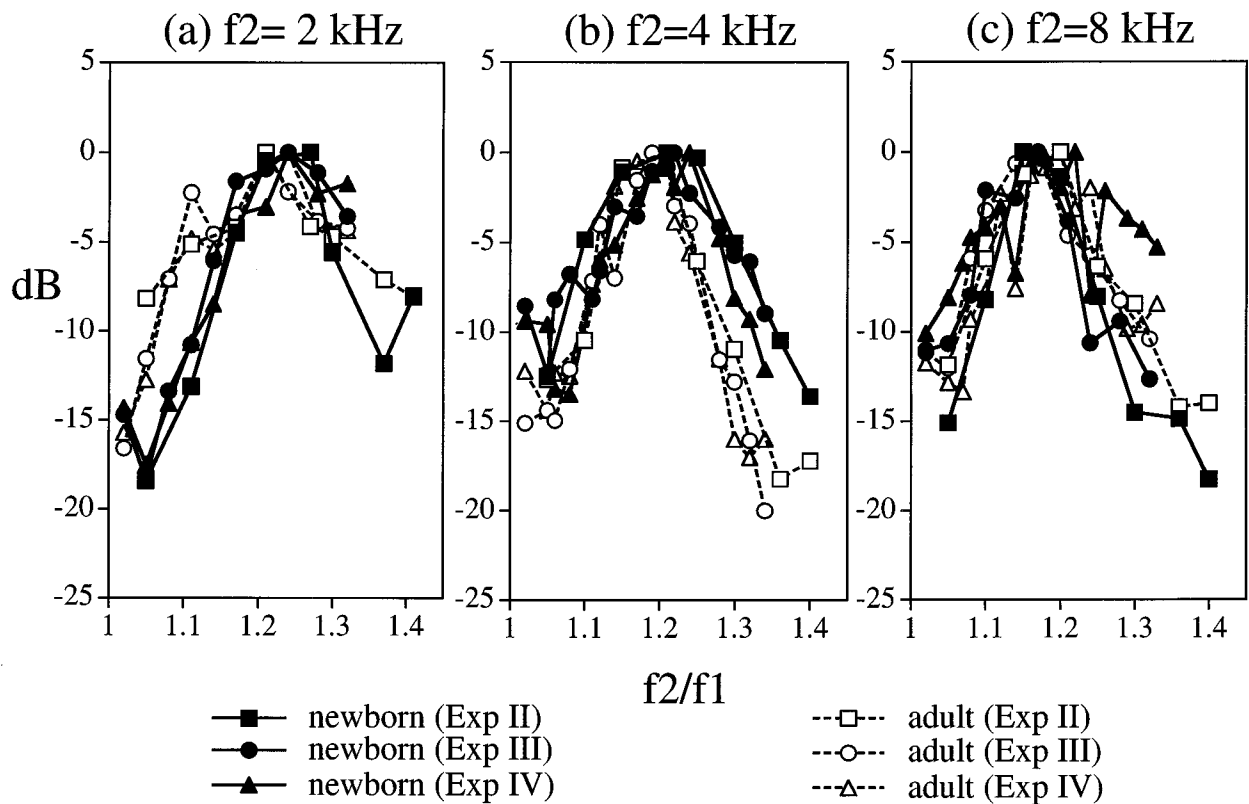


FIG. 6. Mean newborn and adult normalized $2f_1 - f_2$ amplitude by f_2/f_1 functions for $f_2 = 2$ (a), 4 (b), and 8 (c) kHz. The data from experiments II, III, and IV are included in this figure.

at the time of testing = 40.0 weeks, s.d. = 0.9 weeks) and 10 young adults (mean age at the time of testing = 21.3 years, s.d. = 1.4 years) participated as subjects.

The analyses to be presented will focus on the same three DPOAEs considered in experiment II, $2f_1 - f_2$, $3f_1 - 2f_2$, and $2f_2 - f_1$ because few of the other DPOAEs were significant.

2. Results

Figure 6 plots mean normalized (assigning the peak value of each function as the referent sound pressure) $2f_1 - f_2$ amplitude $\times f_2/f_1$ functions for newborns and adults in experiments II, III, and IV. Again, nonsignificant values at the extremes of the f_2/f_1 range were included to more accurately portray these functions. Experiments III and IV replicated experiment II reasonably well. Some differences between the newborn and adult data replicated as well, suggesting real differences and not measurement variability. Two (age) $\times n$ (f_2/f_1) repeated measures analyses of variance were computed at each f_2 for experiments III and IV. The age $\times f_2/f_1$ interactions for experiment III were significant at $f_2 = 2$ kHz [$F(9,117) = 2.63$; $p = 0.008$] and 4 kHz [$F(15,195) = 2.77$; $p = 0.001$]. At $f_2 = 2$ kHz inclusion of nonsignificant DPOAEs at the extremes of the f_2/f_1 range explained the significant age $\times f_2/f_1$ interaction. At $f_2 = 4$ kHz the adult functions were somewhat sharper than newborn functions especially after the peak in the function. These differences persisted when subjects having nonsignificant DPOAEs were excluded from the analyses. At mid

f_2/f_1 's newborn and adult DPOAE amplitudes were comparable, at the extremes newborn amplitudes were larger ($p < 0.05$ by t-tests at 1.06, 1.30, 1.32, and 1.34). At $f_2 = 8$ kHz the newborn and adult data did not significantly differ.

Newborn and adult functions for all three experiments tended to peak at lower f_2/f_1 with increasing f_2 . This replicates a result reported in other studies (Lonsbury-Martin *et al.*, 1987; Harris *et al.*, 1989; Brown and Gaskill, 1990a; Whitehead *et al.*, 1992; Stover *et al.*, 1994; Prijs *et al.*, 1994; Lasky *et al.*, 1995; Abdala 1996). There is some controversy concerning this result because Brown and Gaskill (1990b) and Gaskill and Brown (1990) reported little variation in this peak as a function of frequency.

In experiment III DPOAE amplitude and phase reproducibilities were calculated in the same manner as in experiment I. For both age groups reproducibility was best for the f_2/f_1 ratios near peak DPOAE amplitudes. For example, at $f_2 = 4$ kHz the best mean reproducibility for the newborn subjects was 0.42 dB (s.d. = 0.42 dB) at $f_2/f_1 = 1.17$. The corresponding best phase reproducibility was 4.82 degrees (s.d. = 2.51) also at $f_2/f_1 = 1.17$. For adults it was 0.36 dB (s.d. = 0.24 dB) at $f_2/f_1 = 1.21$. The corresponding best phase reproducibility was 1.78 degrees (s.d. = 1.25) at $f_2/f_1 = 1.19$. In contrast, at less optimal ratios the worst newborn reproducibilities averaged a little more than 2 dB, while the worst adult reproducibility averaged a little less than 2 dB. For both ages the worst phase reproducibilities were greater than 20 degrees.

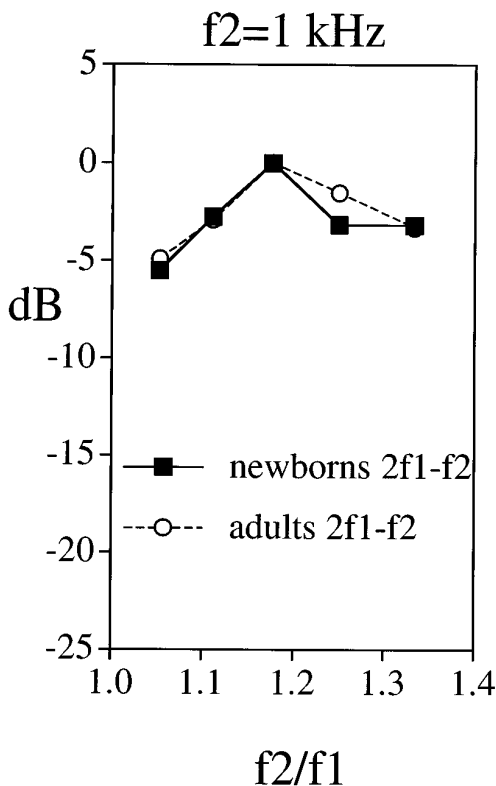


FIG. 7. Mean newborn and adult normalized $2f_1-f_2$ amplitude by f_2/f_1 functions for $f_2=1$ kHz.

Figure 7 presents mean $2f_1-f_2$ DPOAE amplitude $\times f_2/f_1$ functions for $f_2=1$ kHz from experiment IV. Again, the values were normalized by assigning the peak value of each function as the referent sound pressure. The characteristic peak is evident in both the newborn and adult data, and its location did not differ between the two ages. The peak was, however, at a slightly lower f_2/f_1 than expected. The sampling of f_2/f_1 's was sparse (constrained by instrumentation limitations) which may explain, in part, the low f_2/f_1 associated with the peak. The function at this frequency was much less peaked than at higher frequencies in line with previous results from human adults and monkeys (Lasky *et al.*, 1995).

Additional averaging in experiment IV also resulted in more reliable recordings of higher order $(n+1)f_1-nf_2$ DPOAEs. Thus it was possible to further investigate the cochlear filtering hypothesis. At all f_2 frequencies the peak of the $3f_1-2f_2$ function was about a half-octave down from f_2 consistent with that hypothesis. At $f_2=4$ and 8 kHz it was possible to measure $4f_1-3f_2$ and $5f_1-4f_2$ functions as well. Those functions peaked at progressively smaller f_2/f_1 ratios approximately half an octave down from f_2 consistent with the cochlear filtering hypothesis. There were no striking developmental differences with respect to these results.

III. DISCUSSION

The different types of distortion products recorded were similar in newborns and adults implying generally similar displacements of the cochlear partition. The shapes of new-

born and adult I/O functions also seem to be similar (Popelka *et al.*, 1995; Lasky, 1997). Because emission nonlinearities are explained by cochlear dynamics, a conclusion of relatively mature cochlear function in the human newborn seems compatible with the data. It is also compatible with Pujol and Uziel's (1988) conclusion based on anatomical findings.

The different DPOAEs that are recorded is a function of the recording parameters. For example, at low frequencies and high levels (exceeding the ranges presented in this study) the prominence of the f_2-f_1 DPOAE grows. Different nonlinearities are involved at high (over-loading) and low to moderate (essential) primary levels (see Plomp, 1976). The filtering characteristics of outer, middle, and inner ear structures and other factors unrelated to the generation of the DPOAEs also affect the likelihood of recording different DPOAEs. Thus at low frequencies $2f_2-f_1$ was actually more prominent than $2f_1-f_2$ for newborns and adults. This may be explained, in part, by the decrease in the noise floor as DPOAE frequency increases ($2f_2-f_1$ is higher frequency than $2f_1-f_2$).

The prominence of the $2f_2-f_1$ DPOAE at low frequencies may have clinical implications. Recording the $2f_2-f_1$ DPOAE may facilitate low-frequency assessment. Furthermore, it is clear that optimizing stimulus parameters can positively affect the likelihood of recording DPOAEs (optimization varies as a function of frequency, f_2/f_1 , and primary level: Lasky *et al.*, 1995; Whitehead *et al.*, 1995; Abdala, 1996).

The significant differences that were recorded between newborn and adult DPOAEs could generally be described by linear operations (e.g., differences in DPOAE amplitude across frequency). Therefore, structures that respond linearly to sound such as the outer and middle ears may be implicated. Those structures are also known to change significantly over the age range assessed (Saunders *et al.*, 1983; Eby and Nadol, 1986; Kruger and Rubin, 1987; Relkin, 1988; Keefe *et al.*, 1993, 1994; Ikui *et al.*, 1995; Margolis and Trine, 1997).

Outer and middle ear acoustics are largely responsible for the shape of the minimum audibility curve (Dallos, 1973). Similarly, they must also shape DPOAE amplitude \times frequency functions although their forward and reverse contributions are involved. Development of the efferent pathways may also affect emissions. Different structures comprising the peripheral auditory pathway directly affect the DPOAEs recorded. This study cannot differentiate the independent contributions of those structures. However, a consideration of those structures is important in the interpretation of developmental differences in DPOAEs.

Depending on probe placement and the physical dimensions of the ear canal nulls caused by standing waves are present at frequencies above 2–3 kHz in adults (Shaw, 1974; Siegel, 1994; Siegel and Hirohata, 1994). The instrumentation used in this study adjusted the stimulus output after calculating the ear canal frequency response so that the stimulus levels measured by the probe microphone were as specified. For stimulus frequencies whose standing wave nulls were near the probe microphone location, the output of the earphones had to be increased relative to frequencies not

in a null. It was often not possible to present 65 dB SPL stimuli to adults at the higher frequencies. This was less of a problem for newborns whose smaller outer ear canals resulted in probe placements closer to the tympanic membrane (increasing the frequency that nulls were encountered) and greater sound pressure for the same voltage applied to the earphone.

Because the probe was farther from their tympanic membranes, standing waves developed at lower frequencies in adults. At the highest frequencies tested standing waves affected measurements in both newborns and adults although their effects differed because of different newborn and adult canal sizes. Standing waves altered the primary levels at the tympanic membrane, thereby altering the effective L_1-L_2 which has predictable effects on DPOAE amplitude (Gaskill and Brown, 1990; Mills and Rubel, 1994; Lasky *et al.*, 1995; Lasky, 1997; Whitehead *et al.*, 1995; Abdala, 1996). The effect of standing waves on DPOAE amplitude also depends on the distortion product I/O function. At primary levels that function is compressive, the gain in emission amplitude should also be compressed. Standing waves also affected reversely traveling emissions from the cochlea (note that forward transmitting primaries and reversely transmitting distortion products are not the same frequencies). The combined effects of standing waves on forward and reverse transmission are complicated. Nevertheless, standing waves do affect emission amplitudes and do so differentially in newborns and adults.

It was more difficult to record low-frequency DPOAEs from newborns than adults. Newborn ear canal noise levels were higher than adult noise levels at low frequencies. Thus poorer SNRs at low frequencies contributed to the difficulty of recording low-frequency DPOAEs in newborns. Furthermore, the impedance of the newborn outer ear canal is relatively high at low frequencies due to their small canal size and small middle ear cavities. Although the stimuli that were presented were equated for impedance differences at the probe location, reversely traveling low-frequency emissions from the cochlea would be reduced in amplitude in newborns because of their greater canal impedance. On the other hand, smaller newborn tympanic membranes would imply less emission attenuation as a consequence of the differences in areas between the stapes footplate and the tympanic membrane. At least in rats (Rosin *et al.*, 1994) this may not be the case. Despite large changes in the dimensions of the developing rat's outer ear, the ratio between the tympanic membrane and the oval window (stapes footplate) reached mature values early in development. Whether this relationship holds for humans is unknown.

Although the lowest-frequency DPOAEs were harder to reliably record in newborns, reliable low- to mid-frequency (f_2 's < 4 kHz) DPOAE amplitudes were largest for term newborns, next largest for preterm newborns (32–35 weeks post-conception at testing), and smallest for adults. The amplitude differences between newborns and adults were maximal at an f_2 of approximately 3 kHz replicating a result reported by Lasky *et al.* (1992). Above 4 kHz, developmental differences in DPOAE amplitudes were less apparent. Lasky *et al.* (1992), Brown *et al.* (1995), and Abdala (1996)

have reported a similar frequency effect concerning newborn/adult differences in DPOAE amplitudes.

The preterm/term DPOAE amplitude differences in this study replicated Smurzynski's (1994) and Abdala's (1996) results. In contrast, Popelka *et al.* (1995) reported no preterm/term differences at $f_2=2$ kHz. At $f_2=4$ kHz both Popelka *et al.* and this study reported similar amplitude preterm and term DPOAEs.

An explanation for preterm/term differences in DPOAE amplitudes at low frequencies may involve different mechanisms than an explanation for newborn/adult differences at those frequencies. Cochlear and noncochlear factors may be involved in a complex manner in newborn/adult differences. In contrast to newborns and adults, differences between preterm and full term newborn probe frequency response functions were smaller (Fig. 1) suggesting similarities in their outer and middle ear impedances and in the positioning of the probe. Preterm frequency response functions were smaller in amplitude at frequencies below about 5 kHz and larger in amplitude above that frequency. That implies the impedances measured at the probe location were slightly less in the preterm newborn at low frequencies and slightly higher at high frequencies. Because of their smaller canal and middle ear cavities, the opposite results were expected, i.e., higher preterm impedances at low frequencies. At very low frequencies Keefe *et al.* (1993) hypothesized greater absorption of sound by the more compliant canal walls of newborns than adults. The canal walls of preterm newborns may be more compliant than those of the full term newborn accounting for some of the preterm/full term differences at those frequencies. However, the low-frequency effect extended to higher frequencies than reasonably accounted for by compliant canal walls. Impedances of the canal and middle ear are not well understood in the preterm and full term newborn (Margolis and Shanks, 1991).

If outer and middle ear differences do not explain reduced amplitude low-frequency preterm DPOAEs relative to those of the full term newborn, cochlear structures would seem to be implicated. That reasoning is compatible with Pujol and Uziel's (1988) conclusion that the human cochlea is functionally immature before 35 weeks. On the other hand, the distortion products (this study) and I/O functions (Popelka *et al.*, 1995; Lasky, 1997) recorded in preterm and full term newborns and adults are similar suggesting relatively mature cochlear functioning in newborns. Preterm outer and middle ear coupling to the cochlea at low frequencies may be less efficient than in the full term newborn despite comparable (or lower) impedances measured in the outer ear. In effect, more acoustic energy may have been shunted away from the cochlea in preterm newborns. It is also possible that efferent differences may explain some of the preterm/term DPOAE amplitude differences at these frequencies.

Full term newborn and adult $2f_1-f_2$ DPOAE amplitude $\times f_2/f_1$ functions were similar confirming results reported by Abdala (1996). Abdala recorded DPOAE amplitude $\times f_2/f_1$ functions at $f_2=1.5$ and 6 kHz. However, at $f_2=4$ kHz full term newborn DPOAE amplitude $\times f_2/f_1$ functions were broader than those of adults consistent with

Brown *et al.*'s (1995) results. The present study indicates that measurements reflecting the noise level were not likely to explain developmental differences at 4 kHz, one of the alternative explanations proposed by Abdala (1996). It is surprising developmental differences were recorded at 4 kHz and not other frequencies because animal and anatomical research indicates that is the region of the cochlea likely to mature first. If the 4-kHz region also matures first in humans, noncochlear factors may account for the developmental difference in the $f_2=4\text{ kHz } 2f_1-f_2$ DPOAE amplitude $\times f_2/f_1$ function.

The hypothesized filtering of DPOAEs by cochlear structures (Allen, 1990; Brown and Gaskill, 1990b; Stover *et al.*, 1994) probably does not differ greatly in full term newborns and adults. Full term newborn and adult $2f_1-f_2$ DPOAE amplitude $\times f_2/f_1$ function peaks were at approximately the same f_2/f_1 replicating Abdala's (1996) results and extending them to other frequencies. The low f_2/f_1 ratio slopes in newborns and adults were similar. Furthermore, the peaks of $(n+1)f_1-nf_2$ DPOAE amplitude $\times f_2/f_1$ functions ($n>1$) were about one-half octave down from f_2 for both newborns and adults. It should be noted, however, that similar functions in barn owls and alligator lizards (species lacking the structures, tectorial membranes, hypothesized to be responsible for the peripheral filtering) indicate that the specifics of this hypothesis may require modification (Taschenberger *et al.*, 1995). The data from this study cannot contribute to that issue but indicate the effect is found in full term newborn as well as adult humans.

Reproducibility of responses is another measure of maturation. It is often more variable in immature organisms. DPOAE amplitudes and phases were slightly more variable in newborns than adults. Newborn and adult reproducibility to the most favorable stimuli was quite impressive (repeat measurements differed by less than 0.5 dB and 5° at both ages). Reproducibility was best at f_2/f_1 ratios associated with peak DPOAE amplitudes. In part, the decreased reproducibility at other f_2/f_1 's may be attributed to the increasing influence of the noise floor at those f_2/f_1 's (both because of poor SNRs and because some DPOAEs may have really been noise).

It is hard to account for poorer newborn than adult reproducibility at all frequencies by higher newborn noise levels. Above about 4 kHz newborn and adult noise levels were comparable. Furthermore, the SNRs associated with DPOAEs in newborns and adults at $f_2/s>3$ kHz were frequently more than 20 dB. At those SNRs uncorrelated noise would have only a small effect on the DPOAE measurements.

In summary, this study described the effect of varying the primary frequencies on DPOAEs in newborns and adults. This knowledge can better inform future research and clinical applications. DPOAEs can be recorded reliably in newborns. That statement includes both term and preterm newborns as young as 32 weeks conceptional age at the time of testing. The overall similarity between newborn and adult DPOAEs suggests that the cochlea is quite mature in the pre and full term newborn especially at high frequencies. However, differences between newborn and adult DPOAEs do

exist. The considerable postnatal changes in the geometries of the outer and middle ears may explain some of those differences. Combining measurements of outer and middle ear characteristics (e.g., Keefe *et al.*, 1993, 1994) with emission data will greatly improve the interpretation of peripheral auditory function in newborns.

- Abdala, C. (1996). "Distortion product otoacoustic emission ($2f_1-f_2$) amplitude as a function of f_2/f_1 frequency ratio and primary tone level separation in human adults and neonates," *J. Acoust. Soc. Am.* **100**, 3726-3740.
- Abdala, C., Sininger, Y. S., Ekelid, M., and Zeng, F.-G. (1996). "Distortion product otoacoustic emission suppression tuning curves in human adults and neonates," *Hearing Res.* **98**, 1660-1670.
- Adelman, C., Levi, H., Linder, N., and Sohmer, H. (1990). "Neonatal auditory brain-stem response threshold and latency: 1 hours to 5 months," *Electroencephalogr. Clin. Neurophysiol.* **77**, 77-80.
- Allen, J. B. (1990). "Modeling the noise damaged cochlea," in *The Mechanics and Biophysics of Hearing*, Proceedings of a Conference held at the University of Wisconsin, Madison, Wisconsin, 25-29 June 1990, edited by P. Dallos, C. D. Geisler, J. W. Mathews, M. A. Ruggero, and C. R. Steele (Springer-Verlag, New York), pp. 324-332.
- Bench, R. J., and Metz, D. L. (1974). "On the measurement of fetal auditory responses," in *Sound Reception in Mammals*, edited by R. J. Bench *et al.* (Academic, New York), pp. 11-22.
- Birnholtz, J. C., and Benacerraf, B. R. (1983). "The development of human fetal hearing," *Science* **222**, 516-518.
- Bredberg, G. (1968). "Cellular patterns and nerve supply of the human organ of Corti," *Acta Oto-Laryngol. Suppl.* **236**, 1-135.
- Bonfils, P., Avan, P., Francois, M., Trotoux, J., and Narcy, P. (1992). "Distortion-product otoacoustic emissions in neonates: Normative data," *Acta Oto-Laryngol.* **112**, 739-744.
- Brown, A. M., and Gaskill, S. A. (1990a). "Measurement of acoustic distortion reveals underlying similarities between human and rodent mechanical responses," *J. Acoust. Soc. Am.* **88**, 840-849.
- Brown, A. M., and Gaskill, S. A. (1990b). "Can basilar membrane tuning be inferred from distortion measurement?" in *The Mechanics and Biophysics of Hearing*, Proceedings of a Conference held at the University of Wisconsin, Madison, Wisconsin, 25-29 June 1990, edited by P. Dallos, C. D. Geisler, J. W. Mathews, M. A. Ruggero, and C. R. Steele (Springer-Verlag, New York), pp. 164-169.
- Brown, A. M., Sheppard, S. L., and Russell, P. T. (1995). "Differences between neonate and adult cochlear mechanical responses," *Aud. Neurosci.* **1**, 169-181.
- Brownell, W. E. (1990). "Outer hair cell electromotility and otoacoustic emissions," *Ear Hear.* **11**, 82-92.
- Dallos, P. (1973). *The Auditory Periphery* (Academic, New York).
- Eby, T. L., and Nadol, J. B. (1986). "Postnatal growth of the human temporal bone," *Ann. Otol. Rhinol. Laryngol.* **95**, 356-364.
- Gaskill, S. A., and Brown, A. M. (1990). "The behavior of the acoustic distortion product, $2f_1-f_2$, from the human ear and its relation to auditory sensitivity," *J. Acoust. Soc. Am.* **88**, 821-839.
- Hall, J. W. (1992). *Handbook of Auditory Evoked Responses* (Allyn and Bacon, Boston), p. 134.
- Harris, F. P., Lonsbury-Martin, B. L., Stagner, B. B., Coats, A. C., and Martin, G. K. (1989). "Acoustic distortion products in humans: Systematic changes in amplitude as a function of f_2/f_1 ratio," *J. Acoust. Soc. Am.* **85**, 220-229.
- Henley, C. H., Owings, M. H., Stagner, B. B., Martin, G. K., and Lonsbury-Martin, B. L. (1989). "Postnatal development of $2f_1-f_2$ otoacoustic emissions in pigmented rat," *Hearing Res.* **43**, 141-148.
- Ikui A., Sudo I., and Sudo, M. (1995). "Postnatal development of the tympanic cavity: A computer-aided reconstruction and measurement study," *Abstr. Assoc. Res. Otolaryngol.* **18**, 169.
- Keefe, D. H., Bulen, J. C., Campbell, S. L., and Burns, E. M. (1994). "Pressure transfer function and absorption cross section from the diffuse field to the human infant ear canal," *J. Acoust. Soc. Am.* **95**, 355-371.
- Keefe, D. H., Bulen, J. C., Hoberg Arehart, K., and Burns, E. M. (1993). "Ear-canal impedance and reflection coefficient in human infants and adults," *J. Acoust. Soc. Am.* **94**, 2617-2638.
- Kemp, D. T., Ryan, S., and Bray, P. (1990). "A guide to the effective use of otoacoustic emissions," *Ear Hear.* **11**, 93-105.

- Kruger, B., and Rubin, R. J. (1987). "The acoustic properties of the infant ear," *Acta Oto-Laryngol.* **103**, 578–585.
- Lary, S., Briassoulis, G., de Vries, L., Dubowitz, L. M. S., and Dubowitz, V. (1985). "Hearing threshold in preterm and term infants by auditory brainstem response," *J. Pediatr.* **107**, 593–599.
- Lasky, R. E. (1991). "The effects of rate and forward masking on human adult and newborn auditory evoked brainstem response thresholds," *Dev. Psychobiol.* **24**, 51–64.
- Lasky, R. E. (1997). "Distortion product otoacoustic emissions in human newborns and adults: II, Level effects," *J. Acoust. Soc. Am.* **103**, 992–1000.
- Lasky, R. E., Perlman, J., and Hecox, K. (1992). "Distortion product otoacoustic emissions in human newborns and adults," *Ear Hear.* **13**, 430–441.
- Lasky, R. E., Rupert, A., and Waller, M. (1987). "Reproducibility of auditory brainstem evoked responses as a function of the stimulus, scorer, and subject," *Electroencephalogr. Clin. Neurophysiol.* **68**, 45–57.
- Lasky, R. E., Snodgrass, E. B., Maier, M. M., Hecox, K. E., and Laughlin, N. K. (1995). "Distortion product otoacoustic emissions in Macaca mulatta and humans," *Hearing Res.* **89**, 35–51.
- Lenoir, M., and Puel, J.-L. (1987). "Development of otoacoustic emissions in rat," *Hearing Res.* **29**, 265–271.
- Lonsbury-Martin, B. L., Martin, G. K., Probst, R., and Coats, A. C. (1987). "Acoustic distortion products in rabbit ear canal. I. Basic features and physiological vulnerability," *Hearing Res.* **28**, 173–189.
- Lubchenco, L. (1970). "Assessment of gestational age and development at birth," *Pediatr. Clin. North Am.* **17**, 125–145.
- Margolis, R. H., and Shanks, J. E. (1991). "Tympanometry: basic principles and applications," in *Hearing Assessment*, edited by W. F. Rintelmann (Pro-ed, Austin, TX), pp. 179–245.
- Margolis, R. H., and Trine, M. B. (1997). "Influence of middle-ear disease on otoacoustic emissions," in *Otoacoustic Emissions: Clinical Applications*, edited by M. S. Robinette and T. J. Glatke (Thieme, New York), pp. 130–150.
- Mills, D. M., and Rubel, E. W. (1994). "Variation of distortion product otoacoustic emissions with furosemide injection," *Hearing Res.* **77**, 183–199.
- Mills, D. M., and Rubel, E. W. (1996). "Development of the cochlear amplifier," *J. Acoust. Soc. Am.* **100**, 428–441.
- Neely, S., and Liu, Z. (1993). "EMAV: otoacoustic emission averager," Boys Town National Research Hospital Technical Memorandum 17.
- Norton, S. J. (1993). "Application of transient evoked otoacoustic emissions to pediatric populations," *Ear Hear.* **14**, 64–73.
- Norton, S. J., Bargones, J. Y., and Rubel, E. W. (1991). "Development of otoacoustic emissions in gerbil: Evidence for micromechanical changes underlying development of the place code," *Hearing Res.* **51**, 73–92.
- Pisorski, P., Long, G. R., Talmadge, C. L., and Tubis, A. (1995). "Origin of the fine structure of distortion product emissions in the human ear," *Abstr. Assoc. Res. Otolaryngol.* **18**, 476.
- Plomp, R. (1976). *Aspects of Tone Sensation* (Academic, London), pp. 26–40.
- Popelka, G. R., Karzon, R. K., and Arjmand, E. M. (1995). "Growth of the $2f_1-f_2$ distortion product otoacoustic emission for low-level stimuli in human neonates," *Ear Hear.* **16**, 159–165.
- Prijs, V. F., Baalbergen, R., and Schoonhoven, R. (1994). "Simulation of distortion product otoacoustic emissions using an active nonlinear cochlear model," *Abstr. Assoc. Res. Otolaryngol.* **17**, 53.
- Pujol, R., Calier, E., and Lenoir, M. (1980). "Ontogenetic approach to inner and outer hair cell functions," *Hearing Res.* **2**, 423–430.
- Pujol, R., and Uziel, A. (1988). "Auditory development: Peripheral aspects," in *Handbook of Human Growth and Developmental Biology*, Vol. IB, edited by E. Meisami and P. S. Timiras (CRC, Boca Raton, FL), pp. 109–130.
- Relkin, E. M. (1988). "Introduction to the analysis of middle-ear function," in *Physiology of the Ear*, edited by A. F. Jahn and J. Santos-Sacchi (Raven, New York), pp. 103–123.
- Romand, R. (1983). "Development of the cochlea," in *Development of Auditory and Vestibular Systems*, edited by R. Romand and M. R. Romand (Academic, New York), pp. 47–88.
- Rosin, D. F., Zimmer, W. M., and Saunders, J. C. (1994). "Middle-ear structural development in the rat," *Assoc. Res. Otol.* **17**, 119.
- Rubel, E. W. (1984). "Ontogeny of auditory system function," *Annu. Rev. Physiol.* **46**, 213–219.
- Saunders, J. C., Kaltenbach, J. A., and Relkin, E. M. (1983). "The structural and functional development of the outer and middle ear," in *Development of Auditory and Vestibular Systems*, edited by R. Romand and M. R. Romand (Academic, New York), pp. 3–25.
- Schulman-Galambos, C., and Galambos, R. (1975). "Brainstem evoked response audiometry in newborn hearing screening," *Arch. Otolaryngol.* **105**, 86–90.
- Shaw, E. A. G. (1974). "Transformation of sound pressure level from the free field to the eardrum in the horizontal plane," *J. Acoust. Soc. Am.* **56**, 1848–1861.
- Siegel, J. H. (1994). "Ear-canal standing waves and high-frequency sound calibration using otoacoustic emission probes," *J. Acoust. Soc. Am.* **95**, 2589–2597.
- Siegel, J. H., and Hirohata, E. T. (1994). "Ultra-high-frequency distortion product emissions and thresholds in humans," *Abstr. Assoc. Res. Otolaryngol.* **17**, 55.
- Smurzynski, J. (1994). "Longitudinal measurements of distortion-product and click-evoked otoacoustic emissions of preterm infants: Preliminary results," *Ear Hear.* **15**, 210–223.
- Starr, A., Amlie, R. N., Martin, W. H., and Sanders, S. (1977). "Development of auditory brainstem potentials," *Pediatrics* **60**, 831–839.
- Stover, L., Neely, S. T., and Gorga, M. P. (1994). "Explorations of the 'filter' of distortion product otoacoustic emissions," *Abstr. Assoc. Res. Otolaryngol.* **17**, 54.
- Taschenberger, G., Gallo, L., and Manley, G. A. (1995). "Filtering of distortion product otoacoustic emissions in the inner ear of birds and lizards," *Hearing Res.* **91**, 87–92.
- Tierney, T. S., McGee, J., and Walsh, E. J. (1994). "Development of cubic distortion product otoacoustic emissions in the cat," *Abstr. Assoc. Res. Otolaryngol.* **17**, 198.
- van Trees, H. L. (1968). *Detection, Estimation, and Modulation Theory. Part I* (Wiley, New York), p. 92.
- Walsh, E. J., and Romand, R. (1992). "Functional development of the cochlea and the cochlear nerve," in *Development of the Auditory and Vestibular Systems 2*, edited by R. Romand (Elsevier Science, Amsterdam), pp. 161–219.
- Weitzman, E. D., and Graziani, L. J. (1968). "Maturation and topography of the auditory evoked response in premature infants," *Devel. Psychobiol.* **1**, 79–89.
- Whitehead, M. L., Lonsbury-Martin, B. L., and Martin, G. K. (1992). "Evidence for two discrete sources of $2f_1-f_2$ distortion product otoacoustic emission in rabbit: I. Differential dependence on stimulus parameters," *J. Acoust. Soc. Am.* **91**, 1587–1607.
- Whitehead, M. L., Stagner, B. B., McCoy, M. J., Lonsbury-Martin, B. L., and Martin, G. K. (1995). "Dependence of distortion-product otoacoustic emissions on primary levels in normal and impaired ears. II. Asymmetry in L_1, L_2 space," *J. Acoust. Soc. Am.* **97**, 2359–2377.

Distortion product otoacoustic emissions in human newborns and adults. II. Level effects

Robert E. Lasky^{a)}

Neurology Department, The University of Wisconsin, Madison Medical School, H6/528 Clinical Science Building, 600 Highland Avenue, Madison, Wisconsin 53792-5132

(Received 19 July 1996; revised 16 June 1997; accepted 23 October 1997)

This study varied the levels of the primaries and recorded distortion product otoacoustic emissions (DPOAEs) from human newborns and adults. Preterm as well as term newborns were tested. The $2f_1 - f_2$ DPOAE was the most reliably recorded DPOAE, especially at low levels of the primaries. Amplitude and phase reproducibility deteriorated with decreasing level of the primaries. Newborn DPOAEs were slightly less reproducible than adult DPOAEs. The underlying DPOAE I/O functions were nonmonotonic for both newborns and adults. Unity gain characterized the initial increasing portion of those functions in most subjects. Although newborn and adult I/O functions were similar, they did differ. In particular, adult functions tended to be more linear with saturation at higher primary levels. Some of the newborn functions saturated at very low stimulus levels. Although differences in cochlear mechanics may explain developmental difference in DPOAE I/O functions, developmental differences in the resonance characteristics of the outer and middle ears may also be involved. © 1998 Acoustical Society of America. [S0001-4966(98)02702-7]

PACS numbers: 43.64.Jb, 43.64.Ri [BLM]

INTRODUCTION

Tierney *et al.* (1994) described the development of distortion product otoacoustic emissions (DPOAEs) in the cat. Among other results, they reported that (1) DPOAE thresholds decreased with age (reaching adult values first in the $f_2 = 3$ kHz region), (2) DPOAE input/output (I/O) function slopes increased with age, and (3) the level at which saturation of the I/O function occurred increased with age.

These developmental results in experimental animals may not characterize human newborns because of species related differences in maturation of the ear (Pujol and Uziel, 1988; Walsh and Romand, 1992). Indeed, the existing literature suggests considerable maturity in DPOAE I/O functions in human newborns. Popelka *et al.* (1993, 1995) reported similar DPOAE I/O functions in human newborns and adults. In particular, there were no age related differences in the slopes of those functions. Norton and Widen (1990) reported no developmental differences concerning transient evoked otoacoustic emission I/O function slopes. The slopes of newborn auditory brainstem evoked response (ABR) latency-intensity I/O functions are also adultlike [see Hall (1992) for a review]. In contrast, Lasky *et al.* (1992) reported that the slopes of newborn DPOAE I/O functions were more compressive than adult functions.

Whitehead *et al.* (1993, 1995b, footnote 5), Popelka *et al.* (1995), and Nelson and Zhou (1996) have argued that including DPOAE measurements reflecting noise results in shallower I/O function slopes. Therefore, shallower newborn I/O function slopes reported by Lasky *et al.* (1992) and possibly by Tierney *et al.* (1994) may reflect the fact that newborn canal recordings tend to be noisier than adult recordings. Saturation at higher stimulus levels may also explain

steeper I/O function slopes with maturation (i.e., slope estimates increase as saturating portions of the I/O function are less likely to be included). Norton *et al.* (1991) have hypothesized that the cochlear amplifier saturates at higher stimulus levels with maturation. Tierney *et al.*'s (1994) results support Norton *et al.*'s hypothesis.

Comparing newborn and adult DPOAE I/O functions is complicated because of age related differences in the outer and middle ears. The resulting differences in the acoustics of those structures produce different input to the cochlea for identical input to the outer ears of newborns and adults. Therefore, some newborn/adult differences in DPOAE I/O functions may be explained by developmental differences in noncochlear structures.

The present study investigated developmental differences in human DPOAE I/O functions. Most developmental studies of I/O functions have varied the levels of the two primaries simultaneously. In the present study primary levels were varied simultaneously and independently in order to provide a more complete description of developmental differences concerning DPOAE I/O functions.

I. GENERAL METHODS

General descriptions of the subjects, the apparatus and stimuli, and the procedures are presented in a companion article (Lasky, 1997). In both articles the frequency of the primaries are abbreviated by f . The level of the primaries in dB SPL is abbreviated by L . The subscript 1 refers to the lower-frequency primary, and the subscript 2 refers to the higher-frequency primary. Experiment specific methodological details are presented in the introduction to each experiment.

^{a)}Electronic mail: rlasky@facstaff.wisc.edu

II. EXPERIMENTS

A. Experiment I

1. Introduction

Experiment I was conducted to contrast DPOAE I/O functions in human preterm newborns, full term newborns, and adults at select frequencies. I/O functions were recorded at f_2 's = 1, 2, 3, 4, 6, 8, and 10 kHz. The f_2/f_1 ratio was held constant at 1.2 for all stimuli. The levels of the primaries were equal ($L_1 - L_2 = 0$ dB). The first primaries were presented at 65 dB SPL. The primary levels were then decreased in 5-dB steps until the DPOAEs were subthreshold. At each level duplicate responses were recorded.

Avoiding noise contaminated measurements in DPOAE I/O functions is important because they can alter the shapes of those functions (Whitehead *et al.*, 1993, 1995b; Popelka *et al.*, 1995; Nelson and Zhou, 1996). Consequently, only DPOAEs that were significantly greater than the noise floors ($p < 0.05$ by a General Likelihood Ratio test; van Trees, 1968) were included in the analyses.

Fifteen preterm newborns (mean conceptional age at the time of testing = 34.0 weeks, s.d. = 1.0 weeks), 12 full term newborns (mean conceptional age at the time of testing = 39.4 weeks, s.d. = 1.2 weeks), and 8 young adults (mean age at the time of testing = 21.7 years, s.d. = 1.5 years) were the subjects.

2. Results

The data were explored for families of DPOAEs (see Lasky, 1997). As expected $2f_1 - f_2$ was the most robust DPOAE recorded. Five DPOAEs, $f_1 + f_2$, $2f_1 - f_2$, $3f_1 - 2f_2$, $2f_2 - f_1$, and $3f_2 - 2f_1$, were recorded with some regularity and were considered in the following analyses.

The absolute differences in amplitude and phase of the duplicate DPOAE recordings were calculated for all responses. Amplitude and phase reproducibility was best for the $2f_1 - f_2$ DPOAE. The other DPOAEs were recorded so infrequently as to make statements regarding their reproducibility inconclusive. Too few significant newborn $2f_1 - f_2$ DPOAEs were recorded to the $f_2 = 1$ kHz stimulus to make meaningful statements concerning reproducibility at that frequency.

Amplitude and phase reproducibility deteriorated with decreasing level of the primaries. Absolute differences in $2f_1 - f_2$ amplitude were generally less than 2 dB for all stimuli ($f_2 = 2 - 10$ kHz). Absolute amplitude differences decreased with increasing age. Absolute differences in phase were generally less than 20 degrees and also decreased with age. The rate of decline in reproducibility was greatest for adults, however, at all levels newborn reproducibility was poorer than adult reproducibility.

DPOAE amplitude I/O functions were calculated for each subject. I/O functions were calculated only if the data included a minimum of three different levels. Linear functions explained much of the variability in the $2f_1 - f_2$ data (more so for adults than newborns), however, many functions were nonlinear. Linear functions fit by least squares to the data were generally steeper for adults than newborns. The slopes of these linear functions increased with frequency for

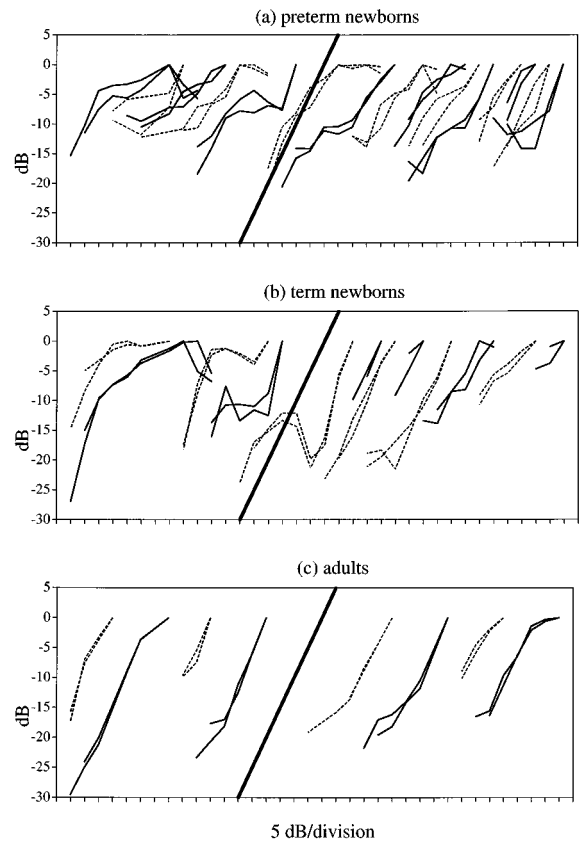


FIG. 1. Individual $2f_1 - f_2$ I/O functions for preterm newborns (a), full term newborns (b), and adults (c) at $f_2 = 4$ kHz ($L_1 = L_2$, $f_2/f_1 = 1.2$). For presentation purposes the DPOAE amplitudes are normalized so that the amplitude of the largest DPOAE for each function is assigned the referent sound pressure level (i.e., 0 dB). Normalized DPOAE amplitudes are specified on the ordinate. Relative primary levels are represented on the abscissa. The levels of the primaries increase 5 dB/division from left to right. Solid and dashed lines have been alternated to characterize adjacent individual I/O functions. Duplicate functions are presented for each subject. The heavy black line bisecting each graph represents the slope of a linear function with a 1 dB/1 dB slope.

newborns and adults. These results replicated those reported by Lasky *et al.* (1992, 1994) and extended them to preterm newborns.

The slope of the best fitting linear regression is only a gross description of the I/O function (Lasky *et al.*, 1995). It indicates a difference among I/O functions at different ages but is not specific, confounding differences in slope and deviations from linearity. Consequently, individual functions are presented graphically for the $f_2 = 4$ kHz amplitude data. Figure 1 presents the preterm, full term, and adult I/O functions. The data at this frequency were selected because they were most complete for all subjects (i.e., significant DPOAEs were recorded to the greatest range of primary levels), thereby permitting the most accurate estimate of the I/O function within the sampled range of primaries. The data for the other frequencies were consistent with the $f_2 = 4$ kHz results.

The individual functions for the same age were plotted on the same graph. Each individual I/O function was arbitrarily displaced on the abscissa for clarity of presentation. Thus the abscissa of Fig. 1 is not a continuum but is interpretable locally for each I/O function represented. Each di-

vision represents a 5-dB step in the level of the primaries. DPOAE amplitudes have been normalized so that the amplitude of the largest DPOAE for each function was assigned the referent sound pressure level (i.e., 0 dB). This was done to eliminate overall level differences in these functions. Solid and dashed lines have been alternated to characterize adjacent individual I/O functions. Duplicate functions are presented to communicate the reproducibility of those functions. The heavy black line bisecting each graph represents a linear function with a 1 dB/1 dB slope.

At all ages portions of most I/O functions could be selected that were approximately linear with a 1 dB/1 dB slope. The data for the other frequencies assessed were similar in this regard. For the range of primary levels presented in this experiment, adult I/O functions were linear with few exceptions. In contrast, a greater portion of the sampled newborn I/O functions were nonlinear, some markedly nonlinear. The prevalence of nonlinear I/O functions seemed to be greater for the preterm newborns than the term newborns.

Other than $2f_1 - f_2$ there were few significant DPOAEs at primary levels less than 60 dB SPL. Therefore, statements concerning the I/O functions of those DPOAEs must be qualified. At low frequencies $2f_2 - f_1$ was actually recorded in more subjects than the $2f_1 - f_2$ DPOAE when primaries were presented at 65 dB SPL (replicating Lasky, 1997). However, at primary levels <65 dB SPL $2f_1 - f_2$ DPOAE was more prevalent even at low frequencies ($f_2 = 1$ and 2 kHz). The slopes of quintic ($3f_1 - 2f_2$ and $3f_2 - 2f_1$) DPOAE I/O functions should be 5 dB/dB if they result from an overloading nonlinearity of the type suggested by von Helmholtz (1954). In none of the subjects with relevant data was there evidence for a growth in these DPOAEs by 5 dB for every dB increment in the primaries.

B. Experiment II

1. Introduction

Both primaries were presented at the same level in experiment I ($L_1 - L_2 = 0$). In experiment II the relative levels of the primaries were varied ($L_1 - L_2 = 0$ dB; $L_1 - L_2 = 10$ dB; $L_1 - L_2 = 15$ dB). Altering $L_1 - L_2$ affects DPOAE I/O functions in predictable ways (Gaskill and Brown, 1990; Mills and Rubel, 1994; Lasky *et al.*, 1995; Whitehead *et al.*, 1995a, b). $L_1 - L_2$'s > zero are frequently used in research and clinical applications because DPOAE amplitudes tend to be largest (at least for primary levels <60–70 dB SPL) at positive $L_1 - L_2$'s. Abdala (1996) has reported that human newborn and adult DPOAE amplitudes are differentially affected by $L_1 - L_2$.

Experiment II extended the results of experiment I to positive $L_1 - L_2$'s. Furthermore, different portions of the DPOAE I/O function (e.g., the linear and saturating portions of that function) suggest different cochlear processes (Lasky *et al.*, 1995; Nelson and Zhou, 1996). Extending the range of primary levels (25–80 dB SPL) and varying their relative levels provided information not evident from experiment I data (e.g., saturation of adult I/O functions).

I/O functions were recorded at f_2 's = 2, 4, and 8 kHz. The f_2/f_1 ratio was held constant at 1.2 for all stimuli. Three

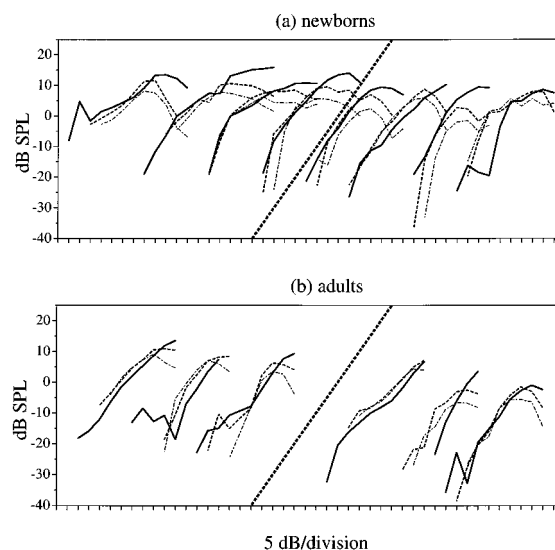


FIG. 2. Individual $2f_1 - f_2$ I/O functions for newborns (a) and adults (b) at $f_2 = 4$ kHz ($f_2/f_1 = 1.2$). Three I/O functions are represented for each subject—the $L_1 - L_2 = 0$ dB I/O function (solid line), the $L_1 - L_2 = 10$ dB I/O function (dashed line), and the $L_1 - L_2 = 15$ dB I/O function (dot/dashed line). Relative primary levels are represented on the abscissa. The levels of the primaries increase 5 dB/division from left to right. The heavy dashed line bisecting each graph represents the slope of a linear function with a 1 dB/1 dB slope.

ascending series defined by 5-dB steps were presented, one for each of the three $L_1 - L_2$'s. L_2 's ranged from 25 through 80 dB SPL for the $L_1 - L_2 = 0$ dB series, 25 through 70 dB SPL for the $L_1 - L_2 = 10$ dB series, and 25 through 65 dB SPL for the $L_1 - L_2 = 15$ dB series. The corresponding L_1 's ranged from 25 through 80 dB SPL for the $L_1 - L_2 = 0$ dB series, 35 through 80 dB SPL for the $L_1 - L_2 = 10$ dB series, and 40 through 80 dB SPL for the $L_1 - L_2 = 15$ dB series. At high primary levels stimuli could not always be presented due to instrumentation limitations.

Eight full term newborns (mean conceptual age at the time of testing = 39.1 weeks, s.d. = 1.5 weeks) and 6 young adults (mean age at the time of testing = 21.8 years, s.d. = 1.7 years) served as subjects.

2. Results

Figure 2 plots the $2f_1 - f_2$ amplitude I/O functions for each newborn and adult for the $f_2 = 4$ kHz data. Again, the data at this frequency were selected because they were most complete for all subjects. Individual functions for subjects of the same age were plotted on the same graph. Each individual's I/O functions were arbitrarily displaced on the abscissa for clarity of presentation. The abscissa is not a continuum but is interpretable locally for each individual's I/O functions represented. Each division represents a 5-dB step in the level of the primaries. The heavy black dashed line bisecting each graph represents a linear function with a 1 dB/1 dB slope. Three I/O functions are presented for each subject, the $L_1 - L_2 = 0$ (solid line), 10 (dashed line), and 15 (dot/dashed line) dB I/O functions. The level of f_1 (i.e., L_1) was the independent variable (abscissa) for each of these three functions. Plotting the data in this manner emphasizes the similarities and differences in these functions more clearly than

the more usual plot of DPOAE amplitude as a function of L_2 . With one exception all of the DPOAEs presented in this figure were significant (i.e., unlikely to be noise, $p < 0.05$). The exception was the DPOAE to the primaries one step less intense than the softest primaries eliciting a significant DPOAE (this did not apply to all subjects because some subjects had significant DPOAEs to the least intense primaries presented). This exception was included to characterize the transition from no DPOAE to a significant DPOAE.

All three I/O functions for newborns and adults could be characterized as approximately linear functions with a 1 dB/1 dB slope that saturated as the presentation level of the primaries increased. After saturating, DPOAE amplitudes often declined with further increases in the primaries. This was more obvious for the $L_1 - L_2 = 10$ and 15 dB I/O functions. Finally, the transition from a nonsignificant response (noise) to a significant response was variable as expected from near noise level responses. However, it often seemed to be very rapid (i.e., often much greater than the 1 dB/dB increment that characterized the remaining portion of the I/O functions prior to saturation).

Between threshold and saturation all three I/O functions had similar amplitude DPOAEs. The three I/O functions differed primarily in the saturating portions of those functions. Saturation was most pronounced for the $L_1 - L_2 = 15$ dB I/O functions, less pronounced for the $L_1 - L_2 = 10$ dB I/O functions, and least pronounced for the $L_1 - L_2 = 0$ dB I/O functions. The onset of saturation occurred at higher primary levels for the $L_1 - L_2 = 0$ dB I/O functions than for the other two functions. The onset of saturation occurred at slightly higher primary levels for the $L_1 - L_2 = 10$ dB than the $L_1 - L_2 = 15$ dB I/O functions.

At the highest levels of L_1 , the greater the L_2 associated with that L_1 the larger amplitude the DPOAE. Specifically, the $L_1 - L_2 = 0$ dB DPOAE was of greater amplitude than the $L_1 - L_2 = 10$ dB DPOAE which was of greater amplitude than the $L_1 - L_2 = 15$ dB DPOAE. These results apparently contrast with the expectation that the largest amplitude DPOAEs are recorded when $L_1 - L_2$ is positive (see Gaskill and Brown, 1990; Lasky *et al.*, 1995; Whitehead *et al.*, 1995a; Abdala, 1996). The discrepancy is only apparent because largest amplitude DPOAEs are associated with positive $L_1 - L_2$'s (up to saturating levels) when comparing stimuli having equal L_2 's (not equal L_1 's as in this figure). Plotting the I/O functions for constant L_1 emphasizes that L_1 determines DPOAE amplitude up to saturation levels regardless of L_2 (within limits) and that saturation depends on both L_2 and $L_1 - L_2$. Plotting these same data for equal L_2 's displaces them along the abscissa (L_2) such that the functions with larger $L_1 - L_2$'s have the largest amplitude DPOAEs for the same L_2 until they saturate. Functions with larger $L_1 - L_2$'s saturate before functions with smaller $L_1 - L_2$'s which is why the largest amplitude DPOAEs are associated with decreasing $L_1 - L_2$'s with increasing L_2 (Gaskill and Brown, 1990; Mills and Rubel, 1994; Lasky *et al.*, 1995; Whitehead *et al.*, 1995a).

The shapes of the newborn and adult I/O functions at $f_2 = 2, 4,$ and 8 kHz were similar, however, there was a frequency effect. The saturation level of the I/O functions in-

creased with increasing frequency. In addition, higher thresholds were recorded at decreasing frequency (reflecting, in part, higher noise levels). (This latter result was more pronounced for newborns possibly because their noise levels were higher than those of adults at low frequencies.) These two results may explain a frequency effect previously reported by a number of researchers (Martin *et al.*, 1988; Harris and Probst, 1990; Lonsbury-Martin *et al.*, 1990; Hauser and Probst, 1991; Lasky *et al.*, 1992, 1994, 1995; Tierney *et al.*, 1994), i.e., more compressive I/O functions with decreasing frequency.

Confirming experiment I results, newborn I/O functions tended to include more nonlinear portions than adult I/O functions. The higher noise levels in newborn canals at low frequencies increased the likelihood of sampling the saturating portion of the I/O function. Furthermore, saturation was more apparent for newborns at all frequencies, in part, because the 75 and 80 dB SPL primaries could be presented to most newborns, whereas, they could be presented to few adults because of instrument output limitations exacerbated by ear canal acoustics. With increasing frequency, saturation of the I/O functions occurred at higher levels and noise level differences between newborns and adults decreased. Thus differences in newborn and adult I/O functions would be expected to decrease with increasing primary frequencies. There is empirical support for this reasoning (this experiment; experiment I; Lasky *et al.*, 1992).

Other DPOAE I/O functions were also examined. The results described in experiment I concerning other DPOAEs were replicated. Differences in $L_1 - L_2$ did not differentially affect the DPOAEs recorded.

C. Experiment III

1. Introduction

Experiment III was conducted to address two issues not addressed by experiments I and II. In experiment III L_2 was held constant ($L_2 = 45, 50, 55, 60,$ or 65 dB SPL for newborns and, in addition to these levels, $L_2 = 40$ dB SPL for the adults), while L_1 was varied from the L_2 level through 65 dB SPL in 5-dB steps. This was done for four different f_2 's (1, 2, 4, and 8 kHz). These functions differ in predictable ways from $L_1 - L_2 = a$ constant I/O functions (Lasky *et al.*, 1995). L_2 I/O functions provided another comparison of newborn and adult cochlear function.

The second issue specifically addressed by experiment III concerned changes in I/O functions as a function of f_2/f_1 . This issue has received little empirical attention. An exception is the comprehensive study by Whitehead *et al.* (1992) in rabbits. Whitehead *et al.* reported similar $L_1 - L_2 = 0$ dB I/O slopes across a range of f_2/f_1 's except at the lowest f_2/f_1 ratio assessed. For small f_2/f_1 's I/O slopes were much steeper than at other ratios. [Humes (1980) addressed the same issue psychophysically. Human adults had similar I/O functions across a range of f_2/f_1 's except at the highest f_2/f_1 's assessed where thresholds were much higher and slopes were steeper. It is possible that Humes was measuring a different nonlinearity (an overloading nonlinearity) at these wide separations of f_1 and f_2 .] Whitehead *et al.*'s

results are difficult to explain by the cochlear mechanics assumed to account for DPOAE I/O functions (Lasky *et al.*, 1995; Whitehead *et al.*, 1995b). Specifically, as the traveling waves of the primaries approach (the f_2/f_1 ratio decreases), two tone suppression increases and the overlap of the traveling waves is more likely to include the compressive nonlinear regions of the traveling wave (near the peak). Both of these factors imply that if anything I/O functions should become more compressive as f_2/f_1 decreases.

Three different f_2/f_1 ratios were examined, 1.1, 1.2, and 1.3. The same I/O functions (described above) were defined at each f_2/f_1 . In addition, for a subset of three adults additional f_2/f_1 's (1.05, 1.15, 1.25, and 1.4) were also assessed in order to address this issue in greater detail. For these three subjects duplicate measurements were made to each stimulus presented. The testing time required for these additional stimuli was excessive for newborn subjects.

Eleven full term newborns (mean conceptional age at the time of testing=39.2 weeks, s.d.=1.2 weeks) and 6 young adults (mean age at the time of testing=22.4 years, s.d.=1.6 years) were tested.

2. Results

With some exceptions as L_1 increased, DPOAE amplitude increased, saturated, and then decreased in amplitude. These results are exemplified by the $f_2=4$ kHz data represented in Fig. 3. Except for overall shifts in amplitude the similarity between the newborn and adult functions is apparent. (Many factors including the resonance characteristics of peripheral structures may explain the overall shifts in amplitude between newborns and adults.) The level at which these I/O functions saturated (and the level of the maximum amplitude DPOAE) increased with increasing f_2/f_1 ratio and level of the primary held constant (L_2). These results extended previously reported results (Lasky *et al.*, 1995) to newborns.

The primary frequencies also affected the saturation level. Figure 4 plots mean $2f_1-f_2$ $L_2=45$ dB SPL amplitude I/O functions for newborns and adults for four different f_2 's at each f_2/f_1 . Only the $L_2=45$ dB SPL results were presented to simplify the figure. The results of the other L_2 functions can be predicted from the $L_2=45$ dB SPL results. Each graph represents the data for one f_2/f_1 . The I/O functions for the four different f_2 's were arbitrarily displaced along the abscissa. The abscissa (L_1) is divided into 5 dB/division steps which are locally interpretable. For presentation purposes the DPOAE amplitudes have been normalized so that the amplitude of the largest DPOAE for each function was assigned the referent sound pressure level (i.e., 0 dB). This normalization equated for level differences such as those resulting from differences in the resonance characteristics of peripheral auditory structures. The saturation level (and the maximum amplitude DPOAE) was recorded at higher levels with increasing f_2 (and also f_2/f_1). These results characterized newborns and adults whose I/O functions were very similar.

The three adult subjects with more extensive data offered an opportunity to describe DPOAE I/O functions as a function of f_2/f_1 in greater detail. These data were similar to

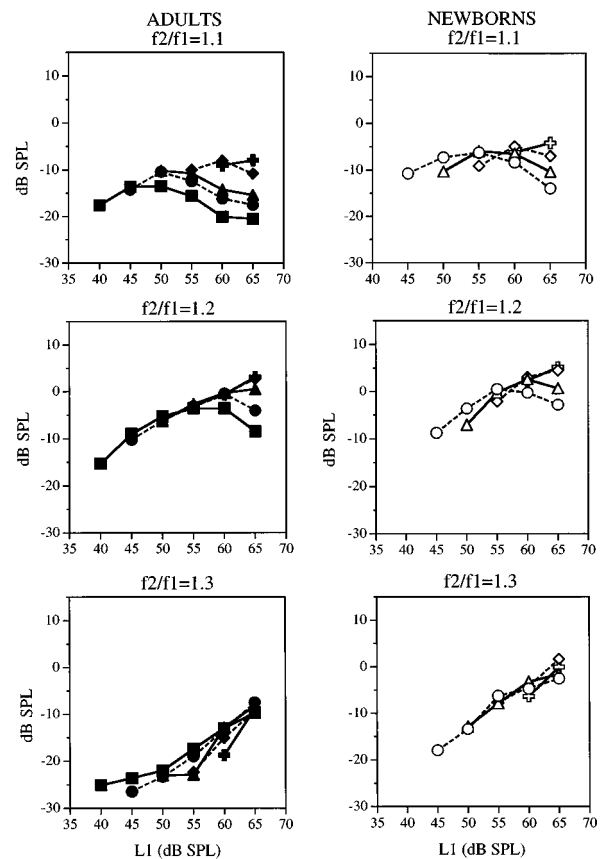


FIG. 3. Mean L_2 I/O functions for full term newborns and adults as a function of f_2/f_1 at $f_2=4$ kHz. The ordinate for these graphs is $2f_1-f_2$ amplitude. The abscissa is L_1 . The parameter is L_2 . $L_2=40$ dB SPL for the I/O functions represented by squares connected by a solid line. $L_2=45$ dB SPL for the I/O functions represented by circles connected by a dashed line. $L_2=50$ dB SPL for the I/O functions represented by triangles connected by a solid line. $L_2=55$ dB SPL for the I/O functions represented by diamonds connected by a dashed line. $L_2=60$ dB SPL for the I/O functions represented by crosses connected by a solid line. Adult symbols are filled; newborn symbols are not filled.

the group data at common f_2/f_1 's. For the same L_2 , $2f_1-f_2$ amplitude $\times f_2/f_1$ functions were calculated for different L_1-L_2 's. As L_1-L_2 increased, these functions peaked at increasingly large f_2/f_1 's. Abdala (1996) has reported the same result in newborns and adults. Figure 5 presents an example of this result for one subject. Smaller amplitude DPOAEs at small f_2/f_1 's (not observed in corresponding psychophysical functions) have been explained by the characteristic resonances of cochlear structures, specifically the tectorial membrane (Allen, 1990; Brown and Gaskill, 1990; Stover *et al.*, 1994; Abdala, 1996). Figure 5 implies that this filtering changes significantly as the relative levels of the primaries were varied. It should be noted that Taschenberger *et al.* (1995) have questioned filtering DPOAEs by the tectorial membrane on other grounds. Specifically, they have reported the hypothesized result of this filtering (reduced DPOAE amplitudes at small f_2/f_1 's) in barn owls and alligator lizards (species lacking tectorial membranes).

III. DISCUSSION

The shapes of the newborn and adult $2f_1-f_2$ DPOAE I/O functions recorded in this study were similar. Unity gain

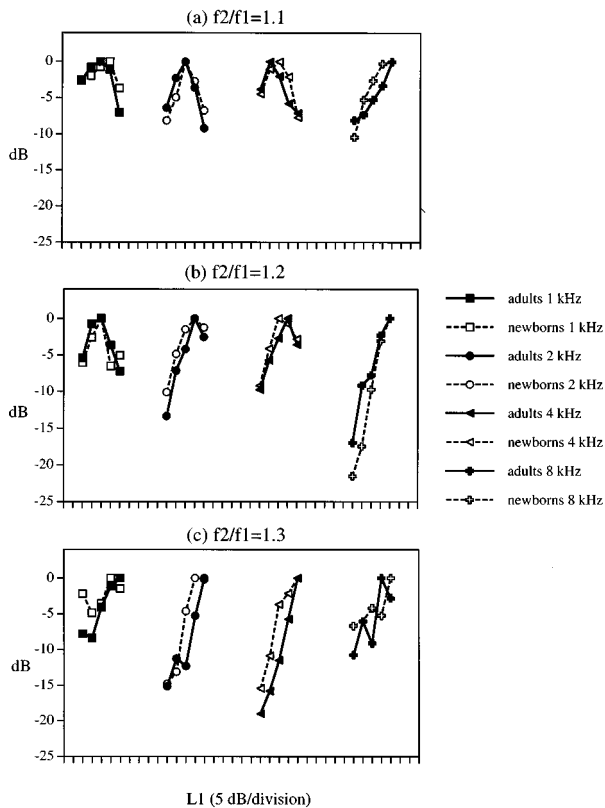


FIG. 4. Mean $L_2=45$ dB I/O functions for full term newborns and adults as a function of f_2 (1, 2, 4, and 8 kHz) and f_2/f_1 [1.1 (a), 1.2 (b), and 1.3 (c)]. The ordinate for these graphs is normalized $2f_1-f_2$ amplitude. Relative L_1 is represented on the abscissa. L_1 increases 5 dB/division from left to right for each function. The parameters are age and f_2 frequency.

(1-dB increase in DPOAE amplitude/1-dB increase in primary level) characterized the initial increasing portion of those functions in most subjects. At the highest stimulus levels presented, those functions saturated and then decreased in amplitude with further increases in primary levels.

At higher primary levels than presented in this study, the $2f_1-f_2$ DPOAE may again increase in amplitude with increasing level of the primaries. Fahey and Allen (1986) have reported I/O functions in the cat that behaved according to a simple overloading polynomial transfer function at very high levels of the primaries. Several other researchers have also reported steeper I/O functions at high primary levels (Brown and Gaskill, 1990; Gaskill and Brown, 1990; Whitehead *et al.*, 1992) although those functions do not seem to be quite as steep as predicted by an overloading polynomial transfer function. I/O functions at high levels seem to be unaffected by loop diuretics that reduce OHC function (Whitehead *et al.*, 1992; Mills and Rubel, 1994,1996). In contrast, I/O functions at low levels are markedly affected by loop diuretics. These data suggest different DPOAE generation processes at low and high input levels (Brown and Gaskill, 1990; Gaskill and Brown, 1990; Norton and Rubel, 1990; Whitehead *et al.*, 1992; Mills and Rubel, 1994,1996). The evidence for different DPOAE generators at low and high stimulus levels is less compelling in primates than nonprimate laboratory animals (Whitehead *et al.*, 1992; see Lonsbury-Martin *et al.*, 1997 for a review and discussion of this issue).

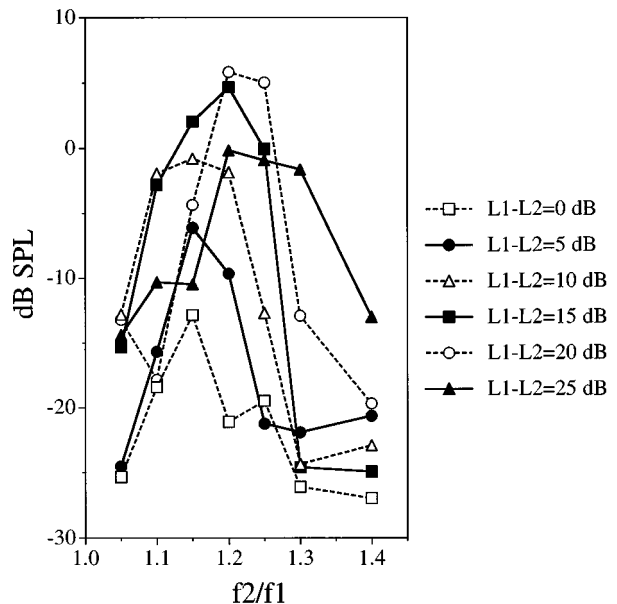


FIG. 5. $2f_1-f_2$ amplitude Xf_2/f_1 functions for one subject at $f_2=4$ kHz. The ordinate is $2f_1-f_2$ amplitude (dB SPL), the abscissa is f_2/f_1 , and the parameter is L_1-L_2 ($L_2=40$ dB SPL).

Although newborn and adult I/O functions were generally similar, the recorded functions did differ. In particular, adult functions tended to be more linear with less evidence of saturation (experiment I) or saturation at higher primary levels (experiment II). Some of the newborn functions saturated at very low stimulus levels. These functions often increased in amplitude after saturating [similar to Nelson and Kimberley's (1992), "diphasic" I/O functions]. These results are consistent with previously reported results for humans (Lasky *et al.*, 1992), i.e., more compressive functions with decreasing age. They are also consistent with more compressive (Tierney *et al.*, 1994) and lower saturating (Tierney *et al.*, 1994; Norton *et al.*, 1991) I/O functions reported in immature experimental animals.

Norton *et al.* (1991) and Tierney *et al.* (1994) have offered physiologic explanations for their animal data, focusing on immaturity of the cochlear amplifier. Other explanations are also plausible. In this study the levels of the primaries presented to newborns and adults were equated at the probe microphone and not at the stapes footplate. Because of developmental differences in peripheral auditory structures, the range of primary levels presented to the cochleae of newborns and adults may have differed in this study. Higher newborn noise levels were also more likely to obscure the contribution of low level DPOAEs to newborn I/O functions. Depending on the stimulus and recording parameters, only the initial linear portion of the I/O function, the saturating portion, the increasing portion after saturation, or some combination of the above may be recorded. In effect, different portions of the I/O function may have been sampled in newborns and adults in this study and other developmental studies reported in the literature.

A comprehensive study contrasting I/O functions developmentally is a rather daunting task. Two-dimensional I/O functions are slices of a multidimensional function mini-

mally characterized by five dimensions (frequency of the source $Xf_2/f_1XL_1XL_2X$ DPOAE amplitude). Even that is a simplification because a complete description would be a nonlinear transfer function which would characterize the output given any input. The input to that function would include the physiologic range of stimuli. The output would include the complete response to the input and not just the response at the frequency of one distortion product. Furthermore, because the peripheral auditory system consists of different structures which contribute in an indeterminate fashion to the recorded responses, a comprehensive description of newborn and adult differences would also include the transfer functions of those structures.

Nevertheless, the conclusion to be drawn from a comparison of a limited sample of human newborn and adult DPOAE I/O functions is that they are quite similar. Furthermore, many of the observed differences can be accounted for by a scaling factor (a linear operation) which may be explained by cochlear maturation and/or by differences in structures (outer ear, middle ear, efferent suppression from the medial olivocochlear bundle) that affect emissions. This study cannot resolve those alternatives.

In the absence of definitive biophysical models, heuristic biophysical explanations have been proposed to account for some distortion product results (Zwicker, 1981; Humes, 1985; Gaskill and Brown, 1990; Norton *et al.*, 1991; Lasky *et al.*, 1995; Whitehead *et al.*, 1995b). Although generally not quantitative [Zwicker (1981) and Humes (1985) are exceptions], these explanations are useful in organizing and interpreting data. They assume that distortion products result from the overlap between the traveling waves to the primaries. Insight into the effects of stimulus parameters on DPOAE amplitudes are gained by translating the acoustic parameters of the stimuli into traveling wave displacements. Such a translation is imperfect at present for a number of reasons including the unspecified effects of the resonance characteristics of the peripheral auditory structures.

The general shape of the DPOAE I/O function described in this study is similar to that of basilar membrane $2f_1-f_2$ distortion product I/O functions (Rhode and Cooper, 1993). The shapes of psychophysical $2f_1-f_2$ distortion product I/O functions are also similar (Plomp, 1976). The similarity in these data adds credence to the hypothesized relationship between DPOAE amplitude and basilar membrane displacement.

Despite the general correspondence of these data, there are differences. The slopes of basilar membrane $2f_1-f_2$ DPOAE I/O functions in rodents and cats at low stimulus levels (Robles *et al.*, 1990; Ruggero *et al.*, 1992; Rhode and Cooper, 1993) are close to unity (1 dB/1 dB). Similar slopes are calculated from human DPOAE I/O function slopes at low levels in this and other studies (Popelka *et al.*, 1993, 1995; Nelson and Zhou, 1996). In contrast, low level DPOAE I/O function slopes for laboratory animals including rodents and cats are generally greater than unity gain (Brown and Gaskill, 1990; Whitehead *et al.*, 1992; Tierney *et al.*, 1994; Mills and Rubel, 1994; Lasky *et al.*, 1995). More specifically, they are between one and two. These data cast some

doubt on a simple correspondence between DPOAE amplitude and basilar membrane displacement.

Another difference concerns the diversity of DPOAE I/O functions as can be appreciated from Figs. 1 and 2 and from the literature (e.g., Nelson and Kimberley, 1992). This diversity does not seem to be present in the more limited basilar membrane and psychophysical data. Other factors than basilar membrane displacement seem to contribute to the diversity of DPOAE I/O shapes (Wiederhold *et al.*, 1986; Brown, 1987; Harris and Probst, 1990; Nelson and Kimberley, 1992; Lasky *et al.*, 1994; Nelson and Zhou, 1996). Harris and Probst (1990) explain the unusual shapes of DPOAE I/O functions they recorded by the fact that "... two tones are interacting not only with each other in both the forward and reverse directions, but also with multiple combination tones generated within the cochlea coincident with two-tone stimulation" (p. 183). Brown and Beveridge (1997) have argued that there may be at least two generators of DPOAEs. As a consequence, even modest level changes in the primaries may cause changes in the phases of the DPOAEs generated that have dramatic consequences on the recorded DPOAE amplitudes. He and Schmiedt (1993) have demonstrated that small differences in frequency and level of the primaries can cause major DPOAE amplitude differences.

Despite limitations, some of the results in this study may be explained by considering displacements of the basilar membrane. Differences among $L_1-L_2=a$ constant, L_1 , and L_2 I/O functions may be a case in point. The $L_1-L_2=0$ dB I/O function peaks at a higher level of the primaries than the corresponding L_2 I/O function peak which in turn is at a higher level than the L_1 I/O function peak (Brown, 1987; Lasky *et al.*, 1995; Whitehead *et al.*, 1995b). When L_1 and L_2 increase simultaneously their interaction increases until the two traveling waves saturate. In contrast, when one of the primaries is held constant (L_1 or L_2 I/O functions) the overlap between the primaries can increase only until the amplitude of the constant primary is exceeded. As Gaskill and Brown (1990) have reasoned, this will occur at higher levels of the varying primary for L_2 than L_1 I/O functions.

Incrementing L_1 while holding L_2 constant should increase DPOAE amplitude as the overlap between L_1 and L_2 increases. As long as the L_1 displacement does not exceed that of L_2 at the location of the $2f_1-f_2$ generator, L_1 and not L_2 should determine the amplitude of the $2f_1-f_2$ distortion product. This was demonstrated in Fig. 2. However, once the L_1 displacement at the location of distortion product generation exceeds that of L_2 , further increasing L_1 cannot increase the overlap with L_2 . The L_2 I/O function should saturate (DPOAEs actually decrease in amplitude with increasing L_1 after saturating). As L_2 is increased, the level of L_1 that can overlap with the high frequency primary at the location of distortion product generation should increase. Thus the L_1 at saturation of the L_2 I/O function should increase with L_2 . In addition, the L_1 at saturation should increase with frequency because f_1 and f_2 are more tuned at higher frequencies, and, therefore, maximum overlap of the two primaries occurs at higher L_1 's. These results have been reported in this study and Lasky *et al.* (1995). Furthermore, because traveling waves flatten as input levels increase (i.e.,

they are less tuned), the L_1-L_2 associated with optimal DPOAE amplitudes should decrease with increasing L_2 . This reasoning also has empirical support (Gaskill and Brown, 1990; Mills and Rubel, 1994; Lasky *et al.*, 1995; Whitehead *et al.*, 1995a).

The present study also provided data concerning the effect of f_2/f_1 on I/O functions consistent with predictions based on traveling wave considerations. As the separation in frequency between the primaries (f_2/f_1) increases, their interaction resulting in distortion products decreases. Thus DPOAE I/O functions should and do saturate at higher primary levels with increasing f_2/f_1 .

This study contrasted the effect of varying the levels of the primaries on human newborn and adult DPOAEs. In addition to addressing important developmental questions concerning peripheral auditory function in newborns, this research has implications for clinical efforts to assess newborn hearing. Otoacoustic emissions are an attractive alternative for those interested in screening hearing in the newborn period. Indeed, an NIH Consensus Statement (1993) recommends otoacoustic emission testing as the first stage of a universal hearing screening program for newborns. Understanding how stimulus and recording parameters affect emission recordings in newborns is critical to that effort.

Abdala, C. (1996). "Distortion product otoacoustic emission ($2f_1-f_2$) amplitude as a function of f_2/f_1 frequency ratio and primary tone level separation in human adults and neonates," *J. Acoust. Soc. Am.* **100**, 3726-3740.

Allen, J. B. (1990). "Modeling the noise damaged cochlea," in *The Mechanics and Biophysics of Hearing*, Proceedings of a Conference held at the University of Wisconsin, Madison, Wisconsin, 25-29 June 1990, edited by P. Dallos, C. D. Geisler, J. W. Mathews, M. A. Ruggero, and C. R. Steele (Springer-Verlag, New York), pp. 324-332.

Brown, A. M. (1987). "Acoustic distortion from rodent ears: A comparison of responses from rats, guinea pigs, and gerbils," *Hearing Res.* **31**, 25-38.

Brown, A. M., and Beveridge, H. A. (1997). "Unravelling acoustic distortion from the human cochlea," *Abstr. Assoc. Res. Otolaryngol.* **20**, 88.

Brown, A. M., and Gaskill, S. A. (1990). "Measurement of acoustic distortion reveals underlying similarities between human and rodent mechanical responses," *J. Acoust. Soc. Am.* **88**, 840-849.

Fahey, P. F., and Allen, J. B. (1986). "Characterization of cubic intermodulation distortion products in the cat external auditory meatus," in *Peripheral Auditory Mechanisms*, edited by J. B. Allen, J. L. Hall, A. Hubbard, S. T. Neely, and A. Tubis (Springer-Verlag, New York), pp. 314-321.

Gaskill, S. A., and Brown, A. M. (1990). "The behavior of the acoustic distortion product, $2f_1-f_2$, from the human ear and its relation to auditory sensitivity," *J. Acoust. Soc. Am.* **88**, 821-839.

Hall, J. W. (1992). *Handbook of Auditory Evoked Responses* (Allyn and Bacon, Boston), pp. 129-134.

Harris, F. P., and Probst, R. (1990). "Growth functions of tone burst evoked and distortion product otoacoustic emissions in humans," in *The Mechanics and Biophysics of Hearing*, Proceedings of a Conference held at the University of Wisconsin, Madison, Wisconsin, 25-29 June 1990, edited by P. Dallos, C. D. Geisler, J. W. Mathews, M. A. Ruggero, and C. R. Steele (Springer-Verlag, New York), pp. 178-185.

Hauser, R., and Probst, R. (1991). "The influence of systematic primary-tone level variation L_2-L_1 on the acoustic distortion product emission $2f_1-f_2$ in normal human ears," *J. Acoust. Soc. Am.* **89**, 280-286.

He, N.-J., and Schmiedt, R. (1993). "Fine structure of the $2f_1-f_2$ acoustic distortion product: Changes with primary level," *J. Acoust. Soc. Am.* **94**, 2659-2669.

Helmholtz, H. von (1954). *On the Sensations of Tone as a Physiological Basis for the Theory of Music* (Dover, New York).

Humes, L. E. (1980). "On the nature of aural nonlinearity," *J. Acoust. Soc. Am.* **67**, 2073-2083.

Humes, L. E. (1985). "An excitation-pattern algorithm for the estimation of ($2f_1-f_2$) and (f_2-f_1) cancellation level and phase," *J. Acoust. Soc. Am.* **78**, 1252-1260.

Lasky, R. E. (1997). "Distortion product otoacoustic emissions in human newborns and adults: I. Frequency effects," *J. Acoust. Soc. Am.* **103**, 981-991.

Lasky, R. E., Perlman, J., and Hecox, K. (1992). "Distortion product otoacoustic emissions in human newborns and adults," *Ear Hear.* **13**, 430-441.

Lasky, R. E., Snodgrass, E., and Hecox, K. E. (1994). "Distortion product otoacoustic emission input/output functions as a function of frequency in human adults," *J. Am. Acad. Audiol.* **5**, 183-194.

Lasky, R. E., Snodgrass, E. B., Maier, M. M., Hecox, K. E., and Laughlin, N. K. (1995). "Distortion product otoacoustic emissions in Macaca mulatta and humans," *Hearing Res.* **89**, 35-51.

Lonsbury-Martin, B. L., Martin, G. K., and Whitehead, M. L. (1997). "Distortion product otoacoustic emissions," in *Otoacoustic Emissions: Clinical Applications*, edited by Robinette and T. J. Glatke (Thieme, New York), pp. 83-109.

Lonsbury-Martin, B. L., Harris, F. P., Stagner, B. B., Hawkins, M. D., and Martin, G. K. (1990). "Distortion-product emissions in humans: I. Basic properties in normally hearing subjects," *Ann. Otol. Rhinol. Laryngol.* **147**, 3-14.

Martin, G. K., Lonsbury-Martin, B. L., Probst, R., and Coats, A. C. (1988). "Spontaneous otoacoustic emissions in a nonhuman primate. I. Basic features and relations to other emissions," *Hearing Res.* **33**, 49-68.

Mills, D. M., and Rubel, E. W. (1994). "Variation of distortion product otoacoustic emissions with furosemide injection," *Hearing Res.* **77**, 183-199.

Mills, D. M., and Rubel, E. W. (1996). "Development of the cochlear amplifier," *J. Acoust. Soc. Am.* **100**, 428-441.

Nelson, D. A., and Kimberley, B. P. (1992). "Distortion product otoacoustic emissions and auditory sensitivity in human ears with normal hearing and cochlear hearing loss," *J. Speech Hear. Res.* **35**, 1142-1159.

Nelson, D. A., and Zhou, J. Z. (1996). "Slopes of distortion-product otoacoustic emission growth curves corrected for noise-floor levels," *J. Acoust. Soc. Am.* **99**, 468-474.

NIH Consensus Statement. (1993). "Early Identification of Hearing Impairment in Infants and Young Children," Vol. 11, Number 1, March 1-3.

Norton, S. J., Bargones, J. Y., and Rubel, E. W. (1991). "Development of otoacoustic emissions in gerbil: Evidence for micromechanical changes underlying development of the place code," *Hearing Res.* **51**, 73-92.

Norton, S. J., and Rubel, E. W. (1990). "Active and passive components in mammalian and avian ears," in *The Mechanics and Biophysics of Hearing*, Proceedings of a Conference held at the University of Wisconsin, Madison, Wisconsin, 25-29 June 1990, edited by P. Dallos, C. D. Geisler, J. W. Mathews, M. A. Ruggero, and C. R. Steele (Springer-Verlag, New York), pp. 219-226.

Norton, S. J., and Widen, J. E. (1990). "Evoked otoacoustic emissions in normal hearing infants and children: Emerging data and issues," *Ear Hear.* **11**, 121-127.

Plomp, R. (1976). *Aspect of Tone Sensation* (Academic, London), pp. 26-40.

Popelka, G. R., Karzon, R. K., and Arjimand, E. M. (1995). "Growth of the $2f_1-f_2$ distortion product otoacoustic emission for low level stimuli in human neonates," *Ear Hear.* **16**, 159-165.

Popelka, G. R., Osterhammel, P. A., Nielsen, L. H., and Rasmussen, A. N. (1993). "Growth of distortion product otoacoustic emissions with primary-tone level in humans," *Hearing Res.* **71**, 12-22.

Pujol, R., and Uziel, A. (1988). "Auditory development: Peripheral aspects," in *Handbook of Human Growth and Developmental Biology*, Vol. IB, edited by E. Meisami and P. S. Timiras (CRC, Boca Raton, FL), pp. 109-130.

Rhode, W. S. (1971). "Observations of the vibration of the basilar membrane in squirrel monkeys using the Mossbauer technique," *J. Acoust. Soc. Am.* **49**, 1218-1231.

Rhode, W. S., and Cooper, N. P. (1993). "Two-tone suppression and distortion production on the basilar membrane in the hook region of cat and guinea pig cochlea," *Hearing Res.* **66**, 31-45.

Robles, L., Ruggero, M. A., and Rich, N. C. (1990). "Two-tone distortion in the basilar membrane of the chinchilla cochlea," in *The Mechanics and Biophysics of Hearing*, Proceedings of a Conference held at the University of Wisconsin, Madison, Wisconsin, 25-29 June 1990, edited by P. Dallos,

- C. D. Geisler, J. W. Mathews, M. A. Ruggero, and C. R. Steele (Springer-Verlag, New York), pp. 304–313.
- Ruggero, M. A., Robles, L., Rich, N. C., and Recio, A. (1992). “Basilar membrane responses to two-tone and broadband stimuli,” *Philos. Trans. R. Soc. London* **336**, 307–315.
- Stover, L., Neely, S. T., and Gorga, M. P. (1994). “Explorations of the ‘filter’ of distortion product otoacoustic emissions,” *Abstr. Assoc. Res. Otolaryngol.* **17**, 54.
- Taschenberger, G., Gallo, L., and Manley, G. A. (1995). “Filtering of distortion product otoacoustic emissions in the inner ear of birds and lizards,” *Hearing Res.* **91**, 87–92.
- Tierney, T. S., McGee, J., and Walsh, E. J. (1994). “Development of cubic distortion product otoacoustic emissions in the cat,” *Abstr. Assoc. Res. Otolaryngol.* **17**, 198.
- van Trees, H. L. (1968). *Detection, Estimation, and Modulation Theory. Part I* (Wiley, New York), p. 92.
- Walsh, E. J., and Romand, R. (1992). “Functional development of the cochlea and the cochlear nerve,” in *Development of the Auditory and Vestibular Systems 2*, edited by R. Romand (Elsevier Science, Amsterdam), pp. 161–219.
- Whitehead, M. L., Lonsbury-Martin, B. L., and Martin, G. K. (1992). “Evidence for two discrete sources of $2f_1-f_2$ distortion product otoacoustic emission in rabbit: I. Differential dependence on stimulus parameters,” *J. Acoust. Soc. Am.* **91**, 1587–1607.
- Whitehead, M. L., Lonsbury-Martin, B. L., and Martin, G. K. (1993). “The influence of noise on the measured amplitudes of distortion-product otoacoustic emissions,” *J. Speech Hear. Res.* **36**, 1097–1102.
- Whitehead, M. L., McCoy, M. J., Lonsbury-Martin, B. L., and Martin, G. K. (1995a). “Dependence of distortion-product otoacoustic emissions on primary levels in normal and impaired ears. I. Effects of decreasing $L2$ below $L1$,” *J. Acoust. Soc. Am.* **97**, 2346–2358.
- Whitehead, M. L., Stagner, B. B., McCoy, M. J., Lonsbury-Martin, B. L., and Martin, G. K. (1995b). “Dependence of distortion-product otoacoustic emissions on primary levels in normal and impaired ears. II. Asymmetry in $L1, L2$ space,” *J. Acoust. Soc. Am.* **97**, 2359–2377.
- Wiederhold, M. L., Mahoney, J. W., and Kellogg, D. L. (1986). “Acoustic overstimulation reduces $2f_1-f_2$ cochlear emissions at all levels in the cat,” in *Peripheral Auditory Mechanisms*, edited by J. B. Allen, J. L. Hall, A. Hubbard, S. T. Neely, and A. Tubis (Springer-Verlag, New York), pp. 322–329.
- Zwicker, E. (1981). “Formulas for calculating the psychoacoustical excitation level of aural difference tones measured by the cancellation method,” *J. Acoust. Soc. Am.* **69**, 1410–1413.

Analysis of the micropipet experiment with the anisotropic outer hair cell wall

Alexander A. Spector

Department of Biomedical Engineering, The Johns Hopkins University, Baltimore, Maryland 21205

William E. Brownell

Bobby R. Alford Department of Otorhinolaryngology and Communicative Sciences, Baylor College of Medicine, Houston, Texas 77030

Aleksander S. Popel

Department of Biomedical Engineering, The Johns Hopkins University, Baltimore, Maryland 21205

(Received 4 April 1997; revised 12 August 1997; accepted 18 October 1997)

The in-plane and bending stiffnesses of the outer hair cell wall are characteristics crucial to the understanding of force and energy transmission between cochlear elements. A mathematical interpretation is given of the micropipet experiment directed at determining the outer hair cell wall stiffness. On the basis of the microstructural observation of the wall showing that it comprises protein networks with different elastic properties, the model of an orthotropic cylindrical shell is used. The boundary-value problem is analyzed corresponding to the stress-strain state of the wall (shell) caused by the action of the micropipet. The solution is given in terms of Fourier series with respect to the circumferential coordinate. An asymptotic analysis of the solution is developed and an approximate formula for the length of the tongue aspirated within the pipet is derived. This leads to an analytical expression for the stiffness parameter measured in the micropipet experiment in terms of Young's moduli and Poisson's ratios of the wall. This expression is an important part of the estimation of the elastic constants of the wall. © 1998 Acoustical Society of America. [S0001-4966(98)03602-9]

PACS numbers: 43.64.Ld, 43.64.Kc, 43.64.Bt [RDF]

INTRODUCTION

The outer hair cell is considered the major candidate for the active component within the cochlea, principally because of the cell's ability to change its length in response to changes of the membrane potential (Brownell, 1990). It may have a strong effect on the force and energy transmission between the vibrating elements of the cochlea and may explain sharp tuning of the basilar membrane. The cell stiffness, a characteristic crucial to this transmission, is important for understanding the role of the outer hair cell in the hearing process. According to results from computer simulation of the *in vivo* dynamics of the organ of Corti (e.g., Bohnke and Arnold, 1996), outer hair cells undergo axial, bending, and torsional modes of loading. Therefore, to determine the wall stiffness, the wall resistance to bending and twisting has to be characterized as well as the resistance to in-plane extension.

Microstructural studies of the outer hair cell wall show that it is a composite in which two major components, the plasma membrane and the subsurface cisternae, have in-plane isotropic properties. The third component, the cortical lattice, comprises two almost perpendicular networks: actin filaments and spectrin crosslinks, which have different elastic properties. The axes of the frame related to the two networks are slightly inclined with respect to the natural cell axes. The average angle of their inclination was estimated as 15° by Holley and Ashmore (1988) and as 9° by Holley *et al.* (1992).

Steele *et al.* (1993) and Tolomeo and Steele (1995) ana-

lyzed the anisotropic properties of the outer hair cell wall. They used the model of an orthotropic elastic membrane and neglected the angle of inclination of the principal axes of orthotropy with respect to the natural cell axes. Combining the data from the experiment with axial loading (Holley and Ashmore, 1988) and the experiment with inflation of the cell (Iwasa and Chadwick, 1992), they demonstrated considerable anisotropy of the wall.

Several experimental techniques have been developed for measuring of the outer hair cell stiffness. Among them are the experiments with axial loading (Holley and Ashmore, 1988; Russell and Schauz, 1995; Hallworth, 1995), with inflation of the cell (Iwasa and Chadwick, 1992), and with the osmotic challenge (Chertoff and Brownell, 1994; Ratnanather *et al.*, 1996). The micropipet experiment is directed at determining the local stiffness of the outer hair cell wall. Previously, the micropipet technique has been effective in the analysis of the mechanical properties of many types of cells including red blood cells (Evans and Skalak, 1980), white blood cells (Needham and Hochmuth, 1990; Waugh, 1991), and endothelial cells (Sato *et al.*, 1987; Theret *et al.*, 1988). For the outer hair cell, interpretation of the micropipet experiment needs a solution of specific problems related to nonaxisymmetry of the wall stress-strain state and to considerable bending around the pipet (Spector *et al.*, 1996a).

In the present paper, we interpret the micropipet experiment by using the model of an orthotropic cylindrical shell. With regard to the analysis of the composite outer hair cell wall (Spector *et al.*, 1996b), the wall is treated here as an

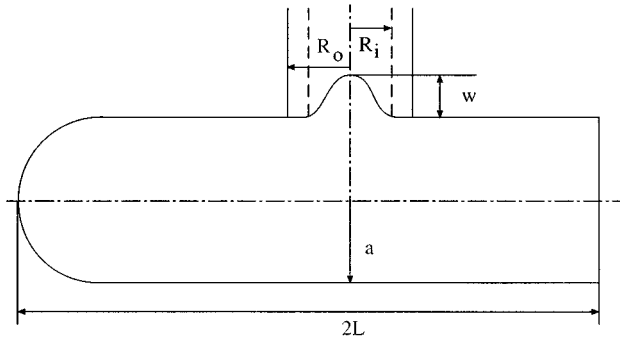


FIG. 1. Schematic sketch of the micropipet experiment.

effective single-layer shell. We assume that the area of the wall located inside the internal contour of the pipet is under the action of a prescribed uniform suction pressure. We also assume that the portion of the wall in contact with the pipet is under the action of a uniform reactive pressure whose magnitude is determined from the force balance of the pipet as a whole.

We use Morley-type equations for the characterization of the orthotropic wall (Lukasiewicz, 1979) and reduce the problem to an eighth-order differential equation in terms of a potential function. It has been shown (Kraus, 1967; Lukasiewicz, 1979) that equations of this type represent an improved version of simplified Donnell's equations and give results close to those of complete higher-order Flügge's equations (Flügge, 1960). Thus, the analysis developed in the present paper is based on a more complete mechanical (orthotropic) model as well as more advanced mathematical description of the stress-strain state of the outer hair cell wall compared to our study (Spector *et al.*, 1996a) where Donnell's equations for an isotropic shell were used. By using Fourier expansion with respect to the circumferential coordinate, we derive a solution of the problem in terms of the eigenfunction of a fourth-order characteristic equation. We develop an asymptotic analysis of leading terms of Fourier series and obtain all characteristics in the closed form. As a result, we derive an analytical formula for the stiffness parameter measured in the experiment. The stiffness parameter is expressed in terms of the elastic constants of the anisotropic wall and the dimensions of the pipet. The derived relationship is used further for the estimation of Young's moduli, Poisson's ratios, and bending stiffnesses of the outer hair cell wall (Spector *et al.*, 1998).

I. MATHEMATICAL FORMULATION AND SOLUTION OF THE PROBLEM

A. Basic equations

We analyze the stress-strain state of the outer hair cell wall caused by the action of the micropipet (Fig. 1). To characterize this state, we use the model of an orthotropic linear elastic cylindrical shell (e.g., Calcote, 1969; Lukasiewicz, 1979; Ambartsumian, 1991). To analyze the orthotropic wall, we use Morley-type equations

(Lukasiewicz, 1979). According to these equations, the problem is reduced to the determination of a potential function $\psi(x, \theta)$ that satisfies the following equation:

$$\left[L_1(D_{ij})L_2(A_{ij}) + \frac{1}{a^2} \frac{\partial^4}{\partial x^4} \right] \psi = p(x, \theta), \quad (1)$$

where $p(x, \theta)$ is the normal pressure acting on the shell surface, and a is the shell radius. Constants A_{ij} ($i, j = 1, 2, 3$) are the elements of the compliance matrix $[\mathbf{A}]$ expressed by the formula

$$[\mathbf{A}] = \frac{1}{h} \begin{bmatrix} E_1^{-1} & -\nu_1 E_1^{-1} & 0 \\ -\nu_1 E_1^{-1} & E_2^{-1} & 0 \\ 0 & 0 & G^{-1} \end{bmatrix}. \quad (2)$$

Here, h is the shell thickness, E_1 and E_2 are Young's moduli for the longitudinal and circumferential directions, respectively, ν_1 is Poisson's ratio corresponding to the extension along the x axis and to the deformation along the θ axis, and G is the independent shear modulus. The second Poisson's ratio is determined by the equation

$$\nu_2 = \nu_1 E_2 E_1^{-1}. \quad (3)$$

The relationship (3) is the necessary and sufficient condition of symmetry of stress-strain relations for a 2-D elastic orthotropic wall (e.g., Kraus, 1967; Ambartsumian, 1991). Constants D_{ij} ($i, j = 1, 2, 3$) are the elements of the bending stiffness matrix $[\mathbf{D}]$ expressed by the following formula:

$$[\mathbf{D}] = \frac{h^3}{12} \begin{bmatrix} E_1(1 - \nu_1 \nu_2)^{-1} & \nu_1 E_2(1 - \nu_1 \nu_2)^{-1} & 0 \\ \nu_1 E_2(1 - \nu_1 \nu_2)^{-1} & E_2(1 - \nu_1 \nu_2)^{-1} & 0 \\ 0 & 0 & G \end{bmatrix}. \quad (4)$$

Similar to the compliance matrix $[\mathbf{A}]$, the bending stiffness matrix $[\mathbf{D}]$ can be expressed in terms of Poisson's ratio ν_1 only, if Poisson's ratio ν_2 is eliminated by using Eq. (3). Operators $L_1(D_{ij})$ and $L_2(A_{ij})$ are determined by the expressions:

$$L_1(D_{ij}) = D_{11} \frac{\partial^4}{\partial x^4} + \frac{2(D_{12} + 2D_{33})}{a^2} \frac{\partial^4}{\partial x^2 \partial \theta^2} + \frac{D_{22}}{a^4} \left(\frac{\partial^4}{\partial \theta^4} + 2 \frac{\partial^2}{\partial \theta^2} + 1 \right) + \frac{2(D_{12} + 2D_{33})}{a^2} \frac{\partial^2}{\partial x^2}, \quad (5)$$

$$L_2(A_{ij}) = A_{22} \frac{\partial^4}{\partial x^4} + \frac{2A_{12} + A_{33}}{a^2} \frac{\partial^4}{\partial x^2 \partial \theta^2} + \frac{A_{11}}{a^4} \frac{\partial^4}{\partial \theta^4}. \quad (6)$$

Membrane forces N_x , N_θ , and $N_{x\theta}$ and normal displacement w are expressed in terms of potential function ψ by the formulas

$$N_x = \frac{1}{a^3} \frac{\partial^4 \psi}{\partial x^2 \partial \theta^2}, \quad N_\theta = \frac{1}{a} \frac{\partial^4 \psi}{\partial x^4}, \quad N_{x\theta} = \frac{1}{a^2} \frac{\partial^4 \psi}{\partial x^3 \partial \theta}, \quad (7)$$

$$w = L_2(A_{ij}) \psi. \quad (8)$$

B. Fourier expansions

Because of symmetry of the pipet, we seek a solution of Eq. (1) in the form

$$\psi = \sum_n \psi_n(x) \cos n\theta. \quad (9)$$

Assuming that the wall is under the action of known suction pressure p_0 inside the internal contour of the pipet and reactive pressure p^* between the internal and external contours of the pipet, we obtain for the Fourier coefficients of pressure p (Spector *et al.*, 1996a)

$$p_n(x) = \frac{1}{\pi n} \begin{cases} p_0 \sin n\phi_1(x) - p^*[\sin n\phi_2(x) - \sin n\phi_1], & 0 \leq x \leq R_i, \\ -p^* \sin n\phi_2(x), & R_i \leq x \leq R_o, \end{cases} \quad (10)$$

$$p^* = \frac{p_0}{\alpha^2 - 1}, \quad \alpha = \frac{R_o}{R_i}, \quad (11)$$

$$\phi_1 = \arcsin \frac{(R_i^2 - x^2)^{0.5}}{a}, \quad (12)$$

$$\phi_2 = \arcsin \frac{(R_o^2 - x^2)^{0.5}}{a}. \quad (13)$$

We seek Fourier coefficients $\psi_n(x)$ of potential function ψ in the following form:

$$\psi_n = \exp \lambda_n x \quad (14)$$

Substituting Eqs. (14) and (9) into Eq. (1), we obtain the following characteristic equation,

$$F_1(\lambda^2)F_2(\lambda^2) + \frac{\lambda^4}{a^2} = 0, \quad (15)$$

where

$$F_1 = D_{11}\lambda^4 - 2(n^2 - 1) \frac{D_{12} + 2D_{33}}{a^2} \lambda^2 + \frac{D_{22}}{a^4} (n^2 - 1)^2, \quad (16)$$

$$F_2 = A_{22}\lambda^4 - n^2 \frac{2A_{12} + A_{33}}{a^2} \lambda^2 + \frac{A_{11}}{a^4} n^4. \quad (17)$$

Equation (15) is an eighth-order equation of a special type. The left-hand side in (15) is a polynomial in terms of λ^2 that has real coefficients. Consequently, the roots of Eq. (15) take the form

$$\lambda_1 = \mu_1 + i\mu_2, \quad \lambda_2 = \mu_3 + i\mu_4, \quad (18)$$

$$\lambda_3 = -\lambda_1, \quad \lambda_4 = \overline{\lambda_1},$$

$$\lambda_5 = -\overline{\lambda_1}, \quad \lambda_6 = -\lambda_2, \quad \lambda_7 = \overline{\lambda_2}, \quad \lambda_8 = -\overline{\lambda_2}. \quad (19)$$

Combining eigenfunctions ψ_n [Eq. (14)] for λ_1 and $\lambda_4 = \overline{\lambda_1}$, we can represent them in the form

$$\psi^* = \exp(\mu_1 x) \sin \mu_2 x, \quad \psi_* = \exp(\mu_1 x) \cos \mu_2 x. \quad (20)$$

The same representation of the eigenfunctions can be obtained for the rest of the pairs of the roots $(\lambda_n, \overline{\lambda_n})$. This analysis is similar to the traditional treatment of the charac-

teristic equations for circular cylindrical shells (e.g., Flugge, 1960; Gol'denveizer, 1961). The range of the outer hair cell length-over-radius ratios is about 4–18 for the *in vivo* conditions. The cells used for the experimental conditions are characterized by ratios in the range 10–15. Based on this, we treat the cell as an infinite cylinder. To guarantee a decay of the solution for high x , we choose half of the roots of Eq. (15) that have the negative real parts. The corresponding eigenfunctions take the form

$$\psi_1 = \exp(-\mu_1 x) \sin \mu_2 x, \quad \psi_2 = \exp(-\mu_1 x) \cos \mu_2 x, \quad (21)$$

$$\psi_3 = \exp(-\mu_3 x) \sin \mu_4 x, \quad \psi_4 = \exp(-\mu_3 x) \cos \mu_4 x, \quad (22)$$

where $\mu_1 > 0$ and $\mu_3 > 0$. Finally, Fourier expansion of potential function ψ takes the form

$$\psi = \sum_n [-C_1 \psi_1(x) + C_2 \psi_2(x) - C_3 \psi_3(x) + C_4 \psi_4(x)] \cos n\theta, \quad (23)$$

where C_i are the coefficients determined by the boundary conditions.

C. Solution of the problem in terms of a Green's function

Following the technique developed for the isotropic case (Spector *et al.*, 1996a), we present a solution of the problem in terms of a Green's function. The solution of the specific problem on the deformation of an infinite cylindrical shell under the action of concentrated normal pressure

$$p(x, \theta) = \delta(x) \cos n\theta \quad (24)$$

plays the role of such a function. Here $\delta(x)$ is the Dirac delta-function. Taking into account the symmetry of the micropipet action on the wall, we reduce the problem of the Green's function determination to the problem for a semi-infinite shell with the following boundary conditions:

$$u^n|_{x=0} = 0, \quad (25)$$

$$N_{x\theta}^n|_{x=0} = 0, \quad (26)$$

$$\frac{\partial w^n}{\partial x}|_{x=0} = 0, \quad (27)$$

$$Q_x^n|_{x=0} = 0. \quad (28)$$

In conditions (25)–(28), u is the longitudinal component of the displacement and Q_x is the x component of the shear force. Let $f_n(x, \theta)$ be a solution of the above formulated boundary-value problem. Using it, we can express the radial displacement in the original problem by the formula

$$w(x, \theta) = 2 \int_0^{R_0} \sum_n f_n(\xi - x, \theta) p_n(\xi) d\xi, \quad (29)$$

where coefficients p_n are given by Eq. (10).

To solve the problem (25)–(28), we express the force and displacement components involved in the boundary conditions (25)–(28) in terms of potential function ψ . For $N_{x\theta}$

and w , such expressions are obtained from Eqs. (7) and (8). For Q_x and u , the corresponding expressions are derived from the following equations (Lukasiewicz, 1979):

$$Q_x = -\frac{\partial}{\partial x} \left[D_{11} \frac{\partial^2 w}{\partial x^2} + \frac{D_{12} + D_{33}}{a^2} \frac{\partial^2 w}{\partial \theta^2} + \frac{D_{12}}{a^2} w \right], \quad (30)$$

$$u = \frac{A_{12}}{a} \frac{\partial^3 \psi}{\partial x^3} + \frac{A_{11}}{a^3} \frac{\partial^3 \psi}{\partial x \partial \theta^2}. \quad (31)$$

Fourier expansions for the displacement and force components take the form

$$Q_x = \sum_n \sum_i C_i^Q \psi_i(x) \cos n\theta, \quad (32)$$

$$u = \sum_n \sum_i C_i^u \psi_i(x) \cos n\theta,$$

$$N_{x\theta} = \sum_n \sum_i C_i^N \psi_i(x) \cos n\theta, \quad (33)$$

$$w = \sum_n \sum_i C_i^w \psi_i(x) \cos n\theta.$$

The expressions for coefficients C_i^Q , C_i^u , C_i^N , and C_i^w in terms of coefficients C_j are determined by Eqs. (30), (31), (7), and (8). These linear expressions can be represented in the following compact form

$$C_i^Q = \sum_j B_{ij}^Q C_j, \quad C_i^u = \sum_j B_{ij}^u C_j \quad (34)$$

$$C_i^N = \sum_j B_{ij}^N C_j, \quad C_i^w = \sum_j B_{ij}^w C_j. \quad (35)$$

Based on Eqs. (34) and (35) and the boundary conditions (25)–(28), we can determine coefficients C_i as

$$\begin{bmatrix} C_1 \\ C_2 \\ C_3 \\ C_4 \end{bmatrix} = [\mathbf{B}] \begin{bmatrix} 0 \\ 0 \\ 0 \\ 0.5 \end{bmatrix} \cos n\theta, \quad (36)$$

where matrix $[\mathbf{B}]$ is expressed by the equation

$$[\mathbf{B}] = \begin{bmatrix} 0 & B_{12}^u & 0 & B_{14}^u \\ 0 & B_{22}^N & 0 & B_{24}^N \\ 0 & \mu_2 B_{31}^w - \mu_1 B_{32}^w & 0 & \mu_4 B_{33}^w - \mu_3 B_{34}^w \\ 0 & B_{42}^Q & 0 & B_{44}^Q \end{bmatrix}^{-1}. \quad (37)$$

Finally, the Green's function for our problem takes the form

$$f_n(\xi - x, \theta) = -C_1^w \psi_1(\xi - x) + C_2^w \psi_2(\xi - x) - C_3^w \psi_3(\xi - x) + C_4^w \psi_4(\xi - x), \quad (38)$$

where coefficients C_i^w are determined by the second equation in formula (35), coefficients C_i are given by Eq. (36), and eigenfunctions ψ_i are given by Eqs. (21) and (22).

II. APPROXIMATE ANALYTICAL SOLUTION

A. Asymptotic analysis of the Fourier coefficients

We obtain now an approximate analytical solution by keeping several leading terms in Fourier expansions and deriving asymptotic formulas for the corresponding coefficients. Our asymptotic approach is similar to one used by Gol'denveizer (1961) in the analysis of isotropic cylindrical shells. We use $\epsilon = h^2/12a^2$ as a small parameter for the asymptotic estimates. Assuming that

$$|-\mu_1 + i\mu_2| \rightarrow \infty \quad \text{when } \epsilon \rightarrow 0 \quad (39)$$

and

$$|-\mu_3 + i\mu_4| \rightarrow 0 \quad \text{when } \epsilon \rightarrow 0, \quad (40)$$

we develop the corresponding asymptotic analysis of Eq. (15) in these two cases. In the case (39), we keep the terms in (15) with the lowest power in terms of λ . In case (40), we keep the terms in (15) with the highest power in terms of λ . Solving the corresponding equations, we obtain the following asymptotic formulas for the eigenvalues of Eq. (15):

$$\mu_1 = \mu_2 = \frac{\sqrt{2} (1 - \nu_1 \nu_2)^{0.25}}{2} \frac{\beta}{\beta^{0.25} \epsilon^{0.25} a} \gg 1, \quad \beta = E_1 E_2^{-1}, \quad (41)$$

$$\mu_3 = \mu_4 = \frac{\sqrt{2} \epsilon^{0.25} n(n^2 - 1)^{0.5}}{2 (1 - \nu_1 \nu_2)^{0.25} \beta^{0.25} a} \ll 1. \quad (42)$$

We give now an asymptotic analysis of the boundary conditions (25)–(28). Keeping the asymptotically leading terms in the expression for $N_{x\theta}$, we obtain the following equation:

$$N_{x\theta}|_{x=0} = 2\mu_1^3(C_2 - C_1) + 2\mu_3^3(C_4 - C_3). \quad (43)$$

Assuming that C_1 and C_2 , C_3 and C_4 are, respectively, the same order of magnitude, we obtain the following estimates:

$$C_1 \sim C_2 \sim C_3 \left(\frac{\mu_3}{\mu_1} \right)^3 \sim C_3 \epsilon^{1.5} \sim C_4 \epsilon^{1.5}. \quad (44)$$

Considering the boundary condition (25) and keeping the asymptotically leading terms in the expression for u , we have

$$u^n|_{x=0} = 2 \frac{A_{12}}{a} \mu_1^3 (C_2 - C_1) - n^2 A_{11} \mu_3 a^3 (C_4 + C_3). \quad (45)$$

Based on estimates (44), we conclude that the second term on the right-hand side of Eq. (45) is much greater than the first term. It leads to the following relationship:

$$C_4 = -C_3. \quad (46)$$

We consider now boundary condition (27). Keeping the leading terms in the expression for w , we obtain

$$\frac{\partial w^n}{\partial x} \Big|_{x=0} = 4\mu_1^5 A_{22} (C_1 + C_2) - \frac{n^4 \mu_3}{a^4} (C_3 + C_4). \quad (47)$$

Because of (44), both terms on the right-hand side of (47) are the same order of magnitude. Taking into account Eq. (46), we obtain

$$C_1 = -C_2. \quad (48)$$

To find asymptotic expressions for coefficients C_i , we consider the boundary condition (28). Taking into account estimates (44), we derive an asymptotic formula

$$Q_x^n|_{x=0} = 16D_{11}\lambda_1^7 A_{22}C_2. \quad (49)$$

From the boundary conditions (28), we obtain

$$C_2 = -C_1 = \frac{\cos n\theta(1-\nu_1\nu_2)}{32a^2\beta\mu_1^7\epsilon}, \quad (50)$$

$$C_4 = -C_3 = \frac{\sqrt{2}\cos n\theta(1-\nu_1\nu_2)^{0.75}\beta^{0.75}a^5}{4n^3(n^2-1)^{0.75}\epsilon^{0.75}}. \quad (51)$$

Taking into account that $C_4 \sim C_3 \gg C_1 \sim C_2$ and keeping the leading terms in the expression for w , we derive the following asymptotic formula for the Green's function:

$$f_n(x, \theta) = \frac{naA_{11}}{(n^2-1)^{1.5}} \frac{\sqrt{2}\cos n\theta(1-\nu_1\nu_2)^{0.75}\beta^{0.75}}{4\epsilon^{0.75}} \times [\psi_3(x) + \psi_4(x)]. \quad (52)$$

Notice that representation (52) is used for several low harmonics in Fourier expansion of displacement w .

B. Analytical formula for the stiffness parameter and its discussion

Substituting Eq. (52) into (29), we obtain

$$w(x, \theta) = \frac{a\sqrt{2}A_{11}}{4} \frac{(1-\nu_1\nu_2)^{0.75}\beta^{0.75}}{\epsilon^{0.75}} \sum_n \frac{n \cos n\theta}{(n^2-1)^{1.5}} \times \int_0^{R_0} \exp[-\mu_3(\xi-x)] [\cos \mu_3(\xi-x) + \sin \mu_3(\xi-x)] p_n(\xi) d\xi. \quad (53)$$

The results of the micropipet experiments are usually formulated in terms of the stiffness parameter (e.g., Sato *et al.*, 1987),

$$K_s = \frac{p_0 R_i^2}{w(0,0)}, \quad (54)$$

which is equal to the ratio of the integral suction force applied via the micropipet over the maximal normal displacement caused by this force. Setting $x=0$ and $\theta=0$ in Eq. (53) and substituting coefficients p_n from Eq. (10), we obtain

$$w(0,0) = \frac{\sqrt{2}ap_0 R_i (1-\nu_1\nu_2)^{0.75}\alpha_1^{0.75}}{\pi E_{11}h\epsilon^{0.75}} \frac{\alpha}{\alpha^2-1} \times \sum_n \frac{1}{(n^2-1)^{1.5}} [\alpha I_n(\alpha_i, \mu_3) - I_n(\alpha_0, \mu_3)], \quad (55)$$

where

$$I_n(\eta, \mu_3) = \int_0^1 \sin(n \arcsin \eta(1-\xi^2)^{0.5}) \times \exp(-\mu_3 \eta a \xi) (\cos \mu_3 \eta a \xi + \sin \mu_3 \eta a \xi) d\xi. \quad (56)$$

Because of the equilibrium conditions for the shell as a whole, the terms with $n=0$ and $n=1$ disappear from the sum in Eq. (55) (e.g., Gol'denveizer, 1961). We keep three leading terms in sum (55) and use an approximation

$$g(\eta, \mu_3) = \sum_{n=2}^4 \frac{1}{(n^2-1)^{1.5}} I_n(A, \mu_3) \approx 0.5A - (0.5 + \mu^2)A^2 + 0.2A^3 = f(\eta, \mu), \quad (57)$$

where

$$\mu = \left[\frac{\epsilon}{(1-\nu_1\nu_2)\alpha_1} \right]^{0.25}. \quad (58)$$

Substituting approximation (57) into Eq. (55), we obtain

$$w(0,0) = \frac{\sqrt{2}ap_0 R_i (1-\nu_1\nu_2)^{0.75}\alpha_1^{0.75}}{\pi E_{11}h\epsilon^{0.75}} \frac{\alpha}{\alpha^2-1} \times [\alpha f(\alpha_i, \mu) - f(\alpha_0, \mu)] \quad (59)$$

and

$$K_s = \frac{\sqrt{2}\pi E_{11}h\epsilon^{0.75} R_i}{2a(1-\nu_1\nu_2)^{0.75}\beta^{0.75}} \frac{(\alpha^2-1)}{\alpha} \frac{1}{\alpha f(\alpha_i, \mu) - f(\alpha_0, \mu)}. \quad (60)$$

All components in Eqs. (59) and (60) for $w(0,0)$ and K_s , except function $g(\eta, \mu_3)$, are exactly reduced to the corresponding expressions for the isotropic case if we set $E_{11}=E_{22}$ and $\nu_1=\nu_2$. Here we use a slightly different approximation of function g than was used for the corresponding function in the analysis of the isotropic case (Spector *et al.*, 1996a). The reason for this difference is related to an improved version of shell theory that we use for the current analysis of the anisotropic case. Independent shear modulus G enters the original governing equations, but the asymptotic estimation shows that its effect on the stiffness parameter is of a higher order of magnitude. This estimation is based on an assumption that shear modulus is the same order of magnitude that Young's moduli. As a result, shear modulus disappears from final expressions (59) and (60).

The developed technique can be routinely extended to the case of a finite-length cylindrical shell with an arbitrary position of the pipet along the wall. In this case, we have to keep all eigenfunctions, including those with the positive real parts, and find the additional constants from the conditions at the edges of the cylinder. The substitution of the experimental data for the stiffness parameter (Sit *et al.*, 1997; Popel *et al.*, 1995) transforms expression (60) into an equation in terms of the elastic constants of the wall. In combination with interpretation of some other experiments, this equation leads to estimates of the elastic characteristics of the outer hair cell wall (Spector *et al.*, 1998).

ACKNOWLEDGMENTS

The work was supported by research grants DC02775 from National Institute of Deafness and Other Communication Disorders and KO1 AG00732 from National Institute of Aging.

- Ambartsumian, S. A. (1991). *Fragments of the Theory of Anisotropic Shells* (World Scientific, New York).
- Bohnke, F., and Arnold, W. (1996). "Displacements and rotations in a cytoarchitectonical model of the organ of Corti," in *Abstracts of the 19th Annual Meeting of the Association for Research in Otolaryngology, St. Petersburg Beach, Florida* (Association for Research in Otolaryngology, Des Moines, IA), p. 103.
- Brownell, W. E. (1990). "Outer hair cell electromotility and otoacoustic emissions," *Ear Hear.* **11**, 82–92.
- Calcote, L. R. (1969). *The Analysis of Laminated Composite Structures* (Van Nostrand Reinhold, New York).
- Chertoff, M. E., and Brownell, W. E. (1994). "Characterization of cochlear outer hair cell turgor," *Am. J. Physiol.* **266**, C467–C479.
- Evans, E. A., and Skalak, R. (1980). *Mechanics and Thermodynamics of Biomembranes* (CRC, Boca Raton).
- Flügge, W. (1960). *Stresses in Shells* (Springer, Berlin).
- Gol'denveizer, A. L. (1961). *Theory of Elastic Thin Shells* (Pergamon, New York).
- Hallworth, R. (1995). "Passive compliance and active force generation in the guinea pig outer hair cell," *J. Neurophysiol.* **74**, 2319–2329.
- Holley, M. C., and Ashmore, J. F. (1988). "A cytoskeletal spring in cochlear outer hair cell," *Nature (London)* **335**, 635–637.
- Holley, M. C., Kalinec, F., and Kachar, B. (1992). "Structure of the cortical cytoskeleton in mammalian outer hair cell," *J. Cell. Sci.* **102**, 569–580.
- Iwasa, K. H., and Chadwick, R. S. (1992). "Elasticity and active force generation of cochlea outer hair cells," *J. Acoust. Soc. Am.* **92**, 3169–3173.
- Kraus, H. (1967). *Thin Elastic Shells* (Wiley, New York).
- Lukasiewicz, S. (1979). *Local Loads in Plates and Shells* (Sijthoff, and Noordhoff, Alphen aan den Rijn, The Netherlands).
- Needham, D., and Hochmuth, R. M. (1990). "Rapid flow of passive neutrophils into a 4 μm pipet and measurements of cytoplasmic viscosity," *ASME J. Biomech. Eng.* **112**, 269–276.
- Popel, A. S., Ratnanather, J. T., Spector, A. A., Sit, P. S., Jerry, R. A., and Brownell, W. E. (1995). "Mechanics of the cochlear outer hair cells," in *Proceedings of the Fourth China-Japan-USA-Singapore Conference on Biomechanics*, edited by G. Yang, K. Hayashi, S. L.-Y. Woo, and J. C. H. Goh (International Academic, Beijing, China), pp. 433–436.
- Ratnanather, J. T., Zhi, M., Brownell, W. E., and Popel, A. S. (1996). "The ratio of elastic moduli of cochlear outer hair cells derived from osmotic experiments," *J. Acoust. Soc. Am.* **99**, 1025–1028.
- Russell, I. J., and Schauz, C. (1995). "Salicylate ototoxicity: effects of the stiffness and electromotility of outer hair cells isolated from the guinea pig cochlea," *Aud. Neurosci.* **1**, 309–320.
- Sato, M., Levesque, M. J., and Nerem, R. M. (1987). "Application of the micropipet technique of the measurement of the mechanical properties of cultured bovine aortic endothelial cells," *ASME J. Biomech. Eng.* **109**, 27–34.
- Sit, S. P., Spector, A. A., Lue, A. J.-C., Popel, A. S., and Brownell, W. E. (1997). "Micropipet aspiration of the outer hair cell lateral wall," *Biophys. J.* **72**, 2812–2819.
- Spector, A. A., Brownell, W. E., and Popel, A. S. (1996a). "A model of cochlea outer hair cell deformations in micropipette experiments: An analytical solution," *Ann. Biomed. Eng.* **24**, 241–249.
- Spector, A. A., Brownell, W. E., and Popel, A. S. (1996b). "A model of elastic properties of cell membranes," in *Contemporary Research in Mechanics and Mathematics of Materials*, edited by R. C. Batra and M. F. Beatty (International Center for Numerical Methods in Engineering, Barcelona, Spain), pp. 55–66.
- Spector, A. A., Brownell, W. E., and Popel, A. S. (1998). "Estimation of elastic moduli and bending stiffnesses of the anisotropic outer hair cell wall," *J. Acoust. Soc. Am.* **103**, 1007–1011.
- Steele, C. R., Baker, G., Tolomeo, J., and Zetes, D. (1993). "Electromechanical models of the outer hair cell sensory systems," in *Biophysics of Hair Cell Sensory Systems*, edited by H. Duifhuis, J. W. Horst, P. van Dijk, and S. M. van Netten (World Scientific, Singapore), pp. 207–214.
- Theret, D. P., Levesque, M. J., Sato, M., Nerem, R. M., and Wheeler, L. T. (1988). "The application of a homogeneous half-space model in the analysis of endothelial cell micropipet measurements," *ASME J. Biomech. Eng.* **110**, 190–199.
- Tolomeo, J. A., and Steele, C. R. (1995). "Orthotropic properties of cochlear outer hair cell wall," *J. Acoust. Soc. Am.* **97**, 3006–3011.
- Waugh, R. E. (1991). "Reticulocyte rigidity and passage through endothelial pores," *Blood* **78**, 3037–3042.

Estimation of elastic moduli and bending stiffness of the anisotropic outer hair cell wall

Alexander A. Spector

Department of Biomedical Engineering, The Johns Hopkins University, Baltimore, Maryland 21205

William E. Brownell

Bobby R. Alford Department of Otorhinolaryngology and Communicative Sciences, Baylor College of Medicine, Houston, Texas 77030

Aleksander S. Popel

Department of Biomedical Engineering, The Johns Hopkins University, Baltimore, Maryland 21205

(Received 4 April 1997; revised 12 August 1997; accepted 18 October 1997)

The outer hair cell makes both passive and active contributions to basilar membrane mechanics. The outer hair cell mechanics is strongly coupled to the elastic properties of the cell lateral wall. The lateral wall experiences both in-plane deformations and bending under physiological and experimental conditions. To characterize the outer hair cell wall, the model of an orthotropic cylindrical shell is used. The elastic constants of the wall are estimated by solving a set of three equations based on the analyses of three independent experiments. The first equation is derived from a new interpretation of the micropipet experiment; the other two are obtained from the axial loading and the osmotic challenge experiments. The two Young's moduli corresponding to the longitudinal and circumferential directions and two Poisson's ratios are estimated. The longitudinal, circumferential, and mixed modes of the bending stiffness are also estimated. The sensitivity of the derived constants to the variation of the cell axial stiffness, which has been measured by several independent groups, is examined. The new estimates are also compared with results obtained by using the assumption of the wall isotropy. © 1998 Acoustical Society of America.

[S0001-4966(98)03702-3]

PACS numbers: 43.64.Ld, 43.64.Kc, 43.64.Bt [RDF]

INTRODUCTION

The cochlear outer hair cell is considered an active element that can add and transmit energy to the vibrating basilar membrane. It has a substantial effect on the amplitude-frequency response of the basilar membrane, and its electromotile properties (Brownell *et al.*, 1985) may explain fine tuning of the mammalian ear. The stiffness of the outer hair cell is a critical characteristic for both the active addition and the passive transmission of energy to the basilar membrane.

A full analysis of outer hair cell mechanics requires consideration of the structural components that make up the cell. The first estimates of the outer hair cell effective stiffness were obtained based on a simplified isotropic single-layer membrane model (Iwasa and Chadwick, 1992). Spector *et al.* (1996a) arrived at a higher but consistent value for the outer hair cell wall stiffness by using an isotropic single-layer shell model and data from the micropipet experiment. Spector *et al.* (1996a) also estimated the effective bending stiffness of the outer hair cell wall and showed that it had a high bending resistance. Steele *et al.* (1993) and Tolomeo and Steele (1995) provided an analysis of the anisotropic properties of the outer hair cell wall. By using the model of a single-layer orthotropic membrane and combining data from the experiment with axial loading and data from the experiment with cell inflation, they showed that the in-plane properties of the wall were considerably anisotropic. Spector *et al.* (1996b) proposed the model of a three-layer anisotropic shell with internal connections between the compo-

nents and used that model for the analysis of the composite structure of the wall.

In the present paper, we use the model of a single-layer orthotropic shell and estimate the in-plane and bending stiffnesses of the cell wall. To find the elastic constants of the wall, we derive three equations based on a combination of the data from three independent experiments. The first equation comes from a new interpretation of the micropipet experiment (Spector *et al.*, 1998). The second equation is a result of an interpretation of the experiment with osmotic pressure change (Ratnanather *et al.*, 1996). The last equation is based on an interpretation of the experiment with axial loading (Holley and Ashmore, 1988).

We give a general solution of these equations where the results of the micropipet and axial loading experiments enter as free parameters. This solution allows us to estimate the elastic moduli for the values of experimental parameters corresponding to the data from several independent research groups. We show that the values of Young's moduli are about 10^{-3} N/m and that the wall is substantially anisotropic. These data are consistent with the results of Steele *et al.* (1993) and Tolomeo and Steele (1995), which were derived by using a different combination of independent experiments. We show that one of the Poisson's ratios is slightly higher than 0.5 and that the second is slightly lower than 2. These values are close to the upper limits of Poisson's ratios in a 2-D orthotropic material. We also estimate

the longitudinal, circumferential, and mixed modes of the bending stiffness and show that they are about 10^{-16} Nm.

I. EQUATIONS FOR THE ELASTIC CONSTANTS

For the determination of the elastic constants characterizing the outer hair cell wall, we use the model of an orthotropic cylindrical shell. Anisotropy of the cell wall is related to the difference between the properties of the filament network and those of the crosslink network. Comprising the cortical lattice, two networks are almost perpendicular to each other and slightly inclined with respect to the natural axes of the cell. The average angle of inclination was estimated as 15° by Holley and Ashmore (1988) and 9° by Holley *et al.* (1992). We neglect this small angle and assume that the principal axes of orthotropy are parallel to the longitudinal and circumferential directions. In this case, the stress-strain relationships are characterized by two Young's moduli, E_1 and E_2 , two Poisson's ratios, ν_1 and ν_2 , and independent shear modulus G (e.g., Lekhnitskii, 1981). Young's moduli, E_1 and E_2 , correspond to the longitudinal and circumferential directions, respectively. Poisson's ratios, ν_1 and ν_2 , correspond to the lateral deformations along the longitudinal and circumferential directions, respectively. Constants E_1 , E_2 , ν_1 , and ν_2 are not independent and are related by the equation

$$\frac{\nu_1}{\nu_2} = \frac{E_1}{E_2}. \quad (1)$$

The longitudinal, circumferential, and mixed modes of the bending stiffness are expressed, respectively, by the following formulas:

$$D_{11} = \frac{E_1 h^3}{12(1 - \nu_1 \nu_2)}, \quad D_{22} = \frac{E_2 h^3}{12(1 - \nu_1 \nu_2)}, \quad (2)$$

$$D_{12} = \frac{\nu_1 E_2 h^3}{12(1 - \nu_1 \nu_2)}, \quad (3)$$

where h is the thickness of the wall.

We now transform the expression for the stiffness parameter measured in the micropipet experiment [Eq. (60), Spector *et al.*, 1998] to an equation in terms of unknown elastic constants. This equation takes the form

$$\begin{aligned} & \frac{(1 - \nu_1 \nu_2)^{0.75} \beta^{0.75}}{E_1 h} [\alpha f(\alpha_i, \mu) - f(\alpha_0, \mu)] \\ &= \frac{\sqrt{2} \pi \epsilon^{0.75} R_i (\alpha^2 - 1)}{2a K_s \alpha}, \end{aligned} \quad (4)$$

where

$$\beta = \frac{E_1}{E_2}, \quad \alpha = \frac{R_0}{R_i}, \quad \alpha_i = \frac{R_i}{a}, \quad \alpha_0 = \frac{R_0}{a}, \quad (5)$$

$$\epsilon = \frac{h^2}{12a^2}, \quad \mu = \left[\frac{\epsilon}{(1 - \nu_1 \nu_2) \beta} \right]^{0.25}, \quad K_s = \frac{p_0 R_i^2}{w(0,0)}. \quad (6)$$

Here, R_o and R_i are, respectively, the outer and inner radii of the pipet, a is the radius of the cell, and K_s is the stiffness parameter determined as a result of the micropipet experi-

ment. In this experiment, the length of the aspirated tongue [radial displacement $w(0,0)$ at the central point under the pipet] is measured. Function $f(A, \mu)$ is determined by the following formula (Spector *et al.*, 1998):

$$f(A, \mu) = 0.5A - (0.5 + \mu^2)A^2 + 0.2A^3. \quad (7)$$

We also use an equation that is based on an interpretation of the experiment with axial loading (Holley and Ashmore, 1988; Russell and Schanz, 1995; Hallworth, 1995; Chan and Ulfendahl, 1996). The straightforward derivation of this equation is based on two equilibrium equations for the cylinder and the preservation condition for the liquid volume inside the cell. The equation is written in terms of the wall in-plane stiffnesses

$$C_{11} = \frac{E_1 h}{1 - \nu_1 \nu_2}, \quad C_{22} = \frac{E_2 h}{1 - \nu_1 \nu_2}, \quad C_{12} = \frac{\nu_1 E_2 h}{1 - \nu_1 \nu_2}, \quad (8)$$

and, neglecting an electrical effect on the mechanical characteristics, it takes the form

$$C_{11} - C_{12} + 0.25C_{22} = \gamma_a. \quad (9)$$

Here

$$\gamma_a = \frac{L}{\pi a} \xi_a; \quad (10)$$

L is one-half of the cell length, a is the radius of the cell, and ξ_a is the measured axial stiffness of the cell as a whole. The axial stiffness of the cell is defined as the ratio of the applied axial force to the corresponding axial displacement of the unfixed end of the cell.

The last equation necessary for the determination of the elastic constants comes from an interpretation of the osmotic pressure change experiment (Ratnanather *et al.*, 1996)

$$1.4C_{11} + C_{22} - 2.7C_{12} = 0. \quad (11)$$

By using Eqs. (9) and (11), we can express β and ν_1 in terms of C_{22} :

$$\beta = 0.25 + 2.08 \frac{\gamma_a}{C_{22}}, \quad (12)$$

$$\nu_1 = 0.5 + 1.08 \frac{\gamma_a}{C_{22}}. \quad (13)$$

Substituting Eqs. (12) and (13) into Eq. (4) and taking into account Eqs. (1) and (8), we obtain the following equation in terms of C_{22} :

$$\begin{aligned} & \frac{0.5 - 0.2(\alpha_0 + \alpha_i)}{F_1(C_{22})} + \left(\frac{\epsilon}{\gamma_a} \right)^{0.5} \frac{1}{F_2(C_{22})} \\ &= \frac{\sqrt{2} \pi \epsilon^{0.75} R_i (\alpha^2 - 1) \gamma_a^{0.25}}{2a K_s \alpha \alpha_0 (\alpha_0 - \alpha_i)}, \end{aligned} \quad (14)$$

where

$$F_1 = C_{22}^{0.75} \left(1 - 1.17 \frac{\gamma_a}{C_{22}} \right)^{0.25}, \quad (15)$$

$$F_2 = C_{22}^{0.25} \left(1 - 1.17 \frac{\gamma_a}{C_{22}} \right)^{1.25}. \quad (16)$$

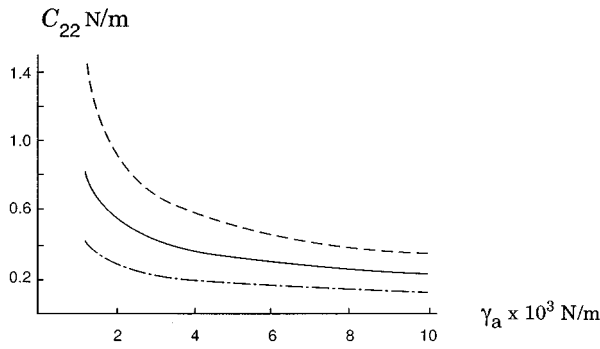


FIG. 1. Circumferential stiffness C_{22} versus cell axial stiffness characteristic γ_a ; --- $K_s=1$, — $K_s=0.75$, and -·- $K_s=0.5$.

Solving Eq. (14) and substituting the results into (12) and (13), we determine C_{22} , $\beta=C_{11}/C_{22}$, and ν_1 . The Young's modulus corresponding to the longitudinal direction is determined by the equation

$$E_1 h = \gamma_a \left(1 - 1.08 \frac{\gamma_a}{C_{22}} \right). \quad (17)$$

The other constants can be calculated from Eqs. (1)–(3) and (8). As a result of the solution of Eq. (14), we obtain the graphs for C_{22} , β^{-1} , and ν_1 versus stiffness characteristic γ_a shown in Figs. 1–3. For each parameter, we give three curves corresponding to three values of stiffness parameter K_s . The intervals

$$10^{-3} \text{ N/m} < \gamma_a < 10^{-2} \text{ N/m} \quad (18)$$

and

$$0.5 \times 10^{-3} \text{ N/m} < K_s < 10^{-3} \text{ N/m} \quad (19)$$

chosen for Figs. 1–3 can be used for the analysis of all available experimental data (see below), as well as for the calculation of the wall moduli that will be based on future experiments.

II. ESTIMATION OF THE STIFFNESS CHARACTERISTICS AND DISCUSSION OF RESULTS

Several independent groups have measured the axial stiffness of the outer hair cell. The data of Holley and Ash-

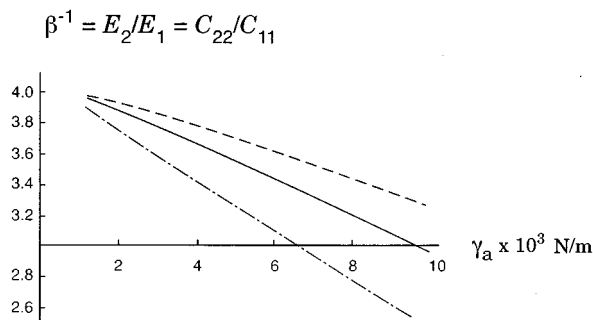


FIG. 2. Ratio of the circumferential Young's modulus over the longitudinal Young's modulus versus cell axial stiffness characteristic γ_a ; --- $K_s=1$, — $K_s=0.75$, and -·- $K_s=0.5$.

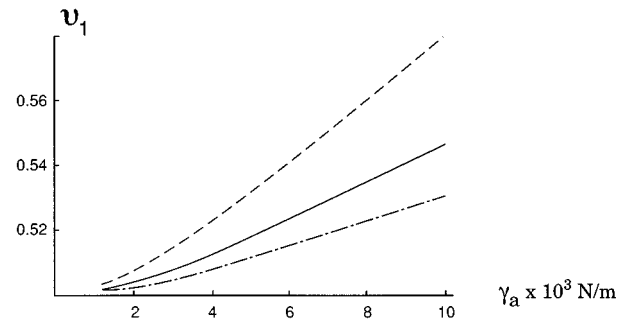


FIG. 3. Poisson's ratio ν_1 versus cell axial stiffness characteristic γ_a ; --- $K_s=1$, — $K_s=0.75$, and -·- $K_s=0.5$.

more (1988), Russell and Schanz (1995), and Chan and Ulfendahl (1996), corresponding to an average 60–65- μm length of the cell, fall inside the range

$$10^{-3} \text{ N/m} \leq \gamma_a \leq 2 \times 10^{-3} \text{ N/m}. \quad (20)$$

The latest data of Hallworth (1997) for cells of the same length give

$$\gamma_a \approx 6.6 \times 10^{-3} \text{ N/m}. \quad (21)$$

We substitute the stiffness parameter along with the dimensions of the pipet (Popel *et al.*, 1995; Sit *et al.*, 1997) and use the axial stiffness value from Holley and Ashmore's (1988) experiment. The corresponding in-plane and bending stiffnesses are given in column 1 of Table I. To characterize the stiffness of the outer hair cell relative to some other types of cell, we compare it with the stiffness of the red blood cell. This cell, structurally somewhat similar to the outer hair cell, has a liquid core that is bounded by a composite membrane including a lipid bilayer and a cytoskeleton. Our results show that the in-plane and bending stiffnesses of the outer hair cell are both about three orders of magnitude greater than those of the red blood cell (Evans and Skalak, 1980). The in-plane stiffness of the outer hair cell wall is four to five orders of magnitude greater than that of neutrophils (Schmid-Schönbein, 1987). On the other hand, the obtained stiffness is about four orders of magnitude lower than that for the Deiter cells (Tolomeo and Holley, 1997). The Deiter cells, located in the cochlea between the outer hair cells and the basilar membrane, transduce the deformations of the outer hair cells into forces affecting vibration of the basilar membrane.

The ratios of Young's moduli in Table I and in Fig. 2 indicate substantial anisotropy of the outer hair cell wall. For the axial stiffness within the range (20), the ratio of the circumferential modulus over the longitudinal modulus is close to 4. For Hallworth's (1997) data, this ratio is about 3.

An interesting feature of the obtained results is related to the values of Poisson's ratios. The basic mathematical analysis valid for any 2-D orthotropic material gives the following upper bounds for Poisson's ratios:

$$\nu_1 \leq \sqrt{\frac{E_1}{E_2}}, \quad \nu_2 \leq \sqrt{\frac{E_2}{E_1}}. \quad (22)$$

TABLE I. The elastic moduli and bending stiffness of the outer hair cell wall.

	Present orthotropic model (cell stiffness data from ^{a)})	Present orthotropic model (cell stiffness data from ^{b)})	Isotropic model ^{c)}	Orthotropic model (interpretation of data from ^{d,e)})	Isotropic model ^{f)}
Young's modulus, E_1h , N/m	1.2×10^{-3}	1.6×10^{-3}	36×10^{-3}	0.98×10^{-3}	25×10^{-3}
Young's modulus, E_2h , N/m	4.8×10^{-3}	6.4×10^{-3}	36×10^{-3}	3.4×10^{-3}	25×10^{-3}
Poisson's ratio, ν_1	0.5016	0.5026	0.9	0.5179	0.82
Poisson's ratio, ν_2	1.979	1.971	0.9	1.81	0.82
Bending stiffness, D_{11} , N×m	1.7×10^{-16}	1.4×10^{-16}	1.6×10^{-16}	0.1×10^{-16}	0.6×10^{-16}
Bending stiffness, D_{12} , N×m	3.4×10^{-16}	2.8×10^{-16}	1.4×10^{-16}	0.2×10^{-16}	0.5×10^{-16}
Bending stiffness, D_{22} , N×m	6.8×10^{-16}	5.6×10^{-16}	1.6×10^{-16}	0.5×10^{-16}	0.6×10^{-16}

^aHolley and Ashmore (1988).
^bRussell and Schauz (1995).
^cSpector *et al.* (1996).
^dSteele *et al.* (1993).
^eTolomeo and Steele (1995).
^fIwasa and Chadwick (1992).

These inequalities are necessary and sufficient for the positiveness of the elastic energy of the material. We can point out that for the material of the outer hair cell wall, Poisson's ratios almost reach their upper limits. It is especially clear from Eqs. (12) and (13) where the ratio γ_a/C_{22} is $10^{-3}-10^{-2}$ if γ_a is within the range (20). This means that one Poisson's ratio has to be slightly greater than 0.5, the second one has to be slightly lower than 2, and the ratio of Young's moduli should be near 4. For the data of column 1 of Table I, the difference between the lower Poisson's ratio and the corresponding upper limit is 0.3%, and it does not exceed 3.5% up to $\gamma_a = 6.6 \times 10^{-3}$ N/m ($K_s = 0.75 \times 10^{-3}$ N/m). To obtain the upper limits for Poisson's ratios, we need to calculate the ratios of Young's moduli on the right-hand side of the inequalities (22). Notice that it has to be done based on the exact expression (12). The Young's moduli in Table I present the values rounded up to two significant digits.

We give a possible explanation of such properties of the obtained values of Poisson's ratios. Our model and the obtained data characterize an effective layer that reflects properties of the major wall components (the subsurface cisternae, the cortical lattice, and the plasma membrane). The elastic parameters of the components have not been determined. However, it is unlikely that Poisson's ratios of the cortical lattice and the subsurface cisternae reach their upper limits. The cortical lattice is a composition of two almost perpendicular networks, and its Poisson's ratio should be small. The subsurface cisternae is a relatively thick (about 30–40 nm) 3-D structure that can be considered isotropic.

This means that its Poisson's ratio is somewhere between 0 and 0.5. The plasma membrane is a 2-D thin (about 5 nm) isotropic layer that is a lipid bilayer with relatively rigid protein inclusions. The limiting value of Poisson's ratio in this case is 1, and it corresponds to an incompressible material. It is known that lipid bilayers have low compressibility (Evans and Skalak, 1980). Thus, the obtained values of the effective Poisson's ratios may be a manifestation of the low compressibility of the outer hair cell plasma membrane.

For comparison with our results, we calculated Young's moduli, Poisson's ratios, and bending stiffnesses based on the values of stiffnesses C_{11} , C_{12} , and C_{22} published by Steele *et al.* (1993) and Tolomeo and Steele (1995). Their data were extracted from a different set of independent experiments [a combination of the axial loading experiment by Holley and Ashmore (1988) and the inflation experiment by Iwasa and Chadwick (1992)]. Notice that we interpreted Holley and Ashmore's (1988) experiment (Eq. 9) slightly differently than did Tolomeo and Steele (1995). The additional terms in Tolomeo and Steele's (1995) version describe strains of the electrical nature that occur during axial loading of the cell. However, these additional terms are very small, and quantitatively the discrepancy between two interpretations is negligible. Comparing the data in columns 1 and 4, we can see that our values of Young's moduli and Poisson's ratios are in a good agreement with the results of Steele *et al.* (1993) and Tolomeo and Steele (1995). The range of our Young's moduli is also consistent with effective Young's modulus extracted by Tolomeo *et al.* (1996) from an experi-

ment with three-point bending. In that analysis, the outer hair cell was treated as a one-dimensional beam.

In column 3, we present the data derived by using the assumption of the wall isotropy. These data were obtained from the combination of the results of the micropipet and the osmotic challenge experiments. Thus in our analysis of the isotropic model, we used two of three experiments on which the current orthotropic model is based. Comparing the data for the present orthotropic model (column 1) with that for the isotropic model (column 3), we can conclude that Young's modulus derived from the assumption of the wall isotropy gives a several-fold overestimate. Another confirmation of this overestimate comes from comparison of Young's moduli in columns 4 and 5. The isotropic model by Iwasa and Chadwick (1992) used the same experimental data with cell inflation as the orthotropic model by Steele *et al.* (1993) and Tolomeo and Steele (1995). The ratio of Young's modulus of the isotropic model of column 5 to the longitudinal (circumferential) Young's modulus of the orthotropic model of column 4 is about the same as the corresponding ratio calculated for the columns 3 and 1. In terms of Poisson's ratios, the value of Poisson's ratio corresponding to the isotropic model is between the values of the two Poisson's ratios for the orthotropic model. This is valid for the data of both column 3 and column 5.

To characterize the sensitivity of the derived moduli with respect to the results of the axial stiffness measurement, in column 2 we present the data obtained from the Russell and Schanz (1995) experiment ($\gamma_a \approx 1.6 \times 10^{-3}$ N/m). The substitution of them for the Holley and Ashmore (1988) data gives about 35% greater and 20% lower, respectively, in-plane and bending stiffnesses. The substitution of the Chan and Ulfendahl (1996) value of the cell axial stiffness ($\gamma_a \approx 1.56 \times 10^{-3}$ N/m) results in the data falling between those in columns 1 and 2, closer to the Russell and Schanz (1995) data. The value of the axial stiffness from the Hallworth (1995, 1997) data results in the longitudinal Young's modulus about 5.5 times greater than that for the data from Holley and Ashmore (1988) and about four times than that for Russell and Schanz (1995). For the circumferential Young's modulus, the differences are about four and three times, respectively. The data in Figs. 1–3 show that all qualitative conclusions regarding properties of the anisotropic outer hair cell wall are valid up to $\gamma_a = 10^{-2}$ N/m.

The obtained elastic constants characterizing the effective passive properties of the outer hair cell wall are also important for the analysis of the active properties of this cell. This is because the molecular motors that are likely responsible for the active cell length changes work against the passive resistance of the surrounding material of the wall. The in-plane and bending moduli are characteristics necessary for developing advanced models of the hearing process where the outer hair cell is a crucial part of the multicomponent cochlear mechanics.

ACKNOWLEDGMENTS

The work was supported by research grants DC02775 from National Institute of Deafness and Other Communica-

tion Disorders and KO1 AG00732 from National Institute of Aging. We would like to thank Dr. Richard Hallworth for providing us with his latest experimental data.

- Brownell, W. E., Bader, C. D., Bertrand, D., and de Ribaupierre, Y. (1985). "Evoked mechanical responses of isolated cochlear outer hair cells," *Science* **224**, 194–196.
- Chan, E., and Ulfendahl, M. (1996). "Compression stiffness of isolated guinea-pig outer hair cell," in *Abstracts of the 19th Annual Meeting of the Association for Research in Otolaryngology*, Des Moines, IA, p. 62.
- Evans, E. A., and Skalak, R. (1980). *Mechanics and Thermodynamics of Biomembranes* (CRC, Boca Raton).
- Hallworth, R. (1995). "Passive compliance and active force generation in the guinea pig outer hair cell," *J. Neurophysiol.* **74**, 2319–2329.
- Hallworth, R. (1997). "Modulation of OHC force generation and stiffness by agents known to affect hearing," *Diversity in Auditory Mechanics*, edited by E. R. Lewis, G. R. Long, R. F. Lyon, P. M. Narins, C. R. Steele, and E. Hecht-Poinar (World Scientific, Singapore), pp. 524–530.
- Holley, M. C., and Ashmore, J. F. (1988). "A cytoskeletal spring in cochlear outer hair cell," *Nature (London)* **335**, 635–637.
- Holley, M. C., Kalinec, F., and Kachar, B. (1992). "Structure of the cortical cytoskeleton in mammalian outer hair cell," *J. Cell. Sci.* **102**, 569–580.
- Iwasa, K. H., and Chadwick, R. S. (1992). "Elasticity and active force generation of cochlea outer hair cells," *J. Acoust. Soc. Am.* **92**, 3169–3173.
- Lekhnitskii, S. G. (1981). *Theory of Elasticity of an Anisotropic Body* (Mir Publishers, Moscow, Russia).
- Popel, A. S., Ratnanather, J. T., Spector, A. A., Sit, P. S., Jerry, R. A., and Brownell, W. E. (1995). "Mechanics of the cochlear outer hair cells," in *Proceedings of the Fourth China-Japan-USA-Singapore Conference on Biomechanics*, edited by G. Yang, K. Hayashi, S. L.-Y. Woo, and J. C. H. Goh (Beijing International Academic Publishing, China), pp. 433–436.
- Ratnanather, J. T., Zhi, M., Brownell, W. E., and Popel, A. S. (1996). "The ratio of elastic moduli of cochlear outer hair cells derived from osmotic experiments," *J. Acoust. Soc. Am.* **99**, 1025–1028.
- Russell, I. J., and Schanz, C. (1995). "Salicylate ototoxicity: effects of the stiffness and electromotility of outer hair cells isolated from the guinea pig cochlea," *Aud. Neurosci.* **1**, 309–320.
- Schmid-Schönbein, G. W. (1987). "Rheology of leukocytes," in *Handbook of Bioengineering* (McGraw-Hill, New York), pp. 13.1–13.25.
- Sit, P. S., Spector, A. A., Lue, A. J.-C., Popel, A. S., and Brownell, W. E. (1997). "Micropipet aspiration of the outer hair cell lateral wall," *Biophys. J.* **72**, 2812–2819.
- Spector, A. A., Brownell, W. E., and Popel, A. S. (1996a). "A model of cochlea outer hair cell deformations in micropipette experiments: an analytical solution," *Ann. Biomed. Eng.* **24**, 241–249.
- Spector, A. A., Brownell, W. E., and Popel, A. S. (1996b). "A model of elastic properties of cell membranes," in *Contemporary Research in Mechanics and Mathematics of Materials*, edited by R. C. Batra and M. F. Beatty (International Center for Numerical Methods in Engineering, Barcelona, Spain), pp. 55–66.
- Spector, A. A., Brownell, W. E., and Popel, A. S. (1998). "Analysis of the micropipet experiment with the anisotropic outer hair cell wall," *J. Acoust. Soc. Am.* **103**, 1001–1006.
- Steele, C. R., Baker, G., Tolomeo, J., and Zetes, D. (1993). "Electromechanical models of the outer hair cell sensory systems," in *Biophysics of Hair Cell Sensory Systems*, edited by H. Duifhuis, J. W. Horst, P. van Dijk, and S. M. van Netten (World Scientific, Singapore), pp. 207–214.
- Tolomeo, J. A., and Steele, C. R. (1995). "Orthotropic properties of cochlear outer hair cell wall," *J. Acoust. Soc. Am.* **97**, 3006–3011.
- Tolomeo, J. A., Steele, C. R., and Holley, M. C. (1996). "Mechanical properties of the lateral cortex of mammalian auditory outer hair cells," *Biophys. J.* **71**, 421–429.
- Tolomeo, J. A., and Holley, M. C. (1997). "The function of the cytoskeleton in determining the mechanical properties of epithelial cells within the organ of Corti," in *Diversity in Auditory Mechanics*, edited by E. R. Lewis, G. R. Long, R. F. Lyon, P. M. Narins, C. R. Steele, and E. Hecht-Poinar (World Scientific, Singapore), pp. 556–562.

Masking by sinusoidally amplitude-modulated tonal maskers^{a)}

Melanie J. Gregan, Sid P. Bacon,^{b)} and Jungmee Lee

Psychoacoustics Laboratory, Department of Speech and Hearing Science, P.O. Box 871908, Arizona State University, Tempe, Arizona 85287-1908

(Received 6 June 1997; accepted for publication 6 November 1997)

In experiment 1, masking patterns were obtained with a tonal masker that was sinusoidally amplitude modulated (SAM) at a rate of 8 Hz and a depth (m) of 1.0. The signal was centered at a masker peak or masker valley. Masker frequency (f_m) was 750, 1350, or 2430 Hz, and signal frequency (f_s) ranged from 0.8 to $1.62 f_m$. Thresholds were generally higher for a signal in a masker peak than in a masker valley. The magnitude of this peak-to-valley (PV) difference was governed by f_s/f_m , rather than by f_s , and was largest for $f_s > f_m$. The PV differences were smallest at the lowest f_m , at least when $f_s > f_m$. In experiment 2, growth-of-masking functions were measured ($f_m = 1350$ Hz, $f_s = 1.44 f_m$). The masker was modulated at a depth (m) of 1.0, 0.75, or 0.50. These thresholds were compared with those obtained with an unmodulated masker in forward or simultaneous masking. The comparisons suggest that thresholds for a signal at a peak of an 8-Hz SAM masker are due to simultaneous masking, while those in a valley are due primarily to forward masking when $m = 1.0$ or simultaneous masking when $m = 0.75$ or 0.50. For these masker depths, the PV difference first increased but then decreased as masker level increased from 60 to 90 dB SPL. This was a consequence of the slope of the masking function for peak placement changing from a value greater than 2.0 to a value of 1.0 at the highest signal levels (an effect that was also observed with the unmodulated simultaneous masker), a result that may be understood in terms of basilar membrane nonlinearity. © 1998 Acoustical Society of America. [S0001-4966(98)05202-3]

PACS numbers: 43.66.Ba, 43.66.Dc, 43.66.Mk [JWH]

INTRODUCTION

Maskers with slowly fluctuating envelopes may produce less masking than those with relatively flat envelopes (Egan and Hake, 1950; Fastl, 1975; Buus, 1985; Mott and Feth, 1986; Moore and Glasberg, 1987; van der Heijden and Kohlrausch, 1995; Nelson and Schroder, 1996). This masking release has been attributed to the ability of subjects to utilize periods of low masker energy (or to “listen in the valleys”) to improve signal detection (Fastl, 1975; Buus, 1985; Mott and Feth, 1986; Moore and Glasberg, 1987). A related explanation was proposed by Buus (1985), who suggested the release may be due to enhanced signal detection as a result of comodulation masking release (CMR). Threshold improvement due to CMR is contingent upon the presence of masker energy within auditory filters centered away from that of the signal. If the masker energy is slowly varying in amplitude, and if the variations are coherent across all involved auditory filters, it is thought that the auditory system makes use of across-channel comparisons of the temporal envelope of the stimulus to aid in signal detection. Both of these hypotheses, “listening in the valleys” and CMR, require adequate temporal resolution that will yield an internal representation of the fluctuating masker envelope that is reasonably faithful to that of the external stimulus.

The auditory processing underlying the masking release also presumably underlies the difference in masking that is

observed when comparing the thresholds for a brief signal placed during a peak versus a valley of a fluctuating masker (Zwicker and Schütte, 1973; Zwicker, 1976a, b, c; Nelson and Swain, 1996). These two thresholds, comprising the peak-to-valley (PV) difference, represent two points on a so-called masking period pattern (Zwicker, 1976a, b, c).

The results published thus far have consistently shown that there is a sizeable temporal effect (masking release or PV difference) when the signal frequency (f_s) is higher than the masker frequency (f_m), but that there is little or no temporal effect when f_s is lower than f_m (Egan and Hake, 1950; Zwicker, 1976c; Buus, 1985; Mott and Feth, 1986; Moore and Glasberg, 1987; Glasberg and Moore, 1994; van der Heijden and Kohlrausch, 1995; Nelson and Schroder, 1996; Nelson and Swain, 1996). Mott and Feth (1986) suggested that the reduced temporal effect for the conditions where f_s is lower than f_m could be attributed to the poorer temporal resolution of the (relatively narrow) auditory filters centered at the lower signal frequencies (i.e., they suggested that the smaller masking release observed when f_s is lower than f_m is tied to the frequency of the signal *per se*, rather than to the frequency of the signal relative to that of the masker). This explanation seems unlikely, however, based on other results in the literature. For example, Glasberg and Moore (1994) found little or no masking release for signal frequencies of 250, 1000, or 4000 Hz ($f_s \approx 0.83$ or $0.91 f_m$), even though the bandwidths of the auditory filters centered at 1000 and 4000 Hz, if not at 250 Hz, would be sufficiently wide to impose little or no smoothing of the envelope fluctuations of their 16-Hz-wide noise masker. Furthermore, the fact that Glasberg and Moore (1994) did not observe a masking re-

^{a)}Portions of this research were presented at the 133rd meeting of the Acoustical Society of America [M. J. Gregan, S. P. Bacon, and J. Lee, “Masking of pure tones by sinusoidally amplitude modulated tonal maskers,” *J. Acoust. Soc. Am.* **101**, 3147(A) (1997)].

^{b)}Corresponding author; electronic mail: spb@asu.edu

lease at 4000 Hz (in the presence of a masker centered at 4400 or 4800 Hz), whereas Mott and Feth (1986) did (but in the presence of a masker centered at 1500 Hz), suggests that the masking release is more closely tied to processing influenced by the frequency of the signal *relative* to that of the masker, rather than to processing influenced by the frequency of the signal *per se*. Further support for this can be observed in a recent paper by Nelson and Swain (1996; their Fig. 3), in which they show that the PV differences that they observe with a 500-Hz masker are similar in magnitude to those observed by Zwicker (1976c) with a 1000-Hz masker, as long as the PV difference is plotted as a function of f_s/f_m .

The influence of f_s/f_m on the size of the temporal effect may be understood in terms of the way in which the masker's excitation grows with level at the place corresponding to f_s (i.e., it may reflect the way in which the response of the basilar membrane grows with masker level at the place corresponding to f_s). In terms of psychophysics, this is akin to suggesting that the size of the effect is influenced by the growth-of-masking function (Zwicker, 1976c; Moore and Glasberg, 1987). If masked thresholds are governed by the instantaneous level of the masker at the time of signal presentation, then the difference between the threshold for a signal at a masker peak and that for a signal at a masker valley (i.e., the PV difference) could be predicted from growth-of-masking functions. In other words, the two thresholds obtained may be considered as representing two points along a growth-of-masking function, one for the masker level at the peak and the other for the masker level at the valley. The difference between the two thresholds, then, would depend upon the slope of that growth-of-masking function: the steeper the slope, the greater the threshold difference. Masking functions in simultaneous masking have a slope greater than 1.0 when f_s is higher than f_m , and a slope less than 1.0 when f_s is lower than f_m (Wegel and Lane, 1924; Egan and Hake, 1950; Schöne, 1977; Bacon and Viemeister, 1985; Stelmachowicz *et al.*, 1987; Murnane and Turner, 1991). Thus the steeper function when f_s is higher than f_m is certainly consistent with the possibility that the greater temporal effect for those conditions is due to processing influenced by the relative frequency of the signal.

Although the results in the literature suggest that the temporal effect is influenced by f_s/f_m rather than by f_s , the evidence exists in the form of comparisons across studies that have used different subjects and, more importantly, different stimulus parameters, such as masker level and masker fluctuation rate. Indeed, no single study has specifically addressed the issue of whether this temporal effect in masking is influenced by f_s/f_m rather than by f_s . This was one of the purposes of the first experiment. The approach was to measure masking patterns for three separate masker frequencies for both a peak and valley signal placement, and to compare the PV difference for various signal frequencies, both when they were higher in frequency than a masker and when they were lower in frequency than a masker. If the magnitude of the effect were dependent upon processing influenced by f_s *per se*, this situation should result in the same PV difference regardless of f_m . Alternatively, if the PV difference were

dependent upon processing influenced by f_s/f_m , the amount of release at a given f_s would depend upon f_m . The other purpose of the first experiment was to examine whether the size of the temporal effect, for a given f_s/f_m , is dependent upon f_m . As noted above, Nelson and Swain (1996) showed that the PV differences they obtained with a 500-Hz masker were similar to those obtained by Zwicker (1976c) using a 1000-Hz masker, when the comparisons were made at similar f_s/f_m ratios. Experiment 1 extends that by evaluating a wider range of masker frequencies, and making the comparisons within the same group of subjects.

I. EXPERIMENT 1: MASKING PATTERNS

A. Apparatus and stimuli

The sinusoidally amplitude-modulated (SAM) masker was digitally generated and produced at a 20-kHz sampling rate. The output of the digital-to-analog converter (TDT DA1) was low-pass filtered at 8 kHz (Kemo VBF 25.01; 135 dB/oct). The masker can be described by the following equation:

$$[1 + m \sin(2\pi F_m t + \phi)] \sin(2\pi f_m t + \theta),$$

where m represents the modulation depth, F_m represents the modulator frequency, ϕ represents the modulator phase (which was 270°), f_m represents the masker carrier frequency, and θ represents the carrier phase (which was 0°). The masker was presented at a level of 80 dB SPL. It was modulated at a rate of 8 Hz and a depth of 1.0. Masker duration was 500 ms; no rise/fall was incorporated, other than that imposed by the modulation.

The signal was a sinusoid, digitally generated and produced at a 20-kHz sampling rate (TDT DA1) and low-pass filtered at 8 kHz (Kemo VBF 25.01; 135 dB/oct). The starting phase was 90° . Signal duration was 30 ms, including a 15-ms \cos^2 rise/fall time (i.e., there was no steady state). The onset of the signal was delayed relative to the onset of the masker by either 172 ms (to be centered in the second masker peak) or 235 ms (to be centered in the second masker valley). The level of the signal was varied adaptively via a programmable attenuator (Wilsonics PATT).

The frequency of the masker was 750, 1350, or 2430 Hz. The frequency of the signal was 0.8, 0.9, 0.95, 1.0, 1.2, 1.44, or $1.62 f_m$. When f_s was greater than f_m , a low-pass noise was presented continuously to mask potential cues due to the detection of the cubic difference tone (CDT) $2f_m - f_s$. The noise (GenRad 1381) was low-pass filtered (Kemo VBF 25.01; 135 dB/octave) at a cutoff frequency equal to the CDT that would be present when $f_s/f_m = 1.2$. Therefore, the cutoff frequency was fixed for a given f_m . The spectrum level of the noise was 20 dB SPL.

The masker, signal, and low-pass noise were added together before being presented monaurally (right ear) through a TDH-49P headphone mounted in an MX/51 cushion.

B. Procedure

Testing was completed in a double-walled, sound-treated booth for both quiet and masked thresholds. An adaptive, two-interval, forced-choice paradigm with a three-

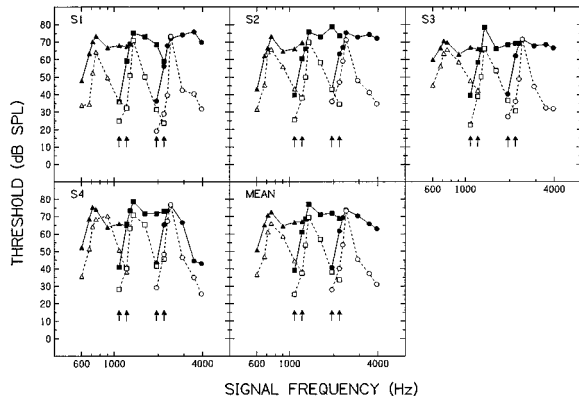


FIG. 1. Individual and mean masking patterns. The filled symbols represent thresholds obtained with the signal at a masker peak and the unfilled symbols represent thresholds obtained with the signal in a masker valley. Masker frequencies of 750, 1350, and 2430 Hz are represented by the triangles, squares, and circles, respectively. The arrows denote the signal frequencies for which a masked threshold was obtained both when a masker was higher in frequency than the signal, and when one was lower in frequency than the signal.

down, one-up decision rule that tracked 79.4% correct performance (Levitt, 1971) was employed. Each run consisted of 60 trials. A 4-dB step size was used for the first two reversals, after which the step size decreased to 2 dB. The first two reversals (three, if the total number of reversals was odd) were discarded, and the threshold estimate for a given run consisted of the average of the signal levels at the remaining reversal points. Runs were discarded if the standard deviation of the threshold estimate was greater than 5 dB or if the number of reversals used for the threshold estimate was less than six; this rarely happened. Three estimates of threshold were averaged to produce an overall threshold for a particular subject and condition. If the standard deviation of this average was greater than 3 dB, an additional estimate was obtained and included in the average. This continued until either the standard deviation of the final threshold average was less than 3 dB, or a total of six threshold estimates were obtained. Most (92%) of the thresholds reported here had standard deviations less than 3 dB.

C. Subjects

Four subjects participated. All had thresholds of 15 dB HL or less (ANSI, 1989) for octave test frequencies from 250 to 4000 Hz. Each subject received 3–6 h of training prior to data collection. Subjects ranged in age from 22 to 26 years. One subject (S1) was the first author; the other three subjects (S2, S3, and S4) were paid an hourly wage for their participation.

D. Results and discussion

Figure 1 shows the masking patterns obtained when the signal was at a masker peak (filled symbols) and when it was in a masker valley (unfilled symbols). The results for the individual subjects and those averaged across subjects are shown in separate panels. The low-frequency and especially the high-frequency slopes of the masking patterns were noticeably steeper when the signal was in a masker valley. The

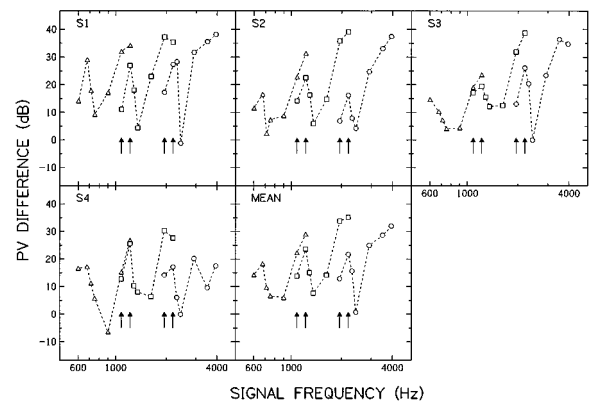


FIG. 2. Individual and mean peak-to-valley (PV) differences. Masker frequencies of 750, 1350, and 2430 Hz are represented by triangles, squares, and circles, respectively. The arrows have the same meaning as for Fig. 1.

especially large differences on the high-frequency side between the two masking patterns for a given f_m confirm previous findings that the PV difference or masking release is especially pronounced when f_s is higher than f_m (Egan and Hake, 1950; Mott and Feth, 1986; Nelson and Swain, 1996). Moreover, the magnitude of the effect observed here is consistent with that observed previously (Buus, 1985; Moore and Glasberg, 1987; Nelson and Schroder, 1996; Nelson and Swain, 1996).

The arrows in each panel denote the signal frequencies for which a masked threshold was obtained both when the signal was higher in frequency than a masker, and when it was lower in frequency than a masker. An important finding revealed in the present results is that, for a given f_s , the PV difference was more pronounced when f_s was higher than f_m than when f_s was lower than f_m . This is seen more clearly in Fig. 2, in which the PV difference is plotted as a function of f_s . The arrows have the same meaning as in Fig. 1. There are 16 conditions (4 signal frequencies for 4 subjects) which provide a test of whether the PV difference is determined by f_s *per se*, or whether it is determined by f_s relative to f_m . For 13 of the 16 conditions, the difference was larger when f_s was higher than f_m than when f_s was lower than f_m . For the other three conditions (1080 Hz for S3 and S4; 1216 Hz for S4) the PV difference was essentially the same, regardless of whether f_s was higher or lower than f_m . Averaged across all 16 conditions, the PV difference was 30 dB when f_s was higher than f_m , but only 18 dB when f_s was lower than f_m . Thus overall, it appears that it is the frequency of the signal relative to the masker that determines the magnitude of the temporal effect.

The PV differences in Fig. 2 have been replotted in Fig. 3 as a function of f_s/f_m , in order to see more clearly whether the size of the temporal effect for a given frequency ratio depends upon f_m . In general, the PV differences are similar across the three masker frequencies at the four lowest frequency ratios ($f_s/f_m \leq 1.0$). At the three highest-frequency ratios ($f_s/f_m > 1.0$), however, the PV differences are clearly smallest for the lowest f_m (750 Hz), but are similar to one another at the two highest masker frequencies (1350 and 2430 Hz). These results thus suggest that the PV difference depends at least somewhat upon f_m , a conclusion

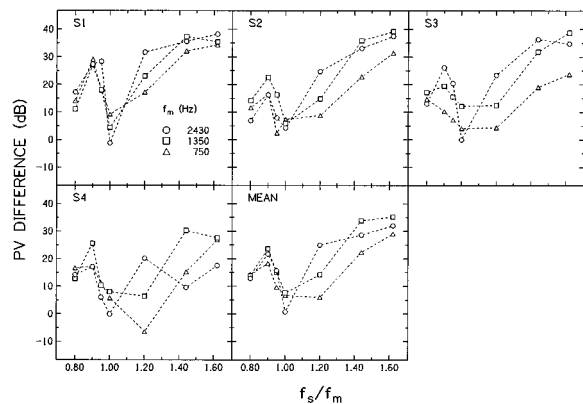


FIG. 3. Data from Fig. 2 replotted as a function of f_s/f_m .

that may seem at odds with the one that might be drawn from Fig. 3 in Nelson and Swain (1996). In that figure, the PV differences at various f_s/f_m ratios are shown to be similar for a 500-Hz (data from Nelson and Swain, 1996) and 1000-Hz masker (data from Zwicker, 1976c). It is unclear why an effect of f_m was observed here and not in the comparisons across the two other studies. Although it could be related to the fact that the comparisons made here were within a single group of subjects tested with comparable stimuli across frequency, another possibility is that it is related to the choice of masker frequencies. In particular, if the PV differences are smaller for masker frequencies below about 1000 Hz than they are for masker frequencies above that, then an effect of f_m would only be observed when masker frequencies are sampled both below and above 1000 Hz (as was done here). Additional research should clarify the situations in which an effect of f_m exists.

II. EXPERIMENT 2: MASKING FUNCTIONS

A. Rationale

Although it is possible, as suggested in the Introduction, that the PV difference for a fluctuating masker could be predicted by considering two points on a single growth-of-masking function (where one masker level represents the masker valley and one represents the masker peak), it is also possible that more than one type of masking could influence threshold. In that case, no *single* growth-of-masking function could accurately predict the PV difference. Consistent with this are results from Moore and Glasberg (1987). They determined that the amount of masking seen in the valley of a 100% SAM masker is greater than would be expected if the masking were due solely to simultaneous masking during periods of low masker energy. They hypothesized that masking during envelope valleys is probably due to a combination of simultaneous masking from the masker energy in the valley and forward masking from the preceding masker peak. Recent results from Nelson and Swain (1996) yield further support for the possibility that forward masking may influence the threshold for a signal in the valley of a modulated masker. Using a 100% SAM tone as a masker, they measured growth-of-masking functions for conditions where the signal's temporal location coincided with either a masker

peak or a masker valley. Their masking functions (f_s higher than f_m) had a slope greater than 1.0 when the signal coincided with a masker peak, but a slope less than 1.0 (consistent with forward-masking results, where slopes are typically less than those seen in simultaneous masking) when the signal coincided with a masker valley. Although it seems likely that forward masking would influence threshold when the signal is located in a masker valley, this has thus far not been explicitly evaluated.

For a given modulation rate, the influence of forward masking would most likely depend upon the modulation depth of the masker; specifically, forward masking would exert a greater influence on masked thresholds in conditions with large modulation depths, while thresholds in conditions with smaller depths would be influenced more by simultaneous masking or perhaps a combination of simultaneous and forward masking. For a given modulation depth, however, the influence of forward masking will depend upon the modulation rate of the masker. As the modulation rate increases, the influence of forward masking on the detection of signals in the valley will increase. Consequently, at higher rates, thresholds in the valley may be influenced by forward masking even at relatively low modulation depths. This interaction between modulation rate and modulation depth makes it unlikely that general statements can be made regarding the depth at which the influence of forward masking gives way to the influence of simultaneous masking. Nevertheless, because most research on the PV difference (or masking release) has concentrated on relatively low modulation rates, the purpose of the second experiment was to determine to what extent thresholds for a signal at a peak or in a valley of the masker used in experiment 1 (rate of 8 Hz) can be accounted for by simultaneous or forward masking produced by an unmodulated masker. This was accomplished by measuring growth-of-masking functions for a signal at a peak or in a valley of a SAM masker modulated at various modulation depths, and comparing those results with

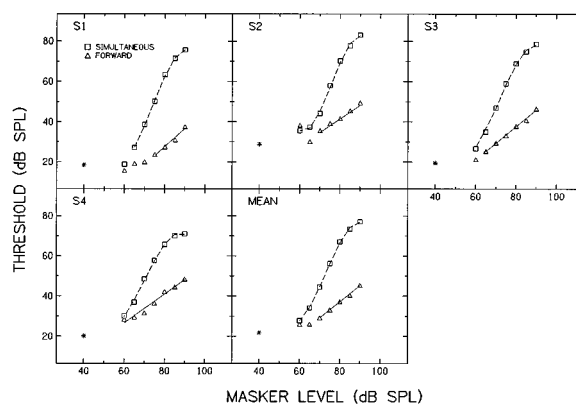


FIG. 4. Individual and mean growth-of-masking functions in simultaneous (squares) and forward (triangles) masking with an unmodulated masker ($f_m=1350$ Hz and $f_s=1944$ Hz). The lines represent the best fits to the thresholds using either linear (forward masking) or polynomial (simultaneous masking) regression. The asterisk represents the absolute threshold for the signal. Only thresholds representing 5 dB or more of masking were included in the fits.

TABLE I. Resulting parameter values (m, b) and goodness-of-fit (r^2) from the best-fitting lines to the forward-masking functions in Fig. 4. The fits can be described by the equation $y = mx - b$.

Subject	m	b	r^2
S1	0.90	44.6	0.977
S2	0.67	12.0	0.995
S3	0.83	28.5	0.995
S4	0.72	16.7	0.970
Mean	0.80	26.8	0.996

growth-of-masking functions obtained in forward or simultaneous masking with an unmodulated masker.

B. Method

The method of stimulus generation, procedures, and subjects were as for experiment 1. The level of the masker was varied in 5-dB steps from 60 to 90 dB SPL. The masker was either unmodulated or SAM at a rate of 8 Hz and a depth (m) of 1.0, 0.75, or 0.5. When m was equal to 1.0, no rise/fall time was incorporated, but when m was less than 1.0, a 5-ms \cos^2 rise/fall time was employed to avoid audible clicks. Total masker duration was 500 ms. Masker frequency was 1350 Hz; f_s was 1944 Hz (i.e., $f_s = 1.44f_m$). Signal duration was 30 ms. When the masker was modulated, the onset of the signal was delayed as described for experiment 1 [i.e., it was delayed by 172 ms (peak) or 235 ms (valley)]. When the masker was unmodulated, the onset of the signal was delayed relative to the onset of the masker by either 408 ms (simultaneous-masking condition) or 500 ms (forward-masking condition). The low-pass noise, with a cutoff frequency of 1260 Hz and a spectrum level of 20 dB SPL, was presented continuously in both the simultaneous- and forward-masking conditions (even though combination tones would not be generated in a forward-masking condition). Most (91%) of the thresholds in this experiment had standard deviations less than 3 dB.

C. Results and discussion

1. Predicting thresholds based on forward or simultaneous masking

The results obtained with the unmodulated masker are shown in Fig. 4. The asterisk in each panel represents the absolute threshold for the signal, the symbols represent the masked thresholds, and the lines represent the best fits to those thresholds. Only thresholds representing 5 dB or more of masking were included in the fits. As can be seen in the figure as well as in Table I, the forward-masked thresholds

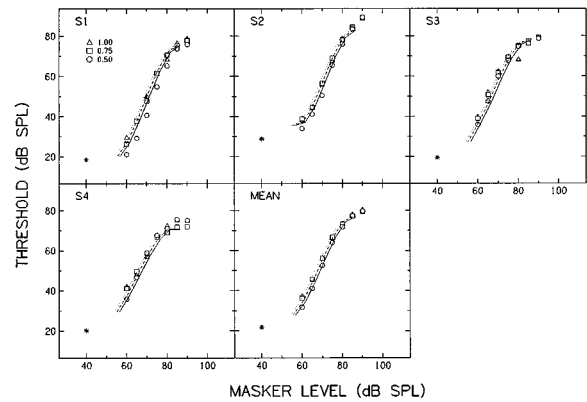


FIG. 5. The symbols represent individual and mean masked thresholds as a function of masker level for a signal located at a peak of a SAM masker modulated at a depth of 1.0 (triangles), 0.75 (squares), or 0.50 (circles). The lines represent the fits to the simultaneous-masking functions in Fig. 4, shifted an appropriate amount to account for instantaneous level differences between the modulated and unmodulated maskers (see text). The asterisk represents the absolute threshold for the signal.

(triangles) were fitted very well using linear regression. Consistent with previous results (e.g., Widin and Viemeister, 1979), the slopes of these functions are less than 1.0. The simultaneous-masked thresholds (squares) were fitted well (not shown) with a linear regression only for masker levels from 60 to about 80 dB SPL. The slope values for this portion of the function were considerably greater than 1.0 (values of 2.40, 2.62, 2.17, and 1.92 for S1 to S4, respectively), consistent with previous reports (Wegel and Lane, 1924; Egan and Hake, 1950; Schöne, 1977; Bacon and Viemeister, 1985; Stelmachowicz *et al.*, 1987; Murnane and Turner, 1991; van der Heijden and Kohlrausch, 1995). For masker levels above 80 dB SPL, the slopes were more shallow, approaching a value close to 1.0. The change in slope at high masker levels will be discussed in Sec. III. Because of the change in slope at high masker levels, the simultaneous-masking functions were fitted with a polynomial regression. The resulting parameter values and goodness of fit are shown in Table II.

The intent of the present experiment was to determine how well the thresholds in Fig. 4 (obtained with an unmodulated masker) could account for thresholds obtained in the presence of a modulated masker. The symbols in Fig. 5 show the growth-of-masking functions obtained with a modulated masker ($m = 1.0, 0.75, \text{ or } 0.5$) and the signal centered at a masker peak. These masking functions are similar to those obtained with an unmodulated masker in simultaneous masking (Fig. 4), even to the extent that the slopes of the functions decrease at high masker levels. Indeed, the lines in Fig.

TABLE II. Resulting parameter values ($b_0, b_1, b_2,$ and b_3) and goodness-of-fit (r^2) from the best-fitting lines to the simultaneous-masking functions in Fig. 4. The fits can be described by the equation $y = b_0 + (b_1x^1) + (b_2x^2) + (b_3x^3)$.

Subject	b_0	b_1	b_2	b_3	r^2
S1	1031.511	-45.279	0.651	-0.00295	0.999
S2	1709.038	-70.477	0.965	-0.00425	0.998
S3	662.922	-30.667	0.466	-0.00219	0.999
S4	636.414	-29.284	0.448	-0.00213	0.999
Mean	978.918	-42.725	0.617	-0.00282	1.000

TABLE III. These r^2 values indicate how well the functions used to fit growth-of-masking data for an unmodulated simultaneous masker (Fig. 4) fit the growth-of-masking data for a SAM masker with the signal at a masker peak (Fig. 5). The functions have been shifted slightly to account for changes in instantaneous masker level caused by modulation (see text for details).

Subject	$m = 1.0$	$m = 0.75$	$m = 0.50$
S1	0.944	0.984	0.929
S2	0.889	0.944	0.959
S3	0.917	0.961	0.966
S4	0.851	0.953	0.944
Mean	0.922	0.967	0.986

5 are the fits to the simultaneous-masking functions in Fig. 4. These lines were shifted slightly in Fig. 5, however, to account for the fact that the masker level at the peak was somewhat greater than the unmodulated carrier level. For example, when the carrier level was 80 dB SPL, the level of the masker at the peak was 85.9 dB SPL when the masker depth was 1.0 (calculated with a 30-ms window centered at the peak). Thus the fit to the function in Fig. 4 was shifted to the left by 5.9 dB to fit the results in Fig. 5 when the masker depth was 1.0. Similarly, the function was shifted to the left by 4.8 and 3.4 dB when the masker depth was 0.75 and 0.50, respectively. As can be seen in Fig. 5 and in Table III, the fits derived from the growth-of-masking functions obtained with an unmodulated masker in simultaneous masking predict the masked thresholds in Fig. 5 reasonably well. These results suggest, not surprisingly, that the threshold for a signal at the peak of a modulated masker is due to simultaneous masking.

The symbols in Fig. 6 show the growth-of-masking functions obtained with a modulated masker ($m = 1.0, 0.75$, or 0.50) and the signal centered in a masker valley. The lines in Fig. 6 are the fits to the masking functions with an unmodulated masker, from Fig. 4. For the case in which the

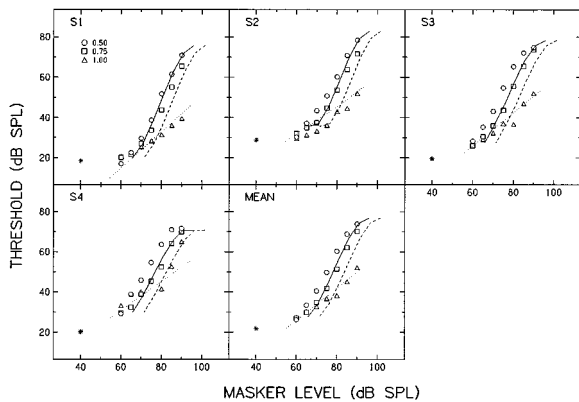


FIG. 6. The symbols represent individual and mean masked thresholds as a function of masker level for a signal located in a valley of a SAM masker modulated at a depth of 1.0 (triangles), 0.75 (squares), or 0.50 (circles). The lines represent the fits to the growth-of-masking functions in Fig. 4. When the masker was modulated at a depth of 1.0 (triangles), the fits were derived from the forward-masking functions in Fig. 4. When the masker was modulated at a depth of 0.75 (squares) or 0.50 (circles), the fits were derived from the simultaneous-masking functions in Fig. 4, shifted to the right by 11.4 dB (dashed curve) and 5.8 dB (solid curve) to account for instantaneous level differences due to modulation (see text). The asterisk represents absolute threshold for the signal.

TABLE IV. These r^2 values indicate how well the functions used to fit growth-of-masking data with an unmodulated masker (Fig. 4) fit the growth-of-masking data for a SAM masker with the signal in a masker valley (Fig. 6). The fits to the forward-masking data were used to fit the results when $m = 1.0$, and the fits to the simultaneous-masking data were used to fit the results when $m = 0.75$ or 0.50 . In all cases, the functions have been shifted to account for changes in instantaneous masker level caused by modulation (see text for details).

Subject	$m = 1.0$	$m = 0.75$	$m = 0.50$
S1	0.943	0.818	0.978
S2	0.667	0.598	0.935
S3	0.919	0.791	0.872
S4	0.660	0.816	0.870
Mean	0.947	0.742	0.919

masker was modulated at a depth of 1.0 (triangles), the dotted line represents the fit to the masking functions obtained in forward masking. This fit thus assumes that the masking in the valley is governed by forward masking by the preceding peak. The function representing the fit was shifted to the left an appropriate amount (5.9 dB) to account for the fact that the instantaneous level of the masker at a peak was greater than the nominal level of the carrier, as described above. This forward-masking function provides a reasonably accurate prediction of the thresholds when the masker was modulated at a depth of 1.0 (see Table IV); at lower modulation depths, the fits based on forward masking were considerably worse (not shown). This suggests that thresholds were governed primarily by forward masking by the preceding masker peak only when the modulation depth was 1.0.

It is worth noting that the forward-masked thresholds predict the thresholds in the presence of a 100% SAM masker especially well for only S1, S3, and the mean across subjects. For S4, the threshold at the highest masker levels inexplicably increased rather abruptly, and hence the forward-masked thresholds underpredict the thresholds in the presence of the modulated masker at high levels. For S2, on the other hand, the forward-masked thresholds overpredict the thresholds over most of the range of masker levels. The lower thresholds in the presence of the SAM masker could reflect the fact that the effective forward-masker duration is shorter in the modulated condition (regardless of whether the effective duration is considered to be that of the single preceding peak or the entire masker prior to signal presentation). The lower thresholds could also reflect the fact that the effective signal delay may be longer in the modulated condition (because the signal occurs near the end of the 62.5-ms “fall” of the 8-Hz masker envelope). Indeed, given these and other differences between the forward-masking condition and the SAM condition ($m = 1.0$), it is perhaps surprising that the fits are generally as good as they are.

The lines representing the fits to the masking functions when the masker was modulated at a depth of 0.75 (squares) or 0.50 (circles) were based on the fits to the simultaneous-masking functions in Fig. 4. As before, these lines have been shifted to account for instantaneous level differences due to modulation. Specifically, they have been shifted to the right by 11.4 (dashed curve) and 5.8 dB (solid curve) when the masker depth was 0.75 and 0.50, respectively, to reflect the

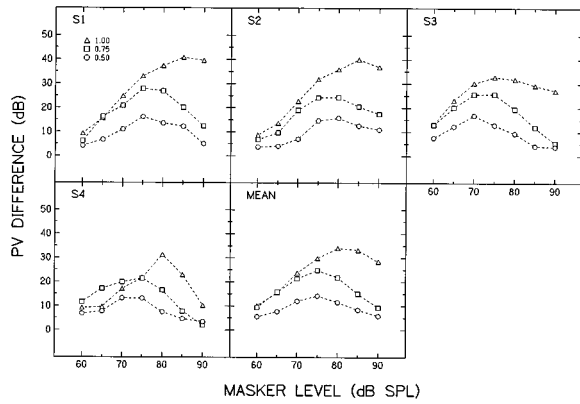


FIG. 7. Individual and mean PV differences (the difference between the thresholds in Fig. 6 and those in Fig. 5) as a function of masker level. The triangles, squares, and circles correspond to a modulation depth (m) of 1.0, 0.75, and 0.50, respectively.

fact that the level in the valley is 11.4 and 5.8 dB lower than the nominal carrier level at those modulation depths. At these two lower modulation depths, the simultaneous-masking functions predict thresholds reasonably well (see Table IV). However, the predicted values were consistently less than the measured values, particularly at a depth of 0.75, where the fits were generally the worst. This suggests that although simultaneous masking plays a greater role in situations where the signal is in a valley of an 8-Hz SAM masker modulated at a depth less than 1.0, there still may be some contribution of forward masking from the masker energy at the preceding peak, as was previously suggested by Moore and Glasberg (1987). That the fits were noticeably worse for a masker depth of 0.75 than 0.50 is consistent with the possibility that forward masking played a greater role when the masker was modulated at a depth of 0.75.

2. PV difference as a function of masker level

Although it was not the intent of the present experiment to examine the effects of masker level on the PV difference, it is possible to do so by subtracting the thresholds in Fig. 6 from those in Fig. 5. The results of this are shown in Fig. 7, where the masker depth is the parameter. In general, the size of the temporal effect first increased but then decreased as masker level increased from 60 to 90 dB SPL. This was particularly true at a masker depth of 0.5 (circles) and 0.75 (squares). At a depth of 1.0 (triangles), the PV difference either decreased to varying degrees or reached an asymptote at the higher masker levels.

To gain a better understanding of this nonmonotonic behavior, the mean thresholds from Figs. 5 and 6 are replotted in Fig. 8, where the modulation depth of the masker is plotted across panels. When the signal was positioned at a masker peak (triangles), the slope of the masking function decreased at a masker level of about 75 dB SPL, regardless of modulation depth.¹ At that and higher masker levels, however, the slope did not decrease when the signal was positioned in a masker valley (squares). (The exception to this was at the highest masker level when the modulation depth was 0.5; this probably reflects the high *signal* level in that

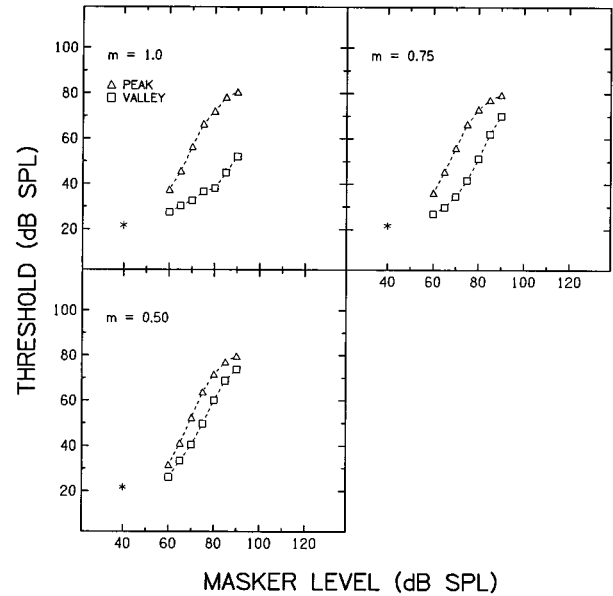


FIG. 8. Mean thresholds from Figs. 5 and 6. The signal was located at a masker peak (triangles) or valley (squares). The modulation depth of the masker varies across panels. The asterisk represents the mean absolute threshold for the signal.

condition—see footnote 1 and Sec. III.) Consequently, the difference between the two functions decreased for masker levels above 75 dB SPL. As can be seen in Fig. 7, the functions relating the PV difference to masker level are very similar to one another at masker depths of 0.5 and 0.75; this is probably because the processes underlying the masking in those cases are likely to be the same. The somewhat different function at a depth of 1.0, on the other hand, reflects the fact that thresholds for a signal in the valley are governed primarily by forward masking. A similar, nonmonotonic effect of level on the PV difference was observed by Zwicker (1976c; his Figs. 4 and 5), who masked a 1600-Hz signal with a 1000-Hz masker modulated at a depth of 1.0 and a rate of 4 or 10 Hz. The PV difference initially increased with an increase in masker level, but then decreased as the masker level increased from 76 to 86 dB SPL. In their study, however, van der Heijden and Kohlrausch (1995) did not observe a decline in masking release at high masker levels. They measured the threshold for a 2000-Hz tone in the presence of various maskers centered at 1300 Hz. The narrow-band noise maskers tended to produce less masking than the sinusoidal masker; this masking release increased with increasing masker level, but then reached an asymptote at a masker level of 78 dB SPL. The discrepancy across studies with regard to whether the temporal effect declines at high levels may be attributed to differences in signal level (see Sec. III). In the present study and in Zwicker (1976c), the PV difference decreased when the signal level (peak placement) exceeded 70–75 dB SPL. In van der Heijden and Kohlrausch (1995), however, where the masking release did not decline at high masker levels, the signal level at threshold never exceeded 70 dB SPL.

III. GENERAL DISCUSSION

A. Predicting the PV difference from thresholds with unmodulated maskers

One purpose of experiment 1 was to determine if the reduced PV difference for conditions in which f_s is lower than f_m can be attributed to processing influenced by the frequency of the signal itself, or if it is due to processing influenced by the frequency of the signal relative to that of the masker. The results suggest that the magnitude of this temporal effect is tied to the relative frequency of the signal; the results from experiment 1 are thus not consistent with the idea (Mott and Feth, 1986) that the reduced temporal effect when f_s is lower than f_m is due to less efficient temporal resolution at the lower f_s . Instead, the results are consistent with the possibility that the temporal effect for a given f_s/f_m is governed by the rate at which masking grows as a function of masker level (Zwicker, 1976c; Moore and Glasberg, 1987); thus the smaller effect when f_s is lower than f_m can be understood by the relatively shallow growth of masking in that condition.

The purpose of experiment 2 was to evaluate quantitatively the relationship between the PV difference and growth of masking. In particular, the goal was to determine to what extent thresholds in the presence of a modulated masker can be accounted for by thresholds in the presence of an unmodulated masker in either simultaneous or forward masking. The results indicated that the threshold for a signal at a masker peak is, as expected, due to simultaneous masking. The type of masking that dominates threshold for a signal in a masker valley, however, appears to depend upon the modulation depth of the masker. Specifically, for the 8-Hz SAM masker used here, thresholds appear to be influenced predominantly by forward masking when the masker is modulated at a depth of 1.0, but by simultaneous masking when the masker is modulated at depths of 0.75 and 0.50. However, for the latter conditions, the finding that the simultaneous-masking functions generally underpredicted masked thresholds for a signal in a masker valley suggests that there is still a contribution from forward masking, and thus that thresholds would be better predicted by a combination of simultaneous and forward masking. Although the modulation depth at which masking can be better predicted by simultaneous masking versus either forward masking or a combination of simultaneous and forward masking will depend upon masker rate, it is still probably the case that the magnitude of the temporal effect can be predicted reasonably well from growth-of-masking functions obtained with unmodulated maskers. Importantly, this strongly suggests that the temporal effect in masking observed here and elsewhere with similar maskers is almost certainly not influenced by factors underlying CMR (see Buus, 1985).

It should be noted that growth-of-masking functions were obtained only for $f_s/f_m = 1.44$; this raises the question of whether growth-of-masking functions from unmodulated maskers will also accurately predict the PV difference for other ratios. Although this should probably be addressed empirically, a comparison of the masking release obtained here with growth-of-masking functions obtained in simultaneous

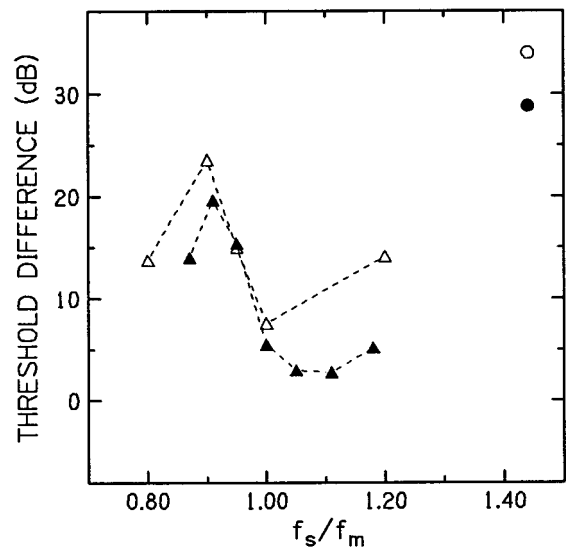


FIG. 9. The filled triangles represent the average difference between simultaneous- and forward-masked thresholds (based on best fits to growth-of-masking functions) from Bacon (1985). The unfilled triangles correspond to average masking release values from Fig. 2. In the upper right corner, the filled circle is the predicted PV difference based on the growth-of-masking functions in Fig. 4 (i.e., the difference between simultaneous- and forward-masked thresholds based on the fits to the data in Fig. 4), whereas the unfilled circle represents the actual PV difference averaged across subjects (Fig. 2).

and forward masking by Bacon (1985) suggests that accurate predictions can probably be made for a wide range of f_s/f_m . In Bacon's experiments, the masker duration was 400 ms and the signal duration was 20 ms. The signal was presented either at the temporal center of the masker or immediately after the masker (the forward-masking results were published by Bacon and Jesteadt, 1987). The frequency of the signal was fixed at 1000 Hz and f_m was varied, with f_s/f_m ranging from 0.87 to 1.18. The masking functions were fitted using linear regression. The difference between the fits to the functions in simultaneous and forward masking, averaged across subjects for a masker level of 80 dB SPL, is shown in Fig. 9 (filled triangles). Also shown is the mean PV difference (over a similar range of f_s/f_m) from Fig. 2 (unfilled triangles) for the 1350-Hz SAM masker modulated at a depth of 1.0. As can be seen, the pattern of results in both sets of data is similar. The data from the present study for $f_s/f_m = 1.44$ are replotted in the upper right corner of Fig. 9. The unfilled circle represents the actual PV difference averaged across subjects, whereas the filled circle is the predicted PV difference based on the fits to the growth-of-masking functions in Fig. 4 (i.e., it is the difference between the fits to the simultaneous- and forward-masked thresholds at a masker level of 80 dB SPL). The agreement within a group of subjects (circles) is similar to that across subjects (triangles). Overall, the data in Fig. 9 suggest that the temporal effect for SAM maskers ($m = 1.0$) is reasonably well predicted from growth-of-masking functions for most, if not all, f_s/f_m .

Inasmuch as PV differences can be accounted for by growth-of-masking with unmodulated maskers, the smaller PV differences observed for the 750-Hz masker compared to the 1350-Hz or 2430-Hz masker (at least when $f_s > f_m$) suggest that growth-of-masking functions may be more shallow

at the lower frequency. Although masking functions were measured only for the 1350-Hz masker, and thus slope comparisons across frequency cannot be made here, unpublished data from our laboratory indicate that masking functions are indeed more shallow for masker frequencies below about 1000 Hz than they are for masker frequencies above 1000 Hz. These slope differences may reflect different degrees of compression across frequency (see below).

B. Change in slope of simultaneous-masking functions at high levels

Both the simultaneous growth-of-masking functions in Fig. 4 (squares) and the growth-of-masking functions in Fig. 5 (also see Fig. 8) obtained with a modulated masker (depth=1.0, 0.75, or 0.50) and the signal at a masker peak show a decrease in slope at high masker levels. The slope is about 2.0 for masker levels from 60 to 75 or 80 dB SPL, but it decreases to an average value of 1.0 for masker levels higher than that. The decrease in slope almost certainly cannot reflect the emergence of the detection of the combination tone $2f_m - f_s$ at high levels, given the low-pass noise that was used to mask the distortion product. Instead, the different slope values may be understood in terms of the nonlinearity of basilar membrane vibration. [Others have also argued that growth of masking may reflect basilar membrane nonlinearity (Oxenham and Moore, 1995; Nelson and Schroder, 1996, 1997; Oxenham and Plack, 1997)].

First consider the initially steep slope of the masking function. For signals of low to moderate intensity, the response to the signal, at the basilar membrane location corresponding to the signal frequency, is presumably compressive. In contrast, the response to the masker, at the location corresponding to the signal frequency, probably grows linearly over the entire range of masker levels when f_s is well above f_m (e.g., Pickles, 1988; Ruggero *et al.*, 1993). Therefore, if masked threshold reflects a constant signal-to-masker ratio (in terms of a physiological response), and the masker level is increased by 10 dB, a greater than 10-dB increase in signal level would be required to yield the same ratio because the basilar membrane response to the signal is compressed. This would account for the expansive slope over the initial range of masker levels. The essentially linear slope at higher levels could be understood if, at high signal levels, the response to the signal (at the signal place) becomes linear. Although some results suggest that the basilar membrane response to characteristic frequency tones changes from compressive to linear at high input levels (e.g., Ruggero *et al.*, 1992, 1993), a more recent study suggests that such a change occurs only in cases of (at least slight) cochlear damage (Ruggero *et al.*, 1997). Although more physiological data are needed to resolve this discrepancy, the recent results of Ruggero *et al.* (1997) suggest that, if the growth-of-masking functions can be understood in terms of basilar membrane responses, then the subjects tested here must have at least a small degree of cochlear damage that may be impervious to standard audiometric testing.

Others have observed a similar change in slope at high levels in simultaneous masking (for $f_s > f_m$). Zwicker (1976c, 1979) reported a decrease in slope at high levels, and

interpreted this as a manifestation of cochlear nonlinearities. He noted in his 1979 paper that the decrease occurred when the signal reached a sensation level (SL) of 40 dB (i.e., at the point where there was 40 dB of masking). For the functions reported in the present study, the decrease in slope occurred at a signal SL of about 50 dB. Schöne (1977) also observed a decrease in slope at high levels, although the signal SL at which the slope changed depended somewhat upon the subject and, for a given subject, the frequency separation between the masker and signal ($f_s > f_m$, in all cases). Finally, the slope of some of the masking functions in Egan and Hake (1950) also decreased at high levels (signal SLs between about 30 and 50 dB).

Although some investigators have observed a change in slope at high levels, others have not (e.g., Bacon and Viemeister, 1985; Moore and Glasberg, 1987; Stelmachowicz *et al.*, 1987; Murnane and Turner, 1991; Nelson and Swain, 1996; Nelson and Schroder, 1997). It is unclear why this is the case. It may, however, be related to whether or not the signal reached a sufficiently high level to place it in a region of linear response growth. In general, the signal levels were lower in the studies that did not observe a decrease in slope of the masking function.

Recently, Oxenham and Plack (1997) found a decrease in slope at high masker (and signal) levels in a forward-masking paradigm ($f_s/f_m = 2.0$), and attributed it to basilar membrane response characteristics. The interpretation of the psychophysical data obtained in forward masking is probably less complicated than that observed with simultaneous masking (present experiment), given the potential for other types of interactions (e.g., suppression) to occur in simultaneous masking. Nevertheless, it seems likely that the decrease in slope at high levels reflects the same processing, regardless of the masking paradigm.

Finally, although the decrease in slope at high signal levels may reflect a change in response growth (from compressive to linear) at the place corresponding to the signal frequency, it could, of course, reflect something else. One possibility is that the change occurs at the point where subjects begin to listen off frequency, on the high-frequency side of the signal's excitation pattern. Because the excitation at this place in response to the signal (as well as to the masker) would grow linearly, the masking function would thus presumably have a linear slope. An excitation pattern analysis (Glasberg and Moore, 1990), however, employing the masker and signal levels (at threshold) used here, suggests that subjects are more likely to listen near the place corresponding to the signal frequency. Further, pilot data from a subject not tested here suggest that the change in slope at high signal levels is not due to off-frequency listening: the addition of a high-pass masker (cutoff of $1.25f_s$) did not alter the slope of the masking function at high levels.

IV. SUMMARY

The present study examined the masking of pure tones by SAM tonal maskers, and attempted to relate it to the masking produced by unmodulated maskers in simultaneous or forward masking. The primary findings can be summarized as follows:

(1) The magnitude of the PV difference (threshold for a signal at a peak of a modulated masker minus threshold for a signal in a valley of that masker) is determined by f_s/f_m , rather than f_s itself, and is largest when f_s is above f_m (experiment 1).

(2) Thresholds for signals at a peak of a modulated masker are determined by simultaneous masking. Thresholds for signals in a valley of a masker modulated at a rate of 8 Hz are influenced mainly by forward masking from the preceding masker peak when $m = 1.0$, or by simultaneous masking from the masker's energy in the valley when $m = 0.75$ or 0.50 (experiment 2). Thus the amount of masking release in the presence of a fluctuating masker may be predicted from growth-of-masking functions obtained with an unmodulated masker, indicating that the masking release is probably not influenced by factors underlying CMR.

(3) When f_s was above f_m , the PV difference (for a given f_s/f_m) was smallest for the lowest f_m (experiment 1). This difference across frequency may be due to a more shallow growth-of-masking function ($f_s > f_m$) at low overall frequencies.

(4) For the condition where $f_m = 1350$ Hz and $f_s = 1944$ Hz, the slope of the masking function (obtained in simultaneous masking with an unmodulated masker or with a SAM masker and the signal at a masker peak) decreased from an average value of 2.0 to an average value of 1.0 at high levels. With a SAM masker, this decrease in slope at high signal levels results in the nonmonotonic effect of masker level on the magnitude of the PV difference (Fig. 7). This change in slope may possibly be understood in terms of basilar membrane nonlinearity, which results in a compressive response to the signal at low to mid stimulus levels, and a (damage-induced?) linear response at high levels, while the response to the masker (when f_s is well above f_m) is linear regardless of the masker level.

ACKNOWLEDGMENTS

This research was supported by NIDCD Grant No. DC01376, and is based on a master's thesis submitted by the first author to the Graduate College at Arizona State University. Dave Nelson and Andy Oxenham provided many helpful comments and suggestions that greatly improved this paper.

¹It was noted previously that the simultaneous-masking functions in Fig. 4 with an unmodulated masker changed slope at a masker level of 80 dB SPL. The discrepancy between this value and the value of 75 dB SPL observed in Fig. 8 is probably due to the fact that the masker level at the time of signal presentation (signal at masker peak) was, in fact, about 80 dB SPL. Further, as we argue in Sec. III, the change in slope is more likely to be governed by the *signal* level, rather than the masker level, and the signal level in Fig. 4 at a masker level of 80 dB SPL is approximately equal to that in Fig. 8 at a masker level of 75 dB SPL.

ANSI (1989). ANSI S3.6-1989, "Specifications for audiometers" (ANSI, New York).

Bacon, S. P. (1985). Unpublished data.

Bacon, S. P., and Jesteadt, W. (1987). "Effects of pure-tone forward masker duration on psychophysical measures of frequency selectivity," *J. Acoust. Soc. Am.* **82**, 1925–1932.

Bacon, S. P., and Viemeister, N. F. (1985). "Simultaneous masking by gated and continuous sinusoidal maskers," *J. Acoust. Soc. Am.* **78**, 1220–1230.

Buus, S. (1985). "Release from masking caused by envelope fluctuations," *J. Acoust. Soc. Am.* **78**, 1958–1965.

Egan, J. P., and Hake, H. W. (1950). "On the masking pattern of a simple auditory stimulus," *J. Acoust. Soc. Am.* **22**, 622–630.

Fastl, H. (1975). "Loudness and masking patterns of narrow noise bands," *Acustica* **33**, 266–271.

Glasberg, B. R., and Moore, B. C. J. (1990). "Derivation of auditory filter shapes from notched-noise data," *Hearing Res.* **47**, 103–138.

Glasberg, B. R., and Moore, B. C. J. (1994). "Growth-of-masking functions for several types of maskers," *J. Acoust. Soc. Am.* **96**, 134–144.

van der Heijden, M., and Kohlrausch, A. (1995). "The role of envelope fluctuations in spectral masking," *J. Acoust. Soc. Am.* **97**, 1800–1807.

Levitt, H. (1971). "Transformed up-down methods in psychoacoustics," *J. Acoust. Soc. Am.* **49**, 467–477.

Moore, B. C. J., and Glasberg, B. R. (1987). "Factors affecting thresholds for sinusoidal signals in narrow-band maskers with fluctuating envelopes," *J. Acoust. Soc. Am.* **82**, 69–79.

Mott, J. B., and Feth, L. L. (1986). "Effects of the temporal properties of a masker upon simultaneous-masking patterns," in *Auditory Frequency Selectivity*, edited by B. C. J. Moore and R. D. Patterson (Plenum, New York), pp. 381–386.

Murmane, O., and Turner, C. W. (1991). "Growth of masking in sensorineural hearing loss," *Audiology* **30**, 275–285.

Nelson, D. A., and Schroder, A. C. (1996). "Release from upward spread of masking in regions of high-frequency hearing loss," *J. Acoust. Soc. Am.* **100**, 2266–2277.

Nelson, D. A., and Schroder, A. C. (1997). "Linearized response growth inferred from growth-of-masking slopes in ears with cochlear hearing loss," *J. Acoust. Soc. Am.* **101**, 2186–2201.

Nelson, D. A., and Swain, A. C. (1996). "Temporal resolution within the 'upper accessory excitation' of a masker," *Acustica* **82**, 328–334.

Oxenham, A. J., and Moore, B. C. J. (1995). "Additivity of masking in normally hearing and hearing-impaired subjects," *J. Acoust. Soc. Am.* **98**, 1921–1934.

Oxenham, A. J., and Plack, C. J. (1997). "A behavioral measure of basilar-membrane nonlinearity in listeners with normal and impaired hearing," *J. Acoust. Soc. Am.* **101**, 3666–3675.

Pickles, J. O. (1988). *An Introduction to the Physiology of Hearing* (Academic, San Diego, CA), 2nd ed., pp. 26–77.

Ruggero, M. A., Robles, L., and Rich, N. C. (1992). "Two-tone suppression in the basilar membrane of the cochlea: Mechanical basis of auditory nerve rate suppression," *J. Neurophysiol.* **68**, 1087–1099.

Ruggero, M. A., Rich, N. C., and Recio, A. (1993). "Alteration of basilar membrane responses to sound by acoustic overstimulation," in *Biophysics of Hair Cell Sensory Systems*, edited by H. Duifhuis, J. W. Horst, P. van Dijk, and S. M. van Netten (World Scientific, Singapore), pp. 258–265.

Ruggero, M. A., Rich, N. C., Recio, A., Narayan, S. S., and Robles, L. (1997). "Basilar-membrane responses to tones at the base of the chinchilla cochlea," *J. Acoust. Soc. Am.* **101**, 2151–2163.

Schöne, P. (1977). "Nichtlinearitäten im mithörschwellen-tonheitsmuster von sinustönen," *Acustica* **37**, 37–44.

Stelmachowicz, P. G., Lewis, D. E., Larson, L. L., and Jesteadt, W. (1987). "Growth of masking as a measure of response growth in hearing-impaired listeners," *J. Acoust. Soc. Am.* **81**, 1881–1887.

Wegel, R. L., and Lane, C. E. (1924). "Auditory masking of one pure tone by another and its possible relation to the dynamics of the inner ear," *Phys. Rev.* **23**, 266–285.

Widin, G. P., and Viemeister, N. F. (1979). "Intensive and temporal effects in pure-tone forward masking," *J. Acoust. Soc. Am.* **66**, 388–395.

Zwicker, E. (1976a). "Influence of a complex masker's time structure on masking," *Acustica* **34**, 138–146.

Zwicker, E. (1976b). "A model for predicting masking-period patterns," *Biol. Cybern.* **23**, 49–60.

Zwicker, E. (1976c). "Mithörschwellen-periodenmuster amplitudenmodulierter töne," *Acustica* **36**, 113–120.

Zwicker, E. (1979). "A model describing nonlinearities in hearing by active processes with saturation at 40 dB," *Biol. Cybern.* **35**, 243–250.

Zwicker, E., and Schütte, H. (1973). "On the pattern of the threshold of tone impulses," *Acustica* **29**, 343–347.

Cross-modality matching and the loudness growth function for click stimuli

Yula C. Serpanos

Adelphi University, Department of Communication Sciences and Disorders, Hy Weinberg Center, Cambridge Avenue, Garden City, New York 11530

Honor O'Malley

Teachers College, Columbia University, and Department of Speech and Language Pathology and Audiology, 525 West 120th Street, New York, New York 10027

Judith S. Gravel

Rose F. Kennedy Center, Albert Einstein Medical Center, 1410 Pelham Parkway South, Bronx, New York 10461

(Received 26 March 1997; revised 17 October 1997; accepted 17 October 1997)

Loudness-intensity functions for click stimuli were obtained from 30 adult listeners having normal ($n = 10$), flat ($n = 10$), or sloping ($n = 10$) high-frequency cochlear hearing loss configurations. The procedure of cross-modality matching (CMM) between loudness and perceived line length [R. P. Hellman and C. H. Meiselman, *J. Speech Hear. Res.* **31**, 605–615 (1988); *J. Acoust. Soc. Am.* **88**, 2596–2606 (1990); *J. Acoust. Soc. Am.* **93**, 966–975 (1993)] was used to validate their loudness growth functions. Mean group loudness exponents were similar to those reported in recent investigations that utilized pure tone stimuli, further supporting the validity and reliability of the CMM task as an estimate of the loudness growth function. The results also suggest that the mean loudness function for clicks is similar to the function obtained with tonal stimuli at least for listeners with moderately impaired hearing or better. Moreover, CMM produced less variability than the more conventional psychophysical methods of magnitude estimation and production for the groups with cochlear hearing loss. Toward direct application of the CMM technique, in lieu of absolute exponential slope values, the individually determined loudness growth function over a range of intensities should be compared to the normal mean function for calculations of deviations. © 1998 *Acoustical Society of America*. [S0001-4966(98)01502-1]

PACS numbers: 43.66.Cb, 43.66.Sr [WJ]

INTRODUCTION

An international standard for loudness (ISO R 131-1959) was formulated in 1959 based on a large scale study of individuals with normal hearing across several laboratories. The ISO standard defines loudness in sound pressure for pure tones as a power function with a slope (exponent) of 0.6 (Robinson, 1957; Stevens, 1955). Loudness measures for individuals with hearing loss are important for the clinical purposes of selecting and evaluating the output of amplification devices (Mueller and Bright, 1994) and to assist in the differential diagnosis of auditory disorders (Hall, 1991).

Recently, several investigators have suggested that loudness scaling methods such as category rating (Robinson and Gatehouse, 1996), magnitude estimation (Geller and Margolis, 1984) or cross-modality matching (Hellman and Meiselman, 1988) should be incorporated into selection procedures for specifying the frequency-gain and compression characteristics of amplification devices that are recommended for use by individuals with cochlear hearing loss. These methods are necessary in order to provide precise information about an individual's loudness growth function, a prerequisite for the fitting of nonlinear circuitry that is increasingly available in current, personal amplification devices (Fabry and Schum, 1994).

Geller and Margolis (1984) hypothesized that the resto-

ration of the normal loudness function is the desired result of any hearing aid fitting. Indeed, several hearing aid manufacturers have developed amplification devices based on this principle (Peterson, 1993; Williams, 1994). The intent of this approach to hearing aid fitting is to abandon the traditional linear response of amplification in lieu of a more appropriate nonlinear model that would account for dynamic sounds, such as those that occur in speech, as well as for the phenomenon of "rapid" loudness growth experienced by listeners with cochlear hearing loss (Brunved, 1994). Toward this end, rather than focus on absolute thresholds, suprathreshold measurements, such as the determination of a patient's loudness sensitivity to frequency- and intensity-specific narrow bands of noise, have been suggested in order to establish the gain, output and compression characteristics of the amplification device (Mikami *et al.*, 1993).

In the clinical setting, several methods exist for assessing loudness although the results are used for different purposes. First, most comfortable loudness (MCL) and uncomfortable listening level (UCL) thresholds are two subjective measures that are commonly obtained at several speech-frequency regions, in order to specify hearing aid gain and output, respectively (Skinner, 1988). Second, loudness growth over a range of intensities has also been examined using a loudness matching procedure, one being the Alter-

nate Binaural Loudness Balance (ABLB) test (Fowler, 1936, 1937). The ABLB test (among other variations) is typically used as a site-of-lesion measure in order to identify the presence or absence of "recruitment" in listeners with sensorineural hearing loss (Hall, 1991; Brunt, 1994).

Several investigators have noted that the conventional clinical procedures used for assessing loudness in individuals with hearing loss are inadequate (Geller and Margolis, 1984; Hellman and Meiselman, 1990; Stevens, 1959; Thalmann, 1965). Specifically, the measures of MCL and UCL do not provide indices of loudness growth over the dynamic range of hearing. Furthermore, the utilization of a loudness-matching procedure is often restricted in individuals with bilateral sensorineural hearing losses. For example, listeners who do not exhibit normal or near normal hearing (for at least one frequency) in the ear contralateral to the test ear are not candidates for the classic ABLB (Hellman and Meiselman, 1990; Knight and Margolis, 1984). Moreover, Thalmann (1965) indicated that bilateral hearing impairment of long duration may alter subjective loudness judgments. Finally, the task of conducting loudness matches may be difficult in individuals with cochlear hearing loss due to the presence of diplacusis and tinnitus (Hellman and Meiselman, 1990).

Numerous studies conducted by Stevens and others revealed that the most accurate representation of the loudness function was obtained by calculating the geometric average of slopes obtained through magnitude estimation and production methods (Hellman, 1976; Stevens, 1969, 1975; Stevens and Greenbaum, 1966). Further, Stevens (1959) suggested that an alternative method for assessing loudness growth for individuals with hearing loss was through the use of a cross-modality matching (CMM) task that would substitute the performance of a normally functioning sensory modality for the impaired ear as the comparison metric. This cross-modality matching procedure would compare judgments of change of sensation in the substituted sensory modality with judgments of changes in loudness.

Hellman and Meiselman (1988, 1990, 1993) investigated the clinical utility of the cross-modality matching (CMM) technique for assessing loudness growth using perceived length as the modality substituted for loudness. Specifically, subjects with normal hearing and cochlear hearing losses were required to match judgments of loudness to perceived magnitudes of line lengths. CMM was determined to be a valid and reliable technique for the estimation of loudness growth in individuals with normal hearing and varying degrees of cochlear hearing loss.

The purpose of this study was to further explore the applicability of the CMM technique as proposed by Hellman and Meiselman (1988, 1990, 1993) by investigating a simple stimulus used in a standard audiological assessment procedure with listeners typical of those frequently presenting with hearing loss in clinical settings. The auditory brainstem response (ABR) remains the most commonly used electrophysiologic procedure for estimating auditory sensitivity and neurologic integrity from the periphery through the brainstem auditory pathways (Jacobson, 1994). The technique has gained popularity in the clinical setting as it is considered

objective. Among other applications, it is useful for examining very young children and other difficult-to-test populations. Owing to the difficulties imposed by obtaining behavioral measures in children younger than 6 months, amplification is often fitted for the pediatric population on the basis of click and tonal ABR findings (Pediatric Working Group, 1996). Moreover, in a recent study, Serpanos *et al.* (1997) found that the click-elicited ABR latency-intensity function could be used to estimate loudness growth in listeners with normal hearing and cochlear hearing loss. Thus, this electrophysiologic procedure shows promise for providing information on an individual's loudness growth function.

Despite the clinical necessity and popularity of the click-evoked ABR, inconclusive data are available on the loudness growth functions with clicks. While inconsistent data exist on the subjective loudness growth function for clicks (Cazals and Stephens, 1975; Davidson *et al.*, 1990; Geisler *et al.*, 1958; Pratt and Sohmer, 1977; Raab and Osman, 1962; Wilson and Stelmack, 1982), there is evidence that the loudness growth function obtained with clicks approximates the loudness function obtained with tonal stimuli (Cazals and Stephens, 1975; Geisler *et al.*, 1958). However, there are no data available from CMM loudness studies that used clicks as stimuli; tones have been used in recent CMM studies (Cefaratti and Zwislocki, 1994; Collins and Gescheider, 1989; Hellman and Meiselman, 1988, 1990, 1993). Therefore, a second purpose of this study was to perform a further investigation of the click loudness function utilizing the CMM technique for the specific purpose of expanding our understanding of the characteristics of this frequently used stimulus for estimating loudness in individuals with normal hearing and with cochlear hearing loss.

I. METHOD

A. Subjects

Subjects in this study included 30 adults, aged 18 to 65 years. Ten subjects comprised each of three test groups, distinguished by the hearing status of one test ear (normal or cochlear hearing loss). Subject sample size was chosen based on previous studies of loudness scaling. Stable, reproducible averaged loudness exponents have been obtained using groups of approximately ten listeners (Hellman, 1981; Stevens, 1959, 1975; Stevens and Guirao, 1964). Subjects were unpaid volunteers or reimbursed participants solicited from the outpatient population of the Hearing and Speech Center at Long Island Jewish Medical Center, New Hyde Park, New York. None of the subjects had any prior experience with loudness scaling.

Subjects in this study were required to demonstrate normal or corrected-normal vision, and normal middle ear function as supported by otoscopy and tympanometry. Aural acoustic immittance testing was performed using an immittance audiometer (GSI-33 Middle Ear Analyzer) and a 226 Hz probe-tone frequency. Normal middle ear function was defined by peak admittance within 0.3 to 1.4 mmho, middle ear pressure within -150 to $+150$ daPa, and ear canal volume between 0.6 and 1.7 daPa (Margolis and Shanks, 1991). The conventional modified Hughson-Westlake technique

was used for the assessment of pure tone air and bone conduction thresholds (Wilber, 1991).

Group I (mean age=35 years) consisted of a group of listeners with normal hearing for the octave frequencies of 250 to 8000 Hz and the 6000 Hz interoctave, bilaterally. Normal hearing was defined by pure tone hearing threshold levels better than or equal to 20 dB HL (*re*: ANSI, 1989) without air–bone (conduction) threshold differences greater than 10 dB.

Groups II and III included subjects with bilateral predominantly cochlear hearing loss of at least five years' duration; one subject (from group II) was unilaterally impaired. Cochlear hearing loss was verified in the test ear by case history information, and the results obtained from a battery of audiometric procedures. The tests that were used to support a cochlear site-of-lesion included speech recognition (Penrod, 1994), contralateral acoustic reflex threshold testing (Gelfand *et al.*, 1990), contralateral acoustic reflex decay (Wilson and Margolis, 1991), high-level Short Increment Sensitivity Index (SISI; Hall, 1991), and suprathreshold ABR assessment (Hall, 1992; Schwartz *et al.*, 1994). The etiologies of the hearing losses were determined by case history information, and were attributed to familial or congenital factors for 9 of 20 subjects. The remaining 11 subjects had acquired, late-onset impairments resulting from noise exposure, ear trauma, or unknown causes.

The hearing losses of subjects in group II (mean age=45 years) were of "flat" audiometric configuration, defined as pure tone thresholds no different than 15 dB between the octave frequencies of 250 to 8000 Hz (including the 6000 Hz interoctave), for at least six of the seven test frequencies. The mean hearing thresholds for each frequency tested ranged from 43 to 53.5 dB. Subjects in group III (mean age=55 years) had sloping high-frequency hearing loss beginning at 2000 Hz. Specifically, hearing thresholds were within normal limits (thresholds better or equal to 20 dB) from 250 to 1500 Hz, with a 5- to 55-dB slope between octave frequencies from 2000 to 8000 Hz and the 6000 Hz interoctave. The mean hearing thresholds at 2000 Hz and above ranged from 34 to 67 dB.

B. Procedures

All audiometric measures were obtained in a double-walled sound-treated test room (IAC 1403 ACT), meeting standards for noise attenuation (*re*: ANSI, 1977). The ABR procedure and the tasks for the loudness growth estimates were conducted in a quiet room.

C. Stimuli

Clicks generated by a clinical auditory evoked potential system (Nicolet Auditory Compact) were the acoustic stimuli. The stimuli consisted of a 1-min train of 100- μ s rarefaction clicks presented monaurally to the test ear through an Etymotic ER-3A insert earphone at a rate of 61.4/s. The amplitude spectrum of this stimulus reveals that the spectral energy of the stimulus is equally concentrated to approximately 3000 Hz where there is a 6 dB per octave roll-off (Gorga and Thornton, 1989). The click train was pre-

sented only once unless the subject requested repeated presentation. Intensities ranging from 20 to 90 dB nHL (*re*: 25 dB peak equivalent sound pressure level) were varied parametrically in 10 dB steps. The duration was chosen to approximate the amount of time required to obtain an ABR recording at each intensity level using the specified rate (Serpanos *et al.*, 1997). The range of intensities were considered a representative range for loudness growth testing.

The visual stimuli consisted of line lengths displayed on 35-mm slides projected (Kodak 860 H) onto a screen located at a distance of 2.74 m from each subject, and 1.83 m from the projector lens (Kodak Zoom Ektanar C). Each slide contained one horizontal 1.5-mm-wide line, with eight variations of length: 0.52, 1.04, 2.08, 5.2, 10.4, 20.8, 41.6, and 65 cm (ratio of 125:1). The line lengths are in accordance with those utilized in the CMM task described by Hellman and Meiselman (1988).

D. Psychophysical tasks for assessing loudness growth

Validation of the CMM procedure using click stimuli was necessary as previous CMM studies utilized tonal stimuli. As noted by the scaling theory of Stevens (1969), the validity of CMM could be established by demonstrations of a close agreement in the slopes of the measured (geometric mean of absolute magnitude estimation [AME] and production [AMP] of loudness: Indow and Stevens, 1966) and predicted [product of CMM and AME of line length] loudness functions among individuals. Calculation of the exponent of the power function relating loudness in perceived number to sound pressure was possible as both perceived number and loudness were matched to the same continuum of line length. Therefore, it was reasoned that when the slope of the loudness function was unknown, the value could be predicted from the products of the slopes obtained from CMM and AME of line length (Stevens, 1969, 1975). Therefore, four sensation-magnitude functions of AME of line length, AME and AMP of loudness, and CMM between perceived line length and loudness were obtained.

Prior to performing the loudness task, thresholds of audibility and discomfort were measured for each subject using an ascending method of limits. The mean click stimulus threshold was 14 dB for group I (normal hearing), 49.5 dB for group II (flat cochlear hearing loss), and 26.5 dB for group III (sloping cochlear hearing loss). The intensity of uncomfortable loudness was established by asking the subject to indicate the intensity level that could not be tolerated for any length of time (Skinner, 1988), and served as the loudness limit of the testing procedure.

For each of the sensation-magnitude functions, eight stimuli (either line lengths or click intensities) were presented by the examiner to each of the subjects with normal hearing. For subjects with impaired hearing, less than eight intensities were often presented for the tasks that involved loudness judgments (AME L and AMP L), due to the limitations imposed by their thresholds of audibility and/or loudness discomfort. The specific intensity ranges were determined individually based on these threshold limitations.

Stimuli were presented one at a time in a randomized order that differed for each of three separate trials per subject. Therefore, each stimulus was judged three times by each subject. The specific procedures, adapted from Hellman and Meiselman (1988) are described below according to the sequential order of testing (for details see the Appendix).

1. Absolute magnitude estimation of line length (AME LL) and absolute magnitude estimation of loudness (AME L)

Each subject was asked to verbally provide a numerical judgment of the perceived length of each one of the eight projected lines for the AME LL task. For the AME L task, subjects were instructed to provide a numerical judgment of the perceived loudness of each of one presented click-train intensity. Eight separate click-train intensities were judged by the listeners with normal hearing (group I). As noted previously, less than eight auditory stimulus intensities were presented to the subjects with cochlear hearing loss due to threshold limitations imposed by their hearing impairments. For the subjects with a flat configuration of hearing loss (group II), four to six click-train intensities were presented. Six to eight stimulus intensities were presented to the subjects with a sloping configuration of hearing loss (group III).

Based on methods utilized in previous studies (e.g., Hellman and Meiselman, 1988, 1990, 1993; Stevens, 1956, 1969; Zwislocki and Goodman, 1980), subjects were asked to assign an appropriate number (including decimals or fractions) to judge the length of each projected line, or the loudness of each intensity. No reference standard was given, and the subjects were permitted to utilize any number, regardless of the number assigned to the previous stimulus. The listener was able to control the duration of the presentation of each stimulus.

2. Absolute magnitude production of loudness (AMP L)

For this task, each subject was required to produce a loudness to match the subjective magnitude of an assigned number. The numbers consisted of the individually averaged estimations provided by each subject from the procedure of AME L.

The subject was blind to the numerical scale of the ABR attenuator, while exact intensity settings were visible to the examiner. The subject controlled the adjustments of loudness using the attenuator control (up and down arrow keys) on the ABR equipment, which ranged from 0 to 100 dB. Subjects were asked to utilize a bracketing technique to set the loudness of the sounds to settings both above and below the perceived magnitude of the assigned number, and then to an approximate equal-sensation point within these limits. The intensity setting was then recorded by the examiner.

3. Cross-modality matching (CMM) between loudness and line length

Cross-modality matches were obtained between loudness and perceived length. The subjects were asked to adjust the loudness of the click sounds produced by the ABR equipment (intensity range of 0 to 100 dB) until judged to be

subjectively equal to the length of a projected line presented by the examiner. The subject was blind to the numerical scale of the attenuator, while the exact decibel settings were visible to the examiner. The line length stimuli for the CMM task were the same as those used for the task of AME of line length. The intensity judgments were recorded by the experimenter after each presentation.

E. Data analysis

1. Overall analysis

Four sensation-magnitude functions were obtained for every individual subject for each of the series of measurements of AME of line length, AME and AMP of loudness, and CMM. All data were analyzed in accordance with procedures described by Hellman and Meiselman (1988, 1990, 1993). The first trial for each task was considered a preliminary training run, and therefore was not included in the overall analysis. The geometric means of each of the stimulus judgments were computed over the last two trials for the AME procedure of line lengths and loudness. For AMP of loudness and CMM between loudness and perceived length, decibel averages over the last two trials were computed (Stevens, 1975). A geometric mean is an appropriate calculation of the AME of line length and loudness tasks as it accounts for any skewness in the data, particularly since subjects are providing numerical estimates presumably in ratio form (Stevens, 1966). For the AMP L and CMM tasks, the subjects provided loudness adjustments and therefore responses are recorded in decibel units. Thus, the decibel data that are referenced relative to an arbitrary standard become interval data, and an arithmetic mean is the proper average (Stevens, 1955).

2. Slope analysis

a. Normal hearing. Slope values for each of the individual sensation-magnitude functions for the subjects with normal hearing were obtained by linear regressions (SPSS for Windows version 6.0.) utilizing the method of least squares.

b. Cochlear hearing loss. Linear regressions were performed for the slope analysis of individual AME LL functions. However, a different slope analysis of the remaining individual loudness functions of AME and AMP of loudness and CMM for the subjects with cochlear hearing loss was performed. Recently, several studies have utilized polynomial regression analysis to describe the slope of the loudness function for listeners with cochlear hearing loss as linear regression analysis may inaccurately represent the presence of nonlinearities (Hellman and Meiselman, 1990, 1993; Knight and Margolis, 1984). Knight and Margolis (1984), however, noted that the slope estimate obtained with polynomial regression in isolation may not accurately characterize the steep pattern in the loudness growth function that is typically displayed by listeners with cochlear hearing loss. Hellman and Meiselman (1990, 1993) therefore supported the use of polynomial regression in combination with linear regression over the steep, low, or mid-range intensity portion of the loudness function.

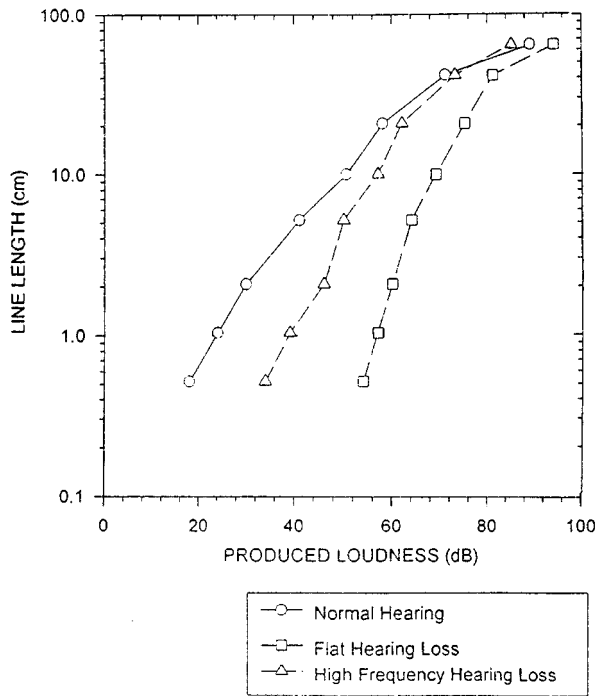


FIG. 1. Group loudness functions obtained with cross-modality matching (CMM) between loudness and perceived line length from listeners with normal hearing, flat and sloping high-frequency configurations of cochlear hearing loss. Each data point represents mean values obtained from ten listeners (see text). Produced loudness is referenced to intensity in dB nHL (re: 25 dB peak equivalent sound pressure level).

The procedures for the slope analysis of individual AME and AMP of loudness and CMM functions were in accordance with those described by Hellman and Meiselman (1990, 1993). Specifically, following a parabolic fit to the data, a localized slope was obtained using linear regression analysis on the partial stimulus range over which the function was linear (SPSS for Windows version 6.0.).

II. RESULTS

A. Group cross-modality matching functions

Figure 1 depicts the averaged data of the loudness functions obtained with CMM by group. Produced loudness in dB (X) is plotted against line length in cm (Y). Each point represents the averaged response for ten listeners. Note that the CMM functions for the groups with cochlear hearing loss are steeper over a wider intensity range than the function for normal hearing (see below).

B. Individual and group exponents

The individual and group exponents for each sensation-magnitude function are described separately for subjects with normal and impaired hearing. The individual measured exponents for loudness were calculated by the geometric mean of the individual exponents obtained for AME and AMP loudness. The individual predicted exponent of loudness was obtained by the product of the individual exponents from AME LL and CMM.

Group exponents were obtained for each sensation-magnitude function by calculating the geometric mean for AME of perceived length and loudness and the arithmetic mean for AMP of loudness and CMM. The group measured loudness exponent was calculated by the geometric mean of the group exponents obtained for AME and AMP of loudness. The predicted loudness exponent for the group was obtained by the product of the exponents from AME LL and CMM.

1. Normal hearing

Table I displays the individual and group exponents for each sensation-magnitude function for subjects with normal hearing (group I). The results suggest that the sensory modality of perceived length is a power function of physical length with a mean exponent of 0.95 (range=0.70 to 1.24). Loudness is a power function of sound pressure with mean

TABLE I. Individual slope values obtained for four sensation-magnitude functions by normal-hearing subjects.^a

Subject	Line length AME LL	Loudness			CMM	Measured (M) (AME LxAMP L)1/2	Predicted(P) (AME LLxCMM)	Deviation (P-M)	Percent deviation
		AME L	AMP L	CMM					
1	0.83	0.55	0.71	0.66	0.63	0.55	-0.08	-12.70	
2	1.09	0.56	0.53	0.61	0.55	0.67	0.12	21.82	
3	0.95	0.62	0.58	0.60	0.61	0.58	-0.03	-4.92	
4	1.01	0.56	0.48	0.64	0.52	0.65	0.13	25.00	
5	0.70	0.63	0.70	0.80	0.67	0.56	-0.11	-16.42	
6	0.80	0.64	0.61	0.73	0.63	0.58	-0.05	-7.94	
7	0.88	0.38	0.58	0.61	0.47	0.54	0.07	14.89	
8	1.07	0.50	0.51	0.72	0.51	0.77	0.26	50.98	
9	1.24	0.37	0.64	0.51	0.49	0.63	0.14	28.57	
10	1.05	0.38	0.80	0.53	0.55	0.54	-0.01	-1.82	
Mean	0.95	0.51	0.61	0.64	0.56	0.61	0.04	9.75	
s.d.	0.15	0.10	0.09	0.09	0.06	0.07	0.11	20.76	

^aNote: Slope values for each of the sensation-magnitude functions were obtained by linear regression analysis; Loudness slopes are referenced in sound pressure; AME LL, AME L, and Measured means are geometric averages (see text for explanation); AME LL=absolute magnitude estimation of line length; AME L=absolute magnitude estimation of loudness; AMP L=absolute magnitude production of loudness; CMM=cross-modality match between loudness and line length; s.d.=standard deviation.

TABLE II. Individual slope values obtained for four sensation-magnitude functions by subjects with flat cochlear hearing loss.^a

Subject	Line length	Loudness		CMM	Measured (M) (AME LxAMP L)1/2	Predicted(P) (AMELLxCMM)	Deviation (P-M)	Percent deviation
	AME LL	AME L	AMP L					
11	0.76	0.70	0.84	1.33	0.77	1.01	0.24	31.17
12	0.97	1.50	2.70	1.70	2.01	1.65	-0.36	-17.91
13	1.08	0.56	1.25	1.64	0.84	1.77	0.93	110.71
14	0.87	1.65	2.68	1.72	2.10	1.50	-0.60	-28.57
15	0.81	0.77	0.92	0.95	0.84	0.77	-0.07	-8.33
16	1.15	0.78	0.72	0.81	0.75	0.93	0.18	24.00
17	0.75	0.96	0.87	1.19	0.91	0.89	-0.02	-02.20
18	0.88	0.92	1.12	1.72	1.02	1.51	0.49	48.04
19	0.67	1.05	1.90	1.94	1.41	1.30	-0.11	-07.80
20	0.91	1.10	1.38	1.68	1.23	1.53	0.30	24.39
Mean	0.87	0.95	1.44	1.47	1.11	1.29	0.99	17.35
s.d.	0.14	0.33	0.70	0.36	0.48	0.34	0.41	38.69

^aNote: Slope values for AME LL were obtained by linear regression analysis; slopes for AME L, AMP L, and CMM were obtained by parabolic fits in combination with linear regression over the steep portion of the curve; loudness curves are referenced in sound pressure; AME LL, AME L, and Measured means are geometric averages (see text for explanation); AME LL=absolute magnitude estimation of line length; AME L=absolute magnitude estimation of loudness; AMP L=absolute magnitude production of loudness; CMM=cross-modality match between loudness and line length; s.d.=standard deviation.

exponents of 0.51 (range=0.37 to 0.64) for AME and 0.61 (range=0.48 to 0.80) for AMP. The cross-modality match between perceived length and loudness is a power function with a mean exponent of 0.64 (range=0.51 to 0.80). For the four functions, the standard deviations (SDs) were 0.15 for AME LL, 0.10 for AME L, and 0.09 for both AMP L and CMM. The median correlation coefficients (*r*) were 0.99 for AME LL and 0.97 for the sensation-magnitude functions of AME L, AMP L and CMM. Individual *r* values ranged from 0.90 to 0.99 for all four functions.

The mean group measured exponent for loudness was 0.56 (s.d.=0.06). The individual measured slopes range from 0.47 to 0.67. The group predicted exponent of loudness was 0.61 slope (s.d.=0.07). Individual predicted exponents

range from 0.54 to 0.77. The deviations of the individual measured from predicted exponents range from -0.11 to 0.26 with a mean deviation of 0.04 (s.d.=0.11). This results in an average 7.1% measured deviation when mean measured and predicted slope values are examined. The high individual and median correlation coefficients demonstrate the excellent approximation of the power function for AME LL, as well as for AME and AMP of loudness and CMM.

2. Cochlear hearing loss

Tables II and III list the individual and mean slope values for each sensation-magnitude function for subjects with a flat or high-frequency sloping configuration of hearing loss,

TABLE III. Individual slope values obtained for four sensation-magnitude functions by subjects with high-frequency cochlear hearing loss.^a

Subject	Line length	Loudness		CMM	Measured (M) (AME LxAMP L)1/2	Predicted(P) (AMELLxCMM)	Deviation (P-M)	Percent deviation
	AME LL	AME L	AMP L					
21	0.85	0.75	1.39	1.33	1.02	1.13	0.11	10.78
22	1.05	0.55	0.84	0.83	0.68	0.87	0.19	27.94
23	0.96	0.60	0.91	0.97	0.74	0.93	0.19	25.68
24	0.73	0.55	1.93	1.39	1.03	1.01	-0.02	-01.94
25	0.80	0.48	0.58	0.95	0.53	0.76	0.23	43.40
26	0.85	1.14	1.76	1.76	1.42	1.50	0.08	05.63
27	0.80	0.57	1.18	0.87	0.82	0.70	-0.12	-14.63
28	0.86	0.42	0.45	0.65	0.43	0.56	0.13	30.23
29	0.80	0.39	0.84	0.97	0.57	0.78	0.21	36.84
30	0.92	0.59	0.52	0.66	0.55	0.61	0.06	10.91
Mean	0.86	0.58	1.04	1.04	0.73	0.88	0.11	17.48
s.d.	0.09	0.20	0.49	0.33	0.29	0.26	0.11	17.39

^aNote: Slope values for AME LL were obtained by linear regression analysis; slopes for AME L, AMP L, and CMM were obtained by parabolic fits in combination with linear regression over the steep portion of the curve; loudness curves are referenced in sound pressure; AME LL, AME L, and Measured means are geometric averages (see text for explanation); AME LL=absolute magnitude estimation of line length; AME L=absolute magnitude estimation of loudness; AMP L=absolute magnitude production of loudness; CMM=cross-modality match between loudness and line length; s.d.=standard deviation.

respectively. The AME LL group mean exponent for subjects with a flat configuration of hearing loss (group II) was 0.87, with individual exponents extending from 0.67 to 1.15 (s.d.=0.14). For the group with sloping high-frequency hearing loss (group III), a 0.86 mean was calculated, and individual slopes range from 0.73 to 1.05 (s.d.=0.09). The individual correlation coefficients were 0.95 or higher for both groups.

a. Group II (flat cochlear hearing loss). For subjects with a flat configuration of hearing loss, the group mean loudness exponents as determined by AME and AMP were respectively 0.95 and 1.44. The individual slope values range from 0.56 to 1.65 for AME L and from 0.72 to 2.70 for AMP L. CMM exponents range from 0.81 to 1.94, with a mean exponent of 1.47. Standard deviations were 0.33 for AME L, 0.70 for AMP L, and 0.36 for CMM.

The individual measured exponents for loudness extended from 0.75 to 2.10 with a group geometric mean of 1.11 (s.d.=0.48). The slope values of the individual predicted exponents of loudness ranged from 0.77 to 1.77 with an average value of 1.29 (s.d.=0.34).

b. Group III (high-frequency cochlear hearing loss).

For subjects with high-frequency sloping hearing loss, individual slope values for AME L ranged from 0.39 to 1.14 with a group geometric mean value of 0.58. A range of 0.45 to 1.93 was calculated for AMP L, yielding an average exponent of 1.04. The analysis of CMM produced individual slope values of 0.65 to 1.76 and a group mean value of 1.04. Standard deviations were 0.20 for AME L, 0.49 for AMP L, and 0.33 for CMM. The group measured exponent was 0.73 (range=0.43 to 1.42; s.d.=0.29). The predicted exponent for the group was 0.88 (range=0.56 to 1.50; s.d.=0.26).¹

C. Validation of cross-modality matching (CMM)

A two-factor with repeated measures analysis of variance (ANOVA) was performed in order to determine whether there were any significant differences between the measured and predicted loudness functions (within-subjects factor= $w1$) among the three test groups of hearing status (normal hearing, flat and sloping high-frequency cochlear hearing loss; between-subjects factor= $w0$). Averaging across groups, the findings indicated that there were no significant differences between the measured and predicted loudness functions ($F=2.86$, $p=0.10$).

Two between-subjects contrasts were generated ($x1$ and $x2$) in order to test for interactions of between and within subjects factors. Specifically, the first contrast ($w1x1$) examined the differential effect of the measured and predicted loudness functions comparing the two hearing-impaired groups (flat and high-frequency cochlear hearing loss). The second contrast ($w1x2$) examined this difference comparing the normal against the two hearing-impaired groups. No significant differences were obtained for either of the interactions ($w1x1: F=0.004$, $p=0.95$; $w1x2: F=0.313$, $p=0.58$). Further, average deviations of measured from predicted exponents of -0.04 and 0.10 were obtained in the normal and hearing-impaired groups, respectively.

D. Effect of the configuration of hearing loss on the loudness-intensity functions

Independent two-sample t -tests assuming equal variance (0.01 level of significance) were performed to determine whether there were any significant differences between the hearing-impaired groups, and for each group when compared to the normal-hearing group. These analyses were performed for both measured and predicted functions.

For the measured loudness functions, significant differences were obtained between the slopes of the groups with flat cochlear hearing loss and normal hearing ($t=3.89$; $p=0.001$). For the predicted loudness functions, significant differences were also obtained between the slopes of the groups with flat cochlear hearing loss and normal hearing ($t=5.89$; $p<0.0001$) and between the high-frequency hearing loss group and normal-hearing group ($t=3.05$; $p=0.007$). No significant differences were noted between the other group comparisons (groups with high-frequency cochlear hearing loss and normal hearing; flat and high-frequency cochlear hearing loss).

III. DISCUSSION

The purpose of this study was to provide information on the utility of clicks for the task of cross-modality matching (CMM) loudness and perceived line length for the assessment of loudness growth as described in recent studies by Hellman and Meiselman (1988, 1990, 1993). An important aspect of this study was to investigate the validity of the CMM task in the prediction of loudness growth using click stimuli. Consistent with Stevens and Greenbaum (1966), AMP generally resulted in steeper functions than AME. No significant differences were obtained between the measured and predicted loudness functions for any of the test groups which were comprised of subjects that exhibited normal hearing, flat, or high-frequency cochlear hearing loss. In addition, the average deviation of the measured from predicted loudness exponents in each of the three test groups was less than 20%. These data support the validity of the CMM task when the stimuli are clicks.

Moreover, the results reveal that the CMM task between loudness and perceived line length is a more precise method of assessing loudness growth in listeners with cochlear hearing loss; better than absolute magnitude estimation and production of loudness techniques. The standard deviations were generally smaller for the predicted than for the measured slope values in both configurations of flat and sloping high-frequency cochlear hearing loss groups. There was essentially no difference in the predicted and measured standard deviation exponent values for the normal-hearing group. The predicted loudness functions for the groups with flat and sloping high-frequency hearing loss are less variable than the measured functions by 29% and 10%, respectively. The greater precision of CMM in estimating the loudness function with clicks is consistent with the findings of Hellman and Meiselman (1993).

A. The loudness function for click stimuli

A second purpose of this study was to provide additional data on loudness functions obtained with clicks. Graphic representation of the group CMM function (Fig. 1) reveals a high-level curvature for the group with normal hearing (group I) unlike the linear CMM functions obtained with tonal stimuli (e.g., Hellman and Meiselman, 1988). This may be explained in two ways. First, it is possible that this effect may have been imposed by the listeners at the maximum intensity level; the subjects may have automatically set the attenuator to its maximum intensity level to match the perceived length of the longest line. Second, the curvature at the highest intensities may have resulted from the broad frequency spectrum of the click stimulus, a similar effect observed in the loudness functions for broadband noise (Scharf and Houtsma, 1986).

The average measured and predicted exponents (slopes) obtained from the normal-hearing group with clicks were 0.56 and 0.61, respectively. Examining other studies of normal listeners that used cross-modality matching or magnitude estimation and production methods with tonal stimuli, these values correspond favorably. The exponents are similar to both the ISO standard loudness exponent of 0.6 (ISO R 131-1959) and the average 0.56 measured/predicted exponents reported by Hellman and Meiselman (1988). In contrast, studies that employed category rating procedures for listeners with normal hearing yielded flatter loudness functions with slopes approximating 0.2 (Ricketts and Bentler, 1996; Robinson and Gatehouse, 1996).

Current data therefore provide further support for the agreement between loudness functions obtained with click and tonal stimuli (Cazals and Stephens, 1975; Geisler *et al.*, 1958). Moreover, the similarity between the loudness exponents yielded in this investigation and from previous studies with normal-hearing listeners suggests that the CMM procedure is a reliable technique for assessing loudness growth.

B. The effect of hearing impairment and configuration of hearing loss on the loudness function

The differentiation of the loudness function obtained from listeners with cochlear hearing loss from those of the subjects with normal hearing would be of clinical value in site-of-lesion assessment. The comparatively different measured/predicted mean slope values among the three test groups suggest that the loudness slopes do vary according to the hearing (loss) configuration. The mean measured/predicted loudness functions obtained with a click stimulus in the hearing impaired groups with sloping high-frequency and flat configurations of hearing loss are approximately one and one half to two times greater than those of the group with normal hearing. Generally lower exponents were calculated for the individual loudness functions in subjects with high-frequency hearing loss (group III) in comparison to the subjects with a flat hearing loss configuration (group II). The mean slope measured/predicted values in group II were 1.5 times greater than those of group III. Furthermore, statistically significant differences between the group mean slopes were found when comparing the measured and predicted ex-

ponents of the subjects with normal hearing to those with flat configuration of hearing loss, and the means of the predicted slopes for high-frequency hearing loss and normal-hearing groups.

The differences in the shape and position of the loudness functions by intensity can also be depicted through graphic representation of the group data obtained from the CMM procedure (Fig. 1). Due to the effect of cochlear hearing loss, the sensation-magnitude functions for the two hearing-impaired groups are steeper and displaced towards higher levels along the intensity axis in comparison to the normal function. The group with flat hearing loss configuration with the poorest mean click threshold, had the steepest and furthest displaced CMM function. At intensity levels approximately 30 dB above the average click threshold in both hearing-impaired groups however, there is a convergence toward the normal function. This is an expected finding at high sound pressure levels for listeners with cochlear hearing loss (Dix *et al.*, 1948; Hellman and Meiselman, 1990, 1993; Moore, 1989; Scharf, 1986).

In addition, the results of this study correspond favorably to recent CMM studies, particularly for the group with a flat configuration of hearing loss (group II). In the current work, the mean slope value of 1.29 for group II lies within ± 1 standard deviation around the mean slope value of 1.2 reported by Hellman and Meiselman (1990) for listeners with 45-dB hearing losses; all of the individual slope values lie within ± 2 standard deviations of this value.

The proximity of the loudness function for the group with sloping impairment (group III) to the function for normal hearing listeners may be explained by the degree of threshold elevations over the tested frequency region. It is possible, for example, that due to the sloping configuration of the impairment that the individual loudness exponents are based primarily on hearing levels at frequencies where thresholds are only slightly elevated.

Hellman and Meiselman (1990) showed that the loudness growth slopes for hearing losses less than 40 dB are similar to those for normal hearing. Recall that for group III, the mean click threshold was approximately 27 dB. Indeed, the majority of these subjects presented with hearing thresholds below 40 dB in the frequency regions over which most of the click-train energy was concentrated. Specifically, eighty percent of the subjects had thresholds better than 40 dB from 250 to 2000 Hz, while 40% of the subjects' thresholds were less than 40 dB at one or more frequencies above 2000 Hz. Similar to the problem of using broadband clicks to estimate audiometric threshold (Stapells *et al.*, 1985), the use of clicks may not be the ideal stimuli for characterizing the rate of loudness growth in specific high-frequency regions of listeners who have sloping high-frequency hearing losses.

C. Clinical application of CMM between loudness and perceived line length

The present study used audiological instrumentation that is commonly available in clinical settings. The CMM task is no more difficult to perform than the present traditional methods of loudness assessment, namely, ABLB, MCL, and UCL tasks. The difficulty with the task may arise in the

computation of the CMM slope value. As noted in the present study, computer analysis and statistical computations were required to derive the slope of the sensation-magnitude functions for hearing-impaired individuals, calculations for which most audiologists and clinics lack the background, time and/or computer support (Knight and Margolis, 1984). A way to circumvent this problem is to abandon the slope value, and examine the CMM loudness function in its entirety over the broad range of intensities. This method may be particularly useful for the fitting of nonlinear amplification devices in hearing-impaired individuals.

IV. CONCLUSION

The CMM task between loudness and perceived line length is a valid, reliable method for predicting the loudness growth function in individuals with either normal or cochlear hearing loss. Moreover, the low variability of the CMM task makes this a viable alternative to the AME and AMP of loudness technique for use with hearing-impaired individuals. In addition, the method of loudness growth assessment via CMM should be easily incorporated into a clinical protocol. The CMM procedure may have applicability for site-of-lesion assessment, and amplification fittings.

ACKNOWLEDGMENTS

This research was funded by a Dean's Grant from Teachers College, Columbia University and the Joanne Schwartz Scholarship. We wish to thank Sigmond K. Schwartz for his support and generosity. We also thank R. Hellman and J. Monroe for their guidance on the statistical analysis of these data. Finally, we are indebted to an anonymous reviewer and particularly R. Hellman for their comments in previous versions of this manuscript.

APPENDIX: INSTRUCTIONS FOR THE PSYCHOACOUSTIC TASKS OF LOUDNESS GROWTH

1. Absolute magnitude estimation of line length (AME LL)

“You are going to view a series of lines of different lengths, one at a time, in random order. Your task is to tell me how long they appear by assigning numbers to them. You may use any positive numbers that appear appropriate to you, whole numbers, decimals, or fractions. Do not worry about running out of numbers; there will always be a smaller number than the smallest you use, and a larger one than the largest you use (note that even between 0 and 1, an infinite range of numbers is possible; repeated use of the same number is acceptable). Do not worry about consistency; just try to assign an appropriate number to each line regardless of the number you may have given to the previous one. You may view the same line as often as you wish before deciding on your number estimate of its length. However, it is best to be as spontaneous and quick in your response as possible. After you have reached a decision, report your judgment. Do you have any questions?”

2. Absolute magnitude estimation of loudness (AME L)

“You are going to hear a series of sounds of different loudnesses, one at a time, in random order. Your task is to tell me how loud they sound by assigning numbers to them. You may use any positive numbers that appear appropriate to you, whole numbers, decimals, or fractions. Do not worry about running out of numbers; there will always be a smaller number than the smallest you use, and a larger one than the largest you use (note that even between 0 and 1, an infinite range of numbers is possible; repeated use of the same number is acceptable). Do not worry about consistency; just try to assign an appropriate number to each loudness regardless of the number you may have given to the previous one. You may listen to the same sound as often as you wish before deciding on your number estimate of its loudness. However, it is best to be as spontaneous and quick in your response as possible. After you have reached a decision, report your judgment. Do you have any questions?”

3. Absolute magnitude production of loudness (AMP L)

“You will be presented with a series of numbers, one at a time, in random order. Your task is to adjust the loudness of the sounds to match your judgment of the size of the assigned number. In order to perform this task, it will be necessary to push the arrow keys in front of you to set an appropriate loudness. When you push the upward arrow key, the loudness will increase. When you push the downward arrow key, the loudness will decrease. Push the arrow keys SLOWLY in order to get an exact setting. First, try to adjust the loudness of the sounds to levels above and below your estimation of the assigned number. Next, attempt to ‘zero’ in on the appropriate setting; that is, bracket the loudness. Press the space bar to turn the signal on and off. After you have reached a decision, keep your final setting intact and turn off the signal. Do you have any questions?”

4. Instructions for cross-modality matching loudness and perceived line length

“You are going to view a series of lines of different lengths, one at a time, in random order. Your task is to make the loudness of the sounds match your judgment of the length of a line you will see projected on the screen. In order to perform this task, it will be necessary to push the arrow keys in front of you to set an appropriate loudness. When you push the upward arrow key, the loudness will increase. When you push the downward arrow key, the loudness will decrease. Push the arrow keys SLOWLY in order to get an exact setting. First, try to adjust the loudness of the sounds to levels *above* and *below* your estimation of the length of the assigned line. Next, attempt to ‘zero’ in on the appropriate setting; that is, bracket the loudness. Press the space bar to turn the signal on and off. After you have reached a decision, keep your final setting intact and turn off the signal. Do you have any questions?” (adapted from Hellman and Meiselman, 1988).

- ¹Though some of the loudness functions for the subjects with cochlear hearing loss appeared linear, parabolic fits were applied as they account for both linear and curvilinear data. The use of a polynomial regression in combination with a linear regression over the steep, low, or mid-range intensity portion of the loudness function, as suggested by Hellman and Meiselman (1990, 1993), accounted for an improvement of 1 to 57% of the total variance versus that of the linear regression in isolation for most subjects in the hearing-impaired groups. This was true for approximately half of the individual sensation-magnitude functions for both hearing-impaired groups.
- ANSI (1977). ANSI S3.1-1977, "American National Standard criteria for permissible ambient noise during audiometric testing" (American National Standards Institute, New York).
- ANSI (1989). ANSI S3.6-1989, "Specifications for audiometers" (American National Standards Institute, New York).
- Brunst, M. A. (1994). "Tests of cochlear function," in *Handbook of Clinical Audiology*, edited by J. Katz (Williams & Wilkins, Baltimore), 4th ed., Chap. 11, pp. 165–175.
- Brunved, P. B. (1994). "How studying loudness growth led to the development of Multifocus," *Hearing Instrum.* **45**, 8–10.
- Cazals, Y., and Stephens, S. D. G. (1975). "The loudness function for click stimuli," *J. Auditory Res.* **15**, 95–105.
- Cefaratti, L. K., and Zwislocki, J. J. (1994). "Relationships between the variability of magnitude matching and the slope of magnitude level functions," *J. Acoust. Soc. Am.* **96**, 126–133.
- Collins, A. A., and Geisheider, G. A. (1989). "The measurement of loudness in individual children and adults by absolute magnitude estimation and cross-modality matching," *J. Acoust. Soc. Am.* **85**, 2012–2021.
- Davidson, S. A., Wall, L. G., and Goodman, C. M. (1990). "Preliminary studies on the use of an ABR amplitude projection procedure for hearing aid selection," *Ear Hear.* **11**, 332–339.
- Dix, M. R., Hallpike, C. S., and Hood, J. D. (1948). "Observations upon the loudness recruitment phenomenon, with especial reference to the differential diagnosis of disorders of the internal ear and VIIIth nerve," *J. Laryngol. Otol.* **62**, 671–686.
- Fabry, D. A., and Schum, D. J. (1994). "The role of subjective measurement selecting and verifying hearing aid fittings," in *Strategies for Selecting and Verifying Hearing Aid Fittings*, edited by M. Valente (Thieme Medical, New York), Chap. 7, pp. 136–155.
- Fowler, E. P. (1936). "Differences in loudness response of the normal and hard-of-hearing ear at intensity levels slightly above the threshold," *Ann. Otol. Rhinol. Laryngol.* **45**, 1029–1039.
- Fowler, E. P. (1937). "The diagnosis of diseases of the neural mechanism of hearing by the aid of sounds well above threshold," *Trans. Am. Otol. Soc.* **27**, 207–219.
- Geisler, C. D., Molnar, C. E., Peake, W. T., Steiberg, C. A., and Weiss, T. F. (1958). "Judgments of the loudness of clicks," Massachusetts Institute of Technology, Research Laboratory of Electronics, Quarterly Progress Report, **50**, 177–184.
- Gelfand, S. A., Schwander, T., and Silman, S. (1990). "Acoustic reflex thresholds in normal and cochlear-impaired ears: effects of no-response rates on 90th percentiles in a large sample," *J. Speech Hear. Disorders* **55**, 198–205.
- Geller, D., and Margolis, R. H. (1984). "Magnitude estimation of loudness I: Application to hearing aid selection," *J. Speech Hear. Res.* **27**, 20–27.
- Gorga, M. P., and Thornton, A. R. (1989). "The choice of stimuli for ABR measurements," *Ear Hear.* **10**, 217–230.
- Hall, J. W. III (1991). "Classic site-of-lesion tests: Foundation of diagnostic audiology," in *Hearing Assessment*, 2nd ed., edited by W. F. Rintelmann (Pro-ed, Austin, TX), Chap. 13, pp. 653–678.
- Hall, J. W. III (1992). *Handbook of Auditory Evoked Responses* (Allyn and Bacon, Needham Heights, MA), Chap. 8, pp. 277–304.
- Hellman, R. P. (1976). "Growth of loudness at 1000 and 3000 Hz," *J. Acoust. Soc. Am.* **60**, 672–679.
- Hellman, R. P. (1981). "Stability of individual loudness functions obtained by magnitude estimation and production," *Percept. Psychophys.* **29**, 63–70.
- Hellman, R. P., and Meiselman, C. H. (1988). "Prediction of individual loudness exponents from cross-modality matching," *J. Speech Hear. Res.* **31**, 605–615.
- Hellman, R. P., and Meiselman, C. H. (1990). "Loudness relations for individuals and groups in normal and impaired hearing," *J. Acoust. Soc. Am.* **88**, 2596–2606.
- Hellman, R. P., and Meiselman, C. H. (1993). "Rate of loudness growth for pure tones in normal and impaired hearing," *J. Acoust. Soc. Am.* **93**, 966–975.
- Indow, T., and Stevens, S. S. (1966). "Scaling of saturation and hue," *Percept. Psychophys.* **1**, 253–272.
- International Organization for Standardization. (1959). *Expression of the physical and subjective magnitudes of sound [ISO/R-131-1959(E)]*. Geneva: International Organization for Standardization.
- Jacobson, J. T. (1994). "Prelude to auditory evoked potentials," in *Principles and Applications in Auditory Evoked Potentials*, edited by J. T. Jacobson (Allyn and Bacon, Needham Heights, MA), Chap. 1, pp. 3–22.
- Knight, K. K., and Margolis, R. (1984). "Magnitude estimation of loudness II: loudness perception in presbycusis listeners," *J. Speech Hear. Res.* **27**, 28–32.
- Margolis, R. H., and Shanks, J. E. (1991). "Tympanometry: Basic principles and clinical applications," in *Hearing Assessment*, edited by W. F. Rintelmann (Pro-ed, Austin, TX), 2nd ed., pp. 179–246.
- Mikami, K. A., Dunckel, D. C., and Whichard, S. P. (1993). *New Dimensions in Diagnostic and Prescriptive Fitting Training Course*. ReSound Corporation.
- Moore, B. C. J. (1989). *An Introduction to the Psychology of Hearing* (Academic, New York), 3rd ed., Chap. 2, pp. 47–83.
- Mueller, H. G., and Bright, K. E. (1994). "Selection and verification of maximum output," in *Strategies for Selecting and Verifying Hearing Aid Fittings*, edited by M. Valente (Thieme Medical, New York), Chap. 3, pp. 38–63.
- Pediatric Working Group Position Statement. (1996). "Amplification for infants and children with hearing loss," in *Amplification for Children with Auditory Deficits*, edited by F. H. Bess, J. S. Gravel, and A. M. Tharpe (Bill Wilkerson Center Press, Nashville, TN), Appendix 1, pp. 399–430.
- Penrod, J. P. (1994). "Speech threshold and word recognition/discrimination testing," in *Handbook of Clinical Audiology*, edited by J. Katz (Williams & Wilkins, Baltimore, MD), 4th ed., Chap. 10, pp. 147–164.
- Peterson, M. E. (1993). "Fitting children with multifocal hearing aids," *Hear. Instrum.* **44**, 33–35.
- Pratt, H., and Sohmer, H. (1977). "Correlations between psychophysical magnitude estimates and simultaneously obtained auditory nerve, brainstem and cortical responses to click stimuli in man," *Electroencephalogr. Clin. Neurophysiol.* **43**, 802–812.
- Raab, D. H., and Osman, E. (1962). "Magnitude estimation of the loudness of clicks," *J. Acoust. Soc. Am.* **34**, 1658.
- Ricketts, T. A., and Bentler, R. A. (1996). "The effect of signal type and bandwidth on the categorical scaling of loudness," *J. Acoust. Soc. Am.* **99**, 2281–2287.
- Robinson, D. W. (1957). "The subjective loudness scale," *Acustica* **7**, 217–233.
- Robinson, K., and Gatehouse, S. (1996). "Test–retest reliability of loudness scaling," *Ear Hear.* **17**, 120–123.
- Scharf, B. (1978). "Loudness," in *Handbook of Perception*, edited by E. C. Carteret and M. P. Friedman (Academic, New York), Vol. IV, pp. 187–234.
- Scharf, B., and Houtsma, A. J. M. (1986). "Loudness, pitch, localization, aural distortion, pathology," in *Handbook of Perception and Human Performance*, edited by K. R. Boff, L. Kaufman, and J. P. Thomas (Academic, New York), Vol. I, Chap. 15, pp. 15.1–15.60.
- Schwartz, D. M., Morris, M. D., and Jacobson, J. T. (1994). "The normal auditory brainstem response and its variants," in *Principles and Applications in Auditory Evoked Potentials*, edited by J. T. Jacobson (Allyn and Bacon, Needham Heights, MA), Chap. 6, pp. 123–154.
- Serpanos, Y., O'Malley, H., and Gravel, J. S. (1997). "The relationship between loudness intensity functions and the click-ABR wave V latency," *Ear Hear.* **18**, 409–419.
- Skinner, M. W. (1988). *Hearing Aid Evaluation* (Prentice-Hall, Engelwood Cliffs, NJ), Chap. 5, pp. 118–148.
- Stapells, D. R., Picton, T. W., Perez-Abalo, M., Read, D., and Smith, A. (1985). "Frequency specificity in evoked potential audiometry," in *The Auditory Brainstem Response*, edited by J. T. Jacobson (College-Hill, San Diego, CA), Chap. 9, pp. 147–180.
- Stevens, S. S. (1955). "The measurement of loudness," *J. Acoust. Soc. Am.* **27**, 815–829.
- Stevens, S. S. (1956). "The direct estimation of sensory magnitudes: Loudness," *Am. J. Psychol.* **69**, 1–25.

- Stevens, S. S. (1959). "On the validity of the loudness scale," *J. Acoust. Soc. Am.* **31**, 995–1003.
- Stevens, S. S. (1966). "A metric for the social consensus," *Science* **151**, 530–541.
- Stevens, S. S. (1969). "On predicting exponents for cross-modality matches," *Percept. Psychophys.* **6**, 251–256.
- Stevens, S. S. (1975). *Psychophysics: Introduction to its Perceptual, Neural, and Social Prospects*, edited by G. Stevens (Wiley, New York), Chap. 4, pp. 99–133.
- Stevens, S. S., and Greenbaum, H. B. (1966). "Regression effect in psychophysical judgment," *Percept. Psychophys.* **1**, 439–446.
- Stevens, J. C., and Guirao, M. (1964). "Individual loudness functions," *J. Acoust. Soc. Am.* **36**, 2210–2213.
- Thalmann, R. (1965). "Cross modality matching in the study of abnormal loudness functions," *Laryngoscope* **75**, 1708–1726.
- Wilber, L. A. (1991). "Pure tone audiometry: Air and bone conduction," in *Hearing Assessment*, 2nd ed., edited by W. F. Rintelmann (Pro-ed, Austin, TX), Chap. 1, pp. 1–38.
- Williams, C. N. (1994). "A 'real life' clinical trial approach opens new avenues of hearing care," *Hear. Instrum.* **45**, 13–15.
- Wilson, R. H., and Margolis, R. H. (1991). "Acoustic-Reflex Measurements," in *Hearing Assessment*, 2nd ed., edited by W. F. Rintelmann (Pro-ed, Austin, TX), Chap. 5, pp. 247–320.
- Wilson, K. G., and Stelmack, R. M. (1982). "Power functions of loudness magnitude estimations and auditory brainstem evoked responses," *Percept. Psychophys.* **31**, 561–565.
- Zwislocki, J. J., and Goodman, D. A. (1980). "Absolute scaling of sensory magnitudes: A validation," *Percept. Psychophys.* **28**, 28–38.

Temporal integration at 6 kHz as a function of masker bandwidth

Andrew J. Oxenham^{a)}

Institute for Perception Research (IPO), P.O. Box 513, 5600 MB Eindhoven, The Netherlands

(Received 14 October 1996; revised 21 August 1997; accepted 26 August 1997)

Thresholds were measured for a 6-kHz sinusoidal signal presented within a 500-ms masker. The masker was either a bandpass Gaussian noise of varying bandwidth, or a sinusoid of the same frequency as the signal. The spectrum level of the noise masker was kept constant at 20 dB SPL, and the level of the sinusoidal masker was 40 dB SPL. Thresholds for signal durations between 2 and 300 ms were measured for masker bandwidths ranging from 60 to 12 000 Hz. The masker was spectrally centered around 6 kHz. For masker bandwidths less than 600 Hz, the slope of the temporal integration function decreased with decreasing masker bandwidth. The results are not consistent with current models of temporal integration or temporal resolution. It is suggested that the results at narrow bandwidths can be understood in terms of changes in the power spectrum of the stimulus *envelope* or modulation spectrum. According to this view, the onset and offset ramps of the signal introduce detectable high-frequency components into the modulation spectrum, which provide a salient cue in narrowband maskers. For broadband maskers, these high-frequency components are masked by the inherent rapid fluctuations in the masker envelope. Additionally, for signal durations between 7 and 80 ms, signal thresholds decreased by up to 5 dB as the masker bandwidth increased from 1200 to 12 000 Hz. The mechanisms underlying this effect are not yet fully understood. © 1998 Acoustical Society of America. [S0001-4966(97)04112-X]

PACS numbers: 43.66.Dc, 43.66.Mk, 43.66.Ba [JWH]

INTRODUCTION

The term temporal integration is often used to describe the way signal thresholds decrease with increasing signal duration. Generally, for a sinusoidal signal in quiet, or in the presence of broadband noise, thresholds decrease by between 8 and 10 dB per decade duration for durations between about 10 and 200 ms (Hughes, 1946; Garner and Miller, 1947; Plomp and Bouman, 1959; Florentine *et al.*, 1988; Gerken *et al.*, 1990).

Most models of temporal integration assume either that the signal intensity is integrated within the auditory system over a duration of around 200–300 ms (Garner and Miller, 1947; Green *et al.*, 1957; Plomp and Bouman, 1959) or that some other transformation of the signal (including compression and/or adaptation) is integrated to give an overall response (Zwislocki, 1960, 1969; Penner, 1978). The signal-to-masker ratio at the output of the integrator is assumed to govern performance. An alternative approach, described by Viemeister and Wakefield (1991), assumes that no such physical integration occurs over durations longer than about 5–10 ms. Instead it is suggested that the auditory system combines information from across independent “multiple looks” at brief segments of a given signal. Nevertheless, for a given segment, it is still assumed that the signal-to-masker ratio provides the relevant decision criterion (although this criterion could be altered without changing the fundamental principle of a multiple-looks hypothesis).

Both types of model (true integration and multiple looks) rely on long- or short-term level cues. This may seem inconsistent with some recent data on the detection of tones gated simultaneously with maskers of equal duration (Kidd *et al.*, 1989; Richards, 1992; Kidd *et al.*, 1993). In these studies, within-channel energy cues were rendered unreliable by roving the overall level of the stimuli. It was shown that the performance of listeners is better than that predicted on the basis of energy cues alone for both narrow- and broadband maskers. In the case of broadband maskers it seems likely that listeners detect a change in the spectral shape of the stimulus by performing a comparison of levels across frequency channels, rather than across trials (e.g., Kidd *et al.*, 1989). For narrowband maskers, other cues, such as changes in the distribution of the envelope or fine structure, probably play a role (Kidd *et al.*, 1989; Richards, 1992; Green *et al.*, 1992; Kidd *et al.*, 1993). Nevertheless, in the case of narrowband maskers, it seems that roving the overall presentation level does produce somewhat higher thresholds than are measured in a constant-level paradigm (e.g., Kidd *et al.*, 1989; Richards, 1992). This may indicate that listeners use level-related cues in most circumstances, and that other cues become dominant only when level cues are no longer reliable.

In most studies of temporal integration, the signal is presented in a longer, or continuous, masker of a constant level. In such situations it is also possible for listeners to detect the signal based on a within-interval *and* within-channel level comparison, by comparing the level of the stimulus before the signal onset with the level within the time period which may contain the signal. Thus, at present the assumption of

^{a)}Present address: Communication Research Laboratory, Department of Speech-Language Pathology and Audiology (133FR), Northeastern University, Boston, MA 02115.

most models of temporal integration, that detection is based on some measure of (integrated) level, seems reasonable for most conditions. Whether levels are compared across trials, across frequency channels, or across time intervals within one trial probably depends on the exact stimulus configuration.

Neither of the integration models mentioned so far predicts an effect of masker bandwidth (BW) on the *slope* of the temporal integration function, as detection is based purely on the signal-to-noise ratio. The prediction of invariant slopes seems to be supported by the two studies that have directly investigated temporal integration as a function of masker BW (Hamilton, 1957; van den Brink, 1964): neither study found that the slope of the integration function varied with masker BW. However, both these early studies used an 800-Hz sinusoidal signal. This frequency may not have been the optimal choice for two reasons. First, this frequency is too low to measure temporal integration at signal durations of less than about 20 ms because the bandwidth of the signal then begins to exceed that of the auditory filter at 800 Hz. For masker BWs narrower than that of the auditory filter, detection may be based on spectral cues associated with the onset and offset of the signal, known as “spectral splatter.” Van den Brink (1964) overcame this problem by filtering both the noise and the signal with a narrow bandpass filter before presentation. However, in this case if the signal bandwidth exceeds the bandwidth of the filter, the temporal characteristics of the signal are affected by the filter, making it difficult to measure true temporal integration. Second, temporal processing is thought to be influenced by the effects of peripheral filtering at frequencies below about 1000 Hz (Moore *et al.*, 1993, 1996). Thus, at 800 Hz the effects of temporal integration, which are thought to be of central origin (Zwislocki, 1960), may be difficult to separate from the influence of peripheral filtering.

In the present study temporal integration was measured as a function of masker BW using a signal frequency of 6 kHz. At this frequency, the equivalent rectangular bandwidth (ERB) of the auditory filter is thought to be about 670 Hz (Glasberg and Moore, 1990), meaning that the bandwidth of even brief signals is less than the ERB. For instance, a Hanning-windowed signal with a half-amplitude duration of only 2 ms has a 3-dB bandwidth of less than 400 Hz. This stimulus configuration therefore enables accurate measurement of temporal integration at much shorter signal durations than was possible in the previous studies using narrowband maskers (Hamilton, 1957; van den Brink, 1964).

I. METHOD

A. Stimuli

The signal was a 6-kHz sinusoid, gated with 2-ms raised-cosine ramps. Thresholds were measured for signal durations of 2, 7, 20, 80, and 300 ms, defined in terms of the half-amplitude duration. The signal was temporally centered around the 300-ms point of a 500-ms masker. The masker was either a band-limited Gaussian noise or a 6-kHz sinusoid. In the latter case, the masker and signal were added in quadrature phase. The BW of the noise masker was varied

between 60 and 12 000 Hz and, unless otherwise stated, was arithmetically centered around 6 kHz. The spectrum level of the noise masker was 20 dB SPL and the level of the sinusoidal masker was 40 dB SPL. As the spectrum level was kept constant, the overall level of the noise masker increased with increasing BW. The possible confounding effect of increasing overall level is addressed in the Discussion and the Appendix. To reduce the possibility of detection of spectral splatter at narrow masker BWs, a background noise with a spectrum level of -5 dB SPL in its passband was gated on and off with the masker. The background noise was broadband (up to 15 kHz) with a spectral notch 1200 Hz wide arithmetically centered around 6 kHz. The masker and background noise were also gated with 2-ms raised-cosine ramps. Both noise stimuli were obtained by generating a 2-s circular buffer of wideband Gaussian noise, performing a discrete Fourier transform, setting the amplitude of the components outside the desired passbands to zero, and applying an inverse Fourier transform. A random starting point within the resulting noise buffers was selected on each presentation interval. All stimuli were generated digitally at a 32-kHz sampling rate, and were played out using the built-in 16-bit D/A converter and reconstruction (antialiasing) filter of a Silicon Graphics workstation. Stimuli were passed through a programmable attenuator (TDT PA4) and a headphone buffer (TDT HB6) before being presented to the left ear of subjects via a Beyer DT990 headset.

B. Procedure

Thresholds were measured using a three-interval forced-choice method with a two-down one-up adaptive procedure, which tracks the 70.7%-correct point of the psychometric function. Each trial consisted of three intervals containing the masker and the background noise. The interstimulus interval was 400 ms. The signal occurred randomly in one of the three intervals and subjects were required to select the signal interval. The signal level was initially adjusted in steps of 8 dB. After every two reversals, the step size was halved until a minimum step size of 2 dB was reached. The run terminated after a further ten reversals. Threshold was defined as the median level at the last ten reversals. For every subject, four such threshold estimates were made for each condition, and the mean and standard deviation of the four estimates were recorded. Subjects were tested in 2-h sessions, including short breaks. Within a session thresholds for up to six different masker BWs were measured. All signal durations for each masker BW were tested contiguously in either ascending (2–300 ms) or descending (300–2 ms) order. The presentation order of the BWs was neither systematic nor completely randomized, but was selected independently for each subject in such a way as to avoid the repetition of a BW within one session. In this way, the four estimates for each data point were collected on four separate days. Responses were made via a computer keyboard, and feedback was provided via a computer monitor. Subjects were tested in a single-walled sound-attenuating chamber, which was situated in a sound-attenuating room.

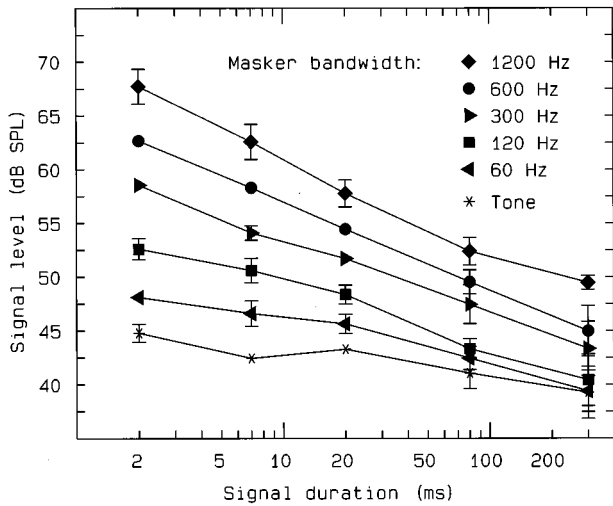


FIG. 1. Signal thresholds as a function of signal duration, with masker bandwidth as the parameter. The signal frequency was 6 kHz and the masker spectrum level was 20 dB SPL (40 dB SPL overall level for the sinusoidal masker). The masker duration was always 500 ms, and the signal was temporally centered around the 300-ms point in the masker. Symbols represent the mean of three subjects. The error bars denote ± 1 standard deviation across the three subjects and are omitted if smaller than the symbol.

C. Subjects

Three subjects took part in the experiment. One subject (the author) had considerable experience in psychoacoustic tasks. The other two were students who had no previous experience in psychoacoustic tasks, and were paid an hourly wage for their participation. All subjects had absolute thresholds of less than 15 dB HL at all octave frequencies between 250 and 8000 Hz, and were given at least 2 h practice before data were collected. No consistent improvements in performance were noted during the course of the experiment; the mean difference between the first and last estimates across all conditions was not significantly different from zero for any of the three subjects.

II. RESULTS

Results across subjects were very similar. Average within-subject standard deviations for each data point were between 1.3 and 1.5 dB for all three subjects. As threshold values were also very similar, only the mean data are shown. Figure 1 shows the data for masker BWs of 1200 Hz and less. Error bars represent ± 1 standard deviation across subjects. The uppermost curve (1200-Hz masker) shows a typical decrease in threshold with increasing signal duration; the difference in threshold between the 2-ms and the 20-ms signal is just under 10 dB, corresponding with previous estimates in quiet and in broadband noise. Reducing the masker BW to 600 Hz produces a decrease in threshold at all durations, resulting in a roughly parallel downwards shift of the integration function. For reductions in masker BW below 300 Hz, however, there is a marked flattening of the integration function, especially for durations of 20 ms and less. For the 60-Hz masker, increasing the signal duration by a factor of 10, from 2 to 20 ms, produces only a 2.5-dB decrease in threshold. For the tonal masker, the difference is even less

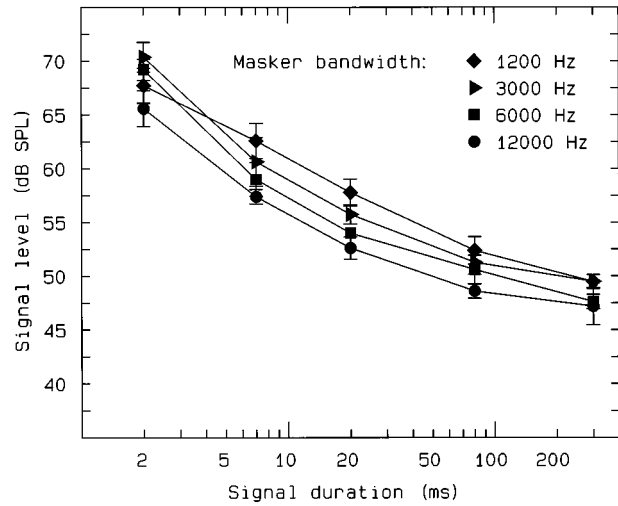


FIG. 2. As in Fig. 1, but for masker bandwidths between 1200 and 12 000 Hz.

(1.5 dB). Thresholds for brief signals at narrow masker BWs are therefore lower than would be predicted based on masker energy. It seems that for narrow masker BWs the slope of the integration function is strongly dependent on masker BW.

Results for the masker BW of 1200 Hz are replotted in Fig. 2, together with the results from the other maskers with BWs greater than the ERB. At the longest signal duration of 300 ms, thresholds are not strongly dependent on masker BW. Taken on their own, the data from the 300-ms signal would probably be interpreted as providing additional support for the idea that thresholds are generally independent of masker BW for BWs beyond the "critical band." At other signal durations the changes with BW are somewhat more marked. For instance, for durations between 7 and 80 ms there is a monotonic decrease in threshold as the BW of the masker increases from 1200 to 12 000 Hz. For the shortest duration, the pattern is again somewhat different, and thresholds seem to reach a maximum for a masker BW of 3000 Hz. Thus, at least for signal durations between 7 and 80 ms, increasing the BW of the masker from 1200 to 12 000 Hz, while keeping the spectrum level constant, resulted in a decrease in thresholds, by as much as 5 dB. This pattern of results was observed for all three subjects. A two-way repeated-measures analysis of variance (ANOVA) was carried out on the results for all signal durations and for BWs of 1200 Hz and greater, in order to assess the significance of the observed changes with BW. The factors were BW and signal duration, and the means of the four threshold estimates for each subject were used as the dependent variable. The main effects of duration and BW were both highly significant [$F(4,8) = 232.6, p < 0.001$ and $F(3,6) = 33.69, p < 0.001$, respectively]. There was also an interaction between BW and duration [$F(12,24) = 4.28, p < 0.005$], reflecting the somewhat different pattern of results at the different signal durations.

In Fig. 3, the data from signal durations of 2, 20, and 300 ms are replotted to show signal level at threshold as a function of masker BW. Consider the data from the 300-ms signal (triangles). Consistent with previous studies, thresh-

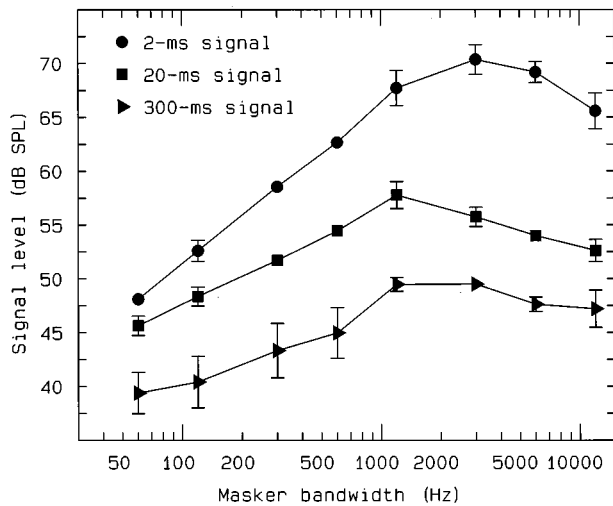


FIG. 3. Data replotted from Figs. 1 and 2, as a function of masker bandwidth, with signal duration as the parameter.

olds increase with increasing masker BW up to a “critical bandwidth” (in this case around 1200 Hz) beyond which the observed change is fairly small. The slope of the function can be measured in terms of signal level (dB) as a function of $10 \log [\text{bandwidth (Hz)}]$. In these units, the slope for BWs between 60 and 1200 Hz is 0.75. This value lies between the slope of unity predicted if only masker power within the critical band is taken into account (Fletcher, 1940) and the slope of 0.5 predicted if performance is limited only by the statistical fluctuations in the level of the noise masker (e.g., Green *et al.*, 1957; Bos and de Boer, 1966). The slope of the mean 20-ms function is 0.92 and so also lies between the predictions from the two models. In contrast, the slope of the 2-ms function is 1.5 and is therefore not in accordance with either model. In analyzing the slopes, it was assumed that there were no significant differences between the subjects, and the three subject thresholds for each condition were treated as three independent estimates of the same variable. Under this assumption a comparison of regression test was performed (Snedecor and Cochran, 1967, p. 432). This confirmed that signal duration had a significant effect on the slope of the function between 60 and 1200 Hz [$F(2,39) = 27.51$, $p < 0.001$]. This effect was due mainly to the 2-ms data, as the slopes from the 20-ms and 300-ms data were not significantly different from each other [$F(1,26) = 2.04$, $p > 0.1$].

Consider next the data for BWs of 1200 Hz and greater. The slope of the function for the 20-ms signal for BWs from 1200 to 12 000 Hz is -0.52 . This is significantly different from zero [$F(1,10) = 62.63$, $p < 0.001$] and confirms that thresholds decrease with increasing BW between 1200 and 12 000 Hz for the 20-ms signal. The slope between 1200 and 12 000 Hz for the 300-ms signal is less steep (-0.26), but is also significantly different from zero [$F(1,10) = 10.95$, $p < 0.01$]. Thus, even in the case of the long-duration signal, the results for a signal frequency of 6 kHz are not consistent with the idea that noise power falling outside the critical band has no effect on threshold (Fletcher, 1940). Thresholds

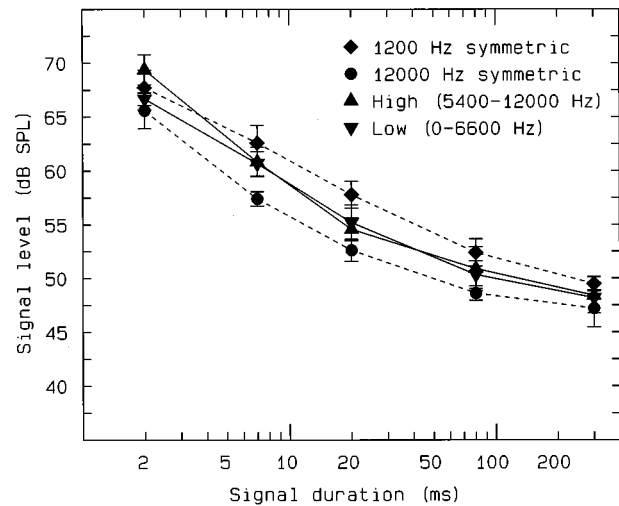


FIG. 4. Additional data using maskers asymmetrically centered around the signal frequency. Symbols joined with solid lines denote signal thresholds in the high-frequency (up-pointing triangles) and low-frequency (down-pointing triangles) asymmetric conditions. Cutoff frequencies for the two maskers are given in the legend. The signal frequency was again 6 kHz, and the masker spectrum level was 20 dB SPL. Data from the 1200-Hz and 12 000-Hz conditions are replotted from Fig. 2.

for the 2-ms signal seem to peak at a masker BW of 3000 Hz and decrease on either side of this.

The difference between the 1200-Hz and the 12 000-Hz conditions is surprising. It seems that adding additional (uncorrelated) noise energy outside the critical band can enhance detection, especially for brief signals. Without yet addressing the underlying mechanisms, the effect could be due to the additional high-frequency masker components, the additional low-frequency components, or a combination of both. In order to narrow the possibilities, two further conditions were tested after the main experiment was completed. All three of the original subjects participated, using the same procedure as in the main experiment. The two additional maskers had BWs of 6600 Hz and were asymmetrically placed around 6 kHz. One had cutoff frequencies of 0 and 6600 Hz (low-frequency condition), and the other had cutoff frequencies of 5400 and 12 000 Hz (high-frequency condition). In this way each masker shared one cutoff frequency with the 1200-Hz masker and one with the 12 000-Hz masker. Results are shown in Fig. 4, together with the replotted results from the 1200-Hz and 12 000-Hz conditions. Both high and low spectral regions seem to contribute about equally to the difference in threshold between the 1200-Hz and the 12 000-Hz conditions at all signal durations except 2 ms. Thus, neither the high- nor the low-frequency portion of the 12 000-Hz masker is solely responsible for the decrease in thresholds.

III. DISCUSSION

A. Masker bandwidths less than 1200 Hz: Role of envelope fluctuations

The main finding of this study is that the slope of the integration function at 6 kHz is strongly dependent on masker BW, for BWs less than 600 Hz. These data cannot be

accounted for by traditional energy detection (integration) models. For instance, in the case of the sinusoidal masker, a more than tenfold increase in signal energy, as the duration is increased from 2 to 20 ms, leads to only a 1.5-dB decrease in threshold. The simplest explanation for the lack of observed integration would be that, at narrow masker BWs, subjects were able to detect the spread of energy into remote spectral regions due to the onset and offset of the signal. A second possibility, mentioned in the Method section, is related to the fact that the overall masker power decreases with decreasing BW. Oxenham *et al.* (1997) recently measured thresholds for a 6.5-kHz sinusoidal signal in a broadband-noise masker. They found that the slope of the temporal integration function at a masker spectrum level of 20 dB SPL was steeper than at masker levels of -10 and 50 dB by a factor of nearly 2. It could therefore be that the decrease in slope with decreasing masker BW is simply due to the decrease in overall masker power. Both these possibilities are examined in the Appendix, and it is concluded that neither can account for the effect. Thus, another explanation is required.

Martens (1982) and Green *et al.* (1992) have proposed that the auditory system is capable of analyzing the power spectrum of the linear envelope, referred to here as the modulation spectrum. The concept of modulation-spectrum analysis is consistent with studies of modulation masking, which have indicated that something analogous to spectral masking occurs in the modulation-spectrum domain (Bacon and Grantham, 1989; Houtgast, 1989). Dau and colleagues have incorporated this concept within a model of auditory processing using a modulation filterbank. Their model can account well for a range of psychoacoustic data on modulation detection and masking (Dau *et al.*, 1996, 1997a,b). So far, such models have been used mainly to account for the detection of steady-state stimuli. It is proposed here that a similar mechanism may account for why brief signals are more easily detectable in narrowband noise than in wideband noise. In the present experiment, the rapid onset and offset of the signal introduce high-frequency components into the modulation spectrum of the stimulus. This could mean that short-duration signals in narrowband maskers are detected by virtue of the high-frequency modulation energy introduced by the ramps. This modulation energy may be resolved from the lower-frequency modulation energy of the narrowband maskers. For broadband maskers, this cue may be masked by the inherent rapid fluctuations of the noise. Subjects may then be forced to rely on the overall increase in stimulus energy due to the addition of the signal. Some simulations are presented in Sec. IV to illustrate how such a scheme might account for the data.

B. Masker bandwidths of 1200 Hz and greater

Increases of masker BW beyond 1200 Hz tended to produce a decrease in thresholds, especially for signal durations between 7 and 80 ms. It is not clear what mechanism could underlie this result, although it should be noted that a similar finding was observed by Bacon and Smith (1991) using a 10-ms, 4-kHz signal. Their Fig. 1 shows that mean thresholds for the signal temporally centered in the noise also decrease by about 2.5 dB for BWs beyond the critical band. A

similar trend can be seen in the data of Wright (1997). Mean thresholds shown in her Fig. 3 for a 20-ms (noise) signal centered around 2500 Hz, temporally centered in a noise masker, also decreased by about 2 dB as the masker BW was increased from 1000 to 8000 Hz.

It is possible that some kind of profile analysis, or spectral shape discrimination, improves performance as the noise covers more peripheral frequency channels (Green, 1988). This interpretation would argue for the importance of across-channel comparisons in detecting a tone in a wideband noise (e.g., Kidd and Dai, 1993). Also, the fact that both low- and high-frequency noise components contribute to the effect is at least qualitatively consistent with this hypothesis. Even so, it is not immediately clear why profile analysis should be most effective for short signal durations. One possibility is that at short signal durations, performance becomes increasingly limited by the trial-to-trial variability of the noise-masker level. In such cases, combining information about the level of the masker across adjacent (independent) frequency channels may improve performance. In the case of long-duration signals, performance may be limited more by “internal” variability, or internal noise. If a dominant proportion of such noise is added after information from different channels is combined, then additional masker energy in adjacent frequency channels would not improve performance.

IV. SIMULATIONS USING ENVELOPE CUES

In the previous section it was postulated that at narrow masker BWs the detection of brief signals is achieved by virtue of the high modulation frequencies introduced by the onset and offset ramps of the signal. To illustrate this, some simulations were carried out using masker BWs of 60 and 600 Hz. Predictions using a simple weighted intensity-summation (energy) model were compared with those of a model using only information from high modulation frequencies (modulation-filter model). It is assumed that only envelope information, and not fine structure, is available at 6 kHz. This is in accordance with physiological results showing that fine-structure information is not coded at frequencies above 4–5 kHz (Rose *et al.*, 1968). Also, the effects of peripheral filtering are not incorporated as the BWs of both the maskers and the signal were less than the estimated BW of the auditory filter at 6 kHz.

A. Description of the models

The task of resolving rapid from less rapid envelope fluctuations can be achieved with a simple bandpass filter in the modulation domain. This filter could be implemented in a number of different ways. For the purposes of illustration, spectral analysis is used here, although similar results could be achieved using a time-domain representation, as discussed in Sec. IV E.

In the present simulations, the selected cutoff frequencies for the modulation filter were based on the following considerations. In a recent study of sinusoidal amplitude-modulation detection using sinusoidal carriers, Fassel and Kohlrausch (1995) found that at carrier frequencies of 5 kHz and above, thresholds remained roughly constant up to modulation frequencies of around 150 Hz. Beyond 150 Hz

thresholds increased sharply before finally decreasing as the sidebands became spectrally resolved. Based on this, it is assumed that the auditory system is equally sensitive to all modulation frequencies up to around 150 Hz at 6 kHz. This value provided the upper cutoff frequency for the model. The lower cutoff frequency of 80 Hz was chosen so that the overall bandwidth (70 Hz) was approximately in line with estimates of modulation-filter bandwidth derived from simulations of modulation detection and masking data (Dau *et al.*, 1997a).

The modulation-filter model was constructed as follows. The Hilbert envelope of each stimulus was calculated, and the magnitude spectrum of the resulting envelope was extracted using a FFT. All the amplitude components were normalized with respect to the 0-Hz component, making the model level-independent for a given stimulus. Then, the rms value of the spectral components between 80 and 150 Hz was calculated and used as the decision criterion. Finally, a normally distributed (Gaussian) random variable was added to the rms value to simulate “absolute threshold” for the detection of high modulation frequencies. The mean of the variable was zero and its variance was set such that the model correctly predicted thresholds for the 2-ms signal in the presence of the tonal masker. In this case, no high modulation frequencies are present in the masking stimulus, and so thresholds are assumed to be limited by internal noise alone.

The following considerations were made for the energy model. It has been shown that it is possible to construct an intensity integration weighting function that will predict any desired (straight-line) integration function with a slope between 0 and -1 (Penner, 1978). The same is true of the multiple-looks theory: it is possible to select an arbitrary set of weights for successive looks, such that any slope between 0 and -1 can be predicted. Both schemes are, however, independent of masker BW. A slope of -0.8 was selected to provide a good fit to the data for masker BWs of 600 Hz and greater. The value of -0.8 is also in good agreement with previous estimates of temporal integration at high signal frequencies (e.g., Florentine *et al.*, 1988; Gerken *et al.*, 1990).¹ The predictions for the 600-Hz masker are 5 dB higher than those for the 60-Hz masker at a given signal duration. This relationship is provided by a model which takes into account trial-to-trial variations in overall masker level (Green *et al.*, 1957; Bos and de Boer, 1966). The absolute levels of the energy-model predictions were selected to provide a good (visual) fit to the 600-Hz data.

B. Description of the simulation procedure

The simulations for the modulation-filter model were run for masker BWs of 60 and 600 Hz, using the same three-interval adaptive procedure as was used in the experiment. The stimuli were also generated and controlled in the same way as in the experiment with the following exception: the noise maskers were generated by constructing a new 512-ms circular buffer of random Gaussian noise for each test interval. The duration was 512 ms, instead of 500 ms, so that the number of samples was a power of 2, making the FFT more efficient. The use of a circular buffer meant that no high

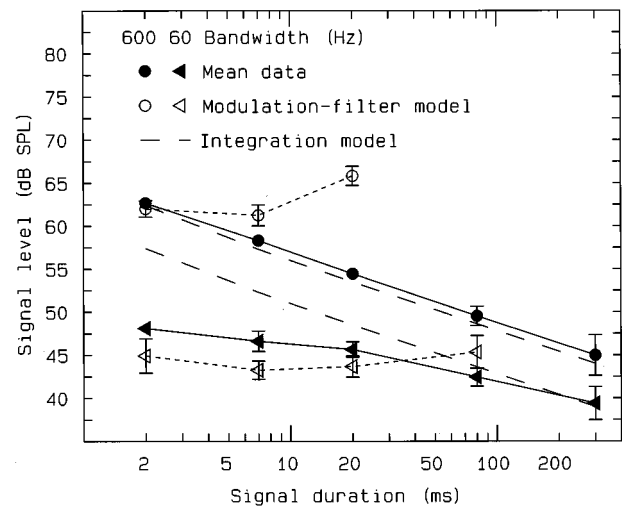


FIG. 5. Predictions using the modulation-filter model (open symbols), together with data replotted from Fig. 1 (filled symbols) for the 60-Hz (triangles) and 600-Hz (circles) conditions. Error bars for the simulations represent ± 1 standard deviation across the 12 estimates for each point. Error bars for the data represent ± 1 standard deviation across the three subjects. The long-dashed lines indicate a decrease in threshold of 8 dB per decade duration.

modulation frequencies were introduced by the onset and offset of the masker, which were instantaneous.

For each trial, three intervals were generated, all containing the masker and one containing the signal. The interval with the largest value for the decision variable was selected by the model. If this interval contained the signal, the answer was deemed “correct,” otherwise it was deemed incorrect and the signal level was increased.

Simulations were also carried out using the sinusoidal masker for the purpose of determining the correct variance of the Gaussian random variable, added to the decision variable of the modulation-filter model. After these values had been determined, simulations were performed with masker BWs of 60 and 600 Hz at all the signal durations tested in the experiment. Each condition was run 12 times through the model, and the means and standard deviations of the predicted thresholds are reported.

C. Model predictions

Predictions from both the energy model (dashed lines) and the modulation-filter model (open symbols) are shown in Fig. 5 together with the mean data replotted from Fig. 1 for the 60-Hz and 600-Hz conditions (filled triangles and circles, respectively). Consider first predictions from the energy model (dashed lines). As expected, this model provides a very good fit to the 600-Hz data (upper dashed line), but not to the 60-Hz data (lower dashed line).

Consider next the predictions of the modulation-filter model (open symbols). These are fairly independent of signal duration up to at least 80 ms at 60 Hz, and at least 20 ms at 600 Hz. Beyond these durations the predictions are not shown as they increase to levels which, in most cases, are undefined. This is because, as the signal duration becomes a significant fraction of the duration of the analysis window, the relative amount of high-frequency modulation energy ac-

tually *decreases* with the addition of the signal, due to the signal's steady-state portion. Thus, for long signal durations, the model consistently selects a nonsignal interval. In such cases, a more suitable criterion would be a reduction in high-frequency modulation energy.

The predictions match the 60-Hz data reasonably well for signal durations up to 20 ms. Note that the predicted thresholds could be increased to match the data better simply by adding an additional internal noise to represent coding inaccuracy in the auditory system. The 600-Hz data are not well described by the predictions of the modulation-filter model; in this condition the energy model provides a better description over the entire range of signal durations.

A number of recent studies have shown that it may be important to take account of peripheral auditory compression when modeling certain psychophysical data (e.g., Oxenham and Moore, 1994, 1995; Moore and Jorasz, 1996; Oxenham and Plack, 1997). Compressing the envelope of a stimulus introduces distortion products into the spectrum that may change the predictions of the model presented here. In order to evaluate the effect of compression, all simulations were repeated with the envelope raised to the power 0.4. This is equivalent to processing intensity raised to the power of 0.2 and is in line with psychophysical estimates of the effective amount of compression (e.g., Oxenham and Moore, 1995). It was found that compression had the effect of raising thresholds by approximately 5 dB for both masker BWs and for all signal durations tested. The pattern of results was, therefore, not affected by the introduction of compression.

In summary, it seems that energy detection provides a reasonable criterion for all signal durations in wideband noise, and for long-duration signals in narrowband noise. For brief signals in narrowband noise, more information may be gained from monitoring increases in high-frequency modulation energy, due to the onset and offset of the signal.

D. Implications for models of temporal resolution

As discussed above, the results from the narrowest BWs cannot be accounted for by current models of temporal integration. Furthermore, current models of temporal *resolution* have time constants which are too long to account for the shallow integration function at the narrowest masker BWs, as shown below.

Two models of temporal resolution were used to predict thresholds at short signal durations in the 60-Hz condition. The first, termed the "lowpass-filter model," is a variant of a model proposed by Viemeister (1979) and adapted by Forrest and Green (1987). In the version used by Forrest and Green (1987), the model comprises an initial bandpass filter with a BW of 4000 Hz, followed by a half-wave rectifier and a first-order lowpass filter with a cutoff frequency of 53 Hz (3-ms time constant). This model has been used to account for amplitude-modulation detection and gap detection in broadband noise. The time constant of the lowpass filter is about two orders of magnitude smaller than that proposed to account for temporal integration (e.g., Plomp and Bouman, 1959). The decision device used by Forrest and Green (1987) was the ratio of the maximum to the minimum instantaneous output of the lowpass filter within one interval (max/min

decision device). This decision device was also used in the present simulations: the interval with the largest ratio was selected by the model. No initial bandpass filter was used as all the stimuli were well within the bandpass region of the 4000-Hz-wide filter proposed by Forrest and Green (1987).

The second model is known as the "temporal-window model." It has been used to account for the decay of forward and backward masking (Moore *et al.*, 1988; Plack and Moore, 1990), the additivity of nonsimultaneous masking (Oxenham and Moore, 1994), and decrement detection (e.g., Plack and Moore, 1991; Peters *et al.*, 1995). The temporal-window model comprises a bandpass filter representing peripheral auditory filtering, a rectifying nonlinearity (often including compression), and a sliding temporal integrator or temporal window. The window is assumed to have a double-sided exponential or rounded exponential form (see, e.g., Moore *et al.*, 1996, for further details). In this model, the random fluctuations of noise maskers are generally ignored, and only the expected noise power within one auditory filter is taken into account.

In the present implementation of the temporal-window model, the initial bandpass filter was again omitted because both the signal and the masker fell within the estimated BW of the auditory filter at 6 kHz. The rectified stimuli were raised to the power 0.7 and passed through a sliding temporal integrator consisting of two back-to-back exponential functions, as done previously by Peters *et al.* (1995) and Moore *et al.* (1996). The equivalent rectangular duration (ERD; see Peters *et al.*, 1995) of the window was set to 9.5 ms. This value corresponds closely to values derived for both decrement detection and forward and backward masking at high (≥ 4 kHz) signal frequencies (Oxenham and Moore, 1994; Peters *et al.*, 1995). The decision device was based on the ratio between the steady-state output of the temporal window in the presence of the masker alone and the maximum output due to the signal and masker together. A constant criterion ratio was selected in these simulations so as to minimize the squared error between the predictions and the mean data for signal durations between 2 and 20 ms.

Thresholds were predicted for signal durations between 2 and 20 ms in the presence of the 60-Hz-wide noise masker. For the lowpass-filter model, simulations were run as they were for the modulation-filter model: 12 estimates were made for each reported data point. Predictions for the temporal-window model, on the other hand, are deterministic, meaning that the adaptive threshold procedure was not necessary. Because of this, a number of additional predicted threshold values were obtained for intermediate durations, in order to define a fairly smooth curve for the temporal-window predictions.

The predictions of both models are shown in Fig. 6, together with the mean experimental data in the 60-Hz condition, for signal durations between 2 and 20 ms. Error bars for the lowpass-filter model (open triangles) represent ± 1 standard deviation across the 12 estimates. Both models show a stronger dependence on signal duration than is observed in the data (filled triangles), although the discrepancy is greater for the temporal-window model (dashed line). The predictions of the lowpass-filter model consistently lie above

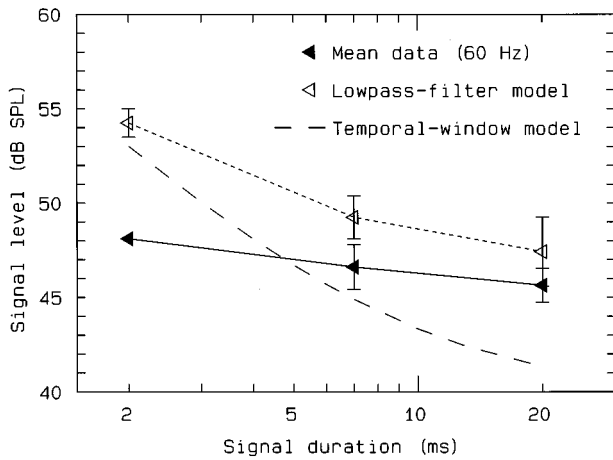


FIG. 6. Predictions for the 60-Hz condition using two models of temporal resolution. Predictions of the lowpass-filter model of Forrest and Green (1987) are shown as open symbols and predictions of the temporal-window model (e.g., Moore *et al.*, 1988) are shown as a long-dashed curve. Mean data (filled symbols) are replotted from Fig. 1.

the data. As no “internal” noise was used in the simulations, it would not be possible for the predictions to match the data more closely without altering the processing or the decision device.

Finally, the predictions of both models show no dependence on masker BW, other than a parallel upward shift in thresholds as the masker energy increases (not shown here). As a result, the temporal-window model provides a better fit to the data from the wideband conditions shown in Fig. 2 than does the lowpass-filter model. In summary, neither models of temporal integration nor models of temporal resolution can account for the shallower integration functions at the narrowest BWs.

E. Concluding remarks

The simulations presented here indicate that the data can be understood if it is assumed that at least two distinct cues are used by the auditory system for the detection of tones in masking noise. The first, and more general, is probably based on a transform of overall signal energy, represented by the dashed lines in Fig. 5. The second may be based on high-frequency modulation energy introduced by the onset and offset of a brief signal. Subjects probably base their judgments on whichever cue produces the lowest thresholds in a given condition. Note that the integration mechanism could be implemented as a lowpass filter within a modulation filterbank, meaning that both types of cue would be incorporated within the same overall structure (see Dau *et al.*, 1996).

The modulation-filter model presented here was designed purely for illustrative purposes. The goal was to show that modulation-frequency analysis could provide an explanation for the data at narrow masker BWs, rather than to present any definitive implementation. As mentioned above, the maskers in the simulations were generated in circular buffers to avoid the introduction of high modulation frequencies due to the maskers’ onset and offset. This could also have been achieved by using an analysis window with ramps of long duration. If the modulation-filter model as imple-

mented here were taken literally, it would imply that the auditory system has a necessarily long time window over which the modulation spectrum is analyzed. Such an assumption could be easily tested by repeating the narrow BW conditions and introducing, for instance, brief gaps in the masker at times before and after the signal. So long as the gaps occurred within the analysis time-window, the high-frequency modulation energy introduced by the gaps should impair performance. The same impairment would not be expected for wider masker BWs.

Another, perhaps more realistic, method of implementing modulation-frequency analysis would not require such a long analysis window: the modulation filters could be implemented in the time domain, and decisions could be based on maximum short-term peaks in the output of such filters around the expected time of the signal, rather than on the summed output over the whole stimulus interval. The response due to the signal onset would be broadly independent of signal duration. Thus, this type of model would also have the advantage of being able to produce threshold predictions for long-duration signals, which the present modulation-filter model was not able to do.

Finally, analysis in terms of the modulation spectrum may offer a new approach to dealing with detection in situations where “qualitative” similarities between masker and signal are thought to play a role. For instance, in forward masking, thresholds for a tonal signal following a narrow-band noise can be affected by signal duration and noise BW in ways that are not predicted by any current models using level cues (e.g., Moore and Glasberg, 1982; Neff, 1985): generally, if the signal is in the same spectral region as the masker, and if the temporal envelope of the signal is similar to a single fluctuation in the masker envelope, thresholds are higher than if some extra cue is available to distinguish the signal from the masker. As discussed by Neff (1985), this effect has been ascribed to a lack of “quality-difference cues” (Weber and Moore, 1981), and the inability to distinguish masker from signal has been referred to as “confusion” (Neff and Jesteadt, 1983). Such confusion may be described by similarities between masker and signal in the modulation spectrum. Thus, using an analysis in the modulation frequency domain may provide a way to quantify such confusion effects, which have so far been described in qualitative terms only.

V. SUMMARY

For a 6-kHz sinusoidal signal, gated with 2-ms raised-cosine ramps, the slope of the integration function is strongly dependent on masker bandwidth below about 600 Hz. The mean difference in threshold between a 2-ms and a 20-ms signal was 8.2 dB for a 600-Hz masker bandwidth, but only 2.5 dB for a 60-Hz masker bandwidth. The results are not consistent with any current model of temporal integration. The lack of dependence of signal threshold on duration for the narrowest masker bandwidths is also not consistent with models of temporal resolution. However, the results can be understood if it is assumed that the auditory system is sensitive to changes in the modulation spectrum, or the power spectrum of the envelope. In this way, the rapid fluctuations

introduced by the onset and offset of the signal may be resolved from the slower fluctuations of the narrowband noise. For wideband noise, the inherent rapid fluctuations of the noise may mask those of the signal's onset and offset, forcing subjects to rely on overall energy cues. A further effect was found for wider masker bandwidths: for signal durations between 7 and 80 ms, thresholds decreased by as much as 5 dB as the masker bandwidth was increased from 1200 and 12 000 Hz. The mechanisms underlying this effect are not fully understood.

ACKNOWLEDGMENTS

This work was supported by a Wellcome Trust Traveling Research Fellowship (0044215/Z/95/Z). I thank Torsten Dau for many stimulating discussions. Steven van de Par, Reinier Kortekaas, Armin Kohlrausch, and two reviewers provided helpful comments on an earlier version of this paper.

APPENDIX: POSSIBLE CONFOUNDING FACTORS

The experimental findings reported here suggest that the slope of the temporal integration function at 6 kHz decreases with decreasing masker BW below about 600 Hz. The simplest explanation of this finding would be that subjects are able to detect the spectral spread of energy associated with the onset and offset of the signal at very narrow masker BWs. In this case, as long as the overall energy cue remained less salient than the splatter, no decrease in threshold with duration would be expected. However, as mentioned in the Introduction, the use of a high-frequency signal and the addition of a background noise should have eliminated any possible spectral cues. The mean threshold (across the three subjects) for the 2-ms signal in the presence of the notched noise alone was 29 dB SPL. As this is only 16 and 19.2 dB below the threshold in the presence of the tonal and 60-Hz masker, respectively, it is unlikely that low-level splatter would be detectable. Nevertheless, if performance were dependent on splatter remote from the signal frequency, thresholds would be determined by the masked threshold of the splatter in the background noise. Thus, thresholds should be dependent on the level of the background noise. If splatter were not detectable, and performance were determined by within-channel processes, then the level of the background noise should have little effect on thresholds, so long as the level is not so high as to cause within-channel masking. This was tested by measuring thresholds for the 2-ms signal in the presence of the 60-Hz-wide masker, with the background noise either 5 dB higher or lower in level than in the original experiment. It was found that changing the level of the background noise over a range of 10 dB had no significant effect on masked thresholds: the mean thresholds of the three subjects for background-noise spectrum levels of -10 , -5 , and 0 dB were 48.6, 48.1, and 49.0 dB SPL, respectively. It therefore appears that detection in narrowband noise was not mediated by spectral splatter.

A second possibility is that the decrease in the slope of the integration function is mediated by the decrease in the overall level of the masker, as the BW is reduced. However,

the change in level between the 600-Hz masker and the 60-Hz masker is only 10 dB. Oxenham *et al.* (1997) found that for a broadband noise carrier the slope of the integration function at 6.5 kHz decreased by a factor of nearly 2 as the masker spectrum level was decreased by 30 dB, from 20 to -10 dB SPL. In the present study, the slope of the mean data decreased by a factor of more than 3 as the overall level was changed by only 10 dB. The effect found by Oxenham *et al.* (1997) was therefore much smaller than that observed here. Nevertheless, the possibility that overall masker level was the dominant variable was tested directly using one subject (AO): thresholds in the presence of the 60-Hz masker were measured using a masker level 10 dB higher than in the original experiment, providing the same overall level as the original 600-Hz masker. Except for a 10-dB overall increase in thresholds, the pattern of results remained essentially the same at the higher level. For durations between 2 and 20 ms, the slope of the integration function was -0.28 at 20 dB and -0.3 at 30 dB. This difference was not significant [$F(1,20) = 0.01$, $p > 0.5$].

In summary, it appears that neither spectral splatter nor the change in overall level can account for the dependence of the slope of the integration function on masker BW.

¹For the energy-model predictions, the equivalent rectangular duration (in terms of energy) of each signal duration was used. The equivalent rectangular duration of a raised-cosine ramp of duration t is $3t/8$ (Dallos and Olsen, 1964).

- Bacon, S. P., and Grantham, D. W. (1989). "Modulation masking: Effects of modulation frequency, depth and phase," *J. Acoust. Soc. Am.* **85**, 2575–2580.
- Bacon, S. P., and Smith, M. A. (1991). "Spectral, intensive, and temporal factors influencing overshoot," *Q. J. Exp. Psychol.* **43A**, 373–400.
- Bos, C. E., and de Boer, E. (1966). "Masking and discrimination," *J. Acoust. Soc. Am.* **39**, 708–715.
- Dallos, P. J., and Olsen, W. O. (1964). "Integration of energy at threshold with gradual rise-fall tone pips," *J. Acoust. Soc. Am.* **36**, 743–751.
- Dau, T., Kollmeier, B., and Kohlrausch, A. (1996). "Modeling modulation perception: Modulation low-pass filter or modulation filterbank?" in *Psychoacoustics, Speech and Hearing Aids*, edited by B. Kollmeier (World Scientific, Singapore), pp. 45–48.
- Dau, T., Kollmeier, B., and Kohlrausch, A. (1997a). "Modeling auditory processing of amplitude modulation. I. Detection and masking with narrowband carriers," *J. Acoust. Soc. Am.* **102**, 2892–2905.
- Dau, T., Kollmeier, B., and Kohlrausch, A. (1997b). "Modeling auditory processing of amplitude modulation. II. Spectral and temporal integration," *J. Acoust. Soc. Am.* **102**, 2906–2919.
- Fassel, R., and Kohlrausch, A. (1995). "Modulation detection as a function of carrier frequency and level," in *IPO Annual Progress Report 30*, edited by M. D. Brouwer-Janse, D. J. Hermes, W. M. C. J. van Overveld, and H. de Ridder (IPO, Eindhoven).
- Fletcher, H. (1940). "Auditory patterns," *Rev. Mod. Phys.* **12**, 47–65.
- Florentine, M., Fastl, H., and Buus, S. (1988). "Temporal integration in normal hearing, cochlear impairment, and impairment simulated by masking," *J. Acoust. Soc. Am.* **84**, 195–203.
- Forrest, T. G., and Green, D. M. (1987). "Detection of partially filled gaps in noise and the temporal modulation transfer function," *J. Acoust. Soc. Am.* **82**, 1933–1943.
- Garner, W. R., and Miller, G. A. (1947). "The masked threshold of pure tones as a function of duration," *J. Exp. Psychol.* **37**, 293–303.
- Gerken, G. M., Bhat, V. K. H., and Hutchinson-Clutter, M. (1990). "Auditory temporal integration and the power function model," *J. Acoust. Soc. Am.* **88**, 767–778.
- Glasberg, B. R., and Moore, B. C. J. (1990). "Derivation of auditory filter shapes from notched-noise data," *Hearing Res.* **47**, 103–138.
- Green, D. M. (1988). *Profile Analysis* (Oxford U.P., Oxford).

- Green, D. M., Berg, B. G., Dai, H., Eddins, D. A., Onsan, Z., and Nguyen, Q. (1992). "Spectral shape discrimination of narrow-band sounds," *J. Acoust. Soc. Am.* **92**, 2586–2597.
- Green, D. M., Birdsall, T. G., and Tanner, W. P. (1957). "Signal detection as a function of signal intensity and duration," *J. Acoust. Soc. Am.* **29**, 523–531.
- Hamilton, P. M. (1957). "Noise masked thresholds as a function of tonal duration and masking noise bandwidth," *J. Acoust. Soc. Am.* **29**, 506–511.
- Houtgast, T. (1989). "Frequency selectivity in amplitude-modulation detection," *J. Acoust. Soc. Am.* **85**, 1676–1680.
- Hughes, J. W. (1946). "The threshold of audition for short periods of stimulation," *Proc. R. Soc. London, Ser. B* **133**, 486–490.
- Kidd, G., and Dai, H. (1993). "A composite randomization procedure for measuring spectral shape discrimination," *J. Acoust. Soc. Am.* **94**, 1275–1280.
- Kidd, G., Mason, C. R., Brantley, M. A., and Owen, G. A. (1989). "Roving-level tone-in-noise detection," *J. Acoust. Soc. Am.* **86**, 1310–1317.
- Kidd, G., Uchanski, R. M., Mason, C. R., and Deliwala, P. S. (1993). "Discriminability of narrow-band sounds in the absence of level cues," *J. Acoust. Soc. Am.* **93**, 1028–1037.
- Martens, J.-P. (1982). "A new theory for multi-tone masking," *J. Acoust. Soc. Am.* **72**, 397–405.
- Moore, B. C. J., and Glasberg, B. R. (1982). "Contralateral and ipsilateral cueing in forward masking," *J. Acoust. Soc. Am.* **71**, 942–945.
- Moore, B. C. J., and Jorasz, U. (1996). "Modulation discrimination interference and comodulation masking release as a function of the number and spectral placement of narrow-band noise modulators," *J. Acoust. Soc. Am.* **100**, 2373–2381.
- Moore, B. C. J., Glasberg, B. R., Plack, C. J., and Biswas, A. K. (1988). "The shape of the ear's temporal window," *J. Acoust. Soc. Am.* **83**, 1102–1116.
- Moore, B. C. J., Peters, R. W., and Glasberg, B. R. (1993). "Effects of frequency on the detection of decrements and increments in sinusoids," *J. Acoust. Soc. Am.* **94**, 3190–3198.
- Moore, B. C. J., Peters, R. W., and Glasberg, B. R. (1996). "Detection of decrements and increments in sinusoids at high overall levels," *J. Acoust. Soc. Am.* **99**, 3669–3677.
- Neff, D. L. (1985). "Stimulus parameters governing confusion effects in forward masking," *J. Acoust. Soc. Am.* **78**, 1966–1976.
- Neff, D. L., and Jesteadt, W. (1983). "Additivity of forward masking," *J. Acoust. Soc. Am.* **74**, 1695–1701.
- Oxenham, A. J., and Moore, B. C. J. (1994). "Modeling the additivity of nonsimultaneous masking," *Hearing Res.* **80**, 105–118.
- Oxenham, A. J., and Moore, B. C. J. (1995). "Additivity of masking in normally hearing and hearing-impaired subjects," *J. Acoust. Soc. Am.* **98**, 1921–1934.
- Oxenham, A. J., and Plack, C. J. (1997). "A behavioral measure of basilar-membrane nonlinearity in listeners with normal and impaired hearing," *J. Acoust. Soc. Am.* **101**, 3666–3675.
- Oxenham, A. J., Moore, B. C. J., and Vickers, D. A. (1997). "Short-term temporal integration: Evidence for the influence of peripheral compression," *J. Acoust. Soc. Am.* **101**, 3676–3687.
- Penner, M. J. (1978). "A power law transformation resulting in a class of short-term integrators that produce time-intensity trades for noise bursts," *J. Acoust. Soc. Am.* **63**, 195–201.
- Peters, R. W., Moore, B. C. J., and Glasberg, B. R. (1995). "Effects of level and frequency on the detection of decrements and increments in sinusoids," *J. Acoust. Soc. Am.* **97**, 3791–3799.
- Plack, C. J., and Moore, B. C. J. (1990). "Temporal window shape as a function of frequency and level," *J. Acoust. Soc. Am.* **87**, 2178–2187.
- Plack, C. J., and Moore, B. C. J. (1991). "Decrement detection in normal and impaired ears," *J. Acoust. Soc. Am.* **90**, 3069–3076.
- Ploomp, R., and Bouman, M. A. (1959). "Relation between hearing threshold and duration for tone pulses," *J. Acoust. Soc. Am.* **31**, 749–758.
- Richards, V. M. (1992). "The detectability of a tone added to narrow bands of equal-energy noise," *J. Acoust. Soc. Am.* **91**, 3424–3435.
- Rose, J. E., Brugge, J. F., Anderson, D. J., and Hind, J. E. (1968). "Patterns of activity in single auditory nerve fibres of the squirrel monkey," in *Hearing Mechanisms in Vertebrates*, edited by A. V. S. d. Reuck and J. Knight (Churchill, London).
- Snedecor, G. W., and Cochran, W. G. (1967). *Statistical Methods* (Iowa State U.P., Ames), 6th ed.
- van den Brink, G. (1964). "Detection of tone pulse of various durations in noise of various bandwidths," *J. Acoust. Soc. Am.* **36**, 1206–1211.
- Viemeister, N. F. (1979). "Temporal modulation transfer functions based on modulation thresholds," *J. Acoust. Soc. Am.* **66**, 1364–1380.
- Viemeister, N. F., and Wakefield, G. H. (1991). "Temporal integration and multiple looks," *J. Acoust. Soc. Am.* **90**, 858–865.
- Weber, D. L., and Moore, B. C. J. (1981). "Forward masking by sinusoidal and noise maskers," *J. Acoust. Soc. Am.* **69**, 1402–1409.
- Wright, B. A. (1997). "Detectability of simultaneously masked signals as a function of masker bandwidth and configuration for different signal delays," *J. Acoust. Soc. Am.* **101**, 420–429.
- Zwislocki, J. J. (1960). "Theory of temporal auditory summation," *J. Acoust. Soc. Am.* **32**, 1046–1060.
- Zwislocki, J. J. (1969). "Temporal summation of loudness: An analysis," *J. Acoust. Soc. Am.* **46**, 431–441.

Factors governing speech reception benefits of adaptive linear filtering for listeners with sensorineural hearing loss^{a)}

Christine M. Rankovic

Northeastern University,^{b)} Department of Speech-Language Pathology and Audiology,
133 Forsyth Building, 360 Huntington Avenue, Boston, Massachusetts 02115

(Received 13 May 1997; revised 8 August 1997; accepted 6 October 1997)

Adaptive linear filtering can improve effective speech-to-noise ratios by attenuating spectral regions with intense noise components to reduce the noise's spread of masking onto speech in neighboring regions. This mechanism was examined in static listening conditions for seven individuals with sensorineural hearing loss. Subjects were presented with nonsense syllables in an intense octave-band noise centered on 0.5, 1, or 2 kHz. The nonsense syllables were amplified to maximize the articulation index; the noises were the same for all subjects. The processing consisted of applying frequency-selective attenuation to the speech-plus-noise with the goal of attenuating the frequency region containing the noise by various amounts. Consonant recognition scores and noise masking patterns were collected in all listening conditions. When compared with masking patterns obtained from normal-hearing subjects, all hearing-impaired subjects had higher masked thresholds at frequencies below, within, and above the masker band except for one subject who demonstrated additional masking above the masker only. Frequency-selective attenuation resulted in both increases and decreases in consonant recognition scores. Increases were associated with a release from upward spread of masking. Decreases were associated with applying too much attenuation such that speech energy within the masker band that was audible before processing was partially below threshold after processing. Fletcher's [*Speech and Hearing in Communication* (Van Nostrand, New York, 1953)] version of articulation theory (without modification) accounted for individual subject differences within the range of variability associated with the consonant recognition test in almost every instance. Hence, primary factors influencing speech reception benefits are characterized by articulation theory. Fletcher's theory appears well-suited to guide the design of control algorithms that will maximize speech recognition for individual listeners. © 1998 Acoustical Society of America. [S0001-4966(98)00102-7]

PACS numbers: 43.66.Dc, 43.66.Sr, 43.66.Ts, 43.71.Gv [WJ]

INTRODUCTION

Adaptive linear filtering refers to a type of hearing aid signal processing in which the frequency-gain characteristic is modified dynamically as a function of input variations. This single-microphone noise-reduction approach is classified as a form of slow compression because the characteristic adapts over periods greater than 200 ms (the approximate length of syllables) whereas fast compression operates with attack times of just a few milliseconds (Braidia *et al.*, 1980). In a previous report conducted with normal-hearing listeners (Rankovic *et al.*, 1992) we examined one mechanism responsible for speech reception improvements under adaptive linear filtering: the release of portions of the speech spectrum from the masking spread caused by band-limited noise interference. The present investigation extends those experiments to listeners with sensorineural hearing loss.

In our earlier report, five normal-hearing subjects were presented with conversational-level nonsense syllables in a high-intensity, steeply-skirted octave band of noise. These listening conditions were chosen so that the noise's spread of

masking would mask speech in neighboring frequency regions. Consonant recognition scores and masking patterns for the noise were collected before and after applying notched-shaped frequency-gain characteristics to the speech-plus-noise complex. The spectral location and depth of the notches were such that they attenuated the frequency region containing the noise by various amounts. We observed systematic increases in consonant recognition with increases in notch depth that were clearly associated with reducing masking spread. Some individual-subject differences in consonant recognition scores were explained by considering the subject-specific masking effects of the noise. It was possible to relate the consonant recognition scores to the masking patterns using an articulation index analysis (ANSI S3.5, 1969).

We anticipated that hearing-impaired listeners would demonstrate even larger increases in consonant recognition under comparable conditions because they are known to exhibit *excess* masking spread whose reduction after processing would unmask *even more* of the speech spectrum. Contrary to this prediction, an evaluation of frequency-selective attenuation by Van Dijkhuizen *et al.* (1991) did not show clear benefits for several of their hearing-impaired subjects. Their interference consisted of a broadband noise that was spectrally shaped to bisect the subject's dynamic range to which they added a low-frequency, octave-wide noise increment to

^{a)}Portions of these data were presented at the 122nd and 125th meetings of the Acoustical Society of America (Rankovic *et al.*, 1991; Rankovic and Zurek, 1993).

^{b)}Data were collected while the author was a post-doctoral fellow with the Communication Biophysics Group in the Research Laboratory of Electronics at the Massachusetts Institute of Technology, Cambridge, MA.

cause masking spread. The aim of their processing algorithm was to attenuate the spectral region containing the increment by the amount necessary to restore the composite noise to the overall level measured before adding the increment. That is, the processing goal was to maintain a constant overall background noise level. Van Dijkhuizen *et al.* found that speech recognition was significantly better with than without processing on the average, although several subjects did not demonstrate significant improvement or showed poorer performance with the processing. This mixed outcome was possible because the averaged data reflected large improvements for some subjects that offset the lack of improvement for other subjects.¹

To explain the ineffectiveness of adaptive filtering for some subjects in Van Dijkhuizen *et al.*'s report, it is essential to ascertain for each subject whether masking spread caused by the noise increment masked speech appreciably, and then, whether the processing introduced enough attenuation to unmask the speech. Given the constant presence of a broadband noise in their test conditions, it is possible for some subjects that the portion of the speech spectrum susceptible to the increment's masking spread was negligible after accounting for the portion masked directly by the broadband noise. Also, the amount of attenuation introduced to suppress the noise increment was always less than required to *eliminate* the increment because the processing goal was to restore the overall intensity level of the noise to its original level rather than to eliminate the increment. Therefore, the release from masking may have been incomplete. To summarize, the processing rules and/or listening conditions may have been such that they provided no opportunity for releasing speech from upward spread of masking for some subjects. Masked thresholds were not obtained by Van Dijkhuizen *et al.* so this hypothesis cannot be tested using their data.

The goal of this investigation is to establish whether the relationship between speech recognition in a band-limited noise and the masking caused by the noise is systematic and/or quantifiable for individuals with sensorineural hearing loss. A predictive relationship is necessary if adaptive filtering algorithms are to effectively exploit the release-from-masking mechanism. As in our previous report, test conditions were selected so that masking spread reduced speech audibility and altering the frequency-gain characteristic unmasked portions of the speech spectrum. Results are analyzed using the articulation index (AI) model, a quantitative framework that predicts speech recognition scores based on physical measurements describing the listening conditions and the masking effects of the noise. The analysis incorporates a comparison of the ANSI S3.5 (1969) AI calculation with the original version of articulation theory presented by Fletcher (1953). Rankovic (1997) reported that Fletcher's calculation was superior to ANSI S3.5 for predicting the nonsense syllable recognition scores of hearing-impaired subjects presented with amplified speech in a quiet background. The present study extends the comparison to conditions with noise interference.

I. METHODS

A. General description

Speech recognition was assessed in static listening conditions with a consonant–vowel nonsense syllable (CV) test presented in each of three octave-band noises geometrically centered on 0.5, 1, or 2 kHz. Briefly, the CVs were digitized using a sampling rate of 10 kHz and were low-pass filtered at 4.5 kHz to prevent aliasing. The entire set of 144 syllables was presented in each test condition. Unprocessed noises had overall intensities of 95 dB SPL. The CV articulation test and noises were identical to those described by Rankovic *et al.* (1992) and further details are provided there. It was necessary to modify listening conditions somewhat to accommodate the wide range of hearing losses of the subjects participating in the present experiment. Here, the CVs were amplified on an individual-subject basis before they were summed with the noise in an attempt to maximize audibility of the average nonsense syllable spectrum in quiet. The frequency-gain characteristics necessary to accomplish this are referred to as MAX AI and their derivation is described below (Section I B). Speech amplification was introduced so that speech scores would not be ultimately limited by the sensitivity loss as defined by absolute thresholds, but rather by the masking effects of the interfering noise.

After the amplified speech was summed with the noise, a second frequency-gain characteristic was applied. The second characteristic constituted the processing under study: frequency-selective attenuation applied to the spectral region containing the noise. Each processing characteristic was from a set of notched-shaped characteristics constructed specifically to attenuate the noise by from 5 to 25 dB in 5-dB steps. Accordingly, processed noises had overall levels of 90, 85, 80, 75, and 70 dB SPL. The notched characteristics were identical to those used by Rankovic *et al.* (1992). Consonant recognition was measured as a function of the notch depth for each octave-band noise condition. Pure-tone thresholds were collected as a function of frequency in the presence of each processed noise to map out masking patterns. AIs were calculated using masking patterns to define the effective noise spectra.

All test stimuli were presented with the same TDH-39 earphone mounted in a GS001 circumaural cushion and testing was conducted in a double-walled sound-treated test chamber. Calibration procedures were described by Rankovic *et al.* (1992).

B. Speech frequency-gain characteristic

MAX AI characteristics were specified based on an assumption derived from ANSI S3.5 (1969) that the best speech recognition scores are expected when the 30-dB short-term band-level distribution of speech is entirely audible (AI=1). The aim of the MAX AI amplification was to equate the effective lower limits of 1/3-octave bands of the short-term speech distribution (band rms in dB minus 18) with absolute thresholds whenever they were found to be below absolute thresholds. The average CV spectrum rather than the ANSI S3.5 speech spectrum was used to determine MAX AI. The MAX AI frequency response was applied to

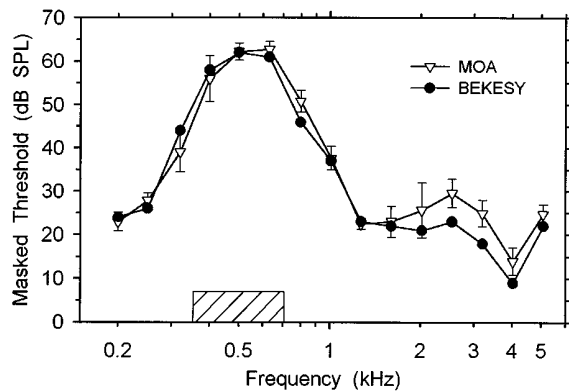


FIG. 1. Masking patterns for an octave-band noise centered on 0.5 kHz (70 dB SPL overall) collected with the method of adjustment (MOA) and Bekesy procedures. The hatched bar indicates the frequency location and bandwidth of the noise. For the MOA masking pattern, each point represents the average of five adjustments. For the Bekesy masking pattern, each point represents the average of the first two thresholds collected that were within 6 dB of one another. The differences between the two masking patterns above 2 kHz reflect the noise floors of two different multifilters used for testing.

each CV off-line with a 1/3-octave digital multifilter. The gain was applied during the experiment with an analog amplifier.

Before beginning data collection, subjects were presented with several amplified CVs in quiet to determine whether loudness discomfort levels were exceeded. SR was the only subject to report that the MAX AI-amplified speech was too loud for consonant recognition testing. Loudness of the syllables was deemed acceptable when the broadband gain was reduced by 5 dB, but consonant recognition was unexpectedly poor [$P(c)=0.29$]. The MAX AI characteristic was abandoned and amplification with a half-gain rule known as POGO (McCandless and Lyregaard, 1983) was applied. The POGO characteristic assigned more mid- but less high-frequency gain than the MAX AI characteristic. The best score for SR was obtained with POGO plus 10 dB of broadband gain [$P(c)=0.49$] and this characteristic replaced MAX AI for subject SR only.

The experimental design is such that speech-to-noise ratios were different for different subjects because the MAX AI characteristics were dependent on absolute thresholds whereas noises were identical for all subjects. For example, subjects with severe hearing losses required more amplification to achieve MAX AI than did subjects with less hearing loss; therefore, subjects with severe losses listened to conditions having higher speech-to-noise ratios. A consequence of this design is that the experiment does not simulate the action of a hearing aid because the speech was amplified separately—before introducing the processing.

C. Masking patterns

In order to expedite data collection, absolute thresholds and masking patterns were collected with a method of adjustment (MOA) procedure rather than the Bekesy tracking procedure used by Rankovic *et al.* (1992). The pure-tone frequencies and presentation time-course parameters were identical to those of the previous report: (1) masked thresholds

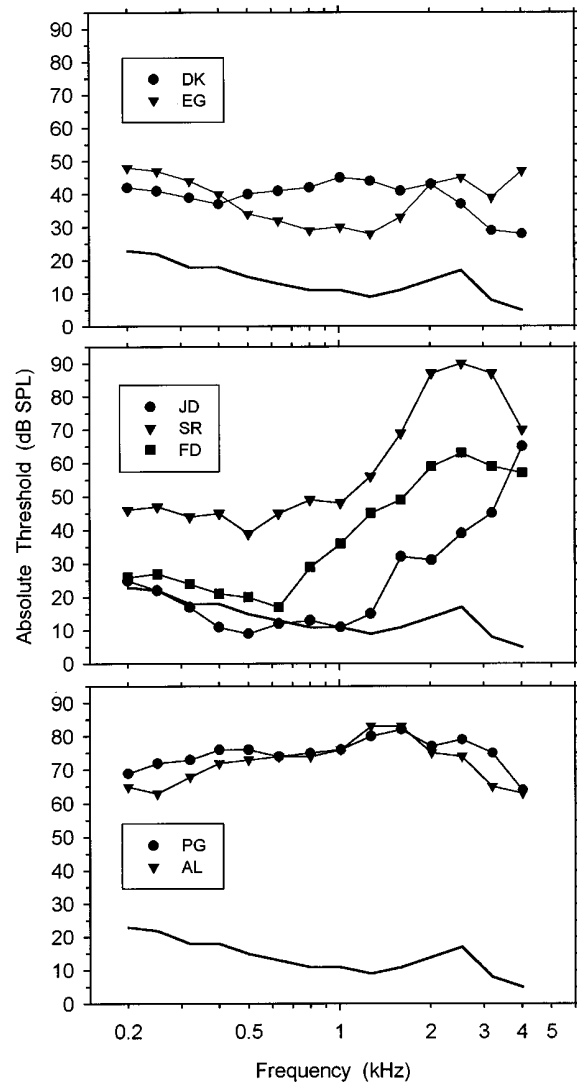


FIG. 2. Absolute thresholds of the seven hearing-impaired subjects obtained with the MOA procedure. The line without data points represents average thresholds for five normal-hearing subjects (Rankovic *et al.*, 1992). Absolute thresholds were obtained without the multifilter in line and, therefore were not affected by noise floor limitations.

were obtained at 15 frequencies ranging from 0.2 to 5.08 kHz at 1/3-octave intervals; (2) the 300-ms test tones had 25-ms rise/fall times and were pulsed on and off with a 200-ms interstimulus interval; and (3) a red light on a response box indicated when the tone was present. For the MOA task, subjects were instructed to “bracket” the detection threshold by rotating a small knob on the response box to the right until the tone was definitely audible, then to the left until it was inaudible, and then to make final adjustments so that the tone was just barely audible. Five masking patterns were collected in each condition with test tones presented in random order for each masking pattern. Three masking patterns were collected in succession and two more were collected either later during the same test session or during another test session. Each masked threshold reported here represents the average of five adjustments. Figure 1 contains a comparison of masking patterns collected with the Bekesy and MOA procedures for a normal-hearing subject. The good agreement of the two masking patterns in the fre-

TABLE I. Subjects with sensorineural hearing loss.

Subject	Age	Hearing loss configuration	Hearing loss onset	Etiology ^a	Hearing aid use	Test ear	S.D. for threshold ^b (dB)
DK	58	mild flat	25 years ago	noise	right daily	R	2.2
EG	59	mild flat	6 years ago	aging	no	R	2.6
JD	76	high frequency	5 years ago	aging	both, rarely	R	3.7
SR	66	high frequency w/loss in lows	unknown	noise/aging	left, 2–3 h daily	R	4.0
FD	38	high frequency	10 years ago	noise/hereditary	right daily	R	2.7
PG ^c	52	severe flat	childhood	hereditary	both daily	R	1.8
AL	26	severe flat	childhood	unknown	both daily	L	2.4

^aAs reported by the subject during the initial test session.

^bFor MOA, averaged across all test conditions.

^cSevere visual impairment.

quency region containing the noise suggests there is no difference between the two procedures. Differences apparent at higher frequencies reflect the different noise floors of the two analog multifilters (both General Radio model 1925) used in the experiments.

D. Subjects

Seven individuals with long-standing, bilaterally symmetrical sensorineural hearing loss served as subjects and completed the experiment. Figure 2 provides their absolute thresholds collected with the MOA procedure. Subjects were divided into three groups according to hearing loss. DK and EG had mild flat losses (top panel) and PG and AL had severe flat losses (bottom panel). Subjects JD, SR, and FD had high-frequency hearing losses (center panel). JD and FD had normal hearing at low frequencies whereas SR had a mild loss at low frequencies.

Table I provides information obtained from subjects during their initial test sessions. All subjects had complete audiologic evaluations before and after participation and demonstrated no change in hearing over the course of the experiment. Subject PG has a severe visual impairment. He did not know how to type, therefore he could not enter responses to the consonant recognition test using a typewriter keyboard. Instead, he responded verbally to the experimenter who sat next to him inside the test chamber and the experimenter entered his responses. PG was able to detect the lights on the response box when the overhead lights were dimmed so it was not necessary to modify procedures for collecting masking patterns. The non-test ear of subject JD was masked with a broadband noise during the entire experiment to prevent participation of that ear. Data were collected during 2-h test sessions and subjects took frequent breaks. Total hours of participation ranged from 12 to 30 (mean=23 h). The last column of Table I contains standard deviations for the five adjustments comprising threshold averaged across all conditions of testing. The averaged standard deviations are representative of performance and indicate that JD and SR performed somewhat more variably than the other subjects.

All subjects were questioned repeatedly about whether test conditions were uncomfortably loud. Conditions were modified or eliminated from the experiment based on their

comments and all modifications are indicated in this report where pertinent. Two other subjects were dropped from the experiment because they reported temporary tinnitus after the first test session. Another subject was dropped after the discovery of a large fluctuating conductive component to the hearing loss.

II. RESULTS

A. Consonant recognition

The bar graphs in Fig. 3 summarize the consonant recognition test results. There is a separate panel for each noise condition. In each panel, there is a set of three bars for each subject that represent (from left to right): (1) the unprocessed score; (2) the best score obtained with processing; and (3) the worst score obtained with processing. Subjects EG and FD indicated that the unprocessed 0.5-kHz noise was too loud and we responded conservatively by eliminating the most intense conditions for all three noises. Their ‘‘unprocessed’’ scores, then, are actually scores obtained with the 10-dB deep notches applied, which they found tolerable. The right-most group of bars in each panel provides the average scores and standard deviations for the five subjects with normal hearing who participated in the Rankovic *et al.* (1992) experiment. Consonant recognition scores for MAX AI-amplified speech in quiet are indicated for each subject by the diamond symbols and are identical across panels.

The consonant recognition scores obtained in quiet (diamonds) are the maximum possible scores for each subject in this experiment. Processed scores are expected to be the same as scores obtained in quiet when: (1) the noise has no masking effect on the speech (several instances for PG and AL); or (2) the processing eliminates the influence of the noise completely (only for AL for the 0.5-kHz noise). None of the scores obtained in quiet from hearing-impaired subjects were as high as the scores obtained from the normal-hearing listeners even though this is predicted by ANSI S3.5 for subjects who received MAX AI amplification (all but SR). In quiet, scores for high-frequency loss subjects JD and SR are particularly low relative to the scores of the other subjects.

The consonant recognition scores ranged from $P(c)$ of 0.20 to 0.70 with few exceptions, therefore ceiling and floor

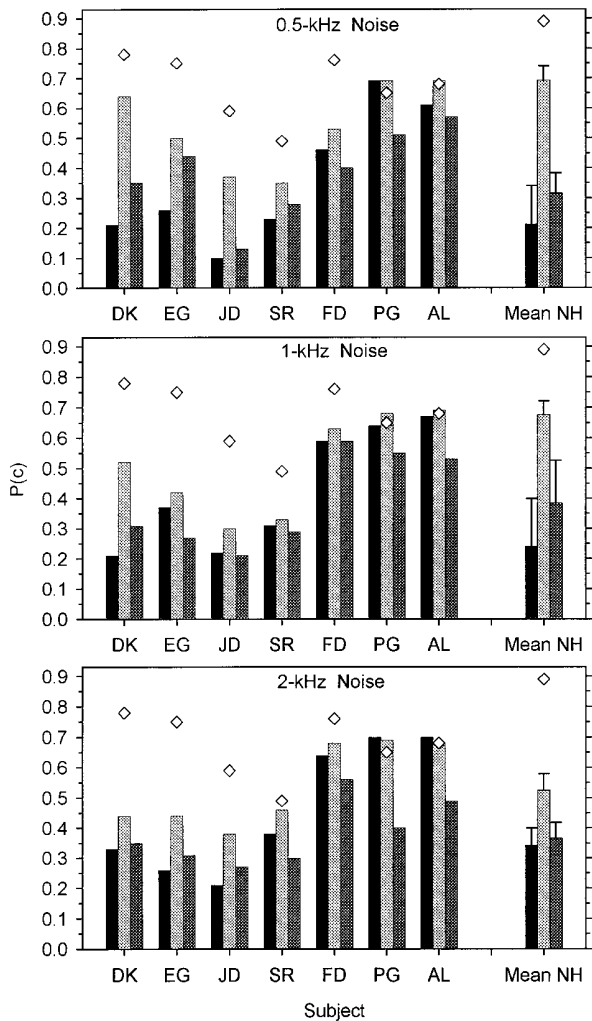


FIG. 3. Summary of consonant recognition test results. $P(c)$ on the ordinate indicates the proportion correct. There are three bars for each hearing-impaired subject. The right-most set indicates the average performance of five normal-hearing subjects (Mean NH). Black bars indicate unprocessed score. Light gray bars indicate the best processed score. Dark gray bars indicate the worst processed score. Diamonds indicate scores obtained in quiet (MAX AI for the hearing-impaired subjects). Error bars indicate 1 standard deviation for the five normal-hearing subjects.

effects were largely avoided. Two patterns of results emerged. For all three octave-band noise conditions, the subjects with mild flat and high-frequency hearing losses (DK, EG, JD, SR, and FD) demonstrated increased consonant recognition scores for some condition of processing when compared with the unprocessed condition. Except for FD, the relationship between the three bars was similar to the pattern demonstrated by the normal-hearing subjects: performance increased with processing and, in most cases, there was no decrease associated with processing. SR and FD demonstrated smaller increases in consonant recognition scores than did DK, EG, and JD. Decreases in scores with processing were demonstrated in some conditions by EG (1-kHz noise), SR (1- and 2-kHz noises), and FD (0.5- and 2-kHz noises). To summarize, subjects with mild flat or high-frequency losses received benefit from the application of at least one of the notched characteristics, however applying the characteristics did not guarantee improvement and was detrimental in several instances.

A second pattern of results was exhibited by the subjects with severe flat hearing loss configurations, PG and AL. They demonstrated little or no increase in score with processing. An exception was an increase in score for AL in the 0.5-kHz noise condition. The similarity of quiet scores and unprocessed scores indicates that the maskers had almost no effect on consonant recognition. However, the worst scores obtained with processing indicate that the processing could be quite detrimental. For both of these subjects, applying the notched characteristics usually resulted in no change or poorer consonant recognition scores.

Not apparent in Fig. 3 is the finding that the best scores did not always occur when the deepest notch was applied. The deepest notch did not result in the best score in 9 of a possible 21 opportunities (3 noise conditions \times 7 subjects). The deepest notch decreased the consonant recognition score substantially in 7 of these 9 instances. Almost all of the decreases occurred for the subjects with severe flat losses, PG and AL.

B. Masking

The first seven three-part panels in Fig. 4 (A through G) contain selected masking patterns of the seven hearing-impaired subjects. (The Appendix contains the complete set of masking patterns.) The last panel (Fig. 4H) provides the complete set of masking patterns obtained from the normal-hearing subjects of Rankovic *et al.* (1992). The three graphs in each set are for the three noise conditions. Each graph includes absolute thresholds (filled circles connected by solid lines), masking patterns for the highest- and lowest-intensity noises tested (top and bottom solid lines with no symbols, respectively), and average masking patterns of the five normal-hearing listeners for the same noises (top and bottom dotted lines, respectively). Many details of the masking patterns are the same as those already noted in the extensive literature on masking (see Moore, 1995; Nelson and Schroder, 1997; Stelmachowicz *et al.*, 1987; Tyler, 1986 for more detailed discussions). Therefore only a general description is presented here.

The major feature of the masking patterns relevant to this experiment is that masked thresholds are higher for hearing-impaired subjects than for the normal-hearing subjects when presented with the identical noise. Higher masked thresholds are apparent for all hearing-impaired subjects at frequencies below, within, and above the masker with the exception of subject FD. FD exhibited additional masking above the masker band but masked thresholds below and within the band were nearly identical to averaged masked thresholds of the normal-hearing subjects. Clearly, the noises were much more deleterious to the hearing-impaired than to the normal-hearing subjects.

For subjects with severe hearing losses (PG and AL), masking patterns were approximately parallel to absolute thresholds (Fig. 4F and G). The noises caused masking over a broad range of frequencies even though the sensation levels of the noises were very low for these subjects.

The following description pertains to the masking patterns obtained from the other subjects (DK, EG, JD, SR, and FD).

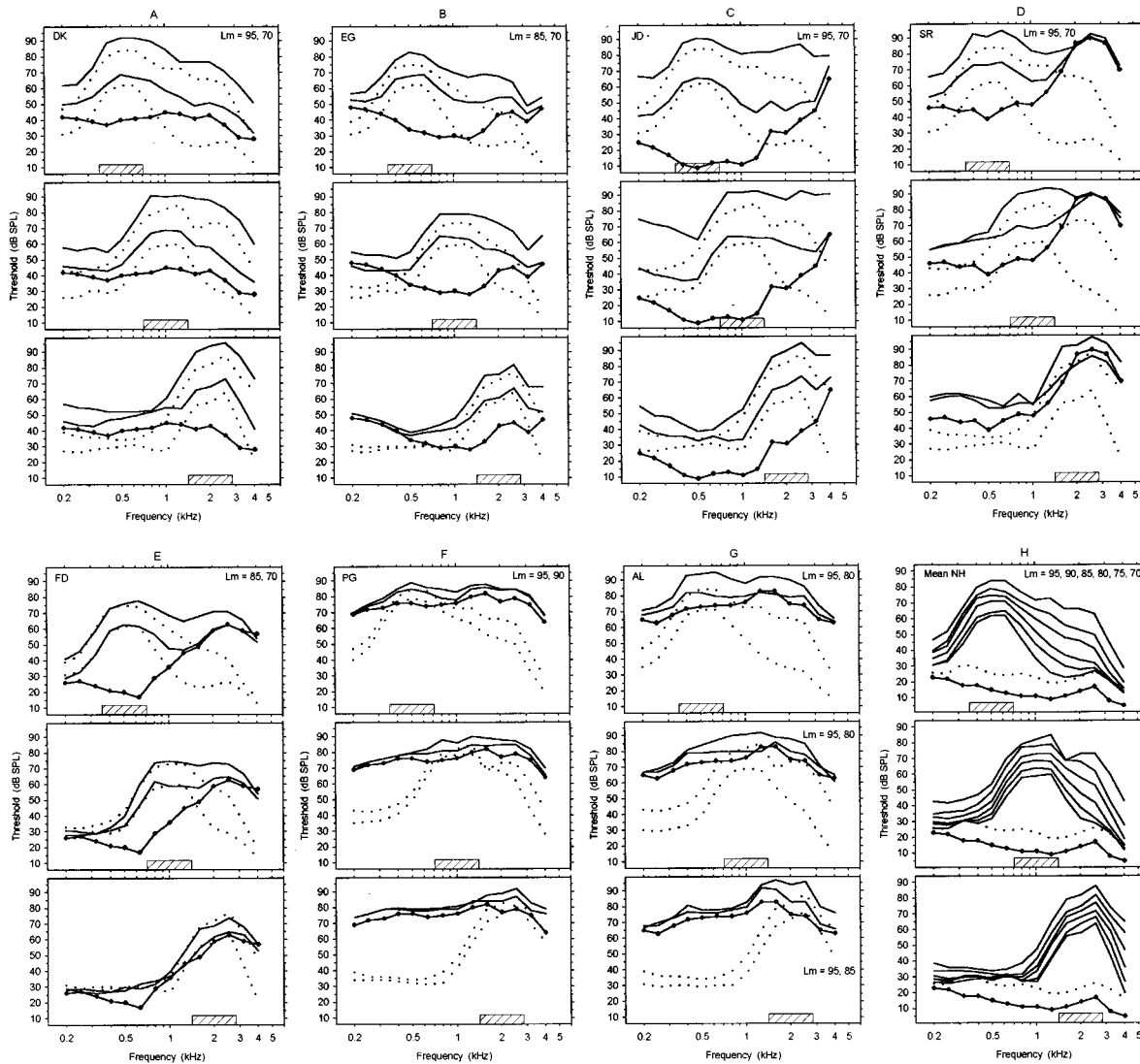


FIG. 4. Selected masking patterns for hearing-impaired subjects (panel sets A through G) and for normal-hearing subjects (panel set H). In each panel, the solid lines with symbols are absolute thresholds. The solid lines without symbols are masking patterns for conditions resulting in the highest (upper solid line) and lowest (lower solid line) intensity noises. The intensity levels are indicated (Lm). Dotted lines are average masking patterns from five normal-hearing subjects for the same noises. The hatched bar indicates the frequency location and bandwidth of the noise. The set of panels labeled "Mean NH" contains the full set of masking patterns of the normal-hearing subjects. The dotted lines in the "Mean NH" panels are the average masking pattern for the noise floor. Masked thresholds collected at 5.08 kHz were not included in the graphs because they were not used in this report. However, they are provided in the Appendix.

1. Below the masker

At test frequencies immediately below the masker (0.25 and 0.32 kHz for the 0.5-kHz noise; 0.5 and 0.63 kHz for the 1-kHz noise; 1 and 1.2 kHz for the 2-kHz noise), masking patterns for hearing-impaired listeners lie above but run roughly parallel to the steep, positive-sloping regions of the averaged masking patterns of the normal-hearing subjects. However, just two data points define these regions so this description is very rough. At frequencies further below the masker, the phenomenon referred to as "remote" masking (Bilger and Hirsh, 1956; Keith and Anderson, 1969; Rittmanic, 1962) is apparent for some subjects. This appears most clearly for thresholds measured at frequencies more than an octave below the masker (for the 1- and 2-kHz-centered noises) and particularly for high-intensity maskers (the top-most solid lines in each graph). The most dramatic

case of remote masking was exhibited by JD for the unprocessed 1-kHz noise (Fig. 4C). The noise caused about 50 dB of masking between 0.2 and 0.5 kHz. This portion of the masking pattern is approximately parallel to JD's absolute threshold curve, consistent with published descriptions of remote masking. Clear instances of remote masking were also exhibited by subjects DK (1- and 2-kHz noises; Fig. 4A), EG (1-kHz noise; Fig. 4B), and SR (1- and 2-kHz noises; Fig. 4D). It is noteworthy that the averaged data of the normal-hearing subjects (Fig. 4H) does not reflect the extent of remote masking demonstrated by some of the individual subjects (see Fig. 5 of Rankovic *et al.*, 1992). This author is not aware of investigations on the impact of low-frequency spread of masking on speech reception. However, the masking patterns suggest that downward spread of masking may substantially decrease audibility of low-frequency speech

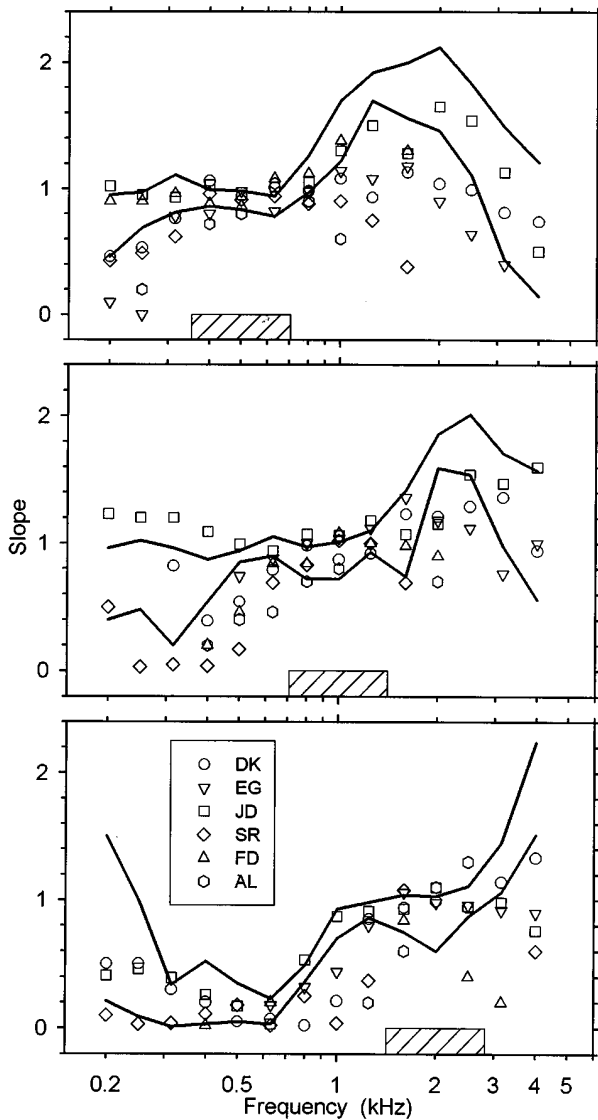


FIG. 5. Slopes of the growth of masking with masker level (dB/dB) as a function of pure-tone test frequency. The curves define the range of slopes obtained from five normal-hearing subjects. Symbols are for the hearing-impaired subjects.

components for some listeners, particularly when high-frequency speech and/or noise components are intense such as under high-frequency emphasis.

2. Within the masker band

Within-band masked thresholds were poorer for hearing-impaired than for normal-hearing subjects with the exception of subject FD. Differences in masked thresholds measured at the center frequency of the masker are presented in Table II. Within-band masked thresholds for hearing-impaired subjects exceeded the averaged masked thresholds of the normal-hearing subjects by more than 5 dB except for EG (1- and 2-kHz noises), FD (all noises), and PG (1-kHz noise). Poorer masked thresholds in broadband noises for hearing-impaired subjects have been reported many times in the literature (see Tyler, 1986, for review) and are typically attributed to broader auditory filter bandwidths. For the octave-band noises used here, the poorer within-band

TABLE II. Within-band masking. Masked thresholds of hearing-impaired subjects minus the average masked thresholds of normal-hearing subjects for test tones at the center frequency of the masker band (dB).

Subject	Octave noise center frequency		
	0.5 kHz	1 kHz	2 kHz
DK	7.7	8.3	11.0
EG	7.3	4.8	2.8
JD	5.0	7.3	6.8
SR	8.5	9.3	11.0
FD	0.8	0.8	0.3
PG	5.5	3.5	8.0
AL	9.8	6.7	12.0

masked thresholds may also be due to an inability to use the off-frequency listening cues available to normal-hearing listeners. Moore (1995) has provided a discussion of these effects.

3. Above the masker

All hearing-impaired subjects demonstrated more masking at frequencies above the masker than did the normal-hearing subjects. For the normal-hearing subjects, upward spread of masking decreased with increasing notch depth: that is, the slope of the high-frequency side of the masking patterns became steeper as the noise intensity was decreased by the processing (Fig. 4H). For the hearing-impaired subjects, the high-frequency slopes of the masking patterns exhibited little or no steepening with increasing notch depth. The most dramatic instances of excessive masking spread were demonstrated by subject JD for the 0.5- and 1-kHz noises (Fig. 4C). The greater-than-normal masking at frequencies above the masker has been described as a manifestation of broader auditory filters combined with absolute threshold limits (e.g., Gagne, 1988). In this study, we attempted to spectrally position the average CV spectrum so that there was an opportunity for the processing to release portions of the speech spectrum from masking spread. Despite this effort, the processing was less effective at unmasking speech for the hearing-impaired than for the normal-hearing subjects because the masking patterns remained broad even with the greatest amount of processing applied.

4. Slopes of masking growth functions

To further characterize the effect of frequency-selective attenuation on masking spread, the slopes of regression lines relating masked thresholds to noise sound pressure level (dB/dB) were calculated. Slopes were calculated at each test frequency for each subject's set of masking patterns and are given in Fig. 5. Masked thresholds were included in the regression only if they exceeded the absolute threshold by more than 5 dB. Regression lines were calculated only when there were at least three such masked thresholds at a particular frequency. The curves in Fig. 5 define the range of slopes for the five normal-hearing subjects from the Rankovic *et al.* (1992) experiment. The symbols represent the slopes calculated from the masking patterns of hearing-impaired subjects. There are no data from subject PG because masking

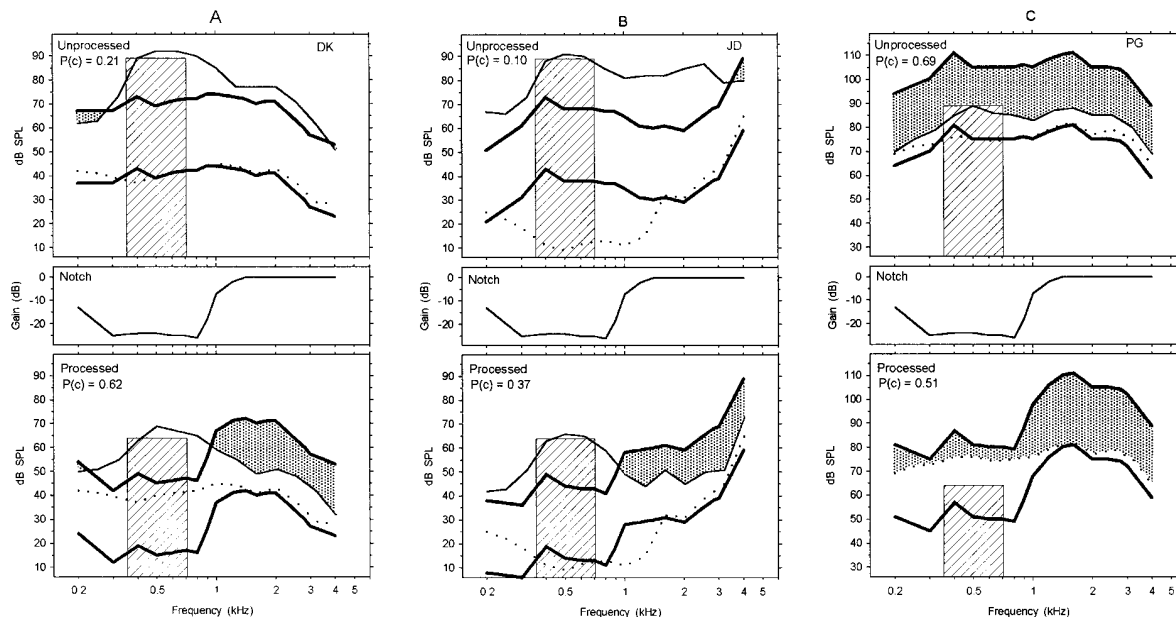


FIG. 6. Examples illustrating the effect of processing for subjects DK, JD, and PG. For each example, the top and bottom panels depict the condition before and after processing, respectively, and the middle panel shows the processing applied. In the top and bottom panels, the hatched bar is an idealized representation of the noise and depicts the bandwidth and effective intensity of the noise. The thin line is the masking pattern for the noise. The heavy lines enclose the effective 30-dB band-level distribution of the nonsense syllables. The dotted lines indicate absolute thresholds. Shaded regions indicate the region of the speech distribution that lies above masked thresholds.

patterns were collected at only two intensities (the other processed noises were inaudible to PG) so there were too few data to calculate slopes.

For normal-hearing subjects, slopes of masking growth functions were near 1.0 when test tones frequencies were within the masker band. The steepest slopes were found in the vicinity of 1 to 2 kHz for the 0.5-kHz noise and 2 to 2.5 kHz for the 1-kHz noise. Slopes ranged from about 1.6 to 2.0 in these frequency regions. This experiment did not include test frequencies high enough to definitely capture the region of fastest growth for the 2-kHz noise; the most rapid growth observed here occurred at the highest frequencies tested. At frequencies below the maskers, most normal-hearing subjects had slopes just less than 1.0 for the 0.5- and 1-kHz noises. For the 2-kHz noise, slopes at frequencies below the masker band were closer to 0.0, reflecting very little change in masking with increasing masker intensity.

As for the normal-hearing subjects, the hearing-impaired subjects had slopes near 1.0 when test tones were within the masker band except for two data points for the 2-kHz noise. At frequencies immediately above the masker, hearing-impaired subjects demonstrated shallower slopes than did the normal-hearing subjects. This is the region in which the normal-hearing subjects demonstrated the most rapid growth of masking. The exceptions were several data points of subject JD in the 0.5- and 1-kHz noises which were within the range defined by the normal-hearing subjects. When considered together with the abnormally broad masking patterns for conditions with the most processing—noises with the lowest intensities—the growth-of-masking slopes reflect that there was little or no steepening of the high-frequency side of the masking pattern when the masker intensity was decreased by the processing. Although the slopes show considerable vari-

ability across hearing-impaired subjects in the frequency region above the masker, results are generally consistent with the notion that response growth is more linear for hearing-impaired than for normal-hearing listeners (e.g., Moore, 1995; Nelson and Schroder, 1997). At frequencies below the masker, slopes are more variable across hearing-impaired subjects except for the 2-kHz condition in which data points were within the range of normal-hearing subjects.

C. Examples illustrating the effects of processing

Increases or decreases in consonant recognition scores can be understood to some extent by considering the spectral location of the speech and the masking patterns, before and after the application of the notched frequency-gain characteristics. Figure 6A and B are schematic depictions of representative test conditions that resulted in increases in consonant recognition scores (for a flat loss and a high-frequency loss) and Fig. 6C depicts conditions that produced a decrease (for a severe loss). All three examples are for the 0.5-kHz octave-band noise condition with the processing consisting of a 25-dB notch. In each example, the top and bottom panels illustrate the unprocessed and processed conditions, respectively, and the middle panel shows the notch. Top and bottom panels contain an idealized noise spectrum (hatched bar), the masking pattern for the noise (thin solid line), the MAX AI-amplified averaged CV spectrum (the region enclosed by heavy lines), and absolute thresholds (dotted line). The shaded regions indicate the portion of the averaged CV spectrum that lies above masked thresholds. The figures were constructed by converting the speech and noise spectra to effective levels so that they could appear on the same graphs with absolute and noise-masked thresholds. Effective levels

were derived by subtracting critical ratios (Fletcher, 1953) (in dB) from measured levels. The ordinate labels refer to effective levels for the noise and speech. The same ordinate labels refer to the pure-tone detection thresholds for absolute and masked thresholds.

1. Mild flat hearing loss

For subject DK (Fig. 6A), the panel for the unprocessed condition (top) shows that the masking pattern for the unprocessed noise was so broad that the speech spectrum was almost entirely masked. After applying the 25-dB deep notched characteristic in the center panel, the bottom panel shows a masking pattern that is lower yet is still very broad. However, a large portion of the speech spectrum higher than 1 kHz lies above masked thresholds after processing, therefore speech audibility has been increased. Consonant recognition increased from 0.21 in the unprocessed condition to 0.62 after processing.

2. High-frequency hearing loss

The situation is similar for subject JD (Fig. 6B). In the top panel, it can be seen that the MAX AI characteristic provided no amplification at low frequencies where absolute thresholds were normal. The MAX AI characteristic provided about 50 dB of gain at about 4 kHz so that the CV spectrum would be above absolute thresholds at high frequencies. After applying the notched characteristic (middle panel), a large portion of the speech spectrum became audible (bottom panel) and the consonant recognition score increased from 0.10 to 0.37.

3. Severe flat hearing loss

Figure 6C provides an example for subject PG who had a severe flat hearing loss. MAX AI amplification is considerable (average overall gain of 44 dB). The masking pattern for the noise is roughly parallel to the absolute threshold curve. Before processing, most of the speech spectrum lies above the masking pattern including the portion within the masker band. After applying the notched characteristic, the low-frequency portion of the speech spectrum falls below the absolute thresholds and some of the high-frequency portion is unmasked. The consonant recognition score decreased from 0.69 to 0.51. No masking pattern was collected in the processed condition because the subject indicated that the noise was not audible. The decrease in score is associated with the removal of a portion of the speech spectrum that apparently had been contributing to consonant recognition in the unprocessed condition.

The increases and decreases in consonant recognition scores are at least partially explained by considering speech spectrum audibility. However, an articulation index analysis provides a more precise characterization of the effects of processing.

D. Articulation index analysis

AIs were calculated for all conditions using procedures recommended by ANSI S3.5 (1969) and by Fletcher (1953). As in Rankovic (1997), these calculations *were not modified*

in any way to account for deficits peculiar to sensorineural hearing loss. For both normal-hearing and hearing-impaired individual data, critical ratios (Fletcher, 1953) were subtracted from masked thresholds to arrive at the effective noise spectrum for each test condition. These inferred noise spectra were submitted to both ANSI S3.5 and Fletcher AI calculations. Consequently, the abnormal frequency resolution as revealed by the hearing-impaired subjects' masking patterns was incorporated into both AI calculations. Fletcher recommended using actual masked thresholds whenever possible. ANSI S3.5 provides an algorithm for calculating spread of masking for normal-hearing listeners that was not used here.

The ANSI S3.5 calculation is a simplified version of articulation theory based on the work of French and Steinberg (1947). French and Steinberg's version is a dramatic reduction of Fletcher's formulation. Unlike these simpler versions, Fletcher's calculation accounts for decreases in speech recognition associated with: (1) deviations of the frequency response from a flat response (Fletcher's F factor); (2) high speech intensities (Fletcher's E factor); and (3) intermodulation distortion caused by speech interacting with noise (Fletcher's H factor). In addition, Fletcher's version represents the speech spectrum in terms of the level of critical bands of speech above threshold. Hence, Fletcher's calculation uses a perceptual speech spectrum that has a 63-dB range whereas the ANSI S3.5 version is based on the 30-dB band-level distribution derived from physical measurements. Fletcher AIs are much smaller than ANSI S3.5 AIs as a consequence of considering these issues in combination. The major difference between the two calculations is conceptual. Fletcher's calculation attempts to transform physical measurements into the perceptual domain using, for example, loudness, critical bands, masking (including speech self-masking), and speech detection thresholds. The ANSI S3.5 version calculates the AI almost directly from physical measurements with only minor consideration given to perceptual correlates. A complete description of Fletcher's calculation has been provided by Fletcher (1953) and Fletcher and Galt (1950).

ANSI S3.5 and Fletcher AIs are compared in Fig. 7. The left panel displays consonant recognition as a function of ANSI S3.5 AIs. The right panel displays the same consonant recognition scores, but now plotted as a function of Fletcher (1953) AIs. The dotted and solid lines represent the averaged consonant recognition scores obtained from five normal-hearing subjects for the same speech test presented in speech-shaped noise. These lines are used as a reference to check the accuracy of predictions of the performance of the hearing-impaired subjects.

The symbols in Fig. 7 represent data collected from the hearing-impaired subjects in this experiment. Black triangles highlight the data of subject SR because his performance was consistently poor. The comparison shows that the performance of hearing-impaired subjects is predicted more accurately from the curves defined for normal-hearing subjects when the Fletcher calculation is used. This is indicated by how well the solid line describes the open circles in the right panel. In the left panel, it is apparent that the ANSI S3.5

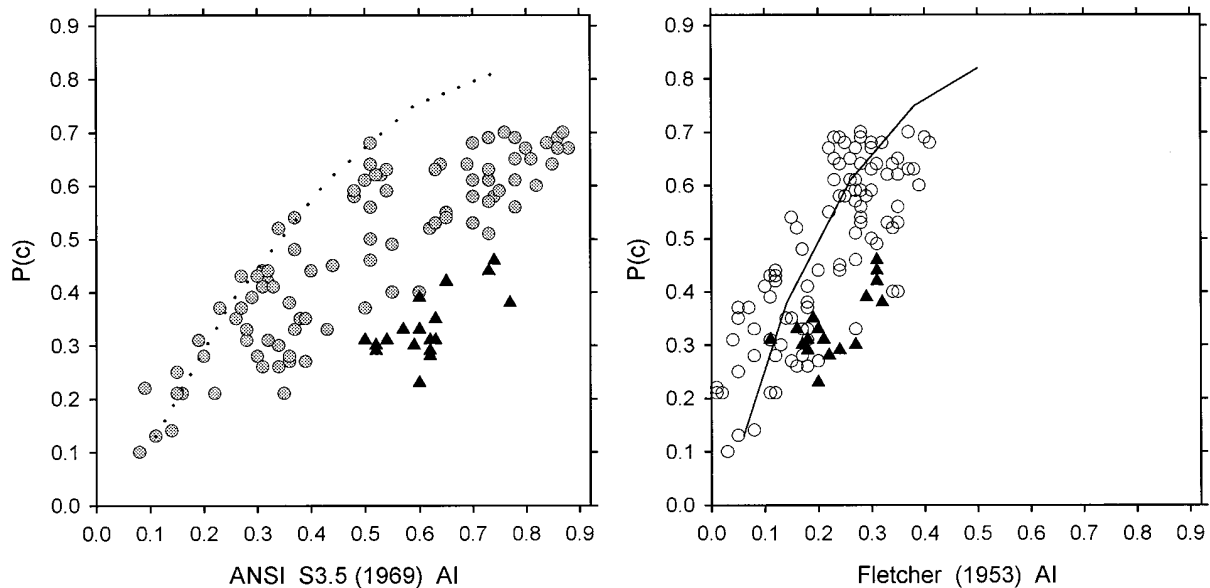


FIG. 7. Comparison of ANSI S3.5 (left panel) and Fletcher AI (right panel) calculations for all subjects. The lines are the averaged consonant recognition scores of five normal-hearing subjects for speech presented in speech-shaped noise (rms-to-rms speech-to-noise ratios: -12 , -6 , 0 , 6 , and 12 dB). Symbols are data collected from the hearing-impaired subjects. The data of subject SR are highlighted (black triangles).

calculation overestimates performance of hearing-impaired subjects by a large amount for AIs greater than approximately 0.35. The range of consonant recognition scores is widest between 0.20 and 0.35 AI for the Fletcher calculation and between 0.50 and 0.60 for the ANSI S3.5 calculation. Particularly for the ANSI S3.5 calculation, the wide range is attributable to the performance of subject SR. Perhaps SR's poorer performance is related to nonauditory factors. This is suggested by the relatively large standard deviations he exhibited in the masking experiment (Table I).

Figure 8 contains the same data but now plotted separately for individual subjects. The dotted and solid lines are identical to those in Fig. 7. The error bars indicate ± 1 standard deviation for the speech-in-speech noise conditions whose means define the functions. For the Fletcher calculation (open symbols) the data generally fall within the ± 2 standard deviation range. Consonant recognition scores tend to increase with AI for both ANSI S3.5 and Fletcher calculations. The data of subjects DK, JD, and SR demonstrate a monotonic relationship between AI and consonant recognition for both calculations. For the other subjects (EG, FD, PG, AL) the data points formed clusters; therefore, test conditions were not sufficiently different to evaluate the monotonicity of consonant recognition scores with AI.

The ANSI S3.5 calculation makes very good predictions of consonant recognition for subject DK but clearly overestimates performance for the other six subjects. The Fletcher calculation underestimates the performance of DK at AIs between 0.0 and 0.1. For subject SR, the errors from Fletcher's calculation are far less than from the ANSI S3.5 calculation. With the exception of only a few data points, the Fletcher AIs predict consonant recognition scores with surprising accuracy.

Table III was constructed to demonstrate the relevance of the differences between the AI calculations for the ex-

amples presented in Fig. 6A and B in which subjects DK and JD demonstrated increased consonant recognition attributable to the processing. Table III provides the consonant recognition scores and AIs calculated for these examples using both ANSI S3.5 and Fletcher methods. Both ANSI S3.5 and Fletcher AIs predict improvement with the processing for both subjects. The roughly equivalent shaded regions in the bottom panels for DK and JD (processed conditions) suggest that the processing increased speech audibility by about the same amount in approximately the same frequency region for both subjects. Accordingly, ANSI S3.5 AIs calculated for the processed conditions are about the same: 0.53 and 0.50, respectively. However the actual consonant recognition scores obtained after processing, 0.62 and 0.37, are quite different from one another. By contrast, Fletcher AIs (0.33 for DK and 0.18 for JD) predict a smaller increase in consonant recognition for JD, in better agreement with the actual scores.

The predictions made by Fletcher's AI calculation are more accurate than those made by ANSI S3.5 (1969). The accuracy of Fletcher's calculation is somewhat surprising given that it was developed to predict speech recognition for listeners with normal hearing.

III. DISCUSSION

A. Factors controlling speech reception benefits

In our previous work with normal-hearing listeners, we observed a close relationship between increased consonant recognition in noise and a reduction in the noise's masking spread that occurred after applying attenuation to the frequency region containing the noise. In the present experiment, most hearing-impaired subjects demonstrated increases in consonant recognition scores following modification of the frequency-gain characteristic, although

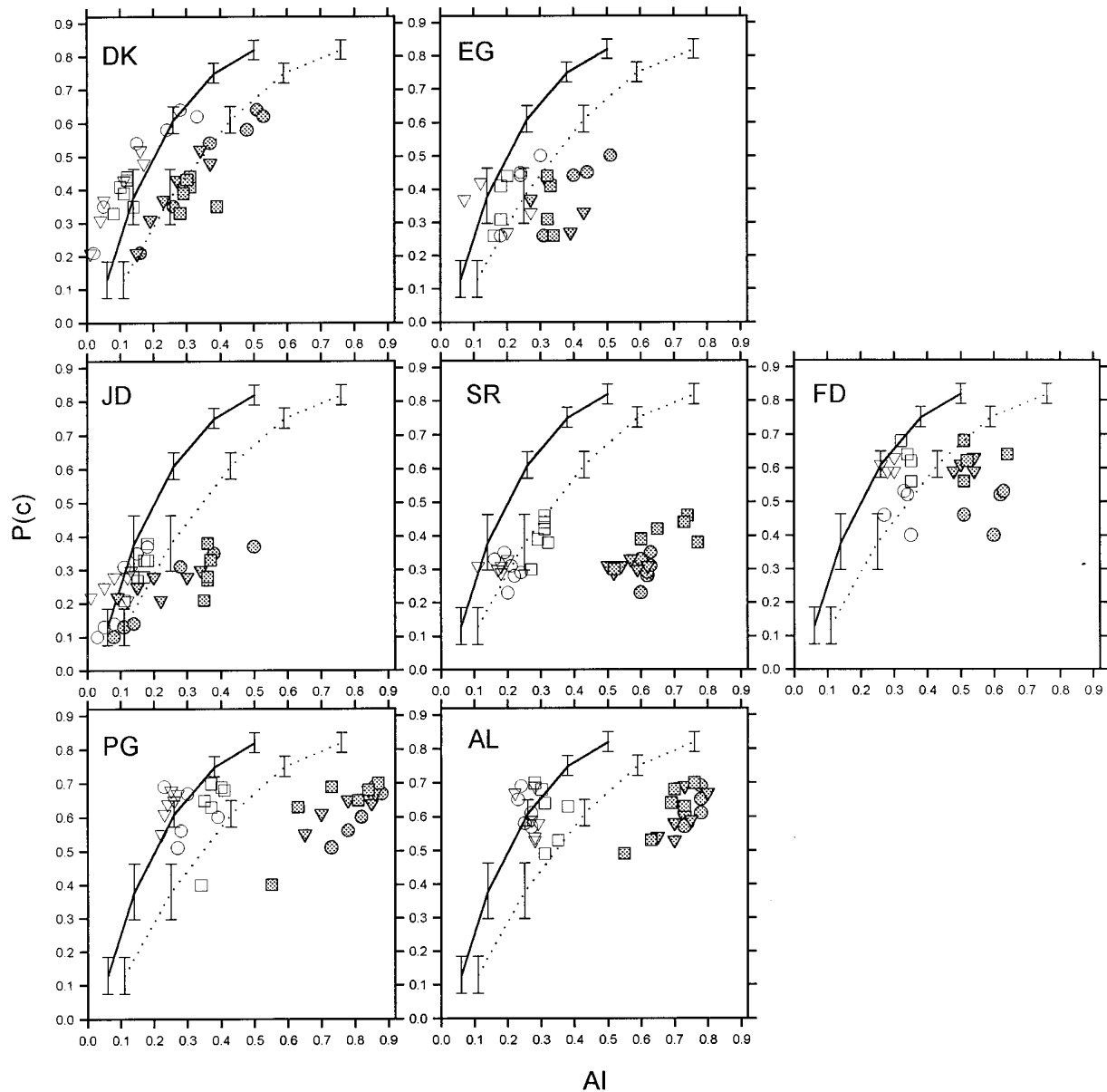


FIG. 8. Comparison of ANSI S3.5 and Fletcher AI predictions for individual subjects. The solid and dotted lines are identical to those presented in Fig. 7 and represent average performance of normal-hearing subjects. Error bars indicate plus/minus 1 standard deviation for the normal-hearing subjects. The open and filled symbols are the data from the hearing-impaired subjects plotted at Fletcher and ANSI S3.5 AIs, respectively. Symbol shapes correspond to noise conditions: circles for the 0.5-kHz noise, inverted triangles for the 1-kHz noise, and squares for the 2-kHz noise.

the size of the increase varied across subjects. Individual subject performance differences were attributable to subject-specific masking effects of the noise, absolute thresholds limits, as well as the spectral location of the speech after the MAX AI amplification was applied. Examination of scores and corresponding masking patterns suggests that improvements in speech reception came about when the test condi-

tions in combination with the subject's residual auditory area and masking effects of the noise were such that a substantial portion of the speech spectrum was unmasked as a consequence of attenuating the spectral region containing the noise.

Masking patterns for hearing-impaired subjects indicated a less rapid growth of masking spread with masker intensity and this was associated with broader-than-normal masking patterns for lower intensity maskers. This excessive spread of masking was related to smaller improvements than would have been expected if based on normal-hearing masking patterns, because lowering the masker intensity did not unmask as much speech for hearing-impaired as it did for normal-hearing individuals. Nevertheless, increases in consonant recognition scores were substantial in many instances

TABLE III. ANSI S3.5 and Fletcher AIs and corresponding consonant recognition scores for the two examples depicted in Fig. 6A and B.

Subject	Unprocessed			Processed		
	$P(c)$	ANSI AI	Fletcher AI	$P(c)$	ANSI AI	Fletcher AI
DK	0.21	0.16	0.02	0.62	0.53	0.33
JD	0.10	0.08	0.02	0.37	0.50	0.18

for the hearing-impaired subjects because sizable portions of the speech spectrum were unmasked by frequency-selective attenuation even without the narrowing of the masking patterns (e.g., Fig. 6A).

When the processing did not increase speech recognition scores, applying the notched characteristic either failed to increase speech audibility, or in some cases actually decreased audibility. Lack of improvement was a consequence of: (1) test conditions in which the noise had very little masking effect; and/or (2) test conditions/masking pattern combinations that allowed little or no release of speech from masking spread. For subjects with severe flat hearing losses, test conditions were such that the noise caused very little masking of speech in the unprocessed condition and application of the notched characteristics rendered portions of the speech spectrum inaudible; this corresponded to decreases in consonant recognition scores. The processing conditions that reduced speech audibility were an unintended side effect of *a priori* experimental design choices. However, these conditions are instructive because they demonstrate that adaptive linear filtering can be *detrimental* if control algorithms are designed without consideration given to the interaction between the exact operation of the processing, the listening conditions, and the listener's absolute thresholds.

B. Articulation theory

An AI analysis incorporating the subjects' masking patterns was effective for explaining the consonant recognition test results. Experimental results agree with those of previous studies indicating that masking spread is a manifestation of frequency resolution that is correlated with speech recognition scores via articulation theory. This relationship has been observed for normal-hearing listeners (Dubno and Ahlstrom, 1995a, 1995b; Kryter, 1962; Rankovic *et al.*, 1992; Saito and Watanabe, 1961) and hearing-impaired listeners (Dubno and Ahlstrom, 1995a, 1995b; Dubno and Schafer, 1992).

The present report demonstrates that when complicated relations between audiogram, frequency-gain characteristic, and noise masking are examined within the framework provided by articulation theory, both the increases and the decreases in consonant recognition scores are predictable. The most important finding pertaining to the AI evaluation is that Fletcher's original version predicted consonant recognition scores within the range of variability associated with the consonant recognition test. Here, as in several published reports, the ANSI S3.5 (1969) calculation or modifications thereof have resulted in poorer-than-predicted performance for subjects with sensorineural hearing loss (e.g., Dugal *et al.*, 1980; Ludvigsen, 1987; Pavlovic, 1984; Rankovic, 1989). Fletcher (1952) also reported poorer-than-predicted performance on speech recognition tests for a simplified version of his own model intended for clinical use. The poorer performance has been attributed to deficits associated with broadened auditory filter bandwidths commonly associated with sensorineural hearing loss.

However, an alternative explanation is possible. The experiments that have yielded discrepancies between normal-hearing and hearing-impaired subject groups have in common that the groups were presented with speech distorted by

different means. This was necessary to achieve conditions with comparable AIs. For example, Rankovic (1989) presented speech in noise to normal-hearing subjects whereas various amplified speech conditions were presented to hearing-impaired subjects. In contrast, Zurek and Delhorne (1987) and Dubno and Schaefer (1992) constructed much more comparable listening conditions for both groups and found that predictions based on ANSI S3.5 calculations were accurate for hearing-impaired listeners. These authors simulated hearing loss in the normal-hearing subjects by presenting a masking noise that was spectrally shaped to shift thresholds to match those of a hearing-impaired subject. Identical noise-masked speech conditions were then presented to both normal-hearing and hearing-impaired subjects. In the simulation studies, then, speech test scores of both types of subjects were compared in conditions that were not only ANSI AI equated but were also matched for speech and noise intensity levels: the audible portions of speech were restricted to identical spectral regions. This way, noise and speech intensity, frequency response, and gain were factored out of the comparisons because they were identical for the two subject groups. It is not necessary to match conditions so carefully when using the Fletcher calculation because these factors are taken into account so dissimilar listening conditions can be compared. This was demonstrated here and in a previous report (Rankovic, 1997).

There is no single explanation for why Fletcher's version of the articulation theory works better than ANSI S3.5. Computationally, this finding is attributable to a combination of factors (see Sec. II D). Fletcher designed articulation theory to make exact predictions of speech test scores and this report indicates that his theory applies when a sensorineural hearing loss is modeled as a masking noise. Given the extensive validation study presented by Fletcher (1953), perhaps it would have been more surprising if the theory *had not* worked.

C. Implications

Results suggest that the control algorithm tested by Van Dijkhuizen *et al.* could be improved if the extent of masking spread were taken into account and relative band gains adjusted accordingly. This may require obtaining masking data from individual subjects. Alternatively, incorporating a model that predicts masking based on the noise spectrum and absolute thresholds (e.g., Glasberg and Moore, 1990; Ludvigsen, 1987) may be a more practical alternative, if the error in predicted thresholds is tolerable. Models of masking could be easily incorporated into Fletcher's articulation theory to test and/or fine-tune proposed algorithms, or to design algorithms that aim specifically to maximize the articulation index. This is a major advantage of a model-based approach to hearing aid design and selection.

ACKNOWLEDGMENTS

This work was supported by grants R29 DC02127, T32 DC00010, and R01 DC00117 from the National Institute on Deafness and Other Communication Disorders (National Institutes of Health).

APPENDIX

TABLE AI. Masking patterns for hearing-impaired and normal-hearing (NH) subjects (dB SPL). Q indicates absolute thresholds.

Frequency Subject	Q	Masker $f_c=0.5$ kHz						$f_c=1$ kHz						$f_c=2$ kHz					
		$L_m=95$	90	85	80	75	70	95	90	85	80	75	70	95	90	85	80	75	70
DK																			
0.20	42	62	55	58	50	51	50	58	51	47	48	48	46	57	51	52	46	48	46
0.25	41	63	60	57	52	51	51	56	49	46	45	45	45	55	52	50	44	50	44
0.32	39	73	71	66	62	58	55	58	47	45	45	43	44	54	52	51	44	51	43
0.40	37	89	87	79	74	70	63	55	49	45	46	46	43	52	49	50	46	47	47
0.50	40	92	88	82	77	73	69	63	55	51	51	50	47	52	49	48	50	52	48
0.63	41	92	88	83	77	73	67	76	70	67	65	56	57	52	49	50	50	48	50
0.80	42	90	83	78	73	69	65	91	85	78	75	69	67	53	49	53	51	50	52
1.01	45	85	79	72	67	61	59	90	86	82	76	72	69	61	55	54	53	53	55
1.27	44	77	72	66	61	56	55	91	87	81	77	73	68	76	69	65	62	57	54
1.60	41	77	68	63	54	52	49	89	83	75	69	63	59	90	83	78	75	69	66
2.02	43	77	70	63	56	55	51	88	78	73	68	59	58	94	87	83	79	74	68
2.54	37	71	66	59	52	49	48	83	74	68	62	56	50	96	90	87	82	75	73
3.20	29	62	56	47	45	43	42	75	65	56	49	43	42	87	80	78	72	64	58
4.03	28	51	52	42	37	40	32	60	49	46	40	36	36	73	66	62	50	46	41
5.08	37	52	47	41	44	40	40	66	51	45	44	40	41	82	73	67	55	56	47
EG																			
0.20	48			57	57	58	53			55	51	52	46			51	44	51	48
0.25	47			58	57	58	52			53	49	47	43			49	42	49	47
0.32	44			67	63	61	55			53	48	46	43			46	42	46	44
0.40	40			78	72	68	66			51	46	45	43			42	39	42	39
0.50	34			83	77	73	68			55	48	44	44			39	39	40	37
0.63	32			81	77	72	69			68	63	58	55			41	42	39	39
0.80	29			74	68	62	60			79	77	69	65			44	44	40	40
1.01	30			70	63	57	53			79	74	67	64			48	47	43	42
1.27	28			67	61	55	51			79	75	67	63			60	55	51	48
1.60	33			69	60	56	51			77	71	63	57			75	68	63	59
2.02	43			68	61	58	54			73	68	60	56			76	70	66	61
2.54	45			64	58	57	54			68	65	57	52			82	75	72	67
3.20	39			49	47	45	44			56	53	48	45			68	63	59	54
4.03	47			54	51	55	49			65	63	55	48			68	59	59	52
5.08	48			54	58	52	56			55	55	52	52			71	63	62	66
JD																			
0.20	25	67	60	52	44	45	42	75	64	53	47	46	44	55	47	45	45	43	43
0.25	22	66	62	53	47	47	43	72	57	50	45	42	40	49	45	42	38	38	38
0.32	17	73	71	62	58	55	51	70	56	46	44	40	38	48	40	38	37	36	36
0.40	11	88	84	76	71	67	63	66	51	44	42	38	36	43	41	37	36	36	36
0.50	9	91	82	80	77	69	66	62	55	46	45	39	37	39	36	35	34	33	33
0.63	12	90	86	81	75	71	65	78	70	66	63	58	53	40	36	35	35	36	36
0.80	13	85	81	77	71	65	59	92	85	77	74	70	64	47	40	37	35	33	33
1.01	11	81	77	72	65	57	49	92	86	79	76	72	64	53	48	43	38	34	34
1.27	15	82	76	72	63	55	44	93	87	80	77	69	63	70	64	62	54	50	50
1.60	32	82	75	71	62	55	51	90	84	79	75	68	63	86	78	75	72	65	65
2.02	31	85	79	72	61	53	45	87	84	78	74	65	59	90	84	80	70	68	68
2.54	39	87	80	73	60	56	50	93	87	79	72	61	56	95	85	84	76	74	74
3.20	45	79	72	65	59	55	51	90	82	73	68	58	54	87	80	75	68	65	65
4.03	65	80	80	75	70	69	73	91	79	75	69	71	66	87	81	74	71	73	73
5.08	82	89	88	87	84	87	86	85	86	83	83	79	81	79	80	87	80	79	79
SR																			
0.20	46	66	58	58	57	53	53	55	58	60	51	59	55	60	58	54	56	55	58
0.25	47	68	68	63	59	56	56	57	55	62	53	58	58	62	60	59	54	63	60
0.32	44	78	77	75	69	66	66	59	58	63	56	63	59	62	59	60	60	63	61
0.40	45	93	87	83	77	73	73	64	59	63	56	64	61	60	64	57	56	61	58
0.50	39	91	89	83	77	73	73	66	64	64	61	62	62	58	56	58	55	55	53
0.63	45	95	88	85	79	75	75	81	76	71	68	65	64	54	52	57	60	54	53
0.80	49	90	83	80	73	69	69	90	87	81	77	73	70	62	60	61	59	56	56
1.01	48	82	78	75	68	63	63	92	90	82	77	72	68	55	61	58	58	57	56
1.27	56	80	77	75	68	64	64	94	88	83	76	72	70	74	68	65	66	63	64
1.60	69	82	80	79	76	74	74	93	88	84	79	78	76	92	84	75	77	70	74
2.02	87	85	83	86	87	85	85	88	88	88	84	87	83	93	88	85	81	81	81
2.54	90	93	93	91	90	91	91	91	81	86	93	87	90	98	94	90	87	86	86

TABLE AI. (Continued.)

Frequency Subject	Q	Masker $f_c=0.5$ kHz						$f_c=1$ kHz						$f_c=2$ kHz					
		$L_m=95$	90	85	80	75	70	95	90	85	80	75	70	95	90	85	80	75	70
3.20	87	90	89	88	88	87	87	86	88	85	90	84	87	94	88	87	84	85	82
4.03	70	73	71	73	73	71	71	75	75	76	80	72	78	82	82	76	71	68	69
5.08	74	76	76	76	74	76	76	77	80	78	80	77	82	80	81	82	81	81	83
FD																			
0.20	26		41	36	32	29				28	31	30	31		28	30	27	29	
0.25	27		46	43	37	33				28	30	28	30		29	30	26	27	
0.32	24		59	51	48	44				29	31	26	29		28	29	26	26	
0.40	21		73	65	63	59				33	33	29	31		27	29	28	27	
0.50	20		76	70	66	63				40	40	35	34		30	29	25	28	
0.63	17		78	71	65	62				60	55	52	47		29	30	31	32	
0.80	29		74	65	60	57				74	70	64	62		32	36	34	34	
1.01	36		69	60	54	48				75	70	64	59		40	41	38	37	
1.27	45		65	55	50	47				74	69	64	59		53	53	48	44	
1.60	49		68	58	55	51				72	67	60	58		67	65	59	55	
2.02	59		71	65	61	60				74	70	65	64		69	72	64	62	
2.54	63		71	65	64	63				73	69	66	65		74	74	70	65	
3.20	59		66	60	60	59				67	65	62	61		68	69	66	63	
4.03	57		54	47	50	52				54	57	52	51		57	55	50	53	
5.08	60		62	56	60	59				59	58	58	58		63	65	59	58	
PG																			
0.20	69	70	68					69	71					74	74				
0.25	72	75	74					74	74					76	76				
0.32	73	79	77					76	76					79	79				
0.40	76	85	83					78	78					80	79				
0.50	76	89	85					80	79					79	78				
0.63	74	86	83					82	79					79	78				
0.80	75	85	79					88	81					80	79				
1.01	76	83	78					86	81					81	79				
1.27	80	87	85					90	85					83	84				
1.60	82	88	86					89	84					88	84				
2.02	77	85	84					88	85					89	84				
2.54	79	85	85					87	85					92	87				
3.20	75	80	81					82	78					83	78				
4.03	64	69	68					70	66					79	76				
5.08	75	80	79					81	77					88	84				
AL																			
0.20	65	71	70	68	68			67	69	64	67			68	66	67			
0.25	63	73	70	69	70			69	69	67	67			68	67	70			
0.32	68	79	77	73	73			73	73	71	71			74	72	73			
0.40	72	93	86	83	82			81	83	79	79			81	77	77			
0.50	73	94	88	84	82			84	84	79	79			78	76	76			
0.63	74	95	90	83	80			87	83	81	80			78	77	76			
0.80	74	91	87	82	79			90	87	82	80			79	78	78			
1.01	76	88	85	82	80			91	88	83	80			83	83	80			
1.27	83	92	87	84	82			92	90	85	80			94	93	92			
1.60	83	92	87	85	81			89	88	88	86			97	93	91			
2.02	75	90	84	80	79			88	86	81	80			94	88	83			
2.54	74	86	83	78	80			85	85	78	78			96	88	83			
3.20	65	74	69	71	68			71	73	69	70			80	74	69			
4.03	63	66	62	63	64			61	64	61	65			76	69	66			
5.08	83	88	86	84	85			83	86	82	87			94	87	87			
NH																			
0.20	23	47	40	39	35	31	31	43	35	33	30	29	26	39	34	31	29	29	27
0.25	22	52	46	43	39	34	33	42	36	32	29	28	26	36	34	29	28	27	26
0.32	18	67	63	60	53	48	44	44	37	34	31	31	31	36	34	30	30	31	28
0.40	18	80	75	73	68	61	58	47	41	37	33	31	29	35	33	30	30	31	29
0.50	15	84	79	75	71	64	62	54	49	43	39	35	32	34	32	29	28	29	30
0.63	13	84	77	74	71	65	62	70	65	59	55	51	46	35	31	30	31	32	31
0.80	11	77	71	67	62	56	48	79	77	71	67	62	58	39	32	30	28	27	28
1.01	11	72	66	60	52	44	35	82	78	73	69	64	59	48	42	37	34	29	27
1.27	9	73	63	54	43	36	26	85	79	73	68	63	60	65	58	53	51	43	42
1.60	11	66	56	48	37	30	23	69	69	64	57	50	44	79	71	68	64	58	56

TABLE AI. (Continued.)

Frequency Subject	Q	Masker $f_c=0.5$ kHz						$f_c=1$ kHz						$f_c=2$ kHz					
		$L_m=95$	90	85	80	75	70	95	90	85	80	75	70	95	90	85	80	75	70
2.02	14	66	53	46	34	28	24	73	68	58	48	39	32	82	75	72	68	64	58
2.54	17	63	50	41	32	29	27	73	62	53	42	32	29	88	82	77	72	68	64
3.20	8	45	33	26	22	21	21	60	43	36	27	24	23	74	69	64	59	51	43
4.03	5	29	20	16	14	13	13	43	28	19	15	12	13	65	58	47	36	27	20
5.08	16	33	25	22	22	23	21	46	31	24	23	21	21	70	57	42	35	25	24

¹Van Dijkhuizen *et al.* (1991) designed their experiment to test the effectiveness of a feasible algorithm in a reasonably realistic noise background (a broadband noise with a spectral prominence) rather than to examine mechanisms responsible for speech reception improvements. Unlike other reports (see Rankovic *et al.*, 1992, for a brief review), Van Dijkhuizen *et al.* supplied detailed descriptions of the listening conditions and the processing as well as the speech reception thresholds obtained from individual subjects in all test conditions. As a result, it is possible to reconsider the performance of their individual subjects here.

Van Dijkhuizen *et al.* presented averaged results in their Fig. 2, p. 890. The individual-subject data referred to here are contained in their Table V, p. 889: the "selective" condition processed with the "100% compression factor." If a difference in speech reception threshold (SRT) greater than 2 dB is taken as significant (Plomp and Mimpen, 1979), the following subjects did not demonstrate significant improvements in SRT with processing for the 0.25–0.5 kHz noise increment condition: subjects 4, 5, 6, 9, 10, and 11. The following subjects did not demonstrate significant improvements with processing for the 0.5–1 kHz noise increment: subjects 1, 4, 9, 11, and 12. In conclusion, 6 of 12 subjects did not show significant improvement with the 0.25–0.5 kHz noise increment condition and 5 of 12 subjects did not show significant improvement with the 0.5–1 kHz noise increment condition.

ANSI (1969). ANSI S3.5-1969, "American National Standard methods for the calculation of the articulation index" (American National Standards Institute, New York).

Bilger, R. C., and Hirsh, I. J. (1956). "Masking of tones by bands of noise," *J. Acoust. Soc. Am.* **28**, 623–630.

Braida, L. D., Durlach, N. I., Lippmann, R. P., Hicks, B. L., Rabinowitz, W. M., and Reed, C. M. (1980). "Hearing aids—A review of past research on linear amplification, amplitude compression, and frequency lowering," *ASHA Monogr.* **19**.

Dubno, J. R., and Ahlstrom, J. B. (1995a). "Masked thresholds and consonant recognition in low-pass maskers for hearing-impaired and normal-hearing listeners," *J. Acoust. Soc. Am.* **97**, 2430–2441.

Dubno, J. R., and Ahlstrom, J. B. (1995b). "Growth of low-pass masking of pure tones and speech for hearing-impaired and normal-hearing listeners," *J. Acoust. Soc. Am.* **98**, 3114–3124.

Dubno, J. R., and Schaefer, A. B. (1992). "Comparison of frequency-selectivity and consonant recognition among hearing-impaired and masked normal-hearing listeners," *J. Acoust. Soc. Am.* **91**, 2100–2121.

Dugal, R. L., Braida, L. D., and Durlach, N. I. (1980). "Implications of previous research for the selection of frequency-gain characteristics," in *Acoustical Factors Affecting Hearing Aid Performance*, edited by G. A. Studebaker and I. Hochberg (University Park, Baltimore).

Fletcher, H. (1952). "The perception of speech sounds by deafened persons," *J. Acoust. Soc. Am.* **24**, 490–497.

Fletcher, H. (1953). *Speech and Hearing in Communication* (Van Nostrand, New York).

Fletcher, H., and Galt, R. H. (1950). "The perception of speech and its relation to telephony," *J. Acoust. Soc. Am.* **22**, 89–151.

French, N. R., and Steinberg, J. C. (1974). "Factors governing the intelligibility of speech sounds," *J. Acoust. Soc. Am.* **19**, 90–119.

Glasberg, B. R., and Moore, B. C. J. (1990). "Derivation of auditory filter

shapes from notched-noise data," *Hearing Res.* **47**, 103–138.

Gagne, J.-P. (1988). "Excess masking among listeners with a sensorineural hearing loss," *J. Acoust. Soc. Am.* **83**, 2311–2321.

Keith, R. W., and Anderson, C. V. (1969). "Remote masking for listeners with cochlear impairment," *J. Acoust. Soc. Am.* **46**, 393–398.

Kryter, K. D. (1962). "Methods for the calculation and use of the articulation index," *J. Acoust. Soc. Am.* **34**, 1689–1697.

Ludvigsen, C. (1987). "Prediction of speech intelligibility for normal-hearing and cochlearly hearing-impaired listeners," *J. Acoust. Soc. Am.* **82**, 1162–1171.

McCandless, G. A., and Lyregaard, P. E. (1983). "Prescription of Gain/Output (POGO) for hearing aids," *Hearing Instrum.* **34**(1), 16–21.

Moore, B. C. J. (1995). *Perceptual Consequences of Cochlear Damage* (Oxford U.P., New York).

Nelson, D. A., and Schroder, A. C. (1997). "Linearized response growth in ferred from growth-of-masking slopes in ears with cochlear hearing loss," *J. Acoust. Soc. Am.* **101**, 2186–2201.

Pavlovic, C. V. (1984). "Use of the articulation index for assessing residual auditory function in listeners with sensorineural hearing impairment," *J. Acoust. Soc. Am.* **75**, 1253–1258.

Plomp, R., and Mimpen, A. M. (1979). "Improving the reliability of testing the speech reception threshold for sentences," *Audiology* **18**, 43–52.

Rankovic, C. M. (1989). "An application of the articulation index to hearing aid fitting," unpublished dissertation, University of Minnesota.

Rankovic, C. M. (1997). "Prediction of speech reception for listeners with sensorineural hearing loss," in *Modeling Sensorineural Hearing Loss*, edited by W. Jesteadt (Erlbaum, Mahwah, NJ).

Rankovic, C. M., and Zurek, P. M. (1993). "A comparison of octave-band noise masking patterns obtained from normal-hearing and hearing-impaired listeners," *J. Acoust. Soc. Am.* **93**, 2314.

Rankovic, C. M., Freyman, R. L., and Zurek, P. M. (1992). "Potential benefits of adaptive frequency-gain characteristics for speech reception in noise," *J. Acoust. Soc. Am.* **91**, 354–362.

Rankovic, C. M., Zurek, P. M., and Freyman, R. L. (1991). "Potential benefits of varying the frequency-gain characteristic for speech reception in noise for hearing-impaired individuals," *J. Acoust. Soc. Am.* **90**, 2319.

Rittman, P. A. (1962). "Pure-tone masking by narrow-noise bands in normal and impaired ears," *J. Aud. Res.* **2**, 287–304.

Saito, S., and Watanabe, S. (1961). "Normalized representation of noise-band masking and its application to the prediction of speech intelligibility," *J. Acoust. Soc. Am.* **33**, 1013–1021.

Stelmachowicz, P. G., Lewis, D. E., Larson, L. L., and Jesteadt, W. (1987). "Growth of masking as a measure of response growth in hearing-impaired listeners," *J. Acoust. Soc. Am.* **81**, 1881–1887.

Tyler, R. S. (1986). "Frequency resolution in hearing-impaired listeners," in *Frequency Selectivity in Hearing*, edited by B. C. J. Moore (Academic, New York).

Van Dijkhuizen, J. N., Festen, J. M., and Plomp, R. (1991). "The effect of frequency-selective attenuation on the speech-reception thresholds of sentences in conditions of low-frequency noise," *J. Acoust. Soc. Am.* **90**, 885–894.

Zurek, P. M., and Delhorne, L. A. (1987). "Consonant reception in noise by listeners with mild and moderate sensorineural hearing impairment," *J. Acoust. Soc. Am.* **82**, 1548–1559.

The effects of different envelope patterns and uncertainty for the detection of a tone added to SAM complex tonal maskers

Virginia M. Richards, Emily Buss,^{a)} and Lijun Tian^{b)}

Department of Psychology, 3815 Walnut Street, University of Pennsylvania, Philadelphia, Pennsylvania 19104

(Received 7 May 1997; revised 10 October 1997; accepted 10 October 1997)

Thresholds for the detection of a tone added in-phase to the carrier of a fully modulated SAM tone were measured. In some conditions the signal was added to a single SAM tone, and in other conditions the signal was added to the sum of three or more SAM tones. Level equalization ensured that the addition of the tonal signal did not lead to increases in energy. When multiple SAM tone maskers were used, a small number of reproducible maskers were tested, each masker being composed of SAM tones with a variety of relative modulator phases. The maskers were either *fixed* across intervals and trials, *roved* across trials but fixed across intervals, or *randomly* chosen across both intervals and trials. The frequency separation between the signal-centered and off-frequency SAM tones was also varied. For small signal-centered/off-frequency SAM tone frequency separations, a separation ratio of 1.3, thresholds in the *fixed* condition depend on the relative modulator phases, and a simple mixture model reasonably predicted thresholds in the *roving* condition based on thresholds in the *fixed* condition for two of the three observers. For signal-centered/off-frequency SAM tone frequency separation factor of 1.68, effects of relative modulator phases were not obtained. Thresholds in the *target-alone* condition were generally superior to thresholds measured with the comodulated masker. Comodulated thresholds were better than *target-alone* thresholds only when level equalization was not used, and so the addition of the signal led to increases in level. © 1998 Acoustical Society of America. [S0001-4966(98)01002-9]

PACS numbers: 43.66.Dc, 43.66.Mk [WJ]

INTRODUCTION

A large number of comodulation masking release (CMR) experiments have demonstrated that the detection of a tone added to the sum of two or more narrow-band maskers can depend on the relative envelope patterns of the narrow-band maskers. Referring to the narrow-band masker centered at the signal frequency as the signal-centered masker and the other narrow-band maskers as the off-frequency maskers, thresholds are typically lowest when the signal-centered and off-frequency maskers have coherent or comodulated envelope patterns; intermediate when just the signal-centered narrow-band masker is present; and largest when the narrow-band maskers have envelopes that do not share modulation patterns (e.g., Hall *et al.*, 1984; Schooneveldt and Moore, 1987; Grose and Hall, 1989; Fantini, 1991). This pattern of results is exaggerated when the signal-centered and off-frequency maskers are relatively nearby in frequency, and appears to occur for signal-centered/off-frequency narrow-band masker separations of an octave or so, the point at which thresholds in the different conditions tend to converge (Cohen and Schubert, 1987; Richards *et al.*, 1997). Not all studies find convergence, however. For example, Schooneveldt and Moore (1987) suggested that the threshold advantage associated with comodulated envelope patterns remains at 3 dB or so even for wide frequency separations, and Co-

hen (1991) found that when the signal-centered and off-frequency maskers were of different levels, effects of across-frequency comodulation were measured for frequency separations as large as three octaves.

Much of the work regarding the dependence of signal detectability on the relative envelope patterns of the signal-centered and off-frequency maskers has emphasized the release from masking associated with comodulation (hence the term comodulation masking release). Relatively less work has examined the basis of the interfering effect of incoherent envelope patterns across frequency. Wright and McFadden (1990) examined the possibility that differences in thresholds measured when envelope patterns are comodulated versus random across frequency reflect different mechanisms. In their study, the degree of certainty with which either comodulated or random envelope patterns would be presented was manipulated. They found relatively little effect of uncertainty, indicating the same mechanisms are likely to underlie detection in the two conditions. In a similar vein, Richards *et al.* (1997) suggested that because thresholds in comodulated and random conditions covary with the frequency of separation between the signal-centered and off-frequency maskers, a single decision rule is likely to underlie detection regardless of consistency of envelope modulation patterns across frequency. Indeed, Richards *et al.* (1997) favored an explanation based on single-channel processing, suggesting effects of envelope modulation pattern, and so the CMR, reflects interactions within a single channel (see also, Berg, 1996).

Whether the elevated thresholds for the detection of a

^{a)}Current address: Otolaryngology, 610 Burnett Womack Building, Campus Box #7070, University of North Carolina, School of Medicine, Chapel Hill, NC 27599-7070.

^{b)}Current address: CB Technologies, Inc., 266 E. Lancaster Ave., Malvern, PA 19355.

tone added to multiple narrow-band maskers with random envelope patterns reflects processing in a single frequency channel versus across-channel processing, the reasons for elevated thresholds in the random conditions are of interest. For example, do the elevated thresholds reflect differential sensitivity to the different envelope patterns presented in the course of the experiment, or does a generalized uncertainty effect lead to increased thresholds (e.g., Moore *et al.*, 1990)? Using sinusoidally amplitude modulation (SAM) narrow-band noise maskers, Fantini (1991) found that the threshold for the detection of an added tone depends systematically on the difference in phase of signal-centered and off-frequency SAM modulators. For narrow-band noise maskers, McFadden (1986) found thresholds for the detection of a tone added to the sum of signal-centered and off-frequency narrow-band noise maskers grew as the envelopes of the two narrow-band maskers were delayed relative to one another. It is plausible, then that thresholds obtained in random conditions reflect a combination of sensitivities associated with the variety of maskers tested.

In an effort to test such a mixture model, and more generally, to evaluate the role of uncertainty for the detection of a tone added to maskers with different across-frequency envelope patterns, two experiments were completed. Both used a limited number of reproducible maskers, which allowed an evaluation of the effect of uncertainty with regard to a particular masker waveform. Based on the results of Fantini (1991), it was anticipated that the different maskers would lead to differential sensitivity, and based on the results of Wright and McFadden (1990) little effect of uncertainty was expected. However, compared to Wright and McFadden, the ‘‘certain’’ stimulus was extreme, that is, the same stimulus was tested in both intervals as well as in all trials of each block of trials that led to a threshold estimate.

I. EXPERIMENT I

In the first experiment, thresholds for the detection of a tone added in-phase to the carrier frequency of a signal-centered SAM tone were estimated. Because level equalization reduced the availability of energy-based cues, this task was equivalent to the detection of a reduction in modulation depth relative to the fully modulated standard. Thresholds were measured in three conditions. First, in the *target-alone* condition, only the signal-centered SAM tone was presented. In the remaining conditions, the signal-centered and two off-frequency SAM tones were presented together to form the masker. For the *fixed* condition, the relative phases of the signal-centered and off-frequency SAM tones were fixed across both intervals of a 2IFC trial and across several blocks of trials. For the *roving* condition, the two intervals of each trial had the same masker, but the masker was randomly chosen on each trial (similar to Wright and McFadden, 1990, random by trial/same within trial condition). In the *random* condition the masker was randomly chosen on each interval of each trial (similar to Wright and McFadden, 1990, random by observation interval/different within trial condition). Finally, a simple mixture model was tested by generating predictions for the *roving* condition based on thresholds measured in the *fixed* condition.

II. METHODS FOR EXPERIMENT I

A. Stimulus generation

The maskers were comprised of one or more fully modulated SAM tones modulated at a rate of 16 Hz. The carrier frequency of the signal-centered SAM tone was identical to the frequency of the signal, 1500 Hz. The signal, when present, was a tone added in-phase to the carrier, yielding a reduction in modulation depth. The off-frequency SAM tones were separated from the signal by a factor of either 1.3 (and 1/1.3) or 1.68 (and 1/1.68), yielding off-frequency SAM tone carriers of 1154 and 1950 Hz in the first case and 892 and 2520 Hz in the second case. The individual SAM tones were presented at 65 dB SPL, and when the signal was added, the signal-centered masker-plus-signal SAM tone was digitally scaled so as to provide a presentation level of 65 dB SPL.

The starting phases of the signal-centered and off-frequency SAM carriers were randomly chosen on each interval from a uniform distribution ranging from 0 to 2π rad. Likewise, the starting phase of the signal-centered modulator was randomly chosen from a uniform distribution ranging from 0 to 2π rad on each presentation. Five different stimuli were tested, each differing in the modulator phases of the off-frequency modulators relative to the signal-centered modulator phase. As a proportion of the modulator period, the relative modulator phases of the low-frequency, signal-centered, and high-frequency SAM tones were 1:(0,0,0), 2:(0.25, 0, -0.25), 3:(-0.4, 0, 0.4), 4:(0.125, 0, -0.1), 5:(-0.2, 0, 0.3). As indicated, these will be referred to as maskers 1–5, with masker 1 denoting the condition in which the signal-centered and off-frequency SAM tones have coherent envelope patterns.

The stimuli were digitally generated and presented using a sample rate of 25 000 samples/s. The signal-centered SAM tone and the signal were presented via one channel of a two-channel digital-to-analog converter, and when off-frequency SAM tones were present, they were presented simultaneously through the second channel. The stimulus duration was 500 ms, including 34-ms cosine-squared onset and offset ramps. The digital outputs were low-pass filtered at 8 kHz (KEMO VBF 8; attenuation skirts approx. 85 dB/oct), summed using an analog adder, and presented diotically through two channels of Sennheiser HD410SL headphones.

B. Procedures and experimental conditions

A 2IFC procedure was used, with the signal interval being as likely to be the first as the second interval. Visual feedback indicated the correctness of each response. Thresholds were estimated using a 2-down, 1-up staircase procedure which estimated the 71 percent correct performance level (Levitt, 1971). Each threshold estimate was generated using blocks of 50 trials and was based on the average of the last even number of reversals, excluding at least the first three. The tracking procedure altered the signal level by changing the modulation depth of the on-frequency SAM tone, using a $20 \log(m)$ scale. A typical initial step size was 0.6 dB, and reduced to 0.3 dB following three reversals. If an observer was particularly sensitive or insensitive in a condi-

tion, the step sizes were reduced or increased, respectively. Observers completed five threshold estimates in turn, with a pause between threshold estimates, then rested. Sessions lasted 1–2 h, yielding 15–30 threshold estimates per session.

Four experimental conditions were tested. In the *target-alone* condition, thresholds were measured for the signal tone added to just the signal-centered SAM tone. For the *fixed* condition, the same masker was used for each presentation, and for the block of five threshold estimates. For the *roving* condition, the same masker was used for the signal and no-signal intervals, but on each trial, the masker was randomly chosen. For the *random* condition, the maskers presented in the signal and no-signal intervals were chosen at random, and with replacement, from the five maskers.

Observers practiced randomly chosen conditions for 5–10 h before data collection began. After practice, ten threshold estimates were measured in the *target-alone* condition. Then the remaining conditions were tested. Two observers first completed the condition in which the signal-centered and off-frequency SAM tones were separated by a factor of 1.3, the other first completed the conditions in which the signal-centered and off-frequency SAM tones were separated by a factor of 1.68. For each observer, 15 threshold estimates were obtained for each condition, and after the 15 estimates were finished, a 1-tailed heteroscedastic Student's *t* test ($p=0.05$ criterion; first 5 threshold estimates against the last five threshold estimates) was used to test for practice effects. As needed, additional threshold estimates were obtained. After finishing all conditions, at least another five threshold estimates were measured in the *target-alone* condition. Thresholds reported below are based on the final nine threshold estimates.

Observers had thresholds in quiet of 10 dB HL or better (for frequencies ranging from 250 to 8000 Hz) and ranged in age from 21 to 30 years. Tests were completed with the observer seated in a double-walled soundproof booth.

III. RESULTS AND DISCUSSION OF EXPERIMENT I

Figures 1 and 2 show the averaged thresholds, as $20 \log(m)$, for the individual observers. Recall that the signal-centered SAM tone was fully modulated and the addition of the signal led to smaller modulation depths [negative $20 \log(m)$ values]. Thus more negative $20 \log(m)$ values are plotted higher on the graph, indicating larger signal magnitudes. Error bars indicate the standard errors of the mean. Figure 1 is for maskers with carriers separated in frequency by a factor of 1.3; Fig. 2 is for a frequency separation factor of 1.68. *Target-alone* thresholds are plotted on the left hand side (cross-hatched), and thresholds for the *roving* and *random* conditions are shown to the right. For the *fixed* conditions, whose thresholds are shown in the middle, each masker number is accompanied by a graph that represents the off-frequency modulator phases relative to the modulator phase of the signal-centered SAM tone. The solid ray is set at an angle of zero: the angle of the signal-centered modulator. The phases of the low- and high-frequency off-frequency modulators relative to the signal-centered modulator, are indicated using dotted and dashed rays, respectively. For the *fixed* conditions, the ordering for different maskers is ascend-

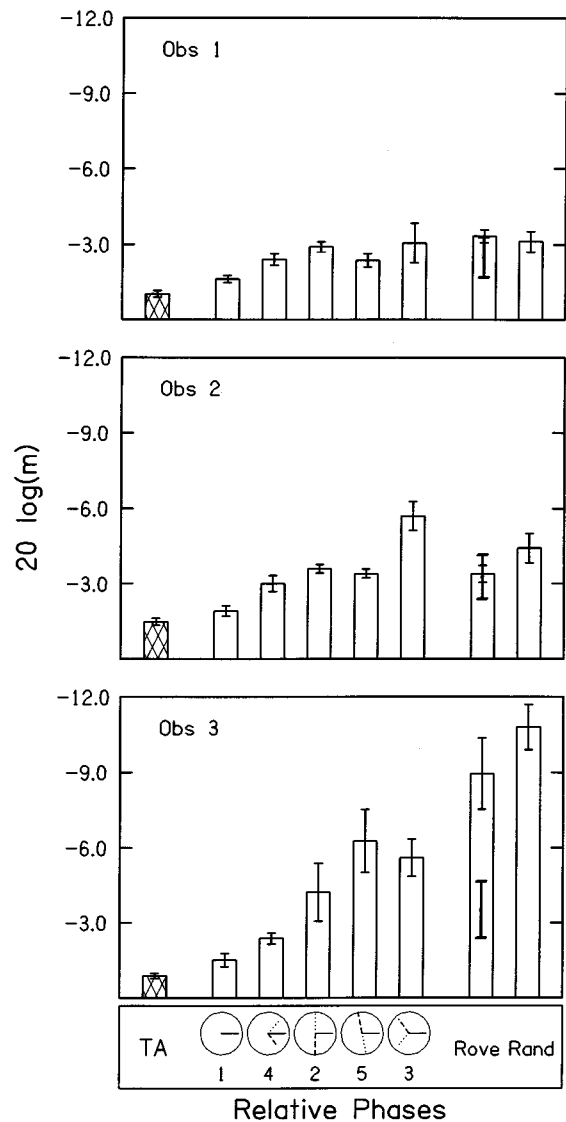


FIG. 1. Thresholds, as $20 \log(m)$, are plotted for three observers. The signal-centered and off-frequency maskers are separated by a factor of 1.3. The *target-alone* condition is plotted to the left (cross-hatched) and the *roving* and *random* conditions are plotted to the right. The results for the *fixed* conditions are plotted centrally, with the masker number shown on the abscissa. Error bars indicate the standard errors of the mean. Bold error bars indicate the standard deviation of the simulated mixture model predictions.

ing based on averaged thresholds. The bold error bars superimposed on the *roving* data are for the predictions of a mixture model, which will be detailed below.

Thresholds are nearly always superior (less negative) for the *target-alone* condition. Comparing thresholds for the *target-alone* condition and the *fixed* condition with comodulated maskers (masker 1), thresholds are lower in the *target-alone* condition, indicating cross-channel masking (e.g., Bacon and Konrad, 1993; Moore *et al.*, 1990) but not a CMR. For Observer 3, thresholds in the *roving* and *random* conditions tend to be inferior (more negative) to the other conditions, a result that does not hold for the other observers.

For the *fixed* conditions, an analysis of variance (ANOVA) indicated a significant main effect of phase and frequency separation [$F(4,8)=4.4$ and $F(1,2)=27$ respec-

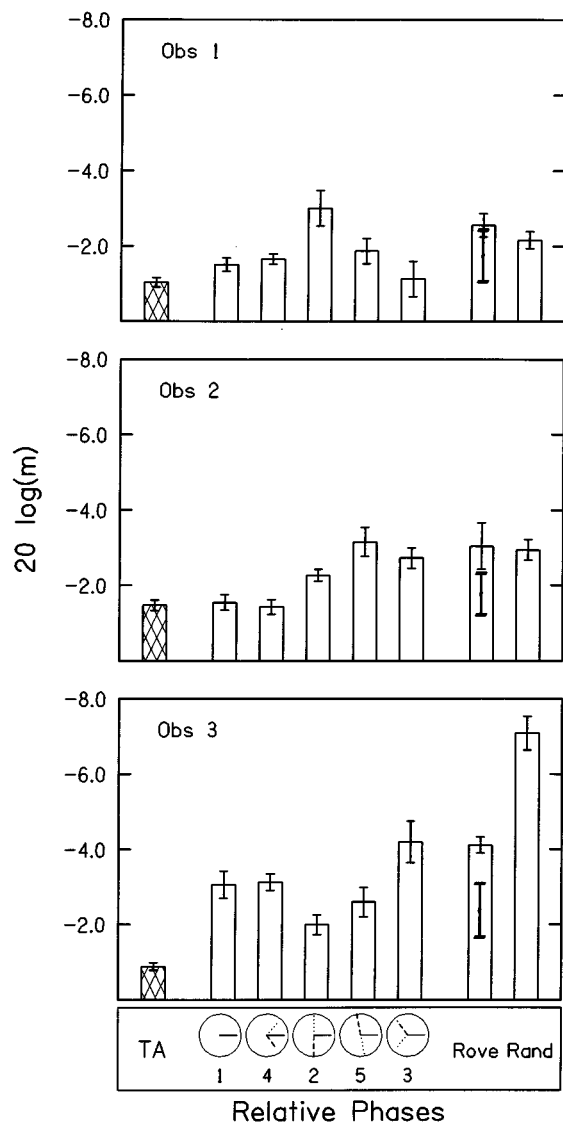


FIG. 2. As Fig. 1, except the signal-centered and off-frequency SAM tones are separated by a factor of 1.68.

tively, $p < 0.05$]. The interaction was not significant [$F(4,8) = 1.4, p > 0.3$]. When analyzed separately, significant phase effects were obtained when the component carriers were separated by a factor of 1.3 [$F(4,8) = 4.4, p < 0.05$] but not when they were separated by a factor of 1.68 [$F(4,8) = 0.33, p > 0.8$]. Using similar experimental conditions, Richards *et al.* (1997) found that randomly choosing the phases of multiple SAM tone maskers on each interval influenced detection thresholds only when the signal-centered and off-frequency SAM tones were separated by less than an octave. Moreover, Richards *et al.* found that the effects of across-frequency modulator phase randomization diminished as the frequency separation between the signal-centered and off-frequency SAM tones grew. The current results conform to that expectation. Thresholds in the random condition were smaller for a frequency separation of 1.7 than for a frequency separation of 1.3 (comparing the *random* conditions in Figs. 1 and 2), although the average difference of 2 dB is small. Taken together, the results of the current study and Richards *et al.* (1997) indicate that phase

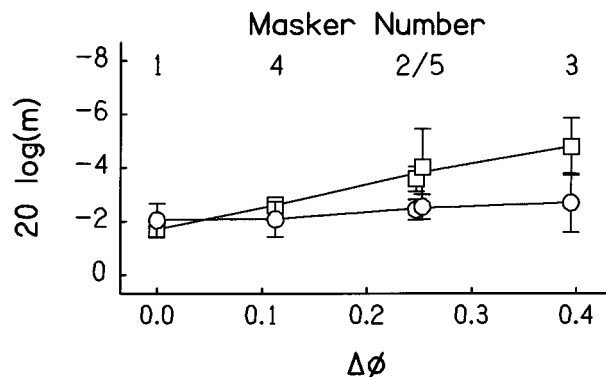


FIG. 3. *Fixed* thresholds averaged across observers as a function of $\Delta\Phi$, the average change in modulator phase, signal-centered modulator re off-frequency modulator, without respect to sign, and as a proportion of modulator phase. Masker number is also shown. Squares and circles are for signal-centered/off-frequency masker separation factors of 1.3 and 1.68, respectively. Error bars are the standard error of the mean across three observers.

effects diminish with increased frequency separation among the components of the complex masker for both *fixed* and *random* conditions.

Figure 3 shows *fixed* thresholds from Figs. 1 and 2 averaged across observers as a function of the average difference in modulator phase ($\Delta\Phi$), signal-centered modulator re off-frequency modulator, without respect to sign, and as a proportion of modulator phase. The masker number is indicated at the top of the figure. Squares are for a frequency separation factor of 1.3; circles are for a frequency separation factor of 1.68. Error bars indicate the standard error of the mean across the three observers. For example, for masker 1, which is comprised of coherent modulator phases, $\Delta\Phi = 0$. For masker 5, which has relative phases as a proportion of the modulator period of $(-0.2, 0, 0.3)$ for the low-frequency, signal-centered, and high-frequency SAM tones, respectively, $\Delta\Phi = 0.25$. Maskers 2 and 5 have the same $\Delta\Phi$, the symbols are offset for the sake of easier viewing. For the frequency separation of 1.3, thresholds grow with $\Delta\Phi$. For the frequency separation of 1.68, the function is flat, consistent with the absence of off-frequency modulator phase effects. The growth in thresholds with $\Delta\Phi$ is consistent with the results of Fantini (1991), who used sinusoidally amplitude modulated bands of noise and a single off-frequency masker.

One interpretation of the averages shown in Fig. 3 is that thresholds depend on a simple, single-channel, additivity of maskers. By this explanation, interactions within a single channel would be significant only for the data obtained using a frequency ratio of 1.3. When interactions occur, thresholds would be poorest when the “dips” in the signal-centered SAM tone are obscured by the “peaks” of the off-frequency SAM tones (i.e., large $\Delta\Phi$). Phase effects would not be obtained for a frequency separation factor of 1.68 due to the absence of single-channel interactions between the signal-centered and off-frequency SAM tones. An alternative explanation is that observers use the minima in the off-frequency SAM tones to cue sampling at the on-frequency masker; but when there are phase differences, this sampling is nonopti-

mal, and might lead to increased thresholds (Buus, 1985; Buss and Richards, 1995). By this explanation, the absence of phase effects for wider frequency separations would reflect diminished comparison sensitivities.

In an effort to determine whether thresholds measured in the *roving* condition could be accounted for using a simple mixture model, several simulations were completed. First signal and no-signal distributions for the fixed conditions were estimated for each observer. For each masker, the signal and no-signal distributions were assumed to be Gaussian and equal variance. It was assumed that changes in the signal level influenced the mean of the signal distribution, but not the variance of the distribution. While a variety of “sensory units” might be assumed, here a $20 \log(m)$ scale was used.¹ At threshold, d' is constant, and so the variance of the signal and no-signal distributions may be directly estimated using the assumptions listed above and the measured threshold value. After estimating the variances of the distributions for each of the fixed maskers, a tracking algorithm was applied to draws from single masker distributions, and the average simulated threshold was within a standard error of the mean of the measured threshold. Then, a mixture model was tested. On each trial of the tracking procedure, a masker, and its associated no-signal and signal *fixed* distributions, was randomly chosen. The model’s “response” was based on draws from the *fixed* distributions. The results of the mixture model are shown in Figs. 1 and 2 using bold error bars that indicate the standard deviation across 40 simulated threshold estimates. For a frequency separation factor of 1.3, and for observers 1 and 2, the mixture model reasonably estimates thresholds in the *roving* condition. For observer 3, the prediction underestimates the threshold, suggesting the presence of additional internal noise, or uncertainty effects. For a frequency separation factor of 1.68, and for observer 1, the mixture model reasonably predicts thresholds in the *roving* condition. For observers 2 and 3, however, the predictions of the mixture model underestimate thresholds, suggesting an uncertainty effect.

For observers 1 and 2, thresholds in the *random* condition are comparable to thresholds in the *roving* condition, regardless of the frequency separation factor. Wright and McFadden (1990), who studied the detection of a tone added to narrow-band noise maskers, similarly found no evidence of additional uncertainty for shifts from conditions parallel to the *roving* and *random* conditions described here. For observer 3, however, the additional randomization associated with the *random* condition relative to the *roving* condition appears to generate sizable uncertainty.

In summary, the three primary results of this experiment are: (1) no CMR was obtained, probably because the addition of the signal did not introduce changes in level (Fantini and Moore, 1994; Richards *et al.*, 1997; in contrast with Hall and Grose, 1988); (2) across-frequency modulator phase effects were obtained when the signal-centered/off-frequency carrier frequency separation was 1.3, but not when the separation factor was 1.68; (3) a mixture model was somewhat successful in accounting for *roving* thresholds when the signal-centered/off-frequency carrier frequency separation was 1.3, and less successful when the separation factor was

1.68. With regard to the third result, the relative success/failure of the mixture model reflects differences across observers. For example, for observer 3 the mixture model underestimated *roving* thresholds for 1.3 and 1.68, possibly reflecting an uncertainty effect. In contrast, for observer 1, the mixture model successfully account for thresholds in the *roving* condition, regardless of frequency separation.

Because the data reflect an effect of frequency separation, it seems plausible that single-channel processing influenced thresholds more for the nearby SAM tones than when the SAM tones were relatively more separated in frequency. Keeping in mind that the mixture model was successful in accounting for thresholds for only two of the three observers when a separation factor of 1.3 was used, the results suggest that for CMR experiments that use multiple narrow-band maskers relatively nearby in frequency, thresholds in the random condition reflect differential sensitivity to the variety of envelope patterns encountered in the course of the threshold measurement.

IV. EXPERIMENT II

In the second experiment, effects of uncertainty were examined using slightly different conditions and procedures. In this experiment, the intent was to more closely evaluate the effects of increased uncertainty that occur with changes from the *fixed* to the *roving* to the *random* conditions. There are four primary differences in the methods used in experiment II compared to experiment I. First, a larger number of maskers was used; seven rather than five. Second, seven simultaneous adaptive tracks were run in parallel. As a result, direct comparisons between the *fixed*, *roving*, and *fixed/random* conditions could be made, where the *fixed/random* condition parallels the *random* condition of experiment I. Third, a larger number of off-frequency components was used, with relatively small frequency separations between signal-centered and off-frequency SAM tones. Fourth, a subset of the experiment was repeated without level equalization, meaning that the addition of the signal led to an increase in level.

A. Stimuli and procedures

In this experiment, four off-frequency SAM tones were used. The signal-centered SAM carrier was 800 Hz, and the off-frequency SAM carriers were 500, 600, 1000, and 1100 Hz. The signal was an 800-Hz tone added in-phase to the carrier of the 800-Hz SAM tone. Seven multi-SAM tone composite maskers were tested, the difference between the seven stimuli being the relative modulator phases of the five SAM tones that comprised each stimulus. Denoting the off-frequency modulator phases relative to the signal-centered SAM tones, in terms of proportion of the period, and in ascending order of carrier frequency, the seven stimuli are: 1:(0,0,0,0,0,0), 2:(-0.1, 0.1, 0, 0, 0), 3:(0, 0.2, 0, -0.1, 0.4), 4:(-0.3, 0.5, 0, -0.1, 0.4), 5:(0.2, -0.3, 0, 0.2, 0), 6:(0.3, 0.2, 0, 0.1, 0.5), 7:(0.5, 0.5, 0, 0.5, 0.5). Maskers 1 and 7 were chosen based on existing data; for these conditions thresholds are expected to be lowest and highest, respectively (Fantini, 1991; Buss and Richards, 1995). The other relative phases were formed according to random

draws with replacement from the distribution of equal-probable values: $[-0.4, -0.3, -0.2, -0.1, 0, 0.1, 0.2, 0.3, 0.4, 0.5]$

As in experiment I, a 2IFC procedure was used. In contrast to experiment I, however, the signal levels were titrated based on the signal-to-carrier ratio, in dB. Unless otherwise noted, digital scaling prevented the change at the signal frequency from leading to a change in the level of the signal-centered SAM tone. The stimuli were digitally generated and presented using a sample rate of 10 000 samples/s. The signal-centered SAM tone and signal were presented via one channel of a two-channel digital-to-analog converter, when the off-frequency SAM tones were present, they were presented simultaneously through the second channel. The stimulus duration was 400 ms, including 34-ms cosine-squared onset and offset ramps. The digital outputs were low-pass filtered at 3 kHz (KEMO VBF 8; attenuation skirts approx. 85 dB/oct), summed using an analog adder, and presented diotically through two channels of Sennheiser HD410SL headphones. The stimuli were presented at a level of 65 dB SPL per SAM tone.

In this experiment, seven interleaved 2-down, 1-up (Levitt, 1971) staircases were used to estimate seven thresholds in parallel. In the *fixed* condition, the same masker was used for all tracks, and in the two intervals of each trial. For this condition, the seven tracks provide seven threshold estimates for the same masker. In the *roving* condition, the signal and no-signal intervals had the same masker, but each of the seven tracks was associated with a different masker. In the *fixed/random* condition, one of the tracks had the same masker in the two intervals. For the remaining six tracks, the signal interval was associated with a single masker; but the non-signal interval had a masker that was randomly chosen from the seven possible maskers. Thus for the single “unchanging” track, the masker was the same in the two intervals, meaning that the threshold estimate could be compared to threshold estimates obtained with less uncertainty (e.g., the *fixed* and *roving* threshold estimates). This threshold will be referred to as the *fixed/random* threshold because the masker is fixed in an environment of randomly chosen maskers. For three of the four observers, *fixed/random* thresholds were measured for maskers 1 (comodulated), 3, and 5. For observer 7, *fixed/random* thresholds were obtained for stimuli 1, 5, and 7. The “thresholds” estimated for the six random tracks (e.g., those with maskers that were not the same in the two intervals) will be referred to as “hit thresholds” because these thresholds are based on the detection of a tone added to one particular masker paired with any one of the seven maskers. “Hit thresholds” presumably reflect the degree to which the signal-plus-masker stimulus “sounds” like a signal-plus-masker rather than a masker-alone stimulus.

Prior to the beginning of each session, the order in which the stimuli associated with the different tracks was randomly chosen, with the constraint that for blocks of 14 trials, each “track” would be represented twice. As in experiment I, thresholds were based on 50 trials per track, and observers paused after completing 50 trials. After each pause, the observer was free to practice prior to resuming

data collection. Because seven tracks were interleaved, observers completed seven sets of 50-trial blocks in a row.

In addition to the *fixed*, *roving*, and *fixed/random* conditions described above, conditions more similar to traditional CMR experiments were tested. For these conditions, thresholds were estimated when the signal was added only to the signal-centered SAM tone (*target-alone* condition of experiment I), when the signal was added to a comodulated masker (masker 1, *fixed* condition; redundant with the condition described above), and when the signal was added to one of the seven maskers, where the masker chosen for the signal and no-signal intervals was random on each interval (*random* condition of experiment I). Thresholds in these three conditions were measured both with and without level equalization. When level equalization was not present, the level of the signal-centered SAM tone increased when the signal was added.

Observers had quiet thresholds of 15 dB HL or better (for frequencies ranging from 250 to 8000 Hz) and ranged in age from 19 to 25 years. Observers were paid for participation, and were tested while seated in a double-walled sound-proof booth. Conditions were tested in random order, blocked by condition: *fixed*, *fixed/random*, etc. Even though several hours of practice preceded data collection, effects of practice were apparent for observer 5. As a result, observer 5 repeated a large portion of the experiment. For the other observers, occasional repetitions of conditions did not reveal practice effects. Unless otherwise noted, the final threshold is the average of seven threshold estimates.

B. Results and discussion of Experiment II

Figure 4 shows the results for the CMR-like auxiliary experiment. Thresholds are for the detection of a tone added to signal-centered SAM tone alone (*target-alone*, left bars), masker 1 (comodulated; middle bars), or maskers that were randomly chosen on each interval (*random*, right bars). Three observers participated, and their data are plotted separately. Level cues associated with the added tone are either available (cross-hatched) or not (unfilled). When level cues are available, thresholds are lowest in the comodulated condition, intermediate in the *target-alone* condition, and largest in the *random* condition, a result common in CMR experiments that employ maskers relatively nearby in frequency (e.g., Schooneveldt and Moore, 1987; Grose and Hall, 1989). When there are no level cues, thresholds in the comodulated and *target-alone* conditions are approximately equal, and lower than thresholds in the *random* condition.

Removing level cues yields higher thresholds in the comodulated and *random* conditions, but not the *target-alone* condition. Although the average change in threshold (level cues absent versus level cues present) is about the same in the comodulated and *random* conditions (5 and 5.3 dB, respectively), in the *random* condition, the effect of removing level cues is most prominent for observer 6. At least for these conditions, it seems that level cues contribute by way of across-channel rather than single-channel processing (e.g., profile analysis, Green, 1988), especially in the comodulated condition (see also Fantini and Moore, 1994). Finally, it would seem that the failure to obtain reduced thresholds in

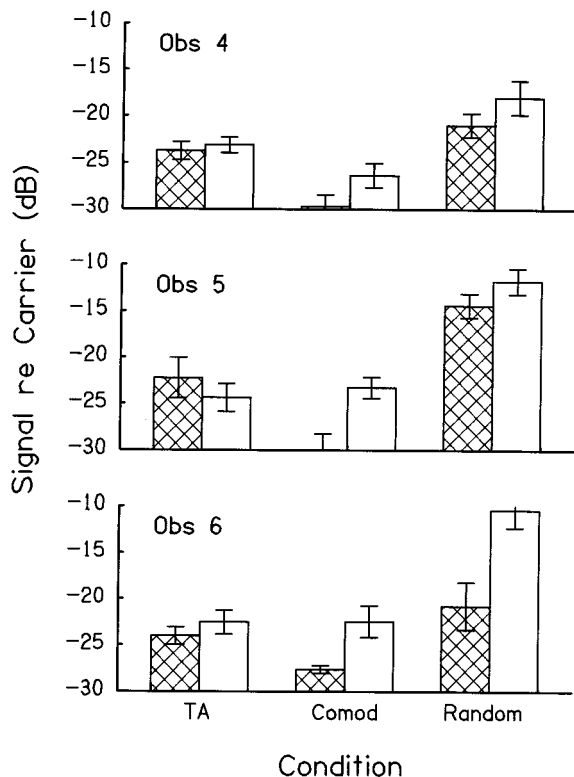


FIG. 4. Thresholds, as signal-to-carrier ratio in dB, are plotted for three observers in three conditions: *target-alone* (left bars), comodulated (middle), and *random* (right). Level cues associated with the addition of the signal were either present (cross-hatched) or absent (unfilled). Error bars indicate the standard error of the mean.

Experiment I's *fixed* condition, masker 1 (comodulation condition) reflects the absence of level cues in that experiment.

Figure 5 plots the results of the main experiment for four observers. The leftmost unfilled circle is the threshold in the *target-alone* condition (replotted from Fig. 4 for observers 4–6). The remaining thresholds are for maskers 1–6. Thresholds are plotted as ascending for the *fixed* condition (unfilled squares, connected using lines), meaning that the abscissa is not the same for each observer. The *roving* and *fixed/random* conditions are plotted using unfilled triangles and asterisks, respectively. Thresholds for masker 7, which had off-frequency modulation patterns shifted 180 degrees relative to the signal-centered SAM tone, are not plotted because thresholds could not be reliably estimated (the signal level rose with no apparent bound).

For multiple SAM tone maskers, thresholds are lowest for masker 1—the comodulated masker. Across observers, the ordering of thresholds as a function of masker number is similar, but not wholly consistent. An ANOVA which included the *fixed* and *roving* conditions reflected what is apparent in the data: a main effect of phase but no significant effect of *fixed* versus *roving* presentation [$F(5,15) = 12.25$, $p < 0.0005$; $F(1,3) = 1.37$, $p > 1.37$, $p > 0.3$, respectively]. Nonetheless, it should be noted that for observer 7, thresholds in the *fixed* condition are consistently lower than thresholds measured in the *roving*. For her, *fixed/random* thresholds are immediate to the *fixed* and *roving* thresholds. Overall, however, these data extend the results described above and

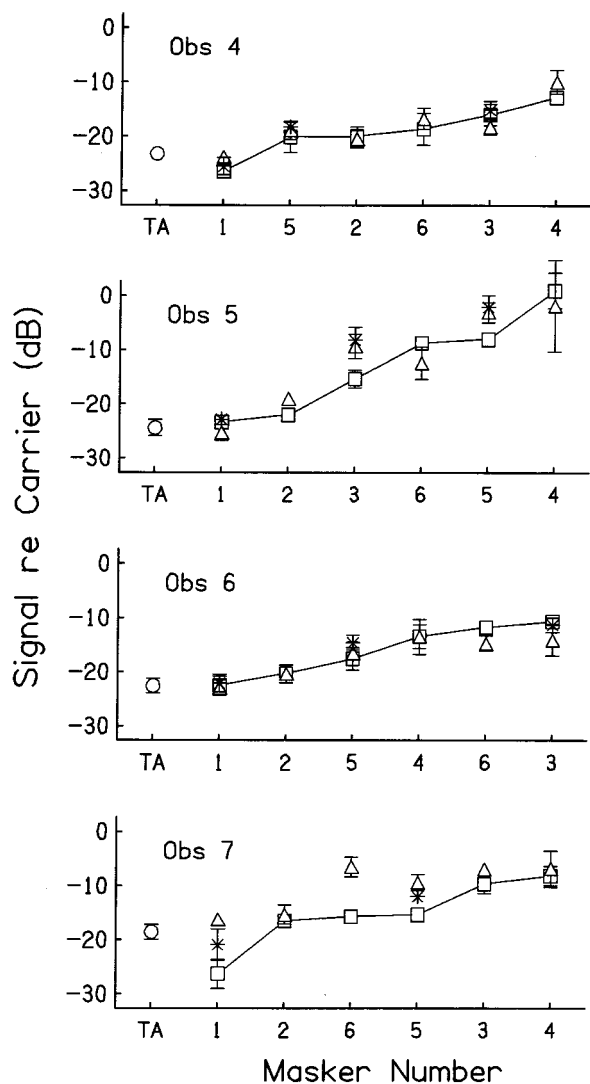


FIG. 5. Thresholds for the *target-alone* condition are plotted to the left (circles). *Fixed* (squares), *roving* (triangles), and *fixed/random* (asterisks) conditions are shown for each masker (1–6). The abscissa indicates masker number, ordered such that for each observer the *fixed* thresholds are ascending. Error bars indicate the standard error of the mean. Note that results are not plotted for masker 7 as thresholds were not reliable.

by Wright and McFadden (1990) in indicating that thresholds measured using different maskers are largely immune to increases in uncertainty.

Figure 6 plots the results for the *fixed* and *roving* conditions averaged across observers (squares) as a function of the average change in modulator phase ($\Delta\Phi$), signal-centered modulator re the two nearest off-frequency modulator phases, without respect to sign, and as a proportion of modulator phase. It should be noted that due to unlucky draws of the modulator phases used to generate the SAM tones, a nearly identical graph would result if $\Delta\Phi$ was based on all off-frequency SAM tones, not just those nearest the signal-centered SAM tone. Masker number is also indicated. As was observed in experiment I, thresholds in the *fixed* condition tend to grow with $\Delta\Phi$, demonstrating an inverse relation between threshold and the magnitude of the difference in modulator phase for the signal-centered and off-frequency

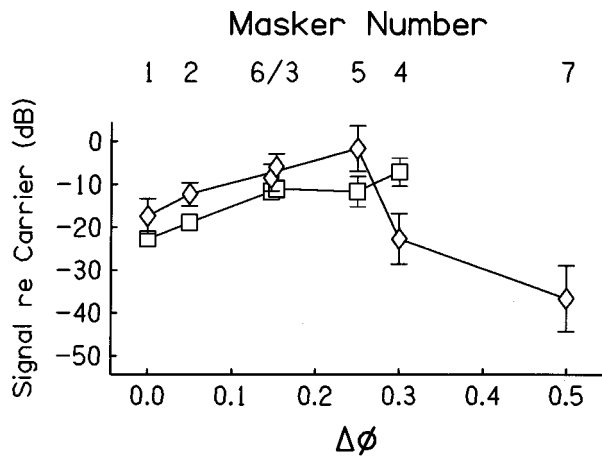


FIG. 6. Squares indicate thresholds as a function of $\Delta\Phi$, as described for Fig. 3. Diamonds show “hit thresholds” for the different maskers. Error bars show the standard error of the mean across four observers. Note that *fixed* thresholds are not plotted for masker 7 as thresholds could not be reliably obtained.

SAM tones. Maskers 6 and 3 have the same $\Delta\Phi$, the symbols are offset to provide easier viewing.

Figure 6 also shows the “hit thresholds” obtained in the *fixed/random* condition (diamonds; at least 18 threshold estimates per observer, averaged across observers). Recall that “hit thresholds” are thresholds obtained when the signal was added to the indicated masker, but the masker in the nonsignal interval was randomly chosen from the seven maskers. First consider the results for masker 7. Thresholds could not be obtained in the *fixed* condition, but the “hit thresholds” are very small. That is, when the signal was added to masker 7, observers nearly always responded “signal.” It seems reasonable to posit that masker 7 sounds as though it has an added signal even when it does not. That would lead to a very low “hit threshold,” and a very high (in this case, unmeasurable) *fixed* threshold. A similar argument was suggested by McFadden and Wright (1990), who pointed to the importance of considering the nonsignal interval when the effect of differences in envelope modulation pattern across frequency are considered. Indeed, one might expect a similar reversal for the masker 1, the comodulated masker. To the degree the masker-alone stimulus sounds devoid of a signal, one might expect the “hit threshold” to be very high—a large signal would be required for observers to detect the addition of the signal compared to the other no-signal stimuli. That result was not obtained. Instead, for all but maskers 4 and 7, a constant difference separates *fixed* and “hit” thresholds. Only for across-frequency modulator patterns that lead to high *fixed* thresholds is there a systematic influence of the differences between the maskers in the signal and no-signal intervals.

V. SUMMARY AND CONCLUSIONS

Experiments I and II indicate that threshold for the detection of a tone added to one of several SAM tones depends systematically on the relative phases of the signal-centered and off-frequency SAM modulators, provided the maskers are near enough in frequency. To a first approximation, for

SAM tones nearby in frequency, thresholds grow with increasing differences in modulator phases of the signal-centered and off-frequency SAM tones (see also Fantini, 1991). Unfortunately, the relative importance of the low- and high-frequency, the nearby and distant SAM tones could not be determined in the current experiment.

Individual differences prevent a clearcut answer to the question of whether thresholds measured in random conditions reflect a combination of sensitivities associated with the variety of maskers used. For two of the three observers, the results of experiment I indicate that when the signal-centered and off-frequency SAM tones are nearby in frequency (a factor of 1.3 in frequency), thresholds measured under uncertainty are reasonably predicted using a simple mixture model. The mixture model was less successful in predicting thresholds measured under uncertainty for larger SAM tone carrier frequency separations (a factor of 1.68), where no significant effects of across-frequency modulator phase were obtained. In this case, the failure of the mixture model may reflect phase-independent increases in masking measured in the modulation detection interference and the across-channel masking paradigms (Yost and Sheft, 1994; Bacon and Konrad, 1993). In experiment II, uncertainty effects were noted for only one of the four observers. For her, *roving* thresholds were consistently higher than *fixed* thresholds, and the *fixed/random* thresholds were intermediate.

Finally, a comodulation masking release in the comodulated versus *target-alone* conditions was obtained when the addition of the signal led to an increase in level, but not when level equalization prevented level differences from contributing to detection. Because the addition of level cues led to lower thresholds in the comodulated and random conditions but not the target-alone condition, it would appear that the level cues contribute by way of across-frequency rather than single-channel processing.

ACKNOWLEDGMENTS

This work was supported by Grant No. RO1 DC 02012 from the National Institutes of Health. Robert L. Jones assisted in data collection. Two anonymous reviews greatly improved the manuscript.

¹When a $20 \log(m)$ scale is used, the distributions include values of m greater than 1. Over modulation was not allowed to occur experimentally, and this result points to the inadequacy of $20 \log(m)$ as a model of the underlying “sensory” scale. Nonetheless, thresholds in the fixed condition were well predicted, meaning that the predictions for the mixture model are expected to be reasonable, even if the underlying scale is inappropriate.

- Bacon, S. P., and Konrad, D. L. (1993). “Modulation detection interference under conditions favoring within- or across-channel processing,” *J. Acoust. Soc. Am.* **93**, 1012–1022.
- Berg, B. G. (1996). “On the relation between comodulation masking release and temporal modulation transfer functions,” *J. Acoust. Soc. Am.* **100**, 1013–1023.
- Buss, E., and Richards, V. M. (1995). “The effects on comodulation masking release (CMR) of systematic variations in on- and off-frequency modulation pattern,” *J. Acoust. Soc. Am.* **99**, 1876–1888.
- Buus, S. (1985). “Release from masking caused by envelope fluctuations,” *J. Acoust. Soc. Am.* **78**, 1958–1965.
- Cohen, M. F. (1991). “Comodulation masking release over a three octave range,” *J. Acoust. Soc. Am.* **90**, 1381–1384.

- Cohen, M. F., and Schubert, E. D. (1987). "Influence of place synchrony on detection of a sinusoid," *J. Acoust. Soc. Am.* **81**, 452–458.
- Fantini, D. A. (1991). "The processing of envelope information in comodulation masking release (CMR) and envelope discrimination," *J. Acoust. Soc. Am.* **90**, 1876–1888.
- Fantini, D. A., and Moore, B. C. J. (1994). "A comparison of the effectiveness of across-channel cues available in comodulation masking release and profile analysis tasks," *J. Acoust. Soc. Am.* **96**, 3451–3462.
- Green, D. M. (1988). *Profile Analysis: Auditory Intensity Discrimination* (Oxford U.P., New York).
- Grose, J. H., and Hall III, J. W. (1989). "Comodulation masking release using SAM tonal complex maskers: Effects of modulation depth and signal position," *J. Acoust. Soc. Am.* **85**, 1276–1284.
- Hall III, J. W., and Grose, J. H. (1988). "Comodulation masking release: Evidence for multiple cues," *J. Acoust. Soc. Am.* **84**, 1669–1675.
- Hall, J. W., Haggard, M. P., and Fernandes, M. A. (1984). "Detection in noise by spectro-temporal pattern analysis," *J. Acoust. Soc. Am.* **76**, 50–56.
- Levitt, H. (1971). "Transformed up-down methods in psychoacoustics," *J. Acoust. Soc. Am.* **49**, 167–177.
- McFadden, D. (1986). "Comodulation masking release: Effects of varying the level, duration, and time delay of the cue band," *J. Acoust. Soc. Am.* **80**, 1658–1667.
- Moore, B. C. J., Glasberg, B. R., and Schooneveldt, G. P. (1990). "Across-channel masking and comodulation masking release," *J. Acoust. Soc. Am.* **87**, 1683–1694.
- Richards, V. M., Buss, E., and Tian, L. (1997). "Effects of modulator phase for comodulation masking release (CMR) and modulation detection interference (MDI)," *J. Acoust. Soc. Am.* **102**, 468–476.
- Schooneveldt, G. P., and Moore, B. C. J. (1987). "Comodulation masking release (CMR): Effects of signal frequency, flanking-band frequency, masker bandwidth, flanking-band level, and monotic versus dichotic presentation of the flanking band," *J. Acoust. Soc. Am.* **82**, 1944–1956.
- Wright, B. A., and McFadden, D. (1990). "Uncertainty about the correlation among temporal envelopes in two comodulation tasks," *J. Acoust. Soc. Am.* **88**, 1339–1350.
- Yost, W. A., and Sheft, S. (1994). "Modulation detection interference: Across-frequency processing and auditory grouping," *Hearing Res.* **79**, 48–58.

Auditory suppression and frequency selectivity in older and younger adults

Mitchell S. Sommers and Sara E. Gehr

Department of Psychology, Washington University, Campus Box 1125, St. Louis, Missouri 63130

(Received 11 March 1997; revised 24 September 1997; accepted 22 October 1997)

Age differences in auditory suppression were examined by comparing auditory-filter shapes obtained with simultaneous and forward masking at 2 kHz in young and elderly normal-hearing listeners. To compensate for the decay of forward masking, growth of masking functions were used to transform thresholds obtained with a notched-noise masker to the level of a continuous noise band that would give the same threshold values. Although both age groups exhibited smaller equivalent rectangular bandwidths (ERBs) when the filters derived from transformed thresholds were obtained with forward masking, the change from simultaneous to nonsimultaneous masking was significantly greater for young adults. Measures of the low- (P_l) and high- (P_u) frequency sides of the filters for young listeners indicated that the slopes of both sides increased following a change from simultaneous to forward masking but that the high-frequency side exhibited significantly greater sharpening. Filter slopes (both upper and lower) for older adults, in contrast, did not differ between the two masking procedures. The findings from the study are discussed as reflecting possible age differences in auditory suppression. However, it is also noted that conclusions regarding differences between filter shapes derived with simultaneous and forward masking are limited to filter parameters determined with transformed (as described above) thresholds. © 1998 Acoustical Society of America. [S0001-4966(98)02402-3]

PACS numbers: 43.66.Dc, 43.66.Sr [JWH]

INTRODUCTION

Auditory-filter shapes measured in young normal-hearing listeners can indicate sharper tuning when they are obtained with nonsimultaneous, compared with simultaneous masking procedures (Houtgast, 1972; Moore and Glasberg, 1981, 1986; Moore and O'Loughlin, 1986). Specifically, studies in which threshold functions are transformed to compensate for the decay of forward masking (by expressing thresholds obtained with a notched-noise masker as the level of a continuous noise band that would give the same threshold values), generally indicate steeper slopes and smaller equivalent rectangular bandwidths (ERBs) for filters measured with forward compared with simultaneous masking paradigms (Moore and Glasberg, 1981, 1986; Moore and O'Loughlin, 1986). Although a number of explanations have been offered to account for the increased frequency selectivity observed with nonsimultaneous masking (Jesteadt and Norton, 1985; Lutfi, 1984, 1988; Moore and O'Loughlin, 1986), accounts based on the operation of auditory suppression are most consistent with empirical findings [Moore and O'Loughlin, 1986; also see, Delgutte (1990) for discussion of within-masker versus masker-to-signal suppression].¹

According to the suppression hypothesis (Houtgast, 1972; Moore and Glasberg, 1981; Moore and O'Loughlin, 1986), lateral suppression can influence auditory-filter shapes in nonsimultaneous masking because the temporal discontinuity between signal and masker allows suppression to reduce the effective level of the masker without altering excitation arising from the signal [i.e., suppression functions to increase signal-to-noise (S/N) ratios at the output of auditory filters]. In simultaneous masking, however, suppression will have equivalent effects on the signal and masker. Conse-

quently, S/N ratios at the output of the filter will remain constant and masked thresholds for the signal will be unaffected by suppression.

The proposal that the effects of suppression on auditory filters are observable only with nonsimultaneous masking has led several investigators (Houtgast, 1972; Moore and Glasberg, 1981; Moore and O'Loughlin, 1986) to suggest that when filters are derived with transformed thresholds, differences between auditory filters measured with simultaneous and forward masking paradigms can provide a quantitative assessment of auditory suppression. The purpose of the present study was to examine age-related changes in the operation of auditory suppression by comparing auditory-filter shapes obtained with forward and simultaneous masking in older and younger listeners.

Although little systematic research has been directed at examining age differences in auditory suppression, findings reported by Moore and Glasberg (1986) provide a preliminary indication that suppression may be reduced as a function of age. Moore and Glasberg (1986) compared auditory-filter shapes obtained with simultaneous and forward maskers in five listeners with unilateral cochlear impairments who ranged in age from 47 to 70. Results from the unimpaired ears indicated that when filter-shape parameters were obtained with transformed threshold values, the two youngest subjects in the study exhibited the greatest increase in tuning following the change from simultaneous to forward masking. In contrast, the unimpaired ear of the oldest participant failed to exhibit significant differences between filters derived with simultaneous and nonsimultaneous procedures. The study by Moore and Glasberg (1986), however, was not designed explicitly to examine age differences in auditory

TABLE I. Age and air-conduction thresholds for all participants. Standard deviations are shown in parentheses for the group means.

Group	Age	Threshold (dB HL)					
		250 Hz	500 Hz	1000 Hz	2000 Hz	4000 Hz	8000 Hz
Young							
1	20	5	5	4	8	8	10
2	18	0	0	6	3	0	7
3	18	0	5	5	11	13	9
4	19	0	3	0	4	7	4
5	21	0	0	0	0	2	2
6	18	7	5	9	6	4	12
7	20	0	7	4	5	2	8
Mean (s.d.)	19.1 (1.2)	1.7 (2.9)	3.5 (2.6)	4.8 (3.9)	5.2 (3.5)	5.1 (4.4)	6.5 (3.4)
Old							
8	75	2	5	0	0	7	15
9	69	0	0	0	4	6	21
10	68	0	5	0	0	9	18
11	73	5	5	7	10	13	26
12	66	5	7	4	8	11	14
13	71	0	0	10	10	10	17
14	67	0	0	0	0	8	14
Mean (s.d.)	69.8 (3.2)	1.7 (2.3)	3.1 (3.0)	3 (4.1)	4.5 (4.7)	9.1 (2.4)	17.8 (4.3)

suppression. As a result, the findings must be considered only suggestive because several important factors for making age comparisons were not included.²

The present study was therefore designed specifically to examine the operation of auditory suppression in younger and older adults by comparing auditory-filter shapes obtained with simultaneous and forward masking in the two age groups. Based on the findings reported by Moore and Glasberg (1986), the working hypothesis for the investigation was that auditory suppression is reduced in older adults. Therefore, auditory filters derived with transformed threshold values were expected to indicate sharper tuning for non-simultaneous than for simultaneous masking but differences between filters derived with the two paradigms were expected to decrease as a function of age. Differential changes in filter tuning following the switch from simultaneous to forward masking would suggest that, under certain conditions, auditory suppression may not function as effectively in older listeners.

I. METHODS

A. Subjects

Seven young (ages 18–20) and seven elderly (ages 66–75) adults served as experimental subjects. Because hearing impairment has been reported to reduce (Moore and Glasberg, 1986) or eliminate (Wightman *et al.*, 1977; Dreschler and Festen, 1986) auditory suppression, only listeners with normal hearing at the signal frequency (2 kHz) were tested. Pure-tone air-conduction thresholds were obtained from the preferred ear of young adults and the better hearing ear (self-reported) of older listeners. All subjects in the present study had thresholds less than 15 dB HL (ANSI, 1989) at 2 kHz. Furthermore, to avoid testing subjects with rapid sensitivity changes in frequency regions adjacent to the signal and to

make hearing levels as similar as possible in the two age groups, subjects were also required to have thresholds less than 15 dB HL for octave frequencies from 250 to 4000 Hz and no greater than 25 dB HL at 8 kHz. A total of 9 younger adults and 37 older listeners were tested to obtain the 7 participants used for each group. Table I lists audiometric and demographic data for all participants. Thresholds for the two groups were quite similar except for a somewhat greater hearing loss at 4 and 8 kHz for the older subjects. All listeners had normal middle ear function (normal tympanograms and presence of acoustic reflex for contralateral stimulation with a 1000-Hz pure tone at 100 dB HL). Both older and younger participants had previous experience in psychoacoustic testing and were paid an hourly rate.

B. Stimuli and equipment

Auditory-filter shapes were measured using the notched-noise procedure developed by Patterson (Patterson, 1976) and later modified by Glasberg and Moore (Glasberg and Moore, 1990). Two separate noise bands, each 800-Hz wide, were positioned either symmetrically or asymmetrically around a 2-kHz pure-tone signal (f_s). Thresholds for detecting the signal were measured as a function of the spectral separation, or notch, between the two bands. Masker duration for both simultaneous and forward masking was 400 ms. The masker was gated on and off with 10-ms cosine squared ramps. Signal duration was 20 ms and was gated on either in the temporal center of the masker (simultaneous masking) or immediately after masker offset (forward masking).

Both masker and signal were generated using a digital-signal processing board (TDT AP2) and a 20-kHz sampling rate. The signal and masker were presented to independent D/A converters (TDT DA1), low-pass filtered at 8.5 kHz (TDT FLT3), and attenuated by two separate programmable

attenuators (TDT PA3). Following attenuation, the signal and masker were mixed (TDT ADD1) and presented to a headphone driver (TDT HB3) connected to Sennheiser HD250 headphones. A new waveform sample was generated for both signal and masker on each observation interval.

The spectrum level of the noise was set to 50 dB (*re*: 20 μ Pa). In the symmetric conditions, the noise bands were positioned above and below f_s such that, expressed relative to the signal frequency, the deviation of the nearer edge of each band (Δf) from f_s (i.e., $\Delta f/f_s$) was 0.0 (no notch), 0.05, 0.1, 0.2, 0.3, 0.4, 0.5, and 0.6. In one set of asymmetric conditions, the nearer edge of the noise band below f_s was closer to the signal with $\Delta f/f_s$ for this band set at 0.05, 0.1, 0.2, 0.3, or 0.4. The nearer edge of the masker above the signal was 0.2 farther away (i.e., $\Delta f/f_s$ for the lower and upper bands, respectively were 0.05, 0.25; 0.1, 0.3; 0.2, 0.4; 0.3, 0.5; and 0.4, 0.6). The remaining set of asymmetric conditions were mirror images of the first with the nearer edge of the upper band closer to f_s and the nearer edge of the lower band 0.2 farther away. Presentation levels were measured at the output of the transducer in a NBS-9A 6-cc coupler with a Bruel & Kjaer sound level meter (model 2204) set on the linear weighting scale.

C. Procedure

Subjects were tested individually while seated in a double-walled sound attenuating booth (IAC). Masked thresholds were determined using an adaptive two-interval forced-choice (2IFC) procedure. Each interval was marked on a CRT screen coincident with stimulus presentation. There was a 500-ms silent period between the two intervals. The interval containing the signal was selected randomly on each trial. Participants received feedback about whether their response was correct or incorrect following each trial. Forward and simultaneous masking was blocked with approximately half the subjects in each group completing all of the simultaneous conditions first and half completing the forward masking first. The order of masker conditions (notch widths) within each type of masker was randomly determined. For each notch width, the signal was initially set at least 10 dB above the subject's estimated threshold. The signal was decreased 10 dB following two consecutive correct detections and increased 10 dB after the first miss. The step size was reduced from 10 to 2 dB after the first incorrect response.

A change from either a correct detection to a miss or vice versa defined a reversal. Threshold was determined as the mean signal level for the final 12 of 16 reversals. In the rare instances (less than 2% of all runs) where the standard deviation of the reversals for a given threshold determination exceeded 5 dB, the threshold was discarded. At least two thresholds were obtained for each notch width. If the two threshold estimates differed by more than 3 dB, additional thresholds were obtained until the standard deviation of all thresholds for that condition was less than 2 dB. This same procedure, without the notched noise, was used to determine the pure-tone air-conduction thresholds displayed in Table I.

D. Growth of masking functions (GOM) for forward and simultaneous masking

In the present study, auditory-filter shapes were determined using a fixed-level notched-noise masker and variable-level pure-tone signal. Several studies (Moore and Glasberg, 1981; Moore, 1985; also see Moore and O'Loughlin, 1986) have provided evidence to suggest that in order to compare auditory-filter shapes in simultaneous and forward masking using this paradigm it is necessary to transform forward masked thresholds to compensate for the decay of forward masking. Others (Lutfi, 1984, 1988; Jesteadt and Norton, 1985), however, have argued against the necessity of transforming thresholds (see general discussion for additional consideration of this issue and its implications for the current investigation). An additional concern for the current investigation were findings from Moore *et al.* (1987) indicating that growth of masking functions for simultaneous masking could vary significantly from unity for some subjects.

Thus to compensate for the decay of forward masking and to minimize the effects of individual differences in GOM for simultaneous masking, all thresholds in the present study (both simultaneous and forward) were transformed using a procedure developed by Moore and Glasberg (1981). In this procedure, thresholds obtained for the notched-noise masker are expressed as the level of a flat-spectrum masker that would give the same thresholds. This transformation requires a calibration experiment in which thresholds for a flat-spectrum masker are measured as a function of masker level (i.e., growth of masking functions).

The procedures for measuring GOM were identical to those used to obtain thresholds at individual notch widths in the auditory-filter experiment except that: (1) the masker for determining GOM functions was continuous (no notch) with a bandwidth of 1600 Hz (1200–2800 Hz); and (2) thresholds were obtained in both simultaneous and forward masking for masker spectrum levels of 5, 15, 25, 35, 45, and 55 dB SL. The growth of masking functions were used to transform thresholds obtained at all notch widths in both the simultaneous and forward masking conditions to the level of a flat-spectrum noise that would give the equivalent threshold value. Filter-shape parameters were derived using the transformed thresholds.

E. Derivation of auditory-filter shapes

Auditory-filter shapes were determined using models developed by Patterson (1976) and Glasberg and Moore (1990). According to these models, filter shapes are determined by fitting smooth line functions to the threshold data and taking the derivative of this function. The response of the filter at a given frequency is therefore proportional to the slope of the threshold function at that frequency. Auditory filters derived using this procedure generally take the form of two exponential functions placed side by side with a rounded top. Patterson *et al.* (1982) termed this the rounded exponential (roex) filter and showed that it can be well fit using two parameters: p which defines the filter's passband and r which limits its dynamic range. The shape of the filter, $W(g)$, is given by

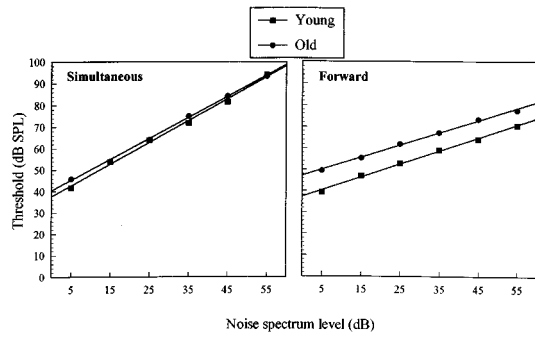


FIG. 1. Growth of masking functions for simultaneous (left) and forward (right) maskers. Solid lines show best-fitting linear regression function.

$$W(g) = (1 - r)(1 + pg)\exp(-pg) + r, \quad (1)$$

where W is the intensity weighting function of the filter and g is the normalized distance from the filter's center frequency. The parameter p defines the slope of the filter's skirts and in the present study, was allowed to differ for the upper and lower halves of the filter (the slope of the lower skirt is given by P_l and the slope of the upper skirt is given by P_u). The value of r places a limit on the dynamic range of the filter and was assumed to be equal for the upper and lower halves.

Filter parameters were derived by: (1) assuming starting values for P_u and P_l ; (2) calculating threshold curves for these values from Eq. (1) (for both symmetric and asymmetric conditions); (3) determining the mean-squared deviation between predicted and obtained thresholds; and (4) altering filter parameters so as to minimize the mean-squared deviation between transformed and predicted threshold curves. It was assumed that the center frequency of the filter used to detect the 2-kHz signal was the one yielding the highest signal-to-noise ratio. The fitting procedure allowed for shifts in the center frequency equivalent to $0.15f_s$ and altered the bandwidth of the filters as described by Glasberg and Moore (1990) to account for changes in filter shape as a function of center frequency. The maximum allowed value for either P_l or P_u was 50.

II. RESULTS AND DISCUSSION

A. Growth of masking functions

Figure 1 displays average growth of masking functions for simultaneous and forward masking in the two age groups. All functions were well fit by the regression lines shown in the figure. The mean slope of the regression line for simultaneous GOM in young adults was 1.01 (range 0.94–1.07). The corresponding values for older listeners was a mean slope of 0.97 with a range of 0.91 to 1.13. Thus both subject groups had comparable simultaneous GOM functions that were quite close to unity. The GOM functions for forward masking, displayed on the right side of Fig. 1, indicated that, although younger listeners exhibited slightly lower thresholds than older adults, the slopes of the masking function regression lines were very similar. The average slope for young adults was 0.61 (range 0.53–0.72). The mean slope for older participants was 0.57 (range 0.44–0.66). These

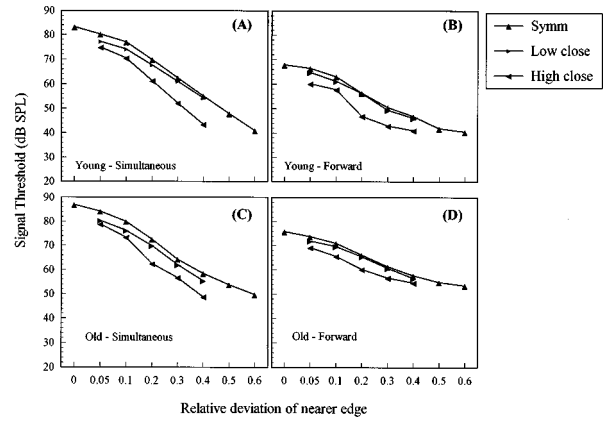


FIG. 2. Thresholds as a function of notch width for younger (panels A and B) and older (panels C and D) listeners. The left panels (A and C) show data for simultaneous maskers. The right panels (B and D) show thresholds for forward maskers. Upright triangles (\blacktriangle) indicate conditions in which the notch was positioned symmetrically about the signal. Right pointing (\blacktriangleright) and left pointing (\blacktriangleleft) triangles indicate asymmetric conditions with the low and high bands, respectively positioned closer to the signal.

findings are consistent with Cheesman *et al.* (1995) who demonstrated that, at least for simultaneous masking, GOM functions do not differ with age.

B. Thresholds as a function of notch width

Figure 2 displays untransformed thresholds for the 2-kHz signal as a function of notch width. Transformed thresholds, expressed as the level of a continuous noiseband (i.e., no notch) that would produce the same thresholds shown in Fig. 2, are displayed in Fig. 3. As noted, Moore and Glasberg (1981) developed the procedure for transforming thresholds from notched-noise masking studies that employ fixed-level maskers to compensate for the decay of forward masking and allow direct comparisons of auditory-filter shapes measured with simultaneous and nonsimultaneous paradigms. Several studies (Lutfi, 1984, 1988) have questioned the appropriateness of this transformation while other investigations (Moore and O'Loughlin, 1986) have presented both theoretical and empirical support for this method of compensating for the

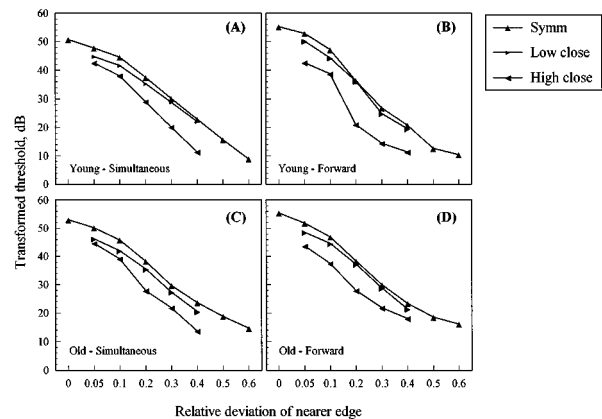


FIG. 3. Same as Fig. 2 except that thresholds have been transformed to the level of a continuous masker (1600-Hz bandwidth; centered at 2 kHz) that would give the same thresholds. The transformed thresholds were derived using the growth of masking functions displayed in Fig. 1.

TABLE II. Auditory-filter shape parameters for young (upper panels) and elderly (lower panels) listeners. Column headings for both simultaneous and forward masking are: P_l —slope of low-frequency side; P_u —slope of high-frequency side; ERB—equivalent rectangular bandwidth (kHz); k —efficiency measure; r —dynamic range. Standard deviations of the means are shown in parentheses.

Subject	Simultaneous masking					Forward masking				
	P_l	P_u	ERB	k	r (dB)	P_l	P_u	ERB	k	r (dB)
Young										
1	19.2	28.4	0.35	6.1	-80.9	19.4	47.8	0.29	-25.9	-45.5
2	18.9	23.2	0.384	3.4	-50.3	22.4	34.3	0.296	-32.9	-46.2
3	23.9	37.2	0.276	11.5	-99	31.3	50	0.208	-19.1	-65.4
4	20.9	28.7	0.33	9.9	-50	26.8	36.8	0.258	-12.2	-53.6
5	19.2	25.9	0.364	4.5	-89.4	22	41.3	0.278	-19.8	-57
6	20.6	26.6	0.35	15.4	-58.3	24.9	48.9	0.24	-28.5	-45.85
7	22.4	32.9	0.303	10.7	-74.5	29.0	43.4	0.233	-15.65	-59.5
Mean	20.7 (1.8)	28.9 (4.6)	0.336 (0.036)	8.7 (4.2)	-71.7 (19.4)	25.1 (4.2)	43.2 (6.1)	0.258 (0.034)	-22.0 (7.3)	-53.2 (7.8)
Old										
8	25.8	43	0.248	18.2	-87.5	27.5	49.9	0.215	-21.5	-53.4
9	24.7	33.4	0.282	15.4	-44.7	23.6	43.8	0.252	-23.5	-57.3
10	14.1	28.6	0.424	7.7	-62.1	20.9	29.1	0.338	-27.5	-39.8
11	17.6	31.9	0.352	7.4	-103	21	33.1	0.312	-29	-39.7
12	17	25.9	0.404	15.4	-44.7	17.1	28.8	0.4	-23.5	-57.3
13	17.5	31	0.372	12.95	-74.8	19.7	28.3	0.356	-24.5	-46.6
14	20.6	32.2	0.317	14.4	-59.7	22.6	34.0	0.296	-24.0	-51.95
Mean	19.6 (4.2)	32.2 (5.3)	0.339 (0.064)	13.0(4)	-68.0 (21.7)	21.7 (3.3)	35.2 (8.6)	0.309 (0.062)	-24.7 (2.5)	-49.4 (7.5)

decay of forward masking. With respect to the current investigation, both transformed and untransformed thresholds are presented and implications for conclusions regarding the role of suppression in accounting for differences between frequency selectivity measured in simultaneous and forward masking are considered in the general discussion.

For both simultaneous and forward masking, thresholds were highest with the symmetric notch conditions. Results from the two asymmetric conditions indicated significant asymmetry in the filters for both types of maskers. Thresholds for conditions with the lower noise band closer to the signal were consistently higher than those with the high-frequency noise band closer. These findings are consistent with previous measures of auditory filters (Moore *et al.*, 1987, 1990; Sommers and Humes, 1993) indicating somewhat sharper tuning for the high-frequency side.

Differences between simultaneous and forward masking for the transformed data (Fig. 3) were relatively small. However, except for one condition (young listeners in the asymmetric condition with the lower noise band closer), the range of transformed thresholds for forward masking was always greater than for the corresponding simultaneous condition (in the one exception, thresholds spanned almost identical ranges). The differences between simultaneous and forward masking obtained in the present study are similar to findings reported by other investigators (Moore *et al.*, 1987) and support the hypothesis that when threshold data are transformed according the procedures developed by Moore and Glasberg (1981), small, but consistent differences can be observed in auditory-filter shapes measured with simultaneous and non-simultaneous procedures. Finally, although masked thresholds for the widest notch widths in the forward masking conditions (both symmetric and asymmetric) approached absolute threshold for the 2-kHz signal, thresholds with the

masking noise were always greater than absolute sensitivity for the signal.

C. Auditory-filter parameters

Table II lists auditory-filter parameters derived by fitting smooth line functions to the transformed threshold data displayed in Fig. 3. Overall, the roex (p,r) model provided a good fit to the transformed threshold values. Average rms deviation of obtained and predicted thresholds for young adults was 1.08 and 1.36 dB for simultaneous and forward masking, respectively. The corresponding rms deviations for older listeners were 1.39 and 1.57 dB.

The average ERB values for simultaneous masking in young and old adults (0.336 and 0.339 kHz) are somewhat higher than has recently been reported by Wright (1996) for a sample size of 80 normal-hearing ears. However, Wright used a masker spectrum level of 40 dB SL, compared with the 50 dB SL level used in the present study. Several investigations have reported that frequency selectivity in simultaneous masking decreases with increasing noise levels (Moore and Glasberg, 1987; Patterson and Moore, 1986). Therefore, the larger ERB values in the current experiment are likely due, at least in part, to the use of a higher level masker. Consistent with this proposal, the ERB values shown in Table II are similar to those reported by Sommers and Humes (1993) using a 50-dB spectrum level masker (Sommers and Humes obtained average ERBs of 0.307 and 0.316 kHz for young and old adults, respectively).

The top panel of Fig. 4 compares average ERB values for simultaneous and forward masking as a function of age. A Kruskal-Wallis analysis of variance (ANOVA)³ conducted on the ERB data indicated that young adults exhibited significantly greater differences ($p < 0.01$) between simulta-

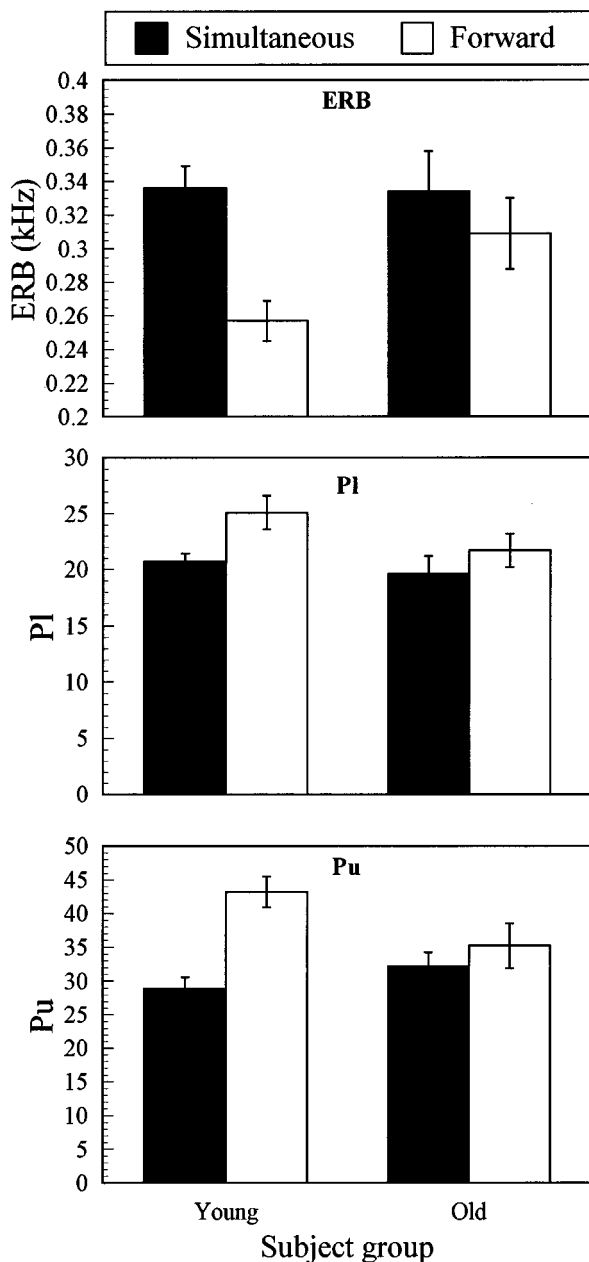


FIG. 4. Values for ERB (top), P_l (middle), and P_u (bottom) with simultaneous and forward maskers in younger and older adults. Error bars show standard deviations of the mean.

neous and forward masking than older listeners. It should be noted, however, that ERB values for both age groups were significantly smaller ($p < 0.001$ for young; $p < 0.05$ for old) in the forward, compared with the simultaneous masking condition. This finding suggests that suppression can operate in both older and younger adults to sharpen frequency selectivity but that this improvement may diminish with age.

The middle and bottom panels of Fig. 4 show values for P_l and P_u in simultaneous and forward masking for the two age groups. Young listeners exhibited significantly steeper low-frequency ($p < 0.01$) and high-frequency ($p < 0.001$) slopes in nonsimultaneous, compared with simultaneous masking. In contrast, older adults failed to show significant effects of masker type for either P_l or P_u . The largest effect

of changing from simultaneous to forward masking was to significantly increase the slope of the high-frequency skirt for younger listeners.

D. Correlations among measures

To examine whether differences between the slopes of auditory filters were related to the absolute values of either P_l or P_u , Pearson product-moment correlations were computed between differences in the values of both P_l and P_u from simultaneous to forward masking (i.e., $P_{l(\text{for})} - P_{l(\text{sim})}$ and $P_{u(\text{for})} - P_{u(\text{sim})}$) and the absolute values of P_l and P_u for the two types of maskers. Only two significant correlations were observed in this analysis. The difference in P_l between forward and simultaneous masking was significantly correlated ($r = 0.59$, $p < 0.05$) with the value of P_l in forward masking and the difference between P_u in simultaneous and forward masking was significantly correlated ($r = 0.81$; $p < 0.001$) with P_u for forward masking. Thus there was some indication that greater frequency selectivity in forward masking was associated with increased differences between auditory-filter slopes in simultaneous and forward masking. This correlation would be expected if both the absolute value for filter slopes in forward masking and differences in slopes between forward and simultaneous masking were due to the operation of a common mechanism such as auditory suppression.

III. GENERAL DISCUSSION

The results of the present study replicate and extend findings from previous investigations of the effects of age on auditory-filter shapes in several ways. First, the similar ERB values obtained for younger and older adults with simultaneous masking are in good agreement with other reports (Peters and Moore, 1992; Sommers and Humes, 1993) that age per se (i.e., independent of hearing loss) does not impair frequency resolution as assessed with a simultaneous notched-noise masking paradigm. Second, the current findings suggest that when transformed threshold values are used to derive auditory-filter shapes, young adults exhibit greater increases in frequency selectivity than older listeners as a consequence of changing from simultaneous to forward masking. To the extent that differences between filter shapes measured with simultaneous and forward masking reflect the operation of suppression, the present results are consistent with the hypothesis of age-related reductions in the operation of auditory suppression.

It is important to note, however, that the role of suppression in explaining differences between auditory filter functions measured with simultaneous and forward masking re-

mains controversial (Lutfi, 1984, 1985, 1988; Moore and O'Loughlin, 1986). Because the present study was not designed to address this issue, it is considered in the current context only to the extent that it may limit the generalizability and interpretation of the obtained data (for additional discussion see Lutfi, 1984, 1985, 1988; Moore and O'Loughlin, 1986). Lutfi (1984) proposed a model that could account for differences in frequency selectivity between simultaneous and forward masking without assuming the existence of additional tuning mechanisms such as suppression. Support for the model was provided in a series of experiments (Lutfi, 1988) that examined the interaction of signal frequency, masker level, and signal delay on measures of frequency selectivity. Lutfi (1988) also demonstrated that if untransformed rather than transformed thresholds were used to derive filter functions, differences between simultaneous and forward masking were quite small. Consistent with this proposal, examination of the untransformed thresholds in Fig. 2 indicates that, if anything, filter functions derived with simultaneous masking are actually sharper than those obtained with forward masking.

Moore (1985; Moore and O'Loughlin, 1986) has countered such arguments by demonstrating that the nonlinearity associated with the decay of forward masking follows, rather than precedes, the auditory filter. This finding has been interpreted (Moore, 1985; Moore and O'Loughlin, 1986) as supporting the validity of transforming thresholds to compensate for the decay of forward masking. In addition, Moore (1985; Moore and O'Loughlin, 1986) has provided evidence to suggest that Lutfi's (1984, 1988) model is inconsistent with evidence from measures of psychophysical tuning curves. Although the current authors believe that the available empirical and theoretical evidence favors the use of transformed thresholds in comparing auditory filters derived with simultaneous and nonsimultaneous procedures, it is important to note that alternative interpretations of the present data are possible. Definitive resolution of this issue will need to await the results of future investigations that can unequivocally support one of the positions.

One finding that supports the role of suppression as a factor mediating the increase in frequency selectivity for nonsimultaneous masking is the differential effects observed for P_l and P_u . Young adults exhibited increases of 21% and 49% for the low- and high-frequency slopes, respectively, as a result of changing from simultaneous to forward masking. Moore *et al.* (1987) reported similar findings (changes of 17% and 40% for P_l and P_u) in listeners 21–35 years old. This differential effect on the high-frequency slope is consistent with the operation of auditory suppression because suppression is generally strongest from high to low frequencies (Houtgast, 1972; Moore and O'Loughlin, 1986). Furthermore, if suppression has greater influence on P_u than P_l , then age-related impairments in auditory suppression should be most apparent for the high-frequency slope of the filter. Consistent with this prediction, the largest age differences in the present study were observed for P_u .

One important feature of the data displayed in Table II is the extensive individual variability evident in slope and ERB values. Differences in ERBs between the two masking con-

ditions ranged from 60 to 110 Hz in young adults and from 4 to 86 Hz in older listeners. Thus even for the highly restricted age range present in the group of young subjects, there was significant variability in the effects of changing from simultaneous to forward masking. Furthermore, one older subject (subject 10) exhibited an 86-Hz decrease in ERB for the nonsimultaneous condition. This value is well within the range observed for young adults and suggests that declines in the operation of auditory suppression may be a consequence of age-related reductions in neural and mechanical processes that also exhibit considerable age variability.

Age-related reductions in auditory suppression could have a number of important clinical implications for assessing and treating speech perception difficulties in older adults. For example, Moore and Glasberg (1983) demonstrated that vowel masking patterns measured with forward masking produced significantly better spectral contrast and formant representations than those obtained with simultaneous masking. Moreover, the spectral contrast observed with forward masking often exceeded that found in the physical spectrum. These findings were interpreted as suggesting that suppression can function to enhance contrast of complex sounds such as speech. Age-related declines in suppression could impair the auditory system's ability to improve spectral contrast for vowel formants and other phonetically important features of speech signals. Such impoverished excitation patterns may account, at least in part, for the finding that speech recognition in older listeners is particularly disadvantaged in noisy environments (CHABA, 1988). Moreover, hearing aids that focus primarily on increasing amplification may prove to be of limited use for patients with impaired auditory suppression.

IV. CONCLUSIONS

- (i) Auditory-filter shapes derived with simultaneous masking were similar for younger and older adults with normal or near-normal hearing.
- (ii) When filter parameters are derived from transformed threshold functions, frequency resolution assessed with nonsimultaneous masking procedures indicates considerably sharper tuning for younger than for older listeners. The increased frequency selectivity for young adults with forward masking was reflected primarily in a steeper slope for the high-frequency side of the filter.
- (iii) Differences between P_l and P_u in simultaneous and forward masking were significantly correlated with absolute values for these two parameters in forward masking.
- (iv) To the extent that differences between simultaneous and forward masking paradigms can be attributed to the operation of auditory suppression, the present findings are consistent with age-related reductions in suppression within the auditory system.

ACKNOWLEDGMENTS

This work was supported by the Brookdale Foundation. The authors would like to thank Robert Peters and an anonymous reviewer for their comments on an earlier version of the manuscript. Melissa Levine and Robin Dorman were extremely helpful in conducting the lengthy testing sessions.

¹See General Discussion section for additional considerations about the role of suppression in accounting for differences between auditory-filter shapes measured with simultaneous and nonsimultaneous masking procedures.

²For example, Moore and Glasberg (1986) did not examine the asymmetry of the auditory filter and this may have obscured some of the differences between filters derived with simultaneous and forward maskers. In addition, only a limited age range (47–70) was tested.

³A recent study (Wright, 1996) reported that the distribution of several auditory-filter parameters departed from normal. Therefore, nonparametric procedures were used in all statistical analyses for the present study.

ANSI (1989). ANSI S3.6-1989, "Specification for audiometers" (American National Standards Institute, New York).

CHABA (Committee on Hearing and Bioacoustics) Working Group on Speech Understanding and Aging (1988). "Speech understanding and aging," *J. Acoust. Soc. Am.* **83**, 859–895.

Cheesman, M. F., Hepburn, D., Armitage, J. C., and Marshall, K. (1995). "Comparison of growth of masking functions and speech discrimination abilities in younger and older adults," *Audiology* **34**, 321–333.

Delgutte, B. (1990). "Physiological mechanisms of psychophysical masking: Observations from auditory nerve-fibers," *J. Acoust. Soc. Am.* **87**, 791–809.

Dreschler, W. A., and Festen, J. M. (1986). "The effect of hearing impairment on auditory filter shapes in simultaneous and forward masking," in *Auditory Frequency Selectivity*, edited by B. C. Moore and R. D. Patterson (Plenum, New York).

Glasberg, B. R., and Moore, B. C. (1990). "Derivation of auditory filter shapes from notched-noise data," *Hearing Res.* **47**, 103–138.

Houtgast, T. (1972). "Psychophysical evidence for lateral inhibition in hearing," *J. Acoust. Soc. Am.* **51**, 1885–1894.

Jesteadt, W., and Norton, S. J. (1985). "The role of suppression in psychophysical measures of frequency selectivity," *J. Acoust. Soc. Am.* **78**, 365–374.

Lutfi, R. A. (1984). "Predicting frequency selectivity in forward masking from simultaneous masking," *J. Acoust. Soc. Am.* **76**, 1045–1050.

Lutfi, R. A. (1985). "A reply to comments by Moore. [*J. Acoust. Soc. Am.* **78**, 253–255]," *J. Acoust. Soc. Am.* **78**, 255–256.

Lutfi, R. A. (1988). "Interpreting measures of frequency selectivity: Is forward masking special?" *J. Acoust. Soc. Am.* **83**, 163–177.

Moore, B. C. J. (1985). "Comments on 'Predicting frequency selectivity in forward masking from simultaneous masking'," *J. Acoust. Soc. Am.* **76**, 1045–1050.

Moore, B. C., and Glasberg, B. R. (1981). "Auditory filter shapes derived in simultaneous and forward masking," *J. Acoust. Soc. Am.* **70**, 1003–1014.

Moore, B. C., and Glasberg, B. R. (1983). "Masking patterns for synthetic vowels in simultaneous and forward masking," *J. Acoust. Soc. Am.* **73**, 906–917.

Moore, B. C., and Glasberg, B. R. (1986). "Comparisons of frequency selectivity in simultaneous and forward masking for subjects with unilateral cochlear impairments," *J. Acoust. Soc. Am.* **80**, 93–107.

Moore, B. C., and Glasberg, B. R. (1987). "Formulae describing frequency selectivity as a function of frequency and level, and their use in calculating excitation patterns," *Hearing Res.* **28**, 209–225.

Moore, B. C. J., and O'Loughlin, B. J. (1986). "The use of nonsimultaneous masking to measure frequency selectivity and suppression," in *Frequency Selectivity in Hearing*, edited by B. C. J. Moore (Academic, London).

Moore, B. C., Peters, R. W., and Glasberg, B. R. (1990). "Auditory filter shapes at low center frequencies," *J. Acoust. Soc. Am.* **88**, 1320–1340.

Moore, B. C., Poon, P. W., Bacon, S. P., and Glasberg, B. R. (1987). "The temporal course of masking and the auditory filter shape," *J. Acoust. Soc. Am.* **81**, 1873–1880.

Patterson, R. D. (1976). "Auditory filter shapes derived with noise stimuli," *J. Acoust. Soc. Am.* **59**, 640–654.

Patterson, R. D., and Moore, B. C. (1986). "Auditory filters and excitation patterns as representations of frequency resolution," in *Frequency Selectivity in Hearing*, edited by B. C. Moore and R. D. Patterson (Academic, London).

Patterson, R. D., Nimmo-Smith, I., Weber, D. L., and Milroy, R. (1982). "The deterioration of hearing with age: Frequency selectivity, the critical ratio, the audiogram, and speech threshold," *J. Acoust. Soc. Am.* **72**, 1788–1803.

Peters, R. W., and Moore, B. C. (1992). "Auditory filter shapes at low center frequencies in young and elderly hearing-impaired subjects," *J. Acoust. Soc. Am.* **91**, 256–266.

Sommers, M. S., and Humes, L. E. (1993). "Auditory filter shapes in normal-hearing, noise-masked normal, and elderly listeners," *J. Acoust. Soc. Am.* **93**, 2903–2914.

Wightman, F. L., McGee, T., and Kramer, M. (1977). "Factors influencing frequency selectivity in normal and hearing impaired listeners," in *Psychophysics and Physiology of Hearing*, edited by E. F. Evans and J. P. Wilson (Academic, London).

Wright, B. A. (1996). "Auditory filter asymmetry at 2000 Hz in 80 normal-hearing ears," *J. Acoust. Soc. Am.* **100**, 1717–1721.

Relative intensity comparisons between a tone and spectrally remote noise: Effects of onset asynchrony

Nicholas I. Hill^{a)} and Peter J. Bailey

Department of Psychology, University of York, York YO1 5DD, United Kingdom

(Received 24 March 1997; revised 3 October 1997; accepted 3 October 1997)

The present experiment investigated the effect of onset asynchrony on listeners' ability to make relative intensity comparisons between a 1-kHz tone and a band of noise high-pass filtered at 3 kHz. In the synchronous condition, the tone and noise were gated on and off simultaneously. In the two asynchronous conditions, either the tone was gated on before the noise or vice versa, both stimuli terminating simultaneously. In the sequential condition, the offset of the tone coincided with the onset of the noise. The task of the six listeners was to indicate in which of the two presentation intervals the level of the tone was incremented relative to that of the noise. To deter the use of strategies based on successive, within-channel level comparisons, the overall level of the stimuli was randomized on each presentation. For all listeners thresholds were lowest in the synchronous condition, and highest in the sequential condition, the difference ranging from approximately 7 to 18 dB (signal *re*: pedestal amplitude). Furthermore, five of the six listeners had significantly lower thresholds in the noise-leading condition than in the tone-leading condition, the average difference across listeners being approximately 5 dB. The results are discussed in terms of auditory grouping and the possible strategies available to the listeners. © 1998 Acoustical Society of America. [S0001-4966(98)00202-1]

PACS numbers: 43.66.Fe, 43.66.Ba [WJ]

INTRODUCTION

The sensitivity of listeners to changes in the spectral profile of broadband stimuli has been the subject of considerable research in recent years (for reviews, see Green, 1988; Hall *et al.*, 1995). In a typical profile analysis experiment, a multi-tone complex is presented in each of two observation intervals, with listeners required to indicate the interval in which the relative level of one component (the pedestal) was increased. To ensure that detection cannot be based on a comparison of the pedestal level in the two observation intervals, the overall level of the stimuli is randomized between presentations. The results from such studies indicate that under conditions of minimal uncertainty, thresholds for detecting across-frequency differences in intensity are similar to those obtained in traditional pure-tone intensity discrimination tasks with no randomization of level.

While the majority of profile analysis studies have employed stimuli comprising sinusoidal components, the results of several studies suggest that listeners can also perform relative intensity discriminations using noise stimuli (Kidd *et al.*, 1989; Versfeld, 1992; Fantini and Moore, 1994). In one of the conditions from their study, Kidd *et al.* (1989) measured thresholds for detecting a relative increment in the level of a sinusoidal pedestal presented in the spectral notch of a band-stop noise. Despite the fact that the spectral notch was wider than the critical band centered on the pedestal, thresholds were approximately 17 dB (signal *re*: pedestal amplitude) below the threshold that would have been obtained were listeners basing their decision on a successive comparison of pedestal level. One interpretation of this result is that dis-

crimination was based on a perceptual attribute derived from an across-frequency integration of information. However, the idea that information is combined over stimuli as perceptually distinct as a tone and a band of noise contrasts with the finding from other profile analysis studies that stimulus manipulations which promote perceptual segregation tend to impair across-frequency comparisons. Such manipulations include presenting the pedestal and flanking components to opposite ears (Green and Kidd, 1983; Bernstein and Green, 1987), applying different patterns of amplitude modulation to the pedestal and flanking components (Green and Nguyen, 1988; Dai and Green, 1991), and gating the pedestal and flanking components on or off at different times (Green and Dai, 1992; Hill and Bailey, 1997).

An alternative account of Kidd *et al.*'s data is that listeners were simply performing an explicit comparison of the levels of the tone and noise in the two observation intervals. Of relevance to this issue is an experiment by Dai and Green (1992) which contrasted listeners' thresholds for discriminating a change in the relative level of a pair of pure tones that were presented simultaneously, with those for the same tones presented sequentially. In the sequential condition listeners had no option but to make an explicit comparison of the levels of the two tones whereas in the simultaneous condition timbre and pitch cues were also potentially available. When the two tones were separated in frequency by more than a critical band, thresholds in the simultaneous condition were approximately 8 dB lower than those obtained in the sequential condition. This result suggests that for stimuli occupying different spectral regions, relative intensity comparisons based on timbral or pitch cues are superior to explicit comparisons. Thus, if performance in the Kidd *et al.* study was based on an across-frequency integration of information,

^{a)}Corresponding author, Electronic mail: nih1@york.ac.uk

then one would predict that presenting the tone and noise sequentially would lead to a substantial elevation of threshold.

It is also possible that discrimination of the relative level of the tone and noise in the study of Kidd *et al.* (1989) was mediated by information in a single frequency channel close to one of the edges of the spectral notch. This follows since the level of the tone relative to the noise was sufficiently great, and the width of the notch sufficiently narrow to ensure that frequency channels close to the edges of the notch received significant excitation from both stimuli. For example, the effective attenuation of the tone at the 3 dB down point of the high-frequency edge of the notch would have been approximately 33 dB (Moore and Glasberg, 1983), implying that the effective level of the tone matched the spectrum level of the noise at that point.

The objective of the present experiment was to determine whether listeners' ability to compare the relative levels of a tone and noise depends upon their temporal relationship. Four conditions were examined: a baseline condition in which the tone and noise were gated on and off simultaneously, a sequential condition in which the offset of the tone coincided with the onset of the noise, and two asynchronous conditions in which either the tone began 200 ms before the noise, or vice versa. The sequential condition provides an estimate of sensitivity in a situation in which listeners are forced to make explicit judgments of the loudness of both the tone and noise. To eliminate the possibility of listeners monitoring a frequency channel which received stimulation from both the tone and noise, the present experiment used a single, high-frequency band of noise with a cut-off frequency substantially above that of the pedestal. Furthermore, the level of the pedestal was only 15 dB above that of the noise in the present experiment compared with 30 dB in that of Kidd *et al.* If, when comparing the relative levels of a tone and noise, listeners base their decision primarily on some perceptual attribute derived from a simultaneous integration of information across frequency, then presenting the stimuli sequentially, or with different onsets would be expected to lead to an increase in threshold. However, if listeners base their decision on an explicit comparison of the levels of the tone and noise, then one would predict little difference in threshold between the four conditions.

I. EXPERIMENT

A. Listeners

The six listeners were aged between 20 and 34. All participants were experienced profile listeners and had normal pure-tone thresholds over the range of frequencies used in this experiment. Listener NH was the first author. The remaining listeners were students at the university and received payment.

B. Stimuli and equipment

The stimulus in each of the four conditions comprised a 1-kHz tone and a wideband Gaussian noise having a lower cut-off frequency of 3 kHz. The upper cut-off frequency of the noise was 8 kHz as determined by an external low-pass

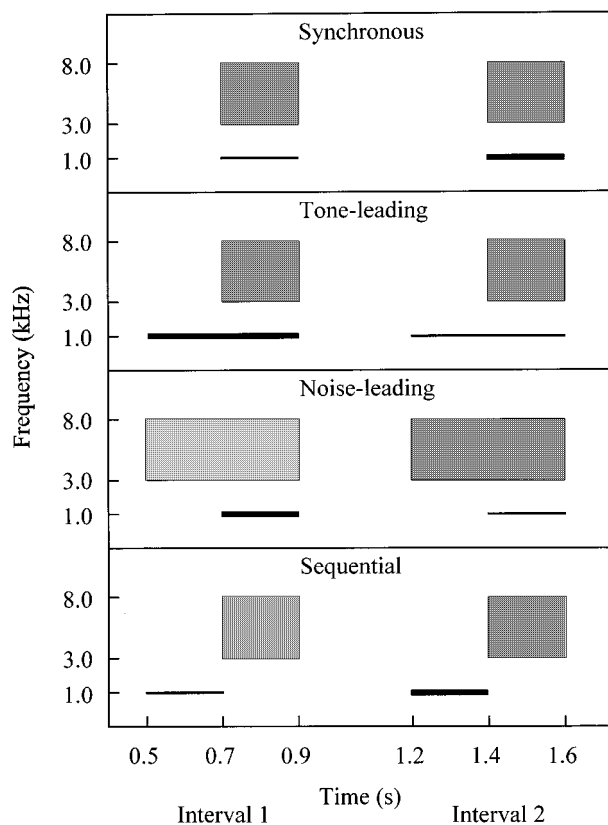


FIG. 1. Schematic illustration of the stimuli used in the four conditions of this experiment. The bold lines indicate relative increments in intensity.

filter used for anti-aliasing. In the synchronous onset condition, both the tone and noise were gated on and off at the same time and had a duration of 200 ms. In the two asynchronous conditions the leading stimulus had a duration of 400 ms and the lagging stimulus a duration of 200 ms, both stimuli being gated off synchronously. The magnitude of the onset asynchrony was therefore 200 ms. In the sequential condition, the tone and noise both had a duration of 200 ms, with the onset of the noise immediately following the offset of the tone. All durations included 10-ms \cos^2 onset and offset ramps. A schematic illustration of the stimuli in the four conditions is given in Fig. 1. The overall level of the stimuli was selected randomly on each presentation from a uniform distribution spanning a 30 dB range. At the midpoint of this range the level of the 1-kHz tone (in the non-signal interval) was 55 dB SPL and the spectrum level of the noise was 40 dB SPL/Hz. The attenuation of the noise relative to the level in the pass band exceeded 60 dB for frequencies below 2 kHz. The starting phase of the tone was randomized on each presentation. In all four conditions, the signal was an increment in the level of the 1000-Hz component.

Stimuli were synthesized in real time at a sampling rate of 20 kHz using custom software running on an IBM-compatible PC. The resulting waveforms were converted to voltages using 16-bit DACs (TDT model DD1) and were

low-pass filtered at 8 kHz (TDT model FT2). The overall level of the stimuli was controlled using a pair of attenuators (TDT model PA4) having a resolution of 0.1 dB. Stimuli were presented diotically over Sennheiser HD414 headphones. Listeners were run individually in a sound-attenuating enclosure.

C. Procedure

Thresholds were determined using a two-alternative, forced-choice, adaptive procedure employing a three-down, one-up rule which targeted the level increment corresponding to 79% correct responses (Levitt, 1971). Each 80-trial run began with the size of the increment, defined as $10 \times \log(1 + \Delta I/I)$, set to 10 dB. During a run the magnitude of the increment was varied logarithmically using an initial ratio of 0.7225. This ratio was increased to 0.85 following the first error so as to increase the resolution of the adaptive procedure near threshold. For example, if the first three responses in a run were correct, the level increment would be reduced to 7.225 dB (0.7225×10.0 dB). An error on the following trial would result in the increment being set to 8.50 dB ($7.225 \text{ dB} / 0.85$). The data corresponding to the first three or four reversals in each run were ignored, estimated threshold being based on the average intensity increment over the remaining even number of reversals. A typical threshold estimate was based on 8–16 reversals. In each session listeners completed 8 runs of the adaptive procedure which took approximately 50 minutes.

The beginning of each trial was signaled by the presentation of a visual alerting signal in the center of a computer screen for 200 ms. In the synchronous condition, the first observation interval followed 500 ms after the offset of the alerting signal, and the inter-stimulus interval was also 500 ms. In the asynchronous and sequential conditions, these intervals were reduced to 300 ms so that the overall duration of a trial was fixed across all four conditions. Listeners were given an unlimited time in which to respond, immediately after which they were presented with visual feedback for 400 ms. The next trial began 1 s after the termination of feedback.

So far as was possible listeners participated on a daily basis over a period of approximately two months. On any given session the same condition was presented on each of the 8 runs in order to minimize effects of uncertainty. All listeners were run first on the synchronous condition, then on the tone-leading condition, then on the noise-leading condition, and finally on the sequential condition. In each condition listeners were run until performance was stable which took between 6 and 11 sessions. The reported thresholds were based on the average of the final two sessions of data collection (16 runs), excluding runs in which the threshold was greater than two standard deviations from the mean. At most one run was excluded on the basis of this criterion for any one listener and condition. To facilitate comparison between the present data and those reported in the majority of previous profile analysis studies, the threshold level increment for each run was converted to the corresponding signal-to-pedestal ratio in decibels [defined as $20 \log(\Delta A/A)$] before averaging.

TABLE I. Threshold signal level defined as $20 \log(\Delta A/A)$ and associated standard error of the mean for each listener and condition. The bottom row shows the mean threshold and associated standard error for each condition averaged across listeners.

Listener	Threshold (dB)							
	Synchronous		Noise leading		Tone leading		Sequential	
NH	-11.89	(0.59)	-9.83	(0.49)	-5.96	(0.62)	-2.24	(0.38)
AK	-9.71	(0.46)	-5.36	(0.82)	-2.65	(0.64)	-1.59	(0.81)
HB	-9.67	(0.47)	-5.75	(0.67)	-2.56	(0.36)	-2.48	(0.46)
KM	-5.04	(0.59)	0.51	(0.80)	1.42	(0.53)	4.98	(0.61)
RW	-9.04	(0.50)	-4.13	(0.68)	5.33	(0.84)	6.41	(0.74)
MF	-9.11	(0.82)	-3.04	(0.58)	7.23	(0.64)	9.35	(0.87)
mean	-9.08	(0.91)	-4.60	(1.39)	0.47	(2.08)	2.40	(2.10)

D. Results

Table I shows the threshold signal-to-pedestal ratio in decibels and associated standard error for each listener and condition. The bottom row shows the mean threshold and standard error for each condition averaged across listeners. For all listeners discrimination thresholds were lowest in the synchronous condition and highest in the sequential condition. The magnitude of the difference ranged from 7.19 dB for listener HB to 18.45 dB for listener MF. Furthermore, all listeners had lower thresholds in the noise-leading condition than in the tone-leading, although for listener KM this difference was probably not reliable.

For a 3-down, 1-up adaptive procedure and a level variation of 30 dB, the expected threshold of a listener basing his/her decision purely on sequential comparisons of tone level is 7.75 dB (Green, 1988). In the synchronous condition therefore, all listeners are clearly able to exploit the presence of the noise referent with average thresholds being approximately 17 dB lower than would be achievable in its absence. This level of performance corresponds closely with the average threshold reported by Kidd *et al.* (1989) for their condition in which a tone was presented in the spectral notch of a wideband noise.

Average thresholds in the noise-leading condition were approximately 4 dB higher than those in the synchronous condition and there was relatively little variation in the magnitude of this difference across listeners. In the tone-leading condition four listeners had thresholds that were approximately 6–7 dB higher than in the synchronous condition. The remaining two listeners had thresholds that were elevated by more than 14 dB with MF apparently making little use of the noise. The average difference in threshold between the tone-leading and sequential conditions was less than 2 dB.

E. Discussion

The data indicate that listeners can perform relatively efficient intensity comparisons between a tone and spectrally remote noise when the two stimuli are gated synchronously. This result replicates the finding of Kidd *et al.* (1989) for a tone presented in the spectral notch of a wide-band noise. The fact that thresholds for all listeners were lower in the synchronous condition than in the other three conditions sug-

gests that performance in the synchronous condition was probably not based on an explicit comparison of the loudness of the tone and noise. Rather, the data support the hypothesis that in the synchronous condition listeners attended to some attribute of the tone-noise stimulus derived from a simultaneous integration of information across frequency. While the average threshold in the synchronous condition is approximately 4 dB higher than that reported by Kidd *et al.* (1989), this difference is probably attributable to the fact that in the present experiment the targeted threshold corresponded to 79% correct responses whereas in the Kidd *et al.* study it was 71%. Indeed, in both studies average thresholds were approximately 17 dB below the theoretical limit for a listener basing his/her decision purely on within-channel comparisons. The close agreement between the studies suggests that for synchronously gated stimuli threshold is relatively independent of factors such as the relative levels of the tone and noise, and the spectral composition of the noise. This result is not entirely surprising given that (a) pedestal level has only a small effect on threshold in conventional profile analysis tasks when the components are sufficiently far apart to avoid masking (Green and Kidd, 1983), and (b) Kidd *et al.*'s study found that for a 900 Hz tone presented in a band of noise, threshold was largely independent of bandwidth for bandwidths exceeding about 100 Hz.

While the deleterious effect of onset asynchrony is consistent with previous studies of the effect of asynchrony on profile analysis performance using tonal stimuli (Green and Dai, 1992; Hill and Bailey, 1997), the finding that most listeners performed significantly better in the noise-leading condition than in the tone-leading condition is somewhat surprising given that in both cases the same value of asynchrony was employed. One interpretation of this result is that gating the tone on ahead of the noise led to greater perceptual segregation than did gating the noise on before the tone, with a corresponding reduction in the amount of information integrated across frequency. However, the fact that thresholds for listeners RW and MF were substantially elevated in the tone-leading condition suggests an alternative interpretation, namely, that gating the tone on ahead of the noise may have led to complete segregation of the two stimuli with the consequence that listeners were forced into basing their decision on an explicit comparison of the levels of the tone and noise. The relatively poor performance of these listeners in the tone-leading condition can then be explained in terms of their general difficulty in performing explicit intensity comparisons, as evidenced by their similarly poor performance in the sequential condition. Given that the thresholds for listeners RW and MF in both the sequential and tone-leading conditions were close to the theoretical limit based on within-channel comparisons, it is possible that these listeners were basing their decision primarily on the absolute level of the tone. Assuming that in both the sequential and tone-leading conditions listeners had to make explicit comparisons of the levels of the two stimuli, the small difference in threshold between the two conditions could be attributed to an improved estimate of the level of the tone in the tone-leading condition due to its increased duration (e.g., Florentine, 1986).

In the sequential condition, three listeners (NH, AK, and HB) had thresholds that were more than 9 dB lower than would be achievable in the absence of the noise. While this result suggests that comparisons of intensity between tonal and noise stimuli are possible even in the absence of timbral cues, it is also possible that listeners were performing across-interval loudness comparisons separately for the tone and noise. In the latter case, the response would be based on whichever of the tone and noise differed most in loudness across the two intervals. In particular, if the loudness of the tone across the two intervals differed more than that of the noise, then the signal interval would correspond to that in which the tone was louder. Conversely, if the loudness of the noise varied most across intervals, then the signal interval would correspond to the interval in which the noise was quieter. The results of an informal control experiment undertaken by NH (the first author) indicated that increasing the ISI to 8 seconds in the sequential condition had no significant effect on threshold. Since thresholds for successive within-channel intensity comparisons (with between-trial roving of level) increase with increasing ISI (e.g., Berliner *et al.*, 1977; Green *et al.*, 1983), this informal result suggests that discrimination in the sequential condition was probably based on explicit comparisons of the levels of the tone and noise.

While the similarity between the present data and those of Kidd *et al.* (1989) suggests that the level of the tone relative to the noise has little effect on threshold in the simultaneous condition, it is possible that performance in conditions requiring an explicit comparison of the levels of two stimuli does depend on their relative level. In particular, it is reasonable to suppose that the more dissimilar the two stimuli being compared the less accurate will be the comparison (Lim *et al.*, 1977). In the present experiment no attempt was made to equate the loudness of the tone and noise and therefore performance in the sequential condition may be somewhat poorer than could be achieved for stimuli matched in loudness.

In summary, the results of the present experiment have extended the observation by Kidd *et al.* (1989) that accurate judgments of relative intensity can be made between a tone and a spectrally remote band of noise. It was found that gating the tone and noise on at different times impaired discrimination performance, although five of the six listeners were still able to perform some sort of relative comparison even when the stimuli were presented sequentially. The results suggest that when the tone and noise are gated synchronously, discrimination is based on a simultaneous comparison of information across frequency, rather than an explicit comparison of the loudness of the tone and noise.

ACKNOWLEDGMENTS

The authors would like to thank the two anonymous reviewers for their constructive comments on an earlier version of this manuscript. Financial support was provided by the U.K. Medical Research Council, Grant No. G9436832N.

- Berliner, J. E., Durlach, N. I., and Braida, L. D. (1977). "Intensity perception. VII. Further data on roving-level discrimination and the resolution and bias edge effects," *J. Acoust. Soc. Am.* **61**, 1577–1585.
- Bernstein, L. R., and Green, D. M. (1987). "The profile-analysis bandwidth," *J. Acoust. Soc. Am.* **81**, 1888–1895.
- Dai, H., and Green, D. M. (1991). "Effect of amplitude modulation on profile detection," *J. Acoust. Soc. Am.* **90**, 836–845.
- Dai, H., and Green, D. M. (1992). "Auditory intensity perception: Successive versus simultaneous, across-channel discriminations," *J. Acoust. Soc. Am.* **91**, 2845–2854.
- Fantini, D. A., and Moore, B. C. J. (1994). "Profile analysis and comodulation detection differences using narrow bands of noise and their relation to comodulation masking release," *J. Acoust. Soc. Am.* **95**, 2180–2191.
- Florentine, M. (1986). "Level discrimination of tones as a function of duration," *J. Acoust. Soc. Am.* **79**, 792–798.
- Green, D. M. (1988). *Profile Analysis: Auditory Intensity Discrimination* (Oxford University Press, Oxford).
- Green, D. M., and Dai, H. (1992). "Temporal relations in profile comparisons," in *Auditory Physiology and Perception*, edited by Y. Cazals, L. Demany, and K. Horner (Pergamon, Oxford), pp. 471–477.
- Green, D. M., and Kidd, G., Jr. (1983). "Further studies of auditory profile analysis," *J. Acoust. Soc. Am.* **73**, 1260–1265.
- Green, D. M., Kidd, G., Jr., and Picardi, M. C. (1983). "Successive versus simultaneous comparison in auditory intensity discrimination," *J. Acoust. Soc. Am.* **73**, 639–643.
- Green, D. M., and Nguyen, Q. T. (1988). "Profile analysis: Detecting dynamic spectral changes," *Hearing Res.* **32**, 147–164.
- Hall, J. W., Grose, J. H., and Mendoza, L. (1995). "Across-channel processes in masking," in *Hearing*, edited by B. C. J. Moore (Academic, San Diego), pp. 243–266.
- Hill, N. I., and Bailey, P. J. (1997). "Profile analysis with an asynchronous target: Evidence for auditory grouping," *J. Acoust. Soc. Am.* **102**, 477–481.
- Kidd, G., Jr., Mason, C. R., Brantley, M. A., and Owen, G. A. (1989). "Roving-level tone-in-noise detection," *J. Acoust. Soc. Am.* **86**, 1310–1317.
- Levitt, H. (1971). "Transformed up-down methods in psychoacoustics," *J. Acoust. Soc. Am.* **49**, 467–477.
- Lim, J. S., Rabinowitz, W. M., Braida, L. D., and Durlach, N. I. (1977). "Intensity perception VIII. Loudness comparisons between different types of stimuli," *J. Acoust. Soc. Am.* **62**, 1256–1267.
- Moore, B. C. J., and Glasberg, B. R. (1983). "Suggested formulae for calculating auditory-filter bandwidths and excitation patterns," *J. Acoust. Soc. Am.* **74**, 750–753.
- Versfeld, N. J. (1992). "On the perception of spectral changes in noise bands," in *The Auditory Processing of Speech: From Sounds to Words*, edited by M. E. H. Schouten (Mouton de Gruyter, New York), pp. 219–227.

Perceptual segregation of a harmonic from a vowel by interaural time difference in conjunction with mistuning and onset asynchrony

C. J. Darwin and R. W. Hukin

Experimental Psychology, University of Sussex, Brighton BN1 9QG, England

(Received 20 May 1997; accepted for publication 10 October 1997)

The two experiments reported here examine how an inter-aural time difference (ITD) interacts with two other cues, mistuning and onset asynchrony, in reducing the contribution of a single frequency component to the perception of a vowel's identity. Previous experiments have shown that although ITD is generally rather ineffective at segregating a simultaneous harmonic frequency component from a vowel, it can produce some segregation when listeners have already been exposed to the isolated segregated component. A difference in ITD increases segregation overall in experiment 1 where the to-be-segregated component can also have a different onset time from the remainder of the vowel, and experiment 2 shows a similar result when the to-be-segregated component is mistuned. However, segregation by ITD is present just as strongly on trials when there is neither mistuning nor a difference in onset-time as on trials where these additional cues are present. Segregation on trials when there is neither mistuning nor a difference in onset-time is however larger in the present experiment which mixed all conditions together than in similar trials in an earlier experiment that had a blocked design [C. J. Darwin and R. W. Hukin, *J. Acoust. Soc. Am.* **102**, 2316–2324 (1997)]. The results show that segregation by ITD increases when other more potent cues are present in the experiment. © 1998 Acoustical Society of America. [S0001-4966(98)00302-6]

PACS numbers: 43.66.Mk, 43.66.Pn, 43.66.Qp, 43.71.Es [JWH]

INTRODUCTION

In the normal environment, a single cue that is useful for the perceptual segregation of a sound source rarely occurs in isolation. Frequency components originating from one sound source will generally differ from those originating from another in a variety of ways: they may have different onset times, be part of different harmonic series, and come from different directions. Experiments that have varied these cues individually have shown that the auditory system can exploit at least some of these cues to perceptually segregate frequency components into different putative sound sources.

For example, there is clear evidence from experiments on vowel perception that mistuning a single harmonic (Darwin and Gardner, 1986; Darwin and Sandell, 1994), giving it a different onset time from the rest of the vowel (Darwin, 1984), or playing it to the opposite ear from the rest of the vowel (Hukin and Darwin, 1995) will substantially remove it from the perception of vowel identity. These cues also affect other tasks, suggesting that the segregation that they provide is a robust phenomenon (Carlyon, 1994; Darwin and Carlyon, 1995; Hill and Bailey, 1997). Such perceptual grouping does not occur so straightforwardly as a result of differences in interaural time difference (ITD). A large difference in ITD (c. $\pm 600 \mu\text{s}$) is either ineffective or very weak, when it is the only cue, at segregating either simultaneous, formantlike noise bands into vowel-like pairs (Culling and Summerfield, 1995) or in segregating an individual harmonic from the perception of the vowel identity of a simultaneous steady-state vowel (Hukin and Darwin, 1995; Darwin and Hukin, 1997).

However, a difference in ITD *can* be effective at en-

hancing the segregation of a harmonic from a vowel under conditions where the listener has been made aware of an appropriate separate sound source. Using the same subjects as are used in the present experiments, Darwin and Hukin (1997, exp. 1) looked at the ability of a difference in ITD to segregate a harmonic from the percept of a vowel's identity under two different types of presentation (measured by a change in the phoneme boundary between /ɪ/ and /ε/ along a F_1 continuum). Under *blocked* presentation subjects heard a block of trials in which one of the harmonics of a vowel had either the same or a different ITD from the remaining harmonics. A difference in ITD gave no change in the phoneme boundary, indicating no segregation of the harmonic from the vowel. However, when these trials were *mixed* with others in which the vowel was preceded by a tone corresponding to the to-be-segregated harmonic, then a difference in ITD did produce segregation, even in trials that lacked the preceding tone sequence. Subsequent experiments (Darwin and Hukin, 1997) showed that this across-trial facilitation required the presence of a tone that corresponded both in identity and ITD to the to-be-segregated tone.

The present experiments ask whether the use of a difference in ITD can also be facilitated by other, more integral cues to segregation. In particular it asks whether the effectiveness of a difference in ITD in segregating a harmonic from a vowel is increased when it has a difference in onset time from the remainder of a vowel, or when it is mistuned relative to the other harmonics in the vowel.

Evidence that the processing of ITD is not independent of perceptual grouping cues such as onset asynchrony and mistuning comes from experiments on the localization of

complex tones. The experiments exploit the result that listeners use consistency of ITD across frequency to localize a band-limited noise (Trahiotis and Stern, 1989) or tonal complex (Hill and Darwin, 1996). A 500-Hz tone with an interaural phase difference that leads on the left ear by three-quarters of a cycle (1.5 ms) will be heard on the right in isolation because of phase ambiguity and a preference of the binaural system for short ITDs. However, if it is presented as part of a broader-band tonal complex whose other components share the same (1.5 ms) ITD, the whole complex will be heard on the left, apparently because the binaural system gives weight to the consistency of (an albeit long) ITD across frequency. This across-frequency integration of ITD can, however, be disturbed either by mistuning or by varying the onset time of the 500-Hz component. A few percent (c. 3%) mistuning, or a few tens of milliseconds (c. 40 ms) delay in onset time is sufficient to perceptually segregate the component from the complex, and to cause it to be heard back towards its original location on the left (Hill and Darwin, 1996). These results argue for the subjective location of a sound being determined after some perceptual grouping has occurred.

The present experiments use vowel identification rather than subjective location as a measure of segregation. Our previous experiments have indicated that grouping by ITD can be influenced by other grouping cues, such as onset asynchrony and mistuning, in two ways. These two ways make different predictions for experiments in which trials which either do or do not have the other grouping cues mixed together in the same block.

First, by analogy with Hill and Darwin's localization experiments, onset asynchrony or mistuning could influence grouping by ITD within a trial by providing a segregated tone which can then be localized separately by its different ITD. This mechanism predicts that ITD should be more effective at segregating a harmonic from a vowel on trials when the other grouping cues are present than on trials when the harmonic is both synchronous and exactly in tune. Informal listening to the sounds used in the present experiments indicated that it was very easy to hear a sufficiently mistuned or asynchronous harmonic that had a different ITD from the rest of the vowel as a separate sound in a distinct location.

Second, other grouping cues can influence grouping by ITD by the across-trial facilitation mechanism described earlier: the segregated and separately localized tone can facilitate segregation by ITD on trials when other grouping cues are not present. This across-trial mechanism predicts that ITD should also be effective on trials which do not have another grouping cue present.

The first experiment examines how segregation by ITD is influenced by onset asynchrony, and the second experiment examines how it is influenced by mistuning.

I. EXPERIMENT 1: ONSET ASYNCHRONY AND ITD

The first experiment examines how the ability of a difference in ITD to segregate a harmonic from the perception of a vowel's identity is influenced by that harmonic also having a different onset time from the rest of the vowel.

The experiment uses a well-established paradigm (Darwin, 1984) to measure the extent to which a 500-Hz component is segregated from a steady-state vowel. The segregation is measured as the shift in the phoneme boundary along a first formant (F_1) continuum between the vowels /i/ and /ε/. Physical, and by inference perceptual, removal of the harmonic results in a phoneme-boundary shift to higher nominal F_1 values. In order to increase the size of phoneme boundary shift that removal of the 500-Hz component produces, conditions are also included in which the level of the 500-Hz component has been increased by 6 dB.

The 500-Hz component is given five different onset asynchronies ranging from 0 to 40 ms in order to provide some, but not complete, segregation by onset asynchrony. The 500-Hz component is also given either the same ITD as the rest of the vowel (which is always presented with an ITD leading on the left ear) or the opposite ITD.

A. Method

The basic stimuli were similar to those used in Hukin and Darwin (1995, exp. 2). On each trial subjects classified a single vowel as /i/ or /ε/. The vowel was 56 ms in duration on a fundamental of 125 Hz and varied in F_1 frequency from 396 to 521 Hz in seven steps. Harmonic amplitudes were calculated from the source and transfer function of the Klatt (1980) synthesizer in serial mode with the first three formant bandwidths at 90, 110, and 170 Hz and the second and third formant frequencies at 2100 and 2900 Hz, respectively. The 500-Hz component of the vowel was presented either with the same ITD as the rest of the vowel (+666 μ s, with the left ear leading) or with the opposite ear leading. The 500-Hz component started 0, 10, 20, 30, or 40 ms before the rest of the vowel. Another condition was run in which the 500-Hz component was physically absent (no 500-Hz). Nine subjects with normal hearing took two different blocks of trials on separate days. The 500-Hz component was given an additional gain of 6 dB in the second block of trials. Each block had 770 trials: 10 replications of $7F_1$ values \times 11 conditions (no 500-Hz + 5 onset asynchronies \times 2 gains). Other experimental details were as in Hukin and Darwin (1995, exp. 2).

B. Results

Phoneme boundaries were estimated from each subject's data in each condition. Mean boundaries are shown in Fig. 1. The results replicate previous results on segregation by onset asynchrony and in addition show a clear effect of segregation by ITD.

Physically removing the 500-Hz 0-dB component increases the phoneme boundary by about 35 Hz and removing the 500-Hz 6-dB component increases the phoneme boundary by about 45 Hz. Giving the 500-Hz component an onset asynchrony of up to 40 ms increases the phoneme boundary by up to about 20 Hz in both the 0- and +6-dB conditions ($F_{4,32} = 21.4$, $p < 0.0001$), indicating that onset asynchrony is partly removing the component from the calculation of vowel quality. Giving the 500-Hz component a different ITD from the rest of the vowel further increases the phoneme

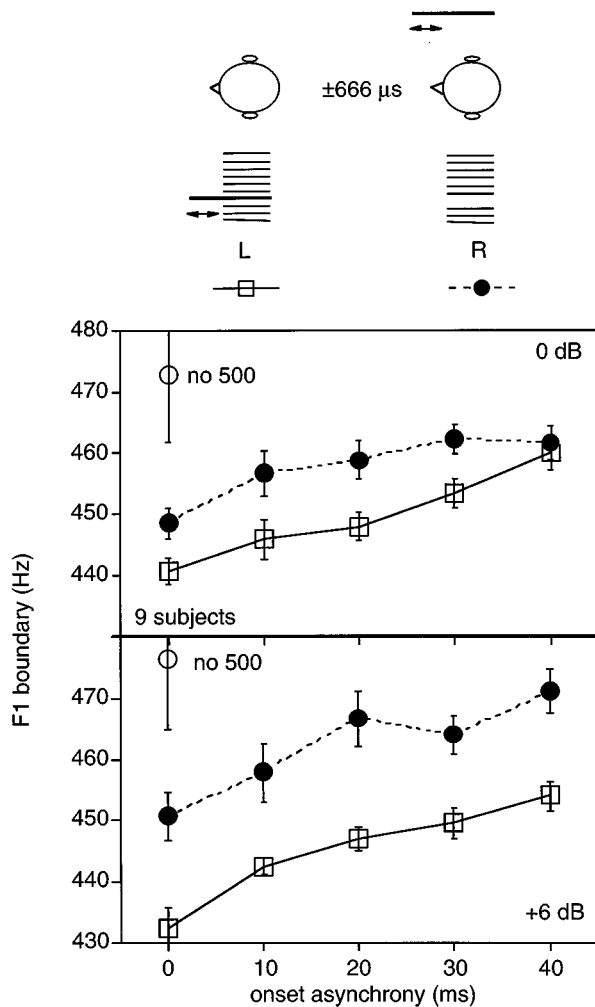


FIG. 1. Phoneme boundaries in experiment 1 along an /t/-/ε/ continuum, for vowels with the 500-Hz component differing in onset asynchrony and in ITD from the rest of the vowel. Stimulus conditions are illustrated in the upper part of the figure, with frequency components placed on the ear that had the ITD lead. In the L condition all components had an ITD of +666 μ s, with the left ear leading. In the R condition the 500-Hz component was given an ITD of -666 μ s. In the lower panel the 500-Hz component has been given an additional gain of 6 dB across all conditions.

boundary ($F_{1,8} = 33.3, p < 0.0005$). Although both the 17-Hz increase with ITD for the +6-dB condition ($F_{1,8} = 27.9, p < 0.001$) and the 8-Hz increase for the 0-dB condition are significant ($F_{1,8} = 16.8, p < 0.005$), the increase is larger for the +6-dB condition ($F_{1,8} = 8.4, p < 0.02$). Overall, the size of the increase with ITD does not depend on onset asynchrony; in particular, it is not smaller at 0-ms onset asynchrony than at other asynchronies.

Across-trial facilitation of segregation by ITD was tested by comparing the size of the phoneme boundary shifts obtained here at 0-ms asynchrony with those found with the same subjects and the same stimuli presented in blocked conditions in Darwin and Hukin (1997, exp. 1). The shift is significantly larger in the present experiment than in the previous experiment, implying across-trial facilitation, for their +6-dB conditions ($F_{1,8} = 8.1, p < 0.025$) but not for their +0-dB conditions.

II. EXPERIMENT 2: MISTUNING AND ITD

The second experiment examines how the ability of a difference in ITD to segregate a harmonic from the perception of vowel's identity is influenced by that harmonic being mistuned relative to the rest of the vowel.

A. Stimuli

The stimuli for this experiment were similar to those of Experiment 1 except that the vowel duration was increased to 200 ms, all components were synchronous, and the 500-Hz component was mistuned by 0%, $\pm 1\%$, $\pm 2\%$, $\pm 3\%$, and $\pm 4\%$. The longer duration of 200 ms was chosen to be the same as that used in the previous vowel experiment on mistuning (Darwin and Gardner, 1986). The amplitude of the mistuned harmonic was held constant when it was mistuned. Again the 0- and +6-dB conditions were run in that order on separate days.

B. Results

Phoneme boundaries were estimated for each subject's data in each condition. Mean boundaries are shown in Fig. 2. The results replicate previous experiments on segregation by mistuning and in addition show a clear, though overall small, effect of segregation by ITD. Physically removing the 500-Hz component again increases the phoneme boundary by about 35 Hz for the 0-dB condition and about 45 Hz for the +6-dB condition. Mistuning the 500-Hz component generally increases the phoneme boundary (quadratic trend $F_{1,8} = 37.0, p < 0.002$), although the increase is more marked for the +6-dB condition than for the 0-dB ($F_{8,64} = 4.4, p < 0.01$) and for negative than for positive mistunings (linear trend $F_{1,8} = 36.5, p < 0.002$). The phoneme boundary is further increased when the 500-Hz component has a different ITD from the rest of the vowel ($F_{1,8} = 67.0, p < 0.0001$). This increase is significant for both the +6-dB condition (8 Hz, $F_{1,8} = 45.2, p < 0.001$) and for the 0-dB condition (4 Hz, $F_{1,8} = 26.0, p < 0.001$) and is larger ($F_{1,8} = 7.3, p < 0.05$) for the +6-dB condition than for the 0-dB condition. The size of the increase with ITD does not vary with mistuning; in particular, it is not smaller for zero mistuning.

Across-trial facilitation of segregation by ITD was tested by comparing the size of the phoneme boundary shifts obtained here at zero mistuning with those found with the same subjects and similar, though shorter, stimuli presented under blocked conditions in Darwin and Hukin (1997, exp. 1). The shift is significantly larger in the present experiment than in the previous experiment for their +6-dB conditions ($F_{1,8} = 5.4, p < 0.05$) but not for their +0-dB condition.

C. Discussion

Both experiments have shown clear evidence of segregation by ITD which adds to but does not interact with the segregation due to onset asynchrony or mistuning. Segregation by ITD is present just as strongly on those trials when there is no onset asynchrony or mistuning, as on those when these additional cues are present. This result contrasts with the weak or lack of segregation found when ITD is the only

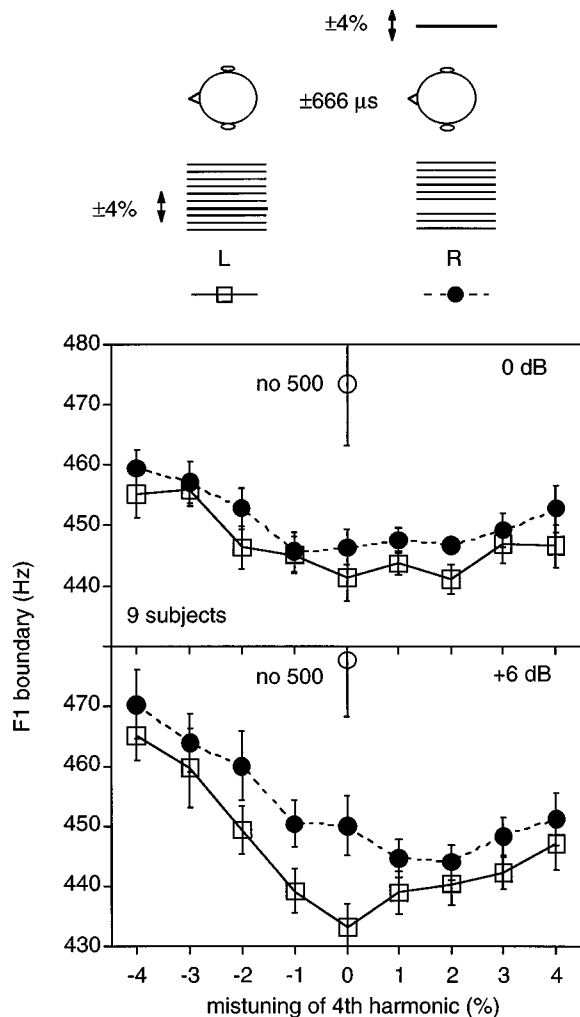


FIG. 2. Phoneme boundaries in experiment 2 along an /t/-/ε/ continuum for vowels with the 500-Hz component mistuned and differing in ITD from the rest of the vowel. In the L condition all components had an ITD of +666 μ s with the left ear leading. In the R condition the 500-Hz component was given an ITD of -666 μ s. In the lower panel the 500-Hz component has been given an additional gain of 6 dB.

cue available to the listener in a block of trials (Culling and Summerfield, 1995; Hukin and Darwin, 1995; Darwin and Hukin, 1997).

It is likely that both the mechanisms proposed in the Introduction are occurring here. First, onset asynchrony and mistuning allow a harmonic from the vowel to be localized as a separate sound source. This may be a sufficient explanation for the additional removal by ITD of the harmonic from the vowel percept that we have found in trials where substantial amounts of onset asynchrony or mistuning are present. However, in order to explain why ITD also removes the harmonic from the vowel percept on trials when neither of these other cues are present, we must also appeal to the across-trial effect previously reported with mixed presentation by Hukin and Darwin (1995, exp. 2) and replicated in Darwin and Hukin (1997). In all these experiments listeners could hear, on some trials at least, an additional sound source corresponding to the tone that was to be segregated by ITD. In the previous experiments that additional sound source was

explicitly present as a precursor tone; in the present experiments the tone could be heard out as a separate sound by virtue of its onset asynchrony or mistuning and localized on the opposite side to the rest of the vowel. The present results thus confirm that such across-trial effects can facilitate segregation by ITD, at least for the +6-dB condition (where phoneme boundary shifts are larger).

Segregation by ITD produces boundary shifts that are twice as large in combination with onset asynchrony than with mistuning. A possible reason for this is that listeners have a clearer image of the 500-Hz tone as a separate and distinctly localized sound source when it starts earlier than the rest of the vowel than when it is synchronous but mistuned. Although the average shifts produced by mistuning and onset asynchrony are comparable in these experiments, it is possible that the 500-Hz tone is more clearly localized to the opposite side when it leads the vowel. We have not formally investigated this possibility.

An entirely separate feature of the mistuning data is that negative mistunings produce more substantial shifts in the phoneme boundary (30 Hz) than do positive mistunings (particularly for the +6-dB condition). Fitting the data in Fig. 2 with a second-order polynomial decomposes the initially asymmetric function into a symmetric second-order component representing the U-shaped results expected from segregation due to mistuning, and a linear component representing the linear asymmetry. The linear component of the phoneme boundaries for the +6-dB L data has a change of about 20 Hz between $\pm 4\%$ mistuning. (The remaining second-order component for the +6-dB L data gives a shift of about 20 Hz for an absolute mistuning of 4%, which is comparable to that produced by an onset asynchrony of 40 ms.)

There are two possible reasons for the asymmetry. One is that it is a result of keeping the level of the mistuned 500-Hz constant rather than letting it follow the spectral envelope. Its constant level deviated from a 450-Hz formant envelope by about +1 and -3 dB for +4% and -4% mistunings, respectively. From the data of Fig. 2 a 6-dB increase in level shifts the boundary by about 10 Hz, so changes of this size could give a total asymmetry of about 7 Hz to the phoneme boundary, which is considerably smaller than that actually found. This explanation could be responsible for the slighter asymmetry seen in the 0-dB data. However, both of the previous experiments (Darwin and Gardner, 1986; Darwin and Sandell, 1994), that have shown phoneme boundary shifts with harmonic mistuning have varied level to maintain spectral envelope, but only the earlier study gave asymmetric data.

The second possible reason is that listener's estimates of the F_1 frequency are being directly influenced by the frequency of the mistuned harmonic. This explanation predicts a change of about 40 Hz, which is twice that observed, so neither explanation is clearly to be preferred.

III. SUMMARY

The two experiments reported here have shown that ITD can be used to perceptually segregate a harmonic from the calculation of a vowel's identity when it occurs in conjunction with other cues to perceptual segregation—onset asyn-

chrony and mistuning. Segregation by ITD also occurred in the present experiments on trials in which other segregation cues were absent. Since a difference in ITD has previously been shown to be ineffective at such perceptual segregation when it is the only cue in a block of trials, two mechanisms are proposed as an explanation for the present results.

First, onset asynchrony or mistuning can segregate a harmonic which may then in turn be localized on the opposite side to the vowel by virtue of a difference in ITD. Second, when listeners hear a separate sound source corresponding to the to-be-segregated harmonic, segregation by ITD was facilitated on other trials in the same experimental block.

In normal listening situations, where there are multiple cues to perceptual segregation, the first mechanism is likely to be the most important. However, the second mechanism does point to the possibility that ITD may be important in tracking a particular sound source over time.

ACKNOWLEDGMENTS

This research was supported by MRC Grant No. G9505738N. Bob Carlyon and Peter Assmann made helpful comments on the paper.

Carlyon, R. P. (1994). "Detecting mistuning in the presence of asynchronous and asynchronous interfering sounds," *J. Acoust. Soc. Am.* **95**, 2622–2630.

- Culling, J. F., and Summerfield, Q. (1995). "Perceptual separation of concurrent speech sounds: Absence of across-frequency grouping by common interaural delay," *J. Acoust. Soc. Am.* **98**, 785–797.
- Darwin, C. J. (1984). "Perceiving vowels in the presence of another sound: constraints on formant perception," *J. Acoust. Soc. Am.* **76**, 1636–1647.
- Darwin, C. J., and Carlyon, R. P. (1995). "Auditory grouping," in *The handbook of perception and cognition, Volume 6, Hearing*, edited by B. C. J. Moore (Academic, London), pp. 387–424.
- Darwin, C. J., and Gardner, R. B. (1986). "Mistuning a harmonic of a vowel: Grouping and phase effects on vowel quality," *J. Acoust. Soc. Am.* **79**, 838–845.
- Darwin, C. J., and Hukin, R. W. (1997). "Perceptual segregation of a harmonic from a vowel by interaural time difference and frequency proximity," *J. Acoust. Soc. Am.* **102**, 2316–2324.
- Darwin, C. J., and Sandell, G. J. (1994). "Effect of coherent frequency modulation on grouping the harmonics of a vowel," *J. Acoust. Soc. Am.* **95**, 2964–2965.
- Hill, N. I., and Bailey, P. J. (1997). "Profile analysis with an asynchronous target: Evidence for auditory grouping," *J. Acoust. Soc. Am.* **102**, 477–481.
- Hill, N. I., and Darwin, C. J. (1996). "Lateralisation of a perturbed harmonic: effects of onset asynchrony and mistuning," *J. Acoust. Soc. Am.* **100**, 2352–2364.
- Hukin, R. W., and Darwin, C. J. (1995). "Effects of contralateral presentation and of interaural time differences in segregating a harmonic from a vowel," *J. Acoust. Soc. Am.* **98**, 1380–1387.
- Klatt, D. H. (1980). "Software for a cascade/parallel formant synthesizer," *J. Acoust. Soc. Am.* **67**, 971–995.
- Trahiotis, C., and Stern, R. M. (1989). "Lateralization of bands of noise: Effects of bandwidth and differences of interaural time and phase," *J. Acoust. Soc. Am.* **86**, 1285–1293.

Comparison of relative and absolute sound localization ability in humans

Gregg H. Recanzone,^{a)} Samia D. D. R. Makhama,^{b)} and Darren C. Guard

Center for Neuroscience and Section of Neurobiology, Physiology & Behavior, University of California at Davis, Davis, California 95616

(Received 25 March 1997; accepted for publication 28 October 1997)

Sound localization ability has traditionally been studied using either a relative localization task, where thresholds to determine a difference in sound source location is approximately 1–10 degrees, or an absolute localization task, where the range of estimates of the source of a sound are 4–30 degrees. In order to directly relate these two psychophysical methods, we compared the psychometric functions from a relative localization task in a human subject to the same subject's performance on an absolute localization task using three different acoustic stimuli: Gaussian noise, 1-kHz tones, and 4-kHz tones. The results showed that the relative localization threshold was a poor indicator of the range of estimates of the same stimulus in absolute space, however, the width of the relative localization psychometric functions was well correlated with the width of the distribution of estimates made in the absolute localization task. It is concluded that the relative localization psychometric functions, but not threshold, provides a reliable estimate of absolute spatial localization ability in human subjects, and suggested that the same neuronal mechanisms can underlie the psychophysical data using both methods. © 1998 Acoustical Society of America. [S0001-4966(98)03002-1]

PACS numbers: 43.66.Qp, 43.66.Ba, 43.64.Bt [JWH]

INTRODUCTION

The ability of humans and animals to localize acoustic stimuli is generally tested using one of two psychophysical procedures: relative localization thresholds measure the ability to determine that a repeated stimulus has changed location (e.g., Mills, 1958; Molino, 1974; Perrott, 1984; Terhune, 1985; Perrott and Saberi, 1990; Chandler and Grantham, 1992; Perrott *et al.*, 1993; see Middlebrooks and Green, 1991), and absolute localization thresholds measure the ability to determine the location in space of a single stimulus (e.g., Stevens and Newman, 1936; Newton, 1983; Oldfield and Parker, 1984; Butler, 1986; Perrott *et al.*, 1987; Wightman and Kistler, 1989; Makous and Middlebrooks, 1990; Middlebrooks, 1992; Ahissar *et al.*, 1992; Butler and Muscant, 1993; Wenzel *et al.*, 1993; Good and Gilkey, 1996). These studies indicate that most individuals have relative localization thresholds of a few degrees, whereas the absolute localization of sounds is broader, depending on the eccentricity and spectral content of the stimulus.

The difference between these two measures is yet to be resolved, and it has been suggested that the relative localization paradigm originally described (Mills, 1958) was actually a reflection of an absolute discrimination task (Hartmann, 1989). However, to date it is difficult to directly compare the results of the two types of studies from the literature due to the differences of the paradigms and subjects, as well as differences in the spectral content, amplitude, and duration of the acoustic stimuli.

Resolution of this issue is important for relating the

sound localization ability to underlying neuronal mechanisms. The growing interest in the cortical and thalamic mechanisms of sound localization (e.g., Imig *et al.*, 1990; Rajan *et al.*, 1990; Middlebrooks *et al.*, 1994; Clarey *et al.*, 1995; Brugge *et al.*, 1996; Barone *et al.*, 1996) and the growing interest in the function of the cortical processing of acoustic information of the primate in general (e.g., Wang *et al.*, 1995; deCharms and Merzenich, 1996; Stricanne *et al.*, 1996; Rauschecker *et al.*, 1997) underscore the importance in understanding how these two measures of sound localization are related. It is likely that the two measures are dependent on the same auditory cortical structures, given the equivalent deficits revealed using both methods following auditory cortical ablations (Neff *et al.*, 1956; Heffner and Masterton, 1975; Heffner, 1978; Kavanagh and Kelly, 1987; Jenkins and Merzenich, 1984; Heffner and Heffner, 1990). It has been demonstrated that the spatial selectivity of auditory cortical neurons recorded in animals are much broader than the relative localization thresholds (Eisenman, 1974; Benson *et al.*, 1981; Middlebrooks and Pettigrew, 1981; Imig *et al.*, 1990; Rajan *et al.*, 1990; Middlebrooks *et al.*, 1994; Clarey *et al.*, 1995; Brugge *et al.*, 1996; Barone *et al.*, 1996), making it difficult to relate these measures of single cortical neurons to perceptual thresholds. Although the relative localization paradigms provide one estimate of localization ability, it may not be appropriate to compare relative localization thresholds to the receptive field sizes of cortical neurons. It may be more appropriate to compare the distribution of absolute localization estimates to the responses of cortical neurons. Alternatively, relative localization paradigms may accurately reflect neuronal processes, but some measure other than threshold could be directly related to single neuron activity. In either case, there should be a clear relationship

^{a)}Electronic mail: ghrecanzone@ucdavis.edu

^{b)}Present address: Department of Physiology, University of Toronto, Toronto, Ontario, Canada.

between relative and absolute localization measures, given deficits in both tasks following cortical lesions.

In order to determine the relationship between these two localization paradigms, we used the same acoustic stimuli, apparatus, and human subjects to compare the psychometric functions from a relative localization task to the estimates of the sound source location from an absolute localization task. These subjects had relative and absolute localization performance similar to that seen from previous studies (cited above). Comparison between the two paradigms showed that the widths of the psychometric functions derived from the relative localization task were strongly correlated with the width of the range of the estimates recorded in the absolute localization task. These results indicate that the difference between the perceived locations in space of acoustic stimuli are in fact within the range of the spatial selectivity of a subset of cortical neurons, and that the width of the relative localization psychometric functions, but not the threshold, provides a good estimate of sound localization ability.

I. EXPERIMENT I: RELATIVE LOCALIZATION MEASURES

A. Methods

1. Subjects

Three male (CK, WG, PS) and two female (AS and CC) subjects between 20–35 years of age at the time of testing performed these tasks with informed consent. Subjects had no known audiological deficits, and detection thresholds for the stimuli used were within normal limits (described below). All subjects had normal or corrected to normal vision. Three of the subjects had extensive psychophysical experience (CK, AS, and PS), and this was the first psychophysical acoustical study for the other two subjects (WG and CC). Subjects CK, WG, and CC completed a full series for each acoustic stimulus, while subject AS completed a full series of the absolute localization paradigm but only a partial series for the relative localization paradigm. Subject PS completed only the control experiments described below, and had partial results from the other two paradigms. The incomplete results from these two subjects were consistent with the findings from the subjects that completed each paradigm and will not be illustrated here.

2. Stimulus parameters

Stimuli were generated using a Tucker-Davis Technologies digital signal processing system. An i486 computer controlled all aspects of the psychophysical task, stimulus generation and delivery, and data collection. Three different stimuli were used: Gaussian noise, 1-kHz tones, and 4-kHz tones. All stimuli were 200 ms in duration with a 5-ms linear rise/fall. Stimuli were delivered through 1 of 15 different speakers (3½-in. Pyle dual cone DD2) located on an arc at a constant distance of 146 cm along the plane of the interaural axis, spanning a range of either –8 to 48 degrees (subjects CK, CC, WG, and PS) or 0 to 56 degrees (AS) in 4-degree increments. The entire behavioral apparatus was located within a double-walled acoustic chamber (6.5-×8.5-ft inner

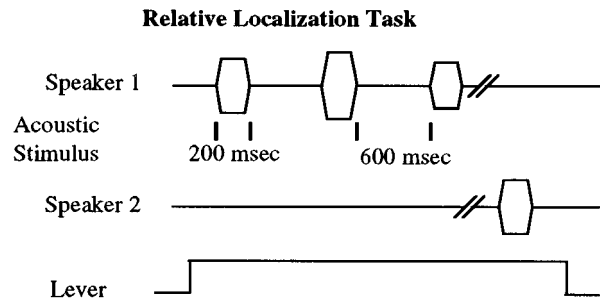


FIG. 1. Schematic of the timing of events during the relative localization task. Subjects initiated a trial by a lever press. A series of 200-ms duration sounds were presented with a 600-ms interstimulus interval. Subjects released the lever when they detected that the speaker changed location. Each acoustic stimulus varied in intensity over a 4-dB range.

dimensions; IAC) with 3-in. sound attenuating foam (Sonex) on all four walls, the ceiling, and much of the floor surrounding the subject.

Physical characteristics: Acoustic stimuli were measured using a B&K sound pressure meter with the microphone placed in the sound booth at the location occupied by the center of each subject's head, with all parts of the apparatus in place. The fast Fourier transform was calculated for all acoustic stimuli from each speaker location in the absence of the subjects. Speaker transformation functions showed a flat portion (± 3 dB) from 200 Hz to 12 kHz with approximately 6-dB/octave rolloff. Comparisons across speakers showed minimal differences in the magnitudes and phases of the FFT components for all three stimuli. Energy of the harmonic components of the tonal stimuli were < 10 dB SPL; echo contributions to all stimuli were < 20 dB SPL.

Psychophysical calibration: The detection threshold for each of the stimuli, at each of the speaker locations used for a given stimulus, were derived using a staircase method for each individual subject during several different periods throughout the study. All subjects had detection thresholds which were consistent with the normal human audiogram. Stimuli were sequentially presented across the speaker array at 30 dB above this threshold and the subjects were asked to adjust the overall intensity of each speaker until they were all the same intensity, which usually resulted in a change of less than 1 dB. These intensity values were randomly varied (± 2 dB) during the course of each trial for each subject. This perceptual equalization ensured that the subjects could not base their localization estimates on absolute loudness, and could only use interaural difference and the spectral cues due to the head-related transfer functions to localize these stimuli.

3. Psychophysical task

All psychophysical tasks were approved by the UC Davis Human Subjects Review Committee and abided by the ethical principles of psychologists. This psychophysical task was based on a go/no-go paradigm described in detail previously (Recanzone *et al.*, 1991; Fig. 1). Subjects were seated in a chair near the center of the sound booth with their heads held stationary by a modified headband attached to the ceil-

ing of the sound booth. All experiments were conducted in sufficient darkness to prevent visualization of the apparatus, and no subject reported the ability to see the apparatus, even after sufficient time for dark adaptation to occur (>1 h).

Subjects initiated a trial by pressing a lever. A series of acoustic stimuli were presented from a single speaker (S1 stimulus) with a 600-ms pause between stimuli. After a randomly determined number of S1 stimulus presentations (2–6), the same acoustic stimulus was then presented from a different speaker location (S2). The subject was required to release the lever when they detected a change in the stimulus location. Additional “catch” trials were presented where stimuli were only presented from the S1 location. For tonal stimuli, seven different S2 speaker locations were used, separated by 8 degrees. Similarly, 15 different speaker locations were used for noise stimuli with the speaker locations separated by 4 degrees. In a given session, 15 trials for each of the S2 locations were presented from 7 of the possible 15 locations for the noise stimuli (separated by 4 degrees), and for 7 locations of 1 of the 2 tonal stimuli (separated by 8 degrees) as well as 15 catch trials for each stimulus for a total of 240 trials. The S2 speaker location and the type of sound stimulus (tone or noise) was randomly interleaved across trials. In three subjects, at least one session was conducted with the S1 stimulus at each of the 8 (tone) or 15 (noise) different S1 locations (16 sessions minimum for these subjects). Subjects AS and PS were not tested at all S1 locations for all stimuli.

Control experiments: Two different classes of control experiments were performed on three subjects (CC, CK, and PS) to ensure that subjects were using spatial cues to perform the task and not nonspatial cues such as differences in the speaker transformation functions. For tonal stimuli, single sessions were run using the same paradigm except that three different S1 locations were used on randomly interleaved trials (0, 24, and 48 degrees). One session each was run (15 trials/location, including catch trials) for 1- and 4-kHz tone stimuli. Each subject then performed a second set of sessions in which the speakers between pairs of locations were exchanged (8 with 16 degrees and 32 with 40 degrees).

The second class of control experiment tested each adjacent pair of speakers using noise stimuli. Subjects oriented their head and body to the location such that one speaker was on either side of the midline. Stimuli were presented sequentially (either right–left or left–right, randomly interleaved) with a 600-ms interstimulus interval. The subjects were required to press one of two switches (left or right) indicating which location the first sound originated from. Following 30 presentations of these stimuli, subjects were cued by a visual stimulus to turn their head as far to the left as possible without moving their body or shoulders (approximately 90 degrees). The same speaker pairs were then tested using the same responses. Each of the possible 14 pairs of adjacent speakers were tested in two sessions in this manner for each of the three subjects.

4. Data analysis

Responses for each trial were recorded as either a (1) hit: the subject released the lever within 700 ms of the S2

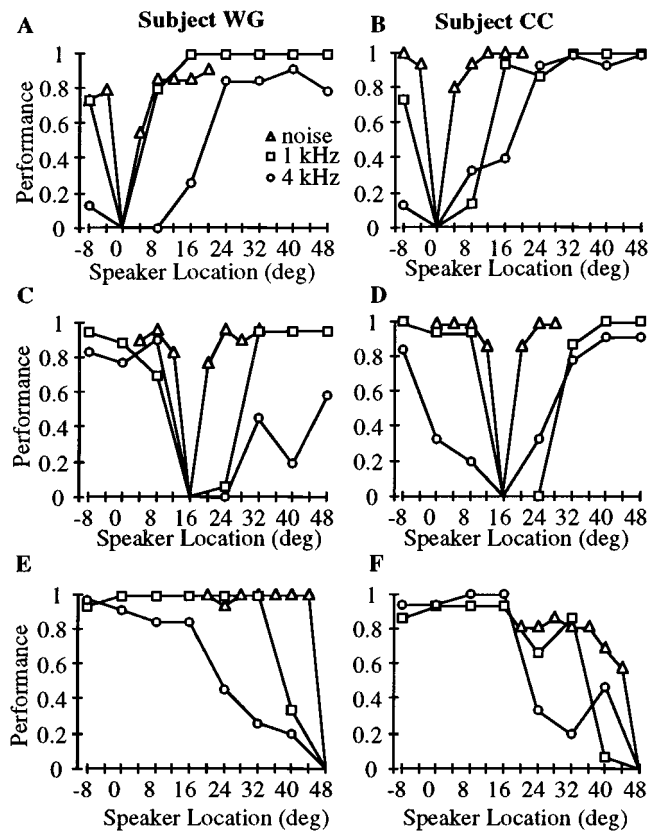


FIG. 2. Representative psychometric functions from two different subjects (WG left, CC right) at three different S1 speaker locations. Open triangles show the performance for noise stimuli, open squares show the performance for 1 kHz tone stimuli and open circles show the performance for 4-kHz tone stimuli. Psychometric functions for S1 speaker locations on the midline are shown in (A) and (B), for S1 speaker locations at 16 degrees to the right are shown in (C) and (D), and for 48 degrees to the right are shown in (E) and (F).

stimulus onset, (2) miss: the subject did not release the lever within 700 ms of the S2 stimulus onset, (3) false-positive: the subject released the lever before the S2 stimulus offset. This time was used because it was well below the minimum reaction time on hit trials (250 ms). The false-positive rate (FP_r) was calculated for each session by the stimulus type (tone or noise) as the number of false-positive responses divided by the total number of trials for that stimulus type, regardless of the outcome of the trial. This value was used to compute the safe rate (S_r) as $(1 - FP_r)$. The hit rate (H_r) was calculated as the number of hits divided by the number of hits and misses for a given stimulus type. The final performance measure (P) for a given S2 condition was calculated as $P = H_r * S_r$. This measure is a reliable measure of performance for safe rates above 0.85 (see Recanzone *et al.*, 1991, 1992a, 1993).

B. Results

Typical psychometric functions for each of the three different acoustic stimuli from three different starting S1 locations are shown for two subjects in Fig. 2. In each case, the performance measured when the S2 stimulus was presented at the same location as the S1 stimulus was zero. This is

because the subjects did not detect any difference in the two stimuli (there was none), and their performance could be considered to be perfect during the “catch” trials. This also indicates that chance performance was very near zero, as the 18 psychometric functions of Fig. 2 represents 270 trials in which a response during a catch trial would be recorded as a hit, and neither subject recorded a hit on any of these trials. Such occurrences of responses during catch trials were very infrequent across subjects, as there were only 15 responses during 1335 catch trials (1.1%) recorded across all sessions for these three subjects.

The psychometric functions shown in Fig. 2 are representative of the data collected across subjects and sessions. The localization ability measured for the noise stimuli was consistently better than that of the tonal stimuli, and the localization ability measured for 1-kHz tonal stimuli was consistently better than the 4-kHz tonal stimuli, regardless of the S1 speaker position. To quantify this more carefully, the threshold for each S1 stimulus location was defined as the speaker separation that would give a performance value of 0.50 (Recanzone *et al.*, 1991) for changes in speaker locations both toward the midline (nasal thresholds) and away from the midline (temporal thresholds). These two threshold measurements were averaged (where possible) and plotted as a function of S1 speaker location in Fig. 3. For all three subjects, these thresholds were consistently best for noise stimuli (open triangles) which were 2–4 degrees, were somewhat worse for the 1-kHz stimuli (open squares) which were 8–10 degrees, and worst for the 4-kHz tonal stimuli (open circles) which were on the order of approximately 20 degrees (ANOVA across stimulus types for each subject, or pooled across subjects; $p < 0.01$ for both cases). These data also show that, within this frontal area of acoustic space, there is very little effect on performance or threshold as a function of distance away from the midline for any of these stimuli.

To verify that averaging the two threshold measurements was not inappropriate, we compared the thresholds measured in both directions for all psychometric functions, pooled across subjects and stimuli, in which such measurements were possible. Speaker locations at the far extremes of the region tested were not used, as only one side of the psychometric function could be measured [e.g., S1 locations at 48 degrees, see Fig. 2(E) and (F)]. These two measures did not show a statistically significant difference (paired, two-tailed t -test; $p > 0.05$).

The subjects had very low false-positive rates over the vast majority of sessions. Pooled across subjects and sessions, the false-positive rate was less than 5% in 89% of all sessions, with the greatest rate measured at 8% in one session. There was no statistically significant difference in the false-positive rates between subjects or stimulus types (ANOVA, $p < 0.001$). We interpret this to indicate that the subjects were biasing their choices to be more likely to miss an S2 stimulus than to make a false-positive response, and these threshold values may consequently be slight underestimates of the actual ability of these subjects to perform this task. This effect, however, has previously been shown to be minor given the manner in which the performance is calculated (see Recanzone *et al.*, 1991, 1992a, 1993).

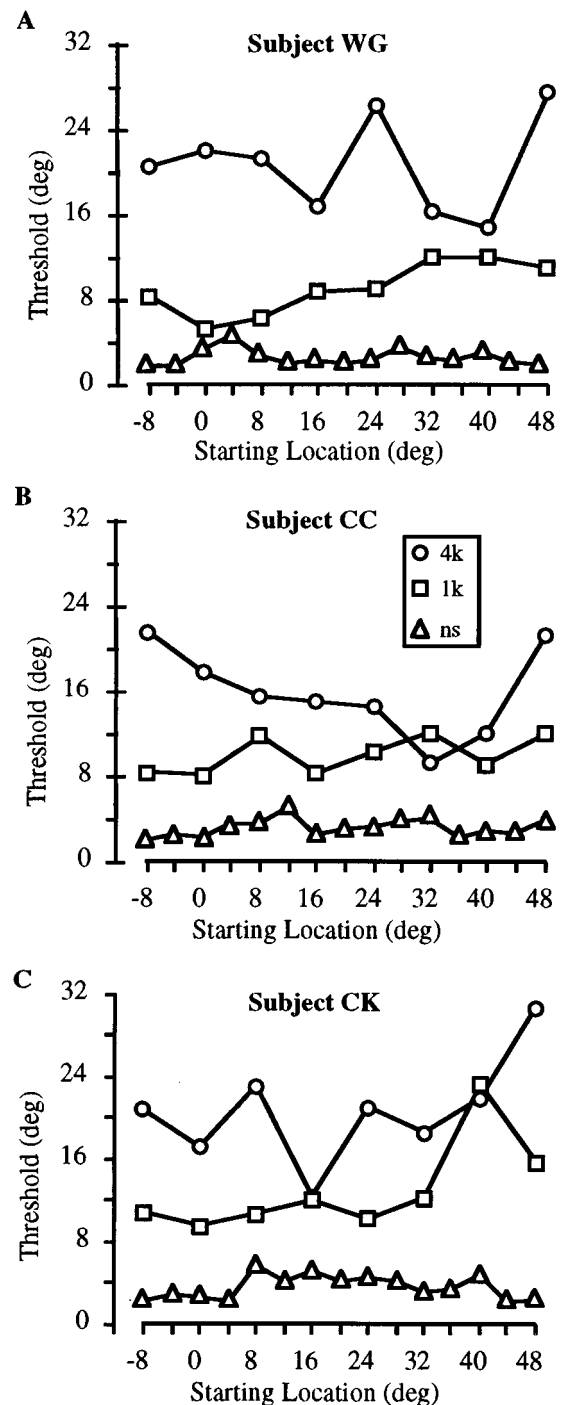


FIG. 3. Relative localization thresholds for each subject. Thresholds were calculated as the location of 0.5 performance from the psychometric functions. In cases where both the nasal and temporal sides of the psychometric function were obtained the two measures were averaged. The x axis shows the S1 speaker location. Open triangles: noise stimuli; open squares: 1-kHz tone stimuli; open circles: 4-kHz tone stimuli.

A major concern when using different speakers to measure relative localization ability is that the subjects could use speaker-specific, nonspatial cues to perform the task. Subjects were instructed to release the lever when they detected a change in the location, but could have been cueing on some other aspect of the acoustic stimulus. Although measurements of the spectrum for each speaker showed very small

differences across the frequency spectrum, the stimuli were psychophysically matched across the array for each subject, and the intensity of the stimuli varied between each stimulus presentation (see Sec. II A), it is still important to ensure that nonspatial cues were not providing the subjects with additional information. To test this possibility for the tonal stimuli, similar sessions were run in which three different starting locations were used on randomly interleaved trials (0, 24, and 48 degrees). After three subjects had performed one session using the 1-kHz tone stimuli and one session using the 4-kHz tone stimuli, the speakers located at positions 8 deg and 16 degrees were exchanged, as well as the speakers located at positions 32 and 40 degrees, and the subjects were tested again the next day. We chose these speaker locations as they were along the slope of the psychometric functions for two of the three different starting speakers. If the subjects were using only spatial localization cues, the psychometric functions obtained pre- and post-exchanging the speakers should be equivalent. If the subjects used nonspatial cues, the performance for each individual speaker should be the same regardless of the speaker location.

An example of such an experiment for subject CK using the 1-kHz tone stimulus is shown in Fig. 4(A). The heavy line shows the psychometric function prior to the speaker exchange and the thin line shows the performance after speaker exchange. It is clear from this example that the two psychometric functions are nearly identical, indicating that this subject used spatial cues to perform the task. If the performance was based on nonspatial cues, the post-exchange psychometric function should have followed the dashed line. Regression analysis of the performance for each speaker before and after the exchange in location across subjects is plotted in Fig. 4(B). There is a close correspondence in performance between speaker locations regardless of which individual speaker is at that location ($r=0.922$; $p<0.0001$; slope=0.856). This can be contrasted with the regression analysis when the performance at each individual speaker is compared pre- and post-exchange regardless of the actual speaker location [Fig. 4(C)]. In this analysis, the correlation coefficient between the pre- and post-exchange sessions is lower ($r=0.553$) and the slope is shallower (0.514) than for the regression between speaker location, indicating again that the speaker location is the most salient cue in performing the task.

A second control addressed the same issue using noise stimuli. Since the performance for noise-stimuli was very good even for 4-degree separations, the speaker exchange paradigm could not be used. Instead we took advantage of the increase in minimum audible angle thresholds for speakers near 90 degrees compared to when the two speakers are located across the midline (Musicant and Butler, 1984; Perrott *et al.*, 1993). In this paradigm, the subjects were asked to determine which of the two speakers were activated first (left-right or right-left; see Sec. II A) when the speakers crossed the midline, and then were immediately tested after the subject turned their head approximately 90 degrees to the left. We reasoned that if there was a noticeable difference between two speakers based on nonspatial cues, the performance when the stimuli crossed the midline would be

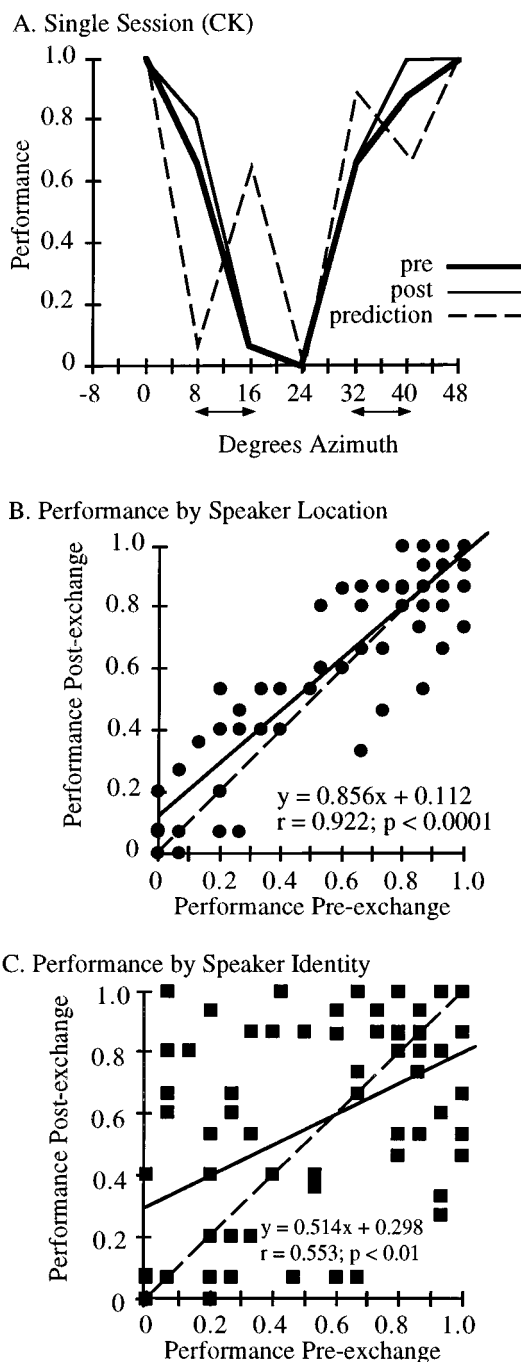


FIG. 4. Relative localization of tonal stimuli control experiments. (A) shows the psychometric functions from the session before (heavy line) and after (thin line) speakers were exchanged between locations at 8 and 16 degrees, and between locations at 32 and 40 degrees. Only the function for S1 locations at 24 degrees are shown for clarity. The dashed line represents the predicted psychometric function if the subject could discriminate between speakers using nonspatial cues. (B) Regression analysis across subjects and stimuli between the performance measured pre- (x axis) and postexchange (y axis) as a function of speaker location. Dashed line: perfect correlation. Solid line: regression line. Regression equation, r , and p values given in the inset. (C) Regression analysis as in (B) as a function of the individual speaker, regardless of spatial location. Conventions as in (B).

equivalent to the performance when the stimuli were far to the right. If only spatial cues could be used, the performance when the speakers crossed the midline should be much better compared to when the two speakers were near 90 degrees to the right.

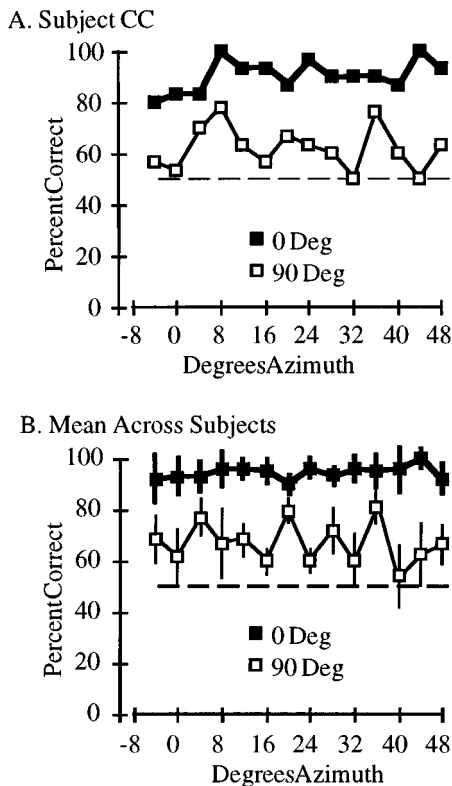


FIG. 5. Percent correct as a function of speaker location for left–right discriminations across the midline (solid squares) or at 90 degrees to the right (open squares). (A) shows the results from a single subject (CC). (B) shows the mean and standard deviations across three subjects. The dashed line indicates chance performance.

A representative example of the results of this experiment are shown in Fig. 5(A), where the solid symbols represent the performance for each speaker pair (plotted as the right speaker on the x axis) when the speakers crossed the midline, and the open squares show the performance when the two speakers were located approximately 90 degrees to the right. It is clear from this example that the performance is much worse with the head turned, consistent with the larger minimum audible angle at these spatial location (Musicant and Butler, 1984; Perrott *et al.*, 1993). The average data across three subjects is shown in Fig. 5(B), demonstrating that this was a consistent effect across subjects, and that there was a statistically significant difference on the performance across subjects and all speaker locations (ANOVA; $p < 0.01$). These two control experiments indicate that the subjects in this report were using predominately, if not exclusively, spatial cues to perform the relative localization task.

A final concern is that subjects were improving their performance at this task as they continued to perform sessions. In every session, both noise stimuli and a tonal stimuli were presented in randomly interleaved order. To determine if there was a training effect in the two naive subjects, the thresholds for the noise stimuli are plotted as a function of the session that they were tested (Fig. 6). These data do not show any significant trends of improved performance over the first ten sessions, and performance was not statistically significantly correlated with the session number for either

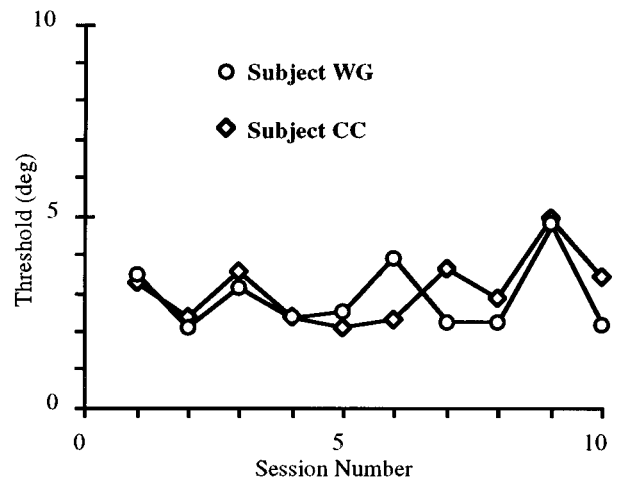


FIG. 6. No improvement in performance with practice. Thresholds for noise trials are plotted for the first ten sessions that were completed for subjects WG (circles) and CC (diamonds). Thresholds ranged from 2–4 degrees, but no significant improvement in performance over time is noted.

subject, or combined across subjects ($r < 0.2$; $p > 0.5$). A similar result was noted when tested with respect to the tonal stimuli. Thus, we conclude that experience had a minimal influence on the ability of these subjects to perform these tasks.

II. EXPERIMENT II: ABSOLUTE LOCALIZATION MEASURE

A. Methods

1. Psychophysical task

This task used the same behavioral apparatus and acoustic stimuli as the relative localization task (200-ms duration; 5-ms linear rise/fall; 30 ± 2 dB *re*: threshold; 1 kHz, 4 kHz, and Gaussian noise). The headband that the subjects wore in this task allowed horizontal head movements. The head position was measured by the current induced in a search coil located on the headband by its position in the magnetic field using standard oculomotor technology (Robinson, 1972). Subjects were signaled to orient their head at the zero position (± 1 degree) by a blinking LED (Fig. 7). When this position was attained, the LED remained on continuously. One to three seconds later a single 200-ms stimulus was presented from any one of eight different speakers spanning a region of 56 degrees. In all sessions, at least one speaker location was at the midline. Subjects were required to move their head to the location they perceived the stimulus to originate from, and to maintain that position until the midline LED began to blink again (2 s from stimulus offset). All subjects consistently refrained from making returning head movements before the midline LED began to blink, which signaled the subject to reorient their head toward the midline.

Each session consisted of a single stimulus (noise, 1 kHz, or 4 kHz tone) with 21 trials for each of eight different locations (168 trials/session). For noise stimuli, a different set of eight locations were used across sessions, so that subjects were tested at all 15 locations. Subjects were not given feedback as to the accuracy of their head movements during

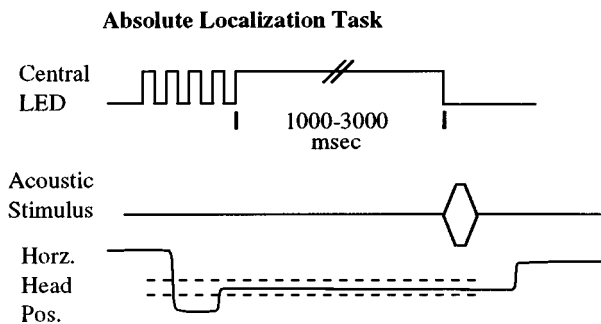


FIG. 7. Schematic of the absolute localization task. Subjects were requested to orient their head to a central flashing LED. Accomplishing this to within ± 1 degree was indicated by the LED remaining continuously illuminated. A single stimulus was then presented from 1 of the 15 speakers in front of them. The subjects were instructed to turn their head to orient to the location in space that they thought the sound came from. Dashed line: electronic head position window at ± 1 degree of the midline.

the course of the session. In addition, no subjects indicated that they could visually perceive any part of the speaker array.

In order to determine the accuracy in which human subjects can orient their head to targets in general, two types of light trials were also introduced. In a “remembered targets” condition, a visual stimulus (LED) was blinked on for 200 ms in a manner identical to the presentation of the acoustic stimulus at one of four possible locations along the array. Subjects were instructed to orient their head to these stimuli, which were always extinguished prior to the onset of the head movement. In the “visible target” condition, a LED was turned on and remained on continuously for 2200 ms, again at one of four different possible locations.

2. Data analysis

Head positions were determined by the average head location measured 1950–2000 ms after the offset of the S2 stimulus (50 ms total). Inspection of the analog head movements showed that this time period was well after any minor adjustments had been made by the subjects after the initiation of the head movement (head movement equivalent to a corrective saccade) and the averaging procedure eliminated the small amount of noise from the signal.

B. Results

A representative data set for a single subject using noise stimuli is shown in Fig. 8 (CK). In this figure, the narrow vertical lines represent the final head position of a single trial. Trials for each speaker location were pooled over five sessions and plotted together. The responses for each speaker location are shown across a single row of thin lines, with the actual target location shown as the thin rectangle in each row. Targets located progressively toward the right are shown progressively offset in the y axis for clarity, but the presentation of the stimulus at each location was randomly interleaved during each session. Data were obtained at 15 different speaker locations from -8 (bottom) to $+48$ degrees (top) in 4-degree increments. What is most obvious

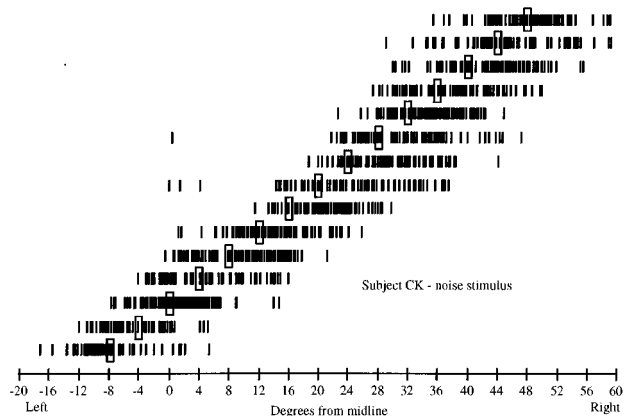


FIG. 8. Absolute localization of noise stimuli. All sessions pooled for subject CK in which the Gaussian noise stimulus was presented. Speakers were separated by 8 degrees in each session, with one speaker always located at the midline. Each small vertical line represents the final head position (estimate) of a single trial. Open rectangles show the location of the target. Each target is represented across a single row, with the rows offset vertically for clarity. The target at -8 degree (left) is shown as the bottom row, while the target at $+48$ degree (right) is the top most row.

from this figure is that, in spite of the fact that this subject had a relative localization threshold of 2–4 degrees for noise stimuli, the subject nonetheless made errors of the actual speaker location by up to 8–10 degrees on any given trial.

These data are representative of all subjects. Each progressively shifted their estimate toward the right for targets located toward the right. It is also evident that, although individual trials could vary over a fairly broad range, it was extremely rare for an estimate to cross into the inappropriate hemifield once the stimulus was beyond about 8 degrees from the midline. Finally, each subject tended to both overshoot and undershoot different target locations.

The absolute localization ability for the tonal stimuli is shown in Fig. 9. These data are presented in a similar manner to the noise data of Fig. 8 for the same subject (CK). In this figure, the longer rectangles show the estimates for all trials using a 1-kHz tone stimulus, whereas the shorter rectangles show the estimates of the 4-kHz tone stimuli. This subject was typical of all subjects tested, with the most salient observation that the tonal stimuli are much more poorly localized than the noise stimuli.

To quantify these data, the accuracy of the estimates was measured as the average error (average estimate-target location). All subjects showed similar errors and the mean across subjects is plotted for each target location and stimulus in Fig. 10(A). The most common error for the tonal stimuli was for the subjects to underestimate the actual target location, indicated by negative values of the mean error. Errors for noise stimuli were much smaller than those for tonal stimuli, with both overshoots and undershoots making the error very near zero. This difference between stimuli was statistically significant (noise versus 1 or 4 kHz: ANOVA, $p < 0.05$). The error for localizing the 4-kHz tonal stimuli were greater than for the 1-kHz stimuli, although this difference did not reach statistical significance ($p = 0.071$). Regression analysis between the error and the speaker eccentricity also did not show a statistically significant correlation ($r = 0.58, 0.06$, and

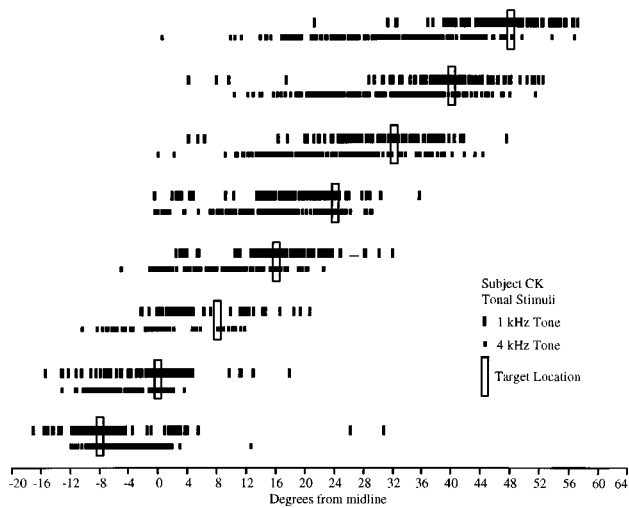


FIG. 9. Absolute localization of tonal stimuli by subject CK. Each row shows the estimates for a single target location. Long rectangles are the single trial estimates when the 1-kHz tone stimulus was presented (top set of lines for each row), the shorter rectangles are the single trial estimates when the 4-kHz tone stimulus was presented. Conventions as in Fig. 8.

0.02 for noise, 1 kHz, and 4 kHz, respectively; $p > 0.05$ for all cases). We take this to indicate that there is not a significant degradation in localization accuracy as a function of eccentricity over this range in frontal space.

The precision of the estimates was measured as the standard deviation of estimates for a given stimulus type and target location [Fig. 10(B)]. There was a statistically significant difference between all three stimulus types, with the noise stimulus having the lowest standard deviation and the 4-kHz tone stimulus having the greatest standard deviation (ANOVA; $p < 0.01$). An interesting observation is that the standard deviation of the estimates to noise stimuli was approximately 5 degrees, even though these same subjects routinely made correct responses to 4-degree separations in the relative localization task. Similarly, the range increased to almost 10 degrees for 1-kHz tonal stimuli, and were often even greater for 4-kHz tonal stimuli.

One apparent trend from the functions of Fig. 10(B) is that the standard deviation of the range of estimates increased with increasing eccentricity of the stimulus. This was tested quantitatively by performing a regression analysis between the standard deviation and the degrees of eccentricity of the target. All three stimuli showed a statistically significant correlation, with r values of 0.851, 0.942 and 0.903 for noise, 1-kHz tone, and 4-kHz tone, respectively. The slopes of the regression line were quite shallow, 0.066, 0.105, and 0.129 for noise, 1-kHz tone, and 4-kHz tone, respectively. These slopes indicate that even though there is a correlation between these two measures, the standard deviation of the estimates increases only approximately 1 degree for every 10 degrees that the target is moved away from the midline across the frontal region of space.

One possible explanation why the range of estimates and the accuracy were much worse than would be expected based on the relative localization results, particularly for that of the noise stimuli, is that these subjects were simply not very accurate or precise at moving their heads in the dark to the

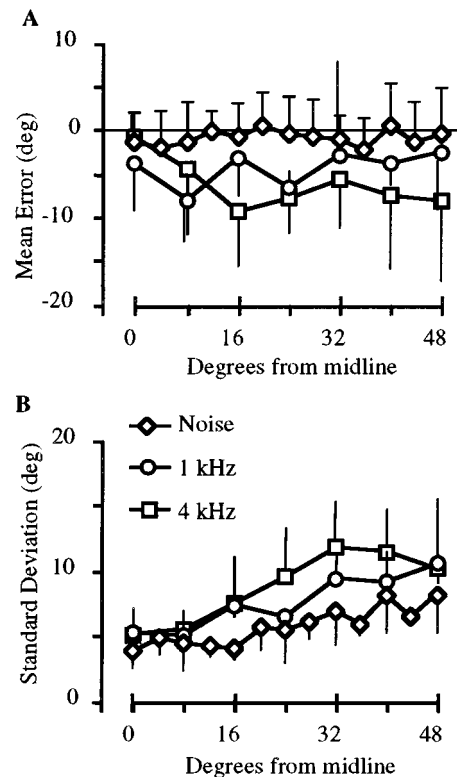


FIG. 10. Averaged errors and standard deviations across subjects. Part (A) shows the average error for noise (diamonds) 1-kHz tones (circles) and 4-kHz tones (squares) measured across subjects and target locations. Points under the dashed line represent underestimates of the targets. Thin lines indicate standard deviations. Part (B) shows the standard deviations of the estimates averaged across subjects for each of the three stimuli at each target location. Thin lines show the standard deviation of this measure.

appropriate location. It may be that many of the errors described for the noise stimuli are due to errors in head orientation, although this would still mean that the localization of tonal stimuli is less accurate and precise than for the noise stimuli. To test this possibility, we also measured head movements to continuous (2200-ms duration) and flashed (200 ms) visual targets. The averaged errors pooled across at least eight sessions for these trials is shown for all subjects in Table I. All subjects were able to localize the continuous visual stimuli to within approximately 1 degree. Only one of the four subjects was statistically significantly more accurate localizing the continuous visual stimuli compared to the flashed visual stimuli (two-tailed t test; $p < 0.001$). For all subjects, the error during both brief and continuous visual stimuli was statistically significantly smaller than for the same spatial locations using noise stimuli (ANOVA, $p < 0.001$ for all subjects).

Given that we were pooling responses across sessions for each of the subjects, and that it was possible that the subjects could be showing an improvement in performance over the course of these sessions, we compared the mean error calculated across stimulus locations from session to session. As subjects CK and AS were already highly experienced at this and similar psychophysical tasks, we reasoned that any training effects would have long since been established, so the analysis was confined to subjects CC and WG

TABLE I. Errors of visual trials. The means and standard deviations of the difference between the estimate and the actual target location for stimuli pooled across at least eight sessions for two classes of visual stimuli. The LED stimuli remained illuminated throughout the duration of the trial (2200 ms, column 2) or were presented for the same duration as the acoustic stimuli (200 ms, column 3). The fourth column shows the p value comparing the two visual stimuli for each individual subject (two-tailed t test). The fifth column compares the errors for the 200-ms visual stimulus to the errors of the 200-ms noise stimulus (two-tailed t test).

Subject	2200 ms	200 ms	Visual p value	ns vs vis p value
WG	-0.11 ± 2.30	0.22 ± 4.23	$p=0.112$	$p<0.001$
CC	1.15 ± 3.00	1.15 ± 5.56	$p=0.101$	$p<0.001$
CK	-0.04 ± 3.99	-0.03 ± 3.16	$p=0.223$	$p<0.001$
AS	-0.80 ± 3.70	0.86 ± 3.51	$p<0.001$	$p<0.001$

as they had just completed the relative localization task, and were performing this type of task for the first time. There was not a measurable learning effect for either subject over the first six sessions (repeated measures ANOVA; $p>0.10$), and no statistically significant difference was noted between any particular speaker location or pooled across speaker locations between the first and sixth session for either subject (two-tailed t test; $p>0.05$). Thus, as in the relative localization task, there was no improvement in performance across sessions for these subjects performing the absolute localization task.

A second consideration is that we used the same intensities as those in the relative localization task, which varied over a 4-dB range. It is possible that, due to the orientation of the speakers, and the random probabilities that different intensities were used, that some bias resulted. To test this possibility, one subject (AS) performed the noise absolute localization task at five different base intensity levels, again with each stimulus randomly presented ± 2 dB for each base intensity. A comparison of both the mean error and the standard deviation showed a statistically significant effect only for stimuli presented 10 ± 2 dB threshold, while both measures remained constant for intensities of 20, 30, 40, and 45 ± 2 dB *re*: threshold across locations (repeated measures ANOVA; $p>0.10$). These results indicate that there is essentially no effect of intensity over this range on either of these localization measures.

The final potential source of artifact that we considered was that subjects might make a mental map of the speaker array, and would therefore create a response bias for particular locations in space. This would ultimately result in making the absolute localization task a multiple-alternative forced choice task. Given that most subjects were tested on well over 3500 trials over the course of the study, it is possible that such position biases would occur. For each subject we pooled all sessions and determined the percentage of total trials wherein responses fell within 0.5-degree bins across the full range of estimates. An example from subject WG is shown in Fig. 11. This plot shows a clear response bias at around 8 degrees to the left and for the midline, with very few estimates located to the immediate left and right of the midline. The overall shape of this curve was consistent across subjects, with only the particular locations for each peak and trough that varied by 2–3 degrees. The peak at the

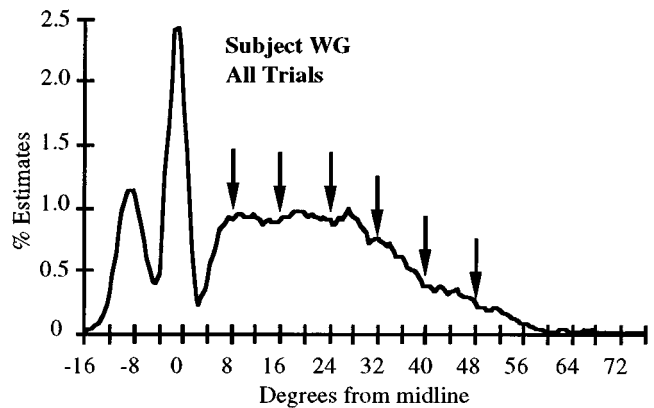


FIG. 11. Cumulative estimates pooled across sessions. All estimates recorded throughout all session were pooled (3882 total trials) for subject WG and plotted as a percentage of total trials in 0.5-degree bins. The general form of this curve, with two distinct peaks followed by a long period in which the percentage of estimates were similar and then ultimately trailing off to zero with a shallow slope, was observed in all subjects. Arrows indicate the location of targets used for both tone and noise stimuli at eight or more degrees to the right of the midline.

midline reflects the poor localization for tonal stimuli presented near the midline. Often the subjects did not perceive these tonal stimuli to originate 8 degrees from the midline, so made no head movement, resulting in the large percentage of estimates at this location (see also Fig. 9). The peak of responses to the left of the midline also probably reflects the subject's knowledge that there was only one possible leftward location during tonal sessions, and only two possible leftward locations for noise sessions. Thus, when the sound was perceived to originate from the left of the midline, most subjects made a head movement to one of the two possible locations. The low percent of estimates immediately left and right of the midline also reflects the subject's knowledge that the next possible location was a few degrees from the starting position, so never made head movements of 1–2 degrees. What we were most concerned with, however, is the possibility that the subjects had response biases at greater eccentricities to the right, where most of the stimuli were presented. For all subjects, this region was relatively flat, and there was no indication that particular locations were selected more often than any others. We also performed a fast Fourier transform over the region beyond 8 degrees for all subjects, and there was no indication of a periodicity of these estimates that would reflect a mental "map" of the speaker array in any subject.

III. COMPARISON BETWEEN RELATIVE AND ABSOLUTE LOCALIZATION PARADIGMS

The main goal of this study was to determine the relationship between the relative and absolute localization paradigms, which seemed to differ significantly across stimulus types. One of the most straightforward comparisons is between the region comprising \pm one standard deviation of the range of estimates during the absolute localization task to an equivalent measure for the same target location in the relative localization task. For the relative localization measure

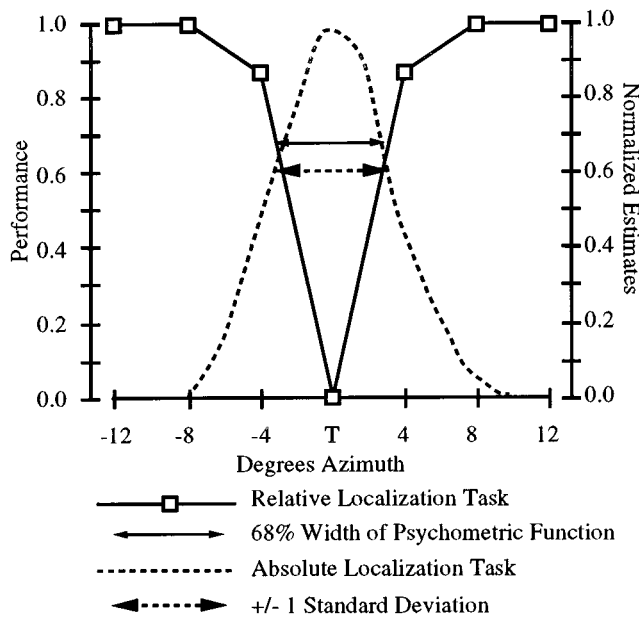


FIG. 12. Method of comparing the relative localization psychometric functions to the distribution of estimates in the absolute localization task: The psychometric function for a noise stimulus presented from a S1 speaker location at 16 degrees in the relative localization task in subject CC (open squares) is plotted with the normalized range of estimates (dashed line) for the same speaker location in the same subject. The normalized estimates were taken as a percentage of estimates in 0.5-degree bins and normalized to the peak. This distribution was shifted to be aligned with the psychometric function. The arrows show the range in degrees for the 0.68 bandwidth of the psychometric function (solid thin arrow) and the (+) and (-) 1 standard deviation for the range of estimates in the absolute localization task (thick dashed arrow). These values were used in the regression analysis shown in Fig. 13(A).

we chose the width of the psychometric functions at 0.68 performance (Fig. 12). This width was chosen as it reflects the area under a Gaussian at \pm one standard deviation about the mean. It is reasonable to assume that the neuronal information of stimulus location provided to these subjects is in the form of a Gaussian (Green and Swets, 1966; Hartmann, 1989), and the distribution of estimates in the absolute localization task were largely Gaussian in shape (Fig. 12—dashed line). For all psychometric functions in which this width could be measured, the distance between the 0.68 performance values when the S2 stimulus moved temporally and nasally was calculated. This procedure limited the sample to the S1 speaker locations between 8 and 32 degrees for tonal stimuli and between 0 and 40–44 degrees for noise stimuli, as a 0.68 performance value could not be determined for speakers beyond this range both nasally and temporally. These values were then plotted against the distance of two standard deviations for the range of estimates for that same S1 speaker location. The results are shown in Fig. 13(A), combining both tonal and noise stimuli and pooled across the three subjects that completed both tasks for all stimuli (CK, CC, and WG). The dashed line is drawn through the origin with a slope of 1.0 and represents perfect correlation. This scatter plots show a good correlation between these two values that is statistically significant ($r=0.813$; $p<0.001$), with the width of the relative localization psychometric functions

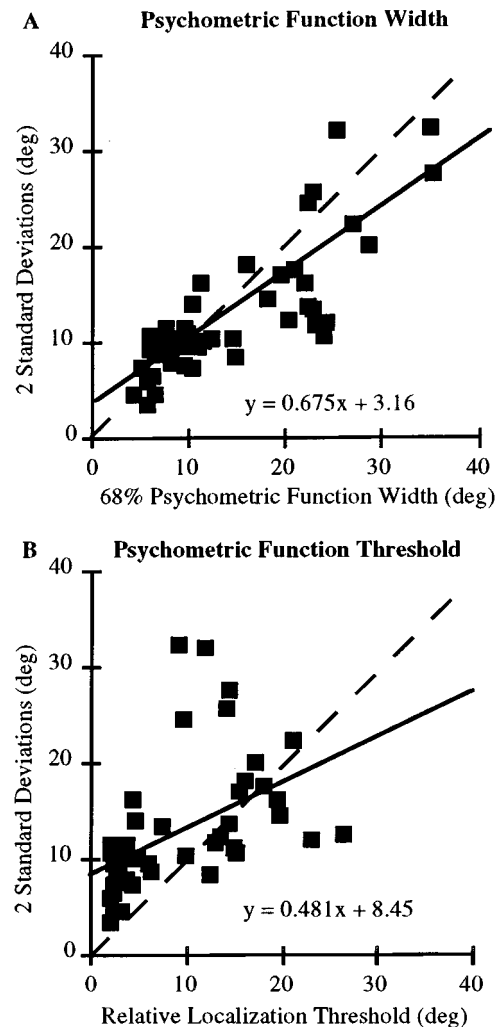


FIG. 13. Correlation between relative and absolute localization data. (A) The distance in degrees across the psychometric function at the 0.68 performance level (x axis) was plotted against two times the standard deviation of estimates for the same target location in the absolute localization task (y axis). Data were pooled across subjects and stimuli ($r=0.752$; $p<0.001$). (B) The same behavioral data as in (A) except the threshold (0.5 performance) for the relative localization task is plotted against the bandwidth measure of the absolute localization task ($r=0.501$; $p<0.001$).

somewhat greater than would be predicted by the standard deviation of the range of estimates in the absolute localization task, resulting in the slope of the regression line of 0.674.

A second comparison that we made was between this standard deviation measure from the absolute localization task to the relative localization thresholds measured for the same subject and stimulus condition [Fig. 13(B)]. In this analysis, the regression coefficient was smaller (0.501) but was nonetheless significant ($p<0.001$). The slope of this regression line was also much lower (0.481) and, as can be seen from the regression plot, the relative localization thresholds were commonly much lower than would be predicted by the standard deviation measure of the absolute localization task, indicated by most points falling above the line showing perfect correlation. Thus, even though the range of estimates for a particular location in absolute space is several-fold

greater than would be predicted by the relative localization threshold, the width of the relative localization psychometric function is well within the range of the estimates of target locations measured in the absolute localization task across both acoustic stimuli and individual subjects.

IV. DISCUSSION

Our relative localization results from noise stimuli are in general agreement with previous studies using a minimum audible angle procedure in normal human listeners employing noise or click stimuli (Perrott and Saberi, 1990; Chandler and Grantham, 1992; Perrott *et al.*, 1993) with similar thresholds and no apparent difference in localization thresholds as a function of distance from the midline over this limited range (Musicant and Butler, 1984; Perrott *et al.*, 1993). The relative localization thresholds obtained in this study for the tonal stimuli are either in agreement (e.g., 1 kHz, Terhune, 1985) or slightly larger than those described in previous studies (e.g., Chandler and Grantham, 1992; Molino, 1974; 4 kHz; Terhune, 1985). Differences between these studies are most likely due to differences in the intensity and duration of the acoustic stimuli, the randomly interleaved trials, and potentially the elimination of absolute loudness cues used in this paradigm.

The results of this report are also consistent with those of others using an absolute localization paradigm (Stevens and Newman, 1936; Newton, 1983; Oldfield and Parker, 1984; Butler, 1986; Perrott *et al.*, 1987; Wightman and Kistler, 1989; Makous and Middlebrooks, 1990; Middlebrooks, 1992; Butler and Musicant, 1993; Wenzel *et al.*, 1993; Good and Gilkey, 1996), particularly with respect to the 1-kHz tone being more easily localized than the 4-kHz tones (Stevens and Newman, 1936). In the most similar studies employing head movements to measure localization ability, subjects showed errors and standard deviations similar to those of this study for noise stimuli (Wightman and Kistler, 1989; Makous and Middlebrooks, 1990). In a similar study using narrow-band stimuli ($\frac{1}{6}$ octave), subjects showed a greater range of estimates and less accuracy (Middlebrooks, 1992) compared to noise stimuli, similar to the results of our subjects when comparing tonal to noise stimuli. The performance for the 4-kHz tones was also in general agreement with previous studies (Perrott *et al.*, 1987) although for most subjects the range of estimates for the 4-kHz tones was greater than previous studies using band-passed stimuli centered at 4 kHz (Abel *et al.*, 1978). This discrepancy is most likely due to the increased spectral content and longer durations of their stimuli compared to the stimuli used in this study.

In the experiments reported here, three different acoustic stimuli were used: noise, 1-kHz tones and 4-kHz tones. We chose these three stimuli because the goal of the study was to directly compare the ability to determine a change in the location of a stimulus to the ability to determine the absolute location of the stimulus. The subjects showed very different localization ability for these three different acoustical stimuli, which allowed for a comparison between these two behavioral measures across a broad range of performances. We obtained a good correlation between the width of the

psychometric functions measured in the relative localization task and the standard deviations of the absolute localization task. Most points of comparison fell near a line through the origin with a slope of 1.0. Those points that fell significantly off the line were due to a larger width of the psychometric function from the relative localization task than would be expected from the standard deviation measured in the absolute localization task. This is probably due to two reasons, the first being that our measure of relative localization ability may have underestimated the subject's true localization abilities. This would be expected from the low false-positive rates, which may be reflecting the subject's bias toward more miss responses. The second is that the relative localization measurements were taken based on 15 trials for each stimulus location, and therefore were more influenced by the normal variance in each subject's performance. The absolute localization measurements were based on at least 105 trials for each speaker location for each stimulus, and were presumably less affected by this normal variance.

We considered the possibility that the subjects were able to use nonspatial cues, such as differences in the speaker transformation functions, to perform the relative localization task, but feel that this is very unlikely for several reasons. First, the thresholds we obtained were similar to those using a single speaker, as noted above. Second, these stimuli were based on each individual subject's threshold for that stimulus at that location, and all speakers were subjectively matched in intensity by each subject before the experiments were initiated. Third, we introduced a variance in the intensity of each stimulus, thereby making each stimulus sound slightly differently and forcing the subject's to concentrate on the spatial location of the stimuli during the task. Last, the control experiments described in Figs. 4 and 5 demonstrate that nonspatial cues provide very little information, if any, for the subjects to perform the task. These four factors taken together indicate that the subjects were using location cues almost exclusively in performing the relative localization task to the tonal and noise stimuli.

One interesting finding is that there was essentially no learning effect over the course of the experiment for either the relative localization task or the absolute localization task. This is a bit curious in that improvements in performance with training is a hallmark of most psychophysical paradigms (see Recanzone *et al.*, 1992a) and can be correlated with changes in the cortical representations of the relevant stimulus parameters (Recanzone *et al.*, 1992b, c, 1993; Nudo *et al.*, 1996). In the absolute localization task, subjects were not given any feedback as to either the actual speaker location or to the orientation of their head. It is therefore not surprising that there was no demonstrable improvement, as the subjects would not have any information about the nature of their error that they could use to adjust their performance. In the relative localization task, however, subjects were given feedback on a trial-by-trial basis. Subjects were aware of miss trials as the stimuli stopped being presented even though the subject never released the lever. Subjects were also indicated of false-positive trials by a longer delay between releasing the lever and the initiation of the next trial. Even with this feedback, the subjects did not show any im-

provement in performance over time. In data shown for one subject, significant improvement in performance at a minimum audible angle task was demonstrated over five blocks of 500 trials using an 8-kHz tone stimulus (Terhune, 1985). A likely explanation for the lack of any training effect in the relative localization task of this study is that a different starting speaker was used for each session (240 trials), so any perceptual gains that could have been acquired on the preceding session may not transfer across acoustic space. A similar lack of transference after a single session where visual stimuli are presented in a different location in the visual field have been noted in human psychophysical studies (e.g., Fahle *et al.*, 1995). It remains to be seen if continued practice at the same locations of acoustic space would generate an improvement in performance.

The most interesting finding of this study is the close correspondence between the widths of the psychometric functions in the relative localization task and the spread of the estimates in the absolute localization task. The fact that this correlation holds up for the three different acoustic stimuli, and the three subjects tested, which all had idiosyncratic localization ability, shows this relationship to be robust. If one assumes that the neuronal representation of these different speaker locations is Gaussian across a population of neurons, and that adjacent locations in space are represented by adjacent and overlapping populations of neurons, then signal detection theory predicts broader absolute localization ability than minimum audible angle thresholds, but similar widths of the two functions (Green and Swets, 1966), and supports the hypothesis that relative localization tasks, such as the minimum audible angle task, are reflecting an absolute localization strategy (Hartmann, 1989).

The representation of acoustic space in the mammalian brain is currently poorly understood (Middlebrooks and Pettigrew, 1981; Imig *et al.*, 1990; Rajan *et al.*, 1990; Middlebrooks *et al.*, 1994; Brugge *et al.*, 1996). It seems clear that the auditory cortex is necessary to localize sounds in the contralateral hemisphere (Neff *et al.*, 1956; Heffner and Masterton, 1975; Heffner, 1978; Kavanagh and Kelly, 1987; Jenkins and Merzenich, 1984; Heffner and Heffner, 1990), yet the spatial selectivity of single neurons are very broad, with only a small subset of neurons with spatial selectivity on the order of 20–40 degrees (see references cited above and Eisenman, 1974; Benson *et al.*, 1981; Ahissar *et al.*, 1992). The results of this study indicate that the measures of the range of estimates in the absolute localization task are within a factor of 2 of the most spatially selective cortical neurons reported in the anesthetized cat and monkeys. Given the current interest in the cortical contributions to sound localization as well as to the cortical contributions to auditory perception in the primate in general (e.g., see Middlebrooks *et al.*, 1994; Clarey *et al.*, 1995; Wang *et al.*, 1995; Brugge *et al.*, 1996; Barone *et al.*, 1996; deCharms and Merzenich, 1996; Stricanne *et al.*, 1996; Rauschecker *et al.*, 1997), the finding that relative localization thresholds are a poor predictor of the absolute localization ability is very important. Any studies that attempt to directly relate the responses of cortical neurons to perception, for example by single neuron spatial selectivity, population responses, or temporal coding

schemes, must be careful in interpreting data based only on relative localization thresholds (i.e., minimum audible angle measurements).

V. SUMMARY

The experiments of this report describe the ability of normal human listeners to localize three different acoustic stimuli using two different behavioral paradigms. As was expected from previous, similar studies, subjects were better able to localize noise stimuli than tonal stimuli. This was true whether the subjects were tested on a relative localization task or an absolute localization task. Although it would initially appear that the ability to determine the absolute location of an acoustic stimulus was much worse than the ability to determine a change in the location of the same acoustic stimulus, these two psychophysical measures were in good agreement when the width of the psychometric function from the relative localization task was compared to the bandwidth of the range of estimates in the absolute localization task. These data indicate that the sound localization ability of normal human listeners is consistent with the spatial receptive field sizes of cortical neurons recorded in other species.

ACKNOWLEDGMENTS

The authors wish to thank M. Phan and P. Geiger for their insightful suggestions during the course of these experiments, and for reviewing previous versions of this manuscript along with M. Sutter, K. O'Connor, and W. Loftus. Funding provided by NIH Grant No. NIDCD DC0271-01A2, the Klingenstein Foundation, and the Sloan Foundation (all to GHR).

- Abel, S. M., Birt, B. D., and McLean, J. A. G. (1978). "Sound localization: value in localizing lesions of the auditory pathway," *J. Otolaryngol.* **7**, 132–140.
- Ahissar, M., Ahissar, E., Bergman, H., and Vaadia, E. (1992). "Encoding of sound-source location and movement: activity of single neurons and interactions between adjacent neurons in monkey auditory cortex," *J. Neurophysiol.* **67**, 203–215.
- Barone, P., Clarey, J. C., Irons, W. A., and Imig, T. J. (1996). "Cortical synthesis of azimuth-sensitive single-unit responses with nonmonotonic level tuning: a thalamocortical comparison in the cat," *J. Neurophysiol.* **75**, 1206–1220.
- Benson, D. A., Hienz, R. D., and Goldstein, Jr., M. H. (1981). "Single-unit activity in the auditory cortex of monkeys actively localizing sound sources: spatial tuning and behavioral dependency," *Brain Res.* **219**, 249–267.
- Brugge, J. F., Reale, R. A., and Hind, J. E. (1996). "The structure of spatial receptive fields of neurons in primary auditory cortex of the cat," *J. Neurosci.* **16**, 4420–4437.
- Butler, R. A. (1986). "The bandwidth effect on monaural and binaural localization," *Hearing Res.* **21**, 67–73.
- Butler, R. A., and Musicant, A. D. (1993). "Binaural localization: Influence of stimulus frequency and the linkage to covert peak areas," *Hearing Res.* **67**, 220–229.
- Chandler, D. W., and Grantham, D. W. (1992). "Minimum audible movement angle in the horizontal plane as a function of stimulus frequency and bandwidth, source azimuth, and velocity," *J. Acoust. Soc. Am.* **91**, 1624–1636.
- Clarey, J. C., Barone, P., Irons, W. A., Samson, F. K., and Imig, T. J. (1995). "Comparison of noise and tone azimuth tuning of neurons in cat primary auditory cortex and medial geniculate body," *J. Neurophysiol.* **74**, 961–980.

- deCharms, R. C., and Merzenich, M. M. (1996). "Primary cortical representation of sounds by the coordination of action-potential timing," *Nature* (London) **381**, 610–613.
- Eisenman, L. M. (1974). "Neural encoding of sound localization: an electrophysiological study in auditory cortex (AI) of the cat using free field stimuli," *Brain Res.* **75**, 203–214.
- Fahle, M., Edelman, S., and Poggio, T. (1995). "Fast perceptual learning in hyperacuity," *Vision Res.* **35**, 3003–3013.
- Good, M. D., and Gilkey, R. H. (1996). "Sound localization in noise: The effect of signal-to-noise ratio," *J. Acoust. Soc. Am.* **99**, 1108–1117.
- Green, D. M., and Swets, J. A. (1966). *Signal Detection Theory* (Wiley, New York).
- Hartmann, W. M. (1989). "On the minimum audible angle—a decision theory approach," *J. Acoust. Soc. Am.* **85**, 2031–2041.
- Heffner, H. (1978). "Effect of auditory cortex ablation on localization and discrimination of brief sounds," *J. Neurophysiol.* **41**, 963–976.
- Heffner, H. E., and Heffner, R. S. (1990). "Effect of bilateral auditory cortex lesions on sound localization in Japanese macaques," *J. Neurophysiol.* **64**, 915–931.
- Heffner, H., and Masterton, B. (1975). "Contribution of auditory cortex to sound localization in the monkey (*Macaca mulatta*)," *J. Neurophysiol.* **38**, 1340–1358.
- Imig, T. J., Irons, W. A., and Samson, F. R. (1990). "Single-unit selectivity to azimuthal direction and sound pressure level of noise bursts in cat high-frequency primary auditory cortex," *J. Neurophysiol.* **63**, 1448–1466.
- Jenkins, W. M., and Merzenich, M. M. (1984). "Role of cat primary auditory cortex for sound-localization behavior," *J. Neurophysiol.* **52**, 819–847.
- Kavanagh, G. L., and Kelly, J. B. (1987). "Contribution of auditory cortex to sound localization by the ferret (*Mustela putorius*)," *J. Neurophysiol.* **57**, 1746–1766.
- Makous, J. C., and Middlebrooks, J. C. (1990). "Two-dimensional sound localization by human listeners," *J. Acoust. Soc. Am.* **87**, 2188–2200.
- Middlebrooks, J. C. (1992). "Narrow-band sound localization related to external ear acoustics," *J. Acoust. Soc. Am.* **92**, 2607–2624.
- Middlebrooks, J. C., and Green, D. M. (1991). "Sound localization by human listeners," *Annu. Rev. Psychol.* **42**, 135–159.
- Middlebrooks, J. C., and Pettigrew, J. D. (1981). "Functional classes of neurons in primary auditory cortex of cat distinguished by sensitivity to sound location," *J. Neurosci.* **1**, 107–120.
- Middlebrooks, J. C., Clock, A. E., Xu, L., and Green, D. M. (1994). "A panoramic code for sound localization by cortical neurons," *Science* **264**, 842–844.
- Mills, A. (1958). "On the minimum audible angle," *J. Acoust. Soc. Am.* **30**, 237–246.
- Molino, J. A. (1974). "Psychophysical verification of predicted interaural differences in localizing distant sound sources," *J. Acoust. Soc. Am.* **55**, 139–147.
- Musicant, A. D., and Butler, R. A. (1984). "The influence of pinnae-based spectral cues on sound localization," *J. Acoust. Soc. Am.* **75**, 1195–1200.
- Neff, W. D., Fisher, J. F., Diamond, I. T., and Yela, M. (1956). "Role of auditory cortex in discrimination requiring localization of sound in space," *J. Neurophysiol.* **19**, 500–512.
- Newton, V. E. (1983). "Sound localization in children with a severe unilateral hearing loss," *Audiology* **22**, 189–198.
- Nudo, R. J., Milliken, G. W., Jenkins, W. M., and Merzenich, M. M. (1996). "Use-dependent alterations of movement representations in primary motor cortex of adult squirrel monkeys," *J. Neurosci.* **16**, 785–807.
- Oldfield, S. R., and Parker, S. P. A. (1984). "Acuity of sound localization: a topography of auditory space. I. Normal hearing conditions," *Perception* **13**, 581–600.
- Perrott, D. R. (1984). "Concurrent minimum audible angle: A re-examination of the concept of auditory spatial acuity," *J. Acoust. Soc. Am.* **75**, 1201–1206.
- Perrott, D. R., and Saberi, K. (1990). "Minimum audible angle thresholds for sources varying in both elevation and azimuth," *J. Acoust. Soc. Am.* **87**, 1728–1731.
- Perrott, D. R., Ambarsoom, H., and Tucker, J. (1987). "Changes in head position as a measure of auditory localization performance: Auditory psychomotor coordination under monaural and binaural listening conditions," *J. Acoust. Soc. Am.* **82**, 1637–1645.
- Perrott, D. R., Constantino, B., and Cisneros, J. (1993). "Auditory and visual localization performance in a sequential discrimination task," *J. Acoust. Soc. Am.* **93**, 2134–2138.
- Rajan, R., Aitkin, L. M., Irvine, D. R. F., and McKay, J. (1990). "Azimuthal sensitivity of neurons in primary auditory cortex of cats. I. Types of sensitivity and the effects of variations in stimulus parameters," *J. Neurophysiol.* **64**, 872–887.
- Rauschecker, J. P., Tian, B., Pons, T., and Mishkin, M. (1997). "Serial and parallel processing in rhesus monkey auditory cortex," *J. Comp. Neurol.* **382**, 89–103.
- Recanzone, G. H., Merzenich, M. M., and Schreiner, C. E. (1992c). "Changes in the distributed temporal response properties of SI cortical neurons reflect improvements in performance on a temporally-based tactile discrimination task," *J. Neurophysiol.* **67**, 1071–1091.
- Recanzone, G. H., Merzenich, M. M., and Schreiner, C. E. (1993). "Plasticity in the frequency representation of primary auditory cortex following discrimination training in adult owl monkeys," *J. Neurosci.* **13**, 87–103.
- Recanzone, G. H., Jenkins, W. M., Hradek, G. T., and Merzenich, M. M. (1991). "A behavioral frequency discrimination paradigm for use in adult primates," *Behav. Res. Methods Instrum. Comput.* **23**, 357–369.
- Recanzone, G. H., Jenkins, W. M., Hradek, G. T., and Merzenich, M. M. (1992a). "Progressive improvement in discriminative abilities in adult owl monkeys performing a tactile frequency discrimination task," *J. Neurophysiol.* **67**, 1015–1030.
- Recanzone, G. H., Merzenich, M. M., Jenkins, W. M., Grajski, K. A., and Dinse, H. A. (1992b). "Topographic reorganization of the hand representation in cortical area 3b of owl monkeys trained in a frequency discrimination task," *J. Neurophysiol.* **67**, 1031–1056.
- Robinson, D. A. (1972). "Eye movements evoked by collicular stimulation in the alert monkey," *Vision Res.* **12**, 1795–1808.
- Stevens, S. S., and Newman, E. B. (1936). "The localization of actual sources of sound," *Am. J. Psychol.* **48**, 297–306.
- Stricanne, B., Andersen, R. A., and Mazzoni, P. (1996). "Eye-centered, head-centered, and intermediate coding of remembered sound locations in area LIP," *J. Neurophysiol.* **6**, 2071–2076.
- Terhune, J. M. (1985). "Localization of pure tones and click trains by untrained humans," *Scand. Audiol.* **14**, 125–131.
- Wang, X., Merzenich, M. M., Beitel, R., and Schreiner, C. E. (1995). "Representation of a species-specific vocalization in the primary auditory cortex of the common marmoset: temporal and spectral characteristics," *J. Neurophysiol.* **74**, 2685–2706.
- Wenzel, E. M., Arruda, M., Kistler, D. J., and Wightman, F. L. (1993). "Localization using nonindividualized head-related transfer functions," *J. Acoust. Soc. Am.* **94**, 111–123.
- Wightman, F. L., and Kistler, D. J. (1989). "Headphone simulation of free-field listening. II: Psychophysical validation," *J. Acoust. Soc. Am.* **85**, 868–878.

Consonant–vowel intensity ratios for maximizing consonant recognition by hearing-impaired listeners

Elizabeth Kennedy,^{a)} Harry Levitt, Arlene C. Neuman, and Mark Weiss

Center for Research in Speech and Hearing Sciences, City University of New York, Graduate School and University Center, 33 West 42nd Street, New York, New York 10036

(Received 9 December 1996; accepted for publication 5 September 1997)

The effect of adjusting the consonant–vowel (C–V) intensity ratio on consonant recognition in 18 subjects with sensorineural hearing impairment was investigated. C–V intensity ratios in a set of 48 vowel–consonant nonsense syllables were adjusted in steps of 3–6 dB depending on the subject's dynamic range of hearing. An increase in consonant intensity is referred to here as consonant enhancement (CE). The value of CE producing the highest consonant recognition score (CR_{max}) is defined as CE_{max}. Both CE_{max} and CR_{max} were determined for each subject for each of the 48 nonsense syllables. Consonant type was found to have a highly significant effect on CR_{max}, the gain in consonant recognition, and CE_{max}. The effect of vowel environment was also significant, but of much smaller magnitude. Audiogram configuration was found to have a small effect and was only significant for CR_{max}. The results of the study also showed that individualized adjustment of the C–V intensity ratio for each subject and consonant–vowel combination can produce substantial improvements in consonant recognition. These data can be used to estimate upper bounds of performance that, in principle, can be obtained by appropriate adjustment of the C–V intensity ratio.

© 1998 Acoustical Society of America. [S0001-4966(98)02502-8]

PACS numbers: 43.66.Sr, 43.66.Ts, 43.71.Ky [JWH]

INTRODUCTION

A major problem limiting the efficacy of acoustic amplification systems for sensorineural hearing impairments is that the dynamic range of hearing is reduced significantly. Unlike a conductive hearing impairment in which both the threshold of hearing and the loudness discomfort level are elevated by roughly equal amounts, a characteristic of sensorineural impairment is that, in addition to an increase in hearing threshold, loudness discomfort level is roughly the same as that for normal-hearing individuals. Since the vast majority of people who are candidates for acoustic amplification have a sensorineural hearing loss, this problem is one of considerable importance.

One approach to the problem is to reduce the dynamic range of the speech signal so as to match the dynamic range of the impaired ear. In order to do so, it is important to take into account the temporal structure of speech. Temporal fluctuations in speech level can be subdivided into two broad categories—slow variations in level (on the order of seconds) associated with changes in overall voice level, and relatively rapid changes in level (on the order of tens of milliseconds) associated with the differences in level among the various sounds of speech (e.g., vowels versus consonants).

The use of compression amplification with relatively long time constants (>0.5 s), often referred to as automatic volume control (AVC), has rarely been used in commercial hearing aids. Theoretically, this type of amplification should allow good speech intelligibility and quality for a large range of input levels. Two recent studies have demonstrated that

this form of compression can improve both the intelligibility (Peterson *et al.*, 1990) and quality (Neuman *et al.*, 1994) of amplified speech for hearing-impaired listeners with small dynamic ranges.

Compression amplification using relatively short time constants (less than 150 ms) can be subdivided into two basic forms, *compression limiting* and *syllabic compression*. Compression limiting is characterized by a high threshold of compression and a high compression ratio; i.e., substantial compression occurs only when the input signal is relatively intense. This form of compression effectively protects the listener from excessive amplification by limiting the output of the hearing aid whenever the input exceeds a critical level (the compression threshold). Compression limiting produces considerably less distortion than peak clipping and results in better speech intelligibility for high input levels (e.g., Davis *et al.*, 1947).

Syllabic compression, in contrast to compression limiting, has a low compression threshold and a relatively low compression ratio (usually on the order of 1.5:1 or 2:1). This type of compression is attractive from a theoretical perspective in that, in principle, weak speech sounds can be amplified well above the threshold of hearing while relatively intense speech sounds are not amplified above the listeners' loudness discomfort level. In practice, however, syllabic compression has not provided the anticipated improvements in speech understanding (Braidia *et al.*, 1979).

Some success has been achieved recently using two-channel syllabic compression. In this type of hearing aid, separate compression amplifiers are used for low frequencies and high frequencies. Several recent studies have demonstrated that this type of hearing aid yields lower speech-reception thresholds (as specified in terms of signal-to-noise

^{a)}Present address: Temple University, Philadelphia, PA 19122.

ratio) than a linear hearing aid with appropriate frequency shaping. In the system evaluated by Moore (1987), for example, improvements were on the order of a 2–3 dB increase in speech-to-noise ratio.

In a recent review of sensory aids for hearing impairment, it was noted that signal processing techniques that take the acoustic–phonetic structure of speech into account promise to be more effective in improving intelligibility than non-phonetically based methods of signal processing, provided that the relevant speech features are extracted reliably (Levitt, 1991). None of the conventional forms of amplitude compression is phonetically based. A form of signal processing which is phonetically based and which holds some promise for improving intelligibility is that of adjusting the ratio of consonant intensity to vowel intensity (C–V intensity ratio). This technique is also an effective means of reducing the dynamic range of the speech signal.

Several studies have demonstrated the relationship between C–V intensity ratio and speech intelligibility. House *et al.* (1965), in their development of the Modified Rhyme Test, made recordings of two talkers. Evaluations with these recordings revealed that the test scores for the two talkers differed significantly. The differences in test score were found to be approximately equivalent to a 3-dB shift in speech-to-noise ratio. An analysis of the recorded utterances showed that, although the vowels for both speakers were approximately equal in level, consonant levels for the less intelligible speaker were 2–4 dB lower than those for the more intelligible speaker (Hecker, 1974).

In making these recordings, a Volume Unit (VU) Meter was used to match the speech levels of the two talkers. Since the VU meter responds primarily to the relatively powerful low-frequency components of speech, this method of equating speech levels should result in the vowel sounds being approximately equal in level, as was observed. The measured levels for the consonantal sounds thus indicated that the C–V intensity ratio was lower for the less intelligible speaker. On the basis of these observations, House hypothesized that the difference in intelligibility between the two speakers was a result of the difference in C–V intensity ratio. House's hypothesis led to a series of studies investigating the relationship between C–V intensity ratio and intelligibility. Williams *et al.* (1966) obtained recordings of the Modified Rhyme Test for eight talkers for whom the C–V intensity ratio for the /s/ consonant covered a large range. Speaker intelligibility was then measured. The data showed a significant correlation between final /s/-vowel intensity ratio and intelligibility. Additional consonant–vowel intensity ratios were measured for six voiceless consonants for two highly intelligible speakers and two less intelligible speakers. The more intelligible speakers were found to have higher C–V intensity ratios than the less intelligible speakers.

Similarly, Salmon (1970) recorded 20 male speakers on Griffith's (1967) Simplified Diagnostic Articulation Test. The test was administered under two conditions of distortion and C–V intensity ratios were measured for the four most intelligible speakers and the four least intelligible speakers. The mean C–V intensity ratio for the most intelligible speak-

ers was just over 6 dB higher than for the least intelligible speakers (–12.5 dB vs –18.9 dB).

Picheny *et al.* (1985, 1986) obtained recordings of “clear speech,” i.e., speech produced so as to be more intelligible for hearing-impaired listeners. They found an increase in the C–V intensity ratio with increased intelligibility, although this was not the only factor linked to increased intelligibility (other factors included more precise articulation and a slower rate of speech production).

Not all studies have shown a correlation between intelligibility and C–V intensity ratio in natural speech. For example, Weiss (1968) recorded the Modified Rhyme Test using 12 different talkers. Intelligibility scores were obtained at two signal-to-noise ratios. Average C–V intensity ratios were determined for each speaker and each signal-to-noise ratio. Unlike other studies of this type, the results did not show a correlation between C–V intensity ratio and intelligibility. It should be noted that C–V intensity ratios (and concomitant test scores) were only obtained for those test words in which the level of the consonant being tested could be measured using a graphic level recorder; i.e., the very weak consonants were omitted from this analysis.

All of the above studies examined the correlation between C–V intensity ratio and intelligibility in natural speech. A series of causal studies has also been performed in which the acoustic speech signal has been processed in order to investigate the effects of modifying the C–V intensity ratio on speech intelligibility.

One of the earliest studies of this type was performed by Hecker (1974). Recordings of the Modified Rhyme Test were obtained for a highly intelligible speaker and a less intelligible speaker. The same two speakers as in the study by House *et al.* (1965) participated, but different recordings were used. The recordings were then modified. The C–V intensity ratios of the more intelligible speech were reduced so as to equal those of the less intelligible speech, and the C–V intensity ratios of the latter were increased to equal those of the more intelligible speech. Intelligibility scores were then obtained for both the modified and unmodified recordings at two signal-to-noise ratios. The test scores for the stimuli in which the C–V intensity ratios had been increased were found to be roughly equal to those of the unmodified, more intelligible speech. Similarly, the test scores for the stimuli in which the C–V intensity ratios had been reduced were roughly equal to those of the unmodified, less intelligible speech.

Gordon-Salant (1986, 1987) investigated the effects of modifying C–V intensity ratio and consonant duration on consonant recognition in noise. Consonant–vowel nonsense syllables were used at a signal-to-noise ratio of 6 dB, the noise consisted of 12-talker babble. Consonant recognition was measured for normal-hearing listeners at stimulus levels of 75 dB SPL and 90 dB SPL, respectively. C–V intensity ratios were increased by 10 dB, consonant durations were increased by 100 percent.

The increase in C–V intensity ratio produced a significant increase in consonant recognition (13 percentage points on the average, for stimuli presented at 75 dB SPL and 9 percentage points, on average, for stimuli at 90 dB SPL).

Increasing consonant duration produced small to negligible improvements in consonant recognition. The study was then repeated for listeners with sensorineural hearing impairments (Gordon-Salant, 1987). Similar results were obtained. In this case, the 10-dB increase in C–V intensity ratio produced improvements of 16 percentage points for the 75 dB SPL stimulus level and 11 percentage points for the 90 dB SPL stimulus level, on the average. Subjects were grouped by audiogram shape (gradually sloping and sharply sloping). Slightly higher improvements were obtained for subjects with the sharply sloping audiograms. The magnitude of the improvement also varied to some extent with vowel type, larger improvements being obtained with the /i/ and /u/ vowels.

Montgomery and Edge (1988) performed a similar experiment using monosyllabic words in quiet. CVC words from the CCT lists developed by Owens and Schubert (1977) were used. Consonant levels were increased to equal those of the vowel; i.e., a C–V intensity ratio of 0 dB was used for both consonants in each CVC word. Stimuli were presented at levels of 65 dB SPL and 95 dB SPL to 20 listeners with moderate sensorineural hearing impairments. The effect of increasing consonant duration (by three pitch periods) was also investigated. The results obtained at the lower stimulus level of 65 dB SPL were similar to those of Gordon-Salant. The increase in C–V intensity ratio produced a 10 to 11 percentage point improvement in consonant recognition while the increase in consonant duration produced a negligibly small change in performance. The results for the 95 dB SPL stimulus level, however, showed a different pattern. The improvement produced by increasing the C–V intensity ratio was relatively small (roughly 2 percentage points, on the average) while the improvement resulting from the increase in consonant duration was approximately twice as large.

Freyman and Nerbonne (1989) adjusted consonant and vowel levels in three different ways. Recordings were obtained for ten talkers producing a set of eight nonsense syllables consisting of a voiceless consonant followed by the vowel /a/. In the first set of adjustments, all the vowels were equated in level to that of the most intense vowel (of the ten talkers) without altering the C–V intensity ratios. In the second set of adjustments, the C–V intensity ratios were equated to equal the largest C–V intensity ratio for that talker. In the third set of adjustments all the consonants for each talker were equated in level to that of the most intense consonant (for that talker) without altering the C–V intensity ratio. White noise was added to the processed stimuli at a signal-to-noise ratio of 0 dB. The stimuli were presented to normal-hearing listeners at a level of 65 dB SPL. The average consonant recognition score for condition 1 (equal vowel levels) was 51.6% increasing to 63.3% for condition 2 (equal C–V intensity ratios) and to 72.5% for condition 3 (equal consonant levels). These data provide further evidence that increasing the C–V intensity ratio is an important factor in improving intelligibility. A concomitant, possibly more important factor, is that of increasing the audibility of the consonantal sounds. Increasing the C–V intensity ratio will increase the audibility of a weak consonant, but, as shown by the results obtained for condition 3, even greater improve-

ments were obtained by increasing consonantal levels directly without altering the C–V intensity ratio. However, increasing both the consonant and vowels levels by the same amount would exceed the available dynamic range of many hearing-impaired listeners.

Studies on improving consonant recognition for severely hearing-impaired listeners by altering the intensity and duration of the consonantal sounds have also been performed by Revoile *et al.* (1986a, 1986b, 1987). For this population, increasing consonant duration had a greater effect than increasing the C–V intensity ratio. Adjustment of vowel duration also helped improve recognition of the voiced–voiceless contrast in the following consonant. This form of processing, however, is beyond the scope of the present paper and the reader is referred to the sequence of papers by Revoile *et al.* for further information.

The studies reviewed above provide strong evidence that adjustment of the C–V intensity ratio can yield significant improvements in consonant recognition for hearing-impaired listeners in quiet, and for both normal-hearing and hearing-impaired listeners in noise. There were, however, large differences in the magnitude of the improvements obtained by different researchers. Montgomery and Edge (1988), for example, obtained relatively small gains in consonant recognition at high signal levels, while Gordon-Salant showed only a small reduction in the gains provided by adjustment of the C–V intensity ratio at comparable signal levels. In view of the conflicting results obtained with hearing-impaired subjects at high signal levels it is likely that for some subjects the increase in C–V intensity ratio may have been excessive, at least on some consonants, while for other subjects many of the consonants may have received insufficient gain.

The purpose of the present study was to determine the C–V intensity ratio for maximizing consonant recognition for speech presented at a comfortable listening level and to investigate the factors affecting this C–V intensity ratio. Factors likely to affect this C–V intensity ratio are consonant type, vowel environment, and audiogram configuration. In order to reduce the problem to tractable form, nonsense syllables were chosen for investigation so as to avoid the confounding effects of linguistic cues. Further, consonant recognition is poorest for nonsense syllables having a vowel–consonant structure and the effects of adjusting the C–V intensity ratio should be easier to measure for stimuli of this type. The results of this investigation should thus provide information on the maximum improvements in consonant recognition that can be obtained by individualized adjustment of the C–V intensity ratio.

I. METHOD

A. Speech stimuli

The test stimuli for this experiment consisted of the vowel–consonant (V–C) subtests of the CUNY Nonsense Syllable Test (Levitt and Resnick, 1978). Six subtests, three unvoiced and three voiced, were used. The test syllables within each voiceless subtest consisted of a vowel (/a/, /u/, or /i/) terminated by one of seven voiceless consonants (/p/, /t/, /k/, /f/, /ʃ/, /s/, and /θ/). The test syllables within each voiced

TABLE I. Vowel level, consonant level, and C-V intensity ratios. All entries are in dB. Vowel levels and consonant levels are specified *re*: rms level of carrier sentence. NS, VL, CL, and CV refer to nonsense syllable, vowel level, consonant level, and C-V ratio, respectively.

Consonant group	Voiceless consonants				Voiced consonants			
	NS	VL	CL	C-V	NS	VL	CL	C-V
Weak fricatives	/af/	3.0	-25.7	-28.7	/av/	2.0	-13.5	-15.5
	/uf/	0.1	-24.5	-24.6	/uv/	1.3	-15.3	-16.6
	/if/	1.6	-25.7	-24.1	/iv/	0.7	-11.7	-12.4
	/aθ/	2.5	-24.5	-27.0	/að/	1.5	-13.6	-15.1
	/uθ/	0.2	-23.6	-23.8	/uð/	1.8	-13.2	-15.0
	/iθ/	-3.1	-23.1	-20.0	/ið/	2.2	-10.4	-12.6
	mean	-0.2	-24.5	-24.7	mean	1.6	-12.9	-14.5
Stops	/ap/	3.2	-23.0	-26.2	/ab/	1.9	-14.6	-16.5
	/up/	2.6	-25.4	-28.0	/ub/	2.0	-15.4	-17.4
	/ip/	-0.1	-23.7	-23.6	/ib/	2.3	-12.1	-14.4
	/at/	2.0	-23.9	-25.9	/ad/	2.2	-12.9	-15.1
	/ut/	1.0	-21.2	-22.2	/ud/	3.3	-12.3	-15.6
	/it/	-2.5	-17.6	-15.1	/id/	-0.7	-10.3	-9.6
	/ak/	0.6	-25.0	-25.6	/ag/	2.5	-12.6	-15.1
	/uk/	1.1	-26.0	-27.1	/ug/	2.5	-13.3	-15.8
	/ik/	-0.6	-20.1	-19.5	/ig/	1.6	-10.0	-11.6
	mean	0.8	-22.9	-23.7	mean	2.0	-12.6	-14.6
Strong fricatives	/aʃ/	1.1	-10.4	-11.5				
	/uʃ/	-1.4	-13.7	-12.5				
	/iʃ/	0.6	-8.9	-9.5				
	/as/	4.0	-8.8	-12.8	/az/	0.6	-10.4	-11.0
	/us/	-0.1	-7.5	-7.4	/uz/	0.3	-8.8	-9.1
	/is/	-2.6	-4.5	-1.9	/iz/	0.9	-7.4	-8.8
mean	0.3	-9.0	-9.3	mean	0.6	-9.0	-9.6	
Nasals					/am/	-4.0	-8.3	-4.3
					/um/	2.2	-3.4	-5.6
					/im/	2.4	-3.3	-5.7
					/an/	0.9	-5.7	-6.6
					/un/	2.0	-0.7	-2.7
					/in/	-0.2	-9.1	-8.9
					/aŋ/	2.7	-5.4	-8.1
					/uŋ/	3.8	-0.5	-4.3
					/iŋ/	0.7	-5.4	-6.1
					mean	1.2	-4.6	-5.8
		VL		CL		C-V		
Means	voiceless		0.5		-19.4		-19.9	
	voiced		1.5		-9.6		-11.1	
	all		1.0		-13.9		-14.9	
Means by Vowel	/a/		1.7		-14.9		-16.6	
	/u/		1.4		-14.1		-15.5	
	/i/		0.0		-12.7		-12.7	

subtest consisted of a vowel (/a/, /u/, or /i/) terminated by one of nine voiced consonants (/b/, /d/, /g/, /v/, /ð/, /z/, /m/, /ŋ/, /n/). Each nonsense syllable was preceded by the carrier sentence "You will mark....."

The consonant and vowel portion of each V-C nonsense syllable was segmented using the waveform editing procedures described in Dubno and Levitt (1981). An auditory analysis was used to confirm the accuracy of the segmentation. This differentiation proved to be easily determined for the stop consonants and fricatives. The nasal consonants, however, showed a gradual merging with the vowel, and a point midway between a pure vowel and a pure nasal consonant was used as the point of segmentation. Note that, in all

cases, the point of segmentation was chosen to coincide with a zero crossing so as to minimize the production of transients when the level of the consonant is increased relative to the vowel.

The levels of each vowel and consonant in the nonsense syllables (prior to processing) are shown in Table I. These levels were obtained by measuring the rms intensity of segmented components of each nonsense syllable. In the case of the stop consonants, the measured level was determined primarily by the noise burst occurring upon the release from closure. The levels in Table I are specified in dB relative to the average rms level of the carrier phrase. As can be seen from this table, each nonsense syllable has a different

consonant–vowel intensity ratio. There is also some variation in vowel level as a function of vowel type.

The primary focus of this study is the effect of increasing consonant intensity (i.e., increasing the C–V intensity ratio) on consonant recognition. The process of increasing consonant intensity is referred to here as consonant enhancement. In order to specify the amount of consonant enhancement, each unprocessed nonsense syllable is defined as having a consonant enhancement (CE) of 0 dB. An increase in consonant intensity of X dB relative to the unprocessed condition is referred to as a CE of X dB.

Nine sets of test stimuli were prepared providing CE's ranging from 0 dB (unprocessed) to 24 dB in steps of 3 dB. The choice of CE's depended on the subject's dynamic range, as described shortly.

B. Subjects

Three groups of six adult hearing-impaired subjects participated. All subjects had sensorineural hearing loss with air-bone gaps no greater than 10 dB and normal tympanograms. Two measures were performed to rule out retrocochlear pathology. Tone decay at 2000 Hz was less than 20 dB in 60 s [using the Olsen–Noffsinger (1974) technique] and no acoustic reflex decay was observed at 500 and 1000 Hz in a 10-s period. Word recognition scores were obtained using an Auditec recording of the NU-6 word lists presented at MCL. All subjects scored below 80% on this test using a 50 item list.

The first group of subjects had a flat audiogram configuration showing relatively little change in hearing loss (within ± 10 dB) over the range from 500 to 5000 Hz. The second group of subjects (sloping audiogram configuration) had sloping audiograms with a maximum slope no greater than 40 dB within the range 500–4000 Hz. The third group (precipitous audiogram configuration) had hearing losses that increased rapidly with frequency (i.e., slopes greater than 40 dB within the 500–4000 Hz range).

C. Instrumentation

The stimuli were stored digitally (20-kHz sampling rate, 16-bit resolution) on the hard disk of a 286-based portable personal computer. On playback, the stimuli were converted to analog form using a Data Translation 2801-A data acquisition board and low-pass filtered with a cutoff frequency of 9500 Hz to remove any aliasing or imaging errors. The analog signals were amplified by means of a power amplifier and then sent to a TDH 39 earphone. The frequency response of the playback system was flat with ± 2 dB from 50 to 7500 Hz.

D. Experimental procedures

Stimuli were presented at the subjects most comfortable level (MCL) for the carrier sentence. MCL was determined using the method of Dirks and Kamm (1976). Uncomfortable listening levels (UCL) were also obtained for each subject using a procedure based on that of Cox (1983). Subjects were presented with each nonsense syllable, with the vowel level at MCL (as determined using the carrier sentence and

the unprocessed nonsense syllable). The level of the consonant in each nonsense syllable was then increased in steps of 3 dB to a maximum CE level of 24 dB. If a subject reported UCL at a CE level of less than 24 dB, the maximum enhancement used with that subject on that consonant was limited to 3 dB below the reported UCL.

Where possible, five CE levels were used with each subject for each nonsense syllable. If a CE level of 24 dB did not reach UCL, then the five CE levels were evenly spaced in 6-dB steps from 0 dB to 24 dB. If, because of UCL constraints, the maximum allowable CE level for a given subject on a given nonsense syllable was less than 24 dB, then a different set of CE levels with closer spacing was used. Three of the 18 subjects were able to tolerate CE levels of 24 dB on all consonants. Two of the subjects found CE levels of 18 dB or higher uncomfortably loud for one or more consonants. Six of the subjects could not tolerate CE levels of 12 dB, four could not tolerate CE levels of 9 dB, and three could not tolerate CE levels of 6 dB on one or more consonants. The UCL's at a CE level of 6 dB were unexpected as the VC's with this amount of enhancement had C–V intensity ratio's below the mean level of the carrier phrase. Subjects were carefully instructed to choose UCL's but may have made these judgements based on sound quality rather than loudness.

The stimuli were divided into two subsets according to whether the consonants were voiced or voiceless. Twenty repetitions of each V–C in each subset were randomized and stored in computer memory. By this means it was possible to present in random order each V–C 20 times at each consonant enhancement (CE). The two subsets of stimuli were presented in a counterbalanced order and were administered in two or more sessions until the entire test was completed.

On each trial, the subject was required to indicate which consonantal sound was heard by pressing a key on an appropriately marked keyboard. Note that there were nine possible response alternatives for the subset involving voiced consonants (/b/, /d/, /g/, /v/, /ð/, /z/, /m/, /ŋ/, /n/), and that for these test stimuli nine keys were marked with the appropriate orthographic symbols. The subtests involving voiceless consonants had seven possible response alternatives (/p/, /t/, /k/, /f/, /j/, /s/, and /θ/), and seven appropriately marked keys were used for these stimuli.

The subjects were encouraged to proceed at their own pace and to take a break whenever they began to feel tired. All of the subjects responses were recorded automatically by the computer which then sorted the responses to obtain percent correct scores and confusion matrices for each subject and experimental condition.

II. RESULTS

The data have been analyzed in three stages. In the first stage, the test scores were analyzed for the unprocessed condition only. This analysis provided a basis for comparing the data of this study with those of earlier studies on consonant recognition in order to establish consistency with previous research.

In the second stage of the analysis, smooth curves were fitted to each set of consonant enhancement data. The result-

TABLE II. Analyses of variance of consonant recognition scores for unenhanced speech. Note: ***=significant at 0.001 level, **=significant at 0.01 level, *=significant at 0.05 level.

Source of variation	Voiced consonants			Voiceless consonants		
	<i>df</i>	Mean Square	<i>F</i> Ratio	<i>df</i>	Mean Square	<i>F</i> Ratio
Consonant (C)	8	7.589	4.52**	6	8.601	8.78***
residual variance	120	0.796		90	0.980	
Vowels (V)	2	8.358	23.16*	2	2.199	5.53**
residual variance	30	0.361		30	0.397	
Audiogram (A)	2	3.842	0.73	2	5.803	1.16
residual variance	15	5.25		15	5.021	
C×V	16	2.805	6.70**	12	1.978	5.66***
residual variance	240	0.418		180	0.349	
C×A	16	0.976	1.22	16	1.695	1.73
residual variance	120	0.796		90	0.980	
V×A	4	0.818	2.26	4	0.547	1.38
residual variance	30	0.361		30	0.397	
C×V×A	32	0.448	1.07	24	0.231	0.35
residual variance	240	0.419		240	0.660	

ing curves are referred to as Consonant Enhancement (CE) functions. A separate CE function was fitted to the data obtained for each subject for each consonant in each vowel environment [i.e., $18 \times (7 + 9) \times 3 = 864$ CE functions were obtained].

The third stage of the analysis was concerned with the factors affecting maximum consonant recognition. The highest point on each CE function was determined, the horizontal and vertical coordinates of which were defined as CEmax and CRmax, respectively. CEmax is the CE level (in dB) at which maximum consonant recognition is obtained. CRmax is the maximum consonant recognition score (in percent).

In all three stages of the analysis, the observed proportions were converted to arc sine units in order to stabilize the error variance (Eisenhart, 1947). The transformation used was

$$Y = 2 \arcsin \sqrt{c/n},$$

where c is the number of correct responses, n is the number of trials for each experimental condition ($n = 20$ in this study), and Y is the transformed value, in arc sine units, of the proportion $p = c/n$.

A useful feature of this transformation is that the error variance is virtually constant over almost the entire range of Y except for $Y = 0$ and $Y = \pi$ (i.e., when $p = 0$ or 1). The magnitude of the error variance is approximately $1/n$ assuming a binomial distribution for estimates of p . The transformed values of p were used for all statistical tests. In reporting the data, however, the transformed values were converted back to percentages to facilitate interpretation of the results.

Analysis of variance techniques were used in stages 1 and 3 of the analysis. The variables for each analysis were consonant (C), vowel environment (V), audiogram configuration (A), and subjects (S). Note that a different group of subjects was used for each audiogram configuration, and

hence a repeated measures analysis of variance was performed with subjects nested within the factor of audiogram configuration. Separate analyses were performed for the voiced and voiceless subtests because of the differences in the number and types of consonants used within each subtest (e.g., there are no voiceless cognates of the nasal consonants). One consequence of this difference is that the score for random guessing is different for the voiced and voiceless subtests (11.1% and 14.3%, respectively).

The factors for each of the analyses of variance were:

Consonant (C)—7 levels for the voiceless consonants

(/p,t,k,f,s,θ/), and

9 levels for voiced consonants

(/b,d,g,v,ð,z,m,ŋ/)

Vowel environment (V)—3 levels (/a,u,i/)

Audiometric configuration (A)—3 levels (flat, sloping, precipitous)

Subject (S)—6 subjects within each audiometric configuration

A. Stage 1: baseline data

Analyses of variance were performed on the data for the unenhanced condition. The results of these analyses for the voiced and voiceless subtests, respectively, are shown in Table II.

Both analyses showed significant main effects for consonant (C) and vowel environment (V), and for the consonant by vowel (C×V) interaction. Histograms illustrating these effects are shown in Fig. 1(a) and (b). Note that the consonants are grouped by manner of articulation with an additional subdivision between strong and weak fricatives. The strong voiceless fricatives are /s/ and /ʃ/, the strong voiced fricative is /z/. As can be seen from Table I the average C-V intensity ratio for these fricatives is just under

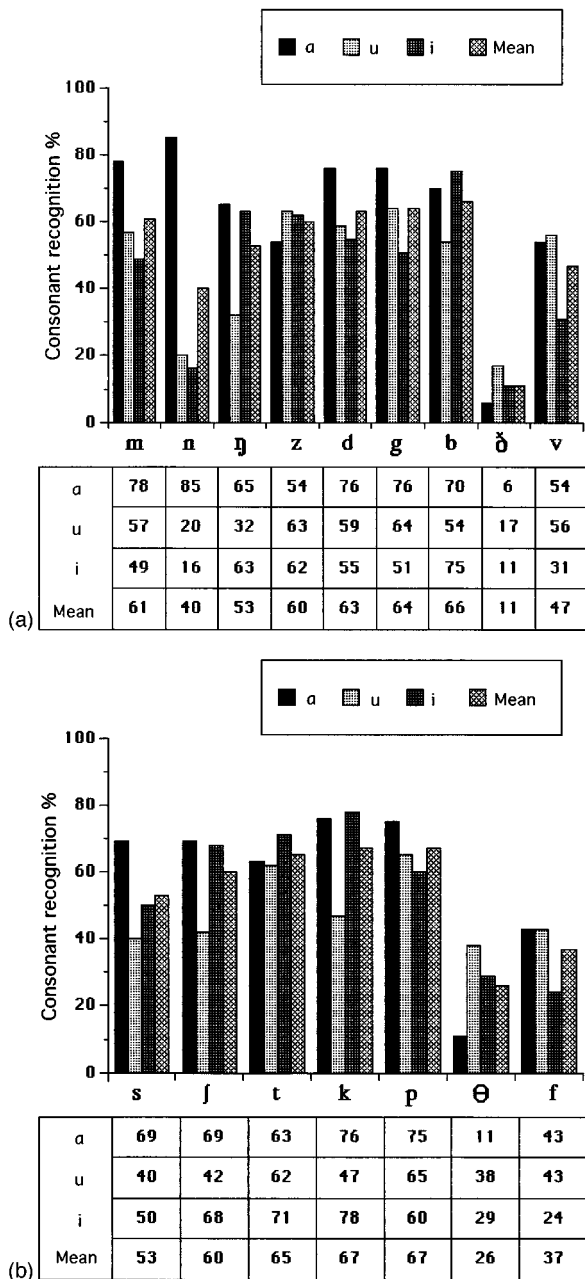


FIG. 1. Consonant recognition scores for the unenhanced condition. The joint effects of consonant (C) and vowel environment (V) are shown. The upper portion shows histograms of the data while the lower portion shows the data in table form. Data for voiced and voiceless consonants are shown separately in (a) and (b) of the figure, respectively.

-9 dB. In contrast, the weak voiceless fricatives /f/ and /θ/ have an average C-V intensity ratio that is just over 15 dB lower, at -24.7 dB. The weak voiced fricatives /v/ and /ð/ also have a relatively poor C-V intensity ratio (average value -14.5 dB). The consonant groups in Fig. 1(a) and (b) are shown in order of decreasing average C-V intensity ratio.

The data for the voiced consonants show that the stops had the highest average score (64.4% averaged over vowel environment, audiogram configuration, and subjects) followed closely by the average scores for the strong fricative (59.6%) and the nasal consonants (51.3%). The weak frica-

tives showing the lowest average score of 29%. Of the three vowel contexts, consonant recognition was highest for /a/ (65.8%, on average) with average scores for /u/ and /i/ being lower at 46.8% and 45.8%, respectively.

The consonant-vowel interaction for the voiced consonants is evident from Fig. 1(a). Consonant-recognition scores for the /a/ vowel context are relatively high for all the consonants except for the weak fricative /ð/. In contrast, scores for the /u/ vowel context are moderately high for only six of the nine consonants and quite low for the remaining three consonants (/ð/, /n/, and /θ/). The results for the /i/ vowel context show a similar pattern in that scores are relatively high for five of the six consonants showing high scores for /u/ with relatively low scores for /ð/, /n/, and /v/.

The data for the voiceless consonants [Fig. 1(b)] show a pattern similar to that for the voiced consonants. As before, the highest average scores were obtained for the stop consonants (66.3%), followed by the strong fricatives with an average score of 56.3%. The scores for the weak fricatives were consistently the lowest (average score of 31.3%). As in the case of the voiced consonants, consonant scores were highest for the /a/ vowel environment (average score 58%). In contrast to the voiced consonants, the average score for the /i/ vowel environment was almost as high (54.2%). The average score for the /u/ vowel environment was relatively low (48.1%).

The consonant-vowel interaction also showed some similarities to that for the voiced consonants. Percent scores for the /a/ vowel environment were high for all consonants except the weak fricative /θ/. Scores for the /i/ vowel context were also relatively high for all consonants except the weak fricatives (/θ/ and /f/). In contrast, the scores for the /u/ vowel context were lower than those for /a/ and /i/ for all consonants except for the weak fricatives. For the latter consonants, the scores for the /u/ vowel environment were relatively high in comparison with those for /i/ and /a/.

B. Stage 2: Derivation of CE functions

The method of orthogonal polynomials (Bennett and Franklin, 1954) was used to find the simplest polynomial curve that provided an adequate fit to each set of consonant enhancement data. Initially, a horizontal line (i.e., a constant) was fitted to the data. If the deviations from the fitted line were statistically significant then a sloping line (i.e., a linear polynomial) was fitted to the data. If this curve did not provide an adequate fit, then a quadratic polynomial was fitted. If the quadratic polynomial did not provide an adequate fit, a cubic polynomial was used, and so on using a polynomial of higher degree at each stage until an adequate fit to the data was obtained.

The CE functions obtained in this way were subdivided into five categories according to their shape.

- (1) Type 1 (decreasing). CE functions of this type show a significant reduction in consonant recognition at all levels of consonant enhancement. These curves were typically of the form shown in Fig. 2(a).
- (2) Type 2 (flat). In this category, a horizontal line provided an adequate fit to the data, indicating that there was no

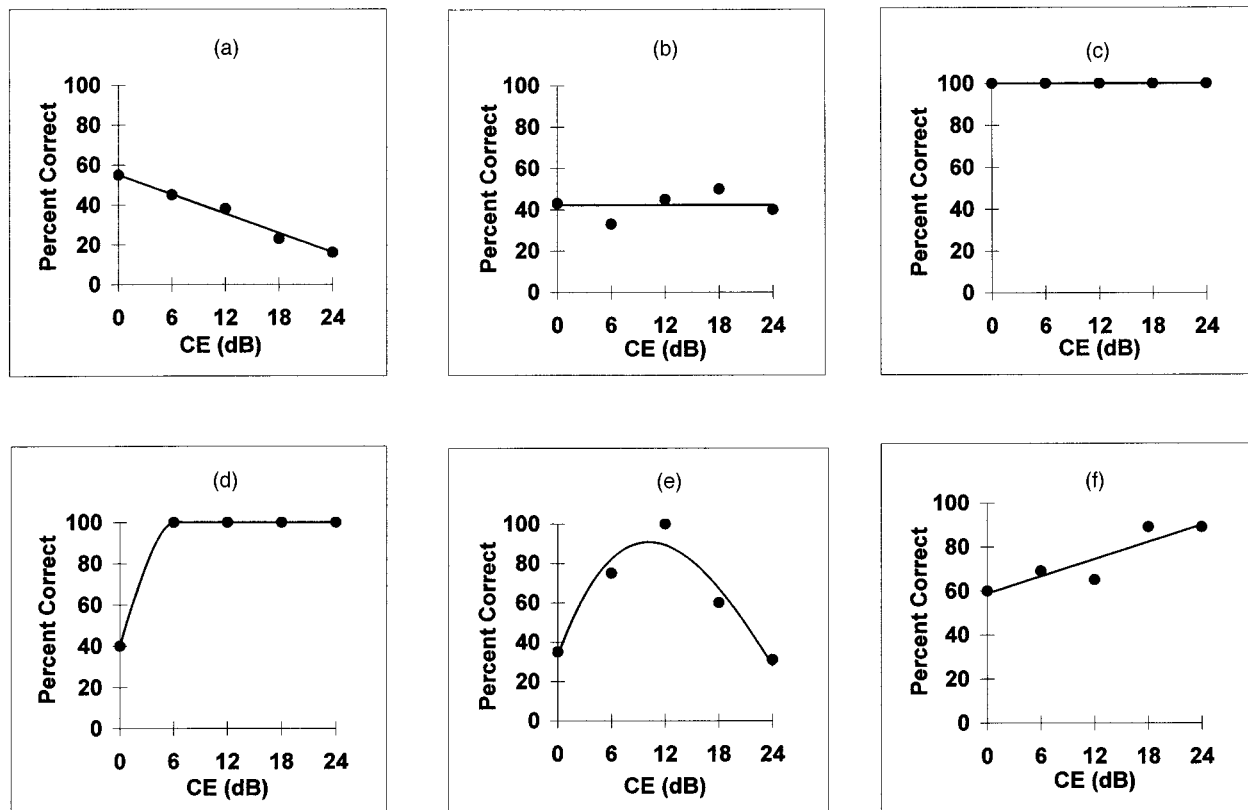


FIG. 2. Types of consonant enhancement (CE) functions. Type 1 (decreasing) CE function is shown in (a). Type 2 (flat, perfect scores) CE function is shown in (b). Type 2 (flat, perfect scores) CE function is shown in (c). Type 3 (increasing, with saturation) CE function is shown in (d). Type 4 (increasing, peak) CE function is shown in (e). Type 5 (increasing, no saturation) CE function is shown in (f).

significant change in performance with consonant enhancement. A common CE function of this type was that in which a consonant recognition score of 100% was obtained at all consonant enhancement levels, including the unenhanced condition. See Fig. 2(b) and (c) for examples of these CE functions.

- (3) Type 3 (increasing, with saturation). CE functions of this type show improved consonant recognition with consonant enhancement, reaching a plateau (typically at a score of 100%) well below the highest CE level used. A typical CE function of this type is shown in Fig. 2(d).
- (4) Type 4 (increasing, peaked). This type of CE function shows improved performance with increasing consonant enhancement until a maximum is reached, after which any further increase in consonant enhancement produces a reduction in test score. A typical CE function of this type is shown in Fig. 2(e). The fitted curves were invariably polynomials of degree 2 (quadratic) or higher.
- (5) Type 5 (increasing, no saturation). In CE functions of this type, consonant recognition increases monotonically with increasing consonant enhancement and without evidence of saturation. The most common CE function of this type is that in which the percent score increases linearly with CE level. A less common, but more dramatic, increase, in performance is that in which the rate of improvement also increases with increasing CE level. An example of the former CE function is shown in Fig. 2(f).

It was of interest to examine whether the frequency of occurrence of the different CE functions was related to the experimental variables being investigated. A four-way contingency table was thus formed for the factors:

Shape of CE function (CE): 5 types as defined above

Consonant group (CG): Stops, strong fricatives, weak fricatives, nasals

Vowel environment (V): /a, u, i/

Audiogram configuration (A): Flat, sloping, precipitous

A log-linear analysis (Bishop *et al.*, 1975) was performed in order to find the simplest model that provided a statistically adequate fit to the data. As before, separate analyses were performed for the voiced and voiceless consonants. In both cases the simplest model was of the form (CE×CG). Note that the main effects of V and A were found to be insignificant. The CE×CG contingency table, summed over V and A, is thus the simplest, statistically adequate model of the four-way contingency table. The CE×CG contingency table for both voiced and voiceless consonants is shown in Table III.

C. Stage 3: Analysis of CR_{max}, CE_{max} and the Improvement in Consonant Recognition at CE_{max}.

CR_{max} and CE_{max} were determined for each CE function. Analyses of variance were then performed on CR_{max}, CE_{max} and on the measured improvement in consonant recognition at CE_{max}.

TABLE III. Frequency of occurrence of CE function types by consonant group. Each entry in the table is the frequency of occurrence (in percent) for each type of CE function within each consonant group.

Consonant group	Type of CF function						Sum
	Decreasing	Flat 100%	Flat 100%	Increasing, saturated	Increasing, peaked	Increasing, no saturation	
Voiceless							
Strong fricatives	2.8	14.8	25.9	20.4	25.9	10.2	100
Stops	5.6	13.6	29.6	7.4	28.4	15.4	100
Weak fricatives	7.4	35.2	1.0	7.4	25.9	23.1	100
Mean	5.3	21.2	18.8	11.7	26.8	16.2	100
Voiced							
Nasals	21.0	39.5	7.4	2.5	17.9	11.7	100
Strong fricatives	3.7	18.5	35.2	11.1	24.1	7.4	100
Stops	5.5	26.5	16.7	13.0	24.1	14.2	100
Weak fricatives	9.2	50.0	3.7	5.6	20.4	11.1	100
Mean	9.9	33.6	15.7	8.1	21.6	11.1	100

Table IV shows the results of the analyses of variance for CRmax. As for the unenhanced case, separate analyses were performed for the voiced and voiceless consonants. The main effects consonant (C) and vowel environment (V) were found to be statistically significant for both voiced and voiceless consonants. Audiogram configuration (A) was significant for the voiceless consonants. In addition, the A×C and C×V interactions were significant for both sets of data. There was also some evidence of an A×V interaction for the voiced consonants, but since this effect was small with a borderline level of significance ($p < 0.05$), it is not described in detail.

Figure 3(a) and (b) shows the relative magnitude of the consonant and vowel environment effects and of the C×V interaction. The mean consonant effect shows consistently high CRmax scores (>78%) for the stops and strong fricatives (both voiced and voiceless) with lower scores for /m/

and /ŋ/ (72.0% and 61.0% on average, respectively). The mean score for /n/ was relatively low (47.0%) because of the very low scores obtained in the /u/ and /i/ vowel environments. The average values of CRmax for these two vowel environments (26.8% and 29.3%, respectively) were only a little higher than those for the unenhanced condition (20.6% and 16.0%, respectively). The mean scores for the weak fricatives showed a pattern similar to those for the unenhanced condition. Low mean scores were obtained for both /ð/ and /θ/ (17.0% and 36.1%, respectively) with moderately good mean scores for /v/ and /f/ (67.7% and 70.4%, respectively).

The mean scores for the three vowel environments showed a pattern similar to that for the unenhanced condition for the voiced consonants, but not for the voiceless consonants. The mean value of CRmax for the voiced consonants was highest (73.4%) for the /a/ vowel environment, with the mean scores for /u/ and /i/ being approximately equal at a

TABLE IV. Analyses of variance for CRmax. Note: ***=significant at 0.001 level, **=significant at 0.01 level, *=significant at 0.05 level.

Source of variation	Voiced consonants			Voiceless consonants		
	df	Mean square	F ratio	df	Mean square	F ratio
Consonant (C)	8	24.739	29.95**	6	20.168	29.2***
residual variance	120	0.826		90	0.689	
Vowels (V)	2	3.809	16.42*	2	1.524	6.52**
residual variance	30	0.232		30	0.233	
Audiogram (A)	2	12.484	6.81	2	16.121	4.13*
residual variance	15	5.304		15	3.907	
C×V	16	2.806	2.17**	12	1.411	5.25***
residual variance	240	0.412		180	0.268	
C×A	16	1.828	2.21***	12	2.196	3.18***
residual variance	120	0.826		90	0.689	
V×A	4	0.472	2.029	4	0.566	2.42
residual variance	30	0.232		30	0.233	
C×V×A	32	0.434	1.05	24	0.412	1.53
residual variance	240	0.413		180	0.268	

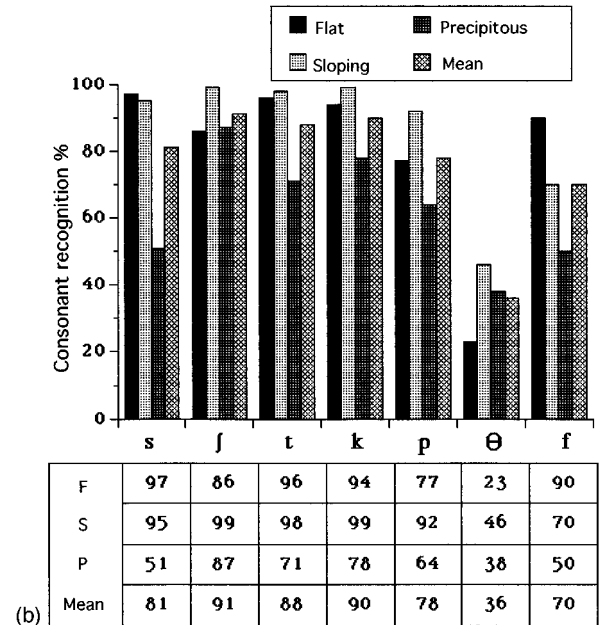
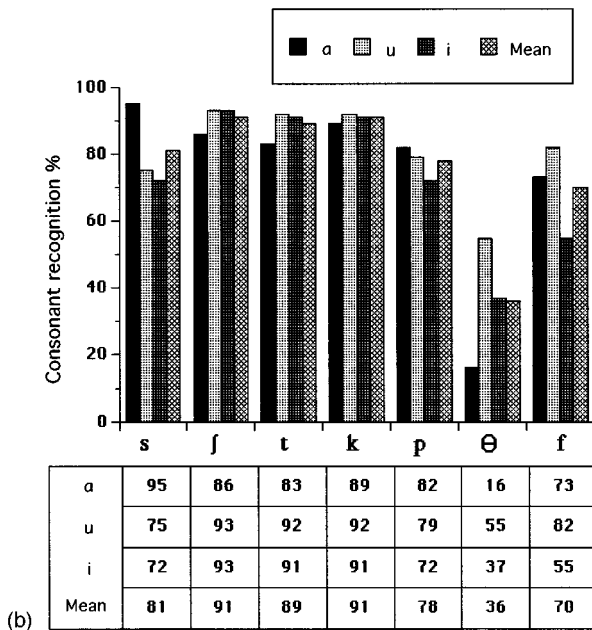
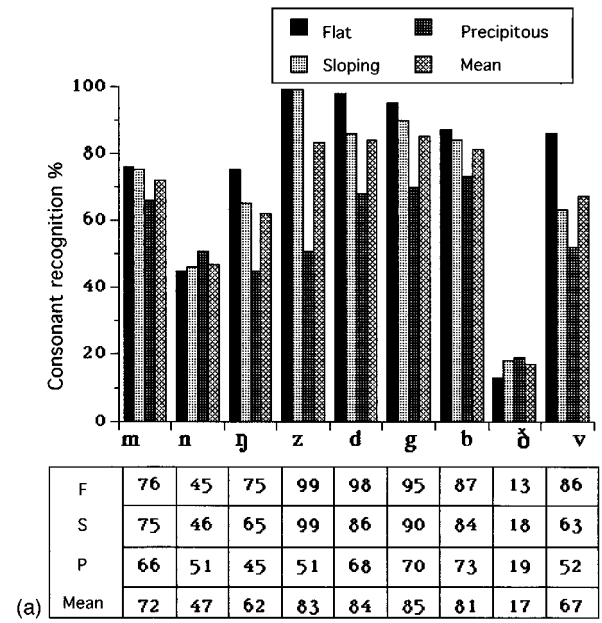
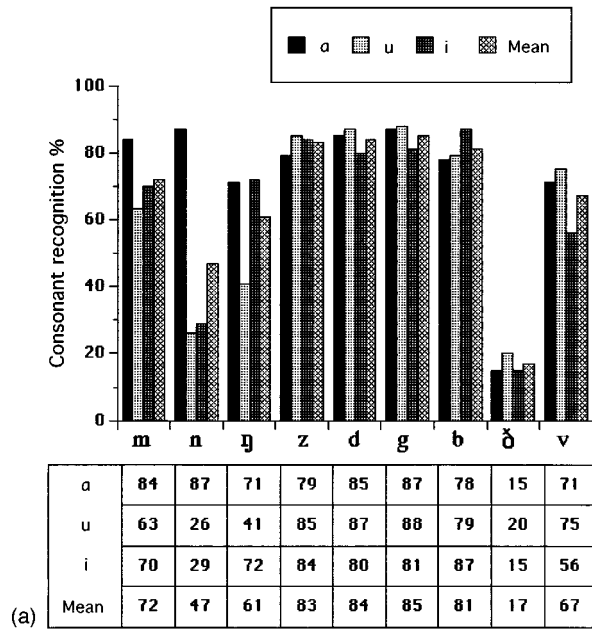


FIG. 3. Maximum consonant recognition scores (CRmax), C×V interaction. The joint effects of consonant (C) and vowel environment (V) are shown. The upper portion shows histograms of the data while the lower portion shows the data in table form. Data for voiced and voiceless consonants are shown separately in (a) and (b) of the figure, respectively.

FIG. 4. Maximum consonant recognition scores (CRmax), A×C interaction. The joint effects of audiogram configuration (A) and consonant (C) are shown. The upper portion shows histograms of the data while the lower portion shows the data in table form. Data for voiced and voiceless consonants are shown separately in (a) and (b) of the figure, respectively.

lower value (62.6% and 63.8%, respectively). The ranking of these mean scores was the same as that for the unenhanced condition. The mean scores for the voiceless consonants, however, showed a very different pattern. The mean value of CRmax for the /u/ vowel environment was higher than that for either /a/ or /i/, whereas in the unenhanced condition the mean score for /u/ was the lowest of the three vowel environments.

The C×V interaction showed a pattern similar to that for the unenhanced condition in that the mean value of CRmax for the /a/ vowel environment was high (relative to the mean scores for /u/ and /i/) for all consonants except the weak

fricatives /ð/ and /θ/. For these two consonants, the mean value of CRmax for /a/ was the lowest of the three vowel environments.

CRmax also showed a significant main effect for audiogram configuration with the voiceless consonants and a significant interaction between consonant and audiogram configuration for both the voiced and voiceless consonants. These effects are illustrated in Fig. 4(a) and (b). The mean values of CRmax averaged over all consonants were relatively high for both the flat and sloping audiogram configurations (77.3% and 76.5%, respectively). The corresponding mean score for the precipitous audiogram configuration was significantly lower at 58.3%.

TABLE V. Analyses of variance for CRmax: Consonant recognition score for the unenhanced condition. Note: ***=significant at 0.001 level, **=significant at 0.01 level, *=significant at 0.05 level.

Source of variation	Voiced consonants			Voiceless consonants		
	<i>df</i>	Mean square	<i>F</i> ratio	<i>df</i>	Mean square	<i>F</i> ratio
Consonant (C)	8	3.008	5.62**	6	4.451	5.18***
residual variance	120	0.534		90	0.859	
Vowels (V)	2	1.337	4.08*	2	8.096	18.0***
residual variance	30	0.327		30	0.449	
Audiogram (A)	2	2.288	2.66	2	3.872	1.42
residual variance	15	0.860		15	2.734	
C×V	16	0.395	2.17**	12	0.798	3.10**
residual variance	240	0.181		180	0.257	
C×A	16	1.506	2.82***	12	1.240	1.44
residual variance	120	0.534		90	0.859	
V×A	4	0.331	1.01	4	0.531	1.18
residual variance	30	0.327		30	0.449	
C×V×A	32	0.227	1.25	24	0.233	0.91
residual variance	240	0.182		180	0.257	

The improvement in consonant recognition in going from the unenhanced condition (CE level=0 dB) to CRmax has been analyzed in terms of the difference between the transformed values of these two scores. Since a difference in transformed scores cannot be converted back to percentages without additional information (see Sec. III), the improvement in consonant recognition is specified in arc sine units.

Table V shows the results of the analyses of variance for the improvement in consonant recognition. As in the previous analyses, the main effects of consonant (C) and vowel enhancement (V) and the C–V interaction were statistically significant for both the voiced and voiceless consonants. In addition, the C×A interaction was found to be significant for the voiced consonants.

The consonant and vowel environment effects are illustrated in Fig. 5(a) and (b). The largest improvements, on average, were shown by the strong fricatives followed by the stop consonants. The nasal consonants showed relatively small improvements with a mixed result for the weak consonants, the improvements for /f/ and /v/ being substantially higher than those for /θ/ and /ð/. Improvements as a function of vowel environment were largest for /u/ (particularly for the voiceless consonants) and smallest, on the average, for the /a/ vowel environment.

A relatively large C–V interaction was observed for the voiced consonants. Six of the nine voiced consonants showed the largest improvement in the /i/ vowel environment (/m, n, ŋ, g, ð, v/), while the improvements obtained in the /u/ vowel environment were largest for only two consonants, /b/ and /d/. The magnitude of these improvements was relatively large, however, resulting in an average improvement for the /u/ vowel environment that was essentially equal to the average improvement observed for the /i/ vowel environment (0.459 compared to 0.460 arc sine units). For the voiceless consonants, the improvement observed in the /u/ vowel environment was consistently larger for all conso-

nants compared to that obtained for each of the other two vowel environments. The significant C–V interaction for the voiceless consonants resulted primarily from the differences in the improvements obtained in the /a/ and /i/ vowel environments. For example, improvements in the /a/ vowel envi-

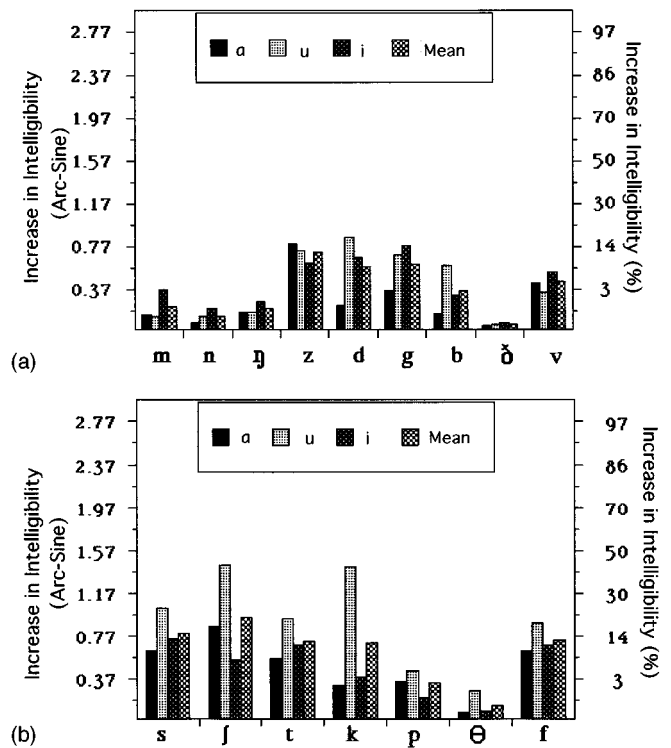


FIG. 5. Improvement in consonant recognition score at CEmax, C×V interaction. The joint effects of consonant (C) and vowel environment (V) are shown. The left vertical axis shows CRmax consonant recognition score for the unenhanced condition, in arc sine units while the right vertical axis shows CRmax in percentage units. Data for voiced and voiceless consonants are shown separately in (a) and (b) of the figure, respectively.

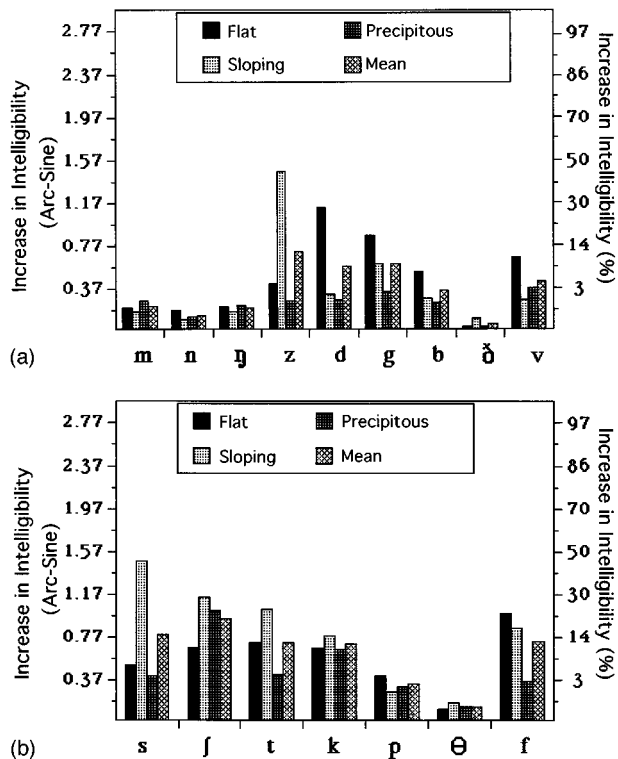


FIG. 6. Improvement in consonant recognition score at CEmax, A x C interaction. The joint effects of audiogram configuration (A) and consonant (C) are shown. The vertical axis shows CRmax consonant recognition score for the unenhanced condition, in arc sine units while the right vertical axis shows CRmax in percentage units. Data for voiced and voiceless consonants are shown separately in (a) and (b) of the figure, respectively.

ronment were larger than those in the /i/ environment for /j/ and /p/, whereas the opposite result was obtained for /s/, /f/, /k/, and /θ/.

The effects of audiogram configuration and consonant on the improvements in consonant recognition are shown in

Fig. 6(a) and (b). The improvements, on average, were largest for the flat audiogram configuration on the voiced consonants and for the sloping audiogram configuration on the voiceless consonants. The precipitous audiogram configuration showed the smallest average improvements for both the voiced and voiceless consonants. The C x A interaction was significant for the voiced consonants only and was a result of the very large improvement shown on the strong fricative /z/. For all other consonants, the improvement for the sloping audiogram configuration was less than that for the flat audiogram configuration.

Table VI shows the results of the analyses of variance for CEmax. The voiced consonants showed substantially more significant effects than the voiceless consonants. For the voiced consonants, the main effects of consonant (C) and vowel environment (V) were significant as well as the C x A and V x A interactions. For the voiceless consonants, only the consonant (C) effect and the C x V interaction were significant.

Figure 7(a) and (b) shows the effects of consonant (C) and vowel environment (V) on CEmax. The largest values of CEmax were obtained for the voiceless stops /t/ and /k/ (14.4 and 12.6 dB on average, respectively). The next largest values of CEmax were obtained for the strong fricatives, ranging from 12.6 dB for /s/ to 14.3 dB for /j/, respectively. The remaining stop consonants (/p/ and the three voiced stops) had values of CEmax ranging from an average of 11.5 dB for /s/ to 12.6 dB for /j/, respectively. The remaining stop consonants (/p/ and the three voiced stops) had values of CEmax ranging from 8.1 dB on average to 13.1 dB on average. These overlapped with the values of CEmax for the weak fricatives /v/ and /f/ (9.5 and 12.9 dB on average, respectively.) Low values of CEmax were obtained for the two weak fricatives (8.8 and 5.3 dB for /ð/ and /θ/ on average, respectively). The lowest values of CEmax were obtained for the nasal consonants (CEmax ranging from an average of 4.5

TABLE VI. Analyses of variance for CEmax. Note: ***=significant at 0.001 level, **=significant at 0.01 level, *=significant at 0.05 level.

Source of variation	Voiced consonants			Voiceless consonants		
	df	Mean square	F ratio	df	Mean square	F ratio
Consonant (C)	8	366.9	6.99***	6	514.0	7.76***
residual variance	120	52.5		90	66.2	
Vowels (V)	2	191.6	3.96**	2	377.6	7.53**
residual variance	30	48.4		30	50.1	
Audiogram (A)	2	158.3	1.25	2	272.1	1.49
residual variance	15	126.9		15	182.3	
C x V	16	63.7	2.01	12	57.8	1.88*
residual variance	240	31.7		180	30.8	
C x A	16	125.6	2.39**	12	28.2	0.43
residual variance	120	52.5		90	66.2	
V x A	4	44.6	0.92	4	29.7	0.59
residual variance	30	48.4		30	50.1	
C x V x A	32	52.2	1.65*	24	47.5	1.54
residual variance	240	31.7		180	30.8	

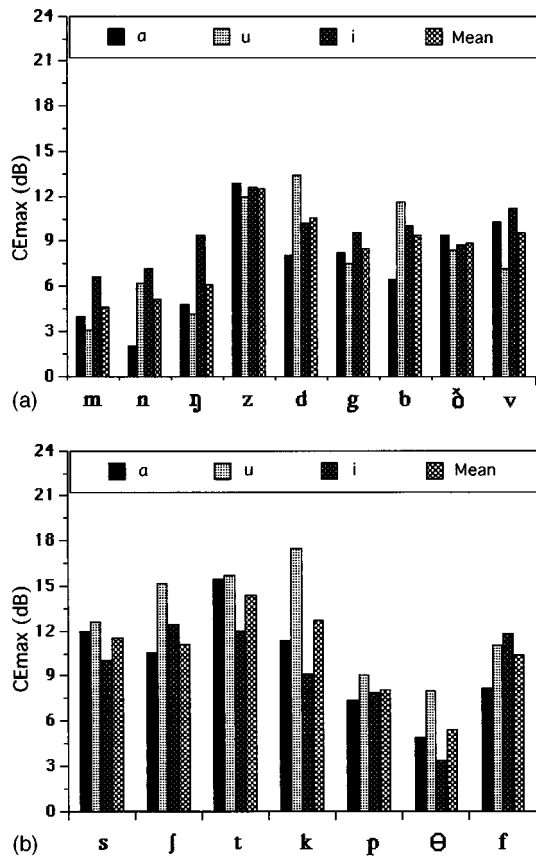


FIG. 7. Consonant enhancement level corresponding to CRmax, C×V interaction. The joint effects of consonant (C) and vowel environment (V) on CEmax are shown. Data for voiced and voiceless consonants are shown separately in (a) and (b) of the figure, respectively.

to 6.1 dB). The average value of CEmax for the voiced consonants was 8.3 dB as compared to 10.7 dB for the voiceless consonants.

The variation of CEmax with vowel environment was significant for both the voiced and voiceless consonants. The range of variation was greater for the voiceless consonants on average, ranging from 9.5 dB with /i/ to 12.7 dB with /u/. For the voiced consonants, the average value of CEmax ranged from 7.3 dB for /a/ to 9.5 dB for /i/. The C×V interaction interaction was significant for both the voiced and voiceless consonants. For the voiced consonants, CEmax was virtually the same for most of the consonants, the exceptions being the stops /b/ and /d/ which showed increases with /u/ and /i/ and the nasals which showed increases for /i/. The CEmax values were essentially the same for each of the voiceless consonants, except /k/ and /θ/ where there is a substantial increase in CEmax for the /u/ vowel.

The only significant effect involving audiogram configuration (A) was the C×A interaction for the voiced consonants which is illustrated in Fig. 8(a). In this case, CEmax was relatively large for the flat audiogram configuration for the stop consonants and for /v/. In contrast, CEmax for this audiogram configuration was relatively small (in comparison with CEmax for the sloping and precipitous audiogram configurations) for the nasals and the strong fricative /z/.

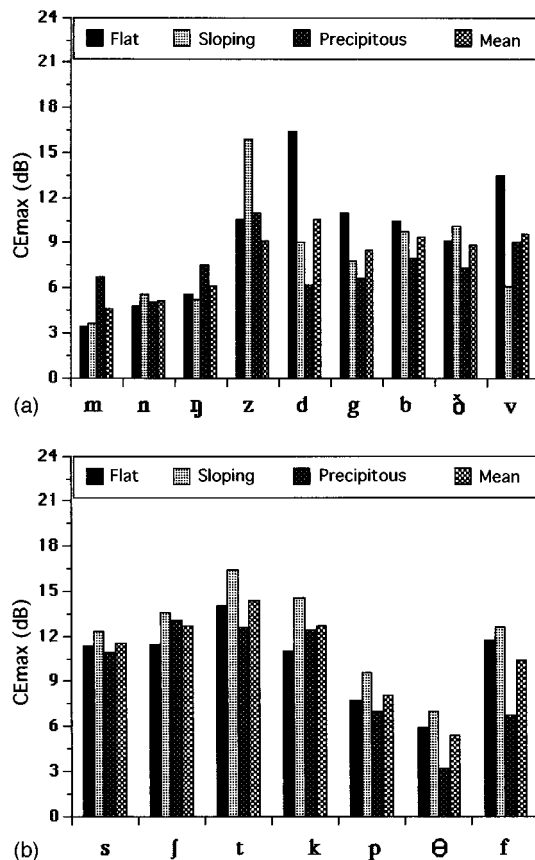


FIG. 8. Consonant enhancement level corresponding to CRmax, A×C interaction. The joint effects of audiogram configuration (A) and consonant (C) on CEmax are shown. Data for voiced and voiceless consonants are shown separately in (a) and (b) of the figure, respectively.

III. DISCUSSION

The first stage of the analysis was concerned with the unenhanced condition. The data for this condition not only serve as a baseline for measuring improvements in consonant recognition, but also allowed for comparisons with the previous studies using the same test stimuli.

The most direct comparison is with the data obtained by Margulies (1980). She used the same nonsense syllables for the voiceless consonants and a smaller set of nonsense syllables for the voiced consonants in which only the /a/ vowel environment was used. Her hearing-impaired subjects included three groups of subjects with sensorineural hearing losses having flat, moderately sloping, and steeply sloping audiometric configurations, respectively. The results obtained in the present study for the unenhanced condition were reasonably consistent with those obtained by Margulies for her unprocessed condition. Both studies showed the same pattern of results for consonant, vowel environment, and audiogram configuration. One area of difference between the two studies related to the scores obtained for the voiceless fricatives in the /a/ and /u/ vowel environments. The data obtained by Margulies showed higher scores for the weak voiceless fricatives in the /u/ vowel context and lower scores for /s/ in the /a/ vowel environment.

A second detailed comparison can be made with data obtained by Dunn (1993). This study used the same subtests

of the CUNY Nonsense Syllable Test as in the present investigation. The subjects in Dunn's study were also diagnosed as having hearing impairment of sensorineural origin but were not grouped according to audiogram configuration. His subjects typically had moderately sloping audiograms. The selection criterion for Dunn's subjects was that they exhibit rollover in their Performance-Intensity (PI) function for moderate amounts of background noise ($S/N=10$ dB for cafeteria noise). Three presentation levels were used, at 5 dB below the subject's loudness discomfort level, at the presentation level corresponding to the peak of the PI function, and a third level 5–10 dB below the peak of the PI function. This lowest presentation level corresponded roughly to the presentation level used in the present study and the data obtained at this level were used for the comparison.

The data of the Dunn study showed a high degree of consistency with those of the present study. For the four conditions in which a difference was observed with the Margulies study, the data of the Dunn study compared favorably with the data of the present study. Differences with the Dunn study that were observed related to the average scores for the voiceless stops and fricatives. The Dunn data showed lower average scores for the voiceless stops and slightly higher average scores for the voiceless fricatives compared to those of the present study.

Apart from the above mentioned differences, which were not substantial considering the many sources of variability involved, the three sets of data showed an acceptably high level of consistency. The baseline data obtained in this study were thus considered to be reasonably reliable.

The second stage of the analysis was concerned with the shapes of the fitted CE functions. The results obtained provided several very useful insights with respect to the potential of C–V intensity ratio adjustment for improving consonant recognition. Of the five types of CE function identified, only the type 1 (decreasing) functions show a decrement in performance. This type of CE function was found to occur relatively infrequently. Roughly 1 in 20 of the voiceless consonants exhibited a PE function of this type. These occurred mostly with the weak fricatives and may have been a result of the increased frequency of /f/–/θ/ confusions for some of the enhancement conditions. A similar result was also observed for the weak voiced fricatives /v/ and /ð/.

The nasal consonants benefitted least from adjustment to the C–V intensity ratio. For these consonants, the type 1 PE functions occurred most frequently (roughly 1 in 5 nasal consonants exhibited a PE function of this type). Nasal consonants already have a relatively high C–V intensity ratio and additional amplification of these consonants may be excessive in many cases. Bear in mind that all three nasal consonants have a similar acoustic structure and place-of-articulation errors are quite common in the perception of nasal consonants.

The type 2 (flat) CE function was found to be the most common of all. Just over 45% of the PE functions were of this type. Approximately one third of these flat PE functions showed perfect scores (100%) for all levels of consonant enhancement, including the no enhancement condition. These CE functions indicate that the listener is able to rec-

ognize the consonant reliably and that there is no need for consonant enhancement, although no harm is being done by increasing the C–V intensity ratio (at least to consonant intelligibility, but not necessarily with respect to overall sound quality).

It is possible that consonants exhibiting a flat CE function might benefit from consonant enhancement for speech at a lower presentation level. The presentation level used in this investigation placed the powerful speech components (the vowels) at the listener's most comfortable listening level. At this level many of the stronger consonants are both audible and intelligible in quiet. This would not be the case for speech reaching the listener at a relatively low level.

All of the remaining CE functions (types 3, 4, and 5) show significant improvements in consonant recognition with an increase in CE level. Well over 50% of the CE functions for the voiceless consonants and just over 40% of the PE functions for voiced consonants were of these types.

The type 3 (increasing, with saturation) CE function is attractive from a signal-processing point of view. This CE function not only reaches a score of 100%, but the consonant enhancement needed for CRmax covers a range of CE levels. As a consequence, the exact value of CE that is used is not critical, provided it lies within the saturated range. The strong voiceless fricatives showed the highest percentage of type 3 CE functions. These fricatives are also relatively easy to identify from an acoustic analysis of the speech signal.

The type 4 (increasing, peaked) CE function is not as useful from a signal processing perspective in that precise adjustment of the CE level is needed in order to maximize consonant recognition. For CE functions of this type, an increase in CE level will improve consonant recognition, but if the increase is too large, a decrement in performance will be obtained. It is significant to note that almost a quarter of the CE functions were of this type. These curves were also distributed roughly equally among all consonant types (except for the nasals which showed a slightly lower but not insubstantial percentage of type 4 CE functions).

The relatively high frequency of type 4 CE functions may help explain why Montgomery and Edge (1988) obtained a reduction in intelligibility at a high presentation level (95 dB SPL). It is likely that at this high level, many of the consonants have been amplified beyond the peak of a type 4 CE function, resulting in a consequent reduction in intelligibility.

The type 5 (increasing, no saturation) CE functions were the most intriguing in that they indicate the possibility of even greater improvements in consonant recognition had higher CE levels been used. Not surprisingly, most of these CE functions were obtained with the less powerful consonants, such as the weak voiceless fricatives and the stop consonants. It should be noted that for the stop consonants, the release burst (which is relatively low in level) was amplified.

The frequency of occurrence of the different CE functions (Table III) indicates that for slightly under half of the nonsense syllables considered in this study, adjustment of the C–V intensity ratio had little or no effect on consonant recognition, as indicated by the high incidence of type 2 CE functions. In addition, for 5%–10% of the nonsense syl-

lables, any adjustment of the C–V intensity ratio produced a decrement in performance (the type 1 CE function).

On the positive side, approximately half of the CE functions were types 3, 4, or 5, indicating that significant improvements in consonant recognition can be obtained if the enhancement is applied appropriately. Of the CE functions showing a significant increase in consonant recognition, at least half require careful adjustment of the CE level (type 4 CE functions). On the other hand, the remaining CE functions either do not require sensitive adjustment, either because the CE function saturates at a score of 100% over a range of levels (type 3 CE functions) or because a fixed enhancement at the maximum CE level used in the study will produce a significant improvement in consonant recognition (type 5 CE function). In many cases, the maximum CE level was determined by the listener's dynamic range of hearing. In other cases, it is likely that even greater improvements in consonant recognition could have been obtained had a larger CE level been used.

The third stage of the analysis was concerned with CR_{max}, CE_{max}, and the improvement in consonant recognition. The factors affecting CR_{max}, in order of their relative magnitude, were consonant (C), vowel environment (V), and audiogram configuration (A). The last factor was only significant for the voiceless consonants and had a relatively small effect, as shown in Fig. 4(a) and (b). In contrast, the consonant (C) effect was substantial, scores close to 100% being obtained for the strong fricatives and stop consonants while average scores for the weak fricatives /ə/ and /ð/ were under 30%. The effect of vowel environment was much smaller although significantly greater than that for audiogram configuration, as shown in Fig. 3(a) and (b). The magnitudes of these effects need to be known if theoretical models accounting for the observed effects are to be developed.

Of particular interest in this investigation was the magnitude of the improvement in consonant recognition at CE_{max}. This improvement is specified in arc sine units since it involves the difference between two percentages, (CR_{max} minus the consonant recognition score for the unenhanced condition). As noted earlier, the arc sine transformation was used in order to avoid the problems associated with nonhomogeneity of the error variance when dealing with data in the form of proportions or percentages. This transformation also improves the likelihood that the factors affecting data of this type will be additive and interpretable in a rational way (Studebaker, 1985).

The largest gains in consonant recognition were obtained with the voiceless stops and the strong voiceless fricatives. The magnitude of these improvements (averaged over vowel environment, audiogram configuration, and subjects) ranged from 0.34 arc sine units (for /p/) to 0.95 arc sine units (for /ʃ/). The largest improvement for the voiced consonants was also obtained with a strong fricative, 0.72 arc sine units for /z/. The smallest improvements were obtained with the weak fricatives /ð/ and /θ/ and the nasal consonants. The magnitude of these improvements ranged from 0.05 arc sine units (for /ð/) to 0.13 arc sine units (for /θ/). The average improvement for all of the consonants considered in this study was 0.48 arc sine units.

In order to obtain some appreciation of what these improvements mean in terms of percentages, it should be noted that an improvement of 0.95 arc sine units (as obtained for /ʃ/) corresponds to a gain of 45.8 percentage point for test scores in the vicinity of 50% (i.e., in going from 27.1% to 72.9%). For test scores in the vicinity of 10%, this improvement corresponds to a gain of 18.6 percentage point (in going from 0.7% to 28.1%). For small changes in arc sine units (e.g., ± 0.1 arc sine units) the ratio between the change in percent score in the vicinity of 50% and the change in percent score in the vicinity of 10% is approximately 1.6.

The large improvements in consonant recognition obtained with the strong fricatives was surprising in view of the fact that these consonants, prior to processing, are already fairly powerful. Similarly, the relatively small improvements exhibited by the weak voiceless fricatives was unexpected since these sounds have very poor C–V intensity ratios (on the order of -25 dB) and are often not audible to hearing-impaired listeners without some form of compression amplification.

A possible explanation for the poor performance exhibited by the weak fricatives (with or without consonant enhancement) is that these sounds are often confused with each other (i.e., /f/ with /θ/ and /v/ with /ð/), thereby resulting in low scores in terms of percent correct. It should also be noted that most of the subjects exhibited a bias towards the /f/ or /v/ response in that scores for these consonants were relatively high in comparison with the scores for /θ/ and /ð/, respectively. The relatively high score for /f/ and /v/ should be interpreted with caution because of this bias. A possible approach to this problem is to use average scores for each member of these two fricative pairs. With this change in scoring procedure, the increase in consonant recognition at CE_{max} for the weak fricatives is similar to the other consonant types.

A factor to be considered in future experiments on C–V intensity ratio adjustment for continuous speech is the extent to which predictable consonant substitutions (as opposed to random substitutions) contribute or detract from overall intelligibility. For example, the reduction in uncertainty in going from not knowing what consonant was produced to a choice between two similar sounding alternatives (e.g., /f/ or /θ/) may be helpful to overall intelligibility, although this effect is not taken into account using traditional methods of scoring.

The improvements in consonant recognition obtained in this study are substantial in comparison with those obtained previously for hearing-impaired listeners. The average improvement reported by Montgomery and Edge (1978) for a presentation level of 65 dB SPL was 10.5 percentage points from an initial score of 42.7% for the unprocessed condition. This improvement corresponds to a gain of 0.21 arc sine units, which is about one-third of the improvement obtained in the present study averaged over all consonants. Similarly, the average improvement obtained by Gordon-Salant (1987) at a comparable signal level (75 dB SPL) was 0.33 arc sine units, which was larger than that obtained by Montgomery and Edge, but substantially less than that obtained in the present study. Bear in mind that Gordon-Salant used back-

ground noise and that her results, although useful, are not directly comparable to those of the present study.

The relatively large improvements in consonant recognition obtained in the present study are a result of the individualized adjustments made for each subject for each consonant–vowel combination. It is unlikely that such precise, individualized adjustment of the C–V intensity ratio could be obtained in a practical hearing aid, but it is useful to know that substantial improvements in consonant recognition can be achieved with appropriate adjustment of the C–V intensity ratio.

A particularly valuable aspect of the data reported here is that it provides an estimate of the upper bound of performance that could, in principle, be obtained by adjustment of the C–V intensity ratio; i.e., by means of uniform gain applied to the consonant without additional processing or frequency shaping. If, for example, the upper bound on the improvement in consonant recognition with C–V intensity ratio adjustment is small, then there would be little practical value in attempting to develop signal-processing techniques for the practical implementation of C–V intensity ratio adjustment in hearing aids. Fortunately, this does not appear to be the case.

The data summarized in Figs. 3–6 should be viewed as providing a conservative estimate of the upper bounds of performance for several reasons. First, approximately 15% of the CE functions were of the “increasing, no saturation” type, indicating that further improvements in consonant recognition might have been obtained had higher CE levels been used, particularly with the weaker consonants.

Second, many of the subjects had relatively good scores for the unenhanced condition, hence the high proportion of type 2 (flat) CE functions showing scores of 100% at all CE levels. Examination of the data indicates that if subjects with relatively good consonant recognition scores for the unprocessed condition were excluded (e.g., subjects with scores in excess of 90% for the unenhanced condition) then the average improvement in consonant recognition is increased by at least 10%.

Third, the change in gain at the start of a consonant was relatively rapid producing an audible transient distortion for many of the higher CE levels. It is likely that more gradual gain changes matched to the acoustic structure of each consonant would provide significant improvements in overall sound quality as well as possibly further improvements in consonant recognition. This refinement, however, was beyond the scope of the present study and represents an area worthy of further investigation.

The average values obtained for CEmax are of great practical interest since they can be used as guidelines in developing practical signal-processing strategies for C–V intensity ratio adjustment. It is significant to note that, with the exception of the weak fricatives, the average value of CEmax did not vary substantially within consonant classes, although there was a significant variation as a function of audiogram configuration and, to a lesser extent, vowel environment. The magnitude of these variations are shown in Figs. 7 and 8.

The values obtained for CEmax, as illustrated in these diagrams, suggest that a practical, approximate method of

adjusting the C–V intensity ratio would be to use the average values of CEmax obtained for the different consonant classes and vowel environments (as estimated from an analysis of the acoustic speech signal) and then to make subsequent adjustments when fitting the hearing aid depending on the subject’s audiogram configuration and tolerance levels. An important caveat at this stage is to bear in mind that all data in this investigation relate to nonsense syllables and not to continuous speech. Experimental investigations are still needed to determine the improvements in speech understanding that can be achieved with individualized adjustment of C–V intensity ratios in continuous speech.

It is interesting to note that for certain consonant classes, the value of CEmax raised the consonant level above that of the vowel. For example, the average C–V intensity ratio for /ʃ/ in the unprocessed condition is -11.1 dB, whereas the average value of CEmax for this consonant is 14.3 dB. Thus on average, the level of /ʃ/ was raised above the level of the vowel by 3.2 dB. Taking individual differences into account, there were many instances in which the level of /ʃ/ was substantially higher than that of the vowel. For example, CEmax for subject 2 of the flat audiogram group was 21.6 dB for /iʃ/. The unprocessed C–V intensity ratio for this nonsense syllable (see Table I) was -9.5 dB. This subject thus obtained a maximum recognition score for /ʃ/ in the /i/ vowel environment at a C–V intensity ratio of $+12.1$ dB. Even greater C–V intensity ratios were obtained for those cases in which the subject exhibited a type 5 (increasing, no saturation) CE function. The latter situation occurred fairly frequently with /s/ (11 of the 18 subjects exhibited a type 5 CE function for this consonant).

Conventional methods of compression amplification can be quite effective in improving the C–V intensity ratio of weak consonants. However, increasing consonant levels above that of neighboring vowels requires a different form of compression amplification. In this respect, phonetically based compression amplification, such as that implicit in the adjustment of C–V intensity ratios, represents a fundamentally different form of compression amplification. The evidence presented in this paper indicates that this approach to compression amplification (e.g., approximating CEmax in a practical system) is worthy of further investigation.

ACKNOWLEDGMENTS

This research was supported by PHS Grant No. 5P50DC00178 from the National Institute on Deafness and Other Communication Disorders. We are grateful to Linda Ashour and Chris Oden for their help in the preparation of this paper.

- Bennett, C. A., and Franklin, N. L. (1954). *Statistical Analysis in Chemistry and the Chemical Industry* (Wiley, New York), Sec. 6.32.
- Bishop, Y. M., Fienberg, S. E., and Holland, P. W. (1975). *Discrete Multivariate Analysis—Theory and Practice* (MIT, Cambridge, MA).
- Braida, L. D., Durlach, N. I., Lippman, R. P., Hicks, B. L., Rabinowitz, W. M., and Reed, C. M. (1979). *Hearing Aids: A Review of Past Research on Linear Amplification, Amplitude Compression, and Frequency Lowering*, ASHA Monograph No. 19 (American Speech-Language-Hearing Association, Rockville, Maryland).
- Cox, R. M. (1983). “Using MCL measures to find frequency/gain and SSPL 90,” *Hearing Instrum.* **34** (7), 17–39.

- Davis, H., Stevens, S. S., Nichols, R. H., Hudgins, C. V., Peterson, G. E., Marquis, R. J., and Ross, D. A. (1947). *Hearing Aids—An Experimental Study of Design Objectives* (Harvard U. P., Cambridge, MA).
- Dirks, D. D., and Kamm, C. (1976). "Psychometric functions for loudness discomfort and most comfortable loudness levels," *J. Speech Hear. Res.* **19**, 613–627.
- Dubno, J. R., and Levitt, H. (1981). "Predicting consonant confusions from acoustic analysis," *J. Acoust. Soc. Am.* **69**, 249–261.
- Dunn, J. (1993). "A study of consonant confusions in a group of cochlear impaired individuals demonstrating rollover," Doctoral Dissertation, City University of New York, New York.
- Eisenhart, C. S. (1947). "Inverse sine transformation of proportions," in [edited by C. Eisenhart, M. W. Hastay, and W. A. Wallis] *Selected Techniques of Statistical Analysis* (McGraw-Hill, New York), pp. 395–416.
- Freyman, R., and Nerbonne, G. (1989). "The importance of consonant-vowel intensity ratio in the intelligibility of voiceless consonants," *J. Speech Hear. Res.* **35**, 524–535.
- Griffith, J. D. (1967). "Rhyming minimal contrasts: A simplified diagnostic articulation test," *J. Acoust. Soc. Am.* **42**, 236–241.
- Gordon-Salant, S. (1986). "Recognition of natural and time/intensity altered CV's by young and elderly subjects with normal hearing," *J. Acoust. Soc. Am.* **77**, 664–670.
- Gordon-Salant, S. (1987). "Effects of acoustic modifications on consonant recognition by elderly hearing-impaired subjects," *J. Acoust. Soc. Am.* **81**, 1199–1202.
- Hecker, M. H. L. (1974). "A study of the relationship between consonant-vowel ratios and speaker intelligibility." Unpublished doctoral dissertation, Stanford University, Palo Alto.
- House, A. S., William, C. E., Hecker, M. H. L., and Kryter, K. D. (1965). "Articulation-testing methods: Consonantal differentiation with a closed-response set," *J. Acoust. Soc. Am.* **37**, 158–166.
- Levitt, H. (1991). "Signal processing for sensory aids: A unified view," *Am. J. Otol.* **12**, 52–55.
- Levitt, H., and Resnick, S. B. (1978). "Speech reception by the hearing-impaired: Methods of testing and the development of new tests," *Scand. Audiol.* **6**, 107–129.
- Margulies, M. K. (1980). "Effects of talker differences on speech intelligibility in the hearing impaired," Doctoral dissertation, City University of New York, New York.
- Montgomery, A. A., and Edge, R. A. (1988). "Evaluation of two speech enhancement techniques to improve intelligibility for hearing impaired adults," *J. Speech Hear. Res.* **31**, 386–393.
- Moore, B. C. J. (1987). "Design and evaluation of a two-channel compression hearing aid," *J. Rehab. Res. Develop.* **24** (4), 181–192.
- Neuman, A. C., Bakke, M. H., Hellman, S., and Levitt, H. (1994). "The effect of compression ratio in a slow-acting compression hearing aid: Paired-comparison judgments of quality," *J. Acoust. Soc. Am.* **96**, 1471–1478.
- Olsen, W., and Noffsinger, D. (1974). "Comparison of one new and three old tests of auditory adaptation," *Arch. Otolaryngol.* **99**, 94–99.
- Owens, E., and Schubert, E. D. (1977). "Development of the California Consonant Test," *J. Speech Hear. Res.* **20**, 463–474.
- Peterson, M. E., Feeney, P., and Yantis, P. A. (1990). "The effect of automatic gain control in hearing-impaired listeners with different dynamic ranges," *Ear Hear.* **11**, 185–194.
- Picheny, M. A., Durlach, N. I., and Braidia, L. D. (1985). "Speaking clearly for the hard of hearing. I: Intelligibility differences between clear and conversational speech," *J. Speech Hear. Res.* **28**, 96–103.
- Picheny, M. A., Durlach, N. I., and Braidia, L. D. (1986). "Speaking clearly for the hard of hearing II. Acoustic characteristics of clear and conversational speech," *J. Speech Hear. Res.* **29**, 434–446.
- Revoile, S. G., Holden-Pitt, L., Edward D., and Pickett, J. (1986a). "Some rehabilitative considerations for future speech-processing hearing aids." *J. Rehab. Res. Dev.* **23**, 89–94.
- Revoile, S. G., Holden-Pitt, L., Pickett, J., and Brandt, F. (1986b). "Speech cue enhancement for the hearing impaired: I. Altered vowel durations for perception of final fricative voicing," *J. Speech Hear. Res.* **29**, 240–255.
- Revoile, S. G., Holden-Pitt, L., Edward, D., Pickett, J. M., and Brandt, F. (1987). "Speech-cue enhancement for the hearing-impaired: Amplification of burst/murmur cues for improved perception of final stop voicing," *J. Rehab. Res. Dev.* **24**, 207–216.
- Salmon, R. D. (1970). "Talker variation as related to intelligibility," CSL/ONR Tech. Report 31, Communication Sciences Laboratory, University of Florida, Gainesville, Fla.
- Studebaker, G. (1985). "A 'rationalized' arcsine transform," *J. Speech Hear. Res.* **28**, 455–462.
- Weiss, M. S. (1968). "A study of the relation between consonant-vowel amplitude ratio and talker intelligibility," Unpublished M.S. Dissertation, Purdue University.
- Williams, C. E., Woods, B., Hecker, M. H. L., and Stevens, K. N. (1966). "Consonant-vowel ratio and speaker intelligibility," *J. Acoust. Soc. Am.* **39**, 1257(A).

Using joint geometry to determine the motion of the cricoarytenoid joint

W. Scott Selbie

Voice and Speech Section, National Institute on Deafness and Other Communication Disorders,
10 Center Drive, MSC 1416, Bethesda, Maryland 20892-1416

Lei Zhang and William S. Levine

Department of Electrical Engineering, University of Maryland, College Park, Maryland 20742

Christy L. Ludlow

Voice and Speech Section, National Institute on Deafness and Other Communication Disorders,
10 Center Drive, MSC 1416, Bethesda, Maryland 20892-1416

(Received 12 August 1995; accepted for publication 6 November 1997)

Facet surfaces of the cricoarytenoid joints from two cadaver larynges were digitized. The data were used to compute the optimal axis of rotation for each of the joints in the sense that the computed axis minimized the variance of the joint gap over the full range of joint motion. The optimal axis corresponded to a rocking motion of the arytenoid on the corresponding cricoid. This motion was consistent with experimental data from digitized recordings of vocal fold movement. Using the rigid laryngoscopic view, a similarity in vocal process movement, over the range in motion, between the rocking axis and the vertical axis described in the literature was found, resolving the controversy between two conflicting views of motion of the vocal processes. © 1998 Acoustical Society of America. [S0001-4966(98)04902-9]

PACS numbers: 43.70.Aj, 43.70.Bk [AL]

INTRODUCTION

The functions of the human larynx, respiration, voicing, and protection of the airway require precise control of glottal opening and closing. Control of the glottal opening is constrained principally by the properties of the cricoarytenoid joints. The goal of this research was to develop a simple yet realistic three-dimensional biomechanical model to describe the motion of the cricoarytenoid joint quantitatively.

Considerable effort by many investigators have addressed the biomechanics of the cricoarytenoid joint (Fink, 1975). However, some question remains as to how the joint works because it is difficult to obtain precise three-dimensional motion data from an intact larynx. Joint motion has been interpreted using the different experimental modalities of endoscopy, joint anatomy, joint facet structure, *in vivo* tomography, and analysis of movement imposed on cadaveric tissue.

Laryngeal movements are most commonly viewed from an endoscope situated within the posterior pharynx. From this superior vantage point, the laryngeal cartilages are completely enveloped by tissues. The low contrast of the visible surfaces produces a perception of the motion as mostly two dimensional. From this perspective, the vocal processes are seen to rotate about an axis through the line-of-sight of the endoscope. This axis has been described as a "vertical" axis (Gray, 1980).

Qualitative anatomical studies have suggested that the dominant motions of the arytenoid cartilages are a rocking motion about and sliding along the longitudinal axis of the cricoid facet (von Leden and Moore, 1961; Maue and Dickson, 1971; Fink and Demarest, 1978). Sonesson (1959) described the cricoarytenoid joint as a cylinder joint with its

long axis coincident with the longitudinal axis of the cricoid facet. He suggested that the arytenoid rocks around this axis, with a very limited sliding motion along this axis. Von Leden and Moore (1961) described the cricoarytenoid joint as a shallow ball and socket joint with two principal types of motion: an inward and outward rocking, and a lateral and medial sliding. They also suggested that a very limited rotary motion might be possible.

The properties of the cricoarytenoid (CA) joint have also been inferred from the arrangement of the collagen fibers on the articular surfaces of the cricoarytenoid joint (Kahane and Kahn, 1986). The collagen fibers on the articular surface of the arytenoid cartilages were orientated orthogonal to the collagen fibers on the articular surface of the cricoid cartilage. The authors concluded that the orientation of the collagen fibers supported a "rocking" axis because the orientation of the collagen fibers reinforces the articular surfaces along the path of CA joint motion associated with "rocking."

Ardran and Kemp (1966) presented tomographic observations in living subjects demonstrating that the arytenoid cartilage rocked on the cricoid facet during movements of the vocal folds. Although these authors measured the CA joint *in vivo* the data were not quantified and could not be used for biomechanical modeling.

Several studies have examined the motion of the CA joint from cadaveric tissue. Frable (1961) photographed a cadaveric larynx stripped of muscle. The movements of the arytenoid were produced by pulling on strings attached to the cartilage. A mirror was placed in the field of view of the camera to determine the three-dimensional motion. Although an equation was provided to describe the plane of rotation

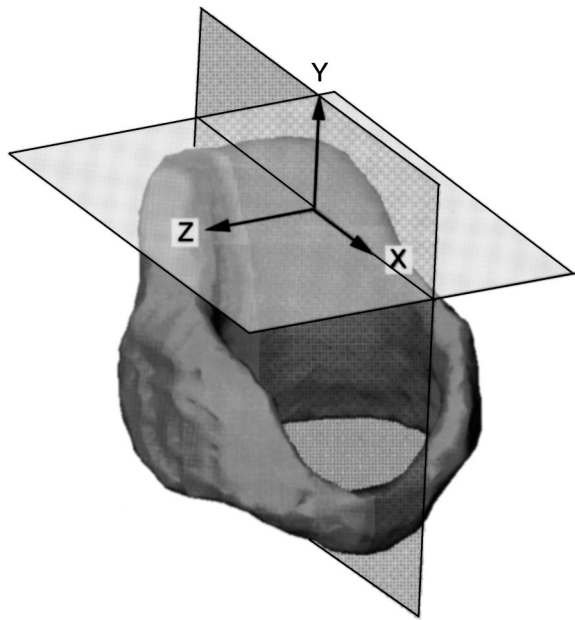


FIG. 1. A reconstructed 3-D model of the cricoid cartilage (M1) displaying the coordinate system defined by the plane of symmetry through the cricoid cartilage.

for the CA joint, a definition of the coordinate system by which the parameters of the equation could be interpreted was not provided.

Sellars and Keen (1978) dissected the joints of 45 larynges and found 3 types of movement of the arytenoid cartilages during adduction: inward rocking, sliding up the slope of the cricoid facet, and twisting to bring the vocal processes together. Sellars and Vaughan (1983) then collected three-dimensional arytenoid movement data from dissected larynges and calculated the principle axes of motion for rocking, sliding, and twisting. The motion of the CA joint was produced by moving a forceps attached to the arytenoid cartilage. The removal of the intrinsic musculature, leaving only the ligaments and joint capsule, and the unquantified applied forces render their results difficult to use for biomechanical modeling.

Neuman *et al.* (1994) calculated the helical axis of rotation from successive 3D CT images of a cadaveric larynx. Vocal fold adduction was achieved by placing a suture at the muscular process of cadaveric larynges and applying tension to it. Because the direction and magnitude of the applied forces were not quantified, and the movements were not verified by *in vivo* motion data, their application for model development is limited.

This paper presents a different approach to quantifying the motion at the cricoarytenoid joint—a quantitative anatomical approach. The dimensions of the joint facets have been reported. Frable (1961) and Maue and Dickson (1971) measured the width and length of the joint facets for both the cricoid facet and the arytenoid facet. Sellars and Keen (1978) measured the dimensions of the cricoid facet, which included the length, breadth at three different points, and arc length at three different points. Neither of these studies provided the necessary data on the articular surfaces, however, for developing a biomechanical model.

The purpose of this study was (1) to measure points on the surfaces of the cricoarytenoid joint facets, (2) to identify the anatomically optimal axes of arytenoid rotation, and (3) to compare vocal process trajectories produced by the resultant axes with observed kinematic data.

A coordinate system, determined quantitatively from the anatomy of the cricoid cartilage, was used to specify the parameters of the CA joint. The data explain the apparent dichotomy of the joint axis rotating about a “vertical” axis versus “rocking” about an oblique axis. Anatomical studies have claimed to reject the theory that the cricoid rotated about a vertical axis because the cricoarytenoid joint facet is roughly ellipsoidal, and the long axis of the ellipse is not vertical (Sawashima, 1974). Rotation about a vertical axis would therefore sublux the joint. The results of this study demonstrate a congruence between the rotation and rocking axis if one assumes that the “vertical” axis is actually an axis along the line of sight of an endoscope.

I. MEASUREMENT AND RECONSTRUCTION OF THE CARTILAGES AND JOINTS

A. Methods

1. MRI scanning protocol

Larynges were excised from two male (67 and 70 years old) fresh frozen cadavers. The specimens were fixed in 5% formalin, secured rigidly, and oriented axially inside acrylic cylinders. Each of these cylinders was inserted into a 2.5-in. (63.5-mm)-i.d. search coil and scanned with a 2.0-Tesla Omega Scanner (GE-NMR Instruments, Fremont, California) using a TR of 200 and a TE of 6.7. A 3-D Fourier transform acquisition was used to produce isotropic resolution. One larynx (M1) was scanned at a voxel resolution of (256×256) pixels for 128 slices over a field of view of (90×90×45 mm) yielding cubic voxels with 0.35-mm sides. The other larynx (M2) was scanned at a voxel resolution of (128×128) pixels for 256 slices over a field of view of (55×55×110) yielding cubic voxels with 0.43-mm sides.

2. Segmentation of scanned cartilages

The voxels comprising each cartilage were segmented from the MRI volume manually using VoxelView_ULTRA (Vital Images, Inc., Fairfield, Iowa). An enveloping polygonal surface for each cartilage was implemented (Edelsbrunner and Mucke, 1994).

The orientation of the larynx was specified in a coordinate system attached to the cricoid cartilage (Fig. 1). We have adapted Broad’s (1968b) definition of a coordinate system for the larynx in order to quantify the axes with respect to our anatomical data. The ($x-y$) plane was defined by the sagittal plane of symmetry. The ($x-z$) plane was defined parallel to the plane where the airway luminal opening was maximum through the cricoid cartilage. We have chosen not to define this plane relative to a line through the cricothyroid joints as in Broad (1968b) because the joint is not well-defined in the MRI images. Both the ($x-y$) and ($x-z$) planes were determined using an optimization algorithm developed for this purpose. The origin of the coordinate system was placed at the center of the airway opening in the $x-z$

plane at the level of the most superior point on the cricoid cartilage. The x axis was directed anteriorly, the y axis was directed rostrally, and the z axis was directed to the right. In Sec. III this coordinate system becomes more similar to Broad's (1968b) when it is rotated so that the $(x-z)$ plane is perpendicular to the line-of-sight of the camera in order to compare the model predictions to laryngoscopic data. Because the line-of-sight is determined subjectively (Broad, 1968b) we first defined a coordinate system based exclusively on quantitative anatomical data.

3. Joint surface measurement

The larynges were removed from the cylinders and dissected. All contiguous soft tissue was removed. The cricoarytenoid joint facets from both sets of cartilages were then digitized with a milling machine [ACER ULTIMA-3VK Vertical Turret Milling Machine with ACU-RITE Mill-Mate $(x-y)$ axis digital readout]. Note that the $(x-y-z)$ coordinate system of the milling machine is not the same as the $(x-y-z)$ coordinate system for the larynx. This difference in coordinate systems is accommodated during the fitting of the joint surface to the MRI segmented surface. The resolution of the mill table is 0.025 mm in each direction. The repeatability with which the mill table could be returned to a given position was 0.005 mm in each of the horizontal directions and 0.02 mm in the vertical direction.

The cartilage was mounted on an aluminum cylinder, clamped in the dividing head mounted on the mill table, with the facet exposed to an indicator (Stimulator, John O. Butler Company) inserted into the mill's tool chuck. The cartilage was held in place by inserting two pins into it. The diameter of the pins was negligible compared to the size of the cartilage. The pins did not pass through the joint facets to prevent damage to the joint surface. The 3-D coordinates of the contact point were determined by moving the mill's table so that the indicator's tip was in contact with the joint facet. The x and y axes corresponded to the horizontal directions of the mill table and the z axis was the vertical direction. Data were collected with respect to a $(y-z)$ grid. The indicator made contact with the cartilage along the x axis because the repeatability of the mill in the horizontal directions was better than in the vertical direction. The dividing head was used to rotate the cartilage whenever necessary to allow the indicator to contact the cartilage. On each facet, 150–250 points were measured. The points were not evenly spaced; the distance between them varied from 0.127 mm to 0.381 mm. Fewer points were measured in the areas of least curvature.

The accuracy of the procedure depended on identifying the contact point between the tip of the indicator and the cartilage surface. Several steps were taken to minimize the human error. First, the visibility of the contact area was improved by using high intensity lighting and positioning the cartilage at the best viewing angle by using the dividing head to allow rotation. Second, each point was measured several times to make certain the readings were repeated within 0.075 mm. Third, the experiment was performed by two people. The first one operated the milling machine and determined the contact. The second person recorded the data

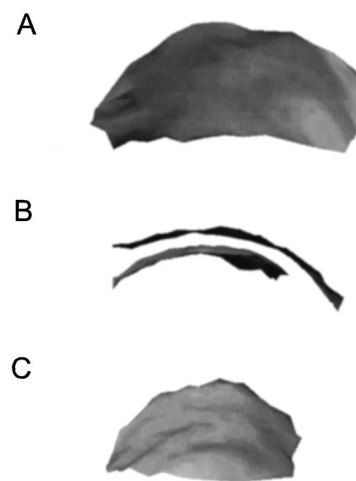


FIG. 2. A. The reconstructed cricoid joint facet (M1-RHS); B. the reconstructed cricoarytenoid joint facets (M1-RHS); C. the arytenoid joint facet (M1-RHS).

after a contact was declared. The second person also determined whether a measurement should be repeated or whether a smaller step size should be taken.

To estimate the error, 16 randomly selected points on the joint surfaces (6 on the cricoid facet, 10 on the arytenoid facet) were measured 10 times. For each point, two out of three coordinates of the mill table were fixed, the table was moved along the third direction (x axis) until the tip of the indicator touched the cartilage surface, then the reading of this x value was recorded.

4. Reconstruction of the joint surface

A 3-D triangular mesh was generated by connecting the joint surface data points (Fig. 2). The surface normal vector (a unit vector perpendicular to the surface) at each vertex of the triangular mesh was calculated by averaging all the normal vectors of the surface triangles sharing the same vertex.

5. Alignment of digitized surface with cartilage images

To orient the joint surfaces with the reconstructed images from the MRI scan, landmark points on the surface of the cartilage were digitized along with the joint surfaces. Landmark points were measured on the posterior-superior surface of the cricoid cartilage, on the anterior-superior surface of the cartilage and on each lateral side (Fig. 3). On the arytenoid, two landmark points were measured, one at the tip of the apex and the other at the tip of the muscular process.

The facet pictures were aligned with the reconstructed cartilage image manually using an interactive graphics program. The landmark points had been marked on the cartilage before digitizing the joint surface, but could not be marked on the cartilage reconstructed from the MRI scan. Because there was no absolute reference between the two data sets, the "fit" between them was an approximation. The position of the joint surface picture (as constructed from the digitized joints) was adjusted manually until all the landmark points were judged to be at homologous locations on the cartilage (Fig. 3).

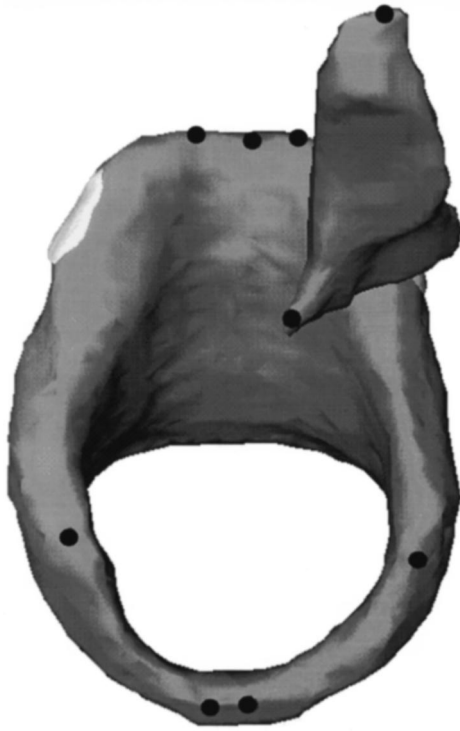


FIG. 3. The reconstructed model of the cricoid and one arytenoid cartilage displaying the landmark points used to align the articular facets.

B. Results

Figure 2 reveals the curved shape of the two surfaces. Looking directly along the long axis of the surfaces the two surfaces appear to be small arcs of concentric ellipses but it is not possible to measure accurately if they are concentric circles. It is necessary to have an arc length greater than 90 degrees in order to fit a circle accurately. However, this image, and that of the other three joints, lends credence to the approximation of the cricoarytenoid joint as concentric circles even if the small arc length precludes mathematical verification.

Measurement errors in the digitization procedure came from two sources: (1) equipment error (the resolution of the milling machine), and (2) human error when judging the contact between the indicator and the cartilage surface. The machine's backlash was eliminated automatically by using a digital readout. The resolution of the mill was 0.025 mm (approximately 10% of the mean distance between two points).

The results of the repeated measures of selected points described in Sec. I A 3 are presented in Table I. The mean absolute difference and the standard deviations were calculated using all the data for the right facets (Wall, 1986). The

average length of the cricoid joint surfaces was 6.2 mm, and the width was 4.1 mm, similar to those reported by Frable (1961) and Mori *et al.* (1990), and which implied that the errors were less than 1% of the facet dimension. The worst case error was within 2%.

The measurement of the cricoid facet was more accurate than that of the arytenoid facet because the joint surface of the cricoid cartilage is convex, making it easier to identify contact.

II. DETERMINATION OF OPTIMAL JOINT AXES

A. Rationale

From the close apposition and conformity in shape of the cricoid and arytenoid articular facets, we assumed that the alignment of the facets throughout the range of joint motion determined the joint properties (Fig. 2). As a first approximation, the arytenoid rotates about an axis that could be determined quantitatively as an optimal axis defined with respect to the relative apposition of the joint surfaces during movement. The measure of the performance of a joint was defined as the variation in distance between the joint surfaces over the range of joint motion. This criterion was established on the basis that joints generally dissipate less energy and cause less stress on the facets while operating if the joint gap is a more uniform surface (Armstrong-Helouvy *et al.*, 1994; Hamrick, 1986). Even variations in the joint gap that are too small to cause jamming will, nonetheless, waste energy by squeezing lubricant into or out of the gap or by distorting the joint.

B. Methods

1. Axis description

Each joint axis of rotation was represented by a straight line in 3-D space that was defined by the intersection of two planes (Fig. 4). Any line which did not lie in a plane parallel to the $x-z$ plane could be defined uniquely by the intersection of these two planes using four parameters (k_x, d_x, k_z, d_z):

$$\begin{aligned} x &= k_x y + d_x, & -\infty < k_x, d_x < \infty, \\ z &= k_z y + d_z, & -\infty < k_z, d_z < \infty. \end{aligned} \quad (1)$$

The orientation or slope of the planes is determined by parameters k_x and k_z . Parameters d_x and d_z determines the intersection of the planes with the y axis. Assuming that the axis did not lie in the $x-z$ plane simplified the description of the axis. This assumption is clearly satisfied for the axes proposed in the literature but it can readily be determined if

TABLE I. Measurement differences of the digitization procedure for joint M1-RHS.

Joint surface	Number of distinct data points measured	Number of measurements per point	Mean absolute difference (mm)		Range of differences (mm)
			Mean absolute difference (mm)	s.d. (mm)	
Cricoid	6	10	0.014	0.020	-0.038 to 0.064
Arytenoid	10	10	0.027	0.036	-0.094 to 0.084
Combined	16	10	0.022	0.031	-0.094 to 0.084

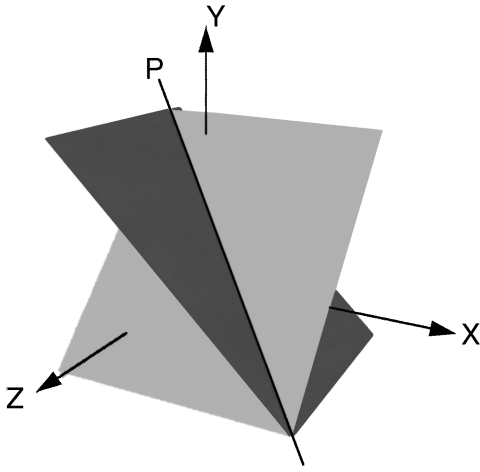


FIG. 4. The axis of rotation (P) of the cricoarytenoid joint is represented as a line defined by the intersection of two planes.

the algorithm was converging to a solution parallel to the $x-z$ plane.

2. Cost function for the optimization

In order to calculate an optimal axis it was necessary to define a precise scalar measure of the uniformity of the joint gap.

The cricoid facet consisted of N_c discrete vertices. For each arytenoid position, the joint gap to the cricoid was measured as the length along the normal vector (r_{ki}) to the cricoid facet (positive if outward and negative if inward) to the intersection with a polygon of the arytenoid facet. If no intersection occurred, then no value was given for the joint gap at that vertex and position. The total number of cricoid vertex normals that intersected the arytenoid facet for one posture was N_k :

$$\text{average joint gap: } \bar{r} = \frac{1}{N} \sum_{k=0}^K \sum_{i=0}^{N_k} r_{ki}; \quad (2)$$

$$\text{number of measurements: } N = \sum_{k=0}^K N_k. \quad (3)$$

The joint gap at each cricoid data point was determined for a range of motion of the arytenoid, from an angle θ_0 to θ_k , about a given joint axis of rotation. This angular range was discretized into $K+1$ values, with $\theta_k = \theta_0 + k\Delta\theta$, $k = 0, 1, \dots, K$. In each case, one of the θ_k 's was the original alignment of the facets. Each value of k determined one position of the arytenoid. The joint gap (r_{ki}) was determined for each of the N_k cricoid vertices at each of the $k+1$ arytenoid angles.

The optimal joint axis of rotation was the one that minimized the variance in the joint gap (Φ) and penalized for joint surface intersections ($\hat{\Phi}$), throughout the range of motion of the joint:

$$\begin{aligned} \text{Variance: } \Phi &= \Phi(k_x, d_x, k_z, d_z) \\ &= \frac{1}{N-1} \sum_{k=0}^K \sum_{i=0}^{N_k} (r_{ki} - \bar{r})^2. \end{aligned} \quad (4)$$

Anatomical feasibility required that the joint would not dislocate and the cartilages would not jam when the arytenoid rotated around this axis within the normal range of motion. By minimizing the variance (Φ), a joint axis could be determined which produced the most uniform gap while the arytenoid rotated through its range of motion. This would not guarantee, however, that there was no interdigitation between the two surfaces. To penalize for interdigitation, the cost function ($\hat{\Phi}$) included the penalty for intersection:

$$\begin{aligned} \text{cost function: } \hat{\Phi} &= \hat{\Phi}(k_x, d_x, k_z, d_z) \\ &= \frac{1}{N-1} \sum_{k=0}^K \sum_{i=0}^{N_k} (\hat{r}_{ki} - \bar{r})^2, \end{aligned} \quad (5)$$

where

$$\begin{aligned} \hat{r}_{ki} &= r_{ki} \quad \text{if } r \geq 0, \\ \hat{r}_{ki} &= 100r_{ki} \quad \text{if } r \leq 0. \end{aligned}$$

The range of motion was determined from the overlap of the facts. The extreme postures in the range of motion were set at 33% of the arytenoid polygons being intersected by normals from the cricoid facet. This range was likely an overestimate of the physiological range of motion (Frale, 1961) but the larger range of motion was determined to be better for mathematical convergence of the algorithm.

3. Computer algorithm for solving the optimization problem

The optimal solution was calculated using a nonlinear simplex method (Press *et al.*, 1988). The computations required the range of positions of the joint surfaces and initial parameter values for the axis parameters (k_x, d_x, k_z, d_z). The range of movement of the arytenoid facet with respect to the cricoid facet varied with the axis of rotation. For example, the more distant the axis from the joint, the smaller the range in angle for a given range of relative movement. Through trial and error the number K was kept about the same number of steps.

The cost function ($\hat{\Phi}$) was constructed from the measured data, i.e., no smoothing of any kind was performed on the data. The characteristics of the cost function ($\hat{\Phi}$) near the solutions were also studied by plotting ($\hat{\Phi}$) versus a series of values for each of the parameters (Fig. 5A) and by plotting ($\hat{\Phi}$) versus a series of values for pairs of parameters (Fig. 5B). The lack of smoothness results in local minima. To eliminate anomalous solutions due to the lack of smoothness or to inherent noise in the data which sometimes caused the algorithm to identify convergence erroneously, all solutions were restarted after perturbing the parameters randomly. This process was repeated until there was no change in the optimal solution for three successive optimizations. A thorough search for locally optimal solutions that were not anomalous was conducted for joint M1 by choosing a variety of initial parameter guesses. Figure 5B displays a narrow flat valley near the minimum values. It was conjectured that varying four parameters simultaneously would reveal a similarly flat range of values near the minimum which resulted in the slow convergence we observed.

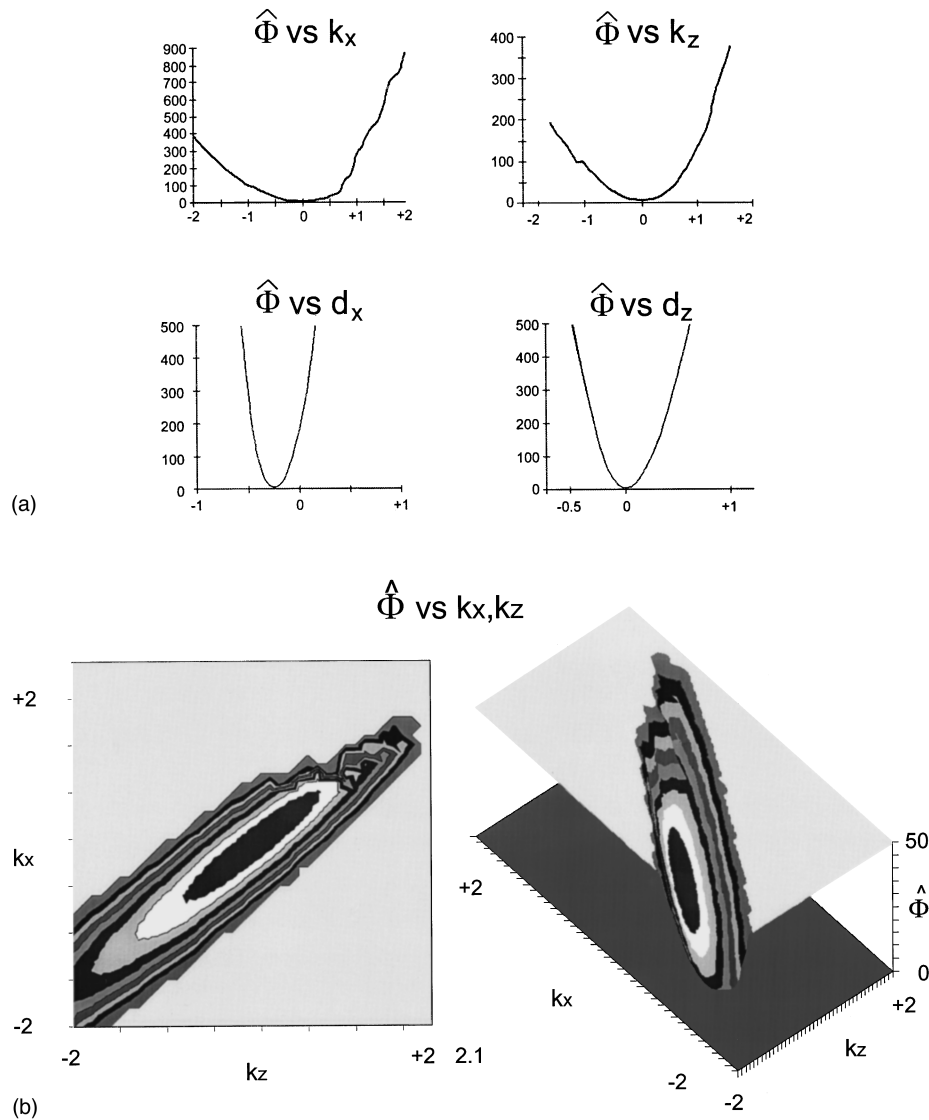


FIG. 5. A. The cost ($\hat{\Phi}$) versus each of the four parameters that define the joint. Note that a minimum is evident in each case but that several local minima exist; B. two views (top and oblique) of the cost ($\hat{\Phi}$) versus two parameters (k_x and k_z). Note the narrow flattened valley in which the optimum solution lies.

4. Sensitivity to alignment

Identifying the orientation of the joint facets from the MRI images was limited by the segmentation of the MRI images (in particular distinguishing the facet vertices from the synovial space) and by the spatial resolution of the MRI images ($M1=0.35$ mm and $M2=0.43$ mm) producing “fuzzy” boundaries. This was further complicated because the distance between the cricoid and the arytenoid surfaces was likely to be on the order of one voxel. A systematic test of the sensitivity of the optimal solution to the alignment of the joint facets was conducted by selecting a range of parameter values around the alignment selected visually.

The sensitivity of the analysis to the alignment of the joint facets with the MRI images was tested using a coordinate system derived from the locally optimal solutions already discovered (Fig. 6). The u axis is defined as an axis which modifies the joint gap (described precisely in a later section). The v axis is defined by the direction of the rocking

axis (as calculated). The w axis is defined by the other two axes:

$$\hat{w} = \hat{u} \times \hat{v}. \quad (6)$$

5. Joint gap

To test different joint gaps, an optimization process was designed to reduce the gap while maintaining the variance of the gap. The criterion was defined to locate the direction vector such that moving the facets closer along this direction maximally reduced the calculated gap with minimal changes in variance.

The unit direction vector \hat{u} can be defined by two parameters (a, b):

$$u_x = a, \quad u_y = b, \quad u_z = \sqrt{1 - (a^2 + b^2)}. \quad (7)$$

When moving a point (x_0, y_0, z_0) along the direction \hat{u} by amount Δ_d the resulting new position of the point is given by

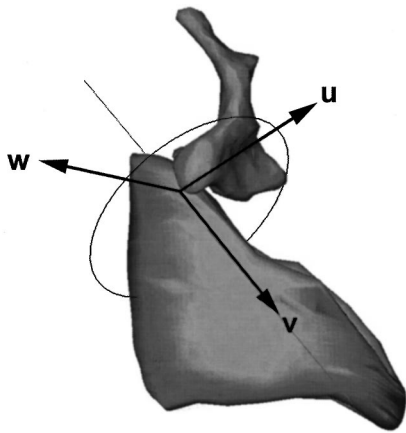


FIG. 6. Local reference frame (u, v, w) for the arytenoid facet relative to the cricoid facet. Note that V is the optimal axis and corresponds with rocking.

$$\begin{aligned} x_1 &= x_0 + u_x \Delta_d, \\ y_1 &= y_0 + u_y \Delta_d, \\ z_1 &= z_0 + u_z \Delta_d. \end{aligned} \quad (8)$$

A cost function different from that used above ($\hat{\Phi}$) was necessary because this was a different criterion. The optimal axis minimizes the cost function Ψ :

$$\begin{aligned} \Psi = \Psi(a, b) &= \frac{1}{N-1} \sum_{i=0}^{N_k} (r_i - \bar{r})^2 + 100.0(\Delta_d - \bar{r})^2 \\ &+ \max(0, a^2 + b^2 - 1)^2. \end{aligned} \quad (9)$$

The objective was to minimize the variance of the joint gap after moving the arytenoid cartilage and to also minimize the difference between the distance moved and the change in the average joint gap. Ψ was minimized using a nonlinear simplex method (Press *et al.*, 1988).

C. Results

The four joints have been classified as M1-RHS (cartilage male 1: right-hand side), M1-LHS (cartilage male 1: left-hand side), M2-RHS (cartilage male 2: right-hand side), and M2-LHS (cartilage male 2: left-hand side).

1. Locally optimal solutions

As a guide for selecting an appropriate joint gap for comparing the four sets of data, we checked the standard recommendation for the clearance limit in mechanical bearings. The clearance limits for loose-running fits between plain cylindrical parts recommended by the ANSI B4.1-1967 (R1979) standard is between 0.1 and 0.4 mm (Baldo, 1987). Because the cricoarytenoid joint surfaces do not fit as well as those in a mechanical bearing (see Fig. 2) the minimum gap tested was different for each cartilage. For this study we have selected a joint gap of 0.40 mm; near the high end of the range defined as a mechanical bearing gap (0.1–0.4 mm). We tested gaps within the ANSI standard and attempted in all joints to reduce the gap to a minimum.

The first series of tests for locally optimal solutions used the joint gap obtained from the alignment procedure. After several tests using a variety of initial guesses, the number of

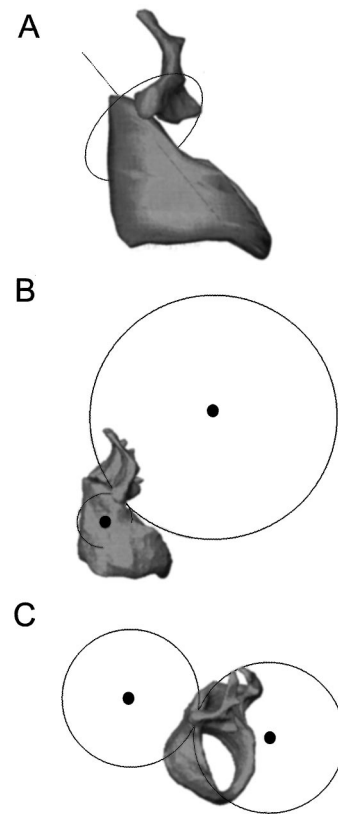


FIG. 7. The five locally optimal solutions for joint M1-RHS. Note that the rocking axis passes through the cricoid cartilage below the joint facet. The other four axes do not pass near the joint and within the vicinity of the joint, over a small range of motion, are all interpreted as manifestations of the “sliding” axis.

locally optimal solutions was reduced to five for M1-RHS, four for M2-RHS, and three for M1-LHS and M2-LHS (Fig. 7). The solution with the lowest performance criterion was consistent with the “rocking” axis described in the literature (Table II). Two axes were perpendicular to the rocking axis and located laterally (to right and left) and parallel to the axis used for reducing the joint gap. Two axes were parallel to each other, (one above and one below the joint) and perpendicular to the other three axes. The solutions other than the rocking axis could be viewed locally as a “sliding” movement of the joint.

For the sensitivity test we have focused on the joint M1-RHS as an example. The next several sections present the results only for this joint.

2. Range of motion

Several ranges of motion were tested. The first was an overestimate of the range based on 33% of the arytenoid polygons being intersected by cricoid normals. It was observed that the greater the range of motion, the better the optimization algorithm worked. The calculation was repeated for a different range of motion to see if the solution was sensitive to the range of motion. Note that the range of motion was different for the different locally optimal solutions. Table III(a) demonstrates that the optimal solution for the three axes common to all joints was not affected substantially by changing the range of motion. The solution corre-

TABLE II. Locally optimal solutions for all joints. Joint M1 had five locally optimal axes on the right side (rocking axis, vertical axis on the right side, vertical axis on the left side, horizontal axis above and horizontal axis below; see Fig. 7) and three locally optimal axes on the left side. Joint M2 had four locally optimal axes on the right side and three locally optimal axes on the left side. For all joints a gap of 0.4 mm was used.

	dx	dz	kx	kz	Optimization criterion ($\hat{\Phi}$) (10^{-3} mm ²)	avg gap (10^{-3} mm)	min gap (10^{-3} mm)
M1-RHS							
rock	-15.55	0.62	-1.25	-1.23	5.66	0.40	0.16
right	-20.35	25.07	0.08	0.95	7.08	0.40	0.16
left	16.70	-20.11	0.45	0.51	7.61	0.40	0.17
above	36.69	-42.22	-0.96	2.17	8.44	0.41	0.18
below	18.14	-188.51	3.01	-20.02	58.62	0.30	-0.43
M1-LHS							
rock	-14.72	-3.14	-1.13	0.64	16.48	0.40	0.03
right	-1.96	-1.53	-0.03	-1.16	33.13	0.41	0.00
left	-25.34	-33.93	0.60	-0.27	21.92	0.39	0.00
M2-RHS							
rock	-13.40	4.86	-0.70	-0.51	11.43	0.40	0.12
right	-27.72	32.65	-0.70	2.07	12.26	0.40	0.14
left	15.82	-26.43	0.89	-0.05	13.55	0.40	0.11
above	22.78	-30.50	0.06	1.18	11.45	0.54	0.26
M2-LHS							
rock	-14.72	-7.39	-1.20	0.29	12.85	0.41	0.10
right	-5.36	-4.73	0.48	-0.33	15.56	0.39	0.01
left	-20.56	-29.75	-1.02	-2.83	14.87	0.41	0.07

sponding to a horizontal axis about the joint was dramatically altered by reducing the range of motion and no solution could be found for the horizontal axis below the joint.

3. Joint gap

The optimal axis parameters were consistent across joint gaps for which there was no intersection for all parameter values for four of the locally optimal solutions [Table III(b)]. The values for the optimal axis of rotation were consistent across joint gaps provided the gap was not small enough to result in intersections between the surfaces. The minimum joint gap identified for any optimal axis gave an indication of the amount the gap can be closed before intersections occur. If the gap was set close to this minimum value the optimal axis changed [Table III(b)]. For a gap of 0.2 mm the optimal solution had the joint surface intersecting. This solution was quite different from the others. If the range of motion was decreased a solution consistent with the other gap was calculated.

The optimization criterion ($\hat{\Phi}$) was consistent between gaps (mean= 5.75×10^{-3} mm², s.d.=0.15) but increased with decreasing gap. The average distance over the range of motion was close to the average distance defined by the single posture used for closing the gap. With decreases in joint gap, there were commensurate decreases in the calculated average distance between the two surfaces.

4. Sliding

This translation had no effect on the “sliding” solutions except to modify the start and end angles for the calculation

[Table III(c)]. For the “rocking” axis the cost function was increased substantially but the parameter values changed only modestly.

5. Perpendicular to “sliding” and “rocking”

Moving along an axis perpendicular to the sliding axis had only a modest effect (Fig. 3D). However, at the point at which the two surfaces intersected the solution did not converge.

6. Rotating the facets about the gap axis

The rotation of the facets about the gap axis had a dramatic effect [Table III(e)]. For a perturbation of -0.2 and 0.5 rad there was a substantial change in the solution.

7. Rotating the facets about the perpendicular axis

Perturbing the facets about the perpendicular axis had a dramatic effect on the solutions [Table III(f)].

D. Discussion

It was conjectured that the properties of the cricoarytenoid joint were constrained by the static geometry of the articular facets. It was possible to identify three locally optimal axes for all four joints. One of these axes corresponded to the “rocking” axis defined in the literature. The other two solutions were all interpreted as describing the “sliding” axis defined in the literature. The results listed in Table II corresponded to feasible rotation axes of the arytenoids in terms of the joint articular surfaces.

No assumptions were made about the shape of the joint facets, because rotation about a single axis requires only that

TABLE III. Results from joint M1-RHS demonstrating the changes in the optimal solution caused by perturbing either the range of motion or the alignment of the joint facets.

(a) Range of motion is defined by the range of angles θ_0 to θ_k .

M1-RHS	dx	dz	kx	kz	θ_0	θ_k	Optimization criterion ($\hat{\Phi}$) (10^{-3} mm ²)	avg gap (10^{-3} mm)	min gap (10^{-3} mm)
rocking	-15.55	0.62	-1.25	-1.23	-80	50	5.66	0.40	0.16
rocking	-15.61	0.41	-1.25	-1.26	-40	25	5.72	0.40	0.16
rocking	-16.17	-0.63	-1.34	-1.44	-20	15	6.27	0.35	0.11
right	-20.35	25.07	0.08	0.95	-14	15	7.08	0.40	0.16
right	-21.24	26.25	0.13	0.90	-6	7	7.08	0.46	0.22
left	16.70	-20.11	0.45	0.51	-10	10	7.61	0.40	0.17
left	16.75	-20.22	0.45	0.50	-6	7	7.54	0.45	0.22
left	16.37	-19.77	0.46	0.49	-6	7	7.61	0.40	0.17
above	36.69	-42.22	-0.96	2.17	-10	10	8.44	0.41	0.18
above	20.43	-23.68	-0.13	1.21	-6	7	7.83	0.41	0.20

(b) Modifying the joint gap.

M1-RHS	Gap	dx	dz	kx	kz	Optimization criterion ($\hat{\Phi}$) (10^{-3} mm ²)	avg gap (10^{-3} mm)	min gap (10^{-3} mm)
rocking	0.45	-15.36	0.79	-1.22	-1.22	5.55	0.45	0.21
	0.4	-15.55	0.62	-1.25	-1.23	5.66	0.40	0.16
	0.35	-15.41	0.72	-1.20	-1.19	5.77	0.35	0.11
	0.3	-15.46	0.60	-1.21	-1.21	5.88	0.30	0.05
	0.25	-15.57	0.48	-1.23	-1.22	5.91	0.25	0.01
	0.2	-15.73	-0.53	-1.21	-1.36	7.83	0.21	-0.83
mean		-15.51	0.45	-1.22	-1.24	6.10		
s.d.		0.13	0.49	0.02	0.06	0.86		
Right	0.45	-21.54	26.53	0.07	0.97	6.92	0.45	0.21
	0.4	-20.35	25.07	0.08	0.95	7.08	0.40	0.16
	0.35	-21.41	26.23	0.09	0.93	7.09	0.35	0.11
	0.3	-21.39	26.13	0.11	0.91	7.06	0.30	0.06
	0.25	-22.92	27.25	0.15	0.87	6.70	0.25	0.03
	0.2	-21.81	25.77	0.29	0.70	6.96	0.21	0.00
mean		-21.57	26.16	0.13	0.89	6.97		
s.d.		0.83	0.73	0.08	0.10	0.15		
Left	0.45	16.80	-20.35	0.45	0.51	7.54	0.45	0.23
	0.4	16.70	-20.11	0.45	0.51	7.61	0.40	0.17
	0.35	16.89	-20.00	0.39	0.58	7.55	0.35	0.12
	0.3	16.74	-19.97	0.40	0.57	7.39	0.30	0.07
	0.25	17.33	-21.10	0.35	0.63	7.43	0.25	0.03
	0.2	19.24	-23.27	0.06	1.00	7.86	0.20	0.00
mean		17.28	-20.80	0.35	0.63	7.56		
s.d.		0.98	1.28	0.15	0.19	0.17		
Above	0.45	29.47	-34.53	-0.64	1.81	8.27	0.46	0.24
	0.4	36.69	-42.22	-0.96	2.17	8.44	0.41	0.18
	0.35	38.94	-44.77	-1.08	2.31	8.46	0.36	0.13
	0.3	31.63	-36.22	-0.74	1.91	8.21	0.31	0.08
	0.25	24.67	-29.67	-0.20	1.30	7.70	0.25	0.02
	0.2	41.43	-46.98	-1.11	2.33	8.30	0.21	0.00
mean		33.81	-39.06	-0.79	1.97	8.23		
s.d.		6.32	6.67	0.34	0.39	0.27		

(c) Perturbing the joint facets along a "sliding" axis (rocking).

M1-RHS	Perturbation (radians)	dx	dz	kx	kz	Optimization criterion ($\hat{\Phi}$) (10^{-3} mm ²)	avg gap (10^{-3} mm)	min gap (10^{-3} mm)
rocking	0.00	-15.55	0.62	-1.25	-1.23	5.66	0.40	0.16
rocking	0.50	-16.30	-0.01	-1.46	-1.52	17.57	0.33	-0.14
rocking	-0.50	-16.48	-1.03	-1.33	-1.34	14.52	0.58	0.30

TABLE III. (Continued.)

(d) Perturbing the joint facets along an axis perpendicular to the “rocking” and “sliding” axes.

M1-RHS	Perturbation (radians)	dx	dz	kx	kz	Optimization criterion ($\hat{\Phi}$) (10^{-3} mm ²)	avg gap (10^{-3} mm)	min gap (10^{-3} mm)
rocking	0.00	-15.55	0.62	-1.25	-1.23	5.66	0.40	0.16
rocking	0.10	-15.94	-0.08	-1.32	-1.36	5.59	0.44	0.20
rocking	0.20	-15.92	-0.30	-1.30	-1.38	5.75	0.43	0.19
rocking	0.50	-16.04	-0.52	-1.30	-1.37	6.44	0.40	0.16
right	0.00	-20.35	25.07	0.08	0.95	7.08	0.40	0.16
right	0.10	-22.07	27.19	0.08	0.95	7.06	0.44	0.20
left	0.00	16.70	-20.11	0.45	0.51	7.61	0.40	0.17
left	0.10	18.14	-22.68	0.46	0.48	7.80	0.43	0.19

(e) Rotating the facets about the gap axis (rocking axis).

Perturbation (radians)	dx	dz	kx	kz	Optimization criterion ($\hat{\Phi}$) (10^{-3} mm ²)	avg gap (10^{-3} mm)	min gap (10^{-3} mm)
0.00	-15.55	0.62	-1.25	-1.23	5.66	0.40	0.16
-0.20	-21.31	-10.63	-2.39	-3.44	9.34	0.44	0.08
0.20	-14.57	3.41	-1.05	-0.68	5.34	0.47	0.26
0.50	-13.36	6.16	-0.80	-0.12	14.89	0.47	0.12
0.70	-16.44	2.87	-1.54	-1.02	110.85	0.53	-5.59

(f) Rotating the facets about the perpendicular axis (rocking axis).

Perturbation (radians)	dx	dz	kx	kz	Optimization criterion ($\hat{\Phi}$) (10^{-3} mm ²)	avg gap (10^{-3} mm)	min gap (10^{-3} mm)
-0.05	-15.55	0.62	-1.25	-1.23	5.66	0.40	0.16
-0.20	-19.51	-0.97	-2.13	-1.73	449.54	0.17	-14.22
-0.10	-20.68	-4.30	-2.35	-2.35	9.75	0.35	0.05
0.20	-22.32	-14.39	-2.26	-3.50	32.28	0.64	0.22
0.30	-22.58	-15.05	-2.30	-3.51	65.41	0.74	0.21
0.50	-22.77	-16.39	-2.23	-3.36	183.82	0.94	0.06

the facets be matching surfaces of revolution. The algorithm required only the location of the polygons comprising each of the joint facets. Minimizing the variance in the gap seemed a sensible choice. It was assumed that the joint displayed properties that approximated an ideal joint. In choosing a representative model the first test calculated the fit of the anatomical data to those of an ideal joint (identified as having zero variation in the joint gap). If the rotation axis was constrained by the geometry, it would be unlikely that the dynamics would alter it substantially.

Rolling joints, such as the human knee or a tire on a road, are exceptions to this uniform gap condition but they do not have fixed axes of rotation. In this investigation, we assumed that the rolling action of the cricoarytenoid is negligible because the facets fit tightly together.

The characteristics of the cost function ($\hat{\Phi}$) near the solutions were also studied by plotting the 3-D surfaces and the 2-D contours obtained by varying two of the four parameters at a time. For example, Fig. 5A shows that the optimum value of each parameter was well-defined when the other three parameters were held constant, but that the minimum was more pronounced for some parameters than for others. Varying two parameters revealed a narrow flat valley near the optimal solution demonstrating why the algorithm observed a slow convergence.

Smoothing the joint surfaces prior to optimization could eliminate the local minimum points introduced by the lack of

smoothness of the cost function. This would have improved the speed of the optimization algorithm. However, because it was thought better to work as directly as possible with the data, the results were obtained without smoothing the joint surfaces.

The minimum joint gap for which a sensible solution could be found for joint M1-RHS was a joint gap of 0.25 mm. This minimum joint gap depends on the quality of the digitization and the quality of aligning the cartilage surfaces. It was not possible to use this small a joint gap for the other three joints. The optimal solution was not sensitive to very small perturbations but as the perturbations increased the cost function and axis parameters were dramatically altered. The extreme perturbations we tested were all identifiable visually and as such an error of this magnitude would not have been made in our manual alignment procedure.

III. TESTING MOTION HYPOTHESES USING VOCAL FOLD TRAJECTORIES

A. Rationale

An important test of an hypothesized axis of arytenoid rotation was to compare the trajectories of the vocal process produced by such a rotation with the trajectories recorded from a human larynx. Because the laryngoscopic data was

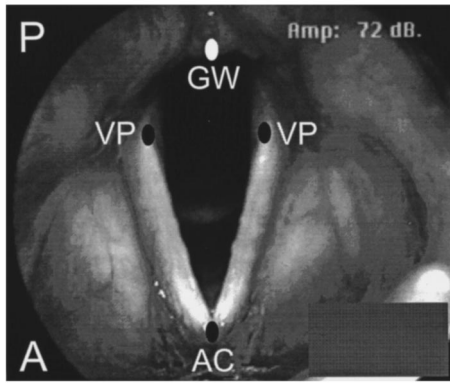


FIG. 8. View of larynx as seen by a 90-degree rigid laryngoscope (A=anterior, P=posterior). Four points were digitized: left and right vocal processes (VP), anterior commissure (AC), and posterior mid-glottic wall (GW).

two dimensional, it was necessary to project the three-dimensional arytenoid rotation into the laryngoscope viewing plane.

B. Methods

1. Movement data collection

The movement data was collected as part of another study (Cooke *et al.*, 1997). A rigid laryngoscope was passed transorally into the posterior pharynx to focus on the vocal folds. The laryngoscope was attached to a SVHS video camera (60 fields per second) videorecorder for analysis. Two normal voice onset gestures from the resting breathing position to vocal fold adduction for each of the ten subjects (five male, five female) were selected for comparison with the model trajectories.

Four sites in the field of view were digitized manually on each 60-Hz video field (Fig. 8): the location of each vocal process (VP), the location of the anterior commissure (AC), and the mid-point along the posterior glottic wall (GW). The data were rotated such that the vector from GW to AC was aligned along the x axis. The data were scaled to the distance between GW and AC.

2. Aligning the cartilages to the vocal fold movements

The coordinate system used for defining the joint axis of rotation was determined by calculating the symmetry of the cricoid cartilages. This coordinate system is not, however, consistent with the coordinate system in which the vocal fold trajectories were measured from the laryngoscope recordings. As suggested by Broad (1968a, b) we have transformed the cartilage coordinate system parallel to the plane of the laryngoscopic image and placed the origin coincident with the interior surface of the posterior glottic wall. Note that this coordinate system is not identical with the one proposed by Broad (1968a). To find the viewing plane onto which the 3-D trajectories of arytenoid motion determined from the joint model should be projected, the 3-D images of the cartilages reconstructed from the MRI were rotated on the computer screen until the laryngoscope viewing angle was obtained (Fig. 9). The angle between this viewing plane and the plane

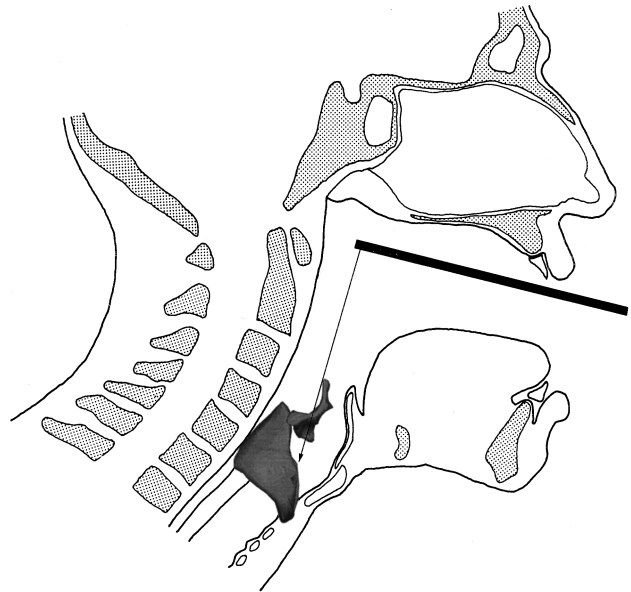


FIG. 9. A line drawing depicting the line of sight of the laryngoscope used for the endoscopy recordings (adapted from Broad, 1968b).

defined by the base of the cricoid was 25 degrees. Our projection was used in only a qualitative fashion as precise data on the projection of the superior tip of the arytenoid was not available.

C. Results

Figure 10 shows the movement trajectories of the arytenoid vocal processes obtained from video (sampled at 60 fields per second). Each trajectory is identified as a connected line. The model trajectories have been superimposed on the experimental data and were extended beyond the range of motion of the joint to identify these trajectories. Figure 10B displays the rocking axis and two of the sliding axes for joint M1-RHS. The “rocking” trajectories fit well with the experimental data while the trajectories for the other axes were reasonable only over a small range of motion.

D. Discussion

These results support the hypothesis that the arytenoid rocks around the longitudinal axis of the cricoarytenoid joint facet on the cricoid. A location and orientation of that axis was found (as the result of Sec. I) which produced a movement trajectory consistent with the recording. Given that the range of motion is different for the rocking and sliding it is likely that the predominant motion is rocking with limited sliding.

IV. DISCUSSION AND CONCLUSIONS

The results indicate that both sliding and rocking are anatomically feasible. The optimization results predict that the rocking axis better represents the relative motion of the surfaces than a rotation axis but the variance is similar enough to conclude that both motions are possible. The controversy described in the literature between a “rocking” axis and a “rotating” axis can be resolved by interpreting the

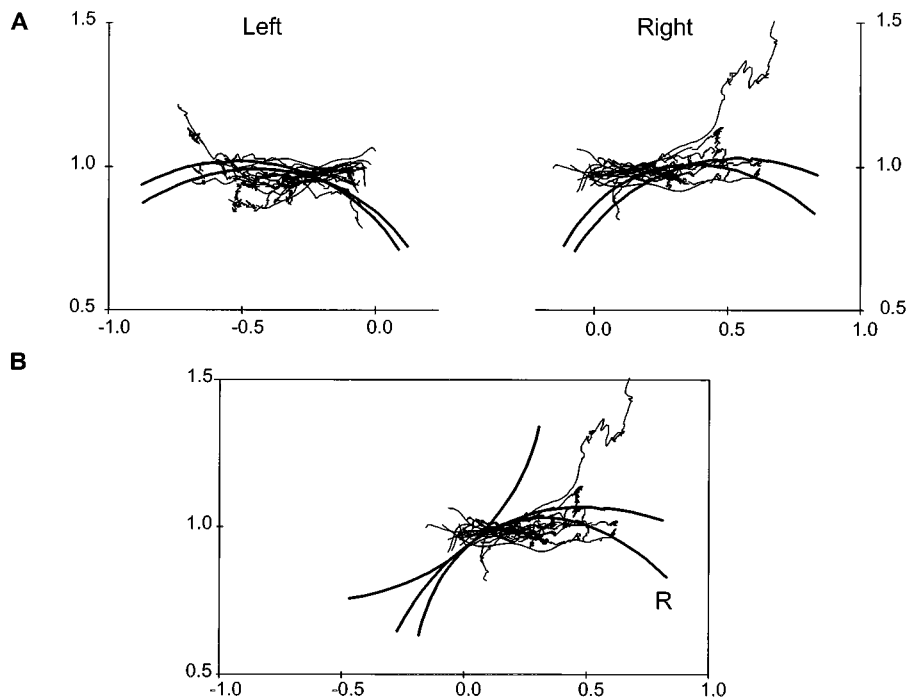


FIG. 10. Two experimental trajectories of the vocal processes, for each of the ten subjects, are indicated by lines. Data were scaled in both x and z to GW-AC distance. The origin is the posterior mid-glottic wall. A. The trajectories for the rocking axis of each of the four joint models have been distinguished by extending them well past their range of motion. Note that the model trajectories lie within the scatter of the experimental trajectories over much of the range of trajectories. B. The trajectories for the rocking axis and two of the "sliding" axes for joint M1-RHS are displayed. Note that the "sliding" axes lie within the range of scatter of the trajectories for only a small range of motion.

definition of the vertical axis to be an axis passing through the line of sight of an endoscopy view (Fig. 9). The placement of the larynx in accordance with an estimated laryngoscope view revealed the rocking axis to be similar to this line of sight.

The resolution of the controversy was not proven mathematically, nor does it imply that the axis of rotation is exactly parallel to the line of sight. We are suggesting that the axis of the joint is sufficiently parallel to the line of sight for the vocal folds to appear to rotate about this axis. Because of the small arc length of the movement about this axis it is not possible to determine if the motion is circular or elliptical but this distinction does not alter our findings substantially.

The measurement of the joint facets was accomplished by means of a simple, albeit labor-intensive, procedure utilizing equipment commonly available in any machine shop. It might be possible to improve the accuracy of the measurements by as much as a factor of ten by using specialized measurement equipment. Although this would improve the reconstruction of the joint facets, it would not change the major results of this project. The influence of random measurement errors on the determination of the rotation axis was substantially reduced by the averaging effect of the summations in the optimization criterion. The measurement technique suggests that the major error sources, detection of indicator contact and resolution of the readout, are random. It is hard to imagine an important source of nonrandom measurement error. The collection of the specimen and its handling, freezing, thawing, and formalin storage could introduce distortion but this is also unlikely to have been a source of nonrandom error. It would certainly be desirable to collect

similar data from a large number of larynges. This would be facilitated by automating the data collection procedure.

The determination of the optimal joint axis of rotation is a precise quantification of the intuitive idea behind many, if not all, of the anatomically determined descriptions of joint motion. That is, that the joint facets describe the possible motions of the cricoarytenoid joint.

The alignment of the joint facets was the weak point of the analysis. The collection and handling of the specimen were more likely to affect this alignment than any of the other relevant aspects of the experiment. The sensitivity analysis, however, demonstrated that the variation in the solution caused by differences in alignment were small for small perturbations. The larger perturbations which changed the results were substantial enough visually that this magnitude of error in alignment was unlikely. The conclusion that there is a rocking and a sliding axis was established unequivocally regardless of the alignment.

In this investigation we assumed that the cricoarytenoid joint was not a rolling joint but rather involved a single axis of rotation. This assumption proved to be reasonable because the variance was small. The real motion of the arytenoids is likely to involve some shifting of the axis of rotation as the cartilages traverse their full range of movement, rather than the exact optimum-axis motion. It would be possible to investigate this possibility by a slight alteration of our approach. The optimal rotation axes for a portion of the arytenoid movement could be determined.

One other possibility exists with regard to the anatomical axis of rotation. If the joint were heavily loaded as is, for example, the human hip joint, then the shape of the facets

under load could be substantially different from the unloaded shape. This is unlikely to be the case for the cricoarytenoid joint because of the small size and rapid movements of the arytenoids which precludes heavy loading. However, the approach taken here can determine the loading once stress versus strain curves are available for the ligaments holding the cricoarytenoid joint together. Such data, combined with rotations about hypothetical joint axes of rotation, could provide precise estimates of the loading forces on the joint. One could even compute the joint axis of rotation that minimizes the stress on the joint.

Our results indicated that the interaction between the cricoarytenoid joint facets does not limit sliding along the optimal rocking axis. Rather, as Sonesson (1959) and others suggested, the motion is presumably limited to about 2 mm. by other structures such as the ligaments of the joint capsule.

Finally, the kinematic data conclusively reject the possibility of a rotation about a vertical axis that passes through the joint. The anatomical data also reject the possibility of a rotation about a vertical axis passing through the joint facets. The sample size is small and we do not know if the motion of the two male larynges would have been similar to the ten subjects studied. Our anatomical results, however, were consistent from one sample to the other and with the literature (Sonesson, 1959; Von Leden and Moore, 1961; Ardran and Kemp, 1966; Fink and Demarest, 1978). In particular, they confirm Sonesson (1959) who was the first to demonstrate that the primary motion of the joint could be expected to be rocking. Further the kinematic results for rocking and vertical rotation are so dramatically different that it is difficult to believe additional data would change the conclusion. Although other small movements are undoubtedly present, the predominant motion of the arytenoids is well-described as rocking.

ACKNOWLEDGMENTS

The work of Dr. Zhang and Dr. Levine was supported by NIH Contract No. N01-DC-1-2116 and, partially, by the National Science Foundation under Grant No. NSF D CDR 8803012.

- Ardran, G. M., and Kemp, F. H. (1966). "The mechanism of the larynx," *Br. J. Radiol.* **39**, 614–654.
- Armstrong-Helouvy, B., Dupont, P., and Canudas De Wit, C. (1994). "A survey of models, analysis tools and compensation methods for the control of machines with friction," *Automatica* **30**, 1083–1138.

- Baldo, A. F. (1987). "Machine elements," in *Mark's Standard Handbook for Mechanical Engineers*, 9th ed., edited by E. A. Avallone and T. Baumeister III (McGraw-Hill, New York), pp. 8–46, Table 8.2.39.
- Broad, D. J. (1968a). "Kinematic considerations for evaluating laryngeal cartilage motions," *Folia Phoniatri.* **20**, 269–284.
- Broad, D. J. (1968b). "Some physiological parameters for prosodic description," SCRL Monograph No. 3, Speech Communications Research Laboratory, Santa Barbara, California.
- Cooke, A., Ludlow, CL, Hallet, N., and Selbie, W. S. (1997). "Characteristics of vocal fold adduction related to voice onset," *J. Voice* **11**, 12–23.
- Edelsbrunner, H., and Mucke, E. (1994). "Three-dimensional alpha shapes," *ACM Trans. Graphics* **13**, 43–72.
- Fink, B. R., and Demarest, R. J. (1978). *Laryngeal Biomechanics* (Harvard U.P., Cambridge, MA), pp. 15–43.
- Fink, B. R. (1975). *The Human Larynx: A Functional Study* (Raven, New York), pp. 121–127.
- Frable, M. A. (1961). "Computation of motion at the cricoarytenoid joint," *Arch. Otolaryngol.* **73**, 551–556.
- Gray, H. (1980). *Gray's Anatomy* (36th ed.), edited by Peter L. Williams and Roger Warwick (Churchill Livingstone, New York).
- Hamrick, B. J. (1986). "Lubrication of machine elements," in *Mechanical Engineer's Handbook*, edited by M. Kutz (Wiley, New York), pp. 457–458.
- Kahane, J. C., and Kahn, A. R. (1986). "India ink pinprick experiments on surface organization of cricoarytenoid joints," *J. Speech Hear. Res.* **29**, 544–548.
- Maue, W. M., and Dickson, D. R. (1971). "Cartilages and ligaments of the adult human larynx," *Arch. Otolaryngol.* **94**, 432–439.
- Mori, K., Kojima, H., and Honjo, I. (1990). "Three-dimensional computer graphics of the larynx," in *Recent Advances in Bronchoesophagology*, Proceedings of the 6th World Congress of Bronchoesophagology, Tokyo, 15–18 October 1989, edited by T. Inouye *et al.* (Elsevier, New York), pp. 259–260.
- Neuman, T. R., Hengesteg, A., Lepage, R. P., Kaufman, K. R., and Woodson, G. E. (1994). "Three-dimensional motion of the arytenoid adduction procedure in cadaver larynges," *Ann. Otol. Rhinol. Laryngol.* **103**, 265–270.
- Press, W. H., Flannery, B. P., Teukolsky, S. A., and Vetterling, W. T. (1988). *Numerical Recipes in C—The Art of Scientific Computing* (Cambridge U.P., Cambridge), pp. 317–324.
- Sawashima, M. (1974). "Laryngeal research in experimental phonetics," in *Current Trends in Linguistics*, edited by T. A. Sebeok (Mouton, Paris), Vol. 12, pp. 2303–2348.
- Sellars, I., and Keen, E. N. (1978). "The anatomy and movements of the cricoarytenoid joint," *Laryngoscope* **88**, 667–674.
- Sellars, I. E., and Vaughan, C. L. (1983). "A biomechanical investigation of cricoarytenoid joint kinematics," in *Biomechanics VIII-A*, edited by H. Matsui and K. Kobayashi (Human Kinetics, Champaign, IL).
- Sonesson, B. (1959). "Die funktionelle Anatomie des Cricoarytenoidgelenkes," *Z. Anat. Entwicklungsgesch.* **121**, 292–303.
- Von Leden, H., and Moore, P. (1961). "The mechanics of the cricoarytenoid joint," *Arch. Otolaryngol.* **73**, 63–72.
- Wall, F. J. (1986). *Statistical Data Analysis Handbook* (McGraw-Hill, New York), p. 4.6.

Speech recognition of hearing-impaired listeners: Predictions from audibility and the limited role of high-frequency amplification

Teresa Y. C. Ching, Harvey Dillon, and Denis Byrne

National Acoustic Laboratories, Australian Hearing Services, 126 Greville Street, Chatswood, Sydney, New South Wales 2067, Australia

(Received 4 February 1997; accepted for publication 6 October 1997)

Two experiments were conducted to examine the relationship between audibility and speech recognition for individuals with sensorineural hearing losses ranging from mild to profound degrees. Speech scores measured using filtered sentences were compared to predictions based on the Speech Intelligibility Index (SII). The SII greatly overpredicted performance at high sensation levels, and for many listeners, it underpredicted performance at low sensation levels. To improve predictive accuracy, the SII needed to be modified. Scaling the index by a multiplicative proficiency factor was found to be inappropriate, and alternative modifications were explored. The data were best fitted using a method that combined the standard level distortion factor (which accounted for decrease in speech intelligibility at high presentation levels based on measurements of normal-hearing people) with individual frequency-dependent proficiency. This method was evaluated using broadband sentences and nonsense syllables tests. Results indicate that audibility cannot adequately explain speech recognition of many hearing-impaired listeners. Considerable variations from audibility-based predictions remained, especially for people with severe losses listening at high sensation levels. The data suggest that, contrary to the basis of the SII, information contained in each frequency band is not strictly additive. The data also suggest that for people with severe or profound losses at the high frequencies, amplification should only achieve a low or zero sensation level at this region, contrary to the implications of the unmodified SII. © 1998 Acoustical Society of America. [S0001-4966(98)05401-0]

PACS numbers: 43.71.Gv, 43.71.Ky, 43.66.Sr [WS]

INTRODUCTION

A major difficulty of hearing-impaired listeners in understanding speech arises from the loss of audibility of some parts of the speech signal that are important for recognition. Therefore, hearing aid amplification systems often aim to restore audibility of those portions of the speech spectrum that are below the listeners' thresholds. It is generally assumed that speech recognition will be optimized when audibility is maximized. The relationship between audibility and speech recognition can be quantified using the Articulation Index (AI) (French and Steinberg, 1947), now called the Speech Intelligibility Index (SII) (ANSI S3.5 Draft, 1993). The SII (AI) assumes that speech recognition increases in direct proportion to speech spectrum audibility, which can be calculated from the hearing thresholds of the listener, and the long term average spectra of the speech and noise reaching the ear of the listener. The SII is represented by the following equation:

$$\text{SII} = \sum I_i A_i, \quad (1)$$

where I_i is the function which characterizes the importance of the i th frequency band to speech intelligibility, and A_i expresses the proportion of the speech dynamic range in the i th frequency band that is above the listener's threshold or masking noise.

Several studies have used the SII to predict speech recognition for hearing-impaired listeners to determine if audibility is the main factor limiting speech performance. While some have reported adequate predictions for mildly and moderately hearing-impaired listeners (Kamm *et al.*, 1985; Dirks *et al.*, 1986; Dubno *et al.*, 1989), many have shown that performance was worse than would be predicted by the unmodified SII, especially for people with moderate or severe losses (Dugal *et al.*, 1978; Pavlovic, 1984; Dubno *et al.*, 1989; Pavlovic *et al.*, 1986), and people with steeply sloping high-frequency losses (Skinner, 1980; Rankovic, 1991).

The role of audibility in speech recognition has also been examined by using masking noise to simulate the effect of elevated thresholds associated with hearing impairment in normal-hearing listeners. This technique is limited to mild or moderate losses, as simulation of more severe losses would require very intense noise. In general, speech scores of the noise-masked normal-hearing listeners were close to those of the hearing-impaired listeners whose thresholds were simulated (Dubno and Schaefer, 1992; Zurek and Delhorne, 1987; Humes *et al.*, 1987). However, performance of simulated steeply sloping losses was sometimes overestimated by audibility.

The overall results of the studies on the effect of audibility demonstrate that audibility cannot adequately predict the reduced speech recognition of hearing-impaired listeners with moderate or severe losses. The contribution of audibility varies for people with different hearing losses, contrary to

the assumptions of the SII, and that other factors affect the listeners' use of speech information in the audible signal.

To improve the accuracy of the SII as a predictive system for hearing-impaired listeners, various attempts have been made to modify the index calculation procedure (Fletcher, 1952; Dugal *et al.*, 1978; Pavlovic *et al.*, 1986; Ludvigsen, 1987). Fletcher and Galt (1950) used a proficiency factor to characterize the enunciation of the talker and the experience of the listener with that talker, as expressed in the following equation:

$$SII = P \sum I_i A_i, \quad (2)$$

where P is the proficiency factor. Fletcher (1952) proposed that the proficiency factor could be used to describe the effects of hearing loss apart from reduced audibility. Dugal *et al.* (1978) adopted the approach, and reported that the effects of frequency-gain characteristics and signal levels were well predicted for a group of six hearing-impaired listeners when the indexes were rescaled by individually derived proficiency factors.

Pavlovic *et al.* (1986) proposed to modify the index by a factor that decreased linearly with hearing loss to characterize the reduced contribution of an audible signal with increase in hearing level. The factor was unity for hearing threshold levels of less than 15 dB HL, and became zero when hearing thresholds exceeded 95 dB HL. This modification improved the accuracy of predictions for four hearing-impaired individuals in various conditions of filtering and noise masking compared with the unmodified procedure. Whether proficiency decreases linearly with hearing level, and whether 95 dB hearing level is the level at which hearing is so extreme that an audible signal makes zero contribution to intelligibility, are open to question.

Another alternative in modifying the SII incorporated models of frequency and temporal resolution (Ludvigsen, 1987). This modified method improved the prediction accuracy of test scores of subjects listening to broadband speech at high levels, but not at moderate levels. Both the modified and the unmodified (ANSI, 1969) methods underpredicted performance of listeners with flat 40 dB losses listening to unfiltered speech, but overestimated performance of normal-hearing subjects and hearing-impaired subjects with flat 40 dB losses when listening to low-pass filtered speech at 1 and 2 kHz. The subjects with sloping losses generally performed worse than predicted by either method when listening in quiet as well as in noise.

The methods of SII modification outlined above to account for the effect of hearing loss on speech recognition were effective in reducing errors for a small number of moderately impaired listeners, but the discrepancies between observed and predicted scores for people with more severe losses have not been examined. The poorer than expected speech abilities of these listeners exemplify the reduced contribution of audibility in frequency regions where the hearing is very impaired. The quantification of this deficit is an important consideration when adopting the index as a basis for specifying adequate amplification characteristics (Popelka

and Mason, 1987; Pavlovic, 1989), and for evaluating options for hearing aid fittings (Humes, 1986; Berger, 1990).

The current interest in applying the SII for hearing aid selection and evaluation is based on the assumption that the frequency-gain characteristic that provides the greatest audibility or highest SII will give the best speech recognition, subject to maintaining constant loudness (Studebaker, 1992). In investigating amplification preferences, Byrne (1986) indicated that listeners who had sloping high-frequency hearing losses judged the amplification scheme which provided the most extended high-frequency emphasis (and therefore provided the highest SII) to be poorest in intelligibility. Similar results were reported by Rankovic (1991) who found that her subjects with steeply sloping losses did not achieve the best speech recognition scores with a frequency response that maximised the SII. Further, Byrne *et al.* (1990) reported that people with severe and profound losses who had extreme hearing losses at the high frequencies preferred amplification that resulted in zero or low audibility for high-frequency components of speech. In tackling the selection problem, it is therefore necessary to understand the way in which audibility is related to speech recognition for people with various degrees and configurations of hearing loss, and the extent to which speech recognition can be explained by audibility. This study was designed to examine the relationship by measuring the amount of speech information that can be extracted from different frequency regions by listeners with a wide range of hearing losses at different sensation levels. Possibilities of improving the predictive accuracy of the SII model for hearing-impaired listeners were explored and evaluated, with the aim of quantifying deficits in speech recognition that cannot be explained by audibility.

I. EXPERIMENT I

This experiment was conducted to achieve three specific aims. The first was to derive an empirical function relating speech scores to audibility for normal-hearing listeners. The second was to quantify speech deficits of hearing-impaired listeners by comparing their performance with scores predicted by the SII. The third was to derive modifications of the SII to minimize the discrepancies between observed and predicted speech scores of hearing-impaired listeners.

A. Method

1. Subjects

Fifty-four subjects participated in this study, comprising 14 normal-hearing (mean age: 31.5 years, s.d.: 16.4 years, range: 20–64 years) and 40 adult listeners (mean age: 55.8 years, s.d.: 21.45 years, range: 20–83 years) with sensorineural hearing loss. The absolute thresholds for the normal-hearing subjects (4 males and 10 females) were no poorer than 15 dB HL at octave frequencies from 250 to 8000 Hz. Audiometric configurations for the hearing-impaired listeners varied. Out of 19 subjects with mild to moderate losses (average loss at 0.5, 1 kHz, and 2 kHz < 65 dB HL), 13 had flat or gradual downward sloping configurations (classification system of Carhart, 1946), and 6 had marked or steep downward slopes. Twenty-one subjects had severe or profound losses; 12 of them had flat configurations, and 9 had

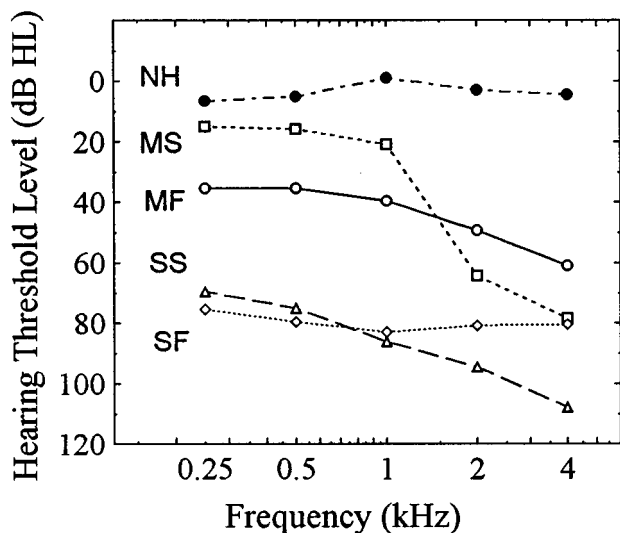


FIG. 1. The mean better ear threshold levels for the normal-hearing group (NH), the mild to moderate flat or gradual downward sloping hearing loss group (MF), the mild to moderate marked or steeply downward sloping hearing loss group (MS), the severe to profound flat group (SF) and the severe to profound downward sloping hearing loss group (SS).

downward sloping audiometric configurations. Figure 1 gives the mean audiograms of the normal-hearing listeners and the four groups of hearing-impaired listeners.

2. Stimuli

The stimuli were digital recordings of the BKB sentence lists (Bench and Doyle, 1979) produced by a native Australian male talker. The overall long-term average rms levels of individual sentences were equalized. The stimuli were filtered with a Kemo filter (48 dB/octave) to obtain six speech bands: lowpass filtered at 0.7 kHz (LP 700), 1.4 kHz (LP 1400), 2.8 kHz (LP 2800); and bandpass filtered at 0.7–1.4 kHz (BP 714), 1.4–2.8 kHz (BP 1428), and 1.4–5.6 kHz (BP 1456).

3. Procedure

The filtered sentence material was played back via a digital cassette tape recorder (Sony-PRO). The output of the tape recorder was routed to a prewhitening filter, a remote attenuator, an antialiasing filter set to bandpass filter at 80–5600 Hz (Kemo filter), an output amplifier (Marantz), and delivered to a TDH-49 earphone mounted in an MX-41/AR cushion. The prewhitening filter was used to shape the speech stimuli with a rising frequency response corresponding to the inverse of the international long-term average one-third-octave band speech spectrum (Byrne *et al.*, 1994).

All subjects were tested monaurally. The threshold levels for each of the six speech bands were first determined using an adjustment procedure. The subjects were instructed to press a button connected to a remote attenuator with 1-dB steps until the stimuli were just audible, then to press another button until the stimuli were inaudible, and then to press the first button again until the speech sounds were just audible. This level was recorded, and the average of five such trials was used to set the speech detection threshold level. The

speech stimuli were presented at 6 levels, ranging from 6 to 36 dB above detection threshold. Half of the subjects were tested at 36-, 24-, 12-, 6-, 18-, and 30-dB sensation level (SL) in that order, and the other half in the reverse order.

For practice, two sentence lists were used for each filter condition. The stimuli were presented at 36 dB SL for subjects to be tested using the first order, and at 30 dB SL for subjects to be tested using the second order. The practice lists were not used in the subsequent testing. Subjects who performed at chance level when listening to the BP 714 stimuli (14 out of a total of 40 hearing-impaired listeners) during practice were given the lowpass filtered 1.4-kHz stimuli for practice and for testing. Similarly, subjects who performed at chance level when listening to the BP1428 stimuli (16 out of 40 listeners) during practice were given the lowpass filtered 2.8-kHz stimuli for further practice and for testing. All subjects took the tests using speech lowpass filtered at 700 Hz and bandpass filtered at 1.4–5.6 kHz as stimuli.

In the actual testing, one sentence list was used for each filter condition at each presentation level. The filter bands were blocked, and sentence lists were randomized. The subjects were required to repeat as much of each sentence as possible, and were encouraged to guess when they were not sure. The speech scores were the number of key words correctly repeated, out of a total maximum of 50 items in each list. A loose key word scoring method was used (Bench *et al.*, 1993).

The speech tests were completed in two experimental sessions, and all testing sessions were preceded by practice.

4. Measurement of third-octave band speech spectra

The acoustic output at the earphone was measured using a Bruel & Kjaer (B&K) 2131 real-time frequency analyser via a 6-cc coupler. Spectral analysis was performed using linear averaging of 125-ms analysis frames over a speech sample of 128 s. Although only key words were scored, the entire sentence provided speech information and was thus used to determine the frequency spectrum of the speech material. The sound-pressure level for each third-octave band was computed by adding a correction for pauses between sentences.

5. Speech intelligibility index calculations

Speech Intelligibility Indexes (SII) were calculated using a third-octave band method (a combination of ANSI S3.5, 1969; Pavlovic, 1987; and ANSI S3.5 Draft v.3.1, 1993) and Eq. (1). SII is the sum of contributions of the proportion of the speech dynamic range that is above the listener's threshold in each third-octave band, weighted by the relative importance of the band to speech intelligibility. Pure tone thresholds were converted into equivalent internal noise by adding ten times the logarithm of the bandwidth of each third-octave band to the difference between the thresholds in dB SPL and the critical ratios as specified in Pavlovic (1987). The effective dynamic range of speech was taken to be 30 dB, and the speech maxima to be 15 dB above the long term equivalent rms level at each third-octave band. The au-

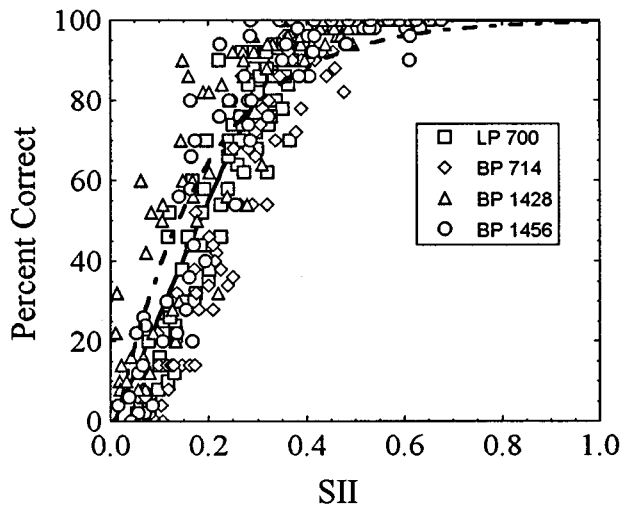


FIG. 2. The observed and predicted scores for 14 normal-hearing listeners as a function of SII. Observed scores of individual subjects for LP700 (squares), BP714 (diamonds), BP1428 (triangles), and BP1456 (circles) are shown. Predicted scores are represented by the transfer functions relating proportion correct (%) to SII. The broken line gives the fitted transfer function based on Eq. (3), and the solid line gives the fitted transfer function based on Eq. (4).

dibility function was estimated by taking the difference between the speech maxima level and the listener's equivalent internal noise level at each third-octave band. This was weighted by the average speech importance function (Pavlovic, 1994) that characterized the relative importance of each third-octave band to speech intelligibility.

B. Results and discussion

1. Recognition of filtered sentences

Normal-hearing listeners and the transfer function. The speech recognition scores obtained using the filtered sentences were normalized for variance using an arcsine transformation (Studebaker, 1985), and all fitting procedures and statistical analyses employed arcsine transformed units. The transfer function first proposed by Fletcher and Galt (1950) was modified by including an additive constant k , and was used to relate speech scores to SII for normal-hearing listeners

$$PC = 1 - 10^{-(SII+k)/Q}, \quad (3)$$

where PC is proportion correct, k and Q are fitting constants to minimize the difference between observed and predicted scores. These were estimated using a least squares procedure. In Fig. 2, the broken line shows the transfer function relating percent correct to SII for all speech bands for the normal-hearing listeners. The proportion of total variance accounted for was 74.6%. An alternative regression equation was formulated to improve on the fitting. This equation has the form

$$PC = \log(10^{(k-a*SII)/Q} + 10^{-1/Q}) - Q, \quad (4)$$

where Q is the curvature, a is the slope, and k shifts the function sideways. The new transfer function accounted for 84.3% of the total variance, and is shown as the solid line in Fig. 2.

TABLE I. The rms error between observed scores and theoretical predictions for normal listeners for different filtered speech bands. Rms errors are expressed in rationalized arcsine units (rau).

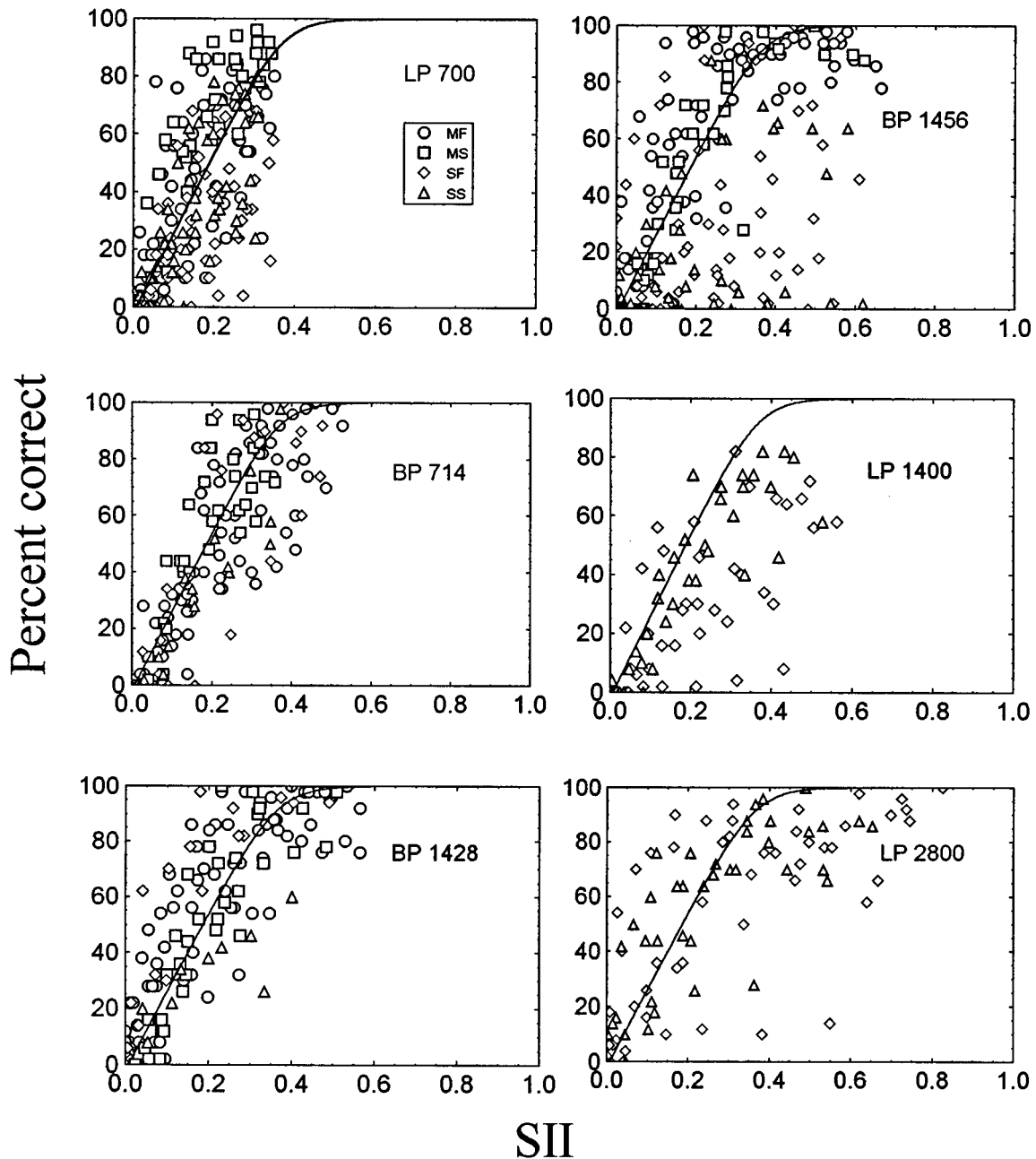
Filter	rms error (rau)
LP700	13.0
BP714	17.6
BP1428	17.6
BP1456	14.9
All bands	15.8

The agreement between the data and the theoretical transfer function can be evaluated by calculating the root-mean-square (rms) error of the difference between the observed scores and the line of best fit. Table I gives the average rms errors for the group of normal-hearing listeners for different frequency bands. The rms errors for the BP 714 and BP 1428 are larger than those for the other two bands. Inspection of the data in Fig. 2 revealed that the BP 714 speech scores were consistently under the fitted curves, and the BP 1428 scores were consistently over the fitted curves. In general, however, the transfer function given by Eq. (4) provided a satisfactory description of the results from normal-hearing listeners for the four speech bands. This function was used in subsequent comparisons of results of hearing-impaired listeners to normal performance.

Hearing-impaired listeners and the normal transfer function. Figure 3 contains the speech scores (in percent correct) of hearing-impaired listeners obtained using each of the filtered sentences as a function of SII. The performance of some subjects was better than the theoretical predictions especially at low sensation levels or low SIIs; and some subjects performed much poorer than predicted at high sensation levels or high SIIs. The overall rms error averaged across all subjects, sensation levels, and filter bands is 30.7 rau. For individual speech bands, the rms errors range from 22.2 rau (BP 714) to 40.7 rau (BP 1456). In its current form (ANSI, 1969), the SII procedure did not predict speech scores accurately. We therefore attempted to modify the procedure to see if the prediction of speech performance of hearing-impaired listeners could be improved.

2. Modification of the SII using a multiplicative proficiency factor

The conventional method of rescaling the index using a multiplicative proficiency factor [Eq. (2)] was first adopted. However, it was found to be inappropriate (Ching *et al.*, 1997). The reason is illustrated in Fig. 4, which shows the speech scores of one subject at six sensation levels. Performance was plotted in relation to the normal transfer function and two curves calculated with two arbitrarily chosen proficiency factors. Although a factor of less than 1, in this case, 0.6, could be used to fit the observed scores at high levels, a factor greater than 1, in this case, 2.2, would be required to improve the fitting at low levels or low SIIs. No single multiplicative proficiency factor would be suitable for all levels. This observation agrees well with the comments of Dugal



SII

FIG. 3. The observed and predicted scores for 40 hearing-impaired listeners as a function of SII. Scores of individuals with mild to moderate flat or gently sloping losses (circles), mild to moderate steeply sloping losses (squares), severe or profound flat losses (diamonds), and severe or profound sloping losses (triangles) are shown. Theoretical predictions are represented by the normal transfer function based on Eq. (4).

et al. (1978) that the predicted scores based on rescaling the index with a single proficiency factor were closer to the observed data for intermediate presentation levels than for the lower or higher levels.

3. Other proposed modifications

Inspection of individual data such as those shown in Fig. 4 suggested that there was a highly nonlinear relationship between audibility and intelligibility, and that the discrepancies were greater at high sensation levels than at low sensation levels. Therefore, several modification schemes were proposed in an attempt to address these aspects. The schemes employed differing numbers of fitting parameters. These

were estimated from the scores from all filtered speech bands using a least squares method. The effectiveness of a scheme was evaluated by calculating the rms errors between observed and predicted scores. For each scheme, Table II gives the rms values (in rau) along with the number of adjustable parameters required for 40 hearing-impaired subjects. The total number of data points used to derive the parameters was 918 (40 subjects * 4 filter conditions * 6 sensation levels, allowing for some subjects who could not be tested at high sensation levels because the stimulus became uncomfortably loud).

Nonlinear growth of effective sensation level. The data suggest that a good fit may be obtained by using two param-

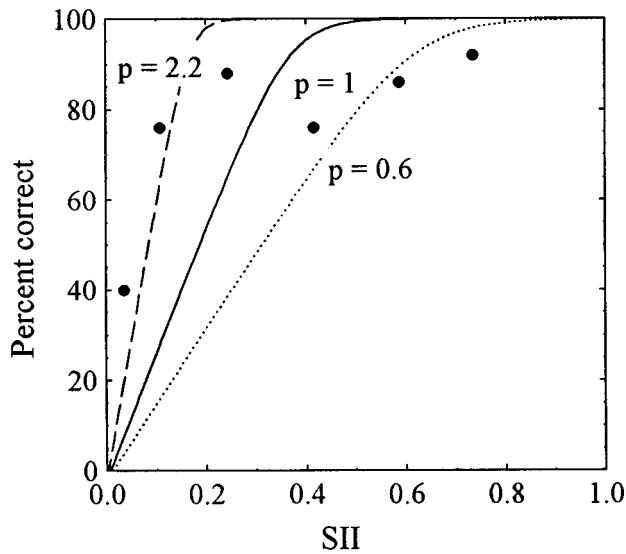


FIG. 4. Speech scores of one subject for one speech band presented at six sensation levels as a function of SII. The solid curve shows predictions using a proficiency (p) of 1, and the broken and dotted lines show predictions based on Eq. (2), using a larger p factor and a smaller p factor, respectively.

eters, one which alters the curvature of the effective audibility function to account for varied performances at low sensation levels, and one which characterizes the reduced asymptotic values at high sensation levels. This modification is shown in the following equation:

$$SII = \sum I_i M_{n,s} (1 - 10^{(-SL_{i,s}/C_{n,s})}), \quad (5)$$

where I_i is the importance function, $SL_{i,s}$ is the sensation level at each third-octave band, $M_{n,s}$ and $C_{n,s}$ are fitting parameters. The subscript s denotes values which differ for individual subjects. The subscript n denotes values that differ for different frequency regions. In this application, n ranges from 1 to 4, which relates to the four frequency regions: 0–700 Hz, 700–1400 Hz, 1400–2800 Hz, and 2800–5600 Hz, respectively. It is assumed that within each of these bands, the parameters $M_{n,s}$ and $C_{n,s}$ are constant.

The modified index accounted for more than 90% of the total variance for 14 hearing-impaired subjects, and between 80% and 90% for 21 hearing-impaired subjects. The overall rms error was reduced to 13 rau.

Modifications using the standard level distortion factor and proficiency factors. The above modification improved the fitting of data by reducing the contribution of audibility at high sensation levels for listeners with severe hearing losses. This effect is compatible with the proposed inclusion of a level distortion factor in the draft SII procedure (ANSI S3.5 Draft v.3.1, 1993). The speech level distortion factor accounts for the fact that the intelligibility of speech decreases at high presentation levels for normal-hearing people (French and Steinberg, 1947). This factor decreases from unity once the overall speech level exceeds 73 dB SPL. Because hearing-impaired listeners had to listen to speech at intensities higher than those needed for the normal-hearing listeners, it was not clear whether the lower than expected scores shown in Fig. 3 were solely the result of the high presentation level, or demonstrated additional individual auditory deficits. To examine the effect of incorporating the level distortion factor as specified in the 1993 Draft, the indexes were recalculated using the following equation:

$$SII = \sum I_i A_i L_i, \quad (6)$$

where L_i is the standard level distortion factor, expressed as

$$L_i = 1 - \frac{(E_i - U_i - 10)}{160}, \quad (7)$$

where E_i is the speech spectrum level and U_i is the standard speech spectrum level for normal vocal effort (ANSI S3.5 Draft v.3.1, 1993) for the i th band.

As shown in Table II, although the prediction errors of Eq. (6) are less than those resulting from Eq. (1), they are greater than those for the more individualised method employing the M and C parameters expressed in Eq. (5). The possibility of improving prediction by combining the level distortion factor with a multiplicative proficiency factor, P_s , was subsequently evaluated. This modification is expressed as

TABLE II. Root-mean-square errors (re: transfer function for normal listeners) for 40 hearing-impaired listeners for each of nine index calculation procedures represented by the corresponding equation number (Eq. No.), together with the total number of fitting parameters for each procedure (Par. No.). Rms errors are expressed in rationalised arcsine units.

Eq. No.	Par. No.	rms error						
		LP700	BP714	BP1428	BP1456	LP1400	LP2800	All bands
1	0	24.3	22.2	23.0	40.7	33.7	32.0	30.7
6	0	21.3	21.2	24.7	29.8	19.3	27.0	24.2
10	2	21.1	20.9	22.3	28.9	18.8	29.7	24.2
11	8	21.1	21.1	21.6	27.1	18.9	27.5	23.3
8	40	18.6	18.7	18.5	23.8	14.7	25.7	20.5
12	162	13.9	14.5	13.6	14.6	12.6	26.4	15.8
9	160	13.6	13.5	13.4	14.5	13.0	22.7	14.9
13	240	12.8	12.6	11.2	12.1	11.8	19.6	13.0
5	320	11.7	12.6	11.3	12.7	12.3	19.4	13.0

$$\text{SII} = \sum I_i A_{i,s} \left(1 - \frac{(E_i - U_i - 10)}{160} \right) P_{n,s}. \quad (8)$$

This formulation required a single parameter to be derived for each listener, and only reduced the rms errors by a further 3.7 rau compared to Eq. (6) where no individual fitting parameter was required.

The fitting was further improved by employing individual frequency-dependent proficiency factors, as expressed in the following equation:

$$\text{SII} = \sum I_i A_{i,s} \left(1 - \frac{(E_i - U_i - 10)}{160} \right) P_{n,s}, \quad (9)$$

where $P_{n,s}$ is the proficiency factor for the n th band for subject s . This method reduced the group rms errors from 30.7 rau [Eq. (1)] to 14.9 rau.

Modifications using a new level-dependent distortion factor and proficiency factor. Since the standard level distortion factor [Eq. (7)] was derived from measurements on normal-hearing people (French and Steinberg, 1947), it was hypothesized that the effect of presentation level on hearing-impaired people could be better accounted for by a parameter derived directly from the data. A reversed logit transformation was used, as expressed by

$$\text{SII} = \sum I_i A_{i,s} \frac{\exp(b_0 - b_1 L_{n,s})}{1 + \exp(b_0 - b_1 L_{n,s})}, \quad (10)$$

where L_n is level in dB SPL averaged across third-octave bands for the n th speech band, and b_0 and b_1 are fitting constants. As shown in Table II, there was no difference in terms of overall rms errors between the procedure which used the standard level distortion factor [Eq. (6)] and the one using the level-dependent distortion factor derived from the data [Eq. (10)]. The mean predictions of both procedures were almost identical, suggesting that on average, the negative effect of high signal level on speech performance was similar for normal-hearing and hearing-impaired listeners.

Further investigations to account for the remaining variance combined the new level-dependent distortion factor with a filter condition factor. It was hypothesized that the hearing-impaired listeners might be more experienced in listening to some of the filtered speech bands than others due to the similarity or dissimilarity of the filtered spectra to the range of frequencies that was usually audible to them. Accordingly, a filter condition factor was included in the equation

$$\text{SII} = F_c \sum I_i A_{i,s} \frac{\exp(b_0 - b_1 L_{n,s})}{1 + \exp(b_0 - b_1 L_{n,s})}, \quad (11)$$

where F_c is the filter condition factor, with c ranging from 1–6 for the six filter conditions used. The overall improvement over the use of the standard level distortion factor was small, with the mean prediction error reduced from 24.2 to 23.3 rau.

To improve on the fitting, the new level-dependent distortion factor was combined with individual proficiency factors, as expressed by the following equation:

$$\text{SII} = \sum I_i A_{i,s} \frac{\exp(b_0 - b_1 L_{n,s})}{1 + \exp(b_0 - b_1 L_{n,s})} P_{n,s}, \quad (12)$$

where b_0 and b_1 are group fitting constants for level-dependent distortion derived by Eq. (10) previously, and $P_{n,s}$ is the fitting constant for the frequency-dependent proficiency factor for the n th band for subject s . An alternative equation was also used to optimize the parameters that allow for individual level-dependent distortion and frequency-dependent proficiency. The equation for deriving these parameters has the form

$$\text{SII} = \sum I_i A_{i,s} \frac{\exp(b_{0,s} - b_{1,s} L_{n,s})}{1 + \exp(b_{0,s} - b_{1,s} L_{n,s})} P_{n,s}. \quad (13)$$

Using individual level-dependent distortion and frequency-dependent proficiency factors considerably improved the fitting, as shown by the reduction of the rms error from 30.7 rau for Eq. (1), to 15.8 rau for Eq. (12), and to 13.0 rau for Eq. (13).

4. Evaluation of SII procedures for predicting speech performance

The relative merit of all modified SII procedures was evaluated in terms of maximal reduction of rms errors between observed and predicted scores utilizing the least number of derived parameters. Table II shows that Eq. (5) and Eq. (13) provided the best fit. However, the expressions used were quite different from the equations in the ANSI standards (ANSI, 1969; ANSI, 1993), and the two equations required the greatest number of adjustable parameters. Equation (5) used eight fitting parameters for each subject (M and C in each of four frequency bands), and Eq. (13) necessitated six parameters per subject (b_0 , b_1 , plus $P_{n,s}$ in each band). The use of the standard level distortion factor proposed in the 1993 Draft, Eq. (6), led to some improvement over Eq. (1), and has the advantage that it is equally applicable to listeners with normal and impaired hearing. Equation (9) combined this factor with a frequency-dependent proficiency factor, and was the modification of choice because the group rms error was reduced by half of the prediction error associated with the unmodified procedure using only four adjustable parameters for each individual.

Figure 5 illustrates the mean predictions of four SII schemes [Eqs. (1), (6), (9), (5)] compared to the observed scores of four groups of listeners at different sensation levels for the LP700 and BP1456 conditions.

The model expressed by Eq. (9) used adjustable proficiency factors to allow for varying degrees of contribution of the audible signal to intelligibility, in addition to the effect of high signal level. The proficiency factors were frequency-specific, and often became zero or negative for individuals with severe losses at the high frequencies. As shown in Fig. 6, an audible signal in the 2.8–5.6 kHz region made no contribution (zero proficiency) to intelligibility, according to the modified SII model, for people whose hearing threshold at 4 kHz exceeded 80 dB HL. In some cases, audibility may even be harmful (negative proficiency).

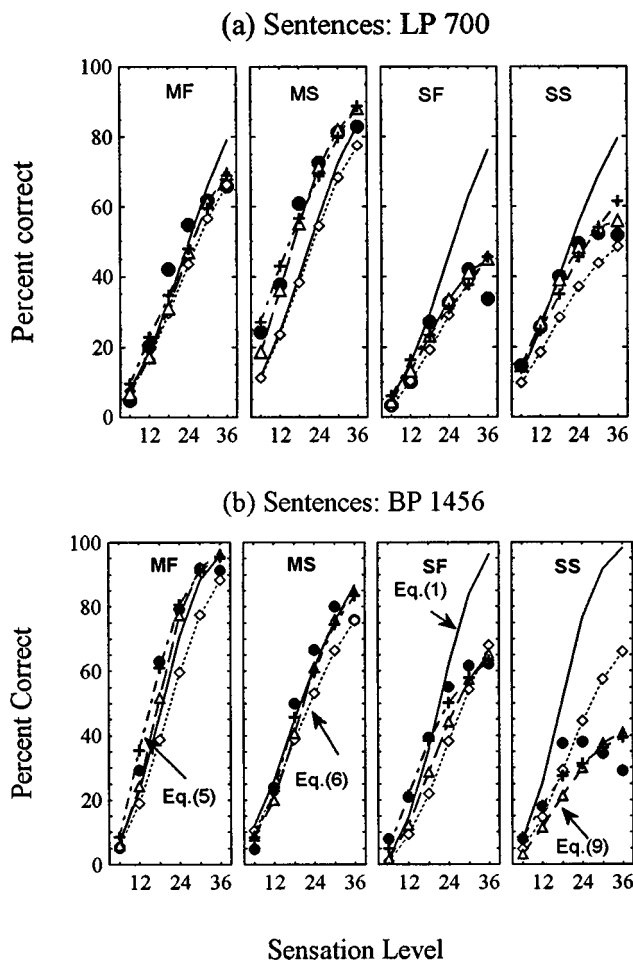


FIG. 5. Mean observed and predicted scores of hearing-impaired listeners for (a) the lowpass filtered 700 Hz (LP 700) condition, and (b) the bandpass filtered 1.4–5.6 kHz (BP 1456) condition. The four panels display performance of listeners grouped according to hearing loss: M(ild or moderate) F(lat or gently sloping losses), M(ild or moderate) S(loping losses), S(evere or profound) F(lat losses), and S(evere or profound) S(teeply sloping losses). Observed mean scores are shown by filled circles, and theoretical predictions are represented by line patterns. Predictions based on Eq. (1) are represented by the solid curve, on Eq. (6) by the curve with diamond patterns, on Eq. (9) by the curve with triangles, and on Eq. (5) by the curve with crosses.

Proficiency factors at frequencies other than 4 kHz did not show similar relations with degree of hearing loss at the same frequency.

An optimal fitting of the data has been achieved by modifying the SII procedure [Eq. (9)], although Fig. 5 shows that considerable variance remained for people with severe sloping losses listening at high sensation levels.

II. EXPERIMENT II

To evaluate the relative effectiveness of the modified and unmodified SII procedures for predicting speech performance, the same subjects were tested using broadband sentences and nonsense syllables. Measured scores were compared to those predicted using the unmodified procedure [Eq. (1)], the draft revised procedure [Eq. (6)], and the proposed modified SII [Eq. (9)] procedure with parameters derived from the filtered speech results in experiment I.

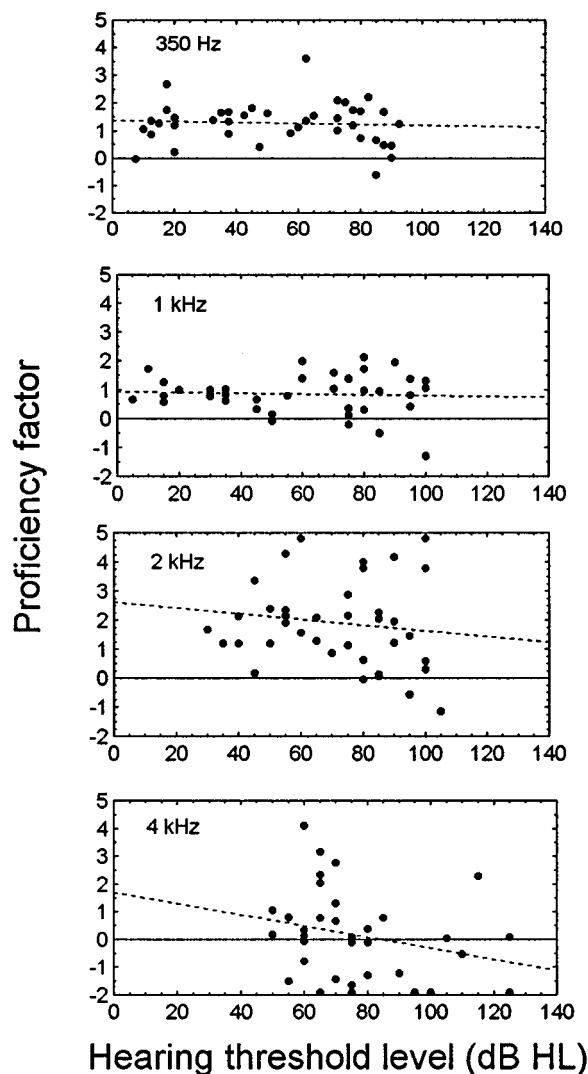


FIG. 6. Individual proficiency factors, deduced by fitting the data to Eq. (9), as a function of hearing threshold level at 350 Hz, 1 kHz, 2 kHz, and 4 kHz.

A. Method

1. Subjects

The subjects were the same as those who participated in Experiment I.

2. Stimuli

The stimuli were digital recordings of BKB sentence lists and VCV syllables. V is one of /i a o/, and C is the entire inventory of 24 English consonants produced by a male talker. The nonsense syllables were extracted from a carrier phrase, and were equalized for overall level. A total of 432 tokens was used, comprising 3 vowels and 24 consonants with 6 repetitions. All speech stimuli were lowpass filtered at 5600 Hz (LP 5600).

3. Procedure

The subjects were tested with the sentence stimuli using the same procedure as that described in experiment I.

The nonsense syllable stimuli were stored on a computer, and played back using custom-designed software at a

25-kHz rate via a 16-bit D/A converter. The playback system was otherwise the same as for the sentence material. All subjects were given practice sessions, which comprised four blocks each of 24 consonants in three vowel contexts. During practice, the stimuli were presented at 30 dB SL for half of the subjects, and at 36 dB SL for the other half. For the actual testing, the vowel contexts were blocked. Consonants were randomised within each block of 24, and four blocks were used for each vowel context at each of six presentation levels. The subjects responded by touching the appropriate symbol displayed on a touch screen that corresponded to the sound heard. All 24 consonants were available responses, and no feedback for correct response was provided. The speech scores were the number of correct responses out of a maximum total of 96 items for each test.

4. Measurement of third-octave band speech spectra

For calculating the audibility function for the sentences, the long term rms spectrum of the broadband sentences was measured as described in experiment I. For the nonsense syllables, a continuous speech sample by the same talker was used to determine the frequency spectrum. This is because the spectrum of the syllables would be dominated by the three vowels forming the VCV syllables. The spectrum, measured as described in experiment I, was corrected for the overall level difference between the nonsense syllables, excluding the pauses, and the continuous discourse. To obtain the overall rms level of the continuous discourse and the nonsense syllables, the output of the earphone was measured via a 6-cc coupler on a B&K 4426 level analyzer.

5. Calculation of the SII

The average speech importance function was used to weight the audibility function for sentence material, and the nonsense syllable importance function (Pavlovic, 1994) was used for the VCV material. Details of the calculation method were otherwise the same as those described in experiment I.

B. Results and discussion

1. Observed and predicted sentence scores

Figure 7 shows the mean observed scores for the LP 5600 sentences in relation to predictions using the three methods of SII calculation expressed by Eq. (1), Eq. (6), and Eq. (9).

For 17 out of 19 listeners with mild and moderate losses, observed performance was superior to all predictions at low sensation levels (6, 12, 18 dB SL). Speech scores were close to and generally better than predictions at high sensation levels. For people with severe or profound losses, all procedures underestimated performance at low sensation levels on average, and for 13 out of 21 individuals. The unmodified procedure greatly overpredicted performance at high sensation levels.

Table III shows the rms errors associated with the different predictions. The magnitude of prediction error was similar for all three equations. Prediction accuracy was

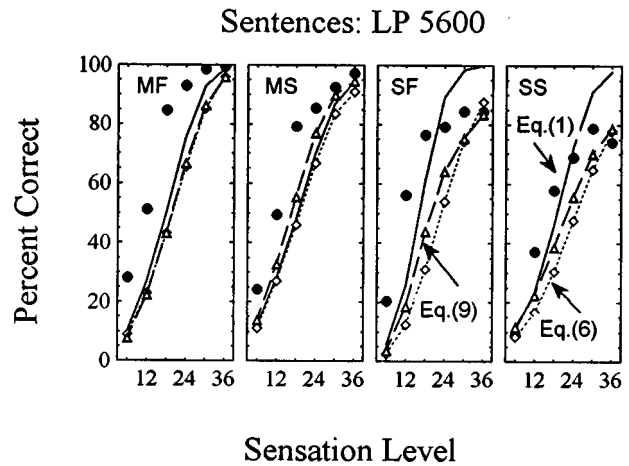


FIG. 7. The mean observed and predicted scores of the four groups of hearing-impaired listeners for sentences lowpass filtered at 5.6 kHz. Mean observed scores are represented by filled circles, and theoretical predictions are represented by line patterns. Predictions based on Eq. (1) are shown by the solid curve, on Eq. (6) by the curve with diamond patterns, and on Eq. (9) by the curve with triangles.

slightly improved by including the effect of frequency-dependent proficiency, but considerable unexplained variance remained.

The extent of improvement was not as great as would be expected on the basis of results from individual bands. This was partly because the performance of listeners with mild and moderate flat and gently sloping losses was underestimated by all procedures. To investigate this issue, the amount of audible signal available to the listeners for LP700 and LP5600 was compared at a level corresponding to a predicted score of 50% based on Eq. (1). Figure 8 gives the maximum short term third-octave band rms sensation levels of the speech spectra [in accordance with ANSI Draft (1993), these levels are 15 dB above the long term rms levels] averaged across 13 listeners with mild-moderate flat and gently sloping losses.

When the predicted score is 50%, the LP700 stimulus resulted in a mean score of 55%, and the LP5600 stimulus resulted in a mean score of 85%. The mean sensation levels shown in Figure 8 indicate that whereas the broadband speech was much less audible below 800 Hz, it was, on average, more audible than the lowpass filtered speech only in the third-octave bands centered at 1000 and 1250 Hz. As both stimuli had the same predicted intelligibility, this decrease and increase in audibility should have exactly compensated for each other. If this were so, why is the broadband

TABLE III. Root-mean-square error (rms error) of hearing-impaired listeners (*re*: transfer function for normal listeners) for sentence material and nonsense syllables lowpass filtered at 5600 Hz. The rms errors are expressed in rationalised arcsine units.

Eq. No.	Equation	rms error (Sentences)	rms error (VCV)
1	$SII = \sum I_i A_{i,s}$	33.5	21.4
6	$SII = \sum I_i A_{i,s} (1 - (E_i - U_i - 10)/160)$	33.5	15.8
9	$SII = \sum I_i A_{i,s} (1 - (E_i - U_i - 10)/160) P_{n,s}$	29.8	14.0

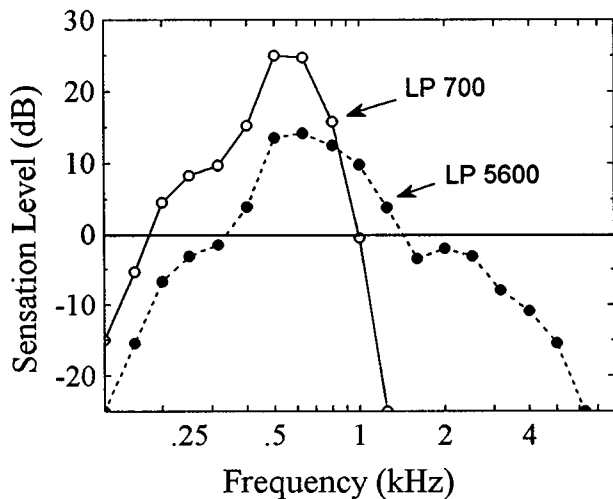


FIG. 8. Third-octave band sensation levels averaged across 13 listeners with mild and moderate flat and sloping losses as a function of frequency. The circles indicate sensation levels for predicted speech performance of 50%. The open symbols represent data for the LP700 stimuli, and the filled symbols represent data for the LP 5600 stimuli.

intelligibility score so much higher than that for the narrow band? If subjects could make use of information that appears to be at a small negative sensation level, then the result would be understandable, as the broadband speech would then have audible information extending up to 2500 Hz. It seems unlikely that subjects can make use of information below their threshold, but small negative sensation levels could actually be small positive sensation levels if the subjects' critical bandwidths were significantly wider than normal, and/or if the effective levels of the speech maxima were more than 15 dB above the long term rms levels. This seems possible because the difference between the speech maxima and rms levels depends on the integration time of the measuring equipment (Cox *et al.*, 1988), and because hearing-impaired people appear to integrate energy over shorter times than do normal-hearing people (Hall and Fernandes, 1983; Carlyon *et al.*, 1990) as a result of reduced compressive nonlinearity in the impaired ear (Moore, 1995; Oxenham *et al.*, 1997).

2. Observed and predicted nonsense syllable scores

Figure 9 shows the measured consonant recognition scores as a function of sensation levels for four groups of subjects in relation to predicted scores based on Eq. (1), Eq. (6), and Eq. (9).

The discrepancy between observed and predicted scores increased with sensation level and with degree of hearing loss. As shown in Table III, the rms errors were much reduced by the level distortion factor, but the effect of frequency dependent proficiency factors was minimal. The huge overpredictions for the severe and profound groups suggest that the proficiency factors may need to be smaller than those derived from the filtered sentences. When listening to sentences, the listeners can draw on contextual cues even though some acoustic cues are not accessible. When listening to nonsense syllables, however, they are heavily

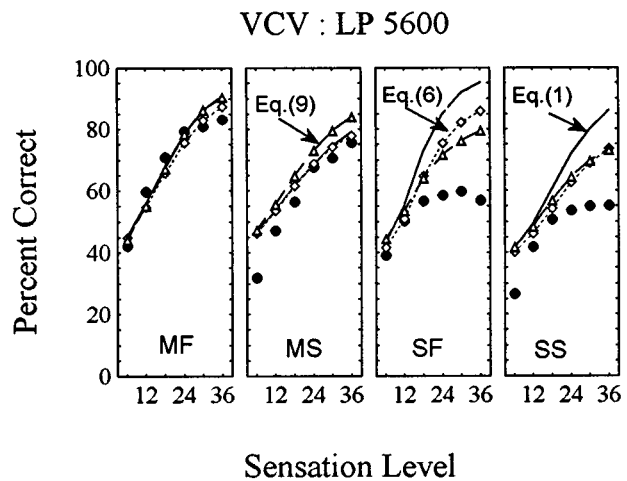


FIG. 9. The mean consonant (VCV) recognition scores and predicted scores of the four groups of hearing-impaired listeners. Symbols are as for Fig. 7.

dependent on extracting information from the impoverished acoustic signal because alternative cues are limited.

III. GENERAL DISCUSSION

A. Why do hearing-impaired people have trouble understanding speech?

Let us try to summarize the findings by providing an answer to this question. The first reason is because of lack of audibility. For people with a mild or moderate hearing loss, this is probably sufficient to account for their speech identification abilities. Consequently, their speech performance, as a group, can be well predicted on the basis of audibility. The only exceptions to this we observed were that, on average, people with mild and moderate losses performed slightly poorer than expected when they listened to filtered sentences at high levels (Fig. 5), better than expected when they listened to wideband sentences (Fig. 7), and slightly poorer than expected when they listened to nonsense syllables at some sensation levels (Fig. 9).

The second reason why hearing-impaired people have trouble identifying speech sounds is because they have to listen at high sound-pressure levels. The inclusion of the level distortion factor in the SII draft standard (ANSI, 1993) reflects the difficulties that normal-hearing people have when they are forced to listen at high levels. It should not be a surprise that the same is true of hearing-impaired people. It is somewhat surprising, however, that when we derived a new level distortion factor from our data, it did not fit the data any better than did the standard level distortion factor [Table II, Eqs. (6) and (10)]. Although we have not shown the data, the mean predictions arising from our derived distortion factor were extremely similar to those derived using the standard factor. It seems that not only are hearing-impaired people disadvantaged by having to listen at high levels, but on average, they are disadvantaged to the same degree as are normal-hearing people. In a subsequent paper we will show that frequency and temporal resolution both degrade with hearing loss. It seems possible that a level distortion factor is

needed for any listener because frequency and temporal resolution ability decrease at high presentation levels, and hence appear to decrease with hearing loss.

Are there more than two reasons why hearing-impaired people have trouble understanding speech? Two results from this experiment suggest that there are. First, consider the results for people with severe sloping losses when listening to high pass filtered speech [right panel of Fig. 5(b)]. The standard level distortion factor [Eq. (6)] overestimated these subjects' performance at high sensation levels. Although it is not shown in the figure, our level distortion factor derived from the data made the same prediction errors. The only one of our models that reflected the rollover nature of this data was the one that incorporated an individual level distortion factor for each person [Eq. (13)]. This suggests that the sensation level, as well as the sound presentation level, affect a listener's ability to make use of audible information. Based on the mean data, when people with this degree of loss receive high pass filtered speech at sensation levels up to about 20 dB, they do as well as one would expect considering the effects of the standard level distortion factor [Eq. (6)]. As sensation level increases further, they rapidly do worse. For broadband filtered sentences (Fig. 7), the same trend for scores to decrease at the highest level is evident.

The second observation that suggests there is more to decreased performance than having to listen at elevated levels relates to the individual proficiency factors. The data in Figs. 5(b) and 7 all relate to relatively broad bandwidths. The individual proficiency factors shown in Fig. 6 for the narrower frequency region from 2800 to 5600 Hz were often zero or negative. Speech intelligibility may thus be less than predicted on the basis of audibility, even when the high presentation level is taken into account, because some frequency regions contribute no information or actually decrease the effectiveness of information available at other frequencies. Possibly no information is extracted because of greatly reduced frequency and temporal resolution, and possibly masking extending to remote frequencies provides a mechanism by which one frequency region can make a negative contribution to intelligibility. Both of these possibilities are very much hypotheses, however.

We do not have the data to know whether the spread of abilities between hearing-impaired people with the same audiogram is greater or less than the spread of abilities between normal-hearing people listening at high levels. Furthermore, these data would be difficult to get, at least at the very high presentation levels that are appropriate to people with profound hearing loss.

B. Relative accuracy of the SII as a predictive system

Two findings in this study undermine the validity of using the SII model to predict speech scores of hearing-impaired listeners. First, the measured scores for the broadband stimuli (LP5600) were better than predictions based on the summed contributions of octave bands within the same bandwidth (see Fig. 7). This suggests that, contrary to the basic assumption of the SII (AI) model, information con-

tained in each frequency band is not strictly additive for these listeners. This lack of additivity did not occur for our normal-hearing listeners.

The second finding relates to the difficulty in deriving any modification that provides a satisfactory explanation of the speech score variation across individuals. The conventional approach of using a multiplicative proficiency factor to rescale the SII is found to be inappropriate, because different proficiency factors have to be used for different sensation levels; and typically, a smaller factor (or lower SII) is required at high than at lower levels. This means that corrections based on utilizing the ratio between the index derived from a test score and the index calculated from hearing level and signal level (e.g., Pavlovic *et al.*, 1986; Studebaker *et al.*, 1995) will only be applicable for predicting performance at some sensation levels, but not at others. Subsequent modifications account for the observed nonlinear growth of effective audibility by using level-dependent distortion factors and proficiency factors derived from the data. The modified SII procedure that seemed to have the best trade-off between accuracy and number of fitting parameters combined the effect of the standard level distortion factor with individually derived frequency-dependent proficiency [Eq. (9)]. Considerable variance remained unexplained, however.

C. Implications for hearing aid amplification

This study shows that, at high sensation levels, the contribution of audibility to speech recognition is less than expected for listeners with severe or profound losses, and that beyond a certain sensation level (sometimes 0 dB), speech recognition decreases with increases in audibility at frequencies where the hearing loss is severe. These considerations are significant when one attempts to select hearing aid frequency-gain characteristics for hearing-impaired individuals on the principle of prescribing the minimum gain in each frequency band to maximize audibility (e.g., Humes, 1986; Rankovic, 1991). For a certain overall loudness, the choice of frequency response affects the relative audibility of speech at different frequencies. Therefore, the key to optimal amplification is to find the best compromise between providing more audibility in some frequencies at the expense of less audibility in others while keeping loudness constant. Is it worth providing audibility at the high frequencies when hearing loss is severe or profound in this region? Possibly not. The C parameter in Eq. (6) can be used to estimate the sensation level at which 90% of the maximum possible SII contribution is reached in any frequency region. This level was 0 dB SL for people with an 80 dB HL hearing loss or greater at 4 kHz. People with this degree of hearing loss could thus not extract any information from an audible signal in the region (Fig. 6), and therefore performed poorer than that expected on the basis of audibility. Increases in audibility can even have negative effects on intelligibility (Fig. 5). These imply that hearing aids for people with severe or profound hearing losses at the high frequencies should not amplify high-frequency components of speech, contrary to the implications of the unmodified SII. Our results are compatible with those of Hogan and Turner (submitted) who re-

ported that providing amplification at 4 kHz was detrimental to speech performance for listeners with severe high-frequency hearing loss. Both our findings and those of Hogan and Turner provide important evidence for the limited role of high-frequency amplification, and practical applications to hearing aid fitting will require further research.

As we have concluded in Sec. III A, there is more to speech recognition of people with severe or profound losses than audibility and the need to listen at high signal levels. Consequently, the general applicability of the SII for hearing aid evaluation must be treated with caution. The assumption that the amplification scheme that maximizes the SII while keeping loudness constant also optimises speech intelligibility is appropriate for listeners with mild losses, but is erroneous when applied to listeners with more severe losses. For these listeners, the amount of information that can be extracted from a speech signal is not proportional to the amount of audibility, and the proportion of potential information that can be extracted depends on absolute sound presentation level, sensation level, hearing loss, frequency, and possibly on other unknown factors.

D. A caveat for practical applications

The findings that the speech scores of some listeners with mild and moderate sloping losses were underpredicted for lowpass filtered sentences at low sensation levels suggests that the relative familiarity of an individual to different speech bands may affect the use of information contained in certain frequency regions. This effect has been estimated mathematically by one of the modified procedures that included a multiplicative filter condition factor as an adjustable parameter [Eq. (11)]. However, the method did not lead to much reduction in rms errors (see Table II). The effect of acclimatization remains to be investigated. In particular, were so many people unable to use high-frequency information because they had not been exposed to high frequency speech cues for many years, or because their hearing mechanism is inherently incapable of using these cues? It is because of this doubt that we are not yet recommending the total removal of high frequency amplification to people whose high frequency thresholds exceed 80 dB HL.

IV. SUMMARY

Two experiments were conducted to examine the extent to which speech recognition for listeners with sensorineural hearing loss, ranging from mild to profound degrees, can be predicted by audibility as quantified by the Speech Intelligibility Index (SII). Speech scores of normal-hearing listeners were used to derive an empirical function relating speech scores to the SII. The performance of hearing-impaired subjects was compared to the predictions based on the index. The following conclusions may be drawn:

(1) Audibility as quantified by the SII overpredicted speech performance at high sensation levels for listeners with severe hearing losses, and in many cases, underestimated speech scores at low sensation levels. These findings indicate that audibility cannot adequately explain speech recognition of hearing-impaired people.

(2) The SII model was modified to improve its predictive accuracy, and the observed data were best fitted by a method which combined the standard level distortion factor (as recommended in ANSI, 1993) with frequency-dependent proficiency factors derived for each person [Eq. (9)]. However, considerable variance remained unexplained, indicating that the general applicability of the SII as a predictive system for hearing-impaired listeners is limited. It also follows that the general validity of using the SII system as a basis for selecting and evaluating hearing aid fittings is questionable.

(3) The contribution of audibility to intelligibility at frequencies where the hearing loss was severe was much reduced or even became nil, and further increases in audibility sometimes had negative effects on speech intelligibility. These findings suggest that it may be counterproductive to attempt to amplify high frequencies to high sensation levels, or sometimes to any positive sensation level, for listeners with severe losses in this region.

(4) The modified SII procedure [Eq. (9)] using proficiency factors derived from narrow speech bands underpredicted speech scores for broadband sentences. This result suggests that, contrary to the implications of the SII, the information contained in individual bands is not strictly additive, and contributions from different bands to speech intelligibility are not independent of each other.

(5) We conclude that hearing-impaired people have difficulty understanding speech because of reduced audibility, and because, for those with severe hearing losses, the individual's proficiency at extracting information from an audible signal is reduced by the need to listen at high sound pressure levels, and is further reduced when sensation level exceeds about 20 dB.

ACKNOWLEDGMENTS

We thank Brian Moore and Larry Humes for their insightful comments on an earlier version of this manuscript. This research was partly funded by the Cooperative Research Centre for Cochlear Implant, Speech, and Hearing Research, Australia.

- ANSI (1969). ANSI S3.5-1969, "American National Standard Methods for the calculation of the articulation index" (American National Standards Institute, New York).
- ANSI (1993). ANSI S3.5 Draft v.3.1-1993, "Proposed American National Standard Methods for the calculation of the speech intelligibility index" (American National Standards Institute, New York).
- Bench, R. J., and Doyle, J. M. (1979). *The BKB/A (Bamford-Kowal-Bench/Australian Version) Sentence Lists for Hearing-impaired Children* (La Trobe University, Victoria).
- Bench, R. J., Doyle, J., and Daly, N. (1993). *The BKB/A Speechreading Test Instruction Booklet* (La Trobe University, Victoria, BC, Canada).
- Berger, K. W. (1990). "The use of Articulation Index to compare three hearing aid prescriptive methods," *Audicibel Summer*, 16–19.
- Byrne, D. (1986). "Effects of frequency response characteristics on speech discrimination and perceived intelligibility and pleasantness of speech for hearing-impaired listeners," *J. Acoust. Soc. Am.* **80**, 494–504.
- Byrne, D., Dillon, H., Tran, K., Arlinger, S., Wilbraham, K., Cox, R., Hagerman, B., Hetu, R., Kei, H., Lui, C., Kiessling, J., Nasser Kotby, M., Nasser, N., El Kholy, W. A. E., Nakanishi, Y., Oyer, H., Powell, R., Stephens, D., Meredith, R., Sirimanna, T., Tavartkiladze, G., Frolenkov, G. I., Westerman, S., and Ludvigsen, C. (1994). "An international comparison of long-term average speech spectra," *J. Acoust. Soc. Am.* **96**, 2108–2120.

- Byrne, D., Parkinson, A., and Newall, P. (1990). "Hearing aid gain and frequency response requirements of the severely/profoundly hearing-impaired," *Ear Hear.* **11**, 40–49.
- Carhart, R. (1946). "An improved method for classifying audiograms," *Laryngoscope* **55**, 640–662.
- Carlyon, R. P., Buus, S., and Florentine, M. (1990). "Temporal integration of trains of tone pulses by normal and by cochlearly impaired listeners," *J. Acoust. Soc. Am.* **87**, 260–268.
- Ching, T., Dillon, H., and Byrne, D. (1997). "Prediction of speech recognition from audibility and psychoacoustic abilities of hearing-impaired listeners," in *Modeling Sensorineural Hearing Loss*, edited by W. Jestaedt (Erlbaum, Hillsdale, NJ).
- Cox, R. M., Matesich, J. S., and Moore, J. N. (1988). "Distribution of short-term rms levels in conversational speech," *J. Acoust. Soc. Am.* **84**, 1100–1104.
- Dirks, D. D., Bell, T. S., Rossman, R. N., and Kincaid, G. E. (1986). "Articulation index predictions of contextually dependent words," *J. Acoust. Soc. Am.* **80**, 82–92.
- Dubno, J. R., Dirks, D. D., and Schaefer, A. B. (1989). "Stop consonant recognition for normal-hearing listeners and listeners with high frequency hearing loss. II: Articulation index predictions," *J. Acoust. Soc. Am.* **85**, 355–364.
- Dubno, J. R., and Schaefer, A. B. (1992). "Comparison of frequency selectivity and consonant recognition among hearing-impaired and masked normal-listeners," *J. Acoust. Soc. Am.* **91**, 2110–2121.
- Dugal, R. L., Braid, L. D., and Durlach, N. I. (1978). "Implications of previous research for the selection of frequency-gain characteristics," in *Acoustical Factors Affecting Hearing Aid Performance*, edited by G. A. Studebaker and I. Hochberg (University Park, Baltimore), pp. 379–403.
- Fletcher, H. (1952). "The perception of speech sounds by deafened persons," *J. Acoust. Soc. Am.* **24**, 490–497.
- Fletcher, H., and Galt, R. H. (1950). "The perception of speech and its relation to telephony," *J. Acoust. Soc. Am.* **22**, 89–151.
- French, N., and Steinberg, J. (1947). "Factors governing the intelligibility of speech sounds," *J. Acoust. Soc. Am.* **19**, 90–119.
- Hall, J. W., and Fernandes, M. A. (1983). "Temporal integration, frequency resolution, and off-frequency listening in normal-hearing and cochlear-impaired listeners," *J. Acoust. Soc. Am.* **74**, 1172–1177.
- Hogan, C., and Turner, C. (submitted). "High frequency audibility: benefits for hearing-impaired listeners." submitted to *J. Acoust. Soc. Am.*
- Humes, L. E. (1986). "An evaluation of several rationales for selecting hearing aid gain," *J. Speech Hear. Res.* **51**, 272–281.
- Humes, L. E. (1991). "Understanding the speech-understanding problems of the hearing impaired," *J. Am. Acad. Audiol.* **2**, 59–69.
- Humes, L. E., Dirks, D. D., Bell, T. S., and Kincaid, G. E. (1987). "Recognition of nonsense syllables by hearing-impaired listeners and by noise-masked normal hearers," *J. Acoust. Soc. Am.* **81**, 765–773.
- Kamm, C. A., Dirks, D. D., and Bell, T. S. (1985). "Speech recognition and the articulation index for normal and hearing-impaired listeners," *J. Acoust. Soc. Am.* **77**, 281–288.
- Ludvigsen, C. (1987). "Prediction of speech intelligibility for normal hearing and cochlearly hearing-impaired listeners," *J. Acoust. Soc. Am.* **82**, 1162–1171.
- Moore, B. C. J. (1995). *Perceptual Consequences of Cochlear Damage* (Oxford U.P., Oxford).
- Oxenham, A. J., Moore, B. C. J., and Vickers, D. A. (1997). "Short-term temporal integration: evidence for the influence of peripheral compression," *J. Acoust. Soc. Am.* **101**, 3676–3687.
- Pavlovic, C. V. (1984). "Use of the articulation index for assessing residual auditory function in listeners with sensorineural hearing impairment," *J. Acoust. Soc. Am.* **75**, 1253–1258.
- Pavlovic, C. V. (1987). "Derivation of primary parameters and procedures for use in speech intelligibility predictions," *J. Acoust. Soc. Am.* **82**, 413–422.
- Pavlovic, C. V. (1989). "Speech spectrum considerations and speech intelligibility predictions in hearing aid evaluations," *J. Speech Hear. Dis.* **54**, 3–8.
- Pavlovic, C. V. (1994). "Band importance functions for audiological applications," *Ear Hear* **15**, 100–104.
- Pavlovic, C. V., Studebaker, G. A., Sherbecoe, R. L. (1986). "An articulation index based procedure for predicting the speech recognition performance of hearing-impaired individuals," *J. Acoust. Soc. Am.* **80**, 50–57.
- Popelka, G. R., and Mason, D. (1987). "Factors which affect measures of speech audibility with hearing aids," *Ear Hear* **8**(5S), 109–118.
- Rankovic, C. (1991). "An application of the articulation index to hearing aid fitting," *J. Speech Hear. Res.* **34**, 391–402.
- Skinner, M. W. (1980). "Speech intelligibility in noise in noise-induced hearing loss: effects of high frequency compensation," *J. Acoust. Soc. Am.* **67**, 306–317.
- Studebaker, G. A. (1985). "A 'rationalized' arcsine transform," *J. Speech Hear. Res.* **28**, 455–462.
- Studebaker, G. A. (1992). "The effect of equating loudness on audibility-based hearing aid selection procedures," *J. Am. Acad. Audiol.* **3**, 113–118.
- Studebaker, G. A., McDaniel, D. M., and Sherbecoe, R. L. (1995). "Evaluating relative speech recognition performance using the proficiency factor and rationalized arcsine differences," *J. Am. Acad. Audiol.* **6**, 173–182.
- Zurek, P. M., and Delhorne, L. A. (1987). "Consonant reception in noise by listeners with mild and moderate sensorineural hearing impairment," *J. Acoust. Soc. Am.* **82**, 1548–1559.

The recognition of vowels produced by men, women, boys, and girls by cochlear implant patients using a six-channel CIS processor

Philipos C. Loizou^{a)}

Department of Applied Science, University of Arkansas at Little Rock, Little Rock, Arkansas 72204-1099

Michael F. Dorman

Department of Speech and Hearing Science, Arizona State University, Tempe, Arizona 85287-0102 and
University of Utah Health Sciences Center, Salt Lake City, Utah 84132

Verelle Powell

Department of Speech and Hearing Science, Arizona State University, Tempe, Arizona 85287-0102

(Received 22 July 1996; revised 22 September 1997; accepted 21 October 1997)

Five patients who used a six-channel, continuous interleaved sampling (CIS) cochlear implant were presented vowels, in two experiments, from a large sample of men, women, boys, and girls for identification. At issue in the first experiment was whether vowels from one speaker group, i.e., men, were more identifiable than vowels from other speaker groups. At issue in the second experiment was the role of the fifth and sixth channels in the identification of vowels from the different speaker groups. It was found in experiment 1 that (i) the vowels produced by men were easier to identify than vowels produced by any of the other speaker groups, (ii) vowels from women and boys were more difficult to identify than vowels from men but less difficult than vowels from girls, and (iii) vowels from girls were more difficult to identify than vowels from all other groups. In experiment 2 removal of channels 5 and 6 from the processor impaired the identification of vowels produced by women, boys and girls but did not impair the identification of vowels produced by men. The results of experiment 1 demonstrate that scores on tests of vowels produced by men overestimate the ability of patients to recognize vowels in the broader context of multi-talker communication. The results of experiment 2 demonstrate that channels 5 and 6 become more important for vowel recognition as the second formants of the speakers increase in frequency. © 1998 Acoustical Society of America. [S0001-4966(98)02202-4]

PACS numbers: 43.71.Es, 43.71.Ky, 43.66.Ts [WS]

INTRODUCTION

In order to perceive speech normally, a listener must sort some physically different acoustic signals into different phonetic categories, and must sort other physically different signals into the same phonetic category. The latter circumstance arises because speakers do not have identical vocal tract geometries. One consequence of different geometries is different formant frequencies for the same phonetic segment. For example, Peterson and Barney (1952) report that, across speakers (men, women and children), F_1 for the vowel /æ/ can range from 625 Hz to 1300 Hz and F_2 can range from 1600 Hz to 2600 Hz. A signal with $F_1 = 625$ Hz and $F_2 = 1600$ Hz is heard as /æ/. A signal with $F_1 = 1250$ Hz and $F_2 = 2550$ Hz is also heard as /æ/. Another consequence of the different geometries of vocal tracts is that some signals with essentially identical formant frequencies are heard as *different* phonetic segments. For example, F_1 and F_2 frequencies of approximately 625 Hz and 1700 Hz can be heard either as /æ/ or as /ɛ/ (Peterson and Barney, 1952). This problem may be partially avoided by attention to vowel length since /ɛ/ is a "short" vowel and /æ/ is a "long" vowel (House, 1961), and/or the speaker's pitch (Miller,

1989). However, the durations of short and long vowels can overlap depending on consonantal context and speaking rate. The mechanisms which allow listeners to sort signals into the appropriate vowel categories, in spite of the complexities described above, continue to be a matter of debate (see the tutorial article by Strange, 1989).

The complexities introduced by different vocal tract geometries, and therefore different formant frequencies, into vowel recognition are of importance to researchers who study speech understanding by patients fit with cochlear implants. If we present single tokens of a small number of vowels from a single speaker to our patients for identification, then the results could be seriously misleading since most of the complexities of vowel recognition have been avoided. Yet the literature on vowel recognition by patients fit with cochlear implants, including studies by the present authors, can be characterized as using a single male speaker (real or synthetic) or, at most, a single adult male and adult female speaker.

Blamey *et al.* (1987) evaluated vowel recognition performance of 28 patients using the F_0/F_1 and the $F_0/F_1/F_2$ coding strategies of the Nucleus device. The stimuli consisted of 11 vowels in /hVd/ context presented live by one male and one female Australian English speaker. Blamey *et al.* (1987) combined the scores for the two speakers. The

^{a)}Electronic mail: loizou@ualr.edu

mean percent correct score for five patients using the $F0/F1/F2$ strategy was 57% in the hearing-alone condition.

Using a set of nine vowels, Skinner *et al.* (1991) reported an overall mean score of 62% correct by patients using the $F0/F1/F2$ processor. The nine vowels were from the Iowa laser videodisc (Tyler *et al.*, 1987) and were produced by one male speaker. Skinner *et al.* (1994) later evaluated the Spectral Peak (SPEAK) coding strategy and the MPEAK strategy for the Nucleus device with patients from three English-speaking countries. For patients from the United States and Canada, a North American vowel set was used which contained 14 vowels in /hVd/ context produced by a single North American male speaker. The Australian patients were tested with an Australian vowel set, which included 11 vowels produced by one Australian male speaker. Skinner *et al.* (1994) reported a mean vowel score of 74.8% correct for the SPEAK strategy and 70.1% correct for the MPEAK strategy.

Vowel performance with the Ineraid device has been found to be similar to that of the $F0/F1/F2$ processor of the Nucleus device. Using a set of 12 synthetic vowels in /bVt/ context, Dorman *et al.* (1989) reported a mean percent correct score of 60% with scores ranging from 49% to 79% correct. Wilson *et al.* (1990) compared the performance of patients fit with the compressed analog (CA) strategy used in the Ineraid device, with the CIS strategy developed at the Research Triangle Institute. In the vowel identification test, the stimuli consisted of eight vowels in /hVd/context produced by one male and one female speaker from the Iowa laser videodisc (Tyler *et al.* 1987). Wilson *et al.* (1990) reported a similar performance for the two strategies on vowel identification. The mean vowel score was 95% correct for the CA strategy (Ineraid) and 92% correct for the CIS strategy. The Ineraid patients in the Wilson *et al.* (1990) study were tested with the CIS strategy in the laboratory, and had no experience (only a few hours) with the new strategy. It was not clear from that study whether the patients' vowel scores would improve over time with experience. This question was addressed by Dorman and Loizou (1997) who investigated the performance of Ineraid patients on vowel identification in three different conditions: (1) with the Ineraid device; (2) within hours of fitting with the CIS processor; and (3) after one month of experience with the CIS processor. The stimuli were 13 synthetic vowels in /bVt/context. The mean percent

correct scores were 35% for the Ineraid device and 41% for the CIS processor at the time of the fitting. The difference was not significant, which was consistent with the findings of Wilson *et al.* (1990) and Boex *et al.* (1994). At one month after fitting with the CIS processor, a significant increase was observed in the mean percent correct vowel recognition (58% correct). This outcome was interpreted to mean that a period of adjustment is necessary, following the fitting of the CIS processor, in which a remapping of the vowel space occurs.

As it can be seen by the preceding literature review on vowel identification by cochlear implant patients, most of the studies have used a single adult male speaker and/or a single adult female speaker. This led us to wonder how well implant patients could identify vowels when the vowels were spoken by a large number of men, women, boy, and girl informants and were produced with widely different, and at times idiosyncratic, vowel durations.

The identification of such a vowel set is of interest not only because it would indicate how well cochlear implant patients can function under conditions of real world complexity, but also because it would give us a unique window on the mechanism underlying vowel recognition. Consider that in the present study the patients used a six-electrode array and, thus, received, at most, six independent channels of stimulation. It is of interest to know how patients can identify vowels with varying formant frequencies when the vowel spectra are represented by a small number of fixed-frequency spectral components.

In the experiments which follow we describe, in experiment 1, the level of vowel recognition obtained by patients who use a six channel, Continuous Interleaved Sampling (CIS) processor when tested with vowels produced by men, women, boys, and girls. We also describe factors which may account for the errors in identification and for individual differences in performance. In experiment 2 we test the hypothesis that channels 5 and 6 of the processor are critical for the recognition of vowels produced for women, boys, and girls, but are not critical for the recognition of vowels produced by men. Finally, we comment on how vowels can be recognized when the vowel spectrum is specified by only a small number of fixed-frequency components (or channels).

TABLE I. Biographical data on implant patients. Subject S5 cannot remember ever hearing in the ear which was implanted. Sound presented to the implanted ear is lateralized to the opposite ear.

Subject	Gender	Age (years) at detection of hearing loss	Age at which hearing aid gave no benefit	Age fit with Ineraid	Age at testing	Etiology of hearing loss	Score on H.I.N.T. in quiet	Score on NU-6 words in quiet
S1	F	7	31	33	40	unknown/ hereditary	100	80
S2	M	19	19	29	41	Cogan's syndrome	100	93
S3	F	23	48	51	57	unknown	100	71
S4	M	20	46	63	68	unknown	88	46
S5	M	5	43	48	58	unknown	92	43

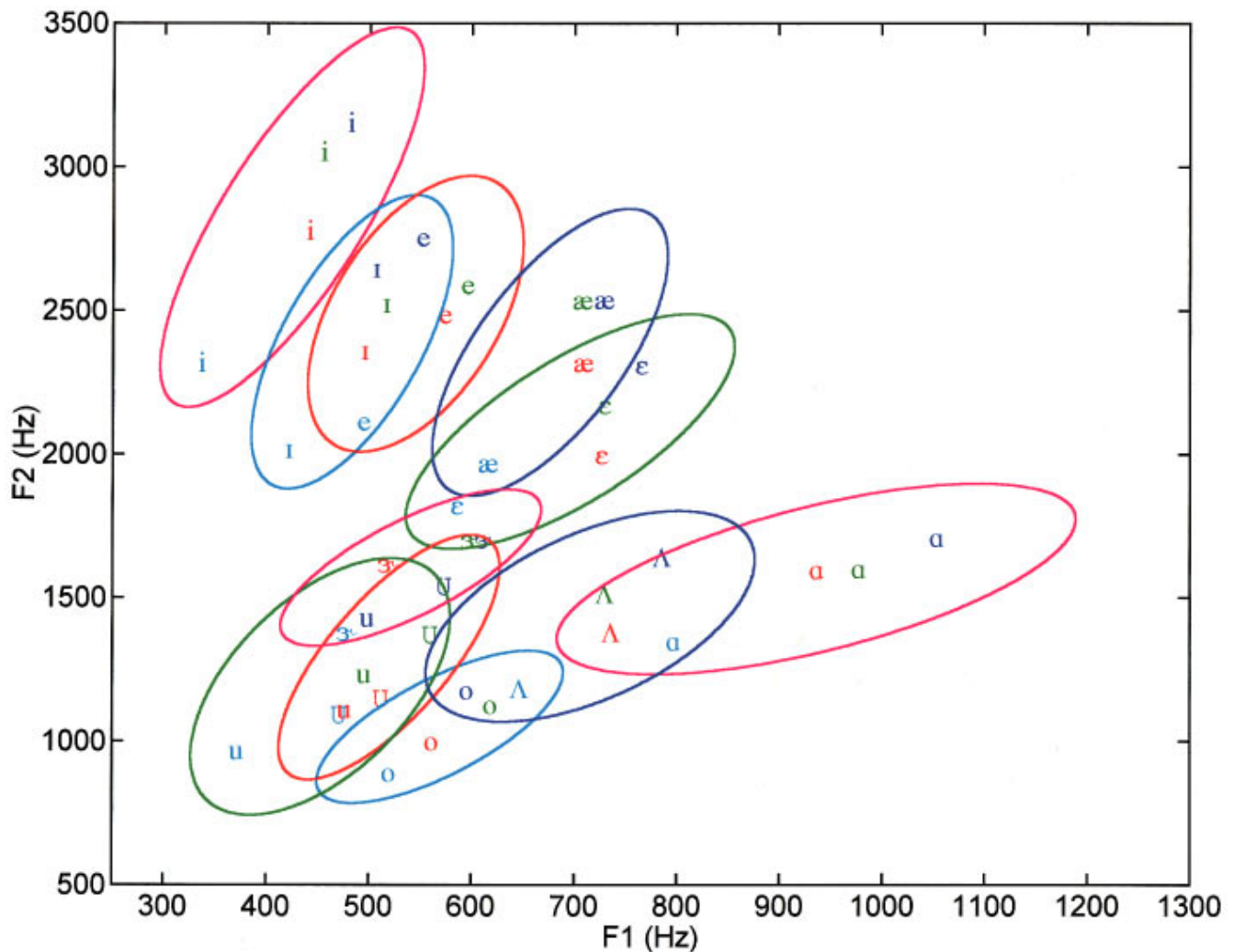


FIG. 1. Average values of $F1$ and $F2$ for men (cyan), women (red), boys (green), and girls (blue) for eleven vowels with ellipses fit to the data.

I. EXPERIMENT 1

A. Method

1. Subjects

The subjects were five post-lingually deafened adults who had used a six-channel CIS processor for periods ranging from six months to a year. All of the patients had used a four-channel, compressed-analog signal processor (Ineraid) for at least 4 years before being switched to a CIS processor. The patients ranged in age from 40 to 68 years and they were all native speakers of American English. Biographical data for each patient are presented in Table I.

2. Stimuli

The stimuli were the words “heed, hayed, hid, had, hod, head, heard, hoed, hood, hud, who’d” spoken by a total of 36 men, 36 women, 25 boys, and 19 girls. There were ten tokens of each vowel from each of the speaker categories, i.e., 10 males produced “heed,” 10 males produced “hid,” etc. In some cases the same speaker contributed tokens to several vowel categories. The stimuli were selected from recordings made by Hillenbrand *et al.* (1995). Note that the vowel /ɔ/ in “hawed” was not used in our study because it

was not identified well (only 82% correct) by the normal-hearing listeners in the Hillenbrand *et al.* study. The tokens of each vowel were selected to represent the complete area of the vowel space, i.e., the tokens came from both the center and the periphery of the vowel space. The means and distributions of the formant values of the tokens selected for this study are shown in Fig. 1. For each vowel from each speaker group the mean of the tokens used in this study were within 100 Hz of the means derived from the entire set used by Hillenbrand *et al.* (1995). This indicates that the tokens were a reasonable representation of the vowel spaces. All of the signals were identified with 90%–100% accuracy by the normal-hearing listeners in Hillenbrand *et al.* (1995).

3. Signal processing

The CIS processor was an implementation of the Wilson *et al.* (1991) design fabricated at the University of Innsbruck (Zierhofer *et al.*, 1994). The signal processor was a sixth-channel design with six-order bandpass filters (Butterworth), full-wave rectification, and a 400-Hz low-pass filter. Signals were pre-emphasized above 1200 Hz. Channel center frequencies were 393, 639, 1037, 1685, 2736, and 4443 Hz. Channel bandwidths were 187, 304, 493, 801, 1301, and

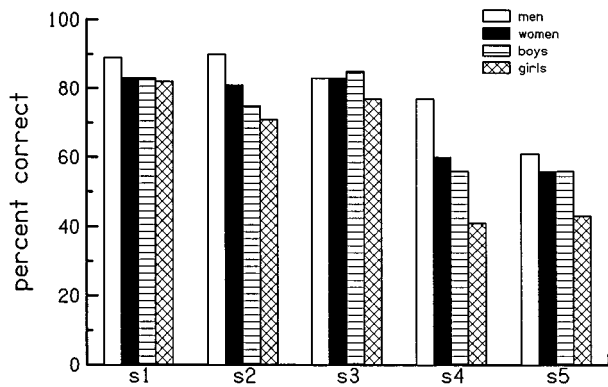


FIG. 2. Average percent correct vowel identification as a function of speaker group for five patients who used a six channel CIS processor.

2113 Hz, respectively. The channels were of equal width on a logarithmic scale. The pulse durations and pulse rates differed for each patient and were chosen after an extensive search through the pulse-duration by pulse-rate space.

4. Procedure

The test was divided into ten sessions. In each session there were three repetitions of each vowel from each of the four speaker groups. The stimuli were completely randomized within each session. Each session consisted of 132 stimuli (= 11 vowels × 4 speaker groups × 3 repetitions). A 5-min recess was allowed following each session. The test sessions were preceded by one practice session in which the identity of vowels was indicated to the listeners. In this practice block one token of each vowel from each of the speaker groups was used.

The stimuli were presented directly to the signal processors via an auxiliary input jack at a comfortable listening level. Responses were collected via a touch sensitive pad.

B. Results

The mean percent correct score for men was 80% correct; for women the mean score was 73% correct; for boys the mean score was 71% correct; and for girls the mean score was 63% correct. The data for each of the five listeners are shown in Fig. 2. A repeated measures analysis of variance indicated a significant main effect for subjects [$F(4,12) = 140.2, p < 0.0001$], a significant main effect for speaker group [$F(3,12) = 32.4, p < 0.0001$], and a significant interaction of subjects and speaker group ($F = 3.79, p < 0.0001$).

For speaker groups, *post hoc* tests according to Scheffe ($\alpha = 0.05$) indicated that (i) the men's vowels were easier to identify than vowels from the other groups, (ii) that vowels from women and boys were more difficult to identify than vowels from men but less difficult than vowels from girls, and (iii) that vowels from girls were more difficult to identify than vowels from any other group. For subjects, *post hoc* tests according to Scheffe ($\alpha = 0.05$) indicated that S1, S2, and S3 performed significantly better than S4 and S5.

The mean scores for each vowel as a function of speaker category are shown in Table II. The most difficult vowels to identify were those in "hod" (38% correct), "had" (59% correct), and "head" (62% correct). The mean score for "head" was reduced by the very poor performance on tokens from women (37% correct).

C. Discussion

In the Introduction it was noted that a test of vowel recognition using tokens from a single speaker from a single speaker group avoids the normally occurring complexities of vowel recognition. As a consequence, data collected in this fashion may overestimate the ability of cochlear implant patients to recognize vowels. The outcome of the present experiment suggests this to be the case. Vowels produced by men were easier to identify than vowels produced by women and boys, and both were easier to identify than the vowels produced by girls.

Other experiments have also found that vowels produced by men are relatively easy to identify for the best performing patients fit with six channel CIS systems. Wilson *et al.* (1990) report a mean score of 92% correct for seven "better" patients who used a CIS processor. The test set was eight vowels spoken by one man and one woman. The three "better" patients in the present experiment averaged 85% correct for the adult male and female speakers (88% and 82%, respectively). The test set included 11 vowels. Both the greater number of vowels in the set and the greater number of speakers undoubtedly contributed to the lower scores in the present experiment. At all events, the data from the present experiment suggest that vowels produced by men can be well identified with six channels of stimulation when a large, but not full, complement of vowels is tested and when the normal variation in formant frequencies for a given vowel exists within the test set.

The potential overestimation of underlying speech perception skills occasioned by the use of only male speakers is

TABLE II. Averaged identification scores (percent correct) for vowels produced by men, women, boys, and girls.

	heed	hid	hayed	head	had	hod	hoed	hood	who'd	hud	heard
Men	94	84	83	73	68	43	89	82	81	83	83
Women	84	82	81	37	55	40	93	82	81	63	92
Boys	77	85	68	75	51	37	74	77	77	63	65
Girls	78	70	67	61	60	31	62	59	65	55	62
Mean	83	80	75	62	59	38	80	75	76	66	76

TABLE III. Results of cluster analysis for distances between channel outputs of vowels produced by men, women, boys, and girls. The between-vowel variance indicates the distance between vowel categories within a speaker group. The measure of within-vowel variance indicates the variability of tokens of a given vowel within a speaker set. The Fisher ratio is the ratio of between-vowel variance to within-vowel variance.

	Between-vowel variance	Within-vowel variance	Fisher ratio
Men	7.30×10^{-2}	2.30×10^{-8}	3.56×10^6
Women	1.15×10^{-2}	1.18×10^{-8}	9.75×10^5
Boys	2.04×10^{-2}	6.20×10^{-8}	3.25×10^5
Girls	1.27×10^{-2}	4.26×10^{-8}	2.99×10^5

illustrated in Fig. 2 by a comparison of the performance of S3 and S4. For S3 performance on the vowel set produced by men (83% correct) suggests that differences in formant frequencies were relatively well resolved. This inference is confirmed by performance on the women's, boys', and girls' vowel sets (83%, 84%, and 77% correct, respectively). Consider, now, the performance of S4. He identified vowels from men with nearly the same accuracy as S3 (77% correct versus 83% correct). In this instance the inference of reasonably good resolution of formant frequencies for the other vowel sets is not appropriate since performance falls from 77% correct for men, to 60% correct for women, to 55% correct for boys, and to 41% correct for girls.

1. Accounting for the difficulty in identification of vowels from different speaker groups

As noted above, vowels produced by men were the easiest to identify. One factor contributing to this effect may be the relatively poor resolution of differences in formant frequencies for women, boys, and girls due to the increased width of the CIS processor filters into which the formants of the women, boys, and girls fall. That is, because a girl's formant frequencies will fall into higher and, therefore, wider filters than a man's, differences in formant frequencies for vowels produced by a girl should be less well resolved. To test this assumption, the signal level at the output of each processor channel for each vowel was measured.¹ To assess the distance between the channel outputs for the different vowels in the set, the results were subjected to cluster analysis (Duda and Hart, 1973) and a measure of between-class scatter was computed (see the Appendix). For this metric the larger the number, the larger the distance between vowels. Therefore, a larger distance between vowels would support the finding that the vowels are more discriminable. The results are shown in the first column in Table III. The largest value occurs for men's vowels. Women's, boys', and girls' vowels have a smaller value, indicating a smaller difference between channel outputs. These results are consistent with the outcome of better performance on men's vowels relative to women's, boys', and girls' vowels. However, the data do not predict the differences in performance on vowels produced by women, boys, and girls.²

It is also reasonable to ask whether the tokens of a given vowel are more variable within one speaker group than another. That is, it could be the case that the channel output patterns for girls, for example, are more variable for a given

TABLE IV. Dynamic range (dB) for electrodes 1–6 for patients S1–S5.

	Dynamic range (dB)					
	Ch. 1	Ch. 2	Ch. 3	Ch. 4	Ch. 5	Ch. 6
S1	15.9	19.1	19.8	22.1	19.4	16.9
S2	28.1	29.2	27.3	28.6	29.8	24.9
S3	16.1	15.7	23.5	21.8	24.5	14.5
S4	10.8	12.0	11.5	11.6	12.2	10.1
S5	15.8	16.2	18.1	18.4	10.8	7.7

vowel than for men. To assess this we used a measure of within-class scatter (see the Appendix). The results are shown in the second column in Table II where a larger number indicates greater variability. The channel output patterns of the boys and girls were found to have greater variability than those of the women and the men. This result is consistent with the poorer performance on vowels produced by boys and girls.

Finally, the measures of between-class variance and within-class variance can be combined using Fisher's ratio which computes the ratio of between-class variance to within-class variance (see the Appendix). The outcome is shown in the third column in Table III. Here a large value indicates a greater distance between items. Men's vowels had the largest value and that value was an order of magnitude larger than the value for women, boys, and girls. Girls had the smallest value. These data are consistent with the outcome that men's vowels were the easiest to identify and that the girls' vowels were the most difficult.

2. Accounting for differences among patients

As described above, subjects S1, S2, and S3 achieved higher scores than S4 and S5. A measure of auditory function—dynamic range, i.e., the range between threshold of detection for electrical stimulation and a high comfortable level of stimulation³—may be related to the better performance of patients S1, S2, and S3 relative to S4 and S5. As shown in Table IV, S1, S2, and S3, relative to S4 and S5, have, most generally, larger dynamic ranges in channels 1–4 and have much much larger dynamic ranges in channels 5 and 6. These data fit the pattern for S1, S2, and S3, relative to S4 and S5, of better recognition of male vowels (88% correct versus 70% correct) and much better recognition of vowels produced by girls (73% correct versus 41% correct). It is possible that for S4 and S5 the small dynamic ranges for electrodes 5 and 6 made coding of girls' formant frequencies more difficult.

3. Accounting for errors in the identification of a given vowel

The three most difficult vowels to identify were those in "hod," "had," and "head." Errors on "head" are the easiest to understand. As shown in Table II, the average identification score for "head" was reduced greatly by the poor identification of /ε/ produced by women. The large difference in identification accuracy among the speaker groups provided a clear window into the difficulty underlying the errors in identification of /ε/ produced by women. The aver-

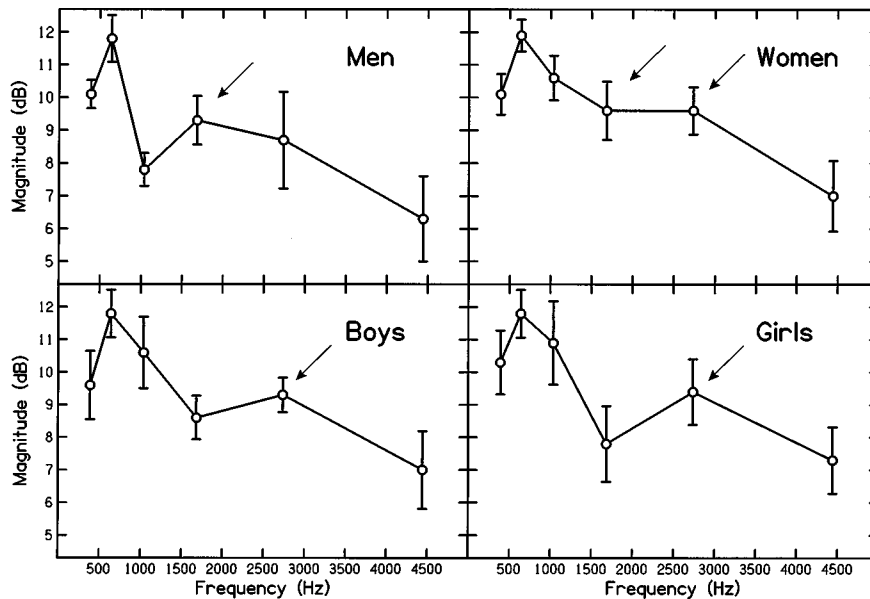


FIG. 3. Average channel output patterns for the vowel / ϵ / (in "head") as a function of speaker group. The arrows point to the channel which codes F_2 for each speaker group.

aged channel output patterns for / ϵ / produced by men, women, boys, and girls are shown in Fig. 3. The output pattern of the women speakers differs from the other patterns in the magnitude of the output for the channel coding F_2 . For men, boys, and girls there is a distinct peak in the pattern corresponding to the channel into which F_2 falls (indicated by the arrows in Fig. 3). This peak is reduced for / ϵ / produced by women. If this too low peak is responsible for the difficulty in identification, then well identified tokens of women's / ϵ / should have a larger peak than less well identified tokens of / ϵ /. As shown in Fig. 4, this was the case. Finally, inspection of the confusion matrix for vowels produced by women indicated that "head" was most often confused with "hud." We would suppose that the channel out-

put pattern of poorly identified tokens of / ϵ / would look much like the output pattern for / Λ /. As shown in Fig. 4, this was the case.

The vowel in "had" was the second most difficult vowel to identify. "Had" was most often confused with "head." A short account of this confusion is as follows. "Had" was produced as a diphthong; the initial portion was similar acoustically to the vowel in "head." In well identified tokens of "had" the channel output pattern during the initial portion of the syllable was similar to that in / ϵ /, while the channel output pattern during the final portion of the syllable was appropriate for / æ /. In poorly identified tokens of "had," the channel output pattern for the initial portion of the vowel was similar to that for / ϵ /, while the output pattern for the final segment was ambiguous between / ϵ / and / æ /.

The vowel in "hod" was the most difficult to identify. The two most common error responses were "had" and "hud." Curiously, there were few similarities between the channel output patterns of the poorly identified tokens of "hod" and the well identified tokens of "had" and "hud." However, the poorly identified tokens of "hod" were distinguishable from the well identified tokens, in that the poorly identified tokens lacked the distinct peak in the output pattern characteristic of the well identified tokens (Fig. 5). As shown in Fig. 5 the poorly identified tokens of "hod" were characterized by a more diffuse distribution of energy across channels 4, 5, and 6. In contrast, the well identified tokens were characterized by a significant drop in channel output level after the fourth channel. Figure 5 illustrates the distinction between the poorly identified and well identified tokens of "hod." The substitution of "had" for "hod" may also have been driven by the similar durations of the two vowels (272 ms, on average, for the vowel in "hod" and 273 ms, on average, for the vowel in "had").

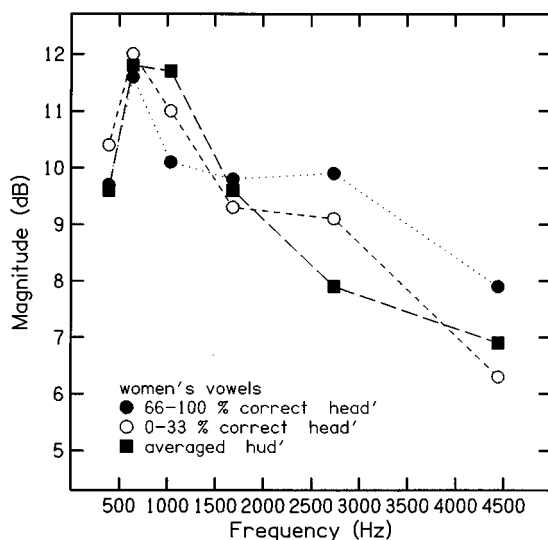


FIG. 4. Average channel output patterns for / ϵ / (in "head") and / Λ / (in "hud") produced by women.

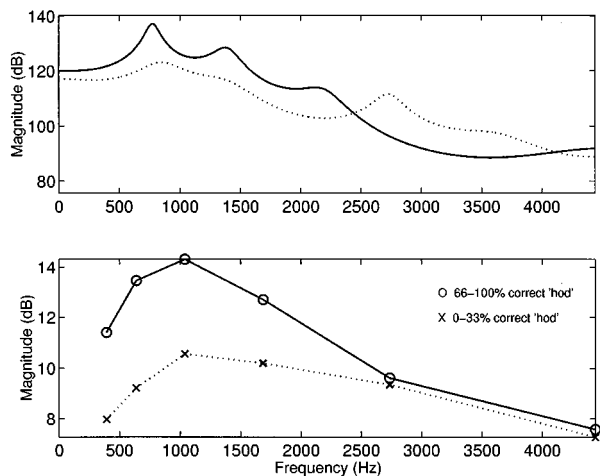


FIG. 5. (top) Spectra of the vowel /a/ (in “hod”) of a well-identified token of “hod” (solid lines) and a poorly identified token of “hod” (dashed lines) produced by male speakers. These spectra were derived using a 20-ms window, centered at the midpoint of the vowel, and a 14-pole LPC analysis. (bottom) Channel output patterns of a well-identified token of /a/ in “hod” (solid lines), and a poorly identified token of /a/ (dashed lines).

II. EXPERIMENT 2

In the discussion of experiment 1 it was suggested that channels 5 and 6 were of particular importance to the recognition of vowels produced by women, boys, and girls because of the higher formant frequencies, relative to men, produced by these speakers. To test this hypothesis, channels 5 and 6 were turned off and the patients were asked to identify vowels as in experiment 1. The hypothesis to be tested was that turning off channels 5 and 6 would have no effect on men’s vowels, but would have a significant effect on the vowels produced by women, boys, and girls.

A. Method

1. Subjects

The subjects were those described in experiment 1.

2. Stimuli

Three of the test blocks used in experiment 1 were used in this experiment. Three blocks, instead of ten, were used in order to reduce patient fatigue.

3. Signal processing

In order to eliminate channels 5 and 6, the value of the high comfortable level for channels 5 and 6 was set to the value of threshold. In this way the bandwidths of channels 1–4 were the same as those in experiment 1.

4. Procedure

The test was divided into three blocks of stimuli. In each block there were three repetitions of each vowel from each of the four speaker groups. The stimuli were completely randomized within each block. The test sessions were preceded by one practice session in which the identity of vowels was indicated to the listeners. In this practice block one token of each vowel from each of the speaker groups was used.

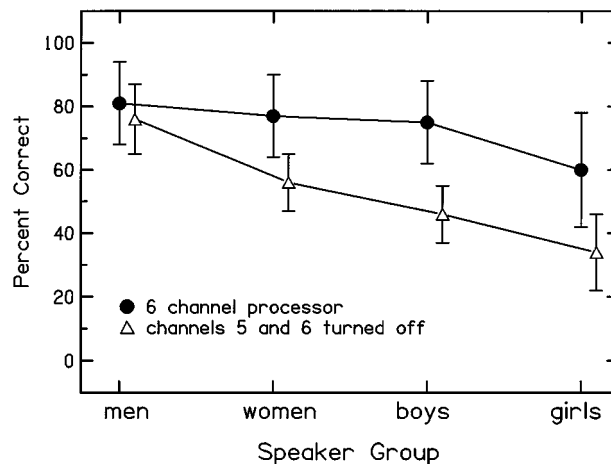


FIG. 6. Average percent correct vowel identification as a function of speaker group. The parameter is processor configuration. The solid circles indicate performance with a six-channel processor, and the open triangles indicate performance with a six-channel processor with channels 5 and 6 turned off.

As in experiment 1, the stimuli were presented directly to the signal processors via an auxiliary input jack at a comfortable listening level. Responses were collected via a touch sensitive pad.

B. Results and discussion

The mean scores with a six-channel processor and with a processor with channels 5 and 6 turned off are shown in Fig. 6. For this analysis, the three test blocks used in experiment 2 were compared to the same three test blocks used in experiment 1. A repeated measures analysis of variance indicated a main effect for speaker group [$F(3,30)=47.8$, $p<0.00001$], a main effect for channel configuration [$F(1,10)=258.4$, $p<0.00001$], and a speaker group by channel configuration interaction [$F(3,30)=11.82$, $p<0.0001$]. *Post hoc* tests according to Scheffe ($\alpha=0.05$) indicated that the scores for vowels produced by men did not differ in the two processor conditions. The scores for women, boys, and girls did differ in the two processor conditions. This outcome, that the identification of vowels produced by men was not significantly affected by elimination of channels 5 and 6 but that the identification of vowels produced by women, boys, and girls was significantly affected, is consistent with our hypothesis that channels 5 and 6 become critical for identification as the second formants of the speakers increase in frequency.

III. GENERAL DISCUSSION

In the discussions following experiments 1 and 2, we commented (i) on differences in the recognition of vowels produced by men, women, boys, and girls, (ii) on the factors which contributed to errors in identification, (iii) on factors which might account for some patients achieving high scores while other patients achieved low scores, and (iv) on the role of channels 5 and 6 in the recognition of vowels produced by men, women, boys, and girls. In this section we suggest how

vowels with varying formant frequencies can be recognized when the spectra of the vowels are specified by only a small number of fixed-frequency components.

Consider, first, the information about vowel identity available to a normal-hearing listener. If the speaker has a low F_0 , then it is likely that harmonics in the source spectrum coincide with peaks in the vocal tract transfer function. In this instance the listener has only to detect the highest amplitude harmonics in the spectrum in order to define the formant values of the signal. However, if the speaker has a high F_0 , then there may not be harmonics which coincide with the peaks in the transfer function. In this instance, the location of the formant peak must be derived from the relative amplitudes of the harmonics which surround the peak, or from the cochlear excitation pattern which results from the pattern of harmonic amplitudes.

The cochlear implant patients in the present study were faced with a situation similar to that of normal-hearing individuals listening to signals with a very high F_0 . In this instance the “ F_0 ” was so high that only six components appeared in the spectrum. Consider, now, how six fixed-frequency components could code F_1 and F_2 for a set of vowels. Figure 3 shows the averaged, channel-output levels for the vowel in “head” spoken by men, women, boys, and girls. The differences in amplitude of the channel outputs in channels 2 and 3 code the frequency of F_1 . For men the highest output level is in channel 2 and the output of channel 3 is very low. This implies a low F_1 (mean $F_1 = 579$ Hz). For women the level of channel 3 is higher than for men indicating a higher frequency F_1 (women’s mean $F_1 = 720$ Hz). For boys the difference between channels two and three is similar to that for women, suggesting that the F_1 is the same as for women (boys’ mean $F_1 = 723$ Hz). For girls, the output of channel 3 is slightly higher than for boys indicating a slightly higher F_1 (girl’s mean $F_1 = 759$ Hz). For men, the peak in energy corresponding to F_2 is in channel 4 (mean $F_2 = 1826$ Hz). For women, channels 4 and 5 have similar levels indicating a higher F_2 than for men (women’s mean $F_2 = 2001$ Hz). For boys, the peak is at channel 5, indicating a higher F_2 than for women (boys’ mean $F_2 = 2176$ Hz), while for girls the peak is also at channel 5 but the output of channel 4 is reduced indicating a higher F_2 relative to that of boys (girls’ mean $F_2 = 2314$ Hz).

The foregoing indicates that differences in channel output levels reflect differences in formant frequencies. The results of the present experiment demonstrate that differences among the output levels of six channels can be used to code the vowel formant frequencies of male voices with reasonable adequacy. More channels will be needed to code the formants of other speakers, especially girls, with similar adequacy.

ACKNOWLEDGMENTS

This research was supported by NIDCD RO1 0000654-6. We thank Jim Hillenbrand for allowing us to use the stimuli he so laboriously gathered and analyzed. We also thank the anonymous reviewers for their helpful comments.

APPENDIX

This Appendix describes the measures used to analyze the vowel channel output vectors. These measures are based on within- and between-class scatter matrices (Duda and Hart, 1973), which are defined as follows.

Let x be a sixth-dimensional channel output vector, and m_i the mean channel vector of the i th vowel. Then, the within-class scatter matrix S_W can be defined as:

$$S_W = \sum_{i=1}^V \sum_{x \in C_i} (x - m_i)(x - m_i)^T,$$

where V is the number of vowels, and C_i is the cluster containing the channel outputs of the i th vowel. Similarly, the between-class scatter matrix S_B can be defined as follows:

$$S_B = \sum_{i=1}^V n_i (m_i - m)(m_i - m)^T,$$

where n_i is the number of channel vectors contained in cluster C_i , and m is the overall mean channel vector.

The matrices S_B and S_W can be used to measure the between- and within-vowel scatter of the channel output vectors. A simple scalar measure of the channel outputs scatter is the determinant of the scatter matrix, which provides an estimate of the hyperellipsoidal scattering volume. An estimate of the *between-vowel variance* can therefore be obtained by taking the determinant of the between-class scatter matrix S_B . Similarly, an estimate of the *within-vowel variance* can be obtained by taking the determinant of the within-class scatter matrix S_W .

The Fisher’s ratio can be constructed as the ratio of between- to within-vowel variance, i.e.,

$$F = \frac{|S_B|}{|S_W|},$$

where $|\cdot|$ denotes the determinant of a matrix. This ratio is a very popular class separability criterion in multiple discriminant analysis (Duda and Hart, 1973). Large values of F indicate that the classes, or vowels in our case, are well separated from each other, and therefore easily discriminable. Small values of F indicate that the classes are possibly intermingled with each other, and therefore easily confusable.

¹Channel output measurements were made at a point 50 ms into the time waveform. The channel outputs were computed as follows. The signal was pre-emphasized and then bandpassed into six logarithmic frequency bands using sixth-order Butterworth filters. The envelopes of the filtered signal were then extracted by full-wave rectification and low-pass filtering with a 400-Hz cutoff frequency. Six channel outputs were computed by estimating the root-mean-square (rms) energy of the six envelopes over a 10-ms frame.

²The variance metrics accounted for the differences in performance for some of the speaker groups, but failed to predict the differences in performance between other groups. This might be because the metrics used static measurements of the vowels taken at a point 50 ms into the time waveform. It is possible that if the metric had used measurements from the onset, middle, and offset segment of each vowel, that the metric might better predict the performances of all speaker groups.

³Measurements of threshold and a high comfortable level of stimulation were made with a 50-ms tone burst using a manual “up-down” procedure.

- Blamey, P., Dowell, R., Brown, A., Clark, G., and Seligman, P. (1987). "Vowel and consonant recognition of cochlear implant patients using formant-estimating speech processors," *J. Acoust. Soc. Am.* **82**, 48–57.
- Boex, C., Pellizzone, M., and Montandon, P. (1994). "Improvements in speech understanding with the CIS strategy for the Ineraid multichannel cochlear implant," in *Advances in Cochlear Implants*, edited by I. Hochmair-Desoyer and E. Hochmair (International Interscience Seminars, Vienna), pp. 136–140.
- Dorman, M., Dankowski, K., McCandless, G., and Smith, L. (1989). "Identification of synthetic vowels by patients using the Symbion multichannel cochlear implant," *Ear Hear.* **10**, 40–43.
- Dorman, M., and Loizou, P. (1997). "Mechanisms of vowel recognition for Ineraid patients fit with CIS processors," *J. Acoust. Soc. Am.* **102**, 581–587.
- Duda, R., and Hart, P. (1973). *Pattern Classification and Scene Analysis* (Wiley-Interscience, New York).
- Hillenbrand, J., Getty, L., Clark, M., and Wheeler, K. (1995). "Acoustic characteristics of American English vowels," *J. Acoust. Soc. Am.* **97**, 3099–3111.
- House, A. (1961). "On vowel duration in English," *J. Acoust. Soc. Am.* **33**, 1174–1178.
- Miller, J. (1989). "Auditory perceptual interpretation of the vowel," *J. Acoust. Soc. Am.* **85**, 2114–2134.
- Peterson, G., and Barney, H. (1952). "Control methods used in a study of vowels," *J. Acoust. Soc. Am.* **24**, 175–184.
- Skinner, M., Clark, G., Whitford, L., Seligman, P., Staller, S., Shipp, D., Shallop, J., Everingham, C., Menapace, C., Arndt, P., Antogenelli, T., Brimacombe, J., Pijl, S., Daniels, P., George, C., McDermont, H., and Beiter, A. (1994). "Evaluation of a new spectral peak coding strategy for the Nucleus 22-channel cochlear implant system," *Am. J. Otolaryngol.* **15** (Suppl. 2), 15–27.
- Skinner, M., Holden, L., Dowell, R., Seligman, P., Brimacombe, J., and Beiter, A. (1991). "Performance of postlinguistically deaf adults with the wearable speech processor (MSP) of the Nucleus multi-channel cochlear implant," *Ear Hear.* **12**, 3–22.
- Strange, W. (1989). "Evolving theories of vowel perception," *J. Acoust. Soc. Am.* **85**, 2081–2087.
- Tyler, R., Preece, J., and Lowder, M. (1987). "The Iowa audiovisual speech perception laser videodisc," Laser Videodisc and Laboratory Report (University of Iowa, Department of Otolaryngology Head and Neck Surgery).
- Wilson, B., Finley, C., Lawson, D., Wolford, R., Eddington, D., and Rabinowitz, W. (1991). "Better speech recognition with cochlear implants," *Nature (London)* **352**, 236–238.
- Wilson, B. S., Lawson, D., and Finley, C. (1990). "Speech processors for auditory prostheses," Fourth Quarterly Progress Report on NIH Project No. N01-DC-9-2401, 1–9.
- Zierhofer, C., Peter, O., Bril, S., Pohl, P., Hochmair-Desoyer, I., and Hochmair, E. (1994). "A multichannel cochlear implant system for high-rate pulsatile stimulation strategies," in *Advances in Cochlear Implants*, edited by I. Hochmair-Desoyer and E. Hochmair (International Interscience Seminars, Vienna), pp. 204–207.

Pitches of concurrent vowels

Peter F. Assmann and D. Dwayne Paschall^{a)}

School of Human Development, The University of Texas at Dallas, Box 830688, Richardson, Texas 75083-0688

(Received 29 October 1996; revised 18 October 1997; accepted 14 November 1997)

When two vowels are presented simultaneously, listeners can report their phonemic identities more accurately if their fundamental frequencies (F_0 's) are different rather than the same. If the F_0 difference (ΔF_0) is large, listeners hear two vowels on different pitches; if the ΔF_0 is small the vowels are identified less accurately and they do not evoke different pitches. The present study used a matching task to obtain judgments of the pitches evoked by "double vowels" created from pairwise combinations of steady-state synthetic vowels /i/, /a/, /u/, /æ/, and /ɚ/. One F_0 was always 100 Hz; the other F_0 was either 0, 0.25, 0.5, 1, 2, or 4 semitones higher. Experienced listeners adjusted the F_0 of a tone complex to assign pitch matches to 50-ms or 200-ms double vowels. For ΔF_0 's up to two semitones, listeners' matches formed a single cluster in the frequency region spanned by the two F_0 's. When the ΔF_0 was 4 semitones, the matches generally formed two clusters close to the F_0 of each vowel, suggesting that listeners perceive two distinct pitches when the ΔF_0 is 4 semitones but only one clear pitch (possibly accompanied by one or more weaker pitches) with smaller ΔF_0 's. When the duration was reduced from 200 ms to 50 ms, only a subset of the vowel pairs with a ΔF_0 of 4 semitones produced a bimodal distribution of matches. In general, 50-ms stimuli were matched less consistently than their 200-ms counterparts, indicating that the pitches of concurrent vowels emerge less clearly when the stimuli are brief. Comparisons of pitch and vowel identification data revealed a moderate correlation between match intervals (defined as the absolute frequency difference between first and second pitch matches) and identification accuracy for the 200-ms stimuli with the largest ΔF_0 of 4 semitones. The link between match intervals and vowel identification was weak or absent in conditions where the stimuli evoked only one pitch. © 1998 Acoustical Society of America. [S0001-4966(98)05702-6]

PACS numbers: 43.71.An, 43.71.Bp, 43.71.Es, 43.66.Hg [WS]

INTRODUCTION

When two voices compete, listeners find it easier to understand the target voice if the interfering voice is on a different pitch (Brokx and Nootboom, 1982). A difference in fundamental frequency (ΔF_0) between two simultaneous vowels helps listeners to identify both vowels (Scheffers, 1983; Zwicker, 1984; Chalikia and Bregman, 1989; Assmann and Summerfield, 1990, 1994; McKeown, 1992; Culling and Darwin, 1993; de Cheveigné *et al.*, 1997). When the vowels differ in F_0 by more than about 2 semitones, the subjective impression is of two voices producing different vowels on different pitches. In contrast, when the F_0 's are the same, listeners hear a blend of two vowels on the same pitch. These findings have provided the motivation for a stage of F_0 -guided segregation in several models of the identification of concurrent vowels (Scheffers, 1983; Assmann and Summerfield, 1990; Meddis and Hewitt, 1992; de Cheveigné, 1997). These models differ primarily in the way they use F_0 information to segregate the components of double vowels in order to predict the improvement in vowel identification with increasing ΔF_0 .

The models proposed by Scheffers (1983) and Assmann and Summerfield (1990) include a stage in which the F_0 's of both vowels are determined. An estimate of the F_0 of each

vowel is used to drive a segregation stage that relies on a spectral or temporal analysis of the composite signal. Since segregation and pitch both depend on an analysis of the F_0 's that are present, these models predict a close link between pitch perception and vowel identification. Specifically, they suggest that the improvement in vowel identification as ΔF_0 increases is coupled with an increased tendency to perceive two pitches rather than one. Consistent with this assumption is the subjective impression of the emergence of two distinct pitches as the ΔF_0 is increased from 0 to 4 semitones. When the duration of the stimulus is reduced from 200 to 50 ms, the impression of two voices on different pitches is less distinct, and the extent of the improvement in identification with increasing ΔF_0 is reduced (Assmann and Summerfield, 1990, 1994; Culling and Darwin, 1994; McKeown and Patterson, 1995).

The model proposed by Meddis and Hewitt (1992) makes the assumption that auditory attention is initially focused on the dominant vowel in the pair. An estimate of its F_0 guides a temporal analysis to group together frequency channels with a common temporal structure. The nondominant vowel is reconstructed by grouping together the remaining channels. Consistent with this approach is the finding that one vowel in the pair is generally perceived as *dominant* relative to the second *nondominant* vowel, and is identified more accurately (Scheffers, 1983). McKeown (1992) found that the relationship between dominant and nondominant

^{a)}Current address: Department of Communication Disorders, Box 42073, Texas Tech University Health Sciences Center, Lubbock, TX 79409-2073.

TABLE I. Formant frequencies of the vowels.

Vowel	F_1 (Hz)	F_2 (Hz)	F_3 (Hz)	F_4 (Hz)	F_5 (Hz)
/i/	250	2250	3050	3350	3850
/a/	750	1050	2950	3350	3850
/u/	250	850	2250	3350	3850
/æ/	750	1450	2450	3350	3850
/ɜ/	450	1150	1250	3350	3850

vowels is determined by the spectral shapes of the constituent vowels, and that the pattern of dominance is maintained across a wide range of vowel intensity ratios. McKeown and Patterson (1995) showed that the improvement in identification accuracy with increasing stimulus duration is primarily due to the nondominant vowel.

Several aspects of the identification of double vowels are not easily accounted for in terms of F_0 -based segregation. Culling and Darwin (1993, 1994) found that the benefits of small ΔF_0 's (1 semitone or less) emerged even when the ΔF_0 was restricted to a subset of the formants, when the two F_0 's were "swapped" across the formants of the two vowels, or when the spectrum envelope of each vowel was defined by the even harmonics of one F_0 and the odd harmonics of the other F_0 . They proposed that the benefits of small ΔF_0 's (1 semitone or less) for vowel identification are based on waveform interactions that enhance the formant patterns of the constituent vowels, rather than a process of F_0 -guided segregation. Consistent with this idea, Assmann and Summerfield (1994) found that some 50-ms segments of double vowels (extracted from a 200-ms stimulus) were easier to identify than other segments. These variations in identification accuracy appeared only when the stimuli differed in F_0 by 1 semitone or less. These findings suggest that waveform interactions over the time course of the stimulus can enhance the spectral patterns to provide "glimpses" of the constituent vowels. These interactions contributed only when the ΔF_0 was small, with stimuli that did not evoke a strong impression of two distinct pitches.

While a number of studies have examined the processes involved in the identification of double vowels, little attention has been given to the pitches evoked by these stimuli. Investigation of the pitches of double vowels is of interest for two reasons. First, these data provide a basis for testing the predictions of models of double-vowel identification that rely on F_0 estimation to account for the improved accuracy as a function of ΔF_0 . A second more basic reason is that models of pitch perception have focused largely on sounds that evoke a single pitch, such as tone complexes and single vowels. Sounds that evoke multiple pitches, such as double vowels, may present special problems for these models because pairs of corresponding harmonics are close in frequency (Beerends and Houtsma, 1989; Assmann and Summerfield, 1990; Darwin *et al.*, 1995).

The present study used a matching paradigm (Moore *et al.*, 1985) to investigate the pitches evoked by double vowels. Listeners adjusted the F_0 of a 25-component tone complex to find the best match in pitch. In experiment 1, they assigned a single match to the dominant pitch. In ex-

TABLE II. Fundamental frequencies of the vowels.

ΔF_0 (semitones)	0	0.25	0.5	1	2	4
F_{01} (Hz)	100	100	100	100	100	100
F_{02} (Hz)	100	101.45	102.93	105.95	112.25	125.99

periment 2, they assigned two matches to the dominant and nondominant pitches.

The purpose of the study was (i) to confirm the subjective impression that double vowels are more likely to evoke two clear pitches (rather than only a single pitch) as the ΔF_0 increases from 0 to 4 semitones, (ii) to determine the F_0 separation at which this change occurs, (iii) to establish whether longer (200 ms) segments are more likely to evoke two distinct pitches than brief (50 ms) segments, and (iv) to examine the relationship between pitch and vowel identification as a function of duration and ΔF_0 .

I. THE EXPERIMENTS

In the pitch-matching paradigm described by Moore *et al.* (1985), listeners were required to adjust the F_0 of a tone complex to find the best match to a target stimulus. Several factors contribute to the difficulty of this task when the target stimuli are double vowels. First, the target and matching stimuli have different spectrum envelopes, and hence differ in timbre. Second, double vowels with large ΔF_0 's are perceived as having two pitches, while the matching stimuli evoke only one pitch. Third, double vowels with small ΔF_0 's frequently evoke a sensation of roughness, created by interactions among corresponding unresolved harmonics of the two vowels (Terhardt, 1974; Carlyon, 1995). Given the complexity of the task, we asked listeners in the first experiment to adjust the F_0 of a tone complex to match only the dominant pitch evoked by the double vowel. In subsequent experiments they made two pitch matches to each double vowel.

A. Experiment 1: Single-pitch matches

1. Test stimuli

The test stimuli were 200-ms double vowels obtained from an earlier study by Assmann and Summerfield (1994, experiment 1: *long* condition). They were constructed by summing the digital waveforms of pairs of single vowels. The single vowels were synthesized using a version of the Klatt cascade formant synthesizer (Klatt, 1980; Summerfield and Assmann, 1991). The vowels were steady-state five-formant approximations to the American English vowels /i/, /a/, /u/, /æ/, and /ɜ/, using the formant frequencies listed in Table I. The single vowels were synthesized with the same amplitude of voicing to simulate approximately equal vocal effort. Six versions of each vowel were constructed using the F_0 's listed in Table II.

Double vowels were constructed by summing a pair of single vowels. In each pair one vowel had an F_0 of 100 Hz; the other F_0 was 0, 0.25, 0.5, 1, 2, or 4 semitones higher. All possible pairwise combinations of the five vowels were used, for a total of 150 test stimuli (25 vowel pair \times 6 F_0 's).

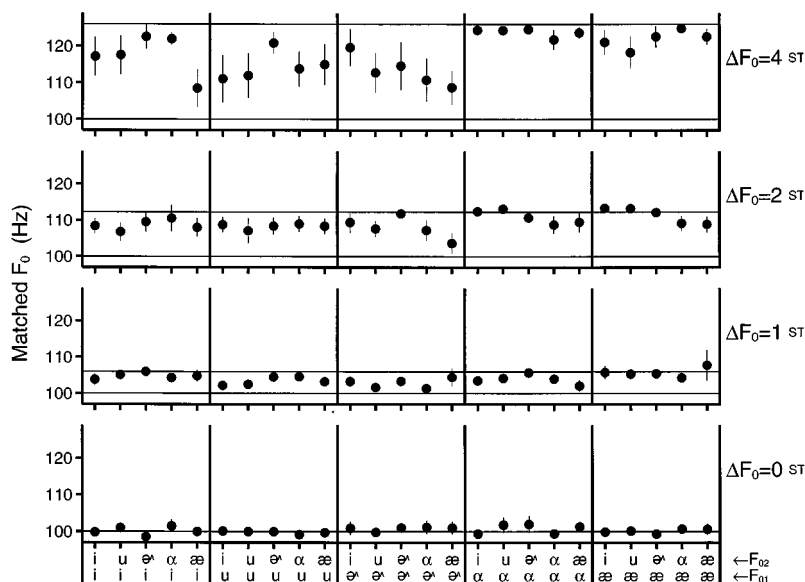


FIG. 1. Single-pitch matches to 200-ms double vowels in experiment 1. Filled circles show the means (across the five listeners) of median matched F_0 (across the five trials). Error bars show ± 1 standard error across listeners. Results for four ΔF_0 's are shown in separate panels for the 25 vowel pairs whose phonetic categories are indicated by the symbols below the abscissa. The solid lines in each panel indicate the actual F_0 's that were present.

2. Matching stimuli

The matching stimuli were tone complexes formed by a harmonic series with a sloping spectrum of approximately -6 dB/oct, similar to the combined glottal source and radiation spectrum of voiced speech (Klatt, 1980).¹ The F_0 of the matching stimulus was adjustable in the range 70–190 Hz with a resolution finer than 0.3 Hz. Onsets and offsets of the matching stimuli were tapered with a 10-ms linear ramp.

3. Procedure

The stimuli were presented on-line (Ariel DSP-16, 16-bit quantization, 10 000 samples/s), low-pass filtered at 4.2 kHz and -110 dB/oct (Stanford Research Systems SR-640), manually attenuated (Kay model 432D), and presented to the left ear via Sennheiser HD-490 headphones. The levels of the test stimuli ranged from 58 to 71 dB SPL, while the matching stimuli ranged from 57 to 65 dB SPL (Bruel & Kjaer type 4152 artificial ear, Bruel & Kjaer type 2235 sound level meter, 6-cc coupler, A-weighting). The test stimuli were synthesized in advance and stored in computer files. The matching stimuli were synthesized on-line. Test and matching stimuli were presented in alternation separated by a 512-ms silent interval. Each pair was repeated at intervals of 1.2 s.

Listeners adjusted the F_0 of the matching stimulus with a computer-controlled mouse to match its pitch with the dominant pitch of the double vowel. They were instructed to bracket their matches, i.e., to approach the target pitch from ascending and descending directions before selecting their match. When satisfied with the match they recorded their response by pressing the mouse button. To prevent listeners from forming an association between the position of the mouse and F_0 range of the matching stimulus, the computer monitor was disabled and the F_0 of the matching stimulus was reset to a random starting value within the 70–190 Hz range at the onset of each trial. The mouse pointer was re-

positioned randomly by dividing the output of a random number generator by a scale factor to place the output in the range between 0 and the maximum number of pixels on the video display (in this case, 640 pixels along the horizontal dimension). Listeners completed 15 listening sessions of approximately 45 min on separate days. Each session included one-third of the 150 test stimuli, presented in a different random sequence for each trial and for each listener.

4. Subjects

Five listeners, including the two authors, took part in experiment 1. All had pure-tone audiometric thresholds within normal limits at octave frequencies between 0.25 and 8 kHz in the left ear. All were native speakers of American English except one (PA) who was a speaker of Canadian English. All subjects participated in a pitch-matching pretest and a double-vowel identification experiment. They identified both constituents of the 200-ms double vowels and their performance was similar to that of other subjects (Assmann and Summerfield, 1994). None of the listeners were professional musicians, although the majority had some musical training.²

5. Results and discussion

The median matched F_0 across the five trials was taken as a summary measure of the dominant pitch. An analysis of variance revealed a significant main effect of ΔF_0 [$F_{(5,20)} = 34.62$; $p < 0.01$]. A significant linear trend was present, with higher matched F_0 's as the ΔF_0 increased [$F_{(1,25)} = 142.82$; $p < 0.01$]. The interaction between vowel pair and ΔF_0 was significant [$F_{(120,480)} = 1.76$; $p < 0.01$] and is shown in Fig. 1.

Figure 1 shows that listeners' matches to the dominant pitch were generally close to 100 Hz when the two vowels had the same F_0 of 100 Hz. There were no significant dif-

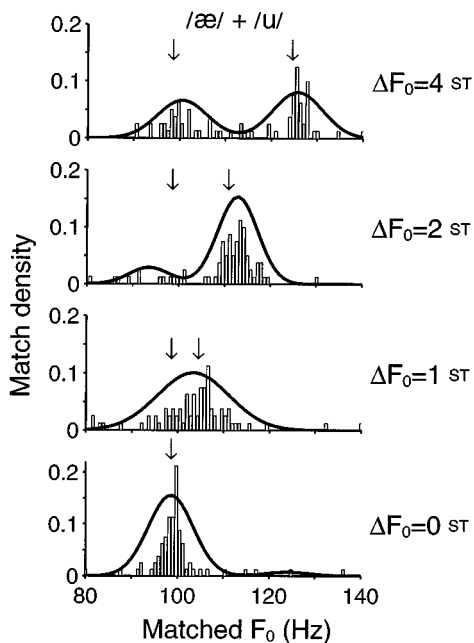


FIG. 2. Histograms of pitch matches for a 200-ms double vowel /æ,u/. The vowel /æ/ had an F_0 of 100 Hz, while /u/ was 0, 1, 2, or 4 semitones higher. The solid line in each panel indicates the result of fitting the histogram with the weighted sum of two Gaussian distributions. Arrows indicate the two F_0 's that were present.

ferences among vowel pairs in this condition, indicating that listeners assigned their matches consistently and without bias when the F_0 's were the same. For small ΔF_0 's up to one semitone, matches generally occupied the frequency region between the two F_0 's (henceforth, F_{01} and F_{02}). Significant differences among the vowel pairs emerged only in the two conditions with the largest ΔF_0 's of 2 and 4 semitones.

An interesting feature of the results was a bias favoring the higher F_0 in listeners' pitch judgments. Across the set of 25 vowel pairs with ΔF_0 's of 2 and 4 semitones, 65.6% of the matches were less than ± 0.5 semitone from F_{02} , while only 16.4% were less than ± 0.5 semitone from F_{01} . In the 4-semitone condition, pitch matches near F_{02} were more prevalent when the vowel with the lower F_0 of 100 Hz had a high $F1$ frequency (i.e., when it was either /a/, or /æ/) rather than a low $F1$ (as in /i/ and /u/). One factor that might help to explain this pattern is that the low-numbered harmonics of vowels in the "spectral dominance region" are the main determinants of pitch (Plomp, 1967; Ritsma, 1967; Moore and Glasberg, 1985). When the first formant ($F1$) has a high frequency, the spectrum levels in the frequency region below the $F1$ peak can be as much as 10 dB lower. This creates a spectral "valley" where a lower-frequency $F1$ from the competing vowel can have an improved signal-to-noise ratio. However, Fig. 1 shows that identical-vowel pairs (such as /æ,æ/) also showed a bias toward the higher F_0 . Identical-vowel pairs have the same spectrum envelope, and the levels of harmonics below $F1$ are similar. For these stimuli, little improvement in signal-to-noise ratio is expected, and hence an alternative explanation must be sought.³

Figure 1 shows that several vowel pairs had mean matched F_0 's that were midway between F_{01} and F_{02} in the

4-semitone condition. The standard errors for these stimuli were consistently larger than those with means near F_{02} . Inspection of individual matches for these stimuli revealed an interesting pattern: Most were clustered either near F_{01} or F_{02} , but few had intermediate values. Four of the five listeners showed this bimodal pattern on different trials, while a fifth consistently assigned all matches close to F_{02} . For these stimuli, the dominant pitch varied as a function of listener and trial and was not adequately characterized by the summary measures reported here.

B. Experiment 2: Double-pitch matches

In experiment 1 listeners were instructed to match only the dominant pitch. In experiment 2 listeners provided judgments of *both* pitches by matching the dominant and non-dominant pitches in succession. If only one pitch was present, they were instructed to assign the same match twice.

1. Procedure

The matching and test stimuli were the same as those used in experiment 1. Test and matching stimuli were presented monaurally in alternation, repeating at 1.2-s intervals. Each trial consisted of two phases. In phase I, listeners adjusted the F_0 of the matching stimulus with a computer-controlled mouse to match its pitch with the dominant pitch of the double vowel. When satisfied with the match, listeners recorded their response by pressing the mouse button. If a second pitch was perceived to be present, listeners adjusted the F_0 of the matching stimulus to match the nondominant pitch. If only one pitch was perceived, listeners assigned the second match to the same pitch selected in phase I. After every five alternating pairs, the response from phase I was repeated as a reminder, following a 51.2-ms interval.

Four experienced listeners, including the two authors, participated in experiment 2. All had previously taken part in experiment 1. Listeners made 10 matches to each of the 150 double vowels over a series of 30 individual listening sessions. Fifty double vowels were presented in each session in random sequence. Sessions lasted approximately 45 min.

2. Results and discussion

Analyses were carried out to determine the conditions in which listeners heard two pitches rather than one, and the accuracy with which their pitch matches reflected both the F_0 's that were present and the interval (ΔF_0) between them. To determine the number of pitches and the relative salience of each pitch, we studied the distribution of pitch matches to each double vowel. We assumed that listeners' matches to each pitch would follow a normal distribution with a mean m centered on the frequency correlate of the perceived pitch, and a standard deviation s determined by internal noise and accuracy of matching. The distribution of matches to double vowels was modeled as the weighted sum of two Gaussian distributions:

$$p(x; m_1, m_2, s, \varphi) = \frac{\varphi}{s\sqrt{2\pi}} e^{-(x-m_1)^2/2s^2} + \frac{1-\varphi}{s\sqrt{2\pi}} e^{-(x-m_2)^2/2s^2}. \quad (1)$$

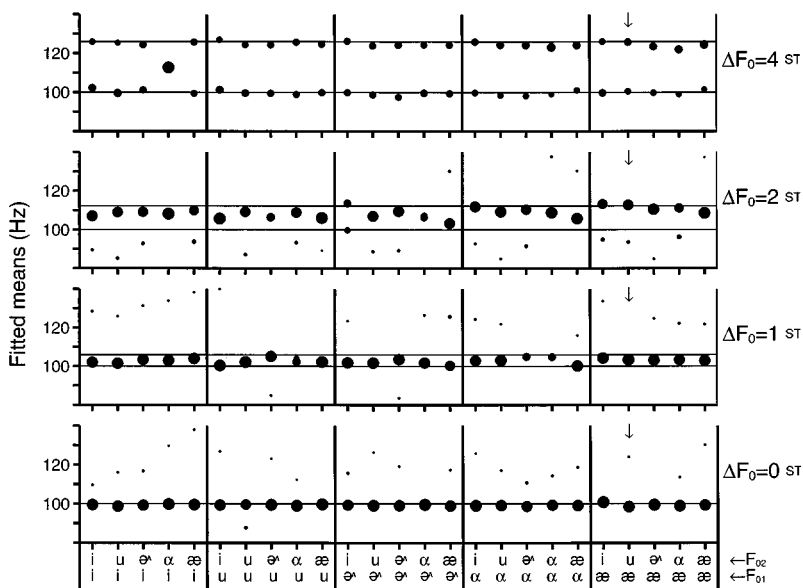


FIG. 3. Double-pitch matches to 200-ms double vowels in experiment 2. Filled circles indicate the means of two Gaussian distributions that gave the best fit to the histogram of pitch matches. The size of the circle reflects the relative weight assigned to each distribution. Results are shown for ΔF_0 's of 0, 1, 2, and 4 semitones and 25 vowel pairs whose phonetic categories are indicated by the symbols below the abscissa. The solid lines in each panel indicate the actual F_0 's that were present. The downward pointing arrows show results for the example in Fig. 2.

The parameters m_1 and m_2 represent the frequency correlates of the two pitches, the standard deviation s is assumed to be the same for each pitch, and the weighting factor φ determines the relative salience of each pitch (in the interval 0–1). When a single pitch is present, the distribution of matches is expected to have a single mode with $m_1 = m_2$. When two pitches of equal salience are present it is expected that $m_2 \neq m_1$, with $\varphi \approx 0.5$.

Estimates of the parameters m_1 , m_2 , s , and φ were obtained by minimizing the log likelihood error function

$$e = - \sum_x \log p(x; m_1, m_2, s, \varphi) \quad (2)$$

with respect to x , the vector of matched F_0 's for a given double vowel. To obtain a sufficient density of matches, pitch matches to each stimulus were combined across the two matches assigned on each trial, ten trials and four listeners and plotted in the form of a histogram as shown in Fig. 2. The example is the vowel pair /æ,u/, with ΔF_0 's of 0, 1, 2, and 4 semitones. The solid line in each panel is the fitted probability density function given by Eq. (1). In this example, the distribution of matches appears unimodal (consistent with the presence of only one pitch) for ΔF_0 's of 0 and 1 semitone. The distribution is bimodal with peaks of roughly the same height (suggesting two pitches) for a ΔF_0 of 4 semitones. The model sometimes generated an estimate of a secondary peak centered on a small cluster of outlying matches, as illustrated in the 2-semitone example in Fig. 2. In these cases the stronger peak was associated with a weighting factor φ close to 1.0. By convention, the parameter associated with the stronger distribution is designated as m_1 , and the weaker distribution as m_2 .

Figure 3 shows the results of fitting the model to stimuli with ΔF_0 's of 0, 1, 2, and 4 semitones. The filled circles

indicate the parameter estimates for m_1 and m_2 . The size of each circle is proportional to φ for m_1 , and proportional to $1 - \varphi$ for m_2 . Large symbols suggest the presence of a single dominant pitch. Small circles may indicate a weak pitch, or the presence of a small cluster of matches of uncertain status. For ΔF_0 's up to 2 semitones, nearly all vowel pairs are represented by large circles, indicating that the distribution of matches was dominated by a single peak. The large circles are generally positioned between F_{01} and F_{02} . Many vowel pairs are also accompanied by small circles, but their frequency locations do not seem to follow a systematic pattern. With a ΔF_0 of 4 semitones, all vowel pairs except one (/i,α/) were represented by two circles of approximately the same size, positioned near the frequencies of F_{01} and F_{02} . The results suggest that listeners generally perceive a single dominant pitch (possibly accompanied by additional, weaker pitches) when the ΔF_0 is 2 semitones or less. With the largest ΔF_0 of 4 semitones, pitch matches generally form two distinct clusters close to the two F_0 's that were present, consistent with the interpretation that these stimuli evoke two distinct pitches.

The above analysis suggests that listeners' pitch matches can provide fairly precise estimates of both F_0 's when the ΔF_0 is 4 semitones, but not when the ΔF_0 is 2 semitones or smaller. A separate question concerns the accuracy of estimation of the interval provided by the ΔF_0 . When the stimuli evoke a single pitch, the frequency interval between the first and second match is expected to be small or zero. When they evoke two pitches, the difference is expected to be proportional to the ΔF_0 .

To determine how accurately listeners' pitch judgments estimated the actual ΔF_0 , the *match interval* (i.e., the absolute frequency difference between listeners' first and second matches) was computed. An analysis of variance was carried

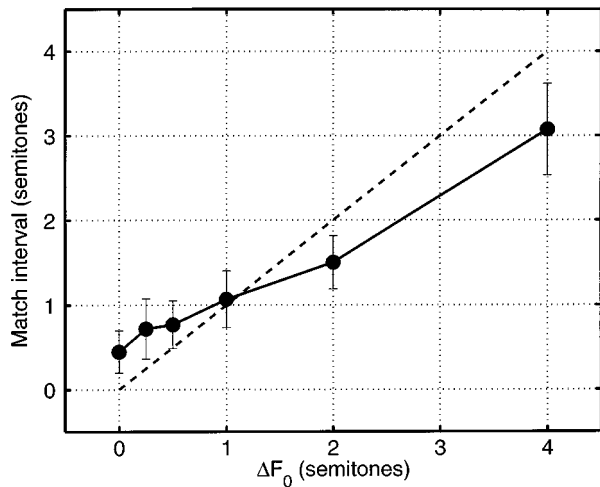


FIG. 4. Match intervals (defined as the absolute frequency difference, in semitones, between the first and second matches assigned on each trial) as a function of ΔF_0 in experiment 2. Filled circles show the means (across the four listeners and 25 vowel pairs) of median match intervals (across the ten trials). Error bars show ± 1 standard error across listeners. The dashed line indicates where the match interval coincides with the ΔF_0 .

out using the median match interval (across the ten trials) as the dependent variable. Figure 4 shows that match intervals tended to follow the ΔF_0 [$r=0.77$; $N=600$; $p<0.01$] although they overestimated the ΔF_0 for ΔF_0 's of 1 semitone or less, and underestimated the ΔF_0 for ΔF_0 's of 2 and 4 semitones. The main effect of ΔF_0 was significant [$F_{(5,15)}=10.70$; $p<0.01$]. *Post hoc* comparisons (Student–Newman–Keuls test, $\alpha=0.05$) showed that match intervals were significantly larger in the 4-semitones condition compared to all other ΔF_0 's. No significant differences were present for ΔF_0 's between 0 and 2 semitones.

The analysis also showed a significant main effect of vowel pair [$F_{(24,72)}=1.85$; $p<0.05$]. The interaction was caused by a small set of vowel pairs in which both members had high $F1$ frequencies (e.g., / $\text{æ}, \text{æ}$ /). Compared to other vowel pairs, these stimuli produced smaller match intervals, with more matches near F_{02} than F_{01} . The interaction between vowel pair and ΔF_0 was not significant.

C. Experiment 3. Double-pitch matches: 50-ms stimuli

Studies of complex tonal stimuli have indicated that pitch strength is reduced when the duration of a complex tonal stimulus is shortened (e.g., Ritsma *et al.*, 1966; Moore *et al.*, 1985; Beerends, 1989). The purpose of experiment 3 was to determine how the pitches of double vowels are affected by reducing the stimulus duration from 200 ms to 50 ms.

1. Procedure

The test stimuli were 50-ms double vowels, derived from the *short* condition of the first experiment in Assmann and Summerfield (1994). A subset of 5 of the 25 vowel pairs were included, at each of the 6 ΔF_0 's for a total of 30 stimuli. The selected vowel pairs were / $\text{ɜ}, \text{a}$ /, / $\text{u}, \text{ɜ}$ /, / a, i /, / $\text{æ}, \text{æ}$ /, and / i, u /.⁴ The matching stimuli and procedures were

the same as those described in experiment 2 for the 200-ms stimuli, except that the duration of the matching stimuli was reduced from 200 ms to 50 ms to conform to the test stimuli. The levels of the 50-ms test stimuli ranged from 59 to 66 dB (A), while the 50-ms matching stimuli ranged from 57 to 63 dB (A). The onsets and offsets of the matching stimuli were tapered with a 10-ms linear ramp. The listeners were the same as those who had participated in experiment 2.

2. Results and discussion

Histograms of pitch matches to each stimulus were constructed by combining the data across the two matches per trial, ten trials and four listeners. The histograms for each double vowel were modeled using a weighted sum of two Gaussian distributions as described in experiment 2. Results for the 50-ms stimuli are shown in the left-hand panels of Fig. 5. Matches to the corresponding subset of five vowel pairs in the 200-ms condition from experiment 2 are shown on the right.

Figure 5 shows that 50-ms and 200-ms double vowels generally showed similar patterns, except at the largest ΔF_0 of 4 semitones. When the ΔF_0 was 2 semitones or less, both 50 and 200-ms stimuli were generally represented by large circles, consistent with the presence of a single dominant pitch. When the ΔF_0 was 4 semitones, the 200-ms stimuli were represented by two circles of medium size, consistent with the presence of two pitches. However, when the duration was shortened to 50 ms, two of the five vowel pairs (/u, ɜ / and /a, i/) were represented by single, large circles positioned in the vicinity of (but lower in frequency than) F_{02} .

To determine how accurately listeners' pitch matches estimated the ΔF_0 , match intervals were computed as in experiment 2. An analysis of variance revealed a significant effect of ΔF_0 [$F_{(5,15)}=6.28$; $p<0.01$]. There was no main effect of vowel pair, but the interaction of vowel pair and ΔF_0 was significant [$F_{(20,60)}=1.84$; $p<0.05$]. The interaction is shown in the left-hand panel of Fig. 6. Student–Newman–Keuls tests indicated a larger match interval for the vowel pair /i, u/ than for the other four vowel pairs in the 4-semitone condition.

The right-hand panel of Fig. 6 shows the results for the corresponding 200-ms stimuli from experiment 2. Match intervals were generally more variable for 50-ms stimuli than for 200-ms stimuli, although the vowel pair / $\text{æ}, \text{æ}$ / provided a notable exception to this pattern. In the 4-semitone condition, three of the 50-ms vowel pairs had smaller match intervals than the corresponding 200-ms stimuli, and provided less accurate estimates of the ΔF_0 . Of the two remaining vowel pairs, / $\text{æ}, \text{æ}$ / provided relatively inaccurate estimates at both durations, while /i, u/ continued to provide reliable estimates of the ΔF_0 even at 50 ms. For the latter both component vowels have a low $F1$ frequency, raising the possibility that intense low-frequency harmonics increase the salience of two pitches at short durations.

The results of experiment 3 suggest that listeners match the pitches of some 50-ms double vowels less consistently and less accurately than the corresponding 200-ms stimuli. One interpretation is that the salience of two pitches is reduced when the stimulus duration is shortened to 50 ms.

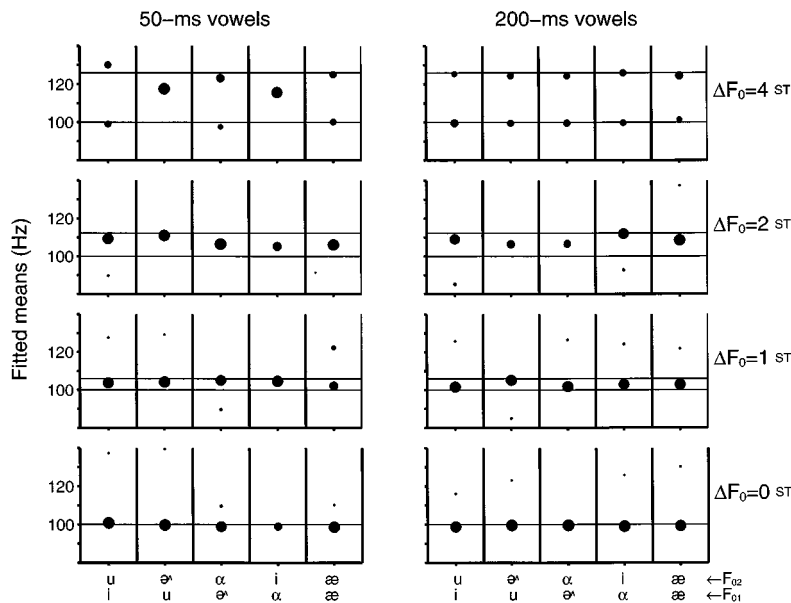


FIG. 5. Double-pitch matches to 50-ms stimuli in experiment 3 (left panel) are compared with results for 200-ms stimuli from experiment 2 (right panel). Filled circles indicate the means of the two Gaussian distributions that gave the best fit to the histogram of pitch matches. The size of the circle reflects the relative weight associated with each distribution. Results are shown for ΔF_0 's of 0, 1, 2, and 4 semitones and five vowel pairs whose phonetic categories are indicated by the symbols below the abscissa. Solid lines in each panel indicate the actual F_0 's that were present.

However, comparisons of experiments 2 and 3 are complicated by differences in the number of stimuli, and because duration differences were confounded with order (all subjects completed the 200-ms set first). For these reasons, further comparisons of 50- and 200-ms stimuli were made in experiment 4 using the set of five vowel pairs from experiment 3 as test stimuli, and order was counterbalanced.

D. Experiment 4. Double-pitch matches: 50- and 200-ms stimuli

Most studies of pitch perception have used tone complexes with a set of equal-amplitude, cosine-phase harmonics as stimuli (e.g., Moore *et al.*, 1985; Shackleton and Carlyon, 1994; Ciocca and Darwin, 1993). The matching stimuli used in experiments 1–3 were atypical, for reasons discussed in Sec. I A 2 and note 1. For comparison purposes, the matching stimuli in experiment 4 were constructed of 25 equal-amplitude, cosine-phase harmonics (cf. Moore *et al.*, 1985). The test stimuli were the 30 double vowels from the 50-ms condition of experiment 3 (5 vowel pairs \times 6 ΔF_0 's), along with the corresponding set of 30 200-ms double vowels from experiment 2. Two of the four listeners from experiments 2 and 3 (PA, DP) matched the pitches of the 50-ms and 200-ms double vowels in counterbalanced order. The procedure was identical to experiments 2 and 3, except that Sennheiser HD 255P headphones were used.

Histograms of matched F_0 were modeled using the weighted sum of two Gaussian distributions as in experiments 2 and 3 and the results were similar to those shown in Fig. 5. Match intervals were computed as in the earlier experiments and subjected to an analysis of variance. There was a significant three-way interaction of duration, ΔF_0 , and vowel pair [$F_{(20,20)} = 2.27$; $p < 0.05$] consistent with the pattern shown in Fig. 6. The interaction can be summarized as

follows: with a ΔF_0 of 4 semitones, two of the five vowel pairs (/i,u/ and /ɘ,ɔ/) gave match intervals which were similar for 50-ms and 200-ms stimuli and were close to the ΔF_0 . For the remaining vowel pairs (/æ,æ/, /α,ɪ/, and /u,ɘ/) the match interval was significantly reduced for the 50-ms stimuli (Student–Newman–Keuls tests, $p < 0.05$). For these vowel pairs, match intervals provided less accurate estimates of the ΔF_0 when the duration was shortened from 200 ms to 50 ms.

II. PARALLELS BETWEEN PITCH AND VOWEL IDENTIFICATION

The pitch-matching experiments reported in Sec. I support the conclusion that listeners perceive a single pitch when ΔF_0 is small, and two pitches when ΔF_0 is 4 semitones. When the stimulus duration is shortened from 200 to 50 ms, the two pitches are perceived less distinctly and listeners' matches provide less accurate estimates of the actual F_0 's for some double vowels. Similarly, vowel identification improves with increasing ΔF_0 , and the benefits of ΔF_0 are less pronounced when the duration is reduced (Assmann and Summerfield, 1990, 1994). To explore the relationship between pitch and phonemic identification of double vowels, listeners' pitch matches to individual double vowels were compared to identification responses obtained previously using the same stimulus set (Assmann and Summerfield, 1994).

In the analyses reported above, we used two measures of pitch salience. First, we used the weighted sum of two Gaussian distributions to model the relative prominence of two pitches. Double vowels with a ΔF_0 of 4 semitones were generally modeled as having two pitches of approximately the same prominence, while stimuli with ΔF_0 's of 2 semitones or less evoked a single strong pitch, possibly combined with a second, weaker pitch. A limitation of the model was

TABLE III. Comparison of identification accuracy (both vowels correct) and pitch judgments (absolute interval between first and second pitch matches) for 200-ms double vowels.

ΔF_0 (semitones)	0	0.25	0.5	1	2	4
Mean identification accuracy (%)	37.3	50.5	62.0	70.4	77.1	76.1
Mean match interval (semitones)	0.4	0.7	0.8	1.1	1.5	3.1
Correlation of identification and match interval	-0.09	-0.01	0.37 ^a	-0.06	0.38 ^a	0.57 ^b

^a $p < 0.05$.

^b $p < 0.01$.

that the weaker pitch generally did not coincide with the either of the two F_0 's and often appeared to be associated with a small cluster of outlying matches. Since it was difficult to separate genuine and spurious pitch matches in these cases, this measure of the prominence of the weaker pitch was of limited utility for comparison with identification data, and generally resulted in nonsignificant correlations.

The second measure was the match interval, defined as the absolute distance between the two matches assigned on each trial. The relationship between match intervals and identification accuracy for the 200-ms double vowels is summarized in Table III. The top row lists the percentage of trials on which both vowels were identified correctly (Assmann and Summerfield, 1994, Fig. 1, "long" condition) for the set of 150 double vowels used in experiments 1 and 2. The second row shows the mean match interval as a function of ΔF_0 . Match intervals and vowel identification scores both increase with increasing ΔF_0 . However, the match interval and vowel identification functions differ in two respects. First, while identification improves sharply over the first

semitone, match intervals increase only by a small amount. Second, identification scores reach a plateau between 1 and 2 semitones, while match intervals show an abrupt increase between 2 and 4 semitones. This outcome is consistent with the finding that the nondominant pitch does not emerge consistently until the ΔF_0 is 4 semitones.

Conceivably, the contribution of ΔF_0 to pitch and vowel identification could vary across vowel pairs. If so, the pattern in the means could obscure aspects of the relationship between pitch and vowel identification. Scheffers (1983) noted that the identification functions for individual double vowels often differed from the pattern in the means, and suggested that these variations were attributable to differences in formant structure between the vowels. Comparisons across the entire data set (25 vowel pairs and 6 ΔF_0 's) revealed a significant correlation of match interval and identification accuracy [$r = 0.44$; $N = 150$; $p < 0.01$]. The partial correlation controlling for the contribution of ΔF_0 was not significant [$r = 0.13$; $N = 150$; $p > 0.5$], suggesting that ΔF_0 is mediating the relationship.

The presence of a significant correlation between match intervals and double-vowel identification is not surprising, given that both are strongly affected by the ΔF_0 . A more meaningful comparison is provided by comparisons involving the same F_0 . Correlations were computed separately for each ΔF_0 ($N = 25$) and are shown in the third row of Table III. Significant but small correlations appeared with ΔF_0 's of 0.5 and 2 semitones ($p < 0.05$), while a moderate correlation appeared when the ΔF_0 was 4 semitones ($p < 0.01$). Thus the relationship between match intervals and vowel identification was strongest in the condition where listeners were most likely to perceive two distinct pitches rather than one.

For the 50-ms stimuli, pitch judgments were available for five vowel pairs at each ΔF_0 . Match intervals were compared with identification scores (averaged across listeners) for the same stimuli from Assmann and Summerfield (1994, Fig. 1, "short" condition). The correlation across all vowel pairs and ΔF_0 's was significant [$r = 0.48$; $N = 30$; $p < 0.01$]. To compare the effects of stimulus duration on pitch and vowel identification, the difference in identification accuracy (between 200- and 50-ms vowel pairs) was compared with the difference in match interval. The decline in identification accuracy was associated with a reduction in the match interval [$r = 0.53$; $N = 30$; $p < 0.01$]. Moreover, the reduction in the effectiveness of the ΔF_0 cue when the stimuli were shortened from 200 to 50 ms (expressed as the accuracy difference between conditions with $\Delta F_0 > 0$ and $\Delta F_0 = 0$) was correlated with the corresponding change in match interval [$r = 0.42$; $N = 25$; $p < 0.05$].

III. GENERAL DISCUSSION

Models of the identification of double vowels that implement F_0 -guided segregation (e.g., Scheffers, 1983; Assmann and Summerfield, 1990; Meddis and Hewitt, 1992; de Cheveigné, 1997) suggest a close link between pitch and vowel identification.⁵ The results of the present study suggest that listeners generally hear two pitches when the ΔF_0 is 4 semitones, but only a single pitch when the ΔF_0 is small or zero. They are also less likely to hear two distinct pitches

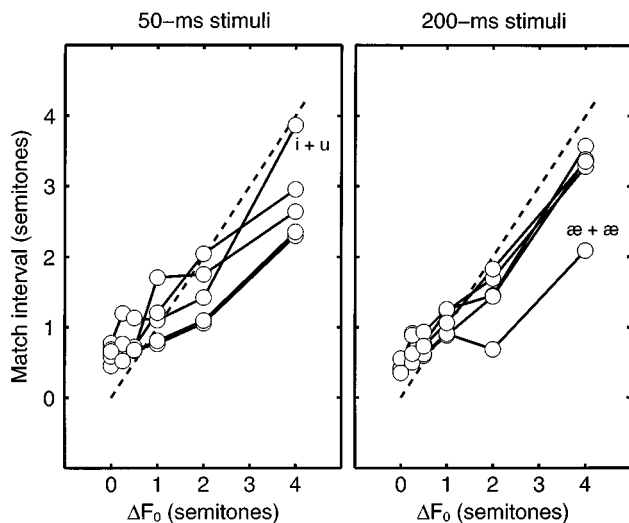


FIG. 6. Match intervals (defined as the absolute frequency difference, in semitones, between first and second matches assigned on each trial) for 50-ms stimuli in experiment 3 (left panel) and 200-ms stimuli from experiment 2 (right panel). Results for the five vowel pairs are shown separately. Unfilled circles indicate the median match interval (across the ten trials) averaged across the four listeners. The dashed line indicates where the match interval coincides with the ΔF_0 .

when the stimulus duration is reduced from 200 to 50 ms. Superficially, this pattern is similar to the vowel identification data which show increased identification accuracy as a function of ΔF_0 (Scheffers, 1983) and reduced benefits of ΔF_0 as the stimulus duration is shortened from 200 to 50 ms (Assmann and Summerfield, 1990; Culling and Darwin, 1993). However, there are clear differences between pitch and double-vowel identification. For example, while vowel identification shows the largest increase with ΔF_0 's between 0.25 and 1 semitone, and little further improvement beyond 2 semitones, two distinct pitches do not appear for most stimuli until the ΔF_0 is 4 semitones.

One reason why pitch judgments and vowel identification do not follow the same pattern with increasing ΔF_0 was provided by Culling and Darwin (1994) who attributed the benefits of small ΔF_0 's (less than 1 semitone) to waveform interactions (beating) between pairs of corresponding low-frequency harmonics of the two vowels. These interactions are influenced both by the overall duration of the stimulus and the frequency separation of the harmonics. When the harmonics are close in frequency and the duration is brief, the wavelength of the beating interaction is longer than the duration of the stimulus. For example, if the ΔF_0 were 3 Hz, the second harmonics of the two vowels would beat together with a period of 167 ms, which is longer than the 50-ms stimulus. The waveform interaction account is supported by three sources of evidence: (i) smaller benefits of ΔF_0 for 50-ms than for 200-ms stimuli (Assmann and Summerfield, 1990; Culling and Darwin, 1993), (ii) reduced identification accuracy with small ΔF_0 's when the F_0 difference is eliminated in the first formant region (Culling and Darwin, 1993) and (iii) the finding that different 50-ms segments (extracted from 200-ms double vowels with small ΔF_0 's) are not equally identifiable (Assmann and Summerfield, 1994). Culling and Darwin (1994) described a computational model of the identification of double vowels that exploits the beating pattern to improve the accuracy of vowel identification. Their model takes advantage of waveform interactions by: (i) performing a frequency analysis using a bank of bandpass filters; (ii) analyzing the waveform in each channel with a brief, sliding temporal window; and (iii) searching for temporal regions of the stimulus where the spectral structure of the component vowels is best defined. Their model predicted the pattern of improvement in identification accuracy for 200-ms stimuli with small ΔF_0 's, and the reduced benefit of ΔF_0 for 50-ms stimuli. Versions of Culling and Darwin's model have also been used to predict effects of formant transitions on the identification of double vowels (Assmann, 1995, 1996).

Does this account imply that the effects of ΔF_0 on judgments of pitch and vowel identification depend on the operation of distinct and unrelated mechanisms? There are three sources of evidence that argue against this conclusion. First, Culling and Darwin's model systematically underpredicted the accuracy of identification in conditions with ΔF_0 's of 2 and 4 semitones, where listeners showed the largest benefits of ΔF_0 . An extended version of Culling and Darwin's model which included a stage of F_0 -guided segregation came closer to predicting the pattern of identification results (Ass-

mann, 1996). Second, de Cheveigné *et al.* (1997) showed strong benefits of ΔF_0 even when the relative amplitudes of the two vowels differed by up to 20 dB and when the phases of the harmonics were manipulated to control the pattern of beats. They attributed their findings to a process of F_0 -guided segregation based on harmonic cancellation rather than waveform interactions. Third, the analyses reported in Sec. II revealed significant correlations between pitch judgments and vowel identification accuracy. A moderate correlation between match intervals and identification accuracy was found with 200-ms stimuli with a ΔF_0 of 4 semitones, the only condition in which listeners consistently perceived two distinct pitches rather than one. Moreover, the drop in identification accuracy when the stimulus duration was shortened from 200 to 50 ms was significantly correlated with the reduction in match interval.

One explanation for the relationship between match intervals and vowel identification is that the benefits of ΔF_0 's for vowel identification depend on the salience with which two distinct pitches are evoked. This account is unlikely to be correct, because double vowels with small ΔF_0 's generally did not evoke two clear pitches. Moreover, the correlation between match intervals and vowel identification was weak in conditions with ΔF_0 's smaller than 4 semitones. Assuming that match intervals provide a reliable measure of pitch salience, and that pitch salience reflects the availability of F_0 information for vowel identification, these findings raise serious doubts about the feasibility of models of double-vowel identification that require precise estimates of the F_0 's of *both* vowels, since the largest benefits of ΔF_0 for vowel identification are observed between conditions with small ΔF_0 's. The results are compatible with alternative models of F_0 -guided segregation that use periodicity information to estimate the dominant F_0 and identify the component vowels (e.g., Meddis and Hewitt, 1992).

IV. SUMMARY

- (1) A matching paradigm was used to study the pitches evoked by double vowels. Experienced listeners adjusted the F_0 of a tone complex to assign two pitch matches to double vowels whose durations were either 200 or 50 ms. When the ΔF_0 was less than 2 semitones, listeners generally matched only one pitch consistently, and the majority of their matches were clustered around the mean of the two F_0 's. Although the histograms of matched F_0 sometimes showed evidence of secondary weaker pitches, bimodal histograms of matched F_0 appeared consistently only for the largest ΔF_0 of 4 semitones.
- (2) When the ΔF_0 was 4 semitones, listeners reported two pitches and assigned their pitch matches close to the two F_0 's that were present.
- (3) When the stimulus duration was shortened from 200 ms to 50 ms, listeners found it more difficult to match two pitches. The histograms of F_0 matches were more variable and provided less precise estimates of the two F_0 's that were present. Subjectively, these stimuli were less likely to give the impression of two distinct pitches.

- (4) With 200-ms double vowels, the dominant pitch was generally evoked by the vowel with the higher F_0 . The majority of matches to the dominant pitch were close to the higher F_0 , and they provided more precise and consistent estimates of its frequency than those assigned near the lower F_0 .
- (5) Comparisons were made between the pitch matching data and vowel identification results obtained for the same stimuli in earlier experiments. Vowel identification accuracy showed a moderate correlation with match interval (the absolute frequency difference between first and second pitch matches) for 200-ms stimuli with a ΔF_0 of 4 semitones. The link between pitch intervals and vowel identification was strongest in conditions where listeners heard two distinct pitches rather than one, and was weak or absent in conditions where only one pitch was heard.

ACKNOWLEDGMENTS

Preliminary reports of portions of this work were presented at the Sixteenth Midwinter Research Meeting of the Association for Research in Otolaryngology, St. Petersburg, Florida, February 8, 1993 (Assmann and Paschall, 1993) and at the 127th Meeting of the Acoustical Society of America, Cambridge, Massachusetts, 6–10 June, 1994 (Assmann and Paschall, 1994). We thank Angela Shoup, Joe Strickland, Tina Socotch, and Linda Oldham for their participation in the experiments, Richard Golden, Hervé Abdi, and Terry Nearey for assistance in statistical analysis and modeling, and Alain de Cheveigné and an anonymous reviewer for helpful suggestions and critique of the manuscript. This work was supported by Grant No. R29-DC01258 from the National Institute on Deafness and Other Communication Disorders of the National Institutes of Health.

¹Matching stimuli were intended to be the sum of 25 cosine components with equal amplitudes and frequencies of $n \cdot F_0$ (where $n=1,2,\dots,25$). For each component a single cycle of duration $1/F_0$ was synthesized, the 25 components were summed, and the resulting period waveform was concatenated to create a 50-ms or 200-ms matching stimulus. However, because of a computational error the frequencies were incorrectly specified as $n + F_0$, creating a discontinuity at each period juncture and thus a falling spectrum of approximately -6 dB/oct. The data reported in Sec. I D indicate that this difference in specification of the matching stimuli had little effect on the pitch matches assigned by listeners.

²Four additional subjects took part in the pretest, but reported considerable difficulty with the matching task and hence were not selected for participation in the experiments.

³A possibility suggested by one of the reviewers (de Cheveigné) is that the dominance of the higher F_0 may be a consequence of the fixed lower F_0 of 100 Hz in all test stimuli. The lower F_0 may have served as a perceptual anchor by focussing listeners' attention on the vowel component that changes from trial to trial. We are currently investigating this possibility by comparing pitch judgments in conditions with fixed and variable baseline F_0 's. In vowel identification one vowel in the pair generally tends to dominate (and is identified more accurately), but the asymmetry appears related to the differences in the formant structure of the constituent vowels rather than their F_0 's (McKeown, 1992; de Cheveigné *et al.*, 1997).

⁴These vowel pairs were chosen on the basis of the following criteria: (i) each of the five single vowels appeared with the same frequency; (ii) the ratio of identical vowel pairs ($/\text{æ}, \text{æ}/$) to nonidentical pairs ($/\text{u}, \text{æ}/$) was the same as in experiment 1; (iii) the selected vowel pairs were representative of the vowel set as a whole in experiment 1.

⁵The models proposed by Meddis and Hewitt (1992) and by de Cheveigné (1997) implement forms of F_0 guided segregation that depend only on an estimate of the dominant F_0 ; they do not require estimates of both F_0 's to segregate the composite stimulus. In Meddis and Hewitt's model, channels that are "captured" by the dominant F_0 are selected and grouped together to identify the first vowel, and then removed to recover the second vowel. In de Cheveigné's model, a within-channel temporal analysis is carried out to "cancel" the contribution of the vowel with the dominant F_0 . The residue after channel selection or cancellation may contain evidence of the periodicity of the nondominant F_0 that contributes both to pitch and phonemic identification. Hence the ability of the models to recover the second, nondominant vowel is likely to be linked to the prominence of its pitch.

- Assmann, P. F. (1995). "The role of formant transitions in the perception of concurrent vowels," *J. Acoust. Soc. Am.* **97**, 575–584.
- Assmann, P. F. (1996). "Modeling the perception of concurrent vowels: Role of formant transitions," *J. Acoust. Soc. Am.* **100**, 1141–1152.
- Assmann, P. F., and Paschall, D. D. (1993). "Perception of concurrent vowels: Pitch Judgements, Judgments," Abstracts of the Sixteenth Midwinter Research Meeting of the Association for Research in Otolaryngology 25.
- Assmann, P. F., and Paschall, D. D. (1994). "Pitches of concurrent vowels," *J. Acoust. Soc. Am.* **95**, 2965(A).
- Assmann, P. F., and Summerfield, Q. (1990). "Modeling the perception of concurrent vowels: Vowels with different fundamental frequencies," *J. Acoust. Soc. Am.* **88**, 680–697.
- Assmann, P. F., and Summerfield, Q. (1994). "The contribution of waveform interactions to the perception of concurrent vowels," *J. Acoust. Soc. Am.* **95**, 471–484.
- Beerends, J. G. (1989). "The influence of duration on the perception of pitch in single and simultaneous complex tones," *J. Acoust. Soc. Am.* **86**, 1835–1844.
- Beerends, J. G., and Houtsma, A. J. M. (1989). "Pitch identification of simultaneous diotic and dichotic two-tone complexes," *J. Acoust. Soc. Am.* **85**, 813–819.
- Brokx, J. P. L., and Noteboom, S. G. (1982). "Intonation and the perception of simultaneous voices," *J. Phonetics* **10**, 23–26.
- Carlyon, R. P. (1995). "Encoding the fundamental frequency of a complex tone in the presence of a spectrally overlapping masker," *J. Acoust. Soc. Am.* **99**, 517–524.
- Chalikia, M., and Bregman, A. (1989). "The perceptual segregation of simultaneous auditory signals: Pulse train segregation and vowel segregation," *Percept. Psychophys.* **46**, 487–496.
- Ciocca, V., and Darwin, C. J. (1993). "Effects of onset asynchrony on pitch perception: Adaptation or grouping," *J. Acoust. Soc. Am.* **93**, 2870–2878.
- Culling, J. F., and Darwin, C. J. (1993). "Perceptual separation of simultaneous vowels: Within and across-formant grouping by F_0 ," *J. Acoust. Soc. Am.* **93**, 3454–3467.
- Culling, J. F., and Darwin, C. J. (1994). "Perceptual and computational separation of simultaneous vowels: Cues from low-frequency beating," *J. Acoust. Soc. Am.* **95**, 1559–1569.
- de Cheveigné, A., Kawahara, H., Tsuzaki, M., and Aikawa, K. (1997). "Concurrent vowel segregation I: Effects of relative level and F_0 difference," *J. Acoust. Soc. Am.* **101**, 2839–2847.
- de Cheveigné, A. (1997). "Concurrent vowel segregation III: A neural model of harmonic interference cancellation," *J. Acoust. Soc. Am.* **101**, 2857–2865.
- Darwin, C. J., Hukin, R. W., and Al-Khatib, B. Y. (1995). "Grouping in pitch perception: Evidence for sequential constraints," *J. Acoust. Soc. Am.* **98**, 880–885.
- Klatt, D. H. (1980). "Software for a cascade/parallel formant synthesizer," *J. Acoust. Soc. Am.* **67**, 971–995.
- McKeown, J. D. (1992). "Perception of concurrent vowels: The effect of varying their relative level," *Speech Commun.* **11**, 1–13.
- McKeown, J. D., and Patterson, R. D. (1995). "The time course of auditory segregation: Concurrent vowels that vary in duration," *J. Acoust. Soc. Am.* **98**, 1866–1877.
- Meddis, R., and Hewitt, M. (1992). "Modeling the identification of concurrent vowels with different fundamental frequencies," *J. Acoust. Soc. Am.* **91**, 233–245.

- Moore, B. C. J., and Glasberg, B. R. (1985). "Relative dominance of individual partials in determining the pitch of complex tones," *J. Acoust. Soc. Am.* **77**, 1853–1867.
- Moore, B. C. J., Glasberg, B. R., and Peters, R. W. (1985). "Relative dominance of individual partials in determining the pitch of complex tones," *J. Acoust. Soc. Am.* **77**, 1861–1867.
- Plomp, R. (1967). "Pitch of complex tones," *J. Acoust. Soc. Am.* **41**, 1526–1533.
- Ritsma, R. J. (1967). "Frequencies dominant in the perception of the pitch of complex sounds," *J. Acoust. Soc. Am.* **42**, 191–198.
- Ritsma, R. J., Cardozo, B. L., and Neelen, J. J. (1966). "The build-up of the pitch percept," *IPO Annual Progress Report* **1**, 12–15.
- Schepers, M. T. (1983). "Sifting vowels: Auditory pitch analysis and sound segregation," Doctoral dissertation, University of Groningen, The Netherlands.
- Shackleton, T. M., and Carlyon, R. P. (1994). "The role of resolved and unresolved harmonics in pitch perception and frequency modulation discrimination," *J. Acoust. Soc. Am.* **95**, 3529–3540.
- Summerfield, A. Q., and Assmann, P. F. (1991). "Perception of concurrent vowels: effects of pitch-pulse asynchrony and harmonic misalignment," *J. Acoust. Soc. Am.* **89**, 1364–1377.
- Terhardt, E. (1974). "Pitch, consonance and harmony," *J. Acoust. Soc. Am.* **55**, 1061–1069.
- Zwicker, U. T. (1984). "Auditory recognition of diotic and dichotic vowel pairs," *Speech Commun.* **3**, 265–277.

Language, context, and speaker effects in the identification and discrimination of English /r/ and /l/ by Japanese and Korean listeners

John C. L. Ingram and See-Gyoon Park

Department of English, University of Queensland, Brisbane 4072, Australia

(Received 12 December 1995; revised 12 September 1997; accepted 6 October 1997)

Japanese and Korean listeners' identification and discrimination of English /r/ and /l/ were compared using a common set of minimal pair stimuli. The effects of speakers (two native speakers of Australian English), position of the contrast within the word (word initial, initial consonant cluster, and medial positions), and listening task (forced choice identification versus oddball discrimination) were examined, with a view to assessing the relative importance of language-specific and language-independent factors operating at the acoustic-phonetic and phonological levels of signal processing in "foreign sound" speech perception. Both prior phonological learning and the relative acoustic discriminability of the items affected subjects' performance on the identification test. Where both factors were engaged, phonological learning effects predominated over the effects of acoustic discriminability. The extent to which a speaker encoded critical acoustic cues for the /r-/l/ distinction was found to affect /r-/l/ identification. Dynamic spectral features known to be relevant for the /r-/l/ contrast were effective in predicting (in a linear regression analysis) speaker-dependent differences in identification scores. Although the discrimination test may have been influenced by ceiling effects, the performance profiles on the identification and discrimination tests were quite different, indicating that the identification and discrimination tests imposed quite different task demands upon listeners and that phonological processing of the signal was more engaged by the former task. © 1998 Acoustical Society of America. [S0001-4966(98)05301-6]

PACS numbers: 43.71.Hw, 43.71.Es, 43.71.Bp, 43.66.Lj [WS]

INTRODUCTION

Difficulties that Japanese and others, whose native language has only a single phonemic liquid, encounter with the English /l-r/ contrast are so well known as to have become a linguistic stereotype. Phonetic studies of this phenomenon have raised, but not resolved, a number of fundamental questions for understanding how novel phonemic contrasts are acquired in second language learning; such as whether beyond a certain age of initial contact with English, the /l-r/ contrast can be reliably perceived (Goto, 1971; Mochizuki, 1981), though it may be consistently realized in production (Sheldon and Strange, 1982); whether phonetic training can facilitate acquisition of the /l-r/ contrast (Logan *et al.*, 1991; Lively *et al.*, 1992, 1993); how language-specific transfer effects influence acquisition of the /l-r/ contrast (Gillette, 1980; Sheldon and Strange, 1982; Henry and Sheldon, 1986), or whether language-independent factors, based upon acoustic phonetic considerations or phonological markedness (Broselow and Finer, 1991; Eckman and Iverson, 1993) play a significant role in acquiring the /l-r/ contrast in different phonological environments in English.

It seems likely that perceptual responses of non-native listeners to foreign speech sounds reflect the simultaneous operation of factors at various levels of signal analysis from the basic acoustic to the linguistic, and that the relevance of prior learning of the first language (L1) may vary depending on parameters of the listening task. It may be that precedence relations operate between different classes of effects in second language speech perception or production. This was pro-

posed by Henry and Sheldon (1986) to account for the relative difficulty that Cantonese listeners experienced with the /l-r/ contrast in syllable codas, an environment that Japanese listeners find relatively easy, presumably because spectral cues for distinguishing /l/ and /r/ syllable finally are distributed over a longer time frame and are hence more discriminable than in other environments. Cantonese (unlike Japanese) has a "clear" (nonvelarized) /l/ in final position and this evidently interferes with the perception of the velarized English /l/, whereas no such interference effects operate for Japanese listeners.

A priori, four major classes of influence may be identified as relevant for the perception of a novel phonemic contrast by second language learners. These are indicated in Table I.

Language specific or language universal influences may express themselves at either the phonetic or the phonological levels of speech processing, and all four combinations of these two factors have found their way into contemporary accounts of interlanguage speech perception. Phonologically oriented theorists, such as Broselow and Finer (1991) who advocate a Parameter Setting model of acquisition, or Markedness theorists, such as Eckman and Iverson (1993), seek to invoke language universal principles of phonological organization to explain patterns of difficulty in mastering L2 phonological contrasts. Phonetically oriented theorists, such as Mann (1986), make an appeal to language universal phonetic constraints, which have their origin in the way articulatory gestures are coded into the acoustic signal of speech.

However, both phonetic and phonological effects on

TABLE I. Factors affecting perception of novel phonemic contrasts.

Type	Label	Source of effect or influence
1.	Transfer effects	Language specific, phonetic, or phonological learning. A language-dependent factor.
2.	Discriminality of sound contrast	Acoustic structure of the signal and nature of the auditory system. A language-independent factor.
3.	Phonological markedness or parameter setting	Universal properties of sound systems and the human language acquisition device. Universal defaults, but language dependent settings.
4.	Task variables	Perceptual or information processing demands of the listening task, e.g., identification versus discrimination. May modulate the effects of factors 1–3 above.

second language speech perception may be language-specific in their operation. The traditional account of interference effects, expressed in the contrastive analysis hypothesis, makes an appeal to structural differences in the sound patterns of L1 and L2, and therefore, to language-specific phonological properties of the languages concerned. But it is also possible that language-specific phonetic influences may play an important role in interlanguage speech perception. For example, perceptual parsing strategies, that operate at a prephonological level of signal processing to aid in the detection of word or morpheme boundaries, and which vary with the language background of the listener, have been found to operate in both monolingual and bilingual speech perception (Cutler *et al.*, 1986, 1992).

In order to understand how these potentially competing influences affect interlanguage speech perception, it is necessary to have some way of separating factors operating at different *levels* of analysis, specifically the phonological and the phonetic, and for distinguishing the *domain* or scope of their operation, whether they are language particular or universal in their application. Only comprehensive cross-language studies comparing speakers of diverse linguistic backgrounds will enable us to distinguish language-specific from universal influences, with the relevant data accumulated over a series of cross-language experiments.

In the present study, phonetic and phonological transfer effects on /l-r/ perception (the first type of effect mentioned in Table I above) were examined by comparing two groups of Japanese and Korean learners of Australian English. Korean and Japanese phonologies differ in ways that are potentially significant for acquisition of the English /l-r/ contrast. These differences enabled the prediction of the pattern of perceptual errors in the two language groups across the three phonological environments where the /l-r/ contrast occurs in Australian English, namely, as single consonants in syllable or word onset position (*red-led*), as second elements of an onset consonant cluster (*pray-play*), and in intervocalic position (*berry-belly*). (Being a nonrhotic dialect, there is no /l-r/ contrast in coda position in Australian English.)

Previous studies have found that /l-r/ perception is more difficult in consonant clusters than other environments (Goto, 1971; Gillette, 1980; Sheldon and Strange, 1982; Lively *et al.*, 1992). This has been attributed to the lower acoustic discriminability of phonemic contrasts within consonant clusters, where segments tend to be shorter, and masking effects due to gestural overlap of adjacent segments are greater. In our experiment, this language-independent effect (type 2 in Table I) was found to operate in an additive manner with transfer effects mentioned above.

Another consideration which is relevant for the acoustic discriminability of phonemic contrasts in L2, concerns pronunciation variability and the adequacy of tokens provided by different L2 speakers. Recent studies have shown that exposing learners to a range of speaker models during the perceptual training phase enhances retention of the /l-r/ contrast and facilitates generalization to new items by Japanese learners of English (Logan *et al.*, 1991; Lively *et al.*, 1992, 1993). In the present study, two male native speakers of Australian English provided stimulus tokens for the identification and discrimination experiments. Speaker effects were also found to be an important source of variance in the perceptibility of the /l-r/ contrast, and subsequent spectrographic analysis indicated an acoustic basis for the differential discriminability of certain tokens over others, in terms the clarity of encoding of key acoustic properties known to be important for distinguishing /l/ and /r/.

However, language-independent effects may not be confined to factors affecting discriminability and basic auditory processing of speech signals. Considerations of phonological markedness (factor 3, Table I) may constitute a separate class of language-universal constraints on phonological restructuring or accommodation to L2 sound patterns. Markedness constraints were originally proposed to remedy perceived inadequacies of contrastive phonological analyses to account for error patterns in second language speech production (Eckman, 1977). In recent years, markedness constraints have been incorporated into the principles and parameters of Universal Grammar (Chomsky, 1986) that supposedly shape the course of first, and possibly also, second language learning. The role of parameter setting in second language learning is controversial, particularly in the phonological domain, where the competing view holds that language-dependent transfer effects exert a much stronger influence (Sato, 1984). Phonological markedness constraints gain expression in cross-language preferences for segment selection and syllable structure. No clear case can be made for the relative markedness of the liquids /l/ or /r/ (Bhat, 1974; Maddieson, 1984). However, it was possible to assign markedness values to items for the range of consonant clusters included in this experiment, based upon proposals by Broselow and Finer (1991) and Eckman and Iverson (1993).

Finally, the perceptual demands of the listening task (factor 4, Table I) exercise a degree of control over listeners' perceptual responses and the foregrounding or backgrounding of factors mentioned above. Mochizuki (1981) found that Japanese listeners' ability to discriminate and label minimal pair /l-r/ contrasts presented in triadic comparisons was highly dependent on the echoic memory load induced by the

response task. Werker and colleagues (Werker and Logan, 1985; Werker, 1994) have manipulated interstimulus intervals (ISIs) to control the amount of phonological processing required of listeners to hold items in echoic memory in a discrimination task. Identification tasks, which involve matching the stimulus to internally stored representations, typically impose greater echoic memory loads than discrimination tasks. More generally, an identification task may be expected to engage linguistic processing of the speech signal more fully than a discrimination test. In their classical study of discrimination and identification of synthetic vowel sounds, Stevens *et al.* (1969) found that Swedish and English subjects exhibited similar performance on vowel discrimination tests, though they yielded somewhat different identification functions, related to phonemic status of the lip rounding in their respective languages.

Lexical familiarity effects have been observed in /l-r/ identification by inexperienced and experienced Japanese learners of English (Yamada and Tohkura, 1992b; Flege *et al.*, 1995), though such effects are likely to be observed in native listeners only under marginal listening conditions or when the stimuli are phonetically ambiguous (Ganong, 1980). It may be hypothesized that lexical familiarity effects will be stronger in an identification task with non-native listeners than in a discrimination task with the same listeners. Such a finding would support the hypothesis (above) that identification tasks engage higher-order linguistic processing of the stimulus to a greater extent than discrimination tasks. Such processing is likely to involve language-specific learning, and consequently, an identification task is also more likely to reflect the influence of the listener's language background than a discrimination task.

Notwithstanding the above, Mann (1986) found that Japanese listeners were sensitive to the acoustic consequences of coarticulation effects in the *discrimination* of synthetic /l-r/ tokens, in a manner similar to native English speakers, even though her subjects were unable to consistently identify /r/ and /l/ as phonological targets. This suggests that a language-independent level of phonetic processing at which articulatory constraints govern speech signal processing may be engaged by a basic discrimination task, even when perceiving "foreign sounds" or incompletely acquired phonemic contrasts. Consequently, the impact of variation of task demands on perceptual performance are difficult to predict. Nevertheless, comparisons of performance on identification and discrimination tasks may throw light upon the perceptual mechanisms involved in acquiring a novel phonemic contrast.

To summarize: In the identification and discrimination experiments of the /l-r/ contrast by Japanese and Korean learners of English reported below, we sought to bring together a range of potentially competing effects operating at different levels (the phonetic and the phonological) and in different domains (the language specific and the language universal) to observe their relative importance and interaction. We argue that the results suggest, (1) an important role for language particular phonetic and phonological factors which reflect the operation of prior perceptual learning, (2) no role for language universal phonological markedness or

parameter setting, and (3) mixed evidence for the operation of language universal factors operating at a phonetic or prephonological level speech signal processing, depending on the source of phonetic variability and how the term "phonetic level of processing" is construed.

I. JAPANESE AND KOREAN LIQUIDS

Japanese possesses a syllable initial liquid, usually phonemicized /r/, which has a range of phonetic variants that have been variously described by linguists as "an alveolar flap," "a retroflexed flap," a "combination of an alveolar lateral and a retroflexed flap," a "lax alveolar stop," and an "alveolar lateral" (Tsuzuki, 1992). There appears to be a wide range of phonetic variation for the Japanese liquid, from a slightly retroflexed lateral approximant, through to an alveolar tap or flap. This phonetic variation occurs across speakers and does not appear to be strongly conditioned by phonological environment. The Japanese liquid is confined to syllable onset position, word initially, or word internally.

Korean also has only one phonemic liquid with a similar range of phonetic variation as its Japanese counterpart. However, the Korean liquid may occur in coda as well as onset position, where there are clearly phonologically conditioned allophones. Syllable initially, the Korean liquid is phonetically realized as a flap [ɾ]. There is, however, a strong sanction against liquids appearing in absolute word initial position in Korean. Word initial liquids are found only in loan words, not in items of native vocabulary. In this special environment, there is, like Japanese, a broader range of phonetic variation, from a flap or tap to a lateral approximant. In coda position, the Korean approximant is consistently realized as a lateral approximant.

Intervocally, the singleton liquid is phonetically realized as an alveolar flap. In geminates (where a liquid in coda position is followed by another in onset position in the next syllable), an alveolar lateral is invariably produced. Thus Korean speakers have a phonetic model available to them for English /l-r/ contrasts, in nonword initial position. They can treat English /r/'s as "singleton" liquids, and /l/'s as geminate liquids, and thereby obtain a phonetic approximation ([ɾ]-[ll]) for the English /r-l/ contrast, as is attested by the phonetic structure of English loan words such as:

<i>orange</i>	[orenʃi]
<i>olympic</i>	[ollimp ^h ik]

However, this model cannot be invoked for word initial position, where, not only is the contrast between the geminate and the singleton liquid unavailable, but any kind of liquid violates canonical native word forms. For Koreans, /l-r/ perception in word initial position would be expected to be doubly difficult, and more so than for Japanese listeners.

With respect to the /l-r/ distinction in onset clusters, Korean phonotactic constraints are practically identical to Japanese. Neither language permits C+liquid clusters and English loan words containing such clusters are typically resyllabified by vowel epenthesis. However, once resyllabification has occurred, Korean speakers will have available to them the phonetic strategy which they employ in word medial position, of treating English /r/ as a singleton and /l/ as a geminate liquid.

TABLE II. Predicted difficulty of /l-r/ perception, based on L1 phonological and phonetic considerations. 1=least difficult, 2=more difficult, 3=most difficult.

L1 background	Phonological environment			Overall Mean
	Initial	Cluster	Medial	
	CV	CCV	VCV	
Korean	3	2	1	2
Japanese	2	3	2	2.3

Table II summarizes cross-language predictions about the relative difficulty of the /l-r/ contrast, based upon phonological differences between Korean and Japanese, in the three environments of occurrence in Australian English.

It was predicted that Koreans would perform somewhat better than the Japanese in intervocalic and cluster environments, but not as well word initially. The predicted patterns of phonological difficulty are neutral with respect to perception and production and should apply equally to each domain. The reduced discriminability of the /l-r/ contrast in the consonant cluster (a language-independent phonetic effect) may be expected as an additional effect upon perception, which would apply equally to listeners of both language backgrounds.

II. IDENTIFICATION EXPERIMENT

A. Stimuli

Two Australian male speakers recorded 50 test words, consisting of (a) 30 /l-r/ words i.e., 15 minimal pairs, five in each of the three phonological environments, and (b) 20 distracter words (see Table III), which were also minimal pair contrasts with the target words. Recordings were made in a sound-attenuated recording booth. The distracter items served to provide a range of perceptual targets, consistent with an identification task, and to promote a linguistic level of stimulus processing. The same 30 target words were used in both the identification and discrimination tests. The 20 distracter words were used only in the identification test. Only common words, likely to be familiar to non-native

TABLE III. Items for identification experiment.

Initial		Cluster		Medial	
target	distracter	target	distracter	target	distracter
read	weed	broom	spoon	lorry	lobby
lead	bead	bloom		lolly	
row	woe	fruit	school	mirror	minute
low	know	flute		miller	
rock	wok	crime	sky	correct	connect
lock	sock	climb		collect	
right	white	pray	stay	arrive	survive
light	might	play		alive	
red	wed	grass	start	berry	heavy
led	bed	glass		belly	

speakers were used as test items. But it proved difficult to balance word familiarity in the choice of /l-r/ words for minimal pairs (see Sec. III D).

The stimuli were digitized at 20 kHz and 16 bit resolution for construction of identification and discrimination test tapes. The identification test contained 200 items (50 words×2 speakers×2 repetitions) in random order, completed in a single session, with a short rest break after every 50 items.

B. Subjects and procedure

Twenty subjects (ten Japanese and ten Koreans, equal numbers of males and females, all students at the University of Queensland) participated in both an identification and a discrimination test. Their age range was 18–37 years. Residency in Australia ranged from 2 to 18 months. Except for one Japanese subject, none had lived in any other English speech community, none had hearing disabilities. Eight of the ten Koreans and four of the Japanese students were undertaking English language courses, to qualify for entry to regular academic programs, thus indicating that the level of English competence may have been higher in the Japanese group.

The identification and discrimination tests were carried out under similar conditions in the same listening environment. Both tests were group-administered in the Language Laboratory of the University of Queensland, using a Tandberg IS9 master station controlling Tandberg 5600 listening stations. The identification test was carried out in two stages. In the initial training session, subjects were familiarized with the test items. The test words were presented on cards and the meaning and correct spelling of each word was reviewed. Subjects were also introduced to the method of filling in the answer sheet, and two practice trials were conducted using distracter items. In the main testing session, subjects were asked to write the word that they heard in the corresponding space on the answer sheet. Responses were scored as correct or incorrect against the target words containing /l/ or /r/. Irrelevant spelling errors (rare) were ignored and responses to distracter items were not scored. Target words were presented twice on a given trial, with an interstimulus interval of 1 s. There was an intertrial interval of 8 s.

C. Data analysis and predictions

The experimental design called for a four way analysis of variance (ANOVA), where the dependent variable was the percentage of correct identifications for the target sound (/l/ or /r/) across the five words in each phonological environment, and the four treatment variables were: (i) The speakers (JI or TM); (ii) the language background of listeners (Japanese or Korean), (iii) the type of target sound ([l] or [r]); and (iv) the position in the word (initial, medial, or cluster). With repetition of the five /l/ or /r/ target words, the maximum score a subject could obtain was 10/10. This score was converted into a percentage correct for the results reported below.

Language-dependent phonological transfer effects will gain expression in main and interaction effects involving the

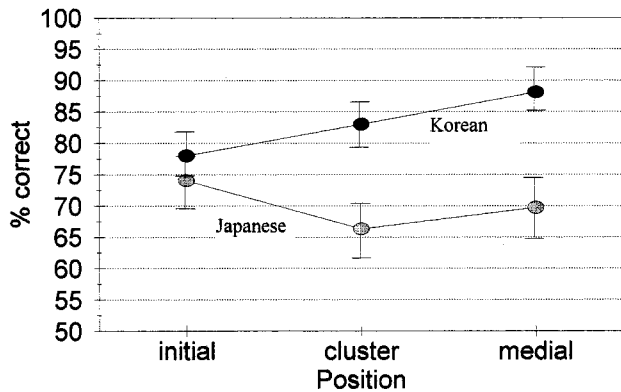


FIG. 1. Two-way interaction: Identification scores (percentage correct) /r-l/ for Japanese and Korean listeners in initial, cluster, and medial environments. Standard error intervals for factor means. (Items “lorry” and “lolly” excluded from set.)

Language factor in the ANOVA. Specifically, we looked for (i) a significant main effect of language, in which the Korean group should identify /l/ and /r/ more accurately than the Japanese, and (ii) a two-way interaction of language by position, whereby the Koreans should perform best in medial position, next best in cluster position, and worst initially, and the Japanese, by contrast, should perform equally well in initial and medial position and but worse in cluster position.

Effects which operate at the (language independent) phonetic level, i.e., at the level of extraction of phonetic features from the acoustic signal, will be reflected in main and interaction effects involving (i) speakers (JI or TM), (ii) phonetic type ([l] or [r]), and (iii) position (initial, medial, cluster), excluding interactions with language.

D. Results

A summary of the ANOVA is shown in Appendix A. The results are complex, with a high proportion of main and interaction effects achieving statistical significance at $p < 0.01$.

1. Language effects

Language-specific transfer effects arising from phonetic or phonological differences between Korean and Japanese were reflected in the main effect of language background and the interaction of language background and phonological environment (language: position). In both instances, the predicted pattern of responses was obtained. The Korean subjects performed better than the Japanese overall (83% vs 70% correct), and the pattern of performance across the three phonological environments was, except for a minor qualification, in agreement with that predicted in Table II above (see Fig. 1).

The minor qualification was that both groups performed less well than expected in intervocalic position. *Post-hoc* analysis revealed why. We made the mistake of including the items “lorry” and “lolly,” which had the effect of increasing the apparent difficulty of perceiving the /l-r/ contrast in intervocalic position. Errors occurred on these two items be-

cause listeners were uncertain of the locus of the contrast. With these items removed, the expected pattern of means was obtained.

As predicted, Korean speakers had more difficulty with word initial position than with the cluster or medial positions. The Japanese, who had greater difficulties with all three environments, relative to the performance of the Koreans, had the most trouble with /r-l/ perception in the consonant cluster, which is what would be expected on grounds of relative acoustic discriminability of the tokens, in the absence of countervailing L1 transfer effects.

2. Type effects

Significant main and interaction effects of segment type, /l/ or /r/ were obtained. The main effect of type ($F[1,198] = 14.86, p < 0.0002$) showed a higher percentage of correct responses for /r/ rather than /l/ (81% correct versus 72%). However, all three of the two-way interactions involving segment type were significant as well as two of the three-way interactions.

The language by type interaction ($F[1,198] = 8.29, p < 0.005$) indicated that while the difference in favor of /r/ over /l/ perception was small (not significant) for the Koreans, (84% to 82%), it was large for the Japanese (75% to 63%). This may reflect the greater phonetic similarity of the English /r/ rather than /l/ to the Japanese liquid, whereas the availability of two phonologically conditioned perceptual targets to map onto the English forms discouraged the development of a response preference for Korean listeners.

The type by position interaction ($F[2,198] = 5.39, p < 0.006$) showed that the perception of /l/ was favored in the cluster environment, but that /r/ perception was easier in initial and medial position. This finding agrees with Gillette (1980) and Sheldon and Strange (1982).

The three-way interaction of type by language by position also reached statistical significance ($F[2,198] = 4.64, p < 0.02$). It indicated that the pattern of difficulty across phonological environments differed for the Korean and Japanese listeners. Two sets of *a posteriori* *t* tests were conducted to identify the nature of this interaction. The results are summarized in Table IV, which shows the cell means and the comparisons that were tested. For the Koreans, /l/ in initial position scored significantly lower than liquids (/l/ or /r/) in any of the other environments (with the exception of /r/ in cluster position). Initial /l/ is the only one of the six phonetic type by position combinations which is excluded by Korean phonology, assuming, as argued above, that English liquid+stop clusters are reanalyzed as intervocalic liquids by Korean listeners, following application of vowel epenthesis. For the Japanese, *a posteriori* *t* tests (Table IV) showed a significant preference for /r/ over /l/ in initial and medial positions, which we noted previously in the two-way language by type interaction, combined with lower scores for both /l/ and /r/ in cluster position.

The other two- and three-way interactions involving segment type and speaker differences are described in Sec. 3 below.

TABLE IV. Identification scores: three-way interaction, language×type×position. Cell means and *t* test comparisons.

Cell means: percent correct							
	Korean				Japanese		
	Position in word				Position in word		
	ini	clu	med		ini	clu	med
l	71.50	85.00	89.38	l	66.50	66.00	55.00
r	84.50	81.00	86.88	r	81.50	66.50	84.38

<i>A posteriori t</i> -test comparisons					
Comparison	Korean		Comparison	Japanese	
	<i>t</i> value	Prob(<i>t</i>) df=38		<i>t</i> value	Prob(<i>t</i>) df=38
l-ini-r-clu	-1.46	>0.15 (n.s.)	l-ini-r-ini	-2.04	<0.05
l-ini-l-clu	-2.75	<0.01	l-med-r-med	-3.08	<0.01
l-ini-l-med	-3.57	<0.001	r-clu-r-ini	-1.96	=0.051 (trend)
l-ini-r-ini	-2.77	<0.01	r-clu-r-med	-2.26	<0.05

3. Speaker effects

Significant speaker effects were observed. Overall, speaker JI provided clearer tokens than speaker TM (77.4% versus 73.5% correct). However, this main effect is small in relation to the two-way interaction of speaker by segment type, or the three-way interaction (speaker×type of sound×position) shown in Fig. 2.

Comparisons among means showed that speaker JI provided more clearly identifiable /l/ tokens than speaker TM in all three positions. With respect to /r/, the identification scores were comparable for both speakers, except for the cluster environment, where speaker JI's tokens were clearly less identifiable than the other stimuli. To ascertain whether the speaker effects could be attributed to differences in the acoustic discriminability of the tokens provided by the two speakers, a spectrographic analysis of the test stimuli was undertaken. Observations focused on the extent to which well-known spectral and temporal cues for the /r-l/ contrast were present in the stimuli and correlated with listener identification scores.

4. Spectrographic analysis of speaker differences

Synthesis studies (Yamada and Tohkura, 1992a) usually manipulate three cues for the /l-r/ contrast: (1) the locus of the third formant, (2) the onset frequency of the second formant, and (3) the abruptness of rise of *F*₁ into the following vowel, which is greater in the case of /l/, imposing a clearer acoustic state change between vowel and consonant in the case of the lateral. In the acoustic analysis, we examined time-varying frequency and amplitude characteristics of the formant transitions of /l/ and /r/ in those environments where speaker effects (differences between JI and TM's productions) had the greatest impact upon listeners' identification scores.

5. Analysis of /r/ in cluster position

As noted earlier, speaker JI's /r/ tokens were more accurately perceived in initial and medial positions than those of speaker TM, except for cluster position where TM's tokens were responded to more accurately. Comparison of spectrograms of JI and TM's /r/ cluster tokens indicated a

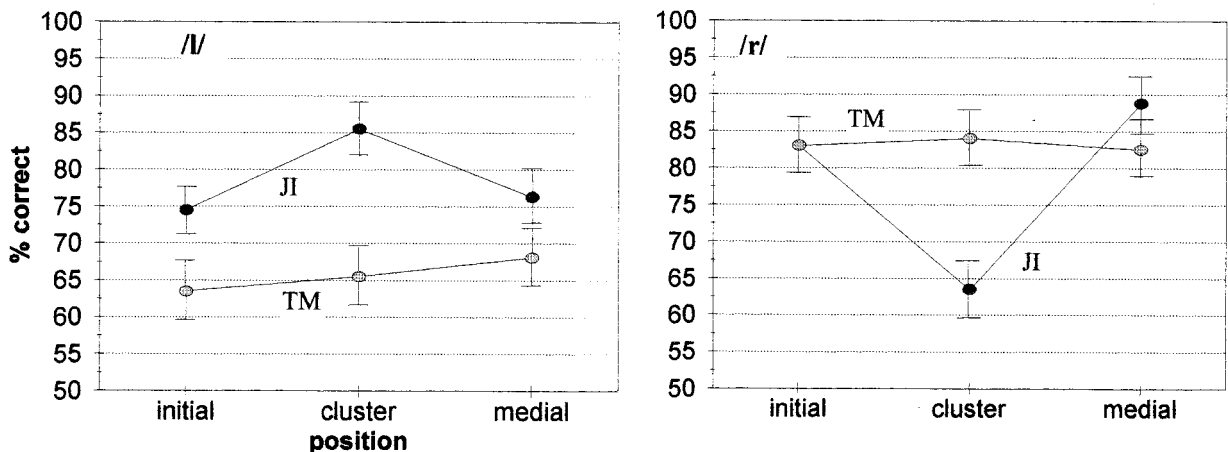


FIG. 2. Three-way interaction: Identification scores (percentage correct) for /l/ and /r/ in initial, cluster, and medial position, in response to tokens from speaker JI and speaker TM.

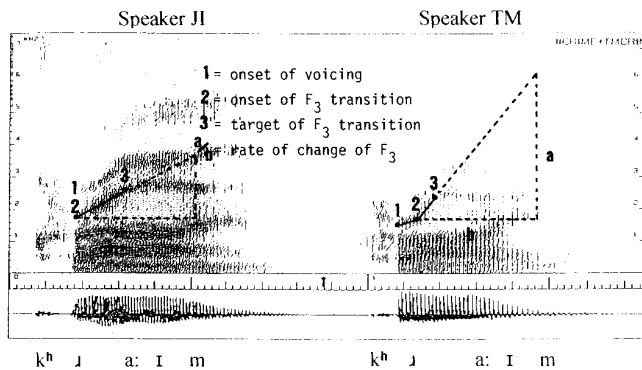


FIG. 3. Spectrograms illustrating differences between speaker JI and speaker TM in rate of change of third formant transition for /r/ tokens in cluster position.

consistent difference in the rate of change (slope) of the third formant trajectory between the tokens of the two speakers. As can be seen from Fig. 3, there was a discernible “elbow” in the third formant trajectory for speaker TM, whereas speaker JI produced a more gradually rising F_3 transition to the steady-state target for the following vowel. To quantitatively assess these differences in formant trajectories, particularly the slope of F_3 , the following measurements were taken.

Starting, midpoint, and end-point measurements were made of the first, second, and third formant frequencies of the /r/ segment. Measurements were made by hand from a spectrogram and power spectrum display (Sensimetrics, SpeechStation™). Starting points for the formant transitions were set so that the first glottal pulse fell within the left skirt of the FFT window. The end point of the formant transition was judged from F_3 , at the (second) “elbow” of the F_3 trajectory into the following vowel. The midpoint of the formant transition was judged, by eye, to fall midway between the start and end points of the formant transitions.

From the formant frequency and duration measurements, the slopes of the F_1 , F_2 , and F_3 transitions were calculated, from onset to midpoint of the /r/, and from midpoint to end point. The greater of these two slope estimates was defined as the maximum slope of the formant transition for a given formant (slFmax). These and other formant frequency change measures, taken in the course of calculating the slopes of the formant trajectories, were then correlated with identification scores for JI and TM’s /r/ tokens in the cluster environment. The two variables with the highest correlations with the dependent variable were the maximum slope of the third formant transition (slF3max) and the overall duration of the formant transition (i.e., the /r/ segment duration: rdur), which were $r=0.76$ and $r=-0.59$, respectively. These two variables were then used as predictors in a linear regression analysis, with the percentage correct responses to /r/ in cluster position for each of the speakers’ tokens as the dependent variable. In view of the small number of observations (ten tokens), not more than two independent variables were justified. The regression equation yielded a multiple R -squared of: $R^2=0.64$ ($F[2,7]=6.34$, $p<0.027$).

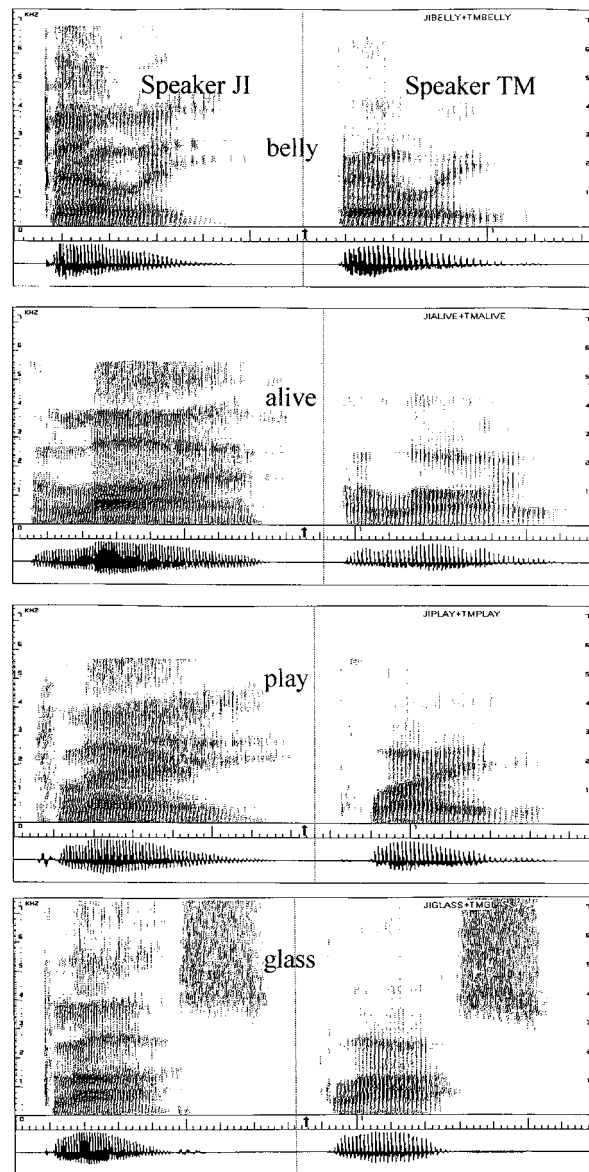


FIG. 4. Spectrograms showing differences in /l/ tokens for speaker JI and speaker TM.

6. Analysis of /l/

As noted previously, in the two-way interaction of type by speaker effects, speaker JI’s /l/ tokens yielded higher identification scores in all three positions than those of TM. Figure 4 shows sample spectrograms of the /l/ tokens by the two speakers. JI’s tokens showed clearer formant structure in the region of F_3 and F_4 and a more abrupt acoustic state change between the consonant and the following vowel nucleus. (These spectral differences were apparent over various dynamic range settings of the spectrogram display.) We sought to derive quantitative indices of the clarity of the higher formant structure from amplitude measurements based upon the short-term power spectrum, averaged over 3 to 4 pitch periods preceding and following the estimated center point of the /l/ segment. Energy maxima at F_1 , F_2 , F_3 , and F_4 were measured in dB and referenced to the major energy peak in the spectrum. Energy minima ($M1$, $M2$, $M3$)

at points midway between formant peaks were also measured. From these spectral maxima and minima, three spectral contrast measures were calculated; one each for $F2$, $F3$, and $F4$, as follows:

$$\text{contrast: } F_n = \text{amplitude: } F_n - \text{amplitude: } M_{n-1} \quad (\text{in dB}),$$

$$\text{where } 2 \leq n \leq 4.$$

The spectral contrast measure for a given formant was thus the difference in decibels between the formant energy maximum and the trough value measured halfway to the preceding formant peak, thus ensuring that the three contrast measures were independent of each other. Two additional acoustic measures, the duration of the /l/ segment, and the stability of the formant pattern (assessed in terms of the change in $F2$ between the onset and offset of the /l/ segment) were also made. The three formant contrast measures, the energy maxima and minima measurements from which the contrast measures were derived, the /l/ segment duration, and the $F2$ change measure were separately correlated with the identification scores for JI and TM's /l/ tokens in the three positions.

Correlation coefficients for the formant contrast measures on $F2$, $F3$, and $F4$ were $r=0.39$, $r=0.46$, and $r=0.65$, respectively, supporting the spectrographic observation that the clarity of the higher formant structure contributed to the higher identification scores for JI's /l/ tokens compared with those of TM. Several linear regression analyses were conducted, taking various combinations of the three formant contrast measures and other acoustic variables mentioned above. These analyses consistently indicated that the only measure which made a statistically significant independent contribution to prediction of the /l/ identification scores was $\text{cn}F4$ (spectral contrast of $F4$).

In summary, the regression analyses of speaker-induced differences in /r/ identification in cluster position and /l/ identification in all three environments found an acoustic basis for the listeners' performance, in terms of the clarity with which acoustic cues for the /l-r/ contrast were encoded by the two speakers JI and TM. For /r/ clusters, the maximum slope of $F3$ and the duration of the formant transitions jointly accounted for approximately 64% of the variance in the dependent variable (the identification scores). The negative loading of the duration factor is notable. The /r/ sound is typically realized as a flap in Korean and Japanese. Speaker TM's shorter /r/ segments and more rapid formant transitions, appear to have favored /r/ perception in the cluster environment.

Speaker-induced differences in the accuracy of /l/ identification were associated with the degree of spectral contrast in the region of $F3$ and $F4$, with the latter dominating the regression model. Prediction of speaker differences for /l/ was less successful, possibly because no readily quantifiable means was found to capture the qualitatively observed feature of the "abruptness of change" between the /l/ segment and the following vowel, which, along with the formant contrast feature, distinguished speaker JI's tokens from those of TM.

7. Phonological markedness and universal grammar

Results presented thus far provide no evidence of language universal markedness constraints or effects of phonological parameter settings affecting listeners' perceptions. Indeed, the language-dependent transfer effects reported thus far suggest the contrary, that phonological effects on perception reflect language particular exigencies. Phonological parameters can potentially affect second language learners' responses either through parametric settings required by the second language, or through settings established in first language acquisition. As mentioned earlier, Japanese and Korean are very similar with respect to constraints on initial consonant clusters, which is the domain where parametric settings may express themselves in the data of this experiment. Hence expressions of markedness constraints should be identical for Japanese and Korean listeners and should reflect the markedness ranking of the different English consonant clusters incorporated in the test stimuli.

Two approaches have been taken to assigning markedness values to consonant clusters. The first, and historically prior approach, which has been dubbed the "typological" (Eckman and Iverson, 1993), establishes the relative markedness of a segment or segment cluster on grounds of distribution frequency of occurrence in a given environment, and cross-linguistic implicational relationships. The second approach, which yields similar results, and some would argue, provides an explanatory basis for the distributional findings, depends upon sonority relations within the syllable and has been most extensively discussed by Clements (1990). A "minimal sonority distance parameter" (MSD; Broselow and Finer, 1991) assigns a markedness value to the range of consonant clusters allowed by the phonotactics of a language. Assuming that segments can be rank ordered on a scale of sonority and that onset and coda sequences respect the sonorance hierarchy, MSD provides a means of calculating the markedness value of any given cluster, establishes an implicational hierarchy among clusters, and provides a quantitative characterization of the relative markedness of any two languages with respect to their phonotactic constraints.

Eckman and Iverson (1993) have argued for the superiority of the typological approach to defining markedness relations among consonant clusters, using as supporting evidence a reanalysis of production errors in consonant clusters made by Japanese and Korean learners of English, originally presented by Broselow and Finer (1991).

Both methods of assigning markedness values to consonant clusters were used to assess the correlation of markedness with rates of identification of the /r-l/ clusters employed in this experiment (see Table V).

Neither the MSD parameter of Broselow and Finer (1991) nor the TM constraint of Eckman and Iverson (1993) accounted for the pattern of identification scores across words or language groups. All four correlations (Spearman's rank-order coefficient) between the two indices of markedness and the cluster identification scores for the Koreans and the Japanese listeners were computed. The correlation coefficients ranged from 0.03 to 0.28. None approached statistical significance on a one-tail test. Nor can the clear differences in favor of the Korean group be attributed to

TABLE V. Markedness and identification of consonant clusters.

	Markedness		Identification scores	
	MSD ^a	TM ^b	Kor.	Jap.
fruit	3	2	93	80
flute	3	2	85	65
broom	2	2	63	53
bloom	2	2	80	73
grass	2	2	90	68
glass	2	2	88	70
pray	1	1	88	65
play	1	1	95	73
crime	1	1	73	68
climb	1	1	78	50
			% correct	

^aMSD=Minimal sonority distance parameter (Broselow and Finer, 1991).

^bTM=Typological markedness (Eckman and Iverson, 1993).

parametric settings, because the phonotactic constraints of Japanese and Korean initial clusters are practically identical.

E. Summary of identification experiment results

Results of the identification experiment suggested a dominance hierarchy among the factors contributing to the perceptibility of the /l-r/ contrast by Japanese and Korean learners of English. For the Korean listeners, the possession of a native-language model for the /l-r/ contrast in intervocalic position appeared to be the dominant factor in determining the pattern of identification scores across the three phonetic environments. The contrast was best perceived in medial position. In cluster position, the /l-r/ contrast was marginally better perceived than in initial position, in spite of the reduced acoustic discriminability of /l/ and /r/ in consonant clusters. Enhanced performance in cluster position appears to have been supported by a compensatory phonological strategy of (re)syllabification through epenthesis (CCV→CvCV, where v=epenthetic vowel), in order to access native language templates for the /l-r/ contrast. It seems appropriate to refer to this enhancement of /l-r/ perception in cluster position by Korean listeners as a *phonological* transfer effect, because any enhancement of the contrast occurs as a result of a linguistic transformation of the input generated by the listener, presumably to render the input signal more compatible with L1 phonotactics, thereby providing a stimulus which is interpretable as an L1 phonological target. Vowel epenthesis may also be observed in Japanese learners' productions of these consonant clusters, but no processing advantage is obtained, because Japanese lacks an L1 model for the /l-r/ contrast in all environments.

The pattern of performance for Japanese listeners, for whom no L1 model of the L2 contrast was available, was consistent with considerations of acoustic discriminability, with performance best in initial position and worst in cluster position.

The extent to which speakers provided clear exemplars for the /r-l/ contrast in various environments also affected identification rates. Speaker differences interacted with the stimulus type and the environment in which the target sound occurred, but they did not interact with the language factor. Acoustic analysis of the stimulus tokens showed that identi-

fication rates were higher for those stimulus tokens which better exemplified spectrographic cues known to be effective for /l-r/ discrimination.

Phonological markedness was found not to be predictive of perceptual error rates among consonant+liquid clusters. Universal markedness constraints apparently had little bearing on the results of this experiment and their relevance for speech perception in second language learning is therefore questionable. On the other hand, language particular factors, arising from a comparative analysis of the relevant phonological structures in Korean and Japanese, were crucial for predicting the pattern of perceptual errors.

III. DISCRIMINATION EXPERIMENT

It was expected that the discrimination task would engage specific linguistic processing of the stimuli less than the identification task reported above. To assess the impact of task variables upon precedence relations and interactions among the factors investigated in the identification experiment, the same group of subjects participated in a discrimination test, using the identical target stimuli. The discrimination experiment was conducted two weeks after the identification task.

A. Procedure

An oddball discrimination test was used, in which, on a given trial, one member of a sequentially presented triad of stimuli differed from the other two, and the listener's task was to identify the odd one out. The advantage of this procedure over the more commonly used ABX or Same-Different discrimination procedures is that it is relatively economical in terms of the number of trials required to map the set of discrimination judgements. Its main disadvantage is that it imposes a greater sensory storage load upon listener's and consequently may be more prone to influences of phonological encoding. Hence the oddball discrimination task may yield conservative estimates of task differences between identification and discrimination on /r-l/ performance.

On a given trial, listeners were presented with one of six possible triads made up of minimal pair /r-l/ triplets (LLR, LRL, RLL, RRL, RLR, LRR) and asked to indicate which word was different. Repetitions of the same token were used for the two stimuli which were "the same" within a given triplet. There were 360 items in the stimulus set, which included one replication (5 pairs×3 positions×2 speakers×6 triplets×2 repetitions). As 360 items were too many for a single experimental session, the subjects were divided into two groups, each of whom responded to half of the trials in the total stimulus set. The interstimulus interval between items in a stimulus triad was approximately 0.5 s and the intertrial interval between triads was 3 s, with a short rest period after each block of 60 trials.

Test conditions were the same as in the identification experiment. Subjects were group tested in the language laboratory listening booths. As in the identification test, there was a pretest in which subjects were familiarized with the test words and then with the response task, using triplets constructed from selected distracter items employed in the identification task.

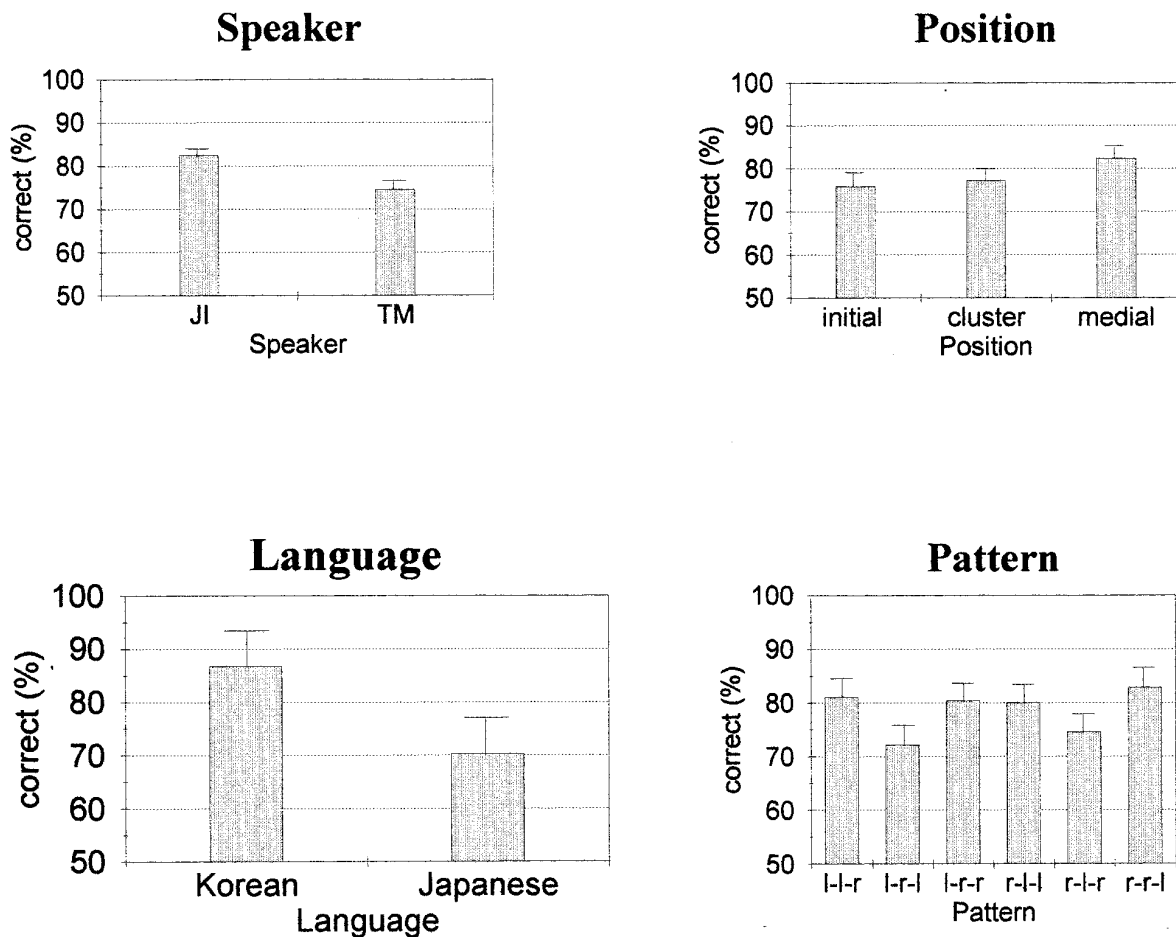


FIG. 5. Main effects: Discrimination experiment.

B. Data analysis

Initial analysis of the data revealed no significant differences between the two groups, who each heard half of the test stimuli, so in further analysis both groups were combined. A four-way analysis of variance was undertaken, with the discrimination scores as the dependent variable, and the same treatment variables as in the identification experiment, except that, in this case, there was no factor for stimulus type (/l/ or /r/), but there was an additional one for the carrier pattern of the discrimination contrast within the triplet (LLR, LRL, LRR, RLL, RLR, RRL).

C. Results

A four-way analysis of variance was conducted. All four main effects were significant at or beyond the $p < 0.001$ level (see Fig. 5), but no significant interactions were obtained. The highly significant main effects of language background ($F[1,648]$, $p < 0.00001$) and speaker ($F[1,648]$, $p < 0.0001$) were in the same direction as for the identification experiment. The Korean listeners performed /l-r/ discrimination better than the Japanese (Mean = 86.7% correct versus 70.2%, respectively). Speaker JI's tokens were more discriminable than those of TM (82.4% vs 74.5%).

A posteriori comparisons among discrimination score means for initial, cluster, and medial positions indicated that medial position was significantly different from the other

two (t test medial versus initial position: $t = -3.03$, $df = 478$, $p = 0.002$, two tailed; t test medial versus cluster position: $t = -2.32$, $df = 478$, $p = 0.021$; t test initial versus cluster position: $t = -0.61$, $df = 478$, $p = 0.54$). This was similar to the pattern of main effects for the identification test. However, the discrimination test did not show any significant interaction effects between the factors of position, language, and speaker.

There was also a strong main effect of the triplet carrier pattern used to elicit discrimination judgments ($F[5,648]$, $p < 0.0002$). As Mochizuki (1981) found, the LRL and RLR triplets resulted in lower discrimination scores (t test [LRL+RLR] versus four other patterns: $t = 4.05$, $df = 718$, $p < 0.001$, two tailed; t test LRL versus RLR: $t = -0.71$, $df = 238$, $p = 0.48$; t test RLL versus RRL: $t = -0.97$, $df = 238$, $p = 0.33$). The LRL and RLR are the two patterns where the "same" stimuli are not contiguous and listeners must hold all three stimuli in sensory storage in order to make a discrimination judgment.

D. Comparison of identification and discrimination tasks

While a similar pattern of main effects was found in the discrimination experiment to those observed in the identification test, the lack of interaction effects suggested that the two tasks may have invoked different processing strategies

on the part of listeners. Phonological transfer effects (language-specific learning effects) were diminished in the discrimination experiment. The main effect of language background was preserved, but no interaction between listeners' language and the position (initial, cluster, medial) of the /l-r/ contrast was found. Similarly, although a strong main effect of speaker was observed, which was in the same direction as the identification experiment, there were no significant interaction effects between the Speaker factor and listeners' language background, or the position of the /l-r/ contrast. These results were consistent with the hypothesis that underlying perceptual mechanisms differed in the identification and discrimination tasks. It was apparent from the identification test results that many of the significant higher-order interactions may have been caused by response preferences towards /r/, which varied with the language background of the listener and the position of the target sound. However, such effects were not apparent in the case of the discrimination data.

If, as hypothesised earlier, identification invokes greater linguistic processing of the signal than does discrimination, then word familiarity effects should operate more strongly in the identification than the discrimination test. An attempt had been made to balance word familiarity effects in the initial selection of /l/ and /r/ minimal pairs, by choosing only items which would be familiar to second language learners. However, in view of the /r/ preference biases observed in the identification task, a comparison of the *relative subjective familiarity* (Flege *et al.*, 1995) of the /l/ and /r/ members of the 15 minimal pairs was warranted, and the impact of any inequalities of lexical familiarity between /l/ and /r/ items on identification and discrimination performance should be assessed.

On the other hand, if identification and discrimination involve similar perceptual processes, then the relative order of difficulty of /r-l/ contrasts across the 15 minimal pairs should be similar across the two tasks. To compare response profiles across the minimal pairs, both the identification and the discrimination data were rescored, so that separate /r/ and /l/ scores were obtained for each of 15 minimal pairs.

1. Scoring the dependent and independent variables

In the case of the discrimination test, a preference towards /r/, or a lexical familiarity effect, could only be expressed as a bias towards or away from the oddball member of a triad. Hence separate /l/ and /r/ scores were obtained by taking account of whether the oddball in a given triad was an /l/ or an /r/ word.

To assess the relative subjective familiarity of the /r/ and /l/ words that comprised the minimal pairs, the authors and two experienced language teachers independently judged which member of each pair would be likely to be more familiar to Japanese and Korean learners of English. There was a high degree of consensus among the four judges. In all but three of the minimal pairs, the /r/ member was rated as more familiar than the /l/ member; the exceptions being: low > row, play > pray, climb > crime. Hence any r bias or lexical familiarity effects would be highly correlated and probably indistinguishable in the present experiment.

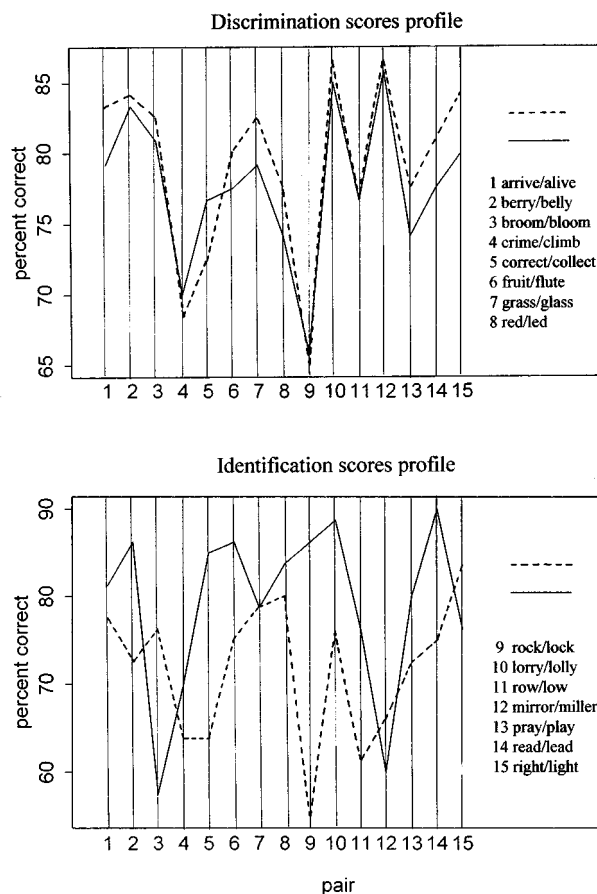


FIG. 6. Interaction plots: Identification and discrimination data. Comparison between the interaction of item type (/l/ or /r/) with minimal pair for identification and discrimination responses. The graphs illustrate different response profiles for the identification and discrimination tests and the presence of an interaction effect for the former, but not the latter.

2. Statistical analysis

Parallel two-way analyses of variance of the identification and discrimination tests were conducted, with the 15 minimal pairs and the item type (/l/ or /r/) as experimental factors. Figure 6, which represents an interaction plot of the two experimental factors, shows the profile of /l/ and /r/ scores across the minimal pairs for the identification and discrimination tests.

A significant main effect of minimal pair was found for both identification and discrimination test ($F[14,570] = 1.99, p = 0.016$; $F[14,570] = 2.88, p = 0.003$, respectively), but the scoring profiles of /r/ and /l/ over the 15 minimal pairs were quite different for the two tests (see Fig. 6). The identification test yielded a significant main effect for item type, ($F[1,570] = 9.17, p = 0.002$) revealing an r bias for most of the minimal pair contrasts. No such effect was found in the case of the discrimination test ($F[1,570] = 0.72, n.s.$). The identification test also yielded a significant minimal pair by item type interaction, ($F[14,570] = 1.77, p = 0.039$) but no significant interaction effect was found for the discrimination test ($F[14,570] = 0.12, n.s.$).

The minimal pair *lorry-lolly*, which was the most difficult on the identification test was the second easiest pair on the discrimination test. The minimal pair *red-led* showed a strong r bias on the identification test, but a slight preference

in the opposite direction on the discrimination test. These differences in performance profile across the minimal pairs indicate that the identification and discrimination tests were tapping different perceptual processes or making different task demands of listeners.

The effects of lexical familiarity were also assessed. However, this factor proved to be statistically indistinguishable in its effects from that of item type (*l/r*), which indicated an *r* bias on the identification test, but no significant effect on the discrimination task. Thus while it was not possible to separate the effects of *r* bias and lexical familiarity in this experiment, the fact that either or both were operative in the identification task, but not in the discrimination task, supports the hypothesized differential sensitivity of the two tasks to the influence of language-dependent processing strategies and linguistic factors in general.

IV. GENERAL DISCUSSION AND CONCLUSIONS

Recent models of cross-language speech sound perception (Flege, 1995; Best, 1995; Kuhl, 1995) stress the importance of naive-language phonemic categorization of non-native (“foreign”) sounds in explaining patterns of perceptual errors or the likelihood or ease of accommodation of the perceptual system to such sounds. Although there is disagreement over the phonetic basis for the categorization of non-native sounds, (e.g., whether it be gestural [Best] or acoustic [Kuhl]), all share the assumption that, at least in the initial stages of L2 exposure, patterns of perceptual assimilation to L1 phonemic categories strongly determine learners’ responses to novel sounds. Best (1995) has elaborated different classes of L1 assimilation for the purpose of predicting pairwise discrimination performance, depending on how sounds in the L2 pair are categorized with respect to L1 targets. Kuhl has postulated “perceptual magnet effects,” whereby phonetic tokens that fall close to a phonemic prototype are less sensitively discriminated than sounds which fall at a distance from such prototypes. Implicit in all three models is the mediating influence of phonological experience and the language-specific nature of the effects on second language speech sound perception.

The major goal of this study was to observe, within a single experiment, the interaction of potentially competing factors, operating at different levels of perceptual processing (the phonetic and the phonological), over different domains (the language specific and the language universal) in the perception of a novel phonemic contrast. The phonetic level of processing was reflected in factors affecting the acoustic discriminability of the tokens, namely, in terms of the present experiment: (a) the position of the target contrast in the word, and (b) the clarity with which the speaker encoded the target contrast in particular tokens across the three contexts. The phonological level of processing was reflected in L1 learning effects, namely: (a) the extent to which Korean provides an L1 model for the foreign *l-r*/ contrast in medial position, whereas Japanese does not, and (b) differences in the extent to which the two listening tasks, phoneme identification and oddball triad discrimination, required specific linguistic processing of the test stimuli. Both prior phonological learning and the relative acoustic discriminability of

the items affected subjects’ performance on the identification test. Where both factors were engaged, phonological learning effects predominated over the effects of acoustic discriminability. This was evident from the differential impact of positional effects on *l-r*/ identification for the Japanese and Korean listeners. Whereas the Japanese listeners’ poorer identification of *l-r*/ in cluster position was attributable solely to the lower acoustic discriminability of *l-r*/ in this environment (supporting findings of previous studies), the Korean listeners’ responses were predominantly influenced by prior L1 phonological learning. Specifically, their performance on the *l-r*/ contrast in cluster position was enhanced by a phonological strategy (vowel epenthesis), which enabled them to deploy the Korean contrast between flaps and geminate liquids in medial position and to aid perception of the English *l-r*/ contrast in initial clusters, such as *play-pray*. Because this L1-driven enhancement of perceptual discrimination depends upon a missyllabification of the input (from the perspective of L2), it seems appropriate to view it as a *phonological* transfer effect, generated by learned phonotactic expectancies for L1 rather than by any inherent phonetic property of the stimulus.

The relative acoustic discriminability of the stimulus items also impacted upon identification scores in terms of the clarity with which a given speakers’ tokens encoded critical acoustic features for *r-l*/ discrimination. Identification rates for tokens from the two speakers (JI and TM) were found to vary depending upon the type of target (*l/* or *r/*) and its position in the carrier word. Speaker JI’s *l/* tokens were more identifiable in all three positions than those of TM. Identification scores for *l/* tokens were found to be quite strongly associated with a measure of the spectral contrastiveness of higher formants *F3* and *F4*. Analogously, speaker TM’s *r/* tokens in cluster position were more accurately perceived than those of JI. Spectral analysis, combined with statistical regression showed that the steepness of *F3* in combination with the segment duration were good predictors of *r/* identification in cluster position.

The pattern of main effects for scores on the discrimination test were similar to those found on the identification test. The Koreans performed better than the Japanese. Speaker JI’s tokens were better discriminated than those of TM. Items in medial position were better discriminated than those in initial and cluster positions. However, there was an absence of factorial interactions of the kind observed in the identification test. Rescoring and comparison of performance profiles across the set of minimal pairs indicated that quite different factors were at work in the identification and discrimination tests. The minimal pair scoring profiles for *r/* and *l/* in the identification and discrimination tests were essentially uncorrelated. A lexical familiarity effect, which was statistically inseparable from a response bias in favor of *r/* items, was found to be significant for identification test performance, but no similar effect was found for performance on the oddball discrimination task. These findings clearly indicate that the identification and discrimination differed in terms of task demands on listeners. The lack of higher-order language, position, and speaker interactions and the absence of a lexical familiarity effect on the discrimination task sup-

ported the hypothesis that a phonological level of signal processing was less engaged by the oddball discrimination task.

However, unlike the identification task, where performance on particular items was found to be linked with the presence of acoustic features known to distinguish /r/ and /l/, no comparable analysis of the acoustic features differentiating hard from easy to discriminate items was undertaken. Except for those triads which imposed some short-term memory load (patterns LRL and RLR), performance on the discrimination task was usually close to the ceiling. This is a topic for further investigation. The main significance of the present findings lies in the predominant role of prior phonological learning in the perception of a non-native phonemic

contrast, which emerged from comparison of Japanese and Korean identifications of English /l/ and /r/, in the face of speaker- and context-dependent phonetic variation. Perception was enhanced in an environment of acoustic disadvantage by the application of an L1 phonological processing strategy that yielded inappropriate syllabification of the input from the perspective of L2, but which enabled listeners to encode the foreign contrast more effectively. A similar interaction between L1 phonological processing strategies and phonetic properties of speech stimuli is reported for the case of foreign vowel perception by Japanese and Korean learners of English in Ingram and Park (1997).

APPENDIX A

TABLE AI. Identification of /l/ and /r/ analysis of variance: repeated measures design.^a

	df	Sum of square	Mean square	F value	Pr(F)
Language (Jap., Kor.)	1	102.3773	102.3773	3.665755	0.071579
Residuals	18	502.7047	27.9280		
Error: Within	df	Sum of square	Mean square	F value	Pr(F)
Main effects:					
Speaker (JI, TM)	1	10.3128	10.312 76	3.485 32	0.063 393 4
Type (/r/, /l/)	1	43.9898	43.989 84	14.866 91	0.000 155 9
Position (Ini., Clu., Med.)	2	7.6443	3.822 14	1.291 74	0.277 098 2
Two-way interactions:					
Speaker:type	1	47.4815	47.481 51	16.046 96	0.000 087 4
Speaker:position	2	6.0818	3.040 89	1.027 70	0.359 728 0
Type:position	2	31.9359	15.967 97	5.396 57	0.005 223 3
Speaker:language	1	1.1690	1.169 01	0.395 08	0.530 364 8
Type:language	1	24.5440	24.544 01	8.294 95	0.004 413 2
Position:language	2	24.9234	12.461 72	4.211 59	0.016 172 1
Three-way interactions:					
Speaker:type:position	2	40.7568	20.378 39	6.887 13	0.001 283 5
Speaker:type:language	1	2.1565	2.156 51	0.728 82	0.394 297 8
Speaker:position:language	2	1.4693	0.734 64	0.248 28	0.780 384 7
Type:position:language	2	27.4693	13.734 64	4.641 79	0.010 713 4
Four-way interaction:					
Speaker:type:posi:lang	2	14.0818	7.040 89	2.379 55	0.095 235 1
Residuals	198	585.8641	2.958 91		

^aResponses to the items "lorry" and "lolly" were excluded from the scoring and the ANOVA. See text for explanation.

APPENDIX B. SPECTROGRAMS FOR MINIMAL PAIR TOKEN CONTRASTS FOR ITEMS IN FIGS. 3 AND 4

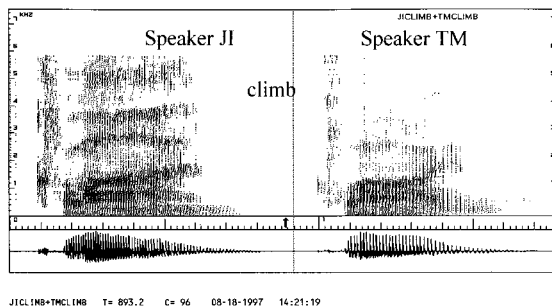


FIG. B1.

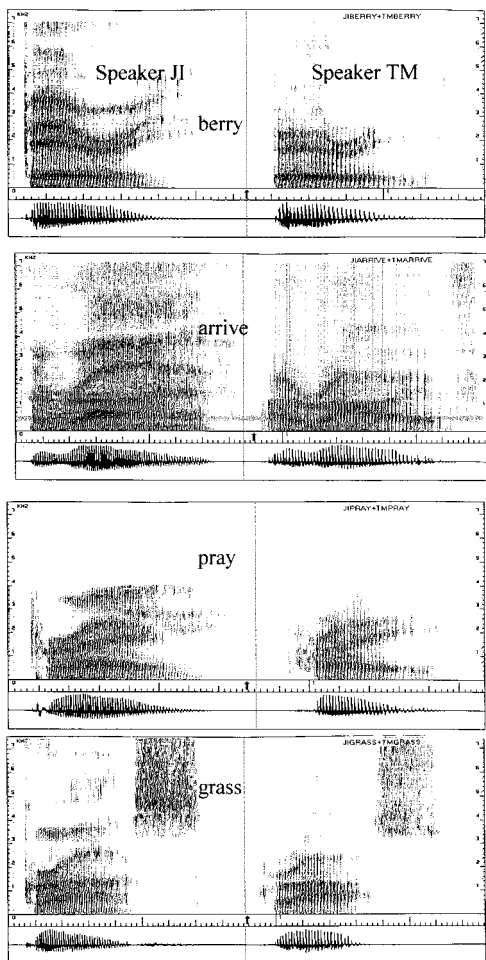


FIG. B2.

Best, C. T. (1995). "A direct realist view of cross-language speech perception," in *Speech Perception and Linguistic Experience: Issues in Cross-language Research*, edited by W. Strange (York, Baltimore), pp. 171–203.

Bhat, D. N. S. (1974). "The phonology of liquid consonants," *Working Papers in Language Universals* (Stanford University, Stanford), Vol. 16, pp. 73–104.

Broselow, E., and Finer, D. (1991). "Parameter setting in second language phonology and syntax," *Second Lang. Res.* **7**, 35–59.

Chomsky, N. (1986). *Knowledge of Language: Its Nature, Origins and Use* (Praeger, New York).

Clements, G. N. (1990). "The role of the sonority cycle in core syllabification," in *Papers in Laboratory Phonology I: Between the Grammar and the Physics of Speech*, edited by J. Kingston and M. Beckman (Cambridge U.P., Cambridge), pp. 283–333.

Cutler, A., Mehler, J., Norris, D. J., and Segui, J. (1986). "The syllable's differing role in the segmentation of French and English," *J. Memory Lang.* **25**, 385–400.

Cutler, A., Mehler, J., Norris, D. J., and Segui, J. (1992). "The monolingual nature of speech segmentation by bilinguals," *Cogn. Psychol.* **24**, 381–410.

Eckman, F. (1977). "Markedness and the contrastive analysis hypothesis," *Lang. Learning* **27**, 315–330.

Eckman, F. R., and Iverson, G. K. (1993). "Sonority and markedness among onset clusters in the interlanguage of ESL learners," *Second Lang. Res.* **9**, 234–252.

Flege, J. E. (1995). "Second-language speech learning: Theory, findings, and problems," in *Speech Perception and Linguistic Experience: Theoretical and Methodological Issues*, edited by W. Strange (Timonium, York, MD), pp. 229–273.

Flege, J. E., Takagi, N., and Mann, V. (1995). "Lexical familiarity and English-language experience affect Japanese adults' perception of /r/ and /l/," *J. Acoust. Soc. Am.* **99**, 1161–1173.

Ganong, W. (1980). "Phonetic categorization in auditory word perception," *J. Exp. Psychol.* **6**, 110–125.

Gillette, S. (1980). "Contextual variation in the perception of L and R by Japanese and Korean speakers," *Minnesota Papers on Linguistics and the Philosophy of Language* (University of Minnesota, Minneapolis), Vol. 6, pp. 59–72.

Goto, H. (1971). "Auditory perception by normal Japanese adults of the sounds 'L' and 'R'," *Neuropsychologia* **9**, 317–323.

Henry, E., and Sheldon, A. (1986). "Duration and context effects on the perception of English /r/ and /l/: A comparison of Cantonese and Japanese speakers," *Lang. Learning* **36**, 505–521.

Ingram, J. C. L., and Park, S.-G. (1997). "Cross-language vowel perception and production by Korean and Japanese listeners," *J. Phonetics* **25**, 343–370.

Kuhl, P. K. (1995). "Linguistic experience and the perceptual magnet effect," in *Speech Perception and Linguistic Experience: Issues in Cross-language Research*, edited by W. Strange (Timonium, York, MD), pp. 121–154.

Lively, S. E., Logan, J. S., and Pisoni, D. B. (1993). "Training Japanese listeners to identify English /r/ and /l/. II: The role of phonetic environment and talker variability in learning new perceptual categories," *J. Acoust. Soc. Am.* **94**, 1242–1255.

Lively, S. E., Pisoni, D. B., and Logan, J. S. (1992). "Some effects of training Japanese listeners to identify English /r/ and /l/," in *Speech Perception, Production and Linguistic Structure*, edited by Y. Tohkura, E. Vatikiotis-Bateson, and Y. Sagisaka (Ohmsha-IOS, Tokyo), pp. 175–196.

Logan, J. S., Lively, S. E., and Pisoni, D. B. (1991). "Training Japanese listeners to identify /r/ and /l/," *J. Acoust. Soc. Am.* **89**, 874–886.

Maddieson, I. (1984). *Patterns of Sounds* (Cambridge U.P., Cambridge, England).

Mann, V. A. (1986). "Distinguishing universal and language-dependent levels of speech perception: Evidence for Japanese listeners' perceptions of 'l' and 'r'," *Cognition* **24**, 169–196.

Mochizuki, M. (1981). "The identification of /r/ and /l/ in natural and synthesised speech," *J. Phonetics* **9**, 283–303.

Sato, C. (1984). "Phonological processes in second language acquisition: Another look at interlanguage syllable structure," *Lang. Learning* **34**, 43–57.

Sheldon, A., and Strange, W. (1982). "The acquisition of /r/ and /l/ by Japanese learners of English: Evidence that speech production can precede speech perception," *Appl. Psycholinguistics* **3**, 243–261.

Stevens, K. N., Liberman, A. M., Studdert-Kennedy, M., and Öhman, S. E. G. (1969). "Crosslanguage study of vowel perception," *Lang. Speech* **12**, 1–23.

Tsuzuki, M. (1992). "A phonetic study of the Korean and Japanese Lateral, Flap, and Nasal," Ph.D. thesis, Seoul National University.

Werker, J. F. (1994). "Cross-language speech perception: Developmental change does not involve loss," in *The Development of Speech Perception: The Transition from Speech Sounds to Spoken Words*, edited by J. C. Goodman and H. C. Nusbaum (MIT, Cambridge, MA), pp. 93–120.

Werker, J. F., and Logan, J. S. (1985). "Cross-language evidence for three factors in speech perception," *Percept. Psychophys.* **37**, 35–44.

Yamada, R. A., and Tohkura, Y. (1992a). "Perception of American English /r/ and /l/ by native speakers of Japanese," in *Speech Perception Production and Linguistic Structure*, edited by Y. Tohkura, E. Vatikiotis-Bateson, and Y. Sagisaka (Ohmsha-IOS, Tokyo), pp. 155–174.

Yamada, R. A., and Tohkura, Y. (1992b). "The effects of experimental variables on the perception of American English /r/ and /l/ by Japanese listeners," *Percept. Psychophys.* **52**, 376–392.

Chaos in segments from Korean traditional singing and Western singing

Myeong-Hwa Lee,^{a)} Jeong-No Lee,^{b)} and Kwang-Sup Soh^{c)}

Department of Physics Education, Seoul National University, Seoul 151-742, Korea

(Received 22 January 1997; revised 7 July 1997; accepted 23 September 1997)

The time series of the segments from a Korean traditional song ‘‘Gwansanyungma’’ and a western song ‘‘La Mamma Morta’’ were investigated using chaotic analysis techniques. It is found that the phase portrait in the reconstructed state space of the time series of the segment from the Korean traditional song has a more complex structure in comparison with the segment from the western songs. The segment from the Korean traditional song has the correlation dimension 4.4 and two positive Lyapunov exponents which show that the dynamic related to the Korean traditional song is a high-dimensional hyperchaotic process. On the other hand, the segment from the western song with only one positive Lyapunov exponent and the correlation dimension 2.5 exhibits low-dimensional chaotic behavior. © 1998 Acoustical Society of America.

[S0001-4966(98)04401-4]

PACS numbers: 43.75.Rs [WJS]

INTRODUCTION

Until recently it has been thought that complicated phenomena result from complicated dynamical systems with many degrees of freedom and they have been usually considered as stochastic processes. But it turned out that even simple systems with few degrees of freedom can exhibit extremely irregular unpredictable behavior when the systems are described by nonlinear deterministic equations. The most typical example is chaos which shows extremely sensitive dependence on initial conditions.

Several authors have analyzed speech data using techniques for studying chaotic dynamics.¹ Despite the apparently complicated mechanism of vocal production, which involves various aspects such as physiological activities and nonlinear fluid mechanics, the concept of deterministic chaos implies the possibility that the complex irregularities may be generated by deterministic nonlinear dynamics with only a few state variables. It has been reported that human speech sounds exhibit bifurcations and chaos,² for example, in fricative consonants,³ vowels,⁴ newborn infant cries,⁵ various phoneme types,⁶ and Korean traditional singing.⁷ In this paper we analyze the irregularities and the dynamics in the time series of the segments from a Korean traditional song and a western song. In order to check our method of analysis a single note ‘‘Si’’ is also analyzed. In Sec. I, our data acquisition from the Korean traditional song, the western song, and the note ‘‘Si’’ is explained. In Sec. II, the power spectra of the time series are given and in Sec. III, the phase portraits which give geometrical information included in the time series are constructed by the delay vector method. In Sec. IV, the correlation dimension of the attractors in the reconstructed space are calculated to characterize properties of the attractor. In Sec. V, Lyapunov exponents are estimated. The

above-mentioned three songs are compared in Secs. II–V. In the last section a brief discussion is given.

I. DATA ACQUISITION

In each section, for the sake of comparison, segments of a Korean traditional song, segments of a western song, and the note ‘‘Si’’ are analyzed at the same time. The song used as Korean traditional singing, ‘‘Gwansanyungma’’ is a SeoDo folk song which has been sung in the northwestern provinces of Korea. It includes various kinds of vocalization of the SeoDo folk song, especially the peculiar vibration. The song we used was sung in 1994 by Pok-Nyŏ O who was born in P’yŏngyang in 1913 and was designated as one of the human cultural assets in 1971. Its length is about 220 s and its words and phonetic transcription using single-symbol

TABLE I. Divided sections of the SeoDo folk song ‘‘Gwananyungma.’’ (The sections with broad power spectrum are marked with an asterisk, a tilde means that the peculiar vibration of the SeoDo folk song is used.)

No	Words	Phonetic transcription	Time
1	ch’ugangi	/CUgaGi/	35 s
2	i~	/i/	10.0 s
3	i~	/i/	14.5 s
4(*)	chŏgma	/Jxma/	10 s
5(*)	ak	/ak/	9.0 s
6(*)	ŏryong	/xrycG/	6.0 s
7	naeng	/nEG/	12.5 s
8(*)	ha~	/ha/	11.5 s
9(*)	ni	/ni/	8.5 s
10(*)	i~	/i/	9.5 s
11(*)	hi~	/hi/	7.5 s
12(*)	injae	/inJE/	3.0 s
13	aei	/Ei/	9.0 s
14(*)	i~	/i/	9.5 s
15(*)	sŏ	/sx/	7.0 s
16	p’u	/pu/	13.0 s
17	u~	/u/	8.0 s
18(*)	~ung	/uG/	13.0 s
19	chungŏnrurŭl	/JUGsxNrUrI/	15.0 s

^{a)}Electronic mail: mhwaltee@gmc.snu.ac.kr

^{b)}Electronic mail: jnlee@gmc.snu.ac.kr

^{c)}Electronic mail: kssoh@phyb.snu.ac.kr

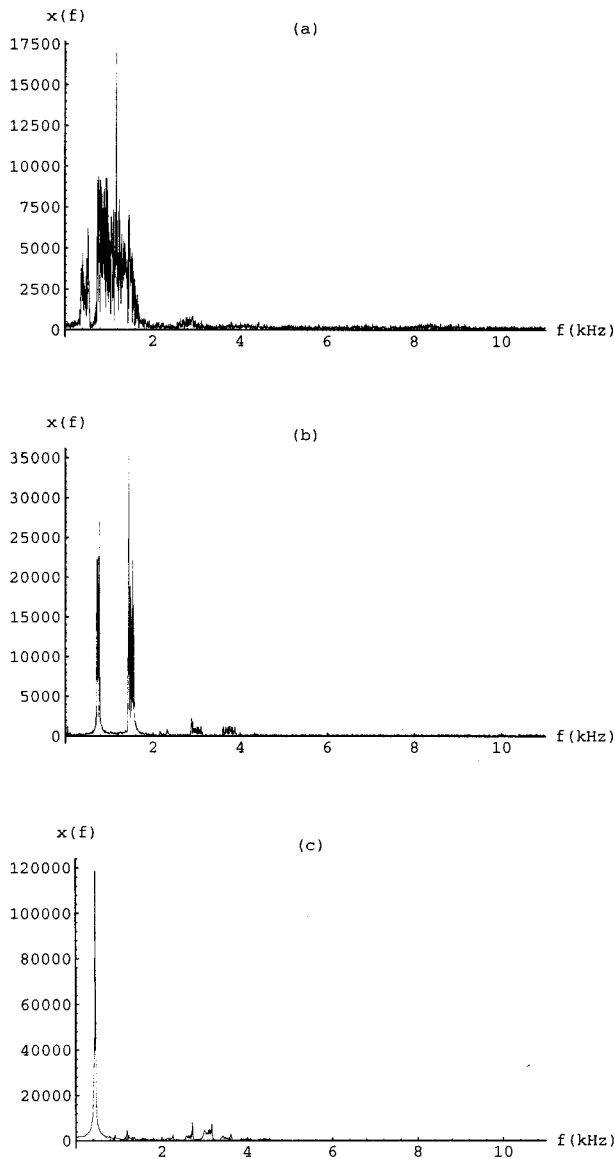


FIG. 1. (a) Fourier transform of the SeoDo folk song shows the very broadened spectrum which is one of the characteristics of a chaotic system. (b) Fourier transform of a western song shows a little broadened spectrum. (c) Fourier transform of “Si” shows δ function which is the characteristics of the periodic system.

ARPA bet are given in Table I. As seen in Table I, they are divided into 19 sections to identify which sections show chaotic behavior. We calculated the power spectrum for each section. After getting insight about the characteristics of each section from the power spectrum, we choose the eighth section for obtaining the phase portrait, correlation dimension, and Lyapunov exponent because the eighth section showed the most broadband power spectrum and was thought to represent the characteristics of the SeoDo folk song most properly. Actually only the latter part of the eighth section is used, whose length is about 1.6 s and its phoneme is described by the vibrating vowel /a/. As a western song, “La Mamma Morta” performed by Maria Callas is used. Especially the segments which do not have background music are used to facilitate the analysis. Its length is about 1 s and the phoneme is also /a/. The single note “Si” of the “Do-re-mi

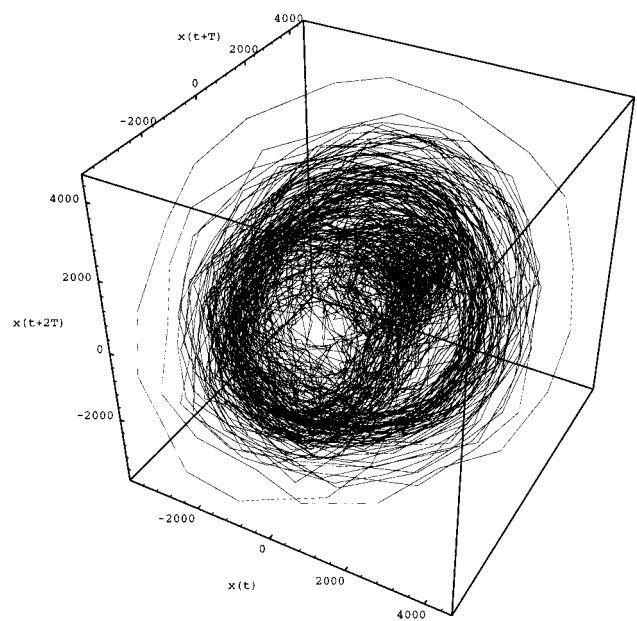


FIG. 2. The three-dimensional phase portrait of the SeoDo folk song wrinkles and occupies an extended region.

song” in the movie “Sound of music” is used to check our methods of analysis. Its length is about 0.5 s. The consonant /s/ is uttered only for a very short time, so the actually recorded and analyzed sound is /i/.

All the data are recorded in the form of wave files with PCM (pulse code modulation) mode using “Sound Blaster AWE32” which is the trademark of Creative Technology Ltd. It is performed with a sampling rate 22 050 Hz and 16 bits except the single note “Si” with 44 100 Hz owing to its short length. Programs to analyze the recorded wave files run on an IBM PC.

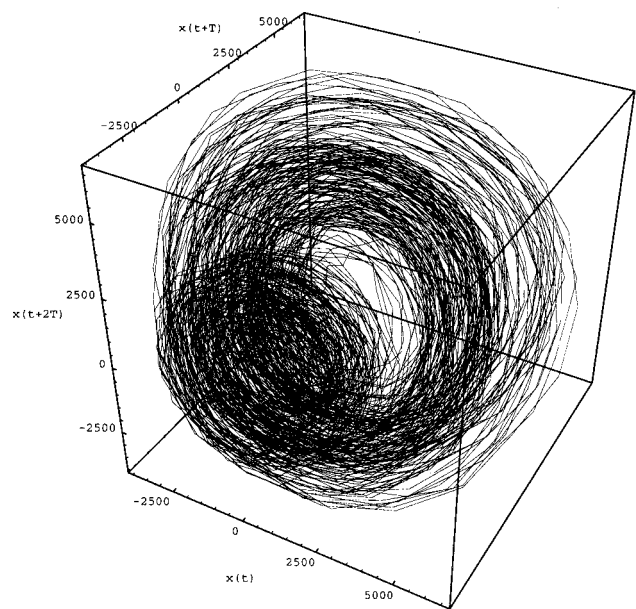


FIG. 3. The three-dimensional phase portrait of the western song also wrinkles and occupies an extended region.

II. POWER SPECTRUM

The Fourier analysis of time series is useful for obtaining, among other things, the frequency components and the power distribution as a function of frequency. In general the power spectrum is a very good tool for the visualization of periodic and quasiperiodic phenomena, and their separation from irregular time evolutions which are characterized by broadband power spectra.⁸ The broadband regions in power spectra can arise from stochastic or deterministic processes, but the decay in the spectral power at large ω is different for the two cases.^{9,10} However, that is not really a good indicator to identify chaotic time series. So we need to estimate correlation dimension and Lyapunov exponents, etc. We use the fast Fourier transform (FFT) to compute a power spectrum.

In the case of Korean traditional song it is obtained for each section divided in order to identify whether each section shows chaotic behavior or not. The sections with broad power spectra are marked with an asterisk in Table I. Figure 1 shows the power spectrum obtained from the time series of the Korean traditional song, western song, and a single note "Si." In the case of the Korean traditional song it is that of the most typical case with the broad power spectrum (eighth section). We can see the broadband regions in the power spectrum of the Korean traditional song which is a characteristic of chaotic systems. The power spectrum of the western song shows less broadband power in comparison with the Korean traditional song and we can see a δ -functionlike peak in the power spectrum of a single note "Si." As the data to investigate phase portrait, correlation dimension, and Lyapunov exponents for the Korean traditional song, we choose the eighth section which shows the most broadband power spectrum.

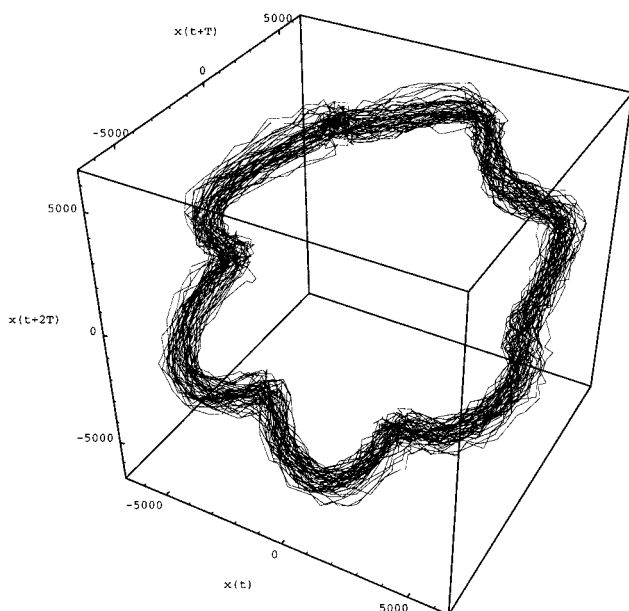


FIG. 4. The three-dimensional phase portrait of "Si" exhibits a limit cycle.

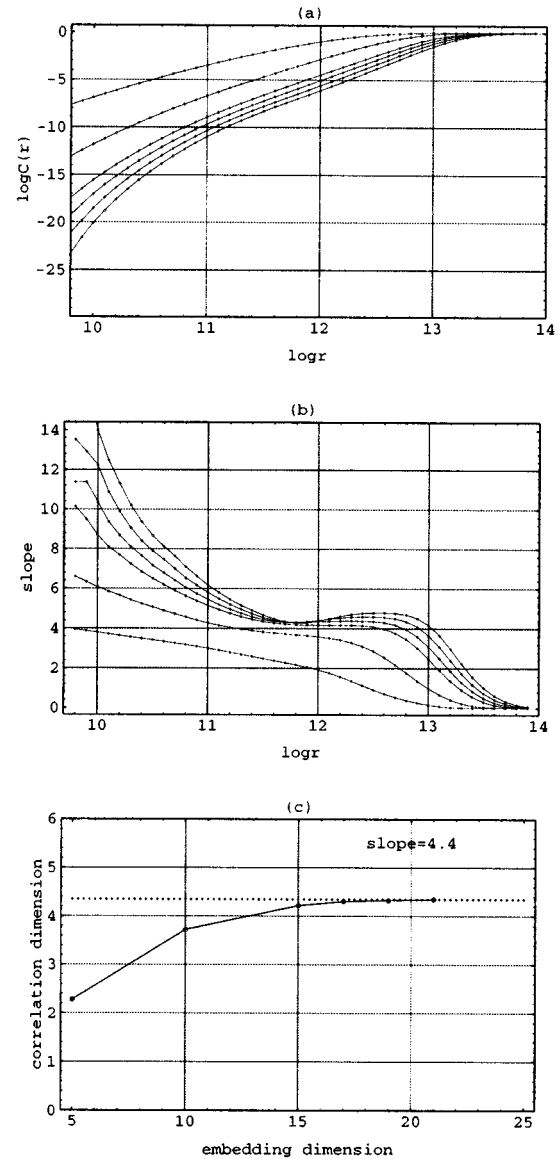


FIG. 5. Correlation integral and correlation dimension for the SeoDo folk song; (a) The plot of $\log_{2.0} C(W, N, r)$ versus $\log_{2.0} r$ for values of r varying from $2.0^{9.8}$ to 2.0^{14} with embedding dimension 5, 10, 15, 17, 19, 21 (top to bottom). (b) The plot of local slopes versus $\log_{2.0} r$ showing the converging scaling region. (c) Correlation dimension ν is saturated at a value of about 4.4 as the embedding dimension is increased.

III. PHASE PORTRAITS

Several variables are usually required to fully describe the state of a system. Thus in order to construct a dynamical model for an experimental time series, we must first reconstruct a state space.¹¹

A simple way to create a state representation is to form vectors of the n consecutive samples of the time series which are delay vectors \mathbf{X}_t . The delay vector \mathbf{X}_t at time t is defined by

$$\mathbf{X}_t \equiv (x_t, x_{t+T}, \dots, x_{t+(n-1)T}), \quad (1)$$

where n , T are called the *embedding dimension*, *delay time*, respectively, and $\{x_t\}$ stands for the time series. This choice of state representation is commonly known as *delay vector method*. Takens¹² proved that if d is the dimension of a

manifold containing the attractor, in order to yield a topological equivalent phase portrait, leaving the dynamical parameters invariant, it is sufficient to choose n such that

$$n \geq 2d + 1. \quad (2)$$

The choice of optimal delay time T is an important and largely unresolved problem. Even though the choice of delay time T is arbitrary for an infinite amount of noise-free data,¹² in the case of real laboratory data a good choice of T is essential for geometrical and numerical analysis of a phase portrait. As $T \rightarrow 0$, the trajectory approaches the identity line. When T is larger than the optimal value, the correlation between the data points is destroyed.

A commonly used rule of thumb is to set T to be the time lag required for the autocorrelation function to become negative, or alternatively, the time lag required for the autocorrelation to decrease by a factor of e (from its value at time lag 0). Another approach, that of Fraser and Swinney¹³ uses the ‘‘mutual information,’’ which measures a more general dependence of two variables. Schuster and Liebert¹⁴ took the first minimum of the logarithm of the generalized correlation integral as a criterion for a proper choice of the delay time. In choosing the optimal delay time, our scheme is as follows: At first we obtain three-dimensional projections of phase portraits with different delay times and then choose delay time T at which value overfolding or the straight line do not appear in the three-dimensional projections as an optimal delay time. Once we reconstruct a n -dimensional space in this way, we can obtain a good representation of the attractor and also obtain an appropriate correlation dimension with this delay time. We also obtain the phase portraits for delay time at which value the autocorrelation decreases to e^{-1} of its initial value and the result is nearly the same as we use the delay time obtained with three-dimensional projection.

Figures 2–4 show the three-dimensional phase portraits of the segments from the Korean traditional song, the western song, and the single note ‘‘Si,’’ respectively. We can see that the phase portrait of the segments from the Korean traditional song wrinkles and occupies an extended region. This does not necessarily imply that the behavior is stochastic, but rather that the dimension of the strange attractor is too large to be determined by visual inspection of the attractor. For these attractors the dimension must be calculated quantitatively. The phase portrait of the segment from the western song also shows a complicated and tangled structure. Comparing these two phase portraits we can infer that the attractor of the segment from the Korean traditional song will have a higher value of dimension than that of the segment from the western song because it has a more complex structure in comparison with the western song. The phase portrait of single note ‘‘Si’’ is supposed to represent a limit cycle but has thickness due to noises. It is essentially a periodic system and accords with the result of the power spectrum.

IV. CORRELATION DIMENSION

The dimension of a phase portrait is clearly the first level of knowledge necessary to characterize its properties and also gives us a lower bound on the number of essential variables needed to model the dynamics. We calculate the

correlation dimension which is relatively easy to compute. It can be calculated by measuring the correlation integral, which represents the spatial correlation of the points on the attractor, defined by¹⁵

$$C(r) = \lim_{N \rightarrow \infty} \frac{2}{N(N-1)} \times \left\{ \begin{array}{l} \text{the number of pairs of points, } (\mathbf{X}_i, \mathbf{X}_j), \\ \text{on the phase portrait with separation } < r \end{array} \right\}, \quad (3)$$

then one observes that as $r \rightarrow 0$,

$$C(r) \propto r^\nu, \quad (4)$$

giving the working definition of the correlation dimension ν . But it is known that for limited data sets with high autocorrelation the correlation integral displays an anomalous shoulder which hinders good estimates of dimension.¹⁶ It is because the distances between these pairs of points which are not well separated in time do not really reflect the geometrical properties of the attractor. So we use the modified correlation integral $C(W, N, r)$, which discards the pairs of points closer together than W in time,¹⁷

$$C(W, N, r) = \frac{2}{(N+1-W)(N-W)} \times \sum_{n=W}^{N-1} \sum_{i=0}^{N-1-n} H(r - \|X_i - X_{i+n}\|), \quad (5)$$

which gives the standard algorithm when $W=1$. In this calculation the autocorrelation time is used as a value of W .

Plotting the value of $C(W, N, r)$ versus r on a log-log plot gives a slope ν for small r . From this plotting of $\log C(W, N, r)$ versus $\log r$, one can distinguish low-dimensional deterministic chaotic signals from stochastic noise. For the deterministic signal, if one increases the embedding dimension n , the slope of $\log C(W, N, r)$ versus $\log r$ at first also increases but settles at a value of ν and becomes independent of the embedding dimension. For random noise, the slope of $\log C(W, N, r)$ versus $\log r$ increases indefinitely as the embedding dimension n is increased.

The correlation dimension is measured using 3.5×10^4 data points for time series of the segment from the Korean traditional song. The slope ν of $\log C(W, N, r)$ versus the $\log r$ plot of the segment from the Korean traditional song is saturated at a value of about 4.4 independent of the embedding dimension, which we assume to be the correlation dimension of the attractor (Fig. 5). The slope ν of $\log C(W, N, r)$ versus the $\log r$ plot of the segment from the Western song measured using 2.0×10^4 data points is saturated at a value of about 2.5 independent of the embedding dimension (Fig. 6). The correlation dimension of the attractor obtained from a single note ‘‘Si’’ with 2.0×10^4 data points is about 1.2 (Fig. 7). It is thought that a noise causes the correlation dimension to be saturated at a higher value than the expected value 1.0. In all these cases we calculated the correlation dimensions for several reasonable values of delay time, which are obtained from phase portrait and autocorrelation. The correla-

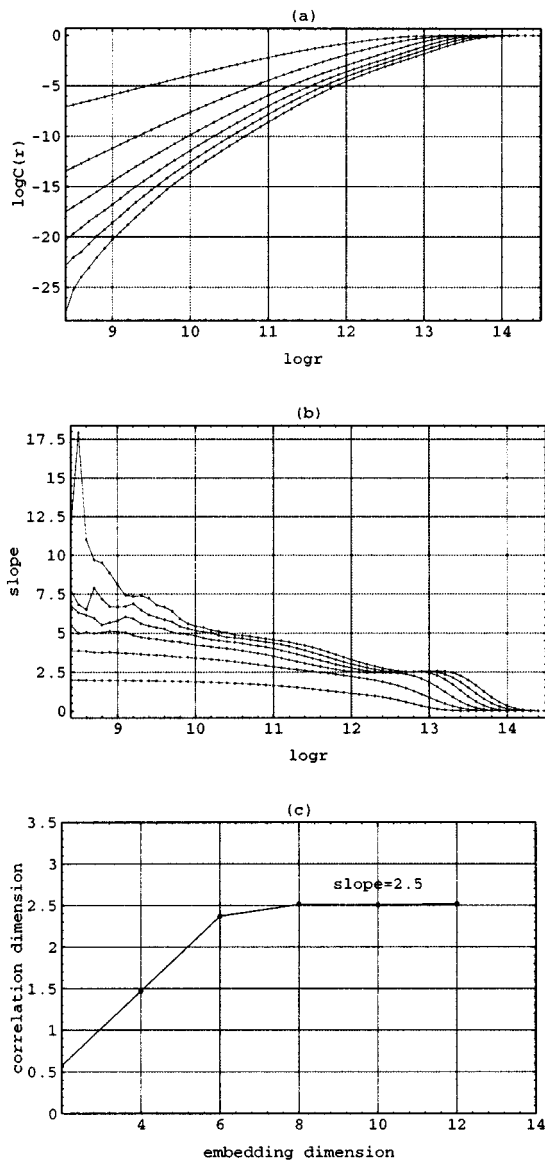


FIG. 6. Correlation integral and correlation dimension for the western song. (a) The plot of $\log_{2.0}C(W,N,r)$ versus $\log_{2.0}r$ for values of r varying from $2.0^{8.4}$ to $2.0^{14.5}$ with embedding dimension 2, 4, 6, 8, 10, 12 (top to bottom). (b) The plot of local slopes versus $\log_{2.0}r$ showing the converging scaling region. (c) Correlation dimension ν is saturated at a value of about 2.5 as the embedding dimension is increased.

tion dimension itself was almost the same except that when the delay time is such that the autocorrelation of the time series decreases to e^{-1} of its initial value the correlation dimension is saturated at a lower embedding dimension.

V. LYAPUNOV EXPONENTS

Lyapunov exponents are one of the most important quantities used to distinguish chaotic from nonchaotic behavior. When a dynamic is chaotic, positive Lyapunov exponents occur that quantify the rate of separation of neighboring (initial) states and give the time duration where predictions are possible. For such experimental works as our case, methods for computing the Lyapunov exponents of a given time series are of great importance. The different al-

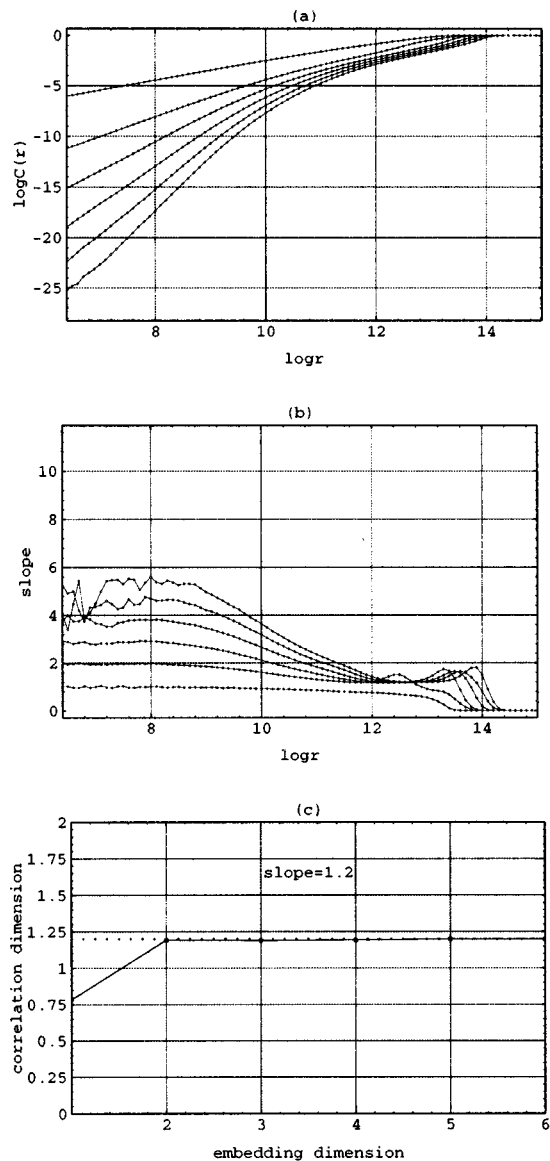


FIG. 7. Correlation integral and correlation dimension for "Si." (a) The plot of $\log_{2.0}C(W,N,r)$ versus $\log_{2.0}r$ for values of r varying from $2.0^{6.3}$ to $2.0^{14.5}$ with embedding dimension 1, 2, 3, 4, 5, 6 (top to bottom). (b) The plot of local slopes versus $\log_{2.0}r$ showing the converging scaling region. (c) Correlation dimension ν is saturated at a value of about 1.2 as the embedding dimension is increased.

gorithms that have been proposed during the last decade for this purpose are all based on the reconstruction of the corresponding attractor by means of the delay vector method with suitable embedding dimension. Most of the methods are based on approximations of the unknown flow governing the dynamics on the reconstructed attractor in embedding space. From the sequence of Jacobians of this flow at the state points along the reconstructed orbit, the Lyapunov exponents can be computed by standard methods.^{18,19} The crucial point of this approach is the accuracy of the approximation of the Jacobian of the unknown flow. The most often used algorithms to achieve this goal are based on linear approximations. In this paper, we used the Eckmann and Ruelle algorithm.¹⁹

In the Eckmann and Ruelle algorithm, it is very impor-

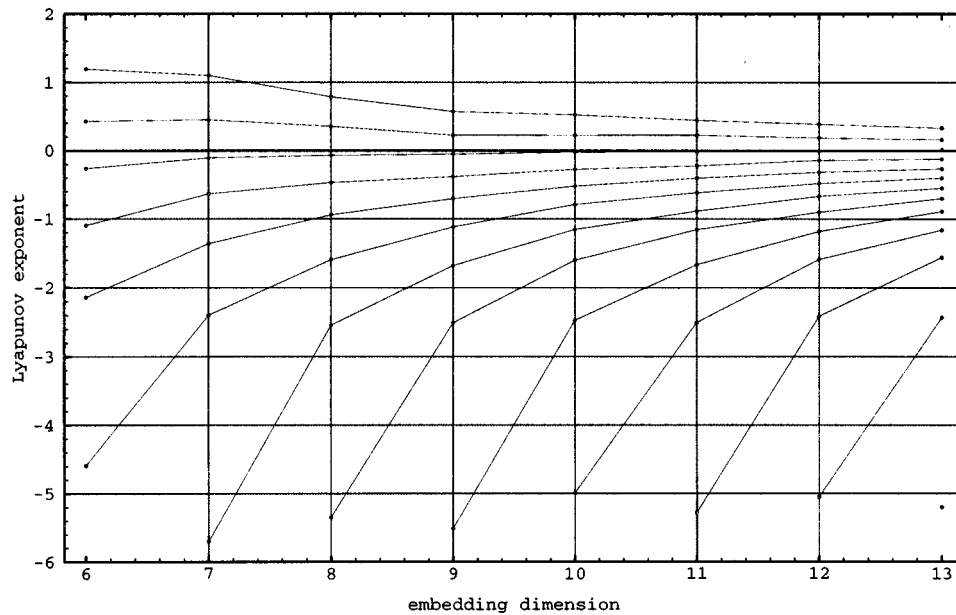


FIG. 8. The SeoDo folk song has two positive Lyapunov exponents under varying embedding dimension 6–13.

tant to choose appropriate values of the embedding dimension n and range r . We choose the range r which is about 3%–5% of the horizontal extent of the analyzed attractor.¹⁸ The delay vector to calculate Lyapunov exponents is obtained the same way for the same data as in the case of correlation dimension. We estimate the Lyapunov spectra at various embedding dimensions and then identify the true Lyapunov exponents and the spurious Lyapunov exponents on the point of view that true Lyapunov exponents do not vary much over a range of n , while the spurious ones wander with n .²⁰ We also calculate the Lyapunov exponents for the different parameters (delay time, range, etc.) and the result is

such that the sign of the largest Lyapunov exponents does not change.

Figures 8–10 show the Lyapunov exponents with n increased using the time series of the segments from the Korean traditional song, the western song and “Si.” We obtain two positive Lyapunov exponents in the time series of the segment from the Korean traditional song, which indicate that the attractor is a hyperchaotic attractor with two directions of expansion. It is known that it is possible to find hyperchaotic attractors with two or more positive Lyapunov exponents only in higher (at least four) dimensional systems,²¹ which accords with our result that the correlation

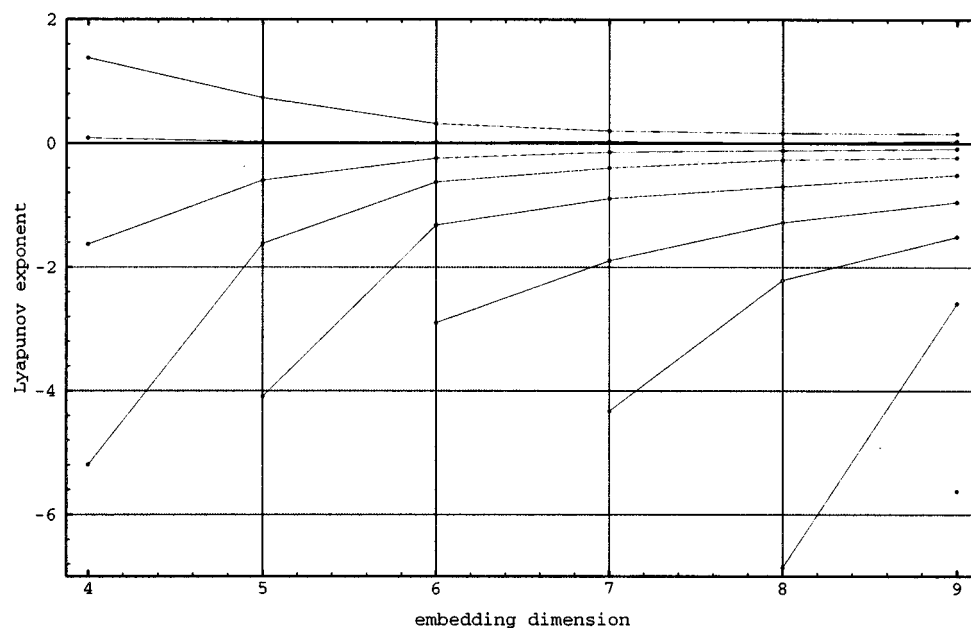


FIG. 9. The western song has one positive Lyapunov exponent under varying embedding dimension 4–9.

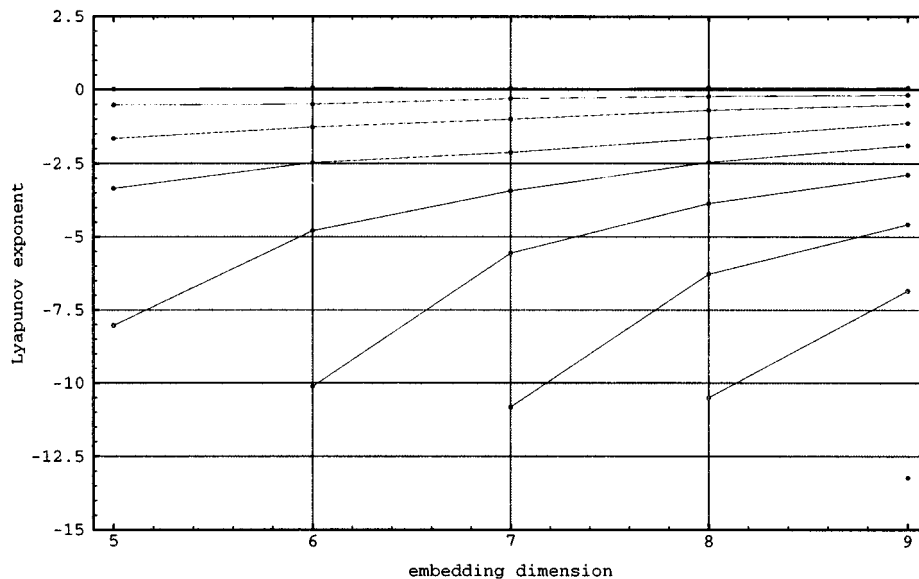


FIG. 10. Lyapunov exponents for “Si” under varying embedding dimension 5–9. It has one zero value and all negative values.

dimension of the Korean traditional song is about 4.4. From the segment of the western song we obtain one positive Lyapunov exponent which means that the dynamic is a chaotic process. The Lyapunov dimension for the time series of segments from the Korean traditional song and western song is calculated by the Kaplan–Yorke formulas.²² In the case of the segment from the Korean traditional song we obtain 4.5–5.3 as the Lyapunov dimension for the embedding dimension from 9 to 13, and 3.1–3.4 with the embedding dimension from 6 to 9 for the segment from the western song. The result turns out that the Lyapunov dimensions in these two cases are a little higher than the correlation dimensions, but it is known that the Lyapunov dimension forms an upper limit for the information dimension as far as higher-dimensional systems are concerned.²³ As we expect, Lyapunov exponents from the single note “Si” are $(0, -, -, \dots)$, which exhibit characteristics of a limit cycle.

VI. DISCUSSION

In this paper, we examine the music signals from the Korean traditional song “Gwansanyungma,” the western song “La Mamma Morta,” and the single note “Si” through power spectra, phase portraits, the correlation dimension, and Lyapunov exponents. From the time series of the segments from the Korean traditional song, we obtain a broadband power spectrum and the phase portrait with a complex and wrinkled structure in the reconstructed phase space. From the result of estimating the correlation dimension and the Lyapunov exponents, we can conclude that the underlying dynamics of the segment from the Korean traditional song is a high-dimensional ($\nu=4.4$) hyperchaotic system which has two directions diverging exponentially. The time series of the segment from the western song gives a power spectrum with a little broadband power and its phase portrait occupies an extended region. Measurement of the correlation dimension of it revealed that its trajectory lies on an attractor with a dimension of about 2.5. The result that

one of the Lyapunov exponents of the segment from the western song is a positive value shows that it is a chaotic system of which nearby trajectories exponentially diverge on the average. The time series of the single note “Si” which is chosen to confirm our analysis methods shows that it is from a periodic system as we expect, that is, it has δ -function shaped power spectrum, a limit cycle blurred by noise in the reconstructed phase space, a correlation dimension of about 1.2, and the largest Lyapunov exponent zero.

In conclusion, we can observe hyperchaotic behavior in the segment from the Korean traditional song and chaotic property in the segment from the western song. It gives some hints for modeling certain aspects of the sound production of the vocal system, especially approaching the vocalization methods. Large dimensionality of the segment from the Korean traditional song in comparison with the segment from the western song means that its system is more complex and has more degrees of freedom. It is thought that it results from the peculiar vocalization of the Korean traditional song, especially vibrating techniques of a SeoDo folk song.

We did not investigate the whole parts but only the segments from the Korean traditional song and the western song, which are thought to reflect adequately the characteristics of the Korean traditional song and the western song. Further study is needed to generalize the above results by investigating more data sets and relate the method of vocalization with chaos more precisely.

ACKNOWLEDGMENTS

This work was supported in parts by the Center for Theoretical Physics, Seoul National University, and by the Basic Science Research Institute, Ministry of Education under Project No. BSRI-96-2418.

¹B. Townshend, in *Nonlinear Modeling and Forecasting*, edited by M. Casdagli and S. Euband (Addison-Wesley, Reading, MA, 1992), pp. 433–453.

- ²H. Herzel, *Appl. Mech. Rev.* **46**, 399 (1993).
- ³S. S. Narayanan and A. A. Alwan, *J. Acoust. Soc. Am.* **97**, 2511 (1995).
- ⁴I. Tokuda, R. Tokunaga, and K. Aihara, *Int. J. Bifurcation Chaos* **6**, 149 (1996).
- ⁵W. Mende, H. Herzel, and K. Wermke, *Phys. Lett. A* **145**, 418 (1990).
- ⁶A. Kumar and S. K. Mullick, *J. Acoust. Soc. Am.* **100**, 615 (1996).
- ⁷M.-H. Lee and K.-S. Soh, *Sae mulli (New Phys.)* **36**, 344 (1996).
- ⁸J. P. Eckmann and D. Ruelle, *Rev. Mod. Phys.* **57**, 617 (1985).
- ⁹H. S. Greenside, G. Ahlers, P. C. Hohenberg, and R. W. Walden, *Physica D* **5**, 322 (1982).
- ¹⁰D. Sigeiti and W. Horsthemke, *Phys. Rev. A* **35**, 2276 (1987).
- ¹¹D. S. Broomhead and G. P. King, *Physica D* **20**, 217 (1986).
- ¹²F. Takens, in *Dynamical Systems and Turbulence*, edited by D. Rand and L. S. Young (Springer-Verlag, Berlin, 1981).
- ¹³A. M. Fraser and H. L. Swinney, *Phys. Rev. A* **33**, 1134 (1986).
- ¹⁴H. G. Schuster and W. Liebert, *Phys. Lett. A* **142**, 107 (1989).
- ¹⁵P. Grassberger and I. Procaccia, *Physica D* **9**, 189 (1983).
- ¹⁶J. Theiler, *Phys. Rev. A* **34**, 2427 (1986).
- ¹⁷J. Theiler, "Quantifying chaos: practical estimation of the correlation dimension," Ph.D. thesis, Caltech, 1988.
- ¹⁸M. Sano and Y. Sawada, *Phys. Rev. Lett.* **55**, 1082 (1985).
- ¹⁹J. P. Eckmann, S. O. Kamphorst, D. Ruelle, and S. Ciliberto, *Phys. Rev. A* **34**, 4971 (1986).
- ²⁰Th.-M. Kruel, M. Eiswirth, and F. W. Schneider, *Physica D* **63**, 117 (1993).
- ²¹O. E. Rossler, *Phys. Lett. A* **71**, 155 (1979).
- ²²J. L. Kaplan and J. A. Yorke, *Lect. Notes Math.* **730**, 204 (1987).
- ²³P. Grassberger and I. Procaccia, *Physica D* **13**, 34 (1984).

The relationship of scattered subharmonic, 3.3-MHz fundamental and second harmonic signals to damage of monolayer cells by ultrasonically activated Albunex[®]

Douglas L. Miller

MS# P7-53, Battelle Pacific Northwest National Laboratory, PO Box 999, Richland, Washington 99352

Shiping Bao

U.S. Transuranium and Uranium Registries, Washington State University, Richland, Washington 99352

(Received 25 June 1997; revised 15 September 1997; accepted 8 October 1997)

Cultured Chinese hamster ovary cells attached to thin Mylar sheets were exposed to 3.3-MHz ultrasound in the presence of Albunex[®] ultrasound contrast agent. The ultrasound beam was directed upward at the exposure chamber with the monolayer on the inside of the upper acoustic window. Cell membrane damage was detected by the firefly enzyme assay for released ATP and the subharmonic, fundamental, and second harmonic scattered signals were recorded. ATP release increased monotonically with increasing pressure amplitude above apparent thresholds of 0.28 MPa for 1-s continuous and 0.56 MPa for 100-s pulsed (10- μ s pulses, 1-ms PRP) exposures with 5% Albunex[®]. The subharmonic signal and, to a lesser extent, the second harmonic signal both increased with the cell membrane damage, which suggests that these signals have predictive value for bioeffects. If the monolayer was positioned on the front window of the exposure chamber, cell membrane damage was greatly reduced, which confirms the protective influence of this configuration of monolayers reported in the literature. The effect decreased both at high (50%) or low (0.5%) concentrations of Albunex[®]. The strong nonlinear scattering of ultrasound by contrast agent gas bodies appears to provide useful indicators of gas body activity including cavitation bioeffects. © 1998 Acoustical Society of America. [S0001-4966(98)06301-2]

PACS numbers: 43.80.Gx, 43.35.Ei, 43.35.Wa [FD]

INTRODUCTION

Contrast agents for diagnostic ultrasound have recently been the subject of energetic commercial development and extensive research on diagnostic medical applications. The purpose of the agents is to enhance echogenicity of blood-filled regions for display in a diagnostic image. This allows better characterization of blood vessels, blood flow, and perfusion both for pulse-echo images and for Doppler modes. The first commercial agents, such as Albunex[®] (Mallinckrodt Medical, St. Louis, MO), have received approval for sale in the United States, and achieved success in clinical use.¹ Newer agents now under development have improved characteristics, such as greater persistence and improved transpulmonary performance.

These agents function by introducing a controlled form of ultrasonic cavitation into the body. Albunex[®], for example, consists of a suspension of microscopic gas bodies roughly 2 μ m–10 μ m in diameter, which are stabilized by a thin shell of denatured human albumin.² Gas bodies of this size produce strong scattering of ultrasound in the megahertz frequency range, which is exploited for enhancing echogenicity. The pulsation of the gas bodies also has nonlinear characteristics: The scattered wave can include discrete signals at harmonic frequencies relative to the incident wave. This nonlinear behavior can also be exploited and is particularly useful for Doppler imaging with the second harmonic.^{3,4} Newer agents show improved nonlinear behavior for second harmonic imaging applications.^{5,6} In addition

to nonlinear scattering, ultrasound exposure can modify the agents, resulting in an apparent loss of stability of the gas bodies.⁷ This phenomenon appears to allow the contrast agent gas bodies to act as cavitation nuclei,⁸ which can result in a strong enhancement of acoustic emissions available for imaging applications.⁹

In ultrasonic cavitation research, acoustic emissions have often been exploited for the purpose of bubble detection and characterization. For example, the second harmonic signal is useful for detection of bubbles in liquid flowing through tubes or blood vessels.^{10,11} The highly nonlinear acoustic emissions of cavitation bubbles can even include subharmonic and broadband noise signals, which have been utilized as diagnostic aids for cavitation activity in bioeffects research. The subharmonic signal at one-half the fundamental frequency has been shown to be a good indicator of ultrasonically induced biological damage under some *in vitro* conditions.^{12,13} A combined signal with subharmonic and wide-band noise emissions has been proposed as a measure of the insult to suspended cells in a cavitating field.¹⁴ The wide band emission, but not the subharmonic signal, has been associated with tissue damage *in vivo*.¹⁵ Recently, the output of a 20-MHz passive cavitation detector has been correlated with ultrasonically induced hemolysis with Albunex[®] at 1 MHz, which lead to a suggestion that cavitation monitoring could be used as a predictor of adverse bioeffects when gas-body-based contrast agents are used clinically.¹⁶

The purpose of this study was to relate the acoustic scattering and emissions from a contrast agent to the *in vitro*

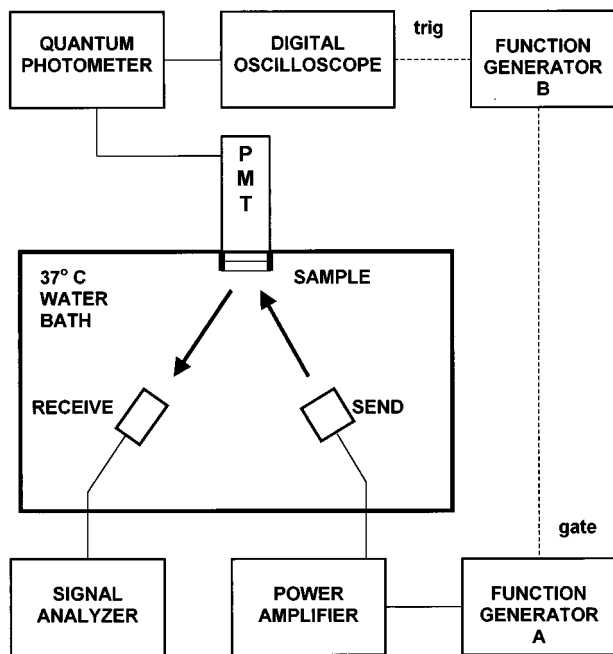


FIG. 1. A diagram of the experimental system. The photomultiplier tube (PMT) assembly was removable to allow placement of the sample chambers in the bath. Function generator B could be used to gate the main generator A, and to trigger the oscilloscope trace.

cavitation bioeffect of cell membrane damage. This goal presents at least three problems in implementation. First, the normal exposure arrangement used for *in vitro* studies of cavitation bioeffects is the rotating tube system. However, contrast agent gas bodies readily nucleate cavitation in this system,⁸ which implies that this system might simply yield the cavitation emissions typical of rotating-tube exposure systems (rather than of the contrast agent). To reduce this problem, a nonrotating chamber shaped like a thin disk was used in this study. Second, gas bodies need to be close to cells for efficient production of cavitation effects. In the rotating tube system, cavities pass back and forth through the cell suspension and affect cells they encounter.¹⁷ In a static system, the gas bodies rise and rapidly separate from the cells. To reduce this problem, a monolayer of cells attached to the inside surface of the upper window of an exposure chamber was employed. In this arrangement, the gas bodies rise under gravity to rest against the cells, and with insonation from below, are driven by the sound beam up into the cells. Cells in monolayers have been reported to be protected from bioeffects,¹⁸ but, as shown below, this appears to occur only when cavities are driven away from the monolayer by the ultrasound. Third, cell damage is normally detected by counts of cells surviving ultrasound exposure relative to sham exposure, which can be an insensitive test. In this study, the ATP release method was used to measure cell damage during exposure, which provides a sensitive differential indication of effects.¹⁹

I. METHODS

A diagram of the experimental system is shown in Fig. 1. The ultrasound exposure was provided by a 19-mm-diam

air-backed transducer (made in the laboratory), which was driven by function generator A (Hewlett-Packard model 3314A) and amplifier (Electronic Navigation Industries Inc., model A300). The unfocused transducer was driven at its nominal thickness resonance frequency of 3.3 MHz. The exposure ultrasound beam was directed upward at a 22.5° angle from vertical toward a sample holder 5 cm away in a 37 °C saline bath. The ultrasound beam was calibrated at 0.2-MPa spatial peak pressure amplitude with a bilaminar shielded hydrophone with a 0.5-mm sensitive spot (Marconi type Y-34-3598, National Physical Laboratory, Middlesex, UK) coupled to a 200-MHz bandwidth digital oscilloscope. Exposure pressure amplitudes were set by linear extrapolation of the function generator voltage from the calibration measurements at low pressure amplitude. The nearfield position of the sample minimized the effect of finite amplitude distortion on the ultrasound. The -6-dB beam width of the central peak was measured at the 5-cm exposure position to be 3.2 mm. A side lobe maxima of -5.7 dB occurred with approximately a 1 cm diam, and the -20-dB beam width was 22 mm. Exposures were either 1-s duration continuous, which were timed by a gating signal from function generator B, or 100-s duration with 10 μs (36 cycle) pulses at 1-ms pulse repetition period, which were manually timed.

A second transducer, 19 mm in diameter and 2.25-MHz nominal frequency (long internal focus, KB-Aerotech, Lewistown, PA) was positioned 22.5° from vertical (and slightly off the axis of the first transducer) to intercept scattered signals from the center of the sample holder 5.5 cm away. The focus was aligned to intersect the central peak of the exposure beam. An absorber was placed at the bottom of the bath to minimize further reflections. The receiving transducer was connected to a signal analyzer (Hewlett-Packard model 89410A) via a high impedance probe. This receiver was not calibrated, since only relative indications at the spectral peaks were needed for the experiment, and was chosen to give good sensitivity at the subharmonic and second harmonic of the exposure frequency, with maxima in response at about 2.25 MHz (-6-dB bandwidth roughly 1 MHz) and about 7.75 MHz, and a minimum in response at about 4.5 MHz.

Above the sample holder, a reservoir of castor oil with a 5-μm Mylar window, a shutter assembly, and a photomultiplier tube were arranged to provide optical detection of light emitted from the sample holder.¹⁹ The castor oil served as an optically transparent ultrasound absorber for the portion of the beam which passed through the sample holder. The light emitted from the sample holder was monitored by the photomultiplier, connected to a quantum photometer (EG&G Princeton Applied Research model 1140A) and oscilloscope (Tektronix model TDS520B). The photomultiplier housing and shutter assembly was moveable to allow placing a sample in the exposure bath.

The sample holder consisted of a 5-μm Mylar film stretched and clamped at 25 mm diam by two plastic rings. The overall inside diameter was 22 mm, which allowed the beam to pass with minimal perturbation. An O-ring was used to clamp a sheet of 12-μm-thick polyvinyl chloride film over the outer ring. The inner ring was 5 mm thick, while the

outer ring was 6 mm thick, so that the chamber contained a disk-shaped 0.5-ml volume, 1 mm thick, and 25 mm in diameter. This normally was placed into the bath such that the chamber faced downward, and the open end of the chamber filled with saline.

Chinese hamster ovary (CHO) cells were maintained as monolayers in 150-cm² tissue culture flasks (Corning, Inc., Corning, NY) at 37 °C, in a humidified atmosphere of 5% CO₂ in air. The growth medium was Ham's F₁₂ supplemented with 10% fetal bovine serum (Sigma Chemical Co., St. Louis, MO) and 50-μg/ml gentamicin (Gibco BRL, Grand Island, NY). On the day of an experiment, these cells were harvested with trypsin, washed by centrifugation and pipetted onto clean Mylar film clamped in sample-holder rings. Approximately 2 million cells in 0.5 ml of growth medium were pipetted onto the Mylar to form a drop covering the central 10 mm of the film. These open sample holders were placed in an incubator for about 4 h, which allowed the cells to settle out and attach to the Mylar, forming a monolayer of cells.

For exposure, a sample holder was rinsed in saline to remove the excess unattached cells. Mixtures of 0.25-ml firefly lantern extract dissolved in water at 20 mg/ml (Sigma Chemical Co. F7771), 0.025-ml Albinex[®] ultrasound contrast agent (Mallinckrodt Medical, Inc.) and 0.225-ml phosphate buffered saline (PBS) were prepared in a small test tube. This mixture was then poured onto the open sample holder, and the chamber was closed by adding the top plastic sheet. When placed in the exposure bath, a delay of 30 s was allowed before exposure for the Albinex[®] to rise up against the monolayer of cells. ATP released from damaged cells mixed with the firefly lantern extract to produce light which was detected by the photomultiplier system. The ATP release is primarily indicative of cell lysis, but some ATP leakage could occur even for sublethal cell membrane damage. An approximate calibration of this signal was obtained each day by replacing the PBS in the mixture with cell lysing reagent in one sample and measuring the light output immediately after placing the holder into the bath. This calibration for 100% ATP release was divided into the measurements during exposure to yield a result in terms of the percentage of ATP released. In interpreting the resulting data, it should be noted that the -6-dB beam width (3.2 mm) encompassed only about 10% of the monolayer area (about 10 mm diam).

II. RESULTS

The light output from a 1-s exposure at 0.8 MPa is shown in Fig. 2. The light signal rises rapidly as ATP is released from the cells and reacts with the firefly enzymes, levels off a few seconds after the end of the exposure, then slowly decays. To characterize the ATP release during an exposure, the difference between the pre-exposure background signal and the signal maximum was used. The spectrum of ultrasound signals received during this same exposure is shown in Fig. 3. This represents an rms average of 32 spectra with 401 points (95-kHz resolution) in the 0–10 MHz span. Stable peaks are discernable at the fundamental (3.3 MHz), subharmonic (1.65 MHz), second harmonic (6.6 MHz), 5/2 harmonic (8.25 MHz), and third harmonic (9.9

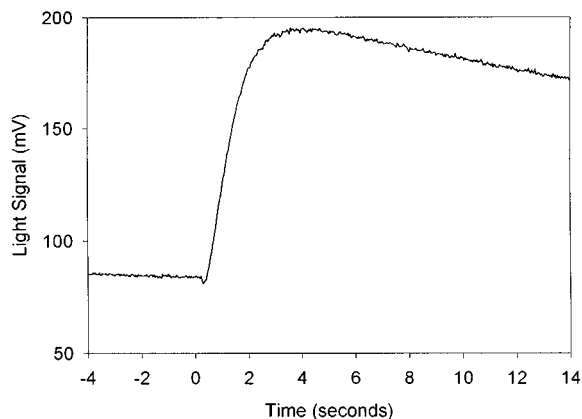


FIG. 2. The signal produced by light coming from the exposure chamber for a 1-s continuous exposure at 0.8 MPa beginning just after the zero time point.

MHz). A peak at the 3/2 harmonic (4.95 MHz) could sometimes be discerned, but the receiver was relatively insensitive at this frequency. Variable noise signals are emphasized around 2.25 MHz because the receiver was most sensitive there. To characterize an exposure, the voltages of the peaks at the subharmonic, fundamental and second harmonic were recorded.

Results are shown in Fig. 4 for the cell ATP release and scattered signal levels for 1-s continuous exposures. The ATP release signal increased monotonically with pressure amplitude above an apparent threshold (the lowest pressure amplitude with a statistically significant increase in the effect) of 0.28 MPa. For the lowest exposures (or sham exposure), the light signal tended to decrease slightly due to the slow decay of the background light signal, which gave a small negative value for the measurement. The subharmonic increased monotonically with exposure and seemed to mirror the ATP release. Linear regression of the mean subharmonic signal versus the mean effect for the four exposures above the threshold gave an r^2 of 0.97, which indicates a good correlation of the effect with the subharmonic signal. The fundamental signal was variable, and changed little over this range of exposures and there was no correlation with the

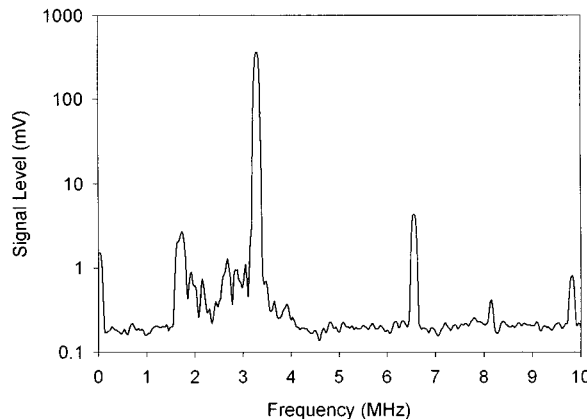


FIG. 3. The rms averaged spectrum of emissions from the exposure chamber obtained during the exposure of the sample used for Fig. 1. The fundamental signal is at 3.3 MHz.

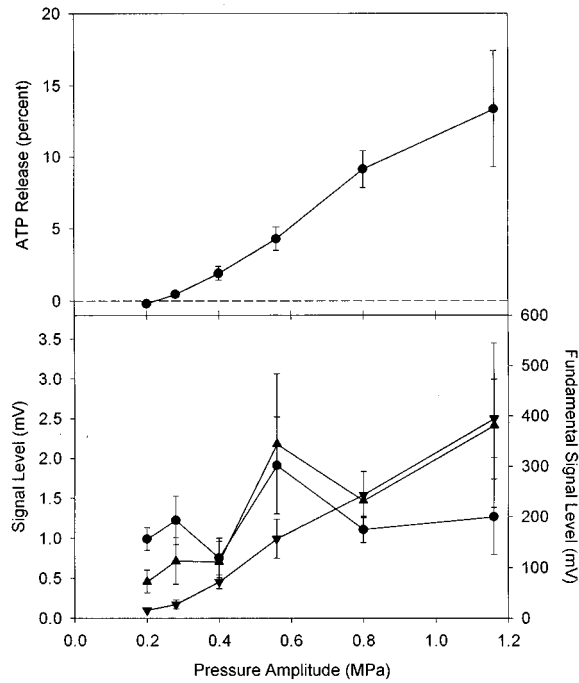


FIG. 4. Upper graph: mean ATP release for 1-s continuous exposures (four repetitions, standard error bars). Lower graph: mean results for scattering for the same exposures for the subharmonic (arrow down), fundamental (circle) and second harmonic (arrow up) signals.

effect ($r^2=0.004$). The second harmonic signal was also variable, but showed a general increase over this range and some correlation with the effect ($r^2=0.41$).

As noted previously, the Alunex[®] gas bodies are somewhat fragile, and can be perturbed by ultrasound exposures above about 0.1–0.2 MPa.²⁰ The gas bodies also seem to disappear gradually after removal from the vial and mixing with other material. The effect of the delay time between placing the sample holder into the bath and the start of 1-s continuous exposure on the results was determined by varying this parameter. ATP release for exposures conducted as soon as possible, after a 30-s delay, and after a 2-min delay were not significantly different from each other. This system therefore appeared to be stable for several minutes, which encompassed all the exposures performed for this study. However, for longer delay times, such as 5 min, the sample deteriorated, yielding more erratic results and reducing the result to about half the result for the 30-s delay.

Results obtained with the chamber placed upside down

TABLE I. ATP release and scattering results (means of four repetitions with standard errors in parenthesis) obtained with the monolayer on the top (the normal configuration) or on the bottom (inverted configuration) for 1-s continuous 0.8-MPa exposure. The ATP release was greatly reduced for the inverted chamber, but the scattered signals were not significantly different (NS).

Chamber configuration	ATP release (%)	Subharmonic (mV)	Fundamental (mV)	Second harmonic (mV)
Normal	12.8 (1.8)	1.4 (0.2)	175 (47)	2.1 (0.6)
Inverted	0.38 (0.17)	1.4 (0.3)	93 (28)	1.2 (0.3)
<i>t</i> -test	$P < 0.001$	NS	NS	NS

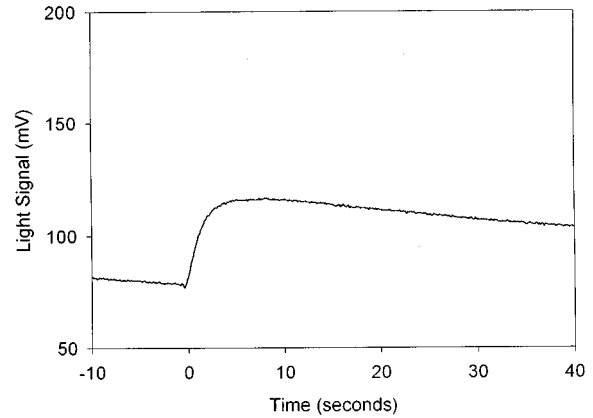


FIG. 5. The signal produced by light coming from the exposure chamber for a pulsed (10- μ s pulses, 1-ms PRP) exposure at 1.12 MPa beginning just after the zero time point.

in the bath were quite different from the normal orientation. When upside down, the monolayer is on the bottom, so that the gas bodies rise under gravity, and are driven by the ultrasound beam, away from the cells. Results for this configuration are compared to the normal configuration in Table I. The scattered signals in the inverted configuration were not statistically different from the normal configuration, which shows that the gas body activity was similar for both. However, the effect was greatly reduced for the inverted configuration.

The light output and ultrasound spectrum obtained for pulsed exposure at 1.12 MPa are presented in Figs. 5 and 6. The light output in this case rose rapidly and leveled off after about 5 s, even though the exposure continued for 100 s. As for the continuous exposure, a slightly negative result was obtained at low exposures (due to decay of the background emission) when the result was obtained 5 s after the start of the exposure. The spectrum was obtained in the gated mode, with the 10- μ s gate centered on the scattered pulse and consisted of the rms average of 3500 spectra with a resolution of 400 kHz. The spectrum has the same general features as the spectrum from the continuous exposure, except that the peaks are broadened in the gated mode (as expected). Results

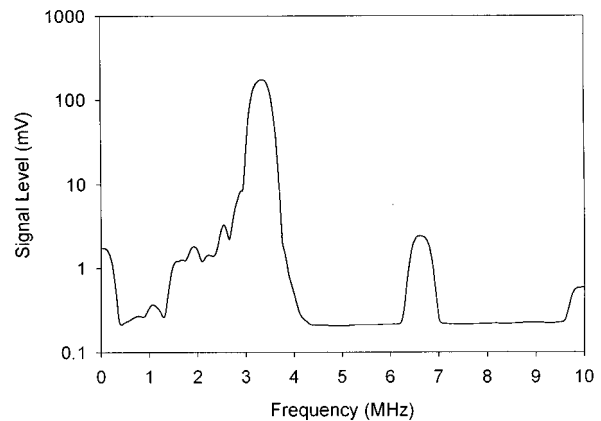


FIG. 6. The rms averaged spectrum of emissions from the exposure chamber obtained during the exposure of the sample used for Fig. 4. The fundamental signal is at 3.3 MHz.

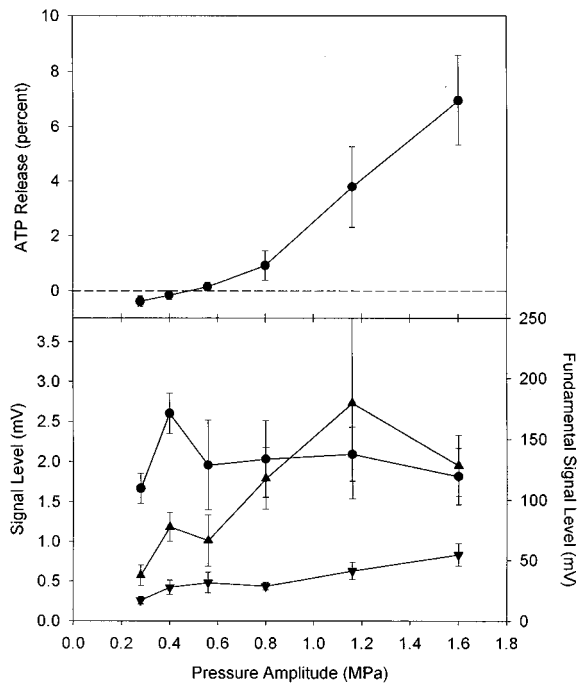


FIG. 7. Upper graph: mean ATP release for 100-s pulsed exposures (four repetitions, standard error bars). Lower graph: mean results for scattering for the same exposures for the subharmonic (arrow down), fundamental (circle) and second harmonic (arrow up) signals.

for pulsed exposure for a range of pressure amplitudes are shown in Fig. 7. The cell membrane damage was reduced from that of continuous exposure, as were the magnitudes of the received signals. ATP release increased monotonically above an apparent threshold of 0.56 MPa. As for the continuous exposure, the fundamental changed little over this range. The effect seemed to be generally tracked by increases in the subharmonic but not in the second harmonic signal: linear regression of the three points above the threshold gave $r^2=0.99$ for the subharmonic but $r^2=0.02$ for the second harmonic. The correlation may have been reduced for pulsed exposures because of the difference in the 5–10 s duration of the measured increase in the light output, and the 100-s duration of the exposure and signal averaging.

The normal 5% concentration of Alburnex[®] was chosen as a compromise between 50%, which was found in previous work with whole blood to produce the highest lysis,²⁰ and low concentrations which minimize the perturbation of the beam by the gas bodies. The transmission of 3.3-MHz ultrasound through the chamber, which was obtained using the same sample and holder but with a straight line transmission to a receiving transducer placed behind the sample, is shown in Fig. 8. At high concentrations, the penetration declines so that the gas bodies at the cell monolayer would be exposed to much lower pressure amplitudes than expected from the free field calibration measurements. The effect of Alburnex[®] concentration on the ATP release and scattering results for 1-s continuous exposure at 0.8 MPa is shown in Fig. 9 for concentrations between 0.5% and 50%. The subharmonic again seemed to follow the ATP release to some extent, but the other signals did not. The background signal levels obtained without Alburnex[®] are plotted as the solid (fundamental),

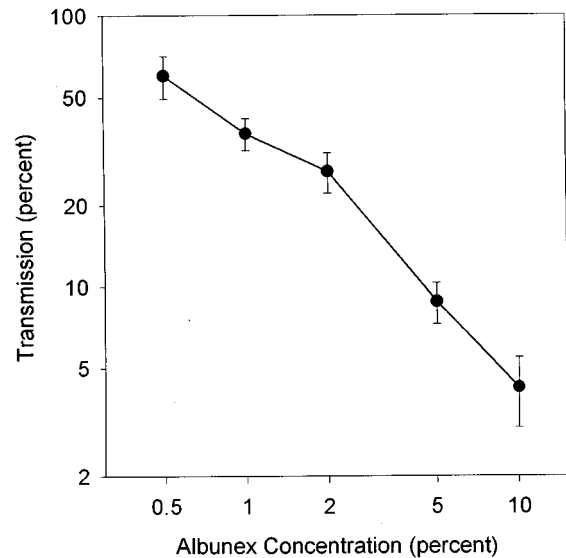


FIG. 8. Transmission through exposure chambers filled with PBS and a range of concentrations of Alburnex[®] expressed as the percent of the receiver voltage for chambers with no Alburnex[®].

dash-dot (second harmonic) and dotted (subharmonic) baselines. For comparison, the signals obtained at this level when a flat piece of highly reflective styrofoam replaced the sample holder were about 0.37 mV at the subharmonic, 682 mV at the fundamental, and 19.4 mV at the second harmonic.

III. DISCUSSION

Cultured Chinese hamster ovary cells attached to thin Mylar sheets were exposed to 3.3-MHz ultrasound in the

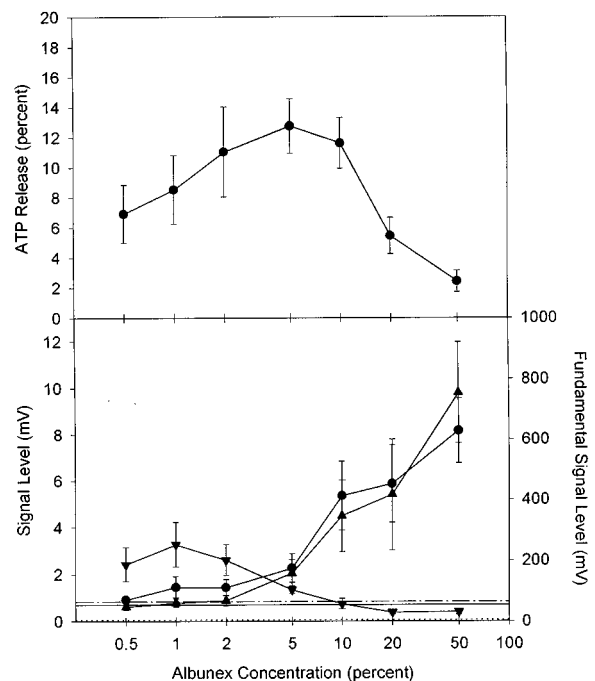


FIG. 9. ATP release (upper graph) and scattered ultrasound signals (lower graph) for a range of Alburnex[®] concentrations. The subharmonic (arrow down), fundamental (circle) and second harmonic (arrow up) had baseline levels (i.e., for no Alburnex[®]) indicated by the dotted, solid and dot-dash lines, respectively.

presence of 5% Albunex[®]. Cell membrane damage was detected by the firefly enzyme assay for released ATP and the subharmonic, fundamental and second harmonic scattered signals were recorded. Cell membrane damage increased monotonically with increasing pressure amplitude above apparent thresholds of 0.28 MPa for 1-s continuous and 0.56 MPa for 100-s pulsed (10- μ s pulses, 1-ms PRP) exposures. The magnitude of the effects appeared to be small, with a maximum of about 10%–15% ATP release. However, as noted in Methods, the central peak of the beam only encompassed about 10% of the monolayer area, which indicates that the actual proportion of cells affected toward the center of the beam was much higher.

Several previous studies have investigated cell lysis in cell monolayers. Some findings have indicated a protective effect for this configuration relative to cell suspensions.^{18,21,22} Other findings have indicated cell damage does occur in monolayer under some conditions.^{23,24} These contrasting results may be explained by the access of cavities to the cells: Studies for which the monolayer was on the window nearest the transducer in traveling wave fields, or at a pressure minimum of a standing wave field, seemed to be protected. In contrast, monolayers on the back window of a chamber in a traveling wave, or at a pressure maximum of a standing wave, were strongly affected. In this study (see Table I) cells on the upper window were destroyed, but cells on the lower window were not, even though the cavitation emissions were the same. The difference in these configurations is that the contrast agent gas bodies rose, and were forced by radiation forces associated with the traveling wave²⁵ upward into the monolayer situated on the upper window, but away from the monolayer when it was on the lower window. In suspensions, the radiation forces in a traveling wave also act to push bubbles in the direction of the beam, which is an important factor in explaining the enhancement of bioeffects obtained by sample-tube rotation.¹⁷

The scattered fundamental signal did not appear to be correlated with the effect. The erratic nature of this signal may reflect the instability of Albunex[®] under ultrasound exposure, noted previously,²⁰ which results in partial loss of the agent during the exposures. The subharmonic signal increased in step with the cell membrane damage, which indicates that this signal has predictive value for bioeffects. The correlation of cell ATP release with the subharmonic signal is in agreement with previous work suggesting this signal makes a good bioeffects indicator.^{12–14} The association of the subharmonic with cavitation activity, and its low background signal level, suggests that it might be a useful signal for ultrasonic imaging of contrast agent distribution and activity in the body. In addition, such an image might provide information on the distribution of potential adverse bioeffects or of therapeutic bioeffects in the tissue.

The reasons for the remarkable correlation of the subharmonic signal with cell membrane damage undoubtedly requires further investigation for a full explanation, but it is interesting to speculate that this phenomenon derives from the behavior of the contrast agent gas bodies relative to free bubbles. The encapsulated gas bodies are highly damped, which limits their response, and are also acoustically labile,

which allows them to serve as cavitation bubble nuclei. The resonance size of an Albunex[®] gas body at 3.3 MHz is roughly 3 μ m in radius, which is more than twice the resonance size of a free spherical bubble.²⁶ The subharmonic signal from a cavitation field has been theoretically determined to originate primarily with bubbles which are twice the linear resonance size at the exposure frequency.²⁷ Thus it seems plausible that shells of resonant Albunex[®] gas bodies break open under suitable conditions, and yield free bubbles of the optimum size for subharmonic emission. The free bubbles would likely be responsible for most of the observed bioeffects owing to their lower damping. This possible explanation may also have a relationship to the enhanced acoustic emission phenomenon noted previously.⁹

The rough correlation of membrane damage with the second harmonic is of interest due to the use of this signal for clinical imaging purposes.^{3–6} This signal is an excellent indicator of bubble activity under some conditions,¹⁰ which makes it a candidate signal for imaging the distribution of contrast agent gas bodies in tissue. This signal was not strongly correlated with bioeffects in this study, possibly because much of the second harmonic signal was due to simple reflection of second harmonic components in the incident beam. Second harmonic components in the incident beam arise from impure oscillator and amplifier signals and from finite amplitude effects.¹⁰ Therefore, the cavitation emission signal at the second harmonic was masked, and was not as clear an indicator of gas body activity as the subharmonic, which was present only at very low levels in the incident beam.

Variations in the concentration of Albunex[®] strongly influenced the results of this study; see Fig. 9. At high concentrations, the beam does not penetrate the chamber, and effects diminished. This trend is indicated to some extent by the subharmonic, but not by the other signals. The second harmonic and fundamental signals increased with increasing concentration, apparently due to linear scattering of these frequency components present in the incident beam. The relationship between subharmonic signal and membrane damage, which peak at different Albunex[®] concentrations, probably reflects the changes in the ratios of cells to gas bodies as well as to the variation in transmission of the beam at the higher concentrations. Albunex[®] contains about 5×10^8 ml⁻¹ gas bodies, which supplies 5×10^6 gas bodies for a 2% concentration of Albunex[®] in the 0.5-ml chamber. This represents about one gas body per 10^{-4} mm² (a square 10 μ m on a side), and only a small part of these would be of a size suitable for strong activation at 3.3 MHz.² Thus for the lower concentrations in Fig. 9, the distribution of strongly activated gas bodies was fairly sparse over the monolayer, which may explain the diminution of effects for the lower Albunex[®] concentrations.

The developing use of contrast agents in medical ultrasound promises to yield valuable new diagnostic information. Gas-body-based contrast agents flowing in blood scatter ultrasound much more strongly than the surrounding cells, which provides the useful signal differentials. This activity represents a controlled form of ultrasonic cavitation, and the scattered signals are essentially cavitation emissions. Intro-

duction of cavitation activity into diagnostic ultrasound exposure situations, for which cavitation would not otherwise occur, prompts the consideration of cavitation bioeffects. Cavitation bioeffects have been analyzed from risk assessment perspective for many years,^{28,29} and this effort has even lead to the development of the Mechanical Index for real-time display of output parameters related to nonthermal bioeffects mechanisms.³⁰ These continuing efforts may be especially pertinent to risk assessment for applications of ultrasound contrast agents. In this study, the scattering and acoustic emissions from ultrasonically activated contrast-agent gas bodies have been found to have some predictive value for the cell membrane damage. In the future, it seems possible that the diagnostically useful acoustic emission signals could also be utilized as a real-time index of gas body activity and bioeffects potential.

ACKNOWLEDGMENTS

We thank P. Young of the Dupont Polymer Division, Circleville OH, for generously providing the Mylar film. This research was supported by the US National Institutes of Health via Grant No. CA42947.

¹N. deJong, "Improvements in ultrasound contrast agents," *IEEE Eng. Med. Biol. Mag.* **15**, 72–82 (1996).
²J. A. Marsh, C. S. Hall, M. S. Hughes, J. Mobley, J. G. Miller, and G. H. Brandenburger, "Broadband through-transmission signal loss measurements of Albunex[®] suspensions at concentrations approaching *in vivo* doses," *J. Acoust. Soc. Am.* **101**, 1155–1161 (1997).
³B. Schrope, V. L. Newhouse, and V. Uhlendorf, "Simulated capillary blood flow measurement using a nonlinear ultrasonic contrast agent," *Ultrason. Imaging* **14**, 134–158 (1992).
⁴P. H. Chang, K. K. Shung, S. Wu, and H. B. Levene, "Second harmonic imaging and harmonic Doppler measurements with Albunex[®]," *IEEE Trans. Ultrason. Ferroelectr. Freq. Control* **42**, 1020–1027 (1995).
⁵P. H. Chang, K. K. Shung, and H. B. Levene, "Quantitative measurements of second harmonic doppler using ultrasound contrast agents," *Ultrasound Med. Biol.* **22**, 1206–1214 (1996).
⁶P. D. Krishna and V. L. Newhouse, "Second harmonic characteristics of the ultrasound contrast agents Albunex[®] and FS069," *Ultrasound Med. Biol.* **23**, 453–459 (1997).
⁷B. F. Vandenberg and H. E. Melton, "Acoustic lability of albumin microspheres," *J. Am. Soc. Echocardiogr.* **7**, 582–589 (1994).
⁸D. L. Miller and R. M. Thomas, "Ultrasound contrast agents nucleate inertial cavitation *in vitro*," *Ultrasound Med. Biol.* **21**, 1059–1065 (1995).
⁹V. Uhlendorf and C. Hoffmann, "Nonlinear acoustical response of coated microbubbles in diagnostic ultrasound," 1994 Ultrasonics Symposium, 1559–1562 (1994).
¹⁰D. L. Miller, "Ultrasonic detection of resonant cavitation bubbles in a flow tube by their second harmonic emissions," *Ultrasonics* **19**, 217–224 (1981).

¹¹D. R. Gross, D. L. Miller, and A. R. Williams, "A search for ultrasonic cavitation within the canine cardiovascular system," *Ultrasound Med. Biol.* **11**, 85–97 (1985).
¹²K. I. Morton, G. R. Ter Haar, I. G. Stratford, and C. R. Hill, "The role of cavitation in the interaction of ultrasound with V79 Chinese hamster cells *in vitro*," *Br. J. Cancer* **45**, 147–150 (1982).
¹³K. I. Morton, G. R. Ter Haar, I. G. Stratford, and C. R. Hill, "Subharmonic emission as an indicator of ultrasonically-induced biological damage," *Ultrasound Med. Biol.* **9**, 629–633 (1983).
¹⁴P. D. Edmonds and P. Ross, "Acoustic emission as a measure of exposure of suspended cells *in vitro*," *Ultrasound Med. Biol.* **12**, 297–305 (1986).
¹⁵P. D. Lele, "Cavitation and its effects on organized mammalian tissue," in *Ultrasound: its Applications in Medicine and Biology*, edited by F. J. Fry (Elsevier Scientific, New York, 1978), Pt. II, App. I, pp. 737–742.
¹⁶E. C. Everbach, I. R. S. Makin, M. Azadniv, and R. S. Meltzer, "Correlation of ultrasound-induced hemolysis with cavitation detector output *in vitro*," *Ultrasound Med. Biol.* **23**, 619–624 (1997).
¹⁷D. L. Miller and A. R. Williams, "Bubble cycling as the explanation of the promotion of ultrasonic cavitation in a rotating tube exposure system," *Ultrasound Med. Biol.* **15**, 641–648 (1989).
¹⁸E. P. Armour and P. M. Corry, "Cytotoxic effects of ultrasound *in vitro* dependence on gas content, frequency, radical scavengers, and attachment," *Radiat. Res.* **89**, 369–380 (1982).
¹⁹A. R. Williams and D. L. Miller, "Photometric detection of ATP release from human erythrocytes exposed to ultrasonically activated gas-filled pores," *Ultrasound Med. Biol.* **6**, 251–256 (1980).
²⁰D. L. Miller, R. A. Gies, and W. B. Chrisler, "Ultrasonically induced hemolysis at high cell and gas body concentrations in a thin-disc exposure chamber," *Ultrasound Med. Biol.* **23**, 625–633 (1997).
²¹J. L. Moore and W. T. Coakley, "Ultrasonic treatment of Chinese hamster cells at high intensities and long exposure times," *Br. J. Radiol.* **50**, 46–50 (1977).
²²S. L. Kerr, D. W. Gregory, M. Shammari, D. J. Watmough, and D. N. Wheatley, "Differing effects of ultrasound-irradiation on suspension and monolayer cultured HeLa cells investigated by scanning electron microscopy," *Ultrasound Med. Biol.* **15**, 397–401 (1989).
²³E. G. Loch, A. B. Fischer, and E. Kuwert, "Effect of diagnostic and therapeutic intensities of ultrasonics on normal and malignant human cells *in vitro*," *Am. J. Obstet. Gynecol.* **110**, 457–460 (1971).
²⁴M. J. Pickworth, P. P. Dendy, P. R. Twentyman, and T. G. Leighton, "Studies of the cavitation effects of clinical ultrasound by sonoluminescence: 4. The effect of therapeutic ultrasound on cells in monolayer culture in a standing wave field," *Phys. Med. Biol.* **34**, 1553–1560 (1989).
²⁵T. G. Leighton, *The Acoustic Bubble* (Academic, New York, 1994).
²⁶C. C. Church, "The effects of an elastic solid surface layer on the radial pulsations of gas bubbles," *J. Acoust. Soc. Am.* **97**, 1510–1521 (1995).
²⁷A. Eller and H. G. Flynn, "Generation of subharmonics of order one-half by bubbles in a sound field," *J. Acoust. Soc. Am.* **46**, 722–727 (1969).
²⁸*AIUM, Bioeffects and Safety of Diagnostic Ultrasound* (American Institute of Ultrasound in Medicine, Rockville MD, 1993).
²⁹WFUMB Symposium on Safety of Ultrasound in Medicine, *Ultrasound Med. Biol.* (in press).
³⁰*AIUM, Standard for Real-Time Display of Thermal and Mechanical Acoustic Output Indices on Diagnostic Ultrasound Equipment* (American Institute of Ultrasound in Medicine, Rockville, MD, 1992).

Control of vocal intensity in budgerigars (*Melopsittacus undulatus*): Differential reinforcement of vocal intensity and the Lombard effect

Kazuchika Manabe, Ehsanee I. Sadr, and Robert J. Dooling
Department of Psychology, University of Maryland, College Park, Maryland 20742

(Received 26 June 1997; revised 10 October 1997; accepted 4 November 1997)

Call production in budgerigars was studied using operant conditioning. In several experiments, budgerigars were reinforced with food for producing calls that were above or below a criterion level of intensity. This differential reinforcement procedure was successful in controlling vocal intensity in both directions showing that the intensity with which budgerigars produce vocalizations is under voluntary control. In additional experiments, call intensity maintained by food reinforcement was measured both in the quiet and in the presence of various levels of broadband noise. Call intensity in budgerigars increased significantly in noise, paralleling the well-known Lombard effect in humans which is the reflexive increase in speech intensity during communication in noise. Call intensity was measured in broadband noise and in a notched noise (no energy between 1.5 and 4.5 kHz) with the same overall level. Results show that noise in the spectral region of contact calls is most effective in causing an increase in vocal intensity. In aggregate, these experiments show that budgerigars have voluntary control over the intensive aspect of their vocalizations, that they normally monitor their vocal output through external auditory feedback, and, like humans, they exhibit the Lombard effect. © 1998 Acoustical Society of America. [S0001-4966(98)04402-6]

PACS numbers: 43.80.Ka, 43.80.Nd, 43.70.Bk [FD]

INTRODUCTION

While there is an extensive and popular literature on animal models of human speech perception (see, for example, Kuhl, 1989), there has been much less work on animal models of human vocal production. In large part, this is because, with the exception of humans, vocal learning at either the phonological or syntactical level does not occur in mammals. Evidence of vocal learning appears to be widespread among birds, probably occurring in over half of the 9000 known species (Kroodsma and Miller, 1982, 1996). For this reason, there have been a number of studies over the years of the effect of hearing loss on the quality of vocal output in both young and adult birds (see, for example, Konishi, 1963, 1964, 1965a,b; Marler *et al.*, 1972, 1973; Nottebohm, 1968; Nottebohm and Nottebohm, 1971). Results show that permanent deafening (i.e., cochlear removal) has a profound effect on the characteristics of vocal output in both young birds and depending on the species, adult birds as well (Nordeen and Nordeen, 1992; Kroodsma and Konishi, 1991). But, aside from these studies that have examined the effects of complete hearing loss on vocalizations, there has been little study of more subtle interactions between hearing and vocalizations in animals. Understanding these more subtle interactions between hearing and vocalizations is probably essential for the full understanding of vocal development, vocal learning, and acoustic communication in both animals and humans. Profound hearing loss in humans can cause tremendous deficits in speech (Binnie *et al.*, 1982; Lane and Webster, 1991). In humans there are also numerous examples of more subtle interactions between hearing and speech production. One such interaction is the Lombard ef-

fect in which speakers adjust their vocal output or speech intensity depending on background noise level (Lane and Tranel, 1971).

As far as we know, there have only been three attempts to look for similar phenomena in animals. Sinnott and her colleagues (Sinnott *et al.*, 1975) showed that two old world monkeys (a female *Macaca nemestrina* and a male *Macaca fascicularis*) could be trained to vocalize for food and increased their vocal intensity when exposed to white noise. Japanese quail (*Coturnix coturnix japonica*) produce louder separation calls when they are visually and acoustically separated from their mate under noise conditions than in the quiet (Potash, 1972). Recent studies of the zebra finch (*Taeniopygia guttata*) also provide evidence that background noise level affects the level of vocal output (Cynx *et al.*, 1997). These studies suggest that some primates and birds may have the ability to monitor their vocal output and adjust their vocal intensity in reference to background noise level.

It is well accepted that changes in speaking level in humans is normally composed of at least two components: a voluntary component and a reflexive component. Clearly humans are able to adjust the intensity of their vocal output in a completely voluntary way in a wide variety of circumstances. But it is also the case that humans adjust their speech intensity in certain situations (increase in background noise, when wearing ear protectors, following temporary threshold shift from noise exposure, etc.) without being consciously aware of making an effort to do so. This “reflexive” increase in vocal intensity provides compelling evidence that humans normally monitor the level or intensity of their vocal output.

We have known for many years from observations and recordings under laboratory conditions that budgerigars

show considerable variability in the peak intensities of their contact calls (ranging from 80 to 100 dB SPL) (Dooling, 1986; Sadr, 1996). Such variation in calling level both between and within birds suggest that budgerigars can control their vocal intensity. The present series of experiments were undertaken to determine whether budgerigars (*Melopsittacus undulatus*), small parrots native to Australia, can adjust the intensity of their vocalizations both voluntarily and in response to environmental conditions such as noise.

I. EXPERIMENT 1

Previous experiments on vocal learning in a wide variety of species of birds, including budgerigars, have shown that many aspects of the spectrotemporal pattern of vocal output are learned (Dooling, 1986; Farabaugh *et al.*, 1994). The intensive features of bird vocalizations, and whether or not these features are learned, have received far less attention (but see Cynx *et al.*, 1990; Williams *et al.*, 1989). Previous experiments in this series have shown that budgerigars can modify the spectrotemporal pattern of their contact calls for food (Manabe and Dooling, 1997; Manabe *et al.*, 1995, 1997). The purpose of the present experiment was to determine whether budgerigars are capable of changing the intensity of their calls in order to obtain food.

A. Method

1. Subjects

Four adult male budgerigars (*Melopsittacus undulatus*) were maintained at 90% of their free-feeding weights. The birds were obtained from a local pet supplier and maintained in an aviary at University of Maryland, under a light–dark cycle correlated with the season. Each bird was caged separately and had free access to water and grit in their home cages.

2. Apparatus

The apparatus and procedure have been detailed previously and are only briefly described here (Manabe and Dooling, 1997).

a. Experimental chamber. Birds were trained in a small experimental chamber (14 cm wide × 12 cm high × 17 cm deep) made of wire mesh which was then housed in a sound-attenuating box (Industrial Acoustics IAC-1). A LED was mounted on each corner of a 3 cm × 3 cm square piece of foam mounted on one side of the test cage just above the food hopper. An electret condenser microphone (SONY ECM-77B) mounted in the middle of the square foam equidistant from the four LEDs was used to record bird's call. The food hopper mounted on the floor at a depth of 3 cm from the front panel delivered yellow millet.

b. Sound sampling. The output of the microphone was sent to a digital signal processing board (National Instruments AT-DSP2200). The board low-pass filtered the analog data at 80 kHz prior to 16-bit digitization. The digital signal was then low-pass filtered at 12 kHz before further processing. When sound intensity exceeded a pre-set criterion, A/D conversion commenced at a sampling rate of 24 kHz for a total duration of 266 ms.

Serial spectra were calculated using the fast Fourier transform (FFT). Calculations for the first 10.67 ms were carried out while the second 10.67 ms of data were being sent to RAM, and so on. For each successive 10.67-ms segment of sound, a power spectrum was calculated (cf. Manabe *et al.*, 1995, 1997; Manabe and Dooling, 1997). In all, 25 successive spectra were computed constituting the entire 266 ms (i.e., 25 × 10.67 ms) of sound analyzed from the beginning of each call. Peak amplitude from the whole call was calculated in real time. Each serial spectrum was normalized to a peak intensity of one for subsequent comparison to the values of the stored template.

In practice, three criteria had to be met in order for a sound to be classified as a contact call. The sound had to have a duration greater than 96 ms, at least 70% of the total energy between 187.5 Hz and 10031.25 Hz had to fall within the range of 937.5 Hz–6843.75 Hz, and no individual call components occurring in the initial 74-ms sampling period could be shorter than 21.3 ms. During testing, every incoming sound classified as a call by these criteria was stored in digital form on disk for further analysis. Programs for experimental control and data collection were written in Microsoft C.

B. Procedure

1. Shaping of vocal responses

After the birds habituated to the experimental chamber, they were allowed to eat millet from the floor-mounted feeder. When the birds became accustomed to eating millet from the feeder whenever it was activated, hand shaping of vocal production began. Typical aviary sounds were played in the test cage to induce the birds to call (cf. Ginsburg, 1960). Whenever the bird produced a contact call, the experimenter activated the feeder. When the birds began to emit calls reliably in the absence of the aviary tape, call productions were reinforced automatically. A test session ended when call productions resulted in a total of 48 reinforcements. Since all calls meeting the criterion for a call were reinforced, this phase was called nondifferential reinforcement of call production. Calls from the last three test sessions were used to establish the call intensity used by each bird in the nondifferential reinforcement of call production phase.

2. Differential reinforcement of call intensity

After the bird's performance stabilized in the nondifferential reinforcement of call production phase, differential reinforcement of high intensity calls was implemented. In this procedure, only calls with an intensity above a pre-set criterion were reinforced. Initially, this criterion was set to the mean intensity of all calls produced in the last three test sessions of nondifferential reinforcement (as described above). Once the bird was producing calls that met or exceeded the criterion intensity level on at least 66% of the trials in a given session, the intensity criterion was increased for the subsequent test session. The intensity criterion chosen for this subsequent test session was set to the mean intensity of calls produced in the previous test session. This procedure

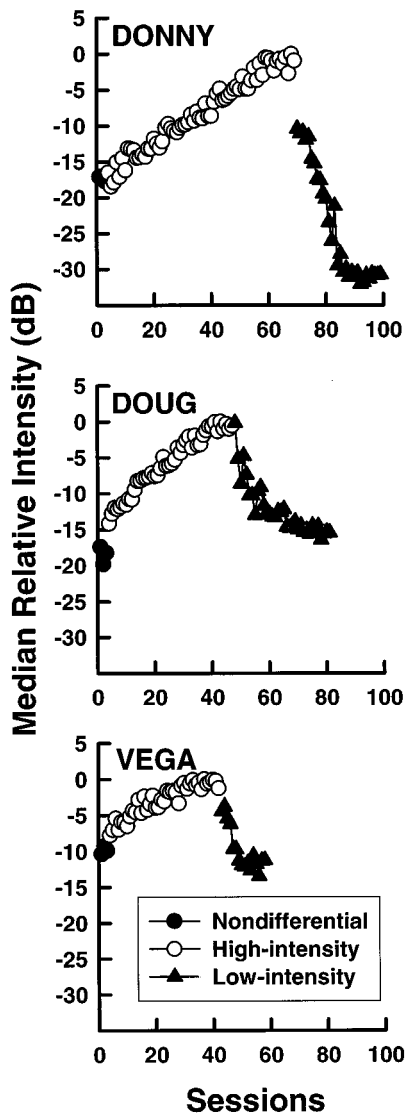


FIG. 1. Median relative call intensities in the nondifferential, differential-reinforcement-of-high-intensity, and differential-reinforcement-of-low-intensity trials. Closed circles show the call intensities produced during nondifferential reinforcement of call intensity, the open circles intensities in differential reinforcement of high intensity schedule and closed triangles intensities in differential reinforcement of low intensity schedules.

continued until there was no increase in intensity over nine successive test sessions. Once this asymptotic level of performance was reached in producing high intensity calls, a second procedure involving the differential reinforcement of low intensity calls was implemented. This procedure was the exact opposite of the first procedure except that the procedure began after the bird reached an asymptotic high intensity call level as opposed to the call intensity level used in test sessions involving nondifferential reinforcement of call production. Now, in the differential reinforcement of low intensity procedure, only calls with intensities below a preset criterion were reinforced.

C. Results and discussion of experiment 1

Figure 1 shows the median call intensity in dB per session for each bird. The call intensities of all birds increased

in the high intensity reinforcement condition and decreased in the low intensity reinforcement condition. The relative difference in intensity between two differential schedules was about 30 dB for DONNY, 20 dB for DOUG, and 11 dB for VEGA. A significant difference was found across conditions [one-way repeated measures ANOVA $F(2,1)=9.29$, $p<0.04$]. In a multiple comparison test, the call intensities in the differential reinforcement of high intensity schedule were significantly greater than those produced in either the nondifferential or differential reinforcement of low intensity schedules (Student–Newman–Keuls method; $p<0.05$). On the other hand, there was no significant difference between nondifferential and differential reinforcement of low intensity schedules. In the present experiment, quiet calls under a predetermined amplitude did not trigger the system. Such calls were therefore never reinforced even under a schedule of differential reinforcement of low intensity calls. Therefore, the lower limit of call intensity probably maintained call intensity above a certain level. Subject DONNY showed a large decrease in intensity during differential reinforcement of low intensity compared to the other two birds. Since Donny's call intensity was much higher than the call intensity of the other birds by 2–17 dB, this bird obviously had sufficient room to decrease call intensity.

II. EXPERIMENT 2

In experiment 1, the birds' call productions were sampled with the microphone in a fixed position on the cage panel. Normally the birds would position themselves on a perch along side the floor-mounted food hopper and facing the fixed microphone on the cage panel. But, with the microphone in a fixed location and the bird free to move about within a few centimeters, there are other possible sources of variation in intensity measured at the microphone other than a variation in output from the bird. It might be possible, for instance, for the bird to affect the intensity of recorded calls by moving closer or farther away from the microphone or turning its head. Because we occasionally observed such behaviors in the birds, experiment 2 was designed to measure the amount of variation that could potentially be attributed to the bird's movement relative to the microphone.

To obtain a measure of call intensity independent of head movement, the distance between the bird's beak and the microphone was fixed. This was accomplished by using a small audio FM transmitter and microphone attached to the bird's head with super glue. We compared the variance in call intensity measured by a microphone on the bird's head with the variance in call intensity recorded from a microphone on the front panel, to see how head movement affected measured call intensity.

A. Method

1. Subjects

Three male adult budgerigars (*Melopsittacus undulatus*) were used.

2. Apparatus

a. Experimental chamber. The same experimental chamber was used as in experiment 1 except for a coil antenna made from audio cable mounted just under the ceiling of the test cage.

b. FM Transmitter. A small audio FM transmitter (1.0 × 0.5 × 0.5 cm) was constructed from a circuit modified from Lancaster *et al.* (1992) for use in bats. The transmitter contained a built-in electret microphone (Knowles Electronics 3068) and a small battery (LR364) so that the bird had complete freedom of movement in the test apparatus. The weight of the transmitter including the microphone and battery was about 1 g and was attached on bird's head by glue during the test sessions. The FM transmissions were monitored with a small FM radio (Radio Shack 12-174), the output of which was sent directly to the DSP board (National Instruments AT-DSP2200). The output level of the FM receiver was calibrated to 0.1-V peak amplitude using a 2-kHz 114 dB SPL pure tone prior to each test session. The tone was produced 4 cm from a microphone on the transmitter. During a test session, contact calls were distinguished from background sounds using the same criteria as described in experiment 1.

B. Procedure

All three birds in this experiment were experienced with the procedure, so shaping of calling behavior for food was not necessary. A transmitter was attached to the bird's head during training sessions. Despite some initial apparent discomfort occasioned by gluing the transmitter to the head, all three birds habituated sufficiently so that useable data could be obtained over the course of an entire test session. Once habituated to the transmitter on its head, the bird was trained to produce a specific call. At first, every call was reinforced if it met the criteria for a contact call as in experiment 1. This phase continued for three sessions, during which the intensity of the bird's calls were measured by a microphone on the front panel of the test cage and by a microphone attached to the transmitter on the bird's head.

C. Results and discussion of experiment 2

The coefficient of variation of call intensities for each bird from a single test session as sampled from both the stationary microphone and the head-mounted microphone are shown in Fig. 2. The variation in call intensity measured by a microphone on the front panel was significantly greater than that measured by a microphone on the head [one-way repeated measures ANOVA $F(2,1) = 18.7$, $p < 0.05$]. We conclude that up to one-third of the variance in call intensity measured by a microphone on the front panel could be due to the movement of the bird in relation to the stationary microphone.

III. EXPERIMENT 3

The results of experiment 2 suggested that the birds could use more than one strategy to affect the intensity of contact calls recorded by a stationary microphone. To establish, unequivocally, whether birds could increase vocal intensity independent of any small changes in position, we se-

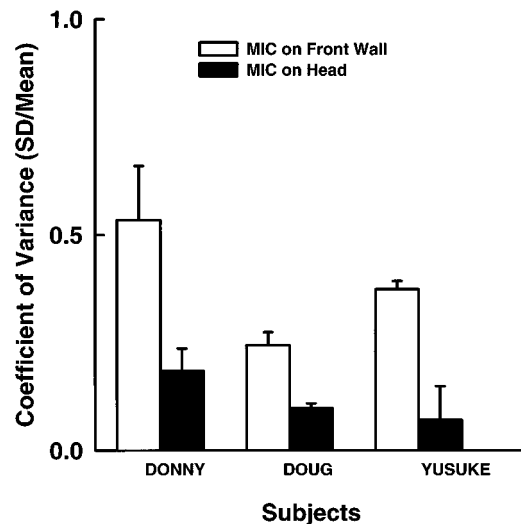


FIG. 2. Coefficient of variance in call intensity. Open bars show coefficient of variances, standard deviation divided by mean call intensity measured by a microphone on the front panel, closed bars coefficient variances measured by a microphone on the bird's head, respectively.

lected one bird from experiment 2 who adapted particularly well to having the transmitter attached to its head for extended testing. With this bird, we repeated the differential reinforcement of high intensity calls used in experiment 1 with the head transmitter in place. We examined call productions both within a test session and across test sessions.

A. Method

One male adult budgerigar (*Melopsittacus undulatus*) from experiment 2 was used.

B. Procedure

This experiment was conducted exactly as described for the intensity increase portion of of experiment 1.

C. Results and discussion of experiment 3

Figure 3 shows intensity changes across trials measured from a microphone attached to the bird's head in the last test session in which the nondifferential reinforcement procedure was in effect (when every call production was reinforced with food) and the first test session when the differential reinforcement of high intensity procedure was introduced (in which only calls with high intensity were reinforced). There was clearly no increase in call intensity during the nondifferential reinforcement of call intensity procedure. On the other hand, there was a marked increase in call intensity within 45 trials of the introduction of the differential reinforcement of high intensity calls.

As in experiment 1, the intensity criterion was adjusted on subsequent test sessions toward higher intensity calling. Figure 4 shows the changes in call intensity across sessions for this bird. Call intensity clearly increased when a procedure involving the differential reinforcement of high intensity calls was instituted thus confirming the results of experiment 1.

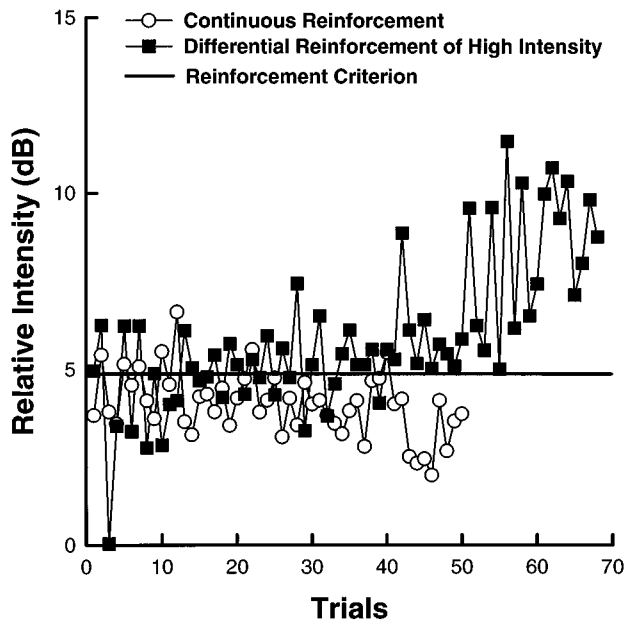


FIG. 3. Relative call intensities across trials in the continuous reinforcement procedure and in differential reinforcement of high intensity procedure using a microphone on the bird's head. Open circles indicate intensities in nondifferential reinforcement, closed circles ones in differential reinforcement of high intensity procedures. The horizontal line indicates the reinforcement criterion.

Interestingly, examination of the calls produced by this bird revealed that it used a strategy not seen in the birds used in experiment 1. This bird produced at least two different calls during training sessions in experiment 3. The sonograms of these two call types—one longer and one shorter—are shown in Fig. 5. Initially the bird made only the longer call during early training sessions (shown in Fig. 4). It began

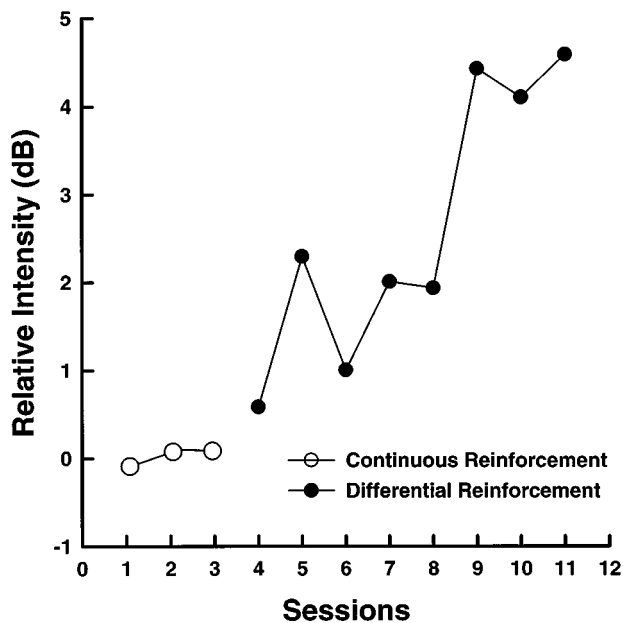


FIG. 4. Relative call intensity in the nondifferential reinforcement and in the differential reinforcement of high intensity procedure. Open circles indicate calls from the nondifferential session and closed circles represent calls from the differential sessions.

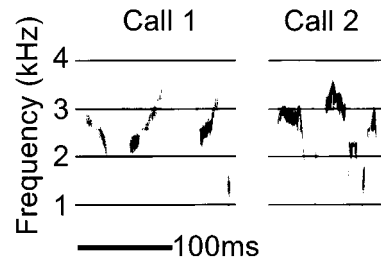


FIG. 5. Sonograms of calls produced by a bird in the differential reinforcement of high intensity procedure.

to produce the shorter call as well only in the later sessions when the intensity criterion was being increased from session-to-session depending on the bird's performance. The intensity of the shorter call was also greater than that of the longer call. One interpretation of this result is that there is a tradeoff in vocal production between intensity and duration. That is, it appears that in order to produce a more intense call, the bird shortened its production. The results of this experiment establish unequivocally that budgerigars can increase the intensity of their vocal productions independent of other strategies such as changes in location.

IV. EXPERIMENT 4

The experiments described above show that budgerigars, like humans, can be directed (or trained) to modify the intensity with which they produce vocalizations. But with humans, there are also clearly instances where the intensity of vocal output is increased in a more reflexive way, as when humans are trying to communicate in a background of noise. This effect, known as the Lombard effect, has been the subject of numerous studies over the years (see, for example, Lane and Tranel, 1971; Dreher and O'Neill, 1958; Pickett, 1958; Gardner, 1964, 1966).

A. Method

1. Subjects

Two female and three male adult budgerigars (*Melopsittacus undulatus*) were maintained at 90% of their free-feeding weights as described in experiment 1.

2. Apparatus

a. Experimental chamber. Birds were trained in the same experimental chamber as in experiment 1.

b. Background noise. White noise was introduced into the test chamber as follows. Noise was digitally generated by the DSP board (National Instruments AT-DSP2200) and delivered through a small 1-in. speaker (Panasonic EAS-45P36S) mounted in foam above and behind the recording microphone and pointed at the bird's head when sitting on the perch. In these experiments, the noise was delivered at two levels and was calibrated using a sound level meter and a 1/2-in. microphone (GenRad Incorporation GR 1982 precision sound-level meter and analyzer) before the experiments.

c. Recording and measurement of call intensity. Since sound intensity recorded by a microphone on the bird's head

could be affected by movement relative to the speaker that was producing the noise in this experiment, a separate, stationary microphone (Radio Shack 33-1063) described above was used to record the birds' calls. The output of this microphone was fed to a tape recorder (Marantz PMD 740). At the end of each session, vocalizations recorded on tape were analyzed with a Kay Sonagraph model 7800 real time analyzer. The intensity of each vocalization was measured using this analyzer.

B. Procedure

After the birds' performance stabilized, a series of test sessions was conducted in which white noise of various levels was presented during the test session. In the first phase, no noise was presented for the first third of the test session, then a noise was presented at an overall level of 55 dB(A) during the middle third of the session, and finally, the noise was turned off again during the last third of the session (A-B-A test sequence). In the second phase, a no noise condition was alternated with a noise presented at a level of 70 dB SPL in the middle third of the session in the same ABA sequence. In the third phase of this experiment, the noise level alternated between 55 dB and 70 dB SPL. Each alternation involved 25 trials resulting in a total of 75 trials in each test session. During these test sessions, every call the bird produced was reinforced by the experimenter rather than automatically, since the masking noise in the test chamber would sometimes trigger the call recognition system.

C. Results and discussion of experiment 4

Call intensities reported in this experiment were normalized to the highest intensity call produced across all test sessions for all birds. The mean relative intensities of the five birds in this experiment are shown in Fig. 6. The significant effects in intensity were found in all three conditions, in the 0-55-0 dB condition [repeated measures one-way ANOVA; $F(4,2)=5.79$, $p<0.03$], in the 0-70-0 dB condition [repeated measures one-way ANOVA; $F(4,2)=13.3$, $p<0.01$] and in the 55-70-55 dB condition [repeated measures one-way ANOVA; $F(4,2)=7.69$, $p<0.02$]. In a multiple comparison test, there was no significant difference in call intensity between the first and the last noise level (two A's) in the A-B-A sequence (Student-Newman-Keuls method) in any of the three conditions. On the other hand, the call intensities produced in the middle third of the test sessions (the "B" noise levels) were all significantly greater than the calls produced in the first or last third of a test sessions (Student-Newman-Keuls method; $p<0.05$). These results show that the intensity with which budgerigars produce their vocalizations is affected by background noise level even when the acoustic dimension of intensity is made irrelevant for the bird obtaining food.

V. EXPERIMENT 5

Experiment 4 showed that budgerigars have a reflexive increase in vocal intensity in the presence of noise. Experiment 5 was designed to further address this issue by examining whether it is overall noise or noise in the spectral re-

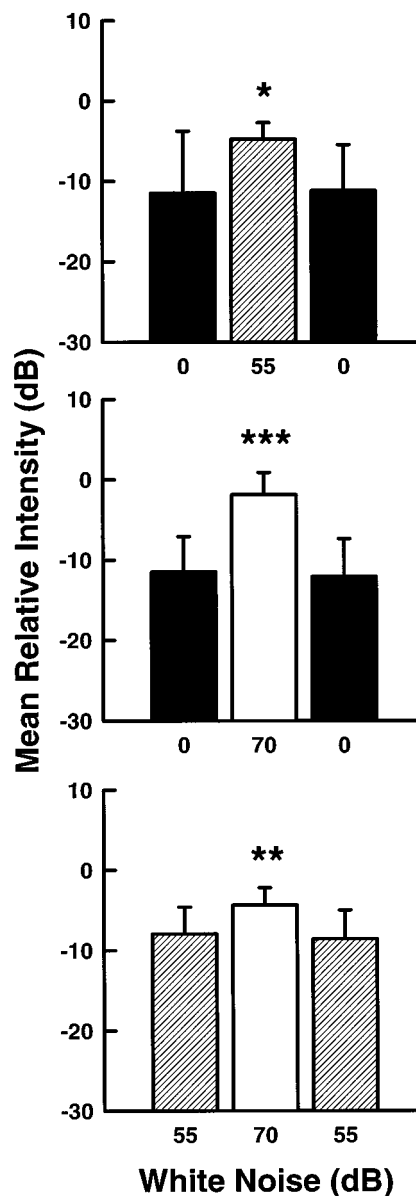


FIG. 6. Mean relative call intensities within a session. The top panel shows relative intensities in the 0-55-0 dB noise condition. The middle panel shows the relative intensities in 0-70-0 dB noise condition and the bottom panel shows the relative intensities in 55-70-55 dB noise condition.

gion of vocalizations that is effective in producing the Lombard effect. If only noise in the spectral region of vocalizations is effective inducing the Lombard effect, this suggests that budgerigars, like humans, are assessing the signal-to-noise ratio between their vocal output and background noise.

A. Method

Subjects and apparatus were the same as in experiment 3.

B. Procedure

In this experiment, noises of two different spectral shapes, but the same overall level, were generated. One noise was the same as the white noise described above which had

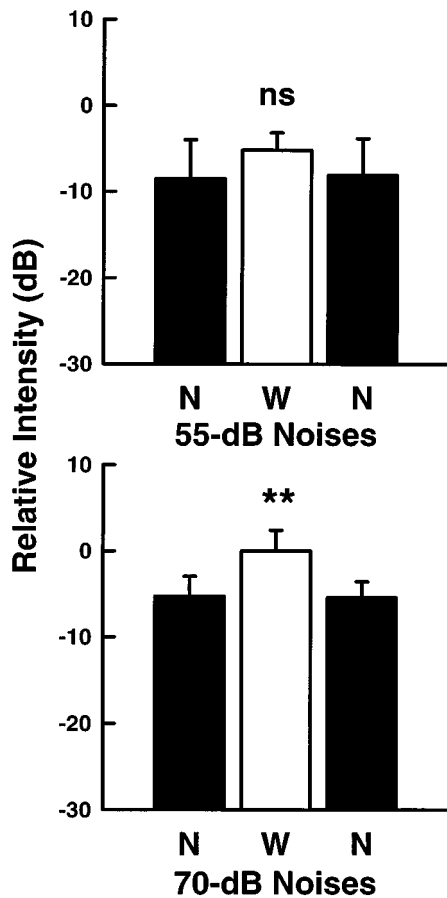


FIG. 7. Mean relative call intensities in notched-white-notched noises condition. The top panel shows relative call intensities produced in the 55-dB noise. The bottom panel shows relative intensities in the 70-dB noise.

a relatively flat spectra. The second noise contained a spectral notch of reduced energy between 1.5 kHz and 4.5 kHz. This spectral notch was greater than 40 dB deep with slopes of 100 dB/octave. The spectral energy of budgerigar contact calls is almost exclusively restricted to this spectral region. Within a single test session, broadband white noise and notched noise were alternated in an A-B-A sequence. The overall sound level of two noises was set either at 55 dB or 70 dB. Each noise condition was tested for 25 trials for a total number of trials in a test session of 75.

C. Results and discussion of experiment 5

The mean relative call intensity of the five birds in the two different sessions is shown in Fig. 7. A significant effect in call intensity was found in the 70-dB background noise condition. [one-way repeated measures ANOVA; $F(4,2) = 6.82$, $p < 0.02$]. A multiple comparison test (Student-Newman-Keuls method) also shows a significant difference in call intensity between notched noise and white noise ($p < 0.05$). On the other hand, there was no significant effect of placing a notch in a noise presented at level of 55 dB SPL [one-way repeated measures ANOVA; $F(4,2) = 2.05$, $p > 0.10$]. These results suggest that it is intense noise in the spectral region of the budgerigar's contact call that is the critical factor for inducing the Lombard effect.

VI. GENERAL DISCUSSION

Understanding the relation between hearing and vocal production in humans depends in large measure on adequate animal models. Hearing loss results in abnormal vocalizations in some birds including the budgerigar (Dooling *et al.*, 1987; Heaton *et al.*, submitted; Konishi, 1963, 1964, 1965a,b). In humans, hearing loss can clearly have a profound effect on the speech of both children and adults (Binnie *et al.*, 1982; Cowie and Douglas-Cowie, 1983; Goehl and Kaufman, 1984; Lane and Webster, 1971; Monsen, 1978a,b, 1979; Waldstein, 1990). The present experiments were designed, in part, to extend the parallels between vocal production in budgerigars and vocal production in humans by examining more subtle aspects of the role that hearing plays in vocal production.

Previous experiments in this series have shown that budgerigars can be trained by food reward to modify the spectrotemporal qualities of their species-specific contact calls (Manabe *et al.*, 1995, 1997; Manabe and Dooling, 1997). The present experiments extend these findings by showing that budgerigars can also be trained to control the intensity of their vocal output just as they can control the spectrotemporal aspects of their complex contact calls. Additional experiments on call production in the presence of background noise also suggest that budgerigars demonstrate a Lombard effect—an increase in vocal intensity in the presence of a background noise.

The Lombard effect, even in humans, is probably the result of very complex processes and it is worthwhile to consider the possible mechanisms that might underlie this specific phenomenon in budgerigars and the general problem of voluntary control of vocal intensity in birds. The experiments in this paper support a case for budgerigars acoustically monitoring their vocal output and making adjustments on the basis of auditory feedback. Other explanations are possible. Most alternative explanations—which we consider unlikely—will probably require additional experiments to resolve. For instance, placing a notch in masking noise in the spectral region of contact calls provides strong evidence that it is energy in the spectral region of the contact call, rather than outside it, which is effective in inducing the Lombard effect. Additional controls might include a systematic investigation of spectral notches placed in other regions of the background noise. Another issue is the extent to which budgerigars can increase or decrease their vocal intensity without auditory feedback. It should be possible to train a bird to change its vocal intensity using operant conditioning, deafen the bird by extirpation of the basilar papillae, and see whether increases and decrease in vocal intensity are still possible under operant control. Although kinesthetic and proprioceptive feedback from the vocal production apparatus could conceivably continue to guide vocal production, such feedback pathways have not been well described in birds. It is well known that deaf humans, even those born deaf, can be trained, albeit with difficulty, to modulate the intensity of their vocal output (Martony, 1968).

In partial support of the hypotheses about nonauditory feedback, recent experiments on vocal production following treatment with the ototoxic drug kanamycin in budgerigars

(which induces extensive but temporary hearing loss) show that call structure is affected by drug-induced hearing loss and that this structure recovers considerably well before significant hearing recovery has occurred (Dooling *et al.*, 1997). This observation argues either for some kind of alternative, non-acoustic feedback in maintaining call phonology or, perhaps, some kind of precise auditory-vocal memory that requires little veridical sensory input in order to maintain well learned behavior patterns.

Another issue is the extent to which birds are stimulated by the addition of background noise to call more frequently and/or produce louder vocalizations independent of external auditory feedback. It is common knowledge among aviculturists that low level background noise such as running water, etc. can be used to elicit calling from birds. Although we did not observe any such tendencies in our operant situation, whether such a phenomenon may have influenced our results simply cannot be determined. Taken together, we think that the results from tests with different noise levels, coupled with the effect of using noise with a notch in the frequency region of vocalizations provide support for the fact that it is the level of auditory feedback (rather than the change in signal-to-noise ratio through auditory feedback) which is the mechanism by which background noise leads to an increase in vocal intensity.

A final issue concerns the fact that several different strategies were employed by budgerigars to affect the intensity of calls as recorded from a stationary microphone. The most obvious strategy was to increase and decrease the intensity of their vocal output. But this strategy in experiment 1 was probably also combined with the second strategy, which was for the bird to alter its location with respect to the stationary microphone. As evidence, consider that the amount of intensity increase for budgerigar DOUG was about 15 dB in experiment 1 but only 5 dB in an identical procedure (experiment 3) when a transmitter was attached to his head. Moreover, a detailed analysis of the call structure produced by this bird across test sessions, revealed yet another possible strategy in that the bird eventually changed call types. In other words, in later sessions, when the bird was producing the highest intensity calls, it was using a different call type. There are several possible interpretations of this latter finding. One is that there is a trade-off between intensity and duration as has been described for humans, such that producing a more intense call requires producing a shorter call. Another possibility is that particular call types that are restricted to a particular intensity may have evolved or developed under functional exigencies. Thus reinforcing the bird for producing a higher intensity call may simply induce it to select a more intense call from its repertoire. Such a strategy could be combined with one of moving closer or further away from a stationary microphone as in experiment 1.

Finally, we think these results are interesting for several reasons. Whether budgerigars monitor their vocal output in the same manner as humans is a critical issue in trying to develop an animal model for understanding the relation between hearing, vocal development, and vocal learning. Birds in general, and budgerigars in particular, are important to

consider in the context of such a model because they exhibit the phenomenon of hair cell regeneration and the return of auditory function following hair cell replacement. Budgerigars, like humans, also show remarkable behavioral plasticity in being able to learn new species-specific vocalizations throughout life. Thus, these birds may provide a unique animal model with which to both assess the effects of temporary hearing loss and hearing restoration on vocal output in humans. Such a model system may therefore have particular relevance for the study of the auditory and vocal sequella of cochlear implantation.

ACKNOWLEDGMENTS

This research was supported in part by NIMH Grant No. MH-00982 to RJD and NIDCD Grants No. DC-01372 to RJD and BMR. Portions of this research were presented at the annual meeting of the Association for Research in Otolaryngology, St. Petersburg, FL, February 1996.

- Binnie, C. A., Daniloff, R. G., and Buckingham, H. W. (1982). "Phonetic disintegration in a five-year-old following sudden hearing loss," *J. Speech Hear. Disorders* **47**, 181–189.
- Borden, G. (1979). "An interpretation of research on feedback interruption during speech," *Brain and Lang.* **7**, 302–319.
- Cowie, R., and Douglas-Cowie, E. (1983). "Speech production in profound postlingual deafness," in *Hearing Science and Hearing Disorders*, edited by M. Lutman and M. Haggard (Academic, New York), pp. 183–231.
- Cynx, J., Williams, H., and Nottebohm, F. (1990). "Timbre discrimination in zebra finch (*Taeniopygia guttata*) song syllables," *J. Comp. Psych.* **104**, 303–308.
- Cynx, J., Lewis, B., Tavel, B., and Tse, H. (1997). "Amplitude regulation of vocalizations in a song bird," Abstracts of the 20th Midwinter Research Meeting of the Association for Research in Otolaryngology.
- Dooling, R. J. (1986). "Perception of vocal signals by budgerigars (*Melopsittacus undulatus*)," *Exp. Biol.* **45**, 195–218.
- Dooling, R. J., Ryals, B. M., and Manabe, K. (1997). "Recovery of hearing and vocal behavior after hair cell regeneration," *Proc. Natl. Acad. Sci. USA* **94**, 14 206–14 210.
- Dooling, R. J., Gephart, B. F., Price, P. H., McHale, C., and Brauth, S. E. (1987). "Effects of deafening on the contact call of the budgerigar (*Melopsittacus undulatus*)," *Animal Beh.* **35**, 1264–1266.
- Dreher, J. J., and O'Neill, J. J. (1958). "Effects of ambient noise on speaker intelligibility of words and phrases," *Laryngoscope* **68**, 539–548.
- Farabaugh, S. M., Linzenbold, A., and Dooling, R. J. (1994). "Vocal plasticity in budgerigars (*Melopsittacus undulatus*): Evidence for social factors in the learning of contact calls," *J. Comp. Psych.* **108**, 81–92.
- Gardner, M. B. (1964). "Effect of noise on listening levels in conference telephony," *J. Acoust. Soc. Am.* **36**, 2354–2362.
- Gardner, M. B. (1966). "Effect of noise, system gain, and assigned task on talking levels in loudspeaker communication," *J. Acoust. Soc. Am.* **40**, 955–965.
- Ginsburg, N. (1960). "Conditioned vocalization in the budgerigar," *J. Comp. Physiol. Psychol.* **53**, 183–186.
- Goehl, H., and Kaufman, D. (1984). "Do the effects of adventitious deafness include disordered speech," *J. Speech Hear. Dis.* **13**, 397–418.
- Heaton, J. T., Dooling, R. J., and Farabaugh, S. M. (submitted). "Effect of deafening on the vocalizations of adult budgerigars (*Melopsittacus undulatus*)," *J. Acoust. Soc. Am.*
- Konishi, M. (1963). "The role of auditory feedback in the vocal behavior of the domestic fowl," *Z. Tierpsychol.* **20**, 349–367.
- Konishi, M. (1964). "Effects of deafening on song development in two species of juncos," *Condor* **66**, 85–102.
- Konishi, M. (1965a). "The role of auditory feedback in the control of vocalization in the white-crowned sparrow," *Z. Tierpsychol.* **22**, 770–783.
- Konishi, M. (1965b). "Effects of deafening on song development in American robins and black-headed grosbeaks," *Z. Tierpsychol.* **22**, 584–599.
- Kroodasma, D. E., and Miller, E. H., Eds. (1982). *Acoustic Communication in Birds* (Academic, New York).

- Kroodsma, D. E., and Miller, E. H., Eds. (1996). *Ecology and Evolution of Acoustic Communication in Birds* (Cornell U.P., Ithaca, NY).
- Kroodsma, D. F., and Konishi, M. (1991). "A subsong bird (eastern phoebe, *Sayornis phoebe*) develops normal song without auditory feedback," *Animal Beh.* **42**, 477–487.
- Kuhl, P. K. (1989). "On babies, birds, modules, and mechanisms: A comparative approach to the acquisition of vocal communication," in *The Comparative Psychology of Audition: Perceiving Complex Sounds*, edited by R. J. Dooling and S. H. Hulse (Erlbaum, Hillsdale, NJ).
- Lancaster, W. C., Keating, A. W., and Henson, O. W. (1992). "Ultrasonic vocalization of flying bats monitored by radiotelemetry," *J. Exp. Biol.* **173**, 43–58.
- Lane, H. L., and Tranel, B. (1971). "The Lombard sign and the role of hearing in speech," *J. Speech Hear. Res.* **14**, 677–709.
- Lane, H. L., and Webster, J. W. (1991). "Speech deterioration in postlingually deafened adults," *J. Acoust. Soc. Am.* **89**, 859–866.
- Manabe, K., and Dooling, R. (1997). "Control of Vocal Production in Budgerigars (*Melopsittacus undulatus*): Selective Reinforcement, Call Differentiation, and Stimulus Control," *Behav. Proc.* **41**, 117–132.
- Manabe, K., Cleaveland, M. J., and Staddon, J. E. R. (1997). "Control of Vocal Repertoire by Reward in Budgerigars (*Melopsittacus undulatus*)," *J. Comp. Psych.* **111**, 50–62.
- Manabe, K., Kawashima T., and Staddon, J. E. R. (1995). "Differential vocalization in Budgerigars: Towards an experimental analysis of naming," *J. Exp. Anal. Behav.* **63**, 111–126.
- Marler, P., Konishi, M., Lutjen, A., and Waser, M. S. (1973). "Effects of continuous noise on avian hearing and vocal development," *Proc. Natl. Acad. Sci. USA* **70**, 1393–1396.
- Marler, P., Mundinger, P., Waser, M. S., and Lujen, A. (1972). "Effects of acoustical stimulation and deprivation on song development in the red-winged blackbird (*Agelaius phoeniceus*)," *Animal Beh.* **20**, 586–606.
- Martony, J. (1968). "On the correction of the voice pitch level for the severely hard of hearing subjects," *Am. Ann. Deaf.* **113**, 195–202.
- Monsen, R. B. (1978a). "Toward measuring how well hearing-impaired children speak," *J. Speech Hear. Res.* **21**, 197–219.
- Monsen, R. B. (1978b). "Acoustic qualities of phonation in young hearing-impaired children," *J. Speech Hear. Res.* **22**, 270–288.
- Monsen, R. B. (1979). "The production of labial occlusives in young hearing-impaired children," *Lang. Speech* **22**, 311–317.
- Nordeen, K. W., and Nordeen, E. J. (1992). "Auditory feedback is necessary for the maintenance of stereotyped song in adult zebra finches," *Behav. Neur. Biol.* **57**, 58–66.
- Nottebohm, F. (1968). "Auditory experience and song development in the chaffinch (*Fringilla coelebs*)," *Science* **110**, 549–568.
- Nottebohm, F., and Nottebohm, M. E. (1971). "Vocalizations and breeding behaviour of surgically deafened ring doves (*Streptopelia risoria*)," *Animal Beh.* **19**, 313–327.
- Pickett, J. M. (1958). "Limits of direct speech communication in noise," *J. Acoust. Soc. Am.* **30**, 278–281.
- Potash, L. M. (1972). "Noise induced changes in calls of the Japanese quail," *Psychon. Sci.* **26**, 252–254.
- Sadr, E. (1996). "The Lombard effect in Budgerigar (*Melopsittacus undulatus*) contact calls," Senior Honor's thesis submitted to the University of Maryland, College Park.
- Sinnott, J. M., Stebbins, W. C., and Moody, D. B. (1975). "Regulation of voice amplitude by the monkey," *J. Acoust. Soc. Am.* **58**, 412–414.
- Waldstein, R. S. (1990). "Effects of postlingual deafness on speech production: Implications for the role of auditory feedback," *J. Acoust. Soc. Am.* **88**, 2099–2114.
- Williams, H., Cynx, J., and Nottebohm, F. (1989). "Timbre control in zebra finch (*Taeniopygia guttata*) song syllables," *J. Comp. Psych.* **103**, 366–380.

Underwater audiogram of a tucuxi (*Sotalia fluviatilis guianensis*)

Matthias Sauerland

Universität Münster, Institut für Neuro- und Verhaltensbiologie, Badestrasse 9, D-48149 Münster, Germany

Guido Dehnhardt

Universität Bonn, Zoologisches Institut, Poppelsdorfer Schloss, D-53113 Bonn, Germany

(Received 7 May 1997; revised 4 September 1997; accepted 3 November 1997)

Using a go/no go response paradigm, a tucuxi (*Sotalia fluviatilis guianensis*) was trained to respond to pure-tone signals for an underwater hearing test. Auditory thresholds were obtained from 4 to 135 kHz. The audiogram curve shows that this *Sotalia* had an upper limit of hearing at 135 kHz; from 125 to 135 kHz sensitivity decreased by 475 dB/oct. This coincides with results from electrophysiological threshold measurements. The range of best hearing (defined as 10 dB from maximum sensitivity) was between 64 and 105 kHz. This range appears to be narrower and more restricted to higher frequencies in *Sotalia fluviatilis guianensis* than in other odontocete species that had been tested before. Peak frequencies of echolocation pulses reported from free-ranging *Sotalia* correspond with the range of most sensitive hearing of this test subject. © 1998 Acoustical Society of America. [S0001-4966(98)03802-8]

PACS numbers: 43.80.Lb [FD]

INTRODUCTION

Sotalia fluviatilis is one of the smallest delphinid species. Two forms are distinguished: a marine form, living along the east coast and in estuaries of northern South America, and a riverine form, inhabiting sections of the Orinoco and Amazon river system (Hershkovitz, 1962; for details, see Borobia *et al.*, 1991). Marine and riverine populations are apparently isolated from each other; they are considered as the subspecies *Sotalia fluviatilis fluviatilis* (Gervais, 1853), the riverine form, and *Sotalia fluviatilis guianensis* (van Beneden, 1864), the coastal and estuarine form. They produce pulses which are presumably used for echolocation (Wiersma, 1982; Kamminga, 1988; Kamminga *et al.*, 1993). However, little is known about the sensory abilities of *Sotalia*. The only available audiometric data is an audiogram of the riverine subspecies obtained with electrophysiological methods (Popov and Supin, 1990), indicating that *Sotalia* might be sensitive over a broader frequency band than most other odontocetes tested so far. To date, the widest frequency range of best hearing was observed in *Tursiops truncatus* (15–110 kHz) and *Delphinapterus leucas* (11–105 kHz) (Au, 1993). The frequency range of best hearing is arbitrarily defined as the bandwidth in which the auditory sensitivity is within 10 dB of the maximum sensitivity (White *et al.*, 1978; Thomas *et al.*, 1988; Au, 1993). Popov *et al.* (1986) supposed that the region of optimal auditory perception corresponds to the acoustic repertoire of an odontocete species.

At present, reliable underwater behavioral audiograms are only available for six odontocete species: *Tursiops truncatus* (Johnson, 1967), *Phocoena phocoena* (Andersen, 1970), *Orcinus orca* (Hall and Johnson, 1971), *Inia geoffrensis* (Jacobs and Hall, 1972), *Delphinapterus leucas* (White *et al.*, 1978), and *Pseudorca crassidens* (Thomas *et al.*, 1988). While all hearing curves have the typical mammalian U shape, the high-frequency cutoff is considered to be species specific (Thomas *et al.*, 1988).

Our objectives were to collect a behavioral underwater audiogram of a tucuxi to (1) relate the shape of the hearing curve to the peak frequency of the echolocation pulses of *Sotalia* and (2) discuss the hearing ability of *Sotalia fluviatilis guianensis* in comparison to those of other odontocetes.

I. METHODS

A. Subject

Two adult male *Sotalia fluviatilis guianensis* have been kept at the Dolphinarium Münster (Germany) since 1991. Both animals were caught in 1977 on the coast of San Antero, Colombia. When we started the experiment on auditory thresholds, they were about 20 years old. They took part in three to five shows daily, except during the winter months. One of them, "Paco," served as the main test subject. This animal was 1.7 m in length and weighed about 60 kg. Of the 3 to 4 kg of sprats and herring fed per day, about 0.5 kg could be used for reinforcement during hearing tests. Despite this small amount of fish available for a test session, a differential reinforcement scheme could have been applied, because the animals were well accustomed to accept half sprats as a reward. Tests were carried out once per day, 3–5 days per week from September 1993 to January 1995.

B. Apparatus

Threshold tests were conducted in the main pool of the Dolphinarium Münster. This concrete tank is rectangular in shape with dimensions of about 20 m (l) × 10 m (w) × 4 m (depth). Considerable background noise at frequencies below 1000 Hz was produced by the filtration system's pumps which worked continuously. Sessions at several test frequencies with pumps turned off proved that the pump noise did not affect the animal's performance. Therefore it was decided to conduct the test sessions without altering the acoustical environment the animal was familiar with. The ambient pool noise was measured at the animal's station using a Brüel & Kjær 8103 hydrophone, a Brüel & Kjær 2635

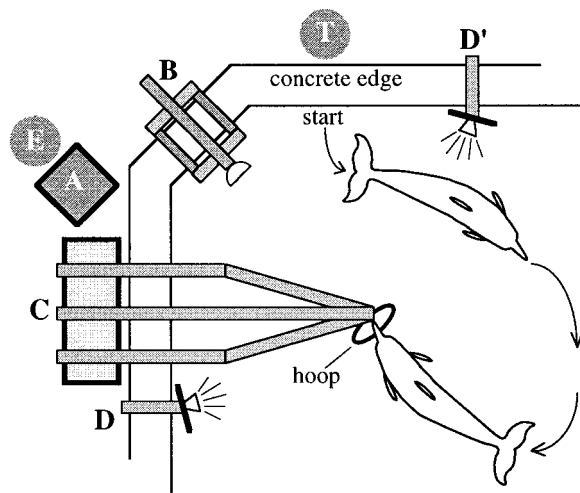


FIG. 1. Top view of the experimental setup: (A) box housing signal-controlling electronics, (B) device supporting the transducer, (C) device supporting the stationing hoop, (D/D') underwater lights, (E) experimenter, and (T) trainer.

charge amplifier, a set of octavepass filters, and a Tektronix oscilloscope model 5 A20N/5B10N. Noise was relatively consistent and decreased from 65 dB/(Hz^{1/2}) at 4 kHz to 52 dB/(Hz^{1/2}) at 16 kHz. At higher frequencies the ambient pool noise was below the measurement limits of our equipment.

The equipment setup is shown in Fig. 1. The electronic instruments were housed in a transportable box positioned adjacent to the concrete edge of the pool (A in Fig. 1). At one corner of the pool a device for installing the underwater transducer at variable water depths was mounted on the concrete edge (B in Fig. 1). Another device, holding a vertical pole supporting a hoop (30 cm in diameter) at the same depth as the transducer, was fixed close to the edge of the pool (C in Fig. 1). The hoop served as a station for the animal during trials. The distance between hoop and transducer was 2.5 m. When in the stationing position, the dolphin touched the hoop with the leading edge of its flippers and with its rostrum pointing to the position of the transducer. To both sides of the transducer an underwater light (D and D' in Fig. 1) was attached to the concrete edge, at the same depth as the hoop corresponding to the eyes of the dolphin.

Initially, considerable fluctuations of the received level of the test signal were measured at the animal's station, which presumably were caused by reflections from the water surface and the walls of the concrete pool. By varying the vertical positions of the transducer and the receiver (which were in most cases installed about 2 m below water surface) and by mounting the transducer within a styropor® (polystyrene) hemisphere (21 cm in diameter, 2-cm wall thickness), thereby enhancing the directivity of the Brüel & Kjær transducer, we were able to reduce signal fluctuations to 5 dB or less.

C. Stimuli

A programmable Kontron function generator (model 8022) produced the sinusoidal test signal. Rise-fall times of

the tests signal (150 ms) as well as the test signal length of 2 s were timed with a control generator connected to the AM-input of the function generator.

The test signal passed an attenuator (1 dB-steps possible) and a power amplifier (both custom designed) before going to the underwater transducer. Because of limitations of the signal transmitting equipment the lowest frequency tested was 4 kHz. For threshold measurements at 4 and 8 kHz a Brüel & Kjær 8104 hydrophone was used as a transducer. At 16, 32, 64, 85, 95, 105, 125, and 135 kHz the test signals were projected by a Brüel & Kjær 8103 hydrophone. The output level to the hydrophone was monitored by a Tektronix oscilloscope (model 5A20N/5B10N) and a Hewlett-Packard 3478 A digital multimeter.

D. Procedure

The animal had been trained by positive reinforcement techniques to perform test cycles according to a go/no go response paradigm. A trial started with the animal stationing at the trainer's hand ("start" position in Fig. 1, T=trainer). Following a hand cue, the dolphin immediately swam to the hoop (see Fig. 1), where it took up its stationing position in the hoop. The experimenter (E in Fig. 1) started the test by switching on the two underwater lights for 15 s thereby marking the beginning and the duration of a test cycle. After a 3-s delay the test signal was projected for 2 s. After another 10 s the lights went out, and the trainer signaled the end of the trial with a release tone by means of a training whistle. During signal-absent trials the procedure was the same, except for the missing test signal. If the animal detected a test signal, it immediately left the hoop and swam to the trainer (go response or "hit") where it received a piece of fish as a reward. In a signal-absent trial, the animal remained in its stationing position until the lights were switched off and the release whistle was given (no go response or "correct rejection"). In order to avoid unintentional cueing, the trainer did not know whether a trial was signal-present or signal-absent. At the end of each test cycle the experimenter informed the trainer of the kind of trial as well as whether the animals response behavior should be rewarded. The animal was not able to observe the experimenter's position at the pool side during a test cycle.

The trainer reinforced the animal's response behavior differentially. It received one fish for proper responses to signal-present trials and half a fish for proper responses to signal-absent trials. Using this type of reinforcement the intention was to bias the animal towards the go response. Remaining in the stationing position during signal-present trials or leaving the station prior to the release whistle ("false alarms") were designated as improper responses and were not rewarded.

The sequence of signal-present and signal-absent trials was based on a modified Gellerman random series table (Gellerman, 1933) with half of the trials being signal-absent. Thresholds were determined by using the "up/down" or "staircase" method, a variance of the method of limits, which results in a 50% correct detection threshold (Levitt, 1971; Gescheider, 1985). The experimenter attenuated the signal amplitude in 2-dB steps on each signal-present trial,

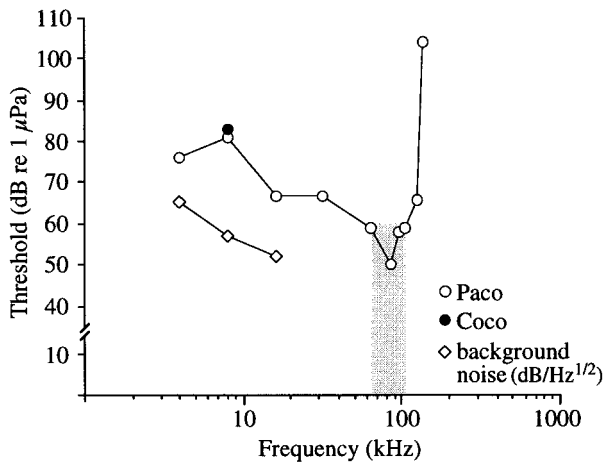


FIG. 2. Underwater behavioral audiogram of *Sotalia f. guianensis*. The grey shade marks the range of best hearing (defined as 10 dB from maximum sensitivity).

until the animal failed to respond to a test signal. The signal level was then increased in 2-dB steps, until the test subject responded “correctly” again, thereby indicating that it could detect the signal. Intensities at which the animal reversed its response behavior were taken as data points. The occurrence of false alarms did not alter the sequence of attenuator settings. Due to the relatively small amount of food that could be used for reinforcement, a day’s data collection merely consisted of 24–36 trials, of which 2–6 trials were reversals. We used the average of the signal levels at ten consecutive reversals for an estimation of the mean threshold at a given frequency. When the estimated thresholds of two consecutive blocks of ten transition points were within 3 dB, the overall threshold was calculated for the tested frequency. If they were the first two blocks, sessions were continued until the next two consecutive blocks with estimated thresholds within a 3-dB range were obtained. We decided to use the criterion of Thomas *et al.* (1988) for determination of high-frequency cutoff, which was based on a 120 dB/oct or greater decrease in sensitivity.

After having completed the collection of threshold data at all frequencies mentioned, mean thresholds were determined from another ten reversals at five frequencies (8, 32, 85, 105, and 135 kHz) in order to estimate the consistency of threshold data over a longer period of time. The time interval between sessions that had been conducted in the first place and the repetition of data collection at those frequencies was about one month (at 135 kHz) or more than one year (at 8 kHz), respectively.

It was also attempted to obtain auditory thresholds with “Coco,” the other *Sotalia* at the Dolphinarium Münster. However, working out the test cycle with this animal appeared to be extremely troublesome. It took one year of training to get a reliable response from this animal to 8-kHz signals with an amplitude well above threshold. However, the animal did not generalize the response to other test frequencies. Since it took several months of extra training to get a response to a new frequency the experiment was stopped with this animal after the successful determination of an absolute threshold at 8 kHz.

TABLE I. Absolute hearing thresholds of *Sotalia f. guianensis* (test subject “Paco”).

Test frequency (kHz)	Number of reversals	Mean thresholds (dB re: 1 μPa)	Range of threshold means (dB re: 1 μPa)	Mean thresholds in repetition tests (dB re: 1 μPa)
4	30	76	74–77	...
8	40	81	78–85	79
16	50	67	65–70	...
32	50	67	66–69	64
64	40	59	57–60	...
85	40	50	48–52	56
95	40	58	57–59	...
105	40	59	57–61	61
125	40	66	65–68	...
135	40	104	101–108	102

II. RESULTS

The hearing sensitivity of both animals is presented in Fig. 2. The overall thresholds and the range of mean values for blocks of ten reversals for each test frequency are shown in Table I. The data of the test subject Paco indicate an increasing sensitivity between 4 and 64 kHz at about 5 dB/oct. The range of best hearing, here defined as 10 dB from maximum sensitivity (which was 50 dB at 85 kHz), was between 64 and 105 kHz. Above 125 kHz the animal’s hearing sensitivity decreased sharply at 475 dB/oct. Therefore it was decided not to test at frequencies above 135 kHz. Estimated mean thresholds from replicated measurements of ten reversals at 8, 32, 85, 105, and 135 kHz were not more than 3 dB apart, except at 85 kHz where the animal’s performance decreased by 6 dB.

The only reliable hearing threshold determined for the test subject Coco was 83 dB at 8 kHz (filled circle in Fig. 2), which was higher by 2 dB than the mean threshold of Paco at the same frequency.

The overall false alarm rates for Paco at different test frequencies (Fig. 3) ranged from 0.7% to 10.8%. Most false alarms occurred at rather low frequencies outside the range of best hearing (except for 8 kHz).

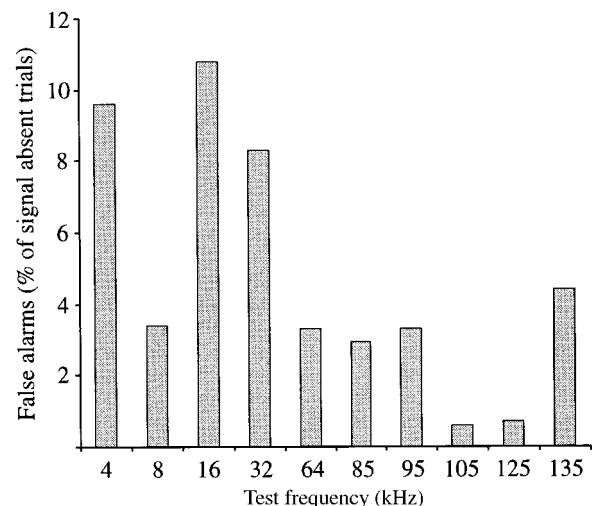


FIG. 3. False alarm rates of test subject Paco as a percentage of signal absent trials.

TABLE II. Comparative aspects of odontocete audiograms.

Species	Maximum sensitivity (dB re: 1 μ Pa)	Range of best hearing ^a (kHz)	Upper frequency limit (kHz)
<i>Tursiops truncatus</i>	42	15–110	150
<i>Phocoena phocoena</i>	47	3–70	150
<i>Orcinus orca</i>	34	15–30	120
<i>Inia geoffrensis</i>	51	12–64	100
<i>Delphinapterus leucas</i>	40	11–105	120
<i>Pseudorca crassidens</i>	39	17–74	115
<i>Sotalia f. guianensis</i>	50	64–105	135

^aDefined as 10 dB from maximum sensitivity.

III. DISCUSSION

The underwater audiogram of *Sotalia fluviatilis guianensis* shows a U-shaped hearing curve which is similar to those of other odontocete species, except for the lowest frequencies measured. At 4 kHz the animal was a little more sensitive than at 8 kHz. From 8 to 64 kHz hearing sensitivity improves at about 5 dB/oct. The audiogram obtained in this study suggests that the most sensitive hearing range in *Sotalia fluviatilis guianensis* is between 64 and 105 kHz (if defined as 10 dB from maximum sensitivity). Only *Tursiops* and *Delphinapterus* have approximately the same hearing sensitivity at this frequency range (Johnson, 1967; White *et al.*, 1978). However, in their range of best hearing most other odontocete species are much more sensitive than *Sotalia fluviatilis guianensis*, except *Phocoena* and *Inia* (Table II).

The comparatively low false alarm rate of the test subject Paco (see Fig. 3) seems to be typical for marine mammals (Schusterman and Johnson, 1975; Schusterman, 1974, 1976). It results from the subject's tendency to respond conservatively by indicating the presence of a signal only in cases where it is strictly confident of perceiving one, though we tried to counteract such a response bias by differential reinforcement (hit:correct rejection=2:1 fish). As such a response behavior results in a low probability of detection score (Au, 1993), the present data might represent a relatively conservative estimate of the auditory abilities of *Sotalia fluviatilis guianensis*. However, this should not affect the shape of the audiogram.

Although the range of best hearing is defined arbitrarily, it appears to be narrower and more restricted to higher frequencies in *Sotalia fluviatilis guianensis* than in other odontocete species (Table II). Hearing sensitivity of our *Sotalia* decreases sharply above 125 kHz, at 475 dB/oct. The upper frequency limit of hearing is concluded to be at, or somewhat beyond 135 kHz, with a threshold 54 dB above maximum sensitivity, which is close to the 60-dB criterion established by Fay for land mammals (Fay, 1992). This frequency limit is only exceeded by *Tursiops* and *Phocoena* (150 kHz; Table II).

Like most studies on auditory abilities of odontocetes this study is based on a single subject. The question remains whether the results presented here do indeed represent hearing characteristics of *Sotalia fluviatilis guianensis*. Regarding the threshold estimate at the lower frequency range (4–16

kHz) one should consider that the animal's performance might have been affected by noise masking. As the critical ratio for *Sotalia fluviatilis* is unknown, the critical ratio for *Tursiops truncatus* (Johnson, 1968; Au and Moore, 1990) might serve as a rough estimate, indicating that background noise may have limited the hearing abilities of the test subject at the lower frequencies. However, one also needs to know the received directivity index to determine if background noise has interfered with the threshold estimate. This parameter has also not been measured for *Sotalia fluviatilis* so far.

We were able to measure a threshold for a second animal (Coco) only at 8 kHz. Compared to the subject Paco, the mean threshold of this subject indicates that it is less sensitive by only 2 dB. This is within the normal range of estimated threshold means of the subject Paco, especially if one considers that even the estimated means from replicated threshold measurements at five frequencies may differ by a certain amount from the means measured originally (Table I). However, the threshold estimate of the second subject also confirms that there is a consistent threshold shift at 8 kHz, compared to the general audiogram curve, in both dolphins. Acoustic trauma experiments with land mammals (including man) reveal that long-term exposures to low-frequency sound may produce an upward spread of threshold shifts along the frequency dimension (see, e.g., Clark *et al.*, 1974; Patterson *et al.*, 1977; Burdick *et al.*, 1978; Lonsbury-Martin *et al.*, 1987; Grenner *et al.*, 1988). Recent studies conducted by Ridgway and Carder (1993, 1997), emphasizing the effect of aging on hearing deficits at high frequencies, suggest that hearing loss in dolphins results from similar mechanisms as in land mammals. Therefore we suspect that the notch in the audiogram at 8 kHz (and possibly some hearing loss at low frequencies in general) may result from a threshold shift due to long-term exposure to low-frequency pump noise.

Popov and Supin (1990) measured auditory brain stem response (ABR) thresholds of a tucuxi. Their audiogram of *Sotalia f. fluviatilis* is similar in shape to the behavioral audiogram that we obtained for *Sotalia fluviatilis guianensis*, although the frequency band over which our test subject Paco is sensitive appears to be much narrower than the ABR data might indicate. Popov and Supin determined the upper frequency limit of hearing at 140 kHz (here defined as a threshold level 60 dB above minimum thresholds). This coincides very well with the upper hearing limit of our test animal Paco. Moreover, the lower thresholds of our behavioral audiogram compared to the data measured by Popov and Supin reveal the typical discrepancy of thresholds measured by means of behavioral methods versus electrophysiological in studies with well-controlled conditions (Bleckmann, 1994).

Kamminga (1988) and Kamminga *et al.* (1993) reported that free-ranging animals of both subspecies of *Sotalia* produce echolocation pulses with peak frequencies at 80–95 kHz. *Sotalia f. guianensis* also produces a second peak at 30 kHz. The frequency range of maximum sensitivity in our test animal corresponds well with the records from free-ranging individuals, indicating that auditory sensitivity and echoloca-

tion signals are well suited to each other. Correspondence between auditory sensitivity and vocal characteristics, especially vocal signals that serve to maximize transmission distance have been shown for a number of mammals and birds (for a review, see Sales and Pye, 1974; Dooling, 1980). However, in a number of odontocete species it has been shown that the peak frequency and spectral shape of echolocation signals is a function of the source level (Au *et al.*, 1995). The source level used for signal production is influenced by several factors including background noise and reverberation (Au, 1993). Accordingly, in a noisy environment peak frequencies of echolocation signals of odontocetes like *Tursiops truncatus*, *Pseudorca crassidens*, and *Delphinapterus leucas* are usually above the range of best hearing and approach their upper hearing limit (Au, 1980; Au *et al.*, 1985; Thomas and Turl, 1990). At least some delphinid species obviously possess highly adaptive echolocation systems, with signal characteristics actively optimized depending on the specific echolocation task (Au *et al.*, 1985; Moore and Pawloski, 1990; Au *et al.*, 1995). However, there are a number of small odontocete species (predominantly from the family Phocoenidae) that seem to emit high-frequency, narrow-band echolocation signals which do not differ with the condition of recording (Au, 1993). Apparently, this point also applies to *Sotalia fluviatilis* (Wiersma, 1982; Kamminga, 1988; Kamminga *et al.*, 1993), suggesting that the echolocation system of this species might have been exposed to similar evolutionary constraints like those of some phocoenid species.

According to Ketten and Wartzok (1990) and Ketten (1992) delphinids living in coastal habitats, estuaries, or rivers require relatively high-frequency echolocation signals to differentiate objects in such structurally complex environments. Though not all audiograms known to date are consistent with this hypothesis (see *Inia geoffrensis*, Table II), our data on *Sotalia fluviatilis guianensis* also suggest that the specialization for upper range ultrasonic audition might be correlated to the habitat characteristics mentioned above. However, we suppose that comparative studies on frequency differentiation abilities could be even more suitable to shed some light on the adaptation of auditory characteristics of different delphinid species to the environment they inhabit.

ACKNOWLEDGMENTS

We are grateful to Ralf Schalk, technical engineer at University Paderborn (Germany), for designing and constructing some of the signal-controlling electronics. Thanks are also due to the training staff at the dolphinarium Münster for their assistance during this study. We are especially indebted to Gerti Dücker of University Münster for her support and encouragement.

- Andersen, S. (1970). "Auditory sensitivity of the harbor porpoise, *Phocoena phocoena*," in *Investigations on Cetacea*, edited by G. Pilleri (Benteli AB, Bern), Vol. 2, pp. 255–258.
- Au, W. W. L. (1980). "Echolocation signals of the Atlantic bottlenose dolphin (*Tursiops truncatus*) in open waters," in *Animal Sonar Systems*, edited by R. G. Busnel and J. F. Fish (Plenum, New York), pp. 251–282.
- Au, W. W. L. (1993). *The Sonar of Dolphins* (Springer-Verlag, New York).

- Au, W. W. L., Carder, D. A., Penner, R. H., and Scronce, B. L. (1985). "Demonstration of adaptation in beluga whale echolocation signals," *J. Acoust. Soc. Am.* **77**, 726–730.
- Au, W. W. L., and Moore, P. W. B. (1990). "Critical ratio and critical bandwidth for the Atlantic bottlenose dolphin," *J. Acoust. Soc. Am.* **88**, 1635–1638.
- Au, W. W. L., Pawloski, J. L., Nachtigall, P. E., Blonz, M., and Gisner, R. C. (1995). "Echolocation signals and transmission beam pattern of a false killer whale (*Pseudorca crassidens*)," *J. Acoust. Soc. Am.* **98**, 51–59.
- Bleckmann, H. (1994). *Progress in Zoology, Vol. 41: Reception of Hydrodynamic Stimuli in Aquatic and Semiaquatic Animals* (Fischer, Stuttgart).
- Borobia, M., Siciliano, S., Lodi, L., and Hoek, W. (1991). "Distribution of the South American dolphin *Sotalia fluviatilis*," *Can. J. Zool.* **69**, 1025–1039.
- Burdick, C. K., Patterson, J. H., Mozo, B. T., and Camp, Jr., R. T. (1978). "Threshold shifts in chinchillas exposed to octave bands of noise centered at 63 and 1000 Hz for three days," *J. Acoust. Soc. Am.* **64**, 458–466.
- Clark, W. W., Clark, C. S., Moody, D. B., and Stebbins, W. C. (1974). "Noise-induced hearing loss in the chinchilla, as determined by a positive-reinforcement technique," *J. Acoust. Soc. Am.* **56**, 1202–1209.
- Dooling, R. J. (1980). "Behavior and psychophysics of hearing in birds," in *Comparative Studies of Hearing in Vertebrates*, edited by A. N. Popper and R. R. Fay (Springer-Verlag, New York), pp. 261–288.
- Fay, R. R. (1992). "Structure and function in sound discrimination among vertebrates," in *The Evolutionary Biology of Hearing*, edited by D. B. Webster, R. R. Fay, and A. N. Popper (Springer-Verlag, New York), pp. 229–263.
- Gellermann, L. W. (1933). "Chance orders of alternating stimuli in visual discrimination experiments," *J. Gen. Psychol.* **42**, 206–208.
- Gescheider, G. A. (1985). *Psychophysics. Method and Theory* (Erlbaum, Hillsdale, NJ).
- Grenner, J., Nilsson, P., Sheppard, H., and Katbamna, B. (1988). "Action potential threshold elevation in the guinea-pig as a function of impact noise exposure energy," *Audiology* **27**, 356–366.
- Hall, J., and Johnson, C. S. (1971). "Auditory thresholds of a killer whale, *Orcinus orca* Linnaeus," *J. Acoust. Soc. Am.* **51**, 515–517.
- Hershkovitz, P. (1962). "Notes on South American dolphins of the genera *Inia*, *Sotalia*, and *Tursiops*," *J. Mamm.* **44**, 98–103.
- Jacobs, D. W., and Hall, J. D. (1972). "Auditory thresholds of a fresh water dolphin, *Inia geoffrensis* Blainville," *J. Acoust. Soc. Am.* **51**, 530–533.
- Johnson, C. S. (1967). "Sound detection thresholds in marine mammals," in *Marine Bioacoustics*, edited by W. N. Tavolga (Pergamon, New York), Vol. 2, pp. 247–260.
- Johnson, C. S. (1968). "Masked tonal thresholds in the bottlenosed porpoise," *J. Acoust. Soc. Am.* **44**, 965–967.
- Kamminga, C. (1988). "Echolocation signal types of odontocetes," in *Animal Sonar. Processes and Performance*, edited by P. E. Nachtigall and P. W. B. Moore (Plenum, New York), pp. 9–22.
- Kamminga, C., van Hove, M. T., Engelsma, F. J., and Terry, R. P. (1993). "Investigations on Cetacean Sonar X: A comparative analysis of underwater echolocation clicks of *Inia* spp. and *Sotalia* spp.," *Aquat. Mamm.* **19**, 31–43.
- Ketten, D. R. (1992). "The mammal ear: Specializations for aquatic audition and echolocation," in *The Evolutionary Biology of Hearing*, edited by D. A. Webster, R. R. Fay, and A. N. Popper (Springer-Verlag, New York), pp. 717–750.
- Ketten, D. R., and Wartzok, D. (1990). "Three-dimensional reconstruction of the dolphin ear," in *Sensory Abilities of Cetaceans. Laboratory and Field Evidence*, edited by J. A. Thomas and R. A. Kastelein (Plenum, New York), pp. 81–105.
- Levitt, H. (1971). "Transformed up-down methods in psychoacoustics," *J. Acoust. Soc. Am.* **49**, 467–477.
- Lonsbury-Martin, B. L., Martin, G. K., and Bohne, B. A. (1987). "Repeated TTS exposures in monkeys: Alterations in hearing, cochlear structure, and single-unit thresholds," *J. Acoust. Soc. Am.* **81**, 1507–1518.
- Moore, P. W. B., and Pawloski, D. (1990). "Investigations of the control of echolocation pulses in the dolphin (*Tursiops truncatus*)," in *Cetacean Sensory Systems: Laboratory and Field Evidence*, edited by J. A. Thomas

- and R. A. Kastelein (Plenum, New York), pp. 305–316.
- Patterson, J. H., Burdick, C. K., Mozo, B. T., and Camp, Jr., R. T. (1977). “Temporal threshold shift in man resulting from 4-hr exposures to octave bands of noise centered at 63 and 1000 Hz,” *J. Acoust. Soc. Am. Suppl.* 1 **62**, S95.
- Popov, V. V., Ladygina, T. F., and Supin, A. Ya. (1986). “Evoked potentials of the auditory cortex of the porpoise, *Phocoena phocoena*,” *J. Comp. Physiol. A* **158**, 705–711.
- Popov, V., and Supin, A. (1990). “Electrophysiological studies of hearing in some cetaceans and a manatee,” in *Sensory Abilities of Cetaceans. Laboratory and Field Evidence*, edited by J. A. Thomas and R. A. Kastelein (Plenum, New York), pp. 405–415.
- Ridgway, S. H., and Carder, D. A. (1993). “High-frequency hearing loss in old (25+ years old) male dolphins,” *J. Acoust. Soc. Am.* **94**, 1830.
- Ridgway, S. H., and Carder, D. A. (1997). “Hearing deficits measured in some *Tursiops truncatus*, and discovery of a deaf/mute dolphin,” *J. Acoust. Soc. Am.* **101**, 590–594.
- Sales, G., and Pye, D. (1974). *Ultrasonic Communication by Animals* (Chapman and Hall, London).
- Schusterman, R. J. (1974). “Low false-alarm rates in signal detection by marine mammals,” *J. Acoust. Soc. Am.* **55**, 845–848.
- Schusterman, R. J. (1976). “California sea lion underwater auditory detection and variation of reinforcement schedules,” *J. Acoust. Soc. Am.* **59**, 997–1000.
- Schusterman, R. J., and Johnson, B. W. (1975). “Signal probability and response bias in California sea lions,” *Psychol. Rec.* **25**, 39–45.
- Thomas, J., Chun, N., Au, W., and Pugh, K. (1988). “Underwater audiogram of a false killer whale (*Pseudorca crassidens*),” *J. Acoust. Soc. Am.* **84**, 936–940.
- Thomas, J. A., and Turl, C. W. (1990). “Echolocation characteristics and range detection threshold of a false killer whale (*Pseudorca crassidens*),” in *Sensory Abilities of Cetaceans Laboratory and Field Evidence*, edited by J. A. Thomas and R. A. Kastelein (Plenum, New York), pp. 321–334.
- White, Jr., M. J., Norris, J., Ljungblad, D., Barton, K., and di Sciara, G. (1978). “Auditory thresholds of two belukha whales (*Delphinapterus leucas*),” in HSWRI Technical Report, No. 78-109, Hubbs Marine Research Institute.
- Wiersma, H. (1982). “Investigations on cetacean sonar IV: A comparison of wave shapes of odontocete sonar signals,” *Aquat. Mamm.* **9**, 57–67.

LETTERS TO THE EDITOR

This Letters section is for publishing (a) brief acoustical research or applied acoustical reports, (b) comments on articles or letters previously published in this Journal, and (c) a reply by the article author to criticism by the Letter author in (b). Extensive reports should be submitted as articles, not in a letter series. Letters are peer-reviewed on the same basis as articles, but usually require less review time before acceptance. Letters cannot exceed four printed pages (approximately 3000–4000 words) including figures, tables, references, and a required abstract of about 100 words.

A note on transient underwater bubble sound

Johan L. Leander

Department of Military Technology, National Defence College, P.O. Box 27805, S-11593 Stockholm, Sweden

(Received 17 April 1997; revised 30 September 1997; accepted 10 October 1997)

This Letter considers scattered sound from transiently oscillating gas bubbles in liquids. The full transient problem including the finite duration of the excitation is analyzed. As a result, the wave front of the radiated sound pulse involving information about the excitation is also studied. The model presented is used to simulate sound pulses from sea-surface bubbles which have been generated by, for example, spilling breakers, capillary-gravity waves, and rain drops. Although very simple in relation to the actual physical process of excitation, this model enables us to predict some of the essential properties of scattered pulses observed experimentally. It is suggested that the time scale of duration of the initial driving that enters into the present analysis might be of some use in a further physical understanding of bubble generation and excitation. © 1998 Acoustical Society of America. [S0001-4966(98)01902-X]

PACS numbers: 43.20.Px, 43.30.Nb [JEG]

INTRODUCTION

The presence of gas bubbles in the sea is of great interest in numerous technical applications from which many concern underwater acoustics.^{1–4} In traveling through a gas–liquid suspension, an acoustic wave can be highly influenced by, for example, attenuation, dispersion, and reflection.^{3,5–7} As a consequence, there exist a variety of sound based methods for the prediction of the amount of bubbles in the sea.^{1–4,8,9} However, yet another aspect of the presence of gas bubbles is that they may also act as separate sound sources and thus contribute to the overall ambient noise level.^{3,9,10} Some examples of natural bubble generation in the sea are wind induced breaking waves, capillary-gravity waves, and rain drops falling on the air–liquid interface.^{4,8–15} Due to the above mentioned processes, bubbles can be brought into or generated in the sea-surface layer and then set into transient motion. The resulting scattered sound pulses and, in particular, the induced acoustic power have been of major concern in a number of recent investigations.^{8–15} From the vast amount of experimental data reported it is found that, to a first approximation, the gas bubbles act as linear spherical sources oscillating with the breathing mode.^{4,9–12,14} Also, due to the interaction with the sea surface the total acoustic field has the character of a transient dipole. By modeling a gas bubble as a linear damped oscillator one can extract information from experimentally obtained sound pulses. Typical examples are the equilibrium bubble radius, transient frequency, damping constant, source strength, and power

spectrum. In all the above investigations, free (undriven) linear oscillations are assumed corresponding to a simple exponentially damped sinusoid. This is indeed justified in looking for the quantities mentioned.

The objective of this Letter is to consider driven pulsations where the bubble undergoes an excitation of finite duration. This means that we solve the full transient problem corresponding to a nonhomogeneous “bubble equation.” As a result, we also model the wave front of the scattered pulses including information about the excitation. This means that a time scale related to the duration of the excitation enters into the analysis. This might be of some use for a further understanding of the generation and excitation of gas bubbles. By manipulation with the governing parameters we are able to simulate scattered pulses, which to a great extent agree well with experimentally obtained data. It is finally noted that although the model presented here has been used as a tool for wind, wave, and rain drop induced underwater transient bubble sound, it actually represents a model for the transient interaction process between a pressure pulse and a gas bubble in a liquid. This is a separate result in itself, which is of interest in for example investigations concerning transient wave propagation in bubbly liquids.⁶

I. MONOCHROMATIC MOTION

In searching for sound pulses from transiently oscillating gas bubbles near the sea surface we first consider sound radiated from a gas bubble undergoing sinusoidal pulsations in

an unbounded liquid. The complex amplitude, $P_{\text{rad}}(r, \omega)$, for the radiated sound from a spherical source is given by³

$$P_{\text{rad}}(r, \omega) = \frac{A}{r} \exp(-ik_0 r), \quad (1)$$

where A is a complex constant and r is the range from the bubble center to the point of observation. The wave number in the surrounding ideal liquid is $k_0 = \omega/c_0$, where ω is the angular frequency and c_0 is the corresponding speed of sound. We also need the particle velocity which is³

$$U(r, \omega) = \frac{A}{r\rho_0 c_0} \left[\frac{1 + ik_0 r}{ik_0 r} \right] \exp(-ik_0 r), \quad (2)$$

where ρ_0 is the liquid density. In order to relate the radiated sound to the excitation, $P_{\text{exc}}(R_0, \omega)$, we look at the bubble surface and find

$$U(R_0, \omega) = i\omega\Delta R, \quad (3)$$

where ΔR denotes the radial displacement and R_0 is the equilibrium bubble radius. ΔR can be expressed in terms of $P_{\text{exc}}(R_0, \omega)$ as⁵

$$\Delta R = -\frac{1 + ik_0 R_0}{\rho_0 R_0 D(\omega)} P_{\text{exc}}(R_0, \omega), \quad (4)$$

where

$$D(\omega) = \omega_t^2 - \omega^2 [1 + 2R_0(\beta_v + \beta_t)/c_0] + i\omega[2(\beta_v + \beta_t) + \omega_t^2 R_0/c_0]. \quad (5)$$

The bubble resonance frequency is ω_t and the viscous and thermal damping functions are denoted as β_v and β_t , respectively. From Eqs. (1)–(4) we finally have

$$P_{\text{rad}}(r, \omega) = P_{\text{exc}}(R_0, \omega) \frac{R_0 \omega^2}{rD(\omega)} \exp[-i\omega(r - R_0)/c_0]. \quad (6)$$

II. TRANSIENT MOTION

We now consider transient bubble oscillations and the complex amplitudes, $P_{\text{rad}}(r, \omega)$ and $P_{\text{exc}}(R_0, \omega)$ are from here on interpreted as Fourier transforms.¹⁶ The transiently scattered pressure profile is thus found on the form

$$P_{\text{rad}}(r, t) = \frac{1}{2\pi} \int_{-\infty}^{\infty} P_{\text{rad}}(r, \omega) \exp(i\omega t) d\omega, \quad (7)$$

where $P_{\text{rad}}(r, \omega)$ is given by Eq. (6). The next step is to find a relevant expression for the acoustic excitation of the gas bubble. Medwin *et al.* denote the driving as shock excited (very short duration), which in this problem means that the excitation is short in relation to the period of the subsequent transient oscillation, as will be clear in the following discussion.^{4,9} In the investigation by Oguz and Prosperetti concerning rain drop induced bubble sound one solved the homogeneous equation and used initial conditions for the radial displacement and its velocity that were positive.¹³ This indicates that we shall use a negative excitation pulse so that the bubble starts with an expanding response. Lastly, it is indeed convenient to work with analytical results so we sim-

ply choose a negative symmetric triangular driving pulse with the Fourier transform¹⁶

$$P_{\text{exc}}(R_0, \omega) = -\frac{4 \sin^2(\omega T_{\text{exc}}/2)}{T_{\text{exc}} \omega^2} \exp(-i\omega T_{\text{exc}}), \quad (8)$$

where the duration is $2T_{\text{exc}}$. In order to evaluate the Fourier integral in Eq. (7) analytically we use the fact that the quantity $D(\omega)$ in Eq. (5) can be conveniently approximated so that it becomes a polynomial in ω . This is done by evaluating $\omega_t(\omega)$ and $\beta_t(\omega)$ for the adiabatic resonance frequency, ω_a ,

$$\omega_a^2 = \frac{P_{b0}}{\rho_0 R_0^2} \left[3\gamma - \frac{2\sigma}{R_0 P_{b0}} \right], \quad (9)$$

where the quantities P_{b0} , γ and σ are the equilibrium pressure in the bubble, the ratio of the specific heats of the gas and the surface tension, respectively. With this approximation, $\omega_t \approx \omega_t(\omega_a)$ and $\beta_t \approx \beta_t(\omega_a)$, the inversion yields the following sum of exponentially damped sinusoids

$$P_{\text{rad}}(r, t + t_0) = g(r, t) - 2g(r, t - T_{\text{exc}}) + g(r, t - 2T_{\text{exc}}), \quad (10)$$

where

$$g(r, t) = \frac{-R_0}{rB\omega_{\text{free}}\beta_{\text{free}}T_{\text{exc}}} \exp(-\beta_{\text{free}}t) \sin(\omega_{\text{free}}t) \quad t \geq 0, \quad (11)$$

and

$$g(r, t) = 0 \quad t < 0. \quad (12)$$

The quantity $t_0 = (r - R_0)/c_0$ is the retarded time and the eigenfrequency, $\omega_{\text{eig}} = \omega_{\text{free}} + i\beta_{\text{free}}$,

$$\omega_{\text{free}}^2 = \frac{\omega_t^2(\omega_a)}{B} - \beta_{\text{free}}^2, \quad (13)$$

where

$$B = 1 + 2R_0[\beta_v + \beta_t(\omega_a)]/c_0, \quad (14)$$

and

$$\beta_{\text{free}} = \frac{2[\beta_v + \beta_t(\omega_a)] + \omega_t^2(\omega_a)R_0/c_0}{2B}. \quad (15)$$

Before continuing, it is perhaps relevant to note that in this work the details of the true excitation process are ignored. Instead, the process is taken to be that of a gas bubble, initially at rest in a liquid, which is hit by a negative pressure pulse. In order to compare our simulations with experimental data we have to model the reflection from the sea surface. If we consider pulses along the vertical below the air-liquid interface the total pressure is given by

$$P_{\text{tot}}(r, t) = P_{\text{rad}}(r, t) - P_{\text{rad}}(r + 2L, t - 2L/c_0), \quad (16)$$

where L is the depth of the bubble. Also, multiple scattering effects where the bubble is reexcited by the sea-surface reflection are neglected.⁷ The parameters of interest in the simulations are the bubble depth L , the equilibrium bubble radius R_0 , the distance to the observation r and the duration of the excitation $2T_{\text{exc}}$ (where we simply use T_{exc}). From the literature we find that the depth can be of the order of a few

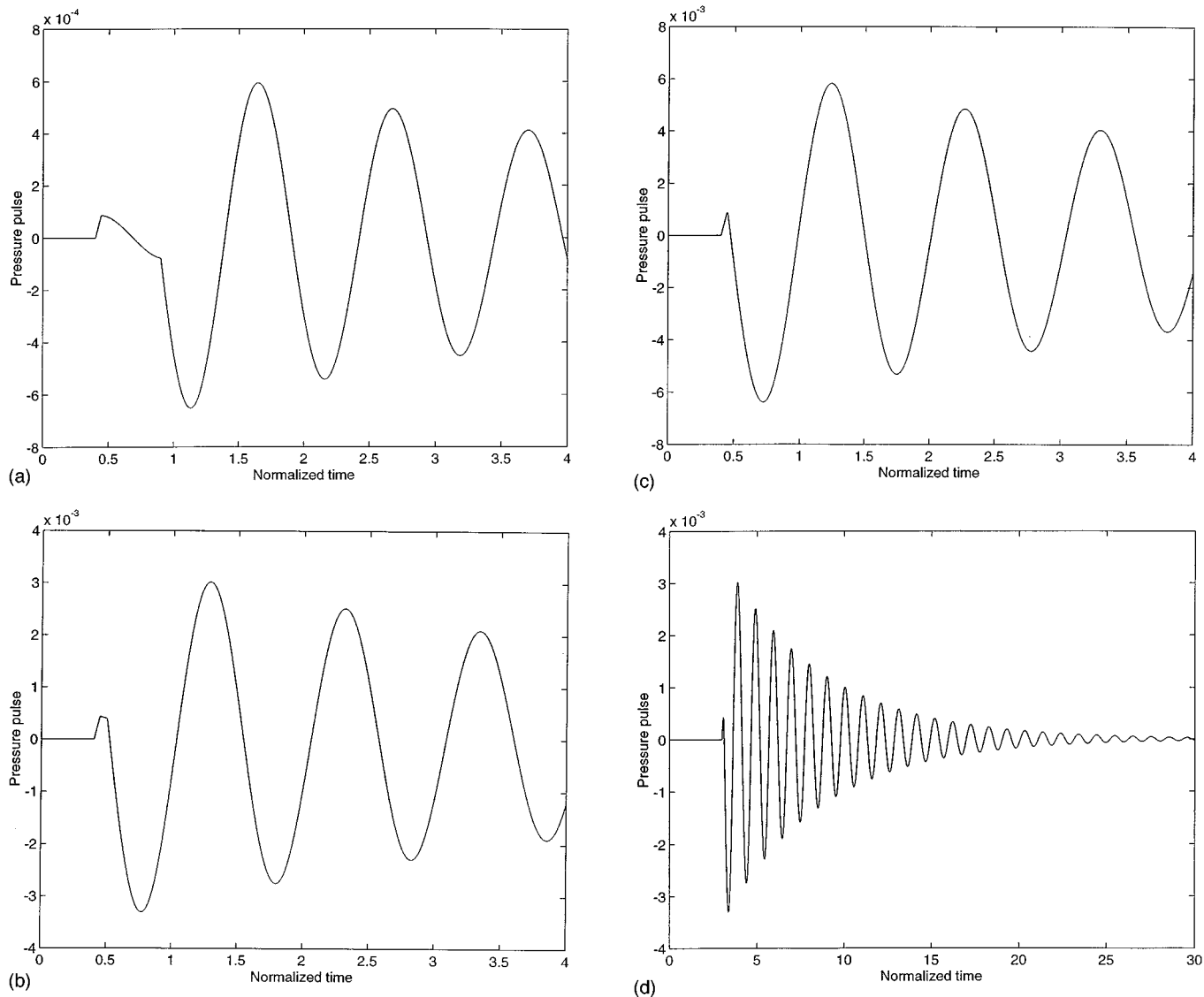


FIG. 1. Total pressure $p_{\text{tot}}(r,t)$ as function of normalized time $t^* = t\omega_d/2\pi$. Bubble depth, $L=3$ mm. Observation distance, $r=3$ dm. (a) $T_{\text{exc}} = \omega_d/4\pi$. (b) $T_{\text{exc}} = \omega_d/20\pi$. (c) $T_{\text{exc}} = \omega_d/40\pi$. (d) Same as (b) but with enlarged time window.

millimeters.^{9,11,13} Moreover, the equilibrium radius is usually in the range, say, 200–400 micrometers and the distance to the observer is of the order of a few decimeters.^{4,9,11–15} Note here that information about the duration of the excitation is missing. With respect to the above numbers and the fact that *three* is the overall lucky number we consider pulses from a 300 micron bubble at a depth of 3 mm observed at a distance of 3 dm. In Fig. 1(a)–(c) some results are shown where we have varied the duration of the excitation. As the excitation becomes shorter a sharp positive initial peak is observed before the exponentially damped sinusoid dominates the picture. The amplitudes in the figures are normalized in the sense that we are dealing with linear analysis and that the maximum amplitude of the driver is set equal to unity. By comparing Fig. 1(d), with the experimentally observed result by Medwin *et al.*¹² (Fig. 4 in their paper) we find a reasonable agreement. This is of course encouraging and it might be suggested that the new parameter introduced in our analysis (the excitation time) can be of some use for a further

physical understanding of underwater transient bubble sound. Let us finally note that the model presented here concerns the transient interaction between a gas bubble and a pulse in a liquid. This is a result in itself and can for example be of use in studying pulses in bubbly liquids.⁶

III. CONCLUSIONS

We have presented in this work a simple model for the interaction of a pressure wave and a gas bubble in a liquid. It can be used in several contexts and we have here considered pulses from wind, capillarity-gravity, and rain drop induced bubbles in the sea. By assuming that a gas bubble also behaves as a linear damped oscillator during the excitation phase, we have been able to simulate pulses which exhibit the essential properties observed in experiments. The true physical generation/excitation has been disregarded and we have simply considered a bubble initially at rest below the sea surface which is suddenly excited by a short acoustic

driver. The time scale of duration of the excitation that enters into our analysis is suggested as a possible tool for further work on the subject.

- ¹H. Medwin, "In situ acoustic measurements of bubble populations in coastal ocean waters," *J. Geophys. Res.* **75**, 599–611 (1970).
- ²H. Medwin, "Acoustic fluctuations due to microbubbles in the near-surface ocean," *J. Acoust. Soc. Am.* **56**, 1100–1104 (1974).
- ³C. S. Clay and H. Medwin, *Acoustical Oceanography: Principles and Applications* (Wiley, New York, 1977).
- ⁴H. Medwin and A. C. Daniel, Jr., "Acoustical measurements of bubble production by spilling breakers," *J. Acoust. Soc. Am.* **88**, 408–412 (1990).
- ⁵K. W. Commander and A. Prosperetti, "Linear pressure waves in bubbly liquids: Comparison between theory and experiments," *J. Acoust. Soc. Am.* **85**, 732–746 (1989).
- ⁶J. L. Leander, "Transient wave propagation through bubbly layers via the Foldy–Twersky integral equation," *J. Acoust. Soc. Am.* **95**, 2378–2386 (1994).
- ⁷J. L. Leander, "Sound propagation in dilute gas–liquid suspensions: Definition of the regime of noninteracting bubbles via scattering theory and the causality approach," *J. Acoust. Soc. Am.* **97**, 1974–1977 (1995).
- ⁸N. Breitz and H. Medwin, "Instrumentation for *in situ* acoustical measurements of bubble spectra under breaking waves," *J. Acoust. Soc. Am.* **86**, 739–743 (1989).
- ⁹H. Medwin and M. M. Beaky, "Bubble sources of the Knudsen sea noise spectra," *J. Acoust. Soc. Am.* **86**, 1124–1130 (1989).
- ¹⁰A. R. Kolaini, L. A. Crum, and R. A. Roy, "Bubble production by capillary-gravity waves," *J. Acoust. Soc. Am.* **95**, 1913–1921 (1994).
- ¹¹H. C. Pumphrey and L. A. Crum, "Free oscillations of near-surface bubbles as a source of the underwater noise of rain," *J. Acoust. Soc. Am.* **87**, 142–148 (1990).
- ¹²H. Medwin, A. Kurgan, and J. A. Nystuen, "Impact and bubble sound from raindrops at normal and oblique incidence," *J. Acoust. Soc. Am.* **88**, 413–418 (1990).
- ¹³H. N. Oguz and A. Prosperetti, "Numerical calculation of the underwater noise of rain," *J. Fluid Mech.* **228**, 417–442 (1991).
- ¹⁴J. S. Stroud and P. L. Marston, "Optical detection of transient bubble oscillations associated with the underwater noise of rain," *J. Acoust. Soc. Am.* **94**, 2788–2792 (1993).
- ¹⁵J. A. Nystuen and H. Medwin, "Underwater sound produced by rainfall: Secondary splashes of aerosols," *J. Acoust. Soc. Am.* **97**, 1606–1613 (1995).
- ¹⁶A. Papoulis, *The Fourier Integral and Its Applications* (McGraw-Hill, New York, 1962).

Acoustic scattering from two junctions in a rectangular waveguide

Jae Y. Kwon, Hyun H. Park, and Hyo J. Eom

Department of Electrical Engineering, Korea Advanced Institute of Science and Technology, 373-1, Kusong Dong, Yuseong Gu, Taejeon, Korea

(Received 20 June 1997; accepted for publication 10 October 1997)

Acoustic scattering from two junctions in a rectangular waveguide is studied. Fourier transform and mode matching are used to represent the scattered wave and the simultaneous equations for the modal coefficients are formulated. The residue calculus is utilized to obtain a solution to the simultaneous equations in fast-converging series. Numerical evaluation shows the behaviors of transmission and reflection in terms of the junction geometry and operating frequency. © 1998 Acoustical Society of America. [S0001-4966(98)00802-9]

PACS numbers: 43.20.Mv [ANN]

INTRODUCTION

Acoustic wave scattering from a T-junction and a right-angle bend in a rectangular waveguide has been studied with an equivalent transmission line approach,¹ a matched asymptotic expansion technique,² and a conformal mapping method.³ The behavior of acoustic wave scattering from multiple junctions in a rectangular waveguide is also of theoretical interest. The purpose of the present Letter is to study the behavior of acoustic wave scattering from two junctions in a rectangular waveguide. We will present a rigorous, exact and analytic solution by using the Fourier transform and mode matching techniques which have been utilized to investigate electromagnetic scattering from junctions in a rectangular waveguide.⁴ The residue calculus is used to represent the transmission and reflection coefficients in rapidly converging series which are numerically efficient. In the next section, we show a field analysis using the Fourier transform and the numerical evaluations are illustrated in Sec. II.

I. FIELD ANALYSIS

Consider two junctions in a rectangular waveguide consisting of a hard surface in Fig. 1. In region (I) ($0 < z < h$), an incident field (velocity potential) Φ^i , propagating along the x direction, impinges on two junctions, thus resulting in a scattered field. The wave number is k ($= 2\pi/\lambda$, λ : wavelength) and an $e^{-i\omega t}$ time-harmonic convention is suppressed. From a velocity potential (Φ), it is possible to obtain the pressure ($i\omega\rho_0\Phi$) and the velocity ($\nabla\Phi$), where ρ_0 is the density of the medium. In region (I) the total field is a sum of the incident and scattered potentials which are

$$\Phi^i(x, y, z) = \cos(b_p y) \cos h_l(z-h) e^{i\beta_{pl} x}, \quad (1)$$

$$\Phi^l(x, y, z) = \frac{1}{2\pi} \int_{-\infty}^{\infty} [\tilde{A}(\zeta) \cos \kappa_p(z-h) + \tilde{B}(\zeta) \cos(\kappa_p z)] \cos(b_p y) e^{-i\zeta x} d\zeta, \quad (2)$$

where $b_p = p\pi/b$, $h_l = l\pi/h$, $\beta_{pl} = \sqrt{k^2 - b_p^2 - h_l^2}$, and $\kappa_p = \sqrt{k^2 - \zeta^2 - b_p^2}$. Note that the Fourier transform of $\Phi^l(x, y, 0)$ is $\int_{-\infty}^{\infty} \Phi^l(x, y, 0) e^{i\zeta x} dx$ given by $[\tilde{A}(\zeta) \cos(\kappa_p h) + \tilde{B}(\zeta)] \cos(b_p y)$.

In region (II) ($-a < x < a, z < 0$) the transmitted field is

$$\Phi^{II}(x, y, z) = \sum_{m=0}^{\infty} C_m \cos a_m(x+a) \cos(b_p y) e^{-i\xi_{mp} z}, \quad (3)$$

where $a_m = m\pi/2a$ and $\xi_{mp} = \sqrt{k^2 - a_m^2 - b_p^2}$.

In region (III) ($d-g < x < d+g, h < z$) the transmitted field is

$$\Phi^{III}(x, y, z) = \sum_{m=0}^{\infty} D_m \cos g_m(x-d+g) \cos(b_p y) e^{i\eta_{mp} z}, \quad (4)$$

where $g_m = m\pi/2g$ and $\eta_{mp} = \sqrt{k^2 - g_m^2 - b_p^2}$.

We use the boundary conditions on the field continuities at $z=0$ and h to find the unknown modal coefficients C_m and D_m . Enforcing the velocity continuity condition at $z=0$ gives

$$\left. \frac{\partial[\Phi^i(x, y, z) + \Phi^l(x, y, z)]}{\partial z} \right|_{z=0} = \begin{cases} \left. \frac{\partial\Phi^{II}(x, y, z)}{\partial z} \right|_{z=0}, & \text{for } |x| < a, 0 < y < b, \\ 0, & \text{otherwise.} \end{cases} \quad (5)$$

Taking the Fourier transform of Eq. (5) results in

$$\tilde{A}(\zeta) = -\frac{a^2 \zeta}{\kappa_p \sin(\kappa_p h)} \sum_{m=0}^{\infty} \xi_{mp} C_m F_m(\zeta a), \quad (6)$$

where

$$F_m(u) = \frac{(-1)^m e^{iu} - e^{-iu}}{(u)^2 - (m\pi/2)^2}. \quad (7)$$

Similarly the velocity continuity condition at $z=h$ gives

$$\tilde{B}(\zeta) = \frac{-g^2 \zeta e^{i\zeta d}}{\kappa_p \sin(\kappa_p h)} \sum_{m=0}^{\infty} \eta_{mp} D_m F_m(\zeta g) e^{i\eta_{mp} h}. \quad (8)$$

Enforcing the pressure continuity condition at $z=0$ gives

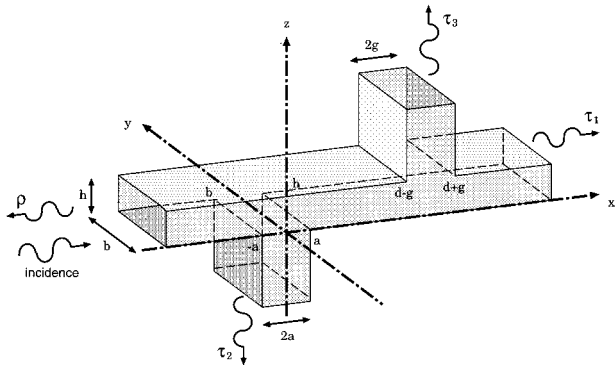


FIG. 1. Acoustic wave scattering from two junctions in rectangular waveguide.

$$\Phi^i(x, y, 0) + \Phi^l(x, y, 0) = \Phi^II(x, y, 0) \quad \text{for } |x| < a, \quad 0 < y < b. \quad (9)$$

Rewriting Eq. (9),

$$\begin{aligned} (-1)^l e^{i\beta_p l x} + \frac{1}{2\pi} \int_{-\infty}^{\infty} [\tilde{A}(\zeta) \cos(\kappa_p h) + \tilde{B}(\zeta)] e^{-i\zeta x} d\zeta \\ = \sum_{m=0}^{\infty} C_m \cos a_m(x+a). \end{aligned} \quad (10)$$

Similarly the pressure continuity condition at $z = h$ gives

$$\begin{aligned} e^{i\beta_p l x} + \frac{1}{2\pi} \int_{-\infty}^{\infty} [\tilde{A}(\zeta) + \tilde{B}(\zeta) \cos(\kappa_p h)] e^{-i\zeta x} d\zeta \\ = \sum_{m=0}^{\infty} D_m \cos g_m(x-d+g) e^{i\eta_{mp} h}. \end{aligned} \quad (11)$$

Substituting $\tilde{A}(\zeta)$ and $\tilde{B}(\zeta)$ into Eq. (10), multiplying (10) by $\cos a_n(x+a)$ ($n=0,1,2,3,\dots$), and performing integration with respect to x from $-a$ to a yield

$$\begin{aligned} ia\beta_{pl}(-1)^{l+1} F_n(\beta_{pl}a) = \frac{ia}{2\pi} \sum_{m=0}^{\infty} [a^2 \xi_{mp} C_m I_{1nm}(a) \\ + g^2 \eta_{mp} D_m e^{i\eta_{mp} h} I_{2nm}] \\ + C_m \varepsilon_n \delta_{nm}, \end{aligned} \quad (12)$$

where

$$I_{1nm}(a) = \int_{-\infty}^{\infty} \frac{\zeta^2 \cot(\kappa_p h)}{\kappa_p} F_m(\zeta a) F_n(-\zeta a) d\zeta, \quad (13)$$

$$I_{2nm} = \int_{-\infty}^{\infty} \frac{\zeta^2 e^{i\zeta d}}{\kappa_p \sin(\kappa_p h)} F_m(\zeta g) F_n(-\zeta a) d\zeta, \quad (14)$$

$$\varepsilon_v = \begin{cases} 2, & \text{when } v=0, \\ 1, & v=1,2,3,\dots \end{cases} \quad (15)$$

Utilizing the technique of the contour integration, we transform $I_{1nm}(a)$ and I_{2nm} into a rapidly converging series. The results are

$$I_{1nm}(a) = \begin{cases} 0, & \text{when } n+m=\text{odd}, \\ p_m(a) \delta_{nm} + q_{nm}(a), & \text{when } n+m=\text{even}, \end{cases} \quad (16)$$

$$\begin{aligned} I_{2nm} = X(\zeta) \\ + \begin{cases} 2\pi i P(\zeta)|_{\zeta=a_n} + 2\pi i Q(\zeta)|_{\zeta=g_m} : & a_n \neq g_m, \\ \frac{2\pi i}{\varepsilon_n a^2 g^2} \frac{f'(\zeta) s(\zeta) - f(\zeta) s'(\zeta)}{s^2(\zeta)} \Big|_{\zeta=a_n} : & a_n = g_m, \end{cases} \end{aligned} \quad (17)$$

where δ_{nm} is the Kronecker delta and $()'$ denotes the differentiation.

$$p_m(a) = \frac{2\pi \varepsilon_m \cot(\xi_{mp} h)}{a^3 \xi_{mp}}, \quad (18)$$

$$\begin{aligned} q_{nm}(a) = -\frac{4\pi i}{a^4 h} \\ \times \sum_{v=0}^{\infty} \frac{\zeta [1 - (-1)^m e^{i2\zeta a}]}{\varepsilon_v (\zeta^2 - a_m^2) (\zeta^2 - a_n^2)} \Big|_{\zeta = \sqrt{k^2 - (v\pi/h)^2 - b_p^2}}, \end{aligned} \quad (19)$$

$$P(\zeta) = \frac{f_1(\zeta)}{a^2 g^2 \kappa_p \sin(h\kappa_p) (\zeta + a_n) (\zeta^2 - g_m^2)}, \quad (20)$$

$$Q(\zeta) = \frac{f_1(\zeta)}{a^2 g^2 \kappa_p \sin(h\kappa_p) (\zeta + g_m) (\zeta^2 - a_n^2)}, \quad (21)$$

$$f(\zeta) = \begin{cases} f_1(\zeta) : & a_n = g_m \neq 0, \\ f_2(\zeta) : & a_n = g_m = 0, \end{cases} \quad (22)$$

$$\begin{aligned} f_1(\zeta) = \zeta^2 [(-1)^{m+n} e^{i\zeta|d-a+g|} - (-1)^m e^{i\zeta|d+a+g|} \\ - (-1)^n e^{i\zeta|d-a-g|} + e^{i\zeta|d+a-g|}], \end{aligned} \quad (23)$$

$$\begin{aligned} f_2(\zeta) = [e^{i\zeta|d-a+g|} - e^{i\zeta|d+a+g|} - e^{i\zeta|d-a-g|} \\ + e^{i\zeta|d+a-g|}], \end{aligned} \quad (24)$$

$$s(\zeta) = \begin{cases} \kappa_p \sin(h\kappa_p) (\zeta + a_n)^2 : & a_n = g_m \neq 0, \\ \kappa_p \sin(h\kappa_p) : & a_n = g_m = 0, \end{cases} \quad (25)$$

$$X(\zeta) = -\frac{2\pi i}{a^2 g^2 h} \sum_{v=0}^{\infty} \frac{f_1(\zeta)}{\zeta \varepsilon_v (-1)^v [\xi_{np}^2 - (v\pi/h)^2] [\eta_{mp}^2 - (v\pi/h)^2]} \Big|_{\zeta = \sqrt{k^2 - (v\pi/h)^2 - b_p^2}}. \quad (26)$$

Similarly, multiplying Eq. (11) by $\cos g_n(x-d+g)$ ($n=0,1,2,3,\dots$), and performing integration yield

$$-ig\beta_{pl}e^{i\beta_{pl}d}F_n(\beta_{pl}g) = \frac{ig}{2\pi} \sum_{m=0}^{\infty} [a^2\xi_{mp}C_mI_{2mn} + g^2\eta_{mp}D_me^{i\eta_{mp}h}I_{1nm}(g)] + e^{i\eta_{mp}h}D_m\varepsilon_n\delta_{nm}. \quad (27)$$

Rewriting Eqs. (12) and (27) in matrix form, we obtain

$$\begin{bmatrix} \Psi_1 & \Psi_2 \\ \Psi_3 & \Psi_4 \end{bmatrix} \begin{bmatrix} C \\ D \end{bmatrix} = \begin{bmatrix} \Gamma_1 \\ \Gamma_2 \end{bmatrix}, \quad (28)$$

where C and D are column vectors consisting of elements C_m and D_m , respectively, and the elements of $\Psi_1, \Psi_2, \Psi_3, \Psi_4, \Gamma_1$, and Γ_2 are

$$\psi_{1,nm} = \frac{ia^3}{2\pi} \xi_{mp}I_{1nm}(a) + \varepsilon_n\delta_{nm}, \quad (29)$$

$$\psi_{2,nm} = \frac{iga^2}{2\pi} \eta_{mp}e^{i\eta_{mp}h}I_{2nm}, \quad (30)$$

$$\psi_{3,nm} = \frac{iga^2}{2\pi} \xi_{mp}I_{2mn}, \quad (31)$$

$$\psi_{4,nm} = \frac{ig^3}{2\pi} \eta_{mp}e^{i\eta_{mp}h}I_{1nm}(g) + e^{i\eta_{mp}h}\varepsilon_n\delta_{nm}, \quad (32)$$

$$\gamma_{1n} = ia\beta_{pl}(-1)^{l+1}F_n(\beta_{pl}a), \quad (33)$$

$$\gamma_{2n} = -ig\beta_{pl}e^{i\beta_{pl}d}F_n(\beta_{pl}g). \quad (34)$$

In the low-frequency regime, the lowest mode ($m=n=0$) becomes dominant; thus

$$C_0 \approx \frac{\psi_{4,00}\gamma_{10} - \psi_{2,00}\gamma_{20}}{\psi_{1,00}\psi_{4,00} - \psi_{2,00}\psi_{3,00}}, \quad (35)$$

$$D_0 \approx \frac{\psi_{1,00}\gamma_{20} - \psi_{3,00}\gamma_{10}}{\psi_{1,00}\psi_{4,00} - \psi_{2,00}\psi_{3,00}}, \quad (36)$$

where Eqs. (29)–(34) simplify to the following expressions for $p=l=0$.

$$\psi_{1,00} = 2i \frac{e^{-ikh}}{\sin(kh)} + 2k \frac{a}{h} \sum_{v=0}^{\infty} \frac{F_0(-a\zeta_v)}{\varepsilon_v\zeta_v} e^{i\zeta_v a}, \quad (37)$$

$$\psi_{2,00} = e^{ikh} \left[-\frac{f'_2(0)}{2a \sin(kh)} + \frac{k}{ah} \sum_{v=0}^{\infty} \frac{f_2(\zeta_v)}{\varepsilon_v(-1)^v\zeta_v^3} \right], \quad (38)$$

$$\psi_{3,00} = -\frac{f'_2(0)}{2g \sin(kh)} + \frac{k}{gh} \sum_{v=0}^{\infty} \frac{f_2(\zeta_v)}{\varepsilon_v(-1)^v\zeta_v^3}, \quad (39)$$

$$\psi_{4,00} = e^{ikh} \left[2i \frac{e^{-ikh}}{\sin(kh)} + 2k \frac{g}{h} \sum_{v=0}^{\infty} \frac{F_0(-g\zeta_v)}{\varepsilon_v\zeta_v} e^{i\zeta_v g} \right], \quad (40)$$

$$\gamma_{10} = -iakF_0(ka), \quad (41)$$

$$\gamma_{20} = -igke^{ikd}F_0(kg), \quad (42)$$

$$\zeta_v = \sqrt{k^2 - (v\pi/h)^2}. \quad (43)$$

II. TRANSMISSION AND REFLECTION COEFFICIENTS

The scattered fields at $x \leq -a$ and $x \geq d+g$ can be evaluated by utilizing the residue calculus.

$$\Phi^l(x,y,z) = \begin{cases} \sum_u K_u^+ \cos(b_p y) \cos h_u(z-h) e^{i\beta_{pu}x}, \\ \text{where } x \geq d+g, \\ \sum_u K_u^- \cos(b_p y) \cos h_u(z-h) e^{-i\beta_{pu}x}, \\ \text{where } x \leq -a, \end{cases} \quad (44)$$

where

$$K_u^\pm = \mp \sum_{m=0}^{\infty} \frac{ia^2 \xi_{mp} C_m F_m(\mp \beta_{pu}a)}{h \varepsilon_u (-1)^u} \mp \sum_{m=0}^{\infty} \frac{ig^2 \eta_{mp} D_m F_m(\mp \beta_{pu}g) e^{\mp id\beta_{pu}}}{h \varepsilon_u} e^{i\eta_{mp}h}, \quad (45)$$

$0 \leq u, u$: integer.

The transmission coefficient is defined as a ratio of the transmitted power through the aperture to the power incident on the aperture.⁵ The reflection coefficient is similarly defined. The transmission (τ_1, τ_2, τ_3) and reflection (ρ) coefficients in Fig. 1 are

$$\tau_1 = |1 + K_l^+|^2 + \sum_{u \neq l} \frac{\varepsilon_u \beta_{pu} |K_u^+|^2}{\varepsilon_l \beta_{pl}}, \quad (46)$$

$$\tau_2 = \frac{2a}{h \varepsilon_l \beta_{pl}} \sum_m |C_m|^2 \varepsilon_m \xi_{mp}, \quad (47)$$

$$\tau_3 = \frac{2g}{h \varepsilon_l \beta_{pl}} \sum_n |D_n|^2 \varepsilon_n \eta_{np}, \quad (48)$$

$$\rho = \sum_u \frac{\varepsilon_u \beta_{pu} |K_u^-|^2}{\varepsilon_l \beta_{pl}}, \quad (49)$$

where $0 \leq u < (h/\pi)\sqrt{k^2 - b_p^2}$, u : integer, $0 \leq m < (2a/\pi)\sqrt{k^2 - b_p^2}$, m : integer, $0 \leq n < (2g/\pi)\sqrt{k^2 - b_p^2}$, n : integer.

In Fig. 2, we show the behavior of transmission (τ_1, τ_2, τ_3) and reflection (ρ) coefficients versus the normalized frequency (kh/π) for the cross junction ($d=0$). The incident field is assumed to be Eq. (1) with $p=l=0$. According to the image theory, the cross junction geometry of height h is equivalent to the geometry of the T-junction of height $h/2$. Our evaluation agrees well with the results of the acoustic T-junction problem² or the electromagnetic E-plane T-junction⁶ for $kh/\pi < 2$. Note that τ_2 (+ + +) of the T-junction should be twice of τ_2 (- - -) of the cross junction. The number of the modal coefficients used in Eq. (28) is corresponding to the number of the propagation modes plus one higher evanescent mode to achieve the numerical accuracy ($\rho + \tau_1 + \tau_2 + \tau_3 = 1$) to within 0.1% error, indicating our series solution is rapidly-converging. Note that our single-mode solution, Eqs. (35) and (36), also give an accurate result for $kh/s\pi < 1$. As the operating frequency in-

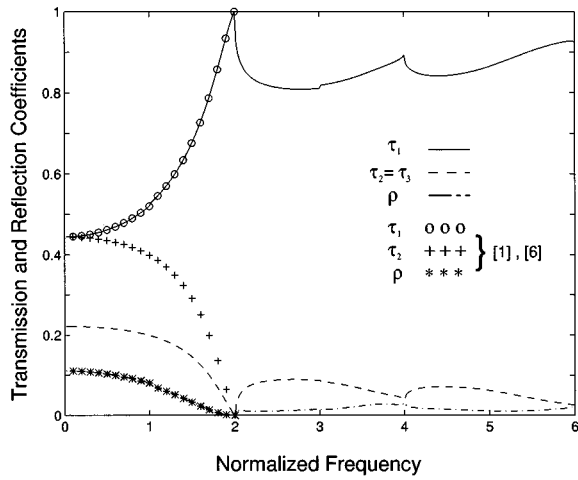


FIG. 2. Behavior of transmission (τ_1, τ_2, τ_3) and reflection (ρ) coefficients versus the normalized frequency (kh/π) for the cross junction ($a/h = 1/4, b/h = 1/2, d/h = 0, g/h = 1/4$).

increases, τ_1 tends to approach to unity, as expected. It is seen that the transmission coefficient τ_1 exhibits peak values at normalized frequencies = 2, 4, 6, Figure 3 shows the behavior of τ_1, τ_2, τ_3 , and ρ versus the normalized distance d/λ between two junctions, when the incident field corresponding to $p=l=0$ in Eq. (1) impinges on the junction. When $d/\lambda \approx 0.25$, τ_2 (τ_1, τ_3, ρ) becomes maximum (minimum) and their resonant behaviors repeat with a 0.5λ periodicity. In order to understand the behaviors of the phases for the

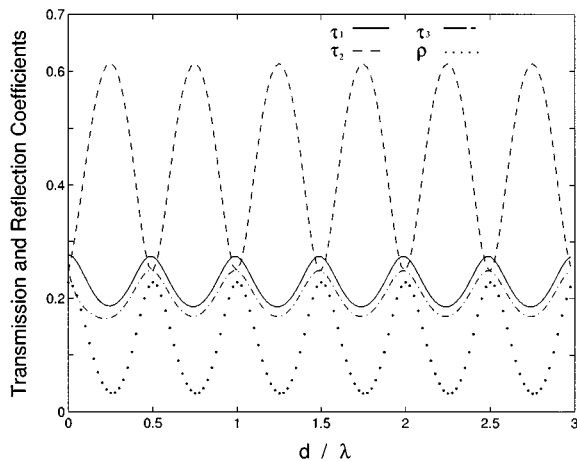


FIG. 3. Behavior of τ_1, τ_2, τ_3 , and ρ versus the normalized distance d/λ between two junctions ($kh = 1, a/h = 1/2, b/h = 1, g/h = 1/2$).

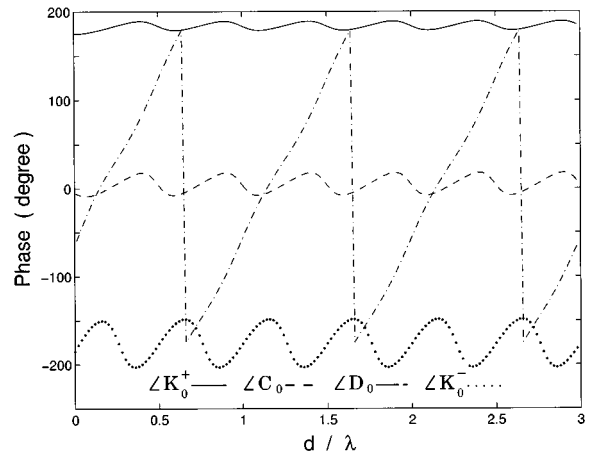


FIG. 4. Behavior of $\angle K_0^+, \angle C_0, \angle D_0$, and $\angle K_0^-$ versus the normalized distance d/λ between two junctions when the same parameters as in Fig. 3 are used in computation.

transmitted and reflected fields, we plot the phases of K_0^+, C_0, D_0 , and K_0^- in Fig. 4. Note that the phase of D_0 fluctuates substantially versus d/λ while the rest of phases remain less sensitive to a change in d/λ .

III. CONCLUSION

Acoustic scattering from two junctions in a rectangular waveguide is investigated using the Fourier transform and the mode matching techniques. The closed-form solutions for the transmission and reflection coefficients are obtained using the residue calculus. A single-mode approximate solution is presented in a simple form which is applicable in low-frequency regime. Numerical computations are performed to illustrate the scattering behavior of the two junctions in terms of the junction geometry.

- ¹J. W. Miles, "The diffraction of sound due to right-angled joints in rectangular tubes," *J. Acoust. Soc. Am.* **19**, 572–579 (1947).
- ²J. C. Bruggeman, "The propagation of low-frequency sound in a two-dimensional duct system with T joints and right angle bends: Theory and experiment," *J. Acoust. Soc. Am.* **82**, 1045–1051 (1987).
- ³C. Thompson, "Linear inviscid wave propagation in a waveguide having a single boundary discontinuity: Part II: Application," *J. Acoust. Soc. Am.* **75**, 356–362 (1984).
- ⁴J. W. Lee and H. J. Eom, "TE-mode scattering from two junctions in H-plane waveguide," *IEEE Trans. Microwave Theory Tech.* **42**, 601–606 (1994).
- ⁵G. P. Wilson and W. W. Soroka, "Approximation to the diffraction of sound by a circular aperture in a rigid wall of finite thickness," *J. Acoust. Soc. Am.* **37**, 286–297 (1965).
- ⁶K. H. Park, H. J. Eom, and Y. Yamaguchi, "An analytic series solution for E-plane T-junction in parallel-plate waveguide," *IEEE Trans. Microwave Theory Tech.* **42**, 356–358 (1994).

Comparison of speech intelligibility between English and Chinese

Jian Kang

The Martin Centre, University of Cambridge, 6 Chaucer Road, Cambridge CB2 2EB, United Kingdom

(Received 4 April 1996; revised 20 September 1997; accepted 14 October 1997)

Most objective indices for speech intelligibility are essentially based on studies of Western languages and not tonal languages like Chinese. Consequently, if speech intelligibility in an enclosure is satisfactory for English, it is not necessarily satisfactory for Chinese, or *vice versa*. In this research, the differences in intelligibility between English and Mandarin (a spoken language of Chinese) have been investigated by carrying out a series of articulation tests in a long corridor and a regularly shaped (i.e., quasi-cubic) seminar room, using loudspeaker sources. The results suggest that in terms of speech intelligibility, Mandarin is slightly better than English under reverberant conditions, and English is considerably better than Mandarin under noisy conditions. © 1998 Acoustical Society of America. [S0001-4966(98)05801-9]

PACS numbers: 43.55.Hy, 43.55.Fw, 43.71.Hw [JDQ]

INTRODUCTION

Most objective indices for speech intelligibility, such as the speech transmission index (STI) and the articulation index (AI), are essentially based on studies of Western languages and not tonal languages like Chinese. Consequently, if speech intelligibility in an enclosure is satisfactory for English, it is not necessarily satisfactory for Chinese, or *vice versa*.

The differences in intelligibility among languages have been noticed. Houtgast and Steeneken, when demonstrating the effectiveness of the rapid speech transmission index (RASTI) with ten Western languages, indicated that language-specific effects could be a factor causing disparity among various tests.¹

In both English and Mandarin (a spoken language of Chinese) there have been considerable investigations on speech intelligibility.¹⁻⁵ For both languages a series of relationship between some objective indices and various measures of speech intelligibility, such as word or sentence intelligibility, has been established. However, it appears to be inappropriate to directly compare these relationships between the two languages because they were established under different conditions. Moreover, these relationships were mainly for diffuse fields and might not be applicable for nondiffuse fields, for example, long enclosures.⁶⁻⁸

In this research, therefore, the differences in intelligibility between English and Mandarin have been investigated by carrying out a series of articulation tests in a long corridor and a regularly shaped (i.e., quasi-cubic) seminar room, using loudspeaker sources.

I. METHOD

Briefly, the articulation tests were in four steps: (1) selecting comparable test materials for the two languages; (2) recording the test materials on a signal tape in an anechoic chamber; (3) designing experimental conditions; and (4) conducting listening tests.

An essential requirement of the articulation tests is that the test materials of the two languages should be comparable. Given the fundamental differences between English and Mandarin, it appears unreasonable to directly compare the phonetically balanced (PB) word scores or syllable scores between the two languages.^{2,3,8} First, the English PB words, especially the monosyllabic ones, only represent the English words with relatively few phonemes and letters, whereas the Mandarin PB words, which include one to four Chinese character words, represent all kinds of words in Chinese. Second, the Mandarin syllables, each corresponding to one Chinese character, are mostly meaningful and tonal and thus, might be more easily understood than the nonsense English syllables. Third, if phonetically marked by Chinese characters, English monosyllabic words correspond to one to three Chinese characters.

Alternatively, the comparison can be made indirectly. One way is to compare the difference of PB word scores or syllable scores from one condition to another between the two languages. Another way is to convert the articulation scores obtained with lists of PB words or syllables into sentence intelligibility scores for comparison. Of course, a more direct way to compare the speech intelligibility of different languages is to use sentences as test materials. The main disadvantage of using sentences is that scores are usually high and not sensitive to small change in listening conditions.³

Accordingly, the articulation tests were carried out using the following test materials: (1) PB words in English and Mandarin. For each language 25 PB word lists were used. In each list 50 words were included. (2) Hong Kong Mass Transit Railway (MTR) public address (PA) messages in English and Mandarin. There were two reasons for using the PA messages rather than conventional sentence lists. First, with the PA messages the test materials in the two languages could have the same meaning. Second, since the original MTR PA messages were in both English and Chinese, possible effects caused by translation can be avoided. According to the original PA messages, 25 sentence lists were care-

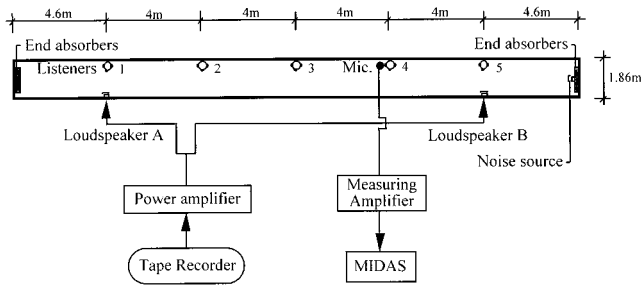


FIG. 1. Experimental arrangement in the corridor, plan view. MIDAS is a software for room acoustic measurements.

fully compiled for each language. Each list contained four sentences. Fifty key words were scored for each list.

The above test materials were recorded on a signal tape in an anechoic chamber for subsequent presentation. Four native talkers for each language, two males and two females, were selected.⁵ Each list of PB words or PA sentences was equally divided into four sections and read by the four talkers consecutively. Each PB word was included, without emphasis, in the same carrier sentence.

The design of experimental conditions was based on two basic requirements: (1) consideration of both reverberation and ambient noise, and (2) coverage of a considerable range of the STI.

The experimental arrangement in the corridor is illustrated in Fig. 1. The length, width and height of the corridor (King's College, Cambridge) were 25.2, 1.86, and 2.34 m, respectively. The sources were loudspeakers (KEF type 103) on a side wall of the corridor. This was, in principle, to simulate a PA system in some long enclosures. The loudspeaker height was 1.2 m. Since the sound field with single and multiple sources could be very different,⁷ experiments were carried out by using a single loudspeaker as well as two loudspeakers. To obtain a wide range of the STI, two loudspeakers were arranged symmetrically with a spacing of 16 m. For convenience, the two loudspeakers are called loudspeakers A and B below. Correspondingly, five listening positions, namely points 1 to 5 in Fig. 1, were arranged between the two loudspeakers at intervals of 4 m. To extend the STI range and investigate the effect of ambient noise, a tape recorder was positioned at an end of the corridor to play white noise.

The articulation tests in the corridor were carried out in the following three cases: Case C1: loudspeaker A only, noise source off, A-weighted signal/noise (S/N) ratio > 25 dB at all listening points. From points 1 to 5 the measured STIs were 0.75, 0.63, 0.6, 0.58, and 0.56, respectively. Correspondingly, the early decay time (EDT) at 500-1 kHz varied from 0.6 s to 1.3 s at points 1 to 5. Case C2: loudspeaker A only, noise source on, A-weighted S/N ratio = 9 dB at point 1. The STIs at points 1 to 5 were 0.6, 0.44, 0.39, 0.29, and 0.19. Case C3: two loudspeakers, noise level the same as Case C2. The STIs at points 1 to 5 were 0.51, 0.47, 0.4, 0.36, and 0.44.

The seminar room (The Martin Centre, Cambridge) was 4.5 m by 7 m by 3.5 m. The EDT of this room was around

0.6–0.8 s at 500-1 kHz. A loudspeaker as used in the corridor was positioned in a corner of the room at the same height as that in the corridor. Again, the tape recorder was used to play white noise. In correspondence with the corridor, five listening points were arranged in the seminar room. To obtain a wide range of the STI, the listening points were along the room diagonally. Accordingly, the loudspeaker and the noise source were at two diagonal corners of the room.

The articulation tests in the seminar room were carried out in the following two cases: Case S1: noise source off, A-weighted S/N ratio > 25 dB at all listening points. The STIs at point 1 (i.e., the nearest point to the loudspeaker) to point 5 were 0.76, 0.66, 0.65, 0.66, and 0.66. Case S2: noise source on, A-weighted S/N ratio = 2 dB at point 1. The STIs at points 1 to 5 were 0.49, 0.41, 0.35, 0.31, and 0.1.

Five native listeners for each language, three males and two females or two males and three females, were selected for the tests. For each acoustic condition (i.e., the Case above) and each language five articulation tests were carried out. Each test included one PB word list and one PA list. The listeners were required to write down the test material as read to them. Neither PB words nor PA sentences were presented to listeners until the test. For each of the five tests, listeners sat at a different position. In other words, for each of the 25 STIs, articulation scores can be averaged over five listeners. The ear height was around 1.2 m.

In addition to the above articulation tests, a subjective rating was also carried out. After each articulation test, listeners were required to give a five-scale rating of the speech intelligibility. The five scales were 1—bad, 2—poor, 3—fair, 4—good, and 5—excellent.

For each acoustic condition, the power amplifier output was adjusted so that the signal level was the same for the two languages. According to the conventional method,^{1,4} the A-weighted signal level was measured by L_{eq} (equivalent continuous sound level) of the PA sentences in three lists.

In brief, from the above tests the following results were obtained for each of the 25 STIs: (1) Word intelligibility: percentage of PB words correctly recorded, average of five listeners; (2) Converted sentence intelligibility: determined from the above word intelligibility according to the conventional relationship between them; (3) PA sentence intelligibility: percentage of correctly recorded key words in PA sentences, average of five listeners; and (4) Subjective rating: scale point of subjective rating, average of five listeners.

II. RESULTS

The analyses below are based on the test results and their regressions. Regressions were performed for three different types of relationship between the STI and articulation scores: logarithmic, linear, and with a form of second order equation. The logarithmic regressions generally gave the best correlation coefficients r , so these are the ones presented. This reflects the conventional relationship between the STI and articulation scores, which is logarithmic.⁴

The comparison of word intelligibility between English and Mandarin, as indicated previously, is only relative. Figure 2 shows the comparison in the corridor. It can be seen that with a relatively high STI which corresponds to a large S/N ratio, the word intelligibility of Mandarin is generally

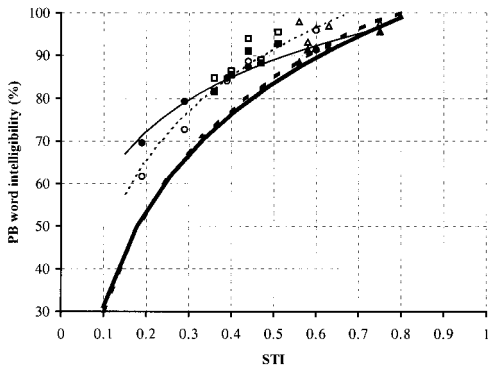


FIG. 2. Word intelligibility of English (filled symbols) and Mandarin (open symbols) in the corridor and the seminar room. ▲ and △, Case C1; ● and ○, Case C2; ■ and □, Case C3. The curves are logarithmic regressions of the test results in English (—, corridor, $r=0.97$; ---, seminar room, $r=0.91$) and Mandarin (·····, corridor, $r=0.96$; -·-·-, seminar room, $r=0.96$).

better than that of English. This means that the decrease in word intelligibility caused by reverberation is greater in English than in Mandarin. A possible reason for this is that under a reverberant condition, some English consonants, such as affricates, fricatives, nasals, and plosives, are very easy to confuse, whereas in Mandarin tones are helpful for word intelligibility. When the STI becomes lower due to the decrease of S/N ratio, the contrary occurs, the word intelligibility of English becomes better than that of Mandarin. Typical examples are at points 4 and 5 in Case C2. It has been observed that in English the SPL dynamic range is considerably greater than that in Mandarin, i.e., typically, with the same A-weighted L_{eq} the peak level of English is about 3 dB higher than that of Mandarin. This may be an explanation of the fact that, under noisy conditions, some English words may be understood by picking up only the high peaks.

To compare the converted sentence intelligibility between English and Mandarin, it is useful to analyze the relationship between word and sentence intelligibility. Such relationships in English and Mandarin have been found from the literature.^{2,3,8} It is interesting to note that for a given word intelligibility, the sentence intelligibility of English is generally better than that of Mandarin. An important reason for this difference, as indicated previously, is that the Mandarin PB words represent all kinds of Chinese words, whereas the English PB words only represent relatively short English words. Given the fact that the word intelligibility improves with increasing number of sounds per word,³ this difference between the two languages is reasonable.

Correspondingly, by converting the word intelligibility in Fig. 2 into sentence intelligibility, the differences between English and Mandarin become more visible, as shown in Fig. 3.

Similarly, in the corridor the differences in PA sentence intelligibility between English and Mandarin, as shown in Fig. 4, are also systematic, especially in Cases C2 and C3, in which the noise source was used. By comparing a typical PA sentence in English and Mandarin, “please use the queuing lines and let passengers leave the train first” and “3qin 2pai

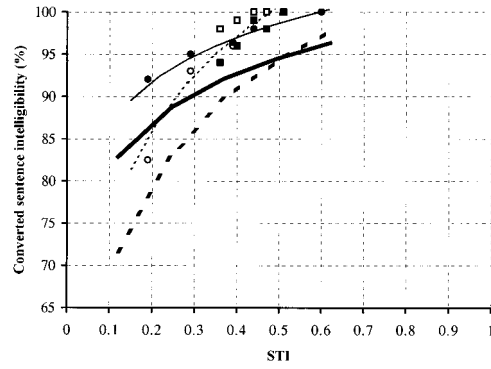


FIG. 3. Converted sentence intelligibility of English (filled symbols) and Mandarin (open symbols) in the corridor and the seminar room. ● and ○, Case C2; ■ and □, Case C3. The curves are logarithmic regressions of the test results in English (—, corridor, $r=0.92$; ---, seminar room, $r=0.81$) and Mandarin (·····, corridor, $r=0.93$; -·-·-, seminar room, $r=0.90$). Cases C1 and S1 are not included in the figure since the converted sentence intelligibility is above 99% at all listening points.

4dui, 1xian 4rang 2cheng 4ke 3xia 1che” (the numbers indicate which tone to use out of four possible tones), it is clear that the total number of sounds in Mandarin is significantly less than that in English. This might be another reason for the lower sentence intelligibility of Mandarin in comparison with English.

In the seminar room, generally speaking, the differences between the two languages are similar to those in the corridor. Figures 2 and 3 also show the comparison of word intelligibility and converted sentence intelligibility between English and Mandarin in the seminar room. In Case S2, in which the STI was relatively low due to the low S/N ratio, the sentence intelligibility of English is considerably better than that of Mandarin, although the difference in word intelligibility between the two languages is not as systematic as that in the corridor. Similarly, the differences in PA sentence intelligibility between English and Mandarin are also considerable, as shown in Fig. 4.

It appears that the above differences between the two languages are unnoticeable in terms of subjective rating. In

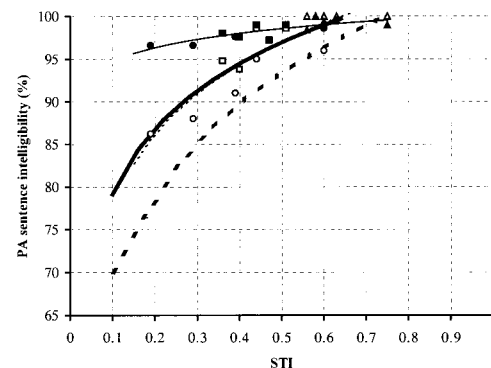


FIG. 4. PA sentence intelligibility of English (filled symbols) and Mandarin (open symbols) in the corridor and the seminar room. ▲ and △, Case C1; ● and ○, Case C2; ■ and □, Case C3. The curves are logarithmic regressions of the test results in English (—, corridor, $r=0.81$; ---, seminar room, $r=0.96$) and Mandarin (·····, corridor, $r=0.91$; -·-·-, seminar room, $r=0.95$).

both enclosures there is no systematic difference in subjective rating between the two languages. Under the noisy conditions, despite the higher sentence intelligibility of English, the subjective rating given by English listeners is not higher, and in some cases even lower, than that of Mandarin. This result suggests that the subjective rating type of test could be rather misleading. However, since a low subjective rating may correspond to less confidence in speech intelligibility, the factor of subjective appraisal should be considered in the acoustic design for an enclosure used for multiple languages.

Since the sound fields in long and regularly shaped enclosures are rather different,⁶⁻⁸ it is useful to compare the speech intelligibility between the corridor and the seminar room. From Figs. 2, 3, and 4 it can be seen that for a relatively high STI there is no systematic difference between the two enclosures, whereas for a relatively low STI, the word or sentence intelligibility in the seminar room is noticeably lower than that in the corridor. This difference is likely to be due to the difference of sound field between the two enclosures. For example, in the corridor the noise was mainly from one direction and thus, could be less disturbing than that in a more diffuse field like the seminar room.

Generally speaking, in the corridor the STI is highly correlated to the articulation scores as well as to the subjective rating, although these relationships are not necessarily the same as that of regularly shaped enclosures like the seminar room. For example, the correlation coefficient between the STI and word intelligibility is 0.97 for English and 0.96 for Mandarin. This means the STI, which has been proved to be effective for regularly shaped enclosures,⁴ is also useful for long enclosures.

It is interesting to note that for a given STI in the corridor, for both languages, with two loudspeakers the word or sentence intelligibility is slightly higher than that with a single loudspeaker. This can be seen by comparing Case C3 with the other two cases in Figs. 2, 3, and 4. The difference is about 3%–5% in word intelligibility and 1%–4% in sentence intelligibility. A *t* test shows that these differences are significant (word intelligibility, $p < 0.001$; sentence intelligibility, $p < 0.01$). This appears to indicate that the intelligibility of sound arriving from two widely separated directions is better than that of sound from one direction.

III. DISCUSSION

It should be noted that for a PA system used for multiple languages the signal level could vary for different languages. For example, since in Mandarin the dynamic range of SPL is less than that in English, the power amplifier output for Mandarin could be higher than that for English. Consequently, for a given ambient noise, the above mentioned differences in intelligibility between English and Mandarin could be diminished.

The research accomplished to date suggests many possibilities for further work. First, since the tests are based on a limited EDT range, 0.6–1.3 s, it would be useful to investigate the differences between the two languages with a greater EDT range. Second, the effect of the spectrum and

direction of ambient noise should be further investigated. It is possible that, for a given S/N ratio, the differences in intelligibility between the two languages are dependent on the spectrum of the ambient noise. Also, in the corridor, if the ambient noise is from more than one direction rather than from the direction of one end wall, the differences between the corridor and the seminar room might be diminished. Third, since the results of sentence intelligibility relate to specific test materials, it might be useful to develop PB sentences for a more general comparison between the two languages. Finally, given the differences in speech intelligibility between one and two loudspeakers in the corridor, it would be interesting to investigate the effect of more loudspeakers.

IV. CONCLUSIONS

To compare speech intelligibility between English and Chinese, a series of articulation tests has been carried out in a long corridor and a regularly shaped (i.e., quasi-cubic) seminar room, using loudspeaker sources. The results suggest that in terms of speech intelligibility, Mandarin is slightly better than English under reverberant conditions, and English is considerably better than Mandarin under noisy conditions. Consequently, for an enclosure which is used for both English and Mandarin, the difference in intelligibility between them should be considered in the acoustic design. For example, in underground stations, where speech intelligibility is significantly affected by the background noise, a higher STI may be required if Mandarin is included. Conversely, the differences in subjective rating between the two languages appear to be unnoticeable. This should also be taken into account in the acoustic design. The discussion suggests that further investigations considering more general cases are still necessary.

ACKNOWLEDGMENTS

The author is indebted to Dr. R. J. Orłowski for his supervision, to Professor J. L. Zhang, Dr. R. Carlyon, and the reviewers for their helpful advice. This work was supported by the ORS, COT, MTRC, and AvH.

¹T. Houtgast and H. J. M. Steeneken, "A multi-language evaluation of the RASTI-method for estimating speech intelligibility in auditoria," *Acustica* **54**, 185–199 (1984).

²J. L. Zhang, "Speech," in *Handbook of Acoustics*, edited by D. Y. Maa and H. Shen (Science Press, Beijing, 1987), Chap. 19, pp. 404–435 (in Chinese).

³L. L. Beranek, *Acoustic Measurements* (Wiley, New York, 1949), Chap. 13, pp. 625–634, Chap. 17, pp. 761–792.

⁴T. Houtgast and H. J. M. Steeneken, "A review of the MTF concept in room acoustics and its use for estimating speech intelligibility in auditoria," *J. Acoust. Soc. Am.* **77**, 1069–1077 (1985).

⁵ANSI S3.2-1989, "American National Standard Method for measuring the intelligibility of speech over communication systems" (American National Standards Institute, New York).

⁶J. Kang, "Reverberation in rectangular long enclosures with geometrically reflecting boundaries," *Acustica* **82**, 509–516 (1996).

⁷J. Kang, "Acoustics in long enclosures with multiple sources," *J. Acoust. Soc. Am.* **99**, 985–989 (1996).

⁸J. Kang, "Acoustics of long enclosures," Ph.D. dissertation, University of Cambridge, 1996.

Transient wave response of a cymbal using double-pulsed TV holography

Staffan Schedin and Per O. Gren

Luleå University of Technology, Division of Experimental Mechanics, S-971 87 Luleå, Sweden

Thomas D. Rossing

Physics Department, Northern Illinois University, DeKalb, Illinois 60115

(Received 21 November 1996; revised 6 October 1997; accepted 7 October 1997)

Using an electronic system for pulsed TV holography with a double-pulsed ruby laser, transient wave propagation during intervals from 30 to 480 μs after impact is recorded. The first observable bending waves, having wavelengths of about 5 mm, propagate at about 1700 m/s, and reach the edge of the cymbal in about 60 μs . These are quickly followed by waves of longer wavelength which scatter at the outer edge of the cymbal and also the central dome and result in standing waves. A phase unwrapping procedure is used to obtain a three-dimensional map of the wave field. Holographic film recordings similarly show scattering of transient bending waves at the central dome. © 1998 Acoustical Society of America. [S0001-4966(98)01802-5]

PACS numbers: 43.75.Kk [WJS]

INTRODUCTION

At least three prominent features have been observed in the sound of a cymbal: the strike sound that results from rapid wave propagation during the first millisecond, the buildup of strong peaks around 700–1000 Hz in the sound spectrum during the 10 or 20 ms, and the strong aftersound in the range of 3–5 kHz that dominates the sound a second or so after striking and gives the cymbal its “shimmer” (Rossing and Shepherd, 1983). The aftersound has been attributed to chaotic behavior taking place at large amplitude which provides a mechanism for the conversion of low-frequency energy to a rich assortment of modes of much higher frequency (Fletcher, 1993).

In this letter, we report the results of using pulsed TV holography to observe the propagation of bending waves during the first 0.3 ms after an impulsive excitation of a Zildjian thin crash cymbal having a diameter of 41 cm. Interferograms were recorded electronically.

I. EXPERIMENTAL METHOD AND RESULTS

The newly developed all-electronic system for pulsed TV holography, which allows quantitative evaluation of interferograms, is described elsewhere (Schedin *et al.*, 1996). Two subsequent holographic images are recorded by a CCD camera whose output can be captured on a personal computer by means of a frame grabber. The optical phase change between the two images is computed at each pixel by a Fourier-transform method. Speckle averaging over the computed phase map is made possible by recording images simultaneously through three 1-mm-diameter apertures.

Two pulses from a ruby laser were separated by times ranging from 30 to 480 μs . Impulses were applied at the edge of the cymbal or 10 cm from the edge by focusing a portion of the first laser pulse on a piece of gel (mostly water) applied to the surface of the cymbal. Rapid evapora-

tion of the water by the laser beam resulted in a local impulse of about 10^{-3} N s (Fällström *et al.*, 1996).

Figure 1 shows a series of phase maps for pulse separations of 30–240 μs when the cymbal is pulsed 10 cm (about half the radius) from the edge of the cymbal. The field of view is 20×15 cm. An increase from dark to bright indicates an out-of-plane displacement in the direction of the impact (out of the paper). The first observable bending waves, having wavelengths of about 5 mm, propagate rapidly out from the impact point and reach the edge of the cymbal in about 60 μs , as seen in Fig. 1(a) and (b). Thus their phase speed is about 1700 m/s and their frequency is about 340 kHz, but they carry much less energy than the longer wavelengths which follow. These longer waves can be seen to reflect at the outer edge of the cymbal (at the right-hand side) and also at the central dome (near the left-hand side) in Fig. 1 (c and following). The reflected waves interfere with the incident waves [Fig. 1(d)–(f)], resulting in complex vibration patterns which eventually will give rise to normal modes of vibration.

In the phase maps in Fig. 1, optical fringes near the impact are very closely spaced and difficult to resolve. Also, discontinuities appear in the images when phase changes of more than $+\pi$ or less than $-\pi$ occur. To eliminate these, a phase unwrapping procedure can be applied (Cusak *et al.*, 1995). The three-dimensional amplitude map in Fig. 2 was obtained from Fig. 1(f) by using such unwrapping procedures.

To observe the scattering of waves by discontinuities, two masses of 6 grams and diameters of 12.8 mm each were attached to opposite sides of the cymbal 10 cm away from the impact point (directly below it in the field of view in Fig. 3). Waves were scattered from the masses, as shown in Fig. 3(a)–(c), which can be compared to the same time intervals in Fig. 1(c)–(e). The position of the masses is marked in Fig. 3(a)–(c).

Figure 4(a) and (b) shows interferograms reconstructed

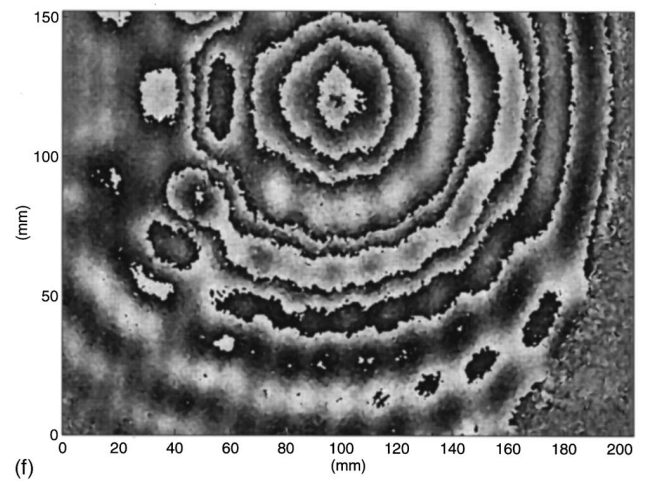
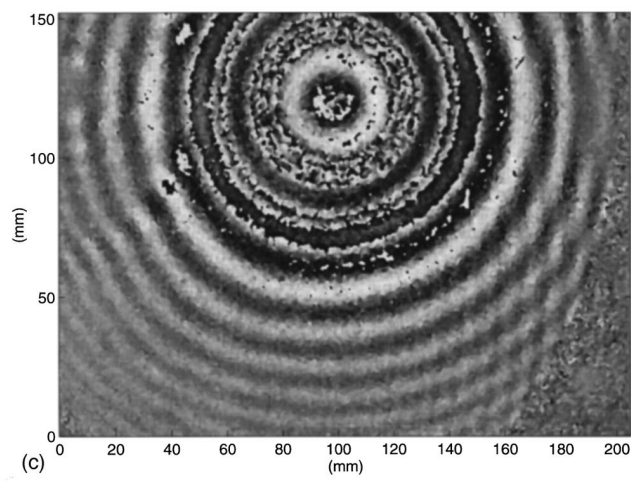
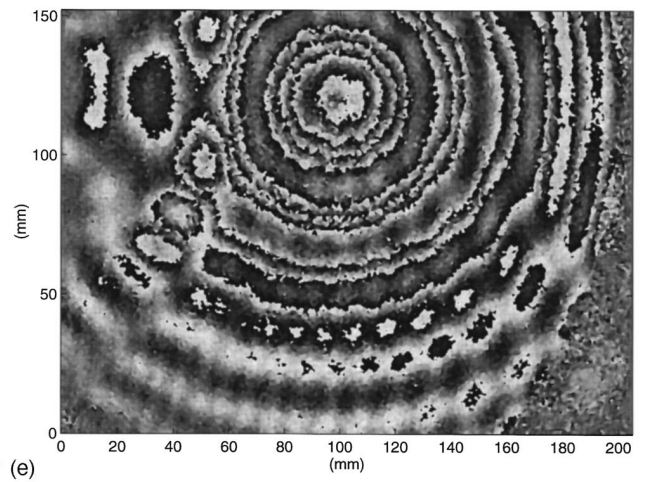
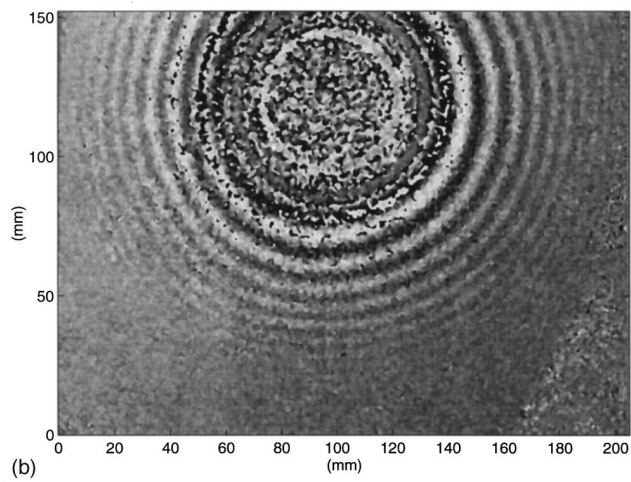
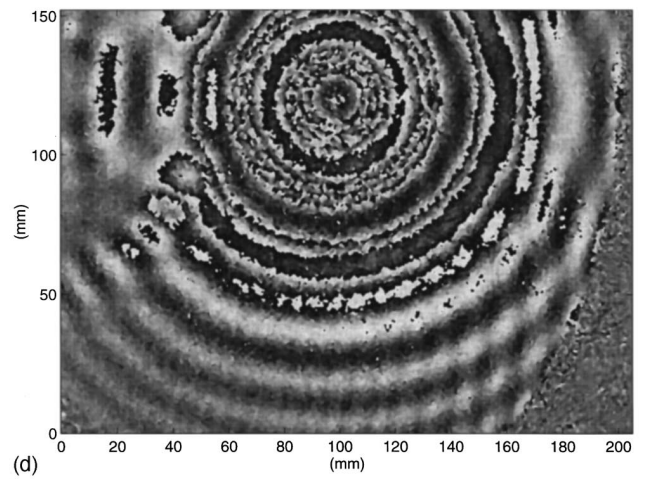
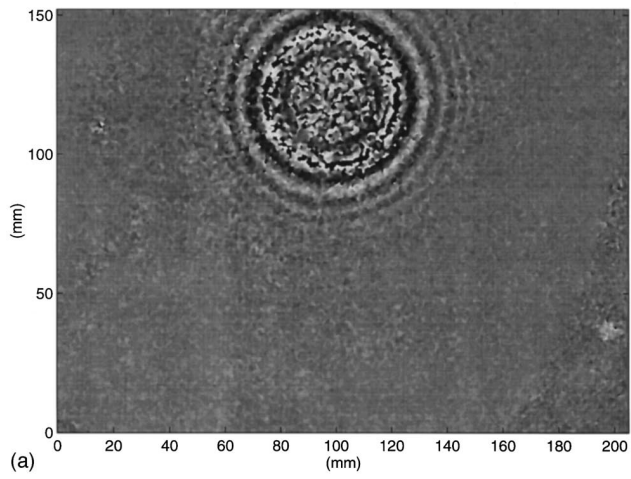


FIG. 1. Phase maps showing wave propagation outward from a point 10 cm from the edge of a 41-cm-diameter Zildjian cymbal. Time after impact: (a) 30 μ s; (b) 60 μ s; (c) 120 μ s; (d) 180 μ s; (e) 240 μ s; (f) 300 μ s.

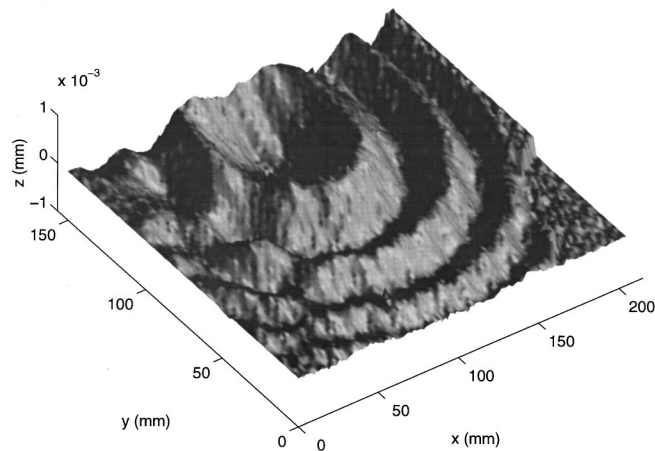


FIG. 2. Three-dimensional amplitude map derived from Fig. 1(f) by phase unwrapping.

from holographic film recordings, when the impulse is applied about a millimeter from the edge of the cymbal. Less wave reflection now occurs at the edge of the cymbal, and significant wave interference does not occur until the waves scatter off the central dome. Thus the normal modes do not develop until later. High-frequency waves are apparent along the edge, with enlarged amplitudes compared to the waves propagating toward the center of the cymbal.

II. DISCUSSION OF THE RESULTS

Percussionists strike cymbals in many different ways. Two commonly used strike points are at the edge of the cymbal and about half a radius away from the center, so these are the points at which the impulses were applied in these experiments. Impacting the cymbal with the laser beam provides a very short impulse, but is not convenient to vary the amplitude over a wide range.

Understanding the initial transient in cymbal sound is important for the cymbal maker, the player, and for composers of electronic music who wish to synthesize cymbal sounds electronically. The onset of cymbal sound is thought to be strongly influenced by wave reflections at the edge, at the central dome or cup, and by the shallow concentric grooves and indentations on the surface.

Wave reflections at the central dome are quite apparent in many of the interferograms, as are reflections at the edge. The waves of very short wavelength (having ultrasonic frequencies) do not appear to be reflected nearly so much as the waves with longer wavelength that arrive later. The two masses attached to the cymbal produce a substantial diffraction effect, giving a decrease in amplitude behind the masses. This effect is more pronounced for longer times when waves of larger amplitudes have reached the masses. (These masses are much larger in size than the grooves on the surface.)

III. CONCLUSIONS

Double-pulsed TV holography provides a convenient and accurate method for studying the initial transient behavior of percussion musical instruments, such as a cymbal. The newly developed electronic system is particularly convenient

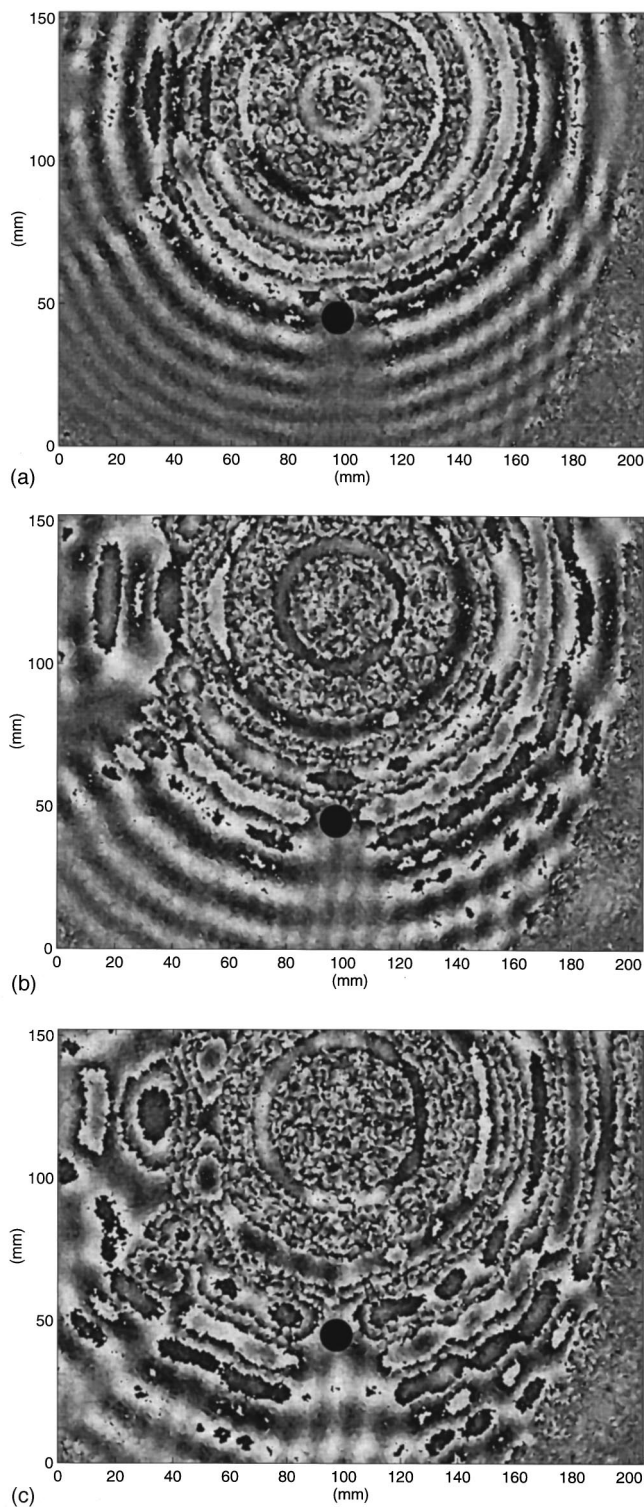


FIG. 3. Phase maps showing wave propagation, as in Fig. 1, but with a pair of 6-gram masses added 10 cm from the impact point (directly below it as seen in these phase maps). Time after impact: (a) 120 μ s; (b) 180 μ s; (c) 240 μ s.

and rapid, and it allow quantitative evaluation of the interferograms. Bending waves of steadily increasing wavelength propagate outward from the point of impact, reflect at edges and discontinuities, and eventually lead to standing wave patterns that form the normal modes of vibration.

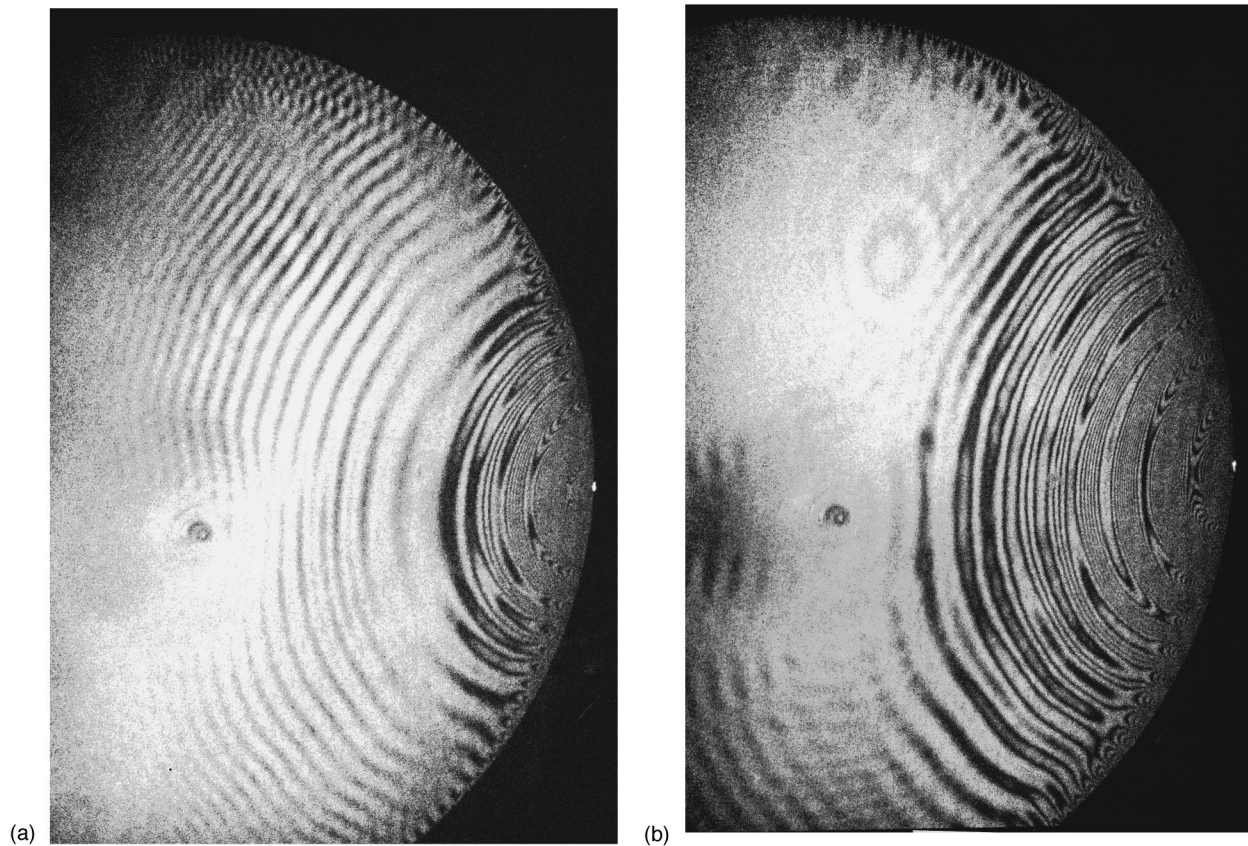


FIG. 4. Interferograms showing wave propagation from an impulse point about 1 mm from the edge of the cymbal. Time after impact: (a) 180 μ s; (b) 300 μ s.

ACKNOWLEDGMENTS

The authors thank Anders Wåhlin for his help in the experiments and also Nils-Erik Molin and Henrik Saldner for valuable comments and discussions.

Cusak, R., Huntley, J. M., and Goldrein, H. T. (1995). "Improved noise-immune phase-unwrapping algorithm." *Appl. Opt.* **34**, 781–789.

Fällström, K.-E., Molin, N.-E., Olofsson, K., Schedin, S., and Wåhlin, A.

(1996). "Mechanical and thermal effects in a steel plate impacted by a focused laser pulse." *Nondestruct. Test. Eval.* **13**, 293–307.

Fletcher, N. H. (1993). "Nonlinear dynamics and chaos in musical instruments," in *Complex Systems: from Biology to Computation*, edited by D. G. Green and T. Bossomaier (IOS, Amsterdam).

Rossing, T. D., and Shepherd, R. B. (1983). "Acoustics of cymbals," *Proc. 11th Intl. Congress on Acoustics (Paris)*, 329–333.

Schedin, S., and Gren, P. (1996). "Phase evaluation and speckle averaging in pulsed TV holography" (submitted for publication).

Erratum: “The perceptual relevance of locus equations” [J. Acoust. Soc. Am. 102, 2997–3008 (1997)]

David Fruchter and Harvey M. Sussman

Department of Linguistics, University of Texas, Austin, Texas 78712

(Received 19 November; accepted for publication 19 November 1997)

[S0001-4966(98)05802-0]

PACS numbers: 43.71.Es, 43.10.Vx [DWM]

Due to an electronics problem, which was not detected, some of the pages of the above-cited article were published with missing elements.

Pages 2999, 3006, and 3007 are republished here in their correct form.

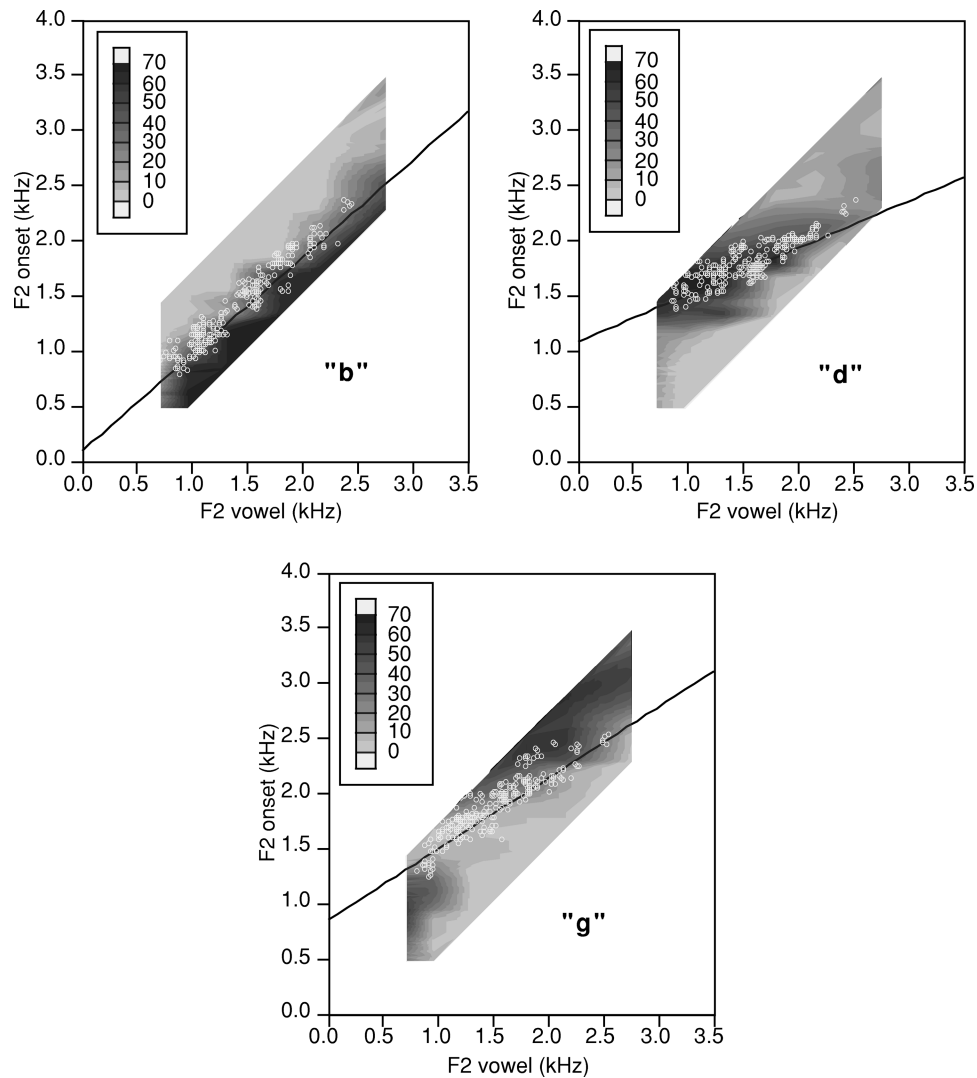


FIG. 1. Identification surfaces for “b,d,g” across seven vowel contexts. Data (F_2 vowel, F_2 onset, identification frequencies) transformed from Liberman *et al.* (1954) and displayed in locus equation coordinate space. Overlaid acoustic data from production (white circles) based on data from five male speakers taken from Sussman *et al.* (1991).

vowel target frequencies (essentially an F_2 -prime vowel) cannot be expected to exactly match F_2 vowels from our speakers (Bladon and Lindblom, 1981), the correspondence between perception results and acoustic data are quite reasonable. The labial consonant identifications closely parallel the acoustic data. The “d” identifications also agree reasonably well with the superimposed locus equation data. The “g” results are noticeably weaker as areas of “g” perception predominate at F_2 onsets >2250 Hz, and little acoustic F_2 onset data falls in this region. Conversion of the Sussman *et al.* acoustic data to F_2 prime values would increase the degree of correspondence to the Liberman *et al.* perceptual data in the upper-right quadrant of these figures, i.e., for /g/ in front vowel contexts.

A more recent perceptual test of locus equation parameters, F_2 onset and F_2 vowel, as cues for stop consonant place perception was performed by Eek and Meister (1995). Using Estonian CVV syllables beginning with voiceless unaspirated stops /p,t,k/ followed by nine long vowels, tokens from one speaker were used as stimuli for identification by 13 listeners. The F_2 onsets “without noise components of

the transitional part of the burst” were varied and presented to listeners for identification. In agreement with the Liberman *et al.* (1954) study, all rising F_2 transitions were heard as “p,” while falling transitions were heard as “t” in back vowel contexts and “k” in front vowel contexts. Missing from the identification responses were alveolar “t” in front vowel contexts and velar “k” in back vowel contexts. The authors concluded that the best perceptual performance (75%–100%) resulted when the strongest peak of the burst was combined with a measure of F_2 vowel-prime (rather than the F_2 onset– F_2 vowel parameters).

The research to be reported below was an attempt to replicate the results of Liberman *et al.* (1954), employing more realistic five-formant stimuli and an expanded vowel space. Also, advantage was taken of the presence of the F_3 by independently manipulating it (three levels of F_3 are employed—one level appropriate for [b], one for [d], and one for [g]). Correspondence of burstless CV stimulus identifications to acoustic locus equation data was evaluated to test the perceptual relevance of locus equation acoustic variables to stop place perception.

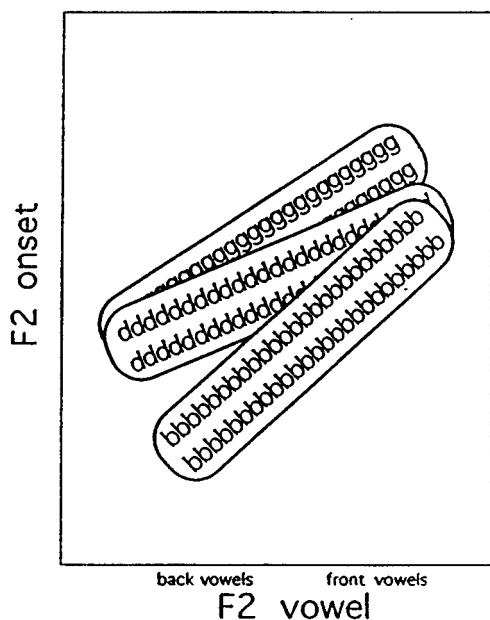


FIG. 6. Schematic of the perceptual dominance hierarchy hypothesis showing $b > d$ in front vowel contexts and $d > g$ in back vowel contexts and two regions of no competition—[b] in back vowel contexts and [g] in front vowel contexts.

bursts versus formant transitions for /b,d,g/ recognition was assayed. Referring, for example, to Dorman *et al.*'s Figure 4, it can be seen that the burst carries significant cue value for /d/ recognition in some front vowel contexts, but not back vowel contexts. Conversely, the burst is most valuable for /g/ recognition in back vowel contexts. Combining these observations with the patterns described by the dominance hierarchy hypothesis, one could simply conclude that the burst carries most weight in those situations in which the $F2$ vocalic transitional cue is not really distinctive—“b” versus “d” in front vowel contexts and “d” versus “g” in back vowel contexts—cueing the alternative disfavored in the dominance hierarchy.

The dominance hierarchy hypothesis should be viewed as relative to stimulus properties, particularly the burstlessness of the current stimuli. The hypothesis describes the pattern of consonant identifications prevailing in nondistinctive $F2$ onset– $F2$ vowel situations when the decisive burst cue is a null. Apparently, in such cases, the stop place with the less prominent burst in natural speech prevails. Probably, if the burst is not null, it can override the default identifications described by the dominance hierarchy. Referring again to Fig. 6, a reversal of dominance relations could be envisioned as switching the position of the clouds, now the “d” cloud obscuring “b” rather than “b” obscuring “d,” for example. The dominance relation based on $F2$ onset– $F2$ vowel is $b > d$ in front vowel contexts, but appropriate burst information should be able to override this, favoring $d > b$, and likewise, the dominance relation based on $F2$ onset– $F2$ vowel is $d > g$ in back vowel contexts, but appropriate burst information should be able to override this, favoring $g > d$ (cf. Walley and Carrell, 1983). Varying VOT or further manipulating $F3$ transition parameters might also produce dominance instabilities or reversals.

Actually, for the [b]–[d] overlap region of front vowel space, the reversal of dominance relations has already been observed. Although the subject-pooled data shows “b” dominating over “d,” at least two of the subjects clearly show the reverse relation, $d > b$. Despite this between-subject variability, the authors are encouraged to suppose that $b > d$ is the prevailing dominance pattern at the group level because group data from the current experiment, Liberman *et al.* (1954), and Eek and Meister (1995) all show a dominance of “b” over “d” perception in front vowel space.

The between-subject variation noted above is one indication that the dominance of “b” over “d” in front vowel space is not as robust as the dominance of “d” over “g” perception observed in back vowel space (the latter dominance relationship showed no between-subject variation). The comparative instability of the $b > d$ relation can also be discerned in the statistical comparisons to be discussed in the next section.

B. Chi square analysis

Significant differences between expected frequencies based on the local densities of acoustic tokens and the observed identification frequencies were found in the areas of overlap between stop consonants (Table IV). This result reinforces the conclusions previously discussed, namely that there is a dominance hierarchy in effect for the stimuli of these experiments, such that one consonant is perceived in preference to another one overlapping it in locus equation acoustic space. In contrast, regions with no overlap among stops show either exact or fairly close agreement between the expected and observed identification frequencies, although this was not always amenable to statistical test due to there sometimes being no degrees of freedom. Inspection of Table IV also indicates that the most consistent dominance effect (i.e., divergence of observed from expected frequencies) is in back vowel space in the region of [d] and [g] overlap (where $d > g$), while the dominance of $b > d$ perception in front vowel space is considerably weaker, indeed at several points absent (the nonsignificant values).

One unanticipated insight afforded by the chi square analysis concerns an apparent contrast in the mode of dominance in the back vowel region versus the front vowel region. The pattern in back vowel space at higher levels of $F2$ onset is very commonly that “d” perceptions are more frequent than would be expected on the basis of the local density of [d] tokens, and there are as well a significant number of [d] tokens in the region, leading to a very strong dominance of “d” perception overall. A somewhat different pattern often occurs among the front vowels at lower levels of $F2$ onset. Here again “d” perceptions are often more frequent than would be expected on the basis of the local density of [d] tokens, i.e., they carry relative perceptual weight, but there are comparatively few [d] tokens in the area and an overwhelming number of [b] tokens. Thus, the somewhat weak and unstable dominance of “b” perception over “d” perception in the front vowel region might be viewed as due in part to an opposing interaction between the greater perceptual weight of [d] tokens and the far greater density of [b] tokens, while the comparatively strong, stable dominance of

“d” perception over “g” perception in the back vowel region could be ascribed to the perceptual weight of [d] reinforced by its considerable density in that region.

C. Conclusion

In summary, there is ample evidence that $F2$ onset and $F2$ vowel, in combination, are significant cues for the perception of stop consonant place of articulation. These components of the speech signal are likely to be mapped together and extracted as a feature, which we have termed the vowel-normalized $F2$ transition, during speech perception. Of course, the $F2$ transition has long been considered an important cue for stop consonant place, but we are now considering a particular parametrization/coding of the $F2$ transition: in terms of its endpoints. The form of the postulated feature-extracting map could be a topographic representation of locus equation acoustic space ($F2$ vowel \times $F2$ onset).

A coherent pattern of integration of the $F2$ transition with two other sets of cues, the burst and $F3$, can be noted. In the previous discussion of the pattern of tradeoffs between $F2$ transition cues and burst cues, as described by Dorman *et al.* (1977), it was concluded that the burst carries most weight in those situations in which the $F2$ vocalic transitional cues are not really distinctive—“b” versus “d” in front vowel contexts and “d” versus “g” in back vowel contexts—cueing the alternative disfavored in the postulated dominance hierarchy. The pattern of $F3$ effects in this experiment, as was summarized in Table III, is somewhat parallel to this view of the pattern of burst effects. As with the burst, $F3$ carries most weight in those situations in which the $F2$ vocalic transitional cues are not really distinctive. There is a lack of $F3$ effects in those regions in which there is a lack of overlap between the different stop places of articulation (back vowel [b] and front vowel [g]), while there are tradeoff effects between the overlapping stops in the region of their overlap ([d] and [g] in back vowel space, [b] and [d] in front vowel space). These tradeoffs are in the natural directions, with g-like $F3$ elevating “g” versus “d” identifications, and b-like $F3$ elevating “b” versus “d” identifications. Thus, it seems that one key to understanding the patterns of both burst and $F3$ effects on stop place perception is to view them in relation to the pattern of locus equation data. The way in which burst perceptual weight and $F3$ perceptual weight both correlate with the overlap versus distinctiveness of locus equation acoustic data argues strongly for a locus equation interpretation of $F2$ transitional cues.

As a closing note it is interesting that computational studies exploring properties of time-delayed neural networks also provide indirect support for $F2$ onset– $F2$ vowel playing an important role in stop place perception. When neural networks are fed sampled consonant–vowel waveforms from natural speech and instructed to classify phonetic categories by place of articulation the most effective cues for this task were reported to be $F2$ onset and $F2$ vowel frequencies (Waibel *et al.*, 1989).

ACKNOWLEDGMENTS

This research was supported by Grant No. R01 DC2014, National Institute on Deafness and Other Communication Disorders, to the second author. Portions of this manuscript are based on the Ph.D. dissertation of the first author, presented to the University of Texas at Austin. We would also like to acknowledge the constructive editorial comments of Winifred Strange, Terry Nearey, and Diana Krull.

¹Values for the z axis (ID frequency) were derived by digitizing enlargements ($\times 5.26$) of the ID graphs from the left half of Fig. 3 in Liberman *et al.* (1954). The enlarged figures were divided into /b/ functions, /d/ functions, and /g/ functions and then separately scanned (120 dpi, 8 bit/pixel PICT files) and digitized. Estimated digitizing error was ± 1.5 , i.e., less than 2.5%.

²A complete chi square results table is available from the second author upon request.

- Bakran, J., and Mildner, V. (1995). “Effect of speech rate and coarticulation strategies on the locus equation determination,” in Proceedings of the XIIIth International Congress of Phonetic Sciences, Stockholm, Sweden, Vol. 1, pp. 26–29.
- Bladon, R. A. W., and Lindblom, B. (1981). “Modeling the judgment of vowel quality differences,” *J. Acoust. Soc. Am.* **69**, 1414–1422.
- Celdran, E. M., and Villalba, X. (1995). “Locus equations as a metric for place of articulation in automatic speech recognition,” in Proceedings of the XIIIth International Congress of Phonetic Sciences, Stockholm, Sweden, Vol. 1, pp. 30–33.
- Delattre, P. C., Liberman, A. M., and Cooper, F. S. (1955). “Acoustic loci and transitional cues for consonants,” *J. Acoust. Soc. Am.* **27**, 769–773.
- Dorman, M. F., Studdert-Kennedy, M., and Raphael, L. (1977). “Stop consonant recognition: Release bursts and formant transitions as functionally equivalent, context-dependent cues,” *Percept. Psychophys.* **22**, 109–122.
- Eek, A., and Meister, E. (1995). “The perception of stop consonants: Locus equations and spectral integration,” in Proceedings of the XIIIth International Congress of Phonetic Sciences, Stockholm, Sweden, Vol. 1, pp. 18–21.
- Fowler, C. A. (1994). “Invariants, specifiers, cues: An investigation of locus equations as information for place of articulation,” *Percept. Psychophys.* **55**, 597–610.
- Guilford, J. P., and Fruchter, B. (1978). *Fundamental Statistics in Psychology and Education* (McGraw-Hill, New York), 6th ed.
- Klatt, D. H. (1980). “Software for a cascade/parallel formant synthesizer,” *J. Acoust. Soc. Am.* **67**, 971–995.
- Klatt, D. H. (1987). “Review of text-to-speech conversion for English,” *J. Acoust. Soc. Am.* **82**, 737–793.
- Krull, D. (1988). “Acoustic properties as predictors of perceptual responses: A study of Swedish voiced stops,” *Phonetic Experimental Research at the Institute of Linguistics, University of Stockholm (PERILUS)*, Vol. VII, pp. 66–70.
- Krull, D. (1989). “Second formant locus patterns and consonant-vowel coarticulation in spontaneous speech,” *Phonetic Experimental Research at the Institute of Linguistics, University of Stockholm (PERILUS)*, Vol. X, pp. 87–108.
- Liberman, A. M., and Mattingly, I. (1985). “The motor theory of speech perception revised,” *Cognition* **21**, 1–36.
- Liberman, A. M., Cooper, F. S., Shankweiler, D. P., and Studdert-Kennedy, M. (1967). “Perception of the Speech Code,” *Psychol. Rev.* **74**, 431–461.
- Liberman, A. M., Delattre, P. C., Cooper, F. S., and Gerstman, L. J. (1954). “The role of consonant-vowel transitions in the perception of the stop and nasal consonants,” *Psychol. Mono.* **68**, 1–13.
- Lindblom, B. (1963). “On vowel reduction,” Report #29, The Royal Institute of Technology, Speech Transmission Laboratory, Stockholm, Sweden.
- Lindblom, B., Stark, J., and Sundberg, J. (1997). “From sound to vocal gesture: learning to (co)-articulate with APEX,” to appear in *FONETIK-97*, Phonum **4**, Umea Universitet, Sweden.
- MathWorks, Inc. (1992). *MATLAB Reference Guide*, Natick, MA.
- Nearey, T. M., and Shammass, S. E. (1987). “Formant transitions as partly distinctive invariant properties in the identification of voiced stops,” *Can. Acoust.* **15**, 17–24.

TECHNICAL NOTES AND RESEARCH BRIEFS

Paul B. Ostergaard

10 Glenwood Way, West Caldwell, New Jersey 07006

Editor's Note: Original contributions to the Technical Notes and Research Briefs section are always welcome. Manuscripts should be double-spaced, and ordinarily not longer than about 1500 words. There are no publication charges, and consequently, no free reprints; however, reprints may be purchased at the usual prices.

Transverse vibrations of circular, annular plates with a free inner boundary [43.40.Dx]

Daniel Vega, Sergio A. Vera, and Miguel D. Sánchez

Physics Department, Universidad Nacional del Sur, 8000-Bahia Blanca, Argentina

Patricio A. A. Laura

Institute of Applied Mechanics (CONICET) and Department of Engineering, Universidad Nacional del Sur, 8000-Bahia Blanca, Argentina

The lower natural frequencies of normal modes of transverse vibration of circular annular plates with a free inner edge while the outer boundary is either simply supported or clamped are determined. It is hoped that present results will be useful to mechanical designers since the eigenvalues already available in the technical literature are rather inaccurate in some instances. © 1998 Acoustical Society of America.

INTRODUCTION

As stated by Leissa and Narita:¹ “the free vibrations of circular plates have been of practical and academic interest for at least a century and a half.”

Even when dealing with classical plate theory one encounters a certain degree of mathematical and numerical difficulties since the analytical determination of natural frequencies requires the solution of transcendental functions, the eigenvalues being contained in the arguments of Bessel functions. In general, Poisson's ratio appears explicitly in the transcendental equations. The fact that even a fundamental case—the simply supported, solid circular plate—was very accurately solved in the early eighties¹ illustrates the difficulty of the situation and the lack of accurate results.

The situation is certainly more critical when one considers annular, circular plates, especially when one or both boundaries are free since the Kirchhoff–Kelvin conditions must be satisfied. A practical example will give a clear idea of the lack of accurate results.

It has been shown² that, in order to determine the fundamental frequency of vibration of annular transducer elements of nonuniform thickness and free inner boundary, one can approximate the displacement amplitude $W(r)$ by means of

$$W \approx W_\alpha = A_1(\alpha r^\gamma + \beta r^2 + 1), \quad (1)$$

where α , β are coefficients obtained by substituting (1) in the governing boundary conditions at the outer edge³ and γ is Rayleigh's optimization parameter.⁴

Substituting (1) in the energy functional, evaluating it between the inner and outer radii of the plate, and minimizing the functional with respect to A_1 one obtains the fundamental frequency coefficient $\Omega = \sqrt{\rho h/D} \omega_1 a^2$, where ρ is the density of the plate material, h is the thickness; D is the flexural rigidity, a is the outer radius, and ω_1 is the fundamental circular frequency.

Since

$$\Omega_1 = \Omega_1(\gamma) \quad (2)$$

by requiring

$$\frac{d\Omega_1}{d\gamma} = 0 \quad (3)$$

one obtains an optimized value of Ω_1 .

In general good engineering agreement was obtained with results available in the literature in the case of plates of uniform thickness⁵ but in

some cases the difference was rather large, i.e., when the plates is clamped at the outer edge one has⁵ for $b/a=0.8$ and $v=1/3$, $\Omega_1=85.32$ while the one-term approximation (1) coupled with the variational approach yields $\Omega_1=92.88$. On the other hand a two-term approximation gives $\Omega_1=92.86$.

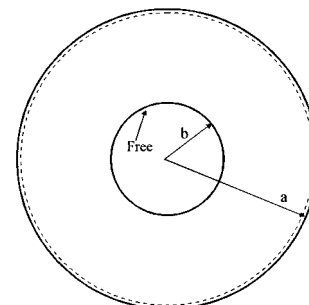
In other situations, using the optimized version of the Rayleigh–Ritz method previously described, one obtains eigenvalues slightly lower than the “exact” results quoted in Leissa's classical treatise.^{2,5} Clearly the approximate eigenvalues should constitute upper bounds with respect to the exact values.

In view of these discrepancies it was decided to calculate the lower eigenvalues using the exact solution and the very convenient Maple V computer system⁶ to generate the frequency coefficient and to obtain the lower eigenvalues.

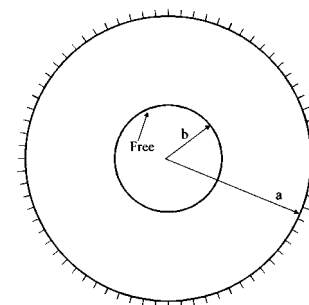
I. EXACT SOLUTION OF VIBRATING, CIRCULAR PLATES

The general solution of the classical plate vibrations problem is, in polar coordinates,⁵

$$W(r, \theta) = \sum_{n=0}^{\infty} [A_n J_n(kr) + B_n Y_n(kr) + C_n I_n(kr) + D_n K_n(kr)] \cos n\theta + \sum_{n=1}^{\infty} [A_n^* J_n(kr) + B_n^* Y_n(kr) + C_n^* I_n(kr) + D_n^* K_n(kr)] \sin n\theta, \quad (4)$$



(A): Simply Supported Outer Edge



(B): Clamped Outer Edge

FIG. 1. Vibrating structural systems under study.

TABLE I. Frequency coefficients $\Omega = \sqrt{\rho h/D} \omega a^2$ for circular annular plates simply supported at the outer edge and free at inside boundary for $\nu=0.3$ and $1/3$; $n=0, 1$, and 2 for several values of b/a .

$\nu=0.3$	b/a	0	0.1	0.2	0.3	0.4	0.5	0.6	0.7	0.8	0.9
$n=0$		4.9351	4.8532	4.7177	4.6640	4.7640	5.0768	5.7107	6.9309	9.5554	17.7087
$n=1$		13.8981	13.8720	13.5686	12.8159	12.0070	11.6073	11.9055	13.3109	17.0869	29.7688
$n=2$		25.6132	25.3944	24.8653	24.1159	23.1484	22.3565	22.4424	24.3292	30.2418	51.1797
$\nu=1/3$											
$n=0$		4.9838	4.8903	4.7327	4.6593	4.7437	5.0432	5.6630	6.8644	9.4550	17.5107
$n=1$		13.9397	13.9114	13.5831	12.7726	11.9066	11.4654	11.7282	13.0889	16.7814	29.2131
$n=2$		25.6525	25.4455	24.9352	24.1618	23.0978	22.1809	22.1517	23.9208	29.6532	50.0928

TABLE II. Frequency coefficients $\Omega = \sqrt{\rho h/D} \omega a^2$ for circular annular plates clamped at the outer edge and free at inside boundary for $\nu=0.3$ and $1/3$; $n=0, 1$, and 2 for several values of b/a .

$\nu=0.3$	b/a	0	0.1	0.2	0.3	0.4	0.5	0.6	0.7	0.8	0.9
$n=0$		10.2158	10.1592	10.4080	11.4237	13.6027	17.7145	25.6742	43.1422	93.0351	360.3503
$n=1$		21.2603	21.1945	20.5507	19.5403	19.5942	22.0145	28.7388	45.3322	94.6139	361.5023
$n=2$		34.8770	34.5353	33.7352	32.5939	31.5346	32.1155	36.8483	51.5852	99.2928	364.9555
$\nu=1/3$											
$n=0$		10.2158	10.1348	10.3470	11.3379	13.5004	17.5979	25.5402	42.9800	92.8154	352.9534
$n=1$		21.2603	21.1893	20.4919	19.3923	19.3892	21.7852	28.4987	45.0776	94.3167	361.0416
$n=2$		34.8770	34.5541	33.7731	32.5593	31.3383	31.7757	36.4202	51.1106	98.7809	364.3064

where $k^2 = \sqrt{\rho h/D} \omega$. In order to determine the natural frequencies, it suffices to consider either the $(\cos n\theta)$ or the $(\sin n\theta)$ component of (4).

The boundary conditions at $r=a$ are (Fig. 1):

simply supported edge:

$$M_r(a, \theta) = -D \left[\frac{\partial^2 W}{\partial r^2} + \nu \left(\frac{1}{r} \frac{\partial W}{\partial r} + \frac{1}{r^2} \frac{\partial^2 W}{\partial \theta^2} \right) \right]_{r=a} = 0; \quad (5)$$

clamped edge:

$$W(a, \theta) = \frac{\partial W}{\partial r}(a, \theta) = 0.$$

On the other hand, the boundary conditions at $r=b$ are⁵

$$M_r(b, \theta) = -D \left[\frac{\partial^2 W}{\partial r^2} + \frac{\mu}{r} \left(\frac{\partial W}{\partial r} + \frac{1}{r^2} \frac{\partial^2 W}{\partial \theta^2} \right) \right]_{r=b} = 0, \quad (6)$$

$$V_r(b, \theta) = Q_r + \frac{1}{r} \frac{\partial M_{r\theta}}{\partial \theta} \Big|_{r=b} = -D \left[\frac{\partial}{\partial r} \nabla^2 W + \frac{1}{r} (1-\nu) \frac{1}{r} \frac{\partial}{\partial \theta} \left(\frac{1}{r} \frac{\partial W}{\partial \theta} \right) \right]_{r=b} = 0.$$

II. NUMERICAL RESULTS

Substituting $W(r, \theta)$ in the governing boundary conditions and implementing the resulting determinantal equation one obtains implementing the algorithmic procedure in the Maple V system,⁶ the desired eigenvalues $\Omega_{ns} = \sqrt{\rho h/D} \omega_{ns} a^2$ as a function of b/a . The subscript “ n ” denotes the number of nodal diameters while “ s ” denotes the number of nodal circles.

Table I depicts the values of Ω_{n0} for the case where the plate is simply supported at the outer boundary, for $\mu=0.3$ and $1/3$ while Table II contains values of Ω_{n0} when the plate is clamped at $r=a$, for the same values of Poisson’s ratio.

For the clamped, outer boundary situation and $b/a=0.8$ one obtains, from Table II, $\Omega_{00}=92.8154$ for $\nu=1/3$ which is in very good agreement

with the eigenvalue determined by means of the optimized Rayleigh–Ritz method, previously quoted (92.88 and 92.86).

When the outer boundary is simply supported, one has for $b/a=0.9$ and $\nu=1/3$, $\Omega_{00}=17.5107$ while the approximate, variational approach⁷ yields 17.51. The eigenvalue available in the literature⁵ is 17.81.

The agreement between the results presented in Tables I and II and those determined by Avalos *et al.*² is remarkably good for $b/a \geq 0.3$. Apparently numerical instabilities arise for smaller values of b/a when applying the optimized Rayleigh–Ritz method coupled with polynomial approximations.²

ACKNOWLEDGMENTS

The present study was sponsored by Secretaría General de Ciencia y Tecnología of Universidad Nacional del Sur (Physics and Engineering Departments) and by Comisión de Investigaciones Científicas (Buenos Aires Province).

¹A. W. Leissa and Y. Narita, “Natural frequencies of simply supported circular plates,” *J. Sound Vib.* **70**, 221–229 (1980).

²D. R. Avalos, H. A. Larrondo, V. Sonzogni, and P. A. A. Laura, “A general approximate solution of the problem of free vibrations of annular plates of stepped thickness,” *J. Sound Vib.* **196**, 275–283 (1996).

³P. A. A. Laura, J. C. Paloto, and R. D. Santos, “A note on the vibration and stability of a circular plate elastically restrained against rotation,” *J. Sound Vib.* **41**, 177–180 (1975).

⁴P. A. A. Laura, “Optimization of variational methods,” *Ocean Eng.* **22**, 235–250 (1995).

⁵A. W. Leissa, “Vibration of Plates,” NASA SP160, 1969.

⁶B. W. Char, K. O. Geddes, G. H. Gonnet, B. L. Leong, M. B. Monagan, and S. M. Watt, *Maple V. Library Reference Manual* (Springer–Verlag, Berlin, 1991).

⁷P. A. A. Laura, S. A. Vera, D. A. Vega, and M. D. Sánchez, “An approximate method for analyzing vibrating simply supported circular plates of rectangular orthotropy,” Institute of Applied Mechanics, CONICET, Bahía Blanca, Argentina, Publication No. 97-34, 1997.

Advanced-degree dissertations in acoustics

Editor's note: Abstracts of Donor and Master's theses will be welcomed at all times. Please note that they must be double spaced, limited to 200 words of text, must include the appropriate PACS classification numbers, and formatted as shown below (don't make the editor retype them, please!). The address for obtaining a copy of the thesis is helpful. Please submit two copies.

Loudness in relation to the autocorrelation function of sound signals in a room [43.55.Hy, 43.66.Cb]—I. Gde Nyoman Merthayasa, *Graduate School of Science and Technology, Kobe University, Kobe, Japan, March 1996 (Ph.D.)*. The loudness is described in relation to the effective duration of the autocorrelation function (ACF) of sound signals. The main results are as follows: (1) The effective duration, τ_e (defined as the ten percentile delay), of ACF of the sound signals in a room is deeply related to the temporal structure of the reflections and the subsequent reverberation time. (2) The loudness in terms of the scale value for a bandpass noise signal with longer τ_e is higher than that of the signal with a shorter τ_e . (3) When a sharp filter with more than 1000 dB/oct is used in producing bandpass noise, then loudness within the "critical band" is not constant in contradiction with the previous theory. (4) The loudness of sound is increased with increasing reverberation time. (5) The loudness is independent of the magnitude of the interaural crosscorrelation (IACC).

Thesis advisor: Yoichi Ando.

Copies of this thesis may be obtained from I Gde Nyoman Merthayasa, Dept. of Engineering Physics, FTI, Institute of Technology Bandung, Jalan Ganesha No. 10, Bandung 40132, Indonesia.

Effects of fluctuation in sound transmission on objective sound fields and subjective evaluations [43.55.Br, 43.55.Hy]—Yasutaka Ueda, *Graduate School of Science and Technology, Kobe University, Kobe, Japan, September 1997 (Ph.D.)*. This study is focused on sound-pressure-level (SPL) fluctuation that was caused by air conditioning in the gymnasium and the relationship between this fluctuation and subjective evaluation. From the results of physical examinations, it is found that significant fluctuations in SPL are observed on sound transmission at high frequencies. The cumulative distribution of the mean-squared amplitude, which was measured in the gymnasium, fits the Nakagami-Rise distribution. The distribution of mean-squared amplitude simulated by the upper impulse response model also fits the Nakagami-Rise distribution. It is confirmed that the mechanism of the fluctuation can be represented by the impulse response in

which the delay time of reflection sound varies with time. From the results of psychological experiments, it is found that sound fluctuation contributes to increase the subjective preference in the case of fast-tempo music which has a short effective duration of autocorrelation function (ACF), τ_e . For such a sound stimulus with $\tau_e=43$ ms, it is found that the most preferred sound field can be obtained when the modulation interval is about 13.0 ms. Other findings are summarized.

Theses advisor: Yoichi Ando.

Copies of this thesis can be obtained from Yasutaka Ueda, Technical Research Institute of Hazama Corp., 515-1 Nishimukai-Karima, Tsukuba City, Ibaraki, 305 Japan.

Analyses of cortical continuous brain waves in relation to subjective preference of physical environments [43.64.Qh, 43.55.Hy]—Chiung Yao Chen, *Graduate School of Science and Technology, Kobe University, Kobe, Japan, September 1997 (Ph.D.)*. The aim of this study is to give an integrative approach to a relationship between the subjective preference and the effective duration (τ_e) of the autocorrelation function (ACF) in the α -wave range of cortical continuous brain waves (CBW) with respect to the simulated changings of the temporal factors for sound fields and a visual field. Typical findings are as follows: (1) The τ_e values of the ACF α -wave range of CBW are prolonged as the scale values of subjective preference increased in each physical factor changed for the sound fields. (2) Cerebral asymmetries lead to a theory of lateral domination of the human brain on specialized physical informations of the sound fields. There are four independent factors which process the temporal and spatial characteristics of sound field. And it is found that the τ_e values of the ACF α -wave range of CBW are significantly prolonged in the left hemisphere in the case where the temporal factors varied (initial time delay of single reflection Δt_1 ; subsequent reverberation time T_{sub}), and in the right hemisphere in the case of the spatial factor (ACC). (3) According to individual difference, the ratios of the τ_e values of the ACF α -wave range of CBW correlate well with the differences of subjective preference in the left hemisphere. (4) Finally, they are successfully applied to basic temporal cognitions, for visual tempo as well as auditory tempo. (5) The τ_e value of the ACF α -wave range of CBW is confirmed as an efficient- and consistent-objective parameter to observe the subjective preference of both auditory and visual perceptions.

Thesis advisor: Yoichi Ando.

Copies of this thesis may be obtained from Chiung Yao Chen, Room 510, Graduate School of Science and Technology, Kobe University, Kobe, Japan.